BSPE19200-100-12

얼음화학 특성연구를 통한 극지방 자연현상 규명 및 응용기술 개발

Investigation of ice chemistry for understanding of environmental processes in polar region and its applications

KOPRI
극지연구소

2020. 2. 28.

한 국 해 양 과 학 기 술 원
부 설 극 지 연 구 소

제 출 문

극지연구소장 귀하

본 보고서를 “얼음화학 특성연구를 통한 극지방 자연현상 규명 및 응용기술 개발” 과제의 최종보고서로 제출합니다.

2020. 2. 28.

연 구 책 임 자 : 김 기 태

참 여 연 구 원 : 이 민 경, 박 기 홍, 김 대 영, 강 정 호, 한 영 철, 박 지 연, 문 홍 수, 허 순 도, 유 규 철, 이 재 일, 김 성 한, 홍 상 범, 황 희 진, 이 강 현, 박 기 태, 윤 영 준, 박 창 근, 이 두 형, 이 윤 학, 한 태 욱, 김 준 태, 이 유 수, 이미리내, 정 현 영, 김 봄 이, 주 진 중, Nguyen Quoc Anh, 김 효 진, 이 승 준, 정 혜 진, 이 승 미, 최 정 옥, 김 연 태. 장 은 호, 안 서 희, 김 지 훈, 안 인 혜

위탁연구기관명(책임자) : 경 북 대(최 철 호), 포 스 텍(최 원 용), 서 울 대(허 영 숙), 포 스 텍(박 문 정), 한 림 대(김 정 원), 서 울 대(강 헌), 강 원 대(이 진 용)

KOPRI 극지연구소

보고서 초록

<table>
<tr><td>과제관리번호</td><td>PE19200</td><td>해당단계
연구기간</td><td>2018.1.1.-2019.12.31.</td><td>단계 구분</td><td>1단계 / 3단계</td></tr>
<tr><td rowspan="2"><u>연구사업명</u></td><td>중 사 업 명</td><td colspan="4">기관고유사업</td></tr>
<tr><td>세부사업명</td><td colspan="4">얼음화학 특성연구를 통한 극지방 자연현상 규명 및 응용기술 개발</td></tr>
<tr><td rowspan="2">연구과제명</td><td>중 과 제 명</td><td colspan="4"></td></tr>
<tr><td>세부(단위)과제명</td><td colspan="4"></td></tr>
<tr><td>연구책임자</td><td>김기태</td><td>해당단계
참여연구원수</td><td>총 : 72 명
내부 : 37 명
외부 : 35 명</td><td>해당단계
연구비</td><td>정부: 4,440,000 천원
기업: 천원
계: 4,440,000 천원</td></tr>
<tr><td>연구기관명 및
소속부서명</td><td colspan="2">한국해양과학기술원 부설 극지연구소 (실용화 연구 사업단)</td><td colspan="2">참여기업명</td><td></td></tr>
<tr><td>국제공동연구</td><td colspan="5">상대국명 : 스페인, 일본, 체코, 스위스, 미국, 뉴질랜드, 이탈리아
상대국연구기관명 : CSIC, 교토대, Masaryk 대학, PSI, 칼텍, UC 어바인, 미시간대, MIT, 오타고대, CNR</td></tr>
<tr><td>위 탁 연 구</td><td colspan="5">연구기관명 : 경북대, 포스텍, 서울대, 한림대, 강원대
연구책임자 : 최철호, 최원용, 허영숙, 박문정, 김정원, 강 헌, 이진용</td></tr>
<tr><td colspan="4">요약(연구결과를 중심으로 개조식 500자이내)</td><td>보고서
면수</td><td>600</td></tr>
<tr><td colspan="6">・얼음화학 연구 인프라 구축 및 기초연구수행
- 얼음화학 연구를 위한 저온실험 및 분석장비 구축
- 얼음표면화학 모델 개발 및 이를 활용한 얼음표면 반응 연구 수행
- 극지방 빙하형성 과정을 모사한 저온고압챔버 초기모델 제작 및 기초데이타 획득
・얼음화학에 기초한 극지방 자연현상의 이해
- 얼음 광화학/지화학 반응 연구 위한 극지환경 모사시스템 구축
- 극지방 구름형성과 관련된 할로겐물질 생성기작 규명
- 극지방 산화물 용출기작에 있어서 얼음의 역할 규명
- 극지방 얼음 매질 내 환경오염물질의 화학반응 특이성 규명
・얼음화학기반 응용기술 탐색 및 기반연구
- 얼음 표면 특성을 활용한 고성능 2차원 전도성 고분자 합성
- 동결 농축 현상을 활용한 오염물질 정화 기술 개발 및 지식재산권 확보</td></tr>
<tr><td rowspan="2">색 인 어
(각 5개 이상)</td><td>한 글</td><td colspan="4">얼음, 화학반응, 할로겐, 화학적 풍화, 동결정화</td></tr>
<tr><td>영 어</td><td colspan="4">ice, chemical reaction, halogen, chemical weathering, freezing purification</td></tr>
</table>

KOPRI 극지연구소

요 약 문

Ⅰ. 제 목

얼음화학 특성연구를 통한 극지방 자연현상 규명 및 응용기술 개발

Ⅱ. 연구개발의 목적 및 필요성

극지방을 포함한 지구 환경에서 얼음이 차지하는 큰 비중에도 불구하고, 지금까지 얼음에 관한 연구는 물에 비해 상대적으로 연구의 수준은 미흡하였다. 그 중에서도 얼음에서 일어나는 화학 반응의 분자 수준 특성 연구는 얼음의 거시적 거동 연구에 비해 소수의 연구만이 진행되었다. 따라서 본 연구과제에서는 얼음에서 일어나는 화학반응의 특이성을 규명하고, 얼음화학반응이 자연현상에 미치는 영향을 연구하며, 얼음의 특성을 활용한 실용화 기술을 개발하는 것을 목적으로 하였다.

Ⅲ. 연구개발의 내용 및 범위

- 기존에 밝혀지지 않았던 얼음의 화학적 특성 규명
- 얼음화학반응에 기초한 극지방 환경변화 요인 규명
- 얼음화학반응의 특이성 기반 응용기술 개발

Ⅳ. 연구개발결과

- 얼음화학 연구 인프라 구축 및 기초연구수행
  - 얼음화학 연구를 위한 저온실험 및 분석장비 구축
  - 얼음표면화학 모델 개발 및 이를 활용한 얼음표면 반응 연구 수행
  - 극지방 빙하형성 과정을 모사한 저온고압챔버 초기모델 제작 및 기초데이타 획득

- 얼음화학에 기초한 극지방 자연현상의 이해
  - 얼음 광화학/지화학 반응 연구 위한 극지환경 모사시스템 구축
  - 극지방 구름형성과 관련된 할로겐물질 생성기작 규명
  - 극지방 산화물 용출기작에 있어서 얼음의 역할 규명
  - 극지방 얼음 매질 내 환경오염물질의 화학반응 특이성 규명

KOPRI 극지연구소

· 얼음화학기반 응용기술 탐색 및 기반연구

- 얼음 표면 특성을 활용한 고성능 2차원 전도성 고분자 합성
- 동결 농축 현상을 활용한 오염물질 정화 기술 개발 및 지식재산권 확보

Ⅴ. 연구개발결과의 활용계획

연구 과제를 통하여 구축한 인프라와 연구 네트워크를 활용하여 얼음의 화학적 특성 연구 뿐 아니라 물리적 성질 및 얼음의 생명활동에서의 역할 규명으로 확장하고, 얼음 특성을 이용한 친환경 수처리 기술 및 신소재 합성 기술을 개발하여 실용화하는 것을 목표로 한 후속 연구과제를 추진한다.

연구 결과는 얼음화학이라는 학문적 미개척 분야를 선도하고 극지방 자연현상 해석에 있어 얼음화학의 새로운 역할 규명에 활용하고, 얼음화학과 기후변화와의 상관관계를 이해함으로써 향후 해빙으로 인한 기후영향 예측과 기후변화모델 개발 및 정확도 향상에 기여할 것이다. 또한 얼음에서 일어나는 특이한 화학반응에 대한 기초연구결과를 교육 자료로 활용할 수 있을 것이며, 기후 변화 대응 정책 마련을 위해 필요한 얼음화학 기초 지식을 제공할 수 있을 것이다.

KOPRI
극지연구소

S U M M A R Y

(영 문 요 약 문)

I. Title

Investigation of ice chemistry for understanding of environmental processes in polar region and its applications

II. Purpose and Necessity of R&D

Despite the importance of ice in the global environment including the polar regions, ice has less attracted researchers' attention than water, and ice research mainly focuses on macroscopic behaviors of ice. Thus, in this research project, we aimed the understanding the intrinsic properties of chemical reaction in ice and the earth/polar environmental systems and finding application technologies based on ice chemistry

KOPRI 극지연구소

III. Contents and Extent of R&D

- To verify previously unknown chemical properties of ice
- To understand the polar environmental system based on ice chemistry
- To develop applications for ice chemistry

IV. R&D Results

- Construction of ice research infrastructure and fundamental studies
  - Construction of low-temperature equipment and analysis instruments for ice chemistry research
  - Development of ice surface molecular model and ice surface reaction studies using the model
  - Production of a low-temperature, high-pressure chamber for modeling polar glacier formation and acquisition of initial data

· Understanding of natural phenomena in polar regions based on ice chemistry
  - Construction of polar environment simulation system for ice photochemistry/geochemistry studies
  - Investigation of halogen formation related to cloud formation in polar regions
  - Investigation of roles of ice in the dissolution of oxide species in polar regions
  - Investigation of properties of chemical reactions of pollutants in polar ices

· Development of applications based on ice chemistry
  - Development of high-performance, two-dimensional conductive polymers using the properties of ice surfaces
  - Development of purification technologies using the freeze concentration effect and securing intellectual property rights

V. Application Plans of R&D Results

Utilizing the infrastructure and the research network constructed in this R&D project, we will carry out the following R&D project that studies not only the chemical properties of ice but the physical properties of ice microstructures and roles of ice in biology and develops the eco-friendly purification technologies and new materials using ice properties for practical use.

The R&D results lead the ice chemistry, an unexplored field, and play a new role in understanding polar natural phenomena, and contribute to the development of climate change models and countermeasures against climate change. Moreover, the results will be used as educational materials for natural climate change and provide fundamental information about climate to prepare a countermeasure for climate change.

KOPRI 극지연구소

C O N T E N T S

(영 문 목 차)

KOPRI 극지연구소

KOPRI 극지연구소

목 차

KOPRI
극지연구소

제 1 장

서 론

김기태

한국해양과학기술원 부설 극지연구소

제 1 절. 연구개발의 배경 및 필요성

얼음은 지구상 담수의 약 70%를 차지하는 물의 저장소이며, 대양 및 지표면의 상당 부분을 덮고 있는 지구 환경의 중요한 구성 요소이며, 대기 중에도 수증기의 상전이에 의해 형성된 얼음 입자가 존재한다. 이러한 지구 환경에 있어 얼음의 존재는 상전이에 의한 물질 및 에너지 순환에 영향을 줄 뿐 아니라, 다른 물질의 화학 반응을 유발하여 극지방 뿐 아니라 전 지구적인 자연 현상에 중요한 역할을 하는 것으로 알려져 있다.

얼음은 자연 현상 뿐 아니라 인간의 생활에도 영향을 미친다. 얼음을 이용한 스키 및 썰매와 같은 수단은 이동 및 수송에 유용하게 사용되지만, 얼음 형성은 자동차 운전 및 항공기 운항의 위험성을 높이고 시설 및 장비를 파손하기도 한다. 얼음 및 동결을 이용한 보존은 실험 시료 및 식품 등의 보존에 널리 사용되지만, 동결 시 생장하는 얼음 결정은 시료를 손상하기도 한다.

얼음의 성질과 얼음에서 일어나는 화학 반응을 연구하여 분자 수준에서 이해하는 것은 자연 현상 이해와 얼음을 이용한 기술 향상을 위해 필수적이다. 그러나 이러한 얼음을 구성하는 물 분자(H_2O)는 화학적으로 단순한 분자이지만, 분자의 성질과 상호 작용에 대해서는 아직 밝혀지지 않은 부분이 많다. 특히 얼음에 대한 연구는 이러한 중요성에 비해 기체상인 수증기, 액체상인 물보다 상대적으로 연구가 적게 진행되었다. 지금까지 수행된 환경 관련 연구들은 대부분 수계 혹은 대기 중에서 일어나는 현상을 중심으로 연구되었고, 소수의 얼음에 관련된 연구도 거시적인 현상 모니터링과 분석 및 현장 시료 채취에 집중되었다. 그러나 얼음에서 일어나는 반응은 수용액이나 기체상에서 일어나는 반응과는 큰 차이가 있어, 이를 규명할 필요가 있다.

얼음 및 얼음에서 일어나는 화학 반응의 특이한 성질을 규명하기 위해서는 얼음 화학을 체계적으로 연구할 필요가 있다. 연구 과정에서 습득한 성질을 통해 극지방 및 전 지구적 자연 현상을 이해하는 단서를 얻을 수 있으며, 얼음 특성에 기반을 둔 실용적인 기술을 개발할 수 있다. 국내에서 거의 연구된 바 없는 얼음 연구를 통해 관련 연구 장비 및 연구 네트워크를 구축할 수 있고, 극지 연구에 대한 학계 및 대중의 관심을 높일 수 있으며, 우리나라 극지 연

구의 대표성과로 부각될 수 있다. 얼음 기반의 응용 기술 개발의 경우, 특히 얼음 미세 구조 내 농축되어 가속되는 화학 반응을 연구하여 오염 물질 분해 및 신소재 합성에 활용 가능하며, 다양한 분야에서 경제적 가치를 창출할 수 있을 것이다.

제 2 절. 연구개발의 목표 및 내용

“얼음화학 특성연구를 통한 극지방 자연현상 규명 및 응용기술 개발” 과제는 2018년 처음 시작하여 2단계로 기획된 과제로(그림 1), 최종목표는 얼음에서 일어나는 화학반응들의 특이성을 규명하고 이를 통해 극지방 및 지구환경의 새로운 현상들을 이해하며, 나아가 얼음화학의 새로운 지식을 활용한 실용적인 응용기술들을 개발하는 것이다. 이를 달성하기 위하여, 얼음화학 연구 인프라 구축 및 기초연구, 얼음화학에 기초한 극지방 자연현상의 이해, 얼음화학기반 응용기술 탐색 및 기반연구, 총 3개의 성과목표를 설정하였다. 이를 통하여 얼음화학연구를 위한 실험적 인프라 및 국내외 연구네트워크를 구축하고 이를 바탕으로 얼음에서 일어나는 다양한 화학반응을 연구해 얼음화학반응에 기초하여 극지방 자연현상을 이해하고, 다양한 극지방 자연현상 중 기존 사전연구에서 얻어진 실험실 기초연구결과를 바탕으로 얼음화학과 관련이 있을 것으로 생각되는 주제들을 심화연구하고 아울러 현장연구를 통해 그 관련성을 규명하고자 하였으며, 아울러 얼음에서 일어나는 특이한 현상을 기반으로 다양한 응용기술을 탐색하고자 하였다.

연구 내용은 1차년도인 2018년에는 얼음화학 연구 인프라구축 및 기초연구에서는 얼음화학 반응 특성연구를 위한 실험적/이론적 인프라구축, 올바른 얼음 표면모델 완성 및 표면 흡착 구조, 흡착 에너지에 대한 연구 수행, 얼음미구조 입자분석을 위한 장비설치, 얼음 표면 흡착반응 계산을 위한 기반 구축 및 얼음-수은 흡착 반응 기초계산 수행을 진행하였다. 얼음화학반응에 기초한 극지방 자연현상의 이해에서는 극지방 모사 시스템 구축, 기후조절가스 현장 관측시스템 구축, 얼음화학반응에 의한 무기요오드의 변환 메커니즘 연구, 얼음 내 무기요오드와 dust의 화학반응 연구, 얼음의 저농도 할로겐원소 분석 최적화, 남극해에서의 휘발성 유기화합물, 할로겐 라디칼 전구물질, 그리고 질소 화합물의 분포 분석, 세종기지 기반 대기 할로겐 물질발생 변화 관측, 할로겐 물질 발생과 에어로졸 입자형성과의 상관성 분석, 극지역의 DMS와 할로겐 화합물의 반응 모델링과 해양 및 대기에서의 DMS관측, 얼음 내 표준광물의 지구화학적 반응 연구, 얼음 내 환경유기 물질의 화학 반응 특성 및 메커니즘 이해를 연구하였다. 얼음화학기반 응용기술 탐색 및 기반연구에서는 얼음표면 특성을 이용한 전도성 고분자 배향 연구 및 얼음 내에서 오염물질간의 산화·환원 반응에 의한 오염물질 제거 연구를 수행하였다.

2차년도인 2019년에는 얼음화학 연구 인프라구축 및 기초연구에서는 얼음 표면 흡착 후 분자들의 추가적인 표면 화학반응의 가능성과 그의 메커니즘을 원자수준에서 연구, 분자-얼음 간 상호 작용 및 반응 연구, 저온고압장비설치 후속작업, 데이터보정 및 기초데이터 획득을 수행하였다. 얼음화학반응에 기초한 극지방 자연현상의 이해에서는 얼음의 할로겐 화학종 분석

법 기초연구, 얼음화학반응에 의한 유기요오드의 변환 메커니즘 연구, 대기 관측을 통한 할로겐 물질 기원 에어로졸 입자 형성 기작 규명, 세종기지 인근 빙권 변화가 할로겐 물질 및 에어로졸 입자형성에 미치는 영향 연구, 남극기지 주변 snowpack과 대기 중의 반응성 미량기체 상호 작용 연구, 얼음-수은 흡착반응의 계산-관찰 결과 상호비교, 극지역의 DMS와 할로겐 화합물의 반응 모델링을 통한 현장관측 자료의 분석, 얼음 내 자연시료의 지구화학적 반응 연구, 얼음 내 환경무기 물질의 화학 반응 특성 및 메커니즘 이해를 연구하였다. 얼음화학기반 응용기술 탐색 및 기반연구로 얼음 표면 특성을 이용한 2차원 구조 전도성 신물질 개발 및 얼음 내에서의 화학 반응에 의한 활성 산소종 생성 및 이에 의한 오염물질 분해 연구를 수행하였다.

위의 목표 달성을 위하여 극지연구소 및 국내외 공동 연구진을 조직하여 연구를 추진하였다. 극지연구소 내에서 연구과제를 총괄하고 연구를 위한 기초 인프라 구축 및 극지 현장연구를 수행하였으며, 학연 및 국제 공동 연구를 통하여 부족한 전문가, 인력 및 연구 시설을 보강하였다. 얼음화학 연구 인프라를 구축하기 위해 국내외 전문 연구자와 협력하여 저온 환경모사 체임버, 고압반응 체임버, 할로겐 물질 관측 장비(MAX-DOAS) 등을 제작하여 극지 환경모사 얼음화학 실험 및 극지 현장연구에 활용하였다. 또한 실험 인프라를 활용하여 응용 기술 개발을 위한 기본 조건을 탐색하였다. 얼음 관련 연구 정보를 확보하기 위하여, 공동연구진과 협력하여 자료를 교환하였으며, 선진 연구 기관과 방문 등의 교류를 하였으며, Goldschmidt Conference, European Geosciences Union (EGU), American Chemical Society (ACS) 와 같은 국제 학술대회에 참여하였다.

KOPRI 극지연구소

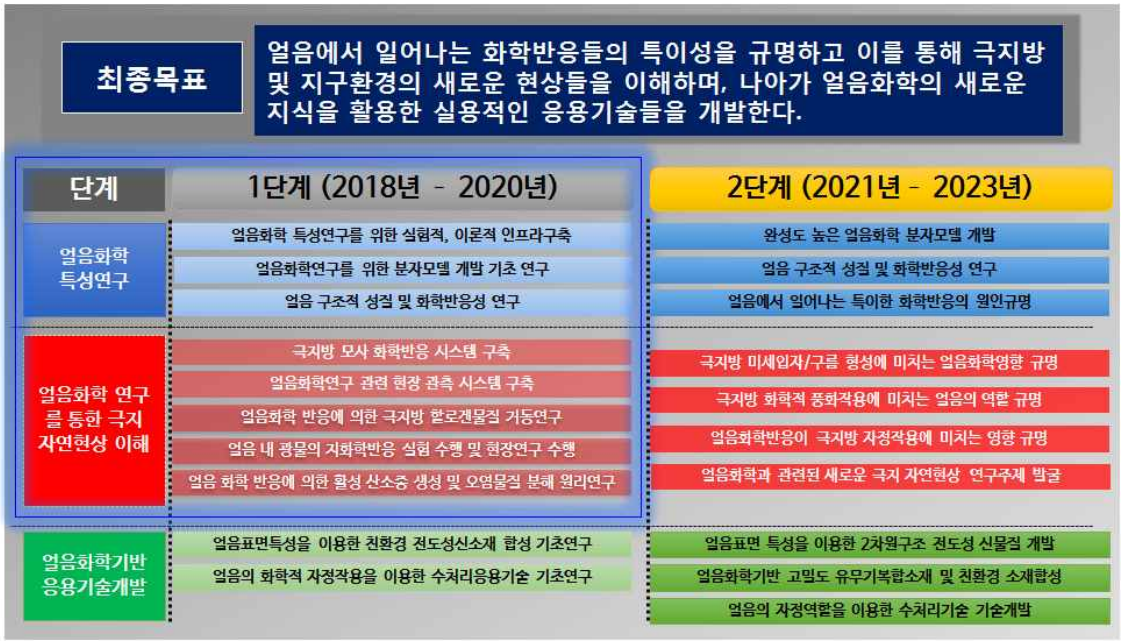

그림 1. 총 연구기간 로드맵

KOPRI 극지연구소

역할	❖ 얼음화학 분석/실험 인프라구축 ❖ 남북극 인프라 지원 및 공동연구	❖ 얼음화학분자모델개발 ❖ 다양한 얼음 환경화학실험 수행 ❖ 얼음화학기반 응용기술개발	❖ 국내 미보유 얼음화학 분석장비 지원 ❖ 현장관측장비 및 현장연구 지원
얼음화학 연구인프라 구축 및 기초연구	▪ 얼음화학 연구를 위한 분석 및 실험적 인프라구축 ▪ 동결농축현상 기반의 얼음화학실험 수행	▪ 얼음화학 분자모델개발 및 얼음표면 화학의 양자역학적 연구	▪ 얼음 표면 및 내부 준액체층 특성연구 (체코 마사릭대, 스위스 PSI) ▪ 얼음특성분석 장비 및 저온고압반응기개발 (뉴질랜드 오타고대, 미국 MIT)
얼음화학 연구를 통한 극지방 자연현상 이해	▪ 극지환경 모사 시스템 구축 ▪ 남북극 기지 및 아라온호 기반 연구지원 ▪ 얼음화학 반응에 의한 할로겐물질 거동연구 및 분석기술 개발 ▪ 얼음에서 일어나는 오염물 제거기작 관련 실험수행 ▪ 얼음에 의한 광물의 화학적 풍화작용 실험수행	▪ 얼음 내부 환경 유무기 물질의 복합 반응계 특성, 메카니즘 규명 및 환경영향 ▪ 얼음의 동결농축에 의한 광물의 차별적 풍화작용 연구	▪ 아라온호 및 세종기지 기반 극지방 할로겐 모니터링((스페인 CSIC ,미국 UC 어바인) ▪ 할로겐 생성물 분석 및 메카니즘 규명 (미국 칼텍, 일본 교토대)
얼음화학기반 응용기술 탐색 및 기반연구	▪ 동결수처리공정 개발을 위한 얼음 내 오염물 분해기작 연구	▪ 얼음화학 기반 신소재 합성 수처리 응용기술 기초연구	

국내 : 극지연, 서울대(2), 포스텍(2), 경북대, 한림대
국외 : 미국(칼텍, MIT, UC Irvine), 뉴질랜드(오타고대, 빅토리아대), 스페인 CSIC, 체코 마사릭 대, 스위스 PSI, 일본 교토대

그림 2. 연구개발 추진 체계 및 역할 분담

제 2 장

국내외 기술개발 현황

제 1 절. 얼음화학반응의 기초 특성 연구

- 얼음의 화학반응은 여러 자연 현상에서 중요한 역할을 함. 예를 들어 지구상에서 눈과 얼음은 대기권의 열평형과 화학적 조성에 지대한 영향을 미치며(Petrenko and Whitworth, 1999), 극지방의 해양 경계층(marine boundary layer)의 해염 얼음(sea salt ice) 또는 에어로졸 입자는 대류권에 활성 할로겐의 생성원으로 여겨짐(Barrie and Plat, 1997). 성층권 구름의 얼음입자는 계절성 오존층 파괴현상에 촉매로써 작용함(Molina *et al.*, 1987). 우주 공간의 얼음 입자는 오랜 기간에 거쳐 생성된 외계 유기물질들의 생성 장소라고 추정됨(Muñoz Caro *et al.*, 2002) (그림 1).
- 얼음촉매하의 광화학 반응은 1985년도에 급격하게 증가한 오존 구멍의 설명에 핵심적인 사항임. 특히 태양빛에 의해 Cl 라디칼이 되고 이것이 오존감소 사이클을 가동시킨다고 제안됨(Solomon *et al.*, 1986) (그림 2). 그 이후 많은 후속연구들이 이루어졌으나 여전히 분자수준에서의 메커니즘에 대한 명확한 실험 및 이론적 일치를 이루지 못하고 있음. 또한 이러한 반응이 일어날 때에 얼음의 구체적인 역할이 무엇인지 역시 여전히 불분명함.
- 서울대학교 강헌 교수 연구진은 저온에서 얼음 표면의 물리적, 화학적 특성에 대한 연구를 지난 10여 년 간 수행해오고 있음. 화학반응의 기초연구로서, 반응이 일어나기 위한 기본 특성들인 물 분자의 얼음표면에서의 확산 속도, 양성자의 이동도, 물 분자의 H/D 교환 반응 등에 대한 지식을 축적함. 또한, HCl, NH_3 등 비교적 간단한 분자들의 얼음 표면에서의 반응 특성을 연구한 바 있음 (그림 3).
- 미국 오클라호마 대학 Paul Devlin 교수 연구진에서 FT-IR 방법을 사용하여 얼음의 기초적 화학반응에 대한 연구를 지난 20여 년 간 수행해 왔음. 얼음의 결합 구조와 이들의 동역학적 특성, HCl 분자의 얼음 내부 및 표면에서의 해리 현상 등을 연구하였음(Devlin *et al.*, 2002) (그림 4). 동일한 분광학적 기법을 활용하여 현재는 얼음 및 얼음 관련 gas hydrates, 또는 액체 nanodroplet 용액들을 포함한 에어로졸의 연구를 헬륨을 활용하여 30-300K 사이의 온도에서 수행 중임.
- 경북대학교 최철호 교수 연구실에서 얼음 표면의 구조 및 화학적 반응성 등에 관한 순 이론적 양자 계산 연구를 수행하고 있음. 얼음 표면의 분자 배열구조 및 간단한 분자들의 흡착 구조에 대한 연구를 수행(Shoaib & Choi, 2012). 세계 최초로 QM/EFP라는 통합 방법론을 활용하여 얼음 표면 모델을 정립하고 HOCl 및 간단한 유기산들의 표면 흡착 구조, 에너지 및 표면 흡착 후 표면 반응들에 대한 연구를 수행함 (그림 5).

- 스웨덴 스톡홀름 대학 L.G.M. Pettersson 교수 연구실에서 얼음 표면에서 분자의 충돌 산란 실험을 수행하는 장치를 제작하고, 이를 사용하여 여러 가지 질소산화물의 얼음 표면에서의 흡착 효율, 반응 행태 등을 연구하고 있음(Romero Lejonthun *et al.*, 2014). 최근에는 X-Ray 레이저를 활용하여 과냉각수용액의 액체-액체상전이에 대한 연구를 수행하여 다양한 온도에서의 얼음의 물성 변화에 대한 체계를 정립하고 있음 (그림 6).
- 얼음 표면에서의 화학 반응은 다양하고 중요한 파급효과를 가지고 있으나 얼음 화학을 연구하는 그룹은 세계적으로 제한적임(Abbatt, 2003). 이와 상보적인 이론적 연구는 더더욱 미미하여 추가적인 노력들이 요구됨. 특히 이론적 연구는 원자수준에서의 반응 메커니즘 및 동역학적 측면을 연구할 수 있는 유일한 방법론임(그림 7). 그러므로 이론은 실험에서 접근하기 힘든 영역들에 대한 중요한 상보적 정보를 제공할 수 있어 기존 실험결과의 올바른 해석과 더 나아가 새로운 실험 방향을 제시 할 수 있음.
- 얼음과 관련된 자연 현상들에 대한 지금까지의 연구는 주로 현상의 관찰 연구가 주를 이루어 왔음. 반면에, 관찰되는 현상들의 근원적인 원인을 이해코자 하는 노력, 특히 얼음 표면 현상의 화학적인 설명은 아직 미미한 단계임. 그 주된 이유의 하나는 얼음에서 일어나는 화학반응에 대한 기초과학적인 연구와 체계적인 화학적 지식이 부족하기 때문으로 생각됨. 본 과제에서는 얼음 표면화학의 기초적 지식을 축적하고 이를 활용하여 상기 현상들에 대한 체계적인 이해를 도모하는 단계를 밟아 나가고자 함.

KOPRI 극지연구소

제 2 절. 얼음화학 연구를 통한 극지 자연현상 이해

1. 자연에서 유·무기 물질들이 얼음상에서 나타내는 특수한 화학 반응 연구 동향

- 지구상 얼음은 고위도 지역 및 대류권과 성층권, 영구동토층, 겨울철 중위도 지방 등에 널리 존재하며 몇몇 현상의 주된 원인임 (그림 8). 지구 상 담수의 대부분은 액체가 아닌 고체인 얼음과 눈의 형태로 존재하나, 얼음상에서 일어나는 환경화학적 반응에 대한 연구는 거의 수행된 바가 없음. 따라서 지구 환경의 깊은 이해를 위해 얼음에서 일어나는 새로운 환경 화학반응들의 연구는 필수적임.
- 용존 유기 물질(Dissolved Organic Matter [DOM])이란 환경에 광범위하게 존재하는 유기물질로서 물에 용해도가 높은 물질들을 의미함. 이러한 DOM은 태양 빛을 받아 활성화된 전자를 생성할 수 있는데, 이 활성 전자는 물에 녹아 있는 용존 산소와 반응하여 활성 산소 중 하나인 singlet oxygen을 생산함. 기존 연구에서는 얼음 내부에서 생성되는 singlet oxygen을 통해 독성 물질 알드린(aldrin)을 분해하는 실험을 진행함. 얼음에 존재하는 DOM으로부터 광조사에 따른 singlet oxygen의 생산량이 액상에서보다 현저히 증가한다는 사실이 발견됨 (그림 9). 이러한 환경에서 얼음으로부터의 singlet oxygen 생산의 향상은 환경의 여러 반응을 촉진할 수 있는 반응이 될 수 있음.

- 에너지가 높은 자외선이 조사되면 물이 분해되면서 수산화 라디칼(·OH)이 생성되는데, 이 수산화 라디칼은 다른 유기물질과 반응하여 물질을 분해하고 산화시키는 역할을 함. 예를 들어, 4-염화페놀(4-chlorophenol)이 들어있는 수용액에 자외선을 조사하면 수산화 라디칼에 의해 하이드로퀴논(hydroquinone)이 생성됨. 이러한 반응을 통해 인공 오염 물질 중 하나인 4-염화페놀은 좀 더 독성이 낮고 환경에 흔한 유기물질 중 하나인 하이드로퀴논으로 분해됨. 반면, 얼음상에서는 자외선 조사로 인해 4-염화페놀로부터 페놀 이합체가 형성되는 현상이 보고됨 (그림 10). 이러한 반응은 페놀류 유기물질의 독성을 증가시키는 반응으로, 인공 오염 유기 물질이 환경에 노출되었을 경우 환경 얼음에 의해 독성이 높은 물질로 변환 될 수 있는 가능성을 시사함.

2. 구름 응결핵으로서의 요오드 생성 연구 동향

- 최근 몇 년 동안 대기의 복사 균형과 기후에 영향을 미치는 구름 응결핵(Cloud Condensation Nuclei)으로 자랄 가능성이 있는 초미세 에어로졸 입자(Ultra Aerosol Particle)가 요오드 산화물 입자(Iodine Oxide Particle)에 의해 형성된다는 연구들이 주목받고 있음. 요오드 산화물 라디칼의 중첩과 재결합으로 요오드 산화물 입자가 형성되고 그 입자는 중합 혹은 알려지지 않은 과정을 통해서 구름 응결핵으로 자람. 지난 연구들은 이러한 활성 요오드종의 원천인 유기 요오드가 많이 형성되는 중위도 지방 해양 경계층에 초점이 맞춰져 있었지만, 최근에 극지방 해양 경계층과 대기에서도 높은 농도의 이러한 입자들이 관측되었으며, 관측된 입자들로부터 지역적 구름 응결핵의 형성이 가능하다는 모델 연구가 확인되었음. 이를 바탕으로 극지의 구름 형성에 요오드 산화물 입자를 만드는 할로카본(Halocarbon-메탄의 수소원자 전부 또는 일부를 할로겐 원자로 치환한 것의 총칭)이 중요한 역할을 할 수 있다는 주장이 제기되고 있음.
- 기존 연구에서는 요오드 산화물 입자로부터 구름 응결핵이 형성되는 과정에 대한 정확한 메커니즘이 밝혀지지 않음. 이전 연구들로는 설명이 불가능한 극지방에서의 높은 농도의 요오드 산화물에 대한 원인, 특히 극지방의 눈과 얼음, 또는 에어로졸에 의한 요오드 산화물 형성에 대한 규명이 필요함 (그림 11).
- 이탈리아 시에나 대학의 Spolaor는 Talos Dome ice core 분석을 통하여 과거 해빙의 면적이 그 시기의 대기 중 요오드 농도와 반비례한다는 것을 밝혀냄. 실제 대기에는 풍부한 iodate(IO_3^-)가 빙하기 ice core에서만 나타나고, 동결된 iodate 용액에 빛을 조사한 실험으로부터 액체상에서 안정하다고 알려진 iodate가 얼음상에서는 안정하지 않고 빛에 의해 활성 요오드 종으로 환원되어 요오드 산화물 입자를 형성할 수 있음을 보여줌 (그림 12).
- 스페인 마드리드의 Gálvez는 얼린 수용액의 iodate염의 광분해로부터 활성 요오드종의 방출을 확인하고, 이를 모델에 적용함으로써 대기 중의 요오드 산화물의 농도가 기존의 모델보다 0.2-1.0 pptv 더 높은 수준으로 나타나는 것을 확인함 (그림 13). 이로써 극지 대기에 핵심적인 역할을 하는 활성 할로겐의 방출 기작과, 활성 요오드의 새로운 방출원을 제시함.
- 미국 미시간 대학의 Pratt 교수는 북극 대기에서 이전 연구들에서 측정된 적 없는 분자 요

오드(I_2)를 봄철에 snowpack 위 대기에서 측정함으로써 눈에서 분자 요오드의 광화학적 형성의 증거를 제시함. 측정값을 이용한 모델링에서 측정된 분자 요오드 농도는 북극 대기에 큰 변화를 야기 할 수 있다는 결과를 보여줌으로써 분자 요오드가 북극 대기의 주요한 요오드 공급원임을 시사함. 또한 해빙수(snow meltwater)에서 요오드 이온(I^-)을 측정한 결과 해수에 비해 농도가 굉장히 높은 것을 확인함으로써 눈에서 요오드가 활성화 된다는 것을 제안함 (그림 14).

3. 극지에서의 화학적 풍화작용 연구 동향

- McMurdo LTER project를 통해 1992년부터 남극의 토양이 가장 많이 드러난 지역인 McMurdo Dry Valleys에서 빙하, 하천, 호수, 토양이 연구되고 있음. 기온이 높고 강수량이 많은 기후에서 화학적 풍화작용이 잘 일어난다는 기존의 인식(White & Blum, 1995)과 다르게 기온이 낮으며 강수량이 적은 극지방에서도 풍화작용이 잘 일어날 수 있다는 주장이 제기되었으나 이는 빙하가 녹아 생기는 하천의 빠른 유속에 의한 물리적 풍화작용에 의한 것으로 여겨짐(Hall *et al.*, 2002; Anderson *et al.*, 1997). 남극에서는 낮은 기온과 적은 강수량에도 불구하고 온대 기후 지역에 상응하는 정도의 풍화작용이 일어나는 것으로 연구되었으며(Nezat *et al.*, 2001; Gooseff *et al.*, 2002), 이는 풍성입자의 풍화작용, 빠른 유속에 의한 물리적 풍화작용, 토양이 물과 맞닿아 있는 혼합대(hyporheic zone)에서의 풍화작용에 의한 것으로 연구됨(Deuerling *et al.*, 2014; Green *et al.*, 2005; Stumpf *et al.*, 2012) (그림 15). 화학반응은 온도가 높을수록 잘 일어난다는 기존의 인식과 달리 최근 광물의 용해와 관련하여 얼음에서 일어나는 특이한 화학반응들이 연구되어(Jeong *et al.*, 2015; Jeong *et al.*, 2012), 대부분이 얼음으로 덮여있는 남극 환경에서 얼음에 의한 화학적 풍화작용이 고려될 필요가 있음.

제 3 절. 얼음화학기반 응용기술개발

1. 얼음 표면 화학을 응용한 전도성 고분자 연구 동향

- 지난 50년간 용액 조건의 다양화를 통해 전도성 고분자의 모폴로지를 제어하고 전자 이동도를 규명하는 연구가 활발하게 진행되어 왔음. 합성된 전도성 고분자는 대부분 구형 혹은 막대 형태의 구조이며, 구조에 따라 확연히 다른 전도도가 보고되어 왔음. 하지만, 실제 디바이스에 활용하기 위해서는 면 형태의 전극을 제작해야 하는데, 합성된 전도성 고분자는 용매에 녹지 않기 때문에 기계적인 방법으로 3차원적인 구조체들을 섞어 2차원적 시트를 제작함. 이 경우 기존에 알려진 연구 결과와 유사하게, 저차원성(low dimensionality)에서 나타나는 장점을 잃고 벌크(bulk) 성질을 보이며 물성이 크게 떨어지는 문제점을 보임.
- 이러한 단점을 해결하기 위해 많은 연구진들은 2차원적 구조를 가지는 그래핀 하드 템플릿(grahpene hard template)의 표면에 전도성 고분자를 합성하여 높은 물성을 보고하여 왔

으나 (그림 16), 이러한 hard template는 합성 후 제거할 수가 없으며, 대면적으로 합성하기 어렵기 때문에 결과에 재현성이 없는 것이 큰 문제점으로 여겨지고 있음.

- 중국과학원(Chinese Academy of Sciences)에서는 그래핀 산화물을 template으로 도입하여 2차원적인 폴리아닐린 마이크로시트(microsheet)를 합성하는 연구를 보고함. 해당 연구에서는 이미 알려져 있는 그래파이트를 Hummer's method를 이용하여 그래핀 산화물로 합성하고, 합성한 그래핀 산화물을 아닐린과 산화제와 함께 넣은 상태로 교반시켜 그래핀 산화물-전도성고분자 복합물을 합성하였음 (그림 17, 18). 합성한 복합물은 아스코르브산(ascorbic acid), 도파민(dopamine), 요산(uric acid)에 대하여 높은 전기적 촉매활성을 보였다는 점에서 의의가 있지만, 그 크기가 수백나노미터에 불과해 실용성이 없음.
- 미국 Northwestern University에서는 Langmuir-Blodgett Assembly 기법을 통하여 물 표면에서 단층의 흑연 산화물, 즉 그래핀 산화물을 합성하는 연구를 보고함. 해당 연구에서는 공기와 수면 사이의 상호작용에 의해 단층의 그래핀 산화물이 합성되었다는 것을 규명. 해당 논문에서 이용한 합성 방법은 2차원적인 층들 사이에 강한 반발력 덕분에 어떠한 계면활성제, 또는 안정제도 사용하지 않고도 뭉치지 않는, 하나의 층으로 된 그래핀 산화물을 합성하였다는 점에서 의의가 있음 (그림 19). 그러나 그래핀 산화물 template 자체의 크기 제어가 어려울 뿐만 아니라, 전도성 고분자가 합성될 핵 생성지점 (nucleation site)의 개수나 위치를 정량화하기가 불가능하기 때문에 합성되는 전도성 고분자 역시 대면적으로 구현하기 어려우며, 그 물성 또한 재현성이 없음.
- 미국 University of California에서는 용액상의 반응 조건을 조절하고 아닐린 단량체가 아닌 아닐린 이량체를 중합하여, 판형, 막대기형, 뇌구조를 모사한 다양한 형태의 폴리아닐린을 합성함. 해당 연구에서는 각 형태에 따라 결정성이 다른 것을 X-선 회절 분석법(XRD)을 통해 확인하였고, 그 결과 리본형, 그리고 판형일 때의 회절 peak이 가장 강했고, 이를 통해 2차원적인 구조가 더 높은 결정성을 갖는다는 것을 확인함. 또한, 각 형태에 따른 전기전도도를 측정한 결과, 막대기형일 때의 전기전도도는 0.3 S/cm에 그친 반면, 판형과 리본형은 각각 0.5 S/cm와 1.1 S/cm 의 더 높은 전기전도도를 가지는 것을 확인하였고, 이를 통해 2차원적 구조가 가지는 장점과 그 이유를 확인함 (그림 20). 하지만 해당 연구에서는 아닐린의 중합도가 낮아서 기존에 보고된 폴리아닐린 관련 논문과 비교하여 평범한 수준에 그친 전기전도도를 갖는다는 한계가 있음.
- 2000년 앨런 히거, 앨런 그레미엄 맥더미드, 시라카와 히데키 교수가 전도성 고분자의 발견과 개발에 대한 공헌으로 노벨상을 받은 이후, 전 세계에서 손쉬운 전도성 고분자 합성법을 개발하기 위해서 연구 노력을 쏟고 있음 (그림 21). 하지만 합성된 전도성 고분자가 실제 디바이스에 활용되기 위해서는 대량생산, 합성의 손쉬움, 가공성 확보 등 해결해야 할 문제점이 많음. 또한 전 세계적으로 그 중요성이 강조되고 있는 "친환경" 프로세스는 전도성 고분자의 합성과는 거리가 먼 것으로 그동안 여겨져 옴. 때문에, 본 연구진이 제안한 얼음을 이용한 2차원적인 전도성 고분자 합성은 그 파급효과가 매우 클 것으로 판단됨.

2. 얼음에서 일어나는 화학적 자정작용 연구 동향

- 물에서 일어나는 화학적 자정작용에 대한 연구는 많이 되었으나, 얼음에서 일어나는 화학적 자정작용 연구는 거의 수행되지 않음. 얼음에서 일어나는 화학적 자정작용은 무궁무진할 것으로 예상되지만, 이를 전문적으로 수행하는 연구그룹은 세계적으로도 10개 내외로 현재 초기 연구 단계에 있음. 기후 변화와 관련하여 환경지구화학에 대한 중요성이 강조되고 있는 현 시점에서 앞으로 물의 상당 부분을 차지하는 얼음에서 일어나는 화학적 자정작용 연구가 더욱 활발하게 진행될 것이며, 이와 더불어 선도적 위치를 선점하고자 하는 경쟁이 치열해질 것으로 예상됨. 하지만, 현재까지 국내 학계에서 본 연구주제와 관련된 연구를 전문적으로 수행하였거나, 수행하고 있는 연구기관은 없음. 따라서 본 연구 수행을 통해 얼음에서 일어나는 화학적 자정작용에 대한 핵심 노하우 및 이론을 정립함으로써 극지방, 영구 동토층에서의 환경 해석과 얼음 반응을 이용한 환경 정화 기술 개발의 세계적 선도 그룹으로 자리매김 할 필요성이 있음 (그림 22).
- 일본 Osaka Prefecture University의 Norimichi Takenaka 그룹은 얼음에서 아질산염의 산화 속도가 물에서보다 10^5배 빨라진다는 것을 보고함. 이는 용액이 어는 과정에서 얼음 결정 주위에 존재하는 준액체층에 화학물질(아질산염, 수소이온, 산소)들이 농축되게 되고(동결농축효과), 화학물질의 농도 증가를 야기함으로써 화학물질간의 산화 · 환원 반응 속도가 향상되었기 때문(Takenaka *et al.*, 1992; Takenaka *et al.*, 1996) (그림 23).
- 미국 Villanova University의 Amanda M. Grannas 그룹은 얼음에서 p-니트로아니솔(nitroanisole)과 피리딘(pyridine)의 광화학 반응 속도가 물에서 보다 최대 40배 빨라진다는 것을 보고함(Grannas *et al.*, 2007) (그림 24). 또한, 물에서보다 얼음에서 용존 자연 유기물(Dissolved natural organic matter)의 광화학 반응에 의한 일중항산소 생산 및 이에 의한 알드린(aldrin) 분해가 1000배 빠르게 진행됨(Fede *et al.*, 2015). 이러한 얼음에서 향상된 광화학 반응 속도는 얼음이나 눈의 특성, 온도, 반응 물질의 종류, 농도 및 용해도에 따라 차이가 있음을 규명함.
- 체코 Masaryk University의 Petr Klán 그룹은 1,1-다이페닐에틸렌 (diphenylethylene)과 오존의 반응으로 인한 벤조페논(benzophenone)의 생성이 물에서보다 눈 표면에서 빨라진다는 것을 보고함. 물이 어는 과정에서 1,1-diphenylethylene은 눈 표면에 농축되고, 따라서 공기 중에 있는 오존과의 반응속도가 향상됨. 극지방 공기 중의 오존의 농도가 20 ppb임을 고려하여 1,1-diphenylethylene이 benzophenone으로 바뀌는 반감기가 5일이라고 추정함 (Ray *et al.*, 2011) (그림 25).
- 일본 Tokyo Institute of Technology의 Tetsuo Okada 그룹은 얼음에서의 fluorescein diacetate의 가수분해 반응이 물에서 보다 빨라진다는 것을 보고함. Fluorescein diacetate는 가수분해 반응에 의해 fluorescein으로 변하며, 이렇게 변환된 fluorescein의 형광을 얼음상에서 측정하여 직접적인 얼음상에서의 동결농축효과 및 fluorescein diacetate의 가수분해 메커니즘을 제시함(Anzo *et al.*, 2013) (그림 26).
- 현재 우리나라는 화학, 물리, 소재, 바이오 분야에서 상당수의 논문을 상위 임팩트 팩터 저널에 발표하고 있지만, 자연 환경 분야에서는 미비한 실정임. 얼음에서 일어나는 화학적

자정작용 연구는 전 지구적 환경 변화 및 오염물질의 거동과 관계된 주제로 high impact factor journal (예: Nature (IF = 38.138), Science (IF = 34.661), Energy & Environmental Science (IF = 25.427))에서 요구하는 연구의 독창성, 대중성, agenda-setting research에 부합하는 연구 주제로 판단됨.

제 4 절. 얼음화학 연구 그룹

1. 스위스 PSI(Paul Scherrer Institut)

- 스위스의 연구기관 PSI는 Matter and Materials, Energy and Environment, Human Health의 세 가지 주요 분야를 연구. Swiss National Science Foundation 재단의 지원으로 이루어진 MiSo(Microscale Distribution of Impurities in SnOw and Glacier Ice) 프로젝트에서는 대기로부터 유래하여 눈과 얼음에서 불순물로 존재하는 물질의 변성과정에서 일어나는 화학적 반응과 빙하로의 물질 이동을 연구하며, 이러한 반응이 human health, 기후, 지구의 지화학적 순환에 미치는 영향을 연구함 (그림 27). Swedish Research Council 재단의 지원으로 XPS(X-ray photoelectron spectroscopy)와 NEXAFS (Near Edge X-Ray Absorption Fine Structure)를 이용하여 얼음 표면에서 일어나는 기체의 반응과 녹는점에 가까운 온도에서 얼음의 표면 특성을 연구함. 환경 화학 부서는 표면 화학과 분석 화학 연구그룹으로 나누어 연구하고 있으며, 표면 화학 연구실에서는 얼음과 관련하여 다음과 같은 연구가 수행되고 있음.
- MiSo 프로젝트의 일환으로 극지 및 중위도 지역에서 정기적으로 관측되는 대규모 오존 파괴 현상과 관련 있는 눈에서의 할로겐화물(halide)과 오존의 화학적 반응을 연구. 온도에 따른 점성 및 상의 변화가 단순히 온도의 영향을 넘어 불균일 반응 속도와 생성물에 영향을 줄 것이라는 가설을 바탕으로 온도가 감소할 때 할로겐화물의 반응성을 연구함 (그림 28).
- 전자 및 형광 NEXAFS 분광법을 이용하여 동결된 염화나트륨 수용액에서 염소 이온을 연구. NEXAFS 분광법은 수용액의 상변화를 관찰하기 용이하며, 전자와 형광 검출법을 함께 이용함으로써 기체와 얼음 경계면 또는 시료 전체를 관찰할 수 있음. 이 연구는 어는점 이하의 온도에서 염화나트륨 수용액이 시료 전체와 얼음 표면에서 상의 차이가 있는지를 밝히는 것을 목표로 하며, 이러한 연구는 눈과 얼음에서의 화학 반응과 이에 따른 환경에의 영향을 모델링하는 데 있어 중요한 의미를 가짐 (그림 29).
- 얼음 내 미세구조의 교차점에서 물질의 물리화학적 특성에 따라 일어나는 얼음의 대기 중 미량 기체 흡수 현상을 분자 수준에서 이해하기 위한 연구 수행. 이 프로젝트에서는 DIFT(Drilled Ice Flow Tube)이라는 유동형 반응기 시스템을 개발하여 얼음 결정도 변화에 따른 표면에서의 미량 기체 흡착을 연구. 얼음 내에서의 미량 기체 거동 연구를 통한 얼음의 화학적 작용과 그에 따른 환경에의 영향, 반응성 미량 기체가 대기 중으로 돌아가

는 정도, 눈과 대기의 조성과 산화능력 등을 연구 (그림 30).

- 얼음과 미량 기체의 상호작용은 대기 조성과 산화능력의 변화를 가져올 수 있음. 미량 기체는 얼음에 포집되어 전환된 후 다시 대기로 방출될 수 있으며, 이때 미량 기체에 의해 얼음의 구조 또한 변할 수 있음. 대기권, 빙권, 생물권에서 일어나는 현상을 이해하는 데 있어 이러한 얼음과 미량 기체의 상호작용을 파악하는 것은 중요하지만 분자 수준에서의 이해는 부족한 실정임. Ambient pressure X-ray spectroscopy를 이용하여 HCOOH, HONO와 같은 산성 미량 기체와 얼음의 상호작용을 연구 (그림 31).

2. 일본 The Institute of Low Temperature Science(ILTS)

- ILTS는 홋카이도 대학과 제휴하여 1941년에 설립된 기관으로 빙권과 극지환경에서의 눈과 얼음, 자연과학에 대한 기초 연구를 수행해오고 있음. Water and Material Cycles, Frontier Ice and Snow Science, Environmental Biology의 세 부서로 이루어져 있으며, Frontier Ice and Snow Division의 Phase Transition Dynamics Group에서 주도적으로 얼음에 대한 연구를 수행하고 있음.
- 동결방지 단백질 분자가 얼음 계면에 흡착되는 과정과 단백질이 얼음 결정 성장에 미치는 영향을 연구. 마커로 표시한 동결방지 단백질을 이용하여 얼음 계면 일어나는 현상을 시각화하였으며, 이를 통하여 동결방지 단백질이 얼음 계면에 흡착하여 결정의 성장을 제어하는 기능을 통해 생체의 동결을 방지할 수 있음을 밝혀냄. 이러한 동결방지 단백질의 작용에 의한 동결 억제 메커니즘은 추운 환경에서 생물이 생존할 수 있는 전략이 될 수 있음 (그림 32).
- 지상에서는 중력의 영향으로 결정 주위에 생기는 열의 대류에 의해 결정의 모양이 고르지 못하게 되거나 대칭이 이루어지지 못하게 되며, 완전한 모양의 얼음 결정을 만들기 위해서는 중력의 영향이 없는 환경에서 실험이 이루어져야 함. 이를 해결하기 위해 지상 400킬로미터의 국제 우주 정거장에서 얼음 결정 성장 연구를 수행하였으며, 동결방지 단백질을 첨가한 수용액의 냉각 및 얼음 결정 성장 모습을 연구 중임 (그림 33).
- 얼음 이외의 결정에서 분자 수준에서 이루어지는 표면의 성장은 지금까지 다양하게 연구되어 왔으나 얼음 결정 구조의 단계적인 성장을 가시화하는 것은 잘 이루어지지 않았음. 연구진이 올림푸스와 공동으로 개발한 레이저 공초점 미분간섭현미경을 이용하여 수증기가 있는 상태에서 성장시킨 얼음 결정의 표면을 관찰하는 연구를 수행. 얼음 결정의 육방정계 기저에서 섬과 같은 분자 층이 형성되며, 이 분자 층이 횡 방향으로 성장하며 퍼져 얼음 결정이 성장하는 모습을 관찰. 두께가 같은 분자 층이 합쳐질 때는 분자 층의 가장자리가 사라지는 현상을 보임 (그림 34).
- 얼음 결정의 표면은 녹는점(0 ℃) 이하의 온도에서도 융해하여 액체상의 표면(유사 액체층)을 형성하며, 이러한 액체상의 표면은 스케이트의 미끄러짐, 서릿발에 의한 동결, 얼음 결정립의 재결정화와 조대화(coarsening), 눈 결정의 모양 변화, 음식 및 인체 장기의 동결 보관, 뇌운의 전기 발생 등 다양한 현상의 열쇠를 쥐고 있다고 여겨짐, 이를 밝히기 위해 액체상 표면에 대한 분자 수준에서의 이해가 필요함. 해당 연구진은 마이클 패러데이에 의

해 1850년대에 이미 주장되었지만 최근까지 시각화하지 못했던 녹는점 이하에서 얼음의 융해에 의한 표면 액체상의 생성을 시각화하는 연구를 수행. 얼음 결정의 육방형 기저면에서 물과 기름처럼 서로 섞이지 않는 두 종류의 표면 액체상이 생성하는 것을 발견함. 이러한 두 개의 액체상 표면은 서로 물리적 및 화학적 성질이 크게 다름. 지금까지 하나의 종류만 존재하며 얼음 표면 전체에서 균일하게 생성되는 것으로 생각되었던 액체상 표면에 대한 새로운 시각을 제시함 (그림 35).

KOPRI
극지연구소

참고문헌

Abbatt, J. P. 2003, Interactions of atmospheric trace gases with ice surfaces: Adsorption and reaction. *Chem. Rev.*, **103**, 4783-4800.

Anderson, S. P.; Drever, J. I.; Humphrey, N.F. 1997, Chemical weathering in glacial environments. *Geology,* **24**, 399-402.

Anzo, K.; Harada, M.; Okada, T. 2013, Enhanced Kinetics of Pseudo First-Order Hydrolysis in Liquid Phase Coexistent with Ice. *J. Phys. Chem. A* 117, 10619-10625.

Bao, Y.; Song, J.; Mao, Y.; Han, D.; Yang, F.; Niu, L.; Ivaska, A. 2011, Graphene Oxide Templated Polyaniline Microsheets toward Simultaneous Electrochemical Determination of AA/DA/UA. *Electroanalysis* **23,** 878-884.

Barrie, L.A.; Platt, U. 1997, Arctic tropospheric chemistry: an overview. *Tellus* **49B**, 450-454.

Bartels-Rausch, T. *et al.* 2014, A review of air-ice chemical and physical interactions (AICI): liquids, quasi-liquids, and solids in snow. *Atmos. Chem. Phys.*, **14**, 1587 - 1633.

Cote, L. J.; Kim, F.; Huang, J. 2009, Langmuir-Blodgett Assembly of Graphite Oxide Single Layers. *J. Am. Chem. Soc.* **131,** 1043-1049.

Deuerling, K. M; Lyons, W. B.; Welch, S. A.; Welch, K. A. 2014, The characterization and role of aeolian deposition on water quality, McMurdo Dry Valleys, Antarctica. *Aeolian Res.* **13**, 7-17.

Devlin, J.; Uras, N.; Sadlej, J.; Buch, V. 2002, Discrete stages in the solvation and ionization of hydrogen chloride adsorbed on ice particles. *Nature* **417**, 269-271.

Fede, A; Grannas, A. M. 2015, Photochemical Production of Singlet Oxygen from Dissolved Organic Matter in Ice. *Environ. Sci. Technol.* **49**, 12808-12815.

Gálvez, Ó.; Baeza-Romero, M. T.; Sanz, M.; Saiz-Lopez, A. 2016, Photolysis of frozen iodate salts as a source of active iodine in the polar environment. *Atmos. Chem. Phys.* **16**, 12703-12713.

Gooseff, M. N.; McKnight, D. M.; Lyons, W. B.; Blum, A. E. 2002, Weathering reactions and hyporheic exchange controls on stream water chemistry in a glacial meltwater stream in the McMurdo Dry Valleys. *Water Resour. Res.* **38**, 15-1-15-17.

Grannas, A. M.; Bausch A. R.; Mahanna K. M. 2007, Enhanced Aqueous Photochemical Reaction Rates after Freezing, *J. Phys. Chem. A* **111**, 11043-11049.

Green, W. J.' Stage, B. R.; Preston, A.; Wagers, S.; Shacat, J.; Newell, S. 2005, Geochemical processes in the Onyx River, Wright Valley, Antarctica: Major ions,

KOPRI 극지연구소

nutrients, trace metals. *Geochim. Cosmochim. Acta* **69**, 839-850.

Hall, K.; Thorn, C.E.; Matsuoka, N.; Prick, A. 2002, Weathering in cold regions: Some thoughts and perspective. *Prog. Phys. Geogr.* **26**, 577-603.

Jeong, D.; Kim, K.; Choi, W. 2012, Accelerated dissolution of iron oxides in ice. *Atmos. Chem. Phys.* **12**, 11125-11133.

Jeong, D.; Kim, K.; Min, D. W.; Choi, W. 2015, Freezing-Enhanced Dissolution of Iron Oxides: Effects of Inorganic Acid Anions. *Environ. Sci. Technol.* **49**, 12816-12822.

Kang, H.; Shin, T.-H.; Park S.-C.; Kim, I. K.; Han, S.-J. 2000, Acidity of hydrogen chloride on Ice. *J. Am. Chem. Soc.* **122**, 9842-9843.

Klánová, J.; Klán, P.; Heger, D.; Holoubek, I. 2003, Comparison of the effects of UV, H_2O_2/UV and ɣ-irradiation processes on frozen and liquid water solutions of monochlorophenols. *Photochem. Photobiol. Sci.* **2**, 1023-1031.

Liu, S.; Gordiichuk, P.; Wu, Z. et al. 2015, Patterning two-dimensional free-standing surfaces with mesoporous conducting polymers. *Nat Commun.* **6**, 8817.

Molina, M. J.; Tso, T. L.; Molina, L. T.; Wang, F. C. Y. 1987, Antarctic Stratospheric Chemistry of Chlorine Nitrate, Hydrogen Chloride, and Ice: Release of Active Chlorine. *Science* **238**, 1253-1257.

Muñoz Caro, G.; Meierhenrich, U.; Schutte, W. A.; Barbier, B.; Arcones Segovia, A.; Rosenbauer, H.; Thiemann, W. H.-P.; Brack, A; Greenberg, J. M. 2002, Amino acids from ultraviolet irradiation of interstellar ice analogues. *Nature* **416**, 403-406.

Nada, H.; Furukawa, Y. 2012, Antifreeze proteins: computer simulation studies on the mechanism of ice growth inhibition. *Polym. J.* **44**, 690.

Nezat, C. A.; Lyons, W. B.; Welch, K. A. 2001, Chemical weathering in streams of a polar desert (Taylor Valley, Antarctica). *GSA Bulletin* **113**,1401-1408.

Petrenko, V. F.; Whitworth, R. W. 1999, *Physics of Ice*; Oxford University Press.

Raso, A. R. W.; Custard, K. D.; May, N. W.; Tanner, D.; Newburn, M. K.; Walker, L.; Moore, R. J.; Huey, L. G.; Alexander, L.; Shepson, P. B.; Pratt, K. A. 2017, Active molecular iodine photochemistry in the Arctic. *Proc. Nat. Acad. Sci. U.S.A.* **114**, 10053-10058.

Ray, D.; Kurkova, R.; Hovorkova, I.; Klan, P. 2011, Determination of the specific surface area of snow using ozonation of 1,1-diphenylethylene. *Environ. Sci. Technol.* **45**, 10061-10067.

Romero Lejonthun, L. S. E,; Andersson, P. U.; Hallquist, M.; Thomson, E. S.; Pettersson, J. B. C. 2014 Interactions of $N_2O_5$and related nitrogen oxides with ice surfaces: Desorption kinetics and collision dynamics. *J. Phys. Chem. B* **118**, 13427-13434.

Sazaki, G.; Zepeda, S.; Nakatsubo, S.; Yokoyama, E.; Furukawa, Y. 2010, Elementary steps at the surface of ice crystals visualized by advanced optical microscopy. *Proc. Nat. Acad. Sci. U.S.A.* **107**, 19702-19707.

Sazaki, G.; Zepeda, S.; Nakatsubo, S.; Yokoyama, E.; Furukawa, Y. 2012, Quasi-liquid layers on ice crystal surfaces are made up of two different phases, *Proc. Nat. Acad. Sci. U.S.A.* **109**, 1052-1055.

Schonhardt, A.; Begoin, M.; Richter, A.; Wittrock, F.; Kaleschke, L.; Gomez Martin, J. C.; Burrows, J. P. 2008, Simultaneous satellite observations of IO and BrO over Antarctica. *Atmos. Chem. Phys.* **12**, 6565-6580.

Shoaib, M. A.; Choi, C. H. 2012, Adsorptions of HOCl on ice surface: Effects of long-range electrostatics, surface heterogeneity, and hydrogen disorders of ice crystal. *J. Phys. Chem. C* **116**, 3694-3701.

Solomon, S.; Garcia, R. R.; Rowland, F. S.; Wuebbles, D. J. 1986, On the depletion of Antarctic ozone. *Nature* **321**, 755-758.

Spolaor, A.; Vallelonga, P.; Plane, J. M. C.; Kehrwald, N.; Gabrieli, J.; Varin, C.; Turetta, C.; Cozzi, G.; Kumar, R.; Boutron, C.; Barbante, C. 2013, Halogen species record Antarctic sea ice extent over glacial-interglacial periods. *Atmos. Chem. Phys.* **13**, 6623-6635.

Stumpf, A. R.; Elwood Madden, M. E.; Soreghan, G. S.; Hall, B. L.; Keiser, L. J.; Marra, K. R. 2012, Glacier meltwater stream chemistry in Wright and Taylor Valleys, Antarctica: Significant roles of drift, dust and biological processes in chemical weathering in a polar climate. *Chem. Geol.* **322 - 323**, 79-90.

Takenaka, N.; Ueda, A.; Daimon, T.; Bandow, H.; Dohmaru, T.; Maeda, Y. 1996, Acceleration Mechanism of Chemical Reaction by Freezing: The Reaction of Nitrous Acid with Dissolved Oxygen, *J. Phys. Chem.* **100**, 13874-13884.

Takenaka, N.; Ueda, A.; Maeda, Y. 1992, Acceleration of the rate of nitrite oxidation by freezing in aqueous solution. *Nature* **358**, 736.

Wang, Y.; Tran, H. D.; Liao, L.; Duan, X.; Kaner. R. B. 2010, Nanoscale Morphology, Dimensional Control, and Electrical Properties of Oligoanilines. *J. Am. Chem. Soc.* **132,** 10365-10373.

White, A. F.; Blum, A. E. 1995, Effects of climate on chemical weathring rates in watersheds. *Geochim. Cosmochim. Acta* **59**, 1729-1747.

Xu, J.; Wang. K.; Zu, S.-Z.; Han, B.-H.; Wei, Z. 2010, Hierarchical Nanocomposites of Polyaniline Nanowire Arrays on Graphene Oxide Sheets with Synergistic Effect for Energy Storage. *ACS Nano* **4**, 5019-5026.

KOPRI 극지연구소

Yokoyama, E.; Yoshizaki, I.; Shimaoka, T.; Sone, T.; Kiyota, T.; Furukawa, Y. 2011, Measurements of growth rates of an ice crystal from supercooled heavy water under microgravity conditions: basal face growth rate and tip velocity of a dendrite. *J. Phys. Chem. B* **115**, 8739-8745.

Zhang, S.; Zeng, M.; Xu, W.; Li, J.; Li, J.; Xu, J.; Wang, X. 2013, Polyaniline nanorods dotted on graphene oxide nanosheets as a novel super adsorbent for Cr(Vi). *Dalton Trans.* **42**, 7854-7858.

KOPRI
극지연구소

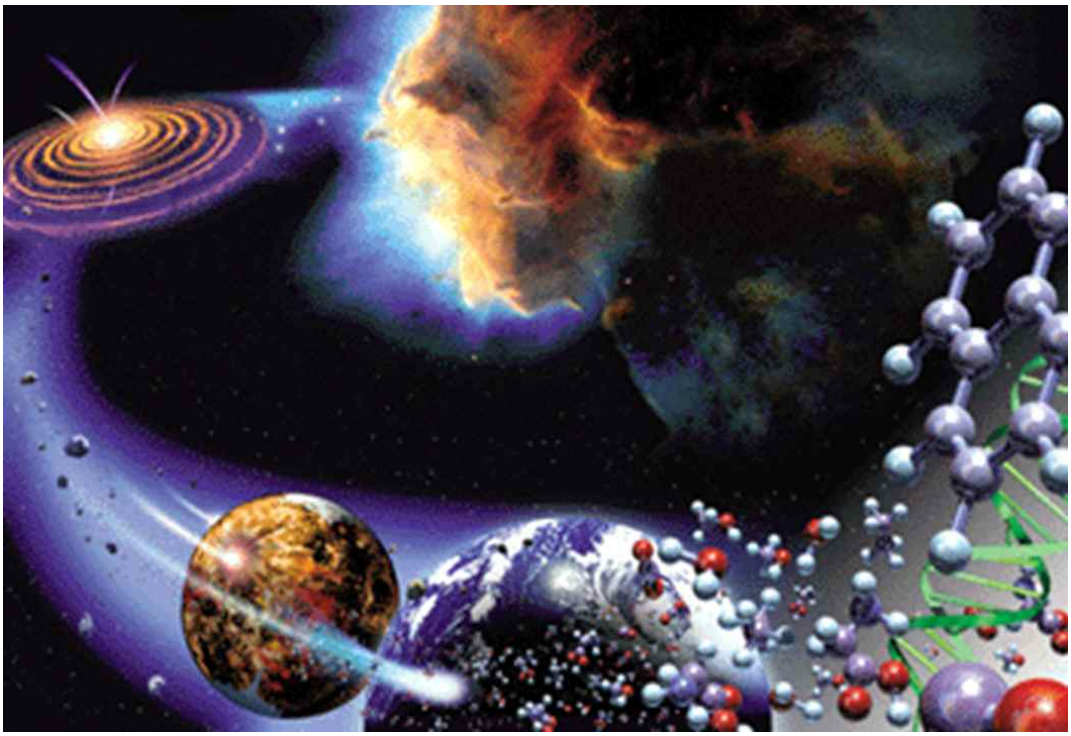

그림 1. 우주의 성간 먼지 구름으로부터 별과 행성이 생성되는 과정을 보여주는 과학적 상상도. 과학자들은 성간 구름을 이루는 얼음 입자에서 간단한 분자들이 합성되고 이들이 오랜 기간 동안 일련의 과정을 거쳐 행성의 구성물을 이루게 된 것으로 유추함.

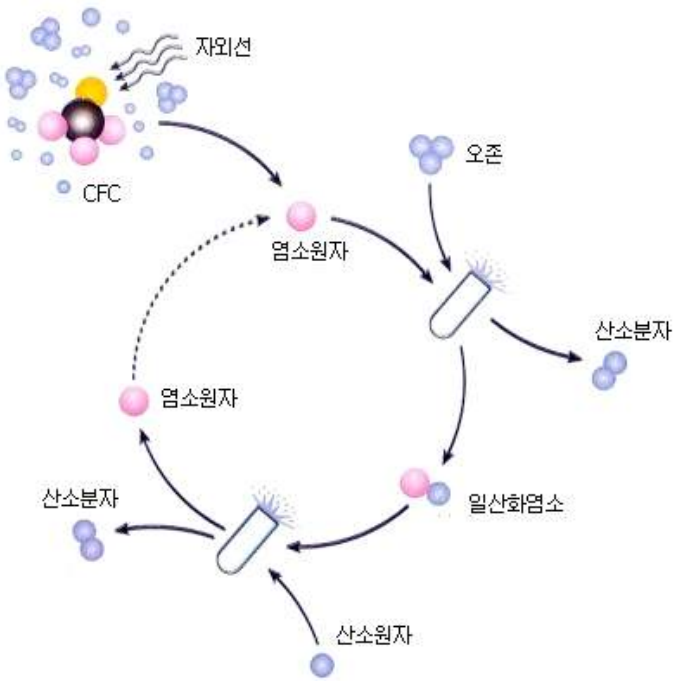

그림 2. 오존 감소 사이클의 개략도.

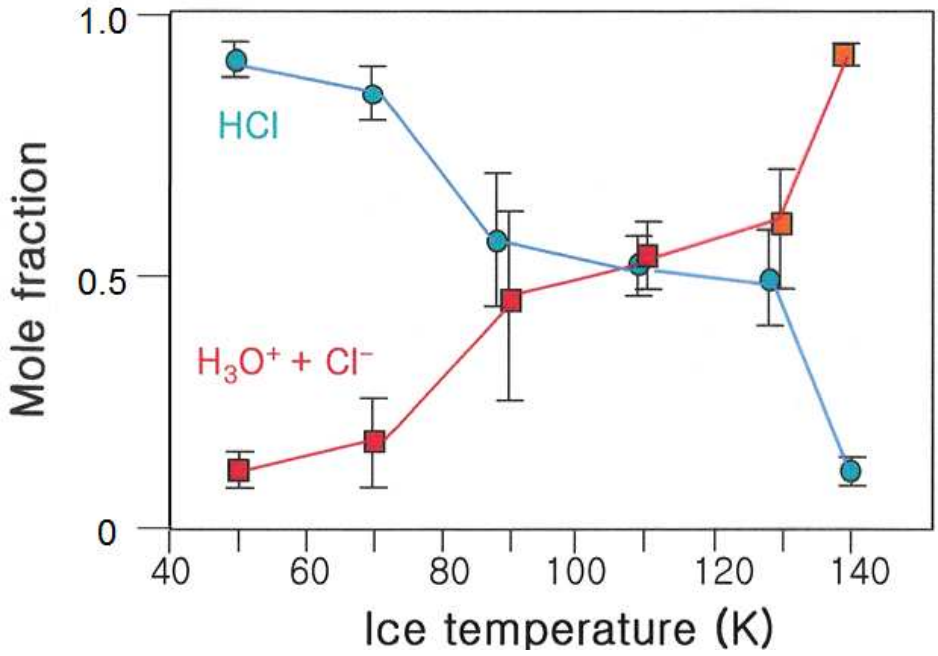

그림 3. 얼음 표면에서 HCl 분자가 온도에 따라 해리되는 정도의 변화를 측정한 자료. 90 K 미만의 저온에서는 HCl의 해리가 불완전하게 되어 약산으로 작용함. (Kang *et al.,* 2000)

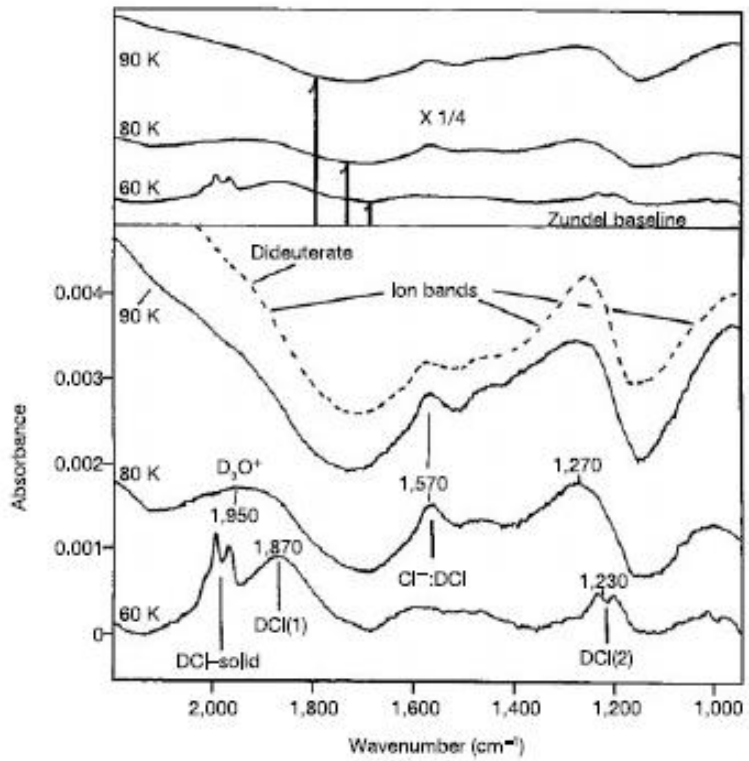

그림 4. DCl 분자가 흡착된 D_2O 얼음 시편의 FT-IR 스펙트럼.

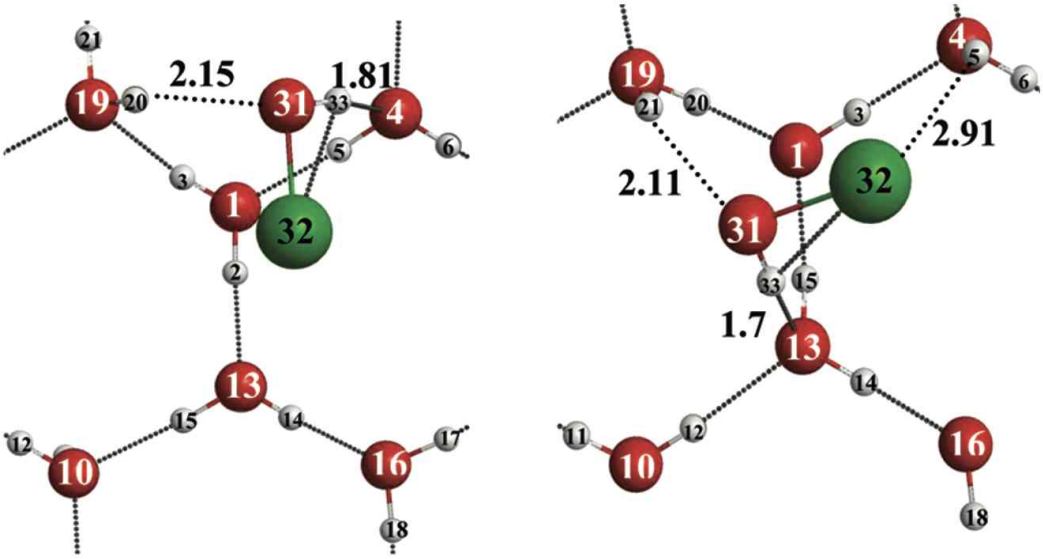

그림 5. HOCl의 얼음 표면 흡착 구조.

KOPRI
극지연구소

그림 6. X-Ray 레이저를 이용한 과냉각수용액의 액체-액체상전이 측정 모식도.

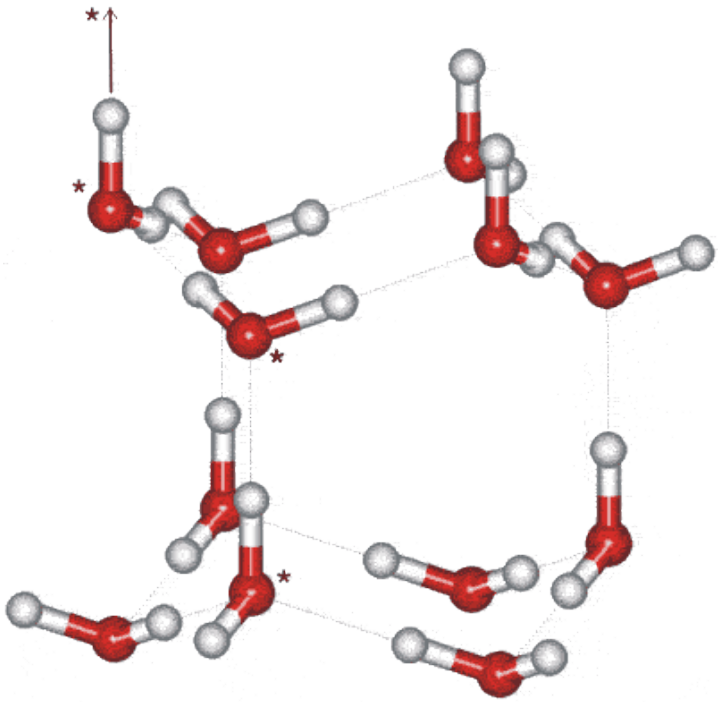

그림 7. I_h 얼음구조의 일부분으로, 원자수준에서의 이해가 필요

그림 8. 지구 환경에 존재하는 얼음 및 환경에 미치는 영향

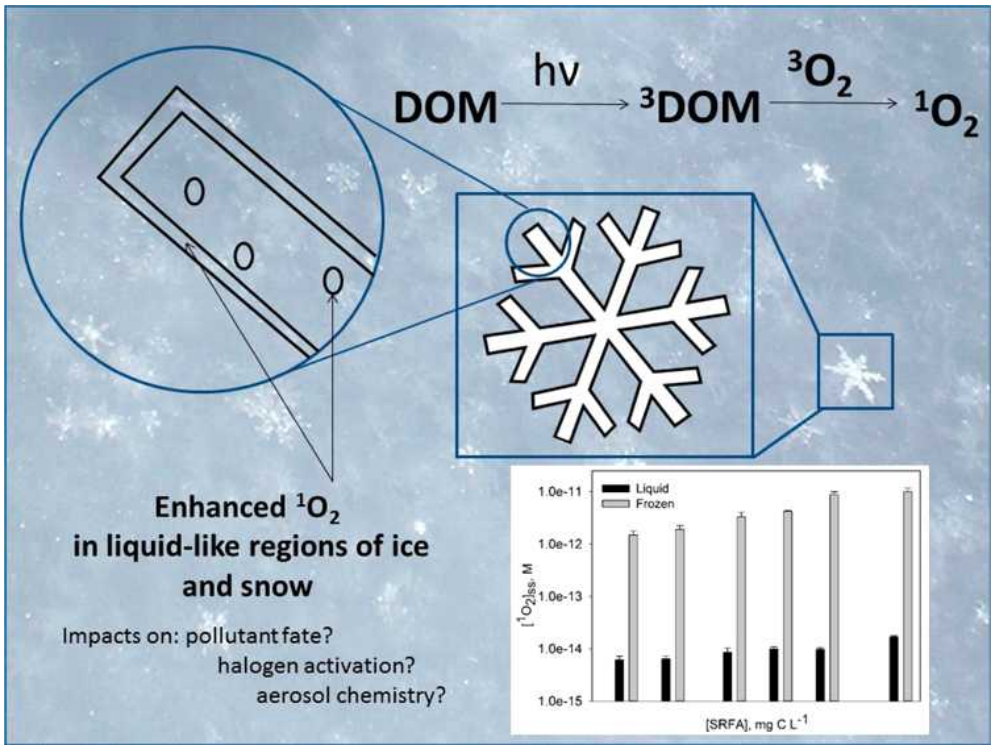

그림 9. 얼음에 존재하는 DOM으로부터 광조사에 따른 singlet oxygen의 생산량이 액상에서보다 현저히 증가함. (Fede *et al.*, 2015)

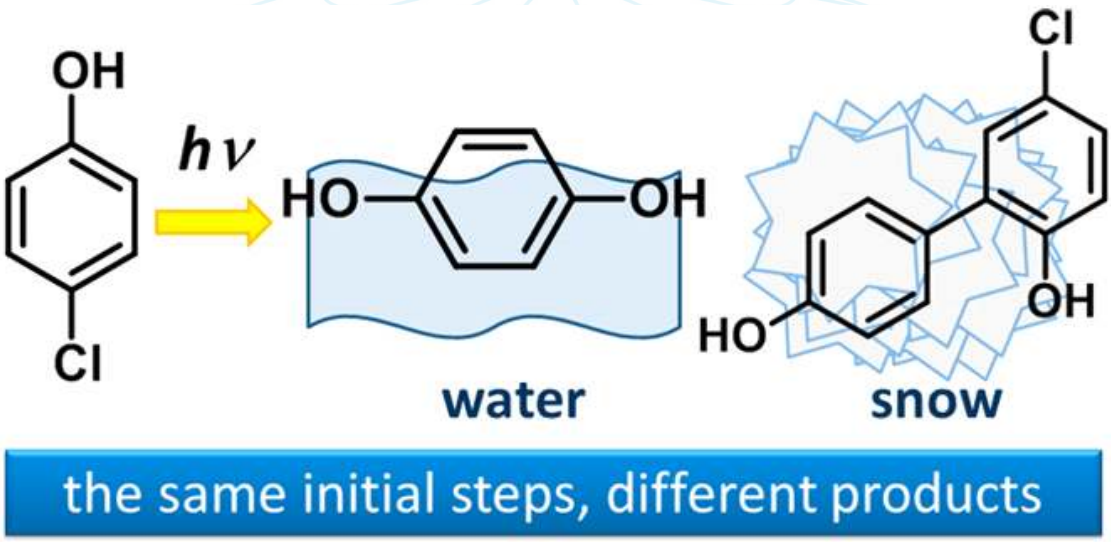

그림 10. 4-염화페놀(4-chlorophenol)이 들어있는 수용액을 자외선으로 조사 시키면 수산화 라디칼에 의해 환경에 흔히 존재하며 독성이 낮은 하이드로퀴논(hydroquinone)이 생성되지만, 얼음상에서는 자외선 조사로 인해 4-염화페놀로부터 페놀 이합체가 형성됨(Klanova *et al.*, 2003)

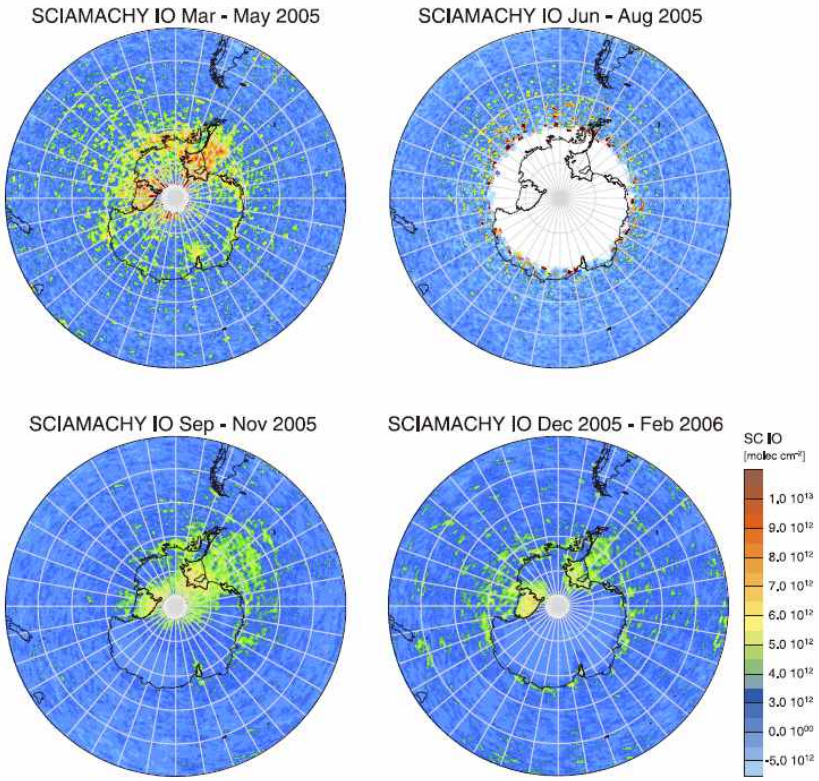

그림 11. 남극 대기에서 관측된 높은 농도의 할로겐 산화물 (Schonhardt *et al.*, 2008).

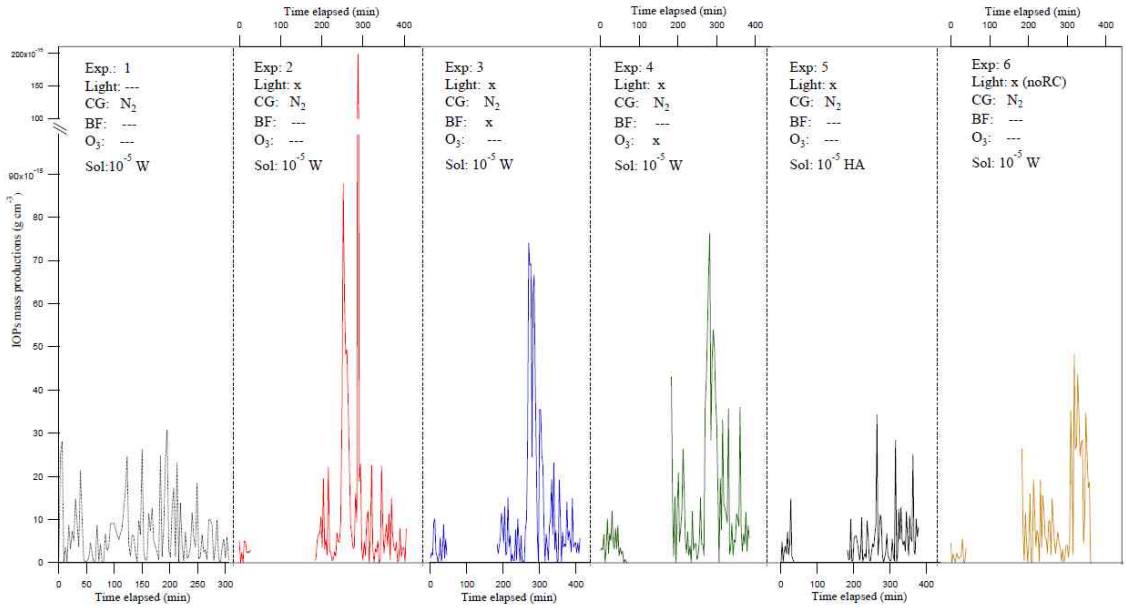

그림 12. 오존이 있는 조건에서 UV를 조사할 때 동결된 iodate 용액으로부터 요오드 산화물 입자 생성됨 (Spolaor *et al.*, 2013).

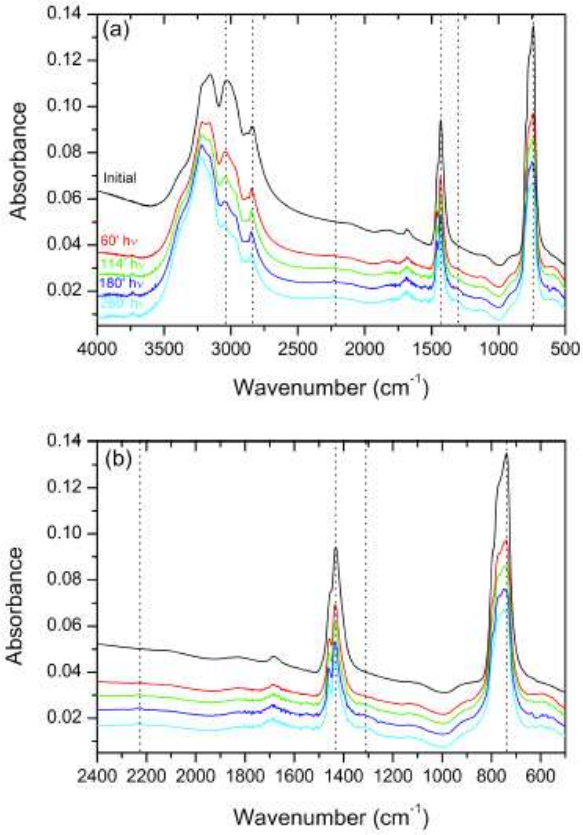

그림 13. Iodate염을 얼릴 때 생성되는 활성 요오드 종 (Gálvez *et al.*, 2016).

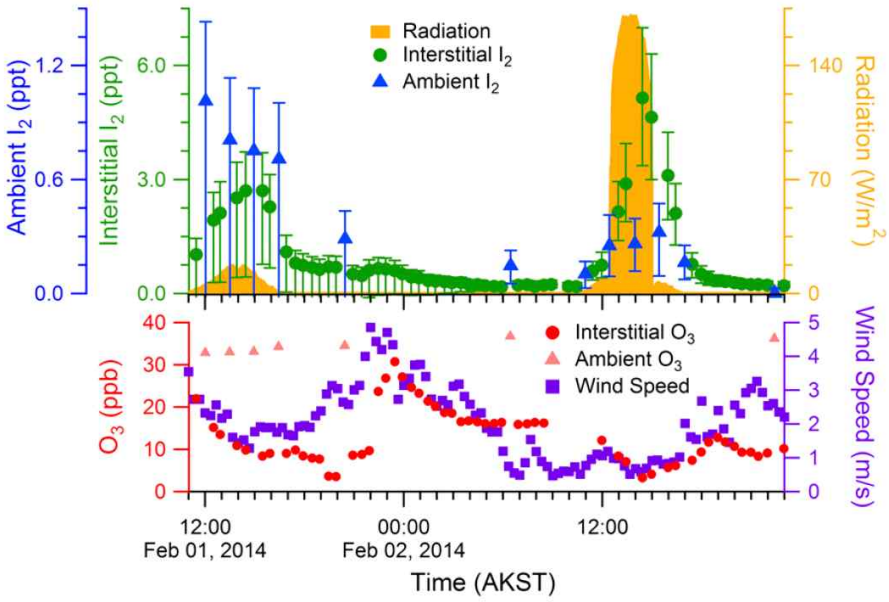

그림 14. 북극 Utqiagvik snowpack에서 측정된 분자 요오드 농도(Raso *et al.*, 2017).

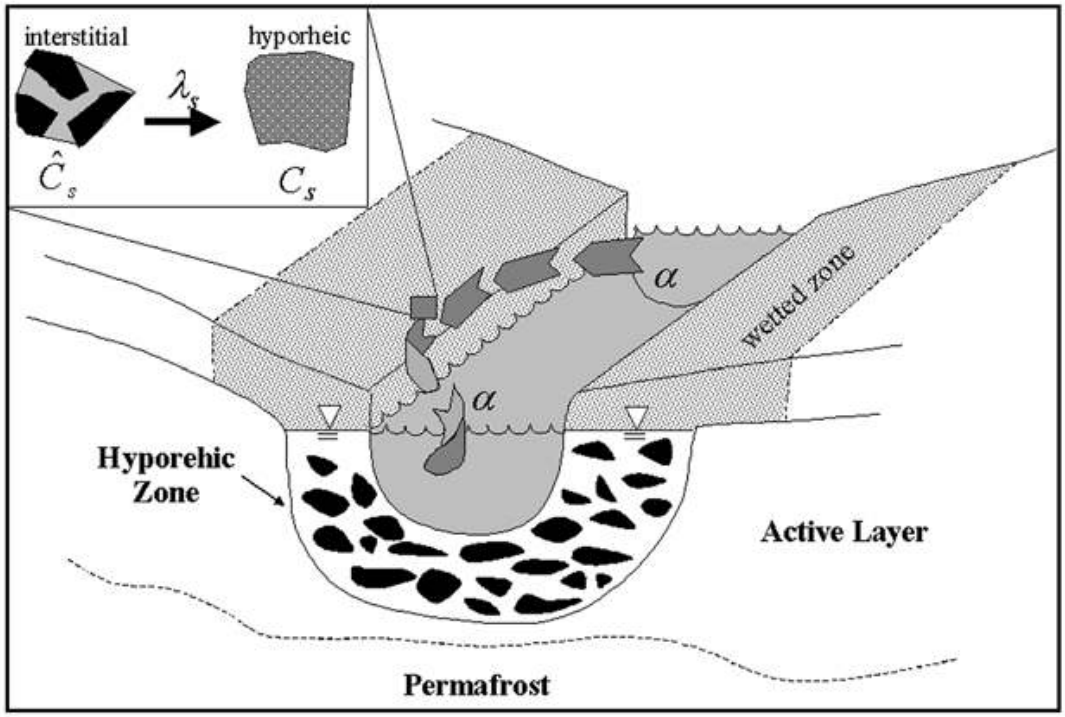

그림 15. 남극 하천의 혼합대에서 일어나는 풍화작용의 개념도(Gooseff *et al.*, 2002).

KOPRI

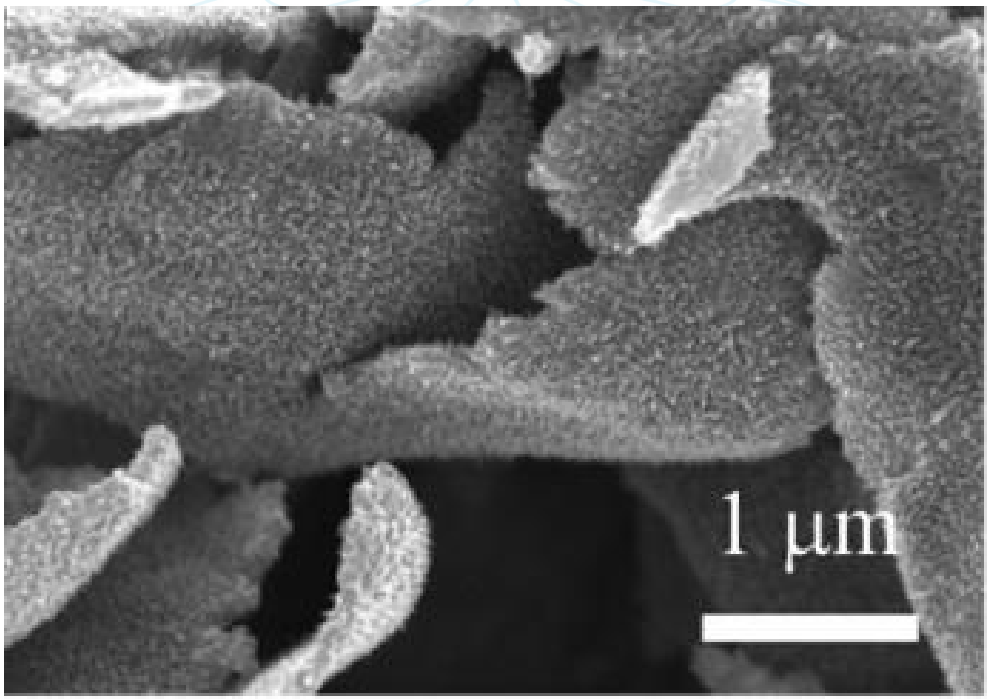

그림 16. 그래핀 산화물을 hard template으로 도입한 전도성고분자-그래핀 산화물 복합물 (Xu *et al.*, 2010).

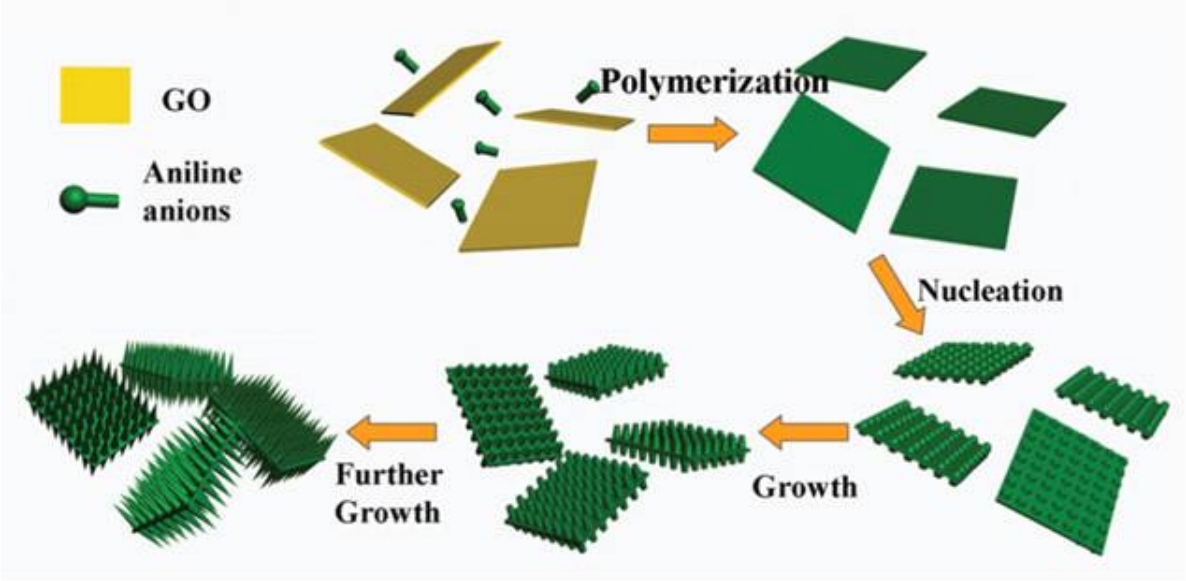

그림 17. 그래핀 산화물을 template으로 이용하여 2차원적인 폴리아닐린을 합성하는 방법 (Zhang *et al.*, 2013).

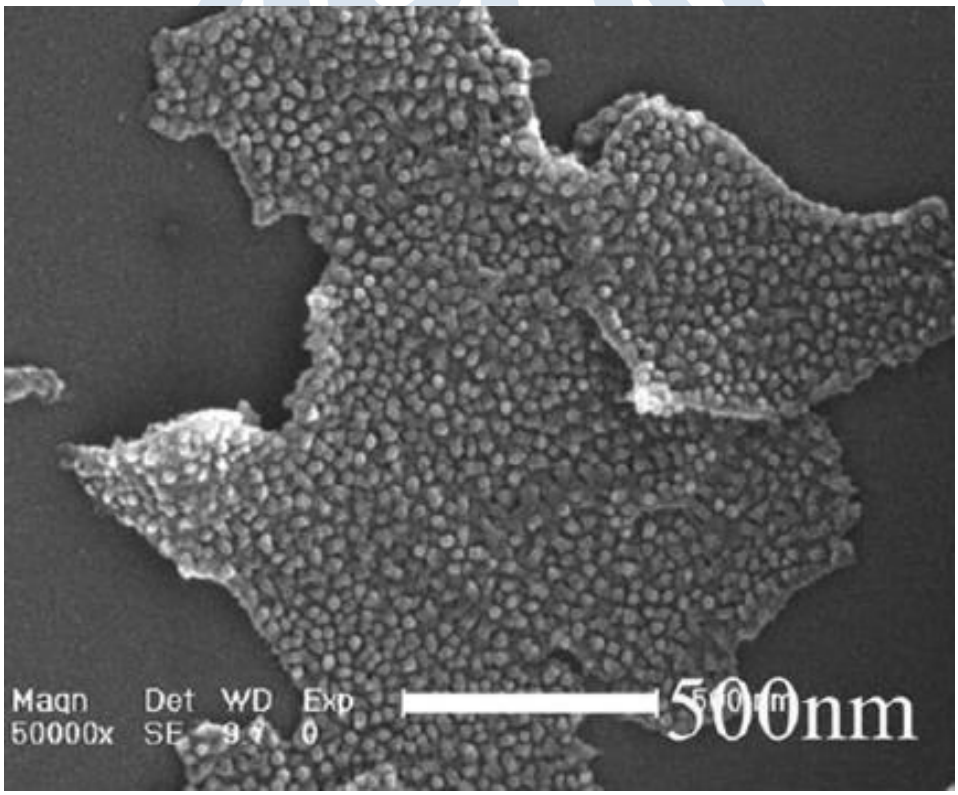

그림 18. 2차원적인 그래핀 산화물-전도성고분자 복합물(Bao *et al.*, 2011)

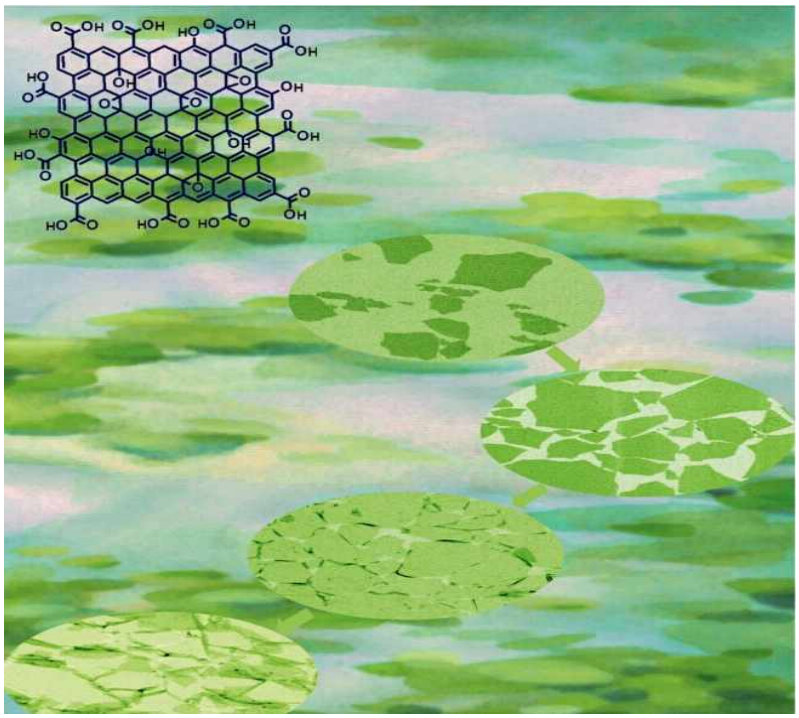

그림 19. Langmuir-Blodgett Assembly 기법을 이용하여 물 위에서 합성한 단층의 그래핀 산화물 (Cote *et al.*, 2009)

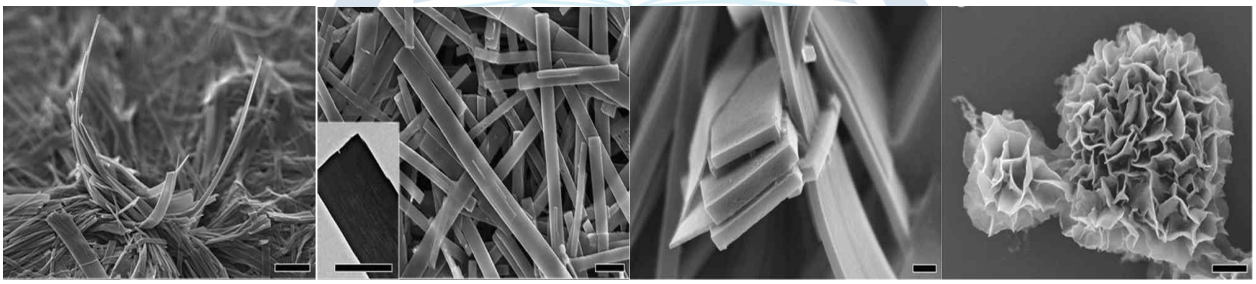

그림 20. 합성 조건을 달리하여 합성한 다양한 형태의 아닐린 중합체(Wang *et al.*, 2010)

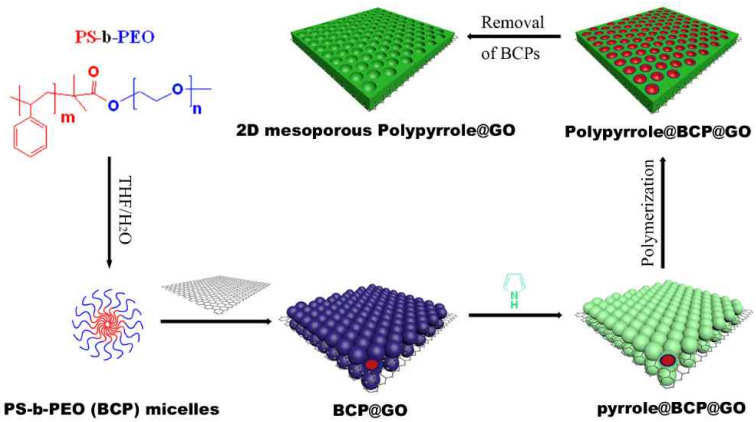

그림 21. 기존에 보고된 2차원 전도성 고분자 합성 방법 (Liu *et al.*, 2015)

그림 22. 얼음에서 일어나는 화학적 자정작용 연구의 필요성 및 응용 기술

KOPRI

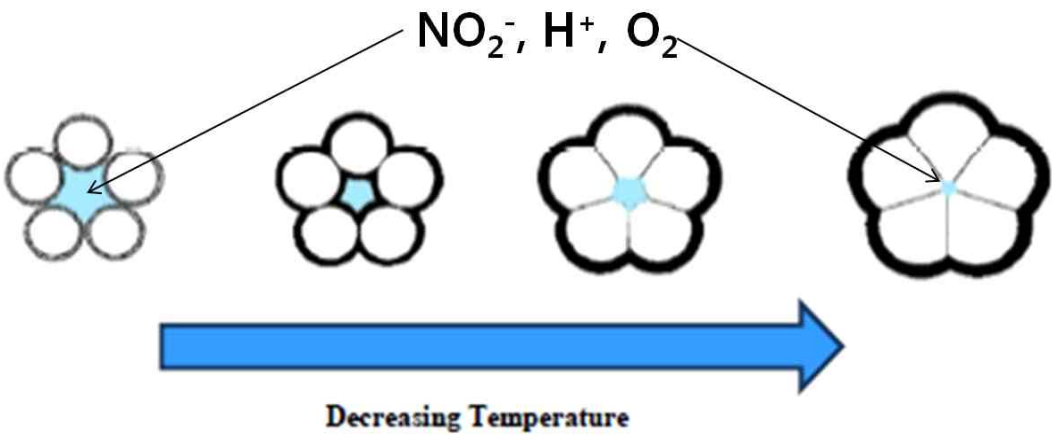

그림 23. 얼음에서 향상된 아질산염의 산화 메커니즘 (동결농축효과)

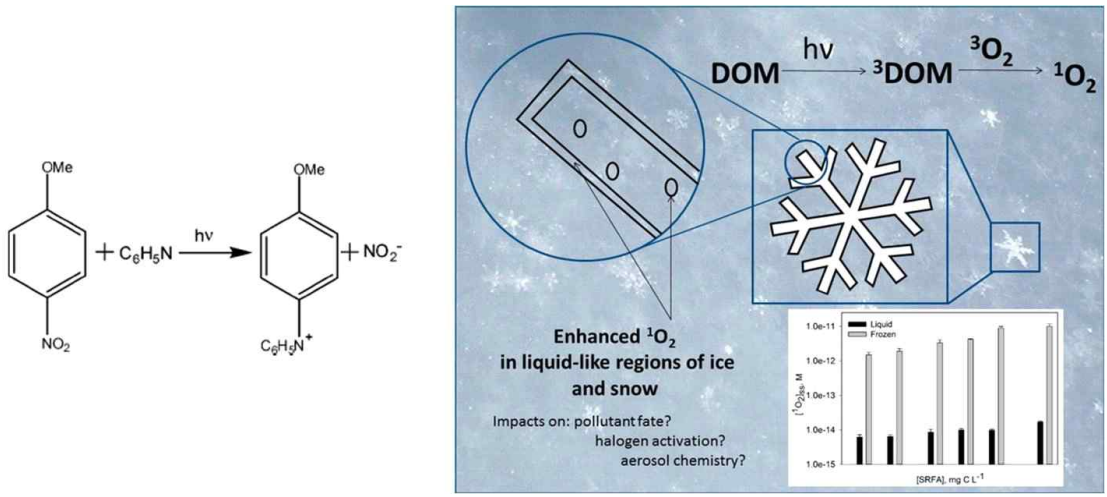

그림 24. 얼음에서 향상된 p-nitroanisole과 pyridine의 광화학 반응 및 용존 자연 유기물의 광화학적 일중항산소 생성

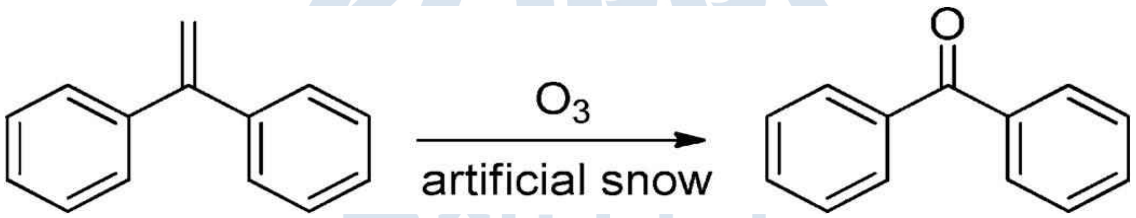

그림 25. 눈 표면에서 1,1-diphenylethylene과 오존의 반응으로 인한 benzophenone의 생성

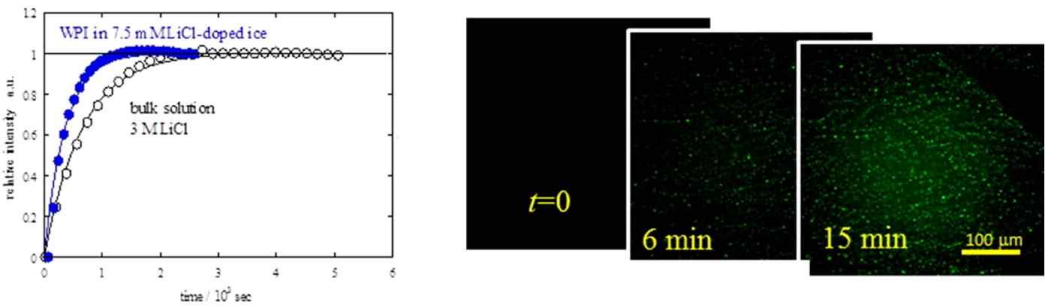

그림 26. 물과 얼음에서 fluorescein diacetate의 가수분해로 생성된 fluorescein의 형광 결과

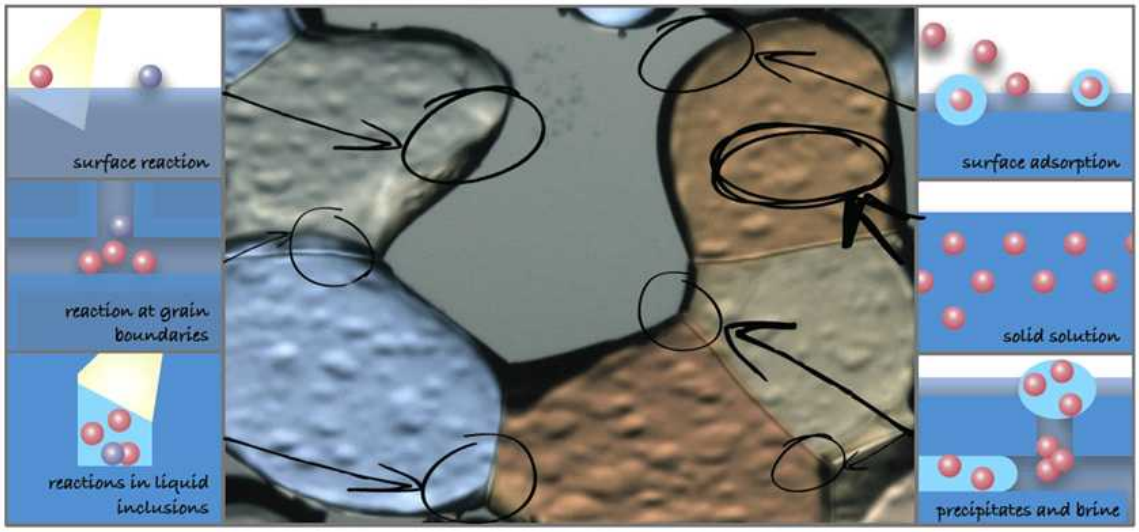

그림 27. 얼음 내 존재하는 불순물과 얼음에서 일어나는 반응의 종류 (Bartels-Rausch *et al.*, 2014).

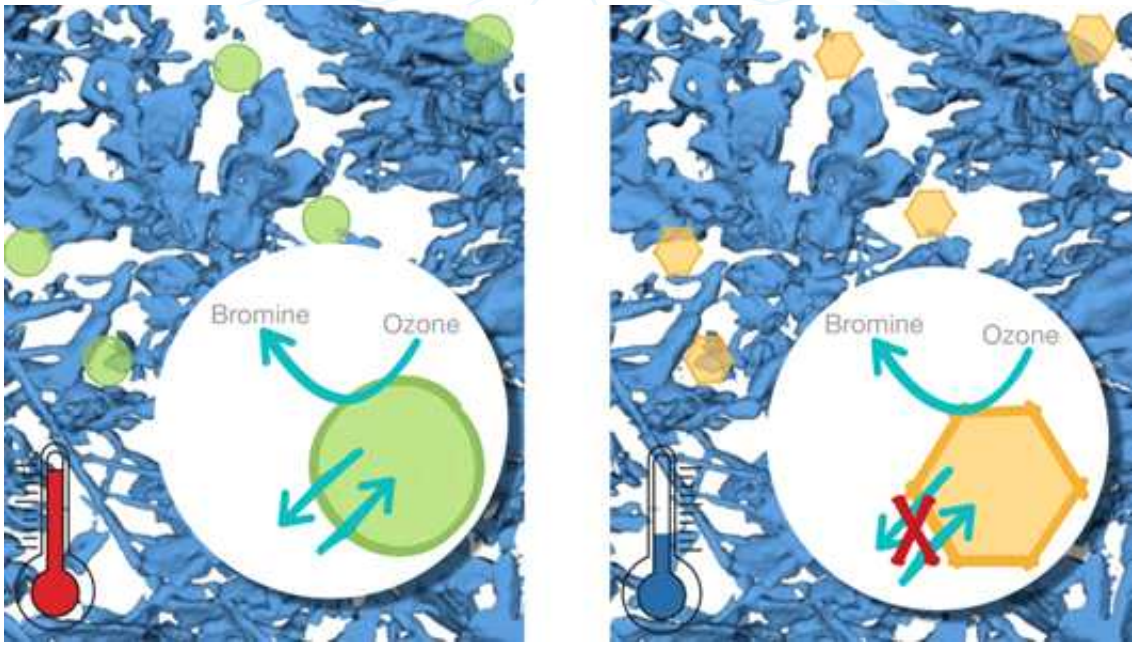

그림 28. 온도 감소에 따라 일어나는 눈 속 에어로졸 입자의 상변화

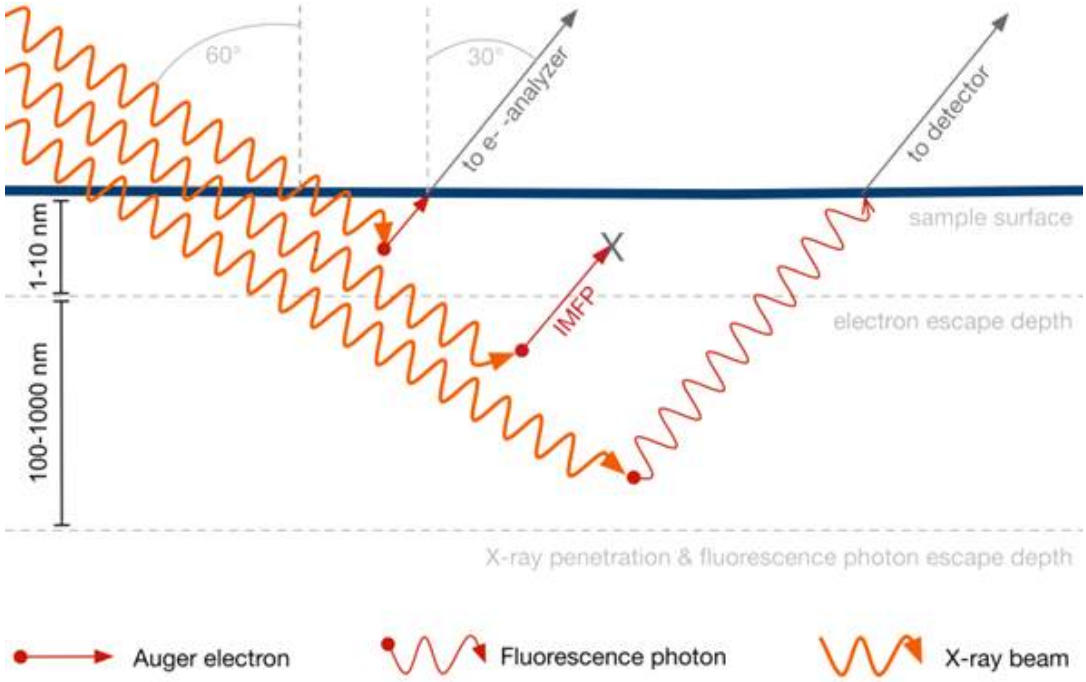

그림 29. 전자 및 형광 NEXAFS 분광법의 모식도

KOPRI

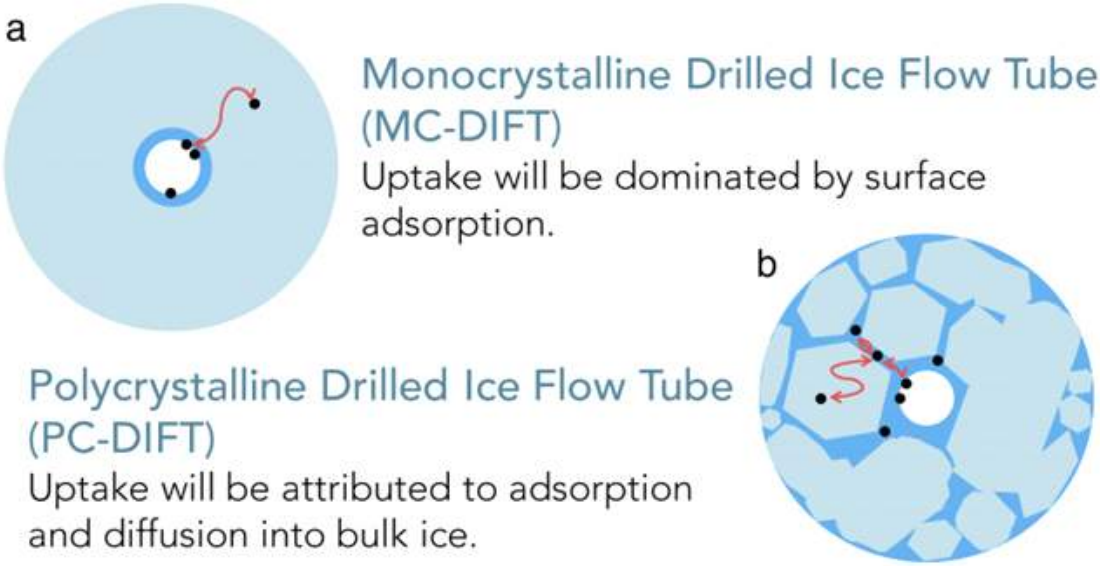

그림 30. 얼음 내 미량 기체 흡착을 연구하기 위해 고안된 DIFT 모식도

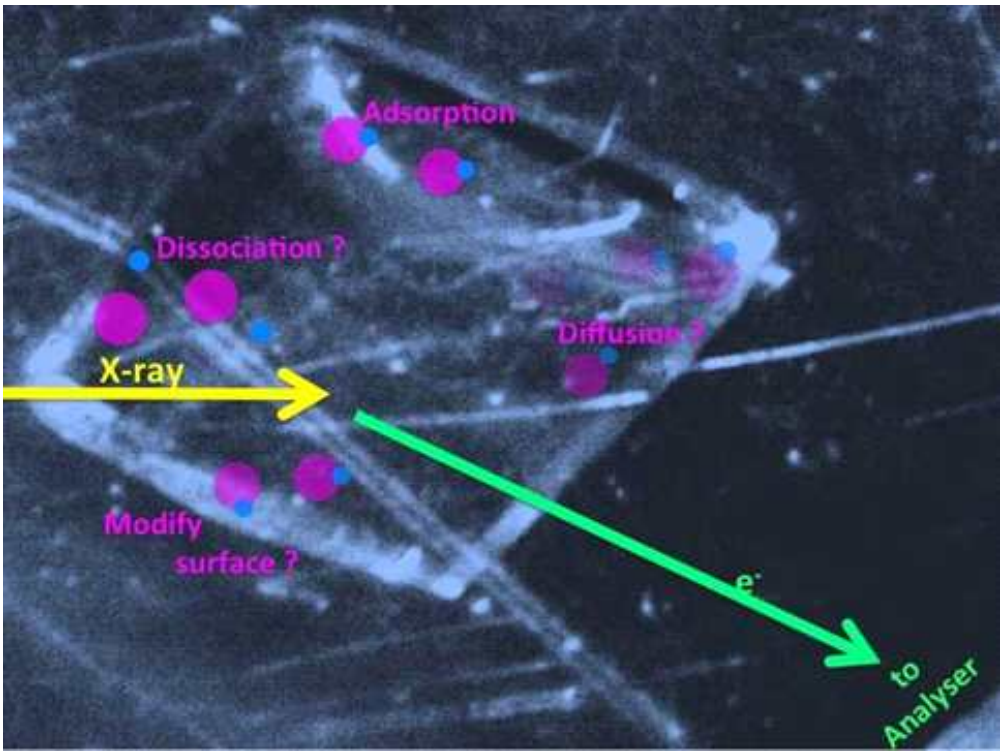

그림 31. 얼음 결정에서 일어날 수 있는 표면에의 흡착, 화학 반응(분리), 확산, 표면 변화 반응.

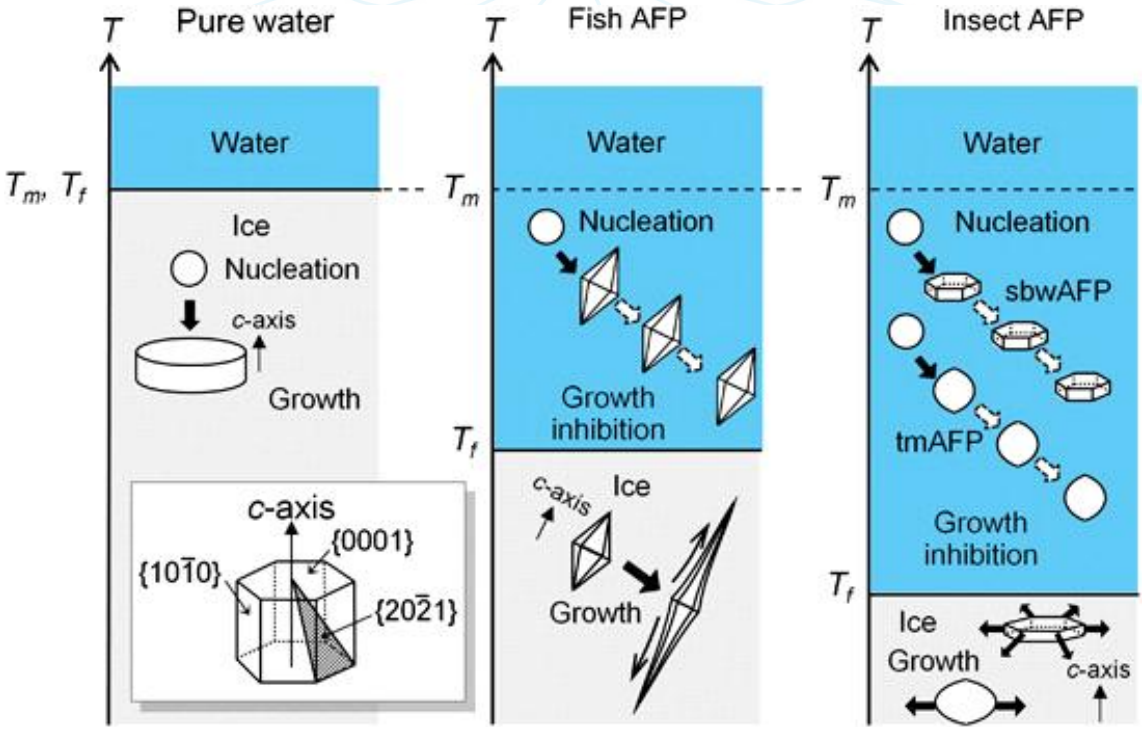

그림 32. 동결방지 단백질에 의한 얼음 성장 억제 메커니즘의 모식도(Nada and Furukawa, 2012).

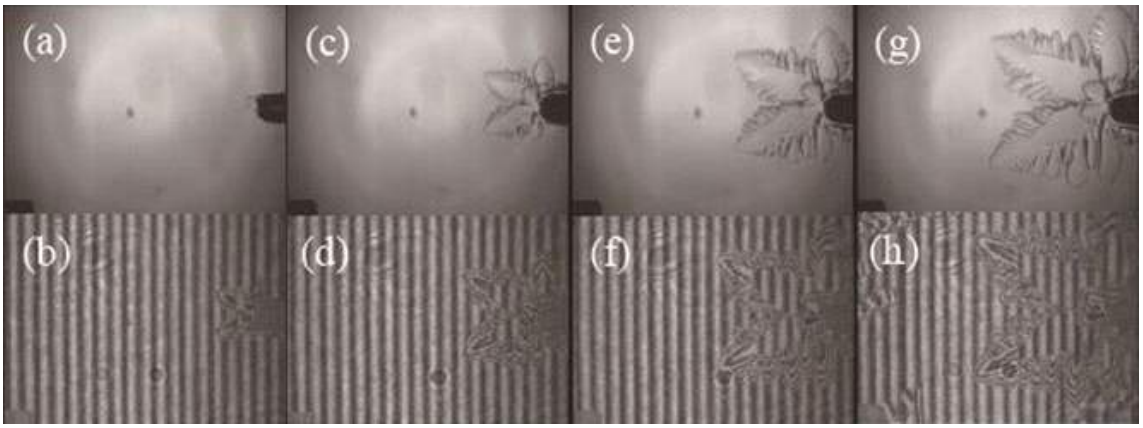

그림 33. 30초 간격으로 관측된 우주 정거장에서의 얼음 결정 성장 과정(Furukawa *et al.*, 2011).

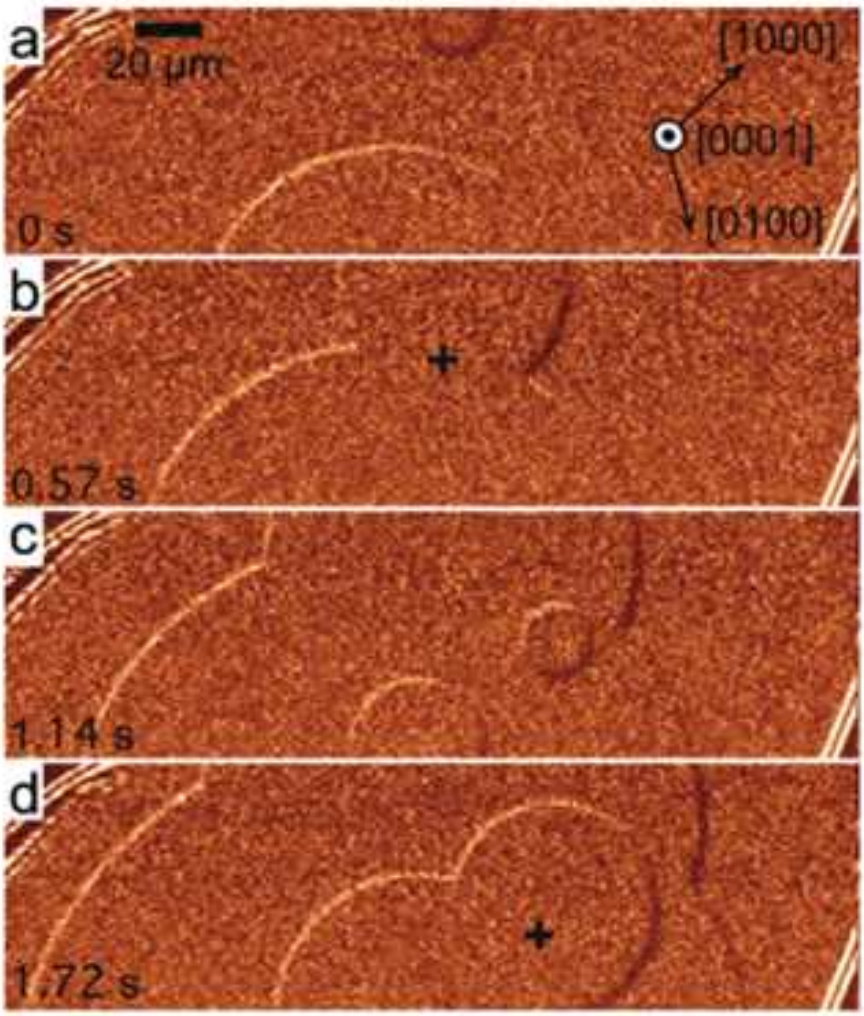

그림 34. 두께가 같은 분자 층이 합쳐질 때 얼음 결정 표면의 현미경 사진(Sazaki *et al.*, 2010).

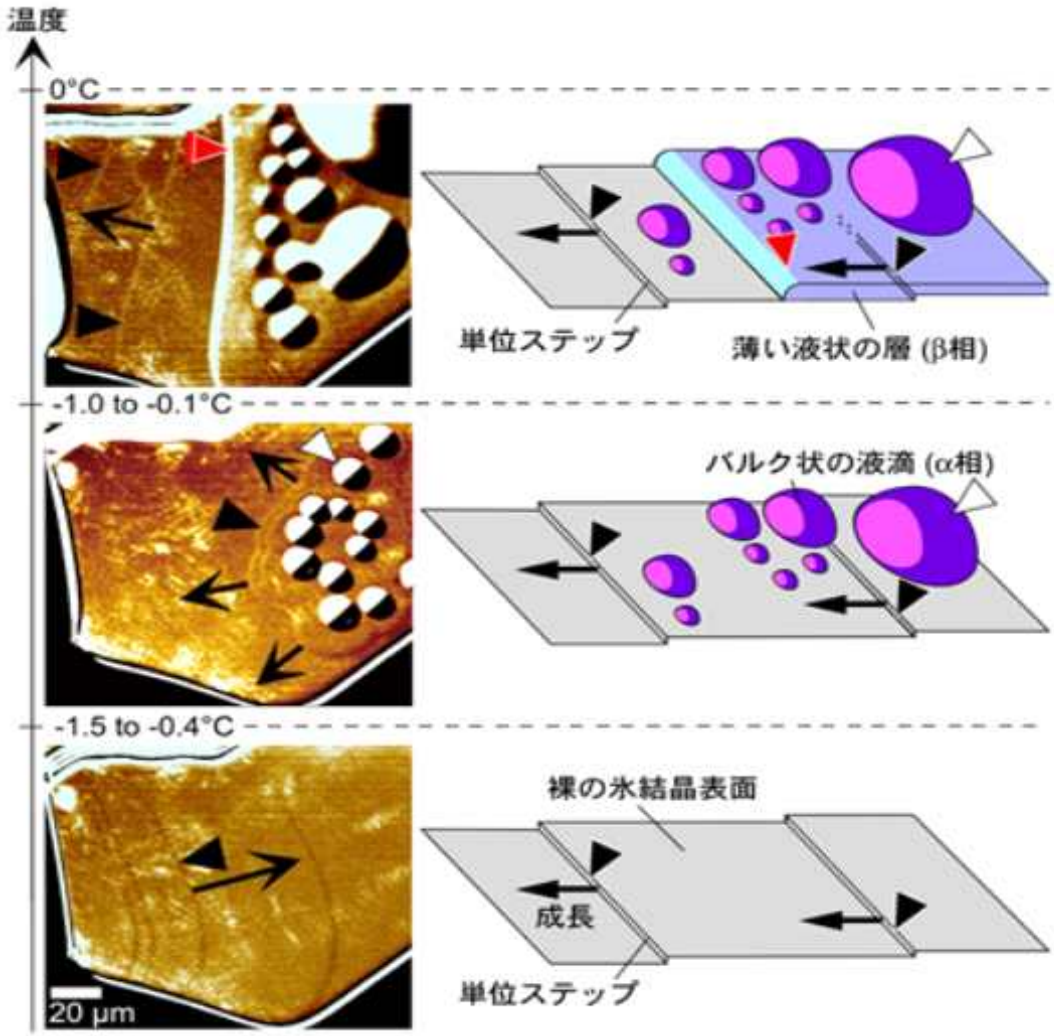

그림 35. 얼음 결정의 기저면에서 생성되는 두 종류의 액체상 표면 (Sazaki *et al.*, 2012)

제 3 장

연구개발수행 내용 및 결과

제 1 절. 얼음화학 현상에 양자역학 및 동력학적 접근

최철호, 호르바텐코예브헨, 백용수, 카힝가, 술토노브라흐맛, 스벳라나쇼스탁, 박우진

경북대학교 화학과

1. 서론

얼음 표면상에서 일어나는 화학적 현상들에 대해 원자수준적 이해를 위한 이론연구를 수행한다. 얼음표면의 올바른 모델을 제시하고 그를 바탕으로 표면 흡착물의 정확한 화학적 흡착구조, 흡착 에너지, 표면 화학반응 메커니즘 및 동력학적 측면들을 규명한다. 또한 표면 온도, 산도 및 빛에너지의 흡수와 같은 외부적 요소에 따른 표면 화학반응들의 변화를 연구한다. 얼음표면 촉매 현상과 그에 따른 화학적 변화과정에 대한 연구는 지표상 물질 순환, 태양에너지 흡수와 관련된 기체상 물질변화들의 근원적인 이해를 높이는데 기여할 것이다.

우리가 알고 있는 많은 화학반응들은 물의 액체 상태를 매질로 하여 이루어지고 있다. 그러나 지구를 제외한 우주에서는 물이 주로 얼음의 형태로 존재한다. 그러므로 우주에서 이루어지는 분자의 진화는(작은 분자에서 더욱 복잡한 분자의 생성) 얼음이라는 매체를 통해 이루어진다고 생각되어진다. 또한 지구상에서도 온도가 낮은 지역 또는 성층권에서 이루어지는 화학 반응들은 눈이나 얼음의 존재와 밀접한 관련이 있다. 특히 남극에서 발견된 오존 구멍과 대기의 화합물 조성의 결정에 중요한 역할을 한다는 것이 알려지면서 얼음표면의 특성과 그 위에서 일어나는 화학반응에 대한 관심은 커지고 있다. 얼음표면 반응의 중요성은 지구에서 일어나는 많은 화학반응에서역시 살펴볼 수 있다. 지표의 약 10%는 항상 얼음과 눈으로 덮여있고 이들은 대기의 조성을 변화시키고 열적 균형을 이루는데 중요한 역할을 하고 있다. 잘 알려진 바와 같이 Molina 와 Rowland는 염불화탄소(chlorofhluorocarbons) 화합물들이 자외선에 의해 분해되어 염소 라디칼이 생성되고 이것이 오존을 산소로 변화시킨다고 제안하였다. 그러나 이렇게 생성된 염소 라디칼이 다시 기체반응에 비해 상대적로 반응성이 떨어지는 염산 (HCl)과 $ClONO_2$ 의 형태로 저장된다는 것이 다시 밝혀졌다. 그러나 1985년도에 급격하게 증가한 오존 구멍의 크기는 이러한 상대적으로 반응성이 약한 기체상 반응으로만 설명하기에는 지나치게 광범위 하였다. 이러한 딜레마를 해결하기 위해 Solomon등은 남극의 겨울동안 성층권에서는 얼음 조각을 포함한 다양한 공기부유 조각들이 생긴다고 주장하며 다음과 같은 반응이 그 표면에서 일어난다고 제안하였다.

$ClONO_2$ + HCl --> HNO_3+Cl_2

이 반응은 HNO_3를 생성하고 또한 중요한 Cl_2를 생성하는데 이는 태양빛에 의해 Cl 라디칼이 되고 이것이 오존감소 사이클을 가동시킨다고 제안되었다. 그 이후 많은 후속연구들이 이루어졌는데 여전히 위 반응이 분자수주에서의 메커니즘에 대한 명확한 실험 및 이론적 일치를 이루지 못하고 있다. 또한 이러한 반응이 일어날 때에 얼음의 구체적인 역할이 무엇인지 역시 여전히 불분명하다.

금속표면이나 염의 표면에서의 반응과 비교하여 분자수준의 이해도 측면에서 살펴보면 이러한 가스들과 얼음표면의 상호작용은 많은 부분에 있어서 여전히 연구해야 할 영역들이 많이 남아있다. 먼저 대기 중에서 얼음표면은 증발과 응축이 일어나고 있는 동적인 상황이다. 많은 경우에 있어서 얼음표면에 물 분자의 흡착보다 기체 분자들의 흡착반응의 반응열이 비슷하거나 더 크다. 이는 표면 흡착반응을 통해 얼음표면은 다양한 재구성 혹은 변화가 일어날 수 있다는 것을 알려준다. 또한 얼음표면은 얼음 내부에 비해 상당한 무질서함이 존재한다. 이러한 이유에 의해서 금속과 같은 표면과 비교하여 얼음표면 화학반응의 엄밀한 정의를 힘들게 만들고 있다.

얼음 표면에서의 화학 반응은 위에서 언급한 것과 같이 다양하고 중요한 파급효과를 가지고 있으나 얼음 화학을 연구하는 그룹은 세계적으로 제한적이다. 이와 상보적인 이론적 연구는 더더욱 미미하여 추가적인 노력들이 요구된다. 그림 1처럼 얼음 구조의 특수성에 기인하여 얼음 표면 흡착 site가 그림 2처럼 다양하다. 이러한 반응 환경에서 이론적 연구는 원자수준에서의 반응 메커니즘 및 동력학적 측면을 연구할 수 있는 유일한 방법론이다. 그러므로 이론은 실험에서 접근하기 힘든 영역들에 대한 중요한 상보적 정보를 제공할 수 있어 기존 실험결과의 올바른 해석과 더 나아가 새로운 실험 방향을 제시 한다.

KOPRI 극지연구소

2. 연구개발수행 내용 및 결과

○ Protonated Hydroxylamine의 얼음표면 흡착 안정도 연구

Protonated Hydroxylamine(PHA)는 얼음상에서 다양한 화학적 특성을 띄고 있으나 PHA의 얼음 표면 흡착 구조에 대한 연구는 미흡하다. 또한, 얼음표면과 얼음 내부와의 상대적 안정도에 대한 연구역시 존재하지 않는다. 본 연구는 먼저 PHA가 다양한 얼음 표면 흡착 site에서 어떠한 결합 구조를 이루는지 그리고 얼마만큼 강한 흡착에너지를 가지는지를 살펴보았다. 본 연구를 하기 전에 PHA는 일반적으로 수용액에서 질소원자가 protonation된다고 알려져 있으나 얼음 표면 흡착연구에서는 질소 및 산소원자가 protonation되는 구조를 각각 연구하였다. 그림 3과 같이 특히 일반적으로 불리한 산소 protonation이 오히려 얼음 표면에서 더 강한 흡착강도를 보임을 알게 되었다. 이는 특히 얼음 표면이라는 특별한 환경에서는 일반적으로 선호되지 않는 구조가 더 안정해 질 수 있음을 보인 예이다.

○ Sulfurous acid가 sulfuric acid로의 변환과정에 오존과 과산화수소수의 역할 연구

최근 본 실험실에는 얼음 표면 상에서 아래와 같은 기체상 SO_2의 반응 연구를 수행하였다.

SO_2 + H_2O on ICE surface -----> H_2SO_3

이 연구결과 얼음 표면상에서는 기체상 SO_2가 쉽게 흡착이 되고 얼음 표면에 존재하는 물분자에 의해 쉽게 H_2SO_3가 될 수 있음을 알게 되었다. 그러므로 얼음표면에 H_2SO_3가 존재할 수 있음을 보였고 이는 다시 얼음 속에 존재하는 H_2O_2에 의해 H_2SO_4가 될 수 있는 가능성을 연구하였다.

$$H_2SO_3 + H_2O_2 \text{ on ICE surface } \text{-----> } H_2SO_4$$

이 결과 다양한 stepwise와 concerted 메커니즘들이 있음을 밝혔고 일반적으로 H_2O_2만으로 이루어지는 H_2SO_3산화는 ~ 40 kcal/mol 이상의 큰 에너지가 필요함을 보인다(그림 4). 그림 4의 첫 번째 경로는 H가 H_2O_2에서 H_2SO_3 이동하는 동시에 H_2O_2의 OH가 S 원자로 친핵 공격을 하는 상황이다. 먼저 이동한 H는 H_2SO_3 의 OH와 결합하여 물분자를 형성하여 제거되는 결과를 주고 동시에 H_2O_2의 OH는 S에 결합하여 H_2SO_4를 형성함을 볼 수 있다.

그러나 이 경로는 반응 활성화 에너지 측면에서 보면 49.52 kcal/mol를 보여 쉽게 기체상에서 일어나기 힘들을 보이고 이고 있다. 그림 4의 오른쪽 반응 경로는 추가로 첨가한 여분의 물분자가 전체적인 반응 활성화를 33.78 kcal/mol로 낮추고 있음이 보인다. 즉, 추가된 물분자가 촉매 역할을 하고 있음을 알 수 있다. 그러나 여전히 높은 반응 활성화 에너지를 보여 기체상에서 여분의 수분이 존재하여도 이 반응이 쉽게 가기는 힘듦을 알 수 있다.

그러나 물 분자 하나의 도움을 받게 되면 그림 5와 같이 이 값이 6 kcal/mol로 낮춰져 물분자의 강한 촉매작용을 밝혔다. 또한, HSO_3^-의 이온의 경우 역시 비슷한 정도의 낮은 활성화 에너지가 필요함을 보였고 이 두 과정은 모두 concerted 경로임을 밝혔다. 이에 반하여 stepwise 반응은 일반적으로 hydroperoxyl (-O-O-H)기를 가지는 중간체를 형성하고 이는 H_2O_2에 의한 친핵공격의 결과이다.

모든 메커니즘에서 H_2SO_4가 형성되면 60 kcal/mol 이상의 발열이 됨을 보여 산이 만들어지는 과정이 열역학적으로 큰 안정도를 줌을 보이고 또한, 이 열반응들은 특히 저온에서 빛의 도움 없이도 일어날 수 있음을 최초로 밝혀 저온 암반응의 가능성을 보여준다.

○ 산소 분자의 얼음 표면 흡착과 iodide 흡착의 상관관계연구

저온에서 I^-에 의한 I_2 및 H_2O_2 생성 반응을 양자역학적인 방법론들을 동원하여 이론적으로 연구 하였다. 지금까지는 IO_2^- 이온의 생성이 중요한 중간체로 알려져 왔으나 이는 전체반응의 강한 pH 의존성을 설명하기 힘들었다. 본 연구 결과 IO_2H라는 새로운 분자단위 중간체가 생김을 최초로 밝혔다(그림 6).

이 중간체는 왜 pH가 낮을 때 반응이 빨라지는 이유를 설명할 수 있다. 즉, protonation이 되면 안정한 분자형태의 생성물이 발생함음 처음 보였다. 또한, 기존 연구과는 다르게 이 중간체의 여기상태 계산결과가 실험값과 더 부합됨을 보여 본 연구에서 주장하는 중간체의 존재가능성을 높였다. 이 중간체는 그림 6처럼 특히 빛을 받아 여기 되었을 때 훨씬 반응이 빨라지는데 이는 실험결과와 완전히 부합되는 내용이다. 그림 6은 이 중간체가 여기 되었을 때 일어날 수 있는 반응의 경로를 나타내고 있고 모든 여기상태에서 반응이 빨리 진행함을 보여준다.

특히, 기존 모델에서는 설명하기 힘들었던 전하전달도 IO_2H에서 I^- --> O_2 로의 전자

전달이 발생함을 예측하였다. 이는 중성 I가 생성되는 메커니즘을 밝힌 것이고 특히 전자적으로 singlet 상태에서 더 잘 생성됨을 보여 명반응시 반응 활성화가 되는 이유를 밝혔다. 이렇게 생성된 라디칼 I는 다시 I^-와 만나 I_2^-를 형성하고 disproportion 반응으로 I_3^-를 형성한다.

라디칼 I 생성 시 동시에 라디칼 O_2H가 생성되는데 이 라디칼이 protonation이 되는 순간 H_2O_2의 형성이 가능함을 최초로 보였다. 저온에서 I^-의 반응이 일어나는데 이러한 환경은 얼음속의 환경이라 할 수 있고 본 연구의 결과는 얼음속 H_2O_2의 축적이유를 설명할 수 있는 최초의 연구 결과이다.

3. 연구개발결과의 활용계획

가. 학술적 파급효과

- 원자수준에서의 얼음 표면화학 반응 이해를 통한 얼음촉매현상 정립
- 본 과제에서 적용할 비단열 동력학을 이용한 얼음 표면에서의 반응 분석은 최초로 시도되어 미개척 분야에 대한 새로운 기준 제시
- 국제 학술지 게재를 통한 학문적 위상정립

나. 경제적 파급효과

- 얼음 표면에서 일어나는 반응들을 체계화함으로써 대기, 환경등의 연구개발에 토대 구축
- 얼음 표면 화학반응들의 특성을 활용하여 신물질 개발에 응용
- 극지방 혹은 성간에서 일어나는 화학반응들의 세밀한 이해를 바탕으로 기후변화, 지구전체적 물질의 순환 및 변화등에 대한 정보를 제공하여 다양한 변화에 대해 능동적으로 대처

KOPRI 극지연구소

3. 참고문헌

(1) Petrenko, V. F. Whitworth, R. W. Physics of Ice. Oxford university: Oxford, 1999.

(2) Barrie, L. A.; Plat, U. Arctic tropospheric chemistry: an overview. *Tellus* 1997, 49B, 450-454.

(3) Molina, M. J. Tso, T-L. Molina, L. T. Wang, F. C.-Y. Antarctic stratospheric chemistry of chlorine nitrate, hydrogen chloride, and ice: release of active chlorine. *Science* 1987, 238, 1253-1257.

(4) Greenberg, J. M. Cosmic dust and our origins. *Surface Sci.* 2002, 500, 793-822.

(5) Devlin, J. P.; Uras, N.; Sadlej, J ; Buch, V. Discrete stages in the solvation and ionization of hydrogen chloride adsorbed on ice particles. *Nature* 2002, 487, 269-271.

(6) Romero Lejonthun, L. S.; Andersson, P. U.; Hallquist, M.; Thomson, E. S.; Pettersson, J. B. Interactions of N2O5 and Related Nitrogen Oxides with Ice Surfaces: Desorption Kinetics and Collision Dynamics. *J. Phys. Chem. B* 2014, 118, 13427-13434.

(7) Cyriac, J.; Pradeep, T.; Kang, H.; Souda, R.; Cooks, R. G. Low-Energy Ionic Collisions at Molecular Solids. *Chem. Rev.* 2012, 112, 5356-5411.

(8) K. A. Pratt, *Trends in Chemistry*, 2019, 1, 545 - 548.

(9) U. S. Bhatt, D. A. Walker, J. E. Walsh *et al.*,, Implications of Arctic Sea Ice Decline for the Earth System, 2014, **39,** 57 - 89.

(10) A. R. W. Raso, K. D. Custard, N. W. May, D. Tanner, M. K. Newburn, L. Walker, R. J. Moore, L. G. Huey, L. Alexander, P. B. Shepson and K. A. Pratt, *Proc. Natl. Acad. Sci. U.S.A.,* 2017, 114, 10053 - 10058.

(11) K. D. Custard, A. Raso, P. B. Shepson and R. M. Staebler, Production and Release of Molecular Bromine and Chlorine from the Arctic Coastal Snowpack, *ACS Earth and Space Chem., 1, 142 - 151,* 2017.

(12) L. A. Barrie, J. W. Bottenheim, R. C. Schnell, P. J. Crutzen and R. A. Rasmussen, *Nature*, 1988, **334**, 138 - 141.

(13) A. Sigg and A. Neftel, *Nature*, 1991, **351**, 557 - 559.

(14) J.-F. Lamarque, J. R. McConnell, D. T. Shindell, J. J. Orlando and G. S. Tyndall, *Geophys. Res. Lett.*, 2011, **38**, n/a - n/a.

(15) C. A. Cuevas, N. Maffezzoli, J. P. Corella, A. Spolaor, P. Vallelonga, H. A. Kjær, M. Simonsen, M. Winstrup, B. Vinther, C. Horvat, R. P. Fernandez, D. Kinnison, J.-F. Lamarque, C. Barbante and A. Saiz-Lopez, *Nature Communications*, 2018, **9**, 1 - 6.

(16) K. Kim, A. Yabushita, M. Okumura, A. Saiz-Lopez, C. A. Cuevas, C. S. Blaszczak-Boxe, D. W. Min, H.-I. Yoon and W. Choi, *Environ. Sci. Technol.*, 2016, **50**, 1280 - 1287.

(17) H. Levanon and G. Navon, *Journal of Physical Chemistry*, 1969, **73**, 1861 - 1868.

(18) D. O'Sullivan and J. R. Sodeau, *J Phys Chem A*, 2010, **114**, 12208 - 12215.

(19) D. Vione, V. Maurino, C. Minero and E. Pelizzetti, *Ann Chim*, 2003, **93**, 477 - 488.

(20) D. E. Heard and M. J. Pilling, *Chem. Rev.*, 2003, **103**, 5163 - 5198.

(21) R. Luc and C. Vergely, *Int J Biomed Sci*, 2008, **4**, 255 - 259.

(22) J. Kästner, J. M. Carr, T. W. Keal, W. Thiel, A. Wander and P. Sherwood, *J Phys Chem A*, 2009, **113**,11856 - 11865.

(23) E. Runge and E. K. U. Gross, *Phys. Rev. Lett.*, 1984, **52**, 997 - 1000.

(24) F. Bernardi, M. Olivucci and M. A. Robb, *Chem. Soc. Rev.*, 1996, **25**, 321 - 328.

(25) J. Yeo and W. Choi, *Environ. Sci. Technol.*, 2009, **43**, 3784 - 3788.

(26) J. M. Gardner, M. Abrahamsson, B. H. Farnum and G. J. Meyer, *J. Am. Chem. Soc.,* 2009, **131**, 16206 - 16214.

KOPRI 극지연구소

(27) M. Sipilä, N. Sarnela, T. Jokinen, H. Henschel, H. Junninen, J. Kontkanen, S. Richters, J. Kangasluoma, A. Franchin, O. Peräkylä, M. P. Rissanen, M. Ehn, H. Vehkamäki, T. Kurten, T. Berndt, T. Petäjä, D. Worsnop, D. Ceburnis, V.-M. Kerminen, M. Kulmala and C. O'Dowd, *Nature*, 2016, **537**, 1 - 3.

(28) Bo Long, Zheng-wen Long, Yi-bo Wang, Xing-feng Tan, Yu-hua Han, Chao-yun Long, Shui-jie Qin, and Wei-jun Zhang, *ChemPhysChem* 2012, 13, 323 - 329.

KOPRI
극지연구소

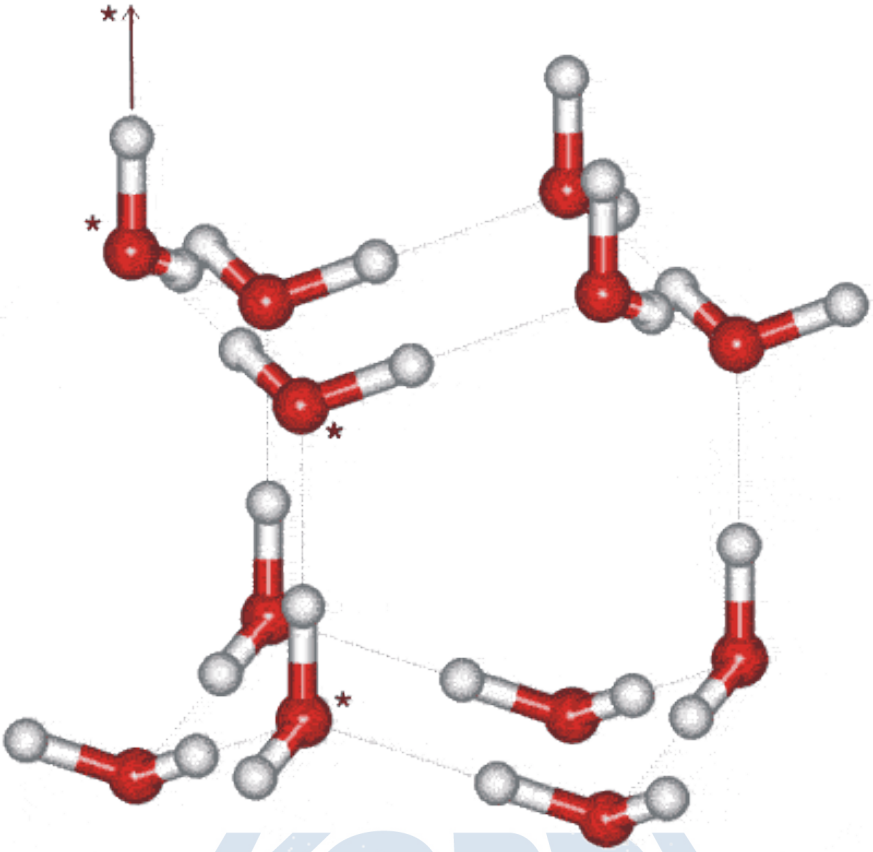

그림 1. Ih 얼음구조의 일부분으로 원자수준에서의 이해가 필요

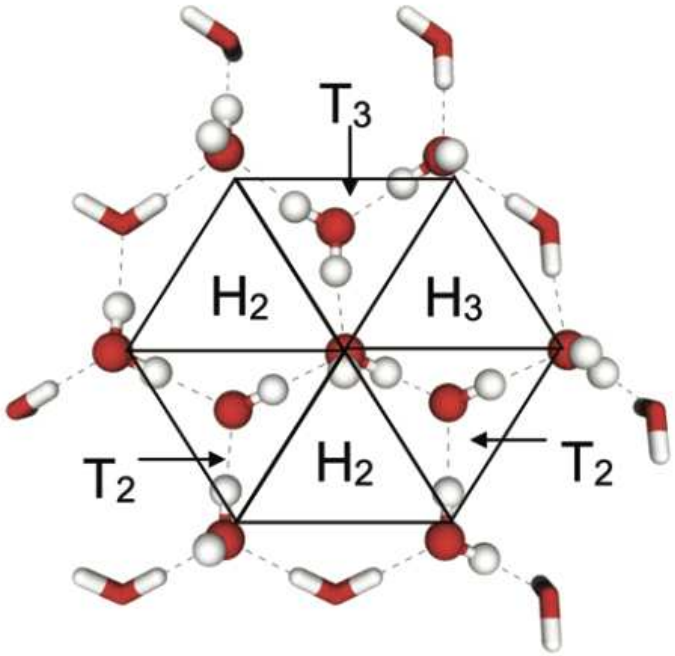

그림 2. 얼음표면의 다양한 흡착구조

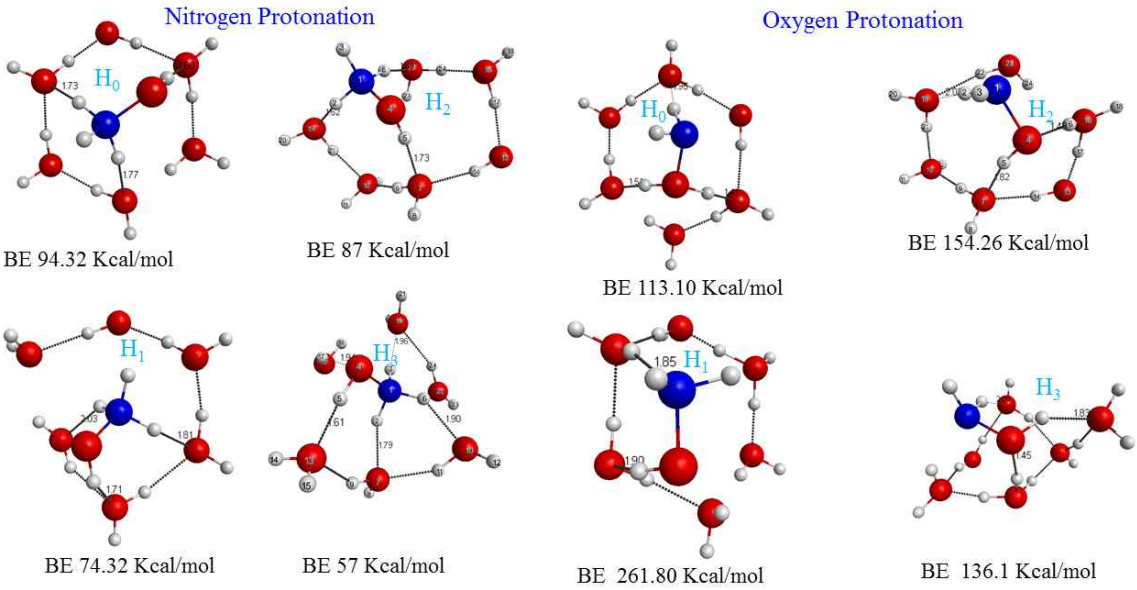

그림 3. PHA의 다양한 표면 흡착구조

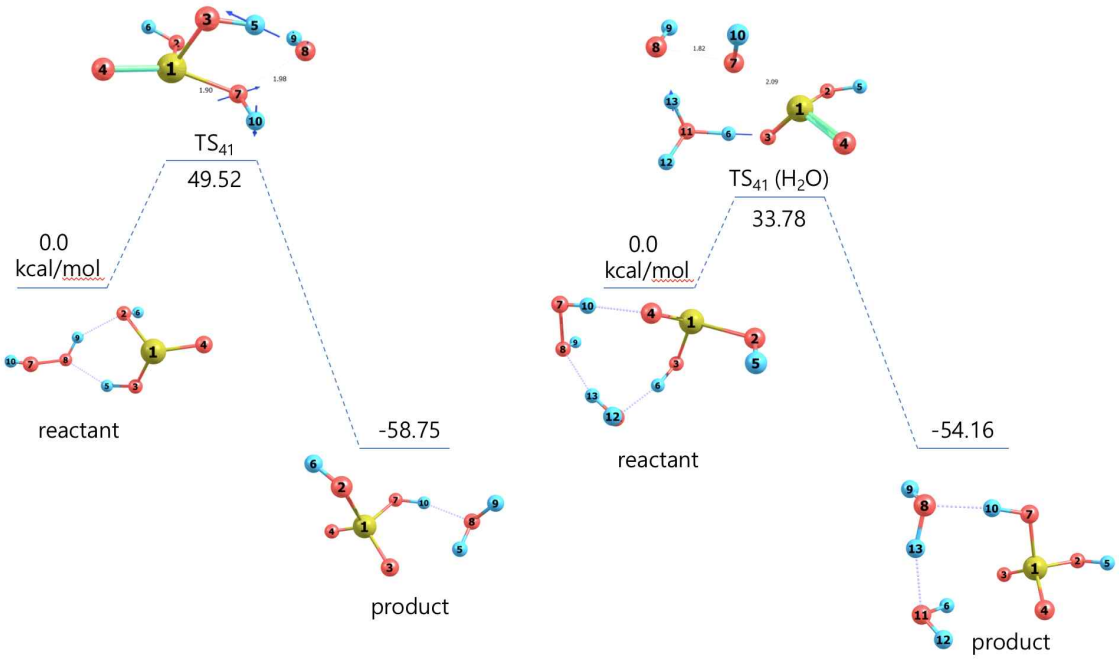

그림 4. 높은 활성화 에너지가 필요한 경로들의 예

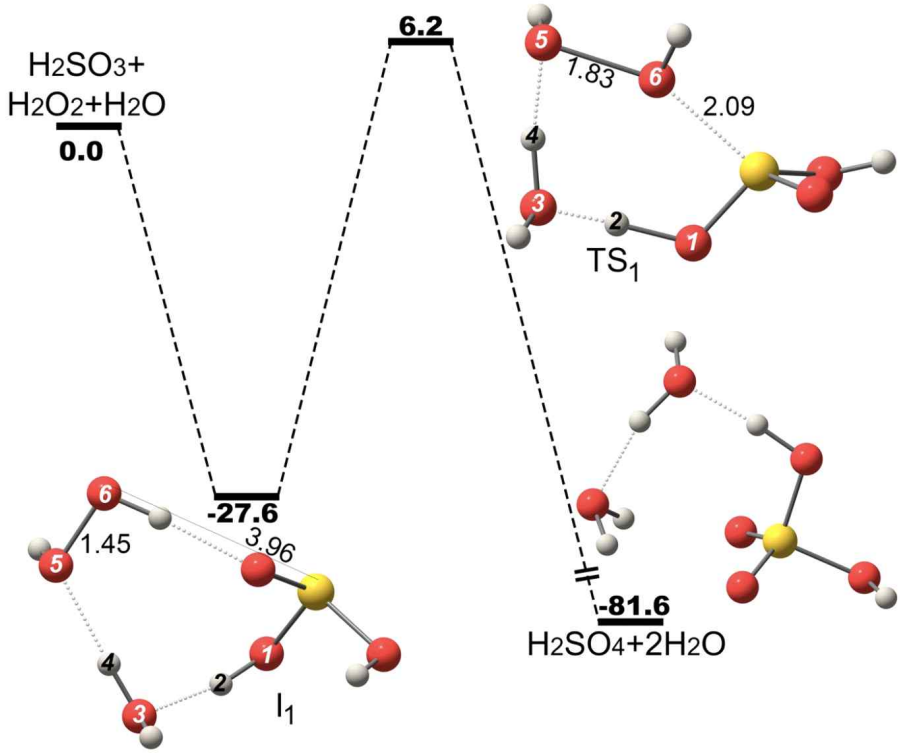

그림 5. 물분자의 촉매 역할을 보여주는 concerted 메커니즘 경로

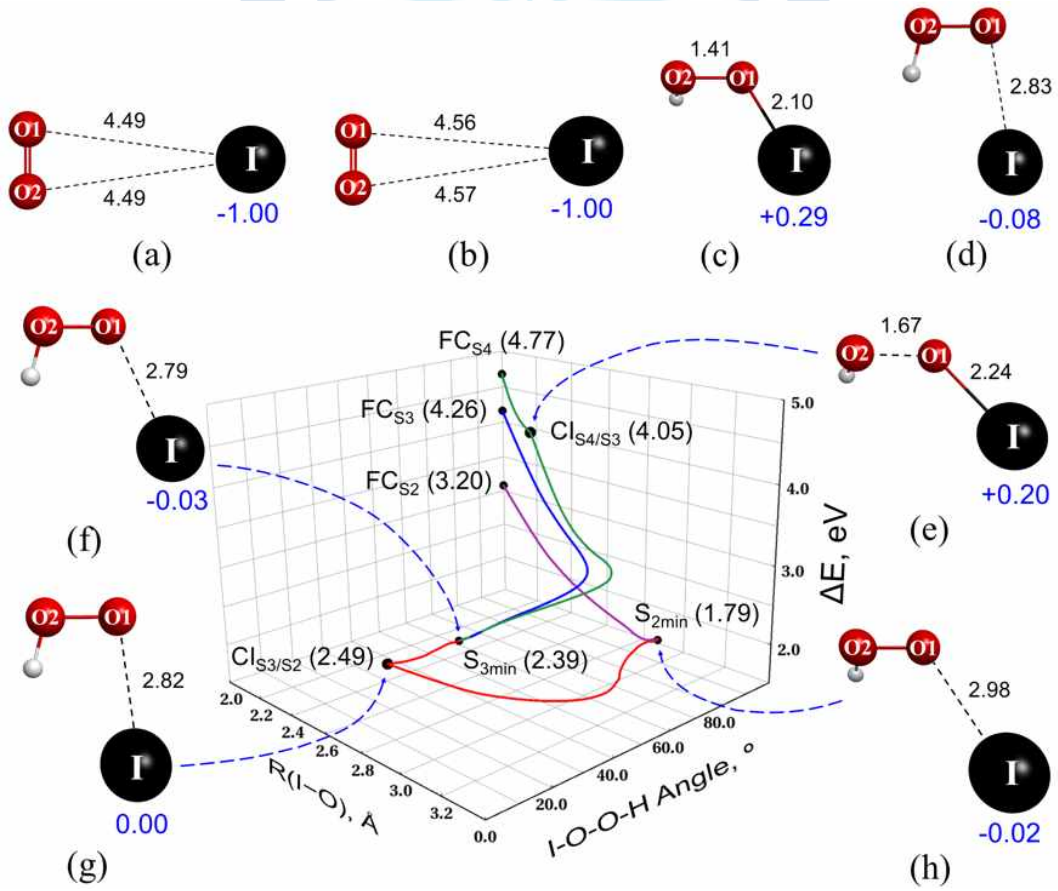

그림 6. IO_2H의 다양한 광화학 반응 경로

제 2 절. 극지방 수은 순환에서의 얼음의 역할: 양자화학계산을 이용한 미시적 접근[1)]

이유수, 한영철

한국해양과학기술원 부설 극지연구소

1. 서론 및 배경

수은(Hg)은 전 지구적인 오염물질로서, 자연환경에서의 거동은 수십 년 동안 집중적으로 연구되어왔음. 극지방의 눈 평원에 도달하는 대부분의 미량 원소들은 단방향 퇴적을 하지만, Hg의 경우 일련의 광화학적 산화-환원 반응을 통하여 대기와 눈 평원의 표면에서 양방향 교환을 하는 것이 알려져 있음 (Steffen et al., 2007). 눈 평원에 퇴적된 미립자로 된 수은(particulate Hg; P_{Hg})은 태양광에 포함된 UV-선에 의하여 환원되어 대기로 다시 방출되는데, 퇴적된 PHg의 수명은 대략 4-24시간으로 알려짐 (Dommergue et al., 2007; Mann et al., 2015). 이때, 소량의 Hg이 표면 눈 평원에 잔류하여 대기-눈 평원 Hg 순환에서 격리되고, 이러한 Hg은 이후 빙하코어에서 검출되어 고기후 분석에 이용됨 (Han et al., 2017; Jitaru et al., 2009). 이 과정에서 눈 평원에 퇴적된 불순물(sedimentary dust, sea salt, etc.)들이 Hg을 강하에 흡착하여 P_{Hg}를 형성한다는 가설이 제시됨. 하지만, 극지방에 가장 많이 존재하고 있는 얼음이 극지방 Hg 순환에 어떤 역할을 하는지 알려지지 않음. 본 연구에서는 양자화학계산을 이용하여 극지방 대기-눈 평원 Hg 순환 과정을 원자단위에서 살펴보고, 이 과정에서 대기중에 존재하는 얼음 입자들과 그리고 이와 공존하는 에어로졸 입자들이 어떠한 역할을 하는지 파악하고자 함. 1차 연구로 Hg^{2+}의 얼음 및 에어로졸 입자 표면에 대한 흡착 경향성을 확인함 (Yi et al., 2019). 그리고, 후속 연구를 통하여 비교적 단순한 구조의 산화된 Hg 화합물(Hg^{II})의 해염(halite), 에어로졸(muscovite and illite), 그리고 얼음(ice-Ih) 표면에 대한 흡착 경향성 및 UV-선에 의한 해리 가능성 등을 파악하고자 함.

2. 재료 및 방법

양자화학계산

본 연구에서는 양자화학계산이라는 이론적 접근 방법을 이용하여 극지방 대기 중에 존재하는 Hg 화합물과 얼음 및 에어로졸 입자들 사이의 흡착 경향성을 밝혀내고자 함. 양자화학계산은 원자와 분자 간의 상호작용을 양자화학 이론을 토대로 묘사하여, 모델 설계에 따라서, 실제 실험결과 및 자연현상을 대부분 설명 가능함. 이뿐만 아니라, 실험적으로 재현이 어려운 극한의 환경(극저온 및 고압)에서 일어나는 현상을 예측하거나, 관련된 실험의 결과들을 설명하기 위

1) 이 연구는 본 과제 지원으로 수행되었으며 그 결과는 다음의 논문으로 출판되었음: Yoo Soo Yi, Yeongcheol Han, Sung Keun Lee and Soon Do Hur, “Atomistic View of Mercury Cycling in Polar Snowpacks: Probing the Role of Hg^{2+} Adsorption Using Ab Initio Calculations”, *Minerals* 2019, 9, 459.

하여 이용됨. 근래에 접어들어 컴퓨터 공학의 발달과 함께 많은 발달하며 다양한 연구 분야에 적용되고 있음. 전자구조를 묘사하는 함수(basis function; 예를 들어, plane wave, projected augmented plane wave, linearized augmented plane wave, Gaussian function 등)의 종류나 원자간 상호작용(interatomic potential and exchange correlation)을 기술하는 방법론(예를 들어, full potential, pseudopotential 등)에 따라 다양하게 나뉘고 있는데, 연구의 목적에 따라 효율성과 정확성을 고려하여 이용됨 (Clark et al., 2005; Schwarz et al., 2002; Tse, 2002). 원자간 물리-화학 반응을 모사하는 과정에서 실험적으로 얻어지는 변수(empirical parameter)들을 최대한 배제하고, 각 원자가 갖는 본질적인 특징(intrinsic property; 예를 들어, 전자숫자, 스핀, 크기, 무게, 등)들에 대한 정보만 이용하기 때문에, 조건이 맞는다면 (계산 자원이나 양자화학 계산의 이론적 한계 등에 의한 제한 조건들) 어렵거나 불가능해 진행된 적 없는 실험에 대해서도, 가상적인 실험을 설계하여 (실제 실험에 비해서 낮은 비용과 시간적 효율성으로) 그 결과를 예측하거나, 기존에 행해진 실험들의 결과를 원자단위에서 어떤 물리-화학적 반응으로 일어났는지 해석을 가능하게 함 (Tse, 2002). 본 연구에서는 Hg의 얼음 및 에어로졸 표면에의 흡착 및 관련된 물리-화학적 현상들을 파악하는 것이 목적으로 projected augmented plane wave (PAW)와 on-the-fly generated pseudopotential (OTFP)을 이용한 양자화학계산 프로그램(CASTEP)을 이용함 (Clark et al., 2005). 극지방 대기중에 존재하는 얼음과 에어로졸 입자에 대한 Hg 화합물의 흡착 경향성을 파악하기 위하여, 예상되는 흡착제의 표면 구조를 준비해야 함. 해염은 halite의 (001) 방향 표면을, 퇴적성 에어로졸은 muscovite와 illite의 (001) 표면을, 그리고 얼음은 ice-Ih의 (0001) 및 (000-1) 표면을 준비함 (그림 1). 각 표면에 흡착되는 Hg 화합물은 Hg0 및 비교적 간단한 구조를 갖는 Hg^{2+}, HgO, $HgBr_2$, $HgCl_2$, HgClBr을 이용함.

KOPRI 극지연구소

전자구조 계산 및 구조 최적화

Hg 화합물의 흡착 경향성 파악을 구조 최적화, 흡착된 Hg 화합물의 진동 에너지, UV-VIS 흡수 스펙트럼을 얻기 위한 전자구조(electronic structure) 계산에는 CASTEP을 이용함 (Clark et al., 2005). 전자구조 계산을 위한 전자-이온 상호작용(electron-ion interaction)은 ultrasoft pseudopotential을 이용하여 묘사함 (Clark et al., 2005). 근거리 전자간 산호작용(on-site electron-electron interaction)은 Perdew-Burke-Ernzerhof (PBE) 방법론을 이용함 (Perdew et al., 1996). Hg 화합물의 흡착과정 및 얼음의 수소결합을 정확하게 기술하기 위하여, 긴-거리 단위의 분산력 상호작용(long-range order dispersion interactions)을 Tkatchenko-Scheffler (TS) 방법론을 이용함 (Gillan et al., 2016). 각 과정에서 안정적인 원자구조를 얻기 위한 구조 최적화 계산은 two-point steepest descent (TPSD) 방법론을 이용함 (Barzilai and Borwein, 1988). 상세한 계산 조건은 관련 논문에 정리되어 있음 (Yi et al., 2019).

흡착 에너지

극지방 대기 중에 존재하는 얼음 및 에어로졸 (해염 및 퇴적성 입자) 표면에 Hg^0 및 반응성 Hg 화합물(Hg^{II})의 흡착 에너지를 계산, 이를 통하여 각각의 상대적인 흡착 경향성을 확인. 그

리고, Hg의 빙상 표면의 침적과 반영구적 잔류에 어떤 역할을 하는지 확인. 흡착과정을 시뮬레이션하기 위하여 이용된 얼음 및 에어로졸 표면의 구조는 이전 실험 및 이론 연구에서 밝혀진, 실험이나 자연계에서 상대적으로 쉽게 형성되는 (easily accessible) 표면 구조들을 참조하였음. Hg의 얼음 및 에어로졸 표면에의 결합 에너지는 다음의 식을 이용하여 계산함 (E_B는 결합 에너지, $E^0_{Hg-surf}$ 및 $E_{Hg-surf}$는 Hg^{II}의 에어로졸 표면 흡착 전후의 에너지, E^0_{Hg} 및 E_{Hg}는 표면 흡착 전후의 Hg^{II}의 에너지, E^0_{surf} 및 E_{surf}는 Hg^{II} 흡착 전후의 에어로졸 표면의 에너지).

$$E_B = \left(E_{Hg-surf} - E^0_{Hg-surf}\right) - \left(E_{Hg} - E^0_{Hg}\right) - \left(E_{surf} - E^0_{surf}\right)$$

UV-VIS 흡수 스펙트럼

UV-VIS 흡수 스펙트럼은 특정 물질의 흡착으로 만들어진 스펙트럼의 특징적인 피크와 해당 결합의 에너지를 비교함으로써, 조사된 UV에 의하여 특정 물리-화학적 결합의 해리 가능성에 대한 정보를 제공함. 얼음 표면에 흡착된 Hg^{II}의 UV-VIS 흡수 스펙트럼을 계산하여, 자외선에 의한 흡착된 Hg의 광해리 및 이를 통한 대기로의 재방출 가능성을 확인. UV-VIS 흡수 스펙트럼은 유전율(dielectric constant; $\varepsilon=\varepsilon_1+i\varepsilon_2$)을 계산한 이후, 아래의 식을 이용하여 얻을 수 있음(α_{abs}는 UV-VIS 스펙트럼의 특정 ω에서의 absorption cross section, ω는 angular frequency, ε는 유전율).

$$\alpha_{abs} = \frac{2\omega}{c}\sqrt{\frac{|\epsilon| - \epsilon_1}{2}}$$

KOPRI 극지연구소

얼음 표면에 흡착된 Hg 화합물의 진동특성

얼음 표면에 흡착된 Hg^{II}의 진동 특성(vibrational normal modes)을 계산. 이를 통하여, 온도 증가에 따른 해리 속도(desorption rate)와 잔류 시간(residence time) 변화를 확인하여 얼음 표면에 흡착된 Hg^{II}가 극지방의 온도 조건(200-273K)에서 얼음 표면에 안정적으로 흡착되어 존재할 수 있는지, 아니면 열적 확산을 통하여 대기 중으로 재방출 될 가능성이 있는지 확인. 얼음 표면에 흡착된 Hg^{II}의 해리 속도(k) 및 잔류 시간(τ)은 다음과 같이 계산됨(ν는 계산에서 얻어진 흡착된 Hg^{II}의 진동 모드, ED는 계산에서 얻어진 결합 에너지의 음의 값, $E_D = -E_B$, T는 온도, k_B는 Boltzmann 상수).

$$k/\nu_0 \sim \exp\left(-\frac{E_D - E_{vib}}{k_B T}\right),\ \tau\nu_0 \sim \exp\left(\frac{E_D - E_{vib}}{k_B T}\right)$$

3. 연구결과

얼음 및 에어로졸 입자 표면에 Hg^0 및 Hg 화합물의 흡착이 가능함을 확인. 그림 2에 halite, illite, ice-Ih 표면에 흡착된 Hg 화합물을 나타냄. 이러한 결과는 각 물질이 극지방 대기 중에 존재하는 Hg 화합물을 표면에 흡착시켜 빙상으로의 침적을 유발할 수 있음을 의미함.

얼음 및 에어로졸 물질(halite, illite, and ice-Ih) 표면에 대한 Hg^0 및 Hg^{II} (HgO, $HgBr_2$, $HgCl_2$, Hg^{2+}, HgClBr)의 결합 에너지(binding energy)를 계산하여, 상대적인 흡착 친화도를 확인 (그림 3). 얼음이 수은 화합물에 대한 흡착 친화도가 halite나 illite와 유사할 정도로 강하게 나타나, 극지방 대기 및 눈 평원에 존재하는 얼음이 Hg의 순환에 적극적으로 참여하고 있을 것으로 예상함. 특히, 얼음 표면에 존재하는 매달린 수소 원자(dangling H)에 의하여 표면의 pH(acidity)와 Hg^{II}에 대한 반응성이 커지며, Hg 화합물의 흡착과정에서 얼음 표면에 할로겐 원소를 남기고 해리성 흡착(dissociative adsorption)이 진행되어 Hg0, HgCl, HgBr이 해리되는 Hg^0 및 HgCl, HgBr의 결합 에너지를 낮춰, 재방출을 촉진할 가능성이 있음. 이뿐만 아니라, 흡착된 수은 화합물들은 극지방에 조사되는 UV-선(280-400 nm)의 광자가 갖는 에너지보다 작은 결합 에너지를 갖고 있어, UV-선에 의한 흡착된 Hg 화합물의 직접적인 광해리(direct photodissociation) 가능성을 시사함.

UV-선에 의한 얼음 표면에 흡착된 Hg의 광해리 가능성을 직접 확인하기 위하여 얼음 표면에 흡착된 Hg^0와 $HgBr_2$의 UV-VIS 흡수 스펙트럼을 계산함. 이를 통하여, UV-선에 의한 Hg 화합물과 얼음 사이의 결합 구조의 전기적 전이(electronic transition)가 해당 결합 에너지보다 커서, 결합을 깨뜨리고 해리될 수 있는지 확인 (그림 4). Ice-Ih^A 표면에 흡착된 Hg^0, ice-Ih^C 표면에 흡착된 Hg^0와 $HgBr_2$의 결과를 보면, 얼음 표면에 Hg 화합물이 흡착되면서 ~250 - ~400 nm 영역에 새로운 흡수 피크가 나타나며, 해당 영역의 UV-선에 의한 전기적 전이가 일어날 수 있음을 의미. 해당 에너지의 세기가 각 결합 에너지보다 크게 나타나기 때문에, 흡착된 Hg^0 및 $HgBr_2$의 UV-선에 의한 광해리가 가능함을 뜻함. 이전 연구는 극지방 눈 평원에서의 Hg의 방출이 광화학적 환원(photo-induced reduction) 반응에 의한 것으로 추측하였으나 (Dommergue et al., 2007; Ferrari et al., 2004), 본 연구의 결과는 이에 더하여 UV-선에 의한 광해리 또한 Hg의 방출에 일부 이바지를 할 수 있음을 의미함.

극지방의 일반적인 온도 환경에서 얼음 표면에 흡착된 Hg^0 및 $HgBr_2$의 진동특성을 계산하여, 진동 에너지 및 해당 온도 구간에서의 흡착된 얼음 표면에서의 탈착 확률(desorption probability)과 체류 시간(residence time)의 온도 의존도를 확인함(그림 5). 극지방의 전형적인 온도 범위에서, 흡착된 Hg^0 및 $HgBr_2$의 탈착은 0.05 - 0.07 eV(E_{vib})만큼 촉진될 것이지만, UV-선 없이 흡착된 Hg 화합물의 자발적 방출(spontaneous release)을 유발하기에는 해당 결합 에너지(E_B)에 비해 크기가 너무 작음. 이에 의한 탈착 확률(온도 증가와 함께 증가)과 체류 시간(온도 증가에 따라 감소)의 변화는 극지방 빙하코어에서 나타나는 Hg 농도의 일주성 및 계절성 변화와 연관이 있을 것으로 생각됨 (Angot et al., 2016; Han et al., 2017).

결정질 얼음 표면 위에 수은의 흡착을 주로 살펴보았지만, 이전 연구에서 premelting 온도(~250 K) 이상에서의 비정질 구조를 갖는 준-액체층의 존재 가능성이 제안됨 (Slater and Michaelides, 2019). 이에 따라, 비정질 얼음 표면에 Hg 화합물의 흡착 경향성을 파악하기 위하여, ice-Ih (0001) 표면 위에 존재하는 준-액체층 구조를 얻기 위하여 계산을 수행 중 (그림 6). 신뢰도가 높은 비정질 얼음 표면 구조가 얻어지면, 이를 통하여 실제 얼음 표면에서 일어나는 다양한 화학적 반응에 대한 이해를 높일 수 있을 것으로 기대됨.

본 연구에서는 비교적 단순화된 얼음 표면 구조를 이용하여 계산을 수행함. 하지만,

실제 자연계에 존재하는 얼음 표면은 다소 복잡함. 표면 dangling H atom의 다양한 분포 (Buch et al., 2008; Pan et al., 2008) 및 비정질 구조를 갖는 준-액체층의 존재(Slater and Michaelides, 2019)가 이전 연구에서 제안되었듯이 극지방에 존재하는 얼음 입자의 표면 구조는 복잡할 것으로 예상. 하지만, 결정질 ice-Ih 표면에서는 줄무늬와 같은 표면 H 원자 분포 (striped ordering)를 보이는 얼음의 표면 에너지가 안정하며 (Buch et al., 2008), 액체상 구조를 갖는 물의 표면은 H_3O^+ 형태를 갖는 여분의 H 원자들이 모여 표면의 산성도(acidity)를 높인다는 것이 알려져 있음 (Buch et al., 2007). 즉, 극지방 대기 중이나 눈 평원에 존재하는 얼음 입자의 표면 구조가 아직 명확하지는 않지만, 본 연구의 결과와 이와 같은 이전 연구의 결과들을 함께 고려할 때, 얼음이 대기 중에 존재하는 Hg 화합물을 흡착시켜 눈 평원에 퇴적을 유발할 수 있을 것으로 생각됨. 얼음 및 에어로졸 표면의 Hg 화합물에 대한 흡착 경향성 및 UV-선에 의한 광해리 및 대기로의 재방출 가능성을 고려하면, UV-선이 있을 때, 충분한 시간이 지나면 침적된 Hg가 눈 평원에서 대부분 빠져나가야 함. 하지만 일정 부분의 Hg가 잔류하여, 빙하코어에서 검출되고 있음. 즉, 이렇게 극지방 눈 평원에 잔류하는 Hg는 대기나 빙원에 가장 많이 존재하는 얼음이나 본 연구에서 살펴본 일반적인 에어로졸(sea salt, sedimentary dust) 표면으로의 흡착이 아닌 다른 원인을 고려해야 함. 최근의 Hg 동위원소 연구에서 눈 평원에 잔류하는 Hg가 초목과 식생(vegetation)에서 기원한 유기물 표면에 흡착에 의한 것이라 제안됨 (Douglas and Blum, 2019). 이처럼 표면 반응성이 높은 유기물과 같은 물질 표면으로의 흡착 또는 승화(sublimation)와 수증기의 침적(vapor deposition) 과정에서 수소결합으로 연결된 얼음 구조 내부에 흡착과 같이 UV-선에 의한 광해리나, 광화학 반응에 참여를 어렵게 하는 과정을 통하여 Hg의 잔류가 유발될 것으로 예상함.

KOPRI 극지연구소

4. 결론

이러한 결과들은, 기존 연구에서 제안된 광화학 반응에 의한 Hg^{II} 또는 에어로졸 표면에 Hg^{II}가 흡착되어 형성된 particulate-Hg의 환원에 더하여, 기존 연구에서 밝혀낼 수 없었던 극지방 빙상 표면에서의 Hg의 순환에 얼음이 어떤 역할을 하는지 밝혀내어 극지방 빙상 표면에서의 Hg의 순환 경로를 제시할 수 있을 것으로 기대함.

5. 참고문헌

Angot, H., Magand, O., Helmig, D., Ricaud, P., Quennehen, B., Gallée, H., Del Guasta, M., Sprovieri, F., Pirrone, N., Savarino, J., and Dommergue, A. (2016) New insights into the atmospheric mercury cycling in central Antarctica and implications on a continental scale. Atmospheric Chemistry and Physics, 16, 8249-8264.

Barzilai, J., and Borwein, J.M. (1988) Two-point step size gradient methods. IMA Journal of Numerical Analysis, 8, 141-148.

Buch, V., Groenzin, H., Li, I., Shultz, M.J., and Tosatti, E. (2008) Proton order in the ice crystal surface. Proceedings of the National Academy of Sciences, 105, 5969-5974.

Buch, V., Milet, A., Vácha, R., Jungwirth, P., and Devlin, J.P. (2007) Water surface is acidic. Proceedings of the National Academy of Sciences, 104, 7342.

Clark, S.J., Segall, M.D., Pickard, C.J., Hasnip, P.J., Probert, M.J., Refson, K., and Payne, M.C. (2005) First principles methods using CASTEP. Zeitschrift Fur Kristallographie, 220, 567-570.

Dommergue, A., Bahlmann, E., Ebinghaus, R., Ferrari, C., and Boutron, C. (2007) Laboratory simulation of Hg0 emissions from a snowpack. Analytical and Bioanalytical Chemistry, 388, 319-327.

Douglas, T.A., and Blum, J.D. (2019) Mercury isotopes reveal atmospheric gaseous mercury deposition directly to the Arctic coastal snowpack. Environmental Science & Technology Letters, 6, 235-242.

Ferrari, C.P., Dommergue, A., Boutron, C.F., Skov, H., Goodsite, M., and Jensen, B. (2004) Nighttime production of elemental gaseous mercury in interstitial air of snow at Station Nord, Greenland. Atmospheric Environment, 38, 2727-2735.

Gillan, M.J., Alf?, D., and Michaelides, A. (2016) Perspective: How good is DFT for water? The Journal of Chemical Physics, 144, 130901.

Han, Y., Huh, Y., Hur, S.D., Hong, S., Chung, J.W., and Motoyama, H. (2017) Net deposition of mercury to the Antarctic Plateau enhanced by sea salt. Science of The Total Environment, 583, 81-87.

Jitaru, P., Gabrielli, P., Marteel, A., Plane, J.M.C., Planchon, F.A.M., Gauchard, P.-A., Ferrari, C.P., Boutron, C.F., Adams, F.C., Hong, S., Cescon, P., and Barbante, C. (2009) Atmospheric depletion of mercury over Antarctica during glacial periods. Nature Geoscience, 2, 505.

Mann, E.A., Mallory, M.L., Ziegler, S.E., Avery, T.S., Tordon, R., and O'Driscoll, N.J. (2015) Photoreducible mercury loss from arctic snow is influenced by temperature and snow age. Environmental Science & Technology, 49, 12120-12126.

Pan, D., Liu, L.-M., Tribello, G.A., Slater, B., Michaelides, A., and Wang, E. (2008) Surface energy and surface proton order of ice-Ih. Physical Review Letters, 101, 155703.

Perdew, J.P., Burke, K., and Ernzerhof, M. (1996) Generalized gradient approximation made simple. Physical Review Letters, 77, 3865-3868.

Schwarz, K., Blaha, P., and Madsen, G.K.H. (2002) Electronic structure calculations of solids using the WIEN2k package for material sciences. Computer Physics Communications, 147, 71-76.

Slater, B., and Michaelides, A. (2019) Surface premelting of water ice. Nature Reviews Chemistry, 3, 172-188.

KOPRI 극지연구소

Steffen, A., Douglas, T., Amyot, M., Ariya, P., Aspmo, K., Berg, T., Bottenheim, J., Brooks, S., Cobbett, F., Dastoor, A., Dommergue, A., Ebinghaus, R., Ferrari, C., Gardfeldt, K., Goodsite, M.E., Lean, D., Poulain, A., Scherz, C., Skov, H., Sommar, J., and Temme, C. (2007) A synthesis of atmospheric mercury depletion event chemistry linking atmosphere, snow and water. Atmospheric Chemistry and Physics Discussions, 7, 10837-10931.

Tse, J.S. (2002) Ab Initio molecular dynamics with density functional theory. Annual Review of Physical Chemistry, 53, 249-290.

Yi, Y.S., Han, Y., Lee, S.K., and Hur, S.D. (2019) Atomistic view of mercury cycling in polar snowpacks: Probing the role of Hg^{2+} adsorption using ab initio calculations. Minerals, 9, 459.

KOPRI
극지연구소

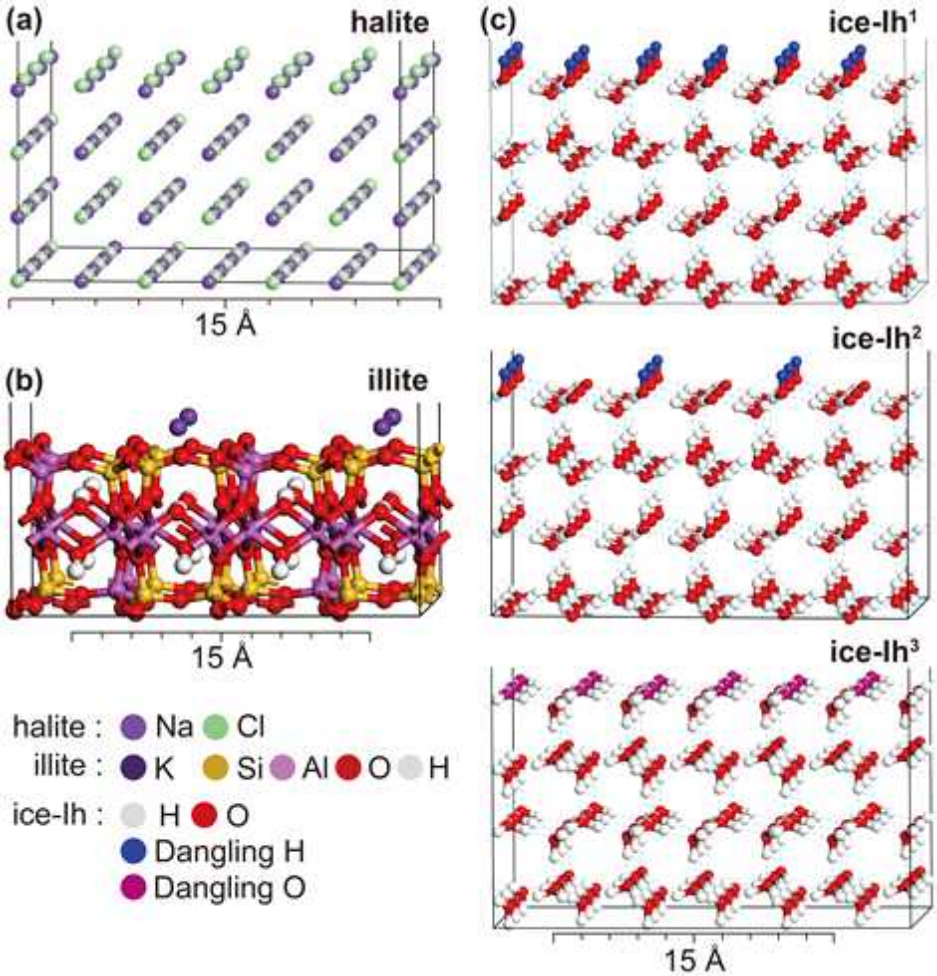

그림 1. Hg 화합물의 흡착 경향성 계산을 위하여 사용된 극지방 대기 중에 존재하는 에어로졸 물질의 표면 구조. (a) halite (001) 표면, (b) illite (001) 표면, (c) 표면 H 원자 분포가 다른 ice-Ih (0001) 표면 및 표면에 H 원자가 존재하지 않는 (000-1) 표면.

극지연구소

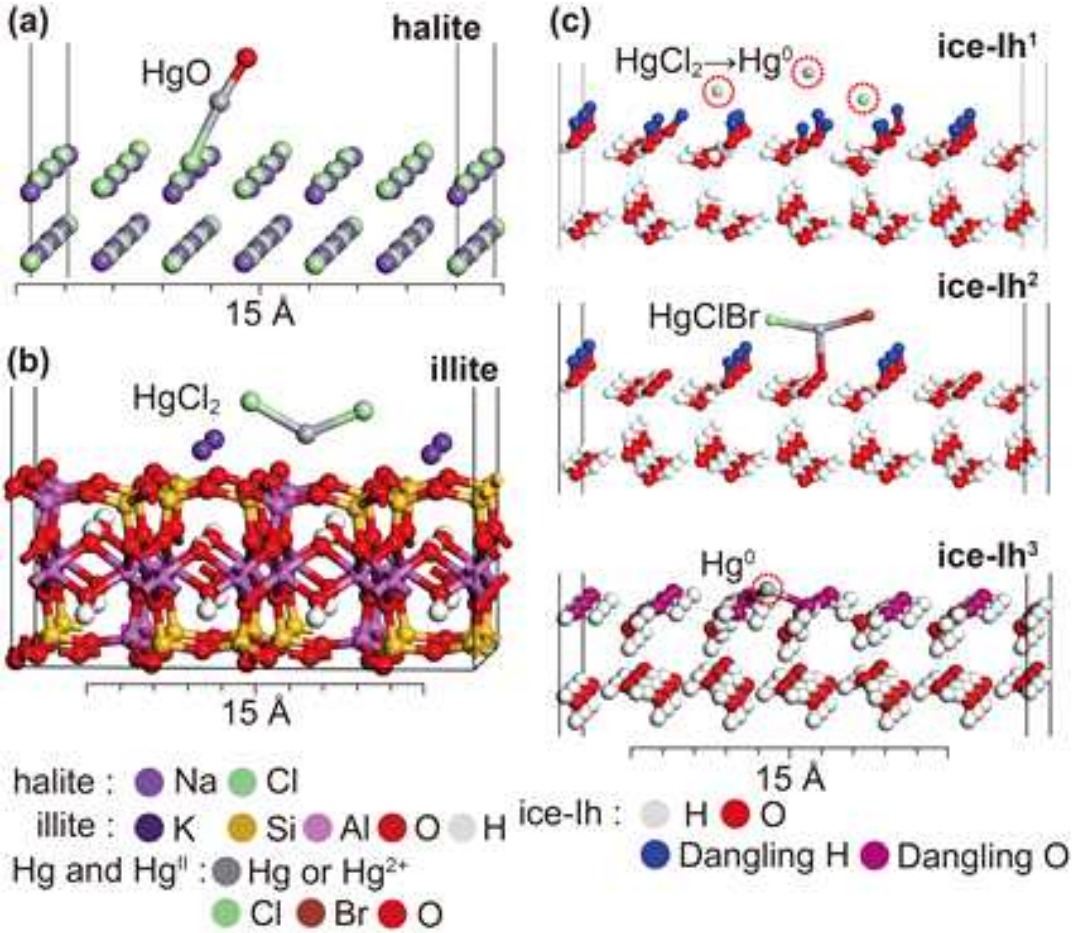

그림 2. Halite, illite, ice-Ih 표면에 흡착된 Hg 화합물. (a) halite (001) 표면에 흡착된 HgO, (b) illite (001) 표면에 흡착된 $HgCl_2$, (c) ice-Ih (0001) 표면에 흡착된 $HgCl_2$, HgClBr 그리고 ice-Ih (000-1) 표면에 흡착된 Hg^0.

국지연구소

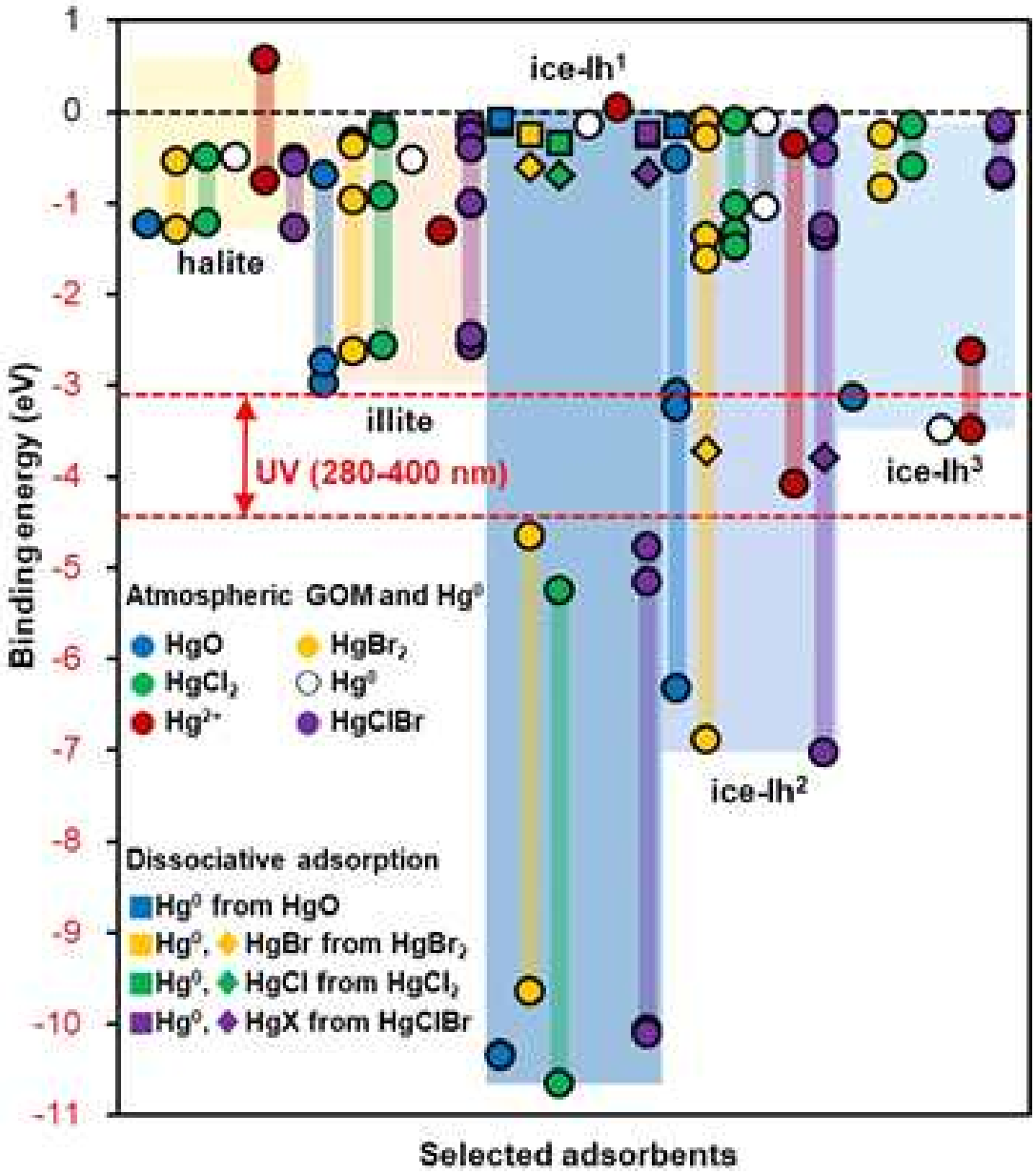

그림 3. Halite, illite, ice-Ih 표면에 흡착된 Hg (HgO, $HgBr_2$, $HgCl_2$, Hg^0, Hg^{2+}, HgClBr)의 결합 에너지(binding energy; E_B). 원형은 흡착된 Hg에 대하여 직접 계산된 결합 에너지. 사각형과 다이아몬드는 Hg의 흡착과정에서 반응성이 높은 얼음 표면에서 해리성 흡착(dissociative adsorption) 때문에 Hg^0, HgCl, HgBr이 해리되는 경우의 결합 에너지. -4.43과 -3.10 eV의 붉은 점선은 극지방에 조사되는 자외선(280-400 nm)의 광자가 갖는 에너지.

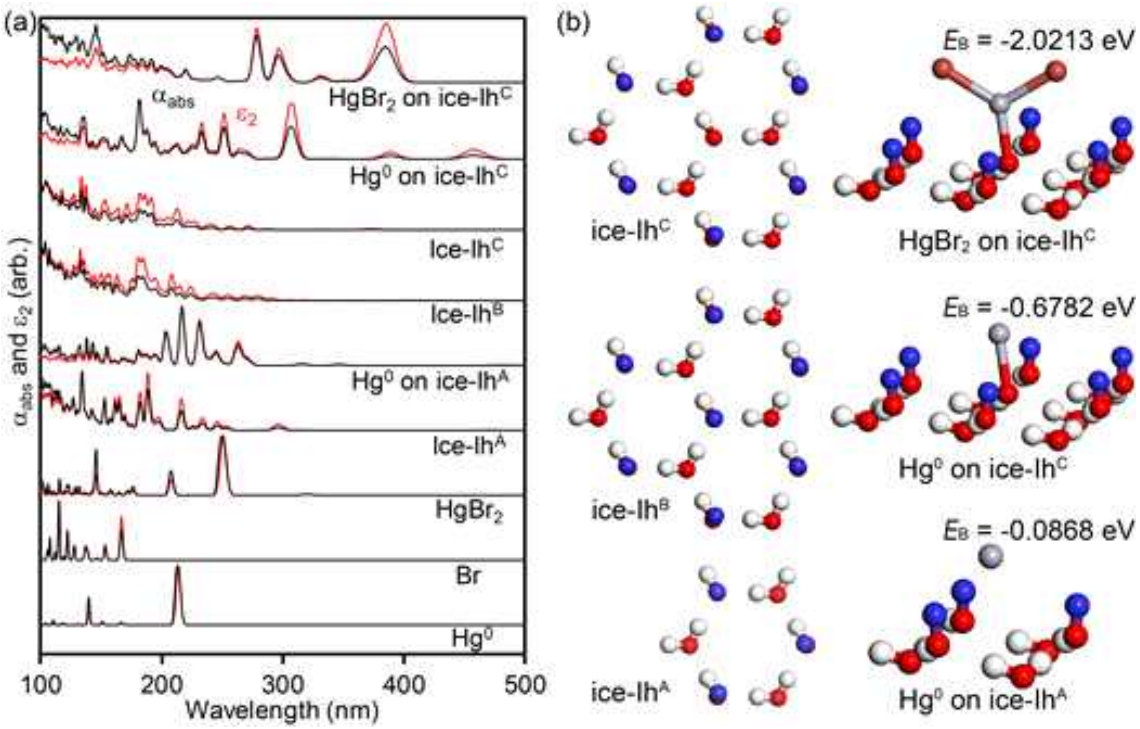

그림 4. (a) Ice-Ih 표면에 흡착된 Hg^0와 $HgBr_2$의 UV-VIS 흡수 스펙트럼(black)과 유전율(imaginary part of dielectric constant; red). (b) Ice-Ih^{A}과 ice-Ih^{B}는 한 개 또는 세 개의 ice-Ih (0001) 표면을 구성하는 육각형 고리(hexagonal ring)로 이루어진 분자 클러스터. Hg^0와 $HgBr_2$는 ice-Ih^B 클러스터 중앙의 매달린 수소(dangling H) 원자 하나를 제거하고 (ice-Ih^C), 해당 위치에 흡착. 표면에 흡착된 Hg^0 및 $HgBr_2$의 결합 에너지(E_B)가 함께 표시됨.

KOPRI 극지연구소

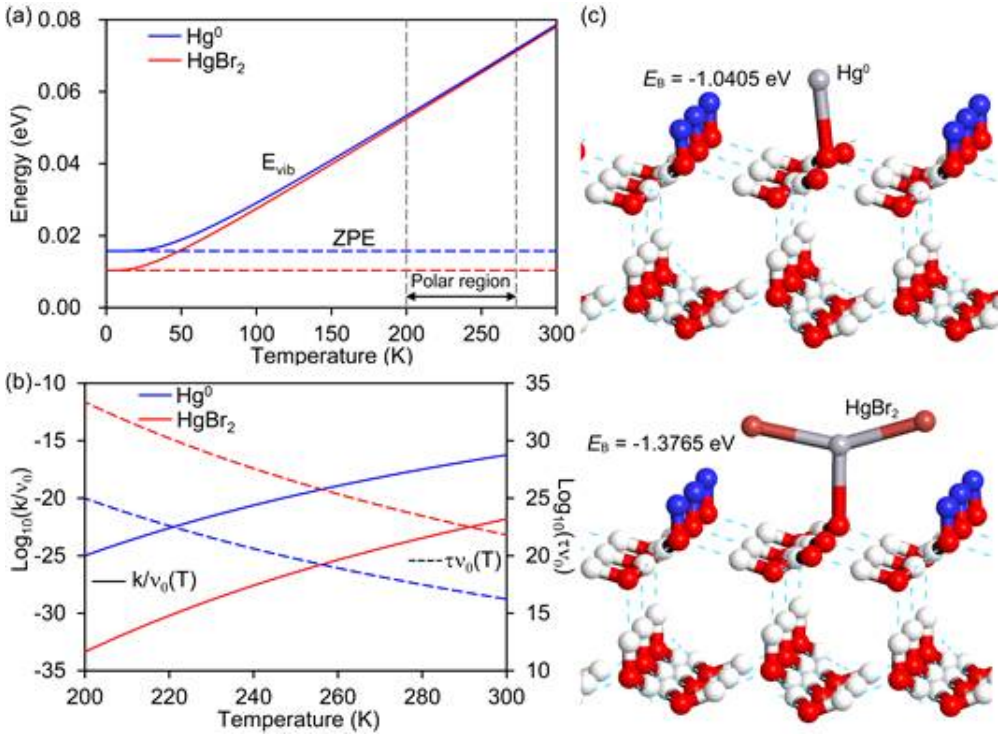

그림 5. (a) Ice-Ih 표면에 흡착된 Hg^0와 $HgBr_2$의 열적 진동 에너지(E_{vib})와 영점 에너지(ZPE). (b) Ice-Ih 표면에 흡착된 Hg^0와 $HgBr_2$의 극지방 온도 환경에서의 탈착 확률(desorption probability)과 잔류 시간(residence time)의 온도 의존도. (c) Ice-Ih 표면에 흡착된 Hg^0 및 $HgBr_2$의 결합 에너지(E_B).

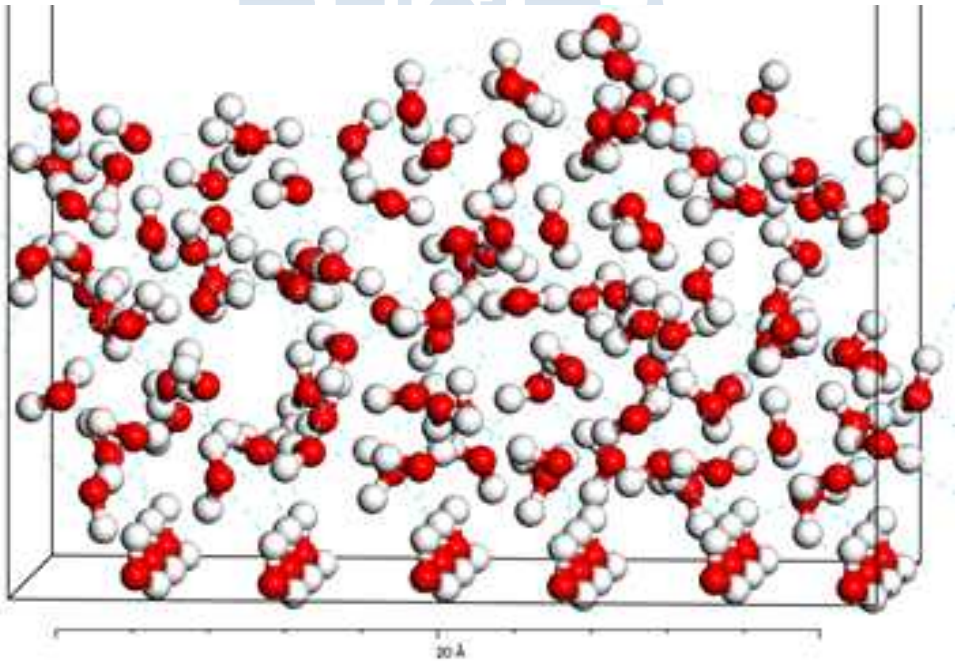

그림 6. Ice-Ih (0001) 단면 위의 220 K의 준-액체상 얼음 구조.

제 3 절. Tunneling Diffusion of Excess Protons in Amorphous Solid Water at 10 and 80 K[2)]

Du Hyeong Lee[1,2], Hani Kang[2], and Heon Kang[2*]

[1]Korea Polar Research Institute
[2]Department of Chemistry, Seoul National University

1. Introduction

The mobility of excess protons (positive protonic defects) in ice is intimately related to the diverse physical (Fletcher, 1970; Petrenko and Whitworth, 1999) and chemical properties of ice (Kang 2005). The general concept of proton transport in ice was originally formulated by Jaccard (1959, 1964) and Onsager (1962) and is now well accepted through extensive experimental verification (Eigen and De Maeyer, 1958; Eigen, 1964; Collier *et al.* 1984; Wooldridge and Devlin, 1988, Fisher and Devlin, 1995, Uritski *et al.*, 2008; Uritski *et al.*, 2009; Presiado *et al.*, 2011; Bove *et al.*, 2009; Park *et al.*, 2010; Lee *et al.*, 2006; Lee *et al.*, 2007; Moon *et al.*, 2008; Moon *et al.*, 2012; Lee *et al.*, 2016; Devlin 2011). The excess protons in ice move along its hydrogen-bonded network via an efficient hopping relay (Grotthuss) mechanism. (Fletcher, 1970; Petrenko and Whitworth, 1999) The proton passage along the hydrogen-bonded water chain polarizes the direction of the hydrogen bonds, which blocks the passage of the subsequent protons hopping along the same path. Therefore, for a continuous flow of protons, reorientation of water molecules (Bjerrum defect motion) must take place to depolarize the hydrogen-bond direction. As water reorientation in ice is activated at temperatures above 130 K (Collier *et al.* 1984; Wooldridge and Devlin, 1988, Fisher and Devlin, 1995), an ice crystal can be an effective protonic conductor only at a high temperature. Acceptance of this elegant mechanism of proton transport in ice in the scientific community, however, was not a straightforward process and there were opposing arguments and confusions, which have been briefly summarized by Devlin (2011). The concept of proton mobility in the ice interior was challenged by the report that H_3O^+ ions that were soft-landed on an ice film surface remained on the surface over a wide temperature range (Cowin *et al.*, 1999), which appeared to reflect a lack of proton mobility in the ice interior. This confusion was clarified by the discovery of Lee *et al.* (2006, 2007) and Moon *et al.* (2008), who showed that

2) 이 연구는 본 과제 지원으로 수행되었으며 그 결과는 다음의 논문으로 출판되었음: Du Hyeong Lee, Hani Kang, and Heon Kang, "Tunneling Diffusion of Excess Protons in Amorphous Solid Water at 10 and 80 K", *J. Phys. Chem. C* 2019, 123, 3657-3663.

excess protons thermodynamically prefer to reside at the ice surface rather than in the interior. Because of this property, protons in fact collected at the surface of ice samples in the proton mobility experiments with soft-landed H_3O^+ ions over a wide temperature range (Cowin *et al.*, 1999), while possessing high mobility in the ice sample interior to be able to reach the surface (Moon *et al.*, 2008; Lilach *et al.*, 2008; Park et al, 2012). The trapping of protons at the ice surface further implies that proton migration along the ice surface does not occur as efficiently as that in the ice interior. Studies of H/D exchange reaction on ice surface indicate that for surface proton transfer, a small but substantial energy barrier (~10 kJ mol^{-1}), which is associated with proton trapping in the surface potential minimum, must be overcome (Moon *et al.*, 2010). Accordingly, proton transfer along the ice surface occurs by thermal activation above a certain temperature or by chemical activation of the ice surface (Park et al, 2004; Moon *et al.*, 2010; Park *et al.* 2014), in contrast to efficient proton transfer in the ice interior over a wide temperature range (Eigen and De Maeyer, 1958; Eigen, 1964; Collier *et al.* 1984; Wooldridge and Devlin, 1988, Fisher and Devlin, 1995, Uritski *et al.*, 2008; Uritski *et al.*, 2009; Presiado *et al.*, 2011).

Theoretical calculations using a hybrid quantum mechanics/molecular mechanics approach indicate that an excess proton is not trapped in a potential energy minimum in the ice crystal but can transfer with a small energy barrier (Kobayashi *et al.*, 2000). The proton hopping along the hydrogen-bonded network of ice is coupled with the lattice geometry relaxation to facilitate sequential proton transfers in a concerted fashion (Kobayashi *et al.*, 2000). An interesting question is whether proton hopping can occur in ice at extremely low temperatures, i.e., when the lattice thermal vibration is minimized and not readily available to assist in the proton transfer. The proton conductivity in ice is closely related to various ice phenomena at low temperatures, including proton order/disorder phase transitions (Castro Neto *et al.*, 2006), charge distributions at the ice surface and interior (Lee *et al.*, 2016), and proton transfer reactions in ice (Kang, 2005). However, direct evidence has not been reported as yet for the mobility of excess protons in cryogenic ice near zero degree, to our best knowledge. There are some observations that indirectly support proton mobility under these conditions (Lee *et al.*, 2016; Shin *et al.*, 2017; Park *et al.*, 2018; Ayotte *et al.*, 2005; Marchand *et al.*, 2012). For example, infrared spectra of acid-doped amorphous solid water (ASW) samples showed an intense absorption of the Zundel continuum, which could be related to concerted proton transfers in the lattice (Lee *et al.*, 2016; Shin *et al.*, 2017; Park *et al.*, 2018; Ayotte *et al.*, 2005; Marchand *et al.*, 2012) The surface voltage measurement of ice films with adsorbed acids showed that the positive protonic charge was spread over a considerable depth from the surface, which was possibly due to fluctuating excess protons near the ice surface (Lee *et al.*, 2016) Spontaneous dissociation of halogenated acetic acids has been observed in ASW at 10 - 140 K, indicating

efficient proton injection and migration in the lattice (Shin *et al.*, 2017; Park *et al.*, 2018). Notably, although slightly different from the transport of excess protons, concerted motion of multiple protons has been observed in *pure* ice samples at temperature 5 K (Bove *et al.*, 2009). Quasi-elastic neutron scattering (QENS) studies of pure crystalline ice (CI) samples in Ih and Ic phases have shown that proton dynamics do not freeze out even at 5 K, which indicates a simultaneous movement of several protons by quantum tunneling in proton-ordered hexagonal loops that are present in a macroscopic, proton-disordered ice crystal (Bove *et al.*, 2009).

The present study aims to explore the possibility of quantum tunneling of excess protons in ice at very low temperatures. An experimental scheme was devised to measure proton transport from a proton donor to an acceptor species that was placed at controlled separation distances within an ice sample. For CI, however, such a sample structure could not be constructed because excess protons in the ice sample interior migrate spontaneously to the surface during crystallization of the sample at high temperatures (Lee *et al.*, 2007; Moon *et al.*, 2012; Lilach *et al.*, 2008), as mentioned above. For this reason, the structure was constructed with an ASW film by vapor deposition in vacuum at a sufficiently low temperature to suppress efficient diffusion of excess protons. The measurement of proton transport in this sample gave information about proton mobility in ASW, most likely in the microscopic ice crystallites present in the sample. Nevertheless, the results may prove to be a useful guide for judging proton mobility in CI as well.

KOPRI 극지연구소

2. Experimental

The experiment was conducted in an ultra-high vacuum (UHV) chamber, which was equipped with a quadrupole mass spectrometer (QMS; Extrel, MAX-500HT) and a Fourier transform infrared (FTIR) spectrometer (Bruker, Vertex 70) (Kang *et al.*, 2016 and Park *et al.*, 2016). A Pt(111) single crystal was cooled by a closed-cycle He cryostat (Sumitomo Heavy Industries, CH-204N) and heated by bombardment of 2 keV electrons from a home-made electron gun attached behind the crystal. The sample could be cooled down to ~10 K and heated above 1200 K. The lowest achievable temperature (~10 K) was estimated from an extrapolation of the sample heating/cooling rates because this temperature was below the range (> 15 K) of the attached N-type thermocouple. The Pt(111) crystal substrate (surface atomic density = 1.5×10^{19} Pt atoms·m^{-2}) was cleaned by 2 keV Ar^+ ion sputtering and heating to 1200 K. The ASW films were grown on the Pt(111) substrate maintained at 80 K at a growth rate < 0.2 monolayer (ML; 1 ML = 1.1×10^{19} water molecules·m^{-2}) per second by backfilling the chamber with water vapor. Water self-diffusion is prohibited at this temperature (Livingston *et al.*, 2002). Hydrogen chloride (HCl, ≥99% purity) and ammonia (NH_3, 99.999% purity) gases were deposited onto the

sample surface by using separate tube dosers and leak values. The background partial pressure of these gases was kept below 4×10^{-8} Pa during deposition to prevent the contamination of the chamber wall.

Temperature-programmed desorption (TPD) experiments were performed to estimate the thickness of the ASW film as well as the amounts of HCl and NH_3 in the samples. The film thickness was estimated by comparing the intensities of water desorption signal (m/z 18) produced from the ASW film and the water monolayer on Pt(111). Similarly, HCl and NH_3 coverages were determined by comparing their desorption intensities to that of their known desorption features on Pt(111) (Daschbach et al, 2005; Fisher, 1981; Gland and Kollin, 1981).

Reflection-absorption infrared spectroscopy (RAIRS) was used to measure the amounts of hydronium ions, ammonium ions, and NH_3 molecules in the samples. Incident p-polarized IR light was reflected from the sample at a grazing angle (85°) and entered an external mercury-cadmium-telluride detector. Dry N_2 gas was used to purge H_2O and CO_2 gases from the beam path. All spectra were recorded at ~10 K to maintain constant baseline intensities and were averaged for 1024 scans with a spectral resolution of 4 cm^{-1}.

3. Results

The transport of excess protons was studied by preparing an ASW sample with a four stacked-layer structure, as shown in Figure 1. The sample consisted of a bottom ASW film grown on a Pt(111) surface, an adsorbed HCl (proton donor) layer, ASW spacer film, and adsorbed NH_3 (proton donor) layer. The sample preparation procedure and the RAIR spectra recorded at each preparation stage are shown in Figure 1. First, a bottom ASW layer was grown on a Pt(111) substrate for a thickness of about 70 ML (Figure 1-I). The corresponding vibrational spectrum showed characteristic features of a pure ASW film (Figure 1a) (Cholette *et al.*, 2009; Smith *et al.*, 2011), which include a strong O-H stretching band (~3400 cm^{-1}) and H-O-H bending vibration (1660 cm^{-1}). An intermolecular libration band (~900 cm^{-1}) appeared outside the spectral display range (Hagen and Tielens, 1982; Severson *et al.*, 2003).

Next, HCl was adsorbed for 0.2 ML on the ASW film surface (Figure 1-II). The two bands at 1225 and 1760 cm^{-1} were discernible in the difference spectrum (Figure 1b), which corresponded to symmetric and asymmetric bending of H_3O^+, respectively (Pursell *et al.*, 2000). The Zundel continuum absorption due to excess protons also appeared in the region of 1000 - 3000 cm^{-1} (Shin *et al.*, 2017; Dahms *et al.*, 2016), as marked by the dotted line. These features, together with the absent H-Cl stretch band (~2500 cm^{-1}) of molecular HCl with hydrogen bonding to the surface, confirmed the complete dissociation of HCl into excess protons and chloride ions at 80 K (Devlin *et al.*, 2002; Parent *et al.*, 2011;

Ayotte *et al.*, 2011; Lee *et al.*, 2018). The negative absorption near 3400 cm^{-1} was consistent with the conversion of a certain portion of water molecules into hydronium ions. Subsequently, on this HCl adsorbate layer, an ASW film was overlaid with a controlled thickness (Figure 1-III), which defined the distance between the proton donor (HCl) and acceptor (NH_3). The difference spectrum of this ASW spacer layer (Figure 1c) was nearly identical to that in Figure 1a.

Lastly, NH_3 molecules were adsorbed for 0.25 ML on top of the ASW spacer film (Figure 1-IV). The NH_3 adsorption was carried out at either ~10 K or 80 K. This temperature defines the temperature of proton transfer through ASW from HCl to NH_3. As presented in Figure 1d, NH_3 adsorption produced various changes in the spectrum. The symmetric bend (ν_2) of NH_3 at 1100 cm^{-1} appeared as a result of ammonia adsorption (Moon *et al.*, 2012; Pursell *et al.*, 2000). The asymmetric bend (ν_4) of NH_4^+ at 1480 cm^{-1} could be attributed to proton transfer to NH_3. The negative absorptions at 1760 and 1210 cm^{-1} indicated a decreased population of hydronium ions because of proton transfer. The complex features at 2800 - 3600 cm^{-1} indicated changes in the N - H stretch intensity of NH_3 and the O - H stretch intensity of water. All these features indicated the occurrence of acid-base reaction (1) by transport of excess protons through the ASW spacer film,

$$H_3O^+(b) + NH_3(s) \rightarrow H_2O(b) + NH_4^+(s) \qquad \text{(Reaction 1)}$$

where (s) and (b) designate surface and bulk species, respectively. It was observed that the reaction instantaneously occurred following the adsorption of ammonia onto the ASW surface. No further increase in the reaction yield was observed after a time delay of RAIRS measurement up to 1 h.

The present sample structure ("HCl-sandwich" structure) was chosen to assess proton transfer because it had two advantages over the "NH_3-sandwich" structure with the reversed positions of HCl and NH_3, which was used in the previous studies (Moon *et al.*, 2012). The first advantage is that the initial amount of excess protons in the sample can be accurately determined for the HCl-sandwich sample because of complete dissociation of HCl inside an ASW film at the temperature (80 K) of the sample preparation (Devlin *et al.*, 2002; Parent *et al.*, 2011; Ayotte *et al.*, 2011; Lee *et al.*, 2018). In contrast, when the NH_3-sandwich film is used, the adsorption of HCl onto the ASW film surface needs to be carried out in the final stage of sample formation at the temperature of proton transfer (10 K or 80 K). However, the degree of HCl dissociation on the ASW surface at 10 K is unknown. Secondly, the sticking coefficient of water molecules on hydronium ions present on the ASW surface is close to unity. This makes an ASW spacer layer grow on them with near uniform thickness. On the other hand, the low sticking probability (~0.14 at ~90

K) of water molecules on NH_3 adsorbates hampers the growth of ASW spacer layer with a uniform thickness in the NH_3-sandwich sample (Moon *et al.*, 2012).

The proton transfer yield in Reaction 1 was measured as a function of the donor-acceptor distance by changing the ASW spacer thickness. Figure 2a displays the difference spectra in the 1000 - 2000 cm^{-1} region measured after ammonia adsorption at 80 K, which were obtained for samples with varying thicknesses of the spacer layer. Figure 2b shows the corresponding results obtained for ammonia adsorption at ~10 K. In both cases, the features arising as a result of Reaction 1, aforementioned in Figure 1d, were clearly observable. The v_2 band of NH_3 at ~1100 cm^{-1} and the v_4 band of NH_4^+ at ~1480 cm^{-1} attributable to ammonia adsorption and proton transfer, respectively, were observed. At the same time, the absorbances of the symmetric (1225 cm^{-1}) and asymmetric (1760 cm^{-1}) bending vibrations of hydronium ions decreased. These changes were more pronounced when the thickness of ASW spacer was narrower and the sample temperature was higher. The weak absorption feature at ~1630 cm^{-1} could be the symmetric bending of NH_4^+ (Martin and Lee, 1996; Jacox and Thompson, 2005). Although this vibrational mode is IR inactive for NH_4^+ in the gas phase, it could be IR active for the surface-adsorbed species because of the symmetry breaking associated with hydrogen bonding to the surface. This feature could also be a visual distortion effect in the spectrum due to the depletion of H_3O^+ asymmetric bend intensity located nearby (~1760 cm^{-1}). The scissoring (asymmetric bending) mode of NH_3 could also appear in this position.

The spectrum displayed at the bottom of each series in Figures 2a and 2b corresponds to the sample without an ASW spacer film. In this sample, proton transfer occurred *along the surface* of the ASW sample between H_3O^+ and NH_3 located on the surface. The efficiency of this surface proton transfer could be estimated from the NH_4^+ band intensities of these samples, as described below. The area of the v_4 band of NH_4^+ at ~1480 cm^{-1} was converted to NH_4^+ population with the help of a calibration experiment, which measured the v_4 band area for a known amount (0.25 ML) of NH_4^+ produced by a stoichiometric reaction between NH_3 (0.25 ML) and HCl (in excess) on the ASW film surface. Separate calibration experiments were performed at ~10 K and 80 K. Then, the efficiency of the surface proton transfer was calculated by dividing the population of NH_4^+ with the initial population of hydronium ions on the sample surface. This quantitation procedure revealed that almost all hydronium ions that are initially present on the surface reacted with adsorbed ammonia molecules to form NH_4^+ at 80 K. This reacted portion was reduced to about 44% at 10 K, indicating that the surface proton transfer efficiency varied significantly depending on the temperature. This behavior is consistent with the fact that an excess proton is trapped in a shallow potential minimum on the ASW surface (Lee *et al.*, 2007, Moon *et al.*, 2008), and its migration along the surface requires it to overcome an

energy barrier of ~10 kJ mol^{-1} with the help of thermal or chemical energy (Moon *et al.*, 2010), as mentioned in Section 1. Accordingly, a substantially large portion of excess protons was trapped in position on the ASW surface without migrating to NH_3 at ~10 K. For the present coverages of HCl (0.2 ML) and NH_3 (0.25 ML), the average distance between the proton donor and acceptor was about two water molecules. Therefore, the result indicated that 44% of excess protons could move across two water molecules at ~10 K. This surface migration of protons could be activated by local heating of the surface upon ammonia adsorption. At 80 K, thermal energy may additionally contribute to overcoming the surface diffusion barrier, which extends the proton transfer distance to significantly longer than two water molecules.

Proton transfer efficiency *through* ASW can be estimated from the results of proton transfer measurements as a function of the ASW spacer thickness. This proton transfer efficiency (η) was calculated only for the "mobile" protons in the sample. A "mobile" proton refers to an excess proton that is not permanently trapped in the potential well in its initially created position at the corresponding temperature. When both hydronium ions and ammonia molecules are placed on the surface of an ASW film, only "mobile" protons can migrate along the surface to produce NH_4^+, whereas "immobile" protons are trapped in the potential well of the surface at fixed positions. Therefore, it was considered that the population of mobile surface protons would be equal to the population of NH_4^+ ions measured in the surface proton transfer experiment in the absence of an ASW spacer film, $\theta_{mobile\,H^+} = \theta_{NH_4^+}(0\,ML)$, where Θ_A is the surface population of A species. As mentioned above, almost all excess protons present on the ASW surface were "mobile" at 80 K, but this portion decreased to about 44% at ~10 K. It was assumed that the same ratio for mobile/immobile excess protons was maintained underneath the ASW spacer layer at corresponding temperatures. This assumption was based on the rationale that thermal rearrangement of the H-bonded water structure does not easily occur at the temperature (80 K) of sample preparation (Coiller *et al.*, 1984; Wooldridge and Devlin, 1988; Fisher and Devlin, 1995). Of course, water adsorption on the surface may perturb the proton trapping structures and may convert some of these immobile protons to mobile protons underneath the ASW spacer film. This effect, however, appeared to be insignificant in the spectra shown in Fig. 2, which showed a smooth decrease, rather than a discontinuous increase, in the ammonium formation yield as a thin ASW layer was overlaid on the surface hydronium ions. Based on these considerations, the proton transfer efficiency through ASW across the film thickness of x could be determined by Eq 1.

$$\eta(x) = \frac{\theta_{NH_4^+}(x)}{\theta_{\text{mobile}\,H^+}} = \frac{\theta_{NH_4^+}(x)}{\theta_{NH_4^+}(0\,ML)} \quad (1)$$

The $\eta(x)$ curves at ~10 K and 80 K estimated from the data set presented in Figure 2 are plotted in Figure 3. The value of $\eta(x)$ decreased from unity at x = 0 to below 0.1 at x = 30 ML at both temperatures. The average distance of proton transfer through ASW was calculated by integrating $\eta(x)$ over x. The average proton-transfer distance calculated in this way was $\langle x \rangle$ = 11.2 ± 1.1 ML at 80 K and 9.4 ± 1.4 ML at ~10 K. In the case of an "NH_3-sandwich" sample, a correction for the non-uniform thickness of ASW spacer layer has previously been implemented for a more realistic estimation of $\langle x \rangle$ (Moon *et al.*, 2008), but this correction had little impact (±1 ML) on improving the $\langle x \rangle$ value of the present samples. Thus, proton transfer distance was considered basically equal to the thickness of the spacer layer.

4. Discussion

When the present samples were prepared by the growth of an ASW spacer layer over the hydronium ions (Stage 1-III) at 80 K, it was assumed that the hydroniums stayed in position without upward diffusion. However, the hydronium ions could undergo thermal diffusion and accumulate at the surface of a growing ASW film at high temperature because of their thermodynamic affinity for the ice surface (Lee *et al.*, 2007; Moon *et al.*, 2008; Park *et al.*, 2012). For this reason, the possibility of upward diffusion of hydronium ions at 80 K was worth investigating. The necessary information could be obtained from the measurement of the surface voltages of HCl-doped ASW films, as described by Lee *et al.* (2016) An analysis of the changes in the film voltage with the growth of the ASW overlayer on the HCl-adsorbed ASW surface at 95 K (Figure 5 in Lee *et al.* (2016)) showed that the average penetration depth of excess protons into the ASW overlayer was 3.5 ML when the HCl adsorbate coverage was 0.04 ML. This penetration depth decreased with an increase in HCl coverage, probably as a result of electrostatic interactions between H^+ and Cl^- ions. Based on this reference, the upward penetration of excess protons into ASW spacer layer in the present samples was expected to be less than 3.5 ML because of a higher HCl content (0.2 ML) and a slightly lower temperature. Therefore, the absolute distance of proton migration in the present measurements likely had this magnitude of uncertainty (< 3.5 ML). When the relative differences in the proton transfer distances at two different temperatures were assessed, this uncertainty would mostly cancel out because the same temperature (80 K) was used for the growth of the ASW spacer in all samples.

Moon *et al.* (2012) conducted similar experiments as described in this study, except that the locations of HCl and NH_3 in the samples were reversed ("NH_3-sandwich" structure), and reported that the average proton migration distance, $\langle x \rangle$, was 11.3 ML in ASW films at 90 K. The two studies show good agreement of the $\langle x \rangle$ values (11.3 and 11.2 ML) at similar temperatures (80 and 90 K), which supports the validity of the

experimental approaches. The upward migration of excess protons did not occur in the experiments conducted by Moon *et al.* (2012) because NH_3 was located in the sandwich layer and hydronium ions were at the surface of the samples. Therefore, the agreement in $\langle x \rangle$ values implied that the upward migration of excess protons in the present samples was not extensive.

In the discussion above, two different quantities relating to proton transport ranges have been mentioned, and it is worthwhile clarifying the differences between them. The proton transport distance (x) measured in the present study and by Moon *et al.* (2012) is the actual migration distance of excess protons from the proton donor to the acceptor species. This proton transport process occurs irreversibly in one direction. On the other hand, the penetration depth of excess protons into an ASW film discussed for the film voltage measurement (Lee *et al.*, 2016) corresponds to the distance of positive charge displacement from the initial injection position of hydronium ions in the sample, in the absence of proton acceptor species. The excess protons in this case may commute back and forth reversibly while residing near the location of the initial hydronium injection. The latter may represent the time-averaged position of protons commuting in the solid lattice. Therefore, the former (9 - 11 ML at 10 - 80 K) is always greater than the latter (3.5 ML at 95 K).

The present study shows two notable features for proton transfer in ASW. One is that proton transfer occurs in ASW at temperatures as low as ~10 K. The observed proton transfer distance in ASW is 9.4 ± 1.4 ML at this temperature, whereas the range of proton transfer along the ASW surface is substantially shorter (about 2 ML). Considering the possibility of local heating of the surface by ammonia adsorption, the surface proton transfer may actually be more restricted if the ammonia adsorption effect is excluded, which is consistent with the fact that surface proton transfer is an activated process (Moon *et al.*, 2010). At 10 K, essentially all atoms and molecules are immobilized with minimal thermal motion at the fixed lattice positions. Theoretical calculations (Kobayashi *et al.*, 2000) indicate that the barrier height for transport of excess proton in ice is about 50 kJ mol^{-1} when the O - O distance of the ice crystal is fixed, and it decreases to 6 kJ mol^{-1} for the minimum energy path with full geometry optimization, although the feasibility of such lattice distortion in cryogenic ice is questionable. These barrier heights are far too large for proton transfer to occur at 10 K. For example, the expected classical rate of proton transfer over the barrier of 6 kJ mol^{-1} is only $k \sim 5 \times 10^{-19}$ s^{-1} at 10 K with a frequency factor of 10^{13} s^{-1}. Therefore, the observed proton transfer must occur via quantum tunneling. The other feature is that the proton transfer distance is independent of the temperature, as indicated by the almost negligible difference (1.8 ± 1.8 ML) between the $\langle x \rangle$ values at 10 K and 80 K. This behavior contrasts with the significantly different

efficiencies of proton transfer along the surface at 10 K and 80 K. If it is considered that the different proton transfer efficiencies on the surface could somehow interfere with the measurements of vertical proton transfer in the present experiment, such a small difference in the $<x>$ values may be physically meaningless. The temperature independence again supports the quantum tunneling of excess protons. Previously, quantum tunneling phenomena of protons have been observed in experiments using pure ice crystals (Bove *et al.*, 2009) and water nanoclusters (Meng *et al.*, 2015) and studied by theoretical calculations (Drechsel-Grau and Marx, 2017). In these cases, concerted tunneling of multiple protons occurs in proton-ordered rings present in ice crystals or nanoclusters without acid additives. This involves simultaneous migration of charge defects in the loop without changing the net dipole moment in the whole proton transfer structure. The present system is different from these cases in that a net charge is carried through the lattice by the transport of excess proton.

The structure of ASW films prepared at 80 K must inevitably have an incomplete hydrogen-bonding network with high density of defects. In this environment, proton tunneling may be possible only in those localized regions of the sample that have a crystalline-like structure with a well-ordered hydrogen-bond network. Abundant defects and incompletely coordinated molecules in the sample may act as permanent traps of excess protons at low temperature (Collier *et al.*, 1984; Wooldridge and Devlin, 1988; Fisher *et al.*, 1995). Consequently, the proton transfer efficiency decreases rapidly with an increase in the donor-acceptor separation distance. In other words, the proton transfer distance in ASW is limited by the hydrogen-bond connectivity of the lattice, which implies that the proton transfer distance may vary depending on the preparation conditions of the ASW sample. Besides, the proton transfer distance is expected to be substantially longer in a macroscopic ice crystal with low defect density.

The occurrence of proton tunneling at low temperature has useful implications for cryogenic ice chemistry. Recent studies have shown that fluoroacetic acids spontaneously dissociate in ASW at low temperature (10 - 140 K) with a higher yield than that in aqueous solutions at room temperature (Shin *et al.*, 2017; Park *et al.*, 2018). These phenomena have been explained in terms of the proposition that acid dissociation is driven by the configurational entropy of mobile excess protons in the ice lattice (Park *et al.*, 2018). The occurrence of proton tunneling in ASW at low temperature supports this interpretation that highly mobile protons can generate a substantially large configurational entropy. Similar effects have also been suggested for the promotion of crystallization of ASW films in the presence of acids (Lee *et al.*, 2018). In general, it has been considered extremely difficult for chemical reactions to occur spontaneously in cryogenic ice because of the immobility of atoms and molecules as well as the lack of thermal energy to

overcome the reaction activation energy. For example, in the ice environments of outer planets of the solar system and the interstellar medium (Greenberg, 2002; Watanabe and Kouchi, 2008), it has thus far been assumed that chemical reactions are driven mostly by external energy input. However, the availability of proton tunneling in cryogenic ice suggests that certain types of proton transfer reactions may be able to occur spontaneously even under these conditions, as has been observed for the dissociation of fluoroacetic acids in ice (Shin *et al.*, 2017; Park *et al.*, 2018).

5. Conclusion

In this study, the transport efficiency of excess protons in ASW was examined at the low temperatures at which only proton hopping motion was possible without thermal reorientation of water molecules. It was found that the diffusion of excess protons occurred in ASW at temperatures as low as ~10 K. The average proton-transport distances were 9.4 ± 1.4 ML and 11.2 ± 1.1 ML at 10 K and 80 K, respectively, through the ASW film prepared by vapor deposition at 80 K. On the other hand, proton diffusion along the ASW surface hardly occurred at 10 K because of an activation energy barrier. The observations that proton transfer through ASW was nearly independent of the temperature and took place over a substantially longer distance than surface proton transfer indicated the quantum tunneling nature of excess protons in ASW. The observed proton transfer may occur in microscopic crystalline-like regions of the ASW samples, implying that the proton transfer distance may be much longer in an ice crystal. This study confirmed the assumption in previous studies (Park *et al.*, 2010; Shine *et al.*, 2010; Park *et al.*, 2018; Lee *et al.*, 2018) that excess protons are uniquely mobile species in ice at low temperatures and may contribute to various physical and chemical phenomena in these environments.

6. References

Ayotte, P.; Hébert, M.; Marchand, P. **2005,** Why Is Hydrofluoric Acid a Weak Acid? *J. Chem. Phys. 123*, 184501.

Ayotte, P.; Marchand, P.; Daschbach, J. L.; Smith, R. S.; Kay, B. D. **2011**, HCl Adsorption and Ionization on Amorphous and Crystalline H_2O Films Below 50 K. *J. Phys. Chem. A 115*, 6002-6014.

Bove, L. E.; Klotz, S.; Paciaroni, A.; Sacchetti, F. **2009**, Anomalous Proton Dynamics in Ice at Low Temperatures. *Phys. Rev. Lett. 103*, 165901.

Castro Neto, A. H.; Pujol, P.; Fradkin, E. **2006**, Ice: A Strongly Correlated Proton System. *Phys. Rev. B 74,* 024302..

Cholette, F.; Zubkov, T.; Smith, R. S.; Dohnalek, Z.; Kay, B. D.; Ayotte, P. **2009**, Infrared Spectroscopy and Optical Constants of Porous Amorphous Solid Water. *J. Phys. Chem. B 113*, 4131-4140.

Collier, W. B.; Ritzhaupt, G.; Devlin, J. P. **1984,** Spectroscopically Evaluated Rates and Energies for Proton-Transfer and Bjerrum Defect Migration in Cubic Ice. *J. Phys. Chem. 88*, 363-368.

Cowin, J. P.; Tsekouras, A. A.; Iedema, M. J.; Wu, K.; Ellison, G. B. **1999**, Immobility of Protons in Ice from 30 to 190 K. *Nature 398*, 405-407.

Dahms, F.; Costard, R.; Pines, E.; Fingerhut, B. P.; Nibbering, E. T.; Elsaesser, T. **2016**, The Hydrated Excess Proton in the Zundel Cation $H_5O_2^+$: The Role of Ultrafast Solvent Fluctuations. *Angew. Chem. Int. Ed. 55*, 10600-10605.

Daschbach, J. L.; Kim, J.; Ayotte, P.; Smith, R. S.; Kay, B. D. **2005**, Adsorption and Desorption of HCl on Pt(111). *J. Phys. Chem. B 109*, 15506-15514.

Devlin, J. P.; Uras, N.; Sadlej, J.; Buch, V. **2002**, Discrete Stages in the Solvation and Ionization of Hydrogen Chloride Adsorbed on Ice Particles. *Nature 417*, 269-271.

Devlin, J. P. **2011**, Relating the Current Science of Ion-Defect Behavior in Ice to a Plausible Mechanism for Directional Charge Transfer During Ice Particle Collisions. *Phys. Chem. Chem. Phys. 13*, 19707-19713.

Drechsel-Grau, C.; Marx, D. **2017**, Collective Proton Transfer in Ordinary Ice: Local Environments, Temperature Dependence and Deuteration Effects. *Phys. Chem. Chem. Phys. 19*, 2623-2635.

Eigen, M.; De Maeyer, L. **1958**, Self-Dissociation and Protonic Charge Transport in Water and Ice. *Proc. R. Soc. London, Ser. A, 247*, 505-533.

Eigen, M. **1964,** Proton Transfer, Acid-base Catalysis, and Enzymatic Hydrolysis. Part I: Elementary processes. *Angew. Chem. Int. Ed., 3*, 1-19.

Fisher, G. B. **1981**, The Electronic Structure of Two Forms of Molecular Ammonia Adsorbed on Pt(111). *Chem. Phys. Lett. 79*, 452-458.

Fisher, M.; Devlin, J. P. **1995**, Defect Activity in Amorphous Ice from Isotopic Exchange Data: Insight into the Glass Transition. *J. Phys. Chem. 99*, 11584-11590.

Fletcher, N. H. **1970**, *The Chemical Physics of Ice*; Cambridge University Press: Cambridge.

Gland, J. L.; Kollin, E. B. **1981**, Ammonia Adsorption on the Pt(111) and Pt(S)-6(111)×(111) Surfaces. *Surf. Sci. 104*, 478-490.

Greenberg, J. M. **2002**, Cosmic Dust and Our Origins. *Surf. Sci. 500*, 793-822.

KOPRI 극지연구소

Hagen, W.; Tielens, A. G. G. M. **1982**, The Librational Region in the Spectrum of Amorphous Solid Water and Ice I_c between 10 and 140 K. *Spectrochim. Acta, Part A 38*, 1089-1094.

Jaccard, C. **1959**, Etude Theorique Et Experimentale Des Proprietes De La Glace. *Helv. Phys. Acta*, *32*, 89-128.

Jaccard, C. **1964**, Thermodynamics of Irreversible Processes Applied to Ice. *Phys. Kondens. Mater.*, *3*, 99-118.

Jacox, M. E.; Thompson, W. E. **2005**, Infrared Spectrum of the NH_4-d_n^+ Cation Trapped in Solid Neon. *Phys. Chem. Chem. Phys. 7*, 768-775.

Kang, H. **2005**, Chemistry of Ice Surfaces. Elementary Reaction Steps on Ice Studied by Reactive Ion Scattering. *Acc. Chem. Res. 38*, 893-900.

Kang, H.; Shin, S.; Park, Y.; Kang, H. **2016**, Electric Field Effect on Condensed-Phase Molecular Systems. III. The Origin of the Field-Induced Change in the Vibrational Frequency of Adsorbed CO on Pt(111). *J. Phys. Chem. C 120*, 17579-17587.

Kobayashi, C.; Saito, S. J.; Ohmine, I. **2000**, Mechanism of Fast Proton Transfer in Ice: Potential Energy Surface and Reaction Coordinate Analyses. *J. Chem. Phys. 113*, 9090-9100.

Lee, C. W.; Lee, P. R.; Kang, H. **2006**, Protons at Ice Surfaces. *Angew. Chem. Int. Ed. 45*, 5529-5533.

Lee, C. W.; Lee, P. R.; Kim, Y. K.; Kang, H. **2007**, Mechanistic Study of Proton Transfer and H/D Exchange in Ice Films at Low Temperatures (100 - 140 K). *J. Chem. Phys. 127*, 084701.

Lee, D. H.; Bang, J.; Kang, H. **2016**, Surface Charge Layer of Amorphous Solid Water with Adsorbed Acid or Base: Asymmetric Depth Distributions of H^+ and OH^- Ions. *J. Phys. Chem. C 120*, 12051-12058.

Lee, D. H.; Kang, H. **2018**, Acid-Promoted Crystallization of Amorphous Solid Water. *J. Phys. Chem. C 122*, 24164-24170.

Lilach, Y.; Iedema, M. J.; Cowin, J. P. **2008**, Proton Segregation on a Growing Ice Interface. *Surf. Sci. 602*, 2886-2893.

Livingston, F. E.; Smith, J. A.; George, S. M. **2002**, General Trends for Bulk Diffusion in Ice and Surface Diffusion on Ice. *J. Phys. Chem. A 106*, 6309-6318.

Marchand, P.; Marcotte, G.; Ayotte, P. **2012**, Spectroscopic Study of HNO_3 Dissociation on Ice. *J. Phys. Chem. A 116*, 12112-12122.

KOPRI 극지연구소

Martin, J. M. L.; Lee, T. J. **1996**, Accurate Ab Initio Quartic Force Field and Vibrational Frequencies of the NH_4^+ Ion and Its Deuterated Forms. *Chem. Phys. Lett. 258*, 129-135.

Meng, X.; Guo, J.; Peng, J.; Chen, J.; Wang, Z.; Shi, J.-R.; Li, X.-Z.; Wang, E.-G.; Jiang, Y. **2015**, Direct Visualization of Concerted Proton Tunnelling in a Water Nanocluster. *Nat. Phys. 11*, 235-239.

Moon, E. S.; Lee, C. W.; Kang, H. **2008**, Proton Mobility in Thin Ice Films: A Revisit. *Phys. Chem. Chem. Phys. 10*, 4814-4816.

Moon, E. S.; Yoon, J.; Kang, H. **2010**, Energy Barrier of Proton Transfer at Ice Surfaces. *J. Chem. Phys. 133*, 044709.

Moon, E. S.; Kim, Y.; Shin, S.; Kang, H. **2012**, Asymmetric Transport Efficiencies of Positive and Negative Ion Defects in Amorphous Ice. *Phys. Rev. Lett. 108*, 226103.

Onsager, L.; Dupuis, M. **1962**, The Electrical Properties of Ice. In *Electrolytes*, Pesce, B., Ed. Pergamon Press: Oxford, pp 27-46.

Parent, P.; Lasne, J.; Marcotte, G.; Laffon, C. **2011**, HCl Adsorption on Ice at Low Temperature: A Combined X-Ray Absorption, Photoemission and Infrared Study. *Phys. Chem. Chem. Phys. 13*, 7142−7148.

Park, S. C.; Jung, K. H.; Kang, H. **2004**, H/D Isotopic Exchange between Water Molecules at Ice Surfaces. *J. Chem. Phys. 121*, 2765-2774.

Park, S. C.; Moon, E. S.; Kang, H. **2010**, Some Fundamental Properties and Reactions of Ice Surfaces at Low Temperatures. *Phys. Chem. Chem. Phys. 12*, 12000-12011.

Park, E.; Lee, D. H.; Kim, S.; Kang, H. **2012**, Transport and Surface Accumulation of Hydroniums and Chlorides in an Ice Film. A High Temperature (140 - 180 K) Study. *J. Phys. Chem. C 116*, 21828-21835.

Park, K.; Lin, W.; Paesani, F. **2014**, Fast and Slow Proton Transfer in Ice: The Role of the Quasi-Liquid Layer and Hydrogen-Bond Network. *J. Phys. Chem. B 118*, 8081-8089.

Park, Y.; Kang, H.; Kang, H. **2016**, Brute Force Orientation of Matrix Isolated Molecules: Reversible Reorientation of Formaldehyde in an Argon Matrix toward Perfect Alignment. *Angew. Chem. Int. Ed. 56*, 1046-1049.

Park, Y.; Shin, S.; Kang, H. **2018**, Entropy-Driven Spontaneous Reaction in Cryogenic Ice: Dissociation of Fluoroacetic Acids. *J. Phys. Chem. Lett.* 4282-4286.

Petrenko, V. F.; Whitworth, R. W. **1999**, *Physics of Ice*; Oxford University Press: Oxford; New York.

KOPRI 극지연구소

Presiado, I.; Lal, J.; Mamontov, E.; Kolesnikov, A. I.; Huppert, D. **2011**, Fast Proton Hopping Detection in Ice I_h by Quasi-Elastic Neutron Scattering. *J. Phys. Chem. C 115*, 10245-10251.

Pursell, C. J.; Zaidi, M.; Thompson, A.; Fraser-Gaston, C.; Vela, E. **2000**, Acid-Base Chemistry on Crystalline Ice: HCl + NH_3. *J. Phys. Chem. A 104*, 552-556.

Severson, M. W.; Devlin, J. P.; Buch, V. **2003**, Librational Modes of Ice. I. *J. Chem. Phys. 119*, 4449-4457.

Shin, S.; Park, Y.; Kim, Y.; Kang, H. **2017**, Dissociation of Trifluoroacetic Acid in Amorphous Solid Water: Charge-Delocalized Hydroniums and Zundel Continuum Absorption. *J. Phys. Chem. C 121*, 12842-12848.

Smith, R. S.; Matthiesen, J.; Knox, J.; Kay, B. D. **2011**, Crystallization Kinetics and Excess Free Energy of H_2O and D_2O Nanoscale Films of Amorphous Solid Water. *J. Phys. Chem. A 115*, 5908-5917.

Uritski, A.; Presiado, I.; Huppert, D. **2008**, Indication of a Very Large Proton Diffusion in Ice I_h. *J. Phys. Chem. C 112*, 11991-12002.

Uritski, A.; Presiado, I.; Erez, Y.; Gepshtein, R.; Huppert, D. **2009,** Temperature Dependence of Proton Diffusion in I_h Ice. *J. Phys. Chem. C 113*, 10285-10296.

Watanabe, N.; Kouchi, A. **2008**, Ice Surface Reactions: A Key to Chemical Evolution in Space. *Prog. Surf. Sci. 83*, 439-489.

Wooldridge, P. J.; Devlin, J. P. **1988**, Proton Trapping and Defect Energetics in Ice from FT-IR Monitoring of Photoinduced Isotopic Exchange of Isolated D_2O. *J. Chem. Phys. 88*, 3086-3091.

KOPRI 극지연구소

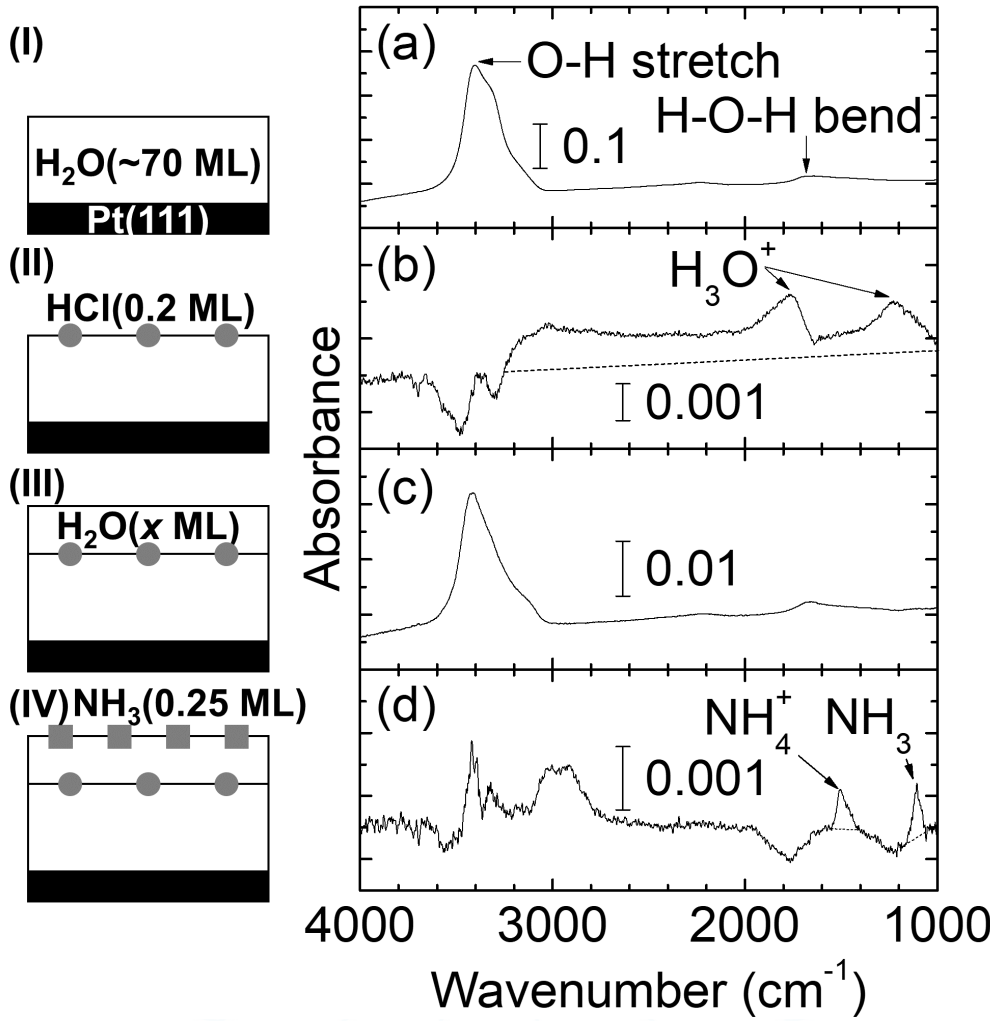

Figure 1. (I) - (IV) Schematics of preparation stages of NH_3(0.25 ML)/ASW(*x* ML)/HCl(0.2 ML)/ASW(~70 ML) film ("HCl-sandwich" structure) on a Pt(111) substrate. The sequence of growth from the bottom to top layer is: (I) ASW substrate film, (II) HCl adsorbate, (III) ASW spacer film, and (IV) NH_3 adsorbate. Steps (I - III) were carried out at 80 K for all samples. Ammonia adsorption (step IV) was performed at either ~10 K or 80 K. (a) - (d) Difference RAIR spectra before and after the corresponding steps. The ASW spacer layer in (c) had a thickness of 7 ML. The dotted line in spectrum (b) is the spectral baseline drawn to indicate the Zundel continuum absorption.

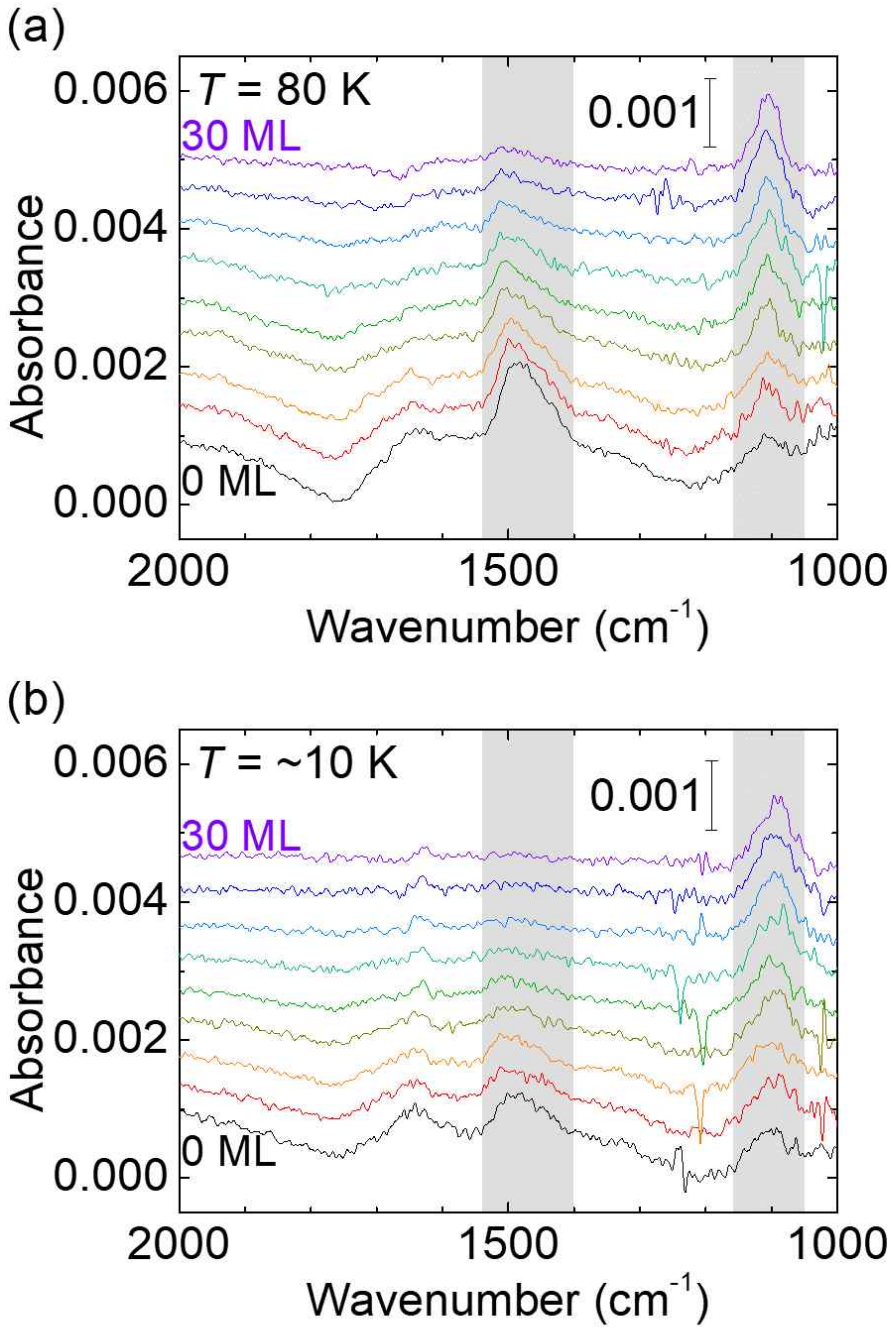

Figure 2. Difference RAIR spectra measured after ammonia adsorption for a coverage of 0.25 ML onto the surface of ASW(0 - 30 ML)/HCl(0.2 ML)/ASW(~70 ML)/Pt(111) samples. Ammonia adsorption was carried out at temperatures (a) 80 K and (b) ~10 K. The thickness of the ASW spacer layer in the samples was 0, 2, 3, 5, 7, 10, 15, 20, and 30 ML, from the bottom to top spectra in (a) and (b). The vertical spacing between the spectra is for visual clarity. Gray shades highlight the positions of the ν_4 band of NH_4^+ (~1480 cm^{-1}) and the ν_2 band of NH_3 (~1100 cm^{-1}). Glitch peaks around 1200 cm^{-1} in several spectra can be attributed to noise that most likely originated from the mechanical vibration of a He cryostat.

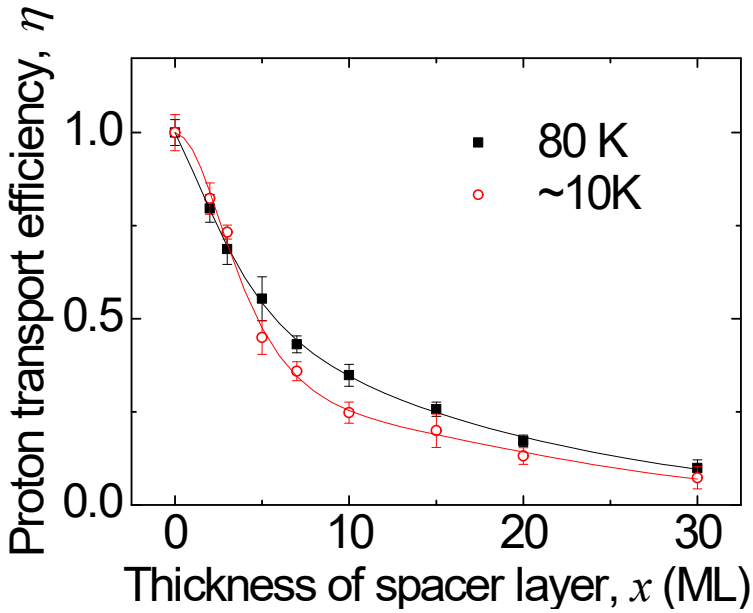

Figure 3. Proton transfer efficiency versus the thickness of ASW spacer layer measured at 80 K (black solid squares) and ~10 K (red open circles). The normalized $\eta(x)$ curves represent the transport efficiencies of "mobile" excess protons in the sample. The error bars correspond to the uncertainty for the quantitation of proton donor and acceptor species through RAIRS measurement.

KOPRI
극지연구소

제 4 절. 얼음의 화학반응과 미구조와의 상관관계 규명

김대영

한국해양과학기술원 부설 극지연구소

1. 서론 및 배경

암석(또는 다결정물질, polymineralic materials)은 취성(brittle), 연성(ductile) 변형, 크게 두 가지로 변형행동을 보인다. 낮은 온도, 또는 높은 변형률(strain rate)이 가해진 상황에서 암석은 취성변형 행동을 보이며, 높은 온도, 또는 낮은 변형률이 가해진 상황에서 연성변형 행동을 보인다. 취성변형 행동은 바이어리의 법칙(Byerlee's law)에 의해 주어진 수직응력(normal stress)과 비례하는 전단응력(shear stress)을 보이며, 연성변형 행동은 파워법칙(Power law)에 의해 변형률이 입자크기, 응력 등에 의해 결정된다(e.g., Kohlstedt et al., 1995; Hirth et al., 2001).

얼음은 특히 기계적으로 약한 암석으로, 대부분의 영역에서 연성변형 행동을 보인다. 일반적으로 얼음의 변형행동은 응력과 변형률이 비례를 보이는 글렌의 법칙(Glen's law)으로 설명된다(Glen, 1952). 추후 향상계수(enhancement factor), 슈미드계수(schmid factor) 등이 추가되며, 얼음 흐름법칙은 수정되었다(Azuma and Higashi, 1985; Budd and Jacka, 1989). 특히 실험에 의해 변형(deformation)을 일으키는 경우, 샘플의 변형을 위한 공간적 제약으로 인해 자연상에서 일어나는 변형에 비해 충분한 변형(strain)을 획득하지 못한 상태가 많다(그림 1). 이는 안정상태(steady state)에 도달하지 못한 상태에서 변형실험이 끝나게 되므로, 올바른 유동법칙을 획득하지 못한 경우가 많았다.

최근 연구에 의해 밝혀진 결빙동안 생기는 요오드, 크롬산염, 아비산염 등 독극물의 정화작용(e.g., Kim et al., 2016, 2017)은 얼음의 변형에 미치는 다른 요인이 될 수 있다. 얼음 내 함유된 불순물의 함량에 따라 얼음의 녹는점(어는점)이 바뀔 수 있고, 이는 얼음의 변형행동에 직접적으로 영향을 미칠 수 있다. 따라서 본 연구를 통해서 화학적 첨가물(독극물, 크롬산염)을 포함한 얼음의 변형실험 과정동안 변형행동에 직접적인 영향을 미치는지 확인하려고 하였다.

2. 재료 및 방법

본 연구는 얼음의 합성실험, 변형실험 이렇게 두 가지 단계로 나눠 실시하였다. 첫 번째 단계는 얼음의 합성실험으로, 크롬이 함유된 표준얼음(standard ice, 입자크기가 180-250 um의 기공이 없는 얼음; Durham et al., 1983)을 만드는 것이 목표였다. 크롬의 합성실험은 미국 펜실베니아대학에서 실시하였다(그림 2). 크롬을 함유한 얼음큐브를 냉동고에서 만든 후, 믹서에 곱게 분쇄한다(그림 3a). 분쇄한 얼음입자는 체(sieve)에 걸러 180-250 um 사이즈의 일정한 입자크기만 골라낸다(그림 3b). 입자크기가 일정한 얼음입자를 원통형 틀에 채운다(그림 3c).

180-250 um 사이즈의 얼음입자가 가득한 원통형 몰드와 물(또는 크롬이 함유된 물)을 얼음물에 담그고 온도를 안정화시켜준 후, 원통형 몰드 내부에 진공을 잡아주며, 물을 흡입시켜 준다(그림 4). 이렇게 완성된 합성얼음은 약 180-250 um 사이즈의 일정한 입자크기를 가지고 크롬을 함유하고 있다.

두 번째로 실시한 실험은 얼음변형실험이다. 얼음변형실험은 압력 14.5-19 MPa, 온도 -30 ~ -10 ℃의 조건에서 총 3가지를 실시하였다(표 1). 변형은 약 8.55-11.79 %까지 주어졌으며, 변형률은 0.85-1.18 × 10^{-5}으로 측정되었다.

얼음변형실험은 펜실베니아대학에 설치된 가스를 이용해 고압을 생성시키는 가스-중간체 장비(gas-medium apparatus)에서 실시하였다(그림 5). 변형실험 후 복구한 샘플은 각각 사진을 찍고, 기계데이터를 획득하였다(그림 6).

3. 연구결과

크롬을 함유한 합성얼음을 만들고, 얼음변형실험을 실시하는 동안, 크롬, 4-CP의 함량이 어떤 변화를 일으키는지 각 단계별로 두 물질의 함량을 측정하였다(표 2). 각각의 함량은 실험을 진행함에 따라서 줄어듬을 알 수 있고, 특히 얼음의 합성이 끝난 시점, 얼음의 변형실험이 끝난 시점에서 가장 큰 변화량을 보인다는 것을 알 수 있다. 이는 얼음의 합성과 변형실험이 크롬의 분해에 영향을 끼친다는 것을 지시한다. 하지만 둘중 어떤 과정이 크롬의 분해에 좀더 큰 영향을 끼치는지에 대한 정확한 자료는 없다. 크롬 외 다른 물질(메탈, 윤활제 등)도 변형실험 과정 속에서 포함될 수 있으므로, 화학반응이 일어나지 않는 장비(예, 플라스틱으로 제작 등)에서 실험을 실시하는 방안을 고안 중에 있다.

추가적으로 뉴질랜드 오타고대학에서 SEM-EBSD를 이용한 샘플의 미구조 관찰을 실시하였다(그림 7). 결정방향성 맵 상에서 나타난 결정은 등입자성(equigranular)이고, 이는 얼음에 집중된 변형이 일정했음을 지시한다(그림 8). 얼음결정의 C-축은 한 곳으로 집중되어 나타나는 경향이 있고(그림 9), 이는 일반적인 극지방 얼음에서 나타나는 지구내부방향으로 배열하는 경향과 같다(e.g., Kamb, 1959; Gow and Williamson, 1976; Gow et al., 1997; Thorsteinsson et al., 1997). 세 샘플이 물질, 압력, 온도, 응력의 조건이 다르기 때문에 이를 비교해 특성을 파악할 수 있다. PIL-170과 PIL-174를 비교하면, 물질과 온도, 압력, 응력 조건이 다르기 때문에, Cr, 압력, 온도, 응력 조건에 따라 미구조가 발달함을 알 수 있다. PIL-174와 PIL-175를 비교하면, 압력, 온도, 응력 조건은 일정하기 때문에, 물질이 달랐을 때 Cr의 양이 적은 샘플이 더 변형된 것을 알 수 있다. 이 결과를 같은 크기의 응력이 작용한 표준얼음시료를 이용한 데이터와 비교했을 때(Craw et al., 2018), Cr을 포함한 얼음이 쉽게 변형되는 것을 알 수 있다. 이는 극지방 얼음이 화학성분을 함유함에 따라 흐름의 속도가 바뀔 수 있으므로 극지방 얼음이동에 중요한 역할을 할 수 있다는 것을 지시한다.

4. 결론

크롬을 함유한 얼음을 이용해 고압저온 변형실험을 실시함으로, 얼음의 화학적 변화가 얼음변

형에 미치는 영향을 연구하고자 하였다. 크롬을 함유한 합성얼음을 제작하고, 합성얼음을 -10 ~ -30도의 온도, 14.5-19 MPa의 압력, 8.55-11.79 %의 변형(strain)을 주어 고압저온 변형실험을 실시하였다. 합성얼음을 제작, 변형하는 과정 중, 각 단계별로 샘플을 녹여 크롬과 4-CP 함량을 측정하였다. 분석결과, 합성얼음을 제작한 직후, 변형실험을 실시한 직후, 크롬과 4-CP 함량이 가장 많이 줄어드는 것으로 나타났다. 이는 얼음의 변형이 크롬의 해독과정과 밀접한 영향이 있음을 지시한다. 하지만, 얼음합성과 변형 두 과정 중 어떤 것이 결정적으로 영향을 미쳤는지에 대한 것은 추가연구가 필요하다. 얼음의 결정방향성 분석결과, 얼음입자가 등입이고 c-축이 압축방향과 평행하게 배열된 것을 알 수 있었다. 이는 변형실험 과정 중, 일정한 힘이 얼음에 작용했다는 것을 지시한다.

5. 참고문헌

Azuma, N., Higashi, A., 1985. Formation processes of ice fabric pattern in ice sheets. Annals of Glaciology 6, 130-134.

Budd, W.F., Jacka, T.H., 1989. A review of ice rheology for ice sheet modelling. 16, 107-144.

Craw, L., Qi, C., Prior, D.J., Goldsby, D.L., Kim, D., 2018. Mechanics and microstructure of deformed natural anisotropic ice. Journal of Structural Geology 115, 152-166.

Durham, W.B., Heard, H.C., Kirby, S.H., 1983. Experimental deformation of polycrystalline H_2O ice at high pressure and low temperature: preliminary results. Journal of Geophysical Research: Solid Earth 88, B377-B392.

Glen, J.W., 1952. Experiments on the deformation of ice. Journal of Glaciology 2, 111-114.

Gow, A.J., Meese, D.A., Alley, R.B., Fitzpatrick, J.J., Anandakrishnan, S., Woods, G.A., Elder, B.C., 1997. Physical and structural properties of the Greenland Ice Sheet Project 2 ice core: A review. Journal of Geophysical Research 102, 26,559-26,575.

Gow, A.J., Williamson, T., 1976. Rheological implications of the internal structure and crystal fabrics of the West Antarctic ice sheet as revealed by deep core drilling at Byrd Station. Geological Society of America Bulletin 87, 1665-1677.

Hirth, G., Teyssier, C., Dunlap, W.J., 2001. An evalution of quartzite flow laws based on comparisons between experimentally and naturally deformed rocks. International Journal of Earth Sciences (Geol Rundsch) 90, 77-87.

Kamb, W.B., 1959. Ice petrofabric observations from Blue Glacier, Washington, in relation to theory and experiment. Journal of Geophysical Research 64, 1891-1909.

Kim, K., Yabushita, A., Okumura, M., Saiz-Lopez, A., Cuevas, C.A., Blaszczak-Boxe, C.S., Min, D.W., Yoon, H.-I., Choi, W., 2016. Production of molecular iodine and tri-iodide in the frozen solution of iodide: Implication for polar atmosphere.

Environmental Science & Technology 50, 1280-1287.

Kim, K., Chung, H.Y., Ju, J., Kim, J., 2017. Freezing-enhanced reduction of chromate by nitrite. Science of the Total Environment 590-591, 107-113.

Kohlstedt, D.L., Evans, B., Mackwell, S.J., 1995. Strength of the lithosphere: constraints imposed by laboratory experiments. Journal of Geophysical Research 100, 17587-17602.

Thorsteinsson, T., Kipfstuhl, J., Miller, H., 1997. Textures and fabrics in the GRIP ice core. Journal of Geophysical Research 102, 26,583-26,599.

KOPRI
극지연구소

표 1. 얼음 변형실험 결과

	Material	P, T	Length (L_0, L_1), displacement (mm)	Strain (%)	Strain rate (measured, initial) (s^{-1})
PIL-170	Pure ice seed + Cr (PH 4.5) flood in	19 MPa, -30 °C	38.61, 35.31, 3.30	8.55	0.85 x 10^{-5}, ~1 x 10^{-5}
PIL-174	Cr (PH 4.5) ice seed + Cr (PH 4.5) flood in	15 MPa, -10 °C	49.53, 43.69, 5.84	11.79	1.18 x 10^{-5}, ~1 x 10^{-5}
PIL-175	Pure ice seed + Cr (PH 4.5) flood in	14.5 MPa, -10 °C	41.91, 37.59, 4.32	10.31	1.03 x 10^{-5}, ~1 x 10^{-5}

표 2. 변형실험한 얼음 내 크롬과 4-CP 함량의 변화과정

	Cr(VI) (uM)	4-CP (uM)
Cr(VI)_pH4.5_after mixing(befor icing)	20	20.60
Cr(VI)_pH4.5_after making cubic ice for (>12)	13.26	13.75
Cr(VI)_pH4.5_ice powder for seed	11.06	10.31
Cr(VI)_pH4.5_after floodin	19.95	20.71
Cr(VI)_pH4.5_after making ice for exp	2.51	0.92
pure ice seed+Cr(VI)flood in before exp	7.45	8.40
PIL-174 deformed sample	0.87	0.39
PIL-174 undeformed (stay as ice to KOPRI)	1.80	0.99

표 3. 얼음 변형실험 결과

	Material	P (MPa), T (℃)	J-index	M-index	Grain size (μm)
PIL-170	Pure ice seed + Cr (PH 4.5) flood in	19, -30	1.02	0.001	206 ± 112
PIL-174	Cr (PH4.5) ice seed + Cr (PH 4.5) flood in	15, -10	1.22	0.034	341 ± 186
PIL-175	Pure ice seed + Cr (PH 4.5) flood in	14.5, -10	1.31	0.051	328 ± 176

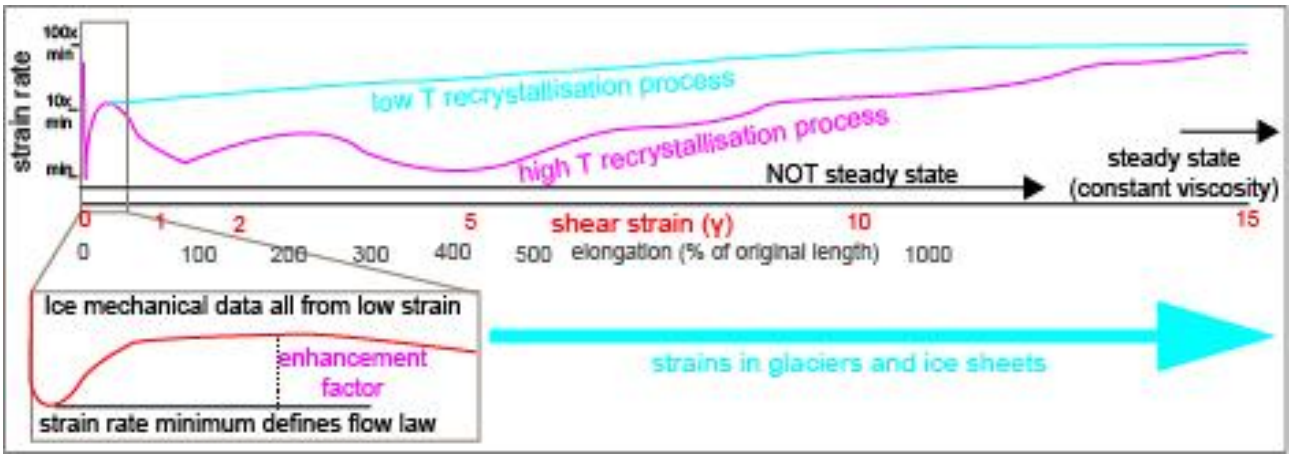

그림 1. 대리석, 석영, 감람석 등의 변형과 변형률 관계의 도식도(큰 그래프). 얼음의 경우(작은 그래프), 실험에 의해 낮은 변형을 가지는 데이터를 이용함으로, 올바른 유동법칙을 흐름법칙을 획득하지 못함.

그림 2. 미국 펜실베니아대학에 있는 합성얼음을 제작하는 원통형 틀과 마개

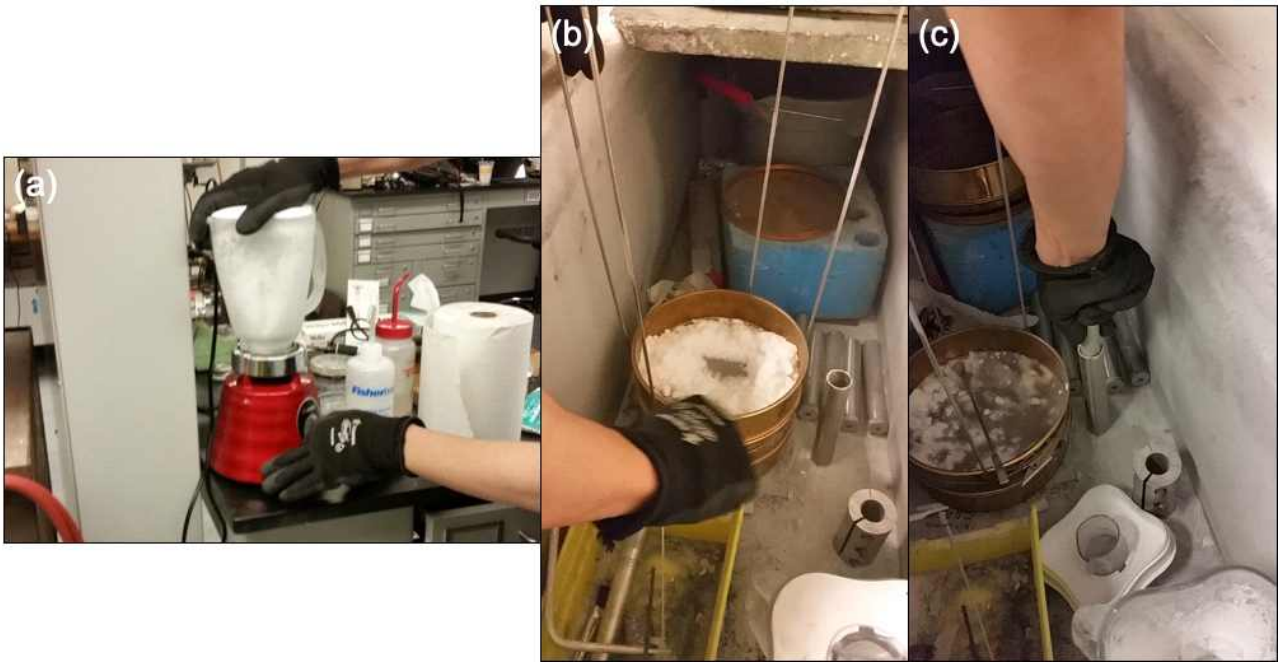

그림 3. 합성얼음을 제작하는 방법(1). 크롬을 함유한 얼음큐브를 냉동고에서 만든 후, 믹서에 곱게 분쇄(a), 체(sieve)에 걸러 180-250 um 사이즈의 일정한 입자크기만 골라낸 후(b), 원통형 틀에 채움(c)

KOPRI

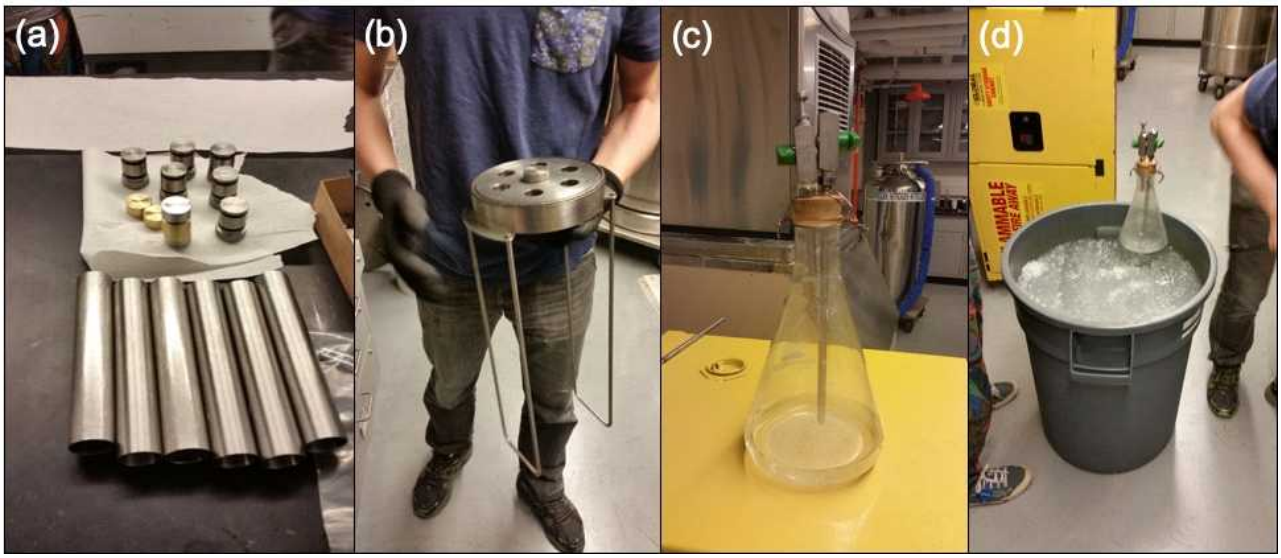

그림 4. 얼음이 가득한 원통형 몰드에 물을 주입시켜 합성얼음을 완성하는 방법. 원통형 몰드(a), 원통형 몰드와 물이 든 비커를 연결시켜주는 장치(b), 물이 든 비커(c), 원통형 몰드를 얼음물에 담궈 온도를 안정화시켜주는 방법(d)

그림 5. 미국 펜실베니아대학에 설치된 고압저온 얼음 변형장비

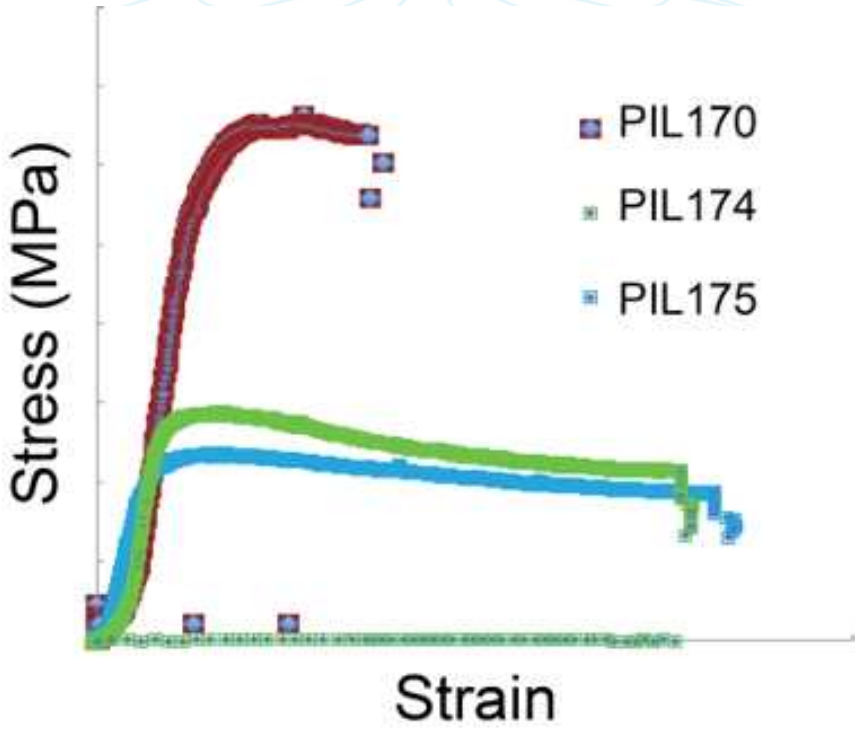

그림 6. 얼음변형실험 도중 샘플에 가해진 응력-변형 상관관계

그림 7. 뉴질랜드 오타고대학에 설치된 얼음의 결정방향성을 측정할 수 있는 cryo-SEM-EBSD 장비

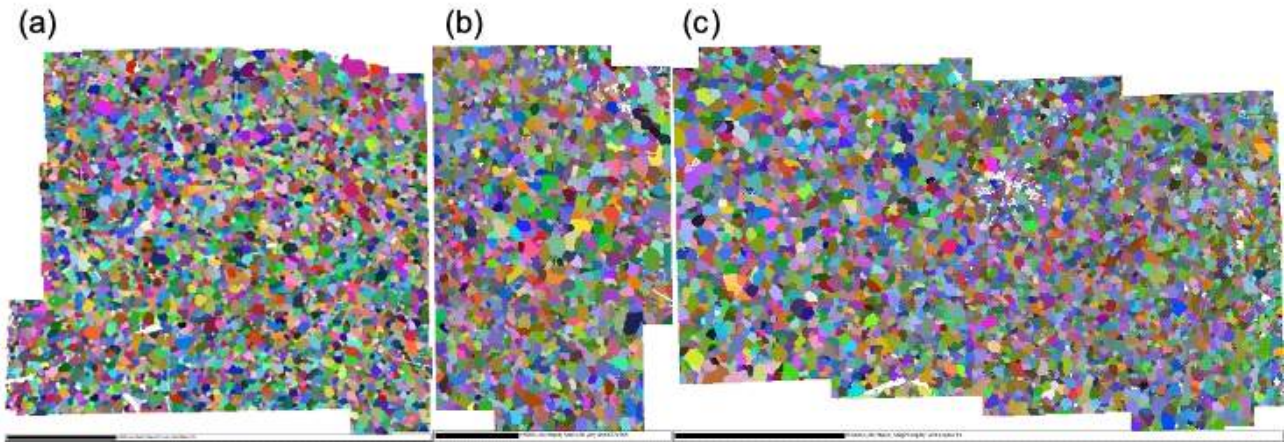

그림 8. 뉴질랜드 오타고대학에서 분석한 얼음샘플의 결정방향성지도(orientation map). 분석함 샘플은 미국 펜실베니아대학에서 변형실험을 통해 합성, 변형된 얼음샘플임. (a) PIL-170, (b) PIL-174, (c) PIL-175.

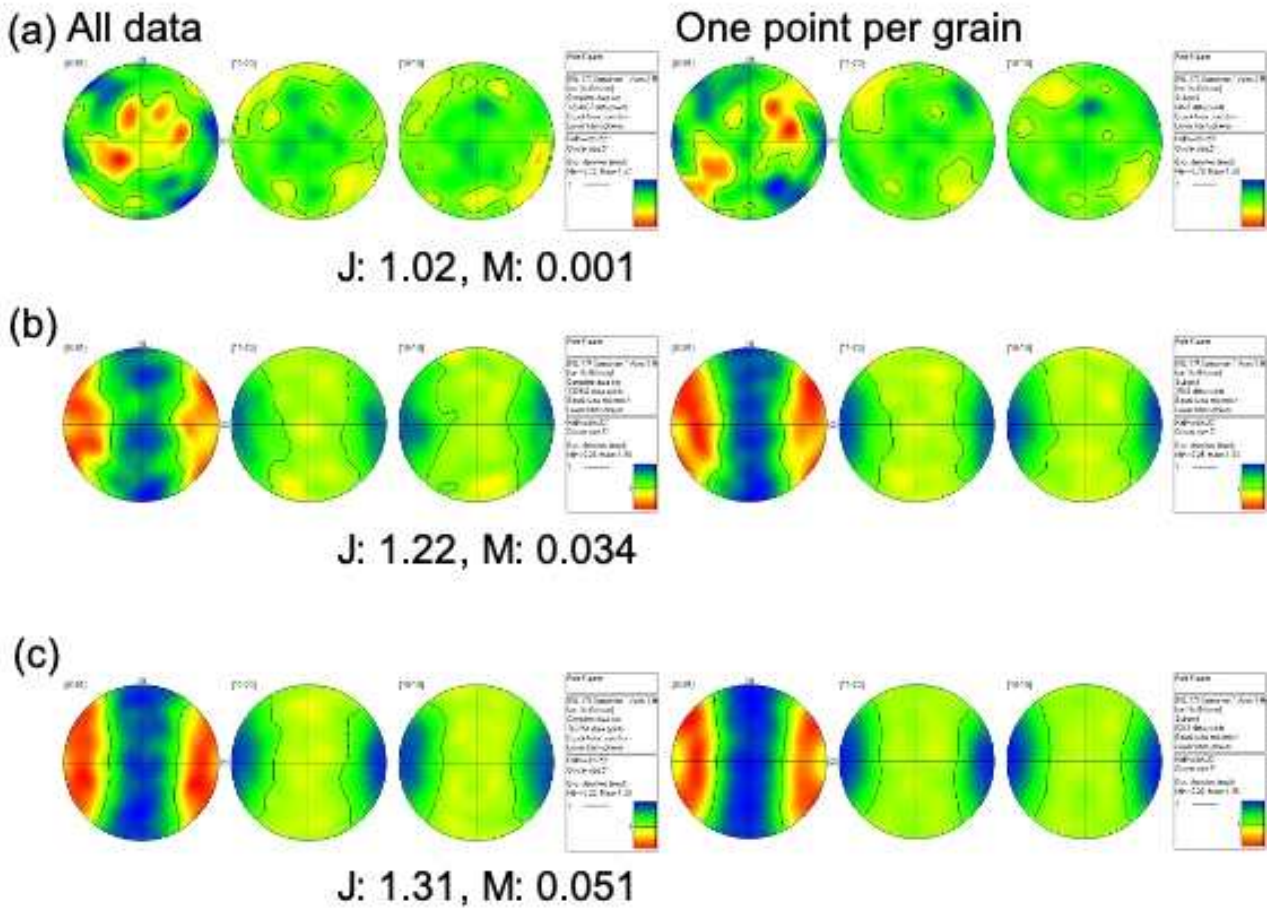

그림 9. 뉴질랜드 오타고대학에서 측정한 얼음의 결정방향성 데이터를 스테레오넷에 도시한 폴피겨(pole figure). 샘플의 압축방향을 양옆으로 배열하도록 샘플을 준비하고 측정을 실시함으로 c-축이 양옆으로 배열됨. 왼쪽은 분석한 전체 데이터를 이용해 도시하였고, 오른쪽은 입자당 한 개의 분석포인트를 반영해 도시한 그림

제 5 절. 얼음의 저농도 할로겐 원소 및 할로겐 화학종 분석법 개발

강정호, 황희진

한국해양과학기술원 부설 극지연구소

1. 서론 및 배경

· 극지역 할로겐 화학

- 대기 중 브롬(Br)과 요오드(I)는 대기 화학반응, 구름핵의 생성과 변화, 오존 농도의 변화에 중요한 역할을 하기 때문에 특히 극지역 대기 중 할로겐 농도 즉 브롬과 요오드의 농도에 대해 많은 연구가 진행되고 있다. 대기 중 브롬이 존재하면 광화학 반응에 의해 대류권의 오존의 농도가 줄어들기 때문에 소위 극지역 봄철에 발생하는 브롬폭발(bromine expolosion) 현상에 의해 오존 농도의 계절적 및 지역적 변화가 발생한다 (그림 1).
- 브롬과 요오드는 주로 해양에서 생성되고 대기로 방출된다. 바닷물의 브롬 농도는 약 70 ug g^{-1}이며 대부분 해염 에어로졸 형태로 방출된다. 바다에서 방출되는 요오드는 구름형성에 관여하는 에어로졸의 형성 및 구름형성의 핵으로 작용할 수 있다. 극지역 요오드의 방출은 주로 계절적 해빙의 아래에서 생성되는 해조류와 같은 해양의 생물학적 활동에 의해 작용한다. 따라서 극지역에서 해빙과 브롬 및 요오드의 농도가 밀접한 연관성을 갖게 된다. 해빙에 갇힌 BrO 와 IO가 봄철 해빙의 변화에 따라 방출되기 때문에 BrO 와 IO의 농도는 극지역 봄철에 증가한다. 또한 극지역에서 브롬과 요오드는 서로 밀접한 연관성을 갖는다. IO가 존재할 때 BrO와 같이 작용하는 촉매작용에 의해 오존파괴가 일어나게 된다.

· 얼음의 저농도 할로겐 원소 분석법 개발 및 최적화

- 극지 해빙에 의해 방출되는 할로겐 원소 즉 브롬과 요오드의 발생원과 방출 머커니즘은 여전히 밝혀지지 않는 부분이 많다. 얼음 내 할로겐 원소의 정량적 화학반응 메커니즘을 규명하기 위해 극지 해빙에서 존재하는 저농도 할로겐 원소의 최적화된 분석이 필요하다. 극지 얼음에서 브롬의 농도는 수십-수천 pg mL^{-1}이고, 요오드의 농도는 수십-수백 pg mL^{-1} 수준이다. 반면 실험실에서 수행되는 결빙과 해빙에 따른 할로겐 원소의 정량적 화학반응실험은 이보다 훨씬 높은 농도에서 수행된다. 실험실 환경모사와 극지 해빙에서 할로겐 화학반응 메커니즘을 동시에 규명하기 위해서는 각각의 농도 수준에 따른 적절한 분석법이 필요하다. 특히 극지 얼음의 농도 범위를 분석할 수 있는 저농도 할로겐 원소의 농도 분석법을 최적화해야 한다. 얼음 내 저농도 할로겐 원소의 정량적 분석은 자동시료도입장치를 연결한 고분해능 유도결합플라즈마 질량분석기(HR-ICP-SFMS)로 분석이 가능하다. HR-ICP-SFMS를 활용한 저농도 할로겐 원소의 정량분석은 현재는 이탈리아 베니스 대학(University of Venice, CNR)과 미국 Desert Research Institute (DRI) 등 일부 연구기

관에서만 분석이 가능하기 때문에 극지연구를 주도하는 극지연구소에서 시급히 분석법을 개발하고 활용할 필요성이 강조된다.

- 극지 얼음 내 할로겐 원소의 정량적 화학반응 메커니즘 규명을 위해서는 할로겐 원소 뿐만 아니라 여러 이온성분의 정량적 변화를 이해해야 한다. 일반적으로 할로겐 원소는 해양성분에 의해 영향을 받기 때문에 비교할 수 있는 해염성분을 같이 비교 분석을 통해 할로겐 원소의 계절적 변화와 할로겐 강화(halogen enrichment) 현상을 이해할 수 있다. 또한 대기 중 먼지입자와 생물성 기원 프록시의 상관관계를 이해하기 위해 얼음의 이온성분을 정량화하는 분석법 개발은 필수적인 연구 주제이다.

· 할로겐 원소 화학종 농도의 정량적 분석을 위한 기초연구

- 극지시료에서 할로겐 원소는 다양한 이온의 형태로 존재한다. 요오드는 일반적으로 I^-와 IO_3^- 및 유기-요오드(organo-I) 형태로 존재하고, 브롬은 Br^-와 BrO_3^-의 형태로 존재한다. 이들 화학종의 농도는 극지 얼음에서 수 pg mL^{-1} 수준으로 매우 낮은 농도 수준이다. 브롬과 요오드 화학종의 분리를 위해서는 이온크로마토그래피 또는 액체크로마토그래피 컬럼을 거쳐 화학종을 분리한 후 사중극자 유도결합플라즈마 질량분석기(ICP-QMS) 또는 고분해능 유도결합플라즈마 질량분석기(HR-ICP-SFMS)로 검출하여 분석할 수 있다. 고농도의 할로겐 화학종 분석법의 개발은 이미 많은 기관에서 분석법을 개발하고 있다. 반면 극지시료의 농도수준인 저농도 및 극미량 할로겐 화학종의 분석법은 현재 이태리, 독일 등 일부 연구기관에서만 분석이 가능한 기술이다. 한편, 극지연구소에는 아직 화학종을 분리하여 분석하는 IC-ICP-MS가 없기 때문에 장비의 구입 또는 외부 기관과의 공동연구를 통해 분석법을 개발을 시도할 수 있다.

KOPRI 극지연구소

2. 재료 및 방법

- 저농도 할로겐 원소 분석법은 극지연구소의 고분해능 유도결합플라즈마 질량분석기를 이용하여 개발하였다. 시료도입을 자동화하기 위해 자동시료주입 장치를 사용하였다. 극지 얼음에 존재하는 저농도 및 극미량의 할로겐 원소를 검출하기 위해 저온 시료도입장치(Peltier Cooled Inlet System; PC3)로 설치하여 할로겐 원소 피크에 대한 간섭을 유발하는 옥사이드 발생을 줄이고, 고분해능 유도결합플라즈마 질량분석기의 이온검출기에 추가 유닛을 장착하여 안정적인 시그널을 얻도록 분석조건을 최적화하였다.
- 저농도 할로겐 원소 분석법에 사용한 기기 조건은 표 1에 표시하였다.
- 최적화된 분석법은 할로겐 원소 인증표준물질(BCR-611)을 설정된 분석법으로 분석하여 분석법을 검증하였다.

3. 연구결과

· 고분해능 유도결합플라즈 질량분석기 (ICP-SFMS)를 이용한 할로겐 원소 분석법 개발 및 최적화

- 극지 얼음 및 눈의 저농도 할로겐 원소를 분석하기 위해 ICP-SFMS의 분석법을 최적화하

였다. 분해능 4000에서 튜닝 파라메타 RF Power, Gas flow rate 등을 최적화하여 Br과 I를 각각 0.1 mL^{-1} 과 0.01 mL^{-1}부터 분석할 수 있다. 최적화된 분석법의 인증표준물질 BCR-611 (low bromine ground water)을 100배 희석하여 분석하여 분석법을 검증하였다.

· 사중극자 유도결합플라즈마 질량분석기(ICP-QMS)를 이용한 할로겐 원소 분석법 개발

- 얼음 중 저농도 (sub-ppb) 수준의 할로겐원소 분석을 위해 ICP-QMS (Elan DRC-e)와 시료도입부를 PC3 (ESI)로 연결하여 Na, Br, I를 동시에 분석하는 분석법을 개발하였다. 분석범위는 Br은 0.7 ng mL^{-1} ~ 6.8 ng mL^{-1}이며, I은 0.07 ng mL^{-1} ~ 0.68 ng mL^{-1}이다. Na은 8.1 ng mL^{-1} ~ 76.2 ng mL^{-1}의 범위에서 분석할 수 있다. 할로겐원소 35Cl을 분석하기 위해 방해물질 ($^{1}H^{18}O^{16}O$)을 메탄을 이용한 Dynamic Reaction Cell (DRC) 모드를 이용하여 제거를 시도하였으나 분리가 되지 않아, Cl은 분석에서 제외하였다. ^{79}Br도 방해물질 ($^{40}Ar^{38}Ar^{1}H$) 때문에 5000 이상의 분해능이 필요하지만 ICP-QMS의 분석 조건을 최적화하여 ^{79}Br을 분석할 수 있게 조정하였다.
- Na, Br, I에 대해 5단계의 검량표준물질을 분석하여 R^2 > 0.95이상의 검량선을 얻었다. 시료매질에 따른 바탕값의 분석을 통해 검출한계를 도출하였다.

· 이온크로마토그래피를 이용한 얼음의 저농도 할로겐 화학종 분석법 개발

- Thermo Dionex ICS 2000 이온크로마토그래피 시스템을 이용하여 저농도의 Br^-와 BrO_3^-을의 브롬 화학종과 I^-및 IO_3^-와의 요오드 화학종을 ng mL^{-1} 수준에서 분석할 수 있는 분석법을 개발하였다. 음이온의 이온크로마토그래피의 분석조건은 IonPac AS 15(2×250 mm)와 IonPac AG 15(4×50 mm) 컬럼을 연결하고 용매는 6 - 55 mM KOH를 gradient 조건으로 흘려서 이온의 화학종을 분리하였다. 써프레서형 전도도 검출기(ASRS 300 suppressor)를 사용하여 저농도에서 브롬과 요오드의 화학종을 분석할 수 있는 조건을 설정하였다. 자동시료주입기로 500 µL를 주입하여 분당 0.5 mL로 흘려주는 조건을 설정하였다.
- 저농도 할로겐 화학종의 분석 조건을 설정하기 위해 Br^-와 BrO_3^-는 inorganic ventures사의 이온크로마토그래피용 표준용액을 사용하여 0.5 ~ 250 ng mL^{-1}의 검량선 표준용액을 제조하였다. I^-는 Supelco사의 이온크로마토그래피용 표준용액을 사용하였고, IO_3^-는 Sigma-Aldrich의 potassium iodate를 1000 mg L^{-1}로 제조하여 희석하여 I^-와 IO_3^-의 0.5 ~ 250 ng mL^{-1}의 검량선표준용액을 제조하여 사용하였다. 분석법은 BCR-611 (bromide in groundwater)과 BCR-408 인증표준물질을 희석해 분석하여 검증하였다. Br^-와는 0.05 ng mL^{-1}에서 RSD가 8.6%이며 검출한계는 0.02 ng mL^{-1}로 나타났다. I^-는 전기전도도 검출기 조건에서 검출되지 않았기 때문에 이온크로마토그래피의 조건을 변경하거나 질량분석기와 같은 다른 검출기를 사용하여 검출할 수 있다.
- 극지 눈과 얼음에서 할로겐 화학종의 농도는 수 ~ 수십 pg mL^{-1} 수준으로 매우 낮은 농도로 존재하기 때문에 이온크로마토그래피(IC)와 유도결합플라즈마(ICP)를 연결한 IC-ICP-MS 분석시스템으로 pg mL^{-1} 수준의 할로겐 화학종을 분석할 수 있다. IC-ICP-MS 시스템은 비소(As) 화학종 분석, 크롬(Cr) 화학종 분석에도 활용할 수 있기

때문에 향후 극지연구소의 얼음화학 연구를 위해 도입이 필요하다.

· **남극 해빙시료 채취**

- 아라온 남극 항해 기간 중 4개의 정점에서 눈, 해빙, 및 해수 시료를 채취하였다. 해빙 위 눈시료는 이번 연구기간 중 최적화한 ICP-SFMS 또는 새로 개발한 ICP-QMS를 이용하여 할로겐 원소의 농도를 분석할 것이다. 해빙 및 해수 시료에서 할로겐 원소의 분석은 연구의 필요에 따라 분석을 진행할 수 있다. 할로겐 이온과 여러 가지 중금속의 농도는 이온크로마토그래피 및 해수시료에 최적화된 ICP-SFMS를 이용하여 분석할 계획이다.

4. 결론

- 극지 얼음 및 눈에 존재하는 할로겐 원소를 분석할 수 있는 저농도 할로겐 원소 분석법을 고분해능 유도결합플라즈마 질량분석기를 이용하여 개발하였다. 또한 저농도 할로겐 원소를 사중극자 유도결합플라즈마 질량분석기로도 분석할 수 있는 분석법을 개발하였다. 이를 통해 극지에서 결빙과 해빙과정에서 일어나는 얼음 내 할로겐 원소의 정량적 화학반응 메커니즘에 대한 이해도를 높을 수 있는 기초연구가 가능하다.
- 할로겐 화학종의 정량적 분석법 기초연구를 통해 실험실 또는 극지 얼음시료에서 할로겐 화학종의 정량 및 화학반응 메커니즘 이해도를 확장할 수 있다.
- 이온크로마토그래피를 이용하여 브롬과 요오드의 화학종을 분리하여 분석할 수 있는 분석법을 개발하였다. 향후 이온크로마토그래피와 유도결합플라즈마 질량분석기를 결합하여 극지 시료의 할로겐 화학종을 분석할 수 있는 분석법을 개발할 수 있다.

KOPRI 극지연구소

5. 참고문헌

Barrie, L., et al. (1988). "Ozone destruction and photochemical reactions at polar sunrise in the lower Arctic atmosphere." Nature **334**(6178): 138-141.

Bu, X., et al. (2003). "Determination of halogens in organic compounds by high resolution inductively coupled plasma mass spectrometry (HR-ICP-MS)." Journal of Analytical Atomic Spectrometry **18**(12): 1443-1451.

De Gois, J. S., et al. (2016). "Bromine isotope ratio measurements in seawater by multi-collector inductively coupled plasma-mass spectrometry with a conventional sample introduction system." Analytical and Bioanalytical Chemistry **408**(2): 409-416.

Ito, K. (1997). "Determination of Iodide in Seawater by Ion Chromatography." Analytical Chemistry **69**(17): 3628-3632.

Louvat, P., et al. (2016). "Determination of Bromine Stable Isotope Ratios from Saline Solutions by "Wet Plasma" MC-ICPMS Including a Comparison between High- and Low-Resolution Modes, and Three Introduction Systems." Analytical Chemistry

88(7): 3891-3898.

Silva, J. S., et al. (2017). "Determination of bromine and iodine in edible flours by inductively coupled plasma mass spectrometry after microwave-induced combustion." Microchemical Journal 133: 246-250.

Tagami, K., et al. (2006). "Determination of chlorine, bromine and iodine in plant samples by inductively coupled plasma-mass spectrometry after leaching with tetramethyl ammonium hydroxide under a mild temperature condition." Analytica Chimica Acta 570(1): 88-92.

Wang, K. E. and S. J. Jiang (2008). "Determination of iodine and bromine compounds by ion chromatography/dynamic reaction cell inductively coupled plasma mass spectrometry." Analytical Sciences 24(4): 509-514.

Xu, S.-Q., et al. (2010). "Extraction and Determination of Total Bromine, Iodine, and Their Species in Atmospheric Aerosol." Chinese Journal of Analytical Chemistry 38(2): 219-224.

Atkinson, H. M., et al. (2012). "Iodine emissions from the sea ice of the Weddell Sea." Atmospheric Chemistry and Physics 12(22): 11229 - 11244.

Cuevas, C. A., et al. (2018). "Rapid increase in atmospheric iodine levels in the North Atlantic since the mid-20th century." Nature Communications 9(1): 1452.

Foster, K. L., et al. (2001). "The Role of Br2 and BrCl in Surface Ozone Destruction at Polar Sunrise." Science 291(5503): 471-474.

Frieß, U., et al. (2010). "Iodine monoxide in the Antarctic snowpack." Atmospheric Chemistry and Physics 10(5): 2439 - 2456.

Gilfedder, B., et al. (2007). "Iodine and bromine speciation in snow and the effect of orographically induced precipitation." Atmospheric Chemistry and Physics 7(10): 2661 - 2669.

Gilman, J. B., et al. (2010). "Ozone variability and halogen oxidation within the Arctic and sub-Arctic springtime boundary layer." Atmospheric Chemistry and Physics 10(21): 10223-10236.

Grannas, A. M., et al. (2007). "An overview of snow photochemistry: Evidence, mechanisms and impacts." Atmospheric Chemistry and Physics 7(16): 4329-4373.

Kim, K., et al. (2016). "Production of Molecular Iodine and Tri-iodide in the Frozen Solution of Iodide: Implication for Polar Atmosphere." Environmental Science & Technology 50(3): 1280-1287.

Legrand, M., et al. (2016). "Year-round records of sea salt, gaseous, and particulate inorganic bromine in the atmospheric boundary layer at coastal (Dumont d'Urville)

and central (Concordia) East Antarctic sites." Journal of Geophysical Research: Atmospheres **121**(2): 997-1023.

Lieb-Lappen, R. and R. Obbard (2015). "The role of blowing snow in the activation of bromine over first-year Antarctic sea ice." Atmospheric Chemistry and Physics **15**(13): 7537-7545.

Maffezzoli, N., et al. (2017). "Bromine, iodine and sodium in surface snow along the 2013 Talos Dome - GV7 traverse (northern Victoria Land, East Antarctica)." The Cryosphere **11**(2): 693 - 705.

Maselli, O. J., et al. (2017). "Sea ice and pollution-modulated changes in Greenland ice core methanesulfonate and bromine." Climate of the Past **13**(1): 39-59.

Roscoe, H. K., et al. (2015). "Particles and iodine compounds in coastal Antarctica." Journal of Geophysical Research: Atmospheres **120**(14): 7144-7156.

Saiz-Lopez, A., et al. (2015). "A mechanism for biologically induced iodine emissions from sea ice." Atmospheric Chemistry and Physics **15**(17): 9731 - 9746.

Saiz-Lopez, A., et al. (2014). "Iodine chemistry in the troposphere and its effect on ozone." Atmospheric Chemistry and Physics **14**(23): 13119-13143.

Saiz-Lopez, A., et al. (2007). "Boundary layer halogens in coastal Antarctica." Science **317**(5836): 348 - 351.

Saiz-Lopez, A., et al. (2008). "On the vertical distribution of boundary layer halogens over coastal Antarctica: Implications for O3, HOx, NOx and the Hg lifetime." Atmospheric Chemistry and Physics **8**(4): 887-900.

Saiz-Lopez, A., et al. (2006). "Measurements and modelling of I2, IO, OIO, BrO and NO3 in the mid-latitude marine boundary layer." Atmospheric Chemistry and Physics **6**(6): 1513-1528.

Saiz-Lopez, A. and R. von Glasow (2012). "Reactive halogen chemistry in the troposphere." Chemical Society Reviews **41**(19): 6448-6472.

Simpson, W. R., et al. (2015). "Tropospheric Halogen Chemistry: Sources, Cycling, and Impacts." Chemical Reviews **115**(10): 4035-4062.

Simpson, W. R., et al. (2007). "First-year sea-ice contact predicts bromine monoxide (BrO) levels at Barrow, Alaska better than potential frost flower contact." Atmospheric Chemistry and Physics **7**(3): 621 - 627.

Simpson, W. R., et al. (2007). "Halogens and their role in polar boundary-layer ozone depletion." Atmospheric Chemistry and Physics **7**(16): 4375 - 4418.

Spolaor, A., et al. (2013). "Sea ice dynamics influence halogen deposition to Svalbard." The Cryosphere **7**(5): 1645-1658.

Spolaor, A., et al. (2016). "Halogen-based reconstruction of Russian Arctic sea ice area from the Akademii Nauk ice core (Severnaya Zemlya)." The Cryosphere **10**(1): 245 - 256.

Spolaor, A., et al. (2012). "Speciation analysis of iodine and bromine at picogram-per-gram levels in polar ice." Analytical and Bioanalytical Chemistry **405**(2-3): 647-654.

Spolaor, A., et al. (2014). "Seasonality of halogen deposition in polar snow and ice." Atmospheric Chemistry and Physics **14**(18): 9613 - 9622.

Spolaor, A., et al. (2013). "Halogen species record Antarctic sea ice extent over glacial - interglacial periods." Atmospheric Chemistry and Physics **13**(13): 6623-6635.

Sturges, W. T. and L. A. Barrie (1988). "Chlorine, Bromine and Iodine in arctic aerosols." Atmospheric Environment **22**(6): 1179-1194.

Thompson, C. R., et al. (2015). "Interactions of bromine, chlorine, and iodine photochemistry during ozone depletions in Barrow, Alaska." Atmospheric Chemistry and Physics **15**(16): 9651-9679.

Vallelonga, P., et al. (2017). "Sea-ice-related halogen enrichment at Law Dome, coastal East Antarctica." Climate of the Past **13**(2): 171 - 184.

Xu, W., et al. (2016). "Bromide and chloride distribution across the snow-sea ice-ocean interface: A comparative study between an Arctic coastal marine site and an experimental sea ice mesocosm." Journal of Geophysical Research: Oceans **121**(8): 5535-5548.

KOPRI 극지연구소

표 1. 저농도 할로겐 원소 분석 조건

Element 2	
Autosampler	SC-4 DX with sample housing
Nebulizer	PFA microflow nebulizer (400 µL min^{-1}) with carbon probe
Spray chamber	PFA chilled cyclonic spray chamber
Sample injector (injector tube)	Sapphire injector
Sampler cone	JET interface nickel sampler cone
Skimmer cone	Nickel skimmer cone (X-version)
RF power (W)	1450
Gas flow rates (L min^{-1})	
Cool	16.00
Auxiliary	0.81
Sample	0.985
Take-up time (sec)	70
Rinse time (min)	10 (2% HNO_3/ 1^{st} UPW/ 2^{nd} UPW)
Resolution	Medium (m • △m^{-1}) = 4000
Runs and passes	3 ´ 3
Mass window (%)	125 (^{23}Na, ^{127}I, ^{129}Xe), 150 (^{79}Br)
Search window (%)	100 (^{23}Na, ^{127}I), 60 (^{129}Xe), 40 (^{79}Br)
Integration window (%)	60 (^{23}Na, ^{127}I, ^{129}Xe), 30 (^{79}Br)

표 2. 할로겐 원소분석을 위한 남극 눈, 해빙, 해수시료 채취 정보

No.	Site	Sampling date	Coordination
7	Weddell Sea	2018. 4. 15	64°20.3524′S, 53°20.6846′E
9	Weddell Sea	2018. 4. 18	64°8.945′S, 55°45.3947′E
10	SW of JRI	2018. 4. 19	64°27.0485′S, 56°40.0292′E
11	W of JRI	2018. 4. 20	64°8.8624′S, 58°32.5993′E

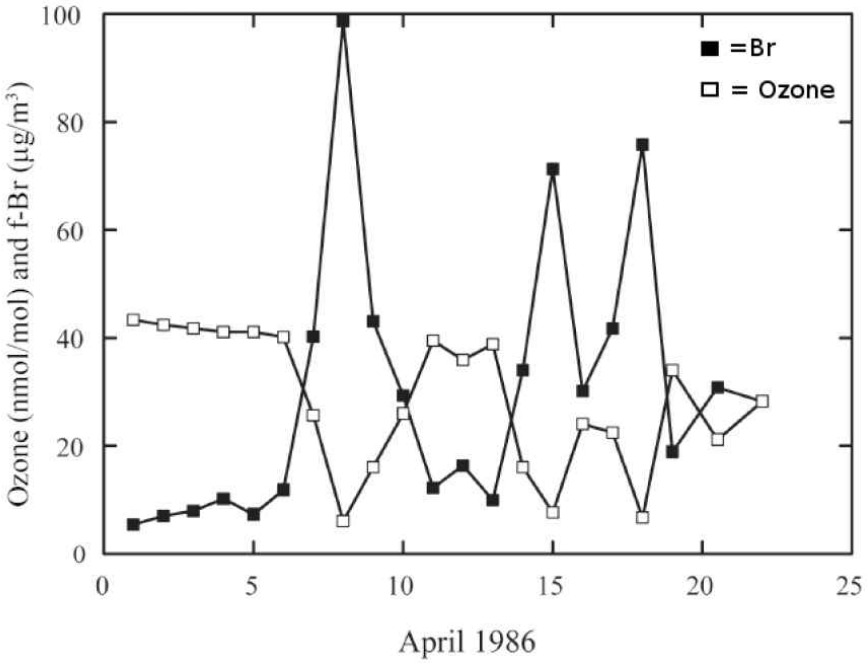

그림 1. BrO의 농도와 Ozone depletion의 연관성 (Barrie et al., 1988)

KOPRI

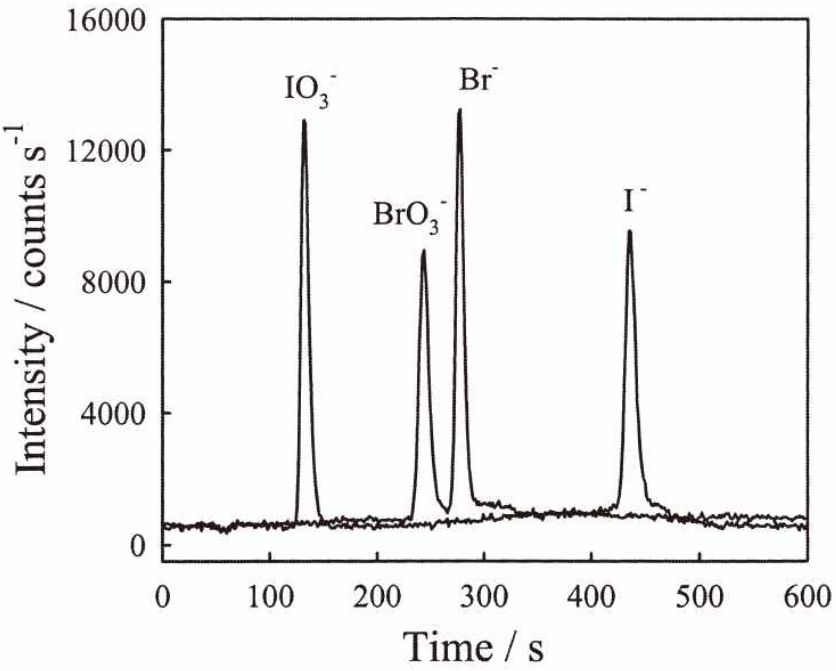

그림 2. 브롬과 요오드 화학종의 IC-ICP-MS 크로마토그램 (Wang and Jian, 2008)

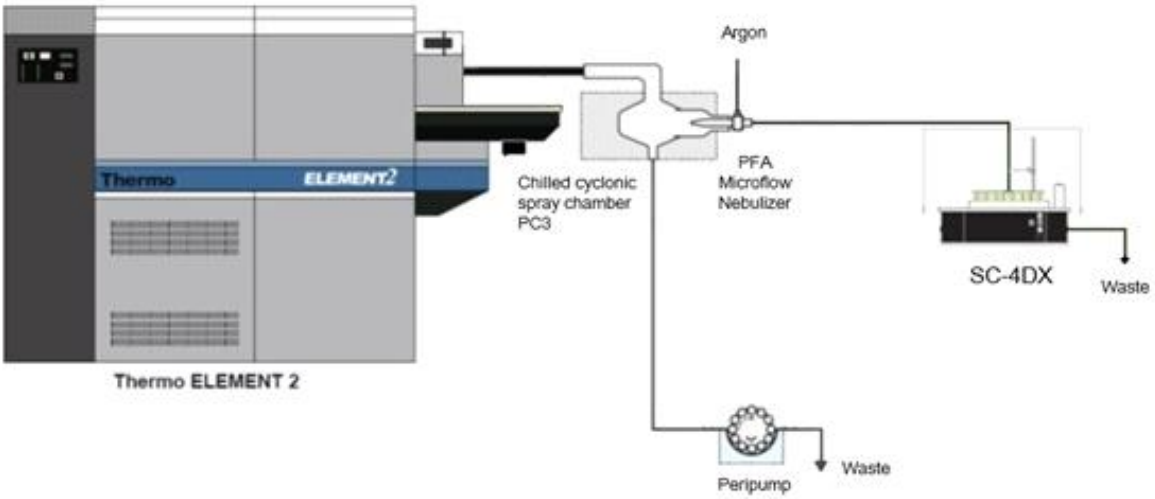

그림 3. PC3와 Autosampler를 연결한 HR-ICP-SFMS 개념

KOPRI

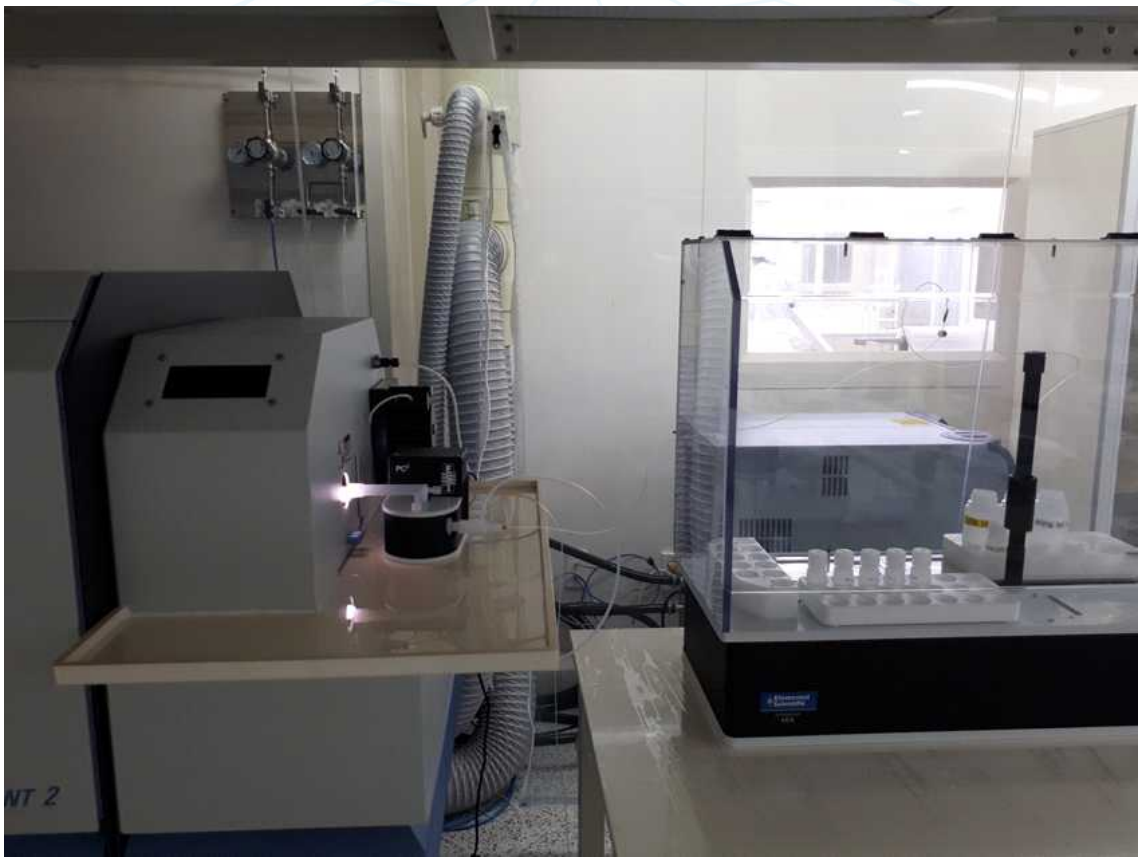

그림 4. 고분해능 유도결합플라즈마 질량분석기(HR-ICP-SFMS)

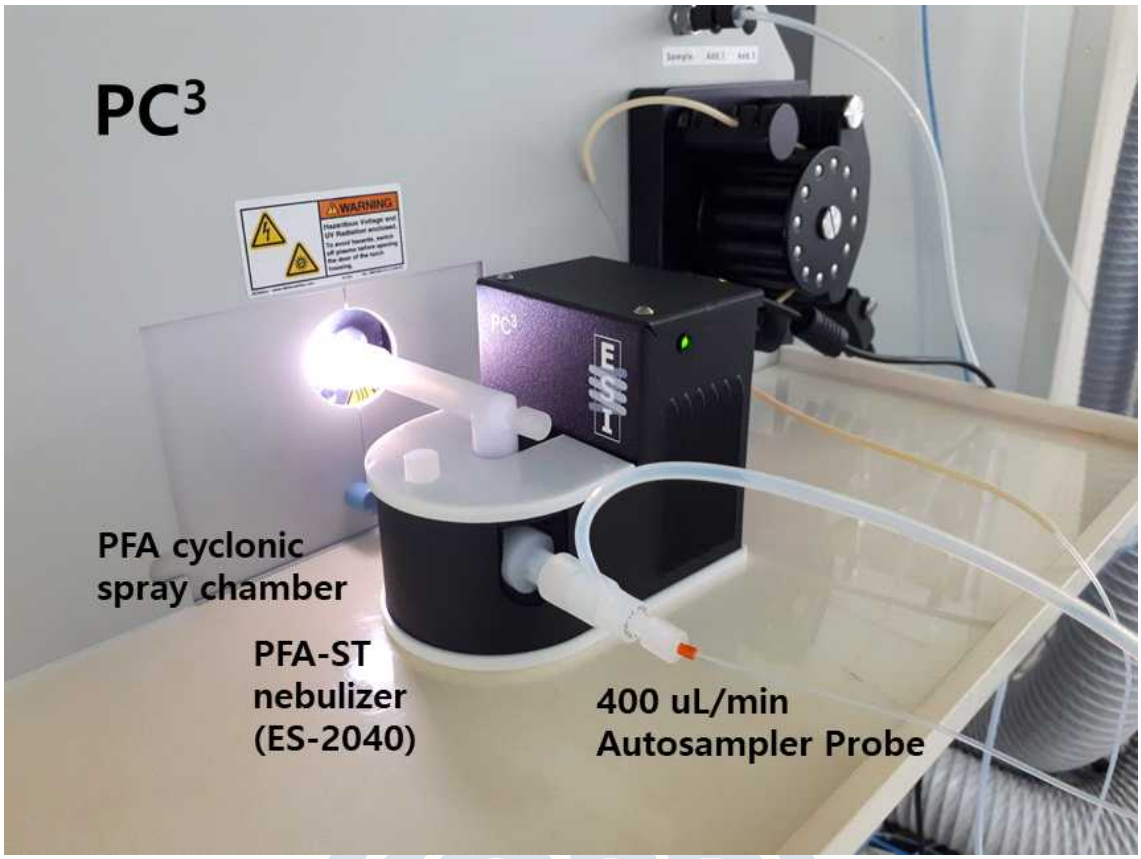

그림 5. PC3 (PC3 시스템)

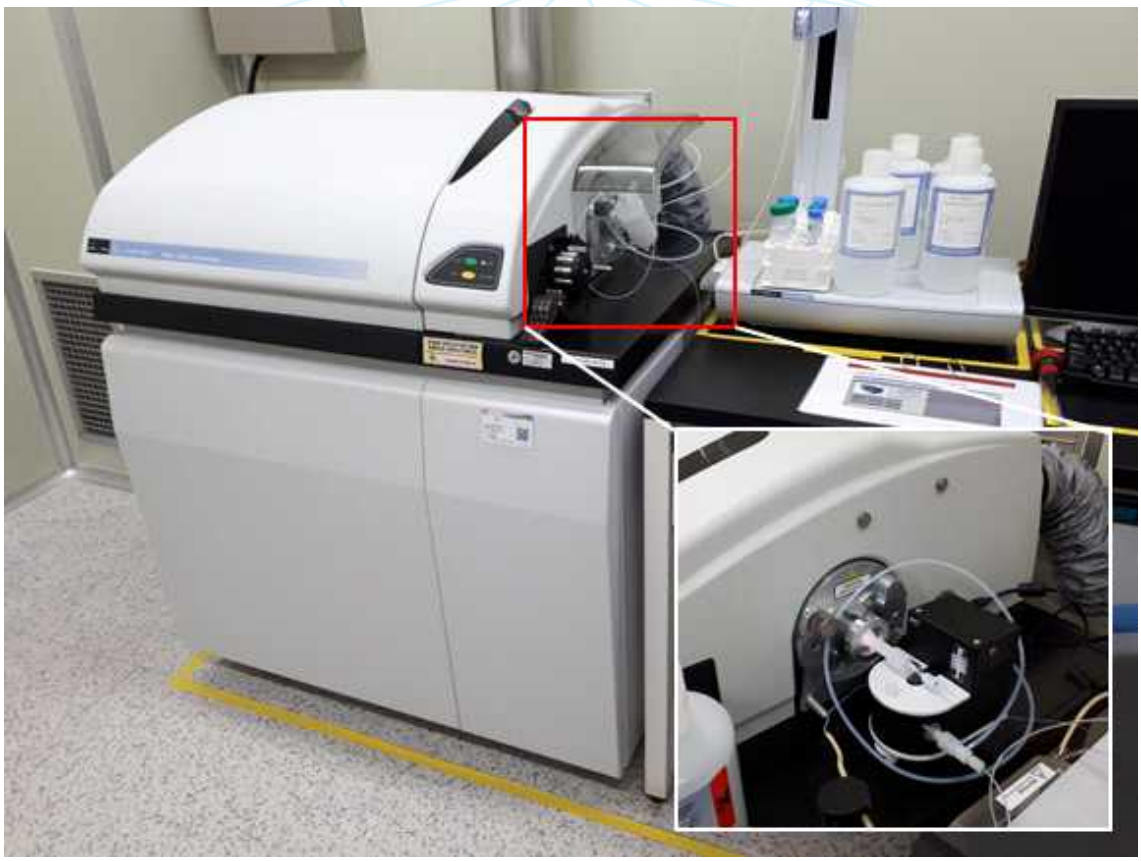

그림 6. 저농도 할로겐 원소를 분석하기 위한 ICP-QMS 시스템(Elan DRC-e)

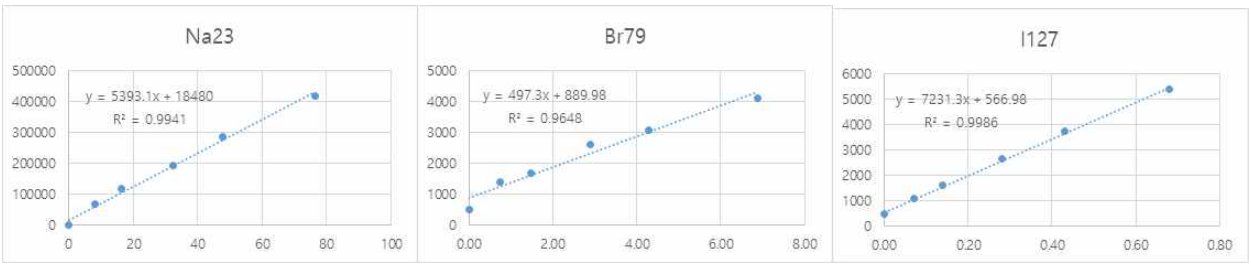

그림 7. Na, Br, I에 대해 5단계 표준물질을 검량선 분석

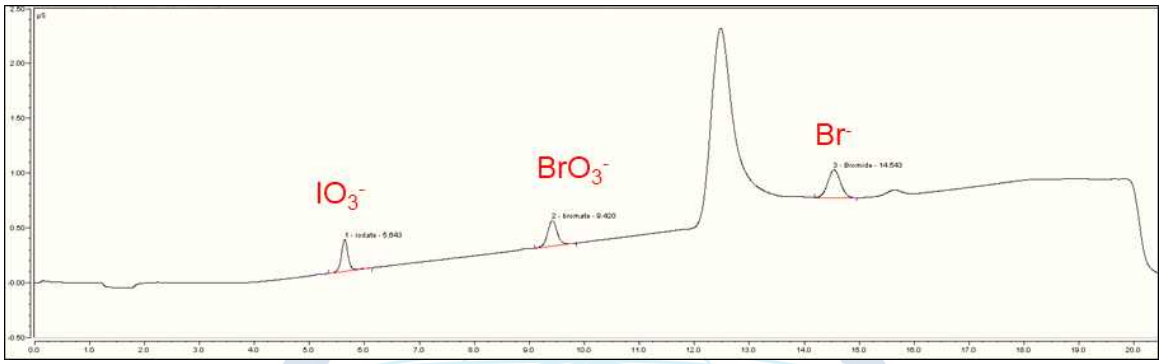

그림 8. 브롬과 요오드 화학종을 분석한 이온크로마토그래피의 크로마토그램

극지연구소

그림 9. IC-ICP-MS 예시(Thermo Scientific)

제 6 절. Nitrite-Induced Activation of Iodate into Molecular Iodine in Frozen Solution[3)]

Kitae Kim[1,2], Jinjung Ju[3], Bomi Kim[1,2], Hyun Young Chung[1,2], Ľubica Vetráková[4], Dominik Heger[4], Alfonso Saiz-Lopez[5], Wonyong Choi[6], and Jungwon Kim[7,*]

[1]Korea Polar Research Institute

[2]Department of Polar Sciences, University of Science and Technology (UST)

[3]Department of Environmental Sciences and Biotechnology, Hallym University

[4]Department of Chemistry and Research Centre for Toxic Compounds in the Environment (RECETOX), Faculty of Science, Masaryk UniversityCzech Republic

[5]Department of Atmospheric Chemistry and Climate, Institute of Physical Chemistry Rocasolano, CSIC, Spain

[6]Division of Environmental Science and Engineering, Pohang University of Science and Technology

1. Introduction

Reactive iodine species, such as atomic iodine (I), molecular iodine (I_2), iodine monoxide (IO), iodine dioxide (OIO), and hypoiodous acid (HOI), play important roles in the tropospheric ozone (O_3) depletion and atmospheric new particle formation in the polar regions [1]. I atoms rapidly react with O_3 to form IO ($I + O_3 \rightarrow IO + O_2$), OIO ($IO + IO \rightarrow I + OIO$), and HOI ($IO + HO_2 \rightarrow HOI + O_2$), which also initiate various tropospheric O_3 depletion cycles [2-4]. In addition, IO and OIO induce the formation of iodine oxides (e.g., I_2O_3, I_2O_4, and I_2O_5) that polymerize to form iodine oxide particles (diameter = 3 - 10 nm), which serve as a cloud condensation nuclei [5-7].

The major origin of atmospheric I atoms is the photolysis of organic iodine (e.g., CH_3I and CH_2I_2) and I_2 biologically generated from marine algae (e.g., seaweeds, phytoplankton, and polar microalgae) ($CH_3I + h\nu \rightarrow CH_3 + I$ and $I_2 + h\nu \rightarrow 2I$) [1]. Organic iodine is produced mainly by marine algae containing I^- and organic matters through the enzyme-induced methylation of I^- and enzyme/H_2O_2-mediated oxidation of I^- [8, 9]. The oxidation of I^- by hydrogen peroxide (H_2O_2) in the cell apoplast of algae produces I_2 through the formation of HOI ($I^- + H_2O_2 \rightarrow HOI + OH^-$; $HOI + I^- + H^+ \rightarrow I_2 + H_2O$) [10, 11]. Although biological processes are regarded as the main route for the production of

3) 이 연구는 본 과제 지원으로 수행되었으며 그 결과는 다음의 논문으로 출판되었음: Kitae Kim, Jinjung Ju, Bomi Kim, Hyun Young Chung, Ľubica Vetrakova, Dominik Heger, Alfonso Saiz-Lopez, Wonyong Choi, and Jungwon Kim, "Nitrite-Induced Activation of Iodate into Molecular Iodine in Frozen Slution", *Environ. Sci. Technol.* 2019, 53, 4892-4900.

organic iodine and I_2 [12, 13], abiotic production routes are also required to explain the total atmospheric iodine budget. A few studies have suggested abiotic mechanisms for the production of organic iodine and I_2. For example, I_2 can be produced on the ocean surface through photochemical ($4I^- + O_2 + 2H_2O + h\nu \rightarrow 2I_2 + 4OH^-$) [14] and chemical reactions ($I^- + O_3 + H^+ \rightarrow HOI + O_2$; $HOI + I^- + H^+ \rightarrow I_2 + H_2O$) [15, 16]. In addition, reactions between methyl radicals (generated from the photolysis of humic substances) and I atoms (generated from the oxidation of I^- by photochemically generated oxidants) [17] and between I_2/HOI (generated from chemical and photochemical reactions) and dissolved organic matter [18] contribute to the formation of organic iodine. However, abiotic routes for the production of organic iodine and I_2 have been much less investigated than biogenic production routes and are largely unknown at this stage.

The freezing point of aqueous solution is the temperature at which the conversion of liquid water to ice crystals starts and the term “frozen solution” in this study refers to the solution containing both liquid regions and ice crystals. At temperatures below the eutectic point, the liquid regions between ice crystals completely disappear. In general, redox chemical reactions in frozen solutions (i.e., at temperatures below the freezing point) are slower than those in aqueous solutions (i.e., at temperatures above the freezing point). However, redox chemical reactions between specific reactants (e.g., NO_2^-/O_2, chromate ($HCrO_4^-$)/H_2O_2, $NO_2^-/HCrO_4^-$, bromate (BrO_3^-)/humic substance, and periodate (IO_4^-)/furfuryl alcohol) proceed more rapidly in frozen solutions [19-23]. Frozen solutions at temperatures between the freezing and eutectic points contain a liquid phase between solid ice crystals, the so-called liquid brine, ice grain boundary, or micropocket [24, 25]. As ice crystals grow, solutes and dissolved gases are gradually accumulated in the liquid regions surrounded by ice crystals [26, 27], which act as micro-sized reactors. In addition, the exclusion of protons (or hydroxides) from ice crystals to the liquid regions changes the pH of the reaction site (i.e., liquid regions between ice crystals) and the speciation of reactants [28]. The concentration of solutes, dissolved gases, and protons (or hydroxides) by freezing (i.e., freeze concentration effect) is regarded as the main reason for the faster redox chemical reactions in frozen solutions.

Recently, the role of ice media on the abiotic production of I_2 has been introduced. The redox chemical reaction between I^- and NO_2^-, which is negligible in aqueous solution, proceeds in frozen solution to generate I_2 (or tri-iodide, I_3^-) and NO_3^- (or nitric oxide, NO) [29-31]. The pH decrease by freezing converts NO_2^- to the nitroacidium ion (H_2ONO^+) and nitrous acid (HONO), which can oxidize I^- to I_2 ($2H_2ONO^+ + 2I^- \rightarrow I_2 + 2NO + 2H_2O$ and $HONO + 2I^- + O_2 + H^+ \rightarrow I_2 + NO_3^- + H_2O$). The photochemical production of I_2 and I_3^- in the presence of I^- is markedly enhanced when aqueous solutions of I^- are frozen [32, 33]. The concentration of I^- and O_2 in the liquid regions between ice crystals by freezing

induces the formation of an $I^-{\cdot}O_2$ complex. UV irradiation ($\lambda > 300$ nm) of the $I^-{\cdot}O_2$ complex enables the electron transfer from I^- to O_2 (inner sphere electron transfer) to generate I atoms as precursors of I_2 and I_3^- ($I^-{\cdot}O_2 + h\nu \rightarrow I + O_2^-$). It has been also reported that I_2 and other reactive iodine species, such as IO and OIO, can be produced from the photolysis of the frozen solution of IO_3^- and the frozen NH_4IO_3 salt [34, 35]. However, a mechanism for this has not been proposed.

The mechanism of organic iodine and I_2 production through biological, chemical, and photochemical processes has been extensively investigated. However, most studies have focused on the conversion of I^- rather than IO_3^- to organic iodine or I_2. Iodine species are mainly found as I^- and IO_3^- in snow, sea ice, sea water, surface water, and atmospheric aerosols. Between these two iodine species, IO_3^- is more abundant [36, 37]. NO_2^- is one of the major inorganic nitrogen species in natural waters and rainwater [38, 39]. NO_2^- is naturally generated by the oxidation of NH_4^+ by *Nitrosomonas europaea* (nitrifying bacteria) and the decomposition of copepod feces and algae in the presence of *Nitrosocystis oceanus* (nitrifying bacteria) [40, 41]. Various industries, such as food preservation, fertilizer manufacturing, and corrosion inhibition, use chemical reagents containing high concentrations of NO_2^- [42]. The agricultural application of fertilizers also contributes to the increase in NO_2^- levels in water and soil [43].

Herein, we report a new mechanism for the production of I_2 from IO_3^-, that is, the abiotic production of I_2 in the frozen solution containing IO_3^- and NO_2^- in the dark. The freezing-induced production of I_2 was measured as a function of various experimental parameters, such as pH, IO_3^- and NO_2^- concentrations, and freezing temperature. Furthermore, the mechanism of I_2 production is proposed based on a variety of experimental evidence.

2. Experimental Section

Chemicals. The following chemicals were used as received without further purification: potassium iodate (KIO_3, Sigma-Aldrich, ≥99.5%), potassium iodide (KI, Junsei, ≥99.5%), sodium nitrite ($NaNO_2$, Sigma-Aldrich, ≥99.0%), sodium nitrate ($NaNO_3$, Sigma-Aldrich, ≥99.0%), cresol red ($C_{21}H_{18}O_5S$, Sigma-Aldrich, ≥95.0%), sodium carbonate (Na_2CO_3, Sigma-Aldrich, ≥99.5%), and sodium bicarbonate ($NaHCO_3$, Sigma-Aldrich, ≥99.7%). All solutions were prepared with ultrapure deionized water (resistivity ≥18.2 MΩ·cm), which was obtained from a Human-Power I+ water purification system (Human Corporation).

Experimental Procedure. Aliquots of IO_3^- and NO_2^- stock solutions were added to deionized water in a beaker to yield the desired initial concentration (usually $[IO_3^-]$ = 1 mM and $[NO_2^-]$ = 1 mM). The solution pH was adjusted using a $HClO_4$ or NaOH solution

to the desired value (usually pH 3.0). Then, 10 mL of this solution was put in a 15-mL polypropylene conical tube that was sealed with a cap. The solution was unbuffered and air-equilibrated. The conical tube containing the aqueous solution of IO_3^- and NO_2^- was placed in a conical tube rack in a cooling bath, which was precooled to the desired temperature (usually −20 °C), to freeze the aqueous solution. Ethanol was used as the coolant. The term "freezing temperature" in this study refers to the temperature of ethanol in the cooling bath. The moment at which the conical tube containing the aqueous solution was introduced into the cooling bath was taken as the reaction starting point (reaction/freezing time = 0 h). The conical tube containing the frozen solution was withdrawn from the cooling bath and then put into lukewarm water bath at 35 °C to thaw the frozen sample for chemical analyses. After thawing, the aqueous sample was immediately analyzed. The experiments in a cooling bath preset at 25 °C were also performed to investigate chemical reactions in aqueous solution as control tests. Multiple experiments were performed for a given set of conditions to confirm the reproducibility of the data.

Chemical Analyses. The quantitative analyses of anions, such as I^-, IO_3^-, NO_2^-, and NO_3^-, were performed using an ion chromatograph (Dionex ICS-1100) equipped with a Dionex IonPac AG14 guard column (4 mm × 50 mm), a Dionex IonPac AS14 column (4 mm × 250 mm), and a conductivity detector. The eluent was a binary mixture of Na_2CO_3 (3.5 mM) and $NaHCO_3$ (1 mM), and its flow rate was 1.0 mL/min. The concentration of I_2 was determined by measuring the absorbance of the aqueous sample at 460 nm (ε = 746 M^{-1} cm^{-1}) [44] using a UV−visible spectrophotometer (Shimadzu UV-2600).

Estimation of the pH of the Frozen Solution. The pH of the frozen solution was estimated by measuring the UV - visible absorption spectra of cresol red (CR) as an acid-base indicator after freezing but without thawing [45, 46]. The relative concentrations of two different CR species ([singly protonated CR]/[doubly protonated CR] or [deprotonated CR]/[singly protonated CR]) were obtained from the UV - visible absorption spectra of CR by non-negative least-squares minimization (eq 1). Then, the pH of the frozen solution was calculated using the simple relationship between the relative concentrations of two different CR species, pK_a, and pH (eq 2) (see Discussion of pH estimation in the Supporting Information (SI) for details).

$$\sum_{\lambda = 400\,\mathrm{nm}}^{650\,\mathrm{nm}} (A \cdot a + B \cdot b - X)^2 = \text{minimum value} \qquad (1)$$

Here, X is the absorbance of frozen solution, A and B are the absorbances of two different CR species, and a and b are the relative concentrations of two different CR species, respectively.

$$\mathrm{pH} = \mathrm{p}K_{a1} + \log\frac{\text{singly protonated CR}}{\text{doubly protonated CR}}$$

$$\left(\text{or } \mathrm{p}K_{a2} + \log\frac{\text{deprotonated CR}}{\text{singly protonated CR}}\right) \quad (2)$$

Measurement of IO_3^- Distribution in Frozen Solution. The distribution of IO_3^- in frozen solution was investigated using confocal Raman microscope (Renishaw inVia). 100 μL of IO_3^- solution ($[IO_3^-]$ = 1 mM and pH 3.0) was dropped on the cover glass on the temperature controlled stage (Linkam scientific THMS600) at lowest temperature = −20 °C. A monochromatic laser with a wavelength of 532 nm was used as the excitation source, and chemical mapping image was obtained by measuring the peak intensity at 942 cm^{-1}.

3. Results and Discussion

Generation of I_2 by Freezing in the Presence of IO_3^- and NO_2^-. The redox chemical reaction between IO_3^- and NO_2^- in frozen solution at −20 °C was investigated and compared with that in aqueous solution at 25 °C (Figure 1). The concentration of NO_2^- gradually decreased with reaction time with the generation of NO_3^- in aqueous solution, whereas the conversion of IO_3^- was negligible during the whole reaction time (Figure 1a). This result indicates that the redox conversion of IO_3^- and NO_2^- does not occur in aqueous solution. Under this situation, the oxidation of NO_2^- to NO_3^- should be attributed to the reaction of NO_2^- with O_2 or H^+ ($2NO_2^- + O_2 \rightarrow 2NO_3^-$, $3NO_2^- + 2H^+ \rightarrow NO_3^- + 2NO + H_2O$, or $4NO_2^- + 2H^+ \rightarrow N_2O + 2NO_3^- + H_2O$) [47, 48]. The generation of NO_3^- in aqueous solution of IO_3^- and NO_2^- was markedly retarded when the solution was purged with Ar gas to remove dissolved oxygen (see Figure S1). This result indicates that the reaction of NO_2^- with O_2 is more favored than that with H^+. In contrast to the aqueous-phase reaction, the concentrations of both IO_3^- and NO_2^- decreased and, at the same time, the concentrations of I^-, I_2, and NO_3^- increased in frozen solution (Figure 1b). The production of I_2 and I^- was initiated after 10 min at which the liquid and solid phases coexisted (see Figure S2 in the SI). The aqueous solution containing IO_3^- and NO_2^- was "apparently" completely frozen after 30 min (see Figure S3 in the SI). However, the liquid regions between ice crystals must have existed longer because the production of I_2 and I^- was observed after 30 min. After 24 h of freezing reaction, 72 (± 2) μM of I_2 and 167 (± 2) μM of I^- were generated from the reduction of 314 (± 1) μM of IO_3^-. At the same time, 961 (± 18) μM of NO_2^- was oxidized and 978 (± 7) μM of NO_3^- was generated.

However, the concentration of IO_3^- in frozen solution was not changed in the absence of NO_2^- (Figure 1c). Therefore, the production of I^-, I_2 (reduction products of IO_3^-), and NO_3^- (oxidation product of NO_2^-) in the frozen solution containing IO_3^- and NO_2^- implies that the redox conversion of IO_3^- and NO_2^- is favored in frozen solution (reactions 3 and 4).

$$IO_3^- + 3HNO_2 \rightarrow I^- + 3NO_3^- + 3H^+, \quad E^0 = 0.151\ V_{NHE} \tag{3}$$

$$2IO_3^- + 5HNO_2 \rightarrow I_2 + 5NO_3^- + 3H^+ + H_2O, \quad E^0 = 0.261\ V_{NHE} \tag{4}$$

Here, E^0 was obtained by combining the half-reduction reactions of IO_3^- to I^- (E^0 = 1.085 V_{NHE}), IO_3^- to I_2 (E^0 = 1.195 V_{NHE}), and NO_3^- to HNO_2 (E^0 = 0.934 V_{NHE}) [49].

The production of I_2 and I^- through the NO_2^--mediated reduction of IO_3^- proceeded only while NO_2^- was oxidized to NO_3^- (i.e., for 24 h). When the oxidation of NO_2^- was complete, the generation of I_2 and I^- stopped, despite the presence of residual IO_3^-. This behavior implies that only NO_2^- acts as a reductant for the conversion of IO_3^- to I^- and I_2. The oxidation of NO_2^- to NO_3^- in the frozen solution of NO_2^- (i.e., in the absence of IO_3^-) was observed, and its rate was much higher than that in the aqueous solution (Figure 1d). The enhanced oxidation of NO_2^- in the frozen solution is due to the accumulation of O_2 in the liquid regions between ice crystals during freezing, which enhances the reaction between NO_2^- and O_2 [20]. However, the observed molar ratio of oxidized NO_2^- to reduced IO_3^- in the frozen solution containing IO_3^- and NO_2^- was 3.1 (Figure 1b), which is similar to the theoretical (stoichiometric) value (2.5−3.0) according to reactions 3 and 4. This result indicates that the oxidation of NO_2^- by IO_3^- is more favored than that by O_2 in frozen solution.

Figures 1e and f show the iodine (($[IO_3^-]$ + $[I^-]$ + 2 × $[I_2]$)/initial $[IO_3^-]$ × 100) and nitrogen mass balances (($[NO_2^-]$ + $[NO_3^-]$)/initial $[NO_2^-]$ × 100) in aqueous and frozen solutions containing IO_3^- and NO_2^-, respectively. Because IO_3^- is inert to NO_2^- in aqueous solution, 100% iodine mass balance was achieved in aqueous solution. However, the nitrogen mass deficits were over 25% after 48 h of reaction. The incomplete nitrogen mass balance is most likely due to both the emission of HNO_2 to the atmosphere in a gaseous form (Henry's law constant of HNO_2 for water as solvent = 37.5−48.6 M atm^{-1}) [50] and the conversion of NO_2^- to other nitrogen species such as nitrogen monoxide (NO) and nitrous oxide (N_2O) [48] (see Figure S1 and accompanying discussion in the SI for details). On the other hand, both iodine and nitrogen mass balances were satisfactory in frozen solution, which confirms that reactions 3 and 4 are the dominant redox chemical reactions between IO_3^- and NO_2^- in frozen solution and other side reactions are negligible.

Figure S4a in the SI shows the images of the samples containing IO_3^- and NO_2^-

as a function of freezing time. The color of I_2 depends on the type of solvent due to different I_2–solvent interactions (e.g., brown in water and ethanol and violet in carbon tetrachloride and chloroform) [51]. The samples gradually turned yellowish-brown with freezing time. These images directly illustrate the production of I_2 in the frozen solution containing IO_3^- and NO_2^-. In accordance with the color change by freezing, the absorbance at 460 nm, which is ascribed to the generation of I_2 [44], gradually increased with freezing time (Figure S4b in the SI).

When the frozen solution was thawed and then kept in the dark under ambient conditions, the absorbance at 460 nm gradually decreased as time went on (Figure S5 in the SI). This result indicates that I_2 trapped in the frozen solution is slowly emitted to the atmosphere after melting (Henry's law constant of I_2 for water as solvent = 11.1−32.4 M atm^{-1}) [50], which may contribute to the significant iodine concentration and ozone depletion in the polar regions during springtime [52, 53].

Mechanism of I_2 Production. It has been reported that the concentration of protons increases when the acidic aqueous solution is frozen due to the freeze concentration effect [28]. The degree of pH decrease by freezing depends on various parameters such as freezing temperature and rate, solute type and concentration, and solvent type. To investigate how much the pH decreases by freezing in our system (i.e., at $[NO_2^-]$ = 1 mM, $[IO_3^-]$ = 1 mM, pH 3.0 in aqueous solution, and freezing temperature = −20 °C), the UV−visible absorption spectra of the frozen solution containing IO_3^-, NO_2^-, and CR were measured without thawing (Figure 2). Only one peak at 434 nm was observed in aqueous solution at pH 3.0. This result is consistent with the fact that about 99% of CR species exist as singly protonated CR (λ_{max} = 434 nm) [54] at pH 3.0 (see Figure S6 in the SI). When the aqueous solution containing IO_3^- and NO_2^- at pH 3.0 was frozen, the peak at 434 nm decreased and the peak at 518 nm increased. This result indicates that some singly protonated CR was changed to doubly protonated CR (λ_{max} = 518 nm) [54] (i.e., the pH decreased) after freezing. The ratio of [singly protonated CR] to [doubly protonated CR] in frozen solution was calculated by fitting the data in Figure 2 to eq 1 and was estimated to be approximately 5:1. Therefore, the pH of the frozen solution with $[NO_2^-]$ = 1 mM, $[IO_3^-]$ = 1 mM, pH 3.0 in aqueous solution, and freezing temperature = −20 °C was 1.8. This value was obtained by inserting the [singly protonated CR]/[doubly protonated CR] value (5.00) and pK_{a1} value of CR (1.10) [55, 56] into eq 2 (see Figure S6 in the SI).

In the aqueous solution containing IO_3^- (pK_a = 0.78) [57] and NO_2^- (pK_{a1} = 1.7 and pK_{a2} = 2.8) [58] at pH 3.0, IO_3^- is the dominant form (99.4%), and NO_2^- mainly exists as NO_2^- (60.2%) and HONO (38.0%). When the aqueous solution containing IO_3^- and NO_2^- at pH 3.0 is frozen (i.e., when the pH decreases to 1.8), the molar fractions of IO_3^-

and NO_2^- species become as follows: 91.3% for IO_3^-, 8.7% for HIO_3, 5.3% for NO_2^-, 52.8% for HONO, and 41.9% for H_2ONO^+ (Figure S7 in the SI). The most striking difference of IO_3^- and NO_2^- speciation between aqueous solution and frozen solution is the existence of H_2ONO^+. The concentration of H_2ONO^+ is negligible in aqueous solution at pH 3.0 but significant in the frozen solution due to the pH decrease to 1.8. It is well known that H_2ONO^+ is much more reactive than HONO and NO_2^-. [59, 60] Therefore, the production of I_2 through the redox chemical reaction between IO_3^- and NO_2^- in frozen solution is most likely due to the generation of H_2ONO^+ by the freezing-induced pH decrease.

Although the reduction of IO_3^- by HONO is thermodynamically possible according to reactions 3 and 4, the negligible conversion of IO_3^- by HONO (38.0%) in aqueous solution at pH 3.0 implies that the redox chemical reaction between IO_3^- and HONO is kinetically very slow. The high reactivity of H_2ONO^+ generated by freezing (by the pH decrease) toward IO_3^- can be ascribed to not only its high reduction power but also the electrostatic attraction between cationic H_2ONO^+ and anionic IO_3^-. The electrostatic attraction between H_2ONO^+ and IO_3^- would facilitate the electron transfer from H_2ONO^+ to IO_3^- by reducing the distance between these species and increasing their collision probability.

The increased concentration of H_2ONO^+ and IO_3^- in the liquid region of frozen solution by exclusion from ice crystals should increase the reaction probability between H_2ONO^+ and IO_3^-, which kinetically accelerates their redox transformation. Figure 3 shows the optical image and IO_3^- distribution of the frozen solution. The pyramidal IO_3^- ions exhibit two strong Raman peaks near 800 cm^{-1} in aqueous solution, which are ascribed to symmetric and antisymmetric stretching of I−O bonds [61]. On the other hand, these two Raman peaks were observed around 900−1000 cm^{-1} in frozen solution (Figure 3a), which indicates that the interaction between IO_3^- and water molecules in frozen solution is different from that in aqueous solution. The IO_3^- mapping image of the frozen IO_3^- solution was obtained based on the peak intensity at 942 cm^{-1}, and its concentrations are represented using a rainbow spectrum (red: high → violet: negligible) (Figure 3b). IO_3^- in frozen solution mainly existed in the liquid regions and IO_3^- trapped in ice crystals was negligible (see Figure S8 and accompanying discussion in the SI for details). Overall, freezing induces the formation of H_2ONO^+ from NO_2^- and increases the concentrations of H_2ONO^+ and IO_3^-. These behaviors act synergistically to enhance the production of I_2 in the frozen solution containing IO_3^- and NO_2^-.

To provide convincing evidence for the above hypotheses, we investigated the effect of solute (IO_3^- or NO_2^-) concentration increase and/or pH decrease on the production of I^- and I_2 in aqueous solution (Figure S9 in the SI). The production of both I^- and I_2 in aqueous solution was negligible at $[IO_3^-]$ = 1 mM, $[NO_2^-]$ = 1 mM, and pH

3.0 (reference conditions). An increase in the IO_3^- or NO_2^- concentration by 10 times (1 mM → 10 mM) at pH 3.0 did not induce the formation of I^- and I_2 (Figures S9a and b in the SI). Despite decreasing the pH to 2.0, where 30% of NO_2^- exists in the H_2ONO^+ form, at $[IO_3^-]$ = 1 mM and $[NO_2^-]$ = 1 mM, the production of both I^- and I_2 was not observed. However, when the concentration of NO_2^- increased to 10 mM and the pH decreased to 2.0, the production of both I^- and I_2 was observed (Figures S9c and d in the SI). This result clearly indicates that the pH decrease and the solute concentration increase by freeze concentration effect synergistically accelerate the redox chemical reaction between IO_3^- and NO_2^- in frozen solution. In contrast to the case of NO_2^-, the increase in the IO_3^- concentration by 10 times (1 mM → 10 mM) at pH 2.0 did not generate I_2 and I^- above the detection limit (Figures S9c and d in the SI). This result implies that the concentration of NO_2^- (more precisely H_2ONO^+) more significantly affects the redox conversion rate of IO_3^- and NO_2^- (i.e., the production of I_2 and I^-) than the concentration of IO_3^-.

Freezing-Induced Production of I_2 under Various Conditions. The effect of pH, IO_3^- concentration, NO_2^- concentration, and freezing temperature on the production of I_2 and I^- in the frozen solution containing IO_3^- and NO_2^- was investigated (Figure 4). Data collection was performed after 24 h of reaction because further freezing to 72 h did not produce more I_2 and I^-. The trend for I_2 production agreed with that for I^- production in all cases. Figure 4a shows the production of I_2 and I^- as a function of pH. The production of I_2 and I^- after freezing increased with decreasing pH. This behavior is ascribed to the fact that the pH of the frozen solution is lower and more H_2ONO^+ is produced when an aqueous solution having a lower pH is frozen.

We also investigated the effect of the IO_3^- and NO_2^- concentrations on the production of I_2 and I^-. The production of both I_2 and I^- increased with increasing concentrations of IO_3^- and NO_2^- (Figures 4b and c). Of those of IO_3^- and NO_2^-, the concentration of NO_2^- has greater influence on the production of I_2 and I^-. When the concentration of IO_3^- increased from 125 μM to 2 mM at $[NO_2^-]$ = 1 mM, the production of I_2 doubled (41.4 μM → 84.1 μM). On the other hand, the increase in the NO_2^- concentration from 125 μM to 2 mM at $[IO_3^-]$ = 1 mM resulted in 130-times greater I_2 production (1.4 μM → 183.8 μM). This result reconfirms that the concentration of NO_2^- has a decisive effect on the rate of the redox chemical reaction between IO_3^- and NO_2^-.

We investigated whether the solution containing IO_3^- and NO_2^- ($[NO_2^-]$ = 1 mM, $[IO_3^-]$ = 1 mM, and pH = 3.0) is frozen or not depending on the temperature (−7, −8, −9, and −10 °C) (see Table S1 in the SI). According to the results, the freezing point is estimated to be about −8 °C. Figure 4d shows the freezing temperature-dependent production of I_2 and I^-. The production of I_2 and I^- in frozen solutions was observed at all

freezing temperatures tested (−10 to −30 °C). However, the amount of I_2 and I^- produced in the frozen solutions varied depending on the freezing temperature. The final production of I_2 and I^- decreased at lower freezing temperatures. After 24 h of reaction, 91.8, 74.1, and 69.2 μM of I_2 (also 212.5, 170.4, and 144.9 μM of I^-) were produced at −10, −20, and −30 °C, respectively. It has been previously reported that the redox chemical reactions in frozen solution last a shorter time at lower freezing temperature because they are stopped (or markedly retarded) when the liquid region completely disappears on complete solidification (i.e., when there is no liquid region in frozen solution because the temperature of liquid region reaches the eutectic temperature) [20, 62-64]. The more rapid complete solidification at lower freezing temperature accounts for why the production of I_2 and I^- decreases with decreasing freezing temperature. The production of I_2 and I^- was higher when the solution was frozen in a refrigerator (relatively slow freezing; coolant: cold air) than when frozen in a cooling bath (relatively fast freezing; coolant: cold ethanol) at the same temperature (−20 °C). This result indicates that the freezing rate at the same temperature affects the final production of I_2 and I^-. However, there are other possibilities of the freezing temperature-dependent production of I_2 and I^-. The growth of ice crystals begins earlier at lower freezing temperatures. Therefore, the concentration of solutes in the liquid regions between ice crystals is higher at lower freezing temperatures in the initial period. The production of I_2 and I^- in the initial period (i.e., after 30 min) was in the order −30 > −20 > −10 °C (see Figure S10 in the SI). However, slow freezing can eventually accumulate a greater amount of solutes in the liquid regions between ice crystals than fast freezing. The local concentration of methylene blue in the grain boundaries of ice at 243 K was higher by 3 orders of magnitude than that at 77 K [27]. The higher production of I_2 and I^- at higher freezing temperatures may be because IO_3^- and NO_2^- are more concentrated in the grain boundaries of ice under slower freezing conditions. In addition, the rate constant of a chemical reaction based on the Arrhenius equation decreases with decreasing temperature. This may also be the reason for the lower final production of I_2 and I^- at lower freezing temperatures. In real aquatic systems, cold air (not ethanol) acts as the coolant. Therefore, the time that it takes to reach the complete solidification would be longer and the production of I_2 and I^- in the frozen solution containing IO_3^- and NO_2^- would be more significant in real aquatic systems.

Environmental Implications. The production of I_2 through the redox chemical reaction between IO_3^- and NO_2^- in frozen solution may make a significant contribution to the global iodine budget because both IO_3^- and NO_2^- are ubiquitous. The concentrations of NO_2^- and IO_3^- vary significantly depending on region, season, and type of environmental media (e.g., NO_2^-: dozens of nM ~ a few μM in snow on the Arctic region [65, 66],

hundreds of nM ~ a few μM in seawater [67, 68], and a few μM ~ hundreds of μM in surface water [69, 70] and IO_3^-: dozens of nM ~ hundreds of nM in sea ice on the Arctic region [71], hundreds of nM in seawater [72-74], and dozens of nM ~ hundreds of nM in surface water [75, 76]). Although the concentrations of IO_3^- and NO_2^- in this study are higher than environmentally relevant concentrations, the proposed mechanism can significantly affect the global production of I_2 because it operates in extensive cold regions, such as polar regions, permafrost, and midlatitudes during the winter season.

Comparing both polar regions, the level of NO_2^- in ice is higher in the Arctic than in the Antarctic due to anthropogenic NO_x (as a precursor of NO_2^-) emissions in the northern hemisphere. In addition, the pH of ice in the Arctic region (4−5) is lower than that in the Antarctic region (4.5−6.5) [77, 78]. Therefore, the production of I_2 through NO_2^--induced activation of IO_3^- in frozen solution should be higher in the Arctic than in the Antarctic. A recent study reported a rapid increase in atmospheric iodine levels in the Arctic since the mid-twentieth century, with potential implications for increased iodine-mediated O_3 depletion in this region in recent decades [79]. Freeze-thaw cycles through day/night temperature variation will produce and emit I_2 in midlatitudes during the winter season. In addition, in permafrost and polar regions, I_2 will be produced and accumulated in ice during the winter season and emitted to the atmosphere in the spring.

No previous mechanisms for the production of organic iodine and I_2 can completely account for the iodine budget in some polar areas, which implies that there is still a missing source and mechanism for organic iodine and/or I_2 production [35, 80]. This new mechanism for I_2 production may help explain why the measured values of iodine are larger than the modeled values in some polar areas. The production of I_2 through the redox chemical reaction between IO_3^- and NO_2^- may be low in the polar regions because there are not many sites that meet the specific requirements (i.e., high concentrations of IO_3^- and NO_2^- and low pH). Even then, the freezing-induced production of I_2 from IO_3^- can be initiated by other inorganic and organic species. The redox couple of IO_3^- and NO_2^- is only one example and there would be other species which could reduce IO_3^- to I_2 during freezing. If so, this mechanism has the potential to have more impact on the I_2 emission flux to the atmosphere.

4. References

(1) Saiz-Lopez, A.; Plane, J. M. C.; Baker, A. R.; Carpenter, L. J.; von Glasow, R.; Martín, J. C. G.; McFiggans, G.; Saunders, R. W. Atmospheric chemistry of iodine. *Chem. Rev.* **2012**, *112*, 1773-1804.

(2) McFiggans, G.; Plane, J. M. C.; Allan, B. J.; Carpenter, L. J.; Coe, H.; O'Dowd, C. A

modeling study of iodine chemistry in the marine boundary layer. *J. Geophys. Res.: Atmos.* 2000, *105*, 14371-14385.

(3) Vogt, R.; Sander, R.; Glasow, R. V.; Crutzen, P. J. Iodine chemistry and its role in halogen activation and ozone loss in the marine boundary layer: a model study. *J. Atmos. Chem.* **1999,** *32*, 375-395.

(4) Saiz-Lopez, A.; Fernandez, R. P.; Ordóñez, C.; Kinnison, D. E.; Martín, J. C. G.; Lamarque, J.-F.; Tilmes, S. Iodine chemistry in the troposphere and its effect on ozone. *Atmos. Chem. Phys.* **2014,** *14*, 13119-13143.

(5) Gálvez, O.; Martín, J. C. G.; Gómez, P. C.; Saiz-Lopez, A.; Pacios, L. F. A theoretical study on the formation of iodine oxide aggregates and monohydrates. *Phys. Chem. Chem. Phys.* **2013,** *15*, 15572-15583.

(6) Saunders, R. W.; Plane, J. M. C. Formation pathways and composition of iodine oxide ultra-fine particles. *Environ. Chem.* **2005,** *2*, 299-303.

(7) Saiz-Lopez, A.; Plane, J. M. C.; McFiggans, G.; Williams, P. I.; Ball, S. M.; Bitter, M.; Jones, R. L.; Hongwei, C.; Hoffmann, T. Modelling molecular iodine emissions in a coastal marine environment: the link to new particle formation. *Atmos. Chem. Phys.* **2006,** *6*, 883-895.

(8) Wuosmaa, A. M.; Hager, L. P. Methyl chloride transferase: a carbocation route for biosynthesis of halometabolites. *Science* **1990,** *249*, 160-162.

(9) Theiler, R.; Cook, J. C.; Hager, L. P.; Siuda, J. F. Halohydrocarbon synthesis by bromoperoxidase. *Science* **1978,** *202*, 1094-1096.

(10) Küpper, F. C.; Schweigert, N.; Gall, E. A.; Legendre, J.-M.; Vilter, H.; Kloareg, B. Iodine uptake in laminariales involves extracellular, haloperoxidase-mediated oxidation of iodide. *Planta* **1998,** *207*, 163-171.

(11) Küpper, F. C.; Carpenter, L. J.; McFiggans, G. B.; Palmer, C. J.; Waite, T. J.; Boneberg, E.-M.; Woitsch, S.; Weiller, M.; Abela, R.; Grolimund, D.; Potin, P.; Butler, A.; Luther, G. W., III ; Kroneck, P. M. H.; Meyer-Klaucke, W.; Feiters, M. C. Iodide accumulation provides kelp with an inorganic antioxidant impacting atmospheric chemistry. *Proc. Natl. Acad. Sci. U. S. A.* **2008,** *105*, 6954-6958.

(12) Carpenter, L. J. Iodine in the marine boundary layer. *Chem. Rev.* **2003,** *103*, 4953-4962.

(13) Saiz Lopez, A.; Plane, J. M. C. Novel iodine chemistry in the marine boundary layer. *Geophys. Res. Lett.* **2004,** *31*, L04112.

(14) Möller, A.; Lovric, M.; Scholz, F. Evidence for the occasional appearance of molecular iodine in sea water. *Int. J. Environ. Anal. Chem.* **1996,** *63*, 99-106.

(15) Garland, J. A.; Curtis, H. Emission of iodine from the sea surface in the presence of

ozone. *J. Geophys. Res.: Oceans* **1981,** *86*, 3183-3186.

(16) Carpenter, L. J.; MacDonald, S. M.; Shaw, M. D.; Kumar, R.; Saunders, R. W.; Parthipan, R.; Wilson, J.; Plane, J. M. C. Atmospheric iodine levels influenced by sea surface emissions of inorganic iodine. *Nat. Geosci.* **2013,** *6*, 108-111.

(17) Moore, R. M.; Zafiriou, O. C. Photochemical production of methyl iodide in seawater. *J. Geophys. Res.: Atmos.* **1994,** *99*, 16415-16420.

(18) Martino, M.; Mills, G. P.; Woeltjen, J.; Liss, P. S. A new source of volatile organoiodine compounds in surface seawater. *Geophys. Res. Lett.* **2009,** *36*, L01609.

(19) Takenaka, N.; Ueda, A.; Maeda, Y. Acceleration of the rate of nitrite oxidation by freezing in aqueous solution. *Nature* **1992,** *358*, 736-738.

(20) Takenaka, N.; Ueda, A.; Daimon, T.; Bandow, H.; Dohmaru, T.; Maeda, Y. Acceleration mechanism of chemical reaction by freezing: the reaction of nitrous acid with dissolved oxygen. *J. Phys. Chem.* **1996,** *100*, 13874-13884.

(21) Kim, K.; Chung, H. Y.; Ju, J.; Kim, J. Freezing-enhanced reduction of chromate by nitrite. *Sci. Total Environ.* **2017,** *590-591*, 107-113.

(22) Min, D. W.; Choi, W. Accelerated reduction of bromate in frozen solution. *Environ. Sci. Technol.* **2017,** *51*, 8368-8375.

(23) Choi, Y.; Yoon, H.-I.; Lee, C.; Vetráková, Ľ.; Heger, D.; Kim, K.; Kim, J. Activation of periodate by freezing for the degradation of aqueous organic pollutants. *Environ. Sci. Technol.* **2018,** *52*, 5378-5385.

(24) Bartels-Rausch, T.; Jacobi, H.-W.; Kahan, T. F.; Thomas, J. L.; Thomson, E. S.; Abbatt, J. P. D.; Ammann, M.; Blackford, J. R.; Bluhm, H.; Boxe, C.; Domine, F. *et al.*, A review of air-ice chemical and physical interactions (AICI): liquids, quasi-liquids, and solids in snow. *Atmos. Chem. Phys.* **2014,** *14*, 1587-1633.

(25) O'Concubhair, R.; Sodeau, J. R. The effect of freezing on reactions with environmental impact. *Acc. Chem. Res.* **2013,** *46*, 2716-2724.

(26) Takenaka, N.; Bandow, H. Chemical kinetics of reactions in the unfrozen solution of ice. *J. Phys. Chem. A* **2007,** *111*, 8780-8786.

(27) Heger, D.; Jirkovský, J.; Klán, P. Aggregation of methylene blue in frozen aqueous solutions studied by absorption spectroscopy. *J. Phys. Chem. A* **2005,** *109*, 6702 - 6709.

(28) Heger, D.; Klánová, J.; Klán, P. Enhanced protonation of cresol red in acidic aqueous solutions caused by freezing. *J. Phys. Chem. B* **2006,** *110*, 1277-1287.

(29) O'Driscoll, P.; Lang, K.; Minogue, N.; Sodeau, J. Freezing halide ion solutions and the release of interhalogens to the atmosphere. *J. Phys. Chem. A* **2006,** *110*, 4615-4618.

(30) O'Driscoll, P.; Minogue, N.; Takenaka, N.; Sodeau, J. Release of nitric oxide and iodine to the atmosphere from the freezing of sea-salt aerosol components. *J. Phys. Chem. A* **2008,** *112*, 1677-1682.

(31) O'Sullivan, D.; Sodeau, J. R. Freeze-induced reactions: formation of iodine-bromine interhalogen species from aqueous halide ion solutions. *J. Phys. Chem. A* **2010,** *114*, 12208-12215.

(32) Kim, K.; Yabushita, A.; Okumura, M.; Saiz-Lopez, A.; Cuevas, C. A.; Blaszczak-Boxe, C. S.; Min, D. W.; Yoon, H.-I.; Choi, W. Production of molecular iodine and tri-iodide in the frozen solution of iodide: implication for polar atmosphere. *Environ. Sci. Technol.* **2016,** *50*, 1280-1287.

(33) Raso, A. R. W.; Custard, K. D.; May, N. W.; Tanner, D.; Newburn, M. K.; Walker, L.; Moore, R. J.; Huey, L. G.; Alexander, L.; Shepson, P. B.; Pratt, K. A. Active molecular iodine photochemistry in the arctic. *Proc. Natl. Acad. Sci. U. S. A.* **2017,** *114*, 10053-10058.

(34) Spolaor, A.; Vallelonga, P.; Plane, J. M. C.; Kehrwald, N.; Gabrieli, J.; Varin, C.; Turetta, C.; Cozzi, G.; Kumar, R.; Boutron, C.; Barbante, C. Halogen species record antarctic sea ice extent over glacial - interglacial periods. *Atmos. Chem. Phys.* **2013,** *13*, 6623-6635.

(35) Gálvez, Ó.; Baeza-Romero, M. T.; Sanz, M.; Saiz-Lopez, A. Photolysis of frozen iodate salts as a source of active iodine in the polar environment. *Atmos. Chem. Phys.* **2016,** *16*, 12703-12713.

(36) Baker, A. R. Inorganic iodine speciation in tropical atlantic aerosol. *Geophys. Res. Lett.* **2004,** *31*, L23S02.

(37) Elderfield, H.; Truesdale, V. W. On the biophilic nature of Iodine in seawater. *Earth Planet. Sci. Lett.* **1980,** *50*, 105-114.

(38) Kieber, R. J.; Rhines, M. F.; Willey, J. D.; Avery, G. B., Jr. Nitrite variability in coastal north carolina rainwater and its impact on the nitrogen cycle in rain. *Environ. Sci. Technol.* **1999,** *33*, 373-377.

(39) Doane, T. A. The abiotic nitrogen cycle. *ACS Earth Space Chem.* **2017,** *1*, 411-421.

(40) Whittaker, M.; Bergmann, D.; Arciero, D.; Hooper, A. B. Electron transfer during the oxidation of ammonia by the chemolithotrophic bacterium *Nitrosomonas europaea*. *Biochim. Biophys. Acta, Bioenerg.* **2000,** *1459*, 346-355.

(41) Carlucci, A. F.; Hartwig, E. O.; Bowes, P. M. Biological production of nitrite in seawater. *Mar. Biol.* **1970,** *7*, 161-166.

(42) Hui, C.; Guo, X.; Sun, P.; Khan, R. A.; Zhang, Q.; Liang, Y.; Zhao, Y.-H. Removal of

KOPRI 극지연구소

nitrite from aqueous solution by *Bacillus amyloliquefaciens* biofilm adsorption. *Bioresour. Technol.* **2018,** *248*, 146-152.

(43) Puckett, L. J. Identifying the major sources of nutrient water pollution. *Environ. Sci. Technol.* **1995,** *29*, 408A-414A.

(44) Awtrey, A. D.; Connick, R. E. The absorption spectra of I_2, I_3^-, I^-, IO_3^-, $S_4O_6^=$ and $S_2O_3^=$. heat of the reaction $I_3^- = I_2 + I^-$. *J. Am. Chem. Soc.* **1951,** *73*, 1842-1843.

(45) Vetráková, Ľ.; Vykoukal, V.; Heger, D. Comparing the acidities of aqueous, frozen, and freeze-dried phosphate buffers: is there a "pH memory" effect? *Int. J. Pharm.* **2017,** *530*, 316-325.

(46) Krausková, Ľ.; Procházková, J.; Klašková, M.; Filipová, L.; Chaloupková, R.; Malý, S.; Damborský, J.; Heger, D. Suppression of protein inactivation during freezing by minimizing pH changes using ionic cryoprotectants. *Int. J. Pharm.* **2016,** *509*, 41-49.

(47) Damschen, D. E.; Martin, L. R. Aqueous aerosol oxidation of nitrous acid by O_2, O_3 and H_2O_2. *Atmos. Environ.* **1983,** *17*, 2005-2011.

(48) Kominami, H.; Gekko, H.; Hashimoto, K. Photocatalytic disproportionation of nitrite to dinitrogen and nitrate in an aqueous suspension of metal-loaded titanium(IV) oxide nanoparticles. *Phys. Chem. Chem. Phys.* **2010,** *12*, 15423-15427.

(49) Lide, D. R. *CRC Handbook of Chemistry and Physics*, 77th, ed.; CRC Press: Boca Raton, FL, 1996.

(50) Sander, R. Compilation of Henry's law constants (version 4.0) for water as solvent. *Atmos. Chem. Phys.* **2015,** *15*, 4399-4981.

(51) Fairbrother, F. Colour of iodine solutions. *Nature* **1947,** *160*, 87.

(52) Sturges, W. T.; Barrie, L. A. Chlorine, bromine and Iodine in arctic aerosols. *Atmos. Environ.* **1988,** *22*, 1179-1194.

(53) Oltmans, S. J.; Komhyr, W. D. Surface ozone distributions and variations from 1973 - 1984: measurements at the NOAA geophysical monitoring for climatic change baseline observatories. *J. Geophys. Res.: Atmos.* **1986,** *91*, 5229-5236.

(54) Rottman, C.; Grader, G.; Hazan, Y. D.; Melchior, S.; Avnir, D. Surfactant-Induced modification of dopants reactivity in sol-gel matrixes. *J. Am. Chem. Soc.* **1999,** *121*, 8533-8543.

(55) Perrin, D. D. Buffers of low ionic strength for spectrophotometric p*K* determinations. *Aust. J. Chem.* **1963,** *16*, 572-578.

(56) Dean, J. A. *Lange's Handbook of Chemistry*, 14th, ed.; McGraw-Hill: New York, 1992.

KOPRI 극지연구소

(57) Perrin, D. D. *Dissociation Constants of Inorganic Acids and Bases in Aqueous Solutions*, Butterworths: London, 1969.

(58) Riordan, E.; Minogue, N.; Healy, D.; O'Driscoll, P.; Sodeau, J. R. Spectroscopic and optimization modeling study of nitrous acid in aqueous solution. *J. Phys. Chem. A* **2005,** *109*, 779-786.

(59) Smith, D.; Wang, T.; Španěl, P. A SIFT study of the reactions of H_2ONO^+ ions with several types of organic molecules. *Int. J. Mass Spectrom.* **2003,** *230*, 1-9.

(60) Turney, T. A.; Wright, G. A. Nitrous acid and nitrosation. *Chem. Rev.* **1959,** *59*, 497-513.

(61) Durig, J. R.; Bonner, O. D.; Breazealel, W. H. Raman studies of iodic acid and sodium iodate. *J. Phys. Chem.* **1965,** *69*, 3886-3892.

(62) Kim, K.; Kim, J.; Bokare, A. D.; Choi, W.; Yoon, H.-I.; Kim, J. Enhanced removal of hexavalent chromium in the presence of H_2O_2 in frozen aqueous solutions. *Environ. Sci. Technol.* **2015,** *49*, 10937-10944.

(63) Kim, K.; Choi, W. Enhanced redox conversion of chromate and arsenite in ice. *Environ. Sci. Technol.* **2011,** *45*, 2202-2208.

(64) Takenaka, N.; Tanaka, M.; Okitsu, K.; Bandow, H. Rise in the pH of an unfrozen solution in ice due to the presence of NaCl and promotion of decomposition of gallic acids owing to a change in the pH. *J. Phys. Chem. A* **2006,** *110*, 10628-10632.

(65) Jacobi, H.-W.; Kleffmann, J.; Villena, G.; Wiesen, P.; King, M.; France, J.; Anastasio, C.; Staebler, R. Role of nitrite in the photochemical formation of radicals in the snow. *Environ. Sci. Technol.* **2014,** *48*, 165-172.

(66) Amoroso, A.; Domine, F.; Esposito, G.; Morin, S.; Savarino, J.; Nardino, M.; Montagnoli, M.; Bonneville, J.-M.; Clement, J.-C.; Ianniello, A.; Beine, H. J. Microorganisms in dry polar snow are involved in the exchanges of reactive nitrogen species with the atmosphere. *Environ. Sci. Technol.* **2010,** *44*, 714-719.

(67) Ito, K.; Takayama, Y.; Makabe, N.; Mitsui, R.; Hirokawa, T. Ion chromatography for determination of nitrite and nitrate in seawater using monolithic ODS columns. *J. Chromatogr. A* **2005,** *1083*, 63-67.

(68) Johnson, K. S.; Petty, R. L. Determination of nitrate and nitrite in seawater by flow injection analysis. *Limnol. Oceanogr.* **1983,** *28*, 1260-1266.

(69) Huang, J.; Liu, P.-r.; Sun, Q.-y.; Zhang, H.; Zhang, Y.; Wang, K. Determination of total nitrogen, ammonia, and nitrite in river water by near-infrared spectroscopy and chemometrics. *Anal. Lett.* **2017,** *50*, 1620-1629.

KOPRI 극지연구소

(70) Zieliński, R.; Dunalska, J.; Grochowska, J.; Bigaj, I.; Szymański, D. Variation of nitrogen forms in lakes with different intensity of anthropogenic pressure. *Limnol. Rev.* **2013,** *13*, 181-188.

(71) Atkinson, H. M.; Huang, R.-J.; Chance, R.; Roscoe, H. K.; Hughes, C.; Davison, B.; Schönhardt, A.; Mahajan, A. S.; Saiz-Lopez, A.; Hoffmann, T.; Liss, P. S. Iodine emissions from the sea ice of the Weddell Sea. *Atmos. Chem. Phys.* **2012,** *12*, 11229-11244.

(72) Schnepfe, M. M. Determination of total iodine and iodate in sea water and in various evaporites. *Anal. Chim. Acta* **1972,** *58*, 83-89.

(73) Yokota, K.; Fukushi, K.; Takeda, S.; Wakida, S.-I. Simultaneous determination of iodide and iodate in seawater by transient isotachophoresis-capillary zone electrophoresis with artificial seawater as the background electrolyte. *J. Chromatogr. A* **2004,** *1035*, 145-150.

(74) Huang, Z.; Ito, K.; Timerbaev, A. R.; Hirokawa, T. Speciation studies by capillary electrophoresis - simultaneous determination of iodide and iodate in seawater. *Anal. Bioanal. Chem.* **2004,** *378*, 1836-1841.

(75) Zhang, S.; Schwehr, K. A.; Ho, Y.-F.; Xu, C.; Roberts, K. A.; Kaplan, D. I.; Brinkmeyer, R.; Yeager, C. M.; Santschi, P. H. A novel approach for the simultaneous determination of iodide, iodate and organo-iodide for ^{127}I and ^{129}I in environmental samples using gas chromatography-mass spectrometry. *Environ. Sci. Technol.* **2010,** *44*, 9042-9048.

(76) Žic, V.; Branica, M. The distributions of iodate and iodide in Rogoznica Lake (East Adriatic Coast). *Estuarine, Coastal Shelf Sci.* **2006,** *66*, 55-66.

(77) Ali, K.; Sonbawane, S.; Chate, D. M.; Siingh, D.; Rao, P. S. P.; Safai, P. D.; Budhavant, K. B. Chemistry of snow and lake water in Antarctic region. *J. Earth Syst. Sci.* **2010,** *119*, 753-762.

(78) Caritat, P. d.; Hall, G.; Gìslason, S.; Belsey, W.; Braun, M.; Goloubeva, N. I.; Olsen, H. K.; Scheie, J. O.; Vaive, J. E. Chemical composition of arctic snow: concentration levels and regional distribution of major elements. *Sci. Total Environ.* **2005,** *336*, 183-199.

(79) Cuevas, C. A.; Maffezzoli, N.; Corella, J. P.; Spolaor, A.; Vallelonga, P.; Kjær, H. A.; Simonsen, M.; Winstrup, M.; Vinther, B.; Horvat, C.; Fernandez, R. P.; Kinnison, D.; Lamarque, J.-F.; Barbante, C.; Saiz-Lopez, A. Rapid increase in atmospheric iodine levels in the north atlantic since the mid-20th century. *Nat. Commun.* **2018,** *9*, 1452.

(80) Saiz-Lopez, A.; Blaszczak-Boxe, C. S.; Carpenter, L. J. A mechanism for biologically induced iodine emissions from sea ice. *Atmos. Chem. Phys.* **2015,** *15*, 9731-9746.

KOPRI
극지연구소

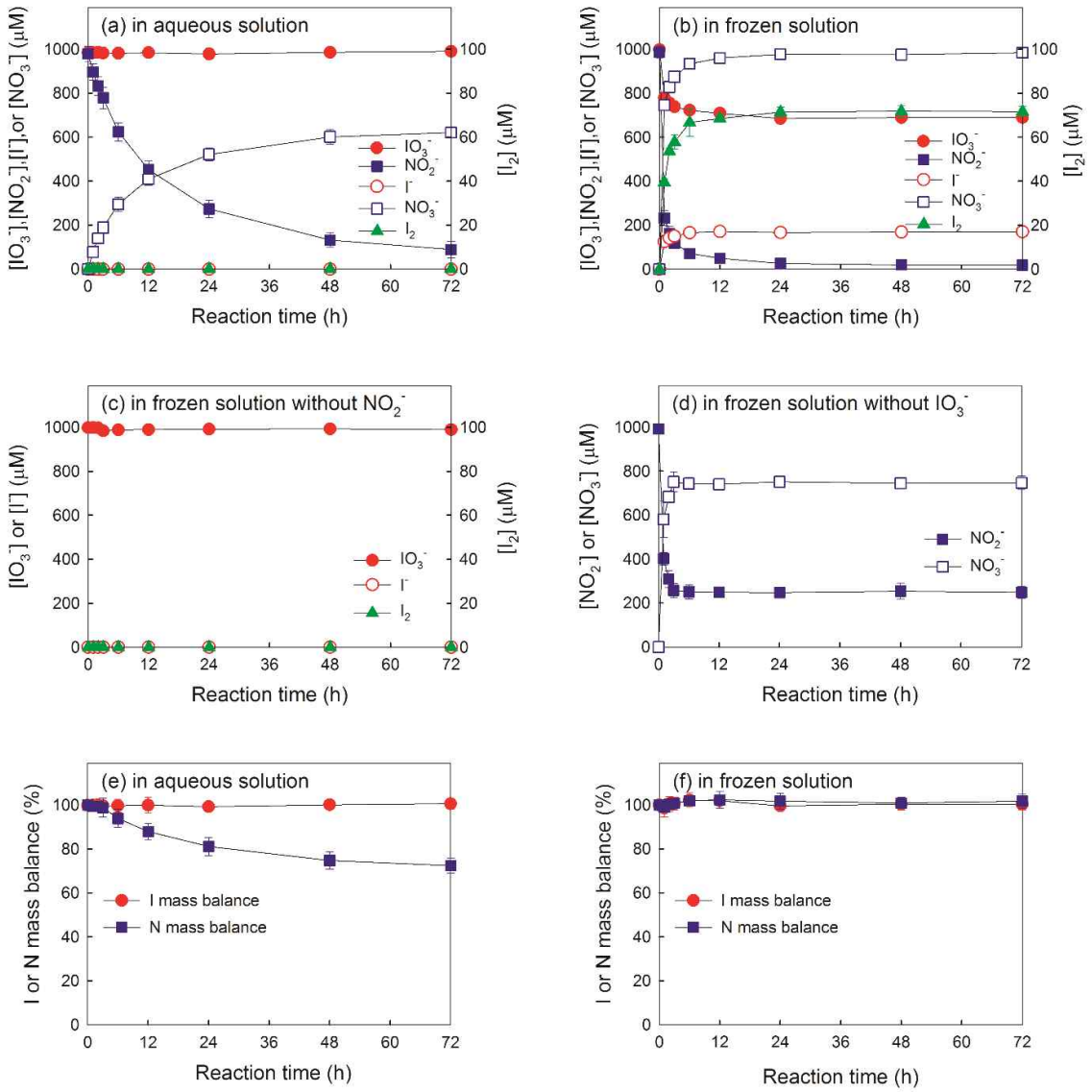

Figure 1. Time profiles of the concentrations of IO_3^-, NO_2^-, I_2, I^-, and NO_3^- in (a) aqueous and (b) frozen solutions containing IO_3^- and NO_2^-. (c) Production of I_2 and I^- in the frozen solution of IO_3^-. (d) Production of NO_3^- in the frozen solution of NO_2^-. Nitrogen and iodine mass balances in (e) aqueous and (f) frozen solutions containing IO_3^- and NO_2^-. Experimental conditions: $[NO_2^-]$ = 1 mM, $[IO_3^-]$ = 1 mM, pH = 3.0, aqueous solution temperature = 25 °C, and freezing temperature = −20 °C.

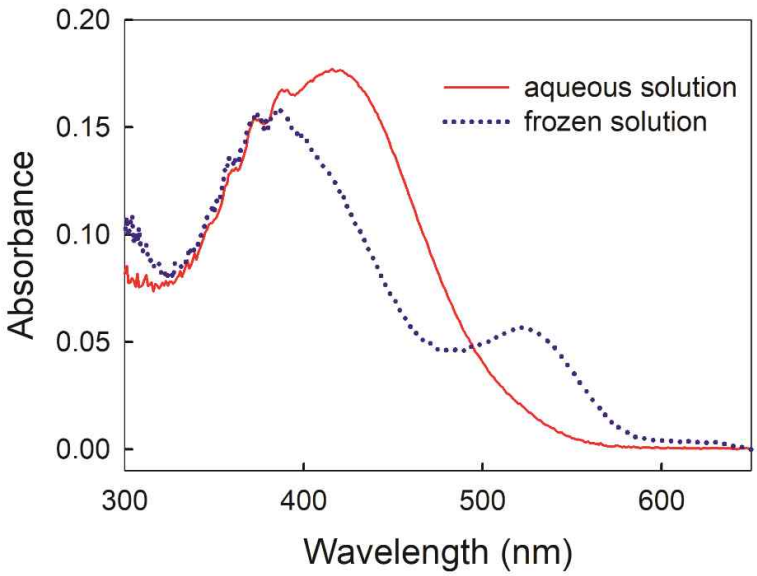

Figure 2. UV－visible absorption spectra of CR in aqueous and frozen solutions containing IO_3^-, NO_2^-, and CR. Experimental conditions: [NO_2^-] = 1 mM, [IO_3^-] = 1 mM, [CR] = 50 μM, pH = 3.0, aqueous solution temperature = 25 °C, and freezing temperature = －20 °C.

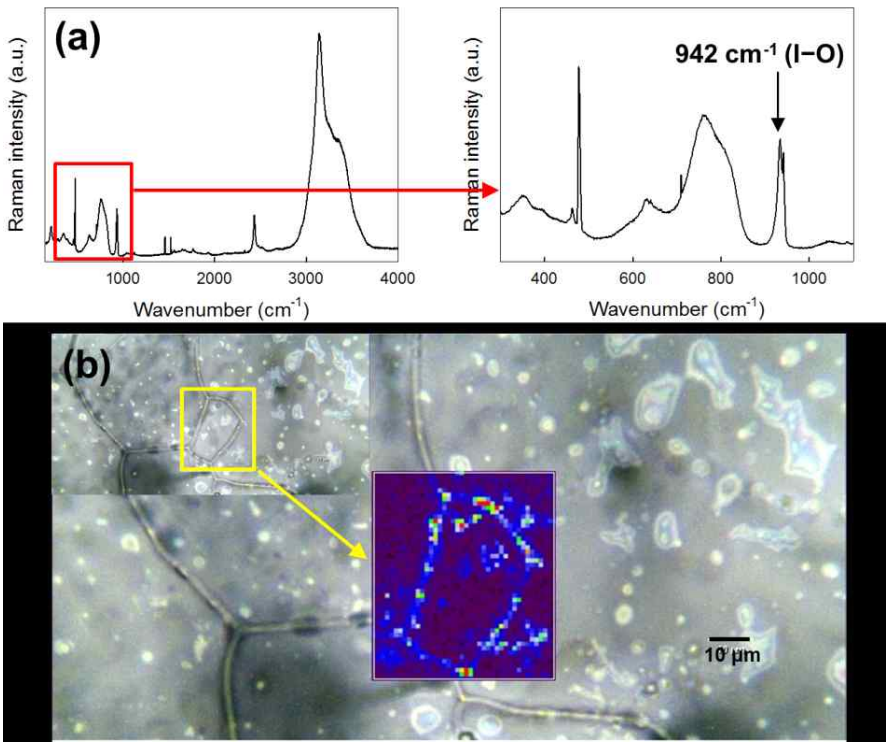

Figure 3. (a) Raman spectra of IO_3^- in frozen solution and (b) optical image of the frozen IO_3^- solution and the distribution of IO_3^- based on the peak intensity at 942 cm^{-1}. Experimental conditions: [IO_3^-] = 1 mM, pH = 3.0, and freezing temperature = decrease from 0 °C to －20 °C at a rate of －1.5 °C/min. The concentration of IO_3^- decreases in the order: red, orange, yellow, green, blue, indigo, and violet.

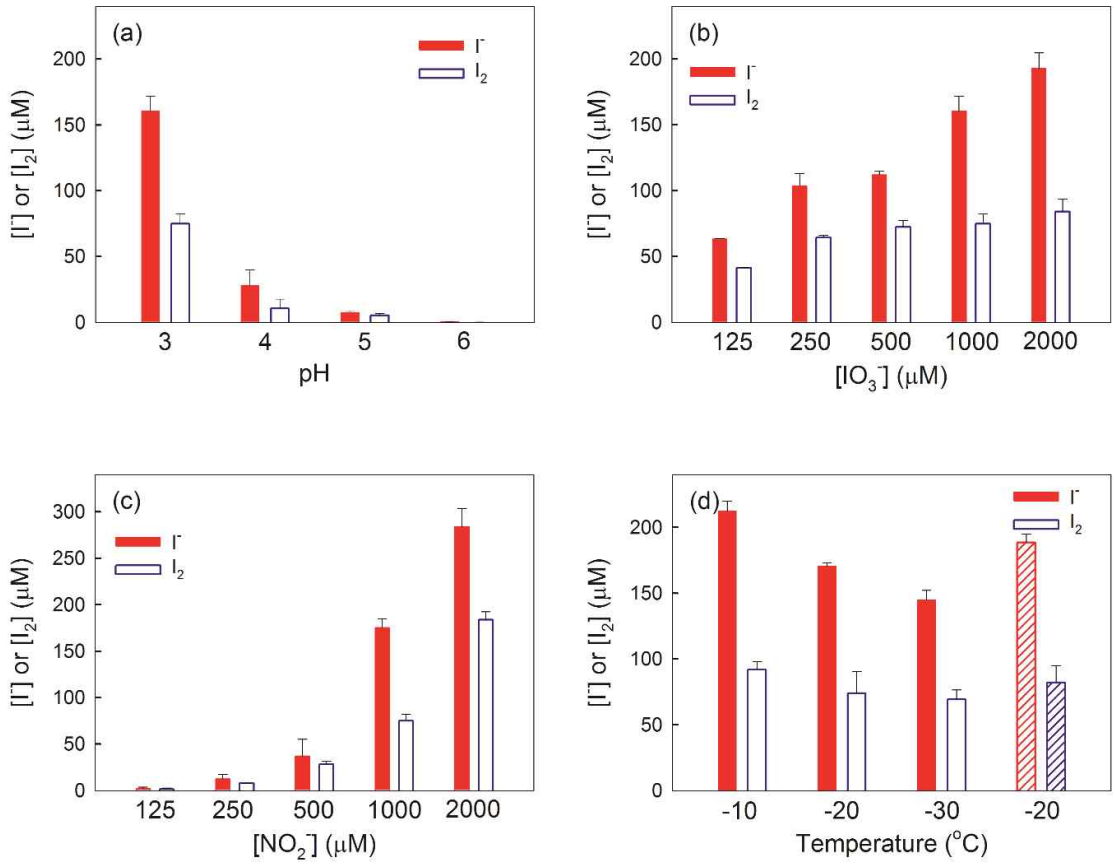

Figure 4. Effect of (a) pH, (b) IO_3^- concentration, (c) NO_2^- concentration, and (d) freezing temperature on the production of I_2 and I^- in the frozen solution containing IO_3^- and NO_2^-. Experimental conditions: $[NO_2^-]$ = 1 mM for parts a, b, and d, $[IO_3^-]$ = 1 mM for parts a, c, and d, pH = 3.0 for parts b, c, and d, and freezing temperature = −20 °C for parts a, b, and c. The bars with diagonal stripes correspond to the experiments performed in a refrigerator.

Supporting Information

Discussion of pH estimation. The maximum absorption wavelength (λ_{max}) of cresol red (CR) is dependent on the pH due to changes in speciation (λ_{max} = 518 nm for doubly protonated CR, λ_{max} = 434 nm for singly protonated CR, and λ_{max} = 573 nm for deprotonated CR) [S1]. All three CR species cannot be in equilibrium because the difference between first and second acid dissociation constants (pK_a) of CR is very large (pK_{a1} = 1.10 and pK_{a2} = 8.15) [S2, S3]. The aqueous solution (pH 3.0 and 3 mL) containing IO_3^-, NO_2^-, and CR ($[IO_3^-]$ = 1 mM, $[NO_2^-]$ = 1 mM, and [CR] = 50 μM) was put in a 4-mL cylindrical quartz tube. Then, this quartz tube was put into a cooling bath at −20 °C. After taking the quartz tube out from the cooling bath, the UV - visible absorption spectra of the frozen samples were immediately recorded using a UV - visible spectrophotometer attached with an integrating sphere (Agilent Cary 5000) and referenced to the background spectrum of pure ice.

Discussion on Figure S1. NO_2^- can be converted not only into NO_3^- (reaction S1) but also into nitrogen monoxide (NO) and nitrous oxide (N_2O) (reactions S2 and S3) under acidic conditions [S4, S5]. Although the aqueous solution containing IO_3^- and NO_2^- was purged with Ar gas to remove dissolved oxygen (to exclude the possibility of reaction S1), the generation of NO_3^- was observed. This result indicates that reactions S2 and S3 are possible. According to reactions S2 and S3 (i.e., in the absence of oxygen), the theoretical (stoichiometric) molar ratio of generated NO_3^- to decreased NO_2^- is in the range 0.33−0.5. The observed molar ratio of generated NO_3^- to decreased NO_2^- (0.30) was only slightly lower than the theoretical (stoichiometric) value. When the aqueous solution containing IO_3^- and NO_2^- was continuously purged with Ar gas, the decrease in the NO_2^- concentration was very fast with the production of a small amount of NO_3^- (observed molar ratio value of generated NO_3^- to decreased NO_2^- = 0.07). This result indicates that the emission of HNO_2 to the atmosphere is possible. Therefore, the incomplete nitrogen mass balance is most likely due to both the emission of HNO_2 to the atmosphere and the conversion of NO_2^- into NO or N_2O.

$$2NO_2^- + O_2 \rightarrow 2NO_3^- \quad \text{(S1)}$$

$$3NO_2^- + 2H^+ \rightarrow NO_3^- + 2NO + H_2O \quad \text{(S2)}$$

$$4NO_2^- + 2H^+ \rightarrow 2NO_3^- + N_2O + H_2O \quad \text{(S3)}$$

Discussion on Figure S8. Not only the concentration of IO_3^- but also other factors, such as a change in the topology at different locations and different scattering efficiencies of the liquid regions and the ice crystals, may affect the Raman peak intensity at a single wavelength. However, the Raman spectra (peak intensity at 942 cm^{-1}) measured at the grain boundaries of ice (liquid regions) were similar to those measured at the ice crystals (solid regions) in frozen pure water (Figures S8a and b). In addition, the average peak intensity at 942 cm^{-1} measured at the grain boundaries of ice was much higher than that measured at the ice crystals in frozen IO_3^- solution (Figures S8c and d). Therefore, the intensity of the Raman peak at 942 cm^{-1} is primarily dependent on the IO_3^- concentration and the effects of other factors on the Raman spectra are negligible.

KOPRI
극지연구소

Table S1. Possibility (%) of freeze[a] depending on the temperature

Temperature (°C)			
−7°C	−8 °C	−9 °C	−10 °C
0	40	65	100

[a]Possibility of freeze: (number of frozen samples)/(number of aqueous samples added to a cooling bath = 20 samples) × 100 (%).

Experimental conditions: $[NO_2^-]$ = 1 mM, $[IO_3^-]$ = 1 mM, pH = 3.0, and reaction time = 4 h.

KOPRI
극지연구소

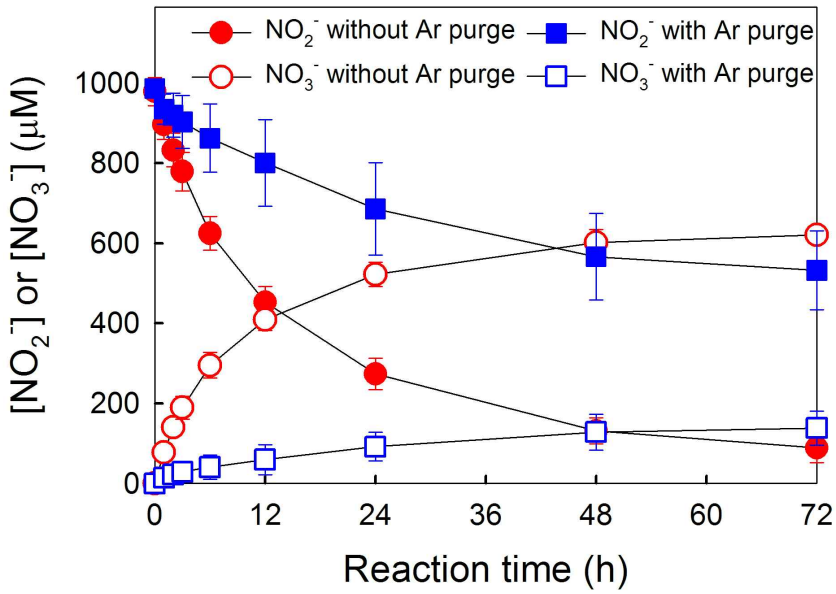

Figure S1. Time profiles of the concentrations of NO_2^- and NO_3^- in aqueous solution containing IO_3^- and NO_2^- with and without an Ar purge. Experimental conditions: $[NO_2^-]$ = 1 mM, $[IO_3^-]$ = 1 mM, pH = 3.0, and aqueous solution temperature = 25 °C. Experimental procedure: A polypropylene conical tube that was sealed with a rubber septum was used as a reactor. An aqueous solution containing IO_3^- and NO_2^- (9.9 mL) and a $HClO_4$ solution were separately purged with Ar gas for 30 min. Then, the $HClO_4$ solution (0.1 mL) was injected into the polypropylene conical tube (containing the aqueous solution of IO_3^- and NO_2^-) using a syringe. The moment when the $HClO_4$ solution was injected into the polypropylene conical tube was noted as the starting point of the reaction (reaction time = 0 h).

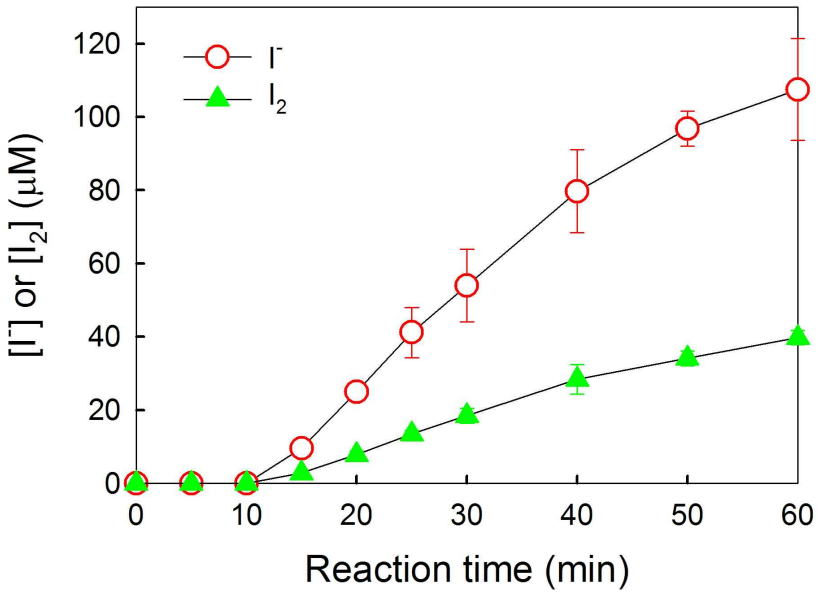

Figure S2. Time profiles of the production of I_2 and I^- in frozen solution containing IO_3^- and NO_2^-. Experimental conditions: $[NO_2^-]$ = 1 mM, $[IO_3^-]$ = 1 mM, pH = 3.0, and freezing temperature = −20 °C.

KOPRI
극지연구소

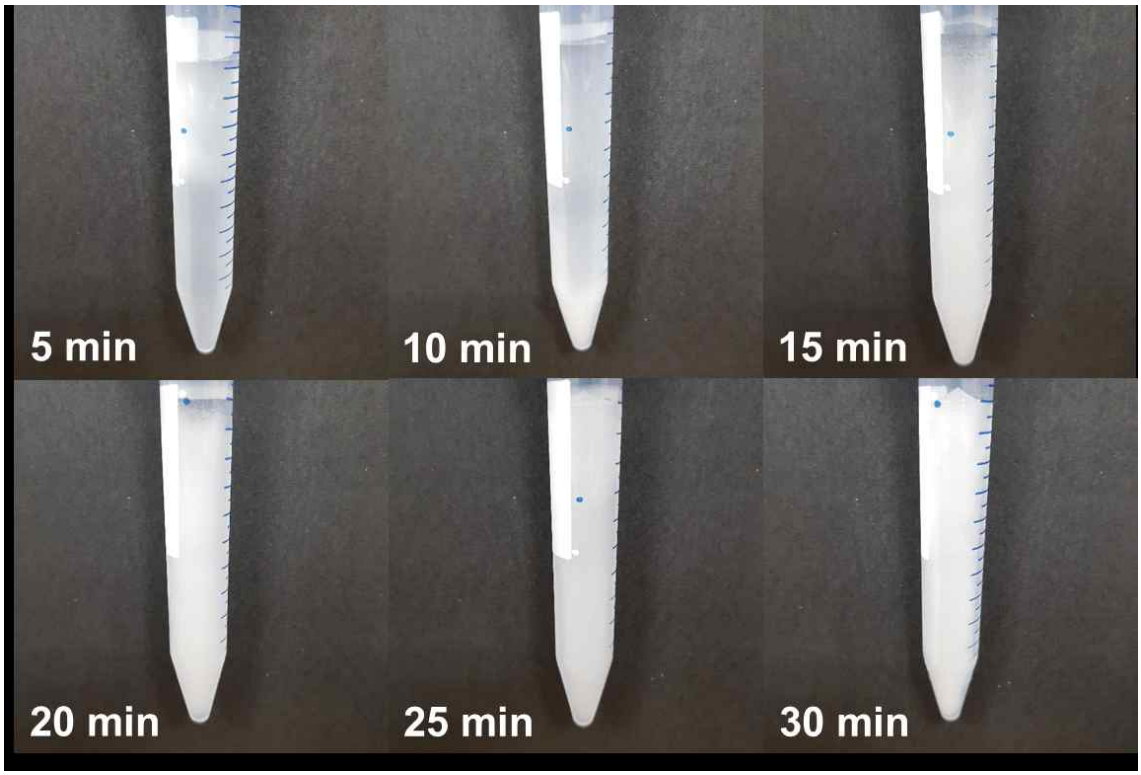

Figure S3. Degree of freezing (solidification) of the solution containing IO_3^- and NO_2^- as a function of reaction time. Experimental conditions: $[NO_2^-]$ = 1 mM, $[IO_3^-]$ = 1 mM, pH = 3.0, and freezing temperature = −20 °C.

KOPRI 극지연구소

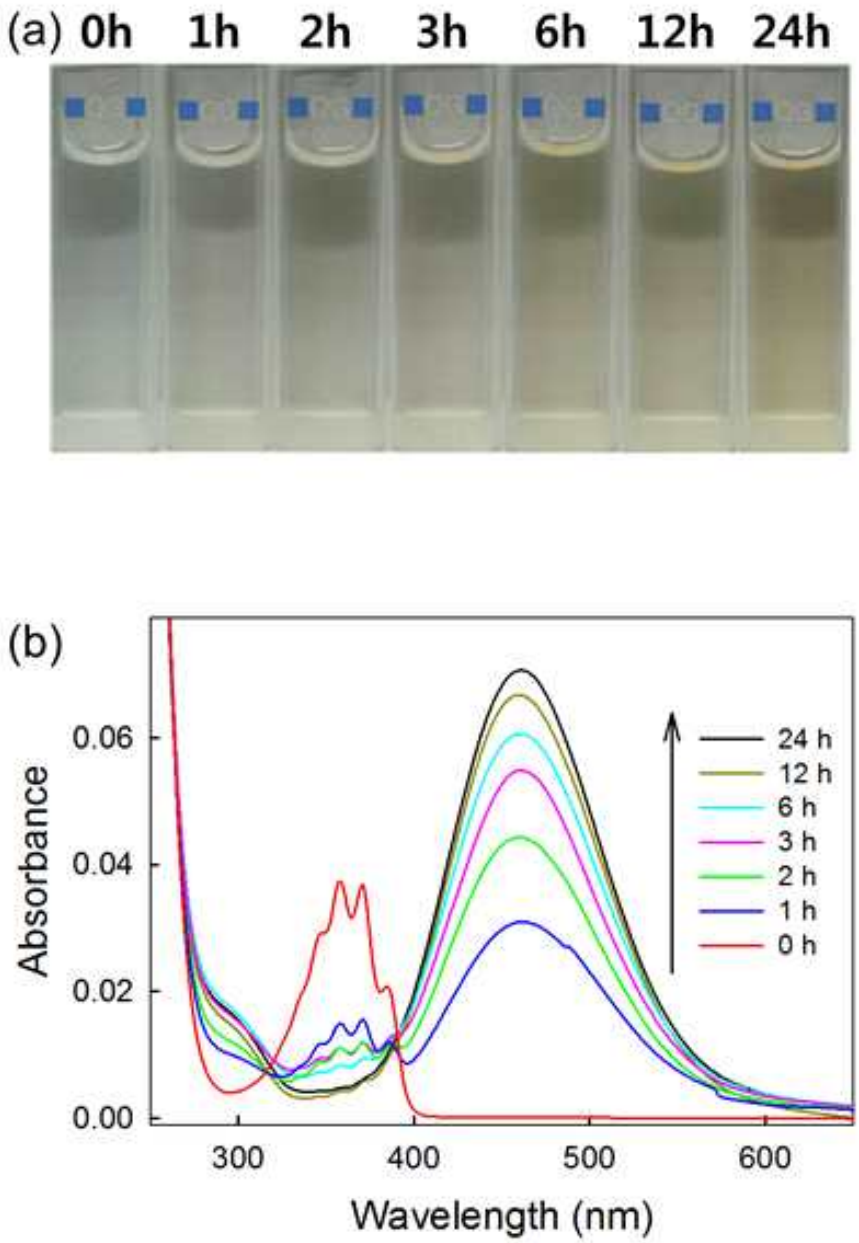

Figure S4. (a) Image and (b) absorbance of the samples containing IO_3^- and NO_2^- as a function of freezing time. Experimental conditions: $[NO_2^-]$ = 1 mM, $[IO_3^-]$ = 1 mM, pH = 3.0, and freezing temperature = −20 °C. They were immediately imaged or measured after thawing the frozen solution.

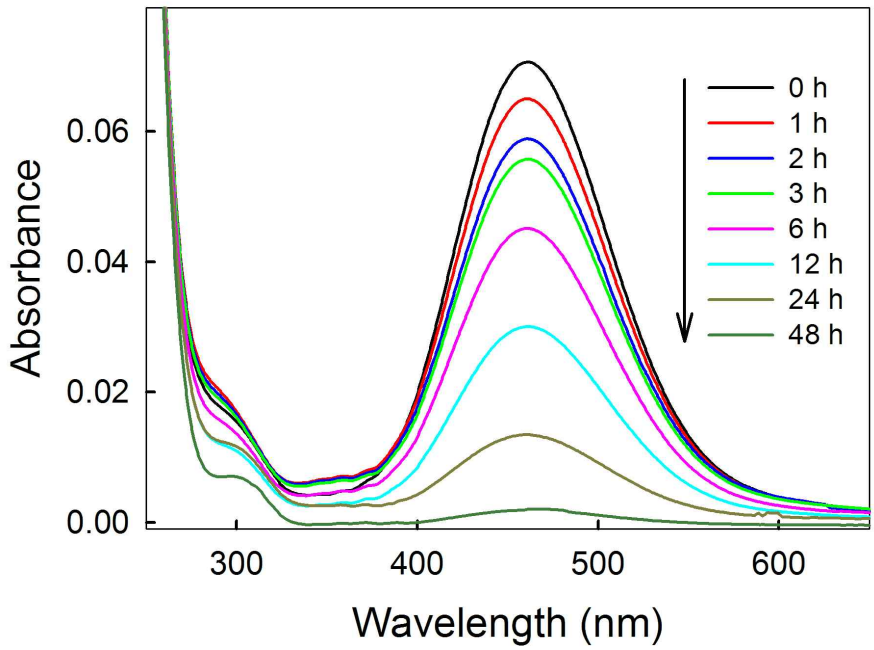

Figure S5. Absorbance change of the melted sample as a function of time. Experimental conditions: $[NO_2^-]$ = 1 mM, $[IO_3^-]$ = 1 mM, pH = 3.0, freezing temperature = −20 °C, and ambient temperature = 25 (± 1) °C. The absorbance was measured after thawing the frozen solution for 24 h and then keeping it in the dark under ambient conditions for 0−48 h.

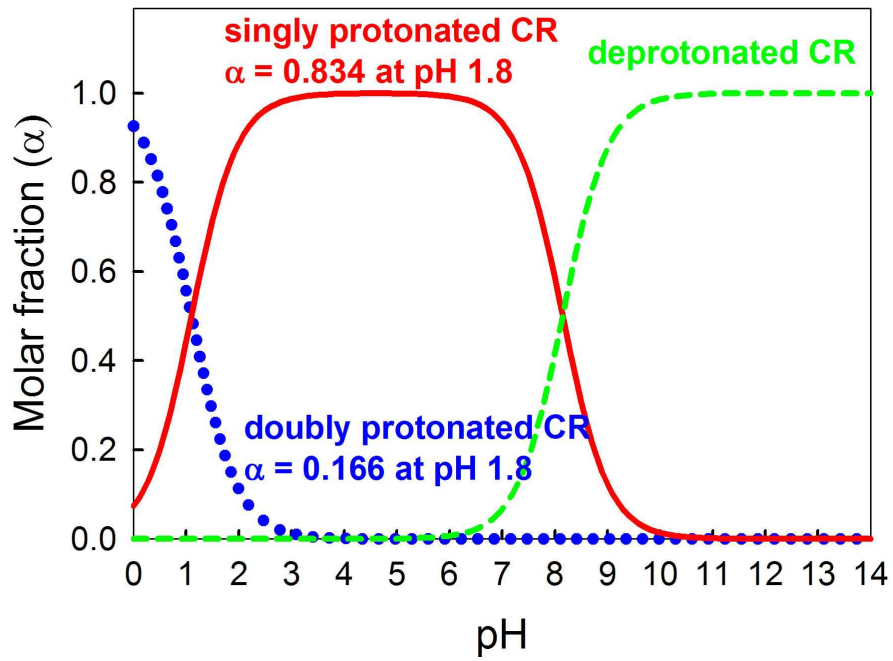

Figure S6. pH-dependent molar fraction of cresol red (CR) species. The acid dissociation constants (pK_a) of CR were obtained from references S2 and S3 (pK_{a1} = 1.10 and pK_{a2} = 8.15).

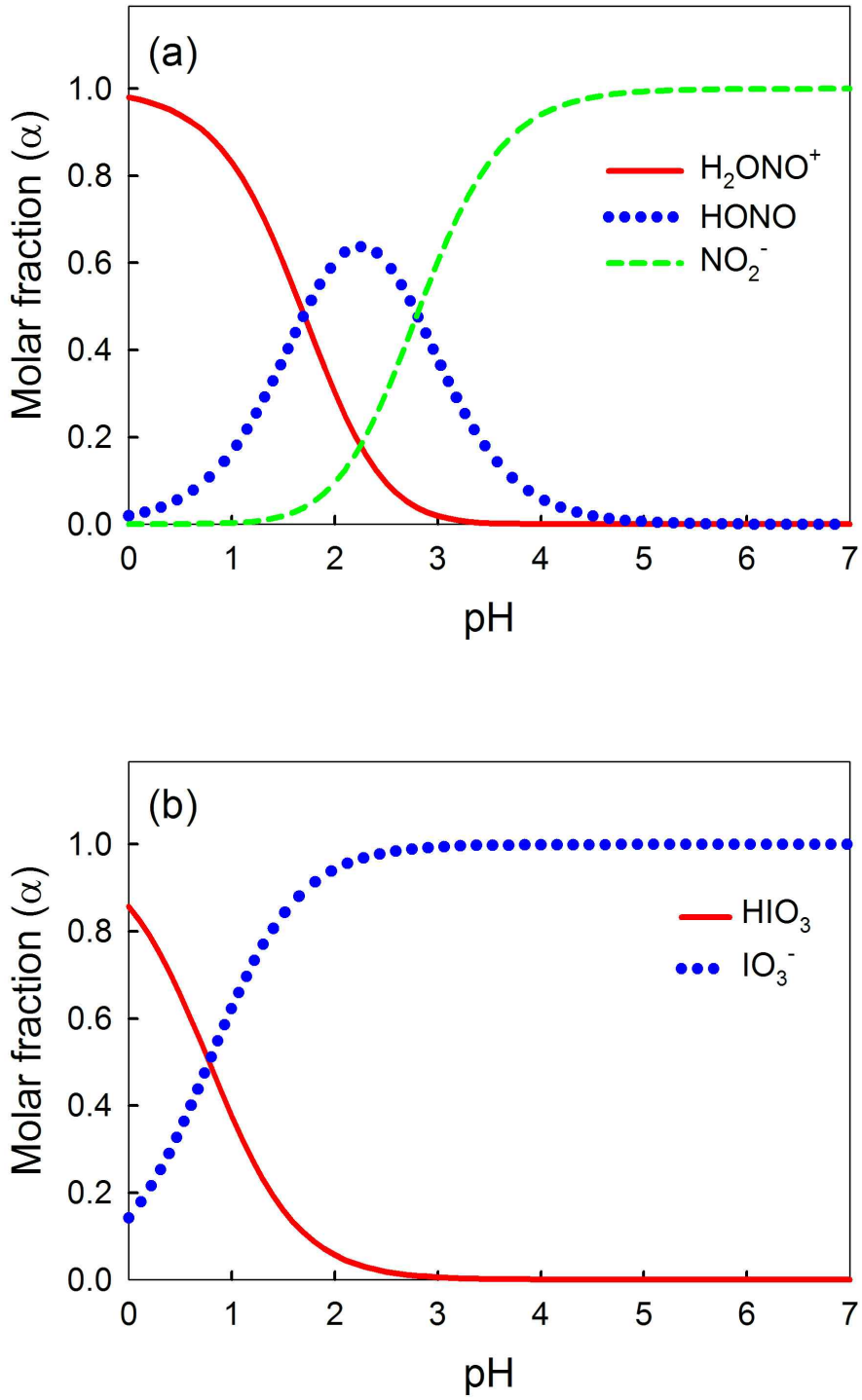

Figure S7. pH-dependent molar fraction of (a) NO_2^- and (b) IO_3^- species. The stepwise acid dissociation constants (pK_a) were obtained from reference S6 for NO_2^- (pK_{a1} = 1.7 and pK_{a2} = 2.8) and reference S7 for IO_3^- (pK_a = 0.78).

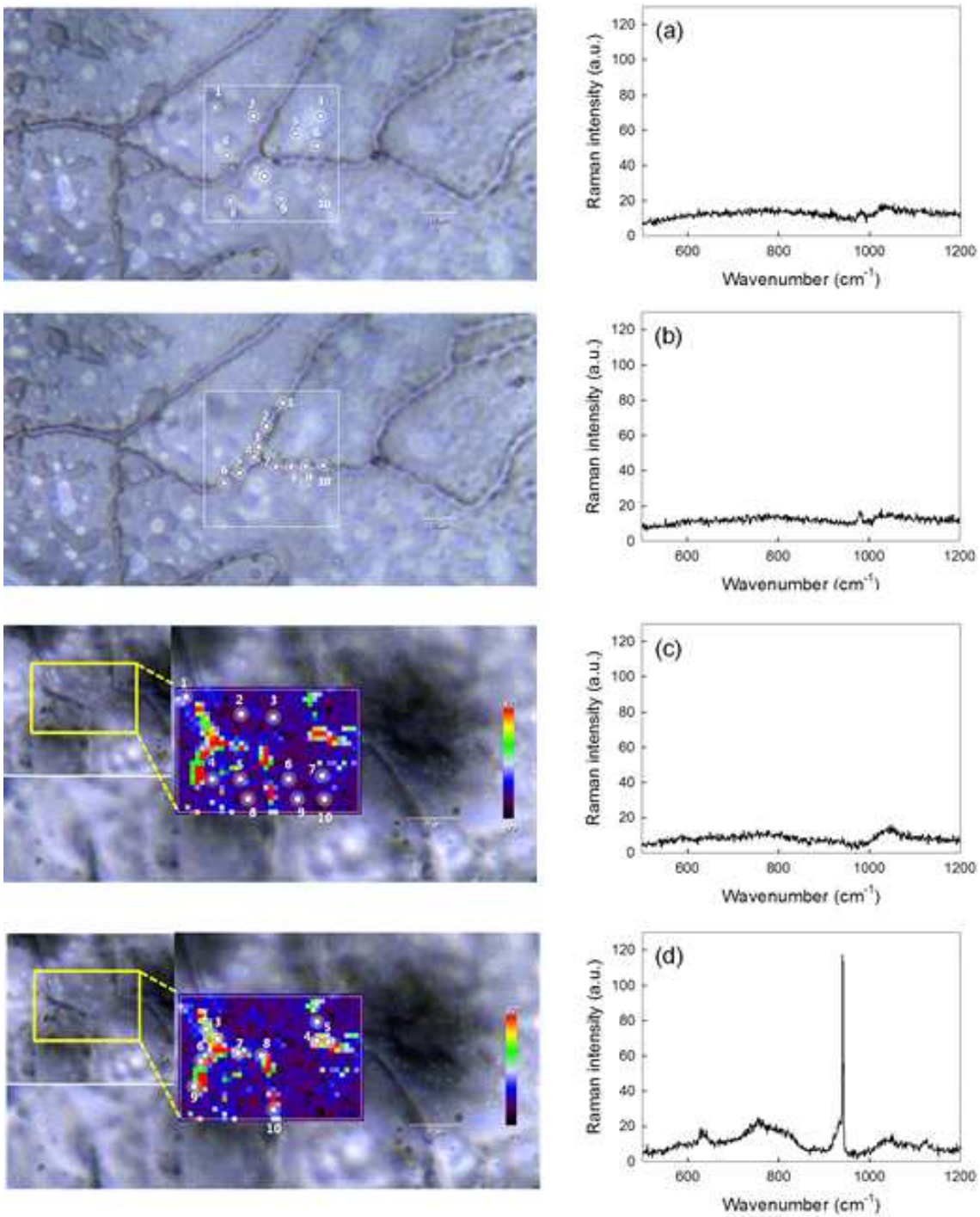

Figure S8. Average Raman spectra of 10 points in (a) ice crystals and (b) liquid regions of frozen pure water and (c) ice crystals and (d) liquid regions of frozen IO_3^- solution. Experimental conditions: $[IO_3^-]$ = 1 mM for parts c and d, pH = 3.0, and freezing temperature = decrease from 0 °C to −20 °C at a rate of −1.5 °C/min. Raman spectra were measured at the points indicated by white circles in the left figures.

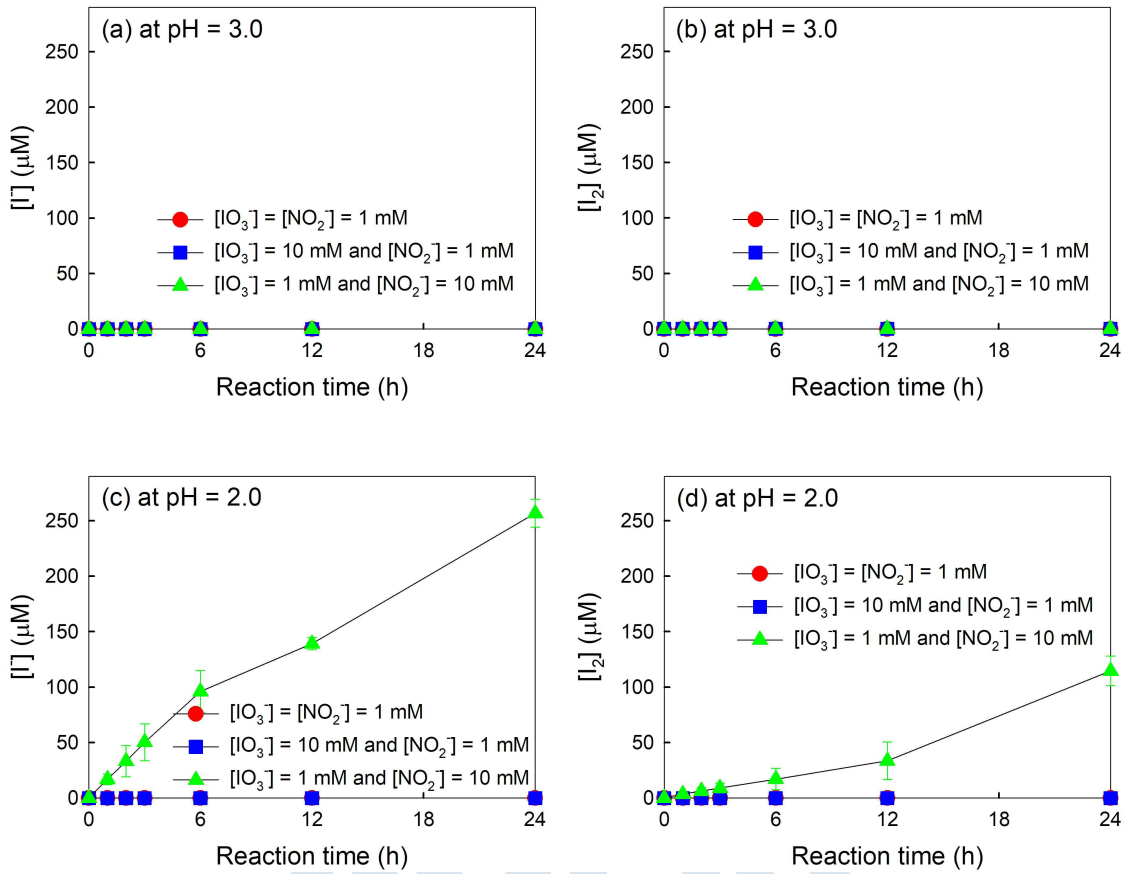

Figure S9. Time profiles of the production of (a and c) I^- and (b and d) I_2 in aqueous solution containing NO_2^- and IO_3^- at (a and b) pH = 3.0 and (c and d) 2.0 depending on the concentration of NO_2^- and IO_3^-. Experimental conditions: $[NO_2^-]$ = 1 or 10 mM, $[IO_3^-]$ = 1 or 10 mM, pH = 2.0 or 3.0, and aqueous solution temperature = 25 °C.

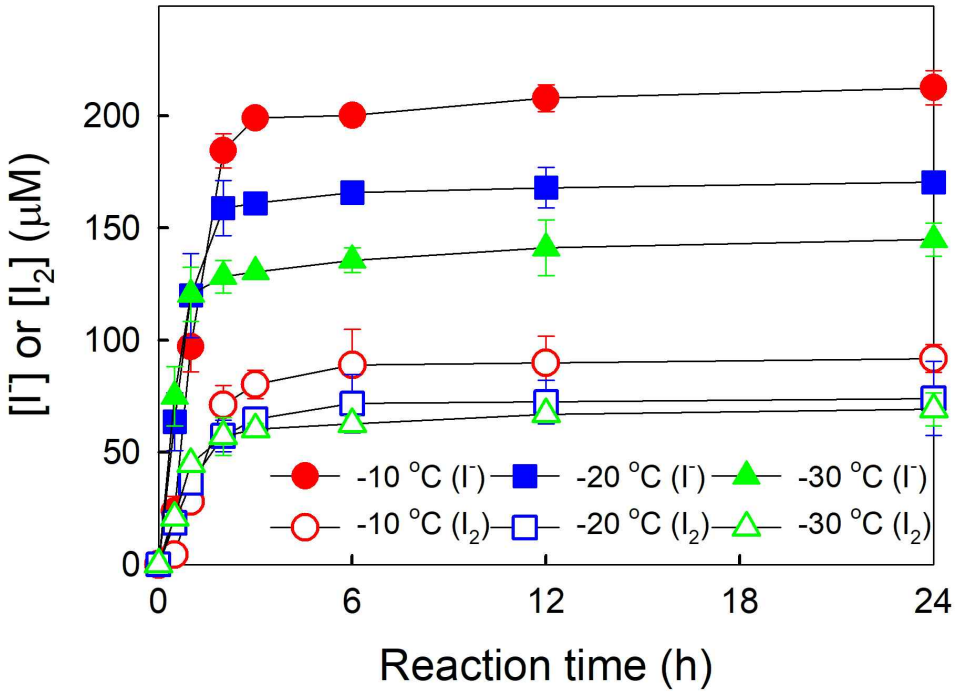

Figure S10. Time profiles of the production of I_2 and I^- in frozen solutions containing IO_3^- and NO_2^- depending on the freezing temperature. Experimental conditions: $[NO_2^-]$ = 1 mM, $[IO_3^-]$ = 1 mM, and pH = 3.0.

KOPRI 극지연구소

References in SI

(S1) Rottman, C.; Grader, G.; Hazan, Y. D.; Melchior, S.; Avnir, D. Surfactant-Induced modification of dopants reactivity in sol-gel matrixes. *J. Am. Chem. Soc.* **1999,** 121, 8533-8543.

(S2) Perrin, D. D. Buffers of low ionic strength for spectrophotometric pK determinations. *Aust. J. Chem.* **1963,** 16, 572-578.

(S3) Dean, J. A. *Lange's Handbook of Chemistry,* 14th, ed.; McGraw-Hill: New York, 1992.

(S4) Damschen, D. E.; Martin, L. R. Aqueous aerosol oxidation of nitrous acid by O_2, O_3 and H_2O_2. *Atmos. Environ.* **1983,** 17, 2005-2011.

(S5) Kominami, H.; Gekko, H.; Hashimoto, K. Photocatalytic disproportionation of nitrite to dinitrogen and nitrate in an aqueous suspension of metal-loaded titanium(IV) oxide nanoparticles. *Phys. Chem. Chem. Phys.* **2010,** 12, 15423-15427.

(S6) Riordan, E.; Minogue, N.; Healy, D.; O'Driscoll, P.; Sodeau, J. R. Spectroscopic and optimization modeling study of nitrous acid in aqueous solution. *J. Phys. Chem. A* **2005,** 109, 779-786.

(S7) Perrin, D. D. *Dissociation Constants of Inorganic Acids and Bases in Aqueous Solutions,* Butterworths: London, 1969.

KOPRI 극지연구소

제 7 절. Simultaneous and Synergic Production of Bioavailable Iron and Reactive Iodine Species in Ice[4)]

Kitae Kim[1,2,3], Sunil Paul M. Menacherry[2], Jungwon Kim[4], Hyun Young Chung[3], Daun Jeong[2], Alfonso Saiz-Lopez[5], and Wonyong Choi[2,*]

[1]Korea Polar Research Institute

[2]Division of Environmental Science and Engineering, Pohang University of Science and Technology

[3]Department of Polar Sciences, University of Science and Technology

[4]Department of Environmental Sciences and Biotechnology, Hallym University

[5]Department of Atmospheric Chemistry and Climate, Institute of Physical Chemistry Rocasolano, CSIC, Spain

1. Introduction

Iron is an essential micronutrient for living organisms and plays an important role in various phytoplankton metabolisms [1,2]. In particular, oceanic primary productivity is limited by bioavailable iron (mainly ferrous species, Fe(II)) in several oceans including the Southern Ocean, which has low phytoplankton production despite the abundant nutrients (HNLC regions: high nutrient low chlorophyll) [3,4]. Since the "iron hypothesis" was firstly proposed by John Martin and coworkers [3,5], various iron fertilization experiments ranging from incubation experiments to mesoscale iron enrichment experiments have been carried out. These experiments have revealed that the iron supply stimulates ocean primary production which is followed by atmospheric carbon sequestration through the biological carbon pump [6, 7]. It is also known that one of the dominant iron sources to the open ocean is aeolian transport of dusts (containing iron) from the desert areas [8]. The speciation, solubility and bioavailability of iron in the oceanic environment are controlled by chemical complexation with organic compounds and photochemical redox processes. The particulate iron (oxyhydr)oxides, which cannot be directly used by phytoplankton, can be transformed to bioavailable forms of iron through photochemical reactions in the ocean [9]. It has been also observed that the photochemical dissolution of iron oxides is enhanced in the presence of various organic compounds [10].

The importance of iodine in the troposphere has been intensively studied due to its

4) 이 연구는 본 과제 지원으로 수행되었으며 그 결과는 다음의 논문으로 출판되었음: Kitae Kim, Sunil Paul M. Menacherry, Jungwon Kim, Hyun Young Chung, Daun Jeong, Alfonso Saiz-Lopez, and Wonyong Choi, "Simultaneous and Synergic Production of Bioavailable Iron and Reactive Iodine Species in Ice", *Environ. Sci. Technol.* 2019, 53, 7355-7362

role in catalytic ozone depletion [11]. In addition to ozone destruction, iodine also plays important roles in i) atmospheric oxidizing capacity by removing various organic and inorganic compounds [12], ii) generation of ultrafine aerosol particles as cloud condensation nuclei (CCN) [13], iii) depletion of gaseous elemental mercury (Hg^0) via oxidation to Hg(II) [11] and iv) perturbation of HO_x and NO_x ratio in mid-latitudes marine boundary layer (MBL) [11, 14]. High concentrations (up to 20 pptv) of iodine oxide (IO) have been detected by ground- and satellite based measurements in coastal Antarctic region during spring time [12]. Furthermore, a remarkable three-fold increase in Arctic atmospheric iodine levels has recently been reported for the period 1950-2011 [15]. Although the environmental impacts of atmospheric iodine are subject to intensive research via field measurements, laboratory and theoretical studies, the plausible production mechanisms of iodine in polar environment are still unclear [16]. Iodine is also suggested to be a potential proxy for past sea ice extent reconstructions [17]. However, the chemical transformation of iodine compounds during transport and after deposition on the ice media is not well known. Understanding chemical transformation of iodine compounds in ice is essential to explain the relationship between iodine recorded in ice cores and paleo sea ice extent or glacial/interglacial variations.

It has been gradually revealed that ice and snow play a significant role as active media for environmental chemical processes such as photochemical, redox, and biological reactions [18-24]. The chemical processes involving organic and inorganic species in the frozen environment are thought to be quite different from their aqueous counterparts and several reactions are significantly accelerated in the ice media. For example, the dissolution of metal oxide particles [19,25] and the reduction of Cr(VI) by organic acids [20] /H_2O_2 [26] /NO_2^- [27] are highly enhanced in the frozen solutions. The photochemical (or dark) transformation of iodide ions to tri-iodide (I_3^-) and gaseous molecular iodine (I_2) is also highly enhanced in the ice phase [28]. It is generally thought that the accelerated chemical reactions in frozen solutions are caused by the freeze concentration effect in ice grain boundaries where organic or inorganic substrates are super-concentrated [29].

Ice edge algal bloom during polar spring time has been observed and input of iron from melting sea ice is regarded as one of the major regulating factors [30]. Atmospheric mineral dusts containing iron oxide are transported and deposited on snow/ice layer on sea ice and the concentration of iron in sea ice is much higher (up to several μM) relative to ice-free waters [31]. Furthermore, iodide exists in sea water at the concentration of tens to hundreds nM [32]. When sea water freezes, the iodide ions and biologically produced iodine species can be concentrated on the surface of sea ice. Considering that the dissolution of iron oxides in ice is sensitively affected by the presence and kind of various organic and inorganic species [19,33,34], the reaction between iron oxides and iodide in ice

may play an important role. Here we investigated the reductive dissolution of iron oxide to bio-available iron ($Fe(II)_{aq}$) and the concurrent oxidation of iodide to reactive iodine species (I_3^-,I_2) in aqueous [35] and frozen solutions to reveal a previously unrecognized chemical transformation in the ice media.

2. Materials and Methods

2.1 Materials.

The synthesis and characterization of optically transparent α-Fe_2O_3 colloid are described in a previous paper [19]. Other commercially available iron oxides of hematite (α-Fe_2O_3, Bayferrox 105 M, LANXESS, BET surface area 6 m^2/g), maghemite (γ-Fe_2O_3, Aldrich, BET surface area 36 m^2/g), goethite (α-FeOOH, Aldrich, BET surface area 178 m^2/g), lepidocrocite (γ-FeOOH, Bayferrox 943, LANXESS, BET surface area 75 m^2/g), and magnetite (Fe_3O_4, Aldrich, BET surface area 50 m^2/g) were also used and compared with the colloidal hematite for the iron dissolution reactions. Arizona test dust (AZTD) containing 2~5% of Fe_2O_3 was employed as a proxy of natural mineral dust. Detailed information on AZTD can be found at www.powdertechnologyinc.com. Commercial iron oxide samples were ground into fine powder before preparing the stock aqueous suspension to enhance the dispersion. KI (99.5%, Samchun Chemical) was used as the iodide source. Argon gas (Linde Korea, 99.999% purity) was used as a purging gas when the dissolved O_2 was removed. Ultrapure deionized water (18 MΩ·cm) prepared by a Barnstead purification system was used in all experiments.

2.2 Photolysis.

The detailed freezing and photolysis methods are described in our previous works [19]. To put it briefly, the samples containing colloidal hematite or various commercial iron oxides with iodide were placed in 12×125-mm quartz tubes, sealed with septa, and were located in a merry-go-round photolysis reactor. The reactor was immersed into the cryogenic ethanol bath cooled at -5 °C. The temperature of cryogenic bath was gradually lowered to -20 °C within 20 minutes in order to prevent the breakage of the quartz tubes. A 100-W mercury lamp (Ace Glass Inc.) was used as a major UV irradiation source and the lamp was placed in a double-jacket Pyrex well (cooled by ethanol circulation through the jacket) to prevent the direct contact between the lamp surface and the frozen solution. Irradiation wavelengths shorter than 300 nm were filtered by the Pyrex jacket surrounding the mercury lamp. After freeze solidification of the samples, the mercury lamp with Pyrex jacket was immersed in the cryogenic ethanol bath to start ice photochemical reaction. Aqueous photochemical reactions of iron oxides with iodide were also carried out as a control at 25 °C using the same experimental setup. For the photochemical experiments in

deaerated condition, the sample tubes were purged with argon gas for 30 min prior to light irradiation. The light intensities absorbed by the aqueous and frozen samples were measured by the ferrioxalate actinometry method. Although the incident light flux from the mercury lamp should be the same, the intensities of the UV light absorbed by the aqueous and ice samples ($\lambda > 300$ nm) were 52.9 and 23.4 mW cm^{-2} (3.4×10^{-4} and 1.5×10^{-4} einstein min^{-1} L^{-1}), respectively. It should be noted that the light intensity absorbed by the frozen sample should be taken only as a rough estimate [36]. The measured value of light intensity in ice phase has some uncertainty because the ferrioxlate actinometry is mainly recommended for liquid phase [37].

2.3 Dark reaction.

A conical centrifuge tube of 15 mL was used as a main reactor for the dark reactions. The samples containing colloidal hematite or commercial iron oxide with iodide were solidified in the cryogenic ethanol bath cooled at - 20 °C. The aqueous samples were solidified within 20-30 minutes. Therefore, defining the time *zero* ("t=0") in the reaction kinetic measurements was ambiguous. In this study, the time *zero* indicates the point when the aqueous sample was placed into the cryogenic ethanol bath pre-cooled at the desired reaction temperature (- 20 °C). Aqueous reactions of iron oxides with iodide were also carried out as a control at 25 °C using the same experimental setup. After reaction, the frozen samples were thawed usually within 5 min in a beaker containing luke warm water (30-40 °C). All reactions were repeated at least three times to confirm the reproducibility.

2.4 Analysis.

The concentration of $Fe(II)_{aq}$ was measured spectrophotometrically by using the ferrozine or 1,10-phenanthroline method [19] and the total dissolved iron (Fe^{2+} and Fe^{3+}) was quantified by the same method following the chemical reduction of $Fe(III)_{aq}$ to $Fe(II)_{aq}$. We also measured the total dissolved iron (Fe^{2+} and Fe^{3+}) concentrations by atomic absorption spectroscopy (AAS, SpectrAA-800) to confirm that the above spectrophotometric method and the AA analysis attain the identical results. The concentration of I_3^- was determined by measuring the absorbance at 352 nm (ε_m = 26,400 $M^{-1}cm^{-1}$) using a UV/visible spectrophotometer (Libra S22).

2.5 Outdoor Experiments.

The outdoor experiments were carried out on the roof of the Environmental Engineering building at POSTECH (Pohang, Korea: 36°00′N, 129°19′E) between 9 AM and 2 PM under clear or partly cloudy sky condition in January (winter season). The solar light

intensity was recorded every minute by using a pyranometer (apogee, PYR-P) and a daily average varied from 20 to 51 mW cm^{-2}. The ambient temperature ranged between -3.7 and 1.9 °C. The same 12×125-mm quartz tubes that were used in the laboratory experiments were also used as a reactor for the outdoor experiments. Quartz tubes containing the desired concentrations of iron oxide and iodide were frozen in an ethanol bath before exposing to sunlight. The frozen samples are placed on the pre-cooled ice pack to keep the samples from melting during the experiments. The control photolysis of aqueous samples was carried out simultaneously under the same irradiation condition and the aqueous samples were placed on an electrically heated mat to prevent the freezing of them. The concentrations of photogenerated $Fe(II)_{aq}$ and I_3^- were immediately determined by a UV/visible spectrophotometer after solar irradiation. We also carried out the same solar experiments in Antarctic region, the King Sejong Station, King George Island (62°13′S 58°47′W, sea level) from December 15 to 24, 2013. The ambient temperature ranged between -5.5 and 1.7 °C (an average of -3.6 °C). The integrated solar irradiance measured at the King Sejong Station varied from 0.08 to 0.97 mW cm^{-2} for UV band of $315 < \lambda < 380$ nm. The quartz tubes containing desired concentrations of iron oxides and iodide in distilled water were frozen in a refrigerator cooled at -20 °C prior to natural solar irradiation. It took about 1 h for full solidification of samples.

3. Results and Discussion

3.1 Enhanced photochemical production of Fe(II)aq and triiodide in ice.

We carried out a series of photoreactions of iron oxides and iodide with monitoring the photoreductive dissolution of $Fe(II)_{aq}$ from iron oxides and the accompanying oxidation of iodide to triiodide. The production of both $Fe(II)_{aq}$ and I_3^- was significantly accelerated in the ice phase while negligible in the aqueous solution (Figure 1a).

$$\alpha\text{-}Fe_2O_3 + 3I^- + 6H^+ \rightarrow 2Fe^{2+} + I_3^- + 3H_2O \quad (1)$$

Although hematite (α-Fe_2O_3) can be reductively dissolved under extremely high concentrations of iodide and protons at high temperature (353 K) [38] in aqueous solution (eq. 1), the reaction was negligible in the present aqueous condition (lower concentrations of proton, iron and iodide, lower temperature). The reaction was apparently accelerated in the frozen solution with producing Fe^{2+} and I_3^- at 2:1 molar ratio, which is close to the eq. 1 stoichiometry. Incidentally, the possible photo-dissolution of Fe^{3+} species from hematite was checked by comparing the total dissolved iron concentration ($[Fe^{2+}] + [Fe^{3+}]$) with $[Fe(II)_{aq}]$: most dissolved iron was Fe^{2+} and the production of Fe^{3+} species was negligible. Therefore, the dissolved iron species is a result of reductive dissolution of iron oxide.

Figure 1b shows that $Fe(II)_{aq}$ production in ice gradually increased with increasing the concentration of iodide. As for the pH effect, the photoreductive production of $Fe(II)_{aq}$ in both aqueous solution and ice was higher at lower pH value [10] (SI Figure. S1a) which is in accord with eq. 1. $Fe(II)_{aq}$ formation was insignificant above pH 5. On the other hand, I_3^- formation via photooxidation of iodide was also faster with lower pH but slightly reduced at pH 2 (Figure S1b). Unlike the case of $Fe(II)_{aq}$ formation, the photooxidative formation of I_3^- was still observed above pH 5, which reconfirms the recent study of photooxidation of iodide in ice [28]. It is well known that I_3^- has equilibrium with I_2 in the presence of I^- ($I_2 + I^- \leftrightarrow I_3^-$: K = 700) and the detection of I_3^- implies the presence of I_2. The chemical equilibrium for the hydration of pyruvic acid was also observed in frozen state [39]. The spontaneous conversion of I_3^- to I_2 in frozen solution and the subsequent evaporation of I_2 to the gas phase over the ice were detected by cavity ring-down spectroscopy (CRDS) [28]. We also monitored the possible production of oxyanions such as IO_3^- and IO_4^- that can be generated from the oxidation of I^- using ion chromatography, but no generation of such oxyanions (within their detection limit of about 0.5 μM) was observed.

To evaluate the role of dioxygen, the photoreactions of hematite and iodide were compared between aerated and deaerated conditions (SI Figure S2). The production of Fe(II) was enhanced in ice both with and without dissolved O_2. The $Fe(II)_{aq}$ formation via photodissolution of hematite should be hindered in the aerated condition since dioxygen can reoxidize the reduced $Fe(II)_{surf}$ or scavenge the conduction band electrons in iron oxide particles [40]. However, it is interesting to note that the inhibiting effect of O_2 on the hematite photodissolution was much lower in ice than that in the aqueous phase. This implies that the iron dissolution reaction (eq. 1) is strongly favored with concentrated reagents (e.g., I^-) in the ice grain boundary and the hindering effect of O_2 is much limited in ice compared with that in the aqueous solution. On the contrary, the concurrent photooxidation of iodide to I_3^- was highly accelerated in the presence of O_2 in both aqueous solution and ice since iodide can be directly oxidized by O_2 (eq. 2)[28].

$$O_2(aq) + 4H^+ + 6I^- \rightarrow 2H_2O + 2I_3^- \quad (2)$$

The photooxidation of iodide to triiodide is negligible in the absence of O_2 in both aqueous and frozen solutions containing the iodide only [28]. However, the present result shows that this anoxic mechanism of iodide photooxidation is enabled in the presence of hematite (SI Figure S2b). This implies that the photoactivation of iodide is possible even in O_2-free (or O_2-deficient) environmental condition as long as iron oxide is available.

3.2 Enhanced production of Fe(II)aq and triiodide under dark condition.

The reaction of hematite and iodide was also tested in the absence of light. Figure 2 shows that the dark redox reaction induced a significant production of $Fe(II)_{aq}$ and I_3^- in the ice phase (though much slower than the photochemical counterpart shown in Figure 1a), while that in aqueous solution was negligible. The final molar ratio of $[Fe(II)_{aq}]$ and $[I_3^-]$ after 96 h reaction was close to the stoichiometric ratio of 2:1 as in the case of photochemical reaction (see Figure 1a).

The simultaneous redox conversion of iron oxide and iodide in ice under dark condition was also tested using various types of iron oxides (commercially available powder) which have different characteristics such as particle size, surface area, and crystallinity [hematite (α-Fe_2O_3), maghemite (γ-Fe_2O_3), goethite (α-FeOOH), lepidocrocite (γ-FeOOH) and magnetite (Fe_3O_4)]. The results are summarized in Table 1. The production of $Fe(II)_{aq}$ and I_3^- under the dark was markedly enhanced in the ice phase regardless of the kind of iron oxides. We also investigated the pH dependence of $Fe(II)_{aq}$ and I_3^- production under dark condition (SI Figure S3). The formation of both $Fe(II)_{aq}$ and I_3^- was enhanced in ice phase and decreased with increasing pH. The generation of $Fe(II)_{aq}$ was negligible above pH 5 even in ice phase. This trend is coincident with the previous finding [33].

3.3 Comparison with the single component freezing systems.

We compared the production of $Fe(II)_{aq}$ or I_3^- in ice between the single component (γ-Fe_2O_3 or iodide only) and the dual (γ-Fe_2O_3 + iodide) components systems (SI Table S1). The production of $Fe(II)_{aq}$ from iron oxide in ice was significantly accelerated in the presence of iodide (the dual components) compared to the case of iron oxide only (the single component) in both dark and irradiated conditions. UV irradiation enhanced the reductive dissolution rate of γ-Fe_2O_3 by iodide in ice about 12 times (initial dissolution rates under dark and UV irradiation are 3.75 μM/h and 45 μM/h, respectively) compared to that under dark condition. However, it seems that the iodide oxidation was not apparently enhanced by the presence of γ-Fe_2O_3 in ice. This implies that triiodide ions are adsorbed or further decomposed back to iodide on γ-Fe_2O_3. The photochemical oxidation of iodide in ice was also accelerated both in the presence and absence of iron oxide.

3.4 Freeze concentration effect and reaction mechanism.

Accelerated chemical reactions in ice are mainly attributed to the freeze concentration effect of reagents in ice grain boundaries [29,41,42]. To investigate this concentration effect on this photo-redox reaction (hematite + iodide) in ice, the aqueous phase reaction was carried out with higher concentrations of iodide and proton. The reference reaction was carried out

with $[I^-]$ = 0.5 mM and pH 3 in both aqueous and frozen solutions, which proceeded only in the ice phase (Figure 3). When either the concentration of $[I^-]$ or $[H^+]$ in aqueous solution was raised by 10-fold (from the reference reaction), the production of $Fe(II)_{aq}$ was also observed in aqueous solution although it was still much lower than that in the ice reference reaction. However, when both $[I^-]$ and $[H^+]$ were raised by 10 times ($[I^-]$ = 5 mM, pH 2), the production of Fe(II) in aqueous solution was comparable to or even higher than that in the ice reference reaction. This implies that the enhanced reaction of hematite and iodide in ice can be ascribed to the concentration of reagents in the ice grain boundary.

The reductive dissolution of hematite by iodide was previously investigated under extreme conditions (i.e., pH 2, high concentrations of iodide (0.5~1.56 M), and high temperature (353 K)) to propose the following rate law (eq. 3) [37]: the first order with respect to proton concentration and the second order with respect to the concentration of iodide.

$$R = k[H^+][I^-]^2 \quad (3)$$

The redox conversion of iron oxide and iodide should require the surface adsorption (or complexation) of iodide on the Fe_2O_3 surface. To verify the adsorption (or complexation) of I^- on the Fe_2O_3 surface, the attenuated total reflection Fourier transform infrared (ATR-FTIR) spectra of pure Fe_2O_3 and I^--adsorbed Fe_2O_3 were measured and compared (SI Figure S4). I^- adsorbed on Fe site in Fe_2O_3 can inhibit the vibration of Fe-O vibration. The peak at 560 cm^{-1}, which is ascribed to Fe-O vibration [43], was significantly reduced by I^- adsorption. This result indicates that the adsorption (or complexation) of I^- on the surface of Fe_2O_3 is favored. The adsorption (or complexation) of I^- on the Fe_2O_3 surface can be enabled by electrostatic attraction between I^- and OH_2^+ group on Fe_2O_3 (outer-sphere surface complex) or ligand exchange between I^- and OH (or OH_2^+) group on Fe_2O_3 (inner-sphere surface complex) [37]. Figure S5 shows high-resolution transmission electron microscope (HRTEM) image, energy-dispersive X-ray (EDX) spectrum, and elemental mapping images of I^--adsorbed Fe_2O_3. The I peak in EDX spectrum reconfirms that I^- can be adsorbed on the surface of Fe_2O_3. I elemental spots are well scattered and exactly coincide the Fe and O elemental spots.

The adsorption of I^- on Fe_2O_3 surface could be followed by the electron transfer from the adsorbed iodide to the iron oxide through two mechanisms: (1) the ligand-to-metal charge transfer (LMCT) from adsorbed iodide to the surface ferric ion or (2) the photo-induced charge transfer on hematite working as a photocatalyst. From a LMCT viewpoint, ferric ion on hematite surface (noted as ≡Fe(III)) forms an inner-sphere

complex with the adsorbed iodide (eq. 4) and the subsequent LMCT reduces ferric to ferrous species with oxidizing iodide (eq. 5-6). It was previously reported that the interfacial process can be highly facilitated in the ice grain boundary region where the concentrations of iron oxide particles and organic/inorganic molecules/ions are highly elevated [19,33,34]. The resulting iodide radical reacts with another iodide anion to produce diiodine radical ($E^0(I_2/I_2^{\cdot-})$ = 0.11 V) (eq. 7), which seems to explain why the overall reaction rate law is the second order with respect to the concentration of iodide (eq. 3). The reduced surface Fe(II) is then dissolved into the solution (eq. 8) and the diiodine radicals disproportionate to produce triiodide (eq. 9).

$$\equiv Fe(III) + I^- \rightarrow \equiv Fe(III)\text{-}I^- \quad \text{(inner-sphere surface complex)} \quad (4)$$

$$\equiv Fe(III)\text{-}I^- \rightarrow \equiv Fe(II)\text{-}I^{\cdot} \quad \text{(LMCT)} \quad (5)$$

$$\equiv Fe(III)\text{-}I^- + h\nu \rightarrow \equiv Fe(II)\text{-}I^{\cdot} \quad \text{(photo-induced LMCT)} \quad (6)$$

$$\equiv Fe(II)\text{-}I^{\cdot} + I^- \rightarrow \equiv Fe(II) + I_2^{\cdot-} \quad (I^- \text{ reaction}) \quad (7)$$

$$Fe(II)_{surf} \text{ (surface site)} \rightarrow \mathbf{Fe(II)_{aq}} \quad \text{(desorption)} \quad (8)$$

$$I_2^{\cdot-} + I_2^{\cdot-} \rightarrow I_3^- + I^- \quad \text{(disproportionation)} \quad (9)$$

An alternative mechanism is the semiconductor photocatalysis where the reductive dissolution of $Fe(II)_{aq}$ and the oxidation of iodide are caused by the photoinduced transfers of conduction band (CB) electron and valence band (VB) hole, respectively, on hematite semiconductor (E_g = 2.2 eV) (eq. 10-13). The photo-generated CB electrons can reduce lattice Fe(III) to Fe(II) (eq. 11) which is subsequently released into the solution phase (eq. 12). On the other hand, iodide is oxidized to I_3^- by VB holes (eq. 13).

$$Fe^{III}{}_2O_3 + h\nu \rightarrow e_{cb}^- + h_{vb}^+ \quad \text{(bandgap excitation)} \quad (10)$$

$$Fe(III) \text{ (surface site)} + e_{cb}^- \rightarrow Fe(II)_{surf} \quad \text{(iron reduction)} \quad (11)$$

$$Fe(II)_{surf} \text{ (surface site)} \rightarrow \mathbf{Fe(II)_{aq}} \quad \text{(desorption)} \quad (12)$$

$$\equiv Fe(III)\text{-}I^- + h_{vb}^+ \rightarrow \equiv Fe(III)\text{-}I^{\cdot}$$

$$\equiv Fe(III)\text{-}I^{\cdot} + I^- \rightarrow \equiv Fe(III) + I_2^{\cdot-} \quad \text{(iodide oxidation)} \quad (13)$$

The redox reaction between ferric ions and iodide ions are thermodynamically spontaneous (eq. 14) [44] and therefore the dark reaction can occur without photoactivation.

$$2Fe^{3+} + 3I^- \rightarrow 2Fe^{2+} + I_3^- \qquad E^0 = 1.01\ V_{NHE} \quad (14)$$

Accordingly, the stoichiometric molar ratio of Fe^{2+} and I_3^- production reached 2:1 in the photostationary state (*see* Figure 1a). However, in the initial reaction period (< 1 h), the

relative concentration of photogenerated $Fe(II)_{aq}$ with respect to I_3^- is significantly lower than the ratio of 2:1. This could be ascribed to the slow dissolution process of $Fe(II)_{surf}$ from the iron oxide surface (eq. 8).

3.5 Solar experiments.

To confirm the applicability to natural solar irradiation, outdoor experiments were conducted under natural environmental conditions in mid-latitude during a winter day (Pohang, Korea: 36°00′N, 129°19′E) (Figure 4). The simultaneous generation of $Fe(II)_{aq}$ and I_3^- was concurrently accelerated in ice under solar irradiation. The production of $Fe(II)_{aq}$ and I_3^- under solar irradiation condition was slightly higher than that in laboratory condition using an artificial light source (100 W medium pressure Hg lamp) (*see* Methods section). We also carried out the solar experiments in an Antarctic environment at King George Island (62°13′S 58°47′W, sea level) (*see* Figure 5). The production of $Fe(II)_{aq}$ and I_3^- in ice was consistently higher than that in the aqueous phase regardless of the kind of iron oxides. Figure 5 compared the production of $Fe(II)_{aq}$ and I_3^- from various iron oxides samples (maghemite, goethite, and lepidocrocite: the properties summarized in Table S2) after 7 h of reaction under Antarctic solar irradiation. The production of $Fe(II)_{aq}$ in ice phase was most closely related with the surface area of the iron oxide sample while other properties of iron oxide such as the surface potential and hydrodynamic diameter seem to have little correlation with the photoactivity. Goethite has the highest surface area (178 m^2/g) and exhibited the highest production of $Fe(II)_{aq}$ (87.4 ± 3.0 μM) after 7 h in ice phase. Maghemite which has the lowest surface area (36 m^2/g) produced the smallest amount of dissolved Fe(II) (27.3 ± 1.0 μM) in ice. Lepidocrocite with a medium surface area (75 m^2/g) showed the medium reactivity (52.7 ± 5.3 μM). Arizona test dust which contained 2~5% of Fe_2O_3 also exhibited an enhanced production of $Fe(II)_{aq}$ in ice phase compared to aqueous solution. The production of $Fe(II)_{aq}$ should depend on the surface area of iron oxide because the ferrous species are dissolved from the surface sites (eqs. 8, 12). On the other hand, the production of triiodide was much less influenced by the type of iron oxides in both aqueous and ice phase (Figure 5b), which is consistent with the observation that the iodide oxidation was not apparently enhanced by the presence of γ-Fe_2O_3 in ice (Table S1). The production of triiodide seems to be little influenced by the iron oxide part. The outdoor experiments confirm that the photoreaction of iron oxide and iodide can be accelerated in frozen solutions not only in the laboratory condition but also under natural solar irradiation.

3.6 Environmental implications.

The reductive dissolution of iron oxides and the accompanying oxidation of iodide to I_3^-

were compared between the aqueous and ice phases. The redox transformation that produces bioavailable $Fe(II)_{aq}$ and reactive iodine species (I_3^- then I_2) proceeded negligibly slowly in aqueous solution but was significantly accelerated in frozen solution both under light irradiation and in the dark. The frozen solution contains iodides, protons, and iron oxide particles concentrated in ice grain boundaries, which should accelerate the heterogeneous reactions. The freeze-enhanced redox reaction of iron oxide and iodide might occur in natural environments. Although the present experimental finding is unlikely applicable to seawater condition because of the high pH of seawater (between 7.5 and 8.4), atmospheric dust particles containing iron can travel long distance and can be trapped in ice aerosols containing sea salts. The pH of aerosols can be decreased to pH 1-2 in the presence of organic and inorganic acids. Acidic aerosols containing iron mineral dusts [45] and frozen sea salt aerosols containing iodide are commonly found in cold environments (atmosphere in polar regions, the upper troposphere and stratosphere) [46]. In addition, snow/ice on frozen sea may contain iron species provided through the atmospheric transport and deposition of mineral dusts and iodide supplied by wind-driven sea water droplets. It is also reported that acid rock drainage and rock weathering site in Antarctica provides acidic (pH 3.2 ~ 4.5) and iron-rich (up to 1.78 mM Fe) drainage water into the ocean. They also measured the concentration of dissolved iron in sea ice (1.9 μM ~ 29 μ M), which is comparable to our study (50 μM as total iron) [47]. The present work suggests that the intrinsic chemical reactions occurring in the ice phase can have important environmental implications and therefore need to be further investigated from the microscopic to the global scale.

We suggest that the concomitant production of active iodine (I_3^-, I_2) along with iron reduction in ice may partly contribute to the abrupt increase of atmospheric iodine concentrations in the Antarctic spring [12,44]. This has implications for CCN formation and radiative forcing48 as reported in previous research connecting atmospheric iodine and particle formation in both the Arctic and Antarctic atmosphere [49].

The supply of bioavailable iron plays a critical role in biogeochemical processes such as enhancement of primary production in HNLC regions. This work suggests that particulate iron oxides present in polar aerosols, snow, sea ice, icebergs, and ice sheets may be quickly converted into the bioavailable form of iron ($Fe(II)_{aq}$) through (photo)reductive dissolution processes. The previously observed high concentration of bioavailable iron and algal bloom near receding ice might be partially explained by the enhanced reduction of iron oxides trapped in ice [30]. The synergically enhanced production of bioavailable iron and active iodine species through the frozen-media transformation path might play a significant role in the global environmental processes.

KOPRI 극지연구소

4. Reference

1. Morel, F. M. M.; Price, N. M. The biogeochemical cycles of trace metals in the oceans. Science 2003, 300, 944-947.
2. Turner, D. R.; Hunter, K. A. The biogeochemistry of iron in seawater. 7 ed.; JOHN WILEY & SONS,LTD: Chichester, 2001.
3. Martin, J. H.; Gordon, R. M.; Fitzwater, S. E. Iron in Antarctic waters. Nature 1990, 345, 156-159.
4. Hopwood, M. Iron from ice. Nat. Geosci. 2018, 11, 462-462.
5. Martin, J. H. Glacial-Interglacial CO2 change : the iron hypothesis. Paleoceanography 1990, 5, 1-13.
6. Boyd, P. W.; Watson, A. J.; Law, C. S.; Abraham, E. R.; Trull, T.; Murdoch, R.; Bakker, D. C. E.; Bowie, A. R.; Buesseler, K. O.; Chang, H.; Charette, M.; Croot, P.; Downing, K.; Frew, R.; Gall, M.; Hadfield, M.; Hall, J.; Harvey, M.; Jameson, G.; Liddicoat, J. L.; Ling, R.; Maldonado, M. T.; McKay, R. M.; Nodder, S.; Pickmere, S.; Pridmore, R.; Rintoul, S.; Safi, K.; Sutton, P.; Strzepek, R.; Tanneberger, K.; Turner, S.; Waite, A.; Zeldis, J. A mesoscale phytoplankton bloom in the polar Southern Ocean stimulated by iron fertilization. Nature 2000, 407, 695-702.
7. Chisholm, S. W. Stirring times in the Southern Ocean. Nature 2000, 407, 685-686.
8. Jickells, T. D.; An, Z. S.; Andersen, K. K.; Baker, A. R.; Bergametti, G.; Brooks, N.; Cao, J. J. Global iron connection between desert dust, ocean biogeochemistry, and climate. Science 2005, 308, 66-71.
9. Finden, D. A. S.; Tipping, E.; Jaworski, G. H. M.; Reynolds, C. S. Light-induced reduction of natural iron(III) oxide and its relevance to phytoplankton. Nature 1984, 309, 783-784.
10. Pehkonen, S. O.; Siefert, R.; Erel, Y.; Webb, S.; Hoffmann, M. R. Photoreduction of iron oxyhydroxides in the presence of important atmospheric organic compounds. Environ. Sci. Technol. 1993, 27, 2056-2062.
11. Saiz-Lopez, A.; Plane, J. M. C.; Mahajan, A. S.; Anderson, P. S.; Bauguitte, S. J.-B.; Jones, A. E.; Roscoe, H. K.; Salmon, R. A.; Bloss, W. J.; Lee, J. D.; Heard, D. E. On the vertical distribution of boundary layer halogens over coastal Antarctica: implications for O3, HOx, NOx and the Hg lifetime. Atmos. Chem. Phys. 2007, 8, 887-900.
12. Saiz-Lopez, A.; Mahajan, A. S.; Salmon, R. A.; Bauguitte, S. J.-B.; Jones, A. E.; Roscoe, H. K.; Plane, J. M. C. Boundary layer halogens in coastal Antarctica.

KOPRI 극지연구소

Science 2007, 317, 348-351.

13. Hoffmann, T.; O'Dowd, C. D.; Seinfeld, J. H. Iodine oxide homogeneous nucleation: An explanation for coastal new particle production. Geophys. Res. Lett. 2001, 28, 1949-1952.

14. Bloss, W. J.; Lee, J. D.; Johnson, G. P.; Sommariva, R.; Heard, D. E.; Saiz-Lopez, A.; McFiggans, G.; Coe, H.; Flynn, M.; Williams, P.; Rickard, A. R.; Fleming, Z. L. Impact of halogen monoxide chemistry upon boundary layer OH and HO2 concentrations at a coastal site. Geophys. Res. Lett. 2005, 32, L06814.

15. Cuevas, C. A.; Maffezzoli, N.; Corella, J. P.; Spolaor, A.; Vallelonga, P.; Kjaer, H. A.; Simonsen, M.; Winstrup, M.; Vinther, B.; Horvat, C.; Fernandez, R. P.; Kinnison, D.; Lamarque, J. F.; Barbante, C.; Saiz-Lopez, A. Rapid increase in atmospheric iodine levels in the North Atlantic since the mid-20th century. Nat. Comm. 2018, 9, 1452.

16. Saiz-Lopez, A.; Blaszczak-Boxe, C. S. The polar iodine paradox. Atmos. Environ. 2016, 145, 72-73.

17. Spolaor, A.; Vallelonga, P.; Plane, J. M. C.; Kehrwald, N.; Gabrieli, J.; Varin, C.; Turetta, C.; Cozzi, G.; Kumar, R.; Boutron, C.; Barbante, C. Halogen species record Antarctic sea ice extent over glacial-interglacial periods. Atmos. Chem. Phys. 2013, 13, 6623-6635.

18. Amoroso, A.; Domine, F.; Esposito, G.; Morin, S.; Savarino, J.; Nardino, M.; Montagnoli, M.; Bonneville, J.-M.; Clement, J.-C.; Ianniello, A.; Beine, H. J. Microorganisms in dry polar snow are involved in the exchanges of reactive nitrogen species with the atmosphere. Envrion. Sci. Technol. 2009, 44, 714-719.

19. Kim, K.; Choi, W.; Hoffmann, M. R.; Yoon, H.-I.; Park, B.-K. Photoreductive dissolution of iron oxides trapped in ice and its environmental implications. Environ. Sci. Technol 2010, 44, 4142-4148.

20. Kim, K.; Choi, W. Enhanced redox conversion of chromate and arsenite in ice. Envrion. Sci. Technol. 2011, 45, 2202-2208.

21. Dubowski, Y.; Hoffmann, M. R. Photochemical transformations in ice: Implications for the fate of chemical species. Geophy. Res. Lett. 2000, 27, 3321-3324.

22. Dubowski, Y.; Colussi, A. J.; Boxe, C.; Hoffmann, M. R. Monotonic increase of nitrite yields in the photolysis of nitrate in ice and water between 238 and 294 K. J. Phys. Chem. A 2002, 106, 6967-6971.

23. Guzman, M. I.; Hoffmann, M. R.; Colussi, A. J. Photolysis of pyruvic acid in ice: Possible relevance to CO and CO2 ice core record anomalies. J. Geophys. Res.

2007, 112, D10123.

24. Cheng, J.; Soetjipto, C.; Hoffmann, M.R.; Colussi, A. J. Confocal fluorescence microscopy of the morphology and composition of interstitial fluids in freezing electrolyte solutions. J. Phys. Chem. Lett. 2010, 1, 374-378.

25. Kim, K.; Yoon, H. I.; Choi, W. Enhanced dissolution of manganese oxide in ice compared to aqueous phase under illuminated and dark conditions. Envrion. Sci. Technol. 2012, 46, 13160-13166.

26. Kim, K.; Kim, J.; Bokare, A. D.; Choi, W.; Yoon, H. I.; Kim, J. Enhanced removal of hexavalent chromium in the presence of H2O2 in frozen aqueous solutions. Envrion. Sci. Technol. 2015, 49, 10937-10944.

27. Kim, K.; Chung, H. Y.; Ju, J.; Kim, J. Freezing-enhanced reduction of chromate by nitrite. Sci. Total. Environ. 2017, 590, 107-113.

28. Kim, K.; Yabushita, A.; Okumura, M.; Saiz-Lopez, A.; Cuevas, C. A.; Blaszczak-Boxe, C. S.; Min, D. W.; Yoon, H. I.; Choi, W. Production of molecular iodine and tri-iodide in the frozen solution of iodide: Implication for polar atmosphere. Environ. Sci. Technol. 2016, 50, 1280-1287.

29. Takenaka, N.; Ueda, A.; Maeda, Y. Acceleration of the rate of nitrite oxidation by freezing in aqueous solution. Nature 1992, 358, 736-738.

30. Sedwick, P. N.; DiTullio, G. R. Regulation of algal blooms in Antarctic shelf water by the release of iron from melting sea ice waters. Geophys. Res. Lett. 1997, 24, 2515-2518.

31. Lannuzel, D.; Vancoppenolle, M.; van der Merwe, P.; de Jong, J.; Meiners, K. M.; Grotti, M.; Nishioka, J.; Schoemann, V. Iron in sea ice: Review and new insights. Elem.Sci. Anth. 2016, 4, 000130.

32. Atkinson, H. M.; Huang, R. J.; Chance, R.; Roscoe, H. K.; Hughes, C.; Davison, B.; Schonhardt, A.; Mahajan, A. S.; Saiz-Lopez, A.; Hoffmann, T.; Liss, P. S. Iodine emissions from the sea ice of the Weddell Sea. Atmos. Chem. Phys. 2012, 12, 11229-11244.

33. Jeong, D.; Kim, K.; Min, D. W.; Choi, W. Freezing-enhanced dissolution of iron oxides: Effects of inorganic acid anions. Envrion. Sci. Technol. 2015, 49, 12816-12822.

34. Menacherry, S. P. M.; Kim, K.; Lee, W.; Choi, C. H.; Choi, W. Ligand-specific dissolution of iron oxides in frozen solutions. Environ. Sci. Technol. 2018, 52, 13766-13773.

35. Pillar, E. A.; Guzman, M. I.; Rodriguez, J. M. Conversion of iodide to hypoiodous

acid and iodine in aqueous microdroplets exposed to ozone. Environ. Sci. Technol. 2013, 47, 10971?10979.

36. Hatchard, C. G.; Parker, C. A. A new sensitive chemical actinometer. II. Potassium ferrioxalate as a standard chemical actinometer. Proc. R. Soc. Lond. A 1956, 235, 518-536.

37. Kuhn, H. J.; Braslavsky, S. E.; Schmidt, R. Chemical Actonometry (IUPAC Technical Report). Pure Appl. Chem. 2004, 76, 2105-2146

38. Ali, S. P.; Blesa, M. A.; Morando, P. J.; Regazzoni, A. E. Reductive dissolution of hematite in acidic iodide solutions. Langmuir 1996, 12, 4934-4939.

39. Guzman, M. I.; Hildebrandt L.; Colussi, A. J.; Hoffmann, M. R. Cooperative hydration of pyruvic acid in ice. J. Am. Chem. Soc. 2006, 128, 10621-10624.

40. Sulzberger, B.; Laubscher, H. Reactivity of various types of iron(hydr)oxides toward light-induced dissolution. Mar. Chem. 1995, 50, 103-115.

41. Takenaka, N.; Ueda, A.; Daimon, T.; Bandow, H.; Dohmaru, T.; Maeda, Y. Acceleration mechanism of chemical reaction by freezing: The reaction of nitrous acid with dissolved oxygen. J. Phys. Chem. 1996, 100, 13874-13884.

42. Grannas, A. M.; Bausch, A. R.; Mahanna, K. M. Enhanced aqueous photochemical reaction rates after freezing. J. Phys. Chem. A 2007, 111, 11043-11049.

43. Namduri, H.; Nasrazadani, S. Quantitative analysis of iron oxides using Fourier transform infrared spectrophotometry. Corro. Sci. 2008, 50, 2493-2497.

44. Laurence, G. S.; Ellis, K. J. Oxidation of iodide ion by iron(III) ion in aqueous solution. J. Chem. Soc., Dalton Trans. 1972, 0, 2229-2233.

45. Fu, H.; Cwiertny, D. M.; Carmichael, G. R.; Scherer, M. M.; Grassian, V. H. Photoreductive dissolution of Fe?containing mineral dust particles in acidic media. J. Geophys. Res. 2010, 115, D11304.

46. Saiz-Lopez, A.; Plane, J. M. C.; Baker, A. R.; Carpenter, L. J.; Glasow, R. v.; Mart?n, J. C. G.; McFiggans, G.; Saunders, R. W. Atmospheric Chemistry of Iodine. Chem. Rev. 2012, 112, 1773-1804.

47. Dold, B.; Gonzalez-Toril, E.; Aguilera, A.; Lopez, E.; Cisternas, M. E.; Bucchi, F.; Amils, R. Acid rock drainage and rock weathering in Antarctica: Important sources for iron cycling in the Southern Ocean. Environ. Sci. Technol., 2013, 47, 6129-6136.

48. Roscoe, H. K.; Jones, A. E.; Brough, N.; Weller, R.; Saiz-Lopez, A.; Mahajan, A. S.; Schoenhardt, A.; Burrows, J. P.; Fleming, Z. L. Particles and iodine compounds in coastal Antarctica. J. Geophys. Res. Atmos. 2015, 120, 7144-7156.

49. Sipila, M.; Sarnela, N.; Jokinen, T.; Henschel, H.; Junninen, H.; Kontkanen, J.;

Richters, S.; Kangasluoma, J.; Franchin, A.; Perakyla, O.; Rissanen, M. P.; Ehn, M.; Vehkamaki, H.; Kurten, T.; Berndt, T.; Petaja, T.; Worsnop, D.; Ceburnis, D.; Kerminen, V. M.; Kulmala, M.; O'Dowd, C. Molecular-scale evidence of aerosol particle formation via sequential addition of HIO3. Nature 2016, 537, 532-534.

KOPRI
극지연구소

Table 1. Formation of $Fe(II)_{aq}$ via reductive dissolution of various types of iron oxides and simultaneous production of I_3^- from I^- oxidation under dark condition[a]

	$[Fe(II)_{aq}]$ (μM)		$[I_3^-]$ (μM)	
	Aq.	Ice	Aq.	Ice
Hematite (α-Fe_2O_3)	1.1±0.6	4.8±1.2	0.1	7.8±0.8
Maghemite (γ-Fe_2O_3)	3.3±0.4	169.1±3.4	0.1	26.8±1.4
Goethite (α-FeOOH)	8.1±1.2	101.1±2.2	0.6±0.3	22.4±0.9
Lepidocrocite (γ-FeOOH)	0.9±0.4	148.4±3.7	0.1	31.6±1.6
Magnetite (Fe_3O_4)	2.5±0.5	218.7±5.5	0.2	30.9±2.1

[a]Experimental condition: [iron oxide] = 0.2 g/L, $[I^-]$ = 1 mM, pH_i = 3, reaction time 72 h in aqueous solution at 25 °C and in ice at − 20 °C.

KOPRI
극지연구소

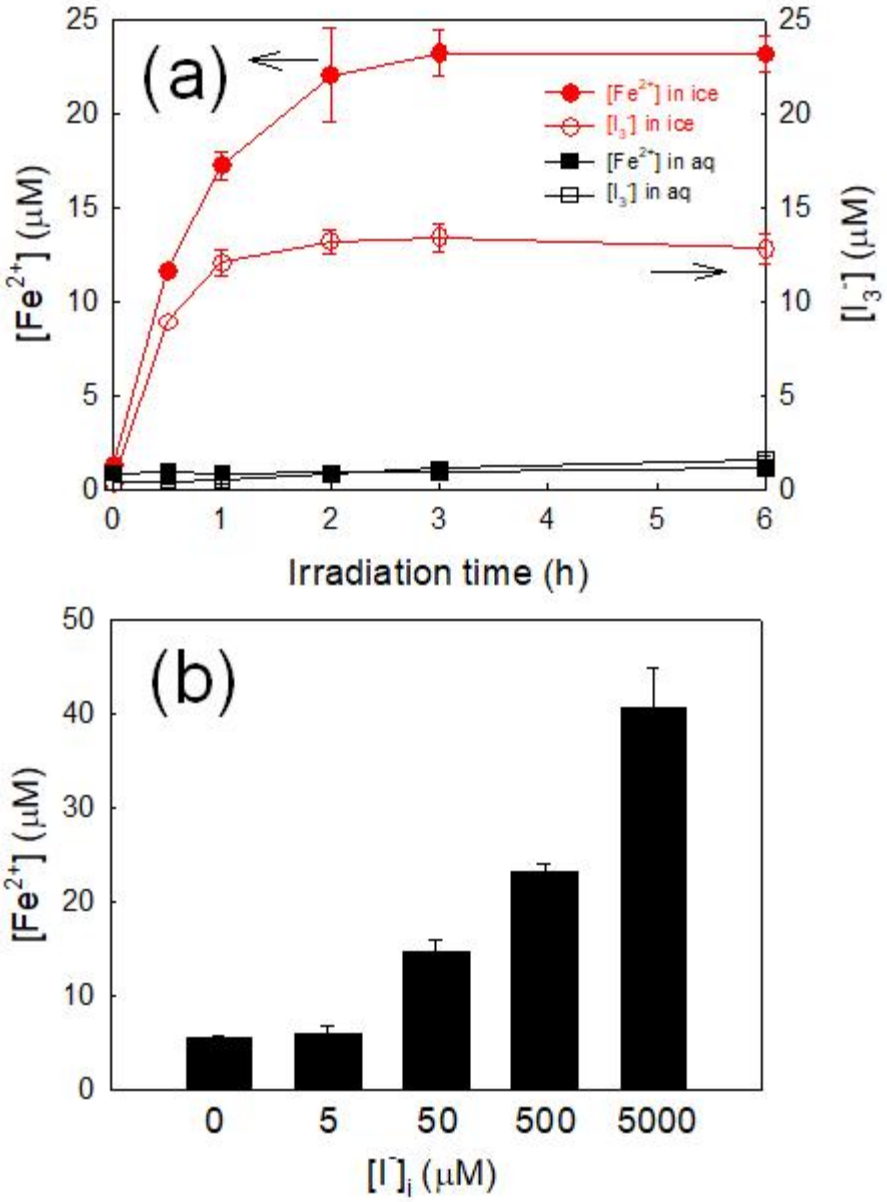

Figure 1. (a) Time profile of the simultaneous generation of $Fe(II)_{aq}$ and I_3^- in the UV-irradiated (λ > 300 nm) colloidal solution of hematite and I^- in aqueous phase (at 25 °C) or in ice (at -20 °C). (b) Production of $Fe(II)_{aq}$ from photoreductive dissolution of hematite with different concentrations of iodide contained in ice at -20 °C (after 6 h reaction). Experimental condition: [α-Fe_2O_3] = 8 mg/L, $[I^-]_i$ = 500 μM (for a), pH_i =3.

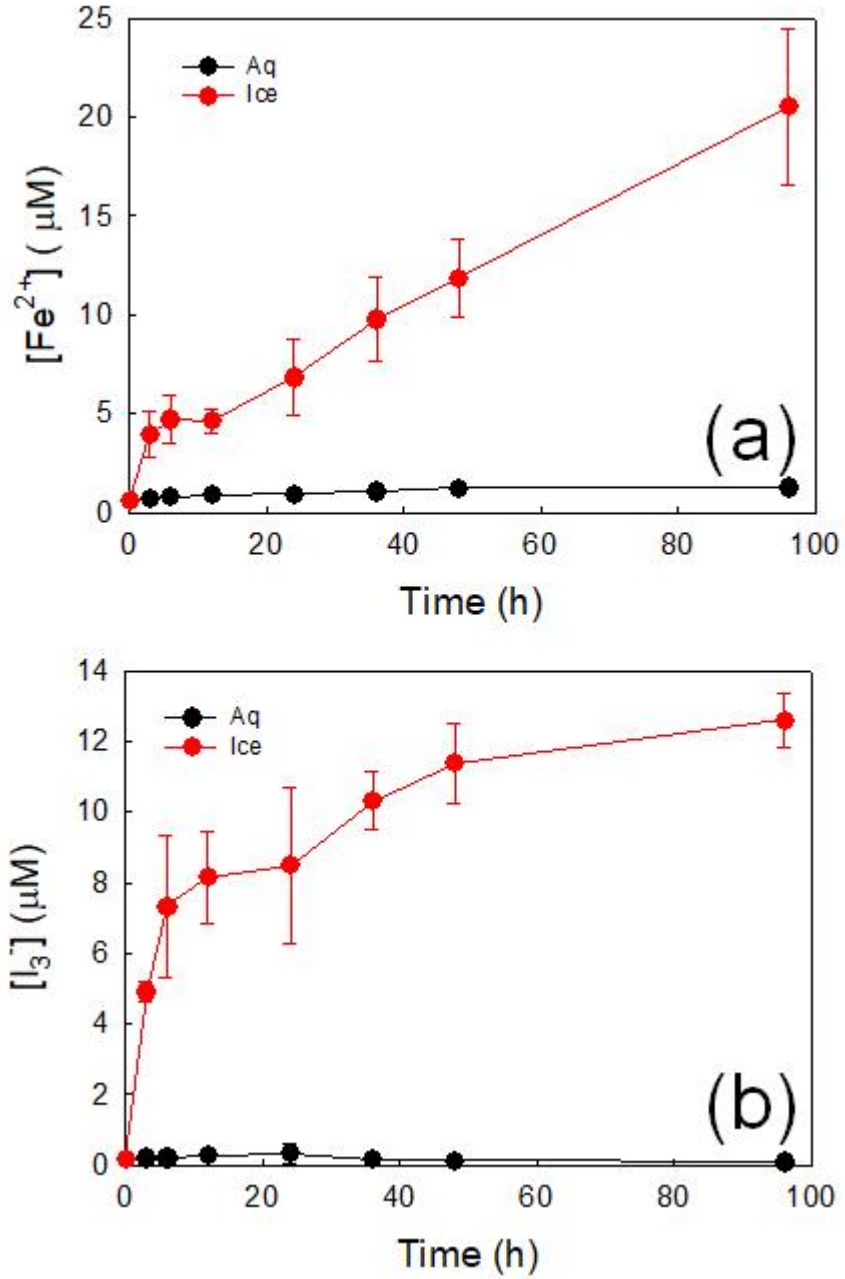

Figure 2. Time profiles of the simultaneous generation of (a) $Fe(II)_{aq}$ and (b) I_3^- in the colloidal solution of hematite and I^- in aqueous phase (at 25 °C) or in ice (at -20 °C) in the dark. Experimental condition: [α-Fe_2O_3] = 8 mg/L, $[I^-]_i$ = 500 μM, pH_i =3.

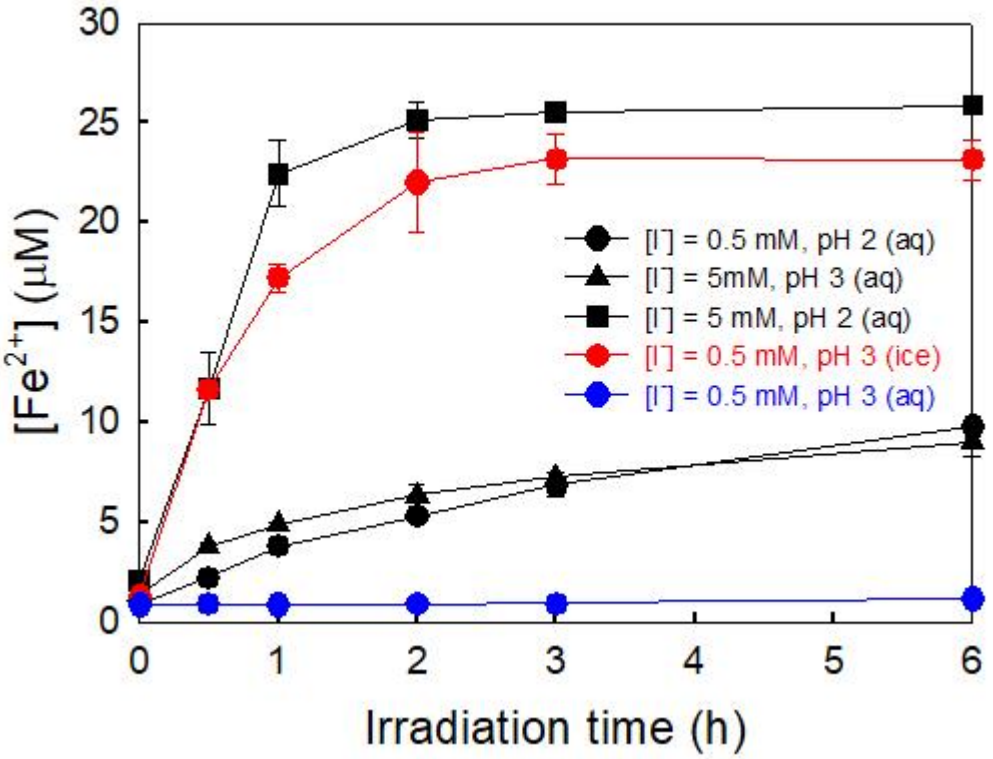

Figure 3. Effect of [I^-] and pH on $Fe(II)_{aq}$ generation via the photoreductive dissolution of hematite (8 mg/L) in aqueous solutions (at 25 °C) in comparison with the reference ice phase reaction performed with [I^-] = 0.5 mM and pH 3 (red circles).

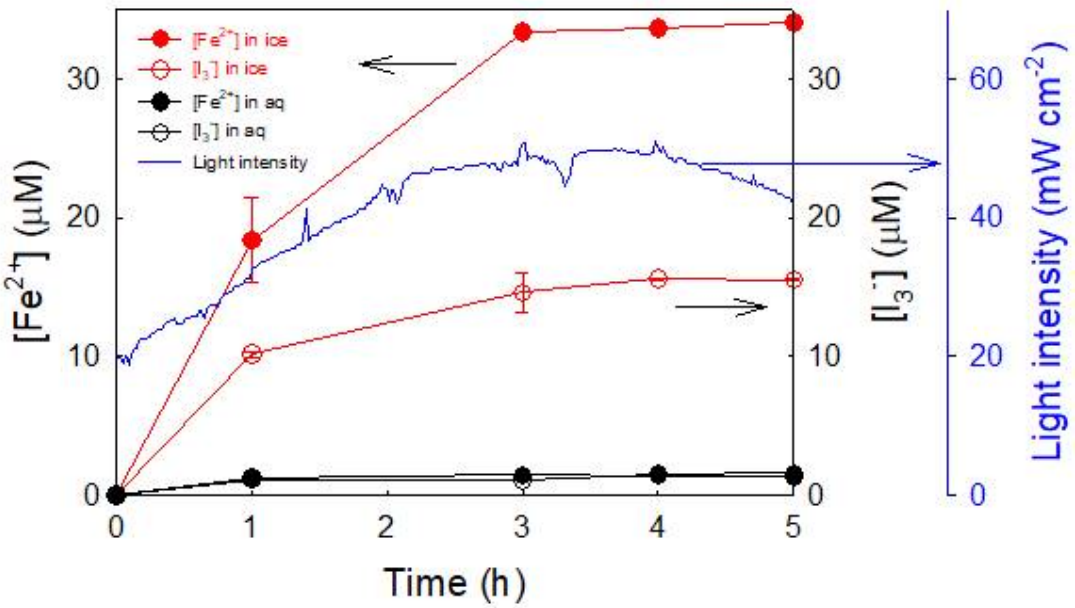

Figure 4. The simultaneous production of $Fe(II)_{aq}$ and I_3^- in the natural solar-irradiated solution of hematite and I^- in aqueous phase (at 25 °C) or in ice (at -20 °C). Experimental condition: [α-Fe_2O_3] = 8 mg/L (50 μM), [I^-] = 500 μM, pH_i = 3.

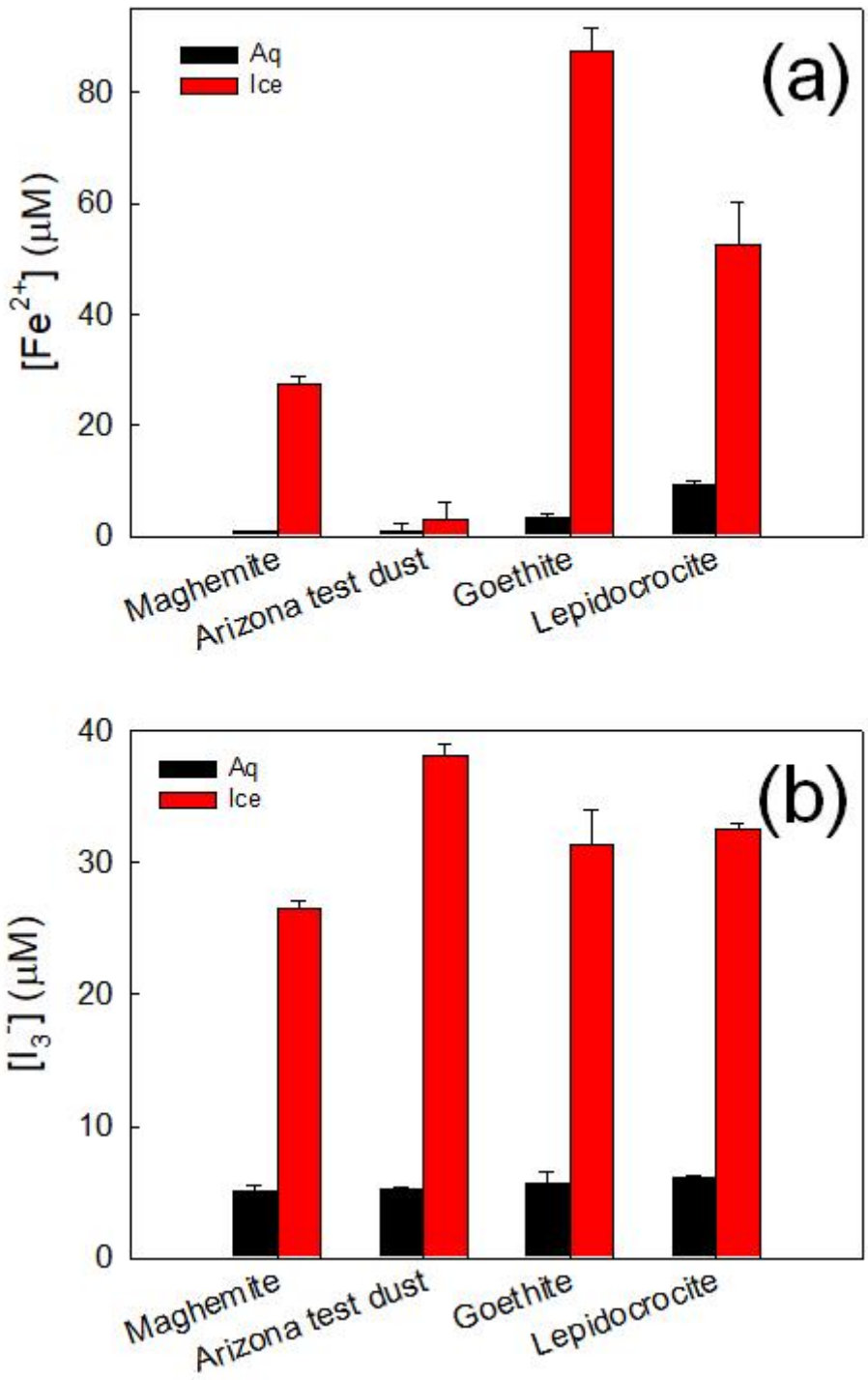

Figure 5. The simultaneous production of (a) $Fe(II)_{aq}$ and (b) I_3^- in the solution of iron oxide and I^- in aqueous phase (at 25 °C) or in ice (at -20 °C) under solar irradiation in Antarctic region (King George Island, 62°13′N, 58°47′E). Experimental condition: [iron oxide or Arizona test dust] = 0.2 g/L, $[I^-]$ = 1 mM, pH_i = 3, 7 h irradiation.

Supporting Information

Table S1. Comparison of production of $Fe(II)_{aq}$ and triiodide in ice between the single and bi-component systems.

	γ-Fe_2O_3 only	I^- only	γ-Fe_2O_3 + I^-	
	$Fe(II)_{aq}$ (μM)	I_3^- (μM)	$Fe(II)_{aq}$ (μM)	I_3^- (μM)
Dark (7 days)	4.6±0.8	38.7±2.2	143.1±3.3	37.1±0.8
UV (12 hours)	4.3±1.1	49.8±1.9	149.6±1.5	42.0±1.4

*Experimental condition: [γ-Fe_2O_3] = 0.1 g/L, [I^-] = 1 mM, pH_i = 3, reaction temperature = aqueous solution at 25 °C and in ice at - 20 °C.

Table S2. Summary of the properties of iron oxide samples

Iron oxide	BET specific surface area ($m^2\ g^{-1}$)	ζ-potential[a] (mV)	crystallite size[b] (nm)	hydrodynamic diameter[a] (nm)
γ-Fe_2O_3 (maghemite)	36	32 ± 1	25 ± 3	292 ± 37
α-FeOOH (goethite)	178	25 ± 1	41 ± 2	480 ± 57
γ-FeOOH (lepidocrocite)	75	21 ± 5	37 ± 3	297 ± 42

[a]values were measured at pH 3 at which the majority of the experiments were conducted. [b]determined by the Scherrer equation from X-ray diffraction analysis

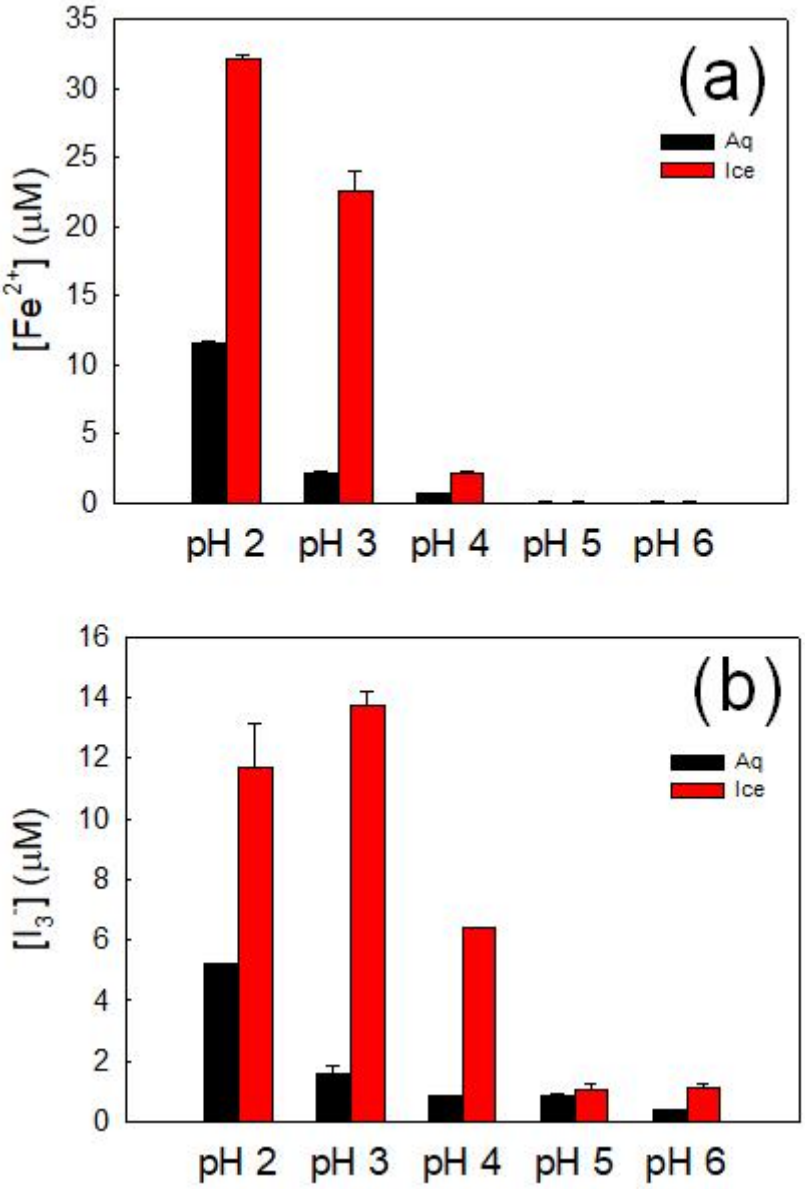

Figure S1. pH effect on the production of (a) $Fe(II)_{aq}$ and (b) I_3^- in the UV-irradiated (λ > 300 nm) colloidal solution of hematite and I^- in aqueous phase (at 25 °C) or in ice (at -20 °C). The pH values in ice indicate the pH before freezing. Experimental condition: [α-Fe_2O_3] = 8 mg/L, $[I^-]_i$ = 500 μM, 6 h irradiation.

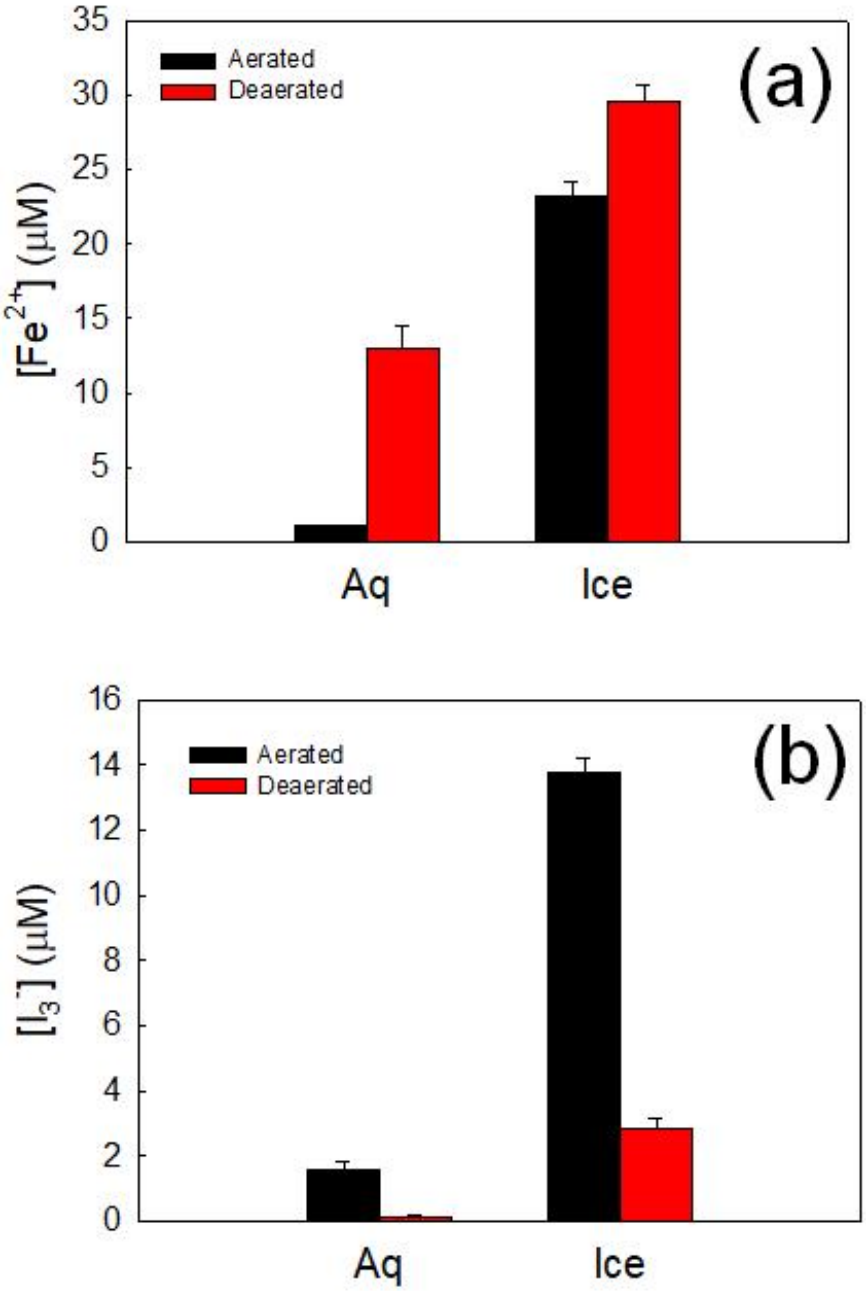

Figure S2. Effect of dissolved O2 on the production of (a) $Fe(II)_{aq}$ and (b) I_3^- in the UV-irradiated (λ > 300 nm) colloidal solution of hematite and I^- in aqueous phase (at 25 °C) or in ice (at -20 °C). The aerated and deaerated solutions are compared. The deaerated ice was prepared by freezing immediately after deaerating the aqueous solution. Experimental condition: [α-Fe_2O_3] = 8 mg/L, $[I^-]_i$ = 500 μM, pH 3, 30-min Ar purging for deaerated condition, 6 h irradiation.

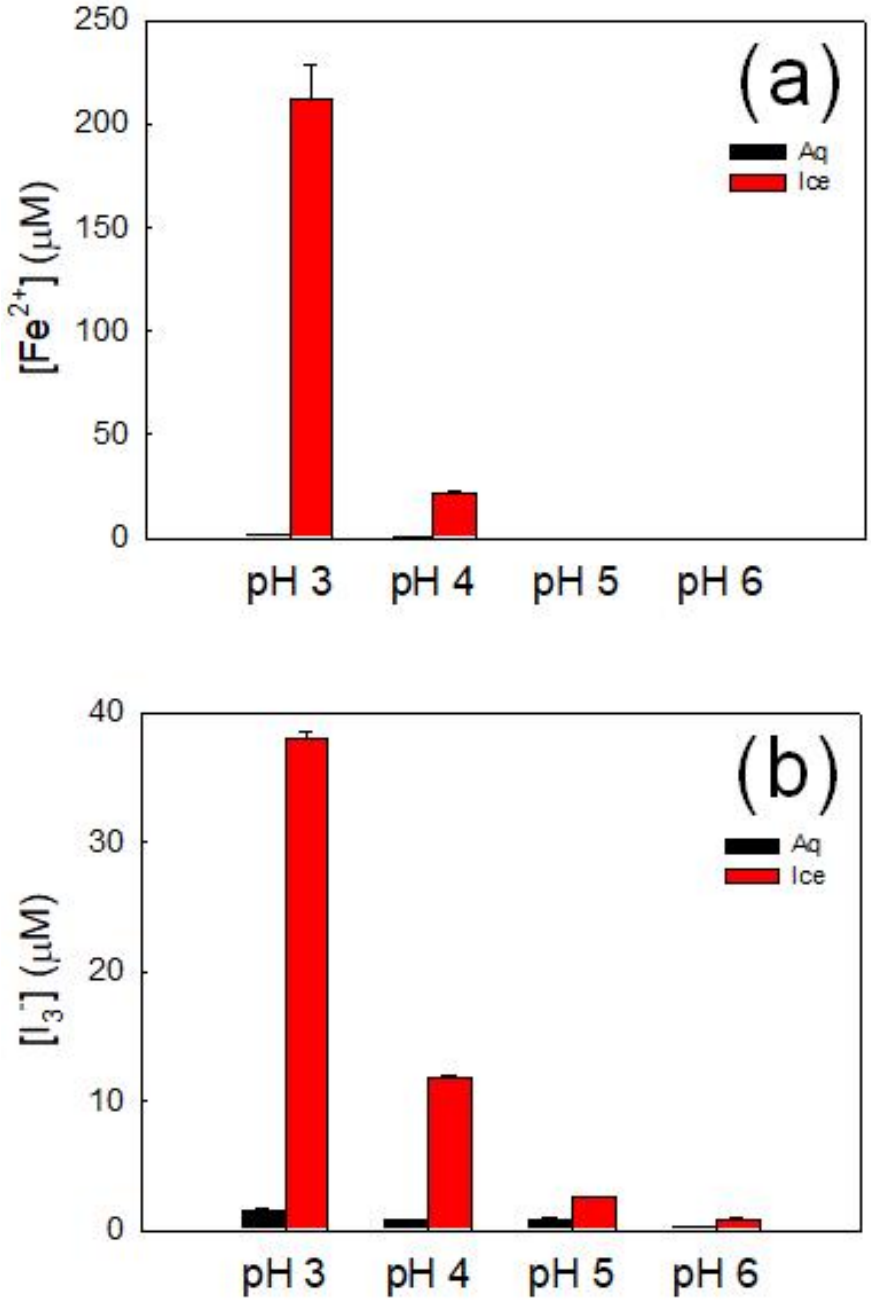

Figure S3. pH effect on the production of (a) $Fe(II)_{aq}$ and (b) I_3^- under dark condition in aqueous phase (at 25 °C) and ice (at -20 °C). The pH values in ice indicate the pH before freezing. Experimental condition: [γ-Fe_2O_3] = 0.2 mg/L, $[I^-]_i$ = 1 mM, 4 days reaction.

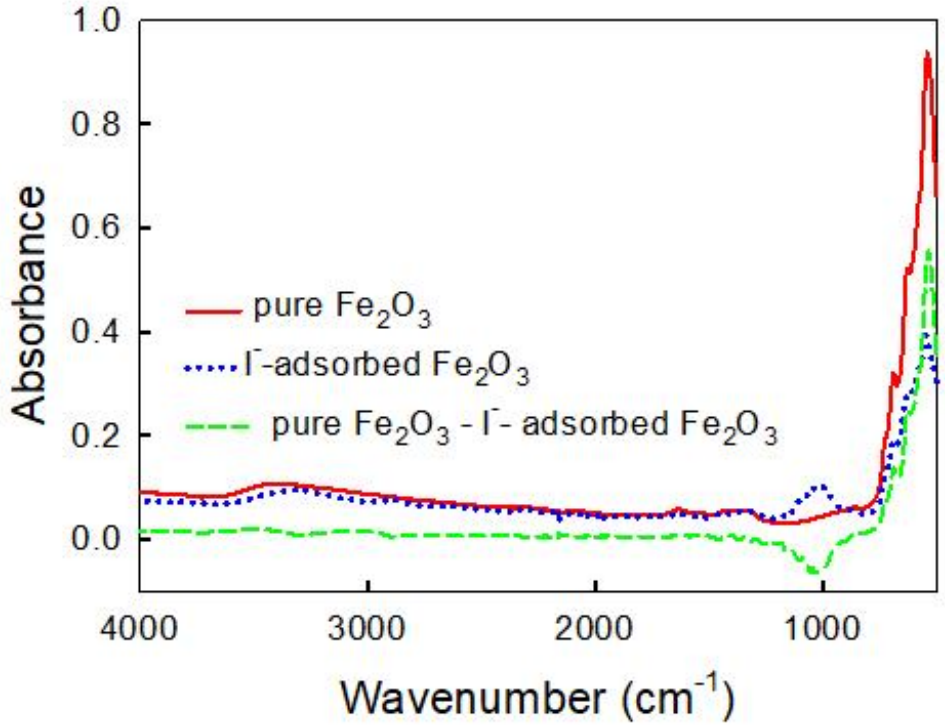

Figure S4. ATR-FTIR spectra of pure Fe_2O_3 and I^--adsorbed Fe_2O_3 and their difference (i.e., (ATR-FTIR spectrum of pure Fe_2O_3) - (ATR-FTIR spectrum of I^--adsorbed Fe_2O_3)). The I^--adsorbed Fe_2O_3 sample was prepared as follows. Iodide solution was added to an aqueous Fe_2O_3 suspension, and the pH of the suspension was adjusted with $HClO_4$ solution. After the suspension was shaken for 30 min, I^--adsorbed γ-Fe_2O_3 powder was collected by filtration, washed with deionized water to remove weakly bound I^-, and dried at room temperature overnight. Experimental condition: [γ-Fe_2O_3] = 1.0 g/L, $[I^-]_i$ = 0.5 M, and pH_i =3. ATR-FTIR spectra were measured using ATR-FTIR spectroscopy (Thermo Scientific Nicolet iS50).

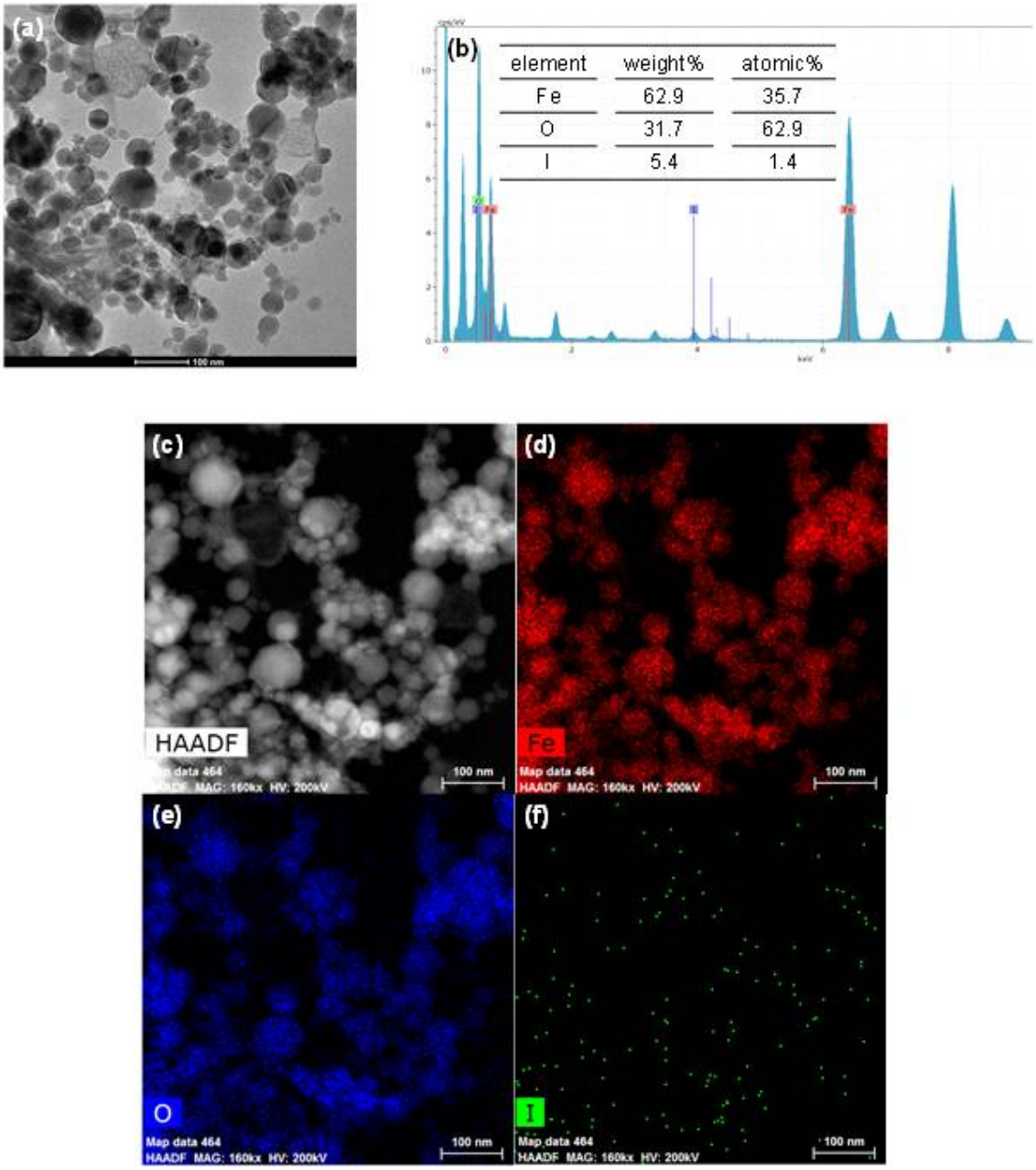

Figure S5. (a) HRTEM image, (b) EDX spectrum, (c) high-angle annular dark-field (HAADF) image, and (d) Fe, (e) O, and (f) I elemental mapping images of I^--adsorbed Fe2O3. The images and spectrum were obtained using TALOS F200X microscope (Thermo Scientific) at an accelerating voltage of 200 kV. Experimental condition: [ɣ-Fe_2O_3] = 8 mg/L, $[I^-]_i$ = 500 μM, pH_i =3.

제 8 절. Ligand-specific Dissolution of Iron Oxides in Frozen Solutions[5)]

Sunil Paul M. Menacherry[1], Kitae Kim[2], Woojin Lee[3], Cheol Ho Choi[4], and Wonyong Choi[1*]

[1]Division of Environmental Science and Engineering, Pohang University of Science and Technology

[2]Korea Polar Research Institute

[3]Department of Civil and Environmental Engineering, Nazarbayev University, Kazakhstan

[4]Department of Chemistry, Kyungpook National University

1. Introduction

Iron is an essential nutrient for nearly all the living organisms [1]. Iron-containing biomolecules are essential cofactors for various cellular level processes (e.g., DNA synthesis, oxygen transport (hemoglobin and myoglobin), electron transport, etc.), which makes this metal an indispensable ingredient of life [2,3]. Since the solubility of most Fe(III)-oxides are extremely low [4], the uptake of iron by living organisms largely requires the reduction to Fe(II) species or the conversion into iron-organic complexes, which are more soluble and more bioavailable [5,6].

The environmentally relevant chemical transformations taking place in ice (frozen solution) have recently attracted attentions among environmental researchers [7-13] and the studies on them are well justified considering the fact that the majority of freshwater on earth exists in the frozen state. The solutes in frozen solutions are highly concentrated in the ice grain boundary region which contains a small fraction of liquid water between the freezing point and the eutectic point of water and the liquid-like grain boundary layer may have reaction conditions (e.g., solute concentration, pH, ionic strength) that are very different from those of aqueous solution [10,12,14,15]. As a result, many kinds of homogeneous and heterogeneous chemical reactions occurring in frozen solutions often exhibit highly accelerated kinetics. Some of the interesting findings of enhanced transformation reactions in/on ice include the accelerated oxidation of nitrous acid [12], the enhanced photolysis of nitrates [16], the formation of dimerized products from the photodegradation of chlorophenols [11,17], the protonation of cresol red [18], the accelerated reductive dissolution of iron oxides and manganese oxides [10,19], the accelerated reduction

5) 이 연구는 본 과제 지원으로 수행되었으며 그 결과는 다음의 논문으로 출판되었음: Sunil Paul M. Menacherry, Kitae Kim, Woojin Lee, Cheol Ho Choi, and Wonyong Choi, “Ligand-Specific Dissolution of Iron Oxides in Frozen Solutions”, *Environ. Sci. Technol.* 2018, 52, 13766-13773.

of hexavalent chromium [8], and the enhanced photooxidation of iodide [9].

In particular, the accelerated dissolution of iron oxides in ice (in both dark and irradiated conditions) is interesting because it may provide an alternative pathway of supplying bioavailable iron [7,19,20]. Kim et al. reported a markedly enhanced photo-reductive dissolution of iron oxides in the presence of various organic electron donors (formic, acetic, butyric, and humic acids) in ice compared to its corresponding aqueous counterpart [19]. Another report by Jeong et al. demonstrated an enhanced non-reductive dissolution of iron (mostly Fe(III) species) from goethite (α-FeO(OH)) and maghemite (γ-Fe_2O_3) in ice under dark condition in the presence of organic ligands [7], which was largely ascribed to the proton-assisted and ligand-promoted dissolution processes in the ice grain boundary region. So far, all the previous studies on the dissolution of iron oxides in ice reported that the presence of organic ligands enhances the dissolution of iron oxides in ice compared with the dissolution in aqueous solution. This study, however, reveals that the iron oxide dissolution in ice is not always accelerated and can be decelerated from its aqueous phase dissolution on the contrary depending on the kind of organic ligands and experimental conditions. The effects of various organic ligands on the iron oxide dissolution were systematically investigated in aqueous and frozen solutions for mostly goethite (regarded as the most thermodynamically stable form of iron oxide in nature [21]) and magnetite (Fe_3O_4) and hematite (α-Fe_2O_3) as well. The highly ligand-specific dissolution of iron oxides in water and ice was investigated by both experimental and computational methods to provide a reasonable understanding of the observed behavior.

2. Materials and Methods

2.1. Materials.

The iron oxides used in this study (goethite, magnetite, and hematite) were purchased from Aldrich chemicals. The specific surface area of these samples was measured as 178, 50, and 8 $m^2\ g^{-1}$, respectively [7]. All other chemicals used in this study including organic acids (formic, acetic, oxalic, citric, and ascorbic acids), hydroxylamine, and alkali halides were of analytical-reagent grade. The sample solutions for the experiments were prepared with doubly distilled water. Dilute solutions of perchloric acid (1 M) and sodium hydroxide (1 M) were used to adjust the initial pH of the samples.

2.2. Experimental procedure.

The sample solutions were prepared by adding 0.01 g of iron oxide sample into 50 mL doubly distilled water to obtain an initial suspension of 0.2 g/L. Then, the calculated amounts of various ligands (e.g., hydroxylamine, ascorbic acid, and iodide) were added to

the iron oxide suspension. To enhance the dispersion of iron oxide particles, the suspension was initially sonicated prior to the addition of organic/inorganic ligands. An initial ligand concentration of 1 mM was added for all the experiments unless otherwise specified. The suspensions (5 mL) were placed in 15 mL polypropylene tubes with or without organic/inorganic ligands and kept in dark condition at room temperature (~25 °C) (for aqueous-phase reactions) or in ethanol bath maintained at -20 °C (for ice-phase reactions). The time at which the aqueous samples were introduced into the pre-cooled ethanol bath was taken as the reaction starting point (t = 0). At each fixed time interval, the aqueous and ice phase samples (after thawing at 40 °C) were filtered through 0.45-μm syringe filter to remove any undissolved iron oxide particles. The filtered samples were used for further analysis. Further details about this experimental setup were already described earlier [7,20]. To confirm the reproducibility, all the experiments were conducted at least in duplicate and the average values were used.

2.3. Analysis.

Ferrous and total iron in various samples were analyzed spectrophotometrically by using a modified 1,10-phenanthroline method [22]. About 1.5 mL of each sample was mixed with 2.0 mL 1,10-phenanthroline (2%) and 1.5 mL acetate buffer. About 100 L of hydroxylamine hydrochloride (10%) solution was added to reduce any dissolved ferric irons to ferrous ions when the total iron concentration was analyzed. This reaction mixture was shaken well and kept in dark condition for at least one hour before the spectrophotometric analysis. The absorbance at 510 nm was recorded on a UV-visible spectrophotometer (Agilent technologies 8453 UV-Vis diode array system) and compared with a set of standard values. The residual concentration of various ligands (mainly iodide) after dissolution experiments were measured using ion chromatography (IC, Dionex, USA).

2.4. Computational Method.

The binding energies of hydroxylamine and iodide ion on ice surface and in ice lattice bulk were calculated and compared. A systematic ice modeling on the basis of QM/EFP [23,24] hybrid scheme was suggested [25,26], which takes into account of the long range electrostatic interactions and hydrogen disorders of crystal ice. The validity and accuracy of our QM/EFP model was thoroughly tested in our earlier studies [25]. The particular combination of a QM and EFP scheme is a three-layer model (QM relaxed region/QM water relax region/EFP water fixed region) for Hydroxylamine/6/762, which is comprised of QM(Solute) relaxed, 6 relaxed QM water molecules and 762 fixed EFP water molecules. For the calculations of QM regions, density functional theory of B3LYP functional was used in combination with 6-31G(d,p) basis sets. We adopted the EFP1-HF (effective

fragment potential 1-Hartree-Fock) water model for the EFP part of our hybrid models [23]. The GAMESS (general atomic and molecular electronic structure system) [27] program was used for all of the computations. Basis set superposition error (BSSE) corrections to binding energies were performed with counterpoise method [28]. Counterpoise (CP) correction including monomer deformations was applied using the following equation,

$$\triangle E_{bind}^{CP}(AB) = [E_{AB}^{AB}(AB) - E_{AB}^{AB}(A) - E_{AB}^{AB}(B)] + [E_{AB}^{A}(AB) - E_{A}^{A}(A)] + [E_{AB}^{B}(B) - E_{B}^{B}(B)] \quad (1)$$

where the subscripts and superscripts denote the geometry and the basis, respectively. The chemical system considered is denoted by the symbols in the parentheses. Here A and B stand for molecule and ice, respectively. Since the geometries of ice (B) in the complex (AB) are different from their isolated forms, the above equation was utilized to accurately perform the BSSE correction.

3. Results and Discussion

3.1. Iron dissolution by organic ligands and halides in ice.

We carried out the dark dissolution of goethite in water and ice containing various organic and inorganic ligands. The amount of total dissolved iron (Fe(II)+Fe(III)) generated from goethite was measured in 24 h reaction in water and ice and compared in Figure 1, which exhibits highly ligand-specific dissolution behaviors. The trend of goethite dissolution induced by formic and acetic acids (Figure 1) is similar to that reported by Jeong et al. [7] Monodentate organic ligands like formic and acetic acids form weak surface complexation with iron oxide surface and their efficiency to induce iron dissolution in water are, thus, very limited, which is little different from that without ligands [7]. On the other hand, freeze concentration effect, which excludes substrates (ligands) and iron oxide particles from the bulk ice (ice-crystal lattice) region upon freezing and subsequently concentrates substrate molecules within a small liquid-like grain boundary region, can enhance the dissolution of iron oxides in ice [7,13,19,20]. Earlier works also reported similar effects, which observed higher reactivity in ice than its aqueous counterpart [7,8,10,19,20]. This work, however, reveals that the freeze concentration effect on the iron oxide dissolution highly varies depending on the kind of ligands, some of which exhibit even negative effect. For example, the total dissolved iron (Fe(II)+Fe(III)) in ice was significantly enhanced by hydroxylamine and iodide from that of aqueous phase dissolution (by a factor of ~6 and 13 times, respectively) whereas the presence of ascorbic acid suppressed the iron oxide dissolution in ice by about 5 times on the contrary. The reductive dissolution of iron oxides induced by strong reducing agents like ascorbic acid [3,5,29,30] can play an

important role in maintaining the iron balance in human body and natural environment. Oxalic and citric acids also suppressed the dissolution of iron oxides in ice phase. This implies that the presence of these ligands in the frozen environment can cause an unusual reduction in the bio-available iron compared to that of the aqueous medium. By considering the possible complexity and differences between the ice and aqueous phase behaviors, the ligand-specific effects on iron oxide dissolution need to be studied.

The concentrations of ferrous and total dissolved iron produced in the presence of various ligands are compared in Table 1. This shows that the dissolution of iron oxides is reductive with ascorbic acid (100%), hydroxylamine (100%), and iodide (91%), whereas the non-reductive dissolution is dominant with formic and acetic acids. The extensive dissolution of iron oxide by ascorbic acid, iodide, and hydroxylamine should be ascribed to their strong reduction power. The mechanism of reductive iron dissolution in water has been extensively studied [4,7,31,32], which is initiated by the complex formation of organic/inorganic ligands (represented as $>Fe^{III}-L^n$ in Reaction 2) on the surface of iron oxide.

$$>Fe^{III} + L \rightarrow >Fe^{III}-L^n \quad (2)$$

The reductive dissolution of iron oxides requires an electron transfer from the ligand to the surface metal ion (Reaction 3). The resulting Fe(II) species is then detached from the surface of the iron oxide and released as dissolved ferrous ions (Reaction 4) [31].

$$>Fe^{III}-L^n \rightarrow >Fe^{II}-L^{(n-1)} \quad (3)$$

$$>Fe^{II}-L^{(n-1)} \rightarrow Fe^{2+}_{aq} \quad (4)$$

The dissolution of ferrous irons from different commercial iron oxide samples (goethite, magnetite, and hematite) in aqueous and ice phases is compared in Figure 2. It seems that the concentration of dissolved ferrous iron is related to the surface area of iron oxide, which is in good agreement with the previous report [7]. Goethite with the highest surface area (BET surface area: 178 $m^2\ g^{-1}$) showed much higher Fe(II) dissolution than magnetite (surface area: 50 $m^2\ g^{-1}$) and hematite (surface area: 8 $m^2\ g^{-1}$) for both cases of ascorbic acid and iodide in water and ice. It should be noted that ascorbic acid consistently suppressed the iron dissolution in ice whereas iodide enhanced it regardless of the kind of iron oxide. The significantly enhanced dissolution of iron oxide in the presence of hydroxylamine and iodide in ice (pH 3) can also be explained in terms of the freeze concentration effect as we did in the previous study [7,20], whereas the opposite results obtained with ascorbic, citric, and oxalic acids cannot. This seems to imply that the freeze

concentration of solutes in frozen solution is not always observed and should depend on the kind of solutes. That is, some solutes like ascorbic acid could be preferentially incorporated within the ice lattice upon freezing. In such case, ascorbic acid molecules become less accessible to the iron oxide concentrated in the ice grain boundary region and hence a suppressed dissolution of iron oxide in ice could occur. The preferential incorporation of anions or cations in ice crystals induces the development of the freezing potential at the ice/water interface, which was experimentally demonstrated [33, 34]. Based on the present observations, it is proposed as a hypothesis that some ligands that suppress the dissolution of iron oxide in ice are not freeze-concentrated in the ice grain boundary region but more preferentially incorporated within the ice crystal lattice on the contrary. To test the validity of such hypothesis, more systematic experimental and theoretical investigations were carried out and discussed below.

3.2. pH-dependent ligand effects on iron oxide dissolution.

It is well known that protons can accelerate the dissolution of iron oxides [4]. Moreover, pH can change the speciation of ligands [35-38] and subsequently their relative distribution between the ice and grain boundary regions to influence the iron oxide dissolution process. Therefore, the effects of pH on the dissolution of iron in ice and water were additionally investigated for ascorbic acid, hydroxylamine, and iodide (*see* Figure 3), which revealed distinguished and contrasting pH-dependent behaviors. Each ligand exhibits a unique pH-dependent behavior. Incidentally, it should be mentioned that the pH values shown in Figure 3 indicate the pH of aqueous solutions before freezing, not the real pH in the liquid-like grain boundary region in the frozen solution. The dissolution of goethite in ice containing ascorbic acid was most suppressed at pH 3, and the relative suppression of the dissolution gradually decreased with increasing pH to show a negligible difference at pH > 4.5 (Figure 3A). On the other hand, hydroxylamine enhanced the iron dissolution in ice at pH 3, but suppressed the iron dissolution in ice at pH 3.5 on the contrary (Figure 3B). Iodide whose speciation is not dependent on pH enhanced the iron dissolution in the tested pH range [39], which was the highest at pH 3 and gradually decreased with pH (Figure 3C). The iron dissolution in iodide-containing ice and water at pH 5 was below the detection limit.

Such pH-dependent behaviors can be related with the pH-dependent relative distribution of each ligand between the ice bulk and the liquid-like grain boundary region. Ascorbic acid exists mainly as the neutral form at pH 3 (pK_{a1} = 4.1) [38,40] and the pH increase causes the deprotonation of this ligand to the anionic form. On the other hand, the protonated cationic form of hydroxylamine ($HONH_3^+$) exists in the acidic pH (pK_a = 6.0) [41,42] and increasing pH should gradually convert the cation to the neutral form. Although

the concentrations of each ligand and pH in the bulk ice and the grain boundary region could not be measured in this work, it is reasonable to assume that the dissolution of iron oxide in ice should be enhanced when the ligands are preferentially concentrated in the grain boundary region along with the iron oxide particles. Similarly, the iron oxide dissolution should be suppressed when the ligands are preferentially incorporated within the ice crystals. On the basis of the pH-dependent dissolution trends observed for ascorbic acid (Figure 3A), hydroxylamine (Figure 3B), and iodide (Figure 3C), it is suggested that some ligands (i.e., the cationic species of hydroxylamine, iodide anion) are preferentially concentrated in the liquid-like grain boundary region and facilitate the dissolution of iron oxide in ice [19,20]. On the other hand, other ligands (*i.e.,* un-dissociated ascorbic acid, neutral hydroxylamine) seem to be preferentially trapped in the bulk ice (not in the grain boundary region) and are consequently less accessible to the iron oxide particles in the grain boundary region, which should result in the suppression of iron oxide dissolution in ice. This seems to be the similar case for citric acid and oxalic acid as shown in Figure 1. The observation that the relative effect of hydroxylamine on the iron oxide dissolution in ice was reversed when the pH increased from 3 to higher values implies that the pH-dependent speciation [41,42] of ligands critically influences the ligand distribution between the ice bulk and the grain boundary.

3.3. Ligand distribution between the ice lattice (bulk) and grain boundary (surface) regions.

From the above considerations, we propose (1) that the ligand molecules that enhance the dissolution of iron oxides in ice (*e.g.,* iodide and protonated hydroxylamine at pH 3) are likely to be excluded from the ice lattice and concentrated in the grain boundary region [19,20]; (2) that ligand molecules that suppress the iron oxide dissolution in ice (*e.g.,* ascorbic acid at acidic pH and hydroxylamine at pH $\geq$ 4) are likely to be trapped in the ice lattice to hinder the direct contacts between the ligand molecules and the iron oxide particles in the grain boundary region. To confirm such hypothesis, we carried out the following experiment to estimate the relative distributions of ligand molecules between the ice lattice (bulk) and the grain boundary (surface) region (*see* Figure 4).

The solidified ice samples containing iron oxide particles and ligand molecules (in both the ice lattice and the grain boundary) were taken out from the ethanol bath and were immediately crushed to fine particles in a mortar, followed by rapid washing with 10 mL of cold water to melt away only the surface region of the crushed ice particles. The washed fine ice particles were immediately recollected via filtration, then fully melted to liquid samples that were analyzed for remaining ligands using ion chromatography. Since the ligand molecules present in the ice surface (grain boundary) region should be

preferentially washed out, it is assumed that the measured concentrations of ligands in the thawed samples represent mostly the ligand molecules trapped in the ice lattice (bulk). Although this is a very rough method and the expected error levels could be high, this should show the relative distribution of the ligand distribution between the ice bulk and surface regions at least qualitatively. Much precaution was made to ensure the reliability of the measurements. The experimental results are summarized in Table 2 which clearly shows the contrasting distribution trends of iodide and ascorbic acid which exhibited the opposite effects on the iron oxide dissolution in ice. The proportion of the iodide ions trapped in the ice lattice (bulk) is very small (< 3%) whereas that of ascorbic acid is markedly higher (>50%). This suggests the preferential concentration of iodide ions in the ice surface region [9,19] and the preferential incorporation of ascorbic acid in the ice bulk region, which is consistent with the proposed hypothesis. As a result, iodide ions highly enhanced the iron oxide dissolution in ice whereas ascorbic acids suppressed it. A similar attempt for the determination of hydroxylamine content in ice, however, was not successful due to the technical difficulties associated with the accurate concentration measurement.

An additional evidence to support the ligand-specific distribution between the ice bulk and ice surface was obtained from theoretical calculations [25,26]. The binding energies of a hydroxylamine (both protonated and neutral forms) and an iodide ion on the ice surface and in the bulk ice lattice were theoretically estimated. The optimized structures and binding energies of protonated hydroxylamine (A), neutral hydroxylamine (B) and iodide (C) on the ice surface (left) and in the bulk ice (right) are compared in Figure 5. As shown in the hydroxylamine case, both the protonated and neutral forms are more stable in the bulk ice lattice. However, the neutral hydroxylamine has a much lower relative surface preference (8.72/133.68 = 0.065) than the protonated hydroxylamine (94.32/226.70 = 0.42), which implies that neutral hydroxylamine should be more easily incorporated into the ice lattice than its protonated form. When more hydroxylamine molecules (reductants) are incorporated within the ice lattice, they should have less contact with the iron oxide particles in the grain boundary (surface) region and hence less reductive dissolution of iron oxide. This calculation result is in good agreement with the observed pH-dependent dissolution of iron oxides with hydroxylamine, which exhibited the enhanced dissolution in ice at pH 3 (where protonated hydroxylamine should be dominant on the surface region) but the suppressed dissolution in ice at higher pH (where the fraction of protonated forms on the surface region is lowered) (*see* Figure 3B). On the other hand, iodide ion strongly prefers the ice surface region (58.89/14.09 = 4.18) and therefore its concentration in the ice surface region should be higher than that in the bulk ice. This explains why iodide always enhances the iron oxide dissolution in ice regardless of pH unlike the case of ascorbic acid and hydroxylamine of which effects on the iron

oxide dissolution in ice are dependent on pH (*see* Figure 3).

3.4. Effects of other factors on the iron oxide dissolution.

According to the previous discussion, the ligands that are preferentially included in the ice bulk (*e.g.,* ascorbic acid) are expected to have less freeze concentration effect than the ligands like iodide [9,19] and protonated hydroxylamine that prefer the ice surface region. To investigate this further, the temperature-dependent production of ferrous ions from goethite dissolution induced by ascorbic acid, hydroxylamine, and iodide was measured and compared in Figure 6. The iron oxide dissolution by ascorbic acid monotonously decreased with decreasing temperature (from 20 to -20 °C) and there is no sign of enhancement below the freezing point, which implies the absence of freeze concentration effect. On the other hand, hydroxylamine and iodide showed a clear sign of enhancement in the iron oxide dissolution below 0 °C, which supports the freeze concentration of the ligands.

The different freeze concentration behaviors of ascorbic acid and iodide can be also related with the different concentration dependences shown in Figure 7. Increasing ascorbic acid concentration almost linearly increased the iron dissolution in water but reached the saturation above 0.1 mM in ice. This indicates that ascorbic acids are not freeze-concentrated in ice. On the other hand, increasing the iodide concentration little increased the iron dissolution in water but efficiently increased it in ice, which implies that iodide ions are indeed freeze-concentrated in ice [9,19]. Both the temperature dependence (Figure 6) and the ligand concentration dependence (Figure 7) support that iodide ions are freeze-concentrated but ascorbic acids are not in the frozen solutions. Such difference causes their opposite effects on the iron oxide dissolution in ice (Figure 1 and 3).

3.5. Environmental Implications.

The present study found that the dissolution of iron oxide under dark condition exhibits highly ligand-specific behavior. While all the previous works on the dissolution of iron oxides in both dark and photo-irradiated conditions reported the enhancement of iron dissolution in ice phase compared with the aqueous phase [7,19,20], this work found that some ligands like ascorbic acid, citric acid, and neutral hydroxylamine suppress the iron dissolution in ice on the contrary. This could be ascribed to the ligand-specific distribution between the ice lattice (bulk) and the ice grain boundary (surface). While most solutes are thought to be freeze-concentrated in the ice grain boundary region upon freezing, some ligands that exhibit the negative effects on the iron oxide dissolution in ice are proposed to be preferentially incorporated in the ice bulk and not freeze-concentrated. The dust particles containing iron oxides can be trapped in ice cloud in the upper atmosphere or deposited on snow and various ice media (sea ice, glacier) in the polar region. In particular,

the iron oxide dissolution is more pronounced in acidic condition which can be often found in the environments such as marine aerosols and cloud droplets with pH < 3.5 [43]. The present study shows that the dissolution rate of iron oxide particles trapped in ice can be sensitively influenced by the kind of organic or inorganic compounds present in various ice media. Some compounds in frozen solutions may enhance the iron dissolution while others may suppress it. The hindered dissolution of iron oxides in ice may cause an iron deficient condition in the environment. This study showing the ligand-specific nature of iron dissolution in ice should provide better understanding of the iron bioavailability in the cold environments [7,20]. However, it should be recognized that the reality is even more complicated. The composition of natural ice samples is far more complex than the controlled laboratory samples because of the co-existence of a wide variety of chemical species including metal ions, inorganic ions, natural organic matters, etc. Furthermore, the pH-dependent behaviors in the iron oxide dissolution may complicate the problems. Therefore, applying the laboratory results to real environments requires more rigorous investigations.

4. Reference

1. Lis, H.; Shaked, Y.; Kranzler, C.; Keren, N.; Morel, F. M. M., Iron Bioavailability to Phytoplankton: An Empirical Approach. ISME J. 2015, 9, 1003-1013.
2. Andrews, N. C., Iron Metabolism: Iron Deficiency and Iron Overload. Annu. Rev. Genom. Hum. Genet. 2000, 1, 75-98.
3. Moretti, D.; van Doorn, G. M.; Swinkels, D. W.; Melse-Boonstra, A., Relevance of Dietary Iron Intake and Bioavailability in the Management of HFE Hemochromatosis: A Systematic Review. Am. J. Clin. Nutr. 2013, 98, 468-479.
4. Schwertmann, U., Solubility and dissolution of iron oxides. Plant Soil 1991, 130, 1-25.
5. Hurrell, R.; Egli, I., Iron Bioavailability and Dietary Reference Values. Am. J. Clin. Nutr. 2010, 91, 1461S-1467S.
6. Abbaspour, N.; Hurrell, R.; Kelishadi, R., Review on Iron and its Importance for Human Health. J Res Med Sci. 2014, 19, 164-174.
7. Jeong, D.; Kim, K.; Choi, W., Accelerated Dissolution of Iron Oxides in Ice. Atmos. Chem. Phys. 2012, 12, 11125-11133.
8. Kim, K.; Choi, W., Enhanced Redox Conversion of Chromate and Arsenite in Ice. Environ. Sci. Technol. 2011, 45, 2202-2208.
9. Kim, K.; Yabushita, A.; Okumura, M.; Saiz-Lopez, A.; Cuevas, C. A.;

Blaszczak-Boxe, C. S.; Min, D. W.; Yoon, H.-I.; Choi, W., Production of Molecular Iodine and Tri-iodide in the Frozen Solution of Iodide: Implication for Polar Atmosphere. Environ. Sci. Technol. 2016, 50, 1280-1287.

10. Kim, K.; Yoon, H.-I.; Choi, W., Enhanced Dissolution of Manganese Oxide in Ice Compared to Aqueous Phase under Illuminated and Dark Conditions. Environ. Sci. Technol. 2012, 46, 13160-13166.

11. Klanova, J.; Klan, P.; Nosek, J.; Holoubek, I., Environmental Ice Photochemistry: Monochlorophenols. Environ. Sci. Technol. 2003, 37, 1568-1574.

12. Takenaka, N.; Ueda, A.; Daimon, T.; Bandow, H.; Dohmaru, T.; Maeda, Y., Acceleration Mechanism of Chemical Reaction by Freezing: The Reaction of Nitrous Acid with Dissolved Oxygen. J. Phys. Chem. 1996, 100, 13874-13884.

13. Takenaka, N.; Ueda, A.; Maeda, Y., Acceleration of the Rate of Nitrite Oxidation by Freezing in Aqueous Solution. Nature 1992, 358, 736-738.

14. Grannas, A. M.; Bausch, A. R.; Mahanna, K. M., Enhanced Aqueous Photochemical Reaction Rates after Freezing. J. Phys. Chem. A 2007, 111, 11043-11049.

15. Takeda, S., Influence of Iron Availability on Nutrient Consumption Ratio of Diatoms in Oceanic Waters. Nature 1998, 393, 774-777.

16. Marcotte, G.; Marchand, P.; Pronovost, S.; Ayotte, P.; Laffon, C.; Parent, P., Surface-Enhanced Nitrate Photolysis on Ice. J. Phys. Chem. A 2015, 119, 1996-2005.

17. Blaha, L.; Klanova, J.; Klan, P.; Janosek, J.; Skarek, M.; Ruzicka, R., Toxicity Increases in Ice Containing Monochlorophenols upon Photolysis: Environmental Consequences. Environ. Sci. Technol. 2004, 38, 2873-2878.

18. Heger, D.; Klanova, J.; Klan, P., Enhanced Protonation of Cresol Red in Acidic Aqueous Solutions Caused by Freezing. J. Phys. Chem. B 2006, 110, 1277-1287.

19. Kim, K.; Choi, W.; Hoffmann, M. R.; Yoon, H.-I.; Park, B.-K., Photoreductive Dissolution of Iron Oxides Trapped in Ice and Its Environmental Implications. Environ. Sci. Technol. 2010, 44, 4142-4148.

20. Jeong, D.; Kim, K.; Min, D. W.; Choi, W., Freezing-Enhanced Dissolution of Iron Oxides: Effects of Inorganic Acid Anions. Environ. Sci. Technol. 2015, 49, 12816-12822.

21. Liu, H.; Chen, T.; Frost, R. L., An Overview of the Role of Goethite Surfaces in the Environment. Chemosphere 2014, 103, 1-11.

22. Stucki, J. W.; Anderson, W. L., The Quantitative Assay of Minerals for Fe2+ and Fe3+ Using 1,10-Phenanthroline: I. Sources of Variability1. Soil Sci. Soc. Am. J.

KOPRI 극지연구소

1981, 45, 633-637.

23. Day, P. N.; Jensen, J. H.; Gordon, M. S.; Webb, S. P.; Stevens, W. J.; Krauss, M.; Garmer, D.; Basch, H.; Cohen, D., An Effective Fragment Method for Modeling Solvent Effects in Quantum Mechanical Calculations. J. Chem. Phys. 1996, 105, 1968-1986.

24. Gordon, M. S.; Fedorov, D. G.; Pruitt, S. R.; Slipchenko, L. V., Fragmentation Methods: A Route to Accurate Calculations on Large Systems. Chem. Rev. 2012, 112, 632-672.

25. Shoaib, M. A.; Choi, C. H., Adsorptions of HOCl on Ice Surface: Effects of Long-Range Electrostatics, Surface Heterogeneity, and Hydrogen Disorders of Ice Crystal. J. Phys. Chem. C 2012, 116, 3694-3701.

26. Shoaib, M. A.; Choi, C. H., Adsorptions of Formic and Acetic Acids on Ice Surface: Surface Binding Configurations and a Possibility of Interfacial Proton Transfer. J. Phys. Chem. C 2013, 117, 4181-4188.

27. Schmidt Michael, W.; Baldridge Kim, K.; Boatz Jerry, A.; Elbert Steven, T.; Gordon Mark, S.; Jensen Jan, H.; Koseki, S.; Matsunaga, N.; Nguyen Kiet, A.; Su, S.; Windus Theresa, L.; Dupuis, M.; Montgomery John, A., General atomic and molecular electronic structure system. J. Comput. Chem. 1993, 14, 1347-1363.

28. Boys, S. F.; Bernardi, F., The Calculation of Small Molecular Interactions by the Differences of Separate Total Energies. Some Procedures with Reduced Errors. Mol. Phys. 1970, 19, 553-566.

29. Hallberg, L.; Brune, M.; Rossander, L., The Role of Vitamin C in Iron Absorption. Int J Vitam Nutr Res Suppl. 1989, 30, 103-108.

30. Lynch, S. R.; Cook, J. D., Interaction of Vitamin C and Iron*. Ann. N. Y. Acad. Sci. 1980, 355, 32-44.

31. Panias, D.; Taxiarchou, M.; Paspaliaris, I.; Kontopoulos, A., Mechanisms of Dissolution of Iron Oxides in Aqueous Oxalic Acid Solutions. Hydrometallurgy 1996, 42, 257-265.

32. Lin, H.-Y.; Chen, Y.-W.; Li, C., The Mechanism of Reduction of Iron Oxide by Hydrogen. Thermochim. Acta 2003, 400, 61-67.

33. Wilson, P. W.; Haymet, A. D. J., Workman-Reynolds Freezing Potential Measurements between Ice and Dilute Salt Solutions for Single Ice Crystal Faces. J. Phys. Chem. B 2008, 112, 11750-11755.

34. Wilson, P. W.; Haymet, A. D. J., Effect of Ice Growth Rate on the Measured Workman-Reynolds Freezing Potential between Ice and Dilute NaCl Solutions. J.

phys. Chem. B 2010, 114, 12585-12588.

35. Ritschel, T.; Totsche, K. U., Quantification of pH-Dependent Speciation of Organic Compounds with Spectroscopy and Chemometrics. Chemosphere 2017, 172, 175-184.

36. Sjoback, R.; Nygren, J.; Kubista, M., Absorption and Fluorescence Properties of Fluorescein. Spectrochim. Acta A 1995, 51, L7-L21.

37. Gramlich, G.; Zhang, J.; Nau, W. M., Increased Antioxidant Reactivity of Vitamin C at Low pH in Model Membranes. J. Am. Chem. Soc. 2002, 124, 11252-11253.

38. Lewin, S., Vitamin C: its Molecular Biology and Medical Potential. Academic Press Inc. (London) Ltd.: London, 1976.

39. Trummal, A.; Lipping, L.; Kaljurand, I.; Koppel, I. A.; Leito, I., Acidity of Strong Acids in Water and Dimethyl Sulfoxide. J. Phys. Chem. A 2016, 120, 3663-3669.

40. Serjeant, E. P.; IUPAC chemical data series.; Ionisation Constants of Organic Acids in Aqueous Solution. Pergamon Press: Oxford; New York, 1979.

41. Fernandez, M. I.; Canle, M.; Garcia, M. V.; Santaballa, J. A., A theoretical analysis of the acid-base equilibria of hydroxylamine in aqueous solution. Chem. Phys. Lett. 2010, 490, 159-164.

42. Kirby, A. J.; Davies, J. E.; Brandao, T. A. S.; da Silva, P. F.; Rocha, W. R.; Nome, F., Hydroxylamine as an Oxygen Nucleophile. Structure and Reactivity of Ammonia Oxide. J. Am. Chem. Soc. 2006, 128, 12374-12375.

43. Zhuang, G.; Yi, Z.; Duce, R. A.; Brown, P. R., Link Between Iron and Sulphur Cycles Suggested by Detection of Fe(n) in Remote Marine Aerosols. Nature 1992, 355, 537-539.

KOPRI 극지연구소

Table 1. Speciation of iron dissolved from goethite in ice in the presence of various ligands[a]

Ligand	[Fe(II)] (μM)	[Fe(II)+Fe(III)](μM))	Reductive dissolution (%)
Ascorbic acid	75.2 ± 0.3	75.2 ± 0.3	100
Iodide	78.2 ± 0.7	85.7 ± 3.1	91.2
Hydroxylamine	48.2 ± 0.1	48.2 ± 0.1	100
Formic acid	7.6 ± 0.1	32.4 ± 0.4	23.6
Acetic acid	2.2 ± 0	18.8 ± 0.0	11.9

[a]Experimental condition: [Goethite] = 0.2 g/L; [Ligand] = 1 mM; pH = 3; Reaction time: 24 h

KOPRI 극지연구소

Table 2. The proportion of ligands trapped in the ice lattice (bulk) out of the total ligands[a]

Ligand	$[Ligand]_{ice\ bulk}$/ $[Ligand]_{total}$	$[Fe(II)]_{ice}/[Fe(II)]_{aq}$
Iodide	2.6%	13.4
Ascorbic acid	58.0%	0.2

[a]Experimental condition: [Goethite] = 0.2 g/L; [Ligand] = 0.5 mM; pH = 3

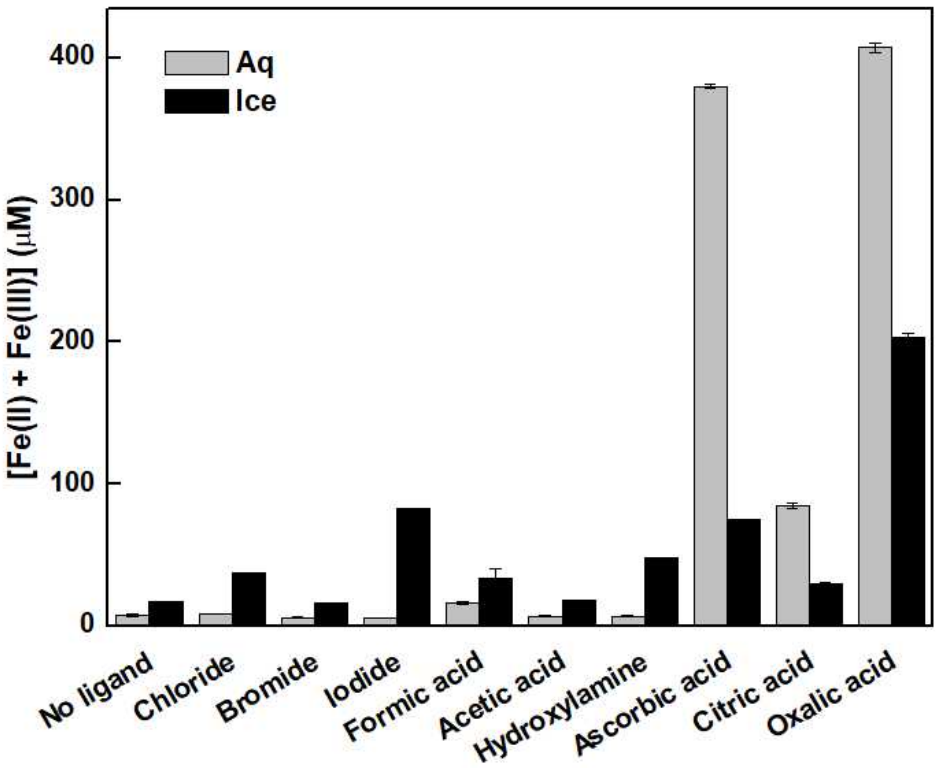

Figure 1. Iron dissolution from goethite in water (grey) and ice (black) at pH 3 in the presence of various ligands. [Goethite] = 0.2 g/L; [Ligand] = 1 mM; Reaction time = 24 h.

KOPRI
극지연구소

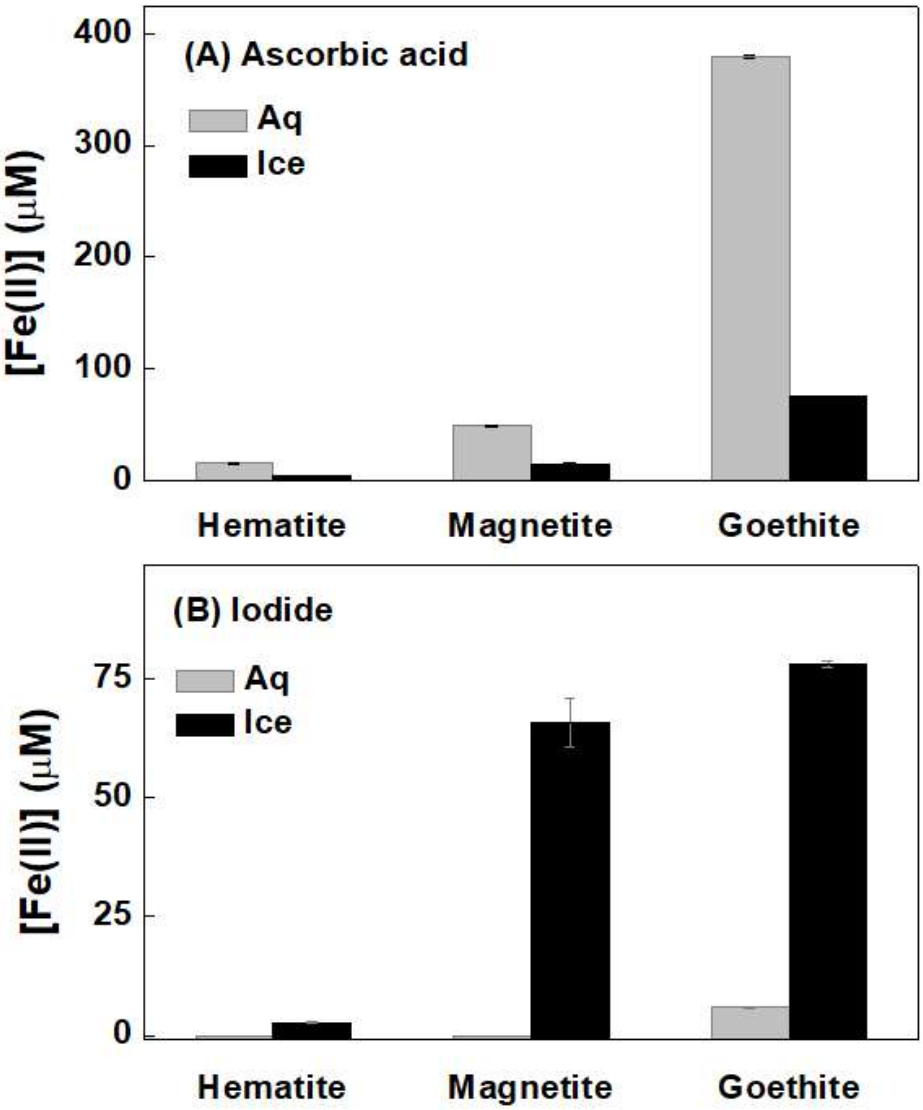

Figure 2. Dissolution of iron from different iron oxides (hematite, magnetite, goethite) in water (grey) and ice (black) at pH 3 in the presence of (A) ascorbic acid and (B) iodide. [Iron oxide] = 0.2 g/L; [Ligand] = 1 mM; Reaction time = 24 h.

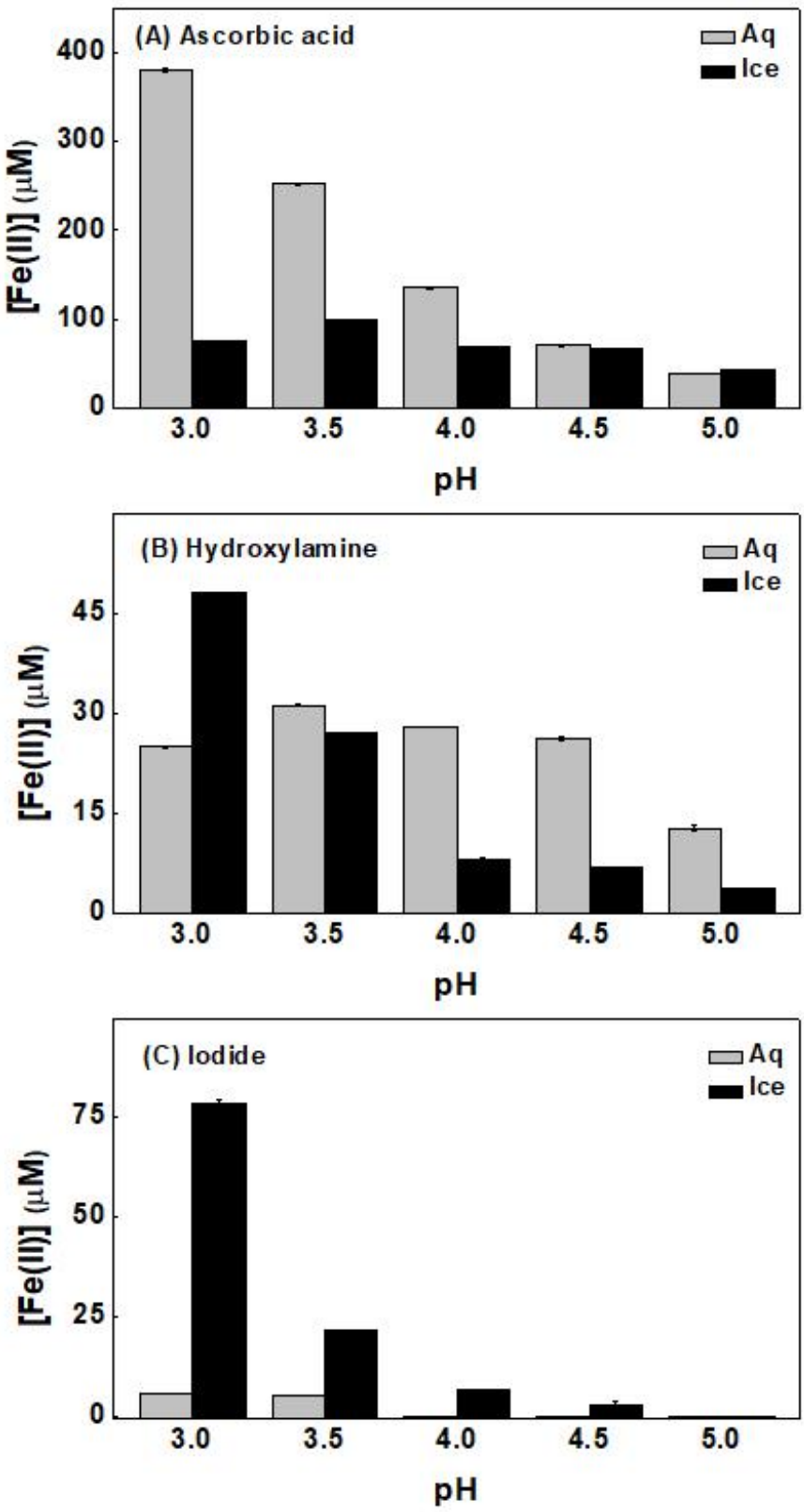

Figure 3. pH-dependent dissolution of ferrous iron from goethite in water (grey) and ice (black) in the presence of (A) ascorbic acid, (B) hydroxylamine, and (C) iodide. The pH values indicate the pH of the aqueous solution before freezing. [Goethite] = 0.2 g/L; [ligand] = 1 mM; Reaction time = 24 h.

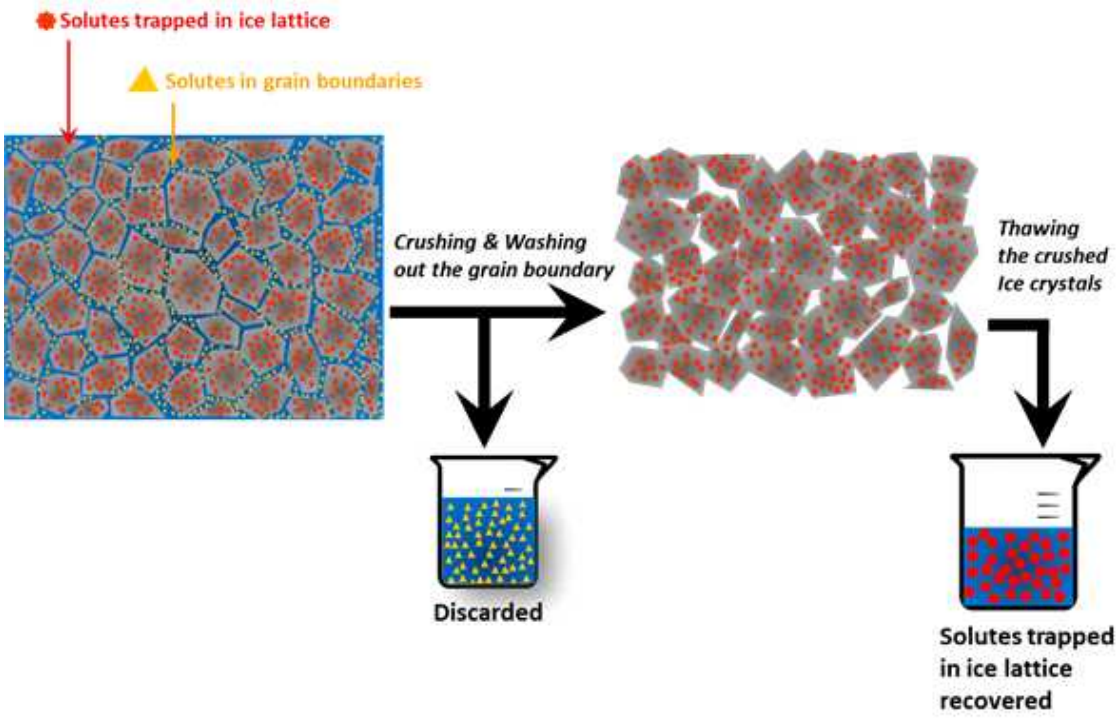

Figure 4. Illustration of the experimental procedure for estimating the concentrations of solutes (ligands) trapped in ice lattice.

KOPRI
극지연구소

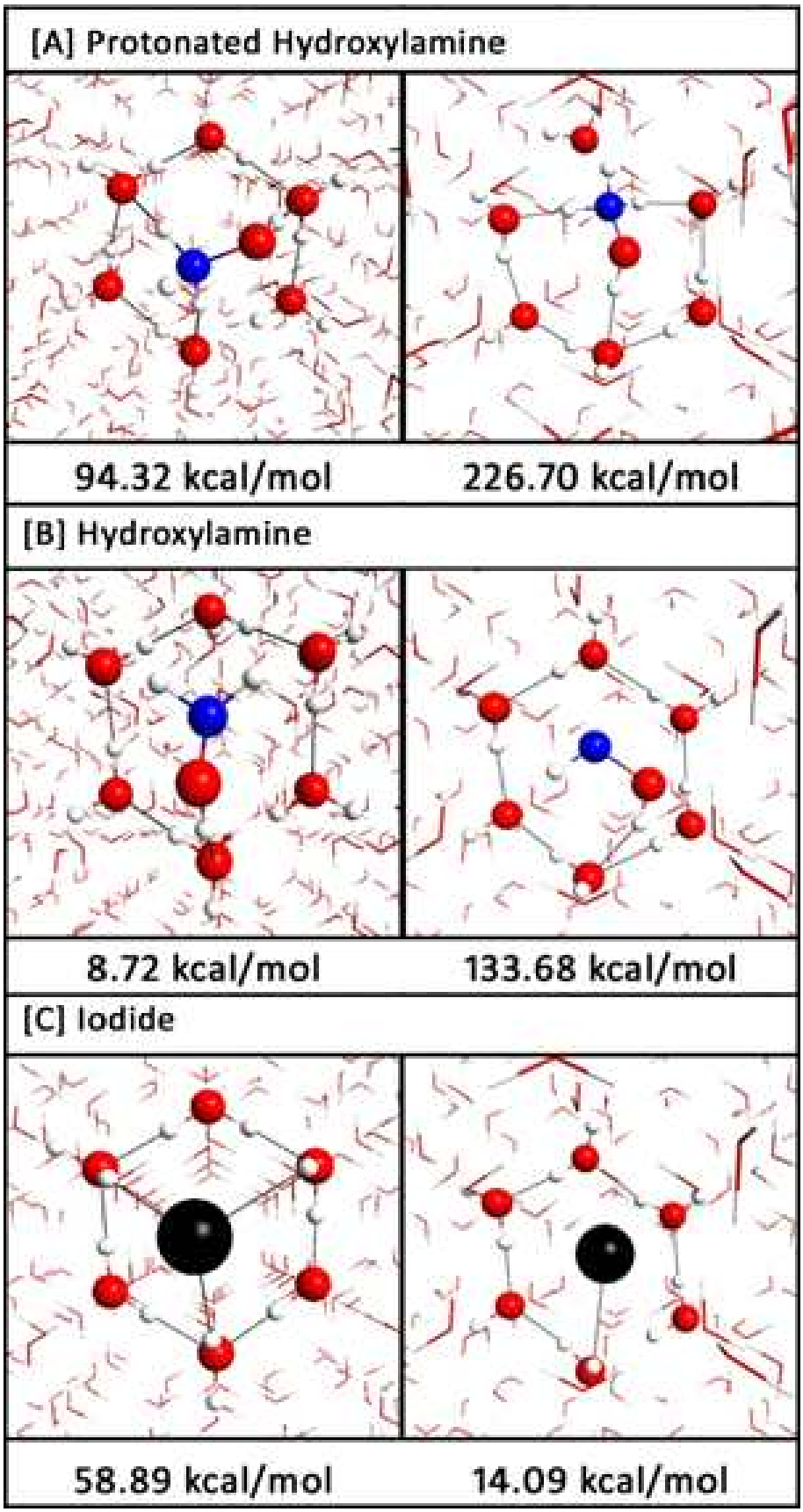

Figure 5. Theoretically optimized structures and binding energies of (A) protonated hydroxylamine, (B) neutral hydroxylamine and (C) iodide on the ice surface (left) and in the bulk ice lattice (right). The colored balls represent O (red), H (white), N (blue), and I (black).

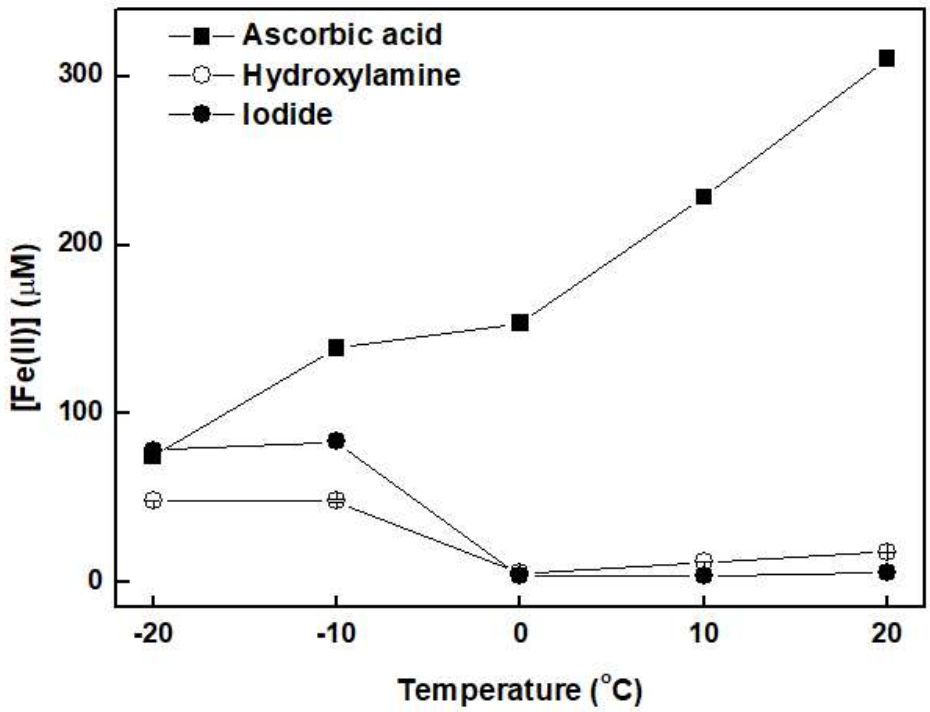

Figure 6. Temperature effect on the production of ferrous ions dissolved from goethite in the presence of ascorbic acid, iodide, and hydroxylamine. [Goethite] = 0.2 g/L; [Ligand] = 1 mM; Reaction time = 24 h; pH = 3 (the error bars are smaller than the symbol size).

KOPRI
극지연구소

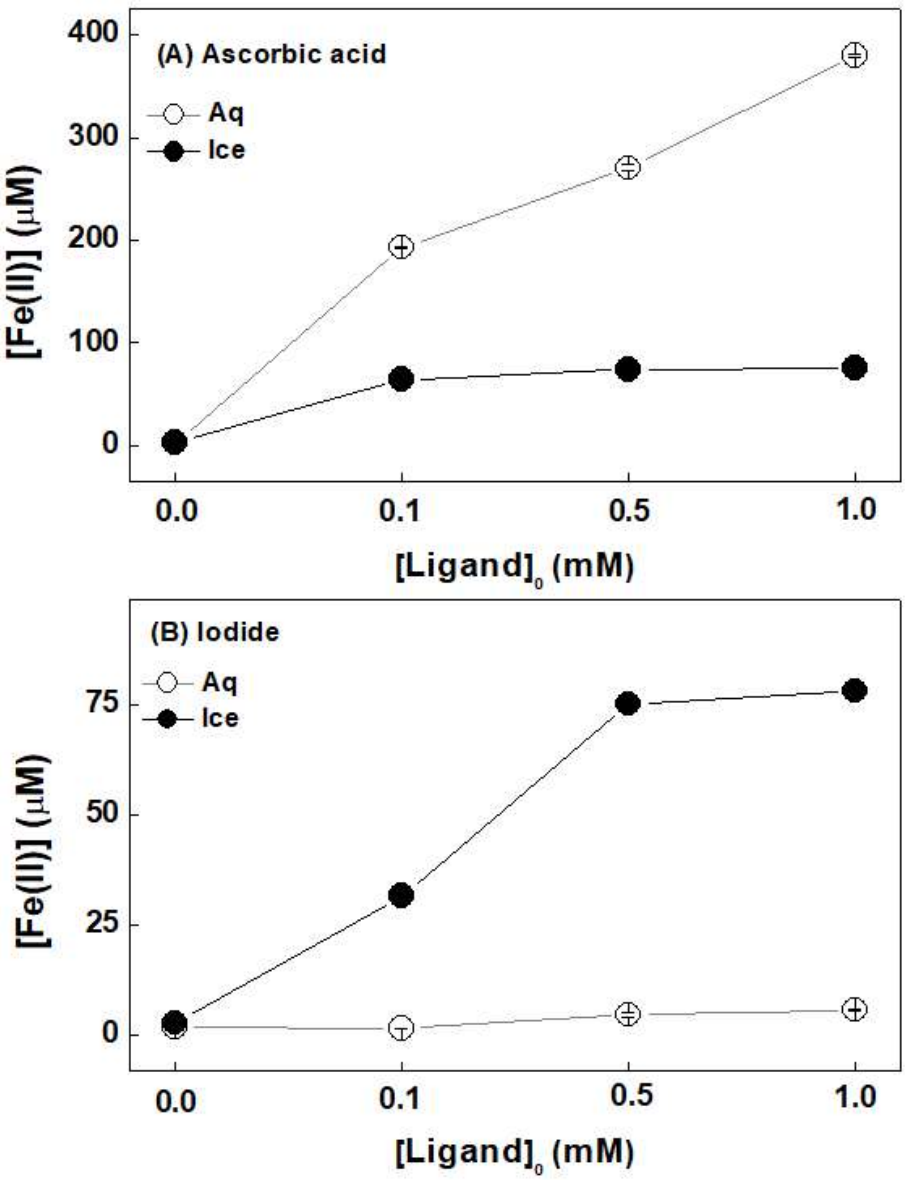

Figure 7. Dissolution of ferrous iron from goethite in water and ice as a function of the ligand concentration: (A) ascorbic acid and (B) iodide. The ligand concentration indicates the aqueous concentration before freezing. [Goethite] = 0.2 g/L; Reaction time = 24 h; pH = 3 (the error bars are smaller than the symbol size)

제 9 절. 대기 관측을 통한 할로겐 물질 기원 에이로졸 입자 형성 기작 규명

박기태

한국해양과학기술원 부설 극지연구소

1. 서론 및 배경

대기 중 할로겐 성분은 대기 구성물질의 산화속도에 영향을 미칠 뿐 아니라, 에어로졸 입자 형성에도 중요한 역할을 한다. 특히, 최근 연구들을 통해서 얼음화학 반응 특이성에 기인한 극지역의 할로겐 가스 생성 기작이 주목 받고 있다 (그림 1) (Saiz-Lopez et al., 2004, Saiz-Lopez et al, 2007, Pratt et al., 2013; Kim et al., 2016; Raso et al., 2017).

대기 중 주요 할로겐 물질 (bromine, iodine)은 ppt 수준의 낮은 농도로 존재하며, 반응 속도가 빠른 탓에 현재까지 연속관측 자료가 극히 희박하다. 특히, 얼음화학 반응에 의한 할로겐 물질의 발생이 극지역에서 활발히 일어날 것으로 예상되지만, 기술의 부재 및 접근성의 어려움으로 현재까지 남극 또는 북극에서의 장기간 대기 할로겐 물질 분석에 대한 기록이 부족하다. 최근 대기 할로겐 물질 연구를 선도하는 연구 그룹에서는 ppt 수준의 다양한 할로겐 물질 관측이 가능한 Differential Optical Absorption Spectroscopy (DOAS) 장비를 개발하였으며, 본 장비를 활용한 현장 관측 연구가 점진적으로 활성화 되고 있다. 특히 스페인 국립연구위원회 (Spanish National Research Council: CSIC)의 Atmospheric Chemistry and Climate group (PI: Dr. Alfonso Saiz-Lopez)에서는 독자적으로 Zenith-sky scattered-sunlight spectroscopy 방식의 Multi-axis Differential Optical Absorption Spectroscopy (MAX-DOAS) 장비를 제작하여 할로겐 물질 발생 기작 및 기후적 기능에 대한 연구를 선도하고 있다 (Plane and Saiz-Lopez, 2006) (그림 2).

세종과학기지가 위치한 서남극 및 남극 반도 지역은 온난화가 빠르게 나타나는 지역으로, 특히 Weddell Sea 부근 해빙 분포는 뚜렷한 계절 변화를 보이고 있다 (그림 3). 극지연구소는 세종과학기지를 기반으로 지난 2009년부터 대기 에어로졸의 다양한 물리적 요소(수농도, 크기분포, 입자산란도 등) 관측 연구를 수행하고 있다 (Kim et al., 2017, Kim et al., 2019). 이에, 세종과학기지 및 남극 반도 인근 해양은 해빙 환경 변화에 의한 할로겐 물질 변화 관측 및 이로 인한 에어로졸 입자 형성 기작 변화를 연구하기 위한 최적의 장소이다, 2018년 남극 하계 현장 조사를 통해 CSIC에서 제작한 MAX-DOAS 장비를 세종과학기지에 설치하였다. 또한, 쇄빙연구선 아라온을 활용하여 남극 항차 기간 동안 할로겐을 포함하는 다양한 에어로졸 전구 물질 연속 관측 및 대기 에어로졸 물리 특성 관측을 통해 극지 환경에서 자연 발생하는 할로겐 물질의 변화 및 에어로졸 입자 형성과의 상관성에 대한 연구를 진행하였다.

2. 재료 및 방법

○ 아라온 남극 항해 기간 중 남극대기 중 에어로졸의 물리적 특성 실시간 관측

2018년 아라온 남극 항해 기간 동안 condensation particle counter (CPC)를 이용하여 에어로졸의 총 수농도를 1분 단위로 측정하였고, Scanning Mobility Particle Sizer (SMPS)를 이용하여 입자의 크기에 따른 수농도 분포 곡선을 3분 단위로 연속 관측하였다. 또한, CCNC Cloud Condensation Nuclei Counter (CCNC)를 활용하여 구름형성응결핵의 수농도를 변화를 1초 단위로 실시간 관측하였고, Athalometer를 이용하여 블랙카본의 질량농도를 5분 간격으로 측정하였다. 총 관측 기간은 2018년 3월 27일부터 5월 4일까지 이며, 해당 기간 동안 아래 그림4에 표시된 경로를 따라 남극해를 이동하였다.

배의 엔진에서 배출되는 인위적 오염원의 영향을 최소화하기 위하여 블랙카본의 농도가 100 ng m^{-3} 이상인 경우, 풍향이 110 - 260°사이에 해당하는 경우 (배의 엔진에서 배출되는 오염 영역) 그리고 풍속이 2 m s^{-1}이하인 경우에 대해 에어로졸 물리 특성 자료를 제거하였다.

○ 세종기지 인근 빙권 변화가 할로겐 물질 및 에어로졸 입자형성에 미치는 영향 연구

다양한 고도각(0-90°)에서의 태양산란광 측정을 바탕으로 차등흡수분광기술(Differential Optic Absorption Spectroscopy: DOAS)과 복사전달모델 (Radiative Transfer Model: RTM)을 이용하여 BrO, IO 등 다양한 할로겐 물질의 연직 분포와 층적분 농도 변화에 대한 정보 획득이 가능하다. 세계 최고 수준의 DOAS 장비 제작 기술을 보유한 스페인 CSIC와 용역 계약을 통해 Multi-Axis DOAS (MAX-DOAS) 제작 완료하였으며 (2018년 11월), 2018년 12월에 신규 제작 장비를 남극 세종과학기지 대기빙하관측동에 설치하였다 (설치 일자: 2018년 12월 10일, 그림 5). 세종과학기지 대기빙하관측동 및 고층대기관측동에 기설치된 대기 관측 장비와의 간섭효과를 최소화하기 위하여 전자기파 차단을 위한 조치를 현장에서 취하였으며, 대기빙하관측동에 기설치 운영 중인 Scanning Mobility Particle Sizer(SMPS)를 통해 남극 대기 중 에어로졸의 입자 크기별 수농도 분포를 동시에 관측하였다.

3. 연구결과

○ 아라온 남극 항해 기간 중 남극대기 중 에어로졸의 물리적 특성 실시간 관측

2018년 아라온 남극 항해 기간 동안 CPC 및 SMPS 장비를 활용하여 2.5 nm-60 nm 크기 범위에 있는 에어로졸의 수농도 분포곡선 분석하였다. 그 결과 20 nm 크기 이하의 나노입자의 수농도가 남극해 이동 기간 중에 크게 증가함을 확인하였으며, 이는 남극대기 중 gas-to-particle conversion (nucleation) 메카니즘에 의하여 나노입자가 생성되었다는 것을 의미한다. 나노입자의 기원을 파악하기 위해서 HYSPLIT 모델을 활용하여 공기역궤적 분석을 수행하였으며, 아라온에서 관측된 에어로졸 입자의 기원지는 크게 대륙기원, 해양기원, sea ice 기원으로 분류할 수 있었다.

○ 세종기지 인근 빙권 변화가 할로겐 물질 및 에어로졸 입자형성에 미치는 영향 연구

할로겐 물질의 발생이 활발히 일어나는 봄-여름철 집중 관측 수행을 통해 남극 대기 중 주요 할로겐 성분 농도 분석을 의한 spectrum intensity 시계열 변화 자료 확보하였다 (관측기간: 2018년 12월 9일~ 2019년 6월 12일). DOAS 장비의 특성상 정상적인 관측을 위하여 충분한 태양광이 확보되어야 하기 때문에, 광량이 부족한 남극 동계 기간에는 관측을 중지하였다.

HYSPLIT 모델 및 인공위성 자료 기반 geographical information을 통합하여 2-day air mass back trajectory를 분석하였다. 최근 10년 동안 세종과학기지로 유입된 공기괴의 이동 경로를 분석한 결과, 남극반도 끝에 위치한 세종과학기지의 지리적 특성으로 인해 해양 기원 공기괴의 비율이 가장 높았으며 (66%), 해빙 (sea-ice) 위를 거쳐 온 공기괴의 비율은 연평균 29%로 나타났다. 그리고, 해빙 면적이 증가하는 겨울철 (6, 7, 8, 9월)에는 해빙 위를 거쳐 오는 공기괴의 비율이 최대 50%까지 증가하였다 (그림 9).

남극 대기 구성물질은 남극 해양, 해빙, 육상에서 발생하는 다양한 성분에 의해 조절된다. 세종과학기지 기반 장기간 대기 에어로졸 입자 특성을 관측한 결과, 남극 대기 입자 수농도 및 크기 분포는 계절별 뚜렷한 물리화학적 차이를 보였다. 선행 연구를 통해, 세종기지 인근의 해양생물 활동의 변화가 봄철 대기 입자 수농도 증가에 미치는 영향에 관한 상관성을 밝혔으나 (Jang et al., 2019, Kim et al., 2019), 생물학적 또는 비생물학적 작용에 의해 발생한 할로겐 물질에 기인한 에어로졸 입자 형성 기작은 관측 자료의 부족으로 인해 정확한 프로세스에 대한 이해가 부족하다.

National Snow and Ice Data Center (https://nsidc.org/)를 통해 1979년부터 2019년까지의 세종과학기지 인근 남극해(40-80°W, 55-65°S)의 연별/계절별 해빙 분포 특성을 파악한 결과, 겨울철(7, 8, 9월) 해빙 면적은 연간 약 0.1% 감소하는 경향을 보였으며, 여름철(1, 2, 3월) 해빙면적은 연간 0.03% 감소하는 경향을 보였다 (그림 10).

4. 결론

○ 아라온 남극 항해 기간 중 남극대기 중 에어로졸의 물리적 특성 실시간 관측

남극해 현장관측 중 4월 22일에서 4월 26일 기간 동안 공기괴가 주로 sea-ice에서 기원하고 풍속 (~30 m s^{-1})이 매우 높을 때, 높은 수농도의 나노입자 (< 20 nm)가 관측되었고, 이는 얼음 화학반응에 의해서 생성된 할로겐 물질이 대기 중 에어로졸의 생성에 기여할 수 있다는 가능성을 간접적으로 제시한다. 하지만, 해빙 기원 할로겐 가스 물질에 의한 극지 대기에서의 에어로졸 입자 형성에 대한 직접적인 관측적 증거를 제시하기 위해서는 할로겐 물질을 포함하는 가스상 전구물질 농도 및 에어로졸의 화학 특성에 대한 추가적인 정밀 분석이 필요하다.

○ 세종기지 인근 빙권 변화가 할로겐 물질 및 에어로졸 입자형성에 미치는 영향 연구

남극해 해빙 환경 변화는 해빙내의 얼음화학 반응에 의해 발생할 것으로 추정되는 다양한 할로겐 물질의 발생 변화에 뚜렷한 영향을 미칠 것으로 추정된다. MAX-DOAS를 통한 주요 할로겐 물질의 파장별 intensity 변화 자료를 동시간에 관측한 대기 에어로졸 수농도 크기 분포 자료 및 공기괴적 이동 자료와 함께 비교 분석한 결과, 공기괴가 해빙 위를 거쳐 세종과학기지

로 유입될 때 할로겐 성분에 의한 spectrum intensity의 증가와 함께 뚜렷한 입자 생성 및 성장 현상이 관측되었다 (그림 11). 후속 연구를 통해 MAX-DOAS 장비에서 확보한 spectrum intensity 자료를 복사전달모델을 통해 주요 할로겐 가스성분의 대기 중 농도 변화로 정량화하고, 기지 인근 해빙 특성 변화 및 에어로졸 입자 성장 관측자료와 정밀 비교 분석함으로서, '해빙-할로겐 성분-에어로졸'에 관한 상호작용 연구를 지속 수행하고자 한다.

5. 참고문헌

Jang, E., Park, K.-T., Yoon, Y. J., Kim, T.-W., Hong, S.-B., Becagli, S., Traversi, R., Kim, J., and Gim, Y., New particle formation events observed at the King Sejong Station, Antarctic Peninsula – Part 2: Link with the oceanic biological activities, Atmos. Chem. Phys., 19, 7595 – 7608, https://doi.org/10.5194/acp-19-7595-2019, 2019.

Kim K, Yabushita A, Okumura M, Saiz-Lopez A, Cuevas CA, Blaszczak-Boxe CS, Min DW, Yoon H-I, Choi W, Production of Molecular Iodine and Tri-iodide in the Frozen Solution of Iodide: Implication for Polar Atmosphere. Environ Sci Technol 50:1280-1287. https://doi.org/10.1021/acs.est.5b05148, 2016

Kim, J., Yoon, Y. J., Gim, Y., Choi, J. H., Kang, H. J., Park, K.-T., Park, J., and Lee, B. Y.: New particle formation events observed at King Sejong Station, Antarctic Peninsula – Part 1: Physical characteristics and contribution to cloud condensation nuclei, Atmos. Chem. Phys., 19, 7583 – 7594, https://doi.org/10.5194/acp-19-7583-2019, 2019.

Kim, J., Yoon, Y. J., Gim, Y., Kang, H. J., Choi, J. H., Park, K.-T., and Lee, B. Y., Seasonal variations in physical characteristics of aerosol particles at the King Sejong Station, Antarctic Peninsula, Atmos. Chem. Phys., 17, 12985 – 12999, https://doi.org/10.5194/acp-17-12985-2017, 2017.

Pratt, K., Custard, K., Shepson, P. et al. Photochemical production of molecular bromine in Arctic surface snowpacks. Nature Geosci 6, 351 – 356, https://doi.org/10.1038/ngeo1779, 2013.

Raso, A. R. W., Custard, K. D., May, N. W., Tanner, D., Newburn, M., Walker, L., Moore, R. J., Huey, G., Alexander, L., Shepson, P., & Pratt, K. A. Active molecular iodine photochemistry in the Arctic. Proceedings of the National Academy of Sciences of the United States of America, 114, 10,053 – 10,058. https://doi.org/10.1073/pnas.1702803114, 2017.

Saiz-Lopez, A. and J.M.C. Plane, Novel iodine chemistry in the marine boundary layer, Geophysical Research Letters, 31, L04112, doi: 10.1029/2003GL019215, 2004.

Saiz-Lopez, A., A. S. Mahajan, R. A, Salmon, S. Bauguitte, A. E. Jones, H. K. Roscoe, and

J. M. C. Plane, Boundary layer halogens in coastal Antarctica, Science, 317, 348-351, 2007.

Plane, J.M.C. and Saiz-Lopez, A. UV-visible Differential Optical Absorption Spectroscopy (DOAS), In: D.E. Heard (ed). Analytical Techniques for Atmospheric Measurement, Blackwell Publishing: Oxford, 2006.

KOPRI
극지연구소

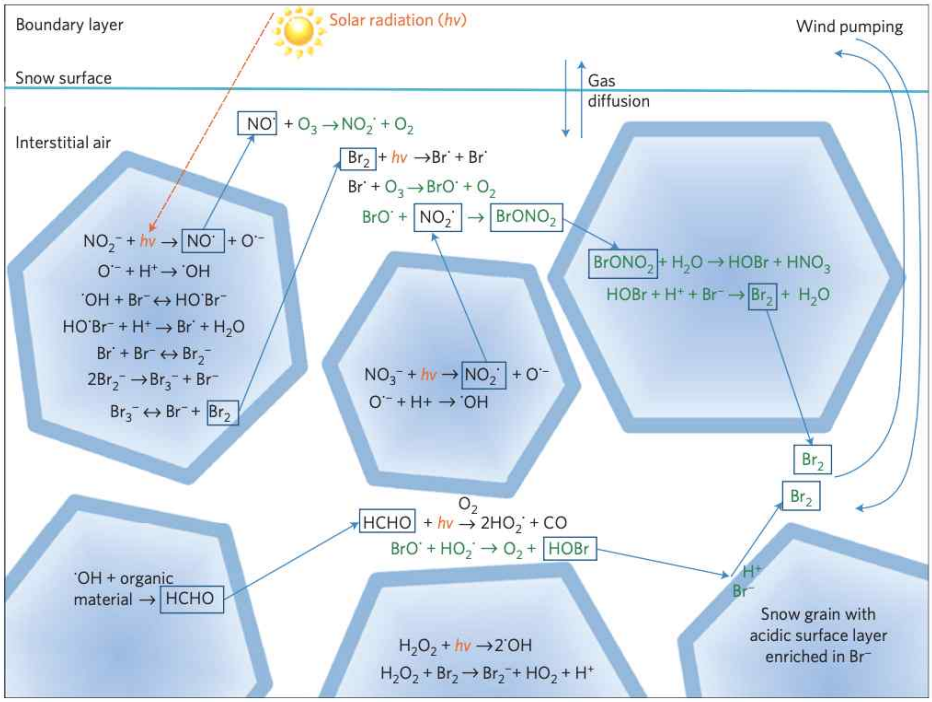

그림 1. 얼음화학 반응에 의한 bromine 활성화 반응 (Pratt et al., 2013)

KOPRI

그림 2. 스페인 CSIC에서 제작한 Multi-axis Differential Optical Absorption Spectroscopy (MAX-DOAS) 장비

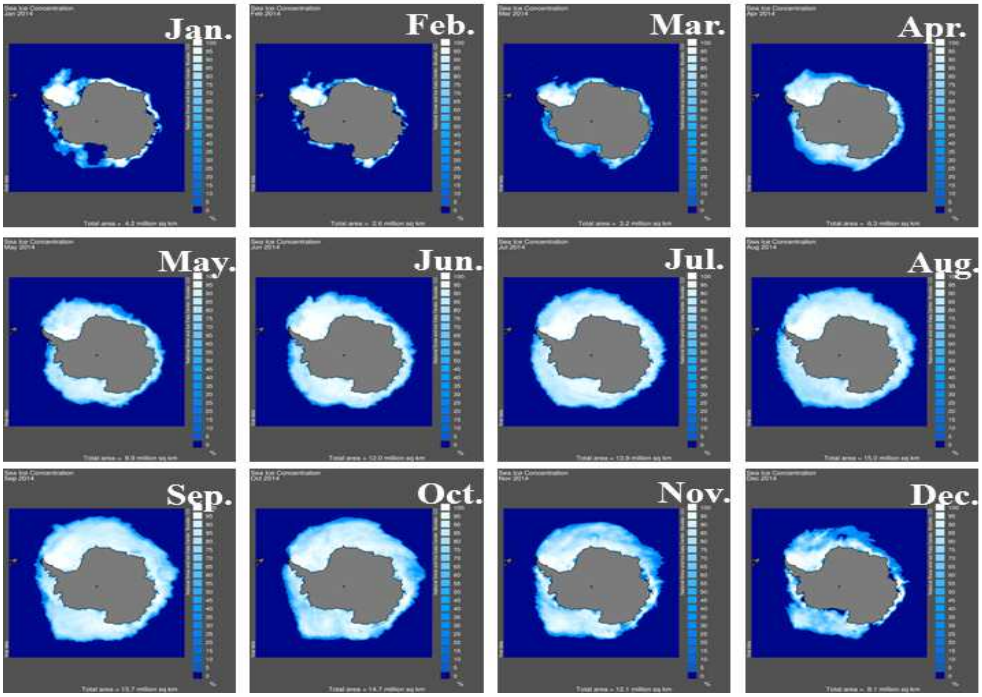

그림 3. 계절별 남극 해빙 분포 변화 (자료 출처: National Ice and Snow Data Center: http://nsidc.org/)

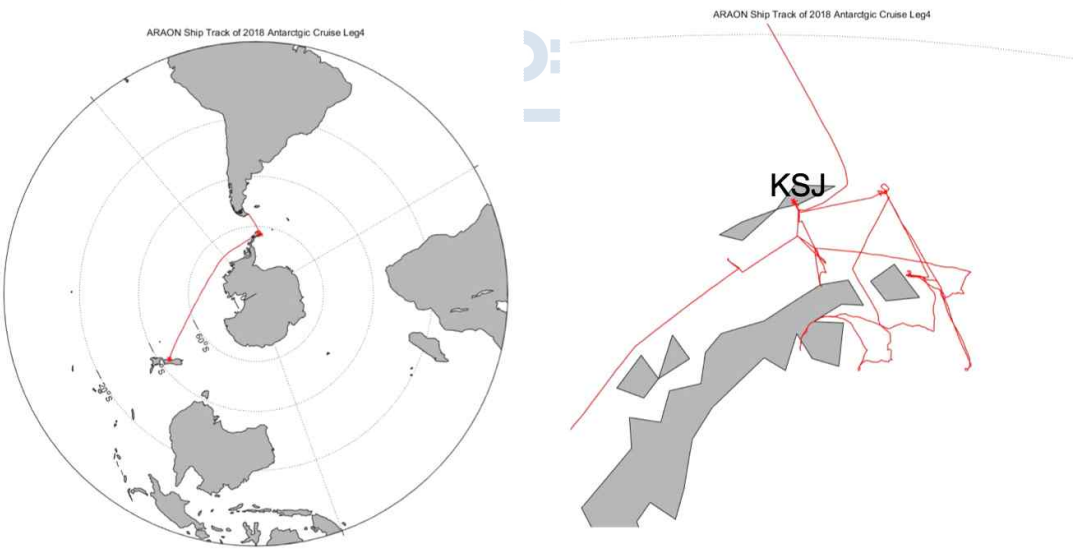

그림 4. 2018년 쇄빙연구선 아라온을 활용한 남극해 에어로졸 현장 관측 crusie track (좌: 전체 항해 기간 중 이동 경로, 우: 세종과학기지(KSJ)인근 해양 이동 경로)

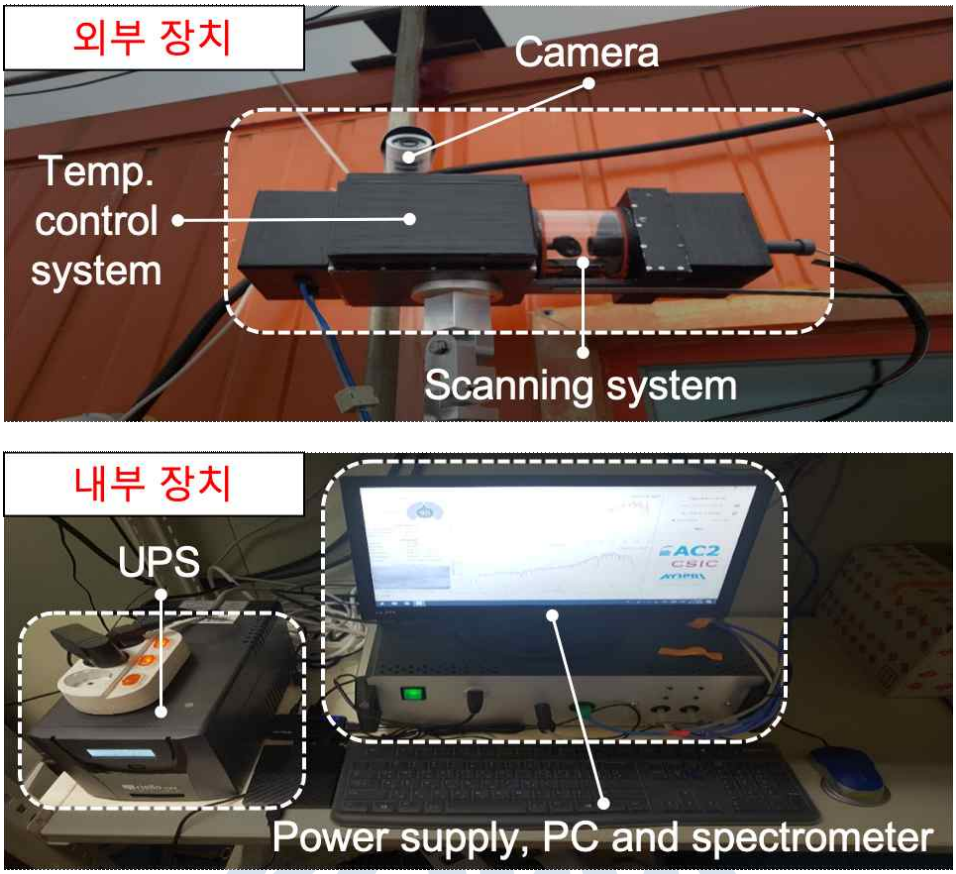

그림 5. 세종기지 대기빙하관측동에 설치된 MAS-DOAS 시스템

극지연구소

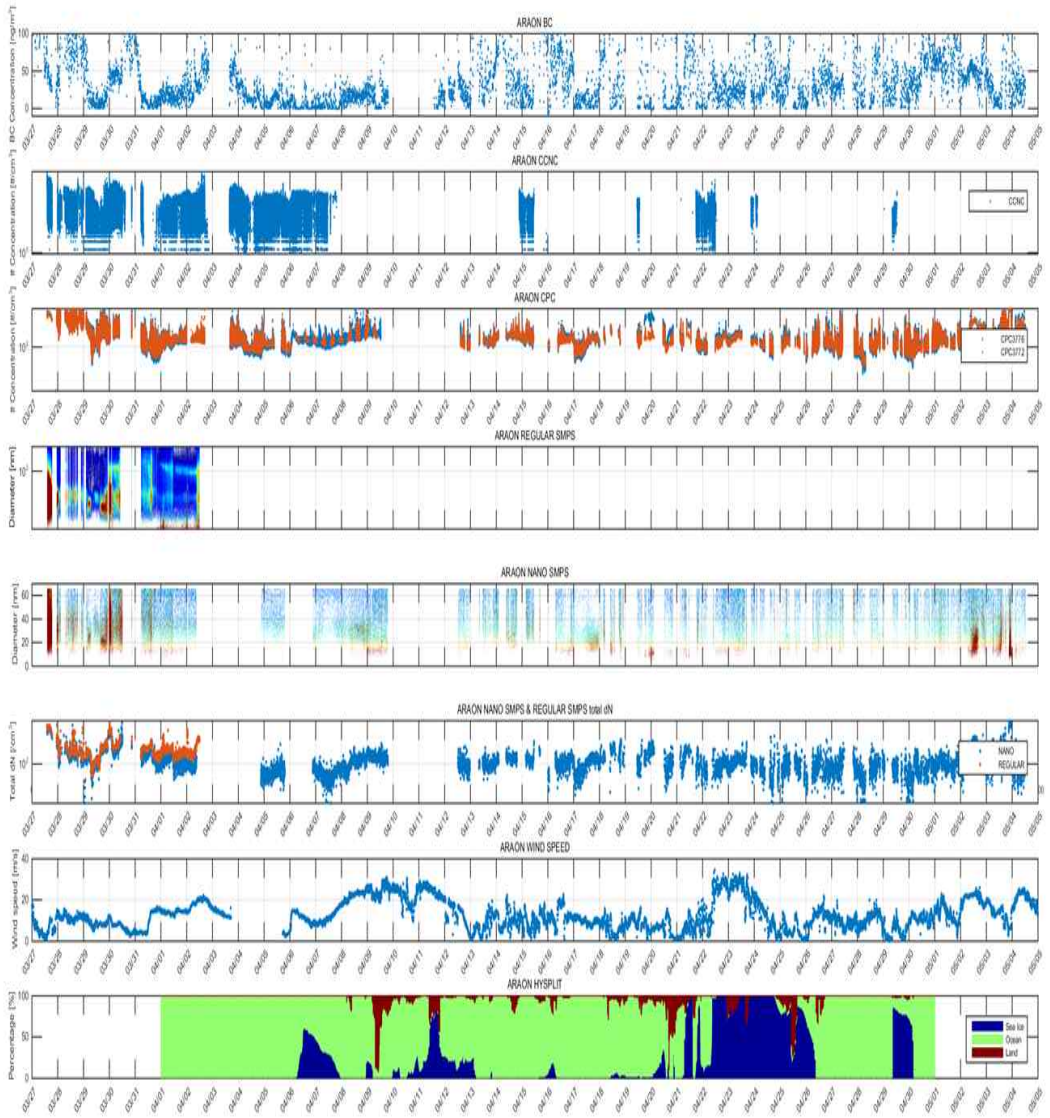

그림 6. 아라온 남극 항해 중 블랙카본 농도, 구름형성응결핵 수농도, 에어로졸 수농도, 수농도 분포곡선, 풍속, 공기역궤적 분석 결과

그림 7. MAX-DOAS 장비를 통한 대기 관측시 spectrum intensity 변화 예시

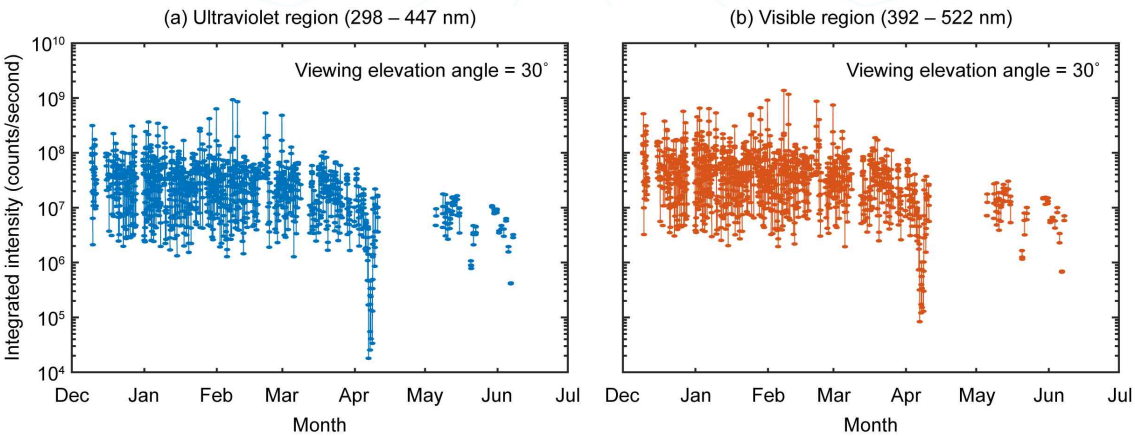

그림 8. 2018년 12월 2019년 6월까지 Max-DOAS를 활용한 대기 주요 할로겐 성분 분석을 위한 (a) 자외선 영역 (298-447 nm), (b) 가시광선 영역 (392-522 nm) 스펙트럼 intensity 시계열 변화

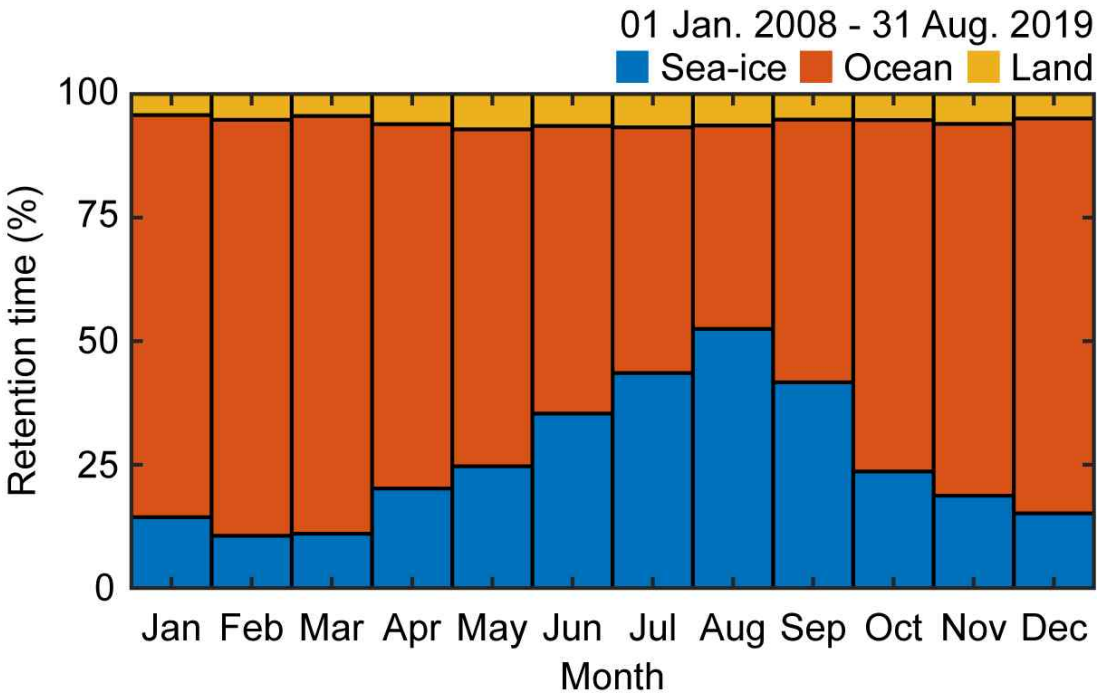

그림 9. 48시간 공기역궤적 분석을 통한, 2008년 1월 부터 2019년 8월까지 세종과학기지로 유입된 공기궤의 주요 도메인 (해빙, 해양, 육상) 체류 시간의 상대적 비율

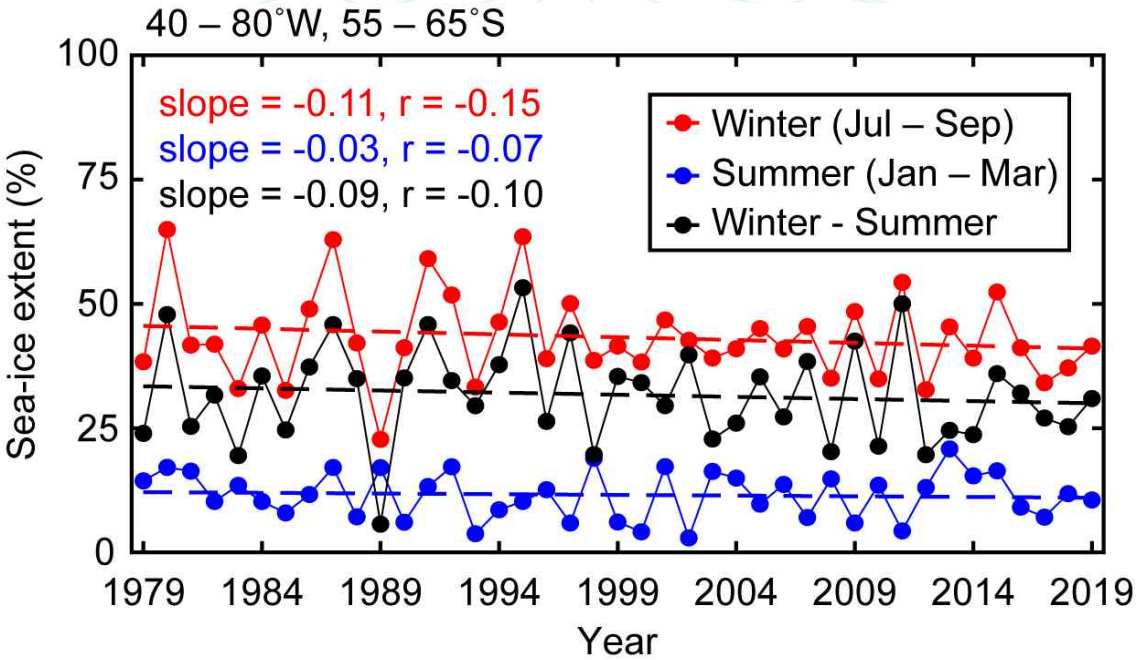

그림 10. 1979년부터 2019년까지의 계절별 세종과학기지 인근 남극해(40-80°W, 55-65°S) 해빙 면적 변화

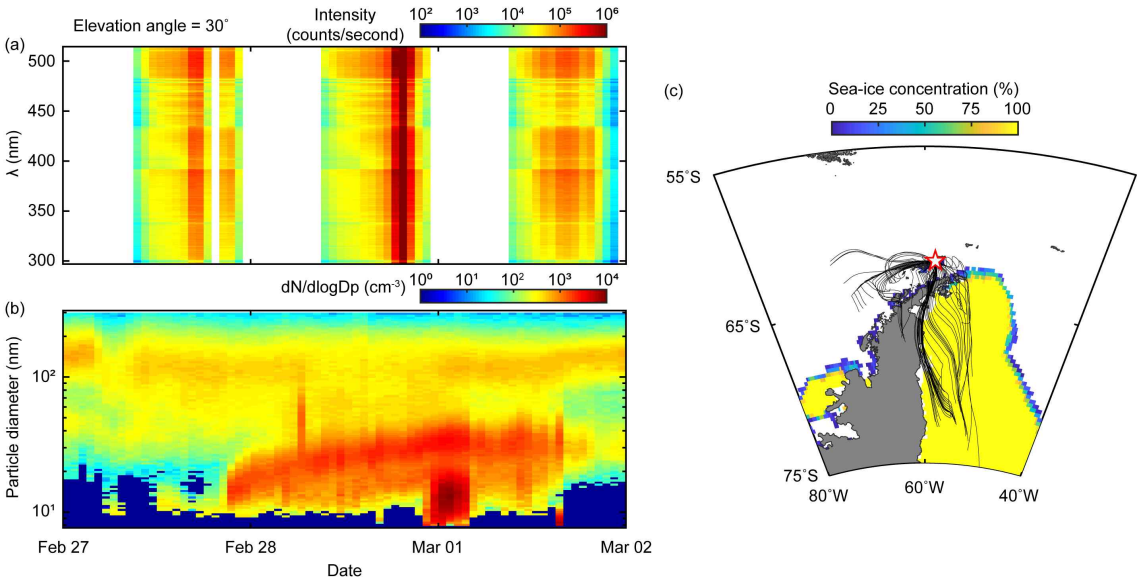

그림 11. (a) MAX-DOAS를 통해 관측한 spectrum intensity 변화, (b) SMPS를 통해 관측한 에어로졸 크기 분포별 수농도 변화, (c) HYSPLIT 모델을 활용한 세종과학기지로 유입되는 공기궤 이동 경로

KOPRI
극지연구소

제 10 절. 구름 생성관련 결빙해역 및 극지 해양의 화학적 특성 연구

박기홍

한국해양과학기술원 부설 극지연구소

1. 서론 및 배경

극지의 해양환경은 다른 온대와 열대 해양과 달리 해빙의 존재로 인하여 독특한 생지화학적인 환경이 조성이 된다. 또한 극지의 경우 광조건 또한 백야 및 극야의 존재 그리고 강한 자외선 등으로 인하여 광화학적인 반응의 조건이 다르게 형성된다. 남극해의 대기중의 브롬은 특히 해빙지역의 조류등에 의해 생성되는 것으로 알려져 있으며 이는 특히 극지에서 햇빛이 나기 시작하는 봄 시기에 집중적으로 형성되며 이들이 DMS등의 휘발성 유기 화합물과 반응하여 대기광화학 과정을 통하여 입자 (구름응결핵)를 생성하는 과정이 시작된다.

남극해에서 대기 중의 브롬은 DMS의 산화에 밀접한 영향을 주어 구름의 형성 및 알베도의 변화등 기후변동과 관련을 가지게 된다: BrO + DMS --> SO_4 or MSA (그림 1). 특히BrO는 남극의 여름철 및 겨울철에 40% 이상 DMS의 산화제로 가장 중요하게 작용하는 것으로 추정된다. 따라서, 해양 및 대기 중의 DMS를 관측함으로 브롬의 관측과 함께 남극 해빙의 변동과 얼음화학이 이들에 미치는 영향을 파악할 수가 있다. 또한 이러한 과정을 NCAR의 지구모델에 도입하고 (그림 2) 모의실험을 통하여 관측 결과를 분석하고 나아가 미래의 변동을 예측할 수 있도록 한다.

나아가, 이러한 DMS를 비롯하여 구름의 입자에 생성에 밀접한 영향을 미치는 휘발성 유기화합물등 다양한 해양-대기 경계층의 특성과 이를 조절하는 해양화학적인 인자들을 파악하기 위하여 현장관측에서는 다양한 해양변수들을 측정하였다. 그리고, 지구모델은 Community Earth System Model을 활용하여 향후 해양-해빙-대기-기후 등의 상호 작용 및 기후변화를 유기적으로 예측할 수 있는 기반을 마련하려 하였다.

2. 재료 및 방법

2.1 아라온 남극해 관측

2018년 3월 ~ 5월 쇄빙연구선 아라온호를 이용하여 남극해의 현장조사를 실시하였다. 항해기간 동안, 수온, 염분, 클로로필 등 기본적인 해양환경 변수들을 관측하였으며 해양내의 용존 DMS와 pCO_2 그리고 순군집생산력을 계산하기 위한 산소-아르곤 비를 측정하였다.

DMS는 MIMS (Membrane-Inlet Mass Spectrometry) 방법을 이용하였다 (그림 3). 이는 반투과성 막을 통해서 해수시료의 용존 기체 성분만 반대편의 사중극자 질량분석기로 주입되어 DMS를 검출기에서 검출하게 된다. 또한 본 장비로 산소-아르곤도 관측하여 그 비를

연속관측하는데 사용하였다.

용존이산화탄소는 Controls사의 Hydro-C모델의 용존이산화탄소 센서 (그림 4)를 이용하여 연속 관측하였다. 이는 항해 중 관측한 DIC와 TA를 이용하여 환산한 pCO_2의 값을 이용하여 보정하여 사용하였다. 이는 보조펌프를 통해 연속으로 흐르는 표층 해수를 끌어들여 반투과성 막을 통과하고, 센서의 내부의 비분산적외선 분석장비로 추출된 용존기체가 보내어진다. 그 다음, 디텍터에서는 용존이산화탄소의 양에 따라 감소되는 적외선을 강도를 농도로 환산하게 된다.

2.2 CESM 모델링

CESM 모델을 활용한 연구는 다음과 같은 방법으로 진행 되었다. 먼저 CESM1의 Large Ensemble (CESM-LE)의 결과를 이용하여 기존의 DMS 모델링의 결과를 분석하고 이에 따른 지금까지의 모델의 문제점을 분석하였다. 그 결과 DMS와 관련된 일련의 화학반응들이 현재 모델에서는 상당히 단순하게 모사되어 있어, 그 부정확도를 개선하기 위해서는 먼저 모델에 DMS와 관련된 화학반응들을 추가하고 그 결과를 관측과 비교하여 개선하는 작업이 필요하다 판단하였다. 또한 극지해양에서의 DMS의 배출량 또한 현재 많은 오차를 가지고 큰 변동성을 기반으로 산정되어 있다. 이에, 더욱 정확한 DMS의 배출량을 얻기 위하여 최적의 배출량 데이터세트를 찾는 작업도 수행할 필요가 있었다.

3. 연구결과

3.1 남극해 관측 결과

그림 5에서 항해기간동안 항로를 따라 연속으로 관측된 관측 자료들을 보였다. 특히 남극반도 부근해역에서 관측된 높은 염도, 낮은 순군집 생산, 그리고 높은 DIC와 TA는 다른 해역과 남극반도 부근이 다른 수괴의 영향을 받고 있음을 간접적으로 알 수 있었다. 반면 이 지역의 강한 바람은 활발한 해양과 대기의 기체교환이 일어날 수 있음을 의미하여, 낮은 농도의 용존 기체라도 입자형성에 중요한 기여을 할 수 있음을 시사하고 있다.

남극항해 기간동안 할로겐 물질과 반응하여 구름응결핵으로 작용하는 해수중의 DMS의 농도를 mmbrane inlet mass spectrometer (MIMS)를 이용하여 연속관측하였다. 항해 지역에서의 DMS의 농도는 전체적으로 10nM 이하의 낮은 농도로 관측되었다. 또한, 남극항해 기간동안 해양에서의 순군집 생산량 (net community production: NCP)을 산소와 아르곤의 비율을 통해 추정하였다. 관측은 MIMS를 통해 이루어 졌으며 항해기간동안 대부분의 지역에서 0에 가깝거나 음의 값을 보였다. 따라서 생물의 활동에 의한 기체교환은 극히 적거나 호흡에 의한 과정이 우세한 것으로 나타났다.

공간분포에서 DMS의 농도는 marginal ice zone에서 상대적으로 높아지는 경향이 보였다. 또한 생산력 또한 같은 경향을 보였다. 따라서 아문젠의 외해역과 남극반도의 지역을 항해시가 벨링스하우젠해와 남극 반도의 좌측을 항해할 때 보다 높은 값들을 보였다. 이는 해빙생태계로부터 일어나는 생명현상과 밀접함을 보이며 또한 이 지역에서 DMS와 할로겐등의 화학 작용등이 활발하게 일어날 수 있음을 의미한다.

또한, 해양의 생산을 나타내는 또다른 인자인 용존이산화탄소의 값은 DIC, TA를 이용해 보정한 값과 센서의 값이 그림 6에서 보는 바와같이 거의 1:1의 비를 나타내며 그 상관성 또한 상당히 견고하다. 따라서, 이러한 pCO_2 센서의 사용으로 아라온의 접근이 어려운 지역의 이산화탄소를 신뢰할 수 있는 센서로 대신하여 측정할 수 있는 가능성을 보였다.

3.2 CESM을 이용한 DMS 모델링

미국의 National Center for Atmospheric Research의 주도로 개발된 지구시스템 모델을 이용하여 대기중의 DMS의 분포를 모사하였다. 현재 모델은 더욱 정교한 모델의 결과를 위하여 DMS의 대기중에서의 화학반응을 추가하는 등의 개선 작업에 있다. 차후 관측된 DMS 자료의 해석 및 변동의 원인 규명, 나아가 기후변화와의 연관성 등에 관한 연구에 활용될 수 있다.

CESM에서 현재 사용되는 DMS의 기존의 이미션 인벤토리대신 최신의 Lana 2011년 논문의 이미션 인벤토리를 적용하기 위해 DMS의 해양의 농도의 climatology를 구하고 이를 남극 지방에 적용하기 위한 준비를 하였다 (그림 8).

마지막으로, 그림 9는 기존의 CESM2에 DMS로부터의 MSA 생성 및 그 비율을 추가하는 민감도 실험의 일부로, 기존의 MSA 관측값과 모델의 값을 비교하였다. 현재 아직까지 대부분의 지역에서 모델이 관측 보다 낮은 값을 보이고 있다. 하지만 DMS로부터의 MSA 생성비율을 늘이는 경우 조금 더 관측치에 가까운 결과를 보여준다. 하지만 전체적인 농도의 공간적 분포 및 월별 변동은 대략적인 수준에서만 일치하고 있다. 따라서 더욱 더 면밀히 모델을 검토할 필요가 있다.

4. 결론

DMS 뿐만 아니라 극지 대기의 산화력을 결정하는 휘발성유기화합물 성분은 그 양의 분포조차 극히 관측이 적다. 따라서 이러한 관측의 결과들은 차후 기후변화와 남극의 환경 변화의 예측에 있어 중요한 배경 자료로 사용될 것으로 믿는다.

아라온을 활용한 결빙해역의 관측은 얼음화학의 측면에서, 특히 그 광화학적 특성이나 식물플랑크톤의 번성시기 등의 해양생지화학적인 환경 조건을 고려할 때 남극의 봄철이 가장 중요하며 의미 있는 시기이다. 하지만 여건상 가을 시기에 남극해를 관측할 수밖에 없었다. 얼음 관련된 화학으로 초점을 맞추어 연구를 처음 하여 기본적인 연구기반의 확립 등을 이룰 수 있었으며, 차후 최적의 여건에 다시 관측하면 의미 있는 결과를 다수 도출 할 수 있으리라 본다.

KOPRI 극지연구소

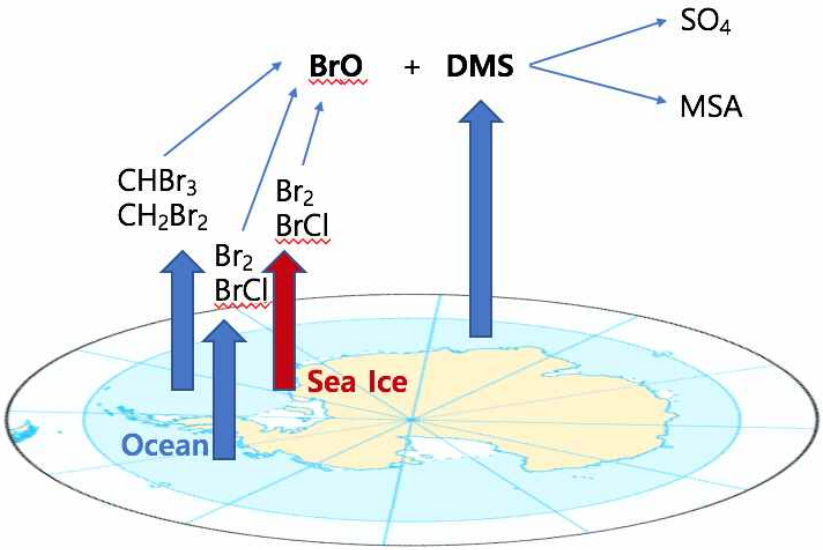

그림 1. 남극의 얼음과 해양에서 배출되는 할로겐물질과 DMS가 반응하여 구름입자를 형성하는 과정의 개요도

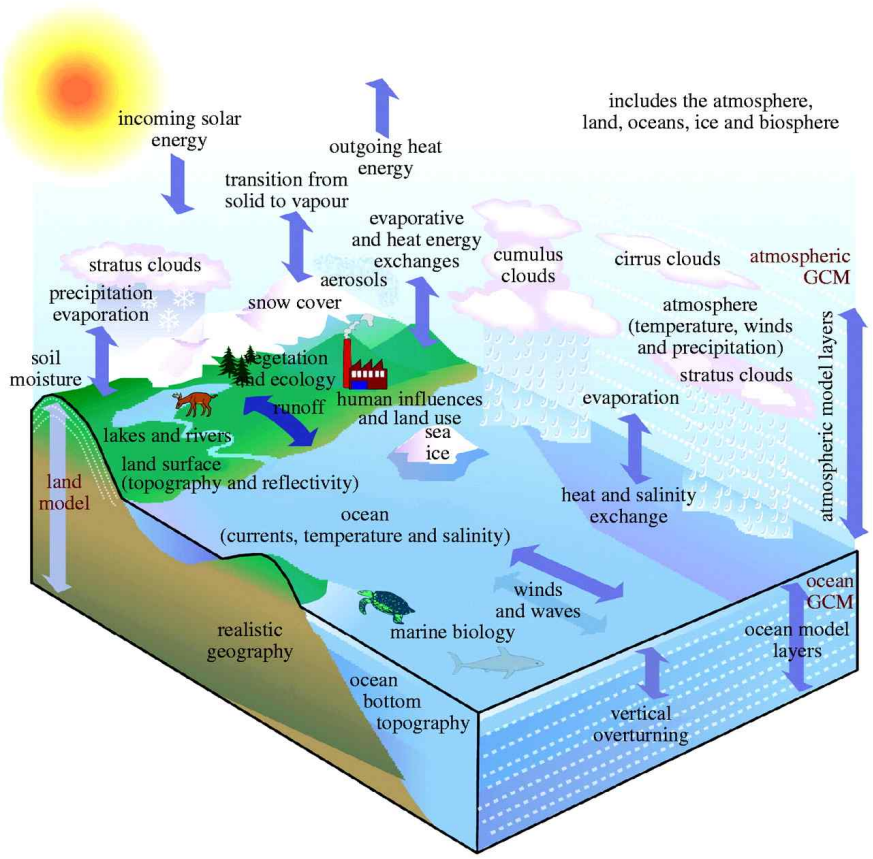

그림 2. 지구모델인 CESM이 개요도. 지구의 기후관련 모든 현상을 모사하므로 우리가 관측한 현상을 분석하고 나아가 기후변화와의 상관을 모의할 수 있음.

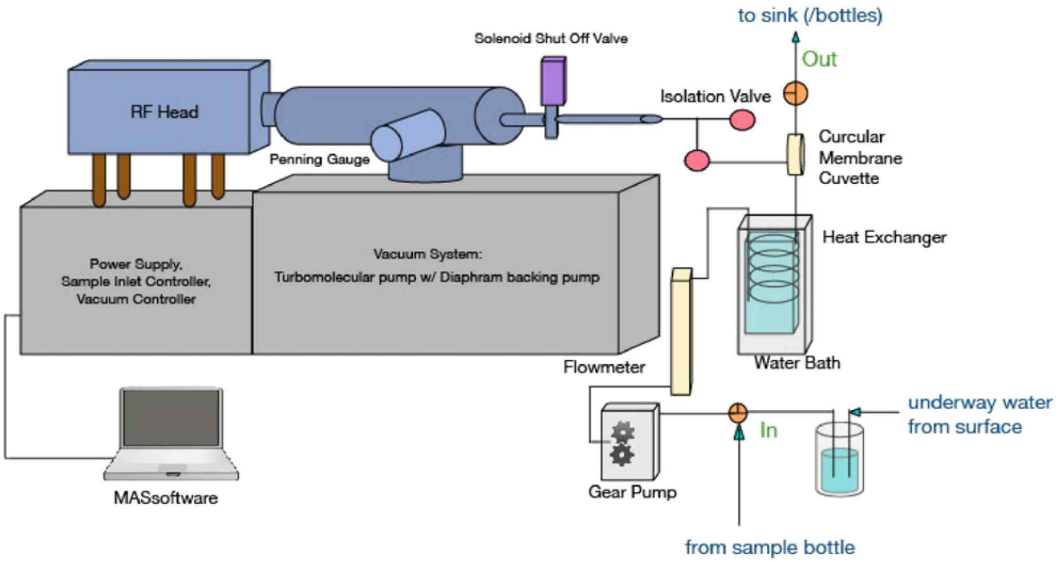

그림 3. 아라온호의 현장관측에서 용존 DMS의 연속관측을 위해 사용된 MIMS 시스템의 개요도

그림 4. 아라온의 현장관측에 사용된 pCO2 센서

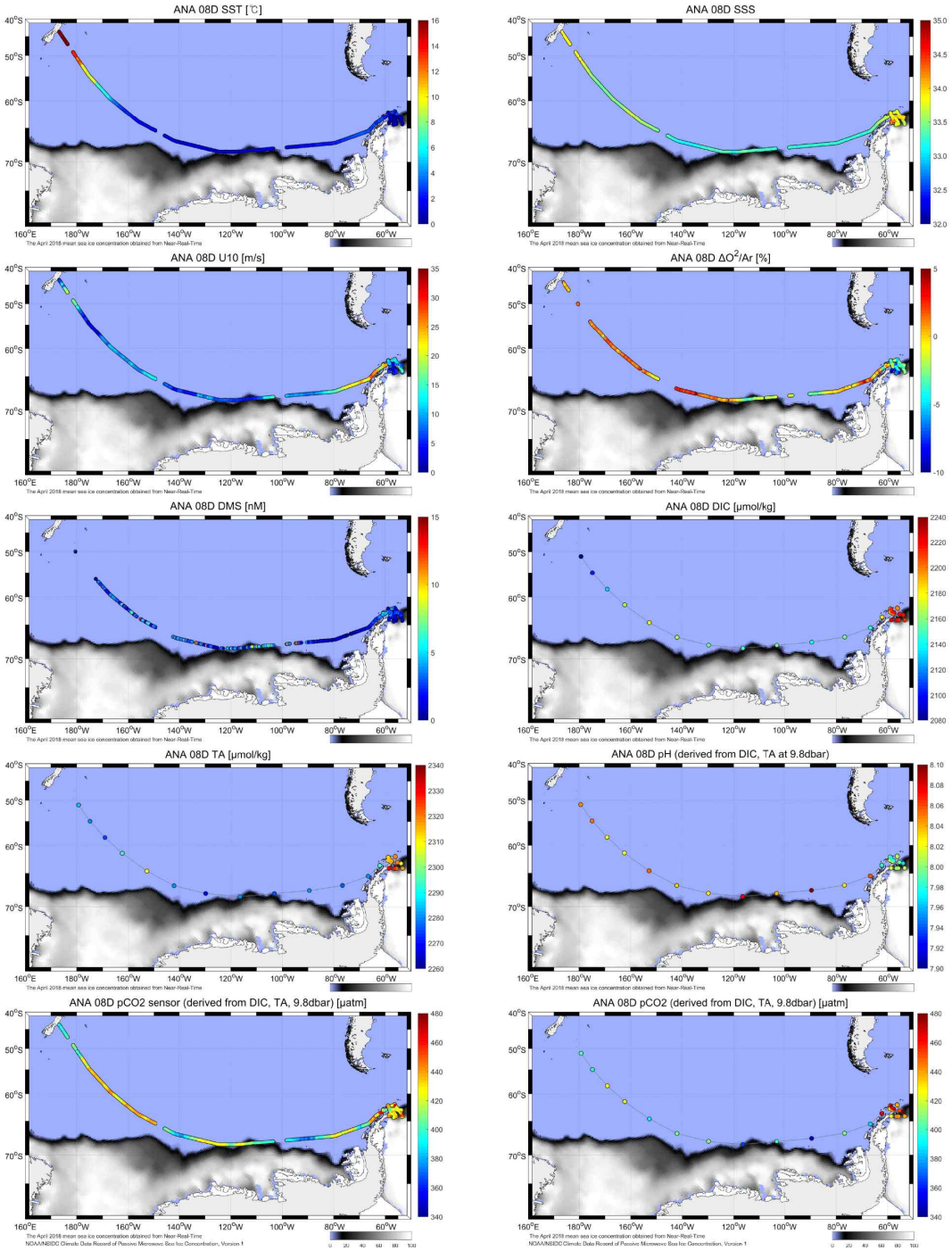

그림 5. 아라온에서 연속 관측한 수온, 염분, 풍속, 산소-아르곤비, DMS, DIC, TA, 그리고 pCO2이다. 그림에서 pH와 pCO2는 DIC와 TA로부터 계산한 값이다.

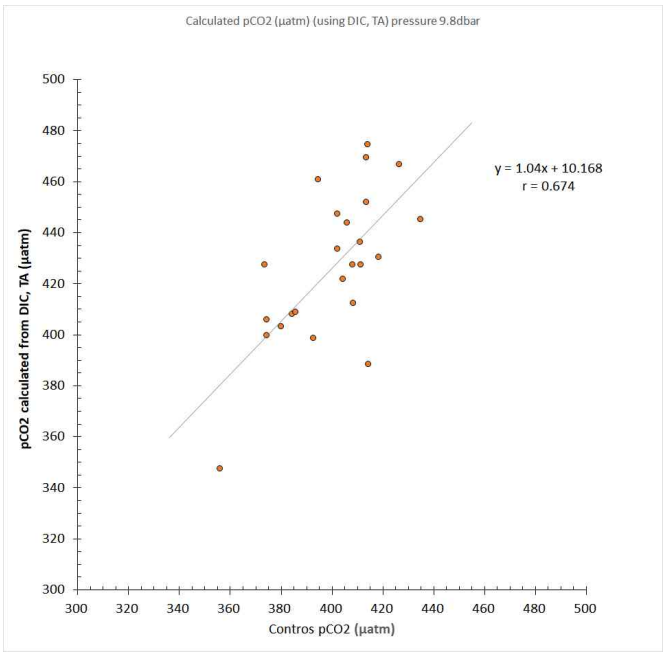

그림 6. pCO_2센서를 통해 관측한 용존이산화탄소의 농도 (x 축)과 DIC와 TA를 통해 계산한 pCO_2값 (y 축)의 비교.

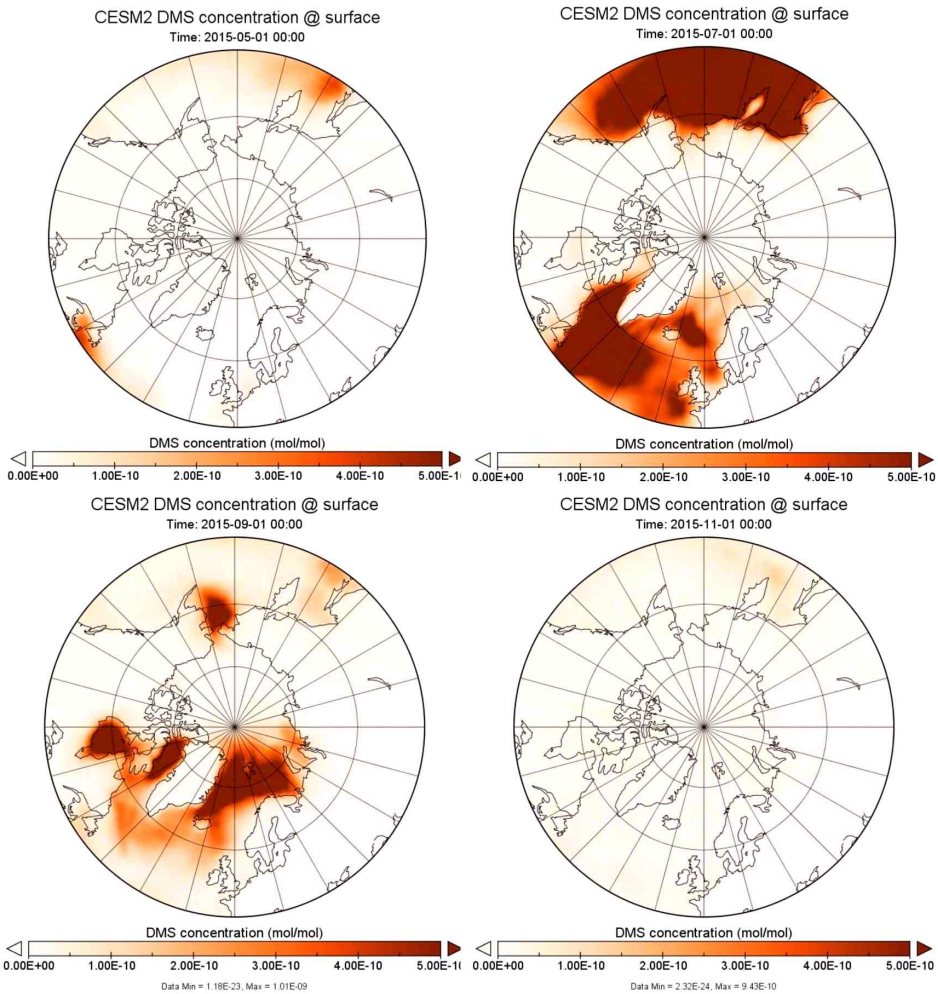

그림 7. CESM2를 활용하여 모사한 2015년 5월, 7월, 9월 및 11월의 DMS의 표층에서의 분포.

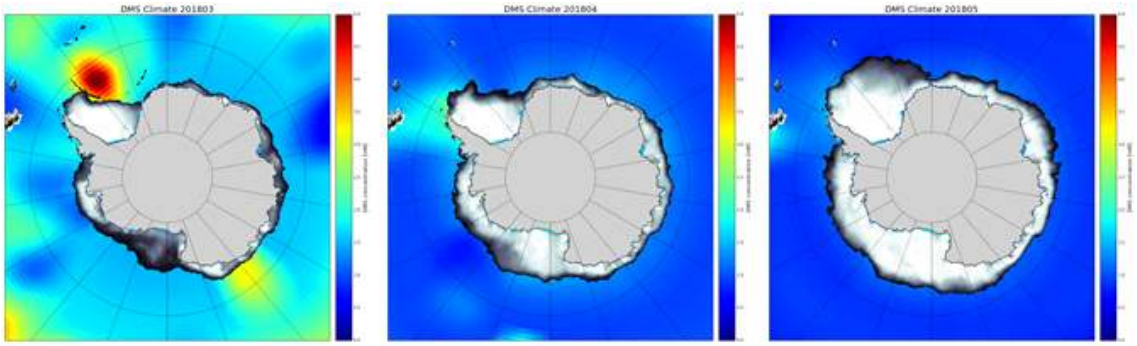

그림 8. Lana et al. (2011)의 해수중 DMS 농도의 climatology data와 2018년 항해자료를 분석하기 위해 2018년 3월(좌), 4월(중), 5월(우)의 해빙 농도와 함께 그린 그림. 남극 반도 및 웨델해 지역에서 4월까지 상대적으로 높은 농도의 DMS가 유지 되는 것을 알 수 있다.

KOPRI

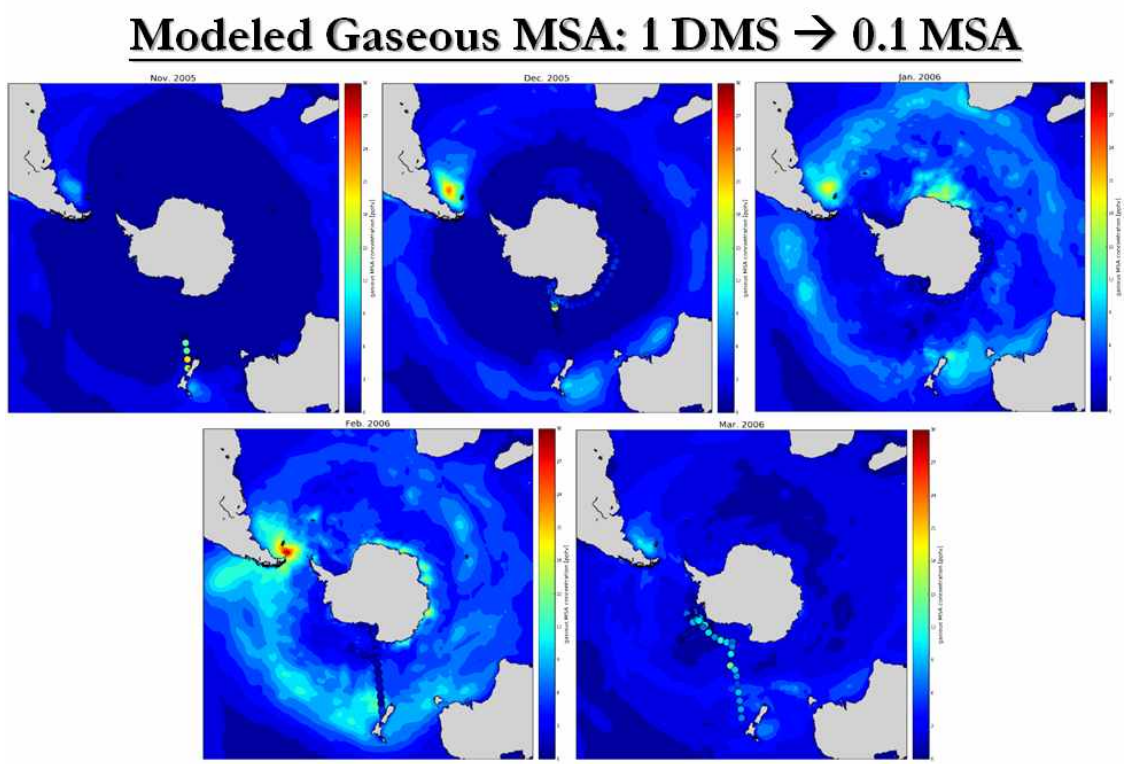

그림 9. CESM2의 모델에 DMS에서 MSA로의 산화비율을 최적화하기 위한 민감도 테스트의 그림. 중국 설룡호에서 관측한 MSA의 결과와 모델의 결과를 비교하였다.

제 11 절. Climatic Factors and Their Robust Evidences Controlling Phytoplankton biomass in the Bransfield Strait[6)]

Hyoung Sul La[1], Keyhong Park[1*], Jeong Yeob Chae[1,2], Taewook Park[1], Jisoo Park[1]

[1]Korea Polar Research Institute
[2]Department of Ocean Sciences, Inha University

1. Introduction

The Antarctic Peninsula is the most rapidly changing region in the Southern Hemisphere, with a rise in atmospheric and ocean surface temperatures, and glacier retreat and thinning (Meredith and King, 2005). The rapid environmental changes on the Antarctic Peninsula have resulted in changes in the adjacent marine ecosystem. The species and population distribution of marine organisms in this region have shown extreme sensitivity to the physical ocean environment (Peck et al., 2004). Biological productivity, inferred from phytoplankton biomass during summertime has significantly declined by 12% along the western shelf of the Antarctic Peninsula over the last 30 years with rapid regional climate change, which could impact the population of higher trophic levels, such as that of krill and penguins (Montes-Hugo et al., 2009).

The Bransfield Strait and adjacent waters west of the Antarctic Peninsula are one of the most productive areas in the Southern Ocean (Comiso et al., 1990; Sullivan et al., 1993). Previous studies reported the role of phytoplankton (Arrigo et al., 1999) and water-column stratification for nutrient supply in ocean biological cycles (Platt et al., 2003a, b). Phytoplankton blooms in the Southern Ocean are frequently controlled by hydrographic features such as fronts (Laubscher et al., 1993), eddies (Heywood and Priddle, 1987), upper mixed layer depths (Loeb et al., 2010; Gonçalves-Araujo et al., 2015), and the seasonal sea ice extent and retreat (Smith et al., 1998). Spatial and temporal variation of phytoplankton distribution has often compared with complex water column structures (Basterretxea and Aristegui, 1999). Additionally, a recent study suggested cloud cover influences phytoplankton biomass in the Southern Ocean (La and Park, 2016). Long-term variation in phytoplankton biomass could be driven by climate change, such as the Southern Annular Mode (SAM) and El Niño-Southern Oscillation (ENSO), since plankton ecosystems are

6) 이 연구는 본 과제 및 PE19060, PE19070 지원으로 수행되었으며 그 결과는 다음의 논문으로 출판되었음: Hyoung Sul La, Keyhong Park, Jeong Yeob Chae, Taewook Park, and Jisoo Park, “Climatic Factors and Their Robust Evidences Controlling Phytoplankton biomass in the Bransfield Strait”, *Terr. Atmos. Ocean. Sci.* 2019, 30, 821-830.

associated with sea ice change and water column stability (Vernet et al., 2008; Venables et al., 2013). Plankton biomass near the northern Antarctic Peninsula has been controlled by fluctuations in ENSO of the southern frontal zone of the Antarctic Circumpolar Current (Loeb et al., 2009). Interpreting the long-term trends of plankton ecosystems requires an understanding of the link between biological and environmental systems. Because phytoplankton biomass has undergone a significant long-term change since the 1970s (Kim et al., 2018), it is necessary to update the previous studies with the recent and longer term environmental and climatic data sets to understand the complexity of phytoplankton biomass variation in the Southern Ocean region.

In the present study, we examined the long-term variability of the phytoplankton biomass in the Bransfield Strait to verify its correlation with climatic and environmental factors. The interannual variability of phytoplankton biomass over the defined Bransfield Strait was assessed by comparing oceanic variables (sea surface temperature (SST) and sea ice concentration (SIC)), climatic variables (SAM, ENSO), and atmospheric variables (cloud fraction, wind speed, and photosynthetically active radiation (PAR)) during the last 12 austral summer periods (2002 - 2014).

2. Methods

2.1. Study region

The Bransfield Strait is a semi-enclosed basin (Bárcena et al., 2002), located between the South Shetland Islands and the Antarctic Peninsula in the Southern Ocean (Fig. 1). The Bransfield Strait is composed of three deep basins (western, central, and eastern basins), which are distinguished from each other by 500 m deep sills (Gordon et al., 2000). The western basin is relatively shallower than the other two basins; the western basin reaches about 1000 m, the central basin reaches about 2000 m, the eastern basin reaches about 2500 m. The Bransfield Strait is characterized by a complex hydrographic structure and a potential of high primary production during austral spring and summer (Gordon et al., 2000; Bölter et al., 1988). In order to assess the relative differences in chlorophyll *a* (Chl-*a*) concentrations between sub-regions, the study area was divided into a central and an eastern basin, as presented in Gordon et al. (2000). The central basin includes coastal water along the Antarctic Peninsula Shelf and the eastern basin includes both coastal water and oceanic waters in the Weddell Sea (Marrari et al., 2008).

2.2. Chl-*a* concentrations

Surface Chl-*a* concentrations were obtained from Moderate-Resolution Imaging Spectroradiometer (MODIS) chlorophyll satellite data from NASA Ocean Biology website for the period from January 2002 to December 2014 (http://oceandata.sci.gsfc.nasa.gov).

Chl-*a* is the main photosynthetic pigment, and thus can be used to represent phytoplankton biomass and primary productivity (Zhang et al., 2014). MODIS Aqua Level 3 monthly averaged data at a 4-km spatial resolution was used for only seven months (October - April) per year because of the limitation of ocean color data in the Southern Ocean. Additionally, because the Bransfield Strait is divided into two regions which are central and eastern basin, we took a look the difference of Chl-*a* variation trend in the two basins (Fig. 2). A time series analysis of monthly averaged Chl-*a* showed that there were no significant seasonal and/or interannual differences between the eastern and central basins of Bransfield Strait. Climatological monthly average of Chl-*a* between 2003 and 2015 also showed no significant regional differences within one standard deviation between two regions (Supplementary Fig. 1). Therefore, we assumed the variation of Chl-*a* biomass in the entire the Bransfield Strait is under the one marine system and, in this study, we used the averaged Chl-*a* from the both basins.

2.3. Oceanographic parameters

Monthly averaged sea ice concentration (SIC) was retrieved from the National Oceanic and Atmospheric Administration (NOAA)/National Snow and Ice Data Center (NSIDC) with nominal 25 km × 25 km grid cells in the study region (http://nsidc.org/data/G02202). Monthly averaged SST was provided by a daily Group for High-Resolution SST (GHRSST) Level 4 with a spatial resolution of 0.2 degrees (https://podaac.jpl.nasa.gov/dataset) (Supplementary Fig. 2).

2.4. Climatic and atmospheric indices

To investigate the climate effect on Chl-*a* biomass, we used two climatic indices: the Oceanic Niño Index (ONI) for ENSO and SAM. The monthly SAM index was available on the BAS website (http://www.nerc-bas.ac.uk/icd/gjma/sam.html), which was based on the methodology in Marshall (2003). The ONI was obtained from the Climate Prediction Center (CPC, http://www.cpc.ncep.noaa.gov).

Cloud fraction and PAR were retrieved from the European Centre for Medium-Range Weather Forecasts (ECMWF) ERA-Interim reanalysis (Dee et al., 2011). ERA-Interim shows a good performance for solar radiation and cloud fraction among the current representative global reanalysis (Zhang et al., 2016). The horizontal resolution was 0.75° × 0.75°, and each parameter was calculated for the monthly mean over this study's pre-defined Bransfield Strait (Fig. 1). Based on the atmospheric pressure, 122 heights of cloud fraction data were defined as low-level (1 - 0.8 sigma; *sigma* = 123 *pressure/surface pressure*), mid-level (0.8 - 0.45 sigma), and high-level (< 0.45 sigma) cloud in the ERA-Interim (Supplementary Fig. 2).

3. Results and discussion

Climatology patterns of the monthly Chl-*a* concentration from July 2002 through December 2014 indicated that the Bransfield Strait had persistently enhanced Chl-*a* during late spring through early fall with high spatio-temporal variability; high standard deviation, especially in February and March (Fig. 2). Chl-*a* in the Bransfield Strait began to increase from November, and blooms continued from December to March. Phytoplankton blooms exceeding 5.0 mg m^{-3} occurred during February and March and rapidly decreased in April. The spatial and temporal changes in Chl-*a* indicate that phytoplankton biomass accumulations initially occurred during November around the South Shetland Islands and Elephant Island. As the season progressed, phytoplankton blooms developed in the northern area of the South Shetland Islands from January and February (Fig. 2a). On the other hand, the phytoplankton blooms in the Bransfield Strait intensified in February and remained until to March. These could be associated with the timing of sea-ice extent retreat, which began to decrease around October and was at a minimum in February (Park et al., 2010).

The seasonal and interannual variability in the monthly Chl-*a* concentration within the study region is clearly shown in Figs. 3 and 4. Chl-*a* was highly variable over the period investigated, but phytoplankton blooms occurred consistently between November and March each year. The strength of phytoplankton blooms during austral summers showed clear interannual variability from the January, February, and March (hereafter as JFM) mean Chl-*a* over the 12-year period investigated (Fig. 3). High phytoplankton biomass > 1 mg m^{-3} occurred during 2006, 2011, and 2012, whereas low phytoplankton biomass < 0.5 mg m^{-3} occurred during 2003, 2004, 2010, and 2014. An intense bloom with a mean Chl-*a* concentration of 1.2 mg m^{-3} appeared in 2011.

The phytoplankton biomass seemed to strongly respond to certain trends in climate variability. The annual cycles of phytoplankton fluctuations have also been associated with variability in vertical stratification, wind mixing, macronutrient amounts, sea ice concentration, and solar irradiance for phytoplankton growth (Smith et al., 2000). To examine the interannual variability of phytoplankton biomass with variations of climatic variables, we analyzed the Pearson correlation between the mean Chl-*a* concentration (JFM) and climatic indices (ONI and SAM) with a time lag (0 - 6 months) (Supplementary Fig. 3 and Table 1).

The phytoplankton biomass showed a significant correlation ($p < 0.05$) with 2 - 6 months lagged ONI, and the maximum correlation was obtained with a 4-month lagged ONI (r = -0.65), whereas it showed an obviously weak and insignificant correlation with SAM (r_{max} = 0.51, p = 0.09 with a 4-month lag). In general, the influence of SAM is stronger than ENSO in the Southern Ocean climate variability. However, because the

Antarctic Peninsula is located in between the Amundsen – Bellingshausen Sea and Weddell Sea and in relatively lower latitude, the region is under the complex climate system including the Amundsen low, which influenced by ENSO and SAM in tandem (Clem et al., 2016; Clem et al., 2017). The result in this study indicates ENSO is more essential driver of climate variability.

Thus, the phytoplankton biomass was negatively correlated with ENSO; moreover, the high phytoplankton biomass within Bransfield Strait was associated with a strong La Niña period (Supplementary Fig. 3b). Smith *et al.* (2008) also observed that a high Chl-*a* biomass offshore in the western Antarctic Peninsula region was associated with La Niña.

Phytoplankton biomass closely varied with some environmental factors as well. Chl-*a* (JFM) exhibited a strong correlation with SST (r = 0.7, $p < 0.05$) and wind speed (r = 0.72, $p < 0.05$) within a 0- and 3-month lag, respectively (Fig. 5). The variation of SST and phytoplankton biomass could be directly caused by ENSO (Zhang et al., 2014), and SST is one of the main factors controlling phytoplankton biomass (Behrenfeld and Falkowski, 1997). As the southern westerly winds drive the Antarctic Circumpolar Current (ACC) around Antarctica, deep waters are forced up to the surface south of the polar front. The westerly winds around the Antarctic continent result in an upwelling region, the Antarctic Divergence at the Southern Front, which is considered to be the Antarctic Circumpolar Current Southern Boundary (ACCSB). The ACCSB is at approximately 65º S (Orsi et al., 1995) moving northward to 55º S. During La Niña the wind strengthens, driving warm, wet storms south across the Southern Ocean, which reduce the sea ice extent along the West Antarctic Peninsula. La Niña drives enhanced upwelling in this region (Martinson et al., 2008). Moreover, a strengthened westerly wind can lead to an increase in the upwelling of subsurface water during austral summer (Purich et al., 2016). Since deep mixing of the Antarctic Surface Water (AASW) occurs during winter months, changes in the intensity with which this relatively warm, nutrient-rich, and CO_2-enriched Circumpolar Deep Water upwells has significant implications for primary productivity (Deppeler and Davidson, 2017) during phytoplankton blooming season. Upwelled nutrient-rich water would fertilize the phytoplankton blooms. Enhanced phytoplankton blooms in surface waters have also been linked with upwelling of iron-rich shelf bottom water (Trimborn et al., 2015).

Furthermore, we performed time lag correlation analyses with other environmental variables influencing Chl-*a* as well, which includes SIC, PAR, and cloud cover (Supplementary Fig. 3). However, no pronounced relationships were observed among these variables with Chl-*a* in the Bransfield Strait. In contrast to La and Park (2016) who presented robust correlations between cloud cover, cloud height, or PAR with Chl-*a* in the Antarctic coastal polynyas, the weak correlations in the present study implied that light

condition is not a key limiting factor for chlorophyll in the Bransfield Strait. Note that the response of Chl-*a* to the high cloud fraction was opposite to the middle and low cloud fractions, albeit their moderate to weak correlations (Supplementary Fig. 3 (h) - (j)). The increase in high cloud cover enhanced Chl-*a*, and the increase in middle or low cloud cover reduced Chl-*a*. This implies a different role of cloud height to the Chl-*a* variation, as well as the complex influence of future cloud cover change associated with climate change (Nazarenko et al., 2015) to the Chl-*a* biomass level. Additionally, the weak correlation between Chl-*a* and SIC (r_{max} = -0.39, p = 0.21 with a 3-month lag) indicated that sea ice-related nutrient or iron release (Wang et al., 2014) was not directly linked to Chl-*a* in this region.

Therefore, we selected the 4-month lagged ONI, 0-month lagged SST, and 3-month lagged wind speed, that exhibited the most robust correlation with Chl-*a*, as the main environmental drivers to the phytoplankton biomass in the Bransfield Strait region (Fig. 5).

We investigated to find a possibility of using these three variables (SST, ONI, and wind speed (WS)) to predict Chl-*a,* since the variation of these factors occurred 0 - 4 months preceding the Chl-*a* change. Assuming Chl-*a* can be estimated by SST, ONI, and WS, and each variable has a linear relationship with Chl-*a* (Eq. (1)), we performed multiple multivariable linear regression analyses.

$$CHL = f(SST, ONI, WS) \tag{1}$$

where SST, ONI, WS denoted 0-, 4-, and 3- month lagged variables.

Each multivariable regression was performed based on the Jackknife sampling which is selecting twelve 11-year data sets (Chl-*a*, SST, ONI, and WS) out of the 12-year data sets (2003 - 2014), and then the coefficients of the multivariable regression curves were calculated by Eq. (2).

$$\hat{\mathbf{b}} = (\boldsymbol{X}'\boldsymbol{X})^{-1}\boldsymbol{X}'\boldsymbol{Y} \tag{2}$$

where n is the number of years used for the regression (n = 11) and

$$\mathbf{b} = \begin{bmatrix} b_0 \\ b_1 \\ b_2 \\ b_3 \end{bmatrix}, \boldsymbol{X} = \begin{bmatrix} 1 & SST_1 & ONI_1 & WS_1 \\ \vdots & \vdots & \vdots & \vdots \\ 1 & SST_n & ONI_n & WS_n \end{bmatrix} \text{ and } \boldsymbol{Y} = \begin{bmatrix} CHL_1 \\ \vdots \\ CHL_n \end{bmatrix}$$

We set aside one-year data set to evaluate the predictability of the empirical multivariable regression. The regression result (Eq. (2)) is applied to estimate the Chl-*a* of the remaining year using the Eq. (3) and repeated for all 12 years.

$$\widehat{CHL_t} = b_0 + b_1(SST_t) + b_2(ONI_t) + b_3(WS_t) \quad (3)$$

where t denotes a year selected for evaluation and is the predicted Chl-*a* derived from the multivariable regression analysis.

In Fig. 6 the predicted mean JFM Chl-*a* values were compared to the Chl-*a* retrieved from the satellite. The predicted values showed a strong positive correlation (r = 0.71, $p < 0.01$) with the observation, and thus implied that SST, ONI, and WS are variables closely associated with Chl-*a* in the Bransfield Strait. In addition, this suggests that the three variables could be used to predict the Chl-*a* level across environments similar to ones found in the Bransfield Strait. In fact, the robust relationship in Fig. 6 was noticeable during the low Chl-*a* years, whereas the regressions underestimated the high Chl-*a* years.

4. Discussion and Conclusion

We performed the same multivariable regression analyses for 2003 - 2015 and 2003 - 2016 (supplementary Fig. 4). Extrapolating until 2015 exhibited almost identical results to the estimates presented in Fig. 6. However, once the 2016 data sets are added in the analysis, the correlation between the model estimates and true values reduced to r = 0.71 to 0.58. An ONI index applied for 2016's estimate is 2.33 while the mean ONI index between 2003 and 2014 is 0.04 ± 0.81. Therefore, different to the previous 12 years, the 2016's result was presumably affected by the extraordinary strong El Niño, and thus the phytoplankton biomass estimate was limited by the description of current model. This also suggests that more robust estimates will be able to acquire by accumulating input data sets with extended time periods covering wider climate and environment variabilities.

The western Antarctic Peninsula has been experienced a dramatic warming trend with a clear interannual variability. The surface temperature has increased by approximately 3°C over the past 50 years (Vaughan et al., 2001). Phytoplankton variability is an essential key driver of the marine ecosystem as a sensitive biological indicator of climate change. Interannual variability of phytoplankton biomass is finely tuned in synchrony with the variation of climatic, atmospheric, and oceanic variables around the fastest warming areas on earth, the Antarctic Peninsula. An ENSO-induced atmospheric variability influences a strength of northwest winds and ocean current in the study area.

During La Niña events, strong northwest winds and associated poleward movement of the Southern Antarctic Circumpolar Current Front tends to increase chlorophyll-a concentrations via upwelling and mixing between oceanic and coastal waters, and vice versa during El Niño events (Loeb et al. 2010, Sprintall 2003). The strong negative correlation between ONI index and chlorophyll-a concentration suggests an important role of the ENSO-related large-scale forcing on phytoplankton dynamics. Sea surface temperature is another regional factor that controls Chl-*a* concentrations by altering metabolic rates. For example, studies of Antarctic phytoplankton indicate that temperature alone causes increase of the growth rate (Boyd et al. 2013, Petrou et al 2016). Strong winds deepen mixed layer depth through turbulent mixing, thereby increasing phytoplankton growth by bringing nutrient-rich water to the surface (Abbott et al. 2000, Deppeler and Davidson, 2017). Our results for a decadal dataset revealed that the phytoplankton biomass undergoes clear seasonal and interannual dynamics. The potential ecological responses, such as biogeochemical variability could vary in this region, depending on the relative interannual variability of climate cycles and other environmental drivers with phytoplankton variability. Therefore, understanding the relationship between climatic factors and phytoplankton biomass is important to forecast the dynamics of the marine ecosystem in the western Antarctic Peninsula. Our results emphasized the long-term trend of phytoplankton biomass to clarify the relationship between phytoplankton biomass and climatic, atmospheric, and oceanic variables. Furthermore, the phytoplankton biomass in the Bransfield Strait increased with higher surface temperatures and wind speeds during La Niña periods, and this trend was especially clear during the low phytoplankton years.

5. Reference

Abbott, M., Richman, J., Letelier, R. and Bartlett, J. 2000. The spring bloom in the Antarctic Polar Frontal Zone as observed from a mesoscale array of bio-optical sensors. Deep Sea Research Part II: Topical Studies in Oceanography. 47, 15-16 (2000), 3285 - 3314, doi: 10.1016/S0967-0645(00)00069-2.

Arrigo, K.R., Robinson, D.H., Worthen, D.L., Dunbar, R.B., Di- Tullio, G.R., VanWoerf, M., Lizotte, M.P., 1999. Phytoplankton community structure and the drawdown of nutrients and CO2 in the Southern Ocean. Science 283, 365 - 367, doi: 10.1126/science.283.5400.365.

Bárcena, M.Á., Isla, E., Plaza, A., Flores, J.A., Sierro, F.J., Masqué, P., Sanchez-Cabeza, J.A., Palanques, A., 2002. Bioaccumulation record and paleoclimatic significance in the Western Bransfield Strait. The last 2000 years. Deep-Sea Res. II 49, 935 - 950, doi: 10.1016/S0967-0645(01)00132-1.

Basterretxea, G., Arístegui, J., 1999. Phytoplankton biomass and production during late austral spring (1991) and summer (1993) in the Bransfield Strait. Polar Biol. 21(1), 11 - 22, doi: 10.1007/s003000050328.

Behrenfeld, M.J., Falkowski, P.G., 1997. Photosynthetic rates derived from satellite based chlorophyll concentration. Limnol. Oceanogr. 42(1), 1 - 20, doi: 10.4319/lo.1997.42.1.0001.

Bölter, M., von Bodungen, B., Liebezeit, G., Meyer, M., 1988. The pelagic ecosystem of the Bransfield Strait, Antarctica: an analysis of microbiological, planktological and chemical characteristics by multivariate analyses. In Antarctic Ocean and Resources Variability (pp. 160 - 166). Springer Berlin Heidelberg.

Boyd, P.W., Rynearson, T.A., Armstrong, E.A., Fu, F., Hayashi, K., Hu, Z., Hutchins, D.A., Kudela, R.M., Litchman, E., Mulholland, M.R., Passow, U., Strzepek, R.F., Whittaker, K.A., Yu, E., Thomas, M.K., 2013. Marine phytoplankton temperature versus growth responses from polar to tropical waters - outcome of a scientific community-wide study. PloS one, 8(5), e63091, doi: 10.1371/journal.pone.0063091.

Clem, K.R., Renwick, J.A., McGregor, J., Fogt, R.L., 2016. The relative influence of ENSO and SAM on Antarctic Peninsula climate. J. Geophys. Res.-Atmos., 121(16), 9324 - 9341, doi: 10.1002/2016JD025305.

Clem, K.R., Renwick, J.A., McGregor, J., 2017. Large-scale forcing of the Amundsen Sea Low and its influence on sea ice and West Antarctic temperature. J. Climate., 30(20), 8405 - 8424, doi: 10.1175/JCLI-D-16-0891.1.

Comiso, J.C., Maynard, N.G., Smith, W.O. Jr, Sullivan, C.W., 1990. Satellite ocean color studies of Antarctic ice edges in summer and autumn. J. Geophys. Res. 95, 9481 - 9496, doi: 10.1029/JC095iC06p09481.

Dee, D.P., Uppala, S.M., Simmons, A.J., Berrisford, P., Poli, P., Kobayashi, S., Andrae, U., Balmaseda, M.A., Balsamo, G., Bauer, P., Bechtold, P., Beljaars, A.C.M., van de Berg, L., Bidlot, J., Bormann, N., Delsol, C., Dragani, R., Fuentes, M., Geer, A.J., Haimberger, L., Healy, S.B., Hersbach, H., Hólm, E.V., Isaksen, L., Kållberg, P., Köhler, M., Matricardi, M., McNally, A.P., Monge-Sanz, B.M., Morcrette, J.J., Park, B.K., Peubey, C., de Rosnay, P., Tavolato, C., Thépaut, J.N., Vitart, F., 2011. The ERA-Interim reanalysis: Configuration and performance of the data assimilation system. Q. J. R. Meteorol. Soc., 137, 553 - 597, doi: 10.1002/qj.828.

Deppeler, S.L., Davidson, A.T., 2017. Southern Ocean Phytoplankton in a Changing Climate. Front. Mar. Sci. 4, 1 - 28, doi: 10.3389/fmars.2017.00040.

Gonçalves-Araujo, R., de Souza, M.S., Tavano, V.M., Garcia, C.A.E., 2015. Influence of

oceanographic features on spatial and interannual variability of phytoplankton in the Bransfield Strait, Antarctica. J. Mar. Sys. 142, 1 – 15, doi: 10.1016/j.jmarsys.2014.09.007.

Gordon, A. L., Mensch, M., Zhaoqian, D., Smethie, W. M., Bettencourt, J., 2000. Deep and bottom water of the Bransfield Strait eastern and central basins. J. Geophys. Res. 105(C5), 11337 – 11346, doi: 10.1029/2000JC900030.

Heywood, R.B., Priddle, J., 1987. Retention of phytoplankton by an eddy. Cont. Shelf. Res. 7, 937 – 955, doi: 10.1016/0278-4343(87)90007-0.

Kim, H., Ducklow, H. W., Abele, D., Ruiz Barlett, E. M., Buma, A. G., Meredith, M. P., Rozema, P.D., Schofield, O.M., Venables, H.J., Schloss, I. R. 2018. Inter-decadal variability of phytoplankton biomass along the coastal West Antarctic Peninsula. Phil. Trans. Math. Phys. Eng. Sci., 376(2122), 20170174, doi: 10.1098/rsta.2017.0174.

La, H.S., Park, K., 2016. The Evident Role of Clouds on Phytoplankton Abundance in Antarctic Coastal Polynyas. Terr. Atmos. Ocean. Sci. 27(2). 293 – 391, doi: 10.3319/TAO.2015.11.30.01(Oc).

Laubscher, R.K., Perissinotto, R., McQuaid, D.C., 1993. Phytoplankton production and biomass at frontal zones in the Atlantic sector of the Southern Ocean. Polar Biol. 13, 471 – 481, doi: 10.1007/BF00233138.

Loeb, V., Hofmann, E.E., Klinck, J.M., Holm-Hansen, O., 2010. Hydrographic control of the marine ecosystem in the South Shetland-Elephant Island and Bransfield Strait region. Deep-Sea Res. II 57(7), 519 – 542, doi: 10.1016/j.dsr2.2009.10.004.

Loeb, V.J., Hofmann, E.E., Klinck, J.M., Holm-Hansen, O., White, W.B., 2009. ENSO and variability of the Antarctic Peninsula pelagic marine system. Antarc. Sci. 21, 135 – 148, doi: 10.1017/S0954102008001636.

Marrari, M., Kendra L.D., Chuanmin, H., 2008. Spatial and temporal variability of SeaWiFS chlorophyll a distributions west of the Antarctic Peninsula: Implications for krill production. Deep-Sea Res. II 55(3), 377 – 392, doi: 10.1016/j.dsr2.2007.11.011.

Martinson, D.G., Stammerjohn, S.E., Iannuzzi, R.A., Smith, R.C., Vernet, M., 2008. Western Antarctic Peninsula physical oceanography and spatio – temporal variability. Deep-Sea Res. II 55(18), 1964 – 1987, doi: 10.1016/j.dsr2.2008.04.038.

Marshall, G.J., 2003. Trends in the Southern Annular Mode from observations and reanalyses. J. Clim. 16, 4134 – 4143, doi: 10.1175/1520-0442(2003)016<4134:TITSAM>2.0.CO;2.

Meredith, M.P., King, J.C., 2005. Rapid climate change in the ocean west of the Antarctic Peninsula during the second half of the 20th century. Geophys. Res. Lett., 32(19),

doi: 10.1029/2005GL024042.

Montes-Hugo, M., Doney, S.C., Ducklow, H.W., Fraser, W., Martinson, D., Stammerjohn, S. E., Schofield, O., 2009. Recent changes in phytoplankton communities associated with rapid regional climate change along the western Antarctic Peninsula. Science 323(5920), 1470 - 1473, doi: 10.1126/science.1164533.

Nazarenko, L., Schmidt, G.A., Miller, R.L., Tausnev, N., Kelley, M., Ruedy, R., ⋯ Bleck, R., 2015. Future climate change under RCP emission scenarios with GISS ModelE2. J. Adv. Model. Earth. Sy. 7(1), 244 - 267, doi: 10.1002/2014MS000403.

Orsi, A.H., Whitworth III, T., Nowlin Jr., W.D., 1995. On the meridional extent and fronts of the Antarctic Circumpolar Current. Deep-Sea Res. 42, 641 - 673, doi: 10.1016/0967-0637(95)00021-W.

Park, J., Oh, I.S., Kim, H.C., Yoo, S., 2010, Variability of SeaWiFs chlorophyll-a in the southwest Atlantic sector of the Southern Ocean: Strong topographic effects and weak seasonality. Deep-Sea Res. 57(4), 604 - 620, doi: 10.1016/j.dsr.2010.01.004.

Peck, L.S., Webb, K.E., Bailey, D.M., 2004. Extreme sensitivity of biological function to temperature in Antarctic marine species. Funct. Ecol. 18(5), 625 - 630, doi: 10.1111/j.0269-8463.2004.00903.x.

Petrou, K., Kranz, S., Trimborn, S., Hassler, C., Ameijeiras, S., Sackett, O., Ralph, P. and Davidson, A., 2016. Southern Ocean phytoplankton physiology in a changing climate. Journal of Plant Physiology. 203, (2016), 135 - 150, doi: 10.1016/j.jplph.2016.05.004.

Platt, T., Broomhead, D.S., Sathyendranath, S., Edwards, A.M., Murphy, E.J., 2003a. Phytoplankton biomass and residual nitrate in the pelagic ecosystem, P. Roy. Soc. Lond. A, 459, 1063 - 1073, doi: 10.1098/rspa.2002.1079.

Platt, T., Sathyendranath, S., Edwards, A.M., Broomhead, D.S., Ulloa, O., 2003b. Nitrate supply and demand in the mixed layer of the ocean, Mar. Ecol. Prog. Ser., 254, 3 - 9, doi: 10.3354/meps254003.

Priddle, J., Brandini, F., Lipski, M., Thorley, M.R., 1994. Pattern and variability of phytoplankton biomass in the Antarctic Peninsula region: an assessment of the BIOMASS cruises. Southern Ocean Ecology: The BIOMASS Perspective. Cambridge University Press, Cambridge, pp 49 - 61.

Purich, A., Cai, W., England, M.H., Cowan, T., 2016. Evidence for link between modelled trends in Antarctic sea ice and underestimated westerly wind changes. Nat. commun. 7, doi: 10.1038/ncomms10409.

Smith, R.C., Baker, K.S., Stammerjohn, S.E., 1998 Exploring sea ice indexes for polar

KOPRI 극지연구소

ecosystem studies. BioScience 48, 83 – 93, doi: 10.2307/1313133.

Smith, R.C.; Martinson, D.G., Stammerjohn, S.E., Iannuzzi, R.A., Ireson, K., 2008. Bellingshausen and western Antarctic Peninsula region: Pigment biomass and sea-ice spatial/temporal distributions and interannual variability. Deep-Sea Res. II 55, 1949 – 1963, doi: 10.1016/j.dsr2.2008.04.027.

Smith, W.O., Marra, J., Hiscock, M.R., Barber, R.T., 2000. The seasonal cycle of phytoplankton biomass and primary productivity in the Ross Sea, Antarctica. Deep-Sea Res. II 47(15), 3119-3140, doi: 10.1016/S0967-0645(00)00061-8.

Sprintall, J. 2003. Seasonal to interannual upper-ocean variability in the Drake Passage. Journal of Marine Research. 61:27-57, doi: 10.1357/002224003321586408.

Sullivan, C.W., Arrigo, K.R., McClain, C.R., Comiso, J.C., Firestone, J., 1993. Distributions of phytoplankton blooms in the Southern Ocean. Science 262, 1832 – 1837, doi: 10.1126/science.262.5141.1832.

Trimborn, S., Hoppe, C.J., Taylor, B.B., Bracher, A., Hassler, C., 2015. Physiological characteristics of open ocean and coastal phytoplankton communities of Western Antarctic Peninsula and Drake Passage waters. Deep-Sea Res I 98, 115-124, doi: 10.1016/j.dsr.2014.12.010.

Vaughan, D.G., Marshall, G. J., Connolley, W. M., King, J. C., Mulvaney, R., 2001. Climate change: Devil in the detail. Science 293, 1777 – 1779, doi: 10.1126/science.1065116.

Vernet, M., Martinson, D., Iannuzzi, R., Stammerjohn, S., Kozlowski, W., Sines, K., Smith, R., Garibotti, I., 2008. Primary production within the sea-ice zone west of the Antarctic Peninsula: I-Sea ice, summer mixed layer, and irradiance. Deep-Sea Res. II 55, 2068 – 2085, doi: 10.1016/j.dsr2.2008.05.021.

Venables, H.J., Clarke, A., Meredith, M.P., 2013. Wintertime controls on summer stratification and productivity at the western Antarctic Peninsula. Limnol. Oceanogr. 58, 1035 – 1047, doi: 10.4319/lo.2013.58.3.1035.

Wang, S., Bailey, D., Lindsay, K., Moore, J.K., Holland, M., 2014. Impact of sea ice on the marine iron cycle and phytoplankton productivity. Biogeosciences. 11(17), 4713 – 4731, doi: 10.5194/bg-11-4713-2014.

Yuan, X., 2004. ENSO-related impacts on Antarctic sea ice: a synthesis of phenomenon and mechanisms. Antarct Sci 16, 415 – 425, doi: 10.1017/S0954102004002238.

Zhang, H., Han, Z., Zhao, J., Yu, P., Hu, C., Sun, W., Yang, D., Zhu, G., Lu, B., Peter, H.U., Vetter, W., 2014. Phytoplankton and chlorophyll a relationships with ENSO in Prydz Bay, East Antarctica. Sci. China Earth Sci. 57(12), 3073-3083, doi: 10.1007/s11430-014-4939-8.

Zhang, X., Liang, S., Wang, G., Yao, Y., Jiang, B., Cheng, J., 2016. Evaluation of the Reanalysis Surface Incident Shortwave Radiation Products from NCEP, ECMWF, GSFC, and JMA Using Satellite and Surface Observations. Remote Sens. 8(3), 225, doi: 10.3390/rs8030225.

KOPRI
극지연구소

Table 1. Correlation coefficients between phytoplankton biomass (Chl-a) and environmental variables (ONI, SAM, PAR, SIC, SST, and wind speed (WS)) with a time lag (0 - 6 months).

	Correlation coefficients with a time lag						
	0	1	2	3	4	5	6
ONI	-0.51	-0.56	-0.61*	-0.64*	-0.65*	-0.64*	-0.62*
SAM	0.05	-0.01	0.22	0.39	0.51	0.43	0.20
PAR	0.31	0.06	-0.17	-0.34	-0.22	-0.06	-0.01
SIC	-0.25	-0.27	-0.32	-0.39	-0.20	-0.11	-0.09
SST	0.70*	0.66*	0.67*	0.65*	0.46	0.15	0.01
WS	0.35	0.48	0.69*	0.72*	0.42	-0.14	-0.24

*Significance at $p < 0.05$

KOPRI 극지연구소

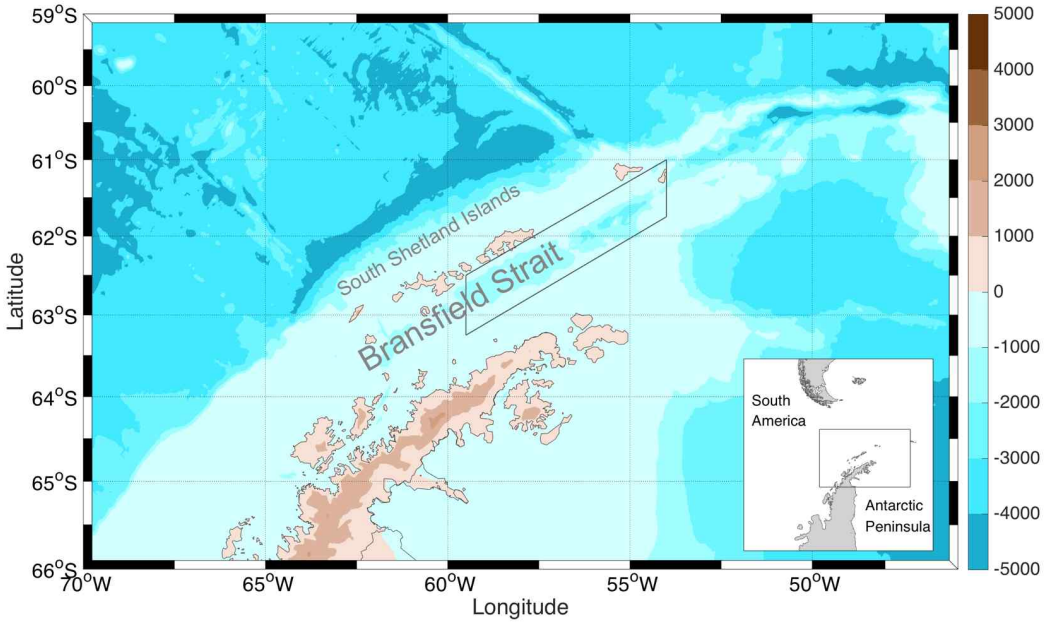

Figure 1. The bathymetry map of the Bransfield Strait in the Southern Ocean. The study region is indicated in the parallelogram. The inset map depicts the position of the Antarctic peninsula.

KOPRI
극지연구소

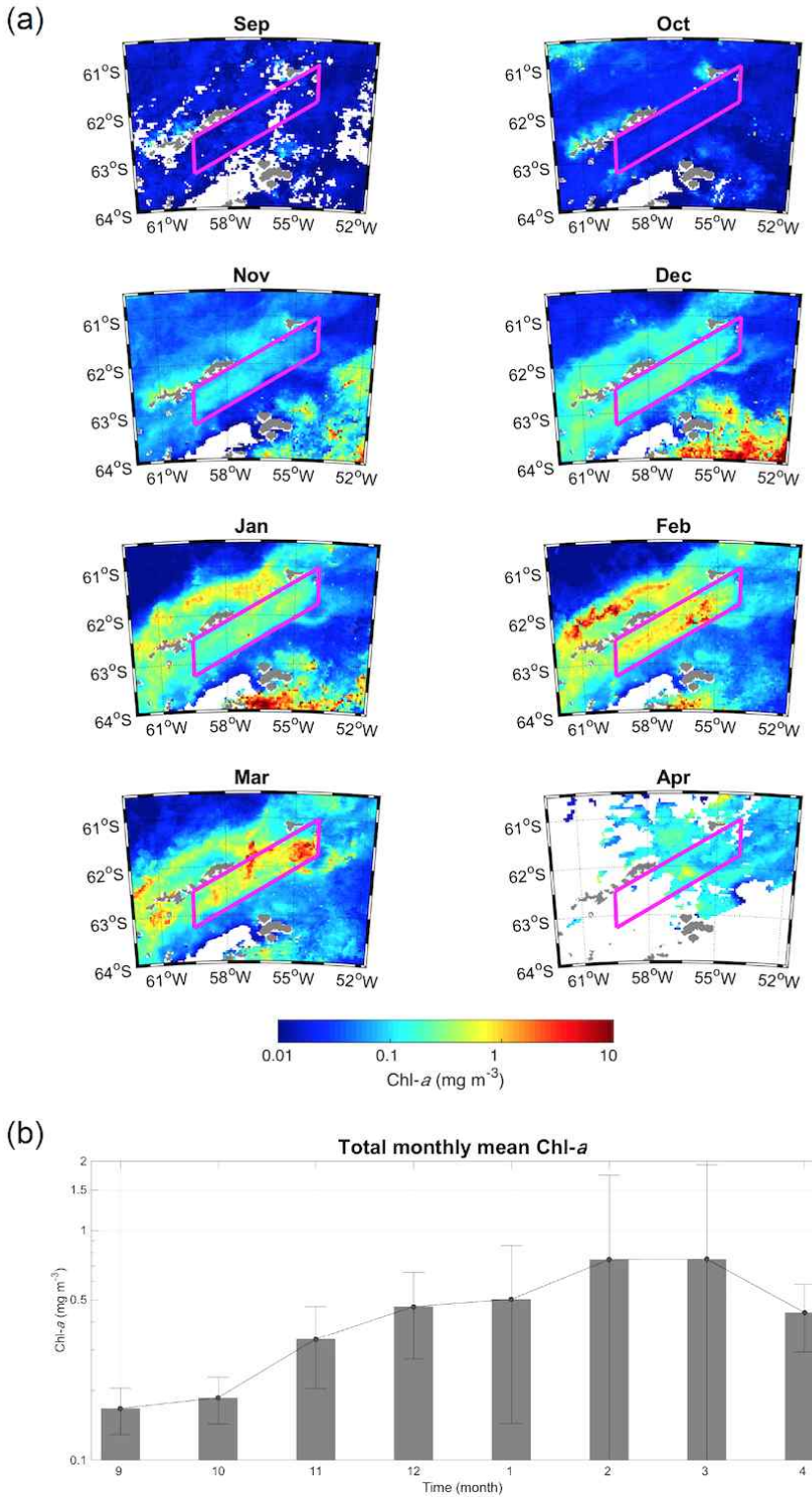

Figure 2. (a) Monthly Chl-a climatology around the Bransfield Strait (purple square) of the Southern Ocean (12-year mean). The color shows the MODIS Chl-a concentration calculated by a standard algorithm. The white region indicates data limited by sea ice, the presence of clouds, and low solar elevation. (b) Monthly Chl-a within the Bransfield Strait over the 12-year period.

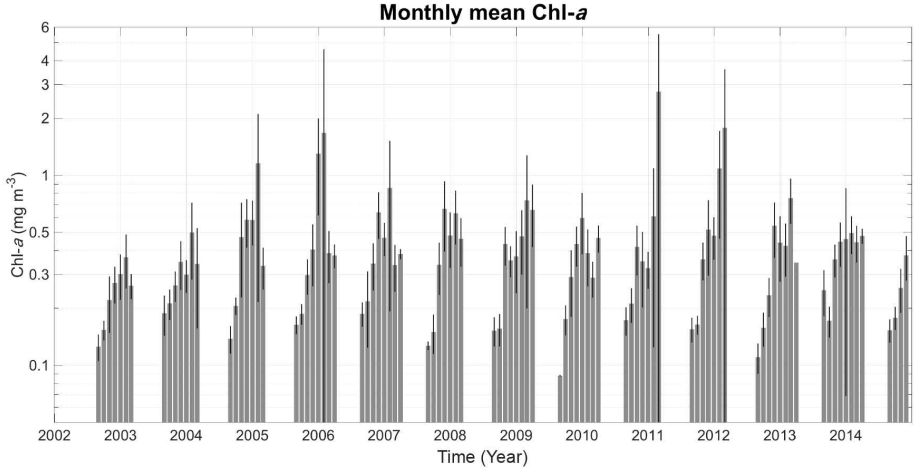

Figure 3. Time-series analysis of the Chl-a concentration over 150 months within the Bransfield Strait from July 2002 to December 2014.

KOPRI

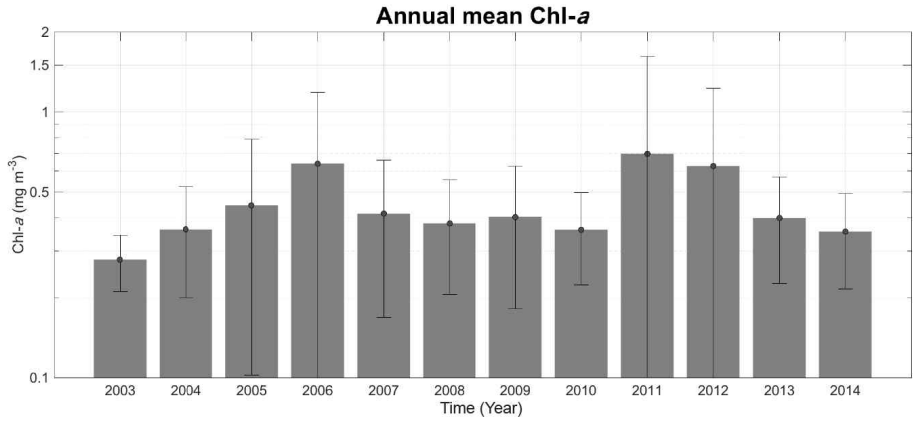

Figure 4. Interannual variation of averaged Chl-a in the Bransfield Strait during the austral summer (JFM), considering the data from July 2002 to December 2014. The error bars denote the 1-s of the three months (JFM).

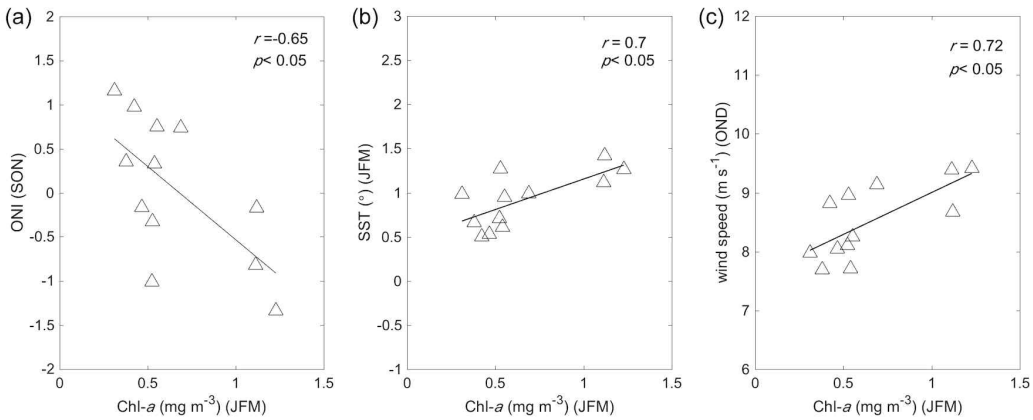

Figure 5. Scatterplots showing the Chl-a concentration against the climatic indices throughout the study period (2002 - 2014): (a) 4-month lagged Oceanic Niño Index (ONI) (b) 0-month lagged Sea Surface Temperature (SST) (c) 3-month lagged surface wind speed.

KOPRI
극지연구소

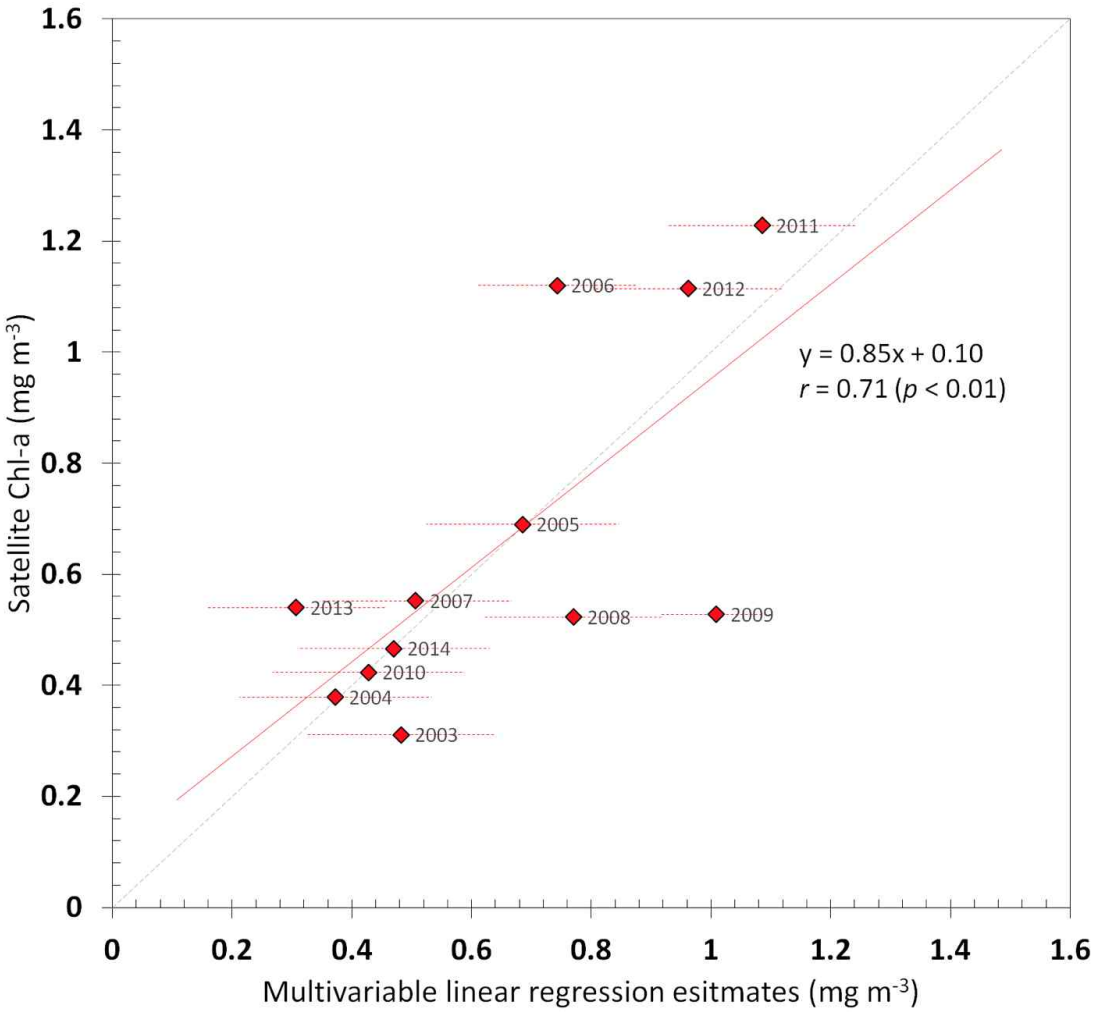

Figure 6. Correlation between the mean JFM satellite Chl-a in the Bransfield Strait and its predicted estimates calculated from the empirical multivariable regression analysis. Each data point is the predicted value for a particular year from the multivariable regression line derived from the data of 12 austral summer periods (2003 - 2014). The error bars are the root mean squared errors (RMSE) of each multivariable regression curve from the 11-year input. The solid red line is the linear regression line and the dotted grey line is the 1-to-1 relation between the predicted and satellite Chl-a.

극지연구소

Supplementary Figures

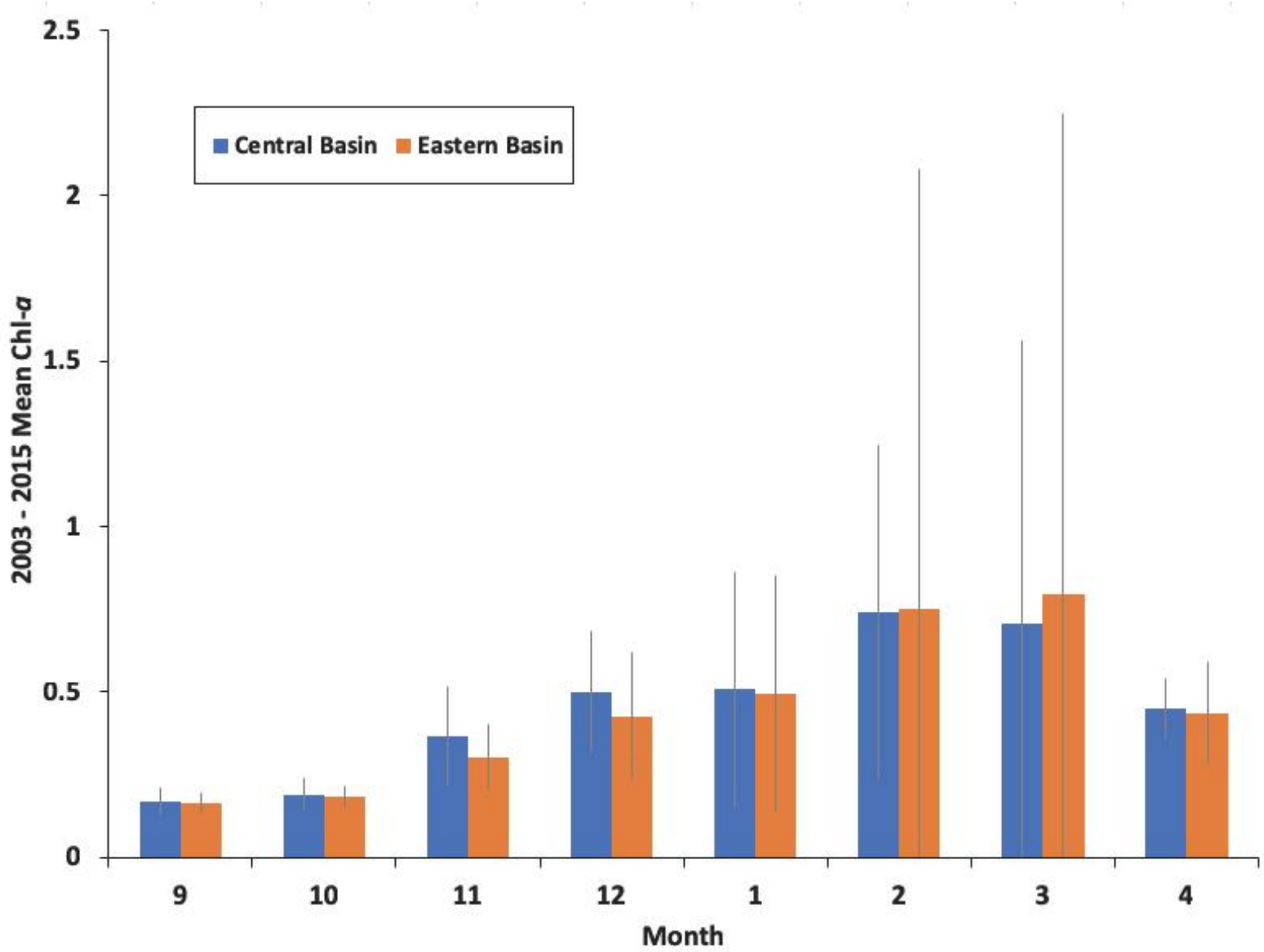

Supplementary Fig. 2. 2002 – 2014 mean monthly distribution of oceanic and atmospheric variables (SST, SIC, PAR, wind speed and cloud cover) in the Bransfield Strait (red square).

(a) Mean SST

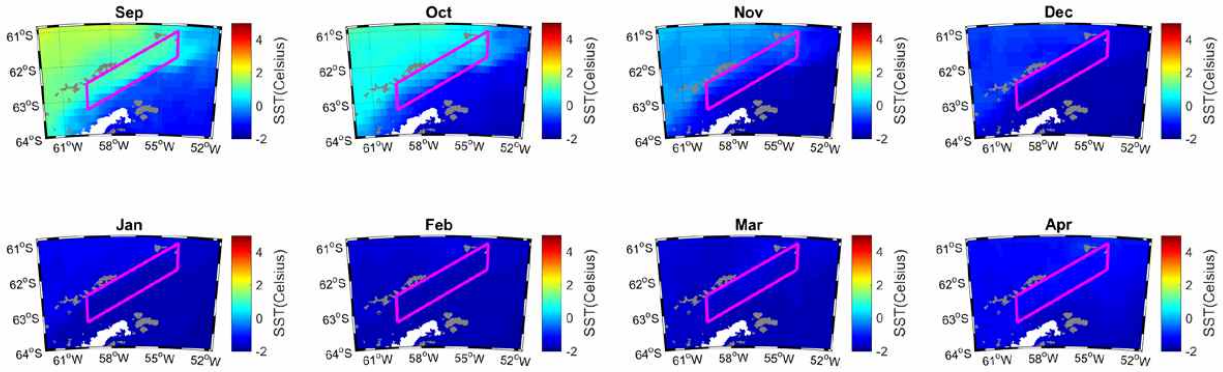

(b) Mean SIC

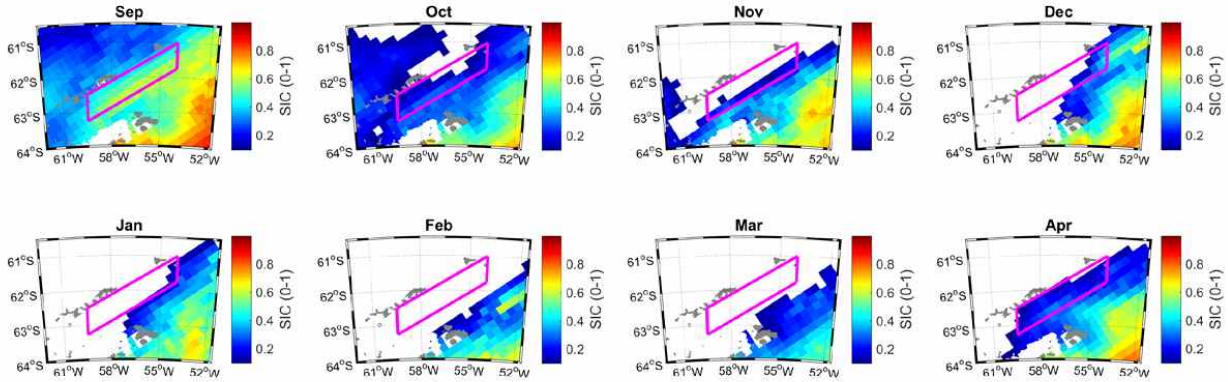

(c) Mean PAR

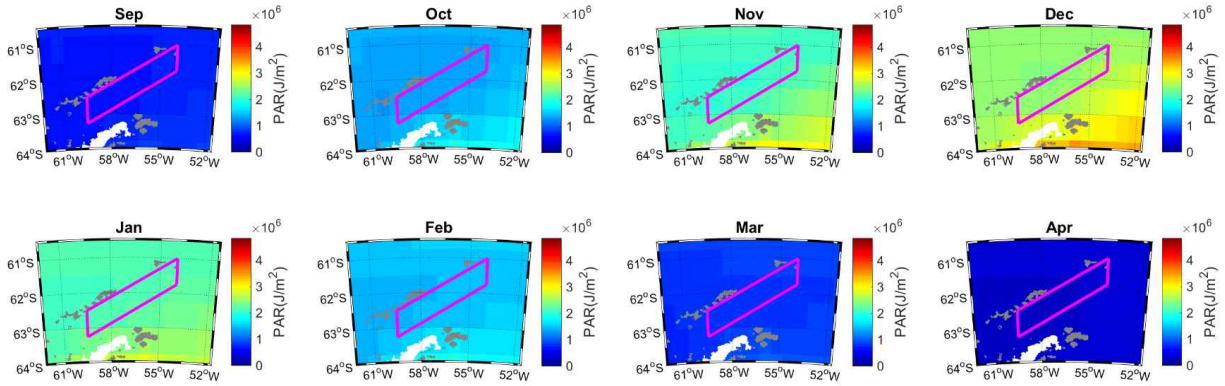

(d) Mean wind speed

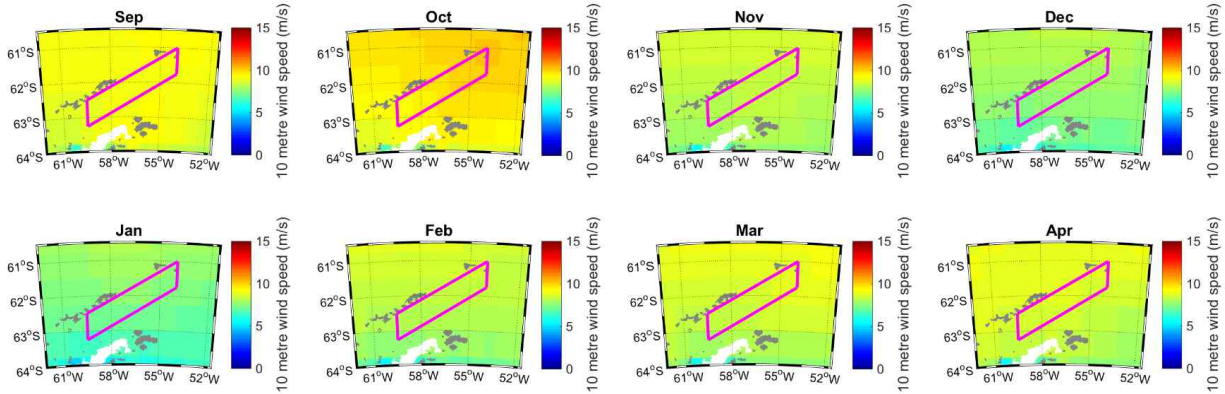

(e) Mean total cloud cover

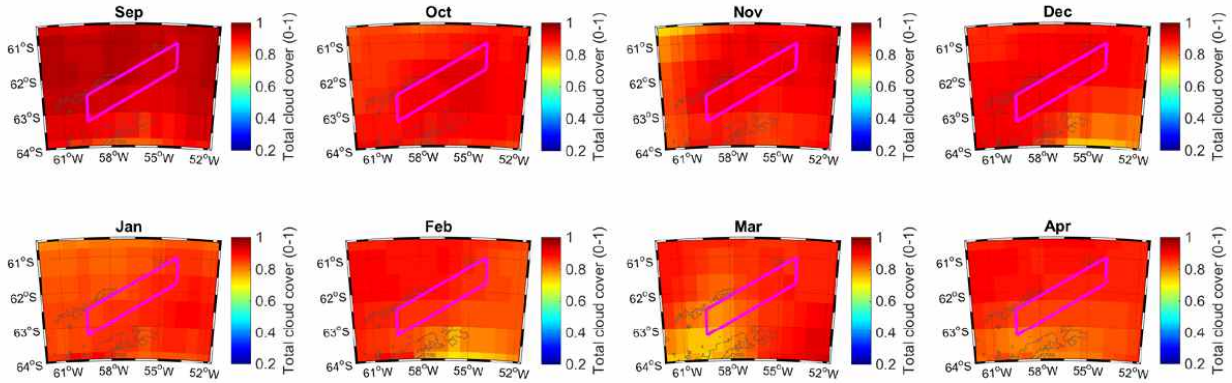

(f) Mean High cloud cover

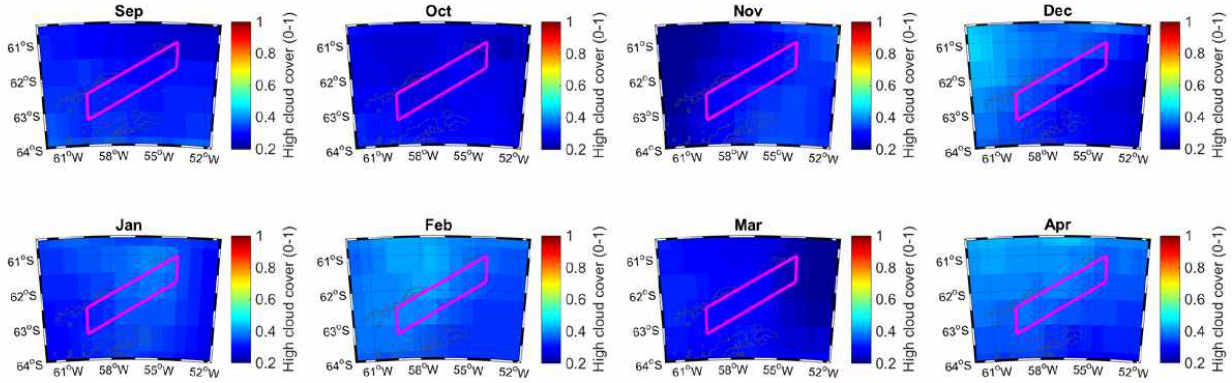

(g) Mean middle cloud cover

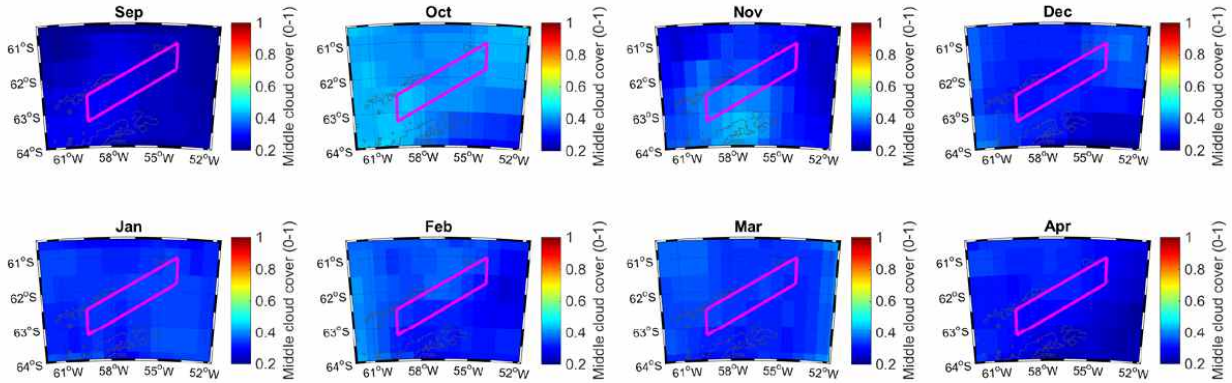

(h) Mean Low cloud cover

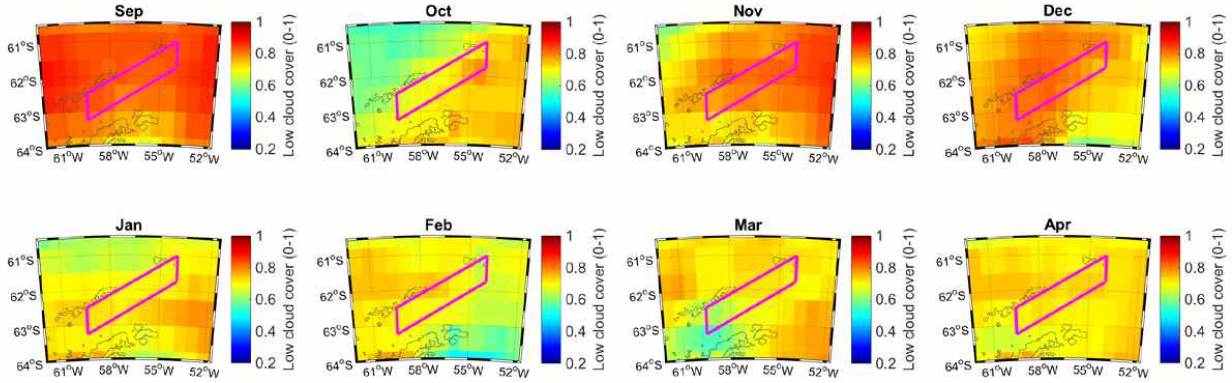

Supplementary Fig. 3. Relationships between JFM mean Chl-*a* and 0 – 6 months (for SAM and ONI) or 0 – 4 months (for SIC, SST, PAR, wind speed, and cloud cover) lagged environment variables in Bransfield Strait.

(a) Chl-*a* vs. SAM (0 – 6 months lag)

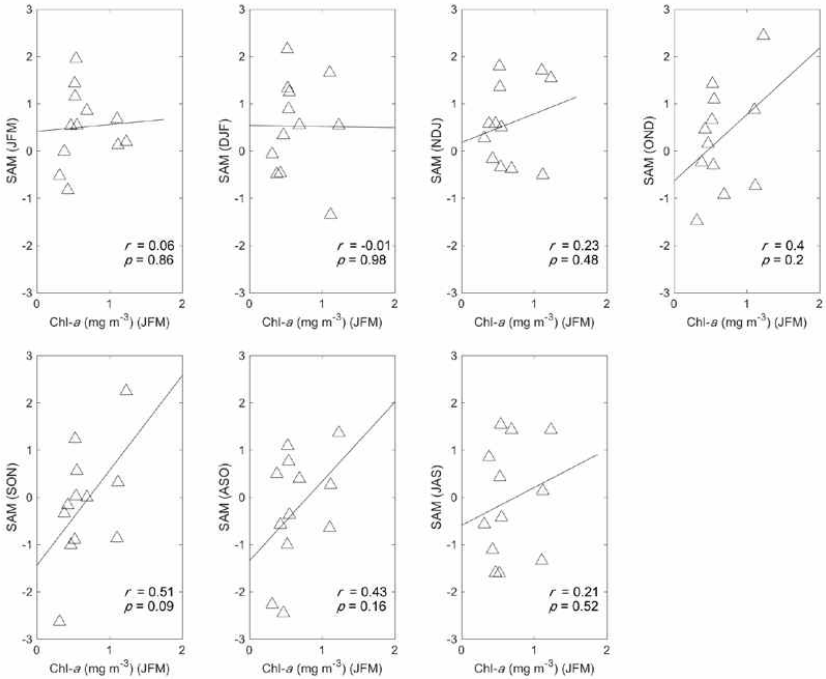

(b) Chl-*a* vs. ONI (0 – 6 months lag)

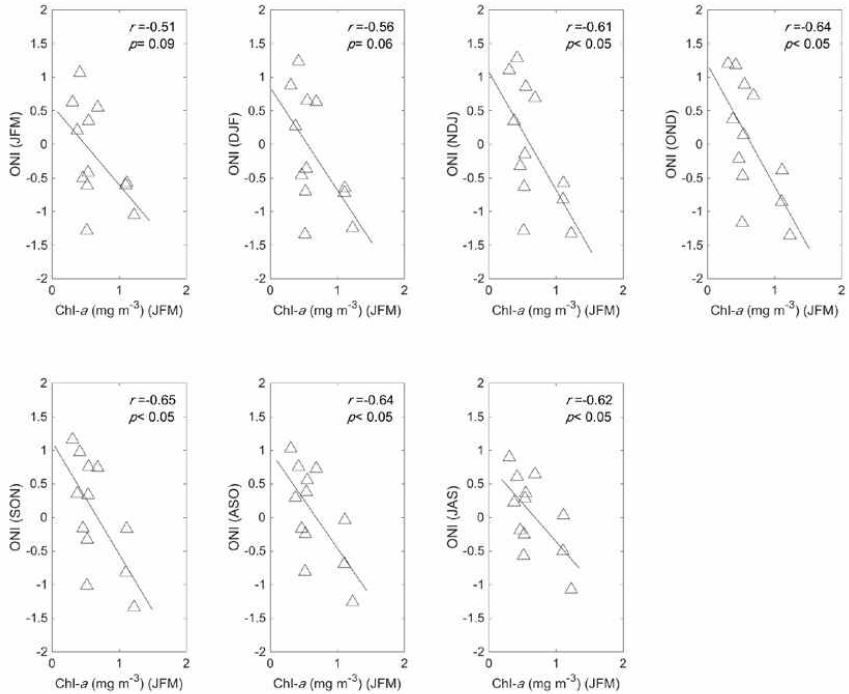

(c) Chl-*a* vs. SST (0 – 4 months lag)

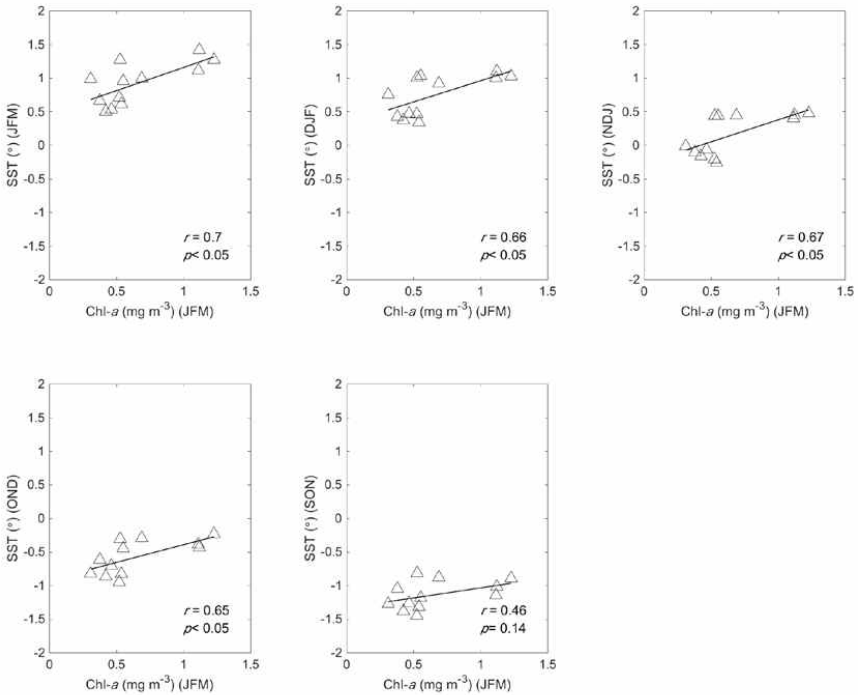

(d) Chl-*a* vs. SIC (0 – 4 months lag)

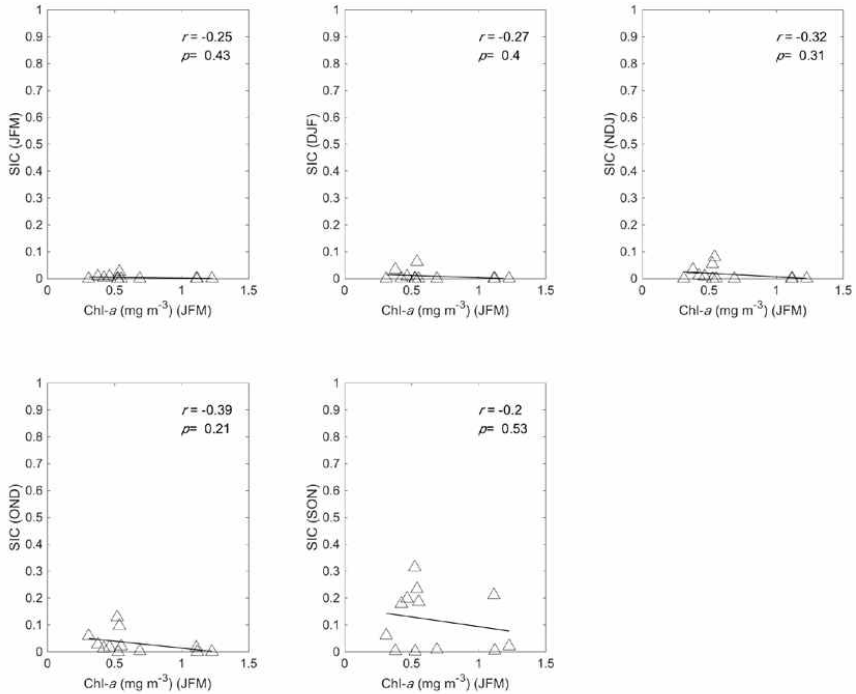

(e) Chl-*a* vs. PAR (0 – 4 months lag)

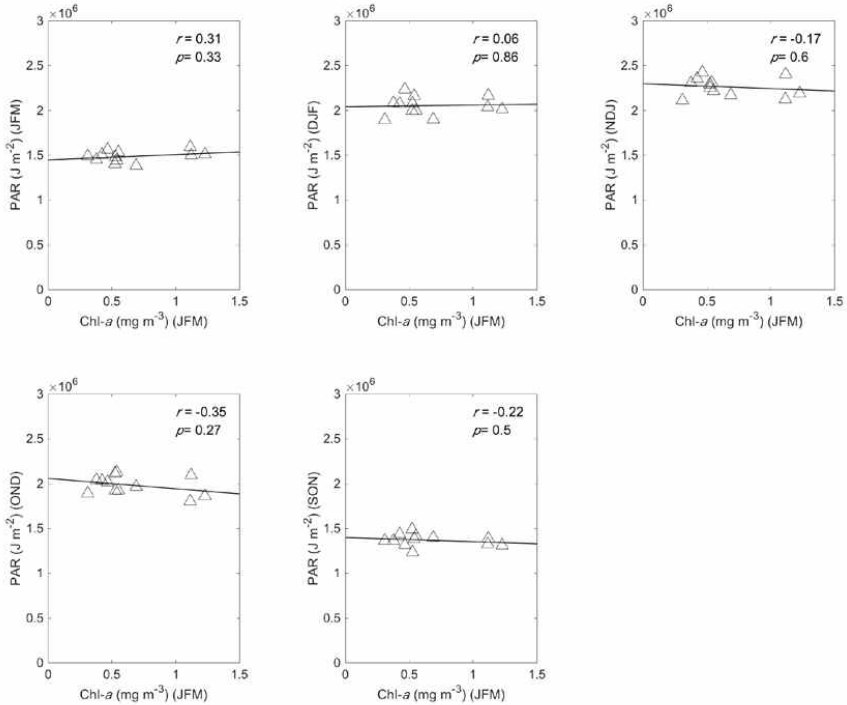

(f) Chl-*a* vs. wind speed (0 – 4 months lag)

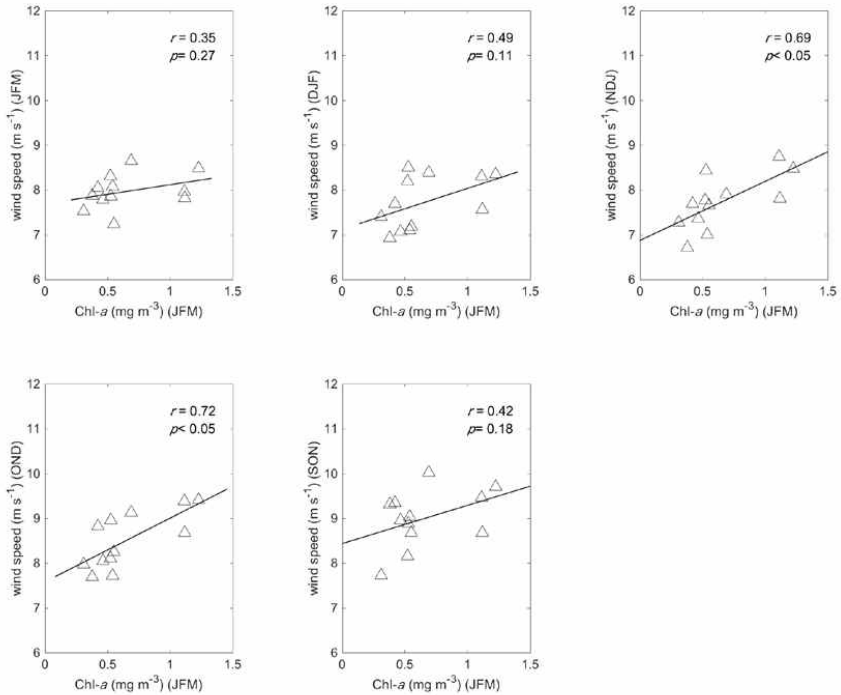

(g) Chl-*a* vs. Total cloud cover (TCC) (0 – 4 months lag)

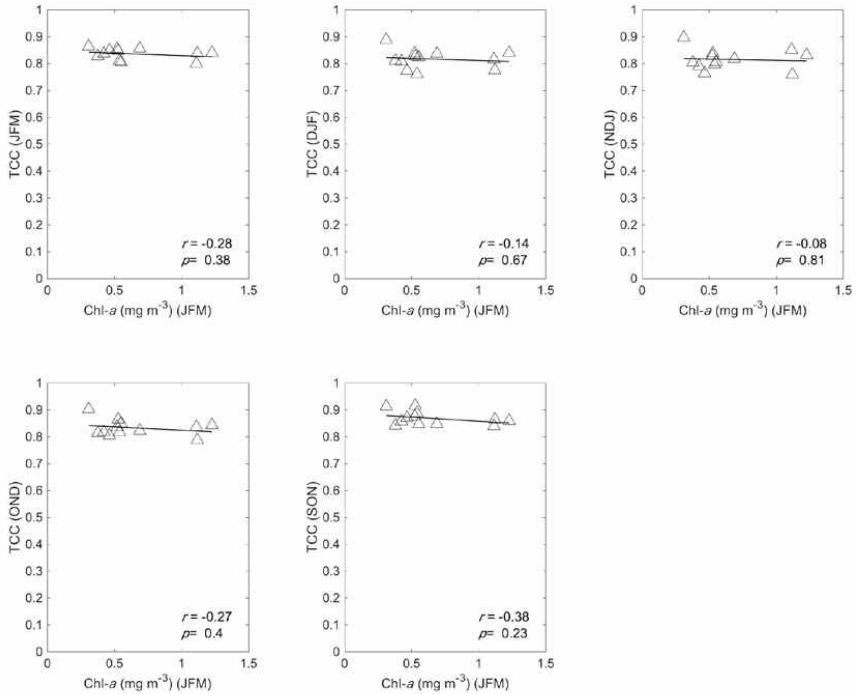

(h) Chl-*a* vs. High cloud cover (HCC) (0 – 4 months lag)

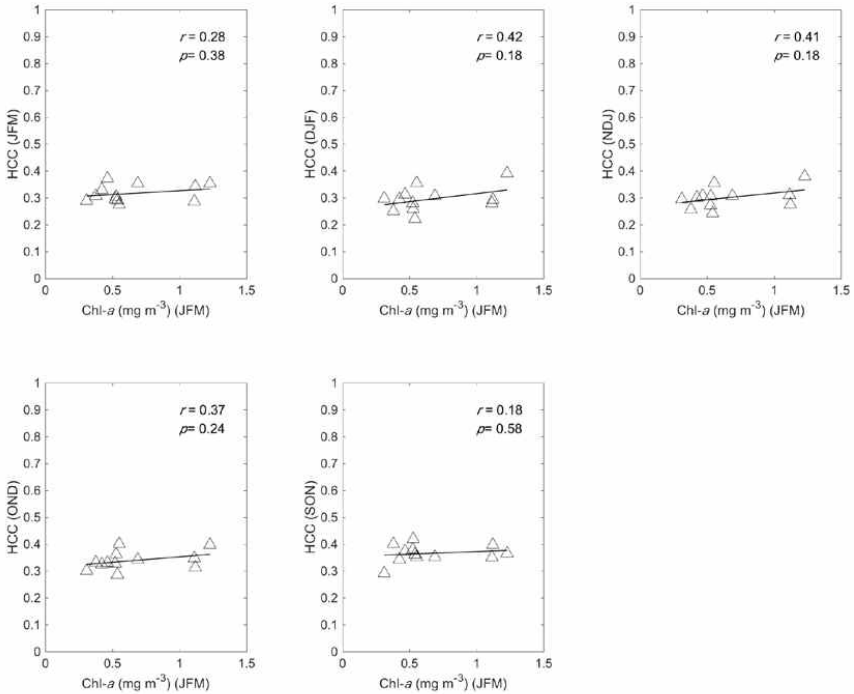

(i) Chl-*a* vs. Middle cloud cover (MCC) (0 – 4 months lag)

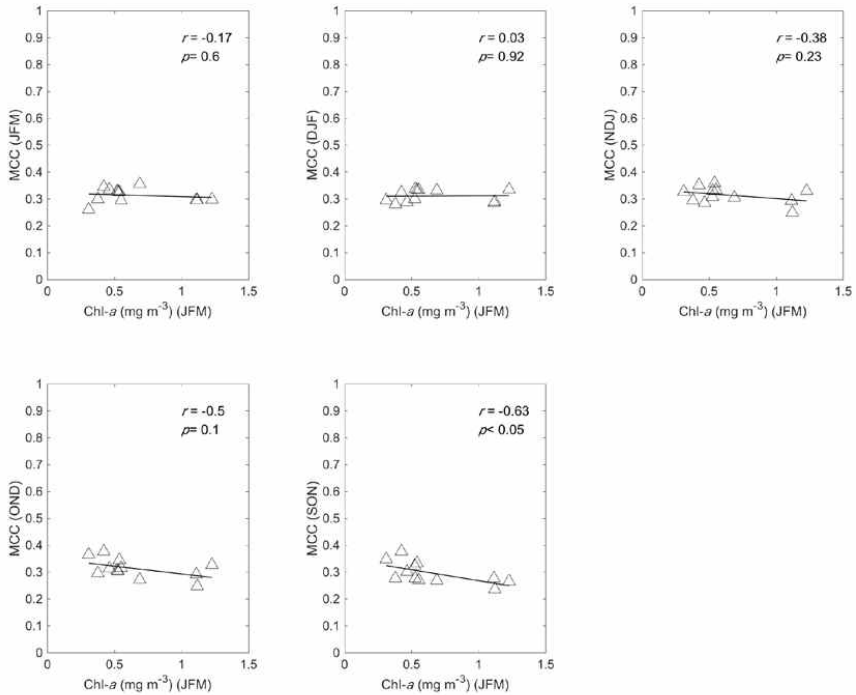

(j) Chl-*a* vs. Low cloud cover (LCC) (0 – 4 months lag)

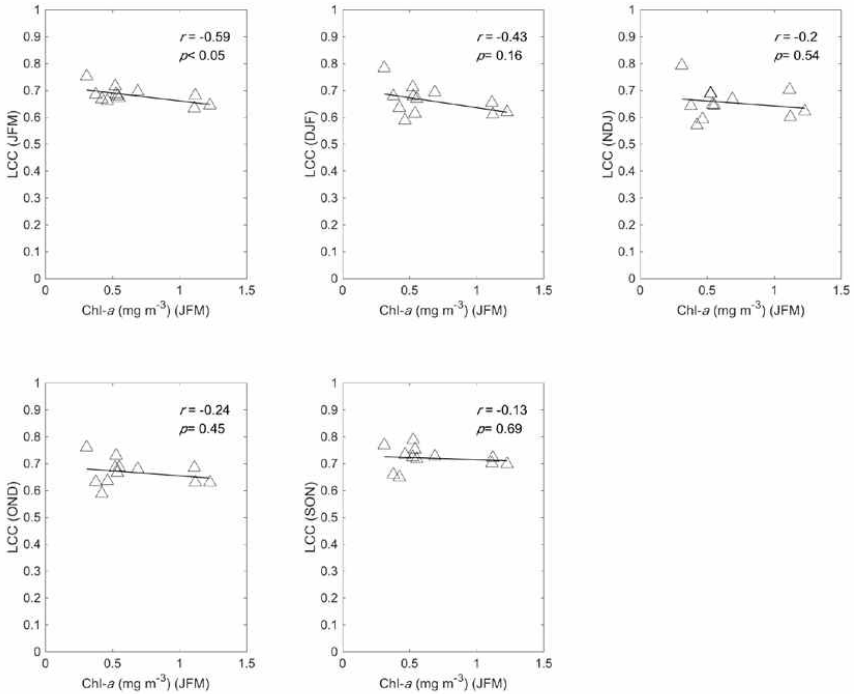

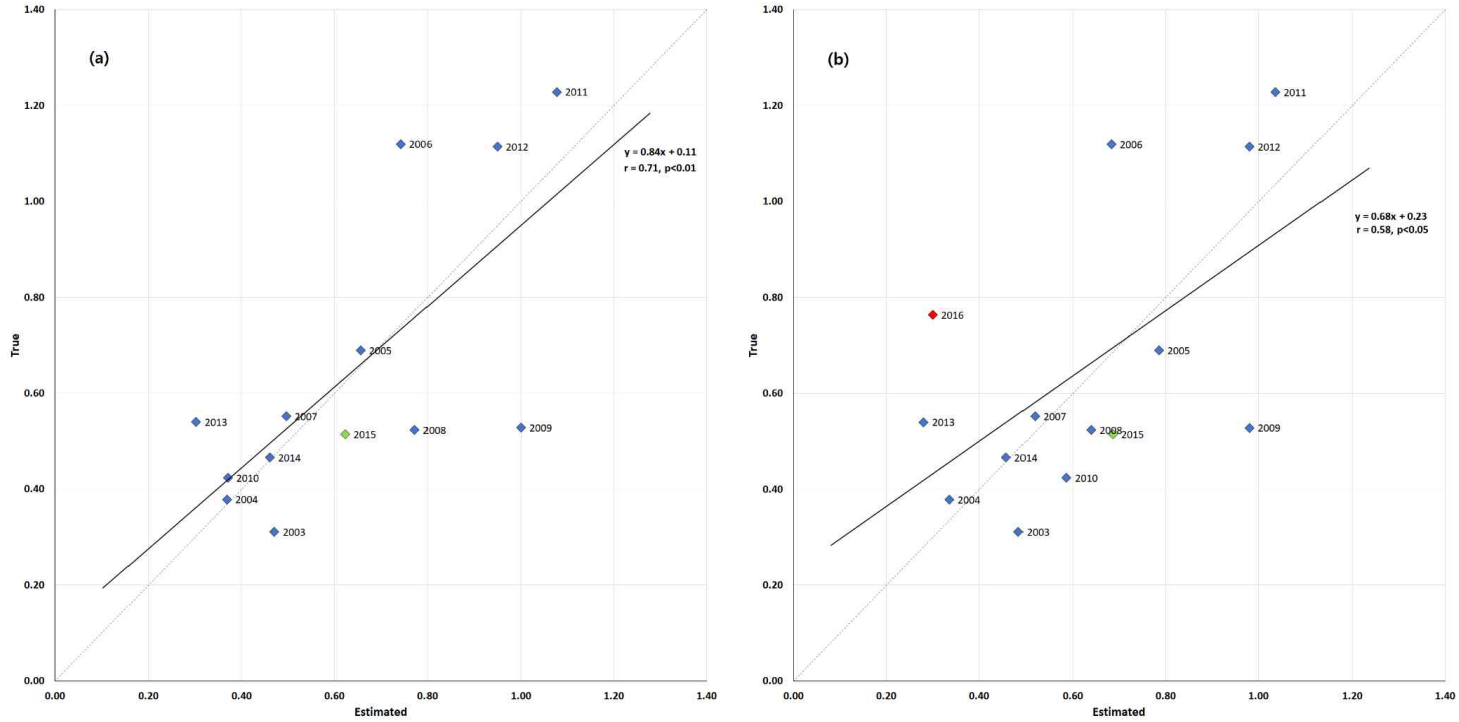

Supplementary Fig. 4. Same multivariable regression analysis as Fig. 6 but with adding 2015 data set (a) and with adding 2015 and 2016 data set (b).

제 12 절. 얼음의 동결농축에 의한 광물의 차별적 풍화작용 연구

허영숙, 이승수, 김미래, 방선화, 이현우, 임준석

서울대학교 지구환경과학부

1. 서론

화학적 풍화작용은 원소의 전 지구적 사이클에 핵심적인 요소이다. 특히, 탄소(C)의 사이클을 살펴보면, 규산염광물이 풍화되면서 이산화탄소(CO_2)의 형태로 대기에 있던 탄소가 탄산염($CaCO_3$)이라는 고체의 형태로 해저 퇴적물에 쌓인다(식 1, 2). 온실기체인 이산화탄소의 이러한 소모는 지질학적 시간스케일에서 기후변화를 초래한다. 따라서 규산염광물의 화학적 풍화에 영향을 주는 요인과 그 기작을 이해하는 것은 기후변화와 원소의 전 지구적 사이클을 이해하는데 매우 중요하다.

$$Ca_2SiO_3(s) + 2CO_2(g) + 2H_2O \leftrightarrow 2Ca^{2+}(aq) + 2CO_3^{2-}(aq) + H_4SiO_4(aq) \quad (식\ 1)$$

$$2Ca^{2+}(aq) + 2CO_3^{2-}(aq) \leftrightarrow 2CaCO_3(s) \quad (식\ 2)$$

또, 과거 빙하기-간빙기의 기후변화 과정에서 화학적 풍화 반응이 어떤 피드백을 일으켰는지를 명확히 밝히는 것은 과거 기후변화뿐만 아니라 미래의 기후변화를 모델링 하는데도 중요하다. 온도가 낮으면 광물이 풍화되는 화학반응의 속도 역시 느려지지만, 물에서 얼음으로의 상변화 때문에 저위도에서 일어나는 풍화반응이 단순한 온도의 연속선상에서 극지방에서도 동일한 기작으로 일어나리라고 생각할 수는 없다. 실제로 유역에 빙하가 존재하는 하천에 대하여 주원소 이온 데이터를 집대성해보면, 빙하가 존재하지 않는 하천에 비해 칼슘(Ca^{2+})과 황산이온(SO_4^{2-})의 비율이 높다(Torres et al., 2017). 이에 대한 현재까지의 개념적 해석은 빙하에 의한 물리적인 풍화가 광물의 표면적을 늘리고, 탄산칼슘과 황화철 등 광물이 그 양은 적지만 용해도가 높아 상대적으로 더 잘 풍화된다는 것이다. 이 가설이 맞는지 밝히는 것이 매우 중요한 이유는 실제로 탄산칼슘과 황화철이 주로 풍화가 된다면 이들 작용들은 대기 이산화탄소를 소모하는 반응이 아니거나 오히려 이산화탄소를 생성하는 반응이어서(식 3, 4) 기후변화에 식1, 2와는 다른 피드백으로 작용하기 때문이다.

$$FeS_2 + 15O_2 + 14H_2O \leftrightarrow 16H^+ + 8SO_4^{2-} + 4Fe(OH)_3 \quad (식\ 3)$$

$$2H^+ + CaCO_3 \leftrightarrow Ca^{2+} + H_2CO_3 \leftrightarrow Ca^{2+} + H_2O + CO_2 \quad (식\ 4)$$

얼음이 화학적 풍화 속도를 증가시키는 요인이 단순히 물리적인 것, 즉 부피 팽창에 의한 암석 파괴와 빙하의 마식작용에 의한 것인지, 아니면 이와는 별개로 얼음 구조 내에 화학적 풍화반

응 속도를 높일 화학적 조건이 조성되는지를 구별하는 것도 중요하다. 최근 일련의 연구에서는 얼음 내부와 표면에 얼지 않는 준액체층이 존재하고, 얼음이 얼면서 얼음 구조에서 배제된 물질들이 이 준액체층에 모여 동결농축현상을 일으키며, 여기서 매우 특이한 화학반응들이 일어남을 밝힌 바 있다(Kim et al., 2010, 2015).

리튬(Li)에는 ^{6}Li과 ^{7}Li의 두 안정 동위원소가 있고, 리튬 동위원소 비($\delta^{7}Li$)는 규산염 광물 풍화의 지시자로 이용되고 있다. 이는 탄산염 광물에 리튬의 함유량이 매우 적기 때문이다. 규산염 광물의 화학적 풍화 과정에는 광물이 완전히 녹아 용존 화학종만 남기는 congruent weathering과 완전히 녹지 않고 2차광물의 형태로 고체가 남게 되는 incongruent weathering이 있다. 리튬 동위원소의 경우 congruent weathering 과정에서는 광물의 $\delta^{7}Li$와 풍화가 일어난 후 용존 리튬의 $\delta^{7}Li$ 값이 같을 것이다. 즉, 동위원소 분별이 일어나지 않을 것이다. 반면, incongruent weathering이 일어날 때에는 2차광물 형성에 ^{7}Li 보다 ^{6}Li이 우선적으로 이용되기 때문에 상대적으로 용존 리튬의 $\delta^{7}Li$이 원래 광물의 값보다 더 크게 된다. 즉 동위원소 분별 작용이 일어나는 것으로 알려져 있다(Pistiner and Henderson, 2003; Wimpenny et al., 2010). 이러한 성질을 이용하여 Misra and Froelich (2012)과 Pogge von Strandmann et al. (2013) 등의 연구에서는 유공충 또는 탄산염암에서 리튬을 추출하여 그 동위원소 비를 분석했고, 이 정보를 통해 100 Ma 이내의 시간 규모에서 과거의 기후 또는 해양 환경의 변화와 규산염 광물의 풍화 양상을 연관지어 해석하였다.

본 연구에서는 얼음의 동결농축 과정에서 촉진되는 풍화 반응을 살펴보고자 모사 실험 시스템을 구축하고, 가장 대표적인 지표 암석 중 하나인 화강암에서 광물의 차별적 풍화와 규산염 광물의 풍화 정도를 모니터하려 하였다. 고체 대 용액의 비, 입자 크기, 반응시간 등 다양한 파라미터를 조절하며 풍화 모사 시스템을 구축하였다. 또, 화강암의 조암광물 중 흑운모가 특히 초기 용해가 빠른 것에 착안하여 흑운모에 대한 풍화 모사 실험도 진행하였다. 규산염 광물의 풍화의 속도와 진행 정도를 검토하기 위해 용존된 주원소를 분석하고 반응 후 남은 화강암 시료에 대한 XRD 분석을 통해 거시적인 광물 조성의 변화도 살펴보았다. 리튬 동위원소($\delta^{7}Li$)를 이용하면 1차광물이 완전 용해되는 congruent weathering과 2차광물을 형성하는 incongruent weathering을 구별해볼 수 있으므로 리튬 동위원소 분석 전처리 과정에 대한 실험을 하였고 일부 초기 분석을 진행하였다. 추후 분석의 재확인과 나머지 시료의 리튬 동위원소 분석도 진행할 예정이다.

2. 국내외 기술개발 현황

최근 극지에 대한 관심이 높아지면서 극지에 분포하는 빙하, 빙산과 같은 얼음이 전 지구적 물질 순환에 어떤 영향을 미치는지에 대한 연구가 활발히 진행되고 있다. 기존의 시각으로는, 얼음이 얼 정도로 낮은 온도에서는 화학반응 역시 거의 일어나지 않는다는 것이 일반적인 견해였으나(White and Blum, 1995) 최근 얼음이 존재하는 환경에서 상온과는 다른 독특한 화학반응이 일어날 수 있다는 연구가 다수 진행되었다(Jeong et al., 2015, 2012). 실험실에서의 자료뿐 아니라 실제 풍화가 일어나는 하천 스케일의 자료에서도 빙하가 존재하는 유역이 빙하가

존재하지 않는 유역에 못지않은 양의 규소를 대륙에서 해양으로 운반하고 있으며 상당량이 비정질 규소로 운반되고 있어 간과되어왔던 이 유입원을 연구해야할 필요성이 대두되고 있다(Hawkings et al., 2017; Hatton et al., 2019). 본 실험 결과와 획득한 시료는 보다 미시적, 기작적인 스케일에서 빙하환경이 풍화에 미치는 영향에 대한 정보를 제공하여, 야외조사 스케일의 거시적 연구 결과를 보완할 수 있을 것이다.

3. 연구개발수행 내용 및 결과

3.1. 얼음상에서의 암석/광물의 풍화 모사 실험

3.1.1. 풍화 모사 실험 설계

본 연구에서는 거시적 스케일의 빙하마식 등 물리적 풍화를 배제하고 미시적 스케일의 동결농축 과정에서 촉진되는 풍화 반응을 살펴보고자 풍화 모사 실험 시스템을 구축하였다. 자연계에 직접 해석을 적용할 수 있도록 지표환경의 대표적인 암석인 화강암에 대해 1차적인 모사 실험을 하였고, 화강암에 포함된 여러 광물들의 차별적 풍화를 확인하기 위해 2차적으로는 흑운모 광물을 대상으로 실험을 설계하고 진행하였다(표1). 얼음상(-20℃)과의 대비를 위해 나머지 조건은 동일하되 온도를 상온(25℃)으로 유지한 비교군을 두었다. 반응용액의 pH는 과제 수행기간 제약에 의해 자연계의 지표수보다는 상당히 산성인 pH 3 이었다. 화강암 실험에는 염산을 사용했으나 흑운모의 실험에는 추후 시료의 ICP-AES, ICP-MS 원소분석의 용이성을 위해 질산으로 교체하였다. 화강암 실험에는 두 가지 입자 크기를 구분하여 실험을 진행하였는데, 빙하 가루(glacial flour) 관련 문헌(Rosenbaum and Reynolds, 2004; Haldorsen, 1981)과 규산염광물 용해 실험 관련 문헌(Stillings and Brantley, 1995)을 참고하였다. 입자크기 63-150 ㎛의 화강암 실험에서 용존 Li의 농도가 낮은 것은 입자의 크기가 커서 표면적이 작고 반응 속도가 느린 것 때문이라고 생각하여, 이것을 보완하기 위해 4-63 ㎛ 입자크기의 암석분쇄물을 이용하고, 고체 대 용액 비를 증가시켜 반응 속도를 증가시켰다. 또한, 63-150 ㎛의 실험에서 반응 초기(1일 이내) 얼음 시스템에서 반응이 빠르고 후기로 갈수록 물 시스템에서 반응이 활발했는데, 얼음 시스템과 물 시스템의 반응추세 변화 시간대를 확인하기 위해서 4-63 ㎛ 실험에서는 더 촘촘한 시간 간격을 두고 실험하였다. 흑운모의 경우 판상광물인 관계로 입자크기를 엄밀히 구별하는데 제약이 있어서 63 - 150 μm 크기에 대해서만 실험을 진행했다. 고체 대 액체의 비율은 용존 리튬의 동위원소를 분석할 수 있을 만큼을 주어진 반응시간 내에 획득할 수 있도록 문헌의 화강암, 흑운모 풍화 실험을 참고해서 정했다(Stillings and Brantley, 1995; Bray et al., 2015).

3.1.2. 풍화 모사 실험 방법

전체적인 실험의 진행은 그림 1에 도시된 순서를 따랐다.

가. 암석과 광물 시료

실험에 사용한 화강암은 Ward's Science사의 Ward's Granite(Gray)로 미국 버몬트 주의 Barre granite이며 세립질에서 중립질이고 흑운모를 포함한다고 설명되어 있다. 흑운모 역시 Ward's Science사의 Ward's Biotite로 캐나다 온태리오 주의 Bancroft biotite이다.

나. 암석과 광물 분쇄

암석/광물은 먼저 Retsch사의 PM400 planetary ball mill을 이용하여 조립질로 분쇄하고, 아게이트(agate) 막자사발로 더 곱게 간 후 체질(sieving)을 하여 목표한 입자 크기 범위의 시료를 확보하였다.

Ball mill의 경우 18 MΩ H_2O(Millipore사 Milli-Q)와 99% 에탄올을 사용하여 세척하였다. 분쇄하려는 암석/광물 약 2g을 넣고 5분 이상 작동시키며 conditioning을 진행했다. 실제 암석/광물은 20g 이하를 넣고 약 20분 진행하였다. 아게이트 막자사발을 사용할 때는 18 MΩ H_2O와 99% 에탄올로 세척을 했고, conditioning을 위해서는 Sigma Aldrich사의 석영 약 5g 그리고 분쇄하려는 암석/광물을 약 1g 사용하였다.

매우 고운 분말 상태로 간 화강암과 흑운모 시료는 금속 체를 이용하여 입자 크기 범위(4-63 μm, 63-150 μm)를 분리했다. 이 과정에는 실내의 습도를 낮게 유지하는 것이 도움이 되었다. 위의 분쇄 과정을 거쳤을 때, 화강암의 경우 4-63 μm 입자 크기가 80%가량이었고, 흑운모의 경우 63-150 μm 입자 크기가 40%가량이었다.

다. 용액 응결 시간 측정

본 실험의 목적이 단순히 저온에서의 풍화 반응이 아니라 얼음상에서 일어나는 풍화를 확인하는 것이기 때문에, 저온반응기(세영과학사의 SH-75SP)에 넣은 시료가 얼기까지의 시간을 가늠할 필요가 있었다. Nalgene사의 HDPE(high-density polyethylene, 500 ml) 사각병에 반응용액 100 ml를 넣은 후 빛 차단과 온도 전달의 효율을 위해 겉면을 알루미늄 호일로 감싸고 넓은 면을 바닥에 눕혀 -20℃로 미리 설정된 저온반응기에 넣었다(그림 2a, c).

용액의 온도가 충분히 낮아져 응결이 시작되기까지 약 30분, 용액이 완전히 얼기까지 약 한 시간이 소요되었다. 화강암 풍화 실험의 경우 첫 시료가 반응 시간 3시간 후였기 때문에 첫 시료도 반응시간의 2/3 이상이 얼음상에서 진행되었다고 볼 수 있다. 흑운모의 경우 화강암보다 반응속도가 빠를 것이 예상되어 첫 시료는 반응 시간 30분 후로 정했고 얼기까지의 시간 단축을 위해 반응용액의 온도를 미리 4℃까지 낮춘 후 광물 분쇄물을 첨가했다.

라. 풍화 모사 실험 진행과 시료 획득

풍화 모사 실험은 표 1의 고체:액체 비에 맞추어 암석/광물과 pH 3의 반응용액을 혼합하여 각각의 정해진 시간 동안 반응을 진행했다. 화강암 4-63 μm의 경우 0, 3, 6, 12, 18, 24, 192 시간에 해당하는 7가지 반응시간에 각각 얼음, 물 두 가지 반응 조건, 그리고 고체 대 액체의 비를 1 : 100과 4 : 100으로 하는 총 7 x 2 x 2 = 28개의 반응용기를 준비하였다. 흑운모의 경우 반응시간 0.5, 1, 2, 3, 4, 5, 6, 435 시간에 해당하는 8가지 반응시간에 각각 얼음, 물 두 가지 반응 조건, 그리고 암석/광물의 비균질성에 대한 정보를 얻기 위해 각각을 중복한 총 32개의 반응용기를 준비하였다. 암석/광물 분쇄물이 얼음/물과의 접촉을 최대화하기 위해 반응용기를 눕혀서 보관했고, 입자들이 최대한 균질하게 바닥에 펼쳐지도록 했다(그림 2b). 교반기는 사용하지 않았다. 반응시간 후에는 해당 반응용기를 저온반응기에서 꺼내 물중탕으로 해동시켰는데 보통 30분 이내에 가능했고 시간이 초과되는 경우 추가로 적외선 램프를 사용하였다. 반응 후 용액

은 Millipore사의 0.2 μm polycarbonate 필터를 이용하여 여과하였다. 여과된 용액은 미리 세척된 Nalgene사의 LDPE 병에 보관하였다. 보관을 위해 ICP급 질산을 이용해 용액의 pH를 2로 맞추었다.

마. 용존 원소 분석

산을 이용한 실험을 진행했기 때문에 음이온 분석은 하지 않았고, 주요 양이온(Ca, Mg, K, Na)과 Al, Si, Li 농도를 분석하였다. 극지연구소의 이온 크로마토그래프, 서울대학교 공동기기원(NCIRF)의 ICP-MS(Perkin-Elmer사의 Optima 8300), 서울대학교 농생명과학공동기기원(NICEM) 먹는 물 분석 센터의 ICP-AES(inductively coupled plasma-atomic emission spectrometry)를 사용하였다.

바. 화강암 분쇄물에 대한 XRD 광물 분석

서울대 공동기기원 분말 X-선 회절분석기(Rigaku사의 SmartLab)를 이용해서 풍화 모사 실험 후 잔류 암석 분쇄물의 광물 조성이 반응 전에 비해 어떻게 달라졌는지 분석하였다.

3.1.3. 풍화 모사 실험 결과

가. 산성도의 변화

버퍼를 사용하지 않은 실험조건 하에서 산성 용액의 수소이온은 화강암/흑운모의 양이온과 이온교환을 하며 용액의 pH가 증가할 것을 예상할 수 있다. 화강암 63-150 μm 실험에서 pH는 암석 입자와 반응시키기 이전(pH 3)에 비해 큰 변화가 없었고, 얼음이 물보다 더 변화가 적었다(그림 3). 입자크기를 4-63 μm 로 줄인 화강암 실험의 경우 pH가 최대 4.0-4.2까지, 고체 대 액체 비를 높인 경우는 최대 6-6.5까지 증가해서 입자 크기와 암석 분말의 양에 따라 풍화가 더 진행된 것을 볼 수 있다(그림 3). 얼음에서는 첫 3시간동안 pH가 급상승했지만 이후 비슷한 수준을 유지했다. 상온에서는 반응 시작부터 192시간까지 pH가 계속해서 상승했다.

흑운모의 경우는 최대 pH 3.7까지 증가하였다(그림 4). 화강암과는 다르게 초기에는 pH가 상승하다가 4-5 시간 경과 후 상온과 얼음에서 모두 pH가 감소한 것이 특징적이다. 특히 얼음에서는 pH가 반응 초기와 비슷한 수준까지 감소하였다. 흑운모 실험에서 반응 후기에 pH가 오히려 감소한 것은 황화 광물의 용해(식 3)를 의심해 볼 수 있어 추후 철과 황산염 이온의 농도도 분석해 볼 필요가 있다.

나. 용존 원소의 농도

화강암 63-150 μm 실험에서 얼음에서는 반응 시작 후 100시간이 경과한 시점부터는 원소들의 농도가 거의 그대로 유지되었다(그림 5). 물에서는 원소 농도가 시간에 따라 증가하는 경향을 보였으며 특히 Mg의 증가폭이 컸다.

입자크기를 4-63 μm 로 줄인 화강암 실험의 경우 고체:용액 비가 높은 4g:100 ml 경우가 1g:100 ml 일 때보다 주요 양이온 농도가 높았고 이는 얼음, 물 공통이었다(그림 6). 화강암 시료에서의 주요 양이온 농도는 얼음과 물에서 시간에 무관하게 모두 Ca > K > Al > Mg

> Na > Si 순이었다. 화강암 1g:100 ml 실험에서는 초기 6시간 동안 농도 증가(특히 칼슘)가 있었으나 이후 시간에 따른 농도 변화가 거의 없었다고 할 수 있다. 화강암 4g:100 ml 물 실험에서는 칼슘의 계속적인 증가가 관찰되기도 하였다. 주요 양이온들의 농도가 처음 6시간 이내에 급격히 증가하다가 그 이후로는 대체로 비슷한 농도를 유지하는 것은, 입자 크기가 작고 표면적이 큰 만큼 쉽게 녹아나올 수 있는 이온들은 산성인 반응용액과 암석 분쇄물을 섞은 직후에 대부분이 녹아나왔고, 그 이후에는 훨씬 느린 속도로 반응이 진행된 것으로 생각할 수 있다. 이것은 동결농축에 의해서 얼음-광물 시스템에서 화학적 풍화반응이 더 빠르게 일어날 것이라는 예상과는 다른데, 물-광물 시스템에서는 이온이 녹아나오는 반응이 지속되지만 얼음-광물 시스템에서는 용해와 침전이 평형을 이루고 있거나 준액체층의 이온 농도가 높아져 포화상태에 도달해서 이온 농도가 변하지 않는 것을 그 이유로 생각할 수 있을 것이다.

흑운모 실험에서 농도는 얼음과 물에서 모두 Ca > K ≈ Mg > Si > Al > Na 순이었다(그림 6). 얼음과 물에서 Ca, Na은 시간에 따라 큰 변화가 없었다. 얼음에서 K, Mg, Al의 농도가 시간에 따라 증가하였고 Si는 감소하여 특히 마지막 435시간 시료에서는 처음 농도의 2% 정도로 크게 감소했다. 물에서는 K, Mg, Al과 Si까지 모두 증가하여 마지막 435시간 시료에서는 초기 농도의 2배 이상이 되었다.

화강암과 흑운모 시료 모두에서 Ca의 농도가 가장 높은 것은 미시적으로 함유된 방해석이 다른 광물에 비해 쉽게 용해되기 때문인 것으로 추측된다. 화강암 4g:100 ml 실험에서 알루미늄의 농도가 화강암 1g:100 ml이나 흑운모 실험보다 10배 낮았던 것이 특징적인데 데이터의 추가 검토가 필요하다(그림 7).

각기 다른 반응시간을 갖게 되는 시료들 간에 암석분쇄물의 균질성이 확보되는지 확인이 필요해 흑운모 실험의 경우 모든 시료를 duplicate로 진행하였다. 얼음 3.7 시간 시료를 제외하면 실험군의 duplicate는 15%이내 일치하였고 대조군의 duplicate는 5% 이내 일치하여서 암석분쇄물의 균질성이 전체 반응의 추세 해석에 지장을 주지는 않는다고 파악하였다.

다. 규산염광물의 풍화 정도

칼슘(Ca)은 방해석과 사장석에 공통인 원소이므로 규산염광물에 특징적인 Na, K, Si 원소들을 중심으로 규산염광물의 풍화 정도를 검토하였다. 일반적으로 Si/K의 비율이 낮을수록 1차 규산염광물이 양이온이 여전히 풍부한 풍화산물을 만드는 반응이 진행되는 것이고, Si/K의 비율이 높을수록 양이온이 결여된 kaolinite, gibbsite로까지 풍화가 진행된다고 생각할 수 있다. 화강암의 4-63 μm의 경우 암석 대 용액 비율에 관계없이 모두 용존 규소의 농도가 매우 낮았고 따라서 매우 낮은 Si/K비, 즉 피상적인 풍화를 지시하고 있다. 즉 규산염광물에서 양이온이 녹아 나오는 단계이다. 이는 용존 Al의 농도가 매우 높은 것과는 상반되는 것이어서 흥미롭다(그림 8). 흑운모의 경우는 Si/K의 비가 비교적 높고(~0.8) 모든 시료가 비슷한 비율을 보였고, 상온에서 Si와 K의 농도가 더 높았다.

용존 원소 분석 자료를 이용하여 풍화 정도를 지시하는 화학적 풍화 지표(chemical weathering index: CIA = chemical index of alteration, CIW = chemical index of weathering)를 계산하였으나, 화강암 실험에서는 물과 얼음 상에 따른 유의미한 차이가 적어도 실험한 시

간 스케일에서 주원소 이온들 자료에서는 보이지 않았다(표 2).

Na-K-Si ternary diagram(Jacobson et al. 2002)에서 사장석에서 kaolinite로, 사장석에서 2차광물이 beidellite로, 흑운모에서 2차광물인 vermiculite로, 흑운모에서 kaolinite로 풍화되는 반응을 고려하여 검토하였다. 화강암 실험의 경우 규소 농도가 낮고 큰 변화가 없어서 반응의 경향성 확인에 효과적이지 않았다. 흑운모 실험의 경우 시료들이 일직선상에 놓였는데 Na:K:Si = 1:7:5 지점을 중심으로 얼음 실험은 흑운모에서 vermiculite로 풍화되는 쪽에, 물 실험은 흑운모에서 kaolinite까지 풍화되는 쪽에 분포했다(그림 9). 여기에 소량 사장석이 kaolinite 또는 beidellite로 풍화하는 것으로 보인다. 이는 흑운모가 반응하는 환경(얼음, 물)에 따라 서로 다른 풍화 반응이 일어남을 지시한다.

라. 풍화 모사 실험 후 잔여물의 광물 조성

XRD 분석 결과 화강암 풍화 모사 실험 후에는 초기 화강암 시료에 비해 장석류(anorthite, $CaAl_2Si_2O_8$; microcline, $KAlSi_3O_8$)와 운모류(muscovite, biotite)가 감소하였고, 특히 albite와 muscovite가 두드러지게 감소하여, 이들 광물이 풍화되었음을 지시하였다(그림 10, 11). 그러나 물과 얼음 상에 따른 유의미한 차이는 보이지 않았다.

3.2. 리튬 동위원소 비 분석 테스팅

3.2.1. 매질로부터 리튬 분리

풍화 모사 실험에서 얻은 액체 시료에 포함된 리튬의 동위원소 비를 분석하기 위해 먼저 양이온 칼럼 크로마토그래피를 이용하였다. 구체적인 분리법 설계는 선행연구(Choi et al., 2013)를 참고하였다. Bio-Rad사의 0.8 cm 직경, 4 cm 길이의 폴리프로필렌 재질 Poly-Prep 크로마토그래피 칼럼에 Bio-Rad사의 AG®50W-X8 200 - 400 mesh 양이온교환수지를 1.8 ml 채웠다. 칼럼에 0.15 M 불산(ASP사의 PC-HF) 10 ml를 흘려 철과 알루미늄을 제거하였고, 6 M 염산(JKC사의 ICP-100) 30 ml를 통과시켜 칼슘과 나트륨을 세척해내었으며, 마지막으로 18.2 MΩ·cm H_2O 5 ml를 흘려 산을 희석했다.

리튬의 양이 100 ng가 될 정도 양의 시료를 준비하여 약 70℃에서 용매를 증발시켰다. 증발시키고 남은 잔여물에 0.5 ml의 용리액(eluent, 1:4 (v/v) 6 M 질산:메탄올)을 넣어 완전히 용해시켰다. 질산은 ASP사의 FC-HNO_3, 메탄올은 Sigma-Aldrich사의 HPLC급(≧99.9%)이었다. 먼저 용리액 5 ml로 칼럼 conditioning을 한 후, 용리액에 용해시킨 시료 0.5 ml를 컬럼에 흘리고 추가로 0.5 ml의 용리액를 더 흘려주었다. 이후 본격적인 용리과정을 시작하는데, 사전에 진행한 칼럼 calibration에 의하면 리튬은 6 - 16 ml에서 용리되므로 최초 6 ml는 취하지 않고 버린다. 용리과정에서 칼럼의 유속을 0.2 ml/min 이하로 맞추기 위해 용리액은 2 ml씩 나눠서 넣었다. 리튬이 용리된 10 ml의 용액은 70℃에서 증발시키고, 5 ml의 2% HNO_3에 녹여 MC-ICP-MS 분석에 이용했다.

3.2.2. MC-ICP-MS 분석

리튬 동위원소 비 분석에는 서울대학교 공동기기원 무기물성분석팀의 MC-ICP-MS (Multi

Collector-Inductively Coupled Plasma-Mass Spectrometer)를 사용했다. 장비는 Nu Plasma 3에 Cetac Aridus II 탈용매화 장치가 부착되어 있다. MC-ICP-MS의 구체적인 세팅은 표 3과 같다.

서울대 공동기기원 MC-ICP-MS 장비는 다양한 원소에 대한 분석을 진행하고 있는데, 다른 원소 세팅에서 리튬 세팅으로 바꾼 당일에는 데이터가 불안정한 경우가 많아서 충분히 안정화시킨 후 분석을 진행했다. 리튬 동위원소 분석을 위한 기기 튜닝에는 20 ppb 농도로 희석한 리튬 표준용액(Sigma-Aldrich사의 Li standard for ICP, 1000 mg/L Li in 2% nitric acid, TraceCERT)을 이용했다. 이 농도는 시료의 리튬 농도와 유사하다. 튜닝은 리튬 신호의 세기가 200 mV/ppb 정도가 되도록 기기조건을 최적화시켰다. 튜닝을 진행한 후 20 ppb L-SVEC(IAEA, Li_2CO_3) 용액과 Li 표준용액을 분석하여 정확도를 확인하였다. 사이사이에 2% HNO_3으로 리튬 바탕값이 표준용액의 0.1% 이하로 떨어질 때까지 세척하였다. 시료를 분석할 때는 표준용액을 시료 앞뒤로 분석하여 시간에 따른 기기의 감도 변화를 보정하였다(Standard-Sample Bracketing).

Li 동위원소 비 스탠다드 용액(L-SVEC)을 약 20 ppb로 희석하여 분석했을 때 ^{7}Li signal intensity는 약 4.4 V, 동위원소 비는 -0.01±0.08‰ (2σ, n=9)의 값을 얻었다(dry plasma, 20 cycles, 1 block, integration time 5 sec). 해수에서 Li 동위원소 비는 L-SVEC에 대하여 31.0±0.1‰ (2σ, Millot et al., 2004) 정도의 값을 갖는 것으로 알려져 있는데, 해수 표준 용액인 NASS-7을 전처리 후 약 20 ppb로 희석하여 분석했을 때 신호세기는 약 5 V, 동위원소 비는 L-SVEC에 대하여 31.4±0.7‰ (2σ, n=3)의 값을 얻었다. 또한, NASS-7에 대해 문헌과 비슷한 값을 얻어 Li의 전처리가 잘 되었을 것이라 판단할 수 있다.

3.2.3. 칼럼분리의 수율(yield) 테스트

칼럼에 도입된 시료의 리튬을 100% 회수하지 않으면 리튬과 같은 질량이 낮은 원소의 경우 이 과정에서 분별이 크게 일어나므로 수율 테스트를 진행했다. 수율 테스트는 Li 표준용액을 이용하여 칼럼분리를 진행하고 MC-ICP-MS를 이용하여 농도와 동위원소 비를 확인했다(그림 12). 수율은 98-104%였고 $\delta^{7}Li$은 0.3 ± 0.2‰로 정확성과 재현성이 테스트 초기에 비해 개선되었다.

3.2.4. 화강암 풍화 모사 실험 중 리튬 동위원소 비 변화

화강암 풍화 모사 실험(4-63 μm 1g:100 ml)에서 얻은 시료의 리튬 동위원소 비를 분석했을 때 얼음과 물 실험 모두 화강암의 평균값에 비해 낮은 값이 나왔다(그림 13). 하지만 이 역시 전 세계적 화강암의 리튬 동위원소 비 범위 안에는 드는 값이다. 일반적으로 용존 리튬에 ^{7}Li이 그리고 잔여 2차광물에 ^{6}Li이 선택적으로 분포한다고 알려져 있는데, 크기가 작기는 하지만 경향성은 어긋난다고 볼 수 있다. 리튬 동위원소 비와 리튬 농도 사이에 뚜렷한 상관관계가 없어서 mixing의 결과로 보기도 어렵다. 얼음 실험의 경우 최종 시료의 리튬 동위원소 비는 다른 시료들보다 $\delta^{7}Li$값이 낮고 화강암의 평균보다 낮아서 특정 광물의 선택적 풍화가 의심된다. 추후 재분석으로 확인이 필요하다.

KOPRI 극지연구소

4. 연구개발목표 달성도 및 대외기여도

1차년도의 목표는 얼음상에서의 화강암 풍화 모사 실험 시스템을 구축하는 것이었고, 세부 목표로는 모사실험의 다양한 파라미터를 정립하고 원소 분석과 특히 리튬 동위원소 분석을 위한 전처리 과정을 확립하는 것이었다. 모사 실험 결과 실제로 동위원소 분석이 가능한 농도의 리튬 시료를 얻었고, 리튬 동위원소 전처리도 해수 시료와 LSVEC 표준물을 교차 분석하여 문헌치를 재현할 수 있었다.

2차년도의 목표는 차별적 풍화에 기여하는 구체적인 광물을 대상으로 풍화 모사 실험을 진행하는 것이었는데, 역시 세부 목표로는 풍화 속도가 1차년도의 화강암과는 다른 흑운모 광물에 대한 모사실험의 다양한 파라미터를 정립하고 (연구진 교체로 인해 다시금 새로이) 리튬 동위원소 분석을 위한 전처리 테스트를 진행하는 것이었다. 모사 실험 결과 실제로 동위원소 분석이 가능한 농도의 리튬 시료를 얻었고, 원소 분석 결과 화강암 실험 때보다 얼음-물 간 더 큰 차이와 시간에 따른 변화를 관찰하였다.

얼음 상에서 진행하는 풍화 모사 시스템을 설계하는데 know-how를 축적하였고, 리튬 동위원소 분석과 MC-ICP-MS 이용에도 경험을 축적하였다.

5. 참고문헌

Bray, Andy & Oelkers, Eric & Bonneville, S.C. & Wolff-Boenisch, Domenik & Potts, Nicola & Fones, Gary & Benning, Liane. (2015). The effect of pH, grain size, and organic ligands on biotite weathering rates. *Geochimica et Cosmochimica Acta*. 56. 10.1016/j.gca.2015.04.048

Choi, M. S., Ryu, J. S., Park, H. Y., Lee, K. S., Kil, Y. and Shin, H. S. 2013. Precise determination of the lithium isotope ratio in geological samples using MC-ICP-MS with cool plasma. *Journal of Analytical Atomic Spectrometry*, 28(4), 505-509.

Haldorsen, S., 1981. Grain size distribution of subglacial till and its relation to glacial crushing and abrasion. *Boreas*, 10(1), 91-105.

Hatton, J.E., Hendry, K.R., Hawkings, J.R., Wadham, J.L., Opfergelt, S., Kohler, T.J., Yde, J.C., Stibal, M. and Žárský, J.D., 2019. Silicon isotopes in Arctic and sub-Arctic glacial meltwaters: the role of subglacial weathering in the silicon cycle. Proceedings of the Royal Society A, 475(2228), p.20190098.

Hawkings, J.R., Wadham, J.L., Benning, L.G., Hendry, K.R., Tranter, M., Tedstone, A., Nienow, P. and Raiswell, R., 2017. Ice sheets as a missing source of silica to the polar oceans. Nature communications, 8(1), pp.1-10.

Jacobson, A.D., Blum, J.D., Chamberlain, C.P., Craw, D. and Koons, P.O., 2003. Climatic and tectonic controls on chemical weathering in the New Zealand Southern Alps. Geochimica et Cosmochimica Acta, 67(1), pp.29-46.

KOPRI 극지연구소

Jeong, D., Kim, K. and Choi, W., 2012. Accelerated dissolution of iron oxides in ice. Atmospheric Chemistry & Physics, 12(22).

Jeong, D., Kim, K., Min, D.W. and Choi, W., 2015. Freezing-enhanced dissolution of iron oxides: effects of inorganic acid anions. Environmental science & technology, 49(21), pp.12816-12822.

Kim, K., Choi, W., Hoffmann, M.R., Yoon, H.I. and Park, B.K., 2010. Photoreductive dissolution of iron oxides trapped in ice and its environmental implications. *Environmental Science & Technology*, 44(11), 4142-4148.

Kim, K., Kim, J., Bokare, A.D., Choi, W., Yoon, H.I. and Kim, J., 2015. Enhanced removal of hexavalent chromium in the presence of H_2O_2 in frozen aqueous solutions. *Environmental Science & Technology*, 49(18), 10937-10944.

Millot, R., Guerrot, C. and Vigier, N., 2004. Accurate and high precision measurement of lithium isotopes in two reference materials by MC ICP MS. *Geostandards and Geoanalytical Research*, 28(1), 153-159.

Misra, S. and Froelich, P. N., 2012. Lithium isotope history of Cenozoic seawater: changes in silicate weathering and reverse weathering. *Science*, 335(6070), 818-823.

Pistiner, J. S., & Henderson, G. M., 2003. Lithium-isotope fractionation during continental weathering processes. E*arth and Planetary Science Letters*, 214(1-2), 327-339.

Pogge von Strandmann, P.A.E., Jenkyns, H.C. and Woodfine, R.G., 2013. Lithium isotope evidence for enhanced weathering during Oceanic Anoxic Event 2. Nature Geoscience, 6(8), pp.668-672.

Rosenbaum, J. G. and Reynolds, R. L., 2004. Record of Late Pleistocene glaciation and deglaciation in the southern Cascade Range. II. Flux of glacial flour in a sediment core from Upper Klamath Lake, Oregon. *Journal of Paleolimnology*, 31(2), 235-252.

Stillings, L. L. and Brantley, S. L., 1995. Feldspar dissolution at 25 C and pH 3: Reaction stoichiometry and the effect of cations. *Geochimica et Cosmochimica Acta*, 59(8), 1483-1496.

Teng, F.Z., Rudnick, R.L., McDonough, W.F. and Wu, F.Y., 2009. Lithium isotopic systematics of A-type granites and their mafic enclaves: Further constraints on the Li isotopic composition of the continental crust. Chemical Geology, 262(3-4), pp.370-379.

Torres, M.A., Moosdorf, N., Hartmann, J., Adkins, J.F. and West, A.J., 2017. Glacial weathering, sulfide oxidation, and global carbon cycle feedbacks. Proceedings of the National Academy of Sciences, 114(33), pp.8716-8721.

White, A.F. and Blum, A.E., 1995. Effects of climate on chemical_ weathering in

watersheds. Geochimica et Cosmochimica Acta, 59(9), pp.1729-1747.

Wimpenny, J., Gíslason, S. R., James, R. H., Gannoun, A., Von Strandmann, P. A. P. and Burton, K. W., 2010. The behaviour of Li and Mg isotopes during primary phase dissolution and secondary mineral formation in basalt. *Geochimica et Cosmochimica Acta*, 74(18), 5259-5279.

KOPRI
극지연구소

표 1. 화강암과 흑운모를 대상으로 얼음과 물에서 진행한 풍화 모사 실험 조건

암석/광물	반응 용액	반응 온도	Grain Size(μm)	고체(g):액체(ml) 비	반응 시간 (hr)
화강암	pH 3 HCl	실험군: -20℃ 대조군: +25℃	63 - 150 4 - 63 4 - 63	1 : 100 1 : 100 4 : 100	1, 24, 96, 480 1, 3, 6, 12, 18, 24, 192 1, 3, 6, 12, 18, 24, 192
흑운모	pH 3 HNO_3		63 - 150	0.5 : 200	0.5, 1, 2, 3, 4, 5, 6, 7, 435

표 2. 주원소이온 분석 결과를 이용해 계산한 화강암의 화학적 풍화도.

Samples	63-150 μm		4-63 μm			
	1 g : 100 ml		1 g : 100 ml		4 g : 100 ml	
	Water	Ice	Water	Ice	Water	Ice
CIA	48.2	48.1	48.5	48.5	63.6	63.6
CIW	68.9	68.9	69.4	69.4	70.5	70.4

극지연구소

표 3. 리튬 동위원소 분석에 사용한 서울대 공동기기원 MC-ICP-MS의 세팅

Parameter	Setting
Plasma type	Dry plasma
RF power	1300 W
Faraday cup	H8(^{7}Li), L5(^{6}Li)
Li concentration	20 ppb (dissolved in 2% HNO_3)
Measurements	1 block 20 cycles
Zero integration/Sample integration	20 s / 5 s
Nebulizer pressure	36.0 psi
Auxiliary gas flow rate	1.5 L / min
Signal intensity	4-6 V
HNO_3 Blank intensity	< 0.002 V
Uptake time	> 30 s
Wash time	> 120 s

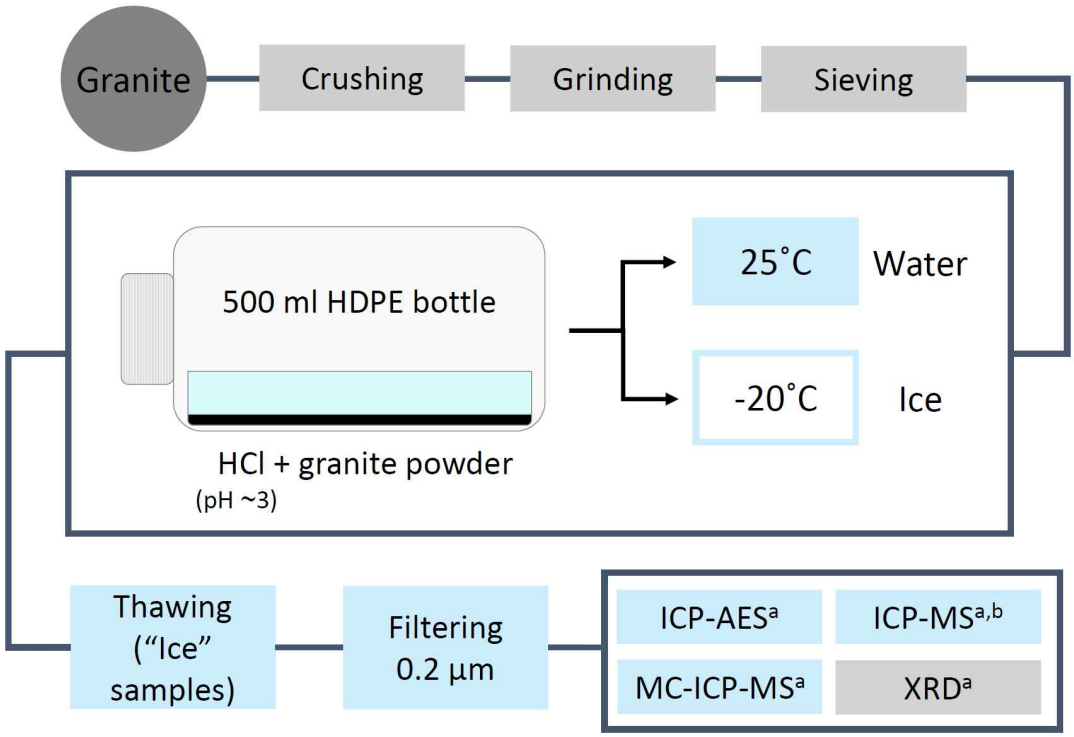

그림 1. 풍화 모사 실험의 진행 모식도. 흑운모도 같은 과정으로 진행했다. a: 서울대 공동기기원, b: KBSI 서울분소.

그림 2. 풍화 모사 실험 진행 사진. (a) 부피 500 ml HDPE 사각병에 암석 분쇄물와 pH 3의 반응용액을 넣는다. (b) 암석 분쇄물을 용기 바닥에 균질하게 펼친다. (c) 반응용기를 밀봉하고, 빛을 차단하기 위하여 은박지로 감싼 후 물-암석/광물 세트는 상온에, 얼음-암석/광물 세트는 영하 20도의 저온반응기에 보관한다.

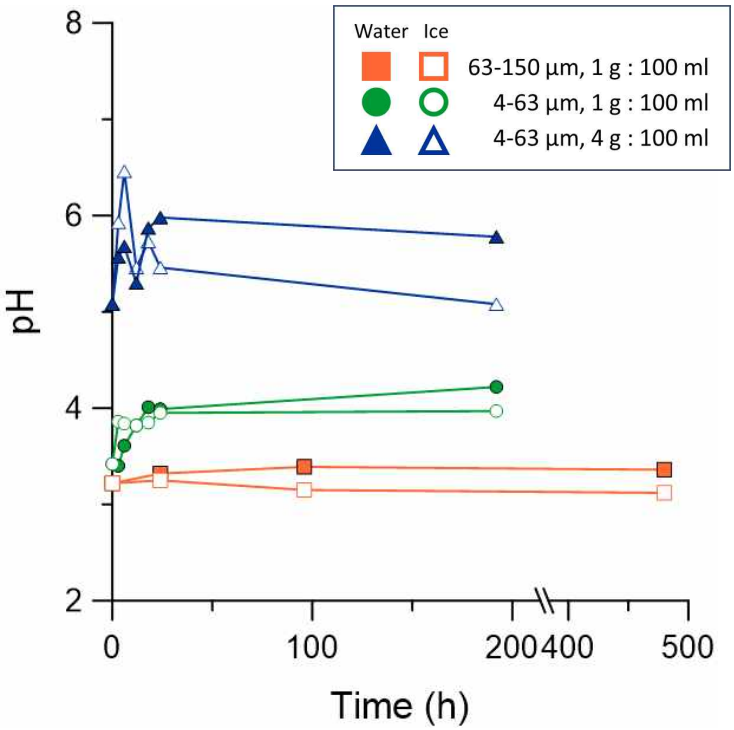

그림 3. 화강암 실험에서 pH 변화.

KOPRI 극지연구소

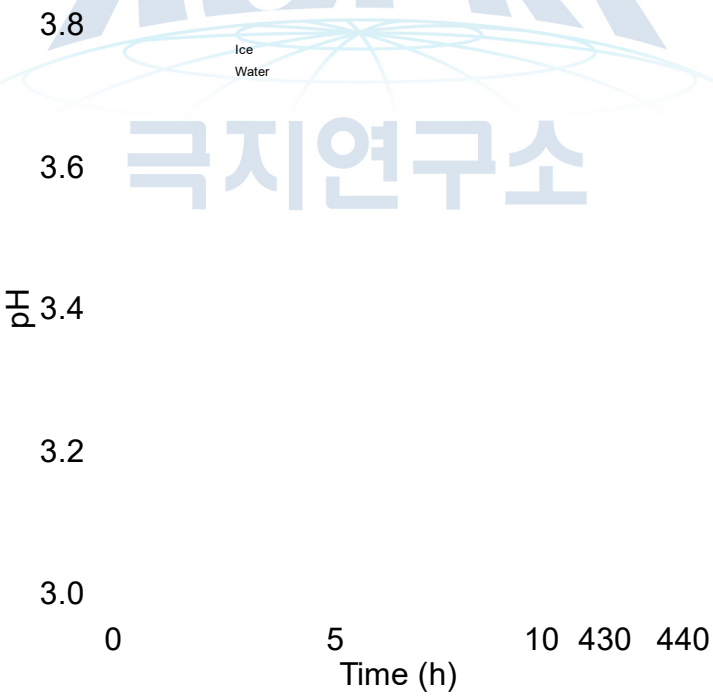

그림 4. 흑운모 풍화 실험에서 시간에 따른 pH의 변화.

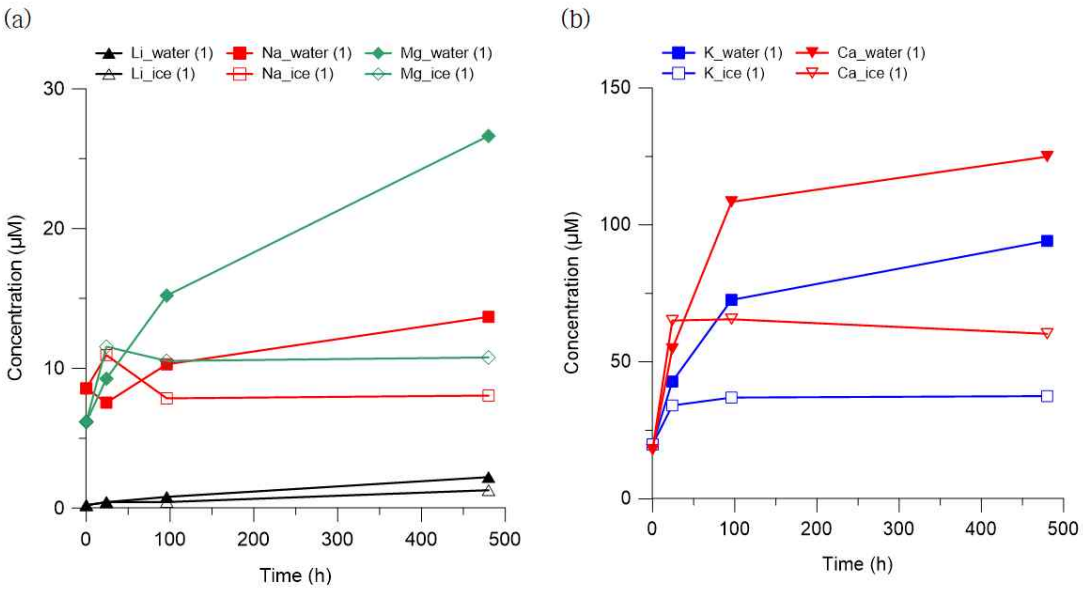

그림 5. 화강암 63-150 μm 실험의 (a) 리튬, 나트륨과 (b) 칼륨, 칼슘 농도 변화.

KOPRI
극지연구소

Granite 4-63 μm 1g:100 ml

Granite 4-63 μm 4g:100 ml

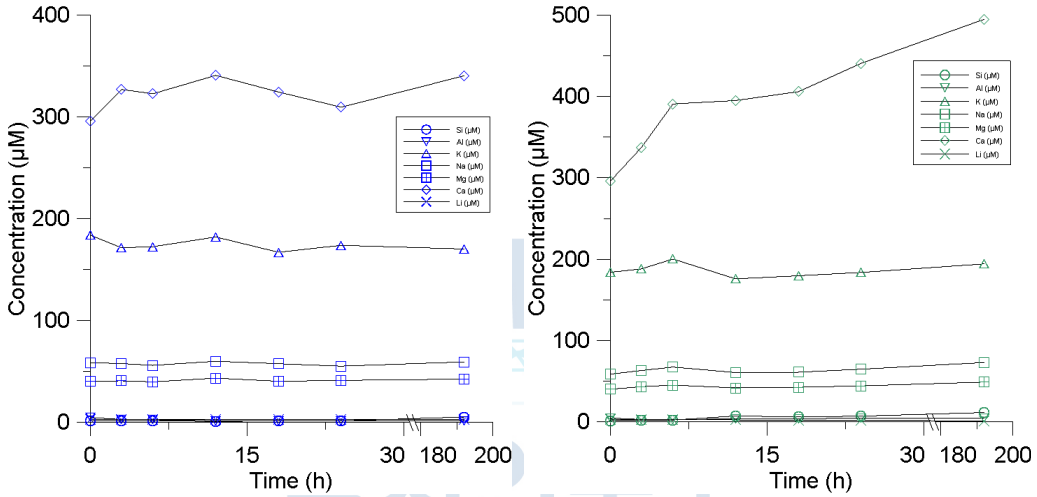

Biotite 63-150 μm 0.5g:200 ml

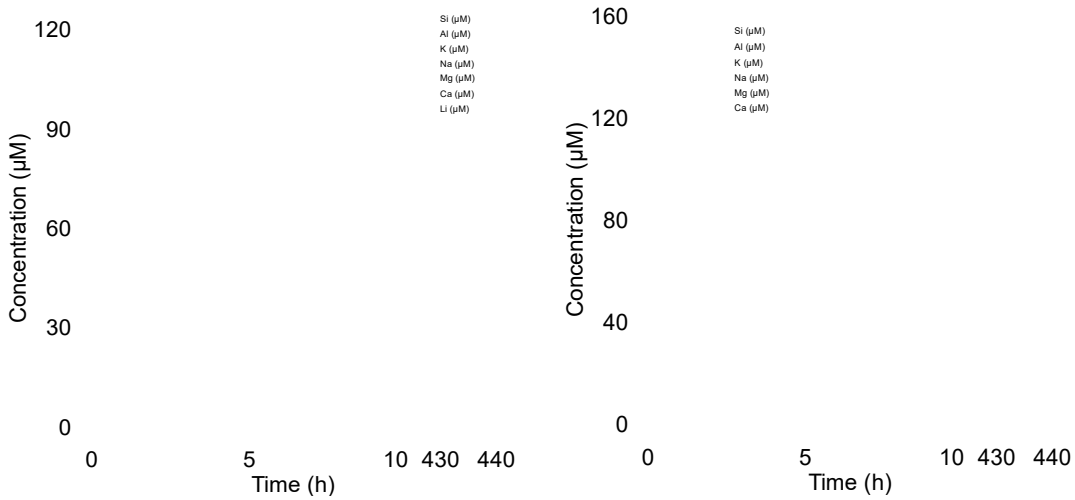

그림 6. 화강암 1g:100ml(상단), 화강암 4g:100ml(중간), 흑운모(하단) 실험결과 용존 원소 농도의 시간 변화. 왼쪽은 -20도 얼음 실험, 오른쪽은 상온 물 실험.

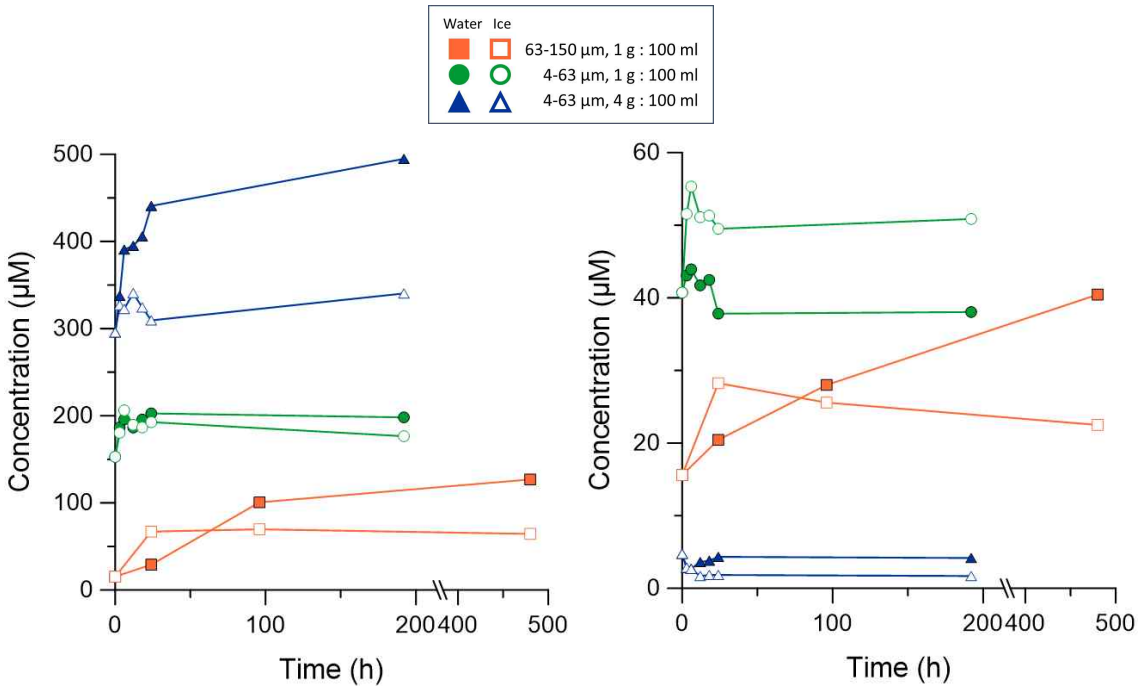

그림 7. 화강암 실험의 (왼쪽)칼슘 농도와 (오른쪽)알루미늄 농도.

KOPRI
극지연구소

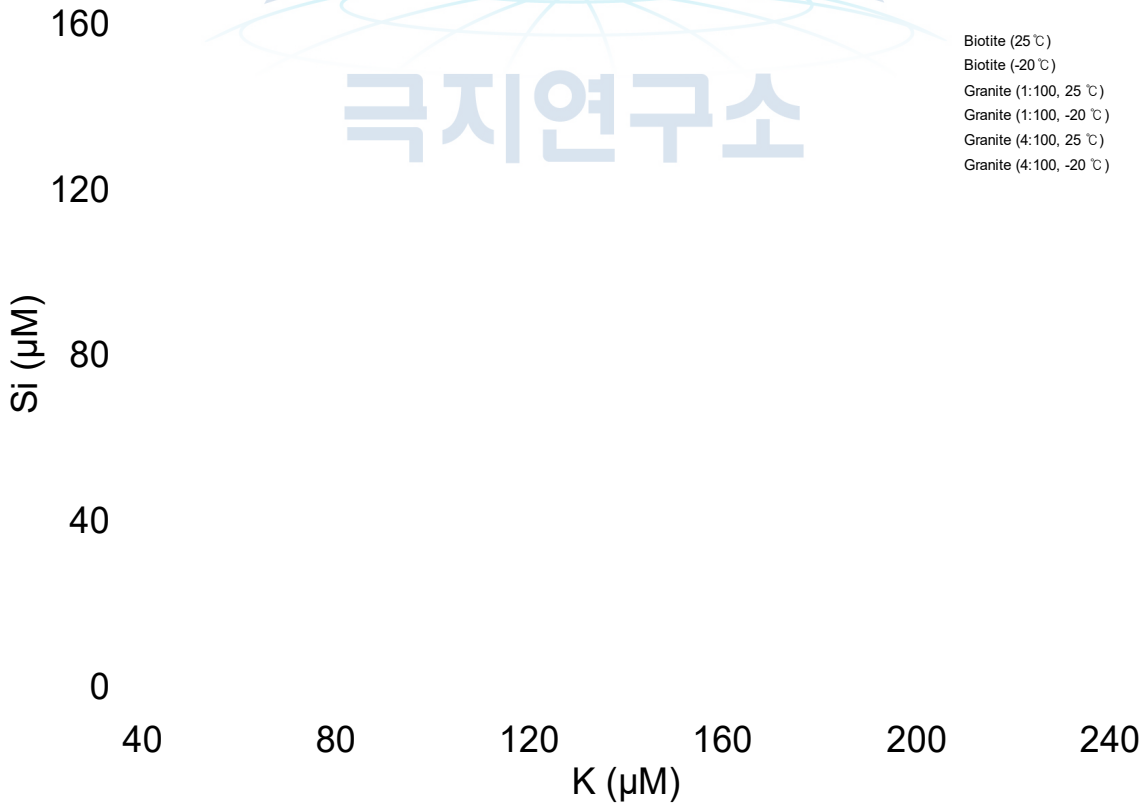

그림 8. 용존 규소 대 칼륨 농도의 비.

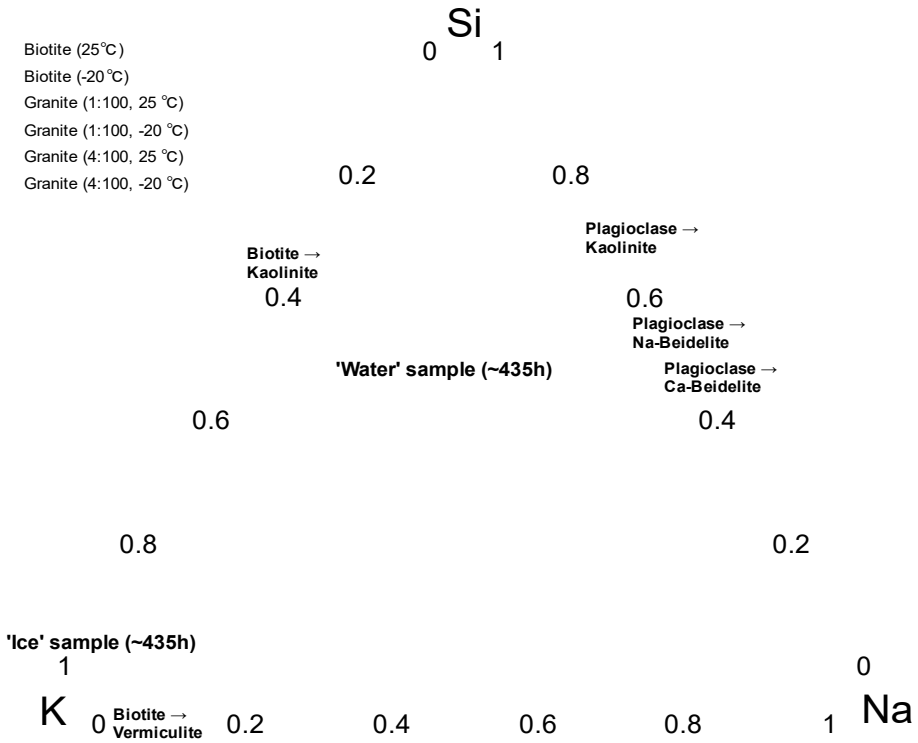

그림 9. Na-K-Si ternary diagram. 각 end-member의 위치는 Jacobson et al. (2002)를 참조했다.

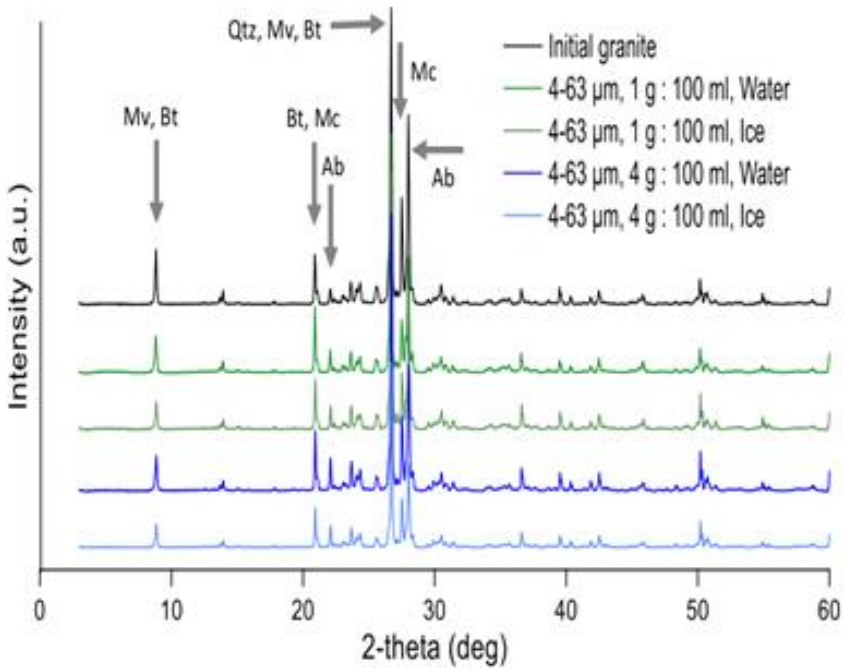

그림 10. 화강암 풍화 모사 실험 후 최종 고체 산물에 대한 XRD 분석 결과. Mv : muscovite, Bt : biotite, Mc : microcline, Ab : albite, Qtz : quartz

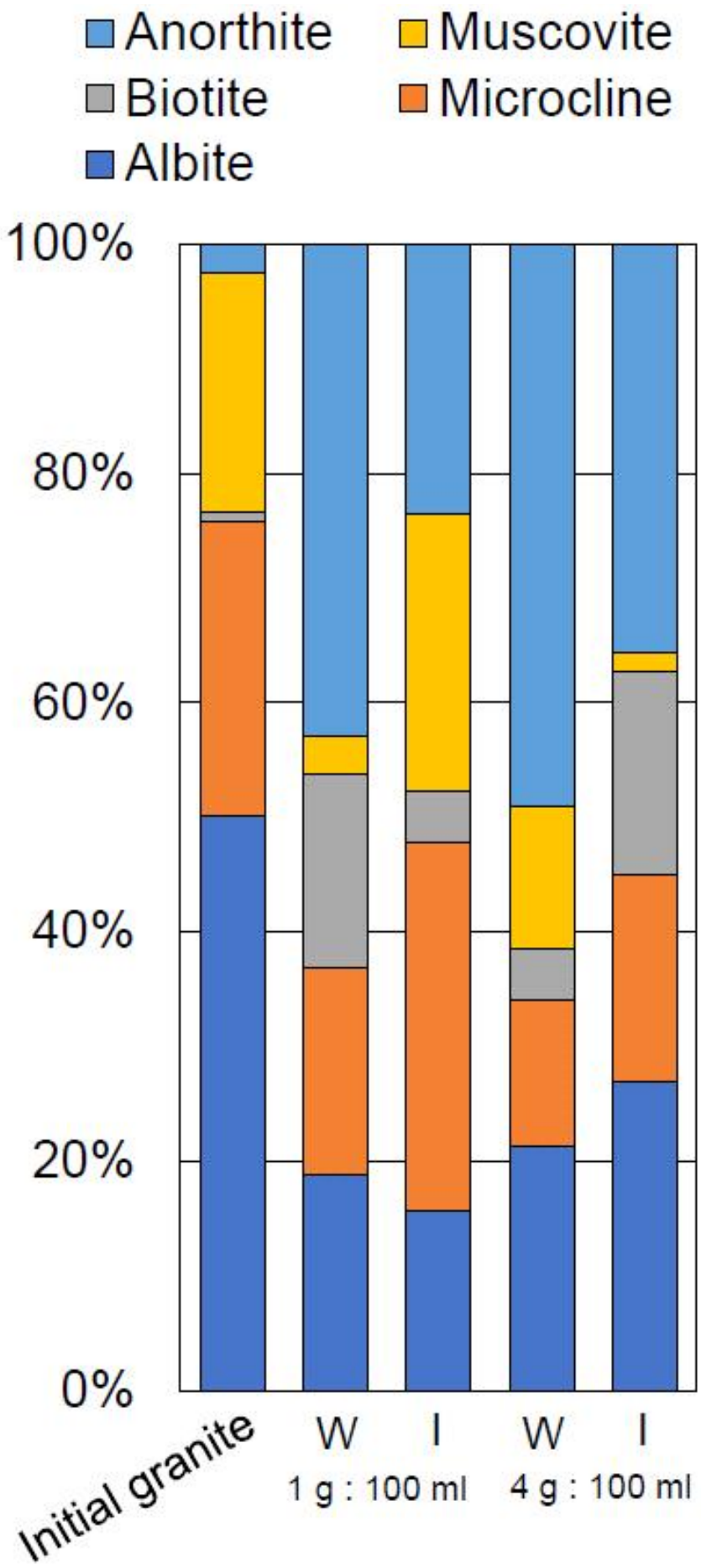

그림 11. Whole Powder Pattern Fitting 결과(quartz-normalized).

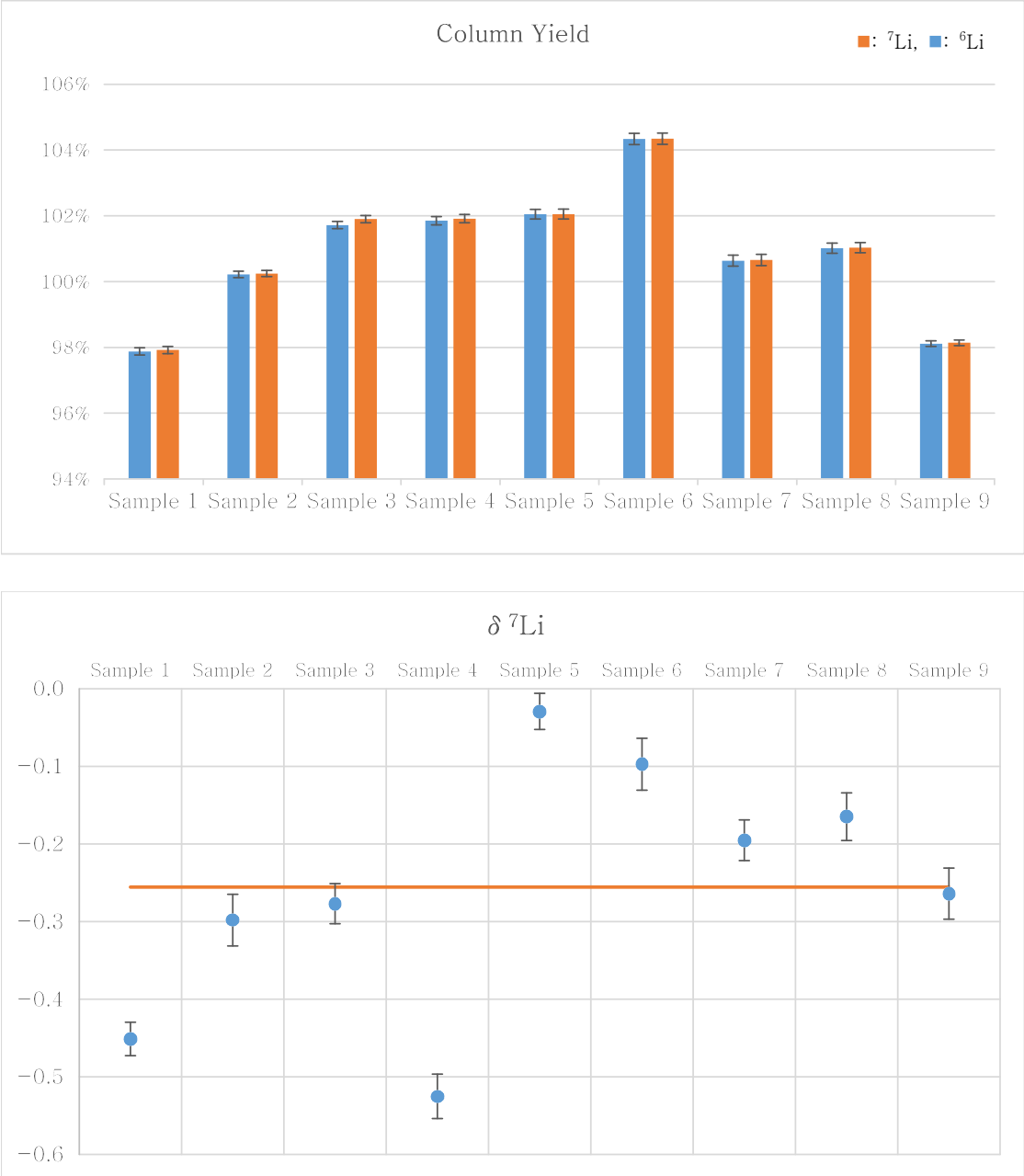

그림 12. 수율테스트 결과. (위) 농도 분석을 통한 수율 추정치, (아래) 리튬 동위원소 비

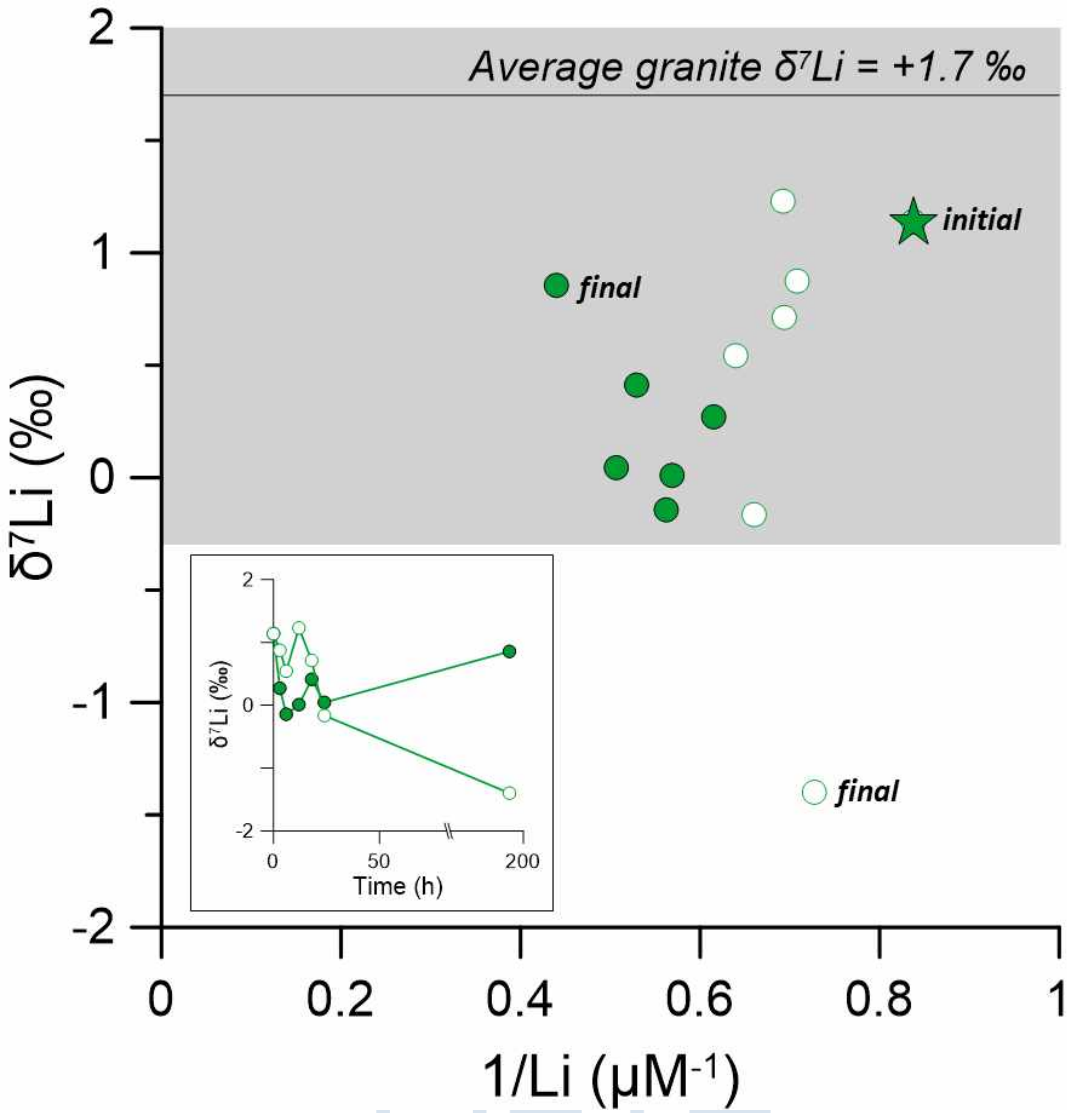

그림 13. 화강암 4-63 μm 1 g : 100 ml 풍화 모사 실험 시료에 대한 리튬 동위원소와 농도 분석 결과.
★ : 풍화 모사 실험 시작 전 초기치
- : 화강암의 평균값 δ^7Li (+1.7 ‰) (Teng et al., 2009)
■ : 화강암의 범위 (Teng et al., 2009)

제 13 절. 얼음에서 일어나는 화학적 풍화작용과 극지방 자연 현상 이해

정현영, 김기태

한국해양과학기술원 부설 극지연구소

1. 서론 및 배경

화학적 풍화는 대기 중 이산화탄소를 흡수하는 기작의 측면에서 연구되어 옴. 특히 규산암의 풍화는 지질학적 시간 규모에서 대기 중 이산화탄소를 흡수하는 순 효과(net effect)가 있지만, 탄산암의 경우 풍화작용에서 흡수한 만큼의 해양과 대기 순환에서 다시 이산화탄소를 내놓아 순 효과가 없는 것으로 알려져 있음(Berner, 1992). 화학적 풍화작용은 암석이 산 또는 산화시킬 수 있는 물질과 반응할 때 일어나며, 기후(온도, 강수량 등), 모재, 생물상 등의 영향을 받음(White & Blum, 1995; Gaillardet *et al.*, 1999; Drever & Stillings, 1997). 물리적 풍화는 화학적인 반응 없이 광물이나 암석이 파편화되거나 그로부터 물질이 빠져나오는 현상을 의미함. 물리적 풍화작용은 유역의 고도, 지형, 유량 등에 영향을 받음.

극지방은 적은 양의 강수량과 낮은 기온, 고등식물의 부재로 화학적 풍화가 거의 일어나지 않을 것으로 생각됨(Bockheim, 1997; Gooseff *et al.*, 2002). 그러나 소수의 극지방 연구에서는 온대지방과 비슷한 수준의 풍화작용이 극지방에서 일어남을 제시함(Prestrud Anderson *et al.*, 1997; Nezat *et al.*, 2001). 기존 연구에서 이러한 극지방에서의 화학적 풍화가 빠른 유속에 의해 새로운 지속적으로 노출되며 증가하는 물리적 풍화 때문인 것으로 설명하고 있음(Prestrud Anderson *et al.*, 1997; Huh, 2003). 또한 기존 연구에서는 극지방에서 높은 농도의 양이온과 상대적으로 낮은 양의 실리카 농도를 보임(Prestrud Anderson *et al.*, 1997). 극지방에서 화학적 풍화를 촉진하는 요인으로는 빠른 유속, 염류풍화작용, 미생물 등이 제시됨(Huh, 2003; Bisson *et al.*, 2015; Maurice *et al.*, 2002). 그러나 기존의 극지방 연구에서는 동결된 상태에서 광물 또는 암석의 풍화작용은 연구되지 않음.

최근의 연구에서 아질산염의 산화, 산화철의 용해와 같은 기존의 인식과 다르게 얼음에서 반응속도가 증가하는 화학반응이 제시됨(Kim *et al.*, 2010; Kim *et al.*, 2019). 이러한 얼음에서의 산화철의 용해반응은 동결농축효과와 준액체층에서 일어나는 양성자에 의한 반응 때문인 것으로 연구됨. 낮은 온도에서 수용액이 고체화될 때 용질은 얼음으로부터 밀려나 준액체층으로 농축되는 것으로 알려져 있음(Takenaka *et al.*, 1996). 이 연구에서는 기존에 고려되지 않은 동결현상과 함께 극지방에서 일어나는 광물과 암석의 풍화작용을 연구하고자 함.

2. 재료 및 방법

2-1. 실험실 실험

2-1-1. 재료 준비 및 실험 방법

실험에 사용한 광물, 암석, 점토 샘플은 Ward's Science에서 구입함. 구입한 광물 및 암석 덩어리는 다이아몬드 날을 이용하여 절단한 뒤 3차 증류수로 세척하여 자연건조시킴. 건조된 광물 및 암석 조각은 링밀(ring mill)을 이용하여 분쇄함. 작은 입자에 의한 영향을 살피기 위한 실험에서는 53 μm 크기의 체를 이용하여 작은 입자의 가루를 분리함. 지름 60 mm의 페트리디쉬에 0.1 g 또는 0.01 g의 광물, 암석, 또는 점토 가루를 넣고 증류수와 pH 조절을 위한 염산 또는 수산화나트륨 수용액을 가함. 유기산의 영향을 살피기 위해 아스코르브산 또는 옥살산을 1 mM 제조하여 가함. 페트리디쉬는 파라필름으로 밀봉하여 상온 또는 -20℃로 설정된 공랭식 저온반응기에 반응시간 동안 놓아둠(그림 1). 각 샘플은 반복성을 위하여 세 개씩 제조함. 동결 샘플은 30-40℃의 미지근한 물에서 해동하였으며, 액상 및 동결 샘플은 공극 크기 0.2 μm의 필터를 이용하여 여과함. 여과된 액체는 이온 크로마토그래피, 분광광도계 등을 이용하여 분석함. 필터에 걸러진 고체상은 풍건시켜 XRD, XRF 등을 이용하여 분석함.

2-1-2. 분석 방법

pH meter(Thermo Scientific, Orion 3 star)를 이용하여 제조한 HCl 및 샘플의 pH를 분석함. 액상 샘플의 양이온 농도 분석을 위하여 이온크로마토그래피 시스템(Ion chromatography, Dionex ICS-1100)을 이용함. 이온크로마토그래피의 분석 조건은 다음과 같음: 유속 1.00 mL/min, CS12A 컬럼, CERS 500 4 mm 서프레서(59mA), MSA(methane sulfonic acid) 용리액. 810 nm에서 UV-Vis spectrophotometer(Shimadzu, UV-2600)를 이용하여 몰리브덴 발색법으로 실리카 농도를 분석함. 시료의 화학적 조성을 분석하기 위하여 마이크로 XRF 분석기(Micro X-ray fluorescence analyzer)를 이용함. XRF의 분석 조건은 다음과 같음: μ-XRF, M4 Tornado, Bruker, Karlsruhe, Germany, 50 kV, 600 μA, 1 s/scanning point. 실험 전후의 광물 조성을 파악하기 위하여 XRD(X-ray diffraction) 분석을 수행함. XRD 분석 조건은 다음과 같음: Rigaku MiniFlex(II), 스캔 속도 1.5 °/min, 0.02° step over the range of 2-theta angles (2 - 80°). 광학현미경(Leika microsystem, Lens HC PLAN 10×20 BR, L 50×/0.50)을 이용하여 준액체층을 관찰하였으며, 광학적 관찰을 위한 시료는 액체질소와 linkam stage를 이용하여 -2℃ min^{-1}의 속도로 -20℃까지 동결함.

2-2. 현장연구 (2018)

2018년 남극 하계 기간 동안 이루어진 현장연구에서 남극세종과학기지 인근 및 바톤반도에서 샘플링을 수행함(그림 2). 얼음에서 일어나는 풍화작용을 연구하기 위하여 눈, 담수, 얼음, 담수 퇴적물, 토양, 해수, 해빙 샘플을 채취함. 채취한 샘플은 남극세종과학기지에서 0.45 μm 공극 크기의 필터로 필터링하였으며, 필터링 전후의 pH 및 전기전도도를 분석함. 0.01 N의 염산을 이용하여 50 mL의 샘플에 대하여 알칼리도를 분석함. 필터링 후의 샘플은 음이온 분석을 위한 냉장 상태, 양이온 분석을 위하여 질산을 가한 후 냉장 상태, 또는 추후 분석을 위한 냉동 상

태로 운반하여 보관함. 양이온 및 음이온 분석을 위하여 이온크로마토그래피 시스템(Ion chromatography, Dionex ICS-1100)을 이용함. 양이온 분석 조건은 다음과 같음: 유속 1.00 mL/min, CS12A 컬럼, CERS 500 4 mm 서프레서(59mA), MSA(methane sulfonic acid) 용리액. 음이온 분석 조건은 다음과 같음: 유속 1.00 mL min, AS19 컬럼, AERS 500 4 mm 서프레서, RFC-30 (Reagent-free controller) 시스템을 이용한 10 mM ~ 45 mM 경사의 KOH eluent. 실리카 농도를 분석하기 위하여 몰리브덴 발색법으로 810 nm에서 UV-Vis spectrophotometer(Shimadzu, UV-2600)를 이용하여 분석. 추가 실험 및 분석 예정.

2-4. 현장연구 (2019-2020)

2019-2020년 남극 하계 기간 동안 이루어진 현장연구에서 남극세종과학기지 인근 및 바톤반도, 위버반도에서 샘플링을 수행함(그림 3). 얼음에서 일어나는 풍화작용을 연구하기 위하여 눈, 담수, 얼음, 담수퇴적물, 토양, 해수, 해빙 샘플을 채취함. 채취한 샘플은 남극세종과학기지에서 0.45 μm 공극 크기의 필터로 필터링하였으며, 필터링 전후의 pH 및 전기전도도를 분석함. 0.01 N의 염산을 이용하여 50 mL의 샘플에 대하여 알칼리도를 분석함. 필터링 후의 샘플은 음이온 분석을 위한 냉장 상태, 양이온 분석을 위하여 질산을 가한 후 냉장 상태, 또는 냉동 상태로 운반하여 보관함. 추가 실험 및 분석 예정.

3. 연구결과

3.1. 암석 및 광물의 액상, 얼음상에서의 풍화실험 결과

산 또는 염기를 가했을 때 초기 pH 조건을 알기 위한 pH 분석 결과. Carbonate 광물인 dolomite의 경우 산성 용액에 대해 높은 완충 능력을 가짐. pH 2의 강산을 가했을 때 대부분 pH 2 정도의 산성 조건이 형성되었으며, pH 3의 산을 가했을 때 oligoclase, anorthite, granite는 pH 3 정도의 비슷한 산성 조건이 형성됨.

다양한 조건(양 또는 입자 크기, pH, 유기산의 종류)에 따른 anorthite, granite, albite, biotite, oligoclase, illite, illite-smectite, kaolinite의 액상 및 얼음상 풍화실험 결과. 대부분의 조건에서 액상에서 얼음상보다 많은 양의 양이온이 용출됨(그림 4 ~ 그림 20). 그러나 기존에 고려되지 않던 얼음상 조건에서도 대부분의 광물, 암석, 점토에서 양이온이 용출되는 것을 확인할 수 있었음. 액상에서는 대부분 시간이 지남에 따라 실리카 농도가 증가하였으나, 얼음상에서는 오히려 초기 농도보다 감소하는 것을 확인할 수 있었음.

액체 질소와 linkam stage를 이용하여 샘플을 -2℃ min^{-1}의 속도로 -20℃까지 천천히 동결한 뒤 광학현미경을 이용하여 준액체층의 이미지를 관찰함. pH 3의 HCl 수용액을 동결하였을 때 준액체층이 형성되는 것을 확인할 수 있었음(그림 21). HCl 수용액과 anorthite 또는 granite 가루를 함께 넣고 동결했을 때 가루 입자가 준액체층에 모이는 것을 확인할 수 있었음(그림 22). 기존 연구에서는 산성 용액을 동결할 때 동결농축효과에 의해 수소 이온이 얼음 가장자리에 형성된 준액체층에 모이게 되어 준액체층의 pH가 낮아짐이 알려져 있음(Takenaka *et al.*, 1996). 동결농축효과에 따라 준액체층에서 높아진 수소이온 농도와 농축된 가루 입자에 의해 용출반응이 높아지는 것을 예상할 수 있음.

실험에 사용된 granite powder는 XRF 분석 결과, 대부분 SiO_2와 Al_2O_3로 존재하지만 K, Na, Ca, Mg 등이 산화물 형태로 소량 존재함을 알 수 있음(표 2). 따라서 앞선 액상 및 동결 실험에서 이러한 산화물 형태로 존재하던 양이온들이 산에 의한 용출 반응으로 빠져나와 실험 후 이온크로마토그래피로 분석한 양이온으로 분석됨.

액상 및 동결 실험 전후 granite 가루 입자의 XRD 분석 결과. 실험 전 초기 상태의 granite은 quartz, plagioclase, mica를 포함하고 있음(그림 23). 액상 및 동결 실험 후 새로운 이차 광물의 형성은 관찰되지 않음. 증류수, pH 3 및 pH 2 수용액의 액상 실험 후 XRD 분석 결과, 실험 전의 광물 조성과 크게 차이가 없었음. 동결 실험 후 XRD 분석 결과에서는 quartz, plagioclase, mica의 피크가 감소함. 따라서 동결 실험에서 granite에 포함된 광물의 결정도가 감소했음을 확인할 수 있음.

4. 결론

규산염 광물과 탄산염 광물의 특성상 액상과 얼음상에서 모두 pH가 낮을수록 광물 및 암석의 용해가 빠르게 일어나는 것을 확인할 수 있었음. 기존 연구에서 얼음상에서의 광물 또는 암석의 풍화작용이 고려되지 않았으나, 실험 조건에 따라 얼음상에서도 상당량의 광물의 용해가 일어남을 확인할 수 있었음. 액상 실험에서는 시간이 지남에 따라 실리카의 농도가 증가하는 반면, 얼음상 실험에서는 초기 농도보다 실리카 농도가 감소함. 이러한 현상은 동결에 의한 실리카의 중합 효과 때문으로 생각되며, 실험 결과를 통해 동결과 해동을 반복하는 극지방 환경에 대한 기존 연구에서 융빙수의 양이온 농도는 높으나 실리카 농도는 낮았던 것을 설명할 수 있을 것으로 생각됨. 광학현미경으로 관찰한 이미지에서 수용액이 동결할 때 형성되는 준액체층을 확인하였으며, 동결농축효과에 의하여 가루입자가 얼음에서부터 밀려나와 준액체층에 모이는 것을 확인함. 실험 결과를 발전시켜 논문 투고 진행 중.

5. 참고문헌

Berner, R.A. Weathering, plants, and the long-term carbon cycle. *Geochim. Cosmochim. Acta* **1992,** 56, 3225-3231.

White, A.F.; Blum, A.E. Effects of climate on chemical weathering in watersheds. *Geochim. Cosmochim. Acta* **1995**, *59*, 1729-1747.

Gaillardet, J.; Dupré, B.; Louvat, P.; Allegre, C.J. Global silicate weathering and CO2 consumption rates deduced from the chemistry of large rivers. *Chem. geol.* **1999**, *159*, 3-30.

Drever, J.I.; Stillings, L.L. The role of organic acids in mineral weathering. *Colloids Surf. A* **1997**, *120*, 167-181.

Bockheim, J.G. Properties and classification of cold desert soils from Antarctica. *Soil Sci. Soc. Am. J.* **1997**, *61*, 224-231.

Gooseff, M.N.; McKnight, D.M.; Lyons, W.B.; Blum, A.E. Weathering reactions and

hyporheic exchange controls on stream water chemistry in a glacial meltwater stream in the McMurdo Dry Valleys. *Water Resour. Res.* **2002**, 38, 15-11-15-17.

Prestrud Anderson, S.; Drever, J.I.; Humphrey, N.F. Chemical weathering in glacial environments. *Geology* **1997**, *25*, 399-402.

Nezat, C.A.; Lyons, W.B.; Welch, K.A. Chemical weathering in streams of a polar desert (Taylor Valley, Antarctica). *Geol. Soc. Am. Bull.* **2001**, *113*, 1401-1408.

Huh, Y. Chemical weathering and climate－a global experiment: a review. *Geosci. J.* **2003**, *7*, 277-288.

Bisson, K.M.; Welch, K.A.; Welch, S.A.; Sheets, J.M.; Lyons, W.B.; Levy, J.S.; Fountain, A. Patterns and processes of salt efflorescences in the McMurdo region, Antarctica. *Arct. Antarct. Alp. Res.* **2015**, *47*, 407-425.

Maurice, P.A.; McKnight, D.M.; Leff, L.; Fulghum, J.E.; Gooseff, M. Direct observations of aluminosilicate weathering in the hyporheic zone of an Antarctic Dry Valley stream. *Geochimica et Cosmochimica Acta* **2002**, *66*, 1335-1347.

Kim, K.; Choi, W.; Hoffmann, M.R.; Yoon, H.I.; Park, B.K. Photoreductive dissolution of iron oxides trapped in ice and its environmental implications. *Environ. Sci. Technol.* **2010**, *44*, 4142-4148.

Kim, K.; Menacherry, S.P.M.; Kim, J.; Chung, H.Y.; Jeong, D.; Saiz-Lopez, A.; Choi, W. Simultaneous and synergic production of bioavailable iron and reactive iodine species in ice. *Environ. Sci. Technol.* **2019**.

Takenaka, N.; Ueda, A.; Daimon, T.; Bandow, H.; Dohmaru, T.; Maeda, Y. Acceleration mechanism of chemical reaction by freezing: The reaction of nitrous acid with dissolved oxygen. *J. Phys. Chem.* **1996**, *100*, 13874-13884.

KOPRI 극지연구소

표 1. 광물 또는 암석 가루 0.1 g과 pH를 조절한 HCl 또는 NaOH 수용액 10 mL의 혼합물의 pH.

Mineral/rock	pH 2	pH 3	DW	pH 9	pH 10
Dolomite	5.97	7.78	10.20	10.22	10.38
Albite	2.33	4.90	10.05	10.08	10.35
Oligoclase	2.06	3.39	8.95	9.15	10.16
Anorthite	2.09	3.69	9.72	9.79	10.18
Olivine	2.16	6.39	10.21	10.24	10.43
Granite	2.01	3.94	9.74	9.80	10.30

표 2. 실험 전 granite powder의 XRF 분석 결과

Oxide Composition	SiO_2	Al_2O_3	K_2O	Na_2O	Fe_2O_3	CaO	MgO	TiO_2	MnO
Weight Percentage(%)	72.50	13.59	7.56	1.83	1.65	1.04	0.58	0.37	0.10

KOPRI 극지연구소

표 3. 2018 남극세종과학기지 현장 샘플의 pH, EC, alkalinity, H_4SiO_4, 양이온 및 음이온 분석 결과

Type		pH (before filtering)	EC (μS/cm)	pH (after filtering)	EC (μS/cm)	alkalinity (μeq L^{-1})	Ca^{2+}	Mg^{2+}	Na^+	K^+	H_4SiO_4	Cl^-	NO_3^-	SO_4^{2-}
Snow (n=6)	minimum	5.31	6.60	4.89	6.70	-	0.16	0.21	0.57	0.10	0.18	1.12	0.04	0.17
	maximum	6.41	21.80	6.25	28.80	-	0.52	0.44	2.49	0.30	1.94	4.63	0.10	0.71
	Mean	5.68	12.86	5.41	14.63	-	0.25	0.29	1.24	0.15	0.63	2.36	0.06	0.42
	Standard deviation	0.34	5.19	0.43	8.44	-	0.12	0.09	0.62	0.07	0.76	1.12	0.02	0.23
Meltwater (n=6)	minimum	5.91	74.80	5.86	73.00	38.00	1.23	0.97	6.87	0.39	14.03	14.47	0.05	2.16
	maximum	7.22	155.40	7.17	147.10	282.00	7.75	2.97	12.49	0.57	50.03	25.62	0.58	13.46
	Mean	6.63	118.53	6.56	116.53	123.33	3.37	1.73	9.62	0.49	36.60	19.38	0.25	6.06
	Standard deviation	0.53	33.09	0.53	32.12	104.37	2.65	0.71	2.08	0.06	12.86	4.44	0.22	3.87
Pondwater (n=9)	minimum	5.66	80.40	5.75	85.50	38.00	0.89	0.92	6.75	0.35	15.29	14.52	0.12	2.73
	maximum	7.16	152.60	7.05	146.70	212.00	6.04	1.97	12.47	0.58	39.46	29.68	0.39	11.79
	Mean	6.59	105.27	6.56	107.81	106.44	2.61	1.48	9.46	0.46	28.69	20.70	0.26	5.59
	Standard deviation	0.47	25.14	0.41	23.37	56.76	1.70	0.39	1.71	0.07	7.52	5.22	0.09	3.12
Ice (n=1)		5.55	31.00	5.41	24.80	-	0.32	0.47	2.53	0.30	5.97	4.61	0.12	0.95
Iceberg (n=1)		-	-	-	-	-	0.17	0.25	0.58	0.09	n.a.	1.12	n.a.	0.23

이온 단위: ppm, H_4SiO_4: μM

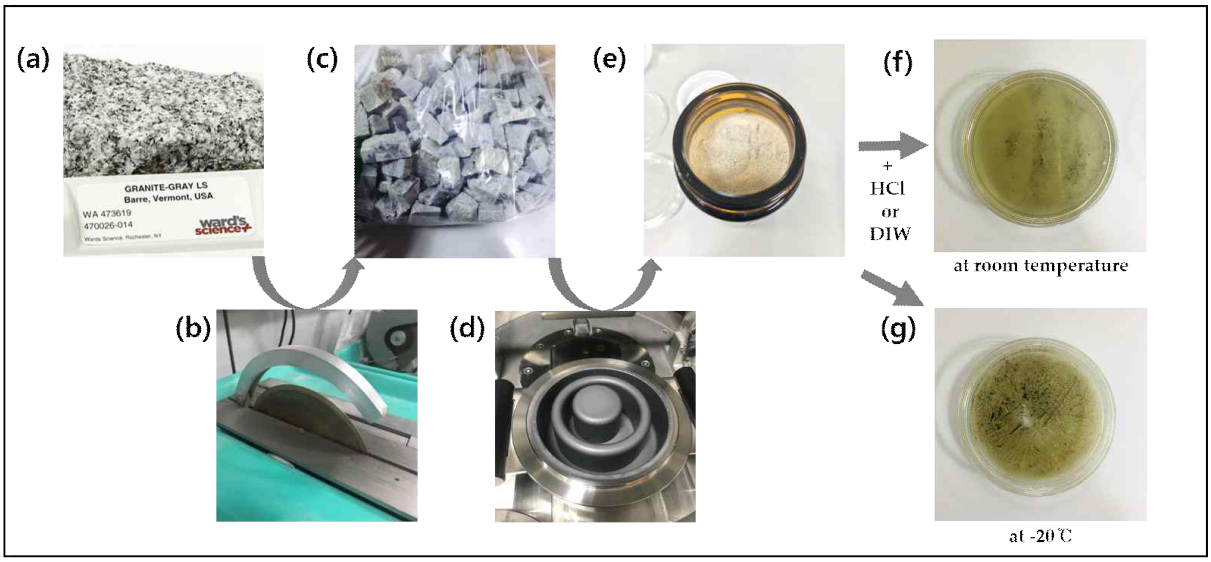

그림 1. 실험 방법의 모식도. (a) 벌크 형태의 광물 또는 암석을 (b) 다이아몬드 날로 절단하여 (c) 조각 형태로 만든 뒤, (d) 링밀을 이용하여 (e) 파우더 형태로 만들어 (f) 액상과 (g) 얼음 상 실험 수행.

그림 2. 2018년 남극세종과학기지 현장연구 샘플링 사진.

그림 3. 2019-2020년 남극세종과학기지 현장연구 샘플링 사진.

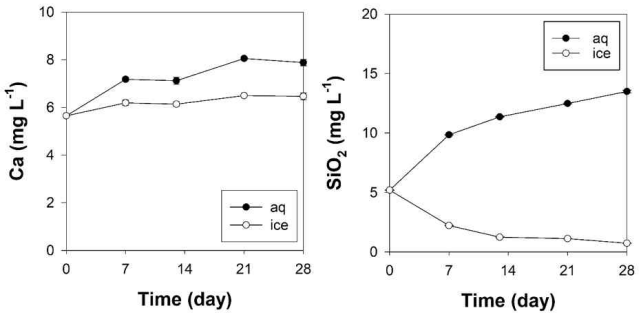

그림 4. Anorthite 0.1 g과 pH 3 HCl 수용액의 액상 및 얼음상 풍화실험 결과.

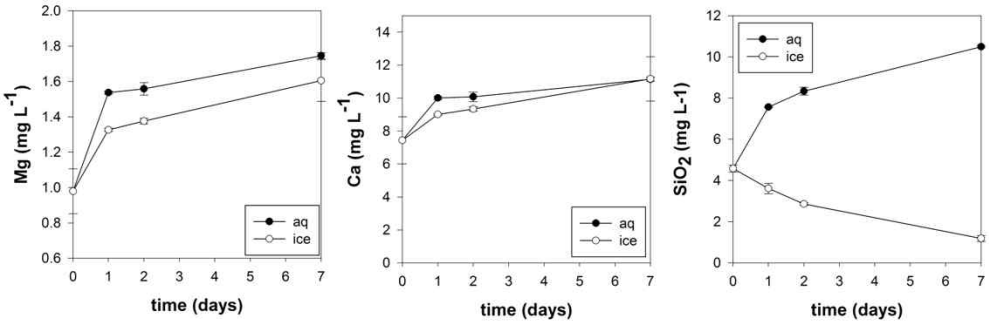

그림 5. 53 μm 이하의 anorthite 0.1 g과 pH 3 HCl 수용액의 액상 및 얼음상 풍화실험 결과.

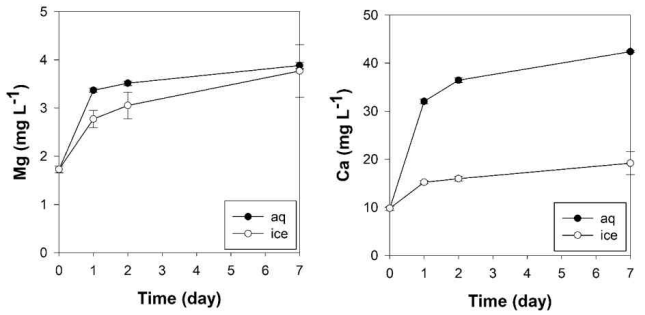

그림 6. Anorthite 0.1 g과 pH 2 HCl 수용액의 액상 및 얼음상 풍화실험 결과.

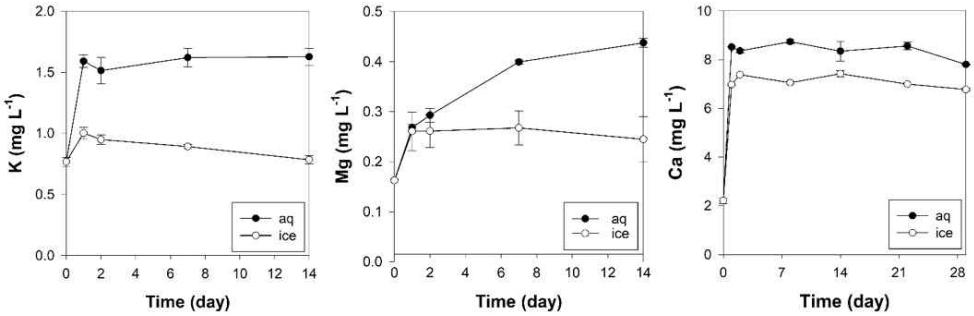

그림 7. Granite 0.01 g과 pH 3 HCl 수용액의 액상 및 얼음상 풍화실험 결과.

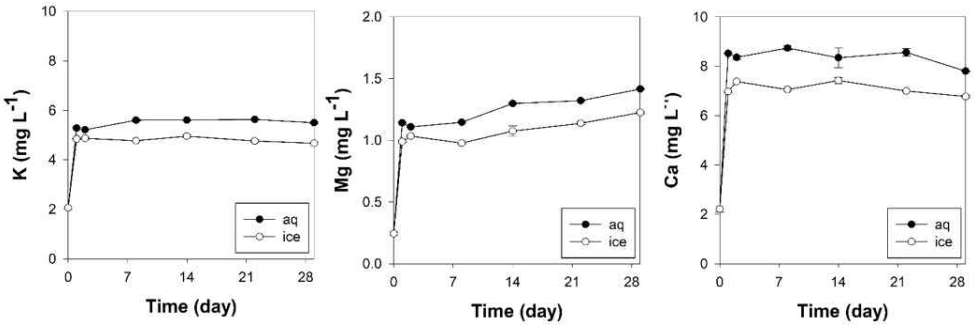

그림 8. Granite 0.1 g과 pH 3 HCl 수용액의 액상 및 얼음상 풍화실험 결과.

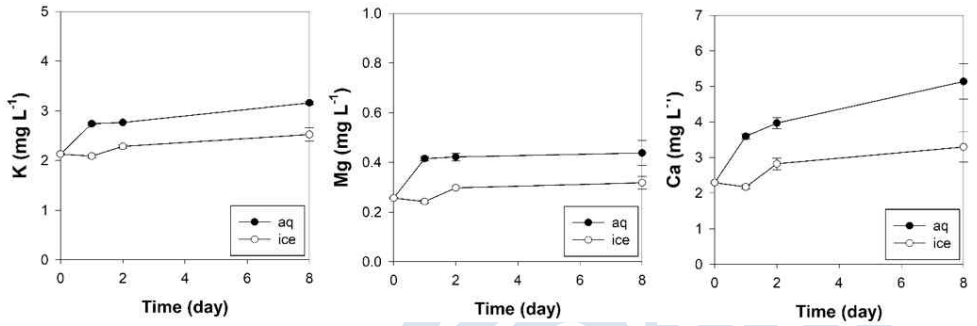

그림 9. Granite 0.1 g과 pH 10 NaOH 수용액의 액상 및 얼음상 풍화실험 결과.

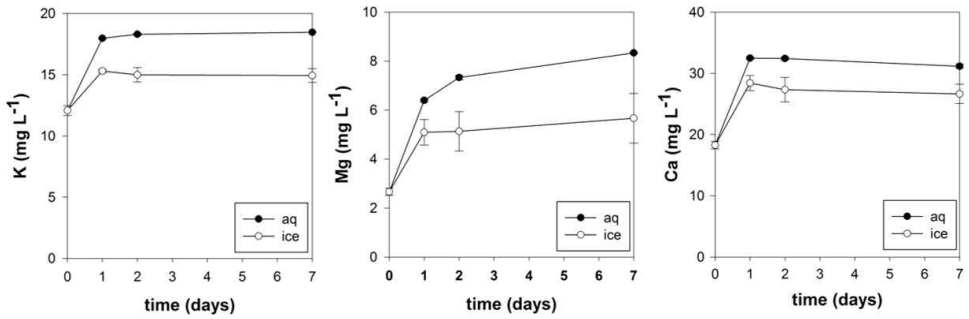

그림 10. 53 μm 이하의 Granite 0.1 g과 pH 2 HCl 수용액의 액상 및 얼음상 풍화실험 결과.

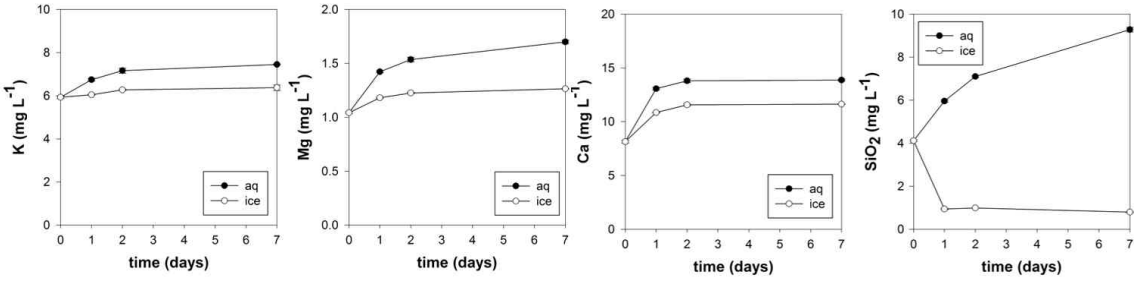

그림 11. 53 μm 이하의 Granite 0.1 g과 pH 3 HCl 수용액의 액상 및 얼음상 풍화실험 결과.

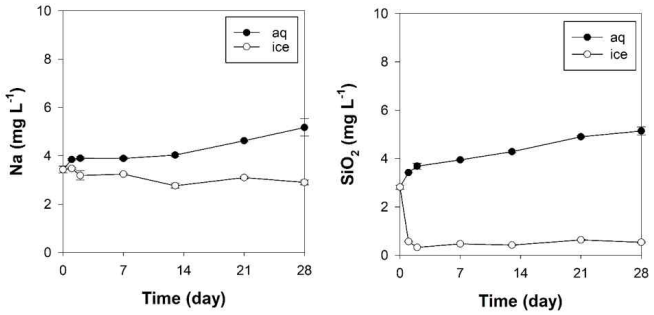

그림 12. Albite 0.1 g과 pH 3 HCl 수용액의 액상 및 얼음상 풍화실험 결과.

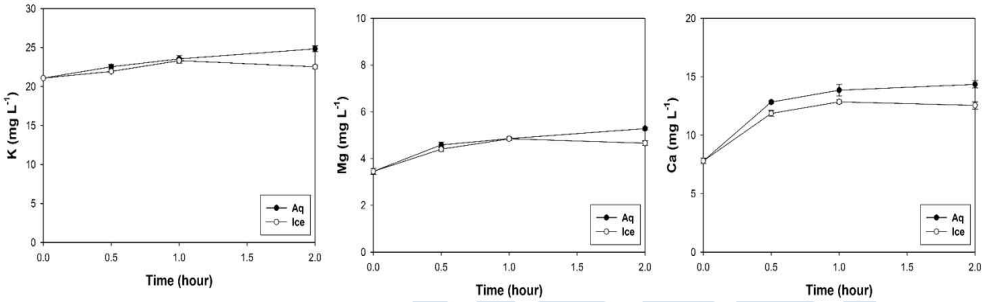

그림 13. Biotite 0.1 g과 pH 5 HCl 수용액의 액상 및 얼음상 풍화실험 결과.

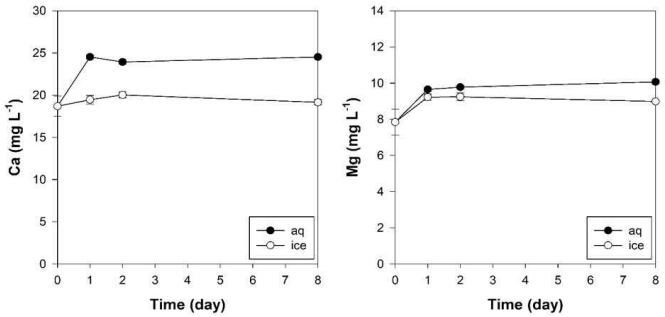

그림 14. Dolomite 0.1 g과 pH 3 HCl 수용액의 액상 및 얼음상 풍화실험 결과.

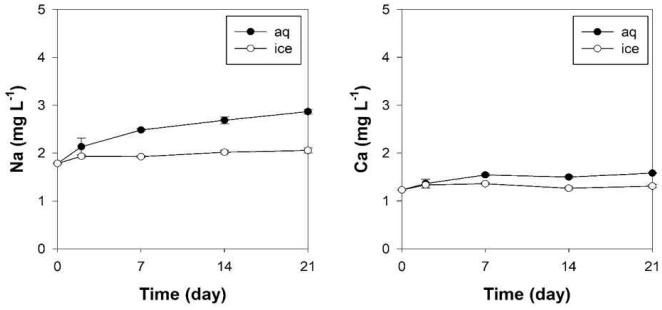

그림 15. Oligoclase 0.1 g과 pH 3 HCl 수용액의 액상 및 얼음상 풍화실험 결과.

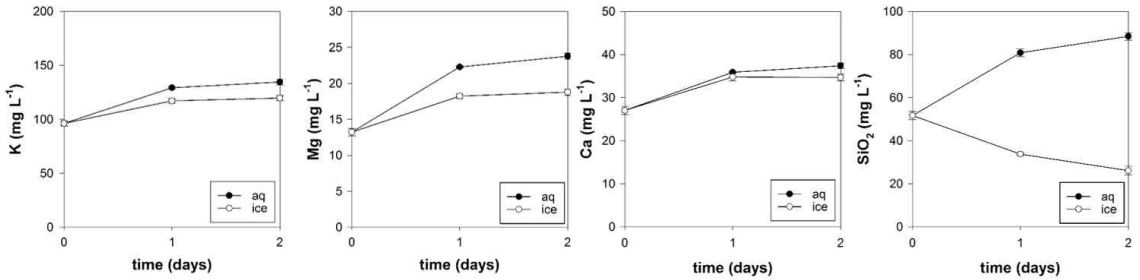

그림 16. Illite 0.1 g과 pH 2 HCl 수용액의 액상 및 얼음상 풍화실험 결과.

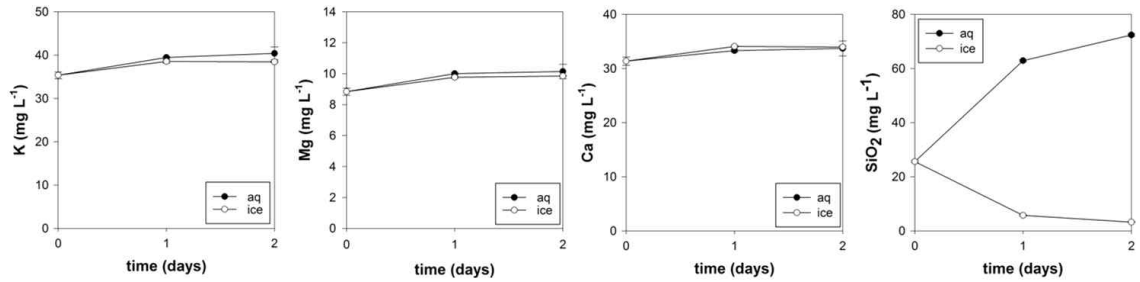

그림 17. Illite-smectite 0.1 g과 pH 2 HCl 수용액의 액상 및 얼음상 풍화실험 결과.

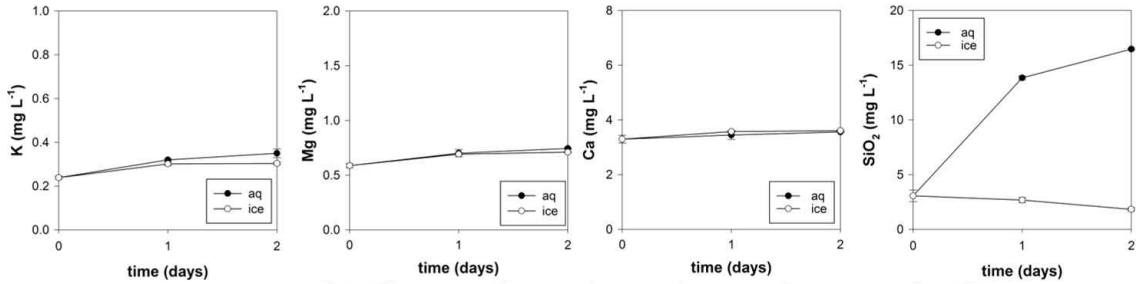

그림 18. Kaolinite 0.1 g과 pH 2 HCl 수용액의 액상 및 얼음상 풍화실험 결과.

극지연구소

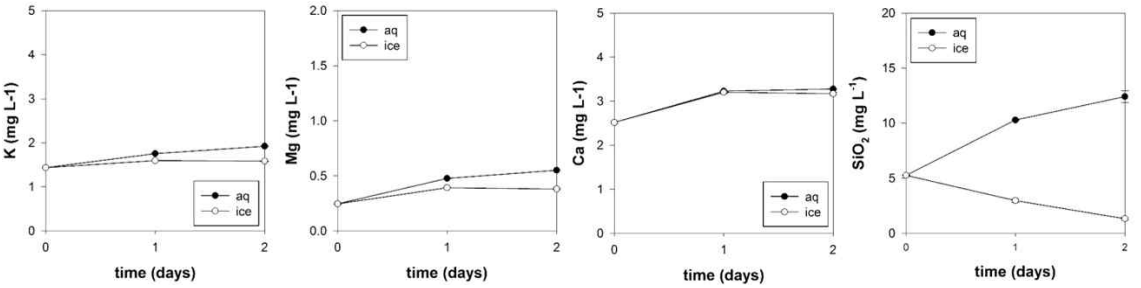

그림 19. Granite 0.1 g과 pH 3 HCl 수용액, ascorbic acid 1 mM의 액상 및 얼음상 풍화실험 결과.

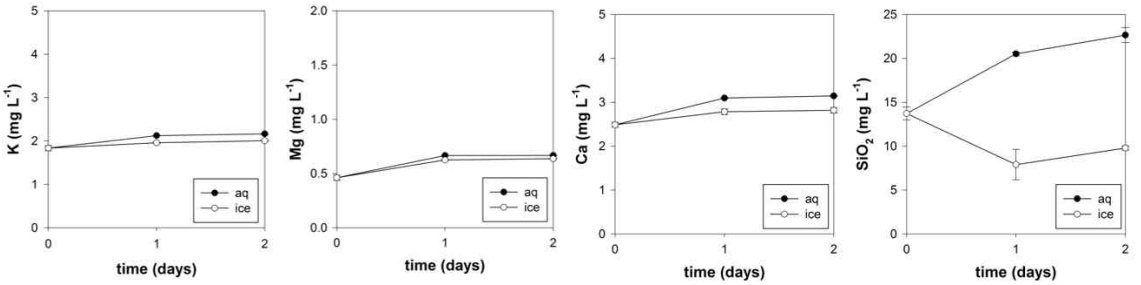

그림 20. Granite 0.1 g과 pH 3 HCl 수용액, oxalic acid 1 mM의 액상 및 얼음상 풍화실험 결과.

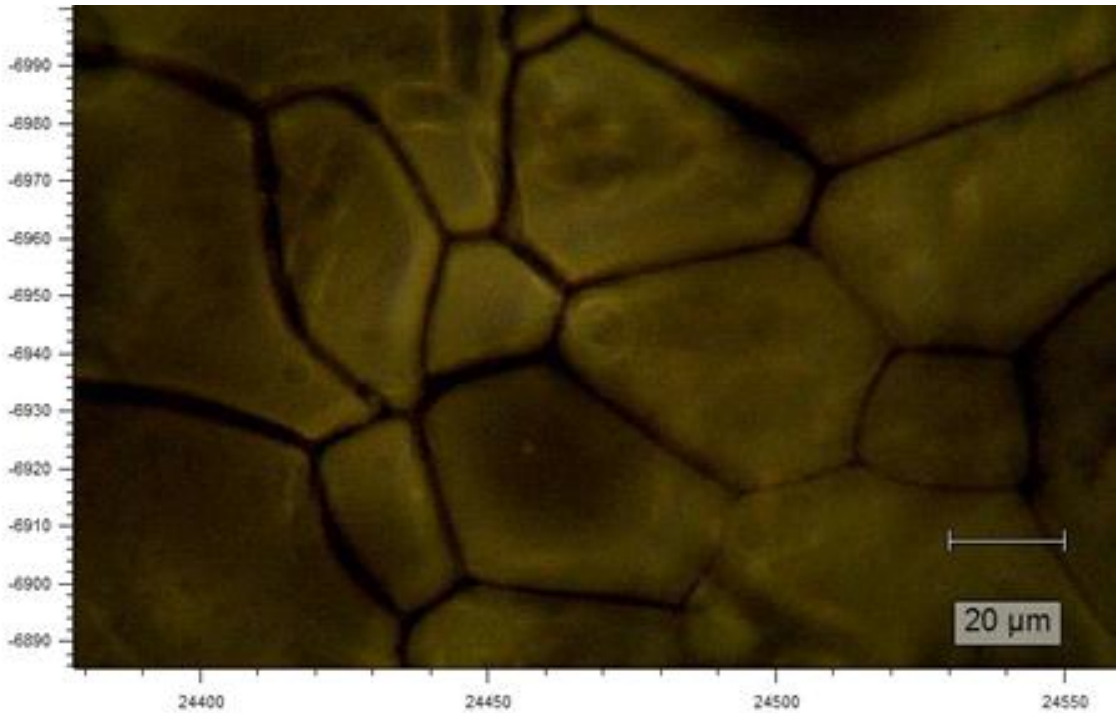

그림 21. Anorthite 0.1 g 과 pH 3 HCl solution의 동결 후 광학현미경으로 관찰한 준액체층 이미지.

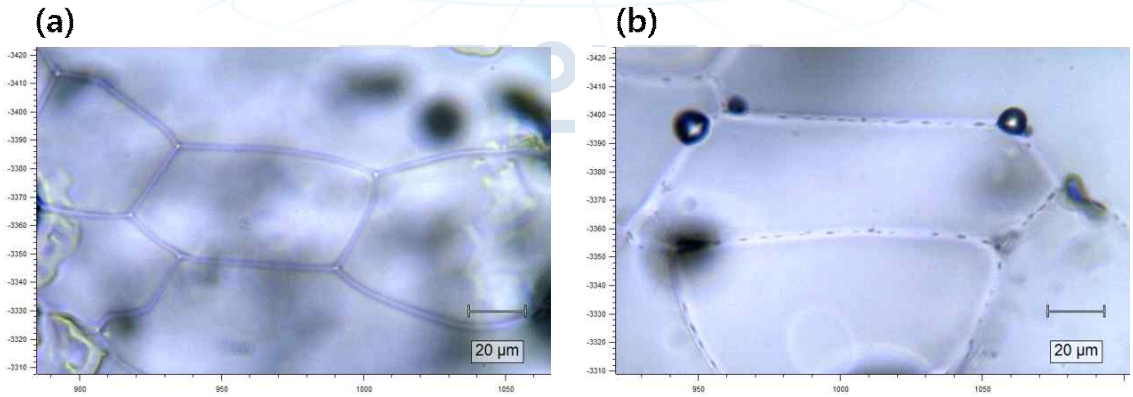

그림 22. (a) pH 3의 HCl 수용액을 동결하여 현미경으로 관찰한 준액체층. (b) granite 0.1 g 과 HCl 수용액을 동결하여 현미경으로 관찰한 준액체층과 준액체층에 모여있는 granite 입자.

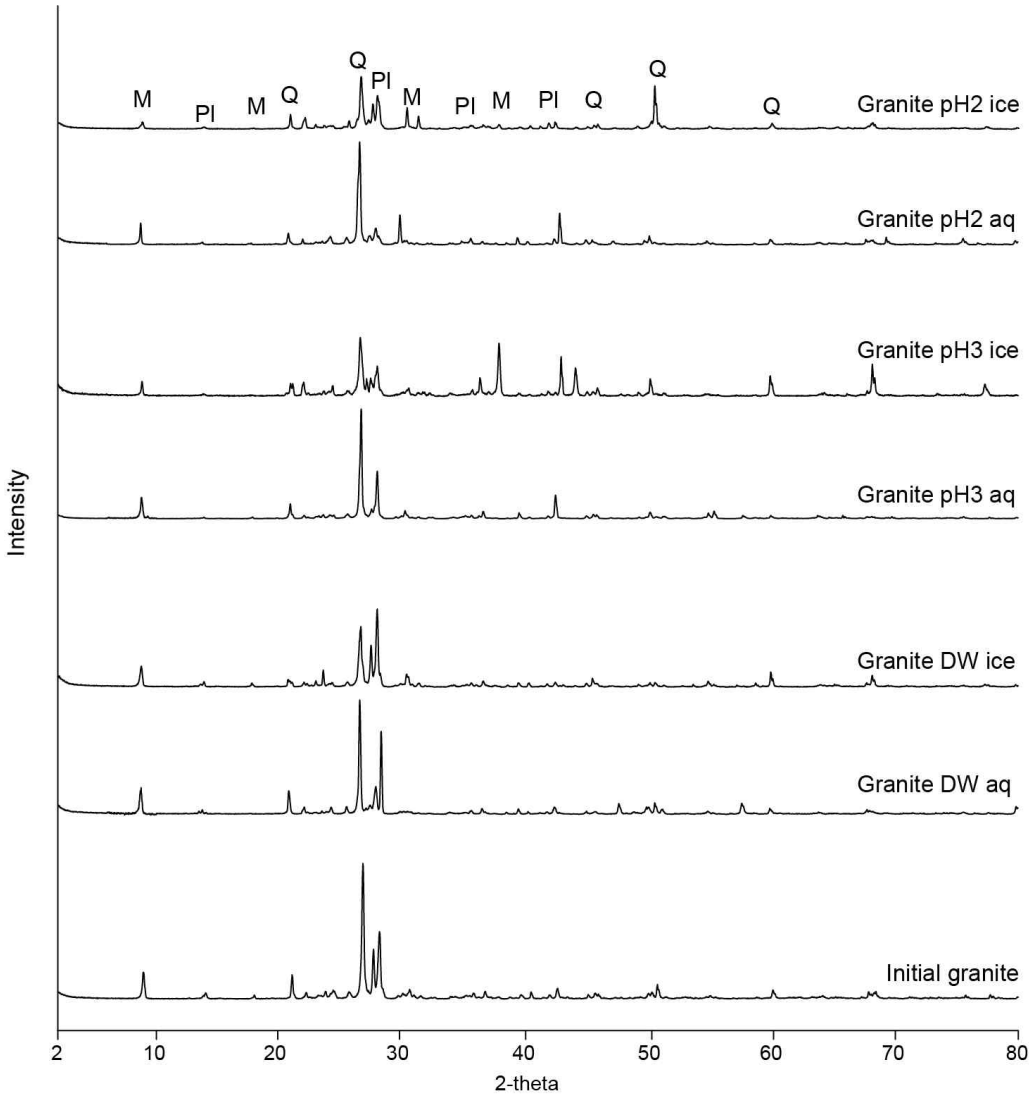

그림 23. 실험 전, 액상 및 동결 실험 후 granite의 XRD 분석 결과. Q: quartz, Pl: plagioclase, M: mica.

제 14 절. Estimation of Thermal Diffusivity of Soils in Antarctica Using Temperature Time Series Data[7)]

Heejung Kim[1], Jin-Yong Lee[1], and Kitae Kim[2]

[1]Department of Geology, Kangwon National University
[2]Korea Polar Research Institute

1. Introduction

Polar regions are one of the regions most affected by climate change, a phenomenon caused by global warming that humanity faces today. Polar regions also have a strong influence on the global climate. Therefore, a number of researchers are conducting studies on polar regions to understand their role in climate (Roth and Boike, 2001; Pringle et al., 2003; Pringle et al., 2007; Wu and Zhang, 2010; Weismuller et al., 2011; Lee et al., 2016; Kim et al., 2018). In doing so, quantitative consideration of the thermal and physical properties of the active layers layers of permafrost in polar regions is essential in understanding the meteorological characteristics of permafrost regions as well as predicting the interaction between the atmosphere and permafrost surface (Pringle et al., 2003; Boike et al., 2008; Ikard et al., 2009; Jeon et al., 2016).

Permafrost refers to ground made up of earth rocks and sediments that maintains a temperature of 0°C or below for two years or more. Permafrost covers approximately one-fourth of exposed land in the Northern Hemisphere and plays a key role in the global thermal system (Bockheim et al., 2007; Vieira et al., 2010; Bockheim et al., 2013). The thermal characteristics of soil depend on its porosity and water content as well as the density, specific heat, and thermal conductivity of its particles.

In polar regions, temperature changes on the surface and active layer are sensitive to atmospheric temperature, and the area of the active layer is changing owing to global warming (Yoshikawa and Hinzman, 2003; Marchenko et al., 2008; Koven et al., 2013). Heat transfer is extremely complex, especially in these active layers of permafrost, and depends on different mechanisms such as heat generation from conduction and phase changes as well as movements of water and vapor (Boike et al., 1998; Pradhan et al., 2019). Thermal conduction refers to the transfer of heat from areas of high temperature to tangential areas of low temperature without physical mass transfer; it is widely known as the primary method of heat transfer in soil (Han et al., 2006; Ebel et al., 2019).

7) 이 연구는 다음의 논문으로 출판되었음: Heejung Kim, Jin-Yong Lee, and Kitae Kim “Estimation of thermal diffusivity of soils in Antarctica using temperature time series datat”, *Episodes* 2019, 42, 245-252.

Nonconductive heat transfer mediums, particularly those associated with groundwater convection, are available with suitable temperature gradient in a liquid or vapor state. Thermal diffusivity is a physical quantity that represents the thermal properties of soil. Methods for estimating thermal diffusivity of soil exist in various literatures (Romanovsky et al., 2003; Wu and Zhang, 2010; Wang et al., 2019). In the case of rocks, thermal diffusivity can be measured by experimenting with collected samples (Nabelek et al., 2012). However, as it is impossible to collect undisturbed soil samples, the thermal diffusivity of soil is usually determined by analyzing temperature observation data (Han et al., 2005; Koo and Song, 2008; Kim et al.,2018).

A number of publications have estimated the thermal diffusivity of soil using equations such as amplitude equations, phase equations, algebraic equations and finite-difference equations derived from the analytical or numerical solution of one-dimensional thermal conductivity equations (Hinkel, 1997; Pringle et al., 2003; Cui et al., 2012). These methods of estimating thermal diffusivity that use analytical or numerical solutions of the heat conductivity equation generally neglect nonconductive heat transfer processes such as fluid flow in air gaps, freezing and melting of water, evaporation, etc. Moreover, thermal diffusivity calculated using such methods may be over- or underestimated as the coefficient itself is affected by the method used to obtain it. This is especially true for methods using amplitude equations and algebraic equations, whose results are affected by nonconductive heat transfer from water flowing within the soil.

Similarly, methods using finite-difference equations exhibit large sensitivity to observational error of the truncation error, making them less reliable in applying measured data (Koo et al., 2003). Therefore, in this study, thermal diffusivity was estimated with temperature time series data simulated using the finite element method, and depth-specific temperature data collected from four different locations near the King Sejong Station.

2. Methods and Materials

Geology of Study Area

The area of study is the region surrounding the King Sejong Station located in the Barton peninsula of King George Island of the South Shetland Islands, northwest of the Antarctic peninsula. The region is populated with bases of diverse nationalities that study the Antarctic's ecology and environment. King George Island is the largest island among the South Shetland Islands, with length, width and area of 72 km, 27 km and 1,338 km^2, respectively (Chang, 2003). It is one of many volcanic islands (Smellie et al., 1984) associated with the subduction of oceanic plates that occurred between the late Mesozoic and early Cenozoic.

The Barton peninsula and Weaver peninsula located southwest of the island mainly

consist of volcanic granules in their lower sections and calk-alkaline volcanic/plutonic rocks in their upper sections. The Barton peninsula is an elevated glacial landform (Yoo et al., 2001). The fact that Maxwell Bay and Marian Cove are fjords, and that the surface of the Barton Peninsula is rather flat, proves that Barton Peninsula is a glacial landform. Likewise, the remains of rounded pebbles found in the higher areas of the peninsula prove that it is an elevated landform as well (John and Sugden, 1971).

The surface of the Barton Peninsula mainly consists of bedrock, moraine, weathered volcanic materials, structural soil and back beach (Lopez-Martinez et al., 2002). Rocks pressed and packed by drift ice form patterned intertidal flats and patterned beaches at the intertidal zones near the King Sejong Station. The station is located near the shores at the northwest end of the Barton Peninsula, southwest of King George Island. The base of the Barton peninsula on which the station is located is a layer of sedimentary volcanic rock known as the Sejong layer covered by alkaline with unconformity.

At the bottom of the Barton-Weaver Peninsula's geological stratum is the Sejong layer, which mainly consists of lapilli and lapilli tuff. It also contains various types of silt and volcanic rock fragments. The layer is a pyroclastic layer with total thickness of approximately 100 m. According to the sedimentary rocks and sedimentary structure, the Sejong layer has five major layers: first, structureless substrate conglomerate; second, structureless pebbly conglomerate; third, stratified pebbly conglomerate; fourth, lamellar sandstone; and finally, lapilli tuff.

Plant fossils found within the silt and fine sandstone of the Sejong layer are leaves that belonged to ferns and broadleaf trees that inhabited the region from the late Paleocene to Eocene. The presence of such fossils indicates a tropical-subtropical climate (Chun and Chang, 1991; Chang et al., 2003; Lee et al., 2019). Rock fragments mainly consist of andesite, basaltic andesite and pumice, and a large number of rhyolitic shards are formed in some layers (Fig. 1).

Acquisitions of Soil Temperature Data

Thermal temperature loggers (iButton, Dallas Semiconductor, USA) were installed in four different locations at depths of 10, 20 and 30 cm: two locations (SJL1 and SJL2) in the east and two locations (SJL3 and SJL4) in the west of the living hall of the King Sejong Station (Fig. 2) The iButton loggers were installed to measure temperature over time, and have an accuracy of 0.5°C with a resolution of 0.0625°C. Soil temperature measurements were taken every 4 h from December 23, 2010 to November 28, 2011. According to Lee et al. (2013), the effects of time delay and attenuation on the temperature measurements of an iButton placed in soil in a glass bottle are not significant. Using the methodology proposed by Lee et al. (2013), depth-specific soil temperature time series data were obtained at four

different locations (SJL1, SJL2, SJL3, and SJL4) near the Antarctic King Sejong Station (Fig. 2).

Theoretical Background

The law of conservation of energy can be expressed as the following equation.

$$\frac{\partial}{\partial t}[cT] + \nabla \cdot \vec{q} = A \tag{1}$$

where c = heat capacity

T = temperature (°C)

$\vec{q}$ = heat flux

A = heat production rate

Heat flow by Fourier's law is according to the following.

$$\vec{q} = -k \nabla T \tag{2}$$

Thus, the heat transfer equation can be derived from equations (1) and (2).

$$\nabla^2 T + \frac{A}{k} = \frac{1}{\alpha}\frac{\partial T}{\partial t} \tag{3}$$

where k = thermal conductivity

a = thermal diffusivity

When equation (3) is given as a function in which the initial temperature is 0, and surface temperature is $T(0, t)$ in a semi-infinite medium where the production and extinction of soil heat do not occur, its solution is given as the convolution of the surface temperature function and the transfer function (f_τ) (Carslaw and Jaeger, 1986).

$$T(z,t) = \int_0^t T(0,\tau) f_t(t-\tau, z) d\tau \tag{4}$$

Here, the transfer function is as follows.

$$f_1(t,z) = \frac{z}{2[\pi\alpha t^3]} \exp\left(-\frac{z^2}{4\alpha t}\right) \tag{5}$$

Accordingly, the change of temperature in the subsurface, which occurs only by heat conduction in a uniform medium without production and extinction of soil heat, can be calculated using equations (4) and (5). In addition, since the soil temperature measurement is performed discretely according to depth, equation (2), as a finite difference method approximation, can calculate heat flow according to depth as follows.

$$q = -k \frac{T(z_{i+1}, t) - T(z_i, t)}{z_{i+1} - z_i} \tag{6}$$

Here, the heat production rate at $[z_i, z_{i+1}] \times [t^j, t^{j+1}]$, the small section of depth and time, can be obtained as follows by Roth and Boike's equation (Roth and Boike, 2001; Han et al., 2006).

$$A = \frac{1}{[t^{j+1} - t^j][z_{i+1} - z_i]} \int_{t^j}^{t^{j+1}} \int_{z_i}^{z_{i+1}} A(z,t)dzdt = \frac{1}{[t^{j+1} - t^j][z_{i+1} - z_i]}$$

$$c\left[\int_{z_i}^{z_{i+1}} \{T(z,t^{J+1}) - T(z,t^j)\}dz - \alpha \int_{t^j}^{t^{j+1}} \{T'(z_{i+1},t) - T'(z_i,t)\}dt\right] \quad (7)$$

T' = differential difference according to the depth of soil heat

To compensate for the fundamental problems with the aforementioned methodologies such as amplitude equation, the phase equation, the logarithmic equation and the finite difference equation the thermal diffusivity was estimated using the FEM in this study (Kim et al., 2018). The reasons of the widely used of the FEM are well known. That are local character of approximations, ability to deal with complex geometric domains, existence of large set of approximation schemes adapted to various problems but embedded in a unified formulation. Furthermore, FEM procedures are generally used in structural problems and in non-structural problems, such as fluid flow and heat transfer problems (Bathe, 1996; Kim et al., 2018).

3. Results and Discussion

The assumption of thermal diffusivity of active layer in Antarctic soils was scored by calculating the root-mean-squared (RMS) error between the measured target and calculated response signals. The RMS error was used because it is a widely recommended measure of tracking accuracy (Kim et al., 2018). Fig. 3 shows the RMS errors between the temperature measured points. The time range between 5,500~6,000 h was adopted for RMS error calculation for SJL1 and SJL4 points. However, the locations of SJL2 andSJL3 were unsuccessful to give a satisfactory result of RMS errors. Therefore, we tried to set another time range for RMS error calculation for SJL2 and SJL3. For SJL2 was possible to find RMS error time range for RMS error calculation, which was between 3,500 and 4,000 h. Despite these efforts, SJL3 could not find satisfactory time range for RMS error calculation (Fig. 3).

The FEM includes the conduction mode of heat transfer and should be applied to the soil regions having temperatures lower than 0°C. Fig. 4 also represents the conduction results at temperatures higher than 0°C; these include temperatures calculated at depths of 0.1, 0.2 and 0.3 m, measured at 4-h time intervals over 6,000 h using the FEM. This section evaluates the calculated distributions of these temperatures that were measured at the King Sejong Station in Antarctica (see Fig. 2). To investigate quantitatively the effects of the time interval and monitoring depth on thermal diffusivity, numerical FEM experiments were performed for the temperatures measured at King Sejong Station.

Thermal diffusivity values of 14 × 10^{-7} m^2/s in SJL1, 12× 10^{-7} m^2/s in SJL2 and

11× 10^{-7} m^2/s in SJL4 were obtained through time series obtained from the application of finite element analysis to the measured 0.1, 0.2 and 0.3 m soil depths, respectively (Table 1). It is consistent with previous reports (Kim et al., 2018). The diffusivity of SJL2 was recalculated with a time window change in order to obtain the optimum thermal diffusivity. The best-fit thermal diffusivity was determined by minimizing the RMS error between the monitored the SJL2 point time series data, for a period between 3,500 and 4,000 h followed by 5,500 and 6,000 h (Fig. 4). However, the temperature time series data at point SJL3 demonstrated problems in estimating thermal diffusivity despite changes in the time window.

4. Conclusions

Because heat transfer in both soil and rock is mainly caused by conduction, estimating thermal diffusivity in Antarctica is a necessity in order to cope with climate change. This study estimates thermal diffusivity using FEM analysis of the soil in the King Sejong station, Antarctica. The conclusions drawn from this study are as follows:

Thermal diffusivity in the study area was shown to be in the range 11×10^{-7} to 14×10^{-7} m^2/s. The time range for RMS error calculations of the monitoring points SJL1 and SJL4 was 5,500 to 6,000 h; in contrast, the SJL2 and SJL3 points did not demonstrate adequate thermal diffusivity results using the same time range for this calculation. The best-fit thermal diffusivity for the SJL2 point was determined by minimizing the RMS error between the monitored time series data for a period between 3,500 and 4,000 h. The distribution of thermal diffusivity values represented by both negative and positive reflects the drop and rise of the temperature, respectively.

For the SJL3 point, this tendency was not present and it was, therefore, impossible to estimate thermal diffusivity using temperature data. Heat transfer by convection played a major role in the polar activity layer in the SJL1, SJL2 and SJL4 locations. However, as the SJL3 point demonstrated problems in estimating thermal diffusivity using only temperature data, the phase change of environmental factors such as pore water, atmospheric temperature and snow cover should be considered in addition to heat conduction.

5. References

Bathe, K., 1996, Finite element procedures, 2nd edition: Prentice Hall, Upper Saddle River, NJ.

Bockheim, J.G., Campbell, I.B., and McLeod, M., 2007, Permafrost distribution and active-layer depths in the McMurdo Dry Valleys, Antarctica. Permafrost and

Periglacial Processes, v. 18, pp. 217 - 227.

Bockheim, J., Vieira, G., Ramos, M., López-Martínez, J., Serrano, E., Guglielmin, M., Wilhelm, K., and Nieuwendam, A., 2013, Climate warming and permafrost dynamics in the Antarctic peninsula region. Global and Planetary Change, v. 100, pp. 215 - 223.

Boike, J., Roth, K., and Overduin, P.P., 1998, Thermal and hydrologic dynamics of the active layer at a continuous permafrost site (Taymyr peninsula, Siberia). Water Resources Research, v. 34, pp. 355 - 363.

Boike, J., Hagedorn, B., and Roth, K., 2008, Heat and water transfer processes in permafrost affected soils: a review of field and modeling based studies for the Arctic and Antarctic. Proceedings International Conference on Permafrost, 2008, Institute of Northern Engineering, v.1, p. 149 - 154

Carslaw, H.S., and Jeager, J.C., 1986, Conduction of Heat in Solids (2nd edition). Oxford University Press, England, 520 p.Chang, S.K., Lee, J.I., Choe, M.Y., and Hur, S.D., 2003, Geology around the King Sejong station, King George Island off the Antarctic peninsula. Journal of the Geological Society of Korea, v. 39, pp. 271 - 286.

Chun, H.Y., and Chang, S.K., 1991, Study on the gymnospermous fossil woods from the King George Island. Korean Journal of Polar Research, v. 2,pp. 179 - 185.

Cui, M., Gao, X., and Zhang, J., 2012, A new approach for the estimation of temperature-dependent thermal properties by solving transient inverse heat conduction problems. International Journal of Thermal Sciences,v. 58, pp. 113 - 119.

Ebel, B.A., Koch, J.C., and Walvoord, M.A., 2019, Soil physical, hydraulic, and thermal properties in Interior Alaska, USA: implications for hydrologic response to thawing permafrost conditions. Water Resources Research, v. 55, pp. 4427 - 4447.

Han, U., Lee, C.K., Nam, S.H., Lee, B.Y., and Kim, Y., 2005, Thermal dynamics of active layer at the Dasan station, Svalbard. Journal of the Geological Society of Korea, v. 41, pp. 91 - 100.

Han, U., Lee, C.K., Jeong, S.H., Lee, B.Y., and Nam, S.H., 2006, The studies on the temperature and thermal properties of the active layer soil at the Sejong Station, Antarctica. Journal of the Geological Society of Korea,v. 4, pp. 577 - 586.

Hinkel, K.M., 1997, Estimating seasonal values of thermal diffusivity in thawed and frozen soils using temperature time series. Cold Regions Science and Technology, v. 26, pp. 1 - 15.

Ikard, S.J., Gooseff, M.N., Barrett, J.E., and Takacs-Vesbach, C., 2009, Thermal characterisation of active layer across a soil moisture gradient in the McMurdo

Dry Valleys, Antarctica. Permafrost and Periglacial Processes, v. 20, pp. 27 – 39.

Jeon, W.H., Lee, J.Y., Lim, H.S., and Yoon, H.I., 2016, Comparison of thermal characteristics of soil in austral summer and winter at King Sejong station, King George Island, Antarctica. Journal of the Geological Society of Korea, v. 52, pp. 901 – 915.

John, B.S., and Sugden, D.E., 1971, Raised marine features and phases of glaciation in the south Shetland Islands. British Antarctic Survey Bulletin,v. 24, pp. 45 – 111.

Kim, H., Lee, K.K., and Lee, J.Y., 2018, Comparison of Carslaw and Jaeger method and finite element method to estimate temperature of soil in Antarctica. Episodes, v. 41, pp. 1 – 8.

Koo, M.H., Kim, Y., Suh, M.C., and Suh, M. S., 2003, Estimating thermal diffusivity of soils in Korea using temperature time series data. Journal of the Geological Society of Korea, v. 39, pp. 301 – 317.

Koo, M.H., and Song, Y., 2008, Estimating apparent thermal diffusivity using temperature time series: a comparison of temperature data measured in KMA boreholes and NGMN wells. Geosciences Journal, v.12, pp. 255 – 264.

Koven, C.D., Riley, W.J., and Stern, A., 2013, Analysis of permafrost thermal dynamics and response to climate change in the CMIP5 Earth system models. Journal of Climate, v. 26, pp. 1877 – 1900.

Lee, J.Y., Lim, H., Yoon, H., and Park, Y., 2013, Stream water and groundwater interaction revealed by temperature monitoring in agricultural areas. Water, v. 5, pp. 1677 – 1698.

Lee, J.Y., Lim, H.S., and Yoon, H.I., 2016, Thermal characteristics of soil and water during summer at King Sejong station, King George Island, Antarctica. Geosciences Journal, v. 20, pp. 503 – 516.

Lee, Y.I., Choi, T., and Lim, H.S., 2019, Petrological and geochemical compositions of beach sands of the Barton and Weaver peninsulas of King George Island, West Antarctica: implications for provenance and depositional history. Episodes, v. 42, pp. 149 – 164.

López-Martínez, J., Serrano, E., and Lee, J. I., 2002, Geomorphological map of Barton and Weaver peninsulas, King George Island, Antarctica (1:10,000). Polar Science Laboratory, Korea Ocean Research and Development Institute, Seoul.

Marchenko, S., Romanovsky, V., and Tipenko, G., 2008, Numerical modeling of spatial permafrost dynamics in Alaska. Proceedings International Conference on Permafrost, 2008, Institute of Northern Engineering, v.2, p. 1125 – 1130

Nabelek, P.I., Hofmeister, A.M., and Whittington, A.G., 2012, The influence of

KOPRI 극지연구소

temperature-dependent thermal diffusivity on the conductive cooling rates of plutons and temperature-time paths in contact aureoles.Earth and Planetary Science Letters, v. 317, pp. 157 - 164.

Pradhan, N.R., Downer, C.W., and Marchenko, S., 2019, Catchment hydrological modeling with soil thermal dynamics during seasonal freeze-thaw cycles. Water, v. 11. doi:10.3390/w11010116

Pringle, D.J., Dickinson, W.W., Trodahl, H.J., and Pyne, A.R., 2003, Depth andseasonal variations in the thermal properties of Antarctic dry valley permafrost from temperature time series analysis. Journal of Geophysical Research: Solid Earth, v. 108. doi:10.1029/2002JB002364.

Pringle, D.J., Eicken, H., Trodahl, H.J., and Backstrom, L.G.E., 2007, Thermal conductivity of landfast Antarctic and Arctic sea ice. Journal of Geophysical Research: Oceans, v. 112. doi:10.1029/2006JC003641.

Romanovsky, V.E., Sergueev, D.O., and Osterkamp, T.E., 2003, Temporal variations in the active layer and near-surface permafrost temperatures at the long-term observatories in northern Alaska. Proceedings International Conference on Permafrost, 2003, Institute of Northern Engineering,v. 1, p. 989 - 994.

Roth, K., and Boike, J., 2001, Quantifying the thermal dynamics of a permafrost site near Ny-孲esund, Svalbard. Water Resources Research, v. 37, pp. 2901 - 2914.

Smellie, J.L., Pankhurst, R., Thomson, M.R.A., and Davies, R.E.S., 1984, The geology of the south Shetland Islands: VI. Stratigraphy, geochemistry and evolution. British Antarctic Survey, Cambridge, 85 p.

Vieira, G., Bockheim, J., Guglielmin, M., Balks, M., Abramov, A.A., Boelhouwers, J., Cannone, N., Ganzert, L., Gilichinsky, D.A., Goryachkin, S., López-Martínez, J., Meiklejohn, I., Raffi, R., Ramos, M., Schaefer, C., Serrano, E., Simas, F., Sletten, R., and Wagner, D., 2010, Thermal state of permafrost and active - layer monitoring in the Antarctic: advances during the international polar year 2007 - 2009. Permafrost and Periglacial Processes, v. 21, pp. 182 - 197.

Wang, Q., Yang, Q., Guo, H., Xiao, X., Jin, H., Li, L., Zhang, T., and Wu, Q., 2019, Hydrothermal variations in soils resulting from the freezing and thawing processes in the active layer of an alpine grassland in the Qilian Mountains, northeastern Tibetan Plateau. Theoretical and Applied Climatology, v. 136, pp. 929 - 941.

Weismüller, J., Wollschläger, U., Boike, J., Pan, X., Yu, Q., and Roth, K., 2011, Modeling the thermal dynamics of the active layer at two contrasting permafrost sites on Svalbard and on the Tibetan Plateau. The Cryosphere, v. 5, pp. 741 - 757.

KOPRI 극지연구소

Wu, Q., and Zhang, T., 2010, Changes in active layer thickness over the Qinghai-Tibetan Plateau from 1995 to 2007. Journal of Geophysical Research: Atmospheres, v. 115. doi:10.1029/2009JD012974.

Yoo, C.M., Choe, M.Y., Jo, H.R., Kim, Y.D., and Kim, K.H., 2001, Volcaniclastic sedimentation of the Sejong formation (late Paleocene - Eocene), Barton peninsula, King George Island, Antarctica. Ocean and Polar Research, v. 23, pp. 97 - 107.

Yoshikawa, K., and Hinzman, L.D., 2003, Shrinking thermokarst ponds and groundwater dynamics in discontinuous permafrost near Council, Alaska. Permafrost and Periglacial Processes, v. 14, pp. 151 - 160.

KOPRI
극지연구소

Table 1. Time range for RMS error calculation and calculated thermal diffusivity

Location	Time range for RMSE cal.	$\alpha_{opt}(\times 10^{-7}\ m^2/s)$	RMSE (°C)
SJL1	5,500 - 6,000	14	0.19953
SJL2	5,500 - 6,000	4	0.18515
SJL2	3,500 - 4,000	12	0.21182
SJL3	5,500 - 6,000	9	0.70905
SJL4	5,500 - 6,000	11	0.32168

KOPRI
극지연구소

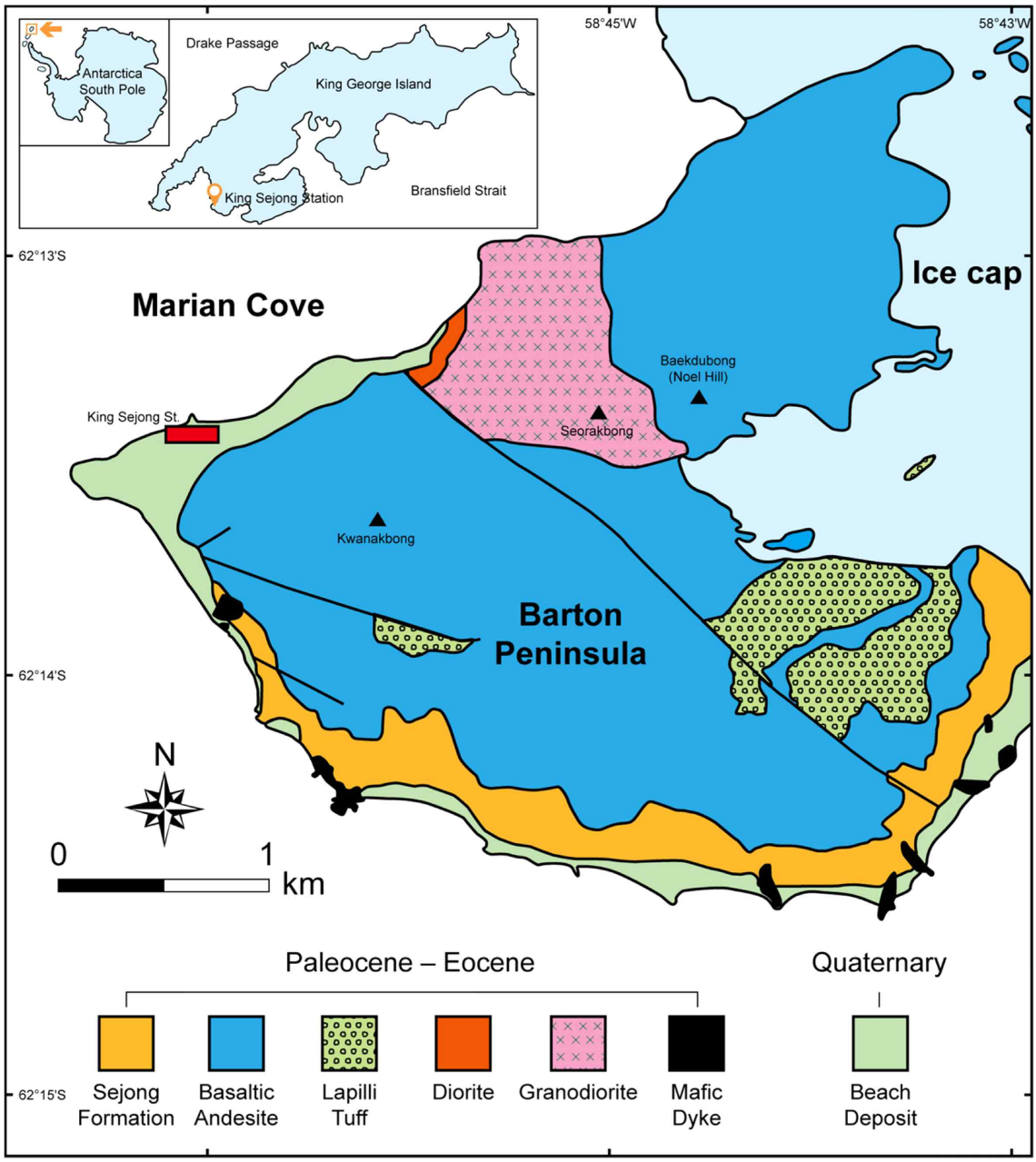

Figure 1. Geological map of Barton-Weaver Peninsulas, King George Island, Antarctica (modified from Lee et al., 2019).

Figure 2. Monitoring locations of surface temperature at the King Sejong Station in the Antarctica (modified from Kim et al., 2018).

극지연구소

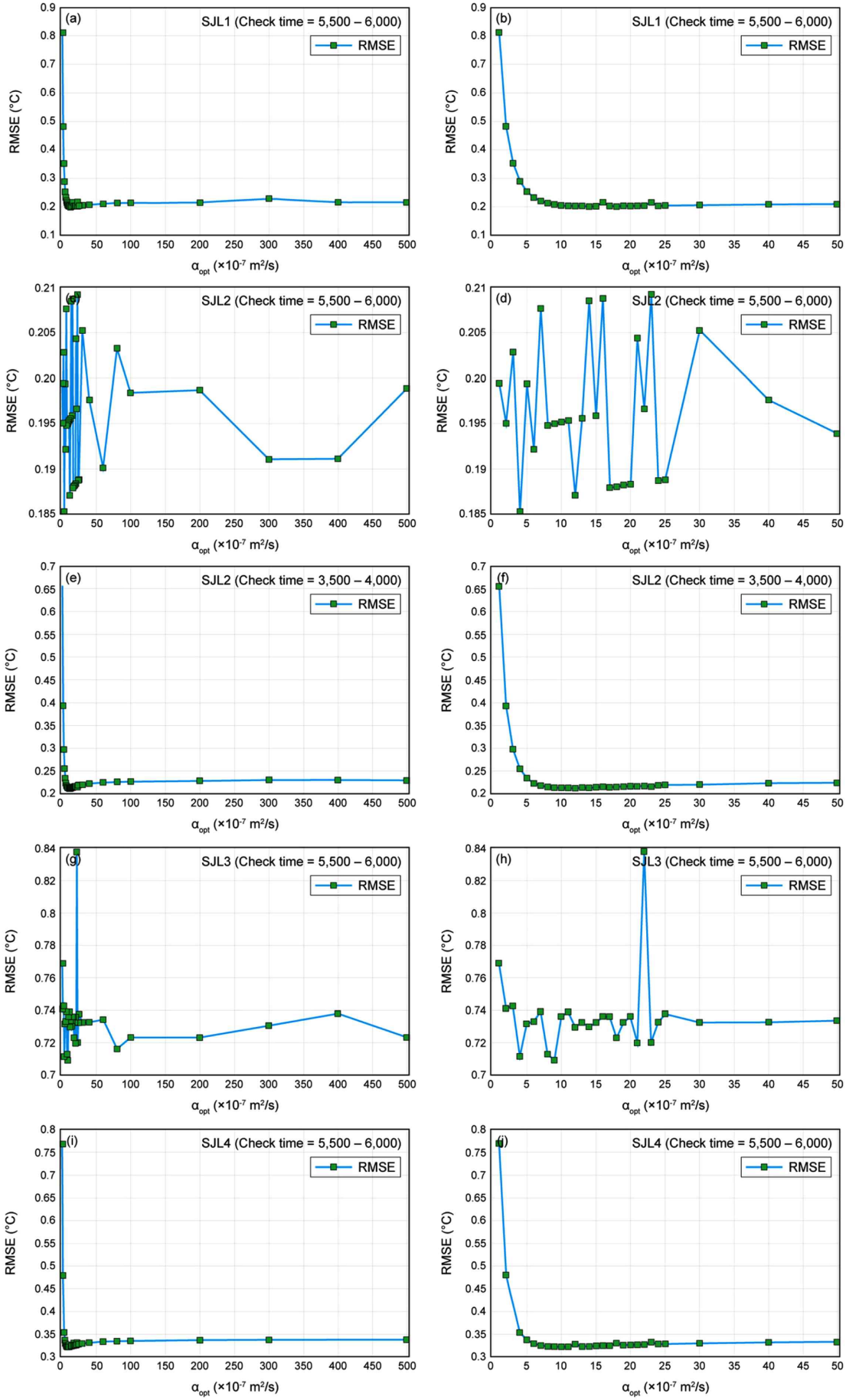

Figure 3. RMS error between the monitoring points.

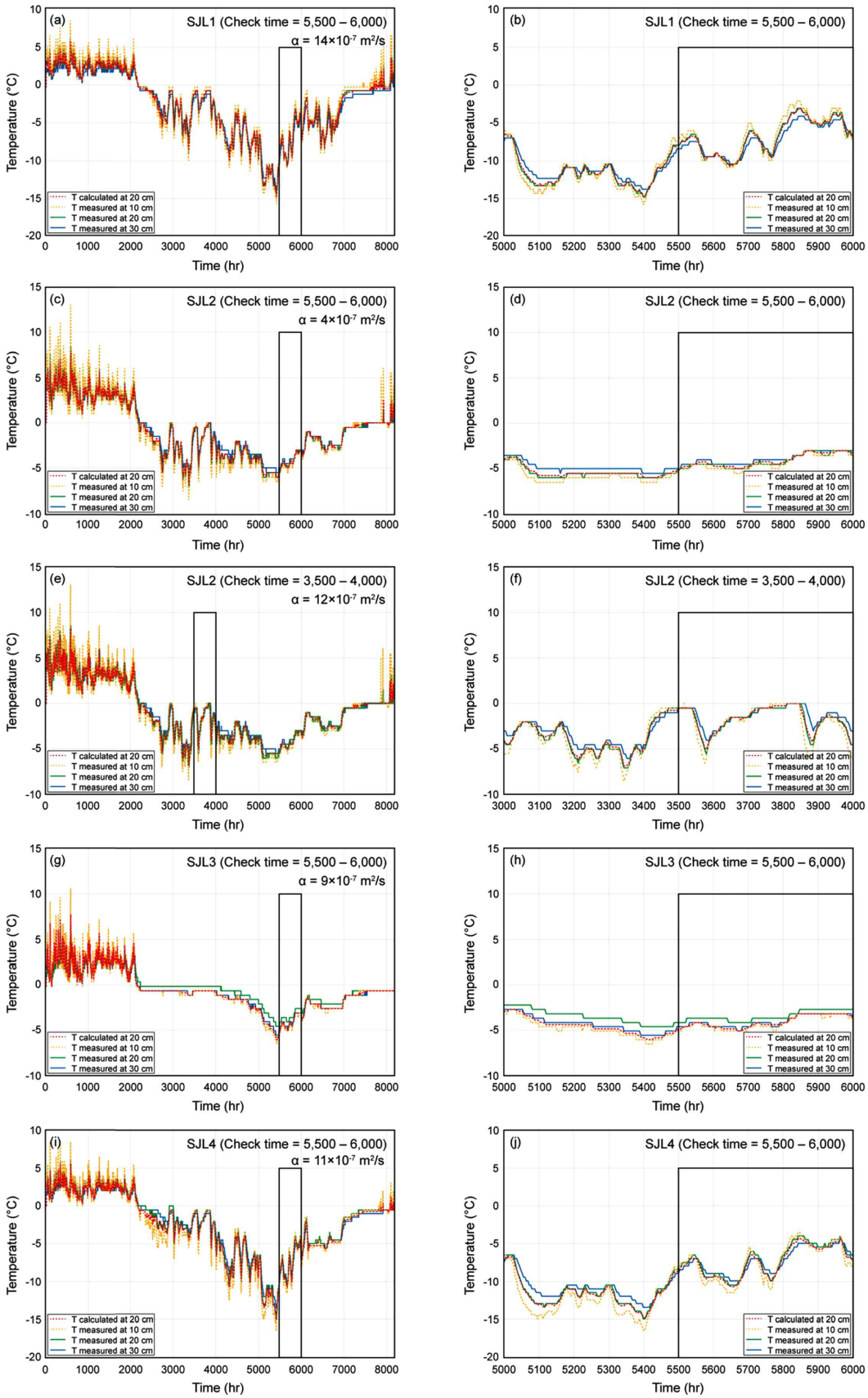

Figure 4. Time series of FEM at points showing a time window for optimum thermal diffusivity; figures on the right are zoomed-in windows of those on the left.

제 15 절. Abiotic Formation of Humic-Like Substances through Freezing-Accelerated Reaction of Phenolic Compounds and Nitrite[8)]

Dae Wi Min[1], Kitae Kim[2], Ka Hei Lui[1], Bomi Kim[2], Sunghwan Kim[3], Jaeweon Cho[4], and Wonyong Choi[*1]

[1]Division of Environmental Science and Engineering, Pohang University of Science and Technology (POSTECH), Pohang 37673, Korea

[2]Korea Polar Research Institude (KOPRI), Incheon, 21990, Korea

[3]Department of Chemistry, Kyungpook National University, Daegu 41566, Korea

[4]School of Urban and Environmental Engineering, Ulsan National Institute of Science and Technology (UNIST), Ulsan 44919, Korea

1. Introduction

Humic substances (HS) are ubiquitous components of natural organic matters (NOM), which play an important role in the environment. NOMs are one of the biggest carbon storages on Earth and contribute significantly to carbon cycle [1]. These organic materials contain nitrogen, phosphorous, and nutrients, which are important for soil fertility and microorganism growth in water [2,3]. In geochemistry, the role of HS can be considered as an electron donor/acceptor and previous studies have shown that several biochemical reactions in geospheres could be mediated by HS [4]. In addition, HS are important chromophores that serve as a photosensitizer in the environment [5]. Under solar irradiation, HS can generate reactive species or solvated electrons that induce redox reactions in nature [6].

HS can be formed via biochemical transformation, re-synthesis, decomposition, and polymerization, all of which are generally defined as humification process [7]. The production pathways can affect the ultimate chemical properties of HS [8]. However, the humification mechanisms are poorly understood and based on many uncertain speculation. A major humification process is the decomposition of macromolecules derived from dead bodies of living organisms [9]. Another important pathway is polymerization of low-molecular-weight materials (e.g., phenolic compounds, glucose, and amino acids) and their conversion to larger sized HS [10,11]. The Maillard reaction [12] is typically regarded

8) 이 연구는 본 과제 지원으로 수행되었으며 그 결과는 다음의 논문으로 출판되었음: Dae Wi Min, Kitae Kim, Ka Hei Lui, Bomi Kim, Sunghwan Kim, Jaeweon Cho, and Wonyong Choi, “Abiotic formation of humic-like substances through freezing-accelerated reaction of phenolic compounds and nitrite”, *Environ. Sci. Technol.* 2019, 53, 7410-7418.

as an important humification process; the effects of phenolic compounds, minerals, and metal oxides towards the reaction products have been studied in previous research [13–18].

However, the Maillard reaction is the only humification pathway yet to be studied and no other possible reactions have been suggested in the literature. In addition, previous studies [13–18] investigated humification with high concentration of organic precursors (e.g., dissolved organic carbon concentration (DOC) over 500 mg L^{-1}), but this concentration range is not comparable to DOC in natural waters [19,20]. Moreover, the above mentioned studies focused only on organic nitrogen (e.g., glycine) as a source of nitrogen in HS instead of inorganic nitrogen species that are commonly present in natural aquatic systems [21]. In this study, the humification was studied with DOC concentration under 10 mg L^{-1} and inorganic nitrogen species.

The aim of this study is to propose and investigate a previously unrecognized and purely abiotic humification process that takes place in the frozen solution containing phenolic compounds and nitrite. It is suggested that nitrite ions initiate the polymerization reaction of phenolic compounds (catechol or phenol), leading to the production of humic-like acids (HLA) and fulvic-like acids (FLA). The chemical characteristics of the produced HS were analyzed and compared with those of natural HS. According to mass spectrometric (MS) and elemental analyses, the humification products (HLA, FLA) have chemical structures and compositions similar to natural humic substances. The reaction is markedly accelerated in frozen conditions, which is attributed to the freeze-concentration effect. The humification rate measured in the frozen phase is much higher than those reported in the previous humification studies. The unique chemical transformation reactions taking place in frozen solutions could have important roles in organic carbon transformation in nature.

2. Methods

2.1. Materials.

Chemicals and reagents used in this study were as follows: catechol ($C_6H_6O_2$, Sigma-Aldrich), phenol (C_6H_6O, Sigma-Aldrich), sodium nitrite ($NaNO_2$, Aldrich), sodium nitrate ($NaNO_3$, Acros Organics), sulfuric acid (H_2SO_4, Sigma-Aldrich), sodium phosphate diabasic (Na_2HPO_4, Sigma-Aldrich), sodium phosphate monobasic (NaH_2PO_4, Sigma-Aldrich), sodium sulfate anhydrous (Na_2SO_4, Shinyo Pure Chemicals Co., Ltd), hydrochloric acid (HCl, Sigma-Aldrich), DAX-8 resin (Sigma-Aldrich), sodium hydroxide (NaOH, Sigma-Aldrich), potassium persulfate ($K_2S_2O_8$, Sigma-Aldrich), humic acid (Aldrich), ethyl acetate (J.T. Baker), and methanol (J.T. Baker). All chemicals were of analytical grade unless specified otherwise. Suwannee River humic acid (SRHA) and fulvic acid (SRFA) were purchased from the International Humic Substances Society (https://ihss.humicsubstances.org/). The deionized water used in the experiments was of

ultrapure (18 MΩ • cm) grade and was prepared using a Barnstead purification system.

2.2. Humification of catechol and phenol with nitrite ion.

Chemical reagent and catechol (or phenol) stock solutions were freshly prepared daily. 10 mL of sample solution with an appropriate substrate concentration was transferred to a 15-mL conical tube. The solution pH was adjusted by sulfuric acid solution (1.0 and 0.1 M). The conical tube was then transferred to a pre-cooled ethanol bath (-20 °C) for the reaction in frozen solutions. The reaction time was measured from the moment when the sample tube was immersed into the ethanol bath (time zero, t=0). After the reaction was completed (6 h), the frozen sample was thawed in a water bath (40 °C) prior to sample analysis. All the above procedures were the same for the control experiments using aqueous phase samples except that the reaction temperature was 20 °C.

2.3. Humic/Fulvic-like acid extraction.

For HLA/FLA extraction, liquid-liquid extraction was used to eliminate the remaining nitrite that might induce further reaction of HLA/FLA products. The sample solution was mixed with ethyl acetate (50 mL) in a separating funnel to extract organic compounds. The mixture was shaken for ~5 min and settled for 10 min. The aqueous layer was discarded and the organic layer was preserved for further analysis. The above procedure was repeated in triplicate. The organic solution was then treated by anhydrous sodium sulfate (Na_2SO_4) to remove excess water in the solution. The solution was then transferred to a round bottom flask and the organic solvent was evaporated by a rotary evaporator (40 °C). The remaining organic substances in the flask were dissolved in deionized water (10 mL) for further separation of HLA and FLA. Over 90% of nitrite was eliminated and ~80% of dissolved organic carbon (DOC) was recovered through this preparation procedure.

The extraction of humic-like acids (HLA) and fulvic-like acids (FLA) was conducted according to the International Humic Substances Society (IHSS) standard protocol. After nitrite elimination, the re-dissolved aqueous solution of humification products was acidified to pH 1.0 and maintained at room temperature for 24 h. The HLA fraction was precipitated and separated by centrifugation (10,000 rpm for 20 min). The HLA precipitates were re-dissolved in NaOH (0.1 M) solution for analysis. The FLA fraction in the supernatant was extracted using DAX-8 resin. 1 mL of the resin was used for each sample. After the absorption of FLA fraction, the DAX-8 resin was washed with deionized water until no monomer (catechol or phenol) was detected (3-5 times). The FLA was re-dissolved in NaOH (0.1M) solution before analysis. The organic substance fraction remaining after extraction HLA and FLA was classified as "residual".

2.4. Quantitative measurement.

The amount of HLA and FLA formation was quantitatively estimated by measuring the concentration of dissolved organic carbon (DOC). The DOC of extracted HLA and FLA was measured by a TOC analyzer (TOC-V CSH, Shimadzu) (detection limit: 0.10 mg L^{-1}).

The humification process can generate dark organic compounds with an elevated background absorption in the visible light region. As an indicating parameter for the humification process [13,15-18], the E_{600} value based on the absorbance at 600 nm can be calculated by the following equation.

$$E_{600}(\mathrm{L\,g^{-1}cm^{-1}}) = \frac{\mathrm{Absrobance\ at\ 600\,nm}}{\mathrm{DOC(g\,L^{-1})} \times \mathrm{light\ path\ length(1\,cm)}} \quad (1)$$

The pH of the sample solution was adjusted to 7 by phosphate buffer before the absorbance measurements which were done by using a UV/Visible spectrophotometer (Agilent 8453).

2.5. Dissolved organic nitrogen (DON) measurement.

DON production from the reaction was calculated from total dissolved nitrogen (TDN), which was measured by the persulfate oxidation method [22], and the following equation.

$$\mathrm{DON} = \mathrm{TDN} - ([NO_2^-] + [NO_3^-] + [NH_4^+]) \quad (2)$$

The concentrations of nitrite, nitrate, and ammonium ions were detected with an ion chromatograph (IC, Dionex DX-120) having a column for anion (Dionex IonPac AS23; 4 mm x 250 mm) or cation (CS12A; 4 mm x 250 mm) analysis, together with a conductivity detector (detection limits for nitrite, nitrate, and ammonium: 0.3~0.6 μM).

The elemental analysis for FLA, HLA, and humic/fulvic acids from Suwannee River and Aldrich was carried out using an elemental analyzer (Vario-Micro Cube, Germany). FLA and HLA samples were freeze-dried prior to the elemental analysis.

2.6. Fluorescence measurement.

The excitation /emission matrix (EEM) of FLA, HLA, and humic/fulvic acids from Suwannee River and Aldrich was measured by using a spectrofluorometer (FluoroMAx-4, HORIBA).

2.7. Pyrolysis-Gas Chromatography/Mass Spectrometry (py-GC/MS).

Prior to py-GC/MS measurement, HLA and FLA samples were freeze-dried. Py-GC/MS

was performed by a GC (Agilent 7890A) with a quadrupole MS (5975C). Approximately 0.5-1.0 mg of powder sample was covered with pyrofoil and placed in a quartz tube. The sample was then heated to the Curie temperature (590 °C) using a Curie point injector (JCI-22; Japan Analytical Industries, Japan). After pyrolysis, organic fragments were went through GC (DB-5MS; Agilent Technologies, USA) equipped with a column (30 m × 0.25 mm × 0.25 μm) for separation. After separation, the organic molecules were identified with a mass spectrometer. For MS measurement, electron energy was 70 eV, scanning arrange was 40-500 amu, and ion source temperature was 220 °C.

2.8. Fourier Transform Ion Cyclotron Resonance/Mass Spectrometry (FT-ICR/MS).

Inorganic ions in the humification product samples (Na^+, Cl^-, SO_4^-, NO_3^- and NO_2^-) were removed by solid-phase extraction prior to FT-ICR/MS measurement. SUPELCLEAN ENVI-8 6-mL tubes (SUPELCO) were used for the extraction following a standard procedure detailed elsewhere [23]. The absorbent tubes were rinsed with methanol before use. The humic sample solution was acidified to pH 2 and passed through the absorbent tube, which was subsequently rinsed again with HCl solution (0.01M) to re-dissolve the ions in the absorbent. The absorbent was dried by purging air for 5 min and the absorbed organic and humic products in the tube were re-dissolved by eluting methanol through the tube.

The samples were analyzed on a 7 Tesla FT-ICR/MS (Solarix 2XR, Bruker Daltonics, GmbH, Bremen, Germany) which was equipped with a quadrupole phase detection (2ω mode) system. The electrospray ionization (ESI) technique was used for the ionization of humic/fulvic substances in the samples. The sample solutions were prepared in 1:1 methanol-water mixture and directly injected into the syringe pump (flow rate: 180 μL/h) using a gastight syringe (Hamilton Co., Reno, NV). The mass spectra were recorded in negative ionization mode within a mass-to-charge (m/z) range of 150.5-3000.0. All recorded spectra were externally calibrated with an ESI-L low concentration tuning mixture (Agilent technologies). For nebulizing and drying, high purity nitrogen (N_2) was used. For ESI source, pressure of nebulizer gas was 0.8 bar and temperature of drying gas was 200 °C with 4.0 L/min flow rate. For the FT-ICR measurement, a capillary voltage of 3.5 kV was used. The ion accumulation time was 10 ms for a single spectrum and nearly 200 scans were summed for the final mass spectra. Voltage of the skimmer was -45.0 V. For the ICR trap, the voltages of both the front and back trap plates were -1.6 V. The ions were excited with a sweep excitation power of 25%.

2.9. Confocal Raman analysis.

To analyze the reagents (catechol and nitrite) in the grain boundary region in the frozen

solution, a confocal Raman microscope (inVia^{TM} Qontor confocal Raman microscope, Renishaw) equipped with a 785-nm edge laser was used. A Linkam stage (THMS 600, Linkam) was used for freezing the sample solution.

2.10. Electron Paramagnetic Resonance (EPR).

Catechol radicals produced by reaction with nitrite in the frozen solution were detected by electron paramagnetic resonance (EPR) analysis with an EMX plus -9.5/2.7 (Bruker). The measurement conditions were as follows: microwave power of 0.6 mW, microwave frequency of 9.4 GHz, and modulation frequency of 100 kHz.

3. Result and Discussion

3.1. Freezing-induced humification of phenolic compounds.

Figure 1A shows the time profiles of humic-like acids (HLA) formation in the presence of catechol and nitrite ions in aqueous and frozen solutions. The concentration of HLA produced from the initial monomer (catechol) was expressed in terms of DOC concentration. The increase of HLA concentration is a result of the humification of catechol. The reaction was markedly enhanced under the frozen condition compared to that in the aqueous phase. The HLA concentration rapidly increased during the initial 2 h of reaction, which leveled off afterwards. Figure 1B compares the time profiles of E_{600} values (eq. 1) under aqueous and frozen conditions. In the frozen phase, there was a rapid increase in E_{600} value over the initial 2 h, which subsequently reached a plateau whereas E_{600} in the aqueous phase was negligible. This is consistent with the behavior of HLA formation (Figure 1A). The HLA and E_{600} values from this study exhibited a reasonably good linear correlation (Figure 1C), indicating that the E_{600} value could be used to estimate the amount of HLA formation. Figure 1D shows the relative composition (%) of three organic fractions (HLA, FLA, and organics residual) after 6 h reaction of catechol and nitrite. The concentration of HLA and FLA fraction generated in the frozen solution was 11% and 34% respectively, which was much higher than those obtained in aqueous solution (0.3% and 2.1%). The fraction of FLA was higher than HLA in both conditions.

Table S1 compares the production rate of HLA and E_{600} values among this and other studies [13-18]. The calculated HLA and E_{600} formation rates in the ice phase were orders of magnitude higher than those in the aqueous phase. The production rates of HLA and E_{600} observed in the frozen condition are significantly higher than any of the reported values measured in the aqueous solution. The production of HLA and E_{600} was favored at lower pH (Figure 2A and C) and increased with increasing [NO_2^-] up to 10 μM (Figure 2B and D). In the absence of nitrite ions, no HLA and E_{600} were generated at all. The humification of catechol essentially requires the presence of nitrite and is highly accelerated

at lower pH. Instead of catechol, phenol was also tested as a humification precursor (Figure 2E and F). The behavior of HLA production in the frozen solution of phenol was very similar to that of catechol although the HLA concentration level was much lower compared with the case of catechol.

3.2. Dissolved organic nitrogen (DON) formation.

Dissolved organic nitrogen (DON) production from the humification process of catechol was measured in aqueous and frozen conditions (Figure 3). The formation of DON and nitrate was significant only in the frozen condition, which was accompanied by a rapid removal of nitrite during the first hour. The nitrate ion should be produced from the oxidation of nitrite ion by dissolved oxygen, which is highly enhanced under frozen condition (eq. 3) [24].

$$2HNO_2 + O_2 \rightarrow 2NO_3^- + 2H^+ \quad (3)$$

Although nitrite ions were quantitatively converted to nitrate ions in the absence of the organic precursor (Figure 3C), a majority of reacted nitrite ions (~84 %) were transformed to DON after frozen reaction in the presence of catechol. This indicates that nitrite-N elements were incorporated into the organic substances during the catechol humification process in the frozen condition whereas such process was negligible in the aqueous solution.

The elemental analysis showed that both HLA and FLA contained the nitrogen content and FLA has higher N content than HLA (see Table S2). The nitrogen composition of HLA was approximately the same as that in natural humic substances. The inorganic nitrogen species is transformed into organic nitrogen species typically through a biotic process in nature [25,26]. However, this study demonstrated that inorganic nitrogen can be incorporated into the organic substances via a purely abiotic pathway occurring in frozen solution.

3.3. Fluorescence spectra of FLA and HLA.

Spectrofluorometric analyses are widely used for chemical characterization of organic matters in nature. Figure S1 shows the excitation/emission matrix (EEM) of catechol, FLA, and HLA. Catechol showed a fluorescence peak at 275/316 nm (= excitation/emission). This peak was shifted to 300/350 nm (= ex/em) for FLA (Figure S1 B and C). Such a red shift of the fluorescence peak was also observed in a humification study [27]. The fluorescence spectra of FLA obtained from aqueous and frozen solution exhibited similar shapes. On the other hand, HLA produced from the frozen solution demonstrated fluorescence peaks at

KOPRI 극지연구소

295/416, 345/424, and 435/480 nm (= ex/em) and the spectra ranged from 360-550 nm emission and 260-450 nm excitation (Figure S1 D). Fluorescence spectra in this excitation/emission region are the typical sign of humic-like substances [28]. HLA was not obtained in the aqueous condition.

3.4. Mass spectrometric analysis of humification products.

Pyrolysis-Gas Chromatography /Mass Spectrometry (Py-GC/MS) was used to analyze the chemical structures of HLA and FLA generated from the humification process. The pyrolysis products of HLA and FLA are composed of various chemical structures formed during humification (Table S3). Alcohol, ketone, aldehyde, carboxylic acid, ester, and methoxy compounds were detected by GC/MS. The formation of such products with functional groups could be induced by the cleavage of aromatic rings during the oxidation of phenolic compounds [29-31]. Several nitrogen-containing compounds (nitrile, amide, indole, and pyrrolidine) were also detected from the humification products, which re-confirmed that organic nitrogen compounds were produced from the reaction of catechol and nitrite. Although the transformation of inorganic nitrogen into organic nitrogen is commonly mediated via plants and microorganisms in ecosystem [25,26], the present result demonstrated the possibility of abiotic mechanism that converts inorganic nitrogen to organic nitrogen in the frozen condition.

FLA, HLA, and standard HS (humic and fulvic acids obtained from Suwannee River) were further analyzed by Fourier Transform-Ion Cyclotron resonance/MS (FT-ICR/MS). A high sample concentration (DOC > 500 ppm) was required for the analysis. Table S4 compares the number of m/z peaks with assigned chemical formula, the average molecular weight (M_n), and percentage of the same m/z peaks among HLA, FLA, and the standard HS (SRFA and SRHA). The number of m/z peaks in SRFA and SRHA was much higher than in HLA and FLA, indicating that natural HS have more diverse chemical compositions than the laboratory-prepared HLA and FLA in frozen conditions. The mass spectra of SRFA and SRHA exhibited broad and evenly distributed peaks in the range of 150-1100 m/z (Figure 4) whereas HLA and FLA samples showed mass peaks in a narrower range of 200-800 m/z. However, in general, HLA and FLA exhibited a high level of similarity (70-80%) to SRHA and SRFA in terms of % peaks identical with SRHA (or SRFA). This implies that HLA and FLA generated in the frozen solution of catechol and nitrite are structurally similar to natural humic substances.

3.5. Freeze concentration effect.

The increase in the humification rate in the frozen solution can be ascribed to the freeze concentration effect occurring in the unfrozen liquid-boundary layer within the ice sample.

When a solution starts to freeze, ice crystals proliferate and expel the solutes into unfrozen areas [32]. The liquid-boundary layer with concentrated solutes remains as a thin interfacial layer between the ice crystals. This unfrozen area, the ice grain boundary, concentrates the solutes in it [24,32-34]. This grain boundary can be observed by various microscopic techniques [35-37]. A confocal Raman microscope was used to observe catechol and nitrite ions concentrated at the ice grain boundary. Figure 5 shows the optical image of the frozen sample and the spacial distribution of catechol and nitrite ions in the same frozen sample. Catechol and nitrite ions exhibit characteristic Raman peak at 772 cm^{-1} and 1326 cm^{-1}, respectively [38,39]. The Raman signals can be used as a probe to locate the distribution of catechol and nitrite ions in the frozen samples. Dark crack observed in the optical image is the grain boundary layer whereas the bright area indicates the ice crystal region in the frozen solution. The spacial Raman image of the same frozen sample shows that both catechol and nitrite are concentrated in the grain boundary region (Figure 5B and 5C) as compared with the optical image (Figure 5A). The Raman signals of 772 cm^{-1} (for catechol) and 1326 cm^{-1} (nitrite) are preferentially detected around the grain boundary region of the optical image. This observation provides a clear evidence that the humification reactions of catechol and nitrite should take place in the ice grain boundary region.

3.6. Mechanism of humification in the frozen solution and environmental implication.

The humification of phenolic compounds should occur via oxidative polymerization since nitrite ions can serve as an oxidant to initiate the humification process. The humification reaction was enhanced under acidic conditions (Figure 2) where nitrite ions are present in the protonated forms. The nitroacidium ions (H_2ONO^+) can be dehydrated to generate nitrosonium ions (NO^+) (eqs. 4 and 5) [40,41].

$$NO_2^- + H^+ \leftrightarrow HONO \ (pK_a = 3.4) \quad (4)$$

$$HONO + H^+ \leftrightarrow H_2ONO^+ \rightarrow NO^+ + H_2O \ (pK_a = 1.7) \quad (5)$$

Nitrosonium ion (NO^+) is a strong oxidant, which can abstract an electron from phenolic compounds to generate phenolic radicals (eq. 6) [42].

$$PhOH + NO^+ \rightarrow PhO\bullet + NO + H^+ \quad (6)$$

$$PhO\bullet \rightarrow \text{polymerization} \rightarrow FLA, HLA \quad (7)$$

The produced phenolic radicals can then induce polymerization and lead to the formation of humic-like substances (eq. 7) [13,14,16,29-31].

The formation of catechol radicals through reaction with nitrite ions was confirmed by electron paramagnetic resonance (EPR) under aqueous and frozen conditions (Figure 6). The EPR measurements were performed at relatively high catechol and nitrite concentration to obtain high signal intensity for phenolic radicals. No phenolic radicals were produced in the absence of nitrite ions, which implies that the humification reaction of phenols should be initiated by nitrite ions. In the presence of nitrite, more radicals were produced under more acidic condition, which confirms that proton concentration is an important factor in the humification process. Phenolic radical peak which is comparable to previous studies [43] were observed only in frozen solution, not in aqueous solution according to the EPR analysis. This is fully consistent with the observed fact that HLA and FLA are produced only under the frozen condition. In the frozen sample, solutes (protons, nitrites, and phenolic compounds) are migrated from the ice crystal lattice and aggregated in a narrow ice grain boundary region [24,32-34]. The increased proton concentration might accelerate the production of NO^+ from nitrite ions in the frozen solution. Under such condition, the enhanced concentration of catechol and NO^+ in the ice grain boundary should provide a unique environment where the humification reaction of phenols are highly accelerated.

Humification processes occurring via the decomposition of living organisms and macromolecular biomass substances ("top-down" mechanism) have been studied for a long time [8,9]. However, HS formation from low molecular weight compounds ("bottom-up" mechanism) has been studied only in limited cases. Furthermore, the bottom-up mechanisms induced very slow humification rates [13-18] which might not be significant as HS formation mechanism in nature. This study demonstrated for the first time that HS could be produced from the freezing-induced polycondesation reaction of phenolic compounds initiated by nitrite ions. The produced HS (HLA, FLA) exhibited the structures and compositions similar to those of standard HS (HASR, FASR). Considering that frozen solutions and ice phases are ubiquitous in natural environments (e.g., ice in polar region, seasonal sea ice, snow, aerosols in upper atmosphere, and frozen soils) and that phenolic compounds and nitrite are also common solutes in various aquatic environments, the present observation of freezing-induced humification process presents a new model of "bottom-up" humification mechanism working in cold environments, which was previously unrecognized.

4. References

1. Araujo, J. R.; Archanjo, B. S.; de Souza, K. R.; Kwapinski, W.; Falcão, N. P. S.; Novotny, E. H.; Achete, C. A., Selective extraction of humic acids from an anthropogenic Amazonian dark earth and from a chemically oxidized charcoal. Biol. Fert. of Soils 2014, 50, 1223-1232.

2. Lal, R., Soil carbon sequestration impacts on global climate change and food security. science 2004, 304, 1623-1627.

3. Canellas, L. P.; Piccolo, A.; Dobbss, L. B.; Spaccini, R.; Olivares, F. L.; Zandonadi, D. B.; Façanha, A. R., Chemical composition and bioactivity properties of size-fractions separated from a vermicompost humic acid. Chemosphere 2010, 78, 457-466.

4. Kl?pfel, L.; Piepenbrock, A.; Kappler, A.; Sander, M., Humic substances as fully regenerable electron acceptors in recurrently anoxic environments. Nature Geosci. 2014, 7, 195.

5. Stemmler, K.; Ammann, M.; Donders, C.; Kleffmann, J.; George, C., Photosensitized reduction of nitrogen dioxide on humic acid as a source of nitrous acid. Nature 2006, 440, 195.

6. Aguer, J.-P.; Richard, C., Influence of the excitation wavelength on the photoinductive properties of humic substances. Chemosphere 1999, 38, 2293-2301.

7. Lehmann, J.; Kleber, M., The contentious nature of soil organic matter. Nature 2015, 528, 60.

8. Rosa, A. H.; Sim?es, M. L.; de Oliveira, L. C.; Rocha, J. C.; Neto, L. M.; Milori, D. M., Multimethod study of the degree of humification of humic substances extracted from different tropical soil profiles in Brazil's Amazonian region. Geoderma 2005, 127, 1-10.

9. Swift, M. J.; Heal, O. W.; Anderson, J. M., Decomposition in terrestrial ecosystems. Univ of California Press, CA, 1979; Vol. 5.

10. Orlov, D. S., Humic substances of soils and general theory of humification. CRC Press, FL, 1995.

11. Tan, K. H., Humic matter in soil and the environment: principles and controversies. CRC Press, FL, 2014.

12. Maillard, L., Formation de mati?res humiques par action de polypeptides sur sucres. CR Acad. Sci 1913, 156, 148-149.

13. Qi, G.; Yue, D.; Fukushima, M.; Fukuchi, S.; Nishimoto, R.; Nie, Y., Enhanced humification by carbonated basic oxygen furnace steel slag-II. Process characterization and the role of inorganic components in the formation of humic-like substances. Bioresource technol. 2012, 114, 637-643.

14. Zhang, Y.; Yue, D.; Ma, H., Darkening mechanism and kinetics of humification process in catechol-Maillard system. Chemosphere 2015, 130, 40-45.

15. Fukuchi, S.; Miura, A.; Okabe, R.; Fukushima, M.; Sasaki, M.; Sato, T.,

KOPRI 극지연구소

Spectroscopic investigations of humic-like acids formed via polycondensation reactions between glycine, catechol and glucose in the presence of natural zeolites. J. Mol. Struct. 2010, 982, 181-186.

16. Nishimoto, R.; Fukuchi, S.; Qi, G.; Fukushima, M.; Sato, T., Effects of surface Fe (III) oxides in a steel slag on the formation of humic-like dark-colored polymers by the polycondensation of humic precursors. Colloid. Surface. A 2013, 418, 117-123.

17. Fukushima, M.; Miura, A.; Sasaki, M.; Izumo, K., Effect of an allophanic soil on humification reactions between catechol and glycine: spectroscopic investigations of reaction products. J. Mol. Struct. 2009, 917, 142-147.

18. Zhang, Y.; Yue, D.; Lu, X.; Zhao, K.; Ma, H., Role of ferric oxide in abiotic humification enhancement of organic matter. J. Mater. Cycles Waste 2017, 19, 585-591.

19. Ogawa, H.; Tanoue, E., Dissolved organic matter in oceanic waters. J. Oceanogr. 2003, 59, 129-147.

20. Sobek, S.; Tranvik, L. J.; Prairie, Y. T.; Kortelainen, P.; Cole, J. J., Patterns and regulation of dissolved organic carbon: An analysis of 7,500 widely distributed lakes. Limnol. Oceanogr. 2007, 52, 1208-1219.

21. Jørgensen, N. O. G., Organic Nitrogen. In Encyclopedia of Inland Waters; Likens, G. E., Eds.; Academic Press: Oxford 2009; pp 832-851.

22. Doyle, A.; Weintraub, M. N.; Schimel, J. P., Persulfate digestion and simultaneous colorimetric analysis of carbon and nitrogen in soil extracts. Soil Sci. Soc. Am. J. 2004, 68, 669-676.

23. Dittmar, T.; Koch, B.; Hertkorn, N.; Kattner, G., A simple and efficient method for the solid?phase extraction of dissolved organic matter (SPE?DOM) from seawater. Limnol. Oceanogr.: Meth. 2008, 6, 230-235.

24. Takenaka, N.; Ueda, A.; Maeda, Y., Acceleration of the rate of nitrite oxidation by freezing in aqueous solution. Nature 1992, 358, 736.

25. N?sholm, T.; Kielland, K.; Ganeteg, U., Uptake of organic nitrogen by plants. New phytol. 2009, 182, 31-48.

26. Bronk, D. A.; Glibert, P. M.; Ward, B. B., Nitrogen uptake, dissolved organic nitrogen release, and new production. Science 1994, 265, 1843-1846.

27. Hur, J.; Park, S.-W.; Kim, M. C.; Kim, H. S., Enhanced binding of hydrophobic organic contaminants by microwave-assisted humification of soil organic matter. Chemosphere 2013, 93, 2704-2710.

KOPRI 극지연구소

28. Chen, W.; Westerhoff, P.; Leenheer, J. A.; Booksh, K., Fluorescence excitation? emission matrix regional integration to quantify spectra for dissolved organic matter. Environ. Sci. Technol. 2003, 37, 5701-5710.

29. Pillar, E. A.; Camm, R. C.; Guzman, M. I., Catechol oxidation by ozone and hydroxyl radicals at the air-water interface. Environ. Sci. Technol. 2014, 48, (24), 14352-14360.

30. Pillar, E. A.; Zhou, R.; Guzman, M. I., Heterogeneous oxidation of catechol. J. Phys. Chem. A 2015, 119, 10349-10359.

31. Pillar, E. A.; Guzman, M. I., Oxidation of substituted catechols at the air-water interface: Production of carboxylic acids, quinones, and polyphenols. Environ. Sci. Technol. 2017, 51, 4951-4959.

32. Takenaka, N.; Ueda, A.; Daimon, T.; Bandow, H.; Dohmaru, T.; Maeda, Y., Acceleration mechanism of chemical reaction by freezing: The reaction of nitrous acid with dissolved oxygen. J. Phys. Chem. 1996, 100, 13874-13884.

33. Kim, K.; Yabushita, A.; Okumura, M.; Saiz-Lopez, A.; Cuevas, C. A.; Blaszczak-Boxe, C. S.; Min, D. W.; Yoon, H.-I.; Choi, W., Production of Molecular Iodine and Tri-iodide in the Frozen Solution of Iodide: Implication for Polar Atmosphere. Environ. Sci. Technol. 2016, 50, 1280-1287.

34. Kim, K.; Choi, W.; Hoffmann, M. R.; Yoon, H.-I.; Park, B.-K., Photoreductive Dissolution of Iron Oxides Trapped in Ice and Its Environmental Implications. Environ. Sci. Technol. 2010, 44, 4142-4148.

35. Kim, K.; Choi, W., Enhanced redox conversion of chromate and arsenite in ice. Environ. Sci. Technol. 2011, 45, 2202-2208.

36. Tokumasu, K.; Harada, M.; Okada, T., X-ray Fluorescence Imaging of Frozen Aqueous NaCl Solutions. Langmuir 2016, 32, 527-533.

37. Inagawa, A.; Harada, M.; Okada, T., Fluidic Grooves on Doped-Ice Surface as Size-Tunable Channels. Sci. Rep. 2015, 5, 17308.

38. Jha, P. K.; Halada, G. P., The catalytic role of uranyl in formation of polycatechol complexes. Chem. Cent. J. 2011, 5, 12.

39. Ianoul, A.; Coleman, T.; Asher, S. A., UV Resonance Raman Spectroscopic Detection of Nitrate and Nitrite in Wastewater Treatment Processes. Anal. Chem. 2002, 74, 1458-1461.

40. Turney, T.; Wright, G., Nitrous acid and nitrosation. Chem. Rev. 1959, 59, 497-513.

41. Riordan, E.; Minogue, N.; Healy, D.; O'Driscol, P.; Sodeau, J. R., Spectroscopic and optimization modeling study of nitrous acid in aqueous solution. J. Phys. Chem. A

2005, 109, 779-786.

42. Zolfigol, M. A.; Madrakian, E.; Ghaemi, E., Silica sulfuric acid/NaNO2 as a novel heterogeneous system for the nitration of phenols under mild conditions. Molecules 2002, 7, 734-742.

43. Khachatryan, L.; Adounkpe, J.; Asatryan, R.; Dellinger, B., Radicals from the gas-phase pyrolysis of catechol: 1. o-semiquinone and ipso-catechol radicals. J. Phys. Chem. A 2010, 114, 2306-2312.

KOPRI
극지연구소

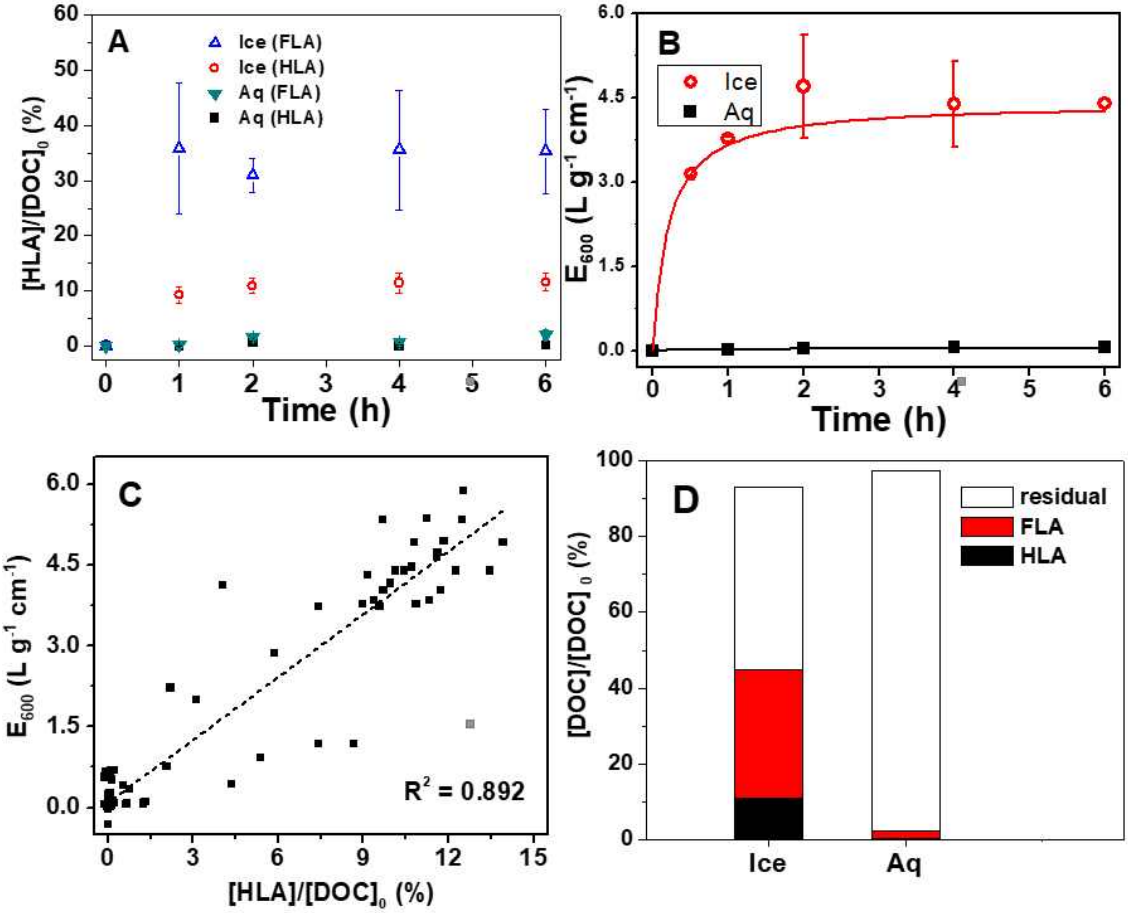

Figure 1. Time profiles of (A) catechol transformation to HLA and FLA(evaluated in terms of DOC) and (B) E_{600} under aqueous (20 °C) and frozen solution (-20 °C) solutions. (C) Correlation between $[HLA]/[DOC]_0$ (%) and E_{600} of this study. (D) Relative composition of HLA, FLA, and residual organics (residual) fractions in frozen (-20 °C) and aqueous (20 °C) solution after 6 h reaction. Experimental conditions: pH_i = 4, $[Catechol]_0$ = 100 μM, $[NO_2^-]_0$ = 5 μM, pH_i = 4.0.

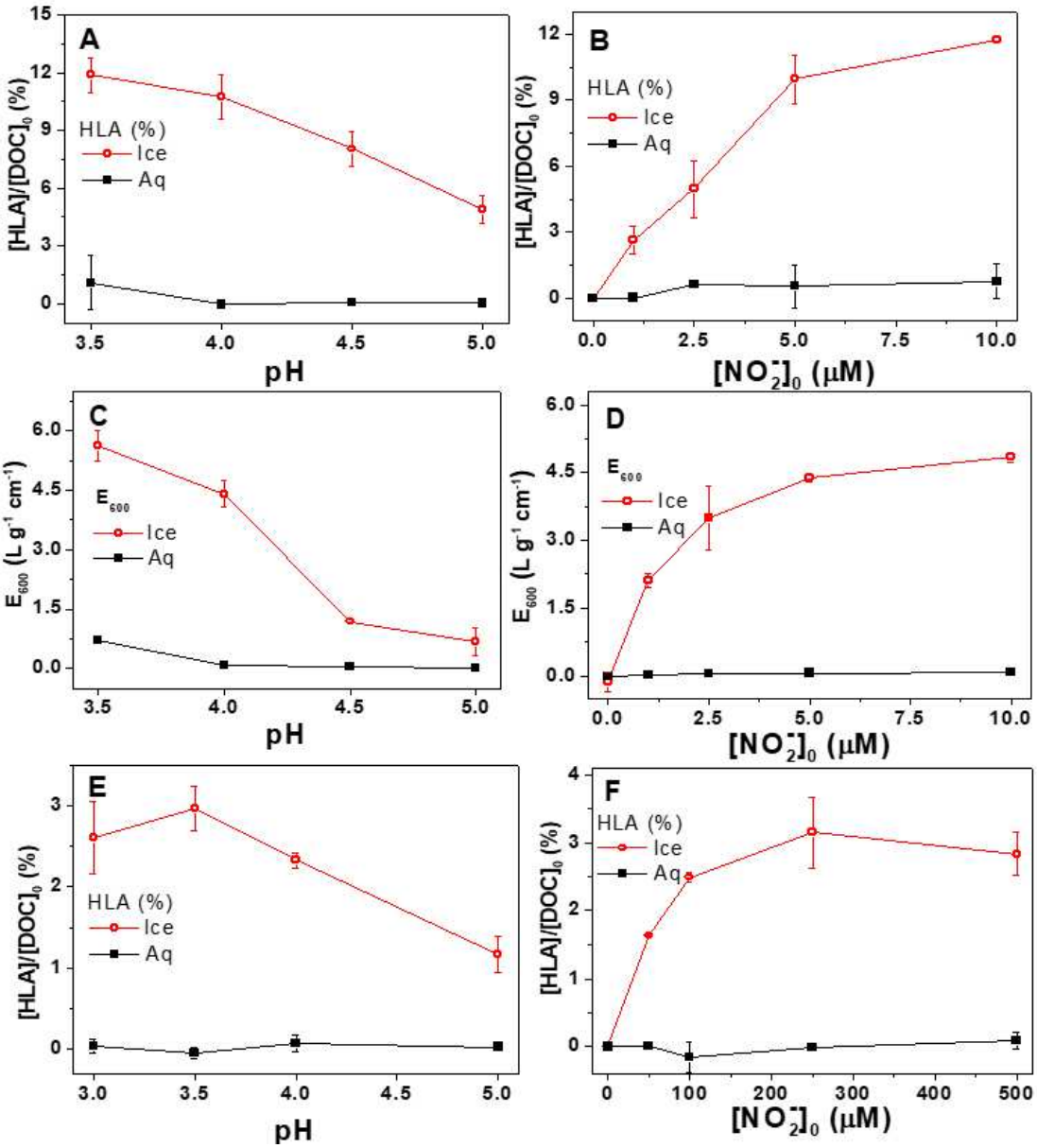

Figure 2. (A, B) HLA production (measured in DOC) and (C, D) E_{600} generation from catechol conversion in frozen (-20 °C) and aqueous (20 °C) solutions as a function of (A, C) pH and (B, D) $[NO_2^-]_0$. (E, F) HLA production from phenol conversion in frozen (-20 °C) and aqueous (20 °C) solutions as a function of pH and $[NO_2^-]_0$. Experimental conditions: $[Catechol]_0$ = 100 μM or $[Phenol]_0$ = 100 μM (for E, F), pH_i = 4.0 (for B, D, F), $[NO_2^-]_0$= 5 μM (for A, C) or 100 μM (for E), reaction time of 6 h.

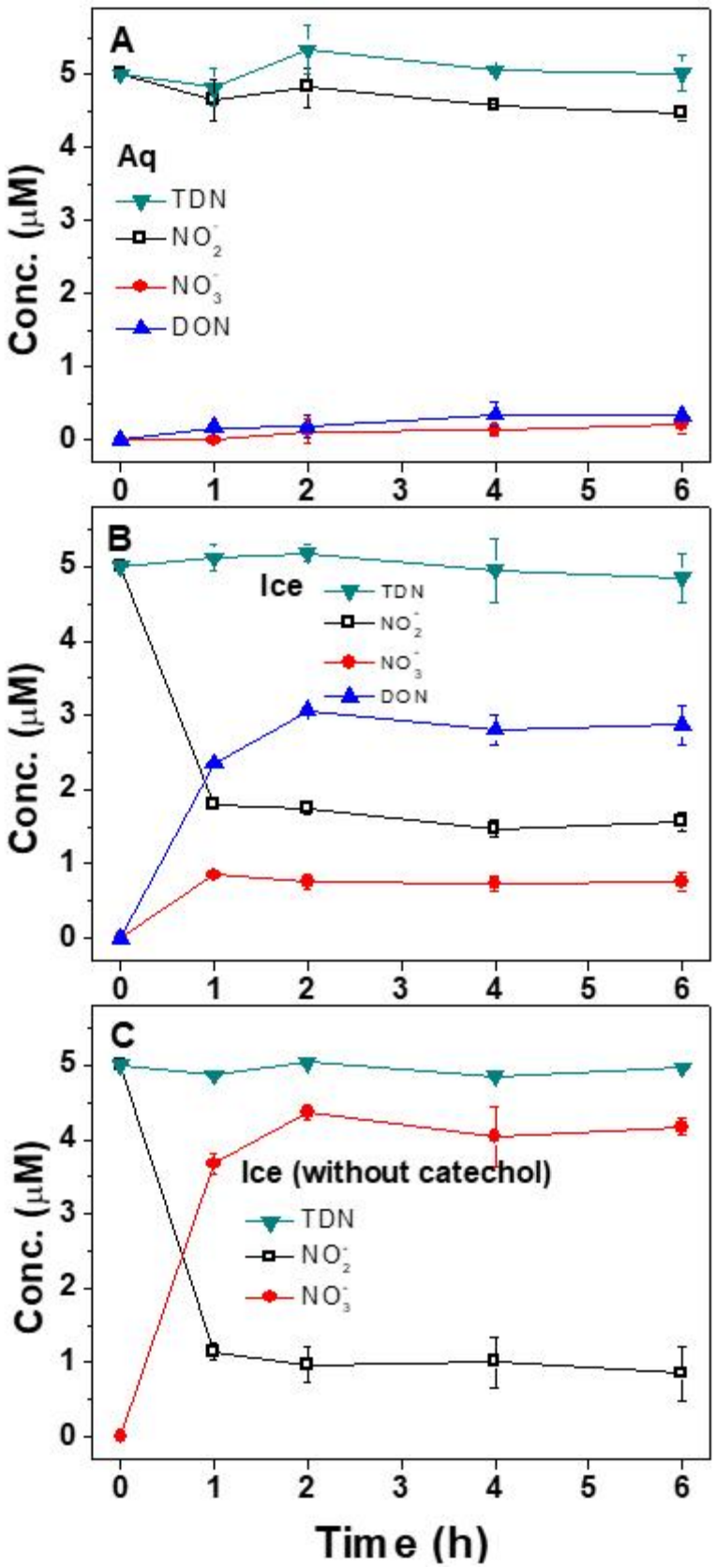

Figure 3. Time profiles of total dissolved nitrogen (TDN), nitrite (NO_2^-), nitrate (NO_3^-), and DON concentration under (A) aqueous (20 °C) and (B) frozen (-20 °C) conditions in the presence of catechol. (C) Conversion of nitrite (NO_2^-) to nitrate (NO_3^-) in the frozen phase in the absence of catechol. Experimental conditions: $[Catechol]_0$ = 100 μM (for A, B), $[NO_2^-]_0$ = 5 μM, pH_i = 4.

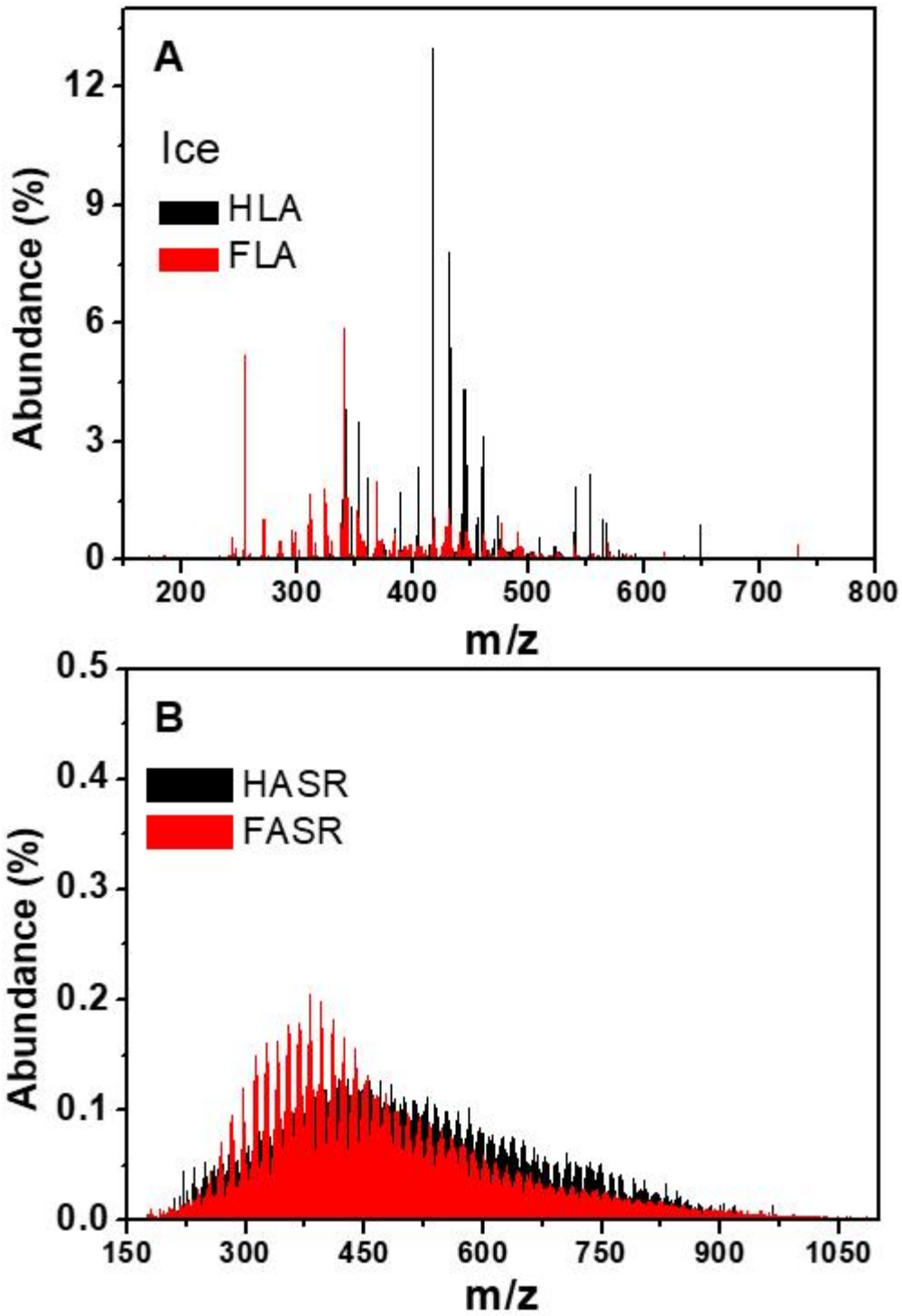

Figure 4. (A) Mass spectra (HLA and FLA) of humification products generated from the catechol transformation in frozen; (B) reference mass spectra of humic and fulvic acids from Suwannee River (SRHA and SRFA). Experimental condition: (A) $[Catechol]_0$ = 100 μM, $[NO_2^-]_0$ = 10 μM, pH_i = 4, reaction time of 6 h.

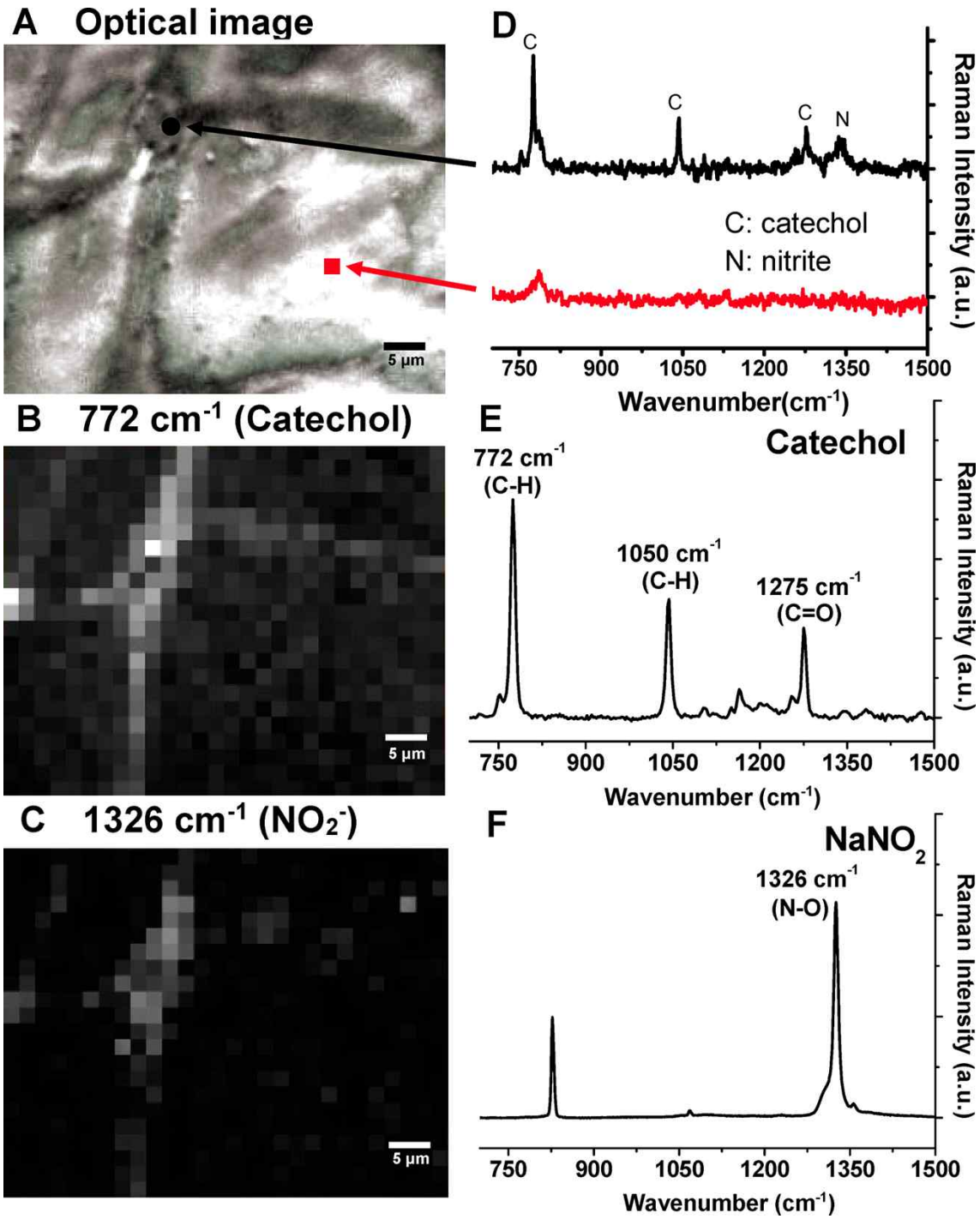

Figure 5. (A) Optical image of the grain boundary in the frozen solution and the corresponding spacial distribution of (B) catechol and (C) nitrite ions detected by a confocal Raman microscope within the frozen solution. (D) Raman spectra of the grain boundary region (black circle) and ice crystal region (red square); Reference Raman spectra of (E) catechol and (F) sodium nitrite. Freezing condition: a solution of catechol (1 mM) and nitrite (0.1 mM) was frozen at 253.2 K (-20 °C).

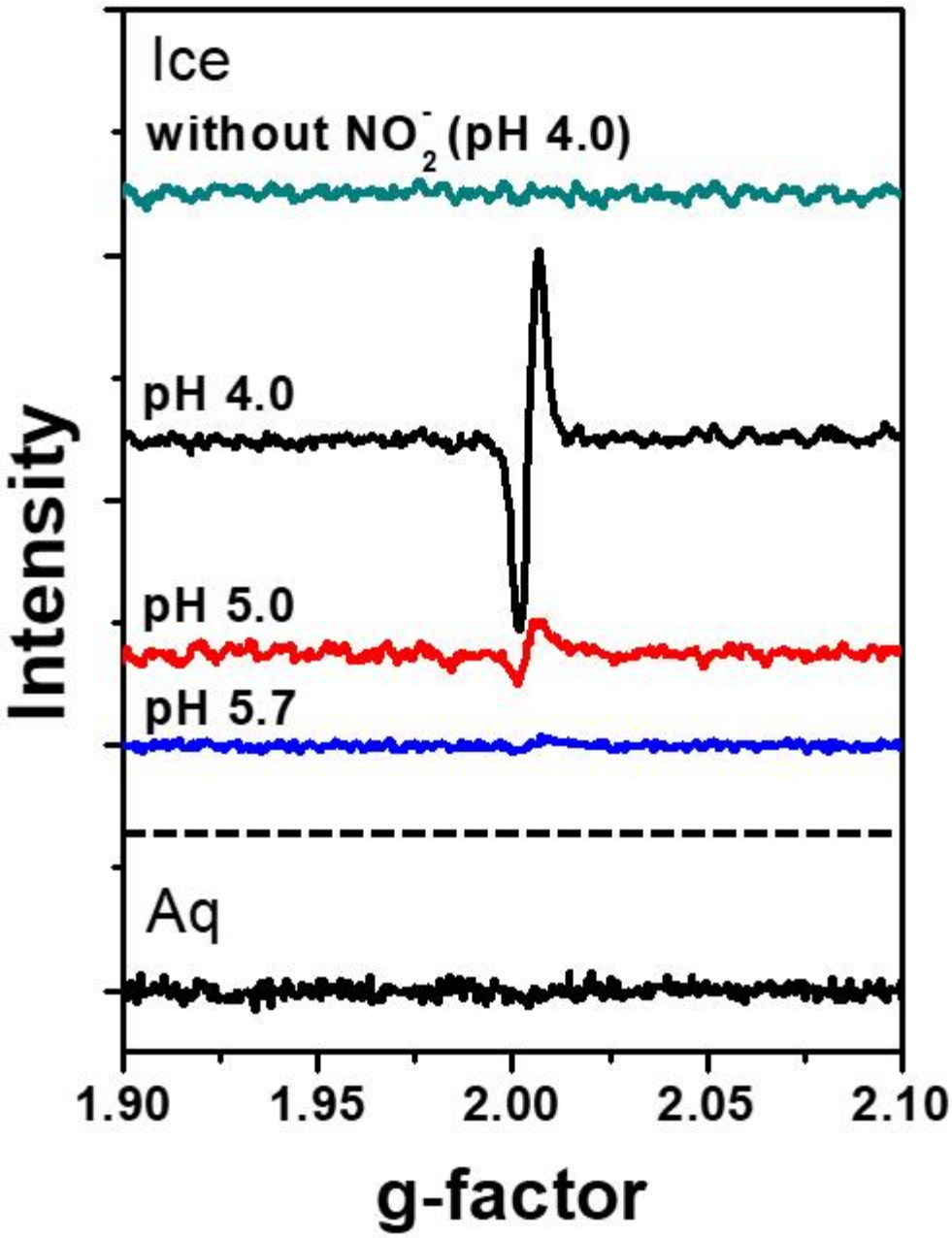

Figure 6. Electron paramagnetic resonance (EPR) spectra of catechol/nitrite solution in frozen (-20 °C) and aqueous (20 °C) solution. The EPR spectra of frozen solution with catechol only (no NO_2^-), with catechol (10 mM)/nitrite (1 mM) at different pH, and aqueous solution with catechol (10 mM)/nitrite (1 mM) at pH 4.0.

Supporting Information

Table S1. Rates of production of HLA and E_{600} via humification of low molecular weight organic precursors in this study† and other reports.

	this study		reference					
	Ice	**Aq**	**ref.13**	**ref.14**	**ref.15**	**ref.16**	**ref.17**	**ref.18**
[HLA]/[DOC]$_0$ (% min^{-1})*	**0.75**	**1.7×10^{-3}**	5.7×10^{-2}	1.8×10^{-2}	-	-	-	-
E_{600} (L g^{-1} cm^{-1} min^{-1})*	**0.36**	**4.2×10^{-4}**	1.2×10^{-2}	-	1.4×10^{-3}	7.7×10^{-4}	5.2×10^{-4}	3.3×10^{-5}
[DOC]$_0$ (ppm)	7.2	7.2	1,680	23,040	8,400	840	480	96
Reactants	Catechol + Nitrite	Catechol + Nitrite	Catechol + Glycine + Glucose	Catechol + Glycine + Glucose	Catechol + Glycine + Glucose	Catechol + Glycine + Glucose	Catechol + Glycine	Catechol + Glycine
pH	4	4	6	8	7	6	7	8
Catalyst	None	None	Birnessite	MnO_2	Zeolite	Steel slag	Allophanic soil	Fe_2O_3

* Initial rate

† Humification condition: [Catechol]$_0$ = 100 μM, [NO_2^-]$_0$ = 5 μM, pH$_i$ = 4, in frozen (-20℃) or aqueous (20℃) phase under dark condition

KOPRI 극지연구소

Table S2. Elemental composition (atom%) of HLA, FLA and standard humic substances

	C	H	N	O
HLA (ice)*	29.8	51.1	**0.4**	18.7
FLA (ice)*	34.9	41.1	**2.1**	21.9
FLA (Aq)*	27.1	49.0	**1.6**	22.4
HA†	34.3	41.2	0.4	24.1
SRHA†	37.3	37.2	0.6	24.8
SRFA†	36.1	38.7	0.3	24.8

* Humification condition: $[Catechol]_0$ = 100 μM, $[NO_2^-]_0$ = 5 μM, pH_i = 4, in frozen (-20℃) and aqueous (20℃) phase under dark condition, reaction time 6 h

† HA = Humic acid from Aldrich, SRHA = Suwannee River Humic acid, SRFA = Suwannee River Fulvic acid

KOPRI 극지연구소

Table S3. Pyrolysis fragments of HLA and FLA detected by GC/MS

Name	Area (%)		
	HLA (ice)	FLA (ice)	FLA (aq)
Acetic acid	0.2	0.3	0.6
Acetonitrile	0.1	1.0	4.0
Albicanol	1.0		
Benzene	0.04		
Benzoic acid	0.3	0.2	0.3
Betulin	1.4	2.1	0.3
Bombykol		0.2	0.2
Catechol	15.5	17.4	23.1
Cembrene	1.9		
Cholest-5-en-3-ol (3β)-		3.6	
Cholest-5-en-3-ol (3β)-, 9-octadecenoate, (Z)-		0.1	
Cholestan-3-one, cyclic 1,2-ethanediyl acetal, (5α)-	0.4	0.4	0.3
Cholic acid	0.1		
Cyclohexyl isocyanate			0.3
Decanenitrile	0.2	0.3	
Deoxy-celidoniol	1.0	1.4	1.4
Dihydrocholesterol	1.1		
Dotriacontane	12.6		
Eicosane	1.9	4.2	2.8
Eicosanoic acid, methyl ester			0.1
Elemol		0.7	
Ergost-5-en-3-ol, (3β)-	2.6		
Formic acid	0.1		
Heptadecanenitrile	0.2	0.4	
Hexadecanamide	0.2	0.9	0.4
Hexadecane	0.4	0.7	
Hexadecanenitrile	0.5	1.6	
Hexadecanoic acid, methyl ester		0.2	
Indole		0.3	
Longifolenaldehyde		0.2	
Methyl 9,9-10,13 tetradeutero octadecanoate		0.1	
Methyl n-hexadecyl ketone		0.7	
N,N- Bis(2-hydroxyethyl) dodecanamide		0.2	0.1
Nonadecane			0.8

(continued)

Name	HLA(ice)	FLA(ice)	FLA(aq)
Nonadecanenitrile	0.3	1.1	
Nonanal	0.1		
Nonanoic acid	0.1		
Octadec-9-en-1-ol	0.4	0.4	0.2
Octadecanal	0.9		
o-Cresol			0.1
Oxirane, 2,2-dimethyl-3-(3,7,12,16,20-pentamethyl-3,7,11,15,19-heneicosapentaenyl)-, (all-E)-	0.5	0.5	
Pentadecanoic acid	6.4	19.2	21.8
Pentadecanoic acid, methyl ester	0.1		
Pentanal		0.2	
Phenol	0.1	0.2	0.5
Phenol, 4-allyl-2-methoxy-, acetate		0.3	0.3
Resorcinol monoacetate	0.5	1.2	1.2
Stigmast-5-en-3-ol, (3β)-	18.3		5.7
Stigmast-5-en-3-ol, (3β,24S)-		1.9	
Stigmast-5,22-dien-3-ol, (3β,22E)-	1.1		
Syringyl acetone		0.2	0.1
Tetradecanal	0.3		1.3
Tetradecanamide			0.1
Tetradecane		0.2	0.4
Tetradecanoic acid		0.2	
Tetratetracontane		0.7	
Tridecanedial	0.2	0.4	0.2
Tridecanoic acid			0.2
Undecanenitrile			0.6
1-(P-Methoxyphenyl)-2-propanone			0.1
1,15-Hexadecadiene			0.2
1,2-Benzenedicarboxylic acid, bis(2-ethylhexyl) ester	1.4		0.8
1,2-Benzenedicarboxylic acid, mono(2-ethylhexyl) ester		0.8	
1,3-Benzodioxol-2-one	0.1	0.7	2.5
1,4-Methano-1H-indene,octahydro-1,7a-dimethyl-4-(1-methylethenyl)-, [1s-(1α,3aβ,4α,7aβ)]-	0.9	0.4	
1,6-Anhydro-β-D-glucopyranose		0.5	
1,8-Octanediol			0.2
14-methyl-(Z)-8-hexadecen-1-ol			0.2

(continued)

Name	HLA(ice)	FLA(ice)	FLA(aq)
16-Hentriacontanone			0.5
1-Cyclohexyl-2-(cyclohexylmethyl)pentadecane			0.1
1-Cyclohexyleicosane		0.3	0.2
1-Decanol			0.9
1-Dodecanol	0.1	0.2	0.2
1-Eicosanol	8.4	11.6	5.1
1-Eicosene	0.4		
1-Hentetracontanol	4.1	3.0	1.5
1-Hexacosene		0.3	
1-Hexanol	0.0		
1-Indanone	0.1	0.3	0.5
1-Nonadecene		0.4	
1-Octadecanol	0.9	2.4	0.9
1-Octadecene	1.6	2.5	1.8
1-Pentacontanol	0.4	5.6	4.1
1-Tetradecanol		0.1	0.1
2(1H)-Naphthalenone, octahydro-3-methyl-,(3α,4aβ,8aα)-			0.1
2,2,7-Trimethyl-octa-5,6-dien-3-one	0.4		
2,3-Butanedione			0.1
2,3-dihydro-Benzofuran			0.1
2,4a,8,8-Tetramethyl decahydrocyclopropa[d] naphthalene	0.2		
2',4'-Dimethoxyacetophenone		0.3	0.2
2,5-Furandione			0.1
2,6,10,14-Tetramethylhexadecane	2.3		0.5
2,6,10,15,19,23-Hexamethyl-2,6,10,14,18,22-tetracosahexaene	0.6		
2,6,10,15-Tetramethylheptadecane			0.9
2,6-Dimethoxy-4-allylphenol		0.1	0.2
2,6-Dimethoxyphenol	0.1		
2,6-Dimethyltridecanenitrile		0.3	
2-Hexadecanone	0.1	0.5	
2-Hexyl-1-octanol		0.2	
2-Methylhexadecane			0.9
2-Methyloctadec-7-yne	0.1		
2-Nonadecanone	0.2		
2-Pentadecanone	3.8	0.2	0.3
2-Propenal, 3-phenyl-	0.1	0.3	0.3

(continued)

Name	HLA(ice)	FLA(ice)	FLA(aq)
2-Tridecanone		0.2	
3,7,11-Trimethyldodecan-1-ol		0.4	1.1
3-Hexanol			0.1
3-methoxy-4-hydroxy-benzaldehyde	0.1		
3-Methoxyacetophenone		0.5	0.5
3-Phenylprop-2-enal	0.1		
3-phenylprop-2-ynal			0.2
3-Pyrrolidin-2-yl-propionic acid		0.3	0.4
4,4-Dimethylandrostan-3-ol	0.1		
4-Hydroxy-3-methoxyphenylacetone		0.3	0.2
5-Methylindole			0.2
6,10,14-Trimethylpentadecan-2-one	0.2	0.3	0.2
6,10-Dimethyl-9-undecen-2-one			0.2
8-Heptadecenoic acid	0.2	0.6	0.6
9-Octadecenoic acid		0.2	0.2
(9Z)-9-Octadecenal		0.6	
(9Z)-9-Tetradecen-1-ol	0.1		
(E)-5-Octadecene		0.3	
(E)-Icos-9-ene	1.1	1.2	3.6
(Z)-11-Hexadecen-1-ol			0.1
(Z)-14-Tricosenyl formate		0.4	
(Z)-9-Octadecenamide	0.5	0.9	0.6
(Z)-9-Tricosene	0.1		
β-Humulene		0.4	
δ-Guaiene		0.3	
unidentified	0.2	0.9	0.6

Table S4. Information of m/z peaks measured by FT-ICR/MS. Average molecular weight (M_n) was calculated as $M_n = \Sigma M_i N_i / \Sigma N_i$ (M_n = average molecular weight, M_i = molecular weight, N_i = abundance).

	Number of Peaks with assigned chemical formula	Average molecular weight (Mn)	% peaks identical with SRHA	% peaks identical with SRFA	% peaks identical with HLA(ice)	% peaks identical with FLA(ice)	% peaks identical with FLA(aq)
HLA (ice)*	99	434.9	84.8	66.7	100	58.6	59.6
FLA (ice)*	490	390.5	83.8	80.2	11.8	100	79.8
FLA (aq)*	544	376.7	86.3	77.8	10.8	71.9	100
SRHA†	3274	510.5	-	-	-	-	-
SRFA	6454	499.2	-	-	-	-	-

* Humification condition: $[Catechol]_0$ = 100 μM, $[NO_2^-]_0$ = 10 μM, pH_i = 4.0.

† SRHA = Suwannee River Humic acid, SRFA = Suwannee River Fulvic acid

KOPRI 극지연구소

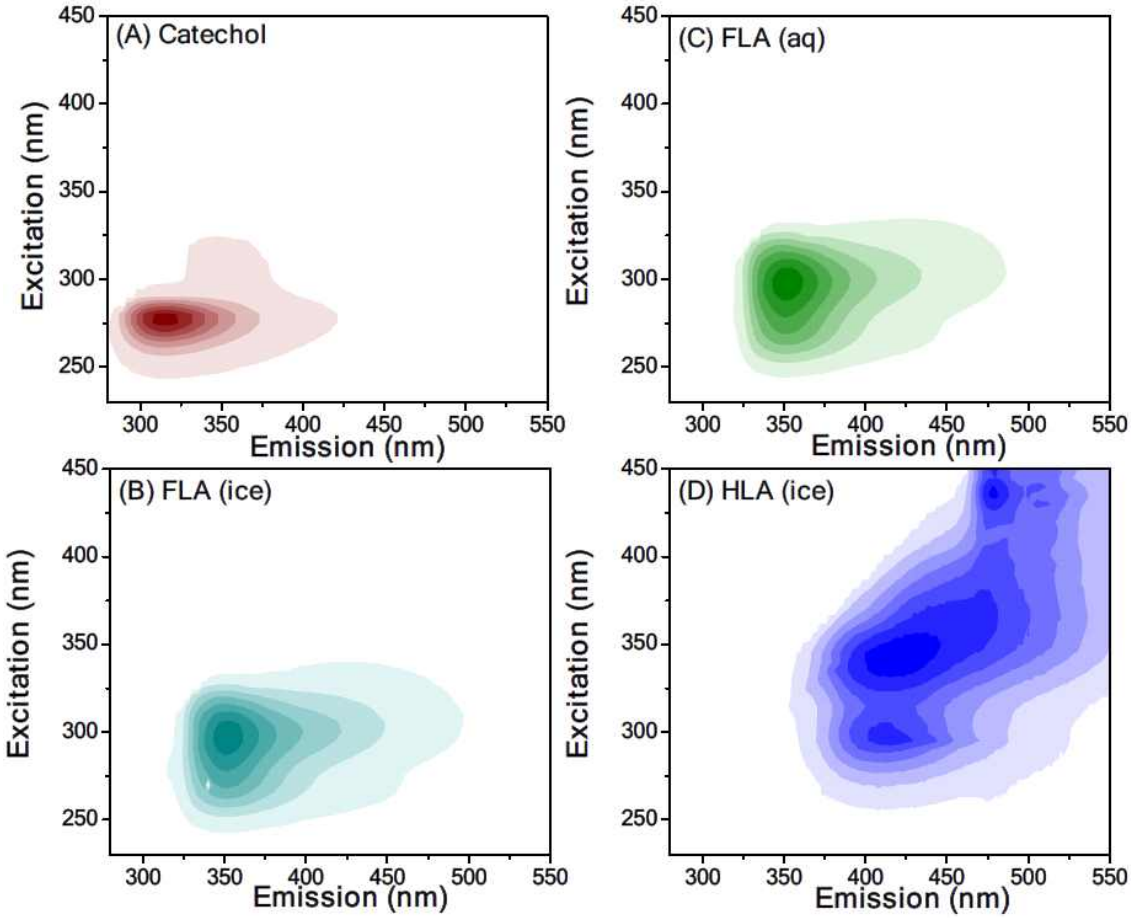

Figure S1. Excitation/emission matrix (EEM) of catechol, FLA and HLA. All spectra were normalized to the total volume of spectra. Experimental condition:(B, C, and, D) $[Catechol]_0$ = 100 μM, $[NO_2^-]_0$ = 5 μM, pH_i = 4, in ice (-20 ℃) and aqueous (20 ℃), reaction time in 6 h.

극지연구소

제 16 절. Halide-Induced Dissolution of Lead(IV) Oxide in Frozen Solution[9)]

Sunil Paul M. Menachery[1,2], Dae Wi Min[1], Daun Jeong[1], Charuvila T. Aravindakumar[2], Woojin Lee[3], and Wonyong Choi[1*]

[1]School of Environmental Science and Engineering, Pohan University of Science and Technology

[2]School of Environmental Sciences, Mahatma Gandhi University, Kottayam, India

[3]Department of Civil and Environmental Engineering, Nazarbayev University, Astana, Kazakhstan

1. Introduction

Lead (Pb) is an essential component in a number of ores (e.g., galena, anglesite, cerrosite, etc.) and a common material used in various industrial products (e.g., lead-acid batteries, cable sheath, solders, radiating shielding, pipelines, etc.) [1-7]. Extensive industrial uses and applications of lead and lead-containing chemical compounds made this toxic metal widely distributed in various media of environments and introduced into plants, animals, and human bodies through polluted air, water, and food [2, 6, 8-13]. The toxicity of this metal is largely ascribed to its binding ability to thiol (-SH) groups in enzymes, which leads to the inhibition of enzymes [14, 15]. Acute lead poisoning in humans causes serious health problems in the kidney, nerve system, brain, and liver, whereas mild poisoning causes anemia and headache [15-19].

Chemical reactions occurring in frozen solutions have attracted the attention of environmental researchers because of the unique chemical reaction characteristics that are clearly different from those of the aqueous counterparts [20-32]. Takenaka et al. observed that the oxidation kinetics of nitrite (NO_2^-) to nitrate (NO_3^-) is 10^5 times faster in frozen solution than in aqueous solution [25, 26]. Heger et al. demonstrated an enhanced protonation of cresol red in frozen solutions by 2-4 orders of magnitude, which is connected to an increase in the local concentration of acids [20]. The photolysis of chlorinated phenols in frozen solutions generated toxic byproducts such as chlorobiphenyldiols and dioxins, whereas such toxic transformation products were not observed in aqueous solution [24, 33]. Our previous studies also demonstrated that the dissolution of inorganic metal oxides (manganese oxide and iron oxide) can be significantly enhanced in frozen solutions [21-23]. Some other interesting examples of the unique

9) 이 연구는 본 과제 지원으로 수행되었으며 그 결과는 다음의 논문으로 출판되었음: Sunil Paul M. Menachery, Dae Wi Min, Daun Jeong, Charuvila T. Aravindakumar, Woojin Lee, and Wonyong Choi, "Halide-Induced Dissolution of Lead(IV) Oxide in Frozen Solution", *J. Hazard. Mater.* 2020, 384, 212198.

chemical reactions in frozen solutions include the enhanced photolysis of nitrates [34], accelerated reduction of bromate [35], enhanced photooxidation of iodide [36], cooperative hydration of pyruvic acid [29], and singlet oxygen-mediated degradation of organic pollutants [27]. On the other hand, a ligand-specific reductive dissolution of iron has been extensively studied using various commercial iron oxide samples [37], which demonstrated an inhibited dissolution of iron from goethite in the presence of some ligands in frozen solutions, which is quite contradictory to most of the above mentioned experimental results. It seems that the mechanisms of chemical reactions occurring in frozen media are complex and sensitively depend on the conditions and the kind of reactants, which warrants more systematic investigations.

The presence of lead in aerosols and frozen environments has been well recognized [38, 39]. The existence of lead in natural frozen media, such as Antarctic and Greenland snow and ice, has been systematically monitored by Boutron and co-workers [40]. Another study by McConnell et al. clearly revealed the ubiquitous deposition of this toxic heavy metal across Antarctic ice [41]. The reduced form of lead (Pb(II)) was reported as a primary species responsible for the lead pollution in environments [42, 43], since the oxidized form such as ß-PbO_2 is insoluble in water. Hence the reduction of insoluble ß-PbO_2 to soluble Pb(II) ions should play a key role in the lead pollution. The dissolution of this toxic metal by diverse chemical species with reducing power has been extensively studied in aqueous solutions. Prior studies by Lin et al., Wang et al., and Shi and Stone reported that the reductive dissolution of lead in aqueous solution was highly enhanced in the presence of reductants such as iodide (I^-), bromide (Br^-), manganese (Mn^{2+}), ferrous ion (Fe^{2+}), and natural organic matter (NOM) [43-48]. However, no studies on the lead dissolution in frozen solutions, which should be essential in understanding the behavior of lead in natural frozen environments (e.g., polar region and upper atmosphere), have been carried out to date. Although lead concentration in natural frozen environments are limited (pg/g to ng/g level), an accelerated reductive dissolution of toxic lead species in the frozen environment, such as cloud droplets and marine mineral aerosols where lead particles exist in highly acidic conditions [38, 39, 49], may cause serious lead pollution. In this study, we systemically investigated the reductive dissolution of lead from a commercial lead oxide sample, plattnerite (ß-PbO_2), in frozen solutions containing halide ions that are ubiquitous in diverse environmental media. This could provide basic knowledge for the clear understanding of the fate and transport of lead in the natural frozen environments and the remediation of lead contamination in cold environments.

2. Materials and Methods

2.1. Materials

Commercially available plattnerite (ß-Pb(IV)O_2; specific surface area = 3.6 m^2/g), which has

been used as a reliable Pb(IV) mineral source in previous studies [44, 46], was purchased from Acros Organics. Halides and all other chemicals used in this study were of analytical reagent grade. All the sample solutions for the experiments in this study were prepared with double-distilled water. Dilute solutions of perchloric acid (1 mM) and sodium hydroxide (1 mM) were used for adjusting the initial pH values of aqueous sample suspensions.

2.2. Experimental procedure

The purchased plattnerite was ground to make fine particles for enhancing its dispersion in aqueous solution. The crystalline structure of ß-PbO2 was confirmed by X-ray diffraction (XRD) analysis (PANalytical X'Pert diffractometer with an X'Celerator detector) using Cu Kα radiation (Fig. S1, Supplementary Data). The particle size of the ground ß-PbO2 sample showed a broad distribution (mostly ranging from sub-mm to 4 mm) and the average particle size was determined as approximately 1.2 μm (Fig. S2-S3, Supplementary Data) using high-resolution Field Emission Scanning Electron Microscopy (JSM-7800F Prime, JEOL Ltd) analysis. Although natural plattnerite particles might exist in an agglomerated form with different sizes, the experimental results obtained using the commercial plattnerite may represent those of natural one, especially in a qualitative aspect. About 0.025 g of ß-PbO2 sample was added into 50 mL of double distilled water to obtain an initial concentration of 0.5 g L^{-1}. An initial halide concentration of 0.1 mM was added for all the experiments, except experiments evaluating their concentration dependence on the reductive dissolution. The initial pH values of these samples, before adjusting into desired values for the dissolution experiments, were found to be between 5.0 - 5.5. Approximately, 5 mL of the lead oxide suspension after pH adjustment was placed in 15 mL polypropylene tubes with or without the ligands and kept in dark at either room temperature (for aqueous phase reaction) or in an ethanol bath maintained at −20 °C (for reaction in frozen condition). The time at which the sample tubes immersed into the dark place or cooling bath was considered as the reaction starting time (t = 0). Aliquots of aqueous and frozen samples (after thawing) were taken at fixed time intervals and filtered through 0.45-micron syringe filter to remove any undissolved lead oxide particles. In the case of a frozen sample, it was taken right after thawing in a water bath maintained at 40 °C. These samples were used for further analyses. The experiments for evaluating the temperature dependence on the reductive dissolution was also conducted using the same experimental setup but changing the temperature to desired values. More experimental details can be found in our previous studies [21-23]. All experimental tasks were conducted at least twice to confirm the reproducibility and the standard errors were indicated in the description of experimental results.

2.3. Analytical Procedure

The concentrations of dissolved lead in both aqueous and frozen samples were measured by inductively coupled plasma – optical emission spectroscopy (ICP-OES: Thermo Scientific iCAP 6000 series). The ICP-OES was initially calibrated to measure lead with a series of standards (Concentration range: 1 – 50 mg/L). The concentrations of halide ions were monitored by ion chromatographic analysis (DX-1200, Dionex Corporation, USA). The individual halides ions were detected (Concentration range: 1 – 500 μM) using a conductivity detector after their separation by a Dionex IonPac AS23 (4 mm x 250 mm) column with an isocratic elution of sodium carbonate (3.5 mM) and sodium bicarbonate (1 mM) at a flow rate of 1.2 mL/min.

3. Results and Discussion

3.1. Dissolution of lead by halides in aqueous and frozen solutions

We first measured the dissolution of lead in aqueous and frozen samples in the absence of the ligands to test the thermodynamic feasibility of lead dissolution [43]. The amount of dissolved lead was greater at lower pH (pH ≥ 3) and gradually decreased with increasing the pH of the aqueous and frozen solutions (Fig 1A), which agrees to the previous research results reporting much enhanced dissolution of lead in acidic conditions [43, 45]. The dissolution of lead was slightly higher in frozen solutions than its aqueous counterpart at pH ≥ 3 (Fig 1A and inset in Fig. 1B) but such enhanced lead dissolution was not observed at higher pH. The concentrations of dissolved lead in both aqueous and frozen solutions were very much closer for pH 1-3. To verify the reliability of those results, statistical analysis (analysis of variance), was conducted. The statistical results revealed a P-value of 0.026 for frozen samples, which is within the accepted limit of α (< 0.05) and, thus, statically significant (i.e., different). On the other hand, the P-values obtained for aqueous samples were 0.151. Since many naturally-occurring environmental media (e.g., cloud droplets and marine mineral aerosols) that may contain lead particles have pH around 3 [38, 39, 49], most of the dissolution experiments in this study were conducted at the relevant pH.

We tested and compared the dissolution of lead in the presence of various halide ions in aqueous and frozen solutions. Halide ions are ubiquitously distributed in the environments [50-52] and their effect on the dissolution of lead oxide is significant for understanding this environmental chemical process. Fig. 1b shows the variance of lead dissolution in aqueous and frozen solutions in the presence of different halide ions. The extent of dissolution in both aqueous and frozen solutions was highly enhanced by bromide and iodide compared to the dissolution without any halides. However, the addition of chloride does not seem to have a significant effect on the dissolution. Among the halide

ions, iodide significantly suppressed the dissolution of lead in frozen solutions compared to that of the aqueous solution. On the other hand, bromide induced a small enhancement (consistently observed) of lead dissolution in frozen solutions. It is known that the dissolution of iron oxide and manganese oxide in the dark frozen condition was enhanced in the presence of various ligands such as formic acid and iodide, which was ascribed to the freeze concentration effect of metal oxide, proton, and ligand molecules in the liquid-like ice grain boundary region [21-23, 36, 53, 54]. The suppressed dissolution of lead in frozen solutions by iodide is clearly contradictory to the dissolution behavior of iron oxide, of which dissolution in frozen solution is enhanced by several times in the presence of iodide [37]. The ligand-specific nature of ß-PbO_2 dissolution implies that the dissolution of toxic lead ions in the frozen environment could be selectively affected by the kind of halide ions that are ubiquitous in the environment.

A stepwise reaction mechanism leading to the dissolution of ß-PbO_2 to soluble Pb(II) by bromide and iodide in aqueous solution has been well documented in earlier reports [45, 46, 48]. The reaction is initiated by the adsorption of halide ion on the surface of metal oxide leading to the formation of an initial surface complex, which is consequently converted into a Pb(III) intermediate species through one-electron transfer process (eqs 1-3).

$$>Pb(IV)\text{-}OH + X^- + H^+ \leftrightarrow >Pb(IV)\text{-}X + H_2O \quad (1)$$

$$>Pb(IV)\text{-}X \rightarrow >Pb(III)\text{-}X^{\bullet} \quad (2)$$

$$>Pb(III)\text{-}X^{\bullet} + X^- + H_2O \rightarrow >Pb(III)\text{-}OH + X_2^{\bullet -} + H^+ \quad (3)$$

The highly unstable Pb(III), due to the unusual $d^{10}s^1$ electronic configuration, could be immediately reduced to more stable Pb(II) by another one-electron transfer process (eqs 4-6), and eventually released from the ß-PbO2 surface and dissolved into bulk aqueous solution (eq 7).

$$>Pb(III)\text{-}OH + X^- + H^+ \rightarrow >Pb(III)\text{-}X + H_2O \quad (4)$$

$$>Pb(III)\text{-}X \rightarrow >Pb(II)\text{-}X^{\bullet} \quad (5)$$

$$>Pb(II)\text{-}X^{\bullet} + X^- + H_2O \rightarrow >Pb(II)\text{-}OH + X_2^{\bullet -} + H^+ \quad (6)$$

$$>Pb(II)\text{-}OH \rightarrow Pb(II)_{aq} \quad (7)$$

A comparison of halide-induced dissolution of lead oxide revealed that the dissolution was the lowest with chloride, intermediate with bromide and the highest with iodide (Fig. 1b). This trend was further confirmed by measuring the concentration of reacted (consumed) halide ions in aqueous and frozen samples during the dissolution

KOPRI 극지연구소

process (Fig. 2). It should be noted that we used five times higher concentration of halide ions (500 μM) for this experiment to achieve better determination of halide concentrations. The results show that the concentrations of bromide and iodide in both aqueous and frozen samples were significantly reduced within 6 h, whereas the chloride concentration was little reduced even after 24 h. This clearly proves that bromide and iodide ions were more highly reactive and involved in the enhanced dissolution of lead oxide particles, while chloride ions seem to be inert for the reductive dissolution. It is also noted that the consumed iodide concentrations in the frozen samples were lower than those in aqueous samples whereas the consumed bromide concentrations in the frozen samples were higher than those in aqueous condition. This result is consistent with the fact that the presence of iodide and bromide suppresses and enhances the lead dissolution in frozen solution, respectively (Fig. 1).

The halide-induced dissolution of lead oxide in both aqueous and frozen solutions increases in the order of $Cl^- < Br^- < I^-$, which is consistent with the electrochemical reduction potential of the halide ions (i.e., $E^0(I^\bullet / I^-) = 1.37\ V_{NHE}$; $E^0(Br^\bullet / Br^-) = 2.04\ V_{NHE}$; $E^0(Cl^\bullet / Cl^-) = 2.59\ V_{NHE}$) [55]. On the basis of the standard potential values, we can postulate that iodide ions with the lowest reduction potential among the halide ions can be most easily oxidized along with the concurrent reductive dissolution of lead oxide ($E^0(PbO_2/Pb^{2+}) = 1.46$ V) [56]. On the other hand, chloride with the highest reduction potential value can be hardly oxidized and cannot be efficiently coupled with the reductive dissolution of lead oxide. However, the observation that the dissolution of lead oxide in frozen condition was retarded by iodide needs more plausible explanation. Moreover, the estimated first order rate constant in a frozen plattnerite solution with iodide ($k = 4.8 \times 10^{-4}\ h^{-1}$) was also lower than its aqueous counterpart ($k = 5.5 \times 10^{-4}\ h^{-1}$). On the other hand, the first order rate constants determined for other frozen systems (i.e., plattnerite with ($k = 4.3 \times 10^{-4}\ h^{-1}$) and without bromide ($k = 2.9 \times 10^{-4}\ h^{-1}$)) were higher than those of aqueous solutions ($3.9 \times 10^{-4}\ h^{-1}$ and $2.6 \times 10^{-4}\ h^{-1}$ with and without bromide, respectively).

3.2. Halide specific dissolution of lead oxide.

Additional experiments in aqueous and frozen solutions were conducted to evaluate the effect of halide ion concentration on the dissolution of lead oxide in an environmentally relevant concentration range. Chloride is the most abundant anionic species in the aquatic environment [51, 52, 57]. The average concentration of chloride in river water varies between 10 and 40 mg/L (170 - 680 μM), whereas more than 20,000 mg/L (2%) of chloride exists in seawater [52]. Therefore, an evaluation of the chloride concentration effect on the lead oxide dissolution is important. Fig. 3(A) shows the dissolution of lead oxide in aqueous and frozen solutions at different chloride concentrations (100-1000 μM) in

the environmentally relevant range.

The results as shown in Fig. 3(A) clearly revealed that the increase of chloride concentration did not influence the lead oxide dissolution in both aqueous and frozen solution, although a slight suppression was observed in the frozen sample at the highest concentration (1 mM). This result confirms that chloride ions are inert toward the dissolution of lead oxide even in the frozen medium.

Bromide is also widely distributed in aquatic environment up to 1 mg/L (~ 8 μM) for fresh water and 80 mg/L (~ 670 μM) for seawater, respectively [52]. A previous study by Lin et al. suggested that the reduction of ß-PbO2 in aqueous solution is significantly influenced by bromide ions [45]. The dissolution of lead oxide induced by a series of environmentally relevant concentrations of bromide ions was, thus, investigated and compared in Fig. 3(B). Unlike chloride, the lead dissolution gradually increased with the increase of bromide concentration (10-100 μM) in both aqueous and frozen conditions, which is in good agreement to the previous study of Lin et. al [45]. Moreover, the concentration of dissolved lead by bromide in the frozen solution was slightly but consistently higher than that in aqueous solution. Concentration-dependent dissolution of lead in the presence of iodide was also conducted to further investigate the reduced dissolution of lead oxide in the freezing condition. Fig. 3(C) shows that the lead oxide dissolution increased with increasing the concentration of iodide, analogous to the case of bromide, but the relative effect of iodide on this dissolution process (frozen vs. aqueous) was the opposite to that of bromide. That is, the iodide ions in all tested concentration range consistently suppress the dissolution of lead oxide in the frozen solution.

Some hypothetical reaction mechanism could be considered to explain the unusual dissolution behavior of PbO_2/I^- in frozen solutions. The most plausible explanation for this observation seems to be that a significant amount of iodide ions are trapped into the bulk ice upon freezing, which should prevent the direct contact of iodide ions with the surface of lead oxide particles that are most likely located in the ice grain boundary region. The hindered reaction of iodide ions with lead oxide would explain the retarded dissolution of lead oxide in the frozen solution. The lower consumption of iodide ions in the frozen samples (Fig. 2C) clearly indicates that the utilization of the iodide ions in the dissolution process is lower in the frozen condition than that in the aqueous solution. A similar effect reducing the availability of ligands in the ice grain boundary region has been also observed in the reductive iron oxide dissolution by ascorbic acid, which was discussed in our previous study [37]. We also evaluated the possible precipitation of an insoluble product (PbI_2: K_{sp} = 4.41× 10^{-9} M^3) [58] during the iodide-induced reductive dissolution of lead oxide. If the reaction of Pb^{2+} and I^- is accelerated in the freezing condition, a portion of dissolved Pb^{2+} ions can be precipitated and filtered out as PbI_2. On the other hand, the

Pb(II) species dissolved out of the PbO_2/Cl^- and PbO_2/Br^- systems might exist as more soluble $PbCl_2$ (K_{SP} = 1.86 × 10^{-5} M^3) and $PbBr_2$ (K_{SP} = 5.89 × 10^{-5} M^3), respectively [58]. To verify the hypothesis of the potential precipitation of dissolved Pb(II), the residual ß-PbO_2 samples obtained after the dissolution experiments using halide ions were recovered and analyzed by X-ray diffraction (XRD). The diffractograms of each sample (Fig. S1, Supplementary Data) were almost identical to each other without showing any evidence for the formation of potential precipitate such as PbI_2. Although the XRD analysis is not sensitive enough to detect the small amount or low crystalline phase, almost exactly identical XRD patterns before and after the reaction even for the PbO_2 sample reacted with iodide, which dissolved out about 4% of lead after 12 h reaction, indicate that the contribution of PbI_2 precipitation to the freezing-suppressed dissolution of lead oxide by iodide is insignificant.

The exclusion of inorganic ions from the ice surface region has been widely known and explained on the basis of Workman-Reynolds Freezing Potential (FP), an electrical charge separation occurred during the freezing of slightly ionized water [59-61]. The measured FP, a non-equilibrium phenomenon, has been reported to be dependent on the nature and concentration of the solutes, freezing rate, and crystalline orientation of the ice [59]. Many earlier studies have shown the capacity of bulk ice to trap the inorganic ions such as halides [59, 60] and organic molecules (e.g., ascorbic acid) [37] and thereby restrict their availability to the chemical processes taking place in the liquid-like ice grain boundary region. Although iodide ions have been known to be concentrated on the ice surface (or grain boundary) upon freezing, and thereby to enhance the dissolution of metal oxide (e.g., goethite) in frozen solutions [37], a contradictory dissolution phenomenon was observed in the ß-PbO_2/I^- case. That is, the trapping of a significant part of iodide ions into the bulk ice during the freezing process could occur in the presence of lead oxide and thereby restrict the reaction of iodide ions with ß-PbO_2 concentrated in the ice grain boundary. To test if this assumption is valid, a simple experimental attempt was made to roughly measure the concentrations of halide ions trapped in the bulk ice. The frozen samples containing ß-PbO_2 and each halide ions were grounded into fine particles using a laboratory mortar and pestle. The ice particles were then washed quickly with cold deionized water at ~0 °C to melt ice particles slightly. The rapid washing process should remove the surface grain boundary region of ice particles more preferentially with leaving the majority of bulk ice intact. The remaining ice crystals recollected after the rapid washing process was completely melted and the resulting melt solution should have the components included not in the ice surface region but in the bulk ice. Therefore, the amount of halide ions recovered through the above process can be considered as a rough measure of the halide ions trapped in the bulk ice region. A graphical illustration and

details of the experimental procedure are described in our earlier report [37]. According to the results shown in Table 1, the amount of chloride, bromide, and iodide ions trapped in the bulk ice is roughly 70, 13, and 35%, respectively.

Since chloride ions are inert toward the dissolution of lead oxide, their relative distribution between the ice bulk and grain boundary region should not be important. However, as for bromide and iodide that are reactive for the reductive dissolution of lead oxide, their relative distribution between the ice bulk and surface region may influence the dissolution process significantly. Note that a significant amount of iodide ions (~35%) are trapped in the bulk ice, which should make iodide less available to the reductive dissolution of lead oxide. This might be responsible for the retarded dissolution of lead oxide in frozen solution containing iodide. This is also in good agreement with the lower consumption of iodide ions in the frozen solution (see Fig 2C). In addition, note that the plot of lead dissolution vs. iodide concentration in frozen solution shows a significant deviation from the linear relation (Fig. 3D). It should be ascribed to the trapping of iodide ions into the bulk ice and thereby limiting their freeze-concentration effect in the grain boundary region. Such deviation was, however, not observed in the frozen solution of bromide ions that are less trapped in the bulk ice.

Fig. 4 shows the dissolution of lead as a function of temperature, which exhibits the different temperature dependence between the bromide and iodide cases. In the aqueous phase (above 0 °C), the decreasing temperature gradually reduces the extent of lead dissolution for both bromide and iodide cases, which is consistent with the common temperature-dependent kinetic behavior of solid dissolution reactions. However, the temperature-dependent dissolution behavior is clearly different below 0 °C. Although a clear sign of enhanced dissolution was observed for the PbO_2/Br^- system when the temperature is lowered from 0 °C to -10 °C, such enhancement was not observed at all for the PbO_2/I^- system in the same temperature range. This indicates that the freezing below 0 °C has different effects for the bromide and iodide cases, which can be related with the different distribution of the halide ions (bromide vs iodide) between the ice bulk and ice grain boundary (see Table 1). Iodide ions seem to be less freeze-concentrated in the ice grain boundary than bromide ions and thus the freezing-enhanced dissolution by iodide seems to be absent. It is interesting to note that the temperature-dependent dissolution of iron oxide in our previous study showed a different dissolution trend for iodide, where the concentration of dissolved iron significantly increased below 0 °C due to the freeze concentration of iodide ions in the ice grain boundary [37]. The temperature-dependent dissolution of lead oxide by iodide observed in this study, however, exhibits an opposite trend as mentioned above. We do not understand why the (lead oxide/iodide) and the (iron oxide/iodide) exhibit the different temperature-dependent behavior but it seems to be

related with the different nature of the halide-metal oxide surface interactions.

3.3. Synergistic effect of halides on the dissolution of lead oxide

Various halide ions coexist in natural environments. The reported concentrations of chloride ions in the real water streams are several times higher than those of bromide and iodide [52]. By considering this fact as well as the inert nature of chloride ions towards the lead dissolution (Fig. 2), the effects of bromide and iodide on the lead dissolution in the presence of an environmentally relevant concentration of chloride were investigated. While the chloride alone has a negligible effect on the lead dissolution, the coexistence of bromide (10 μM) and chloride (500 μM) enhanced the lead dissolution in frozen solution by ~1.8 times compared with the dissolution in aqueous solution (Fig. 5). A similar enhancement of the lead dissolution in frozen solution (~1.2 times higher than the aqueous dissolution) was also observed in the coexistence of iodide (10 μM) and chloride (500 μM), whereas the iodide alone in frozen solution suppressed the lead dissolution compared with the aqueous dissolution on the contrary. The results imply that the coexistence of bromide (or iodide) and chloride induce some synergic mechanism on the halide-enhanced dissolution of lead in the frozen condition.

The enhanced dissolution by mixed halides could be caused by the assistance of chloride ions towards reactions 3 and 6 (see section 3.1) by initiating additional reaction pathways. For example, the >Pb(II)-$Br^{\bullet}$ species can easily react with the excess amount of chloride ions available in the frozen solution (reaction 8).

$$>\text{Pb(II)-Br}^{\bullet} + \text{Cl}^{-} + \text{H}_2\text{O} \rightarrow >\text{Pb(II)-OH} + \text{ClBr}^{\bullet -} + \text{H}^{+} \quad (8)$$

$$\text{Br}_2^{\bullet -} + \text{Cl}^{-} \rightarrow \text{ClBr}^{\bullet -} + \text{Br}^{-} \quad (k = 4.3 \times 10^{10}\ \text{M}^{-1}\text{s}^{-1}) \quad (9)$$

$$\text{Br}^{\bullet} + \text{Cl}^{-} \rightarrow \text{ClBr}^{\bullet -} \quad (k = 1 \times 10^{10}\ \text{M}^{-1}\text{s}^{-1}) \quad (10)$$

Considering that the formation reaction of the mixed halide radicals are diffusion-limited (reactions 9, 10) [48], reaction 8 should be highly favored in the presence of excess chloride concentration. Although chloride ions cannot induce the direct dissolution of lead oxide (Fig. 3A), they can facilitate reaction 8, which subsequently leads to the dissolution of Pb^{2+} ions. Since halide ions should be highly concentrated in the ice grain boundary region through the freeze concentration effect, the reductive dissolution of ß-PbO_2 can be highly accelerated in the frozen state. The formation of $ClBr^{\bullet -}$ has been observed in the pulse radiolysis/laser flash photolysis experiments, which is characterized by an absorption band at 350 nm (ε_{350} = 9300 dm^3mol^{-1} cm^{-1}) [62, 63]. An analogous reaction mechanism leading to the synergically enhanced dissolution of lead oxide could be also possible by mixed halides of Cl^- and I^-. However, the chloro-iodo mixed halide radical anion ($ICl^{\bullet -}$) has not been well studied to date.

The effects of the mixed halide on the lead oxide dissolution were further

investigated by varying the ratio of $[Cl^-]/[Br^-]$ and $[Cl^-]/[I^-]$. Fig. 6. shows the variation of the relative dissolution of lead ($([Pb]_{ice}/[Pb]_{water})$) as a function of the mixed halide ratio. The relative dissolution higher than 1 in Fig. 6 indicates the enhanced dissolution of lead oxide in the frozen samples. The relative dissolution of $[Pb]_{ice}/[Pb]_{water}$ was initially increased with increasing the Cl/Br ratio, maximized at $[[Cl^-]/[Br^-] = 50$, then reduced at higher ratios. On the other hand, the relative dissolution of lead in the mixed chloride-iodide system exhibited much weaker dependence on the chloride/iodide ratio. Since iodide is much more efficient than bromide in inducing the reductive dissolution of lead oxide, the synergic action of chloride in the Cl-I mixture seems to be less important than that in the Cl-Br mixture.

4. Conclusions

In this work, we investigated the dark dissolution of lead oxide, an insoluble corrosion product on lead products (e.g., lead pipeline), into soluble Pb(II) species in the presence of different halide ions in aqueous and frozen conditions. The reductive dissolution process of lead oxide showed distinguishable dissolution behavior depending on solution temperature (aqueous and frozen solutions), halide type and concentrations. The relative distribution of halide ions between the ice bulk and the ice grain boundary during the freezing process should have a sensitive influence on the dissolution of lead in the frozen solution, whereas the reducing power of the halide ions and pH are also important factors controlling the dissolution process. The experimental demonstration of the freezing-enhanced dissolution of PbO_2 by a synergistic effect of mixed halides (chloride/bromide) could be helpful in understanding the dissolution process of toxic lead species in frozen environments since the presence of mixed halide ions is common and ubiquitous. The extent of lead dissolution in the real frozen environment can be greatly enhanced in the unique reaction condition offered by ice-grain boundaries. An increased dissolution of this toxic heavy metal can thus occur in cold environments, which might cause serious lead contamination and potential lead poisoning and related health issues. The enhancement of lead oxide dissolution can be favorable in diverse natural environmental media such as cloud droplets and marine mineral aerosols where lead particles might exist in highly acidic conditions. Frozen soils should present a similar reaction environment in which the enhanced dissolution of the toxic heavy metal may occur. The present study could be informative in understanding and preventing the harmful lead contamination that might be accelerated in the frozen environment.

KOPRI 극지연구소

5. References

[1] D.M. Roundhill, Novel Strategies for the Removal of Toxic Metals from Soils and Waters, J. Chem. Educ., 81 (2004) 275.

[2] J. Markus, A.B. McBratney, A review of the contamination of soil with lead: II. Spatial distribution and risk assessment of soil lead, Environ. Int., 27 (2001) 399-411.

[3] M.M.B. Paoliello, E.M. De Capitani, Environmental Contamination and Human Exposure to Lead in Brazil, Rev. Environ. Contam. Toxicol., 184 (2005) 59-96..

[4] Z. Zhang, G. Guo, Y. Teng, J. Wang, J.S. Rhee, S. Wang, F. Li, Screening and assessment of solidification/stabilization amendments suitable for soils of lead-acid battery contaminated site, J. Hazard. Mater., 288 (2015) 140-146.

[5] E.A. López-Maldonado, O.G. Zavala García, K.C. Escobedo, M.T. Oropeza-Guzman, Evaluation of the chelating performance of biopolyelectrolyte green complexes (NIBPEGCs) for wastewater treatment from the metal finishing industry, J. Hazard. Mater., 335 (2017) 18-27.

[6] X.L. Zhong, S.L. Zhou, Q. Zhu, Q.G. Zhao, Fraction distribution and bioavailability of soil heavy metals in the Yangtze River Delta-A case study of Kunshan City in Jiangsu Province, China, J. Hazard. Mater., 198 (2011) 13-21.

[7] C.W. Lam, S.-R. Lim, J.M. Schoenung, Environmental and risk screening for prioritizing pollution prevention opportunities in the U.S. printed wiring board manufacturing industry, J. Hazard. Mater., 189 (2011) 315-322.

[8] N.S. Duzgoren-Aydin, Sources and characteristics of lead pollution in the urban environment of Guangzhou, Sci. Total Environ., 385 (2007) 182-195.

[9] J. Gasana, A. Chamorro, Environmental lead contamination in Miami inner-city area, J Expo Anal Environ Epidemiol., 12 (2002) 265-272.

[10] R. Malviya, R. Chaudhary, Factors affecting hazardous waste solidification/stabilization: A review, J. Hazard. Mater., 137 (2006) 267-276.

[11] A. Coz, A. Andrés, S. Soriano, Á. Irabien, Environmental behaviour of stabilised foundry sludge, J. Hazard. Mater., 109 (2004) 95-104.

[12] S.L. Lin, W.H. Cross, E.S.K. Chian, J.S. Lai, M. Giabbai, C.H. Hung, Stabilization and solidification of lead in contaminated soils, J. Hazard. Mater., 48 (1996) 95-110.

[13] Z. Shi, L.E. Erickson, Mathematical model development and simulation of in situ stabilization in lead-contaminated soils, J. Hazard. Mater., 87 (2001) 99-116.

[14] K. Nemsadze, T. Sanikidze, L. Ratiani, L. Gabunia, T. Sharashenidze, Mechanisms of lead-induced poisoning, Georgian Medical News, (2009) 92-96.

KOPRI 극지연구소

[15] G. Flora, D. Gupta, A. Tiwari, Toxicity of lead: A review with recent updates, Interdiscip Toxicol., 5 (2012) 47-58.

[16] J. Gasana, W.M. Hlaing, K.A. Siegel, A. Chamorro, T. Niyonsenga, Blood lead levels in children and environmental lead contamination in Miami Inner City, Florida, Int. J. Environ. Res. Public Health, 3 (2006) 228-234.

[17] G.J. Cohen, W.E. Ahrens, Chronic lead poisoning, The Journal of Pediatrics, 54 271-284.

[18] K. Soltaninejad, S. Shadnia, Lead Poisoning in Opium Abuser in Iran: A Systematic Review, Int J Prev Med, 9 (2018) 3.

[19] T.K. Naiya, A.K. Bhattacharya, S. Mandal, S.K. Das, The sorption of lead(II) ions on rice husk ash, J. Hazard. Mater., 163 (2009) 1254-1264.

[20] D. Heger, J. Klánová, P. Klán, Enhanced Protonation of Cresol Red in Acidic Aqueous Solutions Caused by Freezing, J. Phys. Chem. B, 110 (2006) 1277-1287.

[21] D. Jeong, K. Kim, W. Choi, Accelerated dissolution of iron oxides in ice, Atmos. Chem. Phys., 12 (2012) 11125-11133.

[22] K. Kim, W. Choi, M.R. Hoffmann, H.-I. Yoon, B.-K. Park, Photoreductive Dissolution of Iron Oxides Trapped in Ice and Its Environmental Implications, Environ. Sci. Technol., 44 (2010) 4142-4148.

[23] K. Kim, H.-I. Yoon, W. Choi, Enhanced Dissolution of Manganese Oxide in Ice Compared to Aqueous Phase under Illuminated and Dark Conditions, Environ. Sci. Technol., 46 (2012) 13160-13166.

[24] J. Klánová, P. Klán, J. Nosek, I. Holoubek, Environmental Ice Photochemistry: Monochlorophenols, Environ. Sci. Technol., 37 (2003) 1568-1574.

[25] N. Takenaka, A. Ueda, T. Daimon, H. Bandow, T. Dohmaru, Y. Maeda, Acceleration Mechanism of Chemical Reaction by Freezing: The Reaction of Nitrous Acid with Dissolved Oxygen, J. Phys. Chem., 100 (1996) 13874-13884.

[26] N. Takenaka, A. Ueda, Y. Maeda, Acceleration of the rate of nitrite oxidation by freezing in aqueous solution, Nature, 358 (1992) 736-738.

[27] J.P. Bower, C. Anastasio, Degradation of organic pollutants in/on snow and ice by singlet molecular oxygen (1O*2) and an organic triplet excited state, Environ. Sci. Processes Impacts, 16 (2014) 748-756.

[28] M.I. Guzmán, A.J. Colussi, M.R. Hoffmann, Photogeneration of Distant Radical Pairs in Aqueous Pyruvic Acid Glasses, J. Phys. Chem. A, 110 (2006) 931-935.

[29] M.I. Guzmán, L. Hildebrandt, A.J. Colussi, M.R. Hoffmann, Cooperative Hydration of Pyruvic Acid in Ice, J. Am. Chem. Soc., 128 (2006) 10621-10624.

KOPRI 극지연구소

[30] M.I. Guzmán, M.R. Hoffmann, A.J. Colussi, Photolysis of pyruvic acid in ice: Possible relevance to CO and CO2 ice core record anomalies, J. Geophys. Res. Atmos., 112 (2007) D10123.

[31] T. Hullar, C. Anastasio, Direct visualization of solute locations in laboratory ice samples, The Cryosphere, 10 (2016) 2057-2068.

[32] A.S. McFall, C. Anastasio, Photon flux dependence on solute environment in water ices, Environ. Chem., 13 (2016) 682-687.

[33] L. Bláha, J. Klánová, P. Klán, J. Janošek, M. Škarek, R. Růžička, Toxicity Increases in Ice Containing Monochlorophenols upon Photolysis: Environmental Consequences, Environ. Sci. Technol., 38 (2004) 2873-2878.

[34] G. Marcotte, P. Marchand, S. Pronovost, P. Ayotte, C. Laffon, P. Parent, Surface-Enhanced Nitrate Photolysis on Ice, J. Phys. Chem. A, 119 (2015) 1996-2005.

[35] D.W. Min, W. Choi, Accelerated Reduction of Bromate in Frozen Solution, Environ. Sci. Technol., 51 (2017) 8368-8375.

[36] K. Kim, A. Yabushita, M. Okumura, A. Saiz-Lopez, C.A. Cuevas, C.S. Blaszczak-Boxe, D.W. Min, H.-I. Yoon, W. Choi, Production of Molecular Iodine and Tri-iodide in the Frozen Solution of Iodide: Implication for Polar Atmosphere, Environ. Sci. Technol., 50 (2016) 1280-1287.

[37] S.P.M. Menacherry, K. Kim, W. Lee, C.H. Choi, W. Choi, Ligand-specific Dissolution of Iron Oxides in Frozen Solutions, Environ. Sci. Technol., 52 (2018) 13766-13773.

[38] D.J. Cziczo, O. Stetzer, A. Worringen, M. Ebert, S. Weinbruch, M. Kamphus, S.J. Gallavardin, J. Curtius, S. Borrmann, K.D. Froyd, S. Mertes, O. Möhler, U. Lohmann, Inadvertent climate modification due to anthropogenic lead, Nat. Geosci., 2 (2009) 333-336.

[39] D.M. Murphy, P.K. Hudson, D.J. Cziczo, S. Gallavardin, K.D. Froyd, M.V. Johnston, A.M. Middlebrook, M.S. Reinard, D.S. Thomson, T. Thornberry, A.S. Wexler, Distribution of lead in single atmospheric particles, Atmos. Chem. Phys., 7 (2007) 3195-3210.

[40] C.F. Boutron, J.-P. Candelone, S. Hong, Past and recent changes in the large-scale tropospheric cycles of lead and other heavy metals as documented in Antarctic and Greenland snow and ice: A review, Geochimica et Cosmochimica Acta, 58 (1994) 3217-3225.

[41] J.R. McConnell, O.J. Maselli, M. Sigl, P. Vallelonga, T. Neumann, H. Anschütz, R.C. Bales, M.A.J. Curran, S.B. Das, R. Edwards, S. Kipfstuhl, L. Layman, E.R.

KOPRI 극지연구소

Thomas, Antarctic-wide array of high-resolution ice core records reveals pervasive lead pollution began in 1889 and persists today, Scientific Reports, 4 (2014) 5848.

[42] M. Ghaedi, M. Montazerozohori, M. Soylak, Solid phase extraction method for selective determination of Pb(II) in water samples using 4-(4-methoxybenzylidenimine) thiophenole, J. Hazard. Mater., 142 (2007) 368-373.

[43] Y. Wang, J. Wu, Z. Wang, A. Terenyi, D.E. Giammar, Kinetics of lead(IV) oxide (PbO2) reductive dissolution: Role of lead(II) adsorption and surface speciation, J. Colloid Interface Sci., 389 (2013) 236-243.

[44] Y.-P. Lin, R.L. Valentine, The Release of Lead from the Reduction of Lead Oxide (PbO2) by Natural Organic Matter, Environ. Sci. Technol., 42 (2008) 760-765.

[45] Y.-P. Lin, R.L. Valentine, Reductive Dissolution of Lead Dioxide (PbO2) in Acidic Bromide Solution, Environ. Sci. Technol., 44 (2010) 3895-3900.

[46] Y.-P. Lin, M.P. Washburn, R.L. Valentine, Reduction of Lead Oxide (PbO2) by Iodide and Formation of Iodoform in the PbO2/I−/NOM System, Environ. Sci. Technol., 42 (2008) 2919-2924.

[47] Z. Shi, A.T. Stone, PbO2(s, Plattnerite) Reductive Dissolution by Aqueous Manganous and Ferrous Ions, Environ. Sci. Technol., 43 (2009) 3596-3603.

[48] Y. Wang, J. Wu, D.E. Giammar, Kinetics of the Reductive Dissolution of Lead(IV) Oxide by Iodide, Environ. Sci. Technol., 46 (2012) 5859-5866.

[49] G. Zhuang, Z. Yi, R.A. Duce, P.R. Brown, Link between iron and sulphur cycles suggested by detection of Fe(n) in remote marine aerosols, Nature, 355 (1992) 537-539.

[50] Y. Yang, J. Pignatello, Participation of the Halogens in Photochemical Reactions in Natural and Treated Waters, Molecules, 22 (2017) 1684.

[51] M.P. Brooker, P.C. Johnson, The behaviour of phosphate, nitrate, chloride and hardness in twelve welsh rivers, Water Res., 18 (1984) 1155-1164.

[52] Guidelines for Drinking-Water Quality, Second ed., World Health Organization, Geneva, 1996.

[53] D. Jeong, K. Kim, D.W. Min, W. Choi, Freezing-Enhanced Dissolution of Iron Oxides: Effects of Inorganic Acid Anions, Environ. Sci. Technol., 49 (2015) 12816-12822.

[54] K. Kim, W. Choi, Enhanced Redox Conversion of Chromate and Arsenite in Ice, Environ. Sci. Technol., 45 (2011) 2202-2208.

[55] A.A. Isse, C.Y. Lin, M.L. Coote, A. Gennaro, Estimation of Standard Reduction Potentials of Halogen Atoms and Alkyl Halides, J. Phys. Chem. B, 115 (2011) 678-684.

KOPRI 극지연구소

[56] A. Oury, A. Kirchev, Y. Bultel, E. Chainet, PbO2/Pb2+ cycling in methanesulfonic acid and mechanisms associated for soluble lead-acid flow battery applications, Electrochim. Acta, 71 (2012) 140-149.

[57] T. Hiissa, H. Sirén, T. Kotiaho, M. Snellman, A. Hautojärvi, Quantification of anions and cations in environmental water samples: Measurements with capillary electrophoresis and indirect-UV detection, J. Chromatogr. A, 853 (1999) 403-411.

[58] H.L. Clever, F.J. Johnston, The solubility of some sparingly soluble lead salts: An evaluation of the solubility in water and aqueous electrolyte solution, J. Phys. Chem. Ref. Data, 9 (1980) 751-784.

[59] P.W. Wilson, A.D.J. Haymet, Workman－Reynolds Freezing Potential Measurements between Ice and Dilute Salt Solutions for Single Ice Crystal Faces, J. Phys. Chem. B, 112 (2008) 11750-11755.

[60] P.W. Wilson, A.D.J. Haymet, Effect of Ice Growth Rate on the Measured Workman－Reynolds Freezing Potential between Ice and Dilute NaCl Solutions, J. Phys. Chem. B, 114 (2010) 12585-12588.

[61] E.J. Workman, S.E. Reynolds, Electrical Phenomena Occurring during the Freezing of Dilute Aqueous Solutions and Their Possible Relationship to Thunderstorm Electricity, Phys. Rev., 78 (1950) 254-259.

[62] B.G. Ershov, Kinetics, mechanism and intermediates of some radiation-induced reactions in aqueous solutions, Russ. Chem. Rev., 73 (2004) 101-113.

[63] B.G. Ershov, M. Kelm, A.V. Gordeev, E. Janata, A pulse radiolysis study of the oxidation of Br- by Cl2[radical dot]- in aqueous solution: formation and properties of ClBr[radical dot], Phys. Chem. Chem. Phys., 4 (2002) 1872-1875.

KOPRI 극지연구소

Table 1. The proportion of halide ions (X-) trapped in the ice lattice (bulk) out of the total halide ions and the ratio of dissolved Pb(II) between the frozen and aqueous solutions (Each data point represents an average of at least two replicates)[a]

Halide	$[X^-]_{ice\ bulk}$ / $[X^-]_{total}$ (%)	$[Pb]_{frozen}$/ $[Pb]_{aq}$
Chloride	70.1	1.21
Bromide	13.0	1.14
Iodide	35.2	0.73

[a]Experimental conditions: [ß-PbO2] = 0.5 g/L; [halide ion] = 500 μM; pH = 3; Reaction time = 3 h. Note that a higher concentration of halide ions (500 μM) was employed in this experiment to make the analysis of halide concentrations easier.

KOPRI
극지연구소

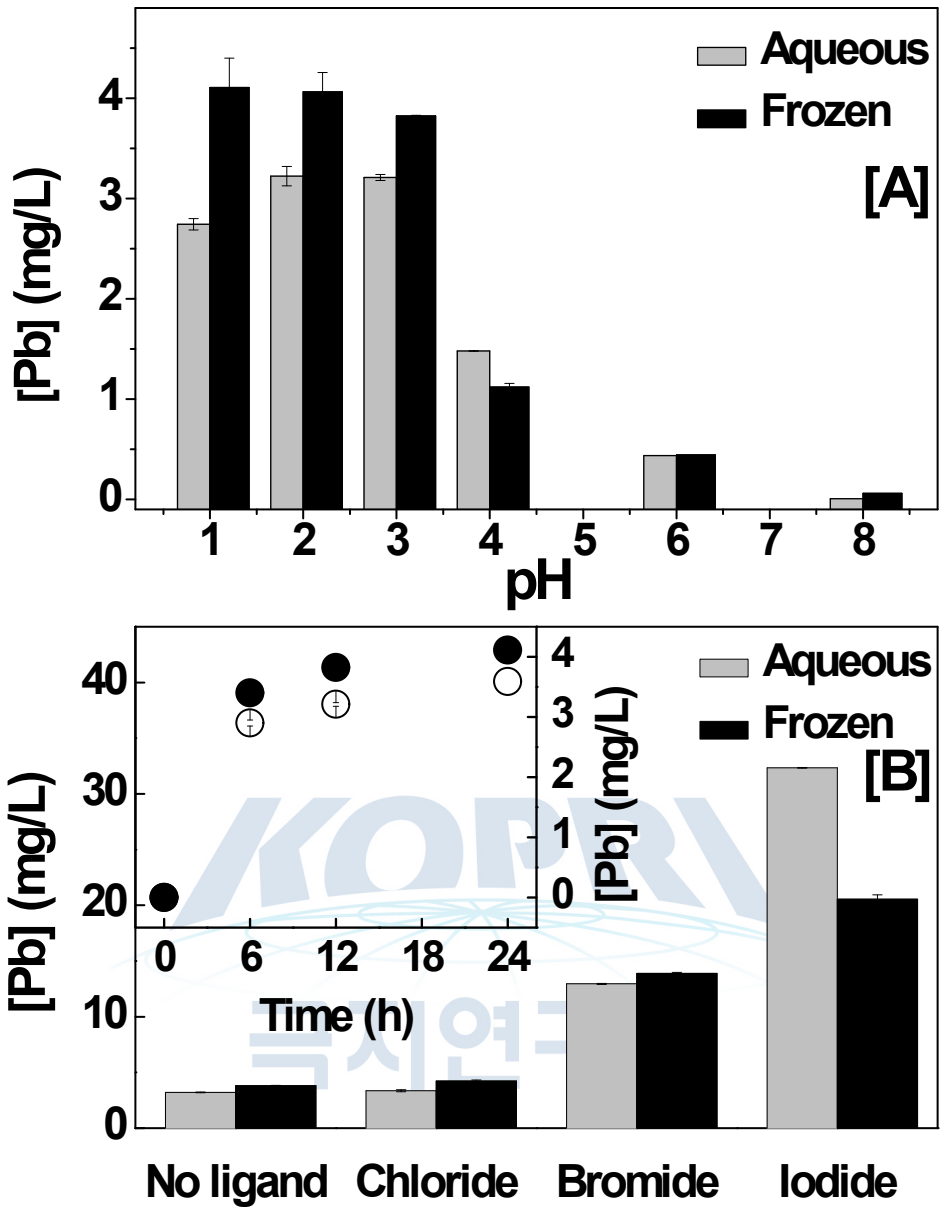

Figure 1. (A) pH-dependent dissolution of ß-PbO_2 in aqueous (grey) and frozen (black) solution without halide ions. Experimental conditions: $[ß\text{-}PbO_2]_0$ = 0.5 g/L; Reaction time = 12 h. (B) Dissolution of lead from ß-PbO_2 in aqueous (grey) and frozen (black) solutions in the presence of different halide ions. (Inset) Time-dependent dissolution of lead in aqueous (o) and frozen (·) solution without halides. Experimental conditions: $[ß\text{-}PbO2]_0$ = 0.5 g/L; [halide] = 100 μM; Reaction time = 12 h; pH = 3 (Each data point represents an average of at least two replicates).

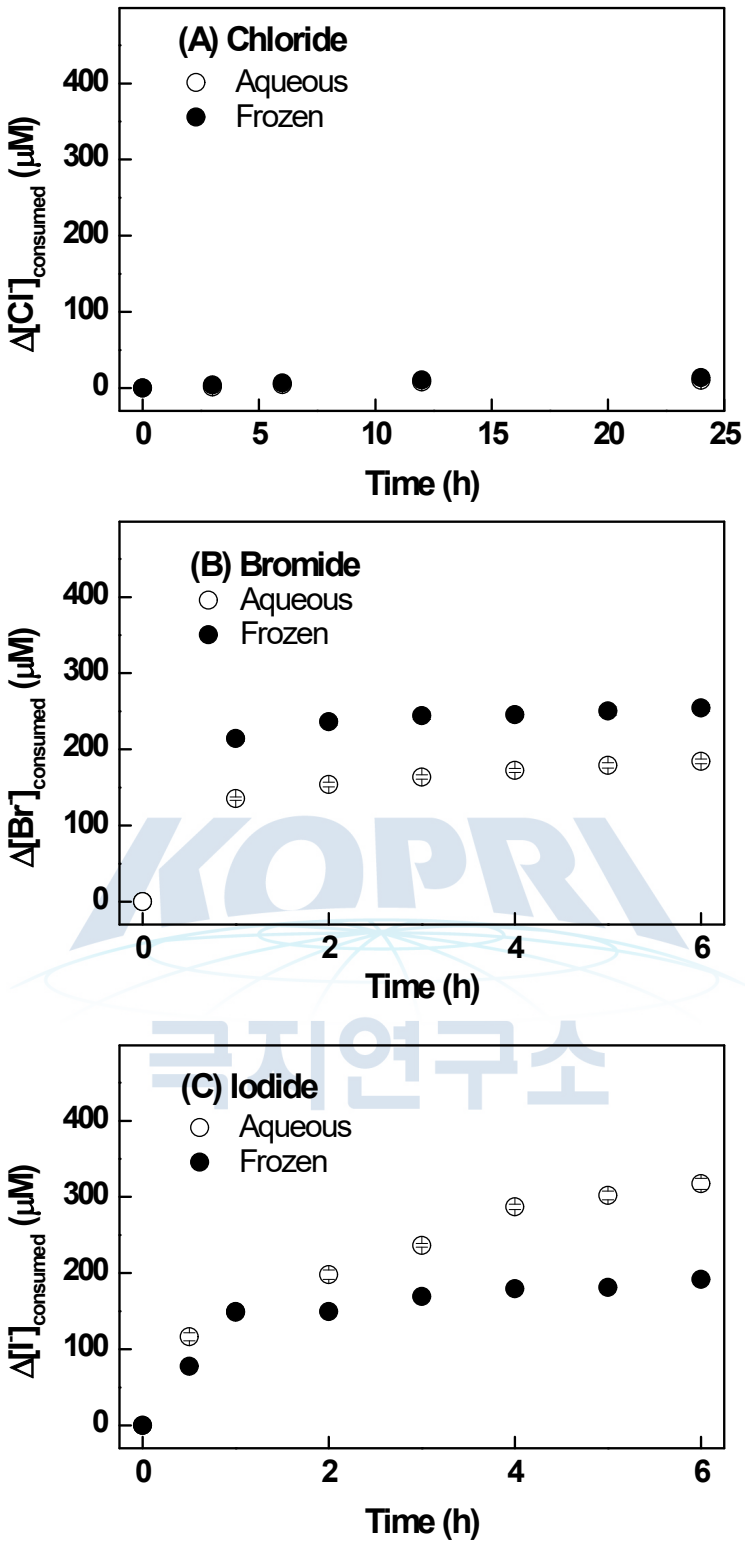

Figure 2. Time-dependent consumption of (A) chloride, (B) bromide, and (C) iodide during the dissolution of lead oxide in aqueous (open) and frozen (solid) solutions. The frozen and aqueous chloride concentration symbols exactly overlap in (A). Experimental conditions: $[ß\text{-}PbO_2]_0$ = 0.5 g/L; $[chloride]_0$ = $[bromide]_0$ = $[iodide]_0$ = 500 μM; pH = 3 (Each data point represents an average of at least two replicates ; Error bars are smaller than the symbol size).

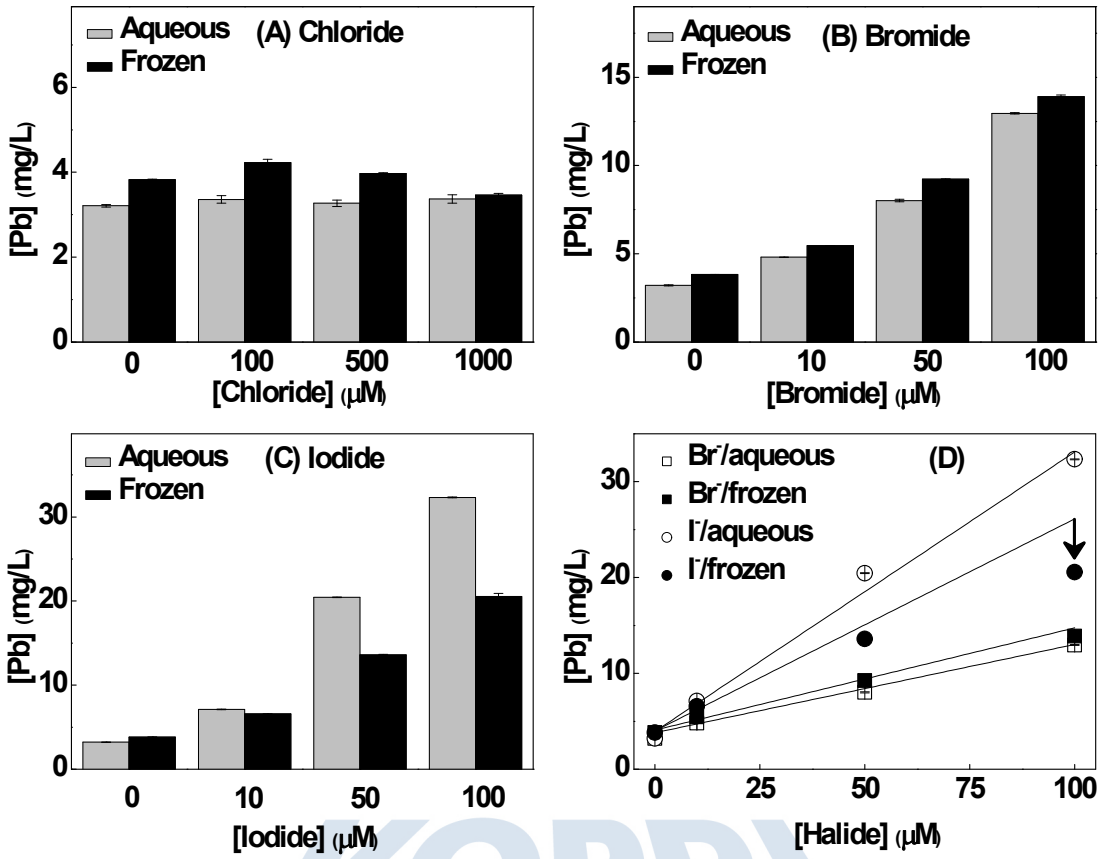

Figure 3. Halide concentration-dependent dissolution of lead ions from ß-PbO_2 in presence of chloride (A), bromide (B), and iodide (C) in aqueous (grey) and frozen (dark) solutions. (D) The lead dissolution as a function of bromide (square) and iodide (circle) concentration in aqueous (open) and frozen (solid) solutions. Experimental conditions: $[ß\text{-}PbO_2]_0$ = 0.5 g/L; pH = 3; Reaction time = 12 h (Each data point represents an average of at least two replicates).

KOPRI 극지연구소

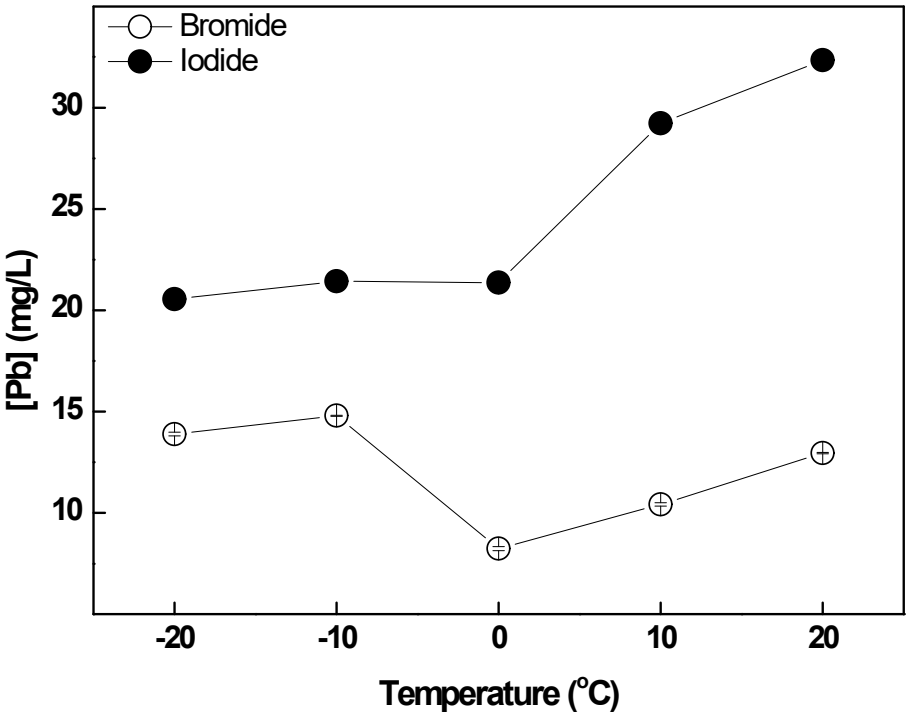

Figure 4. Temperature-dependent dissolution of lead from ß-PbO_2 in presence of bromide (open circle) and iodide (solid circle). Chloride data are not shown because chloride ions are inert for lead dissolution. Experimental conditions: $[ß\text{-}PbO_2]_0$ = 0.5 g/L; [Bromide or Iodide] = 100 μM; pH = 3; Reaction time = 12 h (Each data point represents an average of at least two replicates; Error bars are smaller than the symbol size).

KOPRI 극지연구소

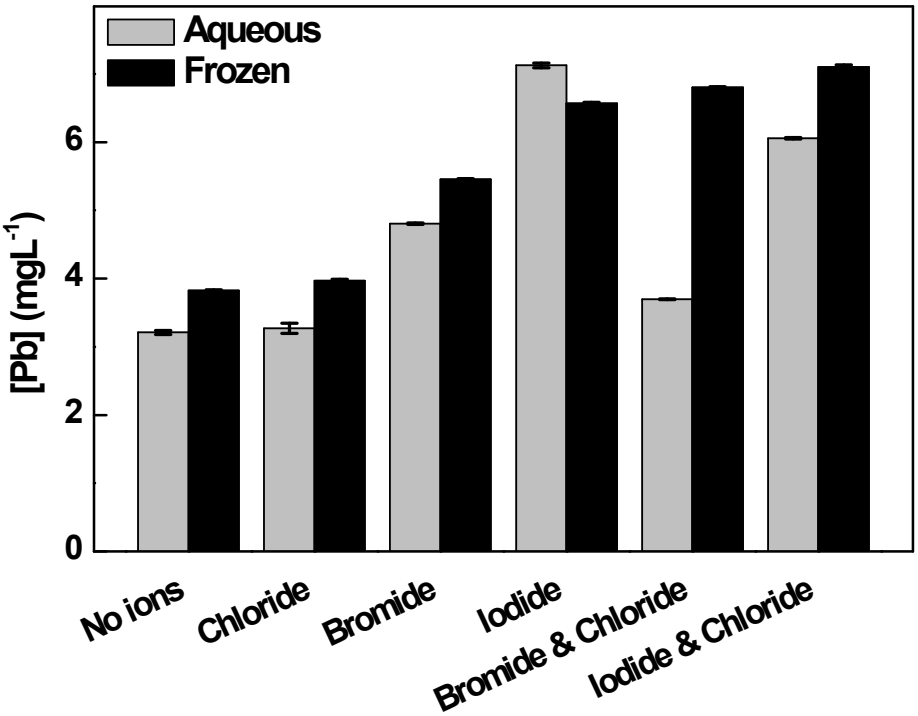

Figure 5. Synergic effect of chloride/bromide and chloride/iodide combinations on the dissolution of lead oxide in aqueous (grey) and frozen (dark) solutions. Experimental conditions: $[ß\text{-}PbO_2]_0$ = 0.5 g/L; $[Cl^-]$ = 500 µM; $[Br^-]$ = $[I^-]$ = 10 µM; pH = 3; Reaction time = 12 h (Each data point represents an average of at least two replicates).

KOPRI 극지연구소

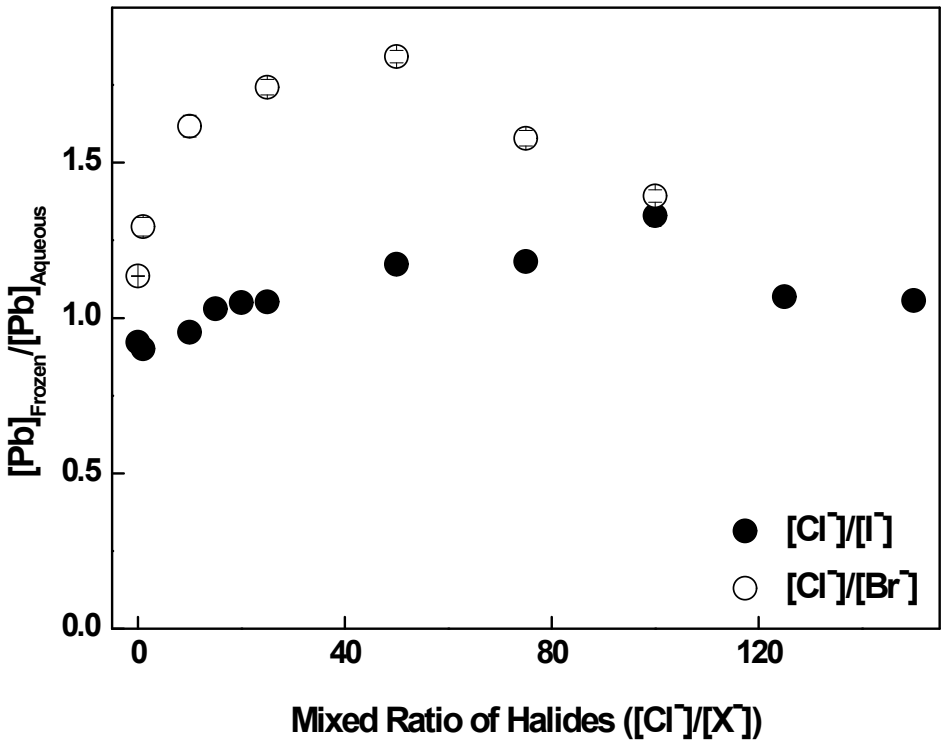

Figure 6. Dissolved lead concentration ratio ($[Pb]_{ice}/[Pb]_{water}$) as a function of the halide ratio ($[Cl^-]/[Br^-]$ (open circle) and $[Cl^-]/[I^-]$ (solid circle)). Experimental conditions: $[ß\text{-}PbO_2]_0$ = 0.5 g/L; $[Br^-] = [I^-]$ = 10 μM; pH = 3; Reaction time = 12 h (Each data point represents an average of at least two replicates; Error bars are smaller than the symbol size).

KOPRI 극지연구소

Supplementary Data

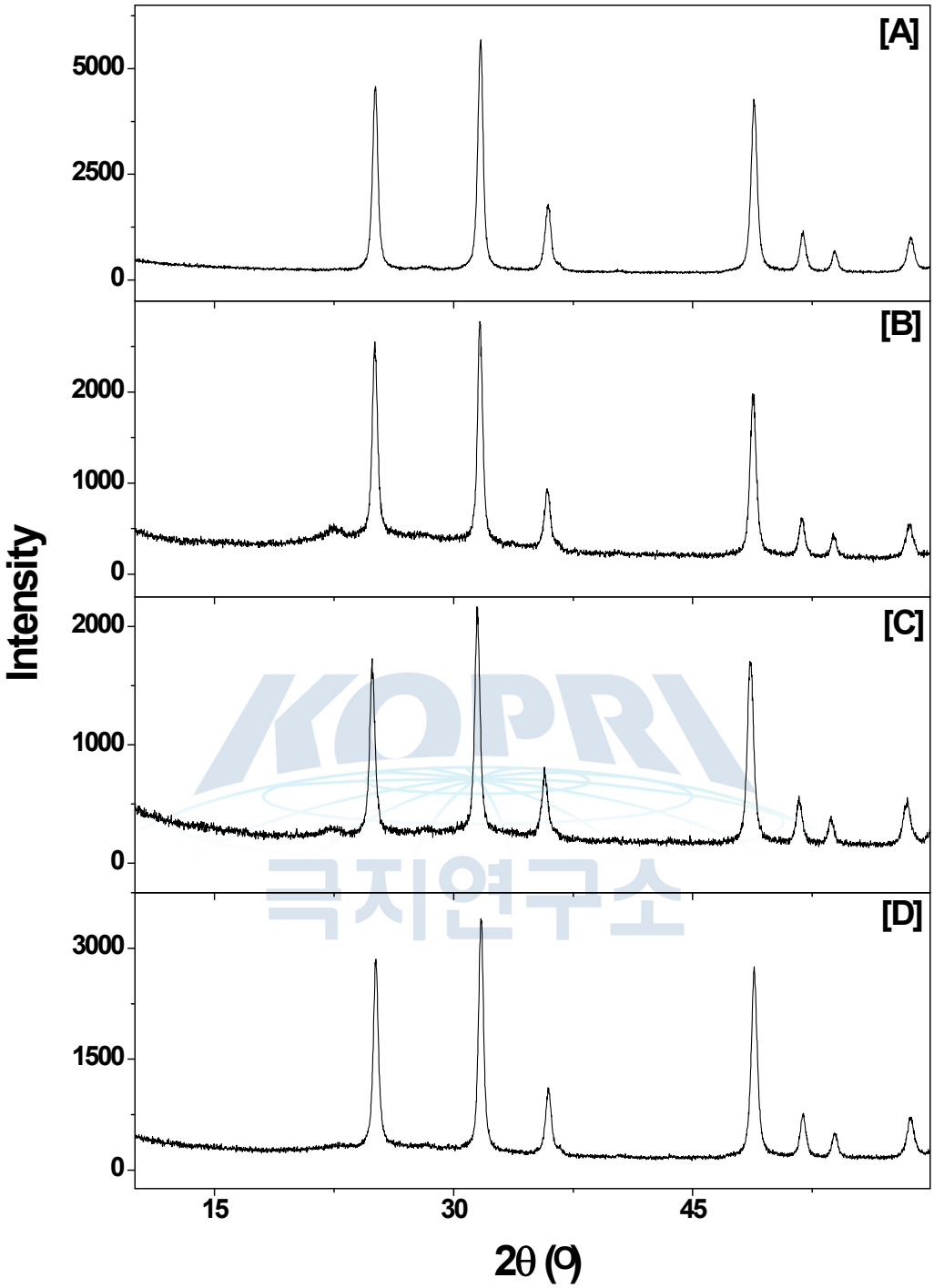

Figure S1. X-ray diffraction pattern of standard β-PbO_2 (plattnerite) [A] and samples after dissolution experiments in the presence of chloride [B], bromide [C], and iodide [D] in frozen solution. Experimental conditions: $[ß\text{-}PbO_2]_0$ = 0.5 g/L; [Halide] = 100 μM; Reaction time = 12 h; pH = 3.

KOPRI 극지연구소

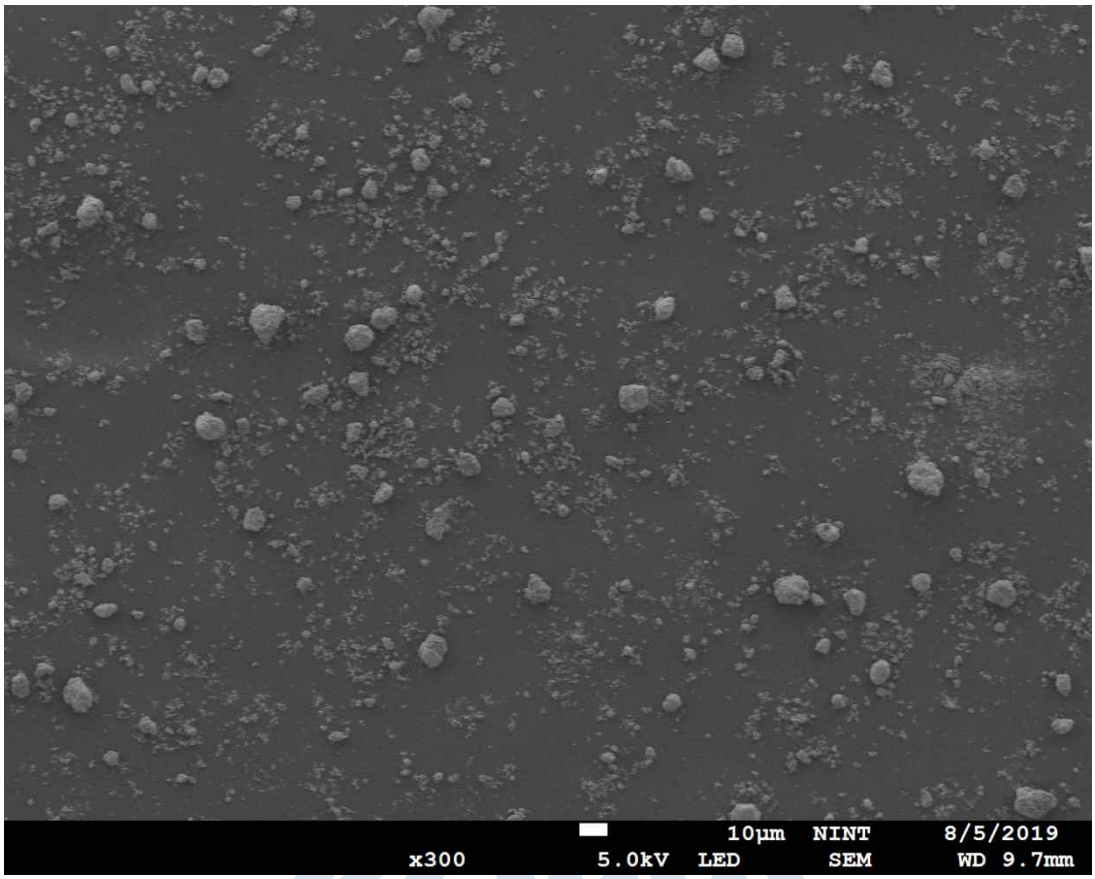

Figure S2. SEM image of ground β-PbO_2 (plattnerite) samples.

KOPRI
극지연구소

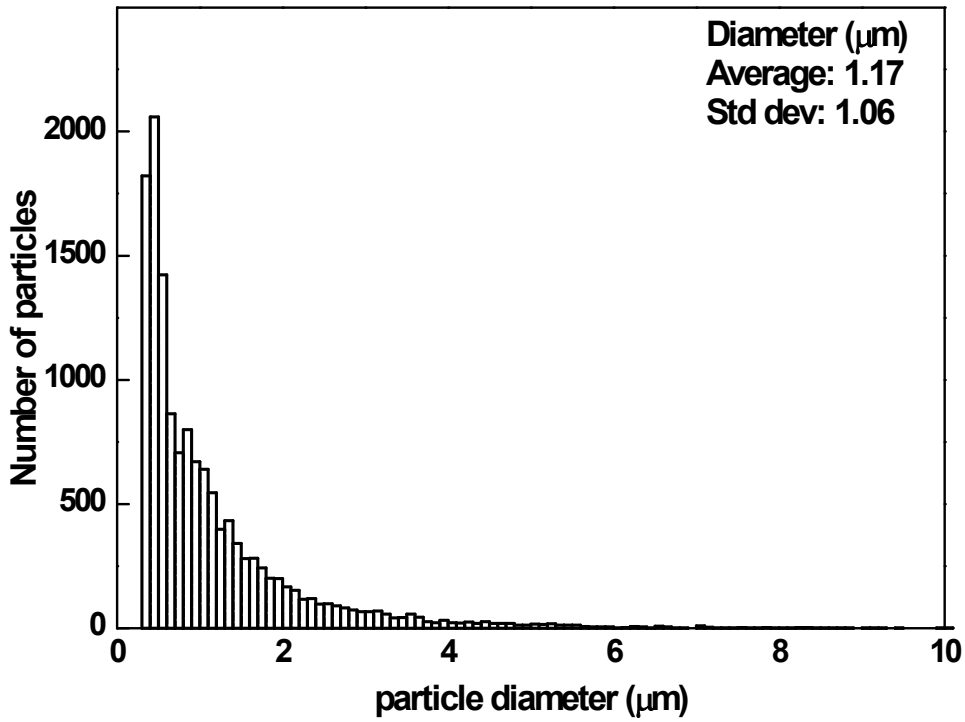

Figure S3. The particle size distribution of ground β-PbO_2 (plattnerite) samples.

KOPRI
극지연구소

제 17 절. Modelling the Sources and Chemistry of Polar Tropospheric Halogens (Cl, Br, I) Ysing the CAM-Chem Global Chemistry-Climate model[10)]

Rafael P. Fernandez[1,2], Antía Carmona-Balea[1], Carlos A. Cuevas[1], Douglas E. Kinnison[3] , Jean-Francois Lamarque[3], Christopher Claszczak-Boxe[4,5], Kitae Kim[6], Wonyong Choi[7], Timothy Hay[8], Anne Blechschmidt[9], Anja Schönhardt[9], Andreas Richter[9], John Burrows[9] and Alfonso Saiz-Lopez[1]

[1]Department of Atmospheric Chemistry and Climate, Institute of Physical Chemistry Rocasolano, CSIC, Madrid, 28006, Spain

[2]National Research Council (CONICET), FCEN-UNCuyo, UNT-FRM, Argentina

[3]Atmospheric Chemistry, Observations & Modelling Laboratory, National Center for Atmospheric Research, USA

[4]Department of Physical, Environmental and Computer Sciences, Medgar Evers College-City University of New York, USA

[5]CUNY Graduate Center, Chemistry Division, Earth and Environmental Science Division, Manhattan, NY 10016, USA.

[6]Korea Polar Research Institute

[7]School of Environmental Science and Engineering, Pohang University of Science and Technology

[8]National Institute of Water and Atmospheric Research (NIWA), New Zealand

[9]Institute of Environmental Physics, University of Bremen, Germany

1. Introduction

The important role played by very short-lived (VSL) halogen chemistry on the global marine boundary layer (MBL), and its impact on ozone and other atmospheric oxidants, has been demonstrated both from experimental (Dorf et al., 2008; Read et al., 2008; Mahajan et al., 2011; Prados-Roman et al., 2015b) and modelling (Yang et al., 2005; Sinnhuber and Folkins, 2006; Hossaini et al., 2010; Liang et al., 2010; Parrella et al., 2012; Saiz-Lopez et al., 2012a, 2014) studies. VSL sources, and their degradation products, affect the

10) 이 연구는 본 과제 지원으로 수행되었으며 그 결과는 다음의 논문으로 출판되었음: Rafael P. Fernandez Antia Carmona-Balea, Carlos A. Cuevas, Javier A. Barrera, Douglas E. Kinnison, Jean-Francois Lamarque, Christopher Blaszczak-Boxe, Kitae Kim, Wonyong Choi, Timothy Hay, Anne-Marlene Blechschmidt, Anja Schonhardt, John P. Burrows, Alfonso Saiz-Lopez, "Modeling the Sources and Chemistry of Polar Tropospheric Halogens (Cl, Br, and I) Using the CAM-Chem Global Chemistry-Climate Model", *J. Adv. Model. Earth Syst.*. 2019, 11, 2259-2289.

tropospheric inorganic halogen loading throughout different geographical regions, expanding from the tropical areas (Aschmann et al., 2009; Saiz-Lopez and Fernandez, 2016) and mid-latitudes (Parrella et al., 2012; Saiz-Lopez et al., 2014) down to the polar regions (Saiz-Lopez et al., 2007, 2008; Pöhler et al., 2010). The additional bromine released from VSL photodecomposition has also been shown to destroy ozone in the lowermost stratosphere (Salawitch et al., 2005), estimating the additional stratospheric injection of VSL bromine to lie within the 5 (3-8) pptv range (WMO, 2014). Recently, the impact of VSL chemistry on the recovery of the Antarctic ozone hole has been evaluated (Oman et al., 2016; Fernandez et al., 2017).

Halogen-mediated Ozone Depletion Events (ODEs) were revealed to be persistent features affecting the polar MBL both in the Arctic and Antarctica (Simpson et al., 2007; Jones et al., 2009; Abbatt et al., 2012). During these events, a very efficient recycling of inorganic bromine species (usually referred as “bromine explosion”) correlates with strong depletion of tropospheric ozone, reducing O3 mixing ratio to very small ambient levels, which in some cases lie below the instrumental detection limit (Simpson et al., 2007, 2015). Even when individual ODEs are usually confined to a small area of a few square kilometers and during periods of time ranging from hours to days, their mean impact on the oxidative capacity of the polar MBL on an annual scale may affect wide extensions over the polar ice-covered areas in both hemispheres. Indeed, bromine oxide (BrO) “clouds”, i.e. regional enhancements on the BrO tropospheric vertical column densities (VCDs), have been observed from different satellite platforms and related to the occurrence of ODEs and bromine explosion events (Theys et al., 2009, 2011; Begoin et al., 2010). The role of chlorine on the generation of ODEs has also been widely studied (Abbatt et al., 2012; Saiz-Lopez and von Glasow, 2012).

Both ice and snow have been recognized as important direct sources of reactive halogen species to the polar atmosphere. The photochemical heterogeneous production of reactive bromine and chlorine species occurring at the snowpack surface have been suggested as a very efficient mechanism in capturing the enhanced halide content prevailing over ice-covered regions (Foster et al., 2001; Dominé and Shepson, 2002; Yang et al., 2010; Abbatt et al., 2012). Additionally, the biologically induced release of inorganic iodine (and possible bromine) from underneath the ice followed by brine diffusion through the ice-shelf (Saiz-Lopez et al., 2015b) can represent the dominant source of iodine and a non-negligible source of bromine to the polar MBL (Atkinson et al., 2012). Likewise, efficient mechanisms of halogen activation of reservoir species occurring on environmental ice and snow have been proposed to represent additional indirect sources (Toyota et al., 2011; Falk and Sinnhuber, 2017). The sea-ice surface recycling process is equivalent to the one occurring on sea-salt aerosols, which has extensively been described in the literature

(Vogt et al., 1996; McFiggans et al., 2000; Fernandez et al., 2014). Many of these recycling processes have been proposed to be controlled by ozone deposition with the subsequent halide oxidation, whose efficiency seems to depend on the Solar Zenith Angle (SZA) and is enlarged within the polar MBL (Toyota et al., 2011; Liao et al., 2014). Even though the presence of frost flowers has originally been suggested to act as an efficient activation indicator (Kaleschke et al., 2004; Granfors et al., 2013), subsequent studies showed that no such a strong correlation between frost-flowers and ODEs existed (Yang et al., 2010). Due to the main differences between the Northern (NH) and Southern (SH) hemisphere ocean salinity, as well as the changes in fresh sea-ice growth rate and the prevalence of different types of microalga underneath the ice-shelf, the efficiency of the biotic and abiotic production of halogens is believed to be very different between both hemispheres, suggesting the existence of an "iodine paradox" between the Arctic and Antarctica (Saiz-Lopez and Blaszczak-Boxe, 2016).

Within the polar regions, oceanic emissions of VSL halocarbons are unlikely to be sufficient to account for the high concentrations of gas phase iodine and bromine observed in the MBL (Pöhler et al., 2010; Saiz-Lopez et al., 2012b; Simpson et al., 2015). For bromine, for example, the photochemical lifetime of CH_2Br_2 within the high latitudes during early spring easily surpass the 0.5 yr limit usually considered for VSL (Carpenter et al., 2014), which notably reduces the organic release of bromine radicals to the polar MBL. For the case of iodine, the dominant inorganic iodine sources arising from the polar oceans does neither account for reproducing the measured iodine levels at different Arctic and Antarctic sites(Saiz-Lopez et al., 2007; Mahajan et al., 2010b). Thus, additional sources arising from the sea-ice surface, or transported from underneath the sea-ice shelf, must be considered in order to reproduce the atmospheric halogen burden in polar regions.

Many of the individual processes described above occur and impact on one of the most pristine regions of the earth, which have been suggested as unambiguous indicators of the advancement of climate change (IPCC, 2013; WMO, 2014). Indeed, box- and 1D-modelling studies have been used to evaluate and describe the role of bromine explosion events on the occurrence of Arctic and Antarctic ODEs (Saiz-Lopez et al., 2008; Jones et al., 2009; Liao et al., 2014), and other oxidative impacts of halogens on Mercury and DMS occurring in the polar regions (Mahajan et al., 2010b; Pöhler et al., 2010). However, most global Chemistry-Climate Models (CCMs) and Chemical Transport Models (CTMs) neglect the contribution of halogen sources and chemistry arising from Antarctica and the Arctic (Parrella et al., 2012; Liang et al., 2014; Hossaini et al., 2016; Sherwen et al., 2016; Fernandez et al., 2017), which certainly produce a non-negligible bias on the global tropospheric ozone burden, as well as on the estimation of the evolution of the oxidative capacity of the global atmosphere. A few attempts have been performed to implement

halogen polar emissions in CTMs/CCMs (Yang et al., 2010; Toyota et al., 2011; Falk and Sinnhuber, 2017), although those studies included a simplified and unique approach to represent direct and indirect polar halogen emissions, were not validated considering direct observations of halogen oxides from Arctic and Antarctic stations, and/or were not oriented to quantify neither the overall additional halogen sources arising from the polar regions respect to the global mean nor to determine the changes in the ozone burden throughout the polar and global troposphere.

Here we present a full-consistent pole-to-pole VSL halogen chemistry scheme, considering *i)* global emissions of VSL halocarbons from the ocean as well as inorganic release of inorganic halogens both from the ocean and from the ice-covered regions within both poles; *ii)* a state-of-the-art halogen gas- and heterogeneous- phase halogen chemical mechanism including reactive and reservoir chlorine, bromine and iodine species; and *iii)* production of sea-salt aerosols, formation of liquid- and ice- clouds and precipitation, as well as dry-/wet- deposition for relevant halogen species at the surface and throughout the troposphere. The additional sea-ice sources have been included interactively into an *on-line polar module* representing the direct photochemical production of bromine and chlorine, the brine diffusion of reactive iodine biologically produced underneath the ice-shelf as well as the indirect recycling of inorganic halogens deposited over the fresh sea-ice surface and sea-salt aerosols.

The paper is structured as follows: Section 2 describes each of the emission sources included in the polar module and how they were parameterized into the CAM-Chem global CCM. Details of the different global model experiments performed, as well as the benchmark CAM-Chem configuration used in this study and the experimental data used for validation, is also provided in Section 2. Results are presented both in sections 3 and 4: while section 3 focuses only on the magnitude, distribution and seasonal variability of each of the bromine, chlorine and iodine implemented sources and their flux strength within each polar region, section 4 emphasizes on evaluating the model performance for the different experiments and validates halogen oxides surface and tropospheric levels against experimental measurements performed both in the Arctic and Antarctica. Discussions of the main implications of considering polar halogen emissions in a global CCM, as well as the main conclusions of the work, are summarized in Section 5.

2. New model Development: Implementation of a Halogen Polar Module in CAM-Chem

Figure 1 represents the different processes releasing inorganic halogens to the atmosphere that compose the polar-module coupled to the CAM-Chem halogen core: *i)* direct emissions

of inorganic halogens either by photochemical oxidation of halide reservoirs at the snowpack surface or due to the biological production by micro-algae activity below the thin ice-shelf followed by brine diffusion; *ii)* indirect deposition and re-emission of inorganic chlorine, bromine and iodine occurring at the surface of 1st-year sea-ice and fresh-now covering the polar continents or multi-year sea-ice; and *iii)* the uptake and recycling of inorganic halogens from sea-salt aerosol, which enhances the total sea-ice flux in the lower troposphere within coastal areas. It's worth noting that while the direct and indirect surface emissions were imposed to occur only on top of ice-covered surfaces, the sea-salt dehalogenation mechanism remains active throughout the whole global lower troposphere up to ~300 hPa. We make the distinction between direct and indirect sources as follows: direct sources are computed at the sea-ice surface and occurs independently of the prior existence of an initial gas-phase halogenated molecule within the lower boundary of the model; while by indirect source we highlight the mandatory requirement of the prior existence of a gas-phase halogenated reservoir capable of being deposited on top of the sea-ice and/or aerosol surface in order to produce the halide uptake and subsequent release of an additional gas-phase halogenated source.

Each of these polar emissions are computed on-line, considering the changes in the fraction of first-year sea-ice covering each polar region (*icefrac*), the net solar irradiance reaching the earth surface at each latitude, longitude and time of the day for each season (*cos(SZA)*), as well as the depositional flux of individual inorganic halogen reservoirs on the surface of the snowpack and or its uptake on sea-salt aerosols occurring both during the day and at night. Additional sea-ice sources of nitrogen oxides occurring due to the deposition of halide nitrates are also considered. Table 1 summarizes the main expressions and parameters associated with each of the three different emission sources, recognizing the similarities and differences observed for the NH and SH polar regions. Before describing the mechanistic details of each additional polar source, the benchmark CAM-Chem halogen configuration used for this study is presented below.

2.1 CAM-Chem benchmark VSL halogen configuration

The novel interactive polar module has been incorporated into the VSL halogenated version of the Community Atmosphere Model with Chemistry (CAM-Chem) (Fernandez et al., 2014; Saiz-Lopez et al., 2014), which constitutes the atmospheric component of the Community Earth System Model (CESM) framework (Lamarque et al., 2012; Tilmes et al., 2016). The VSL halogen setup includes a state-of-the-art halogen chemical scheme including 296 total gas phase inorganic reactions (192 for halogen species, denoted by X and/or Y throughout the text), 33 heterogeneous reactions occurring on sea-salt, sulphates, nitrates and carbonaceous aerosols (19 for halogens), and a complete scheme of gas-phase

organic chemistry based on (Emmons et al., 2010) including more recent updates (145 reactions, 19 for halogens). The implementation and validation of VSL oceanic emissions in the model has been provided by (Ordóñez et al., 2012), while (Prados-Roman et al., 2015a) described the on-line computation of inorganic iodine oceanic sources arising from the ozone mediated oxidation of aqueous iodide (MacDonald et al., 2014). Further descriptions of the VSL halogen mechanism implemented in CAM-Chem can be found elsewhere (Fernandez et al., 2014; Saiz-Lopez et al., 2014).

Within the lower boundary, zonally-averaged distributions of greenhouse gases as well as long-lived halocarbons are specified following their observed surface concentration for year 2000, as done in previous studies (Meinshausen et al., 2011). Climatological sea-surface temperatures and sea-ice extent distributions for the 2000th decade were also considered (Rayner, 2003). Photolysis rate constants are computed online considering both a look-up table and CAM-Chem actinic flux calculations (Lamarque et al., 2012). The stratospheric halogen chemistry in the model is based on (Kinnison et al., 2007; Wegner et al., 2013), including an upper boundary condition which specifies the impact of the ozone column fraction above the model top on the computation of the altitude dependent photolysis rate computations (Lamarque et al., 2008). All rate constants have been updated to JPL-2010 (Jet Propulsion Laboratory, (Sander et al., 2010, 2011) and IUPAC-2008 (International Union of Pure and Applied Chemistry; (Atkinson et al., 2007, 2008).

In this work, all simulations were performed with a horizontal resolution of 1.9° latitude by 2.5° longitude and 26 levels, from the surface up to ~40km, running in Specified Dynamics mode (SD). The model is forced by high-frequency meteorological and dynamical fields obtained from a previous CAM-Chem 5-yrs free-running simulation including the full VSL halogen scheme but without the polar module (Fernandez et al., 2014; Saiz-Lopez et al., 2014). Thus, the CAM-Chem configuration used here only solves for the chemical evolution of the atmosphere while forcing the model to a consistent but fixed meteorological evolution of the troposphere, which in turn is based on prescribed ocean and ice coverage fields that remain identical for all the experiments performed. In this way, the individual appointment to each of the independent sources in each simulation can be considered, as well as the changes in the halogen oxides volume mixing ratios used to validate the model against surface measurements. It is worth noting that all simulations do not pertain to any specific year but are representative of the 2000th decade.

2.2 Direct release of reactive halogens from the sea-ice surface

Equation (1) represents the direct bromine and chlorine flux arising from the photochemical oxidation of the halide content prevailing at the sea-ice surface. The initial bromide and chloride enrichment existent on top of the thin brine layer is assumed to be maintained

either by the deposition of halogen rich sea-salt aerosols or throughout the physicochemical liquation of salty water during the sea-ice solidification (Abbatt et al., 2012; Saiz-Lopez and von Glasow, 2012). Within the model, we assume that the initial bromide and chloride pool is infinitely large (i.e., the fresh sea-ice constitute a non-exhaustible halide reservoir), thus the time-dependent surface flux must be adjusted to respond to the main geophysical parameters controlling the photo-oxidative process. Here we parameterized the direct sea-ice flux (F_{ICE}^{XY}) at each model gridpoint and time (i,t) considering the relative sea-ice extension ($icefrac(i)$) prevailing at each time respect to the maximum sea-ice extension during the whole annual cycle ($maxICE$); as well as the intensity of radiation reaching the model surface at each time of the day (represented by $cos(SZA(i,t))$) normalized by the maximum radiation ($maxSZA$) reaching each gridpoint throughout the year.

$$F_{ICE}^{XY}(i,t) = F_0 \times H_{N/S} \times \frac{icefrac(i)}{\max_{ICE}} \times \frac{\cos(SZA(i,t))}{\max_{SZA}} \quad (1)$$

Note that the direct bromine ($F^{Br2}{}_{ICE}$) and chlorine ($F^{BrCl}{}_{ICE}$) emission is assumed to be abiotic, and thus only respond the geographical changes of the $icefrac(i)$ and $cos(SZA(i,t))$ variables. F_0 is the initial baseline flux, originally taken from a 1-D model of BrO concentrations in Antarctica (Saiz-Lopez et al., 2008), which was iteratively adjusted to improve the CAM-Chem agreement for all measurements performed at different Arctic and Antarctic base stations. $H_{N/S}$ is a hemispheric factor which represents the different chloride and bromide content prevailing on the NH and SH, and relates the efficiency of the process between both polar regions. Although the NH and SH parameters has been adjusted by comparing model results and observations in an iterative manner, their distinct values can be justified due to the well-known differences on sea-ice thickness, ocean salinity and precipitation prevailing between the NH and SH (Yang et al., 2010). It is worth noting that even though the polar module only includes chlorine direct flux in the form of BrCl, homonuclear Cl_2 emissions are also expected to take place in the polar atmosphere (Liao et al., 2014). although they can be rapidly interconverted to heteronuclear BrCl at the sea-ice surface and/or snow (Foster et al., 2001).

For the case of iodine, several mechanisms have been proposed to release reactive halogen species to the atmosphere, such as the production of molecular iodine (I_2) and triiodide (I_3^-) through the photooxidation of iodide in icy surfaces (Kim et al., 2016), and the heterogenous photoreduction of iodate (IO_3^-) in ice releasing an iodine-containing photofragment (Gálvez et al., 2016). Additionally,.micro-algae production of aqueous iodide (I^-_{aq}) and hypoiodous acid (HOI) occurring bellow 1st-year sea-ice, followed by the reactive diffusion through sea-ice brine channels until their ultimate accumulation in the thin brine layer (Saiz-Lopez et al., 2015b), has been suggested as one of the possible missing sources

required to reproduce the high concentrations of iodine oxides observed in coastal Antarctica (Saiz-Lopez et al., 2007; Atkinson et al., 2012). Due to inter-halogen reactions occurring on the brine channels and thin layer, a biologically induced flux of I_2 (and to a lesser extent IBr and/or ICl), can filter throughout the porous sea-ice coverage and reach the bottom of the MBL. A complex mechanism considering the depth-dependent diffusion timescale, the liquid/gas phase equilibrium of halogen species, the temperature gradient between the lower atmosphere and the sea-ice surface underneath, as well as the photochemical diurnal and sea-ice thickness dependence, has been described by means of implementing a detailed 1-D multi-phase scheme (Saiz-Lopez et al., 2015b). In order to implement such a complex mechanism within CAM-Chem, we have simplified the main assumptions and parameterized the emission flux only for gas phase I_2 released to the atmosphere from the sea-ice surface (F_{ICE}^{I2}) as follows:

$$F_{ICE}^{I2}(i,t) = F_0 \times H_{N/S} \times chl_a(i) \times icefrac(i) \times \frac{\cos(SZA(i,t))}{\max_{SZA}} \quad (2)$$

where F_0 is the maximum possible I_2 flux computed for the baseline Antarctic conditions in (Saiz-Lopez et al., 2015b); $chl_a(i)$ is a monthly dependent chlorophyll-a map used as proxy for the biological activity underneath the sea-ice obtained from (Giovanni web page); and the remaining variables are equivalent to the ones described for eq.(1).

2.3 Heterogeneous recycling of reservoir species deposited on top of the sea-ice

The implementation of the heterogeneous recycling of halogenated reservoir species deposited on top of the sea-ice follows the original mechanism described by (Foster et al., 2001), which has already been implemented in many other works (Yang et al., 2010; Toyota et al., 2011; Falk and Sinnhuber, 2017). Briefly, this recycling begins with the initial deposition of a gas-phase oxidized halogenated molecule (in the form of HOX and/or XONO2) on top of the ice and/or snow, which reacts and captures a reduced halide anion (Y−aq) to form a dihalogen molecule (XY), which escapes to the gas-phase due to its small solubility.

$$HOX + H_{aq}^{+} + Y_{aq}^{-} \xrightarrow{sea-ice} XY + H_2O \quad (R1)$$

$$XONO_2 + H_{aq}^{+} + Y_{aq}^{-} \xrightarrow{sea-ice} XY + HNO_3 \quad (R2)$$

The initial reduced halide species must exist in advance on the sea-ice surface to be captured by the redox process. Even when the model considers an infinite halide reservoir prevailing on the sea-ice surface, the additional deposition of halogenated hydracids (HY) must account for the mass-balance required to re-fill the surface halide reservoir through:

$$HY \xrightarrow{sea-ice} H_{aq}^{+} + Y_{aq}^{-} \quad (R3)$$

Note that gas-phase ambient concentrations of these halogenated reservoirs (i.e., $XONO_2$, HOX and HX) must exist within the polar MBL in advance for the deposition and subsequent recycling process to occur; thus constituting an indirect source. It's worth highlighting that not all of the deposited species can follow the redox process, so the initial deposition step also represents an efficient sink of halogens from the atmosphere into a large sea-ice/snow pool that captures reservoir halogen species, which could become available to return to the atmosphere during a later period of time. In this way, the initial depositional flux can be interpreted as a repository compensating the assumption of infinite halogen reservoir for the sea-ice. The parameterized implementation of the abiotic heterogeneous recycling follows:

$$F_{HET}^{XY}(i,t) = RE_{N/S}^{XY} \times \frac{\left(CF^{XONO2} \times D_{FLX}^{XONO2}(i,t) + CF^{HOX} \times D_{FLX}^{HOX}(i,t)\right)}{CF^{XY}} \quad (3)$$

where (F_{HET}^{XY}) represents the surface XY emissions due to the heterogeneous recycling of halogen reservoirs deposited on top of the sea-ice; D_{FLX}^{XONO2} and D_{FLX}^{HOX} represent the dry depositional flux of halogen nitrates and hipo-halogenated acids computed at the lower boundary, respectively, for each model gridpoint and time of the day; CF^{XONO2} and CF^{HOX} are the conversion factors from mass flux (e.g., kg m^{-2} yr^{-1}) to molecular flux (e.g., nmol. m^{-2} day^{-1}) for each deposited species, and CF^{XY} is the equivalent inverse factor for converting nmol. m^{-2} day^{-1} to kg m^{-2} yr^{-1} (see footnote on Table 1). Finally, REN/SXY is the adjusted recycling efficiency for the release of each XY di-halogen source within each polar region (i.e., an analogous to a photochemical quantum yield indicating the probability that the reactive recycling follows each specific production channel). It is worth noting that eq. (3) is only computed over sea-ice covered surfaces (e.g., following the logical condition *icefrac(i)* > 0), although the depositional terms (D_{FLX}^{XONO2} and D_{FLX}^{HOX}) remain active independently of the surface type (the deposition is allowed on all oceanic, icy and continental surfaces). The recycling efficiency for each species was adjusted for each channel depicted in Table 1 starting from their equivalent $RE_{N/S}^{XY}$ values used for sea-salt dehalogenation sources provided in a previous work (Ordóñez et al., 2012; Fernandez et al., 2014; Saiz-Lopez et al., 2014), and adjusted considering the different sea-ice halide content prevailing in each hemisphere (Yang et al., 2010). As many inter-halogen reactions have been suggested to occur on the sea-ice surface and within the thin brine layer covering the Arctic and Antarctic frozen surfaces (Foster et al., 2001), equivalent expressions as those shown by reactions R1 to R3 can proceed forming both homo-nuclear and hetero-nuclear products, releasing a mixture of halogenated species like

IBr, ICl and BrCl, as well to the homonuclear I_2, Br_2 and Cl_2 back to the gas phase (see Table 1).

Note that heterogeneous recycling flux does not explicitly consider the deposition flux of the reduced reservoir HX (i.e., reaction R3) and did not impose any SZA dependence, which is justified considering that: *i)* with a few exceptions, the HX deposition at the model surface largely surpass that arising from D_{FLX}^{XONO2} + D_{FLX}^{HOX}; *ii)* the sea-ice surface is already assumed to be an infinite halide reservoir, and thus the sea-ice halide content should not affect the kinetics of the process; and *iii)* the dial variation of $XONO_2$ and HOX (as well as for HX and all other inorganic halogen species) is already considered in the gas-phase chemical partitioning within our mechanism, which depends on the intensity of solar radiation at each model gridpoint and time of the day. Quantitative evidence of the preceding assumptions is provided in Section 3.3.

2.4 Sea-salt dehalogenation within the polar MBL

Sea-salt aerosols (SSA) are generated by breaking waves on the ocean surface (Monahan et al., 1986; Smith et al., 1993) and can be transported well above the MBL where their washout efficiency decreases. Heterogeneous halogen reactions taking place on the surface of SSA have previously been included in CAM-Chem for HX, HOX and $XONO_2$ species (Ordóñez et al., 2012), based on the assumption that the rate limiting step for the heterogeneous recycling reaction to occur is the uptake of the inorganic halogen species on the aerosol surface (McFiggans et al., 2000). In accordance with the indirect F_{HET}^{XY} sources, we assume the sea-salt aerosol bulk constitute an infinite pool of chloride and bromide, which is large enough for the heterogeneous reactions to occur until the sea-salt aerosol is removed by washout (i.e., we do not consider the temporal aging of the aerosol as the reactive uptake of halides occurs). This is justified considering that the mean lifetime of sea-salt aerosols within the model is less than 1 day (Mahowald et al., 2006; Lamarque et al., 2012), thus it is daily renewed with young-fresh aerosol. Additionally, we imposed a vertical mask to the recycling mechanism above 300 hPa to avoid the SSA dehalogenation computation at high altitudes where it is most probably that aged sea-salt aerosols would prevail.

The implications of the SSA dehalogenation source in CAM-Chem were evaluated for bromine (Fernandez et al., 2014) and iodine (Saiz-Lopez et al., 2014) within the tropical and mid-latitudinal regions. Those works showed that sea-salt recycling in CAM-Chem constitutes significant source of bromine and chlorine to the atmosphere. For the case of iodine, SSA dehalogenation does not represent an additional emission, but only produces a change of partitioning between reservoir and halogen species. Here we extended the SSA dehalogenation process to the high-latitudes and polar lower troposphere, which as shown

in Section 3 constitute a non-negligible source of inorganic chlorine and bromine to the free troposphere. Note that the SSA dehalogenation source is a 3-dimensionall process that is not limited to the surface, but can proceed throughout different vertical levels within the MBL and lower free troposphere. Thus, all this model developments have been implemented within the main driver and chemical-solver instead of constituting a typical additional surface source within the emissions routines. The technical implementation of the SSA dehalogenation source follows a different approach as the one used for the surface emissions, and has been described in detail in the supplementary material of (Ordóñez et al., 2012; Fernandez et al., 2014).

It is worth mentioning that in order to perform a direct comparison of the SSA dehalogenation source respect to the direct and indirect surface sea-ice sources, we have vertically integrated the volumetric dehalogenation flux (i.e., the halogen source derived from the chemical-solver possess units of molec. cm^{-3} s^{-1}) into a mean surface flux at each height (F_{SSA}^{XY} in molec. cm^{-2} s^{-1}, which are the same units as for the sea-ice sources) by means of computing the height thickness of all vertical levels (in cm) at each model gridpoint. We also highlight that, similarly to F_{HET}^{XY} sources, the occurrence of SSA dehalogenation requires the former existence of halogenated reservoirs within the gas-phase which trigger the additional uptake and subsequent release of the pre-existent bromide and chloride aerosol content (i.e., it constitutes an indirect source).

2.5 Photochemical NOx production from the sea-ice surface

In-snow nitrate photolysis occurring on the sea-ice surface has been suggested and measured at several Arctic and Antarctic sites (Domine et al., 2008; Jones et al., 2011; Bauguitte et al., 2012), and represents a non-negligible source of nitrogen to the atmosphere in the polar regions capable of altering the NO/NO_2 ratio and its diurnal cycle, as well as the background ozone levels prevailing in the polar MBL (Bloss et al., 2010). Here, based on (Saiz-Lopez et al., 2008), we introduced a SZA-dependent nitrogen dioxide surface flux (F_{ICE}^{NO2}) arising from the surface of ice-covered regions within the poles following

$$F_{ICE}^{NO2}(i,t) = F_0 \times H_{N/S} \times \frac{\cos\left(SZA(i,t)\right)}{\max_{SZA}} \quad (4)$$

where $\cos(SZA(i,t))$, max_{SZA}, and $H_{N/S}$ are equivalent variables as those defined in Section 2.2. The initial NO_2 flux strength (F_0) has been adjusted iteratively starting from the initial value provided by (Saiz-Lopez et al., 2008) for Antarctic summer conditions (F_0 = 2.0 × 10^8 molec. cm^{-2} s^{-1}), and the final values for all parameters are provided in Table 1.

2.6 Model experiments and experimental observations used for validation

Two independent model experiments were performed to evaluate the changes in the tropospheric halogen loading in the polar regions (Table 2): *i)* a baseline simulation of tropospheric chemistry including VSL sources and the full halogen chemistry scheme, but neglecting the effect of polar emissions (VSL^{PM-off}); and *ii)* the full pole-to-pole setup, where both global VSL sources as well as the complete set of polar emissions were active (VSL^{PM-on}). Within the full pole-to-pole setup, an additional run was designed by turning off the direct sea-ice sources (i.e., those described in Section 2.2) with the intention of evaluate the effectiveness of the indirect heterogeneous recycling of deposited reservoir species (i.e., those described in Section 2.3) whenever the initial direct surface sources are not considered (VSL^{PM-ind}). This multiple model inter-comparison allows to evaluate qualitatively and quantitatively the improvements in the representation of halogen chemistry within the polar regions.

Each of the model experiments was run for 3 years starting from identical initial and boundary conditions, and the output from the last year of simulation was used. All simulations possessed a stabilized stratosphere with approximately 20.5 ppt Br_y, 3250 ppt of Cl_y and less than 0.1 ppt I_y, (where X_y is the total inorganic halogen content within each family, see (Fernandez et al., 2014; Saiz-Lopez et al., 2015a)) in excellent agreement with the last WMO report (Carpenter et al., 2014).

Figure 2 shows the location of each of the Arctic and Antarctic bases where surface experimental observations considered in this study were obtained. Additional relevant information for each of the specific measurements and campaigns considered are compiled in Table 3.

It is worth noting that the vertical extension of the lowest levels of a global CCM like CAM-Chem is in the order of 100-300 m, depending on the model resolution and configuration. In order to compare the surface model estimations respect to BrO, IO and other measured species in the polar campaigns and stations, we performed 1D simulations using the THAMO model for typical polar conditions which allowed to determine the vertical distribution of gas-phase species within the MBL (Saiz-Lopez et al., 2008; Mahajan et al., 2010b). Individual conversion factors were obtained for estimating the surface distribution of the simulated mixing ratios of each halogen species in the lower level of the global model output, and those corrected values were finally compared to the observations. The THAMO model has been used in previous works to study tropospheric halogen chemistry at different locations and environments. Further details including the full chemical scheme can be found elsewhere (Read et al., 2008; Saiz-Lopez et al., 2008, 2016; Mahajan et al., 2010a, 2010c; Lawler et al., 2014). Briefly, THAMO is a 1-D chemistry transport model with 200 stacked boxes at a vertical resolution of 5m (total height 1 km).

KOPRI 극지연구소

The model treats iodine, bromine, O_3, NO_x and HO_x chemistry, and is constrained with typical measured values of other chemical species in the MBL (Saiz-Lopez et al., 2008). The model is initialized at midnight and the evolution of iodine species, O_3, NO_x and HO_x is followed until the model reaches steady state.

3. Quantification of Halogen Emissions from the Polar Regions

This section is presented with the intention of qualitatively depicting the main factors controlling each of the independent sources of inorganic halogens within the polar regions; and most importantly, to quantify the total annual emission and distribution of each individual source. Added together, the north and south polar cap represents almost 15% of the earth surface, highlighting the importance of one of the most pristine regions of the planet where the impact of halogen chemistry on tropospheric ozone and the oxidative capacitive of the atmosphere is expected to be the largest. Thus, we focused our analysis not only on computing the overall emissions from each of the three independent sources considered, but also on comparing the emission strength of this polar sources respect to the main VSL halocarbon and oceanic sources already implemented in the benchmark CAM-Chem setup. This includes the surface and tropospheric photochemical halogen release from the VSL halocarbon emissions inventory (Ordóñez et al., 2012), as well as the inorganic release of inorganic iodine from the ocean surface (Prados-Roman et al., 2015a), which are quantified within the polar regions in Section 3.1. Then in Sections 3.2 and 3.3 we show the spatio-temporal distribution of the direct and indirect polar sources, respectively, as well as the main geophysical factors controlling them. The quantification of the total annual flux of each source, including the individual percentage contribution of each halogen species within each halogen family, is performed separately for the NH and SH, comparing similarities and differences between both polar regions. The quantification of the SSA dehalogenation source presented in Section 3.4 is computed discriminating the surface contribution respect to the total release throughout the tropospheric column, in the same manner as was done for VSL halocarbons in Section 3.1. Section 3.5 presents the abiotic recycling of halide nitrates constituting an indirect source of NO_2. Finally, Section 3.6 compares the contribution of each independent source and provides individual mean results for each specific season. To help going forth-and-back between the technical description of the implementation of each processes in the model and its consequent emission strength computed with CAM-Chem, we ordered the text so results in Sections 3.1 to 3.5 correspond to processes described in Sections 2.1 to 2.5, respectively.

To discern between the Northern and Southern Hemisphere particularities, in the following we will refer to austral seasons as Spring (SON), Summer (DJF), Autumn/Fall (MAM) and Winter (JJA) and to boreal seasons to Spring (MAM), Summer (JJA),

Autumn/Fall (SON) and Winter (DJF). Each of the polar caps (sometimes referred to as polar regions and/or the Arctic and Antarctic subcontinents) is defined poleward of 60º on each hemisphere, and considers all types of model gridpoints including ocean, land and/or ice surfaces. In this manner, the newly implemented polar sources can be compared quantitatively respect to the typical VSL sources already implemented considering latitudinal bands. For the case of sea-ice dependent halogen emissions during winter, when the sea-ice extension is the largest, we included in the polar cap totals those sea-ice sources arising from some latitudes smaller than, but close to, 60º South/North. Note that for these cases, only a few model gridpoints outside the polar caps need to be considered and their contribution to the total polar annual emission represents less than ~1%.

3.1 Oceanic emissions of halocarbons and inorganic halogens

The VSL oceanic sources implemented in CAM-Chem are from the (Ordóñez et al., 2012) inventory, which is based on parametrizations of chlorophyll-a satellite maps within the tropics, but includes constant source strengths for the midlatitudes and polar latitudinal bands, including a time-dependent ice-mask for polar oceans and a monthly seasonality. Table 4 presents the total annual release of halogen atoms from VSL photodecomposition (i.e., considering both hv + OH reactivity) for chlorine, bromine and iodine, separated for the Northern and Southern polar caps (e.g., the Arctic and Antarctic subcontinents). As VSL halocarbon photodecomposition at the ocean surface does not occur instantaneously but depends on the effective chemical lifetime of each species, we separately quantified the release of inorganic chlorine, bromine and iodine arising from VSL degradation occurring only at the ocean surface (F_{VSL}^{srf}, computed by integrating the chemical X atom production rate in the lowest model level) respect to the total halogen release integrated in the whole troposphere (F_{VSL}^{trop}). The release for each halogen family is very similar between both polar regions (F_{VSL}^{srf} = 0.2, 0.6 and 3.1 Gg X yr^{-1} for chlorine, bromine and iodine in the SH, respectively, and accounts for 0.4, 1.0 and 4.6 Gg X yr^{-1} within the Arctic), which is expected to be the case as the (Ordóñez et al., 2012) inventory considers equivalent emission strength for all halocarbons within northern and southern latitudinal bands. The relative release of halogen atoms occurring at the polar surface respect to the overall source throughout the whole polar troposphere is larger for iodine, as the chemical lifetimes are smaller than those for chlorine and bromine(Carpenter et al., 2014; Simpson et al., 2015). Note that the (Ordóñez et al., 2012) emissions inventory considers only natural VSL oceanic sources, so it does not consider anthropogenic chlorocarbon emissions such as dichloromethane (CH_2Cl_2), 1-2 dichloroethane ($C_2H_4Cl_2$), chloroform ($CHCl_3$) and tetrachloroethane (C_2Cl_4), which represents altogether more than 90% of the global surface VSL abundance for chlorine (Carpenter et al., 2014). Thus, within the polar regions, the

chlorine release from VSL is largely influenced by the contribution of mixed brominated and iodinated chloro-carbons (e.g., CH_2BrCl and CH_2ICl, with much shorter lifetimes than anthropogenic VSLs) that increase the relative contribution of chlorine release at the surface (respect to what is observed for bromine). It's worth highlighting that F_{VSLsrf} is more appropriate for comparing the contribution of VSL halocarbons respect to the other sea-ice sources affecting the surface concentrations of halogen oxides (BrO and IO) within the polar regions (i.e., for the validation against surface measurements at Arctic and Antarctic stations), while the overall F_{VSL}^{trop} contribution will impact mostly on the total tropospheric BrO/IO columns and its comparison with the satellite retrievals.

Table 4 also shows the annual mean inorganic iodine source released by the ozone-mediated oxidation of aqueous iodide at the ocean surface (F_{OCN}^{I}, in the form of HOI and I_2), which is computed on-line and released in the lowest layer of the model. Note that for the Antarctic polar cap, F_{VSL}^{srf} and F_{OCN}^{I} for iodine are of the same magnitude, while for the NH the oceanic inorganic source is approximately 6 times larger than the iodocarbon photodecomposition. This respond to the much larger surface ozone background prevailing in the more anthropogenically influenced NH compared to the less polluted SH, which enhances iodine emissions and ozone destruction throughout a negative feedback mechanism (Prados-Roman et al., 2015a).

3.2 Direct emissions from the sea-ice surface: Photochemical and biologically induced sources

Figures 3 and 4 shows the mean seasonal emissions of the direct chlorine, bromine and iodine flux released from the sea-ice surface in the SH and NH, respectively, as well as the geographical distribution of the main factors controlling the spatial features of this polar source. First row in Figs. 3 and 4 highlights the very different distribution of sea-ice extension prevailing in the NH and SH: while the Arctic sea-ice coverage is centered on the North pole and maintain an innermost core with complete ice coverage (icefraction > 0.9) throughout the annual seasonal cycle, the SH sea-ice surrounding the Antarctic continent is renewed year after year (showing ice-fractions smaller than 0.5 during the summer) with the exception of some local features located on the Weddell and Ross seas. This indicates that mostly multi-year (i.e., aged, compacted and thick) sea-ice prevails in the NH; while young, thing and porous 1st year sea-ice encircle Antarctica at most locations. Additionally, the seasonal variation of *cos(SZA)*, representative of the mean irradiance reaching each latitude during each season (second row on Figs. 3 and 4), indicates that during the winter less than 30% of the mean tropical radiation reaches the polar regions (showing a latitudinal variation that minimizes at each pole), while up to 70% (60%) of the tropical average irradiance touches the icy surfaces surrounding the Antarctic

KOPRI 극지연구소

continent (encircling the Arctic periphery) during the summer. The geographical and temporal superposition of these two features determines the dominant pattern of the direct halogen emission arising from the sea-ice surface (F_{ICE}^{XY}) on each hemisphere (whose totals are presented in the 4th, 5th and 6th rows of Figs. 3 and 4 for chlorine, bromine and iodine, respectively). For the case of iodine, further adaptations of the spatial distributions appear at some hot-spot due to the co-location with enhanced chlorophyll-a blooms occurring underneath the sea-ice (see 3rd row on Figs. 3 and 4). With the intention to highlight the very different behavior throughout the seasonal cycle, each F_{ICE}^{XY} panel shows the total flux during each season (i.e., adding the source strength for the three months considered in each column instead of computing a mean seasonal source strength). F_{ICE}^{Br} and F_{ICE}^{Cl} maximize during the summer in the Arctic because the intensity of radiation maximizes during this season while at the same time, a large fraction of the Arctic sea-ice covered areas remain frozen during the warmer months. In contrast, the sea-ice flux in the SH maximizes during spring because during this seasons the sea-ice extension is still large and only starting to decrease, while at the same time the intensity of the radiation is rapidly increasing each day as we move into the summer. Because the dominant sea-ice extension in Antarctica is at comparatively lower latitudes within a warmer ocean (respect to the Arctic), when the surface irradiance maximizes during the summer, the fresh sea-ice extension has been considerably reduced, and thus smaller emissions are modelled to occur.

The sea-ice flux expressions for Br_2 (BrCl) presented in Table 1 consider an initial flux of F_0 = 7.6 × 10^8 molec cm^{-2} s^{-1} (F_0 = 2.85 × 10^8 molec cm^{-2} s^{-1}) and are normalized by the annual mean maximum sea-ice coverage (max_{ICE}) and annual mean maximum radiation (max_{SZA}) within each of the NH and SH polar caps. This implies, for the case of bromine, that the overall flux at a given ice-covered gridbox will reach 7.6 × 10^8 molec cm^{-2} s^{-1} only for those dates and hours of the day where $cos(SZA(i,t))$ = 0.5 and at those locations where the time-dependent ice-fraction is equal to 0.63 in the NH and 0.88 in the SH (see adjusted values in Table 1). If $cos(SZA(i,t)) > max_{SZA}$ and/or $icefrac(i) > max_{ICE}$, then the surface sea-ice flux will be larger than F_0, while the opposite will happen for those times and locations where $cos(SZA(i,t)) < max_{SZA}$ and/or $icefrac(i) < max_{ICE}$. This is a technical heritage of the initial implementation of polar sources within CAM-Chem: as the initial implementation of the polar module parameterization focused on reproducing the 1-D model results of BrO observations performed in coastal Antarctica (Saiz-Lopez et al., 2008), we used as a first F0 guess the maximum springtime value provided for Br_2 sea-ice emissions in that work (i.e., F_0 = 1.0 × 10^9 molec cm^{-2} s^{-1}), and normalized the emissions throughout the annual seasonal cycle considering the maximum values at Halley Base Station (max_{SZA} = 0.443 for Lat = 63.70ºS and max_{ICE} = 0.96 during

August), as that was the location were the experimental BrO measurements had been performed. But even though those initial assumptions worked well for reproducing BrO measurements within the Weddell sea during spring and summer, they did not allow to obtain a proper seasonal representation of the surface measurements at other coastal Antarctic or Arctic stations. Thus, in order to perform the implementation of the sea-ice parameterization from the 1-D model for a specific Antarctic site (Saiz-Lopez et al., 2008) into the 3-D CAM-Chem model for both poles (this work), we iteratively adjusted the F_0, max_{ICE} and max_{SZA} parameters, starting from the initial guess for the Halley base values, until consistent results were obtained for all stations in the Northern and Southern polar caps. Equivalent procedures were performed for the emissions of the other halogen species and for the other sources considered. The final values of the iterative adjustment of all parameters are given for each source and hemisphere in Table 1.

The global annual flux of inorganic chlorine and bromine released from the sea-ice surface reaches 13.4 and 121.1 Gg X yr^{-1}, respectively for the SH, while in the NH it adds up to 21.5 and 194.0 Gg X yr^{-1} (see Table 4). The slightly larger annual values for the NH arise mainly from the larger sea-ice area accumulated throughout the year, as well as the smaller max_{SZA} adjusted parameter for Eq. (1) within the Arctic. Note that the overall bromine emission is ~4 times larger than the one for chlorine. This has important implications in the reproduction of surface BrO and ClO measurements within the Arctic (see Tables 8 and 9 in Section 4).

For the case of iodine, the annual mean global emission of the biologically induced polar source from underneath the sea-ice (F_{ICE}^{I}) in the SH is approximately 14 times larger than the oceanic polar emission and ~20 times larger than the F_{VSL}^{srf} iodine source (see Table 4). For the NH, the sea-ice iodine emission is negligible ($F_{ICE}^{I} \approx 6.6 \times 10^{-2}$ Gg yr^{-1}, which is approximately 3 orders of magnitude smaller than for the SH) and thus more than 90% of the total Arctic iodine source arise in inorganic form from the ocean (F_{OCN}^{I}). The convergence of several emission drivers enhances the relative contribution of F_{ICE}^{I} in Antarctica respect to the Arctic, in what has been called the “iodine paradox” (Saiz-Lopez et al., 2015b): stronger irradiance, larger 1st year sea-ice coverage and thinner sea-ice thickness prevails in the SH, which enhances the photochemical biotic production of iodide underneath the sea-ice and reduces the blocking of gas-phase I_2 produced within the brine channels during their upward transit to the sea-ice surface. In contrast, the dominant thick and compact multi-year sea-ice prevailing in the NH, shields the microalgae colonies underneath the Arctic from the weak solar radiation, reducing the iodide biological production and brine diffusion from below the sea-ice. This fact is represented in the polar module by a reduced efficiency (50 times smaller) in the “production + diffusion coefficient” for the NH ($H_{N/S}$ = 0.015) respect to the SH ($H_{N/S}$ = 0.75), which we applied to the

baseline F_0 flux of 1.2 × 10^9 molec. cm^{-2} s^{-1}, whose final value was determined iteratively as for the parameters for the bromine and chlorine fluxes starting from an initial guess F_0 value provided by (Saiz-Lopez et al., 2015b).

3.3 Indirect abiotic recycling of halide reservoirs at the sea-ice surface

Once the initial direct sources of halogens are released to the atmosphere, the stationary gas-phase reservoir species can be deposited on different types of surfaces. If both reduced (e.g., HY) and oxidized (e.g., $XONO_2$ and/or HOX) halogen reservoirs are deposited on top of the sea-ice, then an heterogeneous recycling of abiotic reservoirs can occur, releasing back to the atmosphere the deposited halogen species plus the uptake of the surface halide. This physicochemical redox process occurs with different efficiencies depending on the rate of deposition of the specific reservoir species deposited, the individual redox potential for each independent inter-halogen reaction, and the halide content of each family prevailing at the sea-ice surface in each hemisphere. Figures 5 and 6 shows the spatial distributions of this abiotic recycling source (F_{HET}^{XY}) for chlorine, bromine and iodine during the different seasons in the SH and NH, respectively. As the geographical distributions of the independent species within each halogen family released to the atmosphere are very similar (for example, sources of I_2, IBr and ICl show equivalent spatial patterns), the total halogen release for each family has been obtained by adding together the recycling contribution from each individual process shown in Table 1. The absolute annual recycling emissions are also shown in Table 4, while the percentage contribution of each independent channel respect to the global annual mean for each family, altogether with the correspondent deposition of reservoir species required for the recycling process to occur, are shown in Table 5.

Due to the larger NH ocean and sea-ice salinity (represented by a larger northern recycling efficiency ($RE_{N/S}^{XY}$) for all NH expressions in Table 1), as well as the larger sea-ice extension, the (F_{HET}^{Cl}) and (F_{HET}^{Br}) contributions to the total polar source is 2 to 3 times larger in the Arctic than in Antarctica (Table 4). An additional factor increasing the NH recycling efficiency respect to the SH is the overall larger NOx background NOx, which shifts the inorganic chlorine/bromine gas-phase partitioning to the formation of $ClONO_2$/$BrONO_2$, thus increasing the initial deposition of oxidized species that initiates the heterogeneous recycling process. In all cases, the indirect F_{HET}^{XY} emission is smaller and, at most, comparable in strength to the total direct emission described in Section 3.2, although for the case of bromine in Antarctica F_{HET}^{Br} represents only 40% of F_{ICE}^{Br}. For the case of iodine, the flux strength is modelled to be smaller in the Arctic (F_{HET}^{I} = 4.5 Gg I yr^{-1}) than in Antarctica (F_{HET}^{I} = 14.2 Gg I yr^{-1}) due to the different types and locations of the initial direct flux releasing gas-phase iodine: while in the NH the dominant

source arises from the ocean which presents increased strength at low latitudes further away from the ice-covered regions, in Antarctica the direct flux arises directly from the sea-ice, at the same locations where the gas-phase halogen reservoirs can be deposited for recycling. In general, the seasonal variation of F_{HET}^{XY} follows the shape of the sea-ice source described in Section 3.2 (see Figs. 3 to 6), indicating the forthright impact of the direct sources from the icy-surfaces on the indirect recycling contribution occurring in both poles.

Besides the $XONO_2$ and HOX depositional flux (D_{FLX}^{ox}) controlling the heterogeneous recycling surface flux rate (see Eq. 3), is worth noting that the HY deposition (D_{FLX}^{red}) must be large enough to account for the halogen mass-balance required to re-fill the halide uptake occurring at the sea-ice surface in both hemispheres. Indeed, Table 5 shows that for both bromine and chlorine $D_{FLX}^{red} > D_{FLX}^{ox}$ both in the Arctic and Antarctica, justifying the assumption that only D_{FLX}^{ox} controls the maximum possible halogen contribution arising from the indirect heterogeneous recycling processes. For the case of chlorine, the deposition of oxidized chlorine species in the Arctic (D_{FLX}^{ox} = 6.7 Gg Cl yr^{-1}) is not enough to provide the total chlorine mass (in the form of Cl_2) to compensate the heterogeneous recycling flux (F_{HET}^{Cl} = 18.3 Gg Cl yr^{-1}). This is compensated by a larger contribution of the heteronuclear BrCl emissions to the total chlorine flux, which arises from the uptake of a chloride anion by the recycling of an oxidized bromine reservoir (mainly BrONO2), whose deposition on the ice-surface largely surpass that from the oxidized chlorine reservoirs (see below). This is not the case for iodine, which presents a marked unbalance in the surface deposition of reduced species (i.e., HI), that represents at most 5% of the heterogeneous recycling flux required to account for the total iodine emission (D_{FLX}^{red} = 0.8 Gg I yr^{-1} for the SH and D_{FLX}^{red} = 0.1 Gg I yr^{-1} for the NH). The reduced HI deposition can be explained by the small HI partitioning within the total inorganic iodine (I_y), which is much smaller than for the equivalent HBr and HCl fractions within the bromine and chlorine families: HCl (HBr) is the most (2^{nd}) abundant tropospheric (Cl_y) Br_y species in the MBL, see (Fernandez et al., 2014; Saiz-Lopez et al., 2014). It's worth noting that the model implementation of the indirect heterogeneous recycling was performed considering an infinite halide reservoir prevailing on top of the sea-ice, thus the mass unbalance between D_{FLX}^{red} and D_{FLX}^{ox} for iodine compounds does not represent a technical limitation to the polar module configuration. But it highlights the omission of additional processes that need to be included in the model to compensate for the additional sea-ice halide content required for maintaining the efficiency of the heterogeneous recycling mechanism. For example, it's possible that a fraction of the aqueous iodide and tri-iodide ions biologically produced underneath the sea-ice can contribute, in addition to the direct F_{ICE}^{I} gas-phase flux, to

re-fill and maintain the iodide abundance on top of the sea-ice surface (Saiz-Lopez et al., 2015b). This assumption could also explain the larger indirect recycling efficiency for Antarctica, where the more porous and thin ice enhances the brine diffusion rates of inorganic iodine.

Table 5 also indicates that for bromine, the homo-nuclear di-halogen re-emission (i.e., Br_2) dominates the percentage contribution of the recycling process: the Br_2 modelled release represents ~55% of the total F_{HET}^{Br} in Antarctica and ~72% in the Arctic. That is not the case for chlorine, where the contribution from BrCl dominates the total surface recycling flux, representing ~70% of the chlorine recycling emission and between (20-30)% of the bromine mass release. This responds to: *i)* the much larger deposition rate of oxidized bromine species respect to their equivalent chlorinated species, both of which can capture the abundant chloride accumulated on top of the sea-ice surface; *ii)* the fact that Cl_2 re-emissions can only occur after deposition of $ClONO_2$ and/or HOCl, while BrCl presents two emission channels arising from the cross-reactions of $ClONO_2$ + Br^- and $BrONO_2$ + Cl^- (or the equivalent processes for HOCl/HOBr, see eqs. (R1 and R2); and *iii)* the larger recycling efficiency factor ($RE_{N/S}^{XY}$) imposed to the cross-reactions respect to the homonuclear release of Cl_2 (see Table 1). Note that for the case of iodine, I_2 and IBr contributions are approximately evenly distributed in both hemispheres.

It is worth noting that for the VSL^{PM-ind} experiment, both the absolute recycling flux and the percentage contribution of each channel are strongly affected by the omission of the direct sea-ice sources in the model. In the SH, the overall recycling flux is reduced by a factor of approximately 3, 8 and 11 for chlorine, bromine and iodine, respectively, highlighting the importance of the direct sea-ice source as a requirement for the initial release of halogen species to the gas phase, which can later be deposited and recycled. It also indicates the much more efficient recycling efficiency of iodine and bromine respect to chlorine on a per atom basis. For the NH, equivalent decreases in F_{HET}^{XY} strength are predicted for bromine and chlorine within the VSL^{PM-ind} experiment. That is not the case for F_{HET}^{I}, which shows equivalent results for VSL^{PM-on} and VSL^{PM-ind}, because the dominant direct iodine source in the Arctic arises from the ocean (F_{OCN}^{I} = 26.9 Gg I yr^{-1}) and not from the sea-ice (F_{ICE}^{I} = 6.62×10^{-2} Gg I yr^{-1}). With regards to the percentage contribution of each specific channel to the overall recycling flux, it's worth noting that due to the large decrease in bromine sources and burden for the VSL^{PM-ind} simulation, chlorine re-emission is no longer dominated by BrCl, but is overpassed by the homo-nuclear Cl_2 flux. As a consequence, the computed depositional fluxes (D_{FLX}^{ox}) for $ClONO_2$ and HOCl within the VSL^{PM-ind} scheme can full-fill the chlorine mass balance required at the sea-ice surface. For the case of bromine, the less efficient recycling produces a shift in the dominant species being deposited on the sea-ice: within the

VSL^{PM-on} experiment, D_{FLX}^{red} is at least 50% larger than D_{FLX}^{ox}, while for the VSL^{PM-ind} experiment $D_{FLX}^{red} < D_{FLX}^{ox}$. Indeed the percentage contribution of BrCl recycling due to the deposition of oxidized chlorine species ($ClONO_2$ and HOCl) reacting with the bromide reservoir increases 6.5 and 3.5 times in the NH and SH, respectively.

3.4 SSA dehalogenation

The annual emission strength of the SSA dehalogenation process, separated into their surface and tropospheric contributions, are also given in Table 4. For comparison, the mean halogen atom release from VSL photochemical decomposition within the surface and throughout the whole troposphere, as well as the individual surface flux of inorganic halogens released from the sea-ice surface (F_{ICE} and F_{HET}), are also shown. Several interesting features can be analyzed from the modelled implementation of the SSA dehalogenation source, which are further exemplified for the southern hemisphere: first, the overall SSA dehalogenation contribution is the largest source of chlorine throughout the troposphere ($F_{SSAtrop}$ = 50.8 Gg Cl yr^{-1}), surpassing the direct (F_{ICE}^{Cl} = 13.4 Gg Cl yr^{-1}) and indirect (F_{HET}^{XY} = 9.9 Gg Cl yr^{-1}) surface fluxes, as well as the photochemical release from VSLs (F_{VSL}^{Cl} = 2.8 Gg Cl yr^{-1}); second, the photochemical surface sea-ice flux is the predominant source of bromine (F^{ICE} = 121.1 Gg Br yr^{-1}) and controls halogen chemistry over the Antarctic surface (F_{HET} = 49.6 Gg Br yr^{-1}, F_{VSL}^{srf} = 0.6 Gg Br yr^{-1} and F_{SSA}^{srf} = 6.3 Gg Br yr^{-1}), but the overall aerosol contribution integrated in the tropospheric column (F_{SSA}^{trop} = 51.2 Gg Br yr^{-1}) surpass those arising from the deposition and recycling of gas-phase bromine (see Table 4); third, there is a marked and rapid decrease on the SSA dehalogenation flux as we move up as well as we move into the continental or completely icy-covered areas and out of the open oceans, which responds to the quite rapid washout lifetime of SSA in the model. Thus, the SSA source possess a large impact on the overall tropospheric column background, mainly above the open ocean areas, but it does not represent a significant contribution to maintaining the large halogen burdens required to reproduce surface observations of BrO and IO presented in Sections 4.1 and 4.2. For these cases, the direct photochemical flux from the sea-ice shelf represents the dominant process controlling the surface polar halogen abundance, followed by the indirect abiotic heterogeneous recycling occurring on the sea-ice surface. Recall that for the case of iodine, SSA dehalogenation does not represent a net source but only constitute an additional process changing the gas-phase partitioning (Saiz-Lopez et al., 2014).

3.5 Quantification of polar NOx sources

The additional photochemical surface denoxification source for each polar region is depicted in Fig. 7 and quantified in Table 6. In order to compare the NO_2 polar emissions to other

nitrogen sources, we've also quantified the polar NO anthropogenic emissions implemented in the benchmark CAM-Chem setup (Lamarque et al., 2012). Notably, while there are not any anthropogenic NO sources implemented for latitudes poleward of 60ºS in the SH, within the NH polar cap the human-induced NO flux surpass the sea-ice NO_2 source arising from the polar module. Indeed, results for NO in Table 6 have been compiled considering an ice-fraction mask (i.e., neglecting the contributions from the NH continents and their surrounding oceans), and indicate that more than half of the nitrogen source in the NH polar cap is anthropogenic (ice-masked F_{NO} = 94.2 Gg N yr^{-1}, while if the oceanic and continental anthropogenic sources are included, it rises up to 5.3 Tg N yr^{-1}). In the Southern Hemisphere, as the sea-ice release is the only nitrogen source, its inclusion impacts on the background ozone levels, and considerably changes the NO/NO_2 ratio, which in turn is correlated with the bromine and iodine halogen cycles through $XONO_2$ and XNO_2 formation (Bloss et al., 2010; Bauguitte et al., 2012). The seasonal variation of polar NO_2 sources shows a similar annual variability as the other sea-ice photochemical processes dependent on the intensity of radiation (i.e., *cos(SZA)*). An equivalent seasonal quantification as the one performed for halogenated sources (see Section 3.6) indicates that in the SH the percentage contribution during DJF, MAM, JJA and SON is 48%, 7%, 4% and 41%, respectively, while for the NH it is distributed as follows: 3%, 40%, 52% and 5%.

3.6 Comparison of polar sources in Antarctica and the Arctic

Figure 8 presents the annual seasonal cycle for all considered polar sources for the SH (top) and NH (bottom), while the monthly total sea-ice area and mean *cos(SZA)* monthly variations are shown in Fig. 9. The percentage distribution of all sources during each season respect to the annual mean is summarized in Table 7. Notably, the contribution of the direct bromine, chlorine and iodine fluxes maximizes during austral mid-spring in the SH (October and November), while for the NH the maximum emissions are observed in the early summer (June). The Antarctic sea-ice direct and indirect bromine source presents a strong seasonality with maximum values of ~35 Gg Br $month^{-1}$ in late austral spring, as a compromise between the still large sea-ice coverage and the increasing rate of incident radiation. Note that even though the intensity of radiation is maximized during the summer, the total sea-ice extension reaches a minimum due to the higher temperatures, reducing the overall halogen emission from the poles. Both direct and indirect sources contribute to the total surface sea-ice flux with similar seasonality that maximizes during the sunlit periods (~60% of the annual emission occurs during Austral Spring, 30% during the Summer, and the remaining 10% during fall and winter), although in absolute values, the direct FICE source represent more than 80% of this total surface source. Note that the

overall contribution from sea-salt recycling integrated within the tropospheric column shows a similar seasonality as the one observed for the surface sources, with slightly larger values during the early austral springtime months. Equivalent total SSA enhancements on top of the dominant sea-ice source are observed for the NH during boreal spring.

For the case of chlorine, even when the sea-salt surface flux still lies below the contribution from direct and indirect sea-ice sources, the total column ($F_{SSA}^{trop} \approx 50.8$ Gg Cl yr^{-1} for the SH and 61.5 Gg Cl yr^{-1} for the NH) largely surpass the overall surface sea-ice flux ($Total_{POLAR}^{srf} \approx 23.4$ Gg Cl yr^{-1} for the SH and 39.8 Gg Cl yr^{-1} for the NH). This would result in an increased background ClO tropospheric column on top of reduced surface ClO clouds (compared to bromine) prevailing in the MBL. It's worth noting that there is a clear minimum of the sea-salt recycling efficiency during SH and NH winters, which is not observed for the bromine SSA dehalogenation (see Table 7).

The annual total flux considering all sources (i.e., surface and tropospheric) released from each polar region reaches 76.9 Gg Cl yr^{-1} and 243.3 Gg Br yr^{-1} for the SH and 106.2 Gg Cl yr^{-1} and 423.3 Gg Br yr^{-1} for the NH. Added together, these sources represents, respectively, 13% and 17% of the annual global chlorine and bromine sources implemented in the model (i.e., the Ordoñez et al., 2012 inventory and the online SSA global dehalogenation), but are circumscripted into an isolated region of the earth where other anthropogenic emissions are negligible, highlighting the importance of considering polar emissions when performing global tropospheric halogen simulations.

For the case of iodine, the seasonal variation follows the results observed for bromine and chlorine, but with a more pronounced springtime enhancement of the biologically induced direct source in Antarctica. Indeed, more than 15 Gg I $month^{-1}$ are emitted from the sea-ice surface during the months of October and November, with 66% of the annual emission occurring during austral spring (see Table 7). Within the NH, the thicker sea-ice coverage blocks the direct emission of iodine from underneath the sea-ice, and the Oceanic source dominates over the other sources such as the indirect heterogeneous recycling flux. Due to the sea-ice shrinkage and ocean expansion occurring during the fall and summer, F_{OCN}^{I} maximizes in July and represent more than 90% of the iodine source to the Arctic atmosphere, in agreement with previous reports (Cuevas et al., 2018). The contribution from iodocarbon photodecomposition represents the 2nd largest contributor in the NH when integrated throughout the whole tropospheric column, with a large variability that can be three times larger during summer than during winter (and 10 times for the SH, although its percentage contribution to the total iodine source is much smaller). It is worth noting that SSA dehalogenation does not constitute an additional iodine source within our modelling approach, and thus sea-salt recycling only represent a

change in partitioning for iodine.

4. Model Validation and Performance: Distribution of Atmospheric Halogens in the Polar Regions

This section is presented with the intention to validate the model performance on reproducing the ambient levels of each halogen family on both polar regions. Sections 4.1 and 4.2 focus on the measurement-model intercomparison of BrO and IO surface volume mixing ratios in Antarctica and the Arctic, respectively, as this are the reactive halogenated species most usually targeted and studied experimentally. However, additional validation for ClO is also presented for the Arctic. Besides the qualitative comparison between experimental and modelled timeseries, a standard statistical analysis is applied to both databases to determine the overall agreement throughout a whole yearly cycle. The total and tropospheric BrO and IO column within the polar regions is also compared against satellite BrO and IO retrievals, with special focus on the geographical distribution of halogen oxides plumes within the MBL and the total VCD which is usually underestimated in global models within the SH and NH polar caps (Section 4.3). Finally, in Section 4.4 the overall changes observed for the different simulations performed in this work are shown, with a special focus on quantifying/estimating the total inorganic halogen burden (i.e., Cly, Bry and Iy) within the polar regions.

4.1 Comparison with Surface Measurements in Antarctica

Figure 10 shows the annual variation of modelled and measured bromine monoxide (BrO) and iodine oxide (IO) surface mixing ratios within the surface measurements performed at the different Antarctic bases compiled in Table 3. In doing so, modelled values have been extracted at the closest model gridpoint respect to the exact location of each database, and the CAM-Chem output at the surface has been re-scaled to account for the large variability in the vertical profile predicted for BrO/IO within the polar MBL (see Fig. 10). A 24 hs (red) and 10 days (blue) moving average has been applied to the hourly model output to allow recognising the short and middle term variability of the modelled data.

We begin the surface validation considering measurements performed in Halley Base station for BrO and IO (Saiz-Lopez et al., 2007), as those are the only experimental datasets existent in polar regions covering a full annual cycle. Both modelled and experimental data shows a marked seasonal cycle, with null values during austral winter and maximum halogen oxides mixing ratios during spring, which rapidly decrease during the summer and fall. Maximum hourly modelled springtime values reach ~45 ppt for BrO and ~9 ppt for IO, with respective daily-mean maximums of ~20 ppt and ~6 ppt which are

maintained during September and October. Measured BrO and IO reached October maximums of 22 and 21 ppt, respectively, with monthly mean maximums of 7.13 and 16.6 ppt. Even when the modelled monthly maximums are in excellent agreement with the observed data, the modelled maximum hourly values for BrO surpass the surface observations by a factor of 2. Most notably, the modelled BrO seasonal cycle shows a secondary maximum during austral fall, in agreement with observations (Saiz-Lopez et al., 2007). This secondary maximum is related with the rapid increase in 1st year sea-ice during march and April, which enhances the surface sea-ice flux before the beginning of the southern polar night. In contrast, the maximum IO levels were observed during September, while the model predicts a maximum peak during late austral spring (October and November). Anyhow, the overall hourly and daily modelled results show a reasonable agreement to the measured IO variability and statistics. This indicates that the initial direct sources of Bromine and Iodine respond to different mechanisms, and that additional sources and/or flux-strength dependence may still be missing in the implemented expressions. During austral summer, and even when the model shows a constant negative bias, the model predicts a continuous and slow decrease of mean daily IO levels until null values are reached during early fall, in replacement of the secondary maximum observed for the case of BrO.

For the case of the MAX-DOAS measurements performed at Arrival Heights (Tim Hay), the modelled BrO and IO values lie within their respective measurements range, showing a similar tendency and a small underestimation for the case of IO. Note, however, that the maximum IO values at Scott Base coincidentally appear during the end of the austral spring. It should also be noticed that for the case of BrO, the secondary maximum appearing during fall is also predicted by the model, although in this case there are no measurements to compare. Finally, the model also show a reasonable agreement and temporal IO evolution during the CEAS summer measurements performed at Dumont Base during 2012 (Grilli et al., 2013).

Table 8 and 9 shows the statistical validation of the model performance in reproducing BrO and IO surface measurements, respectively, for the different polar stations. In general, the model-observations bias is negative, indicating that the model in most cases under-predict the halogen oxides abundance within the polar regions, while both modelled and measured standard deviation (st-dev) largely surpass the absolute bias, indicating that the modelled and measured values are more spread than the mean difference between model an simulation. The only exception within Antarctica is the BrO observations at Halley, which are slightly overestimated in the model, mostly during the spring, where the maximum BrO vmr are predicted.

The seasonal distributions of the large BrO and IO clouds predicted at the

Antarctic surface are shown in Fig. 11. In order to highlight the main seasonal changes, the monthly mean for the middle-month within each season has been selected in each panel. As expected, the BrO and IO clouds follow the spatial patterns of the surface sea-ice flux and heterogeneous recycling observed in Figs. 3 and 5, although additional enhancements appear within the Weddel and Ross seas due to the larger contribution of SSA dehalogenation within these regions. It is worth noting that this enhanced halogen oxides clouds are a persistent feature that appear within the fresh sea-ice covered areas with a daily frequency at different locations, which on average during a full month show the geographical distribution presented in Fig. 12. Note that even when this large BrO and IO plumes are persistent features throughout the whole Antarctic continent, the predicted values within the clouds present consistent maximum values as those reported at the different base stations used for the timeseries validation (Fig. 10). The exact location and magnitude of these spatial clouds is further analysed in Section 4.3 when the model results are compared with satellite retrievals.

4.2 Comparison with Surface Measurements in the Arctic

Equivalent results as those presented for the SH are also observed for the Arctic. Figure 12 shows the temporal evolution of surface modelled BrO, IO and ClO and its comparison with surface Arctic measurements. Daily mean BrO surface mixing ratios measured during boreal spring at Barrow and the Amundsen Gulf are qualitatively well reproduced, showing a very good agreement on the maximum values (BrO^{max}_{obs} = 16 ppt and BrO^{max}_{mod} = 16.77 ppt at Amundsen, while the respective values for Barrow are 27 and 22 ppt) and an overall negative bias (NMB is −0.37 and −0.5 for each respective base). For the case of Alert and Zeppelin stations, the model show a positive bias (NMB is 0.38 and 0.24, respectively), although the maximum predicted values lie in close agreement with the experimental data (see Table 8). It is worth noting that, in agreement with the model predictions within the SH, a secondary BrO maximum appears during the boreal autumn, which still requires experimental validation. Another highlighting point is that, even when the polar surface bromine sources maximize during the summer, BrO mixing ratios maximize during spring, due to the different chemical partitioning of inorganic reactive and reservoir species during each season. This internal partitioning within the different halogen species, as well as its relation with other atmospheric families such as HOx and NOx, is out of the scope of this work and will be further analyzed in a future paper.

For the case of IO, we performed the model validation with the measurement obtained in Zeppelin station (Tuckermann et al., 1997), which were performed in years 1995-1996. Although the timing of the IO modelled peaks is not coincident with the observations (which is expected, as the model meteorology was not forced for any specific

year), there is a general adequate model performance on reproducing the rapid daily changes observed with maximum values that lie within the observations. In contrast to BrO, model IO peaks at Zeppelin are continuously observed throughout the whole boreal spring, summer and fall, without showing any seasonal prevalence. Note that the ovrall NMB = −0.54, indicating that the model underestimate the total polar iodine loading. Finally, the model also predicts maximum ClO surface mixing ratios during boreal spring, equivalently to bromine, although in this case the model clearly under-predict the observations. Several factors, such as the omission of additional anthropogenic chlorinated VSLS sources and the remaining uncertainties related to the direct and indirect sea-ice sources, as well as other mechanistic details that have not been considered within our polar emission approach, certainly impact on the model performance. There is also a reasonable agreement with the Cl_2 measurements recently performed at Barrow (Liao et al., 2014). It's worth mentioning that an equivalent simulation as the VSL^{PM-on} experiment, but replacing the direct sea-ice BrCl emissions by a bimolecular Cl_2 flux, produced equivalent results as those shown here (not shown). Most probably, both BrCl and Cl_2 emissions occur in the real atmosphere, and thus a mixed scheme considering the two related sources can be considered (Foster et al., 2001; Liao et al., 2014). Further research is required to determine the relative contribution of each independent channel to the total chlorine and bromine flux strength.

4.3 Comparison with Satellite Data in the Arctic

Satellite data show the same trends as the surface observations. Figure 14 shows the monthly averaged tropospheric bromine monoxide VCD in the location of the Barrow, Alert and Admudsen Gulf stations, compared to the modelled tropospheric columns. Table 10 includes the statistics of this comparison between GOME-2 observation and modelled data. As in the comparison to surface observation, the model under-predict the bromine oxide levels in the arctic region, showing a negative bias in the model-observation parameter for the Admundsen and Barrow stations. The bias is only positive in the Alert Station, as is the case for the surface observation. Also for the satellite comparison the standard deviation of both modelled and observations are higher than the absolute bias, except in the Alert Station.

5. Discussions and Conclusions

The implementation of the novel polar module considering inorganic halogen emissions from the sea-ice surface and the heterogeneous recycling of reservoir species represents a significant advancement in the complete global representation of halogen chemistry within the troposphere. Indeed, this is the first global model to our knowledge that includes a

complete representation of all chlorine, bromine and iodine sources and chemistry from pole-to-pole, and expanding from the earth surface up to the stratosphere. Even though the parameterized implementation of the natural physicochemical processes releasing inorganic halogens to the polar troposphere has been performed in a simplified manner, it constitute a notorious improvement respect to prior approaches by considering a direct source strength dependence on several geophysical factors that present large seasonal variations within the polar regions, such as the icefraction extension, the intensity of radiation (i.e., *cos(SZA)*) and the influence of marine biological activity (*chl*-a satellite maps). Additionally, this work provides for the first time, quantitative estimations of the annual and seasonal flux strength of each halogen family from each polar region, and compares their magnitude respect to the other halogen oceanic sources usually implemented in global CCMs.

The overall additional contribution of direct and indirect sources within the Antarctic continent accounts for 23.4 and 170.7 Gg X yr^{-1} for chlorine and bromine, respectively, of which approximately 50% occurs during spring and between 70-90% if the summer is also counted for. In comparison, more than half of the bromine and chlorine modelled emissions from the Arctic occurs during the summer (followed by spring) accounting for an annual strength of 39.8 Gg Cl yr^{-1} and 319.5 Gg Br yr^{-1}. Increased local emissions strengths within each model gridbox following the higher irradiance prevailing during the summer is compensated by a reduced sea-ice coverage during the warmer seasons, as the polar icefraction strongly depends on the ocean and atmosphere temperature. The distinct behavior of the sea-ice sources within both polar regions can be explained considering the different compromise between these two geophysical factors, that shows a slightly different trends between the Arctic and Antarctica. This comparably different seasonal behavior between the Arctic (dominant emissions occurring during the summer followed by the preceding spring) and Antarctic (dominant emissions during spring followed by those occurring in the proceeding summer) are attributed to the more concentrated poleward sea-ice distribution in the NH, and the comparatively larger irradiance reaching the summer sea-ice boundary closer to the Antarctic polar circle. Most notably, these polar emissions are between 3 and 5 times larger than the other natural bromine and chlorine natural oceanic sources, highlighting the enormous importance of including the additional sea-ice processes within global models. Indeed, CCAM-Chem strongly underestimates halogen oxides observations if the polar module is turned off.

In contrast to bromine and chlorine, the modelled annual iodine emission strength in Antarctica is 15 times larger than in the Arctic, following the polar iodine paradox suggested by (Saiz-Lopez and Blaszczak-Boxe, 2016). The notable difference in sea-ice thickness and permeability between the Arctic and Antarctic sea-ice, represented in the

model by $H_{N/S}$ (see table 1), produces polar sea-ice emissions (73.8 Gg I yr^{-1}) to dominate the iodine burden in the SH polar cap, while in the NH the polar module accounts only for 4.6 Gg I yr^{-1} and, due to the much higher tropospheric ozone levels, the oceanic release of inorganic iodine (F_{OCN}^{I}) constitute the most important source. Special spatial and seasonal features are also observed for iodine emissions, due to the parameterized dependence on the biologically activity of algae colonies occurring underneath the sea-ice.

Previous attempts to include this additional recycling source on global models have been proposed (Toyota et al., 2011; Falk and Sinnhuber, 2017), although those studies did not considered iodine chemistry and no distinction was made respect to the direct and indirect sources described here. Those studies parameterized the efficiency of an unique heterogeneous recycling mechanism by imposing a molar yield function dependent on the surface type (i.e., 1^{st} year sea-ice, multi-year sea-ice or snow over land) and illumination (discerning only on day/night conditions, but without considering the intensity of solar radiation reaching the surface at each time). Their discrimination of 1^{st}-year and multi-year sea-ice was performed in a very simplified fashion. Similarly as here, those studies assumed an infinite pool of chloride (Cl^-) and bromide (Br^-) for 1^{st} year sea-ice, although they reduce the Br pool for multi-year sea-ice and determine the magnitude of the recycling based on the larger of HOBr + $BrONO_2$ deposition compared to HBr, but they did not assure the halide pool to be re-filled in order to justify the assumed infinite reservoir. Here, the effectiveness of the independent reactions releasing the homonuclear Br_2/Cl_2 respect to the di-halogens BrCl/IBr/ICl species depends on the conversion factors RE^{XY} and FC^{XY}, all of which take different values for each individual species and hemisphere (see Table 1).

The records of BrO,ClO and IO mixing ratios over the entire year show a scattered day-to-day variability as a result of differences in solar incident radiation and halogen source strength, as well as other atmospheric variables such as surface temperature, background atmospheric components and wind speed and direction. However, the overall model performance at different stations within the Arctic and Antarctica shown excellent results, presenting a model-observations bias smaller than both the observed and modelled standard deviation (see Table 8). Is worth noting that, as the modeled considered meteorological conditions representative of the 20^{th} decade (i.e., it was not configured to follow a Specified Dinamics approeach based on reanalysis data), we do not expect the model to present a perfect timing nor an exact spatial co-location for each and all of the rapid BrO and IO peaks recorded in the literature for each campaign. Instead, we focus our development on obtaining an addecuate statistical validation of surface and sattelite observations throughout the whole polar troposphere, capable of reproducing the mean and maximum values, as well as their relative distributions, observed during several different

campaigns performed during different years on different stations.

Note that the modeled the seasonal cycles of IO and BrO are remarkably similar in SH, both in timing (Figs. 11 and 13) and distributions (Figs. 12 and 14). This is quite expected, given the similar sources of the two halogens, and their equivalent *icefraction* and *cos(SZA)* dependence. In NH the differences in absolute concentrations between BrO and IO are more notable, as the IO mechanism of emission is hinder by the greater thickness of the seaice. If we focused in ClO , we can show similar timing cicles respect to BrO, but with a persistent model underestimation. As both halogens have a similar emission parameterization (see Table 1 and Section 2) and also a common BrCl source, we could not further increase the chlorine flux strength because that also produced a BrO enhencement, which was already showing overpredictions at some stations. Further research is required to understand the factors determining the efficiency of each inter-halogen reactive channel both from the experimental and modelling point of view.

6. References

Abbatt, J. P. D., Thomas, J. L., Abrahamsson, K., Boxe, C., Granfors, A., Jones, A. E., King, M. D., Saiz-Lopez, A., Shepson, P. B., Sodeau, J., Toohey, D. W., Toubin, C., von Glasow, R., Wren, S. N. and Yang, X.: Halogen activation via interactions with environmental ice and snow in the polar lower troposphere and other regions, Atmos. Chem. Phys., 12(4), 6237 - 6271, doi:10.5194/acpd-12-8677-2012, 2012.

Aschmann, J., Sinnhuber, B.-M., Atlas, E. L. and Schauffler, S. M.: Modeling the transport of very short-lived substances into the tropical upper troposphere and lower stratosphere, Atmos. Chem. Phys., 9(23), 9237 - 9247, doi:10.5194/acp-9-9237-2009, 2009.

Atkinson, H. M., Huang, R.-J., Chance, R., Roscoe, H. K., Hughes, C., Davison, B., Schönhardt, A., Mahajan, A. S., Saiz-Lopez, A., Hoffmann, T. and Liss, P. S.: Iodine emissions from the sea ice of the Weddell Sea, Atmos. Chem. Phys., 12(5), 4 - 6, doi:10.5194/acpd-12-11595-2012, 2012.

Atkinson, R., Baulch, D. L., Cox, R. A., Crowley, J. N., Hampson, R. F., Hynes, R. G., Jenkin, M. E., Rossi, M. J. and Troe, J.: Evaluated kinetic and photochemical data for atmospheric chemistry: Volume III - gas phase reactions of inorganic halogens, Atmos. Chem. Phys., 7(4), 981 - 1191, doi:10.5194/acp-7-981-2007, 2007.

Atkinson, R., Baulch, D. L., Cox, R. A., Crowley, J. N., Hampson, R. F., Hynes, R. G., Jenkin, M. E., Rossi, M. J., Troe, J. and Wallington, T. J.: Evaluated kinetic and photochemical data for atmospheric chemistry: Volume IV - gas phase reactions of organic halogen species, Atmos. Chem. Phys., 8(15), 4141 - 4496,

doi:10.5194/acp-8-4141-2008, 2008.

Bauguitte, S. J. B., Bloss, W. J., Evans, M. J., Salmon, R. A., Anderson, P. S., Jones, A. E., Lee, J. D., Saiz-Lopez, A., Roscoe, H. K., Wolff, E. W. and Plane, J. M. C.: Summertime NOx measurements during the CHABLIS campaign: Can source and sink estimates unravel observed diurnal cycles?, Atmos. Chem. Phys., 12(2), 989 - 1002, doi:10.5194/acp-12-989-2012, 2012.

Begoin, M., Richter, a., Weber, M., Kaleschke, L., Tian-Kunze, X., Stohl, a., Theys, N. and Burrows, J. P.: Satellite observations of long range transport of a large BrO plume in the Arctic, Atmos. Chem. Phys., 10(14), 6515 - 6526, doi:10.5194/acp-10-6515-2010, 2010.

Bloss, W. J., Camredon, M., Lee, J. D., Heard, D. E., Plane, J. M. C., Saiz-Lopez, A., J.-B. Bauguitte, S., Salmon, R. A. and Jones, A. E.: Coupling of HOx, NOx and halogen chemistry in the antarctic boundary layer, Atmos. Chem. Phys., 10(21), 10187 - 10209, doi:10.5194/acp-10-10187-2010, 2010.

Brooks, S. B., Saiz-Lopez, A., Skov, H., Lindberg, S. E., Plane, J. M. C. and Goodsite, M. E.: The mass balance of mercury in the springtime arctic environment, Geophys. Res. Lett., 33(13), 2 - 5, doi:10.1029/2005GL025525, 2006.

Carpenter, L. J., Reimann, S. (Lead A., Burkholder, J. B., Clerbaux, C., Hall, B. D., Hossaini, R., Laube, J. C. and Yvon-Lewis, S. A.: Update on Ozone-Depleting Substances (ODSs) and Other Gases of Interest to the Montreal Protocol, Chapter 1 in Scientific Assessment of Ozone Depletion: 2014, Global Ozone Research and Monitoring Project-Report No. 55, Geneva, Switzerland., 2014.

Cuevas, C. A., Maffezzoli, N., Corella, J. P., Spolaor, A., Vallelonga, P., Kjær, H. A., Simonsen, M., Winstrup, M., Vinther, B., Horvat, C., Fernandez, R. P., Kinnison, D., Lamarque, J., Barbante, C. and Saiz-lopez, A.: Rapid increase in atmospheric iodine levels in the North Atlantic since the mid-20th century, Nat. Commun., 1 - 6, doi:10.1038/s41467-018-03756-1, 2018.

Custard, K. D., Pratt, K. A., Wang, S. and Shepson, P. B.: Constraints on Arctic Atmospheric Chlorine Production through Measurements and Simulations of Cl 2 and ClO, Environ. Sci. Technol., 50(22), 12394 - 12400, doi:10.1021/acs.est.6b03909, 2016.

Domine, F., Albert, M., Huthwelker, T., Jacobi, H.-W., Kokhanovsky, A. A., Lehning, M., Picard, G., Simpson, W. R. and Cold, A.: Snow physics as relevant to snow photochemistry, Atmos. Chem. Phys., 8(2), 171 - 208, doi:10.5194/acp-8-171-2008, 2008.

Dominé, F. and Shepson, P. B.: Air-snow interactions and atmospheric chemistry., Science, 297(5586), 1506 - 10, doi:10.1126/science.1074610, 2002.

Dorf, M., Butz, A., Camy-Peyret, C., Chipperfield, M. P., Kritten, L. and Pfeilsticker, K.: Bromine in the tropical troposphere and stratosphere as derived from balloon-borne BrO observations, Atmos. Chem. Phys., 8(4), 7265 - 7271, doi:10.5194/acpd-8-12999-2008, 2008.

Emmons, L. K., Walters, S., Hess, P. G., Lamarque, J.-F., Pfister, G. G., Fillmore, D., Granier, C., Guenther, A., Kinnison, D., Laepple, T., Orlando, J., Tie, X., Tyndall, G., Wiedinmyer, C., Baughcum, S. L. and Kloster, S.: Description and evaluation of the Model for Ozone and Related chemical Tracers, version 4 (MOZART-4), Geosci. Model Dev., 3(1), 43 - 67, doi:10.5194/gmd-3-43-2010, 2010.

Falk, S. and Sinnhuber, B.: Polar boundary layer bromine explosion and ozone depletion events in the chemistry-climate model EMAC v2 . 52 : Implementation and evaluation of AirSnow algorithm, Geosci. Model Dev. Discossions, (July), 1 - 15, 2017.

Fernandez, R. P., Kinnison, D. E., Lamarque, J.-F., Tilmes, S. and Saiz-Lopez, A.: Impact of biogenic very short-lived bromine on the Antarctic ozone hole during the 21st century, Atmos. Chem. Phys., 1673 - 1688, doi:10.5194/acp-2016-840, 2017.

Fernandez, R. P., Salawitch, R. J., Kinnison, D. E., Lamarque, J.-F. and Saiz-Lopez, A.: Bromine partitioning in the tropical tropopause layer: implications for stratospheric injection, Atmos. Chem. Phys., 14(24), 13391 - 13410, doi:10.5194/acp-14-13391-2014, 2014.

Foster, K. L., Plastridge, R. a, Bottenheim, J. W., Shepson, P. B., Finlayson-Pitts, B. J. and Spicer, C. W.: The role of Br2 and BrCl in surface ozone destruction at polar sunrise., Science, 291(5503), 471 - 4, doi:10.1126/science.291.5503.471, 2001.

Gálvez, Ó., Baeza-romero, M. T., Sanz, M. and Saiz-lopez, A.: Photolysis of frozen iodate salts as a source of active iodine in the polar environment, Atmos. Chem. Phys., 16, 12703 - 12713, doi:10.5194/acp-16-12703-2016, 2016.

Granfors, A., Andersson, M., Chierici, M., Fransson, A., Gårdfeldt, K., Torstensson, A., Wulff, A. and Abrahamsson, K.: Biogenic halocarbons in young Arctic sea ice and frost flowers, Mar. Chem., 155, 124 - 134, doi:10.1016/j.marchem.2013.06.002, 2013.

Grilli, R., Legrand, M., Kukui, A., Méjean, G., Preunkert, S. and Romanini, D.: First investigations of IO, BrO, and NO2 summer atmospheric levels at a coastal East Antarctic site using mode-locked cavity enhanced absorption spectroscopy, Geophys. Res. Lett., 40(4), 791 - 796, doi:10.1002/grl.50154, 2013.

Hönninger, G., von Friedeburg, C. and Platt, U.: Multi axis differential optical absorption spectroscopy (MAX-DOAS), Atmos. Chem. Phys., 4(1), 231 - 254, doi:10.5194/acp-4-231-2004, 2004.

Honninger, G. and Platt, U.: Observations of BrO and its vertical distribution during surface ozone depletion at Alert, Atmos. Environ., 36(15-16), 2481 - 2489, doi:10.1016/s1352-2310(02)00104-8, 2002.

Hossaini, R., Chipperfield, M. P., Monge-Sanz, B. M., Richards, N. A. D., Atlas, E., Blake, D. R. and Science, A.: Bromoform and dibromomethane in the tropics: A 3-D model study of chemistry and transport, Atmos. Chem. Phys., 10(2), 719 - 735, doi:10.5194/acp-10-719-2010, 2010.

Hossaini, R., Chipperfield, M. P., Saiz-Lopez, A., Fernandez, R., Monks, S., Brauer, P. and von Glasow, R.: A global model of tropospheric chlorine chemistry: organic versus inorganic sources and impact on methane oxidation, J. Geophys. Res. Atmos., 121, 1 - 27, doi:10.1002/2016JD025756, 2016.

IPCC: Climate Change 2013: The Physical Science Basis. Contribution of Working Group I to the Fifth Assessment Report of the Intergovernmental Panel on Climate Change, edited by T. F. Stocker, D. Qin, G. K. Plattner, M. Tignor, S. K. Allen, J. Boschung, A. Nauels, Y. Xia, V. Bex, and P. M. Midgley, Cambridge University Press, Cambridge, United Kingdom and New York, NY, USA,., 2013.

Jones, A. E., Anderson, P. S., Begoin, M., Brough, N., Hutterli, M. A., Marshall, G. J., Richter, A., Roscoe, H. K. and Wolff, E. W.: BrO, blizzards, and drivers of polar tropospheric ozone depletion events, Atmos. Chem. Phys., 9(14), 4639 - 4652, doi:10.5194/acp-9-4639-2009, 2009.

Jones, A. E., Wolff, E. W., Ames, D., Bauguitte, S. J., Clemitshaw, K. C., Fleming, Z., Mills, G. P., Saiz-Lopez, A., Salmon, R. A., Sturges, W. T. and Worton, D. R.: The multi-seasonal NO y budget in coastal Antarctica and its link with surface snow and ice core nitrate : results from the CHABLIS campaign, Atmos. Chem. Phys., 11, 9271 - 9285, doi:10.5194/acp-11-9271-2011, 2011.

Kaleschke, L., Richter, A., Burrows, J., Afe, O., Heygster, G., Notholt, J., Rankin, A. M., Roscoe, H. K., Hollwedel, J., Wagner, T. and Jacobi, H. W.: Frost flowers on sea ice as a source of sea salt and their influence on tropospheric halogen chemistry, Geophys. Res. Lett., 31(16), 4 - 7, doi:10.1029/2004GL020655, 2004.

Kim, K., Yabushita, A., Okumura, M., Saiz-lopez, A., Cuevas, C. A., Blaszczak-boxe, C. S., Min, D. W., Yoon, H. and Choi, W.: Production of Molecular Iodine and Tri-iodide in the Frozen Solution of Iodide: Implication for Polar Atmosphere, Environ. Sci. Technol., 50, 1280 - 1287, doi:10.1021/acs.est.5b05148, 2016.

Kinnison, D. E., Brasseur, G. P., Walters, S., Garcia, R. R., Marsh, D. R., Sassi, F., Harvey, V. L., Randall, C. E., Emmons, L., Lamarque, J. F., Hess, P., Orlando, J. J., Tie, X. X., Randel, W., Pan, L. L., Gettelman, A., Granier, C., Diehl, T., Niemeier, U. and Simmons, A. J.: Sensitivity of chemical tracers to meteorological parameters in the MOZART-3 chemical transport model, J. Geophys. Res., 112(D20), D20302, doi:10.1029/2006JD007879, 2007.

Lamarque, J.-F., Emmons, L. K., Hess, P. G., Kinnison, D. E., Tilmes, S., Vitt, F., Heald, C. L., Holland, E. A., Lauritzen, P. H., Neu, J., Orlando, J. J., Rasch, P. J. and Tyndall, G. K.: CAM-chem: description and evaluation of interactive atmospheric chemistry in the Community Earth System Model, Geosci. Model Dev., 5(2), 369 - 411, doi:10.5194/gmd-5-369-2012, 2012.

Lamarque, J.-F., Kinnison, D. E., Hess, P. G. and Vitt, F. M.: Simulated lower stratospheric trends between 1970 and 2005: Identifying the role of climate and composition changes, J. Geophys. Res., 113(D12), D12301, doi:10.1029/2007JD009277, 2008.

Lawler, M. J., Mahajan, A. S., Saiz-Lopez, A. and Saltzman, E. S.: Observations of I2 at a remote marine site, Atmos. Chem. Phys., 14(5), 2669 - 2678, doi:10.5194/acp-14-2669-2014, 2014.

Liang, Q., Atlas, E., Blake, D., Dorf, M., Pfeilsticker, K. and Schauffler, S.: Convective transport of very short lived bromocarbons to the stratosphere, Atmos. Chem. Phys., 14(11), 5781 - 5792, doi:10.5194/acp-14-5781-2014, 2014.

Liang, Q., Stolarski, R. S., Kawa, S. R., Nielsen, J. E., Douglass, A. R., Rodriguez, J. M., Blake, D. R., Atlas, E. L. and Ott, L. E.: Finding the missing stratospheric Bry: a global modeling study of CHBr3 and CH2Br2, Atmos. Chem. Phys., 10(5), 2269 - 2286, doi:10.5194/acp-10-2269-2010, 2010.

Liao, J., Huey, L. G., Liu, Z., Tanner, D. J., Cantrell, C. a., Orlando, J. J., Flocke, F. M., Shepson, P. B., Weinheimer, A. J., Hall, S. R., Ullmann, K., Beine, H. J., Wang, Y., Ingall, E. D., Stephens, C. R., Hornbrook, R. S., Apel, E. C., Riemer, D., Fried, A., Mauldin, R. L., Smith, J. N., Staebler, R. M., Neuman, J. A. and Nowak, J. B.: High levels of molecular chlorine in the Arctic atmosphere, Nat. Geosci., 7(2), 91 - 94, doi:10.1038/ngeo2046, 2014.

Liao, J., Huey, L. G., Tanner, D. J., Flocke, F. M., Orlando, J. J., Neuman, J. A., Nowak, J. B., Weinheimer, A. J., Hall, S. R., Smith, J. N., Fried, A., Staebler, R. M., Wang, Y., Koo, J. H., Cantrell, C. A., Weibring, P., Walega, J., Knapp, D. J., Shepson, P. B. and Stephens, C. R.: Observations of inorganic bromine (HOBr, BrO, and Br2) speciation at Barrow, Alaska, in spring 2009, J. Geophys. Res. Atmos., 117(6), 1 - 11, doi:10.1029/2011JD016641, 2012.

MacDonald, S. M., Gómez Martín, J. C., Chance, R., Warriner, S., Saiz-Lopez, A., Carpenter, L. J. and Plane, J. M. C.: A laboratory characterisation of inorganic iodine emissions from the sea surface: dependence on oceanic variables and parameterisation for global modelling, Atmos. Chem. Phys., 14(11), 5841 - 5852, doi:10.5194/acp-14-5841-2014, 2014.

Mahajan, a. S., Sorribas, M., Gómez Martín, J. C., MacDonald, S. M., Gil, M., Plane, J. M. C. and Saiz-Lopez, a.: Concurrent observations of atomic iodine, molecular iodine and ultrafine particles in a coastal environment, Atmos. Chem. Phys., 11(6), 2545 - 2555, doi:10.5194/acp-11-2545-2011, 2011.

Mahajan, A. S., Plane, J. M. C., Oetjen, H., Mendes, L., Saunders, R. W., Saiz-Lopez, A., Jones, C. E., Carpenter, L. J. and McFiggans, G. B.: Measurement and modelling of tropospheric reactive halogen species over the tropical Atlantic Ocean, Atmos. Chem. Phys., 10(10), 4611 - 4624, doi:10.5194/acp-10-4611-2010, 2010a.

Mahajan, A. S., Shaw, M., Oetjen, H., Hornsby, K. E., Carpenter, L. J., Kaleschke, L., Tian-Kunze, X., Lee, J. D., Moller, S. J., Edwards, P., Commane, R., Ingham, T., Heard, D. E. and Plane, J. M. C.: Evidence of reactive iodine chemistry in the Arctic boundary layer, J. Geophys. Res., 115(D20), D20303, doi:10.1029/2009JD013665, 2010b.

Mahajan, A. S., Shaw, M., Oetjen, H., Hornsby, K. E., Carpenter, L. J., Kaleschke, L., Tian-Kunze, X., Lee, J. D., Moller, S. J., Edwards, P., Commane, R., Ingham, T., Heard, D. E. and Plane, J. M. C.: Evidence of reactive iodine chemistry in the Arctic boundary layer, J. Geophys. Res. Atmos., 115(20), 1 - 11, doi:10.1029/2009JD013665, 2010c.

Mahowald, N. M., Lamarque, J.-F., Tie, X. X. and Wolff, E.: Sea-salt aerosol response to climate change : Last Glacial Maximum , preindustrial , and doubled carbon dioxide climates, J. Geophys. Res., 111(D05303), 1 - 11, doi:10.1029/2005JD006459, 2006.

Martinez, M., Arnold, T. and Perner, D.: The role of bromine and chlorine chemistry for arctic ozone depletion events in Ny-Ålesund and comparison with model calculations, Ann. Geophys., 17(7), 941 - 956, doi:10.1007/s00585-999-0941-4, 1999.

McFiggans, G., Plane, J. M. C., Allan, B. J., Carpenter, L. J., Coe, H. and O'Dowd, C.: A modeling study of iodine chemistry in the marine boundary layer, J. Geophys. Res., 105(D11), 14371 - 14385, doi:10.1029/1999JD901187, 2000.

Meinshausen, M., Smith, S. J., Calvin, K., Daniel, J. S., Kainuma, M. L. T., Lamarque, J.-F., Matsumoto, K., Montzka, S. A., Raper, S. C. B., Riahi, K., Thomson, A., Velders, G. J. M. and Vuuren, D. P. P.: The RCP greenhouse gas concentrations

and their extensions from 1765 to 2300, Clim. Change, 109(1-2), 213 - 241, doi:10.1007/s10584-011-0156-z, 2011.

Monahan, E. C., Spiel, D. E. and Davidson, K. L.: A Model of Marine Aerosol Generation Via Whitecaps and Wave Disruption, pp. 167 - 174, Springer, Dordrecht., 1986.

Morin, S., Hönninger, G., Staebler, R. M. and Bottenheim, J. W.: A high time resolution study of boundary layer ozone chemistry and dynamics over the Arctic Ocean near Alert, Nunavut, Geophys. Res. Lett., 32(8), 1 - 5, doi:10.1029/2004GL022098, 2005.

Oman, L. D., Douglass, A. R., Salawitch, R. J., Canty, T. P., Ziemke, J. R. and Manyin, M.: The effect of representing bromine from VSLS on the simulation and evolution of Antarctic ozone, Geophys. Res. Lett., accepted, doi:10.1002/2016GL070471, 2016.

Ordóñez, C., Lamarque, J.-F., Tilmes, S., Kinnison, D. E., Atlas, E. L., Blake, D. R., Sousa Santos, G., Brasseur, G. and Saiz-Lopez, A.: Bromine and iodine chemistry in a global chemistry-climate model: description and evaluation of very short-lived oceanic sources, Atmos. Chem. Phys., 12(3), 1423 - 1447, doi:10.5194/acp-12-1423-2012, 2012.

Parrella, J. P., Jacob, D. J., Liang, Q., Zhang, Y., Mickley, L. J., Miller, B., Evans, M. J., Yang, X., Pyle, J. a., Theys, N. and Van Roozendael, M.: Tropospheric bromine chemistry: implications for present and pre-industrial ozone and mercury, Atmos. Chem. Phys., 12(15), 6723 - 6740, doi:10.5194/acp-12-6723-2012, 2012.

Pöhler, D., Vogel, L., Friess, U. and Platt, U.: Observation of halogen species in the Amundsen Gulf, Arctic, by active long-path differential optical absorption spectroscopy., Proc. Natl. Acad. Sci. U. S. A., 107(15), 6582 - 7, doi:10.1073/pnas.0912231107, 2010.

Prados-Roman, C., Cuevas, C. A., Fernandez, R. P., Kinnison, D. E., Lamarque, J.-F. and Saiz-Lopez, A.: A negative feedback between anthropogenic ozone pollution and enhanced ocean emissions of iodine, Atmos. Chem. Phys., 15(4), 2215 - 2224, doi:10.5194/acp-15-2215-2015, 2015a.

Prados-Roman, C., Cuevas, C. a., Hay, T., Fernandez, R. P., Mahajan, a. S., Royer, S.-J., Galí, M., Simó, R., Dachs, J., Großmann, K., Kinnison, D. E., Lamarque, J.-F. and Saiz-Lopez, A.: Iodine oxide in the global marine boundary layer, Atmos. Chem. Phys., 15(2), 583 - 593, doi:10.5194/acp-15-583-2015, 2015b.

Rayner, N. A.: Global analyses of sea surface temperature, sea ice, and night marine air temperature since the late nineteenth century, J. Geophys. Res., 108(D14), 4407, doi:10.1029/2002JD002670, 2003.

Read, K. A., Mahajan, A. S., Carpenter, L. J., Evans, M. J., Faria, B. V. E., Heard, D. E.,

Hopkins, J. R., Lee, J. D., Moller, S. J., Lewis, A. C., Mendes, L., McQuaid, J. B., Oetjen, H., Saiz-Lopez, A., Pilling, M. J. and Plane, J. M. C.: Extensive halogen-mediated ozone destruction over the tropical Atlantic Ocean., Nature, 453(7199), 1232 - 5, doi:10.1038/nature07035, 2008.

Saiz-Lopez, A., Baidar, S., Cuevas, C. A., Koenig, T. K., Fernandez, R. P., Dix, B., Kinnison, D. E., Lamarque, J., Campos, T. L. and Volkamer, R.: Injection of iodine to the stratosphere, Geophys. Res. Lett., 42, 1 - 8, doi:10.1002/2015GL064796.Received, 2015a.

Saiz-Lopez, A. and Blaszczak-Boxe, C. S.: The polar iodine paradox, Atmos. Environ., 145, 72 - 73, doi:10.1016/j.atmosenv.2016.09.019, 2016.

Saiz-Lopez, A., Boxe, C. S. and Carpenter, L. J.: A mechanism for biologically induced iodine emissions from sea ice, Atmos. Chem. Phys., 15(2), 9731 - 9746, doi:10.5194/acp-15-9731-2015, 2015b.

Saiz-Lopez, A. and Fernandez, R. P.: On the formation of tropical rings of atomic halogens: Causes and implications, Geophys. Res. Lett., 43, 1 - 8, doi:10.1002/2015GL067608.Received, 2016.

Saiz-Lopez, A., Fernandez, R. P., Ordóñez, C., Kinnison, D. E., Gómez Martín, J. C., Lamarque, J.-F. and Tilmes, S.: Iodine chemistry in the troposphere and its effect on ozone, Atmos. Chem. Phys., 14(23), 13119 - 13143, doi:10.5194/acp-14-13119-2014, 2014.

Saiz-Lopez, A. and von Glasow, R.: Reactive halogen chemistry in the troposphere., Chem. Soc. Rev., 41(19), 6448 - 6472, doi:10.1039/c2cs35208g, 2012.

Saiz-Lopez, A., Lamarque, J.-F., Kinnison, D. E., Tilmes, S., Ordóñez, C., Orlando, J. J., Conley, A. J., Plane, J. M. C., Mahajan, A. S., Sousa Santos, G., Atlas, E. L., Blake, D. R., Sander, S. P., Schauffler, S., Thompson, A. M. and Brasseur, G.: Estimating the climate significance of halogen-driven ozone loss in the tropical marine troposphere, Atmos. Chem. Phys., 12(9), 3939 - 3949, doi:10.5194/acp-12-3939-2012, 2012a.

Saiz-Lopez, A., Mahajan, A. S., Salmon, R. A., Bauguitte, S. J.-B., Jones, A. E., Roscoe, H. K. and Plane, J. M. C.: Boundary Layer Halogens in Coastal Antarctica, Science (80-.)., 317(5836), 348 - 351, doi:10.1126/science.1141408, 2007.

Saiz-Lopez, A., Plane, J. M. C., Baker, A. R., Carpenter, L. J., von Glasow, R., Martín, J. C. G., McFiggans, G. and Saunders, R. W.: Atmospheric chemistry of iodine., Chem. Rev., 112(3), 1773 - 804, doi:10.1021/cr200029u, 2012b.

Saiz-Lopez, A., Plane, J. M. C., Cuevas, C. A., Mahajan, A. S., Lamarque, J. F. and

KOPRI 극지연구소

Kinnison, D. E.: Nighttime atmospheric chemistry of iodine, Atmos. Chem. Phys., 16(24), 15593 - 15604, doi:10.5194/acp-16-15593-2016, 2016.

Saiz-Lopez, A., Plane, J. M. C., Mahajan, A. S., Anderson, P. S., Bauguitte, S. J.-B., Jones, A. E., Roscoe, H. K., Salmon, R. A., Bloss, W. J., Lee, J. D. and Heard, D. E.: On the vertical distribution of boundary layer halogens over coastal Antarctica: implications for O3, HOx, NOx and the Hg lifetime, Atmos. Chem. Phys., 8(4), 887 - 900, doi:10.5194/acp-8-887-2008, 2008.

Salawitch, R. J., Weisenstein, D. K., Kovalenko, L. J., Sioris, C. E., Wennberg, P. O., Chance, K., Ko, M. K. W. and McLinden, C. A.: Sensitivity of ozone to bromine in the lower stratosphere, Geophys. Res. Lett., 32(5), L05811, doi:10.1029/2004GL021504, 2005.

Sander, S. P., Friedl, R. R., Barker, J. R., Arbor, A., Golden, D. M., Kurylo, M. J., Wine, P. H., Abbatt, J., Burkholder, J. B., Kolb, C. E., Moortgat, G. K., Huie, R. E. and Orkin, V. L.: Chemical Kinetics and Photochemical Data for Use in Atmospheric Studies Evaluation Number 16, JPL_NASA, 09-31(16), 1 - 17, 2010.

Sander, S. P., Friedl, R. R., Barker, J. R., Golden, D. M., Kurylo, M. J., Sciences, G. E., Wine, P. H., Abbatt, J. P. D., Burkholder, J. B., Kolb, C. E., Moortgat, G. K., Huie, R. E. and Orkin, V. L.: Chemical Kinetics and Photochemical Data for Use in Atmospheric Studies, Evaluation No. 17, JPL_NASA, 10-6(17), 2011.

Sherwen, T., Schmidt, J. A., Evans, M. J., Carpenter, L. J., Gro??mann, K., Eastham, S. D., Jacob, D. J., Dix, B., Koenig, T. K., Sinreich, R., Ortega, I., Volkamer, R., Saiz-Lopez, A., Prados-Roman, C., Mahajan, A. S. and Ord????ez, C.: Global impacts of tropospheric halogens (Cl, Br, I) on oxidants and composition in GEOS-Chem, Atmos. Chem. Phys., 16(18), 12239 - 12271, doi:10.5194/acp-16-12239-2016, 2016.

Simpson, W. R., Brown, S. S., Saiz-Lopez, A., Thornton, J. A. and Glasow, R. Von: Tropospheric Halogen Chemistry: Sources, Cycling, and Impacts., Chem. Rev., doi:10.1021/cr5006638, 2015.

Simpson, W. R., von Glasow, R., Riedel, K., Anderson, P., Ariya, P., Bottenheim, J., Burrows, J., Carpenter, L. J., Frieß, U., Goodsite, M. E., Heard, D., Hutterli, M., Jacobi, H.-W., Kaleschke, L., Neff, B., Plane, J., Platt, U., Richter, A., Roscoe, H., Sander, R., Shepson, P., Sodeau, J., Steffen, A., Wagner, T. and Wolff, E.: Halogens and their role in polar boundary-layer ozone depletion, Atmos. Chem. Phys., 7(16), 4375 - 4418, doi:10.5194/acp-7-4375-2007, 2007.

Sinnhuber, B.-M. and Folkins, I.: Estimating the contribution of bromoform to stratospheric bromine and its relation to dehydration in the tropical tropopause layer, Atmos.

Chem. Phys., 6(12), 4755 – 4761, doi:10.5194/acp-6-4755-2006, 2006.

Smith, M. H., Park, P. M. and Consterdine, I. E.: Marine aerosol concentrations and estimated fluxes over the sea, Q. J. R. Meteorol. Soc., 119(512), 809 – 824, doi:10.1002/qj.49711951211, 1993.

Theys, N., Van Roozendael, M., Errera, Q., Hendrick, F., Daerden, F., Chabrillat, S., Dorf, M., Pfeilsticker, K., Rozanov, A., Lotz, W., Burrows, J. P., Lambert, J.-C., Goutail, F., Roscoe, H. K. and De Mazière, M.: A global stratospheric bromine monoxide climatology based on the BASCOE chemical transport model, Atmos. Chem. Phys., 9(3), 831 – 848, doi:10.5194/acp-9-831-2009, 2009.

Theys, N., Van Roozendael, M., Hendrick, F., Yang, X., De Smedt, I., Richter, A., Begoin, M., Errera, Q., Johnston, P. V., Kreher, K. and De MaziÃre, M.: Global observations of tropospheric BrO columns using GOME-2 satellite data, Atmos. Chem. Phys., 11(4), 1791 – 1811, doi:10.5194/acp-11-1791-2011, 2011.

Tilmes, S., Lamarque, J., Emmons, L. K., Kinnison, D. E., Marsh, D., Garcia, R. R., Smith, A. K., Neely, R. R., Conley, A., Vitt, F., Martin, M. V., Tanimoto, H., Simpson, I., Blake, D. R. and Blake, N.: Representation of the Community Earth System Model (CESM1) CAM4-chem within the Chemistry-Climate Model Initiative (CCMI), Geosci. Model Dev., 9, 1853 – 1890, doi:10.5194/gmd-9-1853-2016, 2016.

Toyota, K., McConnell, J. C., Lupu, a., Neary, L., McLinden, C. a., Richter, a., Kwok, R., Semeniuk, K., Kaminski, J. W., Gong, S.-L., Jarosz, J., Chipperfield, M. P. and Sioris, C. E.: Analysis of reactive bromine production and ozone depletion in the Arctic boundary layer using 3-D simulations with GEM-AQ: inference from synoptic-scale patterns, Atmos. Chem. Phys., 11(8), 3949 – 3979, doi:10.5194/acp-11-3949-2011, 2011.

Tuckermann, M., Ackermann, R., Gölz, C., Lorenzen-Schmidt, H., Senne, T., Stutz, J., Trost, B., Unold, W. and Platt, U.: DOAS-observation of halogen radical-catalysed arctic boundary layer ozone destruction during the ARCTOC-campaigns 1995 and 1996 in Ny-Ålesund, Spitsbergen, Tellus, Ser. B Chem. Phys. Meteorol., 49(5), 533 – 555, doi:10.3402/tellusb.v49i5.16005, 1997.

Vogt, R., Crutzen, P. J. and Sander, R.: A mechanism for halogen release from sea-salt aerosol in the remote marine boundary layer, Nature, 383(6598), 327 – 330, doi:10.1038/383327a0, 1996.

Wegner, T., Kinnison, D. E., Garcia, R. R. and Solomon, S.: Simulation of polar stratospheric clouds in the specified dynamics version of the whole atmosphere community climate model, J. Geophys. Res. Atmos., 118(10), 4991 – 5002, doi:10.1002/jgrd.50415, 2013.

WMO: Scientific Assessment of Ozone Depletion: 2010, Global Ozone Research and Monitoring Project-Report No. 55, World Meteorological Organization, Geneva, Switzerland., 2014.

Yang, X., Cox, R. A., Warwick, N. J., Pyle, J. A., Carver, G. D., O'Connor, F. M. and Savage, N. H.: Tropospheric bromine chemistry and its impacts on ozone: A model study, J. Geophys. Res., 110(D23), D23311, doi:10.1029/2005JD006244, 2005.

Yang, X., Pyle, J. a., Cox, R. a., Theys, N. and Van Roozendael, M.: Snow-sourced bromine and its implications for polar tropospheric ozone, Atmos. Chem. Phys., 10(16), 7763 - 7773, doi:10.5194/acp-10-7763-2010, 2010.

KOPRI
극지연구소

Table 1. Additional sea-ice halogen sources implemented in the CAM-Chem polar module

Table 1a. Sea-ice direct emissions implemented in the polar module

Sea-ice Flux Expression based on Eq. (1)[&]	Adjusted Parameters[#]
$F_{ICE}^{BrCl}(i,t) = F_0 \times H_{N/S} \times \frac{icefrac(i)}{\max_{ICE}} \times \frac{\cos(SZA(i,t))}{\max_{SZA}}$	$F_0 = 2.85\times10^8$; $H_{N/S} = 0.4$; $\begin{cases}\max_{ICE} = 0.63\\ \max_{SZA} = 0.50\end{cases}$
	$F_0 = 2.85\times10^8$; $H_{N/S} = 0.4$; $\begin{cases}\max_{ICE} = 0.88\\ \max_{SZA} = 0.50\end{cases}$
$F_{ICE}^{Br2}(i,t) = F_0 \times H_{N/S} \times \frac{icefrac(i)}{\max_{ICE}} \times \frac{\cos(SZA(i,t))}{\max_{SZA}}$	$F_0 = 7.6\times10^8$; $H_{N/S} = 0.6$; $\begin{cases}\max_{ICE} = 0.63\\ \max_{SZA} = 0.50\end{cases}$
	$F_0 = 7.6\times10^8$; $H_{N/S} = 0.6$; $\begin{cases}\max_{ICE} = 0.88\\ \max_{SZA} = 0.50\end{cases}$
$F_{ICE}^{I2}(i,t) = F_0 \times H_{N/S} \times chl_a(i) \times icefrac(i) \times \frac{\cos(SZA(i,}{\max_{SZA}}$	$F_0 = 1.2\times10^9$; $\max_{SZA} = 0.50$; $\begin{cases}H_{N/S} = 0.75\\ if\ (icefrac \geq 0.8) \rightarrow H_{N/S} = 1.0\end{cases}$
	$F_0 = 1.2\times10^9$; $\max_{SZA} = 0.50$; $\begin{cases}H_{N/S} = 0.015\\ if\ (icefrac \geq 0.8) \rightarrow H_{N/S} = 0.02\end{cases}$

[&]The left column on the table present the individual expression for each halogen species emitted from the sea-ice surface based on Eq. (1). F_0 is the initial surface flux for each species; $H_{N/S}$ is a hemispheric factor; *icefrac(i)* is the sea-ice fraction at a given model gridpoint; *cos(SZA(i,t))* is the cosine of the SZA at each model gridpoint and time of the day; max_{ICE} and max_{SZA} are the adjusted maximum sea-ice extension and radiation imposed to normalize the emission strength and *chla(i)* is a monthly dependent chlorophyll-a satellite map. See the text for further details.

[#]The adjusted parameters for each expression on the left column are provided for the NH (top) and SH (bottom). Units for F_0 are molec. cm^{-2} s^{-1}. All the remaining parameters are adimensional and represent relative fractions between 0 (zero) and 1 (one).

Table 1b. Indirect heterogeneous recycling emissions implemented in the polar module

$F_{HET}^{I2}(i,t) = RE_{N/S}^{XY} \times \frac{\left(CF^{IONO2} \times D_{FLX}^{IONO2}(i,t) + CF^{HOI} \times D_{FLX}^{HOI}(i,t)\right)}{CF^{I2}}$	$RE_{N/S}^{XY} = 0.5 \quad ; \quad CF^{spec} = \frac{1.0 \times 10^{12} \times 86400}{MW_{spec}}$
	$RE_{N/S}^{XY} = 0.25 \quad ; \quad CF^{spec} = \frac{1.0 \times 10^{12} \times 86400}{MW_{spec}}$
$F_{HET}^{IBr}(i,t) = RE_{N/S}^{XY} \times \frac{\left(CF^{IONO2} \times D_{FLX}^{IONO2}(i,t) + CF^{HOI} \times D_{FLX}^{HOI}(i,t)\right)}{CF^{IBr}}$	$RE_{N/S}^{XY} = 0.5 \quad ; \quad CF^{spec} = \frac{1.0 \times 10^{12} \times 86400}{MW_{spec}}$
	$RE_{N/S}^{XY} = 0.35 \quad ; \quad CF^{spec} = \frac{1.0 \times 10^{12} \times 86400}{MW_{spec}}$
$F_{HET}^{Br2}(i,t) = RE_{N/S}^{XY} \times \frac{\left(CF^{BrONO2} \times D_{FLX}^{BrONO2}(i,t) + CF^{HOBr} \times D_{FLX}^{HOBr}(i,t)\right)}{CF^{Br2}}$	$RE_{N/S}^{XY} = 0.54 \quad ; \quad CF^{spec} = \frac{1.0 \times 10^{12} \times 86400}{MW_{spec}}$
	$RE_{N/S}^{XY} = 0.3 \quad ; \quad CF^{spec} = \frac{1.0 \times 10^{12} \times 86400}{MW_{spec}}$
$F_{het-rec}^{BrCl} = \begin{cases} RE_{N/S}^{XY}(Cl^-) \times \frac{\left(CF^{BrONO2} \times D_{FLX}^{BrONO2}(i,t) + CF^{HOBr} \times D_{FLX}^{HOBr}(i,t)\right)}{CF^{BrCl}} + \\ RE_{N/S}^{XY}(Br^-) \times \frac{\left(CF^{ClONO2} \times D_{FLX}^{ClONO2}(i,t) + CF^{HOCl} \times D_{FLX}^{HOCl}(i,t)\right)}{CF^{BrCl}} \end{cases}$	$\left.\begin{matrix} RE_{N/S}^{XY}(Cl^-) = 0.36 \\ RE_{N/S}^{XY}(Br^-) = 0.30 \end{matrix}\right\} \quad ; \quad CF^{spec} = \frac{1.0 \times 10^{12} \times 86400}{MW_{spec}}$
	$\left.\begin{matrix} RE_{N/S}^{XY}(Cl^-) = 0.20 \\ RE_{N/S}^{XY}(Br^-) = 0.30 \end{matrix}\right\} \quad ; \quad CF^{spec} = \frac{1.0 \times 10^{12} \times 86400}{MW_{spec}}$
$F_{HET}^{Cl2}(i,t) = RE_{N/S}^{XY} \times \frac{\left(CF^{ClONO2} \times D_{FLX}^{ClONO2}(i,t) + CF^{HOCl} \times D_{FLX}^{HOCl}(i,t)\right)}{CF^{Cl2}}$	$RE_{N/S}^{XY} = 0.1 \quad ; \quad CF^{spec} = \frac{1.0 \times 10^{12} \times 86400}{MW_{spec}}$
	$RE_{N/S}^{XY} = 0.075 \quad ; \quad CF^{spec} = \frac{1.0 \times 10^{12} \times 86400}{MW_{spec}}$

[&]The left column on the table present the individual expression for the indirect recycling emission of each di-halogen species based on Eq. (2).D_{FLX}^{XONO2} and D_{FLX}^{HOX} represent the dry depositional flux of halogen nitrates and hipo-halogenated acids computed at the lower

boundary, respectively, for each model gridpoint and time of the day; CF^{XONO2} and CF^{HOX} are the conversion factors from mass flux (e.g., kg m^{-2} yr^{-1}) to molecular flux (e.g., nmol m^{-2} day^{-1}) for each deposited species, and CF^{XY} is the equivalent inverse factor for converting nmol m^{-2} day^{-1} to kg m^{-2} yr^{-1}; $RE_{N/S}{}^{XY}$ is the adjusted recycling efficiency for the release of each XY di-halogen source within each polar region. The expression is only computed whenever *icefrac(i)* > 1. See the text for further details.

#The adjusted parameters for each expression on the left column are provided for the NH (top) and SH (bottom). The $RE_{HN/S}{}^{XY}$ factor is adimensional and represent relative fractions between 0 (zero) and 1 (one). $CF^{spec} = \frac{1.0 \times 10^{12} \times 86400}{MW_{spec}}$; where MW_{spec} is the molecular weight for each halogen species in g mol^{-1}; 86400 s day^{-1}; 1 × 103 g kg^{-1} and 1 × 109 nmol mol^{-1}.

Table 1c. Direct NO_2 emissions from sea-ice implemented in the polar module

$F_{ICE}^{NO2}(i,t) = F_0 \times H_{N/S} \times \frac{\cos(SZA(i,t))}{\max_{SZA}}$	$F_0 = 1.27 \times 10^8$; $H_{N/S} = 1.0$; $\max_{SZA} = 0.30$
	$F_0 = 1.16 \times 10^8$; $H_{N/S} = 1.1$; $\max_{SZA} = 0.30$

&The left column on the table present the individual expression for each halogen species emitted from the sea-ice surface based on Eq. (3). F_0 is the initial surface flux; $H_{N/S}$ is a hemispheric factor; *cos(SZA(i,t))* is the cosine of the SZA at each model gridpoint and time of the day; max_{SZA} are the adjusted maximum sea-ice extension and radiation imposed to normalize the emission strength. The expression is only computed whenever *icefrac(i)* > 1. See the text for further details.

#The adjusted parameters for the expression on the left column are provided for the NH (top) and SH (bottom). Units for F_0 are molec. cm^{-2} s^{-1}. All the remaining parameters are adimensional and represent relative fractions between 0 (zero) and 1 (one).

Table 2. Description of the polar sources considered in each model experiment.

Sources[&] Experiments	Global Emissions			Polar Module	
	FVSL	FSSA	FOCN	FICE	FHET
VSL^{noPM}	Yes	Yes	Yes	No	No
VSL^{PM-on}	Yes	Yes	Yes	Yes	Yes
VSL^{PM-ind}	Yes	Yes	Yes	No	Yes

[&]Within the Global Emissions, F_{VSL} represents oceanic VSL emissions, F_{SSA} is the sea-salt dehalogenation and F_{OCN} is the inorganic iodine oceanic flux. The additional sources implemented in the polar module are the direct sea-ice source (F_{ICE}) and the indirect heterogeneous recycling (F_{HET}). See the main text for details.

Table 3. Arctic and Antarctic Stations and Measurements used for model validation

Station	Lat/lon	Measured species	Reference	Period measurements
Admundsen Gulf	71N/123'73W	BrO	(Pöhler et al., 2010)	2008
Alert	82.3N/62.2W	BrO	(Honninger and Platt, 2002) (Morin et al., 2005)	2000 2004
Barrow	71.19N/156.37W	BrO	(Brooks et al., 2006) (Liao et al., 2012)	2002 2009
Zeppelin	78.98N/11.89E	BrO	(Martinez et al., 1999) (Tuckermann et al., 1997)	1995 1996 1995-1996
		IO	(Tuckermann et al., 1997)	1996
		ClO	(Tuckermann et al., 1997)	
Halley	75.35S/26.39W	BrO	(Saiz-Lopez et al., 2007)	2004-2005 2004-2005
		IO	(Saiz-Lopez et al., 2007)	
Dumont D'Urville	66.39S/140E	IO	(Grilli et al., 2013)	2012
Scott	77.82S/166.58E	BrO IO	Timothy Hay Timothy Hay	2006-2007 2006-2007

Table 4. Halogen Annual Emission flux arising from each of the independent sources implemented in the polar module

Halogen Species / Source[&]	Antarctica			Arctic		
	Chlorine	Bromine	Iodine	Chlorine	Bromine	Iodine
F_{ICE}	13.4	121.1	59.6	21.5	194.0	0.07
F_{HET}	9.9	49.6	14.2	18.3	125.5	4.5
$Total_{POLAR}$	23.4	170.7	73.8	39.8	319.5	4.6
F_{OCN}^{I}	0.0	0.0	4.2	0.0	0.0	26.9
F_{VSL}^{srf}	0.2	0.6	3.1	0.4	1.0	4.6
F_{SSA}^{srf}	4.8	6.3	0.0	7.2	16.2	0.0
$Total_{SRF}$	28.4	204.4	81.1	47.4	426.7	36.1
F_{VSL}^{trop}	2.8	21.3	32.7	5.0	27.0	32.6
F_{SSA}^{trop}	50.8	51.2	0.0	61.5	76.8	0.0
$Total_{TROP}$	76.9	270.1	110.7	106.2	513.4	64.1

[&]All values are given in Gg X yr^{-1}, where X stands for Cl, Br and/or I. Each shaded row shows the sum of the flux strength of the above non-shaded lines. $Total_{POLAR}$ = F_{ICE}+F_{HET}, i.e., the direct + indirect polar sources. $Total_{SRF}$ are the original sources implemented in CAM-Chem integrated within the surface of each polar cap. $Total_{TROP}$ quantifies the atomic halogen flux integrated within the whole troposphere for each polar cap.

KOPRI 극지연구소

Table 5. Depositional Flux and individual contribution of each species to the total recycling flux for each halogen family.

Region/Experiment / Halogen Source	Antarctic						Arctic					
	Chlorine		Bromine		Iodine		Chlorine		Bromine		Iodine	
	VSL^{PM-on}	VSL^{PM-ind}	VSL^{PM-on}	VSL^{PM-ind}	VSL^{PM-on}	VSL^{PM-ind}	VSL^{PM-on}	VSL^{PM-ind}	VSL^{PM-on}	VSL^{PM-ind}	VSL^{PM-on}	VSL^{PM-ind}
D_{FLX}^{ox} (Gg X yr^{-1})[&]	4.5	3.9	45.4	4.0	17.1	1.6	6.7	3.2	83.7	9.4	3.2	3.3
D_{FLX}^{red} (Gg X yr^{-1}) [&]	18.7	7.5	70.8	3.2	0.8	0.1	30.4	7.1	151.9	6.3	0.1	0.1
F_{HET} (Gg X yr^{-1}) [&]	9.9	3.0	49.6	6.5	14.2	1.3	18.3	3.8	125.5	16.4	4.5	4.7
Cl_2 / Br_2 / I_2 (%)[$]	14.7	42.0	54.2	35.4	41.7	41.7	16.3	36.5	71.8	61.0	50.0	50.0
$BrCl^{(Br)}$ / $BrCl^{(Br)}$ / IBr (%)[$#]	72.2	20.7	32.5	21.2	58.3	58.3	72.9	39.1	23.9	20.3	50.0	50.0
$BrCl^{(Cl)}$ / $BrCl^{(Cl)}$ / none (%)[$#]	13.1	37.3	5.9	38.2	-	-	10.8	24.3	3.6	12.7	-	-
None / IBr / none (%)[$]	-	-	7.4	5.2	-	-	-	-	0.8	6.0	-	-

[&]The depositional fluxes of oxidized and reservoir species, as well as the overall heterogeneous recycling flux, are given in absolute units of Gg X yr^{-1}, where X stands for Cl, Br and/or I.

[$]The relative contribution of each halogen species to the overall annual heterogeneous recycling flux (F_{HET}) is given as percentage (%). The halogen source column indicate, in order, the exact species that represent each tabulated column for the three halogenated species, i.e. Cl_2 / Br_2 / I_2 indicates in order, that the percentage for the Chlorine flux is in the form of Cl_2, for the Bromine flux is in the form of Br_2 and for the Iodine flux is in the form of I_2. The term “none” is given to indicate that we do not consider ICl emissions within the polar module.

[#]For the case of BrCl recycling emissions, $BrCl^{(Br)}$ indicate that the BrCl release arises from the deposition and recycling of oxidized bromine reservoirs that captures a chloride anion within the sea-ice ($BrONO_2$/HOBr + Cl^- à BrCl), while $BrCl^{(Cl)}$ indicate that the BrCl release arises from the deposition and recycling of oxidized chlorine reservoirs that captures a bromide anion within the sea-ice ($ClONO_2$/HOCl + Br^- à BrCl). See text for details.

Table 6. Additional sea-ice NOx Sources implemented in the polar module

	Antarctica			Arctic[&]		
	NO	NO_2	NOx	NO	NO_2	NOx
FNOx (Gg N yr^{-1})	7.7	122.9	130.7	94.2	73.2	167.3
FNOx (%)	6	94	100	56	44	100

[&]Surface NO sources (F_{NO}) within the Arctic has been computed neglecting the oceanic and continental contributions of NO emissions (i.e., by imposing an icemask). If the icemask is not considered, the overall F_{NO} strength within the NH polar cap reaches 5.3 Tg N yr^{-1}.

Table 7. Seasonal evolution of polar emissions for each independent source

Region	Antarctic[&]												Arctic[&]											
Species	Chlorine				Bromine				Iodine				Chlorine				Bromine				Iodine			
Season	Su	Fa	Wi	Sp	Su	Fa	Wi	Sp	Su	Fa	Wi	Sp	Wi	Sp	Su	Fa	Wi	Sp	Su	Fa	Wi	Sp	Su	Fa
F_{ICE} (Gg X yr^{-1})	13.4				121.1				59.6				21.5				194.0				0.1			
FICE (%)	30	5	6	58	30	5	6	58	24	2	8	66	2	41	53	4	2	41	53	4	2	66	32	0
F_{HET} (Gg X yr^{-1})	9.9				49.6				14.2				18.3				125.5				4.5			
F_{HET} (%)	21	12	20	47	23	10	15	52	32	4	7	58	3	32	57	7	2	31	60	7	6	32	54	9
F_{VSL}^{trop} (Gg X yr^{-1})	2.8				21.3				32.7				5.0				27.0				32.6			
F_{VSL}^{trop} (%)	33	16	15	36	34	12	9	46	38	17	12	33	10	31	44	16	8	41	38	13	13	28	39	20
F_{SSA}^{trop} (Gg X yr^{-1})	50.8				51.2				0.0				61.5				76.8				0.0			
$F_{SSAtrop}$ (%)	14	23	28	34	19	15	10	56	-	-	-	-	27	45	10	18	15	53	16	15	-	-	-	-

[&]The top line on each row presents the annual mean flux strength for each independent source in Gg X yr^{-1}, where X stands for Cl, Br and/or I. The bottom line indicates the percentage of the total annual flux released within each independent season. Su, Wi, Fa and Sp stands for Summer, Winter, Autumn/Fall and Spring.

Table 8. Statistical Analysis of CAM-Chem performance in reproducing BrO observations in the Arctic and Antarctica

	Observed			Model			Mod-Obs		
	Mean	Max	St dev	Mean	Max	St dev	Bias	NMB	NME
Admundsen	11.37	16	4.49	9.40	16.77	6.16	-3.08	-0.37	0.63
Alert MAX-DOAS	3.67	4.5	2.26	5.88	10	2.56	2.21	0.38	0.5
Alert LP-DOAS	7.99	17.3	4.91	8.49	17.1	7.42	0.5	0.06	0.66
Barrow	10.89	27	8.17	7.17	22	7.01	-3.62	-0.5	1.23
Zeppelin	5.51	17.5	3.84	7.20	17.84	5.84	1.69	0.24	0.64
Halley	2.66	7.13	2.06	1.66	14.6	2.66	1	0.6	1.23
Scott Base	3.04	7.49	1.44	2.08	6.8	2.39	-0.97	-0.47	1.11

Table 9. Statistical Analysis of CAM-Chem performance in reproducing IO observations in the Arctic and Antarctica

	Observed			Model			Mod-Obs		
	Mean	Max	St dev	Mean	Max	St dev	Bias	NMB	NME
Zeppelin	1.69	3.5	0.83	0.81	4.44	0.95	-0.88	-0.85	2.94
Halley	2.70	16.6	2.88	1.88	5.69	1.71	-0.95	-0.54	0.92
Scott Base	1.43	2.28	0.43	1.00	2.51	0.65	-0.42	-0.62	0.65

극지연구소

Table 10. Statistical analysis of the CAM-Chem ability to reproduce the BrO tropospheric columns observed by GOME-2 in the Arctic stations

	Observed			Model			Mod-Obs		
	Mean	Max	St dev	Mean	Max	St dev	Bias	NMB	NME
Admudsen	1.55×10^{13}	2.80×10^{13}	9.63×10^{12}	1.13×10^{13}	2.03×10^{13}	9.66×10^{12}	-3.66×10^{12}	-0.31	0.32
Barrow	1.46×10^{13}	2.95×10^{13}	1.19×10^{13}	1.36×10^{13}	3.40×10^{13}	1.15×10^{13}	-2.61×10^{11}	-0.02	0.26
Alert	1.12×10^{13}	1.90×10^{13}	5.78×10^{12}	1.26×10^{13}	3.10×10^{13}	9.24×10^{12}	1.41×10^{12}	0.11	0.27

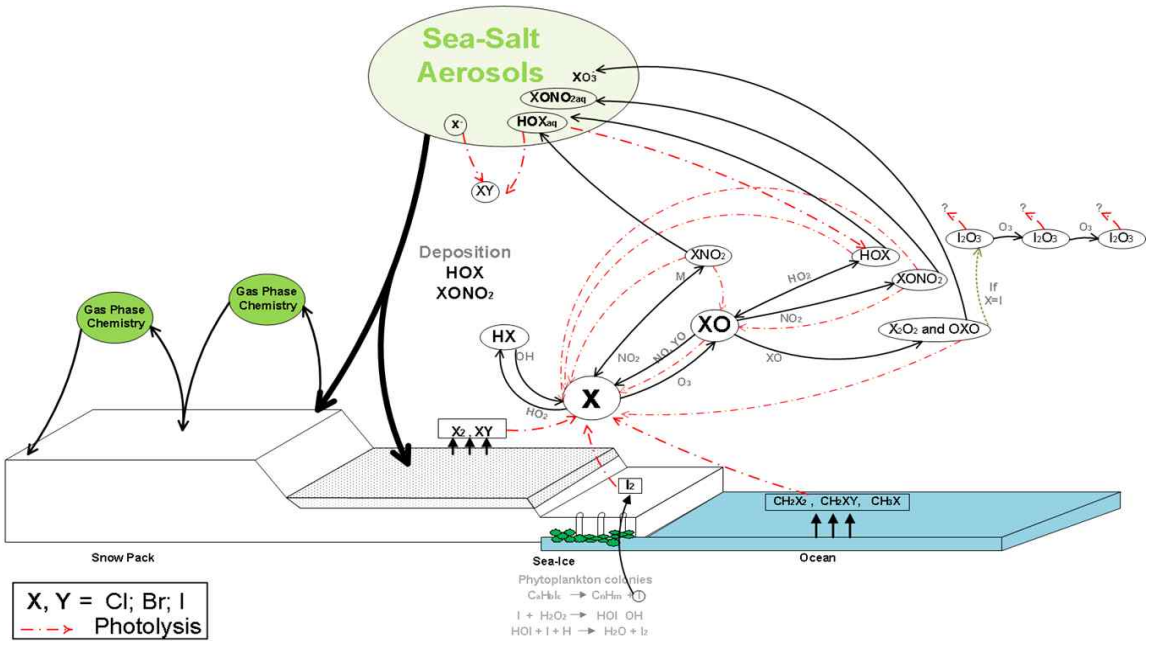

Figure 1. Schematic representation of the direct and indirect halogen sources, gas-phase and heterogeneous-phase chemistry implemented in the polar module.

Figure 2. Geolocation of the Antarctic and Arctic Stations used for model validation. The red line encircles the NH and SH polar caps.

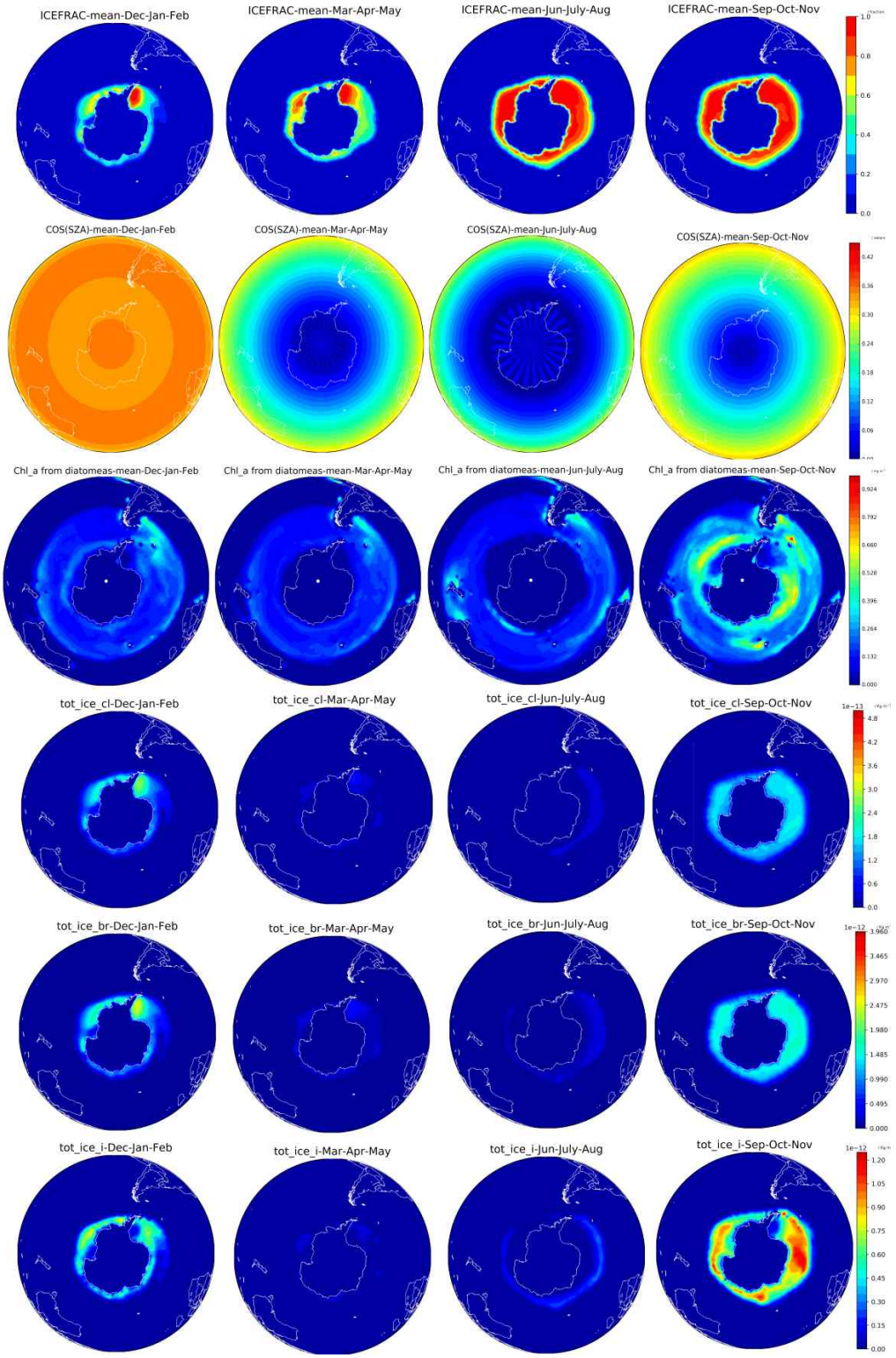

Figure 3. Geographical distribution of the direct Sea-ice Flux (F_{ICE}) and the main geophysical variables affecting the source strength for the SH. Each column presents results for each different season. For the case of the geophysical parameters (icefraction, cos(SZA) and chl-a, each independent row represents the seasonal mean of each magnitude, while F_{ICE}^{XY} panels for each halogen family have been computed by adding the monthly emissions for the three months on each season.

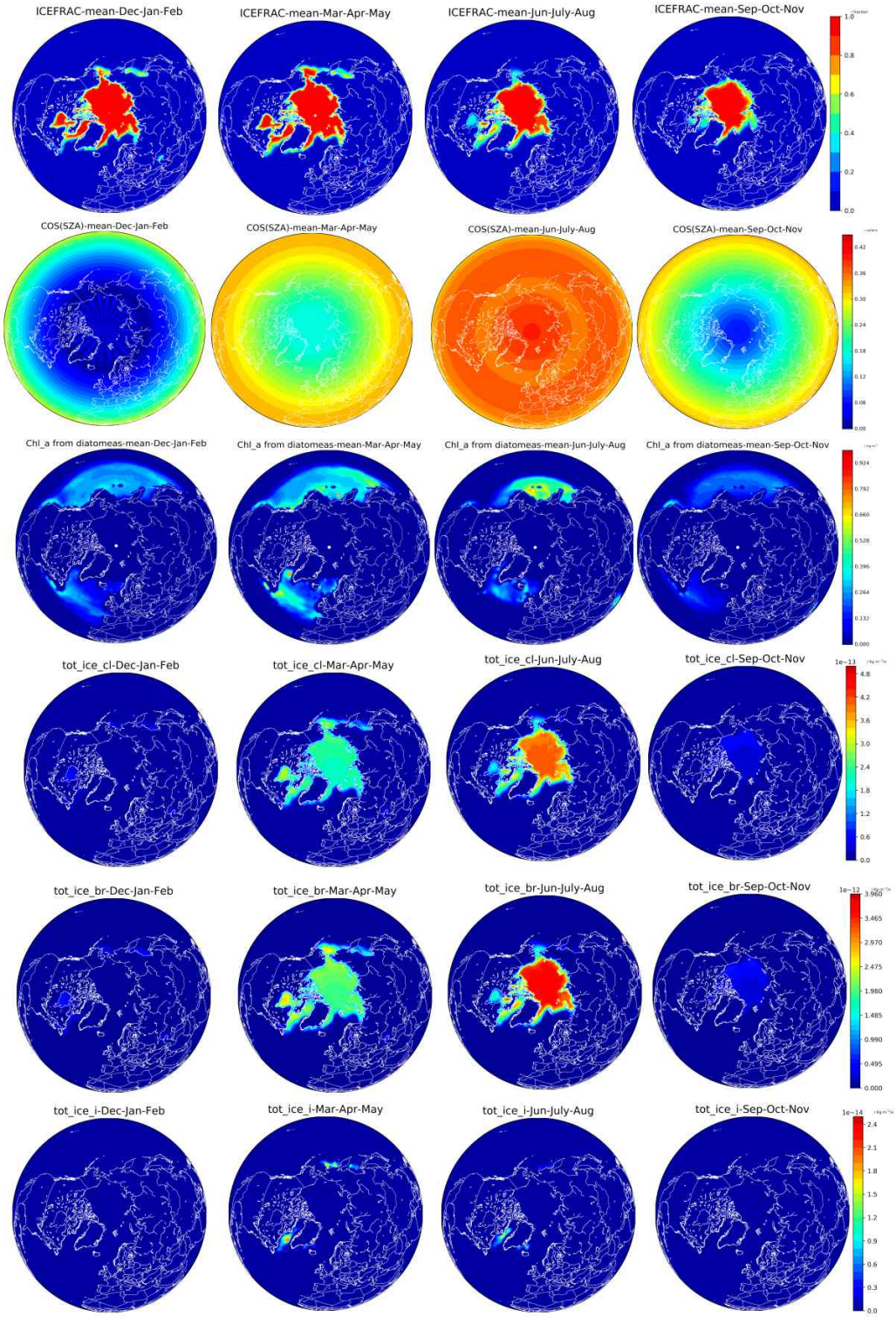

Figure 4. Idem to Fig. 3, but for the NH

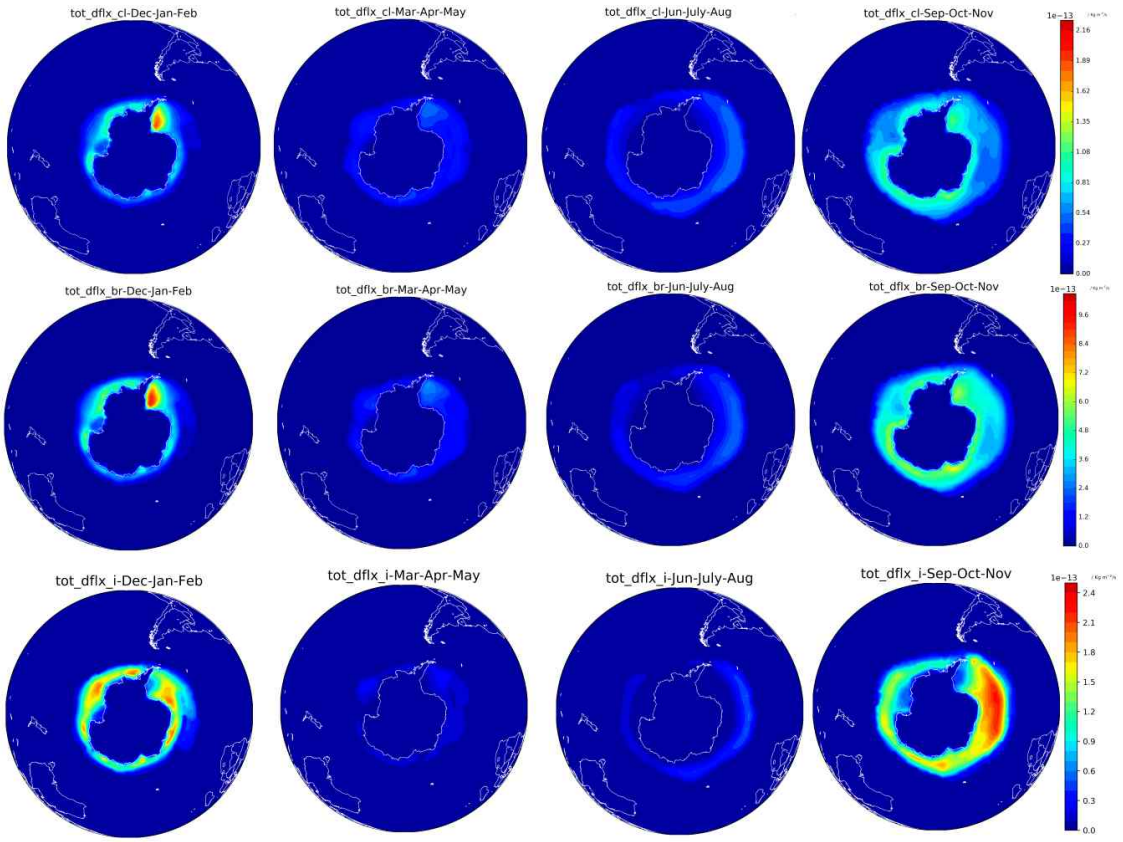

Figure 5. Seasonal distribution of the indirect heterogeneous recycling Flux (F_{HET}) within the SH. The flux strength within each panel has been computed by adding the monthly emissions for the three months on each season. The contribution of all individual species for each halogen families has been added altogether (e.g., $F_{HET}^{Br} = F_{HET}^{Br2}+F_{HET}^{BrCl}+F_{HET}^{IBr}$). The percentage contribution of each individual species is shown in Table 5.

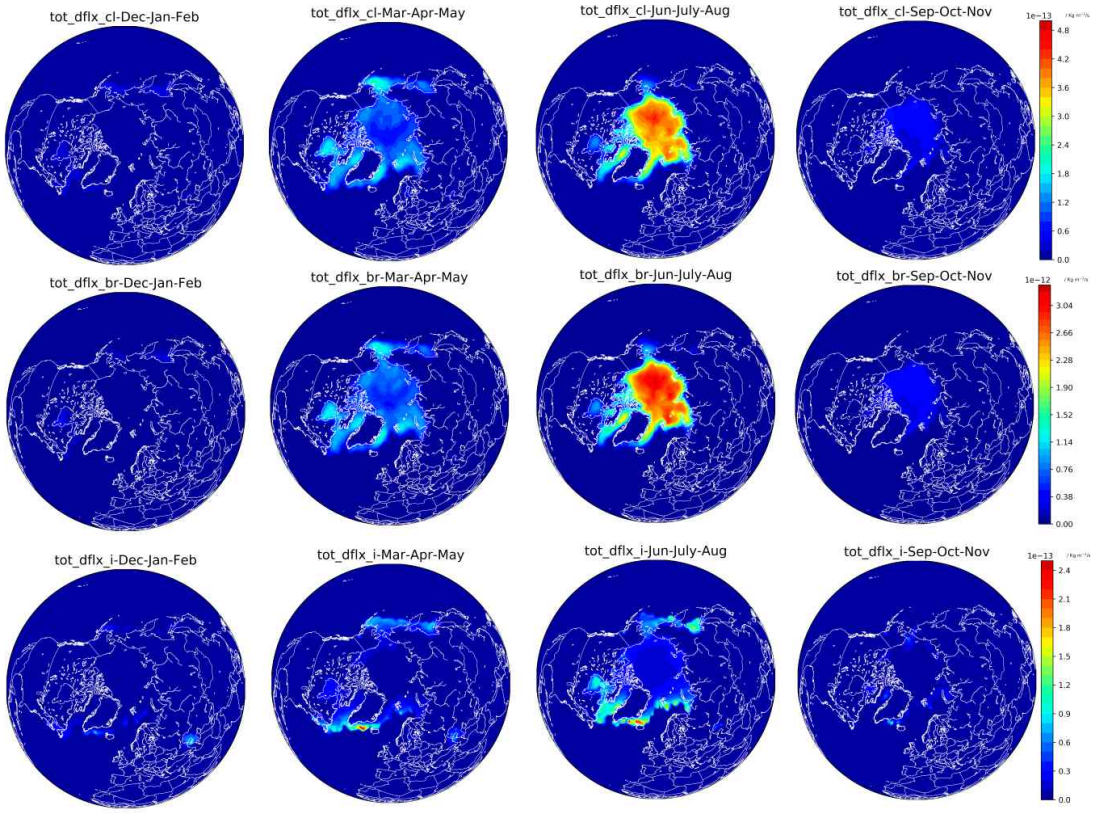

Figure 6. Idem to Fig. 5, but for the NH.

KOPRI
극지연구소

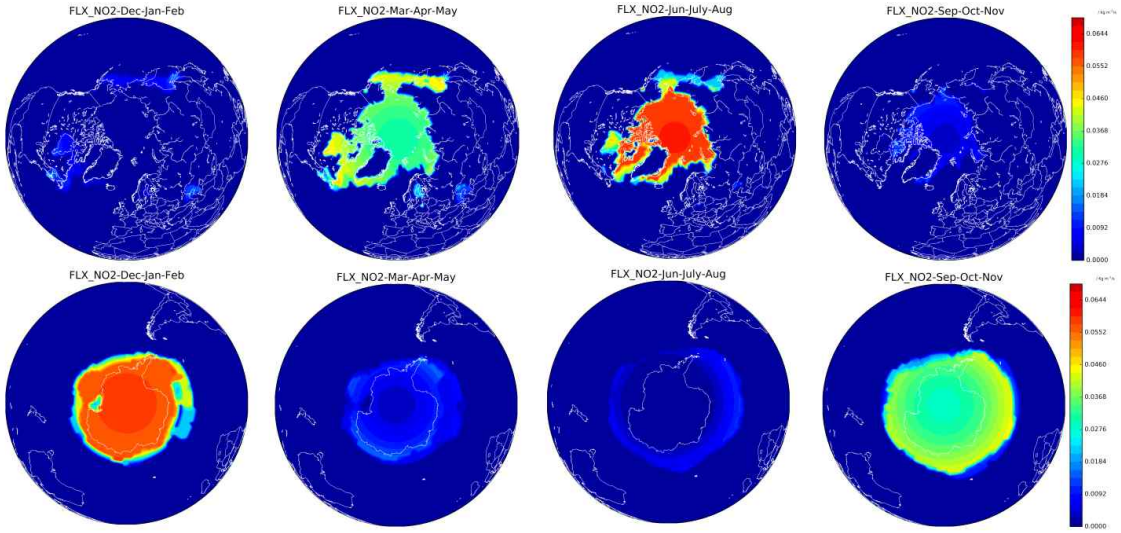

Figure 7. Seasonal distribution of the nitrogen dioxide source (F_{NO2}) within the NH (top) and SH (bottom). The flux strength within each panel has been computed by adding the monthly emissions for the three months on each season.

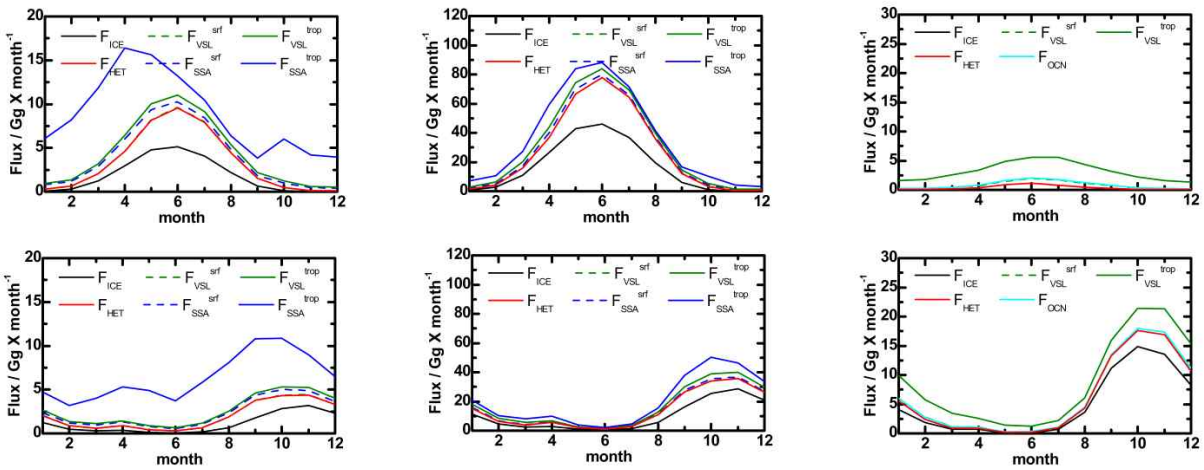

Figure 8. Annual seasonal cycle of direct and indirect emissions from the sea-ice surface, VSL photodecomposition and sea-salt recycling. Each column shows the flux strength of each individual source for Chlorine (left), Bromine (middle) and Iodine (right) within the NH (top) and SH (bottom). The total seasonal flux has been computed by adding the contribution of each independent source (one at a time for each line) in the following order: Flux = F_{ICE}+F_{HET}+F_{OCN}+F_{VSL}^{srf}+F_{SSA}^{srf}+ F_{VSL}^{trop}+F_{SSA}^{trop}. The overall annual emissions and the percentage contribution within each season are given in Table 4 and 7, respectively.

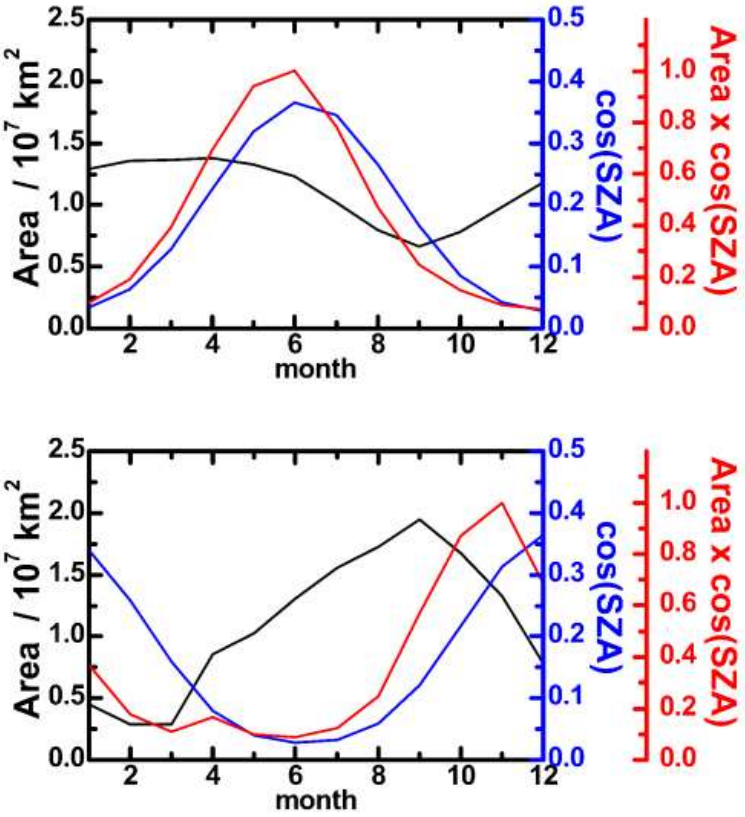

Figure 9. Annual seasonal cycle of the main geophysical parameters affecting the source strength of each halogen source within the NH (top) and SH (bottom). The left column present the total sea-ice area integrated within each polar cap, while the right panels show the monthly mean cos(SZA), representing the intensity of radiation within each polar region,

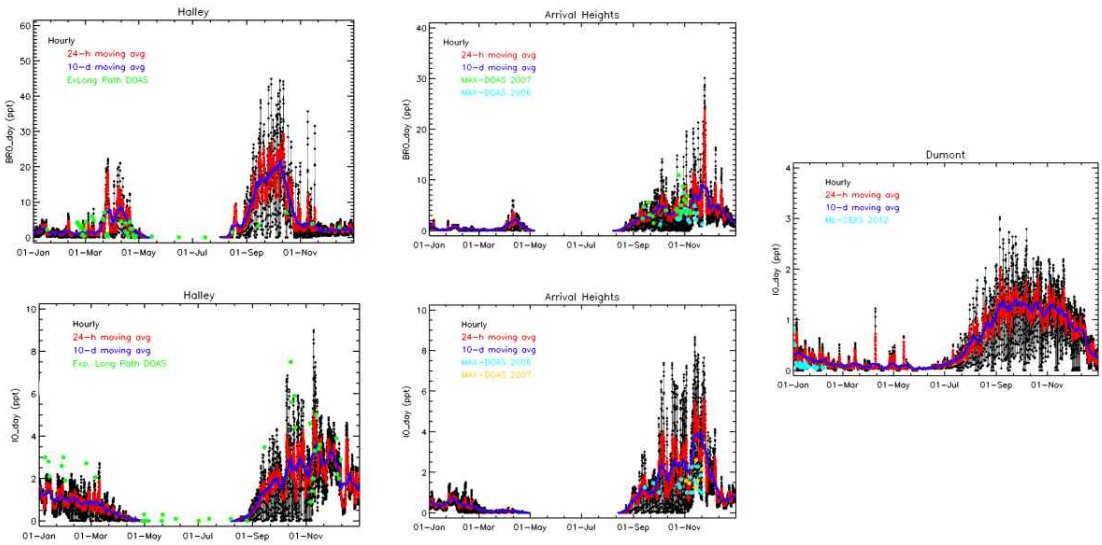

Figure 10. Annual variation of the halogen oxides measured at different SH polar stations. The hourly concentrations, 24-hours moving averages and 10-day moving averages of modelled XO are indicated by a black dot line, red solid line and blue solid line, respectively. Observations are superposed with colored circles.

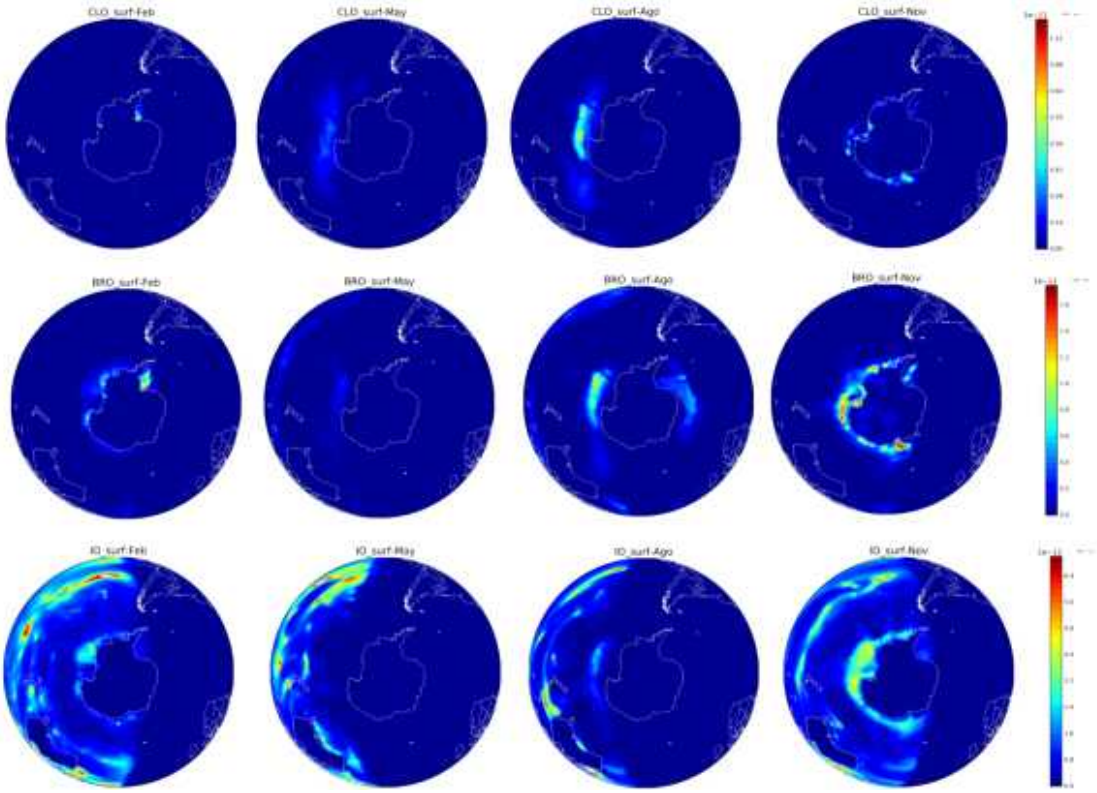

Figure 11. Geographical distributions of ClO (top), BrO (middle) and IO (bottom) surface mixing ratios for the different seasons within the SH. The monthly mean of the central month within each season has been selected. A latitudinal mask has been imposed to the figure to highlight results poleward of 60°S.

KOPRI
극지연구소

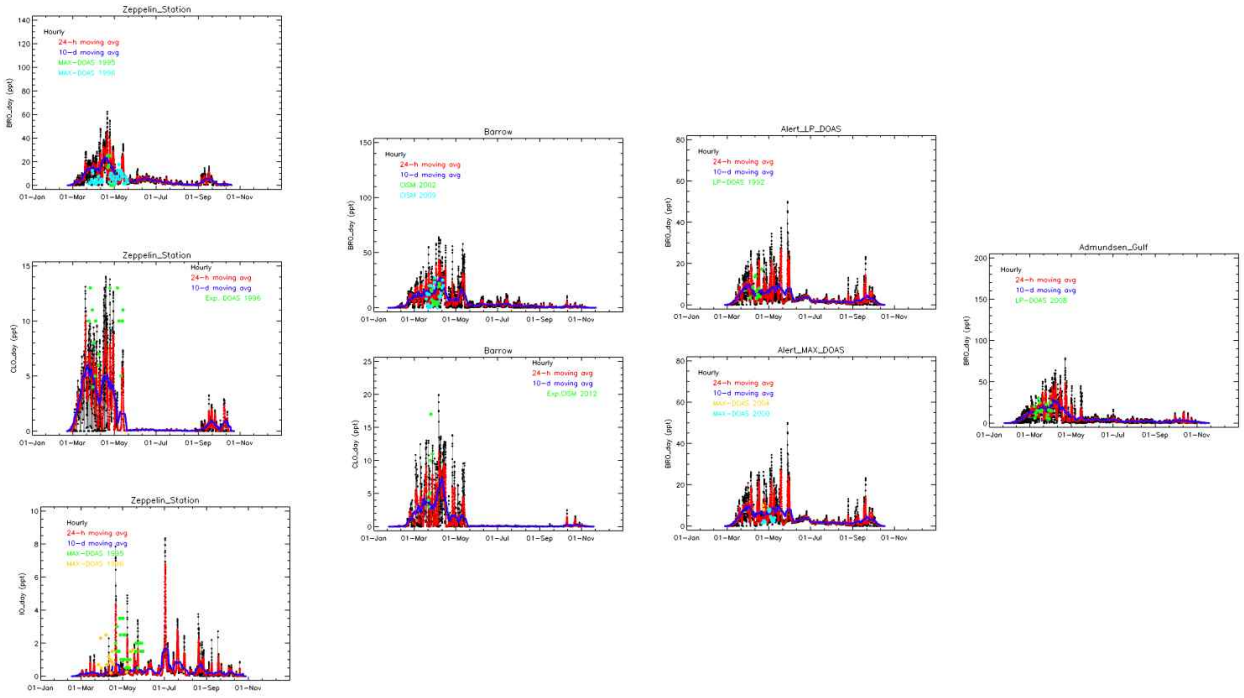

Figure 12. Idem Fig. 10 but for Arctic stations.

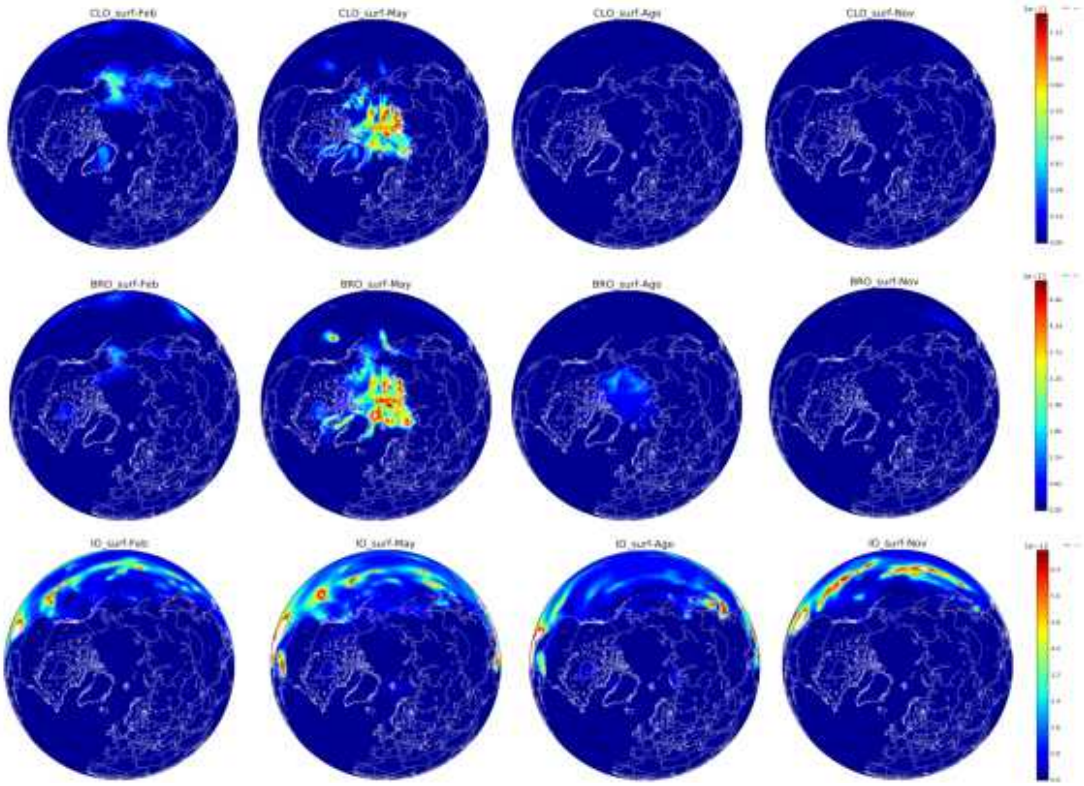

Figure 13. Idem to Fig. 11, but for the NH.

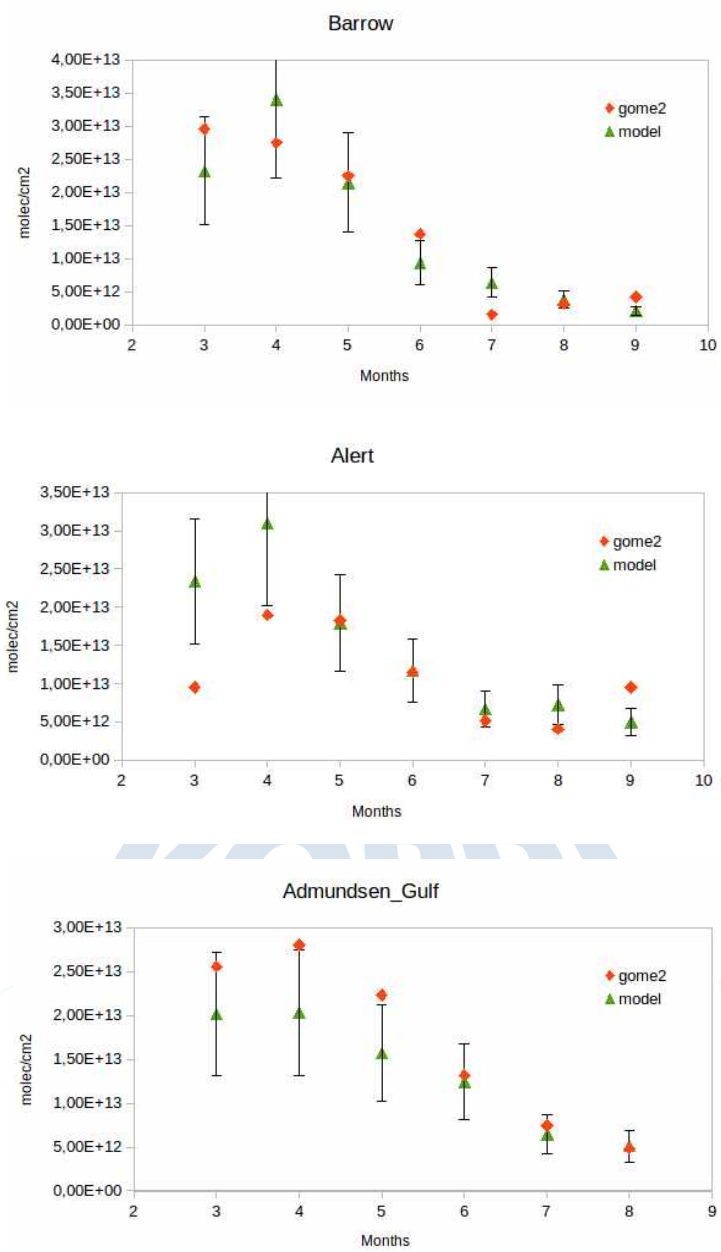

Figure 14. Monthly variation (averaged from 2007 to 2011) of tropospheric bromine oxide VCD measured from GOME-2 at different NH polar stations (in red), and modelled values in the same locations (green dots). Error bars in the modelled values correspond to the standard deviation.

제 18 절. Optimization of Suspect and Non-target Analytical Methods Using GC/TOF for Prioritization of Emerging Contaminants in the Arctic Environment[11)]

Sunggyu Lee[1], Kitae Kim[2], Junho Jeon[3,4], Hyo-Bang Moon[*,1]

[1]Department of Marine Science and Convergence Engineering, Hanyang University
[2]Korea Polar Research Institute
[3]Graduate School of FEED of Eco-Friendly Offshore Structure, Changwon National University
[4]School of Civil, Environmental and Chemical Engineering, Changwon National University

1. Introduction

Numerous chemicals have been manufactured from industrial activities and used as consumer products for humans since the late 18th century. Presently, the Chemical Abstracts Service (CAS) have registered over 145 million chemicals in the database system (CAS, 2019). Although many studies have reported on relationships between chemical exposure and ecotoxicological effects, only a few chemicals have been regulated by international and domestic authorities. It is essential to establish the legislative actions and regular monitoring programs on the chemicals with risks posed to the environment as well as humans. Prioritization is the first step for the monitoring and/or regulation of existing chemicals in the environment. The purpose of prioritization is to designate certain chemicals as either high-priority or low-priority for further risk evaluation. However, targeted analytical method is not enough for the prioritization of environmental contaminants because it always misses non-targeted compounds in environmental samples during experimental procedure and instrumental analysis. In addition, the measured concentrations of target contaminants are not sufficient to account for their whole toxicity in environmental samples (Hong et al., 2016; Simon et al., 2013; Yue et al., 2015).

Accurate measurement of contaminants in environmental samples is a difficult task because the environmental sample matrix such as air, water, soil, and sediment is complex. Despite this, targeted analytical methods have been successfully developed for several decades and provide a good sensitivity and reliable identification and quantification of contaminants existed as trace levels. To date, many scientific approaches have been

11) 이 연구는 본 과제 지원으로 수행되었으며 그 결과는 다음의 논문으로 출판되었음: Sunggyu Lee1, Kitae Kim2, Junho Jeon3,4, Hyo-Bang Moon*,1, “Optimization of suspect and non-target analytical methods using GC/TOF for prioritization of emerging contaminants in the Arctic environment”, *Ecotoxicol. Environ. Saf.*, 2019, 181, 11-17.

developed and upgraded for monitoring of organic contaminants in the environment using gas chromatography (GC) and liquid chromatography (LC) based on mass spectrometry (MS) (Hernández et al., 2015; Park et al., 2018). Recent advances in analytical instrumentation have resulted in the evolution of a high-resolution MS (HRMS) coupled with GC or LC to accurately measure mass of target contaminants (Zhang et al., 2014). Non-target analysis is a new analytical tool to detect all of existing chemicals in environmental samples (Hernández et al., 2015). Time-of-flight (TOF)/MS was recently introduced for non-target analysis, which enables to measure the entire mass spectrum of chemicals with a greater sensitivity than standard quadrupole MS (Moschet et al., 2018; Zhang et al., 2014). In addition, the TOF/MS has been applied for prioritization of contaminants with analytical data processing from environmental samples for a specific site (Guyader et al., 2019).

The Arctic is far away from contamination sources such as industrial and agricultural activities. The Arctic Monitoring and Assessment Program (AMAP) was designated the persistent organic pollutants (POPs) and mercury (Hg) as priority pollutants to disturb the Arctic ecosystems (AMAP, 2016). Contamination by POPs and Hg in the Arctic environment is mostly originated from long-range transport through atmosphere and ocean from low latitudes (Wania, 2003; Gouin et al., 2004). Considering the huge production and consumption of a variety of chemicals, emerging contaminants could be one of important threats to the Arctic ecosystem. Presence of certain chemicals in the Arctic where there is no local source implies an evidence of ubiquitous characters in a global scale. In the present study, the suspect and non-target analytical methods were optimized with a GC/TOF to identify the wide ranges of chemicals existed in multiple environmental samples from the Arctic region. This is the first study to report a scientific-based procedure to prioritize emerging contaminants in the Arctic environment based on suspect and non-target analysis of GC/TOF.

2. Materials and Methods

2.1. Standards and reagents

All standards were obtained from Accustandard (New Haven, CT, USA), Dr. Ehrenstorfer GmbH (Augsburg, Germany), Sigma-Aldrich (St. Louis, MO, USA), Tokyo Chemical Industries America (Portland, OR, USA), Wako Pure Chemicals (Tokyo, Japan), and Wellington Laboratories (Guelph, ON, Canada). The detailed information on all standards used in our study are summarized in Table S1 as Supplementary Materials. Ultra-residue analysis grade hexane and dichloromethane (DCM) were obtained from J.T. Baker (Phillipsburg, NJ, USA). Bio-beads S-X3 for gel permeation chromatography (GPC) was purchased from Bio-Rad Laboratories (Hercules, CA, USA). Sep-Pak Vac C_{18} (500 mg/6

cc), silica gel (1 g/6 cc), florisil (500 mg/6 cc), and Oasis HLB (150 mg/6 cc) cartridges were purchased from Waters (Milford, MA, USA). Nonane (reagent plus grade, 99%) and Granular copper (ACS reagent, 10-40 mesh, ≥ 99.9%) were obtained from Sigma-Aldrich.

2.2. Sample collection

Environmental samples such as seawater, sediment, soil, sludge, and iceberg were collected from Ny-Ålesund, Svalbard during July 2016. Forty liters of surface seawater samples (n=4) were collected in pre-cleaned PP bottles using a stainless steel basket. Water samples were filtered using a glass fiber filter (GF/F, Whatman, 47 mm diameter, >0.7 μm). The filtrate (dissolved phase) was used in a further pretreatment step. Surface sediment samples (n=4) were collected using a Van-veen grab sampler from a research vessel, and soil samples (n=7) were collected using a stainless steel spoon after washing. Sludge sample was taken directly from a wastewater treatment plant (WWTP) located at research stations of Kings Bay. Iceberg sample was also collected near the shoreline of Kings Bay. After washing iceberg samples with distilled water, it was melted at a room temperature and then treated as seawater samples. Particulate matter samples (n=3) from ambient air were collected from Zeppelin station in Ny-Ålesund, Svalbard, using a high volume air sampler (HV-RW, Sibata, Saitama, Japan) between April and September 2015. The detailed information on the sampling information are summarized in Table S1 and the sampling locations are presented in Figure S1. The collected samples were individually wrapped in a pre-cleaned aluminum foil and then kept in a refrigerator. All samples were transported to the laboratory and kept in a freezer at -20 °C until analysis.

2.3. Experimental procedures

Water samples including filtered seawater and melted iceberg were extracted by a solid phase extraction (SPE) cartridge, which was pre-washed with 50% DCM in hexane and conditioned with Milli-Q water. Sediment (~10 g), soil (~10 g), filter paper of ambient air, and sludge (~1 g) were extracted in a Soxhlet apparatus with 200 mL of 25% DCM in hexane for 16 h (Hernández et al., 2015; Moon et al., 2008). Activated copper was added into the extracts to remove sulfur and then the extracts were concentrated to approximately 1 mL using a rotary evaporator. To select the clean-up method, the efficiency was tested and compared with different kinds of SPE sorbents such as HLB (150 mg), C_{18} (500 mg), silica gel (1 g), and florisil (500 mg) in the cartridges. After the clean-up procedure of extracts with the SPE cartridge, the eluants were concentrated to approximately 1 mL and then dried at a room temperature. The residues were dissolved in 100 μL of nonane for instrumental analysis.

2.4. GC/TOF analysis and software for data processing

A gas chromatography (7890B; Agilent Technologies, Santa Clara, CA, USA) coupled to a time-of-flight (7200; Agilent Technologies) (GC/TOF) was used for suspect and non-target analysis for multiple environmental samples. A nitrogen generator (NM32LA; Peak Scientific, Billerica, MA, USA) was used to support the collision cell work. A DB-5MS (30 m length, 0.25 mm inner diameter, 0.25 μm film thickness) capillary column was used to separate organic contaminants existed in the samples. The oven temperature was programmed from 80 °C for 1 min and increased to 200 °C at 10 °C/min, and then finally ramped at 5 °C/min to 300 °C and held for 5 min. The carrier gas used was helium at a constant flow rate of 1 mL/min. The TOF/MS was operated under the positive electron ionization (EI) mode at 70 eV. The ranges of TOF/MS used in our study ranged from 35 to 1,000 as mass-to-charge (m/z) at 100 mS/spectrum. The MS resolution was obtained as approximately 13,000 at m/z 131 and 17,000 at m/z 502 under a high resolution mode of 4 GHz. MS-analysis grade perfluorotributylamine (PFTBA) was used for a mass calibration, which was conducted every sample for obtaining accurate mass in the samples. Helium was introduced into ion source as an internal reference mass (IRM) correction during the TOF analysis. The temperatures of transfer line and ionization source were maintained at 280 °C and 230 °C, respectively. A solvent delay of 4 min was used to prevent damages to the capillary column and filament of ion source. MassHunter Quantitative Analysis B.07.04 and Unknown Analysis B.07.01 (Agilent Technologies) were used for analytical data processing. The National Institute of Standards and Technology (NIST) library (ver. 2014) was also used for identifying the unknown compounds detected in the samples.

3. Results and Discussion

3.1. Establishment of in-house library for suspect analysis

A total of 215 compounds were selected as target contaminants of in-house library for suspect analysis using a GC/TOF. These contaminants are mostly comprised of the POPs and pseudo-POPs reported for the occurrence in low latitude and/or the Artic environments (AMAP, 2016, 2017a, 2017b; Rigét et al., 2010). Some of POPs include polychlorinated dibenzo-*p*-dioxins and furans (PCDD/Fs), dioxin-like polychlorinated biphenyls (DL-PCBs), non-dioxin-like PCBs, organochlorine pesticides (OCPs; e.g., DDTs, HCHs, and chlordanes), polybrominated diphenyl ethers (PBDEs), polychlorinated naphthalenes (PCNs), chlorobenzenes (CLBs), and polycyclic aromatic hydrocarbons (PAHs). Several pseudo-POPs such as dechlorane plus (DP), novel brominated flame retardants (NBFRs), organophosphate flame retardants (OPFRs), phthalates, siloxanes, synthetic musk compounds (SMCs), and benzotriazole ultraviolet stabilizers (BUVSs) were included in the present study. The standard solutions of all the contaminants used in our study were diluted at 100 ng/mL

and then injected into a GC/TOF to obtain total ion chromatogram (TIC) of individual contaminant. The detailed information on retention time, mass spectra, qualification ion, and qualifier ion from individual contaminant were used for the identification in the samples using in-house library for suspect analysis (Table S2). Based on the physico-chemical properties of whole contaminants established in-house library, the optimized analytical method in our study covers organic chemicals with properties of molecular weight from 128 to 1500 and logarithm octanol-water partitioning coefficients (log K_{ow}) from 0.81 to 12.0. This indicates that most organic contaminants existed in the environment could be detectable in the present analytical system by a GC/TOF.

3.2. Selection of a clean-up procedure for GC/TOF analysis

Environmental samples such as water, soil, sediment, and sludge are complex matrices such as 'cocktail of chemicals', which result in many inferences for GC-based analysis. Although GC/TOF analysis provides qualitative and quantitative analysis of wide ranges of organic contaminants, the clean-up procedure is an essential procedure for removing matrix effect in environmental samples. However, the clean-up procedure was carefully considered to minimize the loss of many organic contaminants present in real samples for suspect and non-target analysis. In our study, four kinds of cartridges containing different sorbents such as HLB, C_{18}, silica gel, and florisil were compared for clean-up procedures. All SPE cartridges were pre-washed with 12 mL of 50% DCM in hexane and then conditioned with 12 mL of hexane. After loading of native standard solutions into the cartridges, the solutions were eluted with 12 mL of 50% DCM in hexane. The standards are comprised of 215 contaminants with 100-500 ng, depending on the sensitivity for GC/TOF analysis. The eluants were concentrated and dissolved in 100 μL of nonane for instrumental analysis. Overall, the HLB SPE cartridge showed the best recoveries (mean: 78%) for all spiked standards and was chosen for clean-up procedure in our study. Mean recoveries of spiked standards into the blank samples for silica gel, C_{18}, and florisil were 72%, 65%, and 64%, respectively (Table S3). A previous study also used the HLB SPE cartridge for the clean-up procedure for the determination of organic contaminants by the suspect and non-target analysis with GC/TOF (Hernández et al., 2015). To check the efficiency of the HLB SPE cartridge, the TICs before and after clean-up procedure applied in real samples are presented in Figure S2.

3.3. An optimized method of suspect and non-target analysis

A workflow of suspect and non-target analysis for the determination of organic contaminants in environmental samples with a GC/TOF is presented in Figure 1, which is similar to those reported for previous studies (Portolés et al., 2014; Moschet et al., 2018).

After the sample pretreatments including extraction and clean-up procedure with a SPE cartridge, GC/TOF analysis was conducted to obtain a full-scan mass spectrum in the samples. This step is the same procedure with qualitative and quantitative analysis using a GC/MS or a GC/MS/MS. For suspect analysis, the mass spectrum obtained in the samples was firstly matched with qualification and qualifier ions, isotopic ratio, and retention time of standards archived in-house library using MassHunter software (ver. B.07.04). Examples on TIC, mass spectrum, and extracted ion chromatogram in sediment samples are presented in Figure S3. The qualitative ion and qualifier ion ratios at <30% tolerance and retention time ± 0.5 sec were set as acceptable levels for an identification of contaminants from in-house library. After the confirmation of all contaminants from suspect analysis based on in-house library, the non-target analysis was performed to identify unknown compounds detected in the samples with the NIST library. Due to many overlapped chromatograms of TIC in the samples, all TICs were extracted by the Unknown Analysis software (ver. B.07.04) as deconvoluted ion chromatogram (DIC), which is a possible form to match the mass spectrum provided by the NIST library. Each DIC was used for the identification of unknown compound detected in the samples based on the matching score (> 80) of mass spectra archived in the NIST library. A matched mass spectrum of compound detected in sediment samples based on the DIC and NIST library is shown in Figure S4. In our study, the deconvolution conditions were set as follows; 50, 100, 200, 300, and 400 for retention time size factor, minimum numbers of ion peaks >5, and maximum numbers of ion peaks <10 on the Unknown Analysis software. Contaminants detected in procedure blanks were systemically subtracted in the sample batch.

3.4. Application of suspect and non-target analysis for the Arctic environmental samples

Arctic environmental samples such as seawater, air, soil, sediment, iceberg, and sludge were applied for suspect and non-target analysis with GC/TOF. Based on the number of contaminants commonly detected in multiple environmental samples within the same matrix, the highest number of contaminants detected was found for sludge (n=43), followed by seawater (n=34), sediment (n=25), air (n=23), soil (n=19), and iceberg (n=4) (Figure 2). This suggests that discharges of effluents and sludge could be a potential source of organic contamination in the Arctic environment. Our previous studies have reported that WWTP activity is a major source of organic contaminants for the receiving environments (Moon et al., 2008; Lee et al., 2014a, 2014b, 2015). The contaminants detected in different environmental matrices with suspect analysis are presented in Figure 3. The overall contaminant patterns showed that numbers of emerging contaminants were contributable than those of regulated contaminants such as POPs to the total contaminant numbers

detected in the Arctic samples. In our study, the major contaminants were similar for all environmental samples as siloxanes and OPFRs, which collectively accounted for 44-75% of the total numbers of contaminants for each matrix. In particular, cyclic siloxanes such as decamethylcyclopentasiloxane (D5) and dodecamethylcyclohexasilane (D6) were predominantly detected in all environmental matrices, except for air samples. Similar results were reported for the occurrence of siloxanes in multiple environmental samples in the Arctic (Knudsen et al., 2007; Warner et al., 2010; Krogseth et al., 2017). In particular, cyclic siloxanes and lower-molecular-weight linear siloxanes such as decamethyltetrasiloxane (L4), dodecamethylpentasiloxane (L5), and tetradecamethylhexasiloxane (L6) were predominantly detected in air samples, suggesting the long-range atmospheric transport (LRAT) of these contaminants to the Arctic environment. However, considering the presence of siloxanes in sludge, it should be considered as local contamination originated from research station activities in the surveyed regions (Warner et al., 2010; Krogseth et al., 2017). Our findings suggest a widespread contamination by siloxanes in the Arctic environment as concerns of emerging contaminants.

OPFRs and phthalates were the next predominant contaminants in different types of samples from the Arctic environment. However, these contaminants were not detected in iceberg samples. Previous studies have reported the occurrence of OPFRs and phthalates in air, seawater, sediment, and snow of the Arctic environments (Sühring et al., 2016; Li et al., 2017; Ma et al., 2017). Similar to siloxanes, it should be clarified for contamination pathways (either LRAT or local sources) of these contaminants in the Arctic environment. Several emerging contaminants such as SMCs, BUVSs, and NBFRs were also detected in most samples, implying ubiquitous contaminants in the Arctic environment. The POPs such as PCBs (CBs 8, 18, 110 and 180), OCPs (β-hexachlorocyclohexane and heptachlors), CLBs (1,3,5-chlorobenzene and HCB), and PBDEs (mostly BDE 47) and PAHs (naphthalene, fluorene, acenaphthylene, phenanthrene, anthracene, benzo[ghi]perylene, chrysene, and benzo[a]anthracene) were detected in the samples, which are consistent with those reported for previous studies (Rigét et al., 2010; Hung et al., 2016; Sofowote et al., 2010). In particular, the lower-molecular-weight POPs and PAHs were mainly detected in all environmental samples because these contaminants are easily transported over long distances by atmospheric current (Hung et al., 2016). Despite this, the numbers of POPs detected in the Arctic samples were smaller than those of emerging contaminants because POPs are existed as low levels due to decreasing trends of POPs in the Arctic environments (Rigét et al., 2010; Hung et al., 2016).

Recent studies on non-target analysis with GC/TOF have conducted for multiple environmental samples from specific locations. To our knowledge, this is the first report on suspect and non-target analysis for the Arctic environmental samples. However, it should

be noted that several limitations should be considered for the results observed in our study. Thus, further studies should include more advanced data such as quantification of contaminants, use of internal and surrogate standards for quality control and retention time index (RTI) with alkane mixtures (Zhang et al., 2014; Moschet et al., 2018). Moreover, to assess the bioaccumulation and biomagnification potentials of certain contaminants in the Arctic ecosystems, the biotic samples are used for further studies. Nevertheless, the present study emphasized the presence of several emerging contaminants in the Arctic environment.

4. Conclusions

Suspect and non-target analytical methods with GC/TOF were optimized to propose priority pollutants in the Arctic environment. For suspect analysis, over 200 compounds were registered as target contaminants of in-house library with information on qualification and qualifier ions, isotopic ratio, and retention time. Non-target analytical method was optimized with deconvoluted ion chromatogram, which is a possible form to match the mass spectra of the NIST library. From the suspect and non-target analysis, the commonly detected contaminants in the multiple samples from the Arctic environment were PCBs, PAHs, siloxanes, OPFRs, phthalates, SMCs, similar to those reported for previous studies. In our study, siloxanes and OPFRs were proposed as emerging contaminants for the Arctic environment. This is the first report on an application of suspect and non-target analysis with GC/TOF for the Arctic environment.

KOPRI 극지연구소

5. Reference

AMAP, 2016. AMAP Assessment 2015: Temporal Trends in Persistent Organic Pollutants in the Arctic. Arctic Monitoring and Assessment Programme (AMAP), Oslo, Norway. vi+71pp.

AMAP, 2017a. AMAP Assessment 2016: Chemicals of Emerging Arctic Concern. Arctic Monitoring and Assessment Programme (AMAP), Oslo, Norway. xvi+353pp.

AMAP, 2017b. Chemicals of Emerging Arctic Concern. Summary for Policy-makers. Arctic Monitoring and Assessment Programme (AMAP), Oslo, Norway. 16 pp.

CAS, 2019. CAS registry-The gold standard for chemical substance information. www.cas.org (Accessed 26 March 2019)

Choi, Y., Yoon, H.-I., Lee, C., Vetráková, L'., Heger, D., Kim, K., Kim, J., 2018. Activation of periodate by freezing for the degradation of aqueous organic pollutants. Environmental Science & Technology 52, 5378-5385.

Gouin, T., Mackay, D., Jones, K.C., Harner, T., Meijer, S.N., 2004. Evidence for the

"grasshopper" effect and fractionation during long-range atmospheric transport of organic contaminants. Environmental Pollution 128, 139-148.

Guyader, M.E., Warren, L.D., Green, E., Butt, C., Ivosev, G., Kiesling, R.L., Schoenfuss, H.L., Higgins, C.P., 2019. Prioritization potential endocrine active high resolution mass spectrometry (HRMS) features in Minnesota lakewater. Science of the Total Environment 670, 814-825.

Hernández, F., Ibáñez, M., Portolés, T., Cervera, M.I., 2015. Advancing towards universal screening for organic pollutants in waters. Journal of Hazardous Materials 282, 86-95.

Hong, S., Giesy, J.P., Lee, J.-S., Lee, J.-H., Khim, J.S., 2016. Effect-directed analysis: Current status and future challenges. Ocean Science Journal 51, 413-433.

Hung, H., Katsoyiannis, A.A., Brorstr?m-Lund?n, E., Olafsdottir, K., Aas, W., Breivik, K., Bohlin-Nizzetto, P., Sigurdsson, A., Hakola, H., Bossi, R., Skov, H., Sverko, E., Barresi, E., Fellin, P., Wilson, S., 2016. Temporal trends of persistent organic pollutants (POPs) in arctic air: 20 years of monitoring under the Arctic Monitoring and Assessment Programme (AMAP). Environmental Pollution 217, 52-61.

Ju, J., Kim, J., Vetráková, L'., Seo, J., Heger, D., Lee, C., Yoon, H.-I., Kim, K., Kim, J., 2017. Accelerated redox reaction between chromate and phenolic pollutants during freezing. Journal of Hazardous Materials 329, 330-338.

Knudsen, N.M., Sagerup, K., Polder, A., Schlabach, M., Jossefsen, T.D., Strøm, H., Skåre, J.U., Gabrielsen, G.W., 2007. Halogenated organic contaminants (HOCs) and mercury in dead or dying seabirds on Bjørnøya (Svalbard). Report no. SFT 977/2007. Norwegian Pollution Control Authority (SFT), Oslo, Norway, 45 pp.

Krogseth, I.S., Whelan, M.J., Christensen, G.N., Breivik, K., Evenset, A., Warner, N.A., 2017. Understanding of cyclic volatile methyl siloxane fate in a high latitude lake is constrained by uncertainty in organic carbon-water partitioning. Environmental Science & Technology 51, 401-409.

Lebedev, A.T., Mazur, D.M., Polyakova, O.V., Kosyakov, D.S., Kozhevnikov, A.Y., Latkin, T.B., Yu, I.A., Artaev, V.B., 2018. Semi volatile organic compounds in the snow of Russian Arctic islands: Archipelago Novaya Zemlya. Environmental Pollution 239, 416-427.

Lee, S., Song, G.-J., Kannan, K., Moon, H.-B., 2014a. Occurrence of PBDEs and other alternative brominated flame retardants in sludge from wastewater treatment plants in Korea. Science of the Total Environment 470-471, 1422-1429.

Lee, S., Moon, H.-B., Song, G.-J., Ra, K., Lee, W.-C., Kannan, K., 2014b. A nationwide

survey and emission estimates of cyclic and linear siloxanes through sludge from wastewater treatment plants in Korea. Science of the Total Environment 497-498, 106-112.

Lee, S., Liao, C., Song, G.-J., Ra, K., Kannan, K., Moon, H.-B., 2015. Emission of bisphenol analogues including bisphenol A and bisphenol F from wastewater treatment plants in Korea. Chemosphere 1119, 1000-1006.

Li, J., Xie, Z., Mi, W., Lai, S., Tian, C., Emeis, K.-C., Ebinghaus, R., 2017. Organophosphate esters in air, snow, and seawater in the North Atlantic and the Arctic. Environmental Science & Technology 51, 6887-6896.

Ma, Y., Xie, Z., Lohmann, R., Mi, W., Gao, G., 2017. Organophosphate ester flame retardants and plasticizers in ocean sediments from the North Pacific to the Arctic ocean. Environmental Science & Technology 51, 3809-3815.

Moon, H.-B., Yoon, S.-P., Jung, R.-H., Choi, M., 2008. Wastewater treatment plants (WWTPs) as a source of sediment contamination by toxic organic pollutants and fecal sterols in a semi-enclosed bay in Korea. Chemosphere 73, 880-889.

Moschet, C., Anumol, T., Lew, B.M., Bennett, D.H., Young, T.M., 2018. Household dust as a repository of chemical accumulation: New insights from a comprehensive high-resolution mass spectrometric study. Environmental science & Technology 52, 2878-2887.

Park, N., Choi, Y., Kim, D., Kim, K., Jeon, J., 2018. Prioritization of highly exposable pharmaceuticals via a suspect/non-target screening approach: A case study for Yeongsan River, Korea. Science of the Total Environment 639, 570-579.

Portolés, T., Mol, J.G.J., Sancho, J.V., Hern?ndez, F., 2014. Use of electron ionization and atmospheric pressure chemical ionization in gas chromatography coupled to time-of-flight mass spectrometry for screening and identification of organic pollutants in waters. Journal of Chromatography A 1339, 145-153.

Rigét, F., Bignert, A., Braune, B., Stow, J., Wilson, S., 2010. Temporal trends of legacy POPs in Arctic biota, an update. Science of the Total Environment 408, 2874-2884.

Simon, E., Van Velzen, M., Brandsma, S.H., Lie, E., Løken, K., de Boer, J., Bytingsvik, J., Jenssen, B.M., Aars, J., Hamers, T., Lamoree, M.H., 2013. Effect-directed analysis to explire the polar bear exposome: identification of thyroid hormone disrupting compounds in plasma. Environmental Science & Technology 47, 8902-8912.

Sofowote, U.M., Hung, H., Rastogi, A.K., Westgate, J.N., Su, Y., Sverko, E., D;Sa, I., Roach, P., Fellin, P., McCarry, B.E., 2010. The gas/particle partitioning of polycyclic aromatic hydrocarbons collected at a sub-Arctic site in Canada. Atmospheric

Environment 44, 4919-4926.

Sühring, R., Diamond, M.L., Scheringer, M., Wong, F., Pucko, M., Stern, G., Burt, A., Hung, H., Fellin, P., Li, H., Jantunen, L.M., 2016. Organophosphate esters in Canadian Arctic air: Occurrence, levels and trends. Environmental Science & Technology 50, 7409-7415.

Wania, F., 2003. Assessing the potential of persistent organic chemicals for long-range transport and accumulation in polar regions. Environmental Science & Technology 37, 1344-1351.

Warner, N.A., Evenset, A., Christensen, G., Gabrielsen, G.W., Borg?, K., Leknes, H., 2010. Volatile siloxanes in the European Arctic: Assessment of sources and spatial distribution. Environmental Science & Technology 44, 7705-7710.

Yue, S., Ramsay, R.A., Brown, R.S., Wang, J., Ramsay, J.A., 2015. Identification of estrogenic compounds in oil sands process waters by effect directed analysis. Environmental Science & Technology 49, 570-577.

Zhang, F., Wang, H., Zhang, L., Zhang, J., Fan, R., Yu, C., Wang, W., Guo, Y., 2014. Suspected-target pesticide screening using gas chromatography-quadrupole time-of-flight mass spectrometry with high resolution deconvolution and retention index/mass spectrum library. Talanta 128, 156-163.

KOPRI
극지연구소

Table 1. Non-target screening results in the seawater, sediment, and soil samples collected from the Arctic.

Retention time (min)	Compound Name	CAS No.	Formula	Molecular Weight	Uses
4.25	Benzene, (1-methylethyl)-	98-82-8	C9H12	120	-[a]
4.28	Cyclotetrasiloxane, octamethyl-	556-67-2	C8H24O4Si4	296	Siloxanes
4.81	Decane, 2,4-dimethyl-	2801-84-5	C12H26	170	-
5.76	1-Octanol, 2-butyl-	3913-02-08	C12H26O	186	Fatty alcohol
7.04	4-(2,6,6-Trimethylcyclohexa-1,3-dienyl)but-3-en-2-one	1203-08-3	C13H18O	190	-
8.47	1-tridecanol	112-70-9	C13H28O	200	Fatty alcohol
9.07	2-exo-methyl-2-endo-(1-oxacyclohex-2-yloxy)bicyclo[2.2.1]heptane	-	C13H22O2	210	-
9.67	Octyl tetracosyl ether	-	C32H66O	466	-
9.96	Cycloheptasiloxane, tetradecamethyl-	107-50-6	C14H42O7Si7	518	Siloxanes
10.38	2-(1,3-Dioxolan-2-yl)-1-(2-furyl)ethene	-	C9H10O3	166	-
10.74	4-Methyl-benzoic acid 4-[(3-hydroxy-benzoyl)-hydrazonomethyl]-phenyl ester	-	C22H18N2O4	374	-
11.13	5-Oxo-3,3,6-trimethylbicyclo[4.2.0]octane-7-(exo)-carbonitrile	-	C12H17NO	191	-
11.20	1,2-Benzenedicarboxylic acid, diethyl ester	84-66-2	C12H14O4	222	Phthalates
11.72	Tridecane	629-50-5	C13H28	184	Alkane hydrocarbon
12.17	Docosyl octyl ether	-	C30H62O	438	-
12.41	1,4-Benzenediol, 2-(1,1-dimethylethyl)-5-(2-propenyl)-	73685-60-6	C13H18O2	206	Essential oil of several plant
12.54	cis-1,4-Cyclohexanediamine, N1,N1,N4-triethyl	-	C12H26N2	198	-
13.09	1-Heptadecene	6765-39-5	C17H34	238	-
13.31	1-Nonadecene	18435-45-5	C19H38	266	Natural substances
13.38	3,4-Dihydro-5-methoxy-2,2,8,8-tetramethyl-2H,8H-pyrano[3,2-g]chromen-4-one	-	C17H20O4	288	-
13.46	n-Nonadecanol-1	1454-84-8	C19H40O	284	Fatty alcohol
14.33	Carbonic acid, eicosyl vinyl ester	-	C23H44O3	368	-
14.72	2-tert-Butyl-4-isopropyl-5-methylphenol	-	C14H22O	206	-
15.24	Inosine, 1-hydroxy-	5383-06-02	C10H12N4O6	284	Nucleoside
17.20	Acetic acid, 1,3,3-trimethyl-4-oxo-6-oxabicyclo[3.1.0]hex-2-yl ester	-	C10H14O4	198	-
17.45	Octadecanoic acid, methyl ester	112-61-8	C19H38O2	298	Fatty acid esterified with a methyl group
20.40	2,2',4,4'-TETRA-T-BUTYLDIPHENYL ETHER	-	C28H42O	394	-
24.95	4-(4-(Ethoxycarbonyl)-3-oxo-5-phenyl-2-3-dihydropyrazol-1-yl)benzoic acid	-	C19H16N2O5	352	-
25.06	(R,S)-5-Ethyl-6-methyl-3E-hepten-2-one	57283-79-1	C10H18O	154	Natural substances (tabaco)
25.85	9-Tricosene, (Z)-	27519-02-4	C23H46	322	Insect pheromone/pesticide

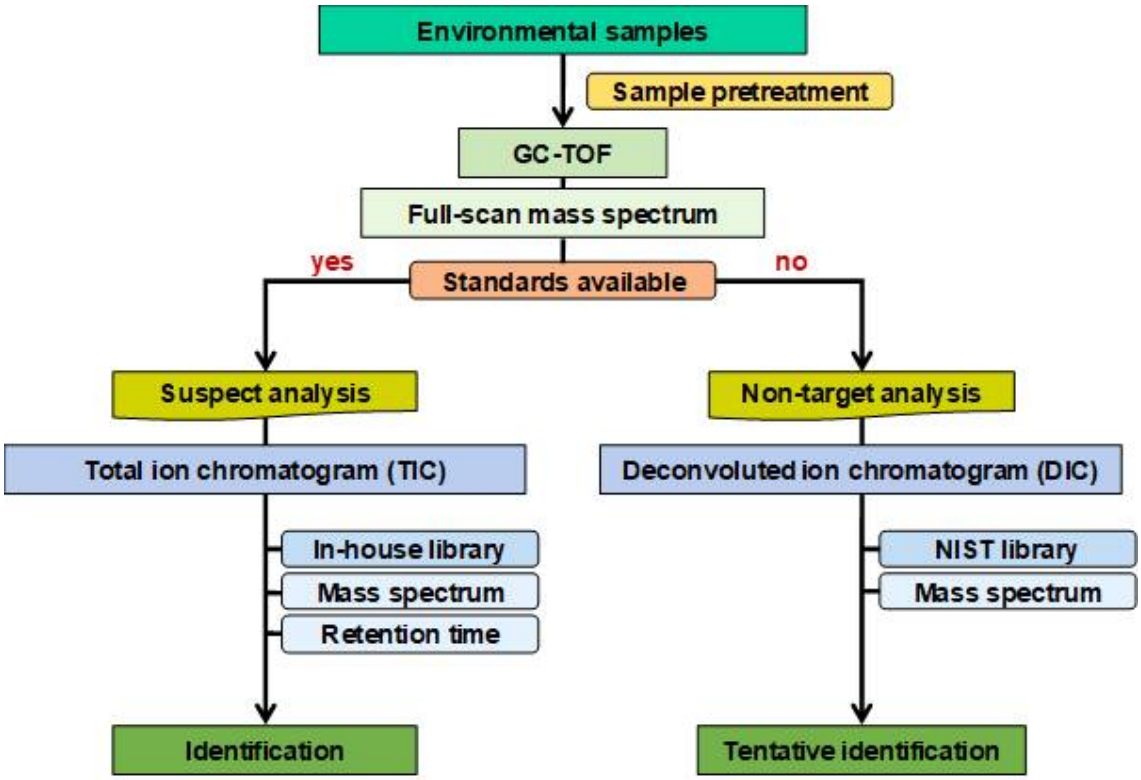

Figure 1. Workflow of suspect and non-target screening analysis with a gas chromatography coupled to time-of-flight (GC/TOF) in multiple environmental samples.

KOPRI

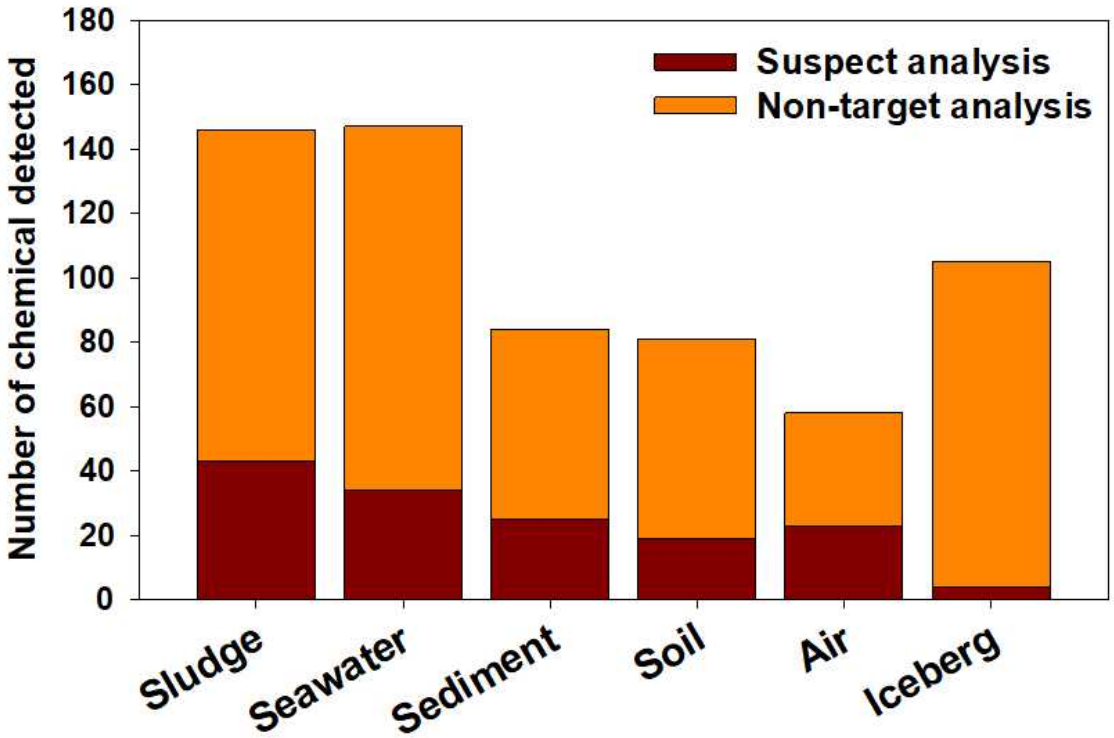

Figure 2. Numbers of identified contaminants by suspect and non-target analysis of GC/TOF in multiple samples such as sludge, seawater, sediment, soil, air, and iceberg samples collected from the Arctic environment.

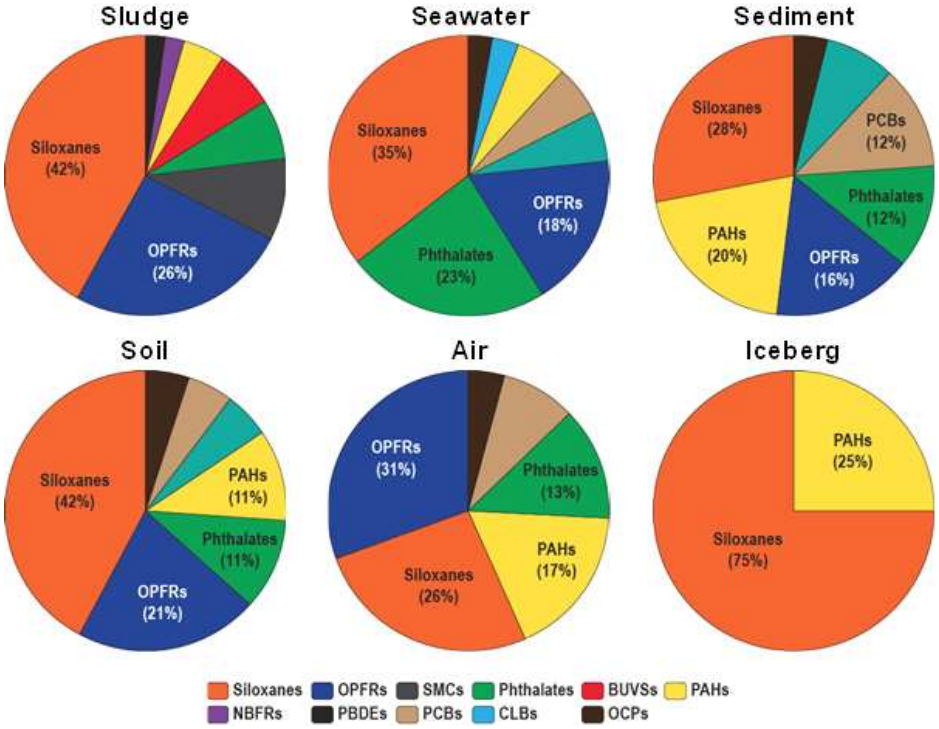

Figure 3. Percentage of detected contaminants by suspect analysis of GC/TOF in multiple environmental samples such as sludge, seawater, sediment, soil, air, and iceberg collected from the Arctic. Contaminant groups over 10% of total contaminant numbers are shown as the label on the pie-graph.

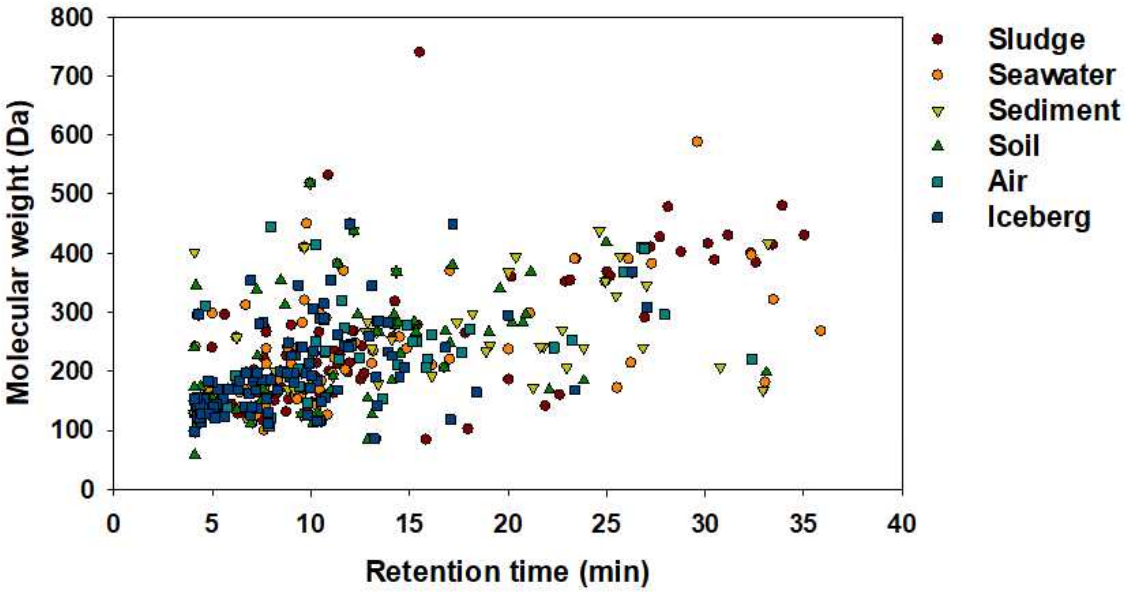

Figure 4. Identified compounds in multiple environmental samples such as sludge, seawater, sediment, soil, air, and iceberg collected from the Arctic regions by non-target analysis of GC/TOF. The graph was illustrated as mass of compounds versus retention time detected. Parenthesis indicates the numbers detected in each environmental matrix.

Supplementary Materials

Table S1. The detail information of particulate matter samples (n=3) from ambient air collected from Zeppelin station in Ny-Ålesund, Svalbard.

No.	Sampling period	Flow rate (m^3/h)	Sampling time (h)	Total volume of sampled air (m^3)
1	2015.04.13 - 2015.04.30	60	456	27021
2	2015.05.02 - 2015.05.20	60	504	30058
3	2015.07.27 - 2015.09.01	60	792	47097

KOPRI
극지연구소

Table S2. Detailed information of the list of 215 suspected compounds.

No	Chemical Group	Compound	Molecular formula	CAS No.	Average mass (Da)	Monoisotopic mass (Da)	Retention time (min)	Qualification ion (m/z)	Qualifier ion (m/z)
1	Organochlorine pesticide	Aldrin	C12H8Cl6	309-00-2	364.910	361.875702	15.753	262.8577	260.8607
2	Organochlorine pesticide	alpha-HCH	C6H6Cl6	319-84-6	290.830	287.860077	12.569	218.9123	180.9384
3	Organochlorine pesticide	beta-HCH	C6H6Cl6	319-85-7	290.830	287.860077	13.132	218.9123	180.9384
4	Organochlorine pesticide	cis-CHL	C10H6Cl8	5103-71-9	409.779	405.797760	17.856	372.8278	374.8252
5	Organochlorine pesticide	cis-NonaCHL	C10H5Cl9	5103-73-1	444.224	439.758789	19.807	408.7867	406.7891
6	Organochlorine pesticide	delta-HCH	C6H6Cl6	319-86-8	290.830	287.860077	13.789	218.9123	180.9384
7	Organochlorine pesticide	Dieldrin	C12H8Cl6O	60-57-1	380.909	377.870636	18.506	262.8577	260.8612
8	Organochlorine pesticide	gamma-HCH	C6H6Cl6	58-89-9	290.830	287.860077	13.269	218.9123	180.9384
9	Organochlorine pesticide	HCB	C6Cl6	118-74-1	284.782	281.813110	12.73	283.8151	281.8154
10	Organochlorine pesticide	Heptachlor	C10H5Cl7	76-44-8	373.318	369.821106	16.911	182.9171	184.9143
11	Organochlorine pesticide	Heptachlor epoxide	C10H5Cl7O	1024-57-3	389.317	385.816010	16.805	352.8451	354.8427
12	Organochlorine pesticide	Isodrin	C12H8Cl6	465-73-6	364.910	361.875702	16.504	192.9379	262.8581
13	Organochlorine pesticide	Mirex	C10Cl12	2385-85-5	545.543	539.626221	23.863	271.8115	236.8419
14	Organochlorine pesticide	o,p′-DDD	C14H10Cl4	53-19-0	320.041	317.953674	18.718	235.0095	237.0061
15	Organochlorine pesticide	o,p′-DDE	C14H8Cl4	3424-82-6	318.025	315.938019	17.581	246.0019	317.9372
16	Organochlorine pesticide	p,p′-DDD	C14H10Cl4	72-54-8	320.041	317.953674	19.696	235.0095	237.0062
17	Organochlorine pesticide	p,p′-DDE	C14H8Cl4	72-55-9	318.025	315.938019	18.47	246.0019	317.9372
18	Organochlorine pesticide	trans-CHL	C10H6Cl8	5566-34-7	409.779	405.797760	17.436	372.8278	374.8253
19	Organochlorine pesticide	trans-NonaCHL	C10H5Cl9	39765-80-5	444.224	439.758789	17.998	408.7867	406.7898
20	Polycyclic aromatic hydrocarbons	1-methyl-Naphthalene	C11H10	90-12-0	142.197	142.078247	7.865	142.0917	115.0557
21	Polycyclic aromatic hydrocarbons	1-methyl-Phenanthrene	C15H12	832-69-9	192.256	192.093903	15.179	191.0996	165.0711
22	Polycyclic aromatic hydrocarbons	2,3,5-methyl-Naphthalene	C13H14	2245-38-7	170.250	170.109543	11.006	170.1335	155.1062
23	Polycyclic aromatic hydrocarbons	2,6-methyl-Naphthalene	C12H12	581-42-0	156.224	156.093903	9.03	156.1085	141.0795
24	Polycyclic aromatic hydrocarbons	2-methyl-Naphthalene	C11H10	91-57-6	142.197	142.078247	7.603	142.0917	115.0557
25	Polycyclic aromatic hydrocarbons	Acenaphthene	C12H10	83-32-9	154.208	154.078247	10.069	154.0959	152.0729
26	Polycyclic aromatic hydrocarbons	Acenaphthylene	C12H8	208-96-8	152.192	152.062607	9.635	152.0866	150.0492
27	Polycyclic aromatic hydrocarbons	Anthracene	C14H10	120-12-7	178.229	178.078247	13.593	178.1103	152.0641
28	Polycyclic aromatic hydrocarbons	Benzo[a]anthracene	C18H12	56-55-3	228.288	228.093903	22.221	228.1132	226.0808
29	Polycyclic aromatic hydrocarbons	Benzo[a]pyrene	C20H12	50-32-8	252.309	252.093903	27.722	252.0971	250.0793
30	Polycyclic aromatic hydrocarbons	benzo[b]fluoranthene	C20H12	205-99-2	252.309	252.093903	26.55	252.1015	250.0795
31	Polycyclic aromatic hydrocarbons	Benzo[ghi]perylene	C22H12	191-24-2	276.331	276.093903	32.484	276.094	274.0767
32	Polycyclic aromatic hydrocarbons	Benzo[k]fluoranthene	C20H12	207-08-9	252.309	252.093903	26.648	252.1025	250.0797
33	Polycyclic aromatic hydrocarbons	Chrysene	C18H12	218-01-9	228.288	228.093903	22.381	228.1132	226.0824
34	Polycyclic aromatic hydrocarbons	Dibenzo[ah]anthracene	C22H14	53-70-3	278.347	278.109558	31.869	278.1094	276.0934
35	Polycyclic aromatic hydrocarbons	Fluoranthene	C16H10	206-44-0	202.251	202.078247	16.904	202.109	200.0693
36	Polycyclic aromatic hydrocarbons	Fluorene	C13H10	86-73-7	166.219	166.078247	11.249	166.1016	164.0644
37	Polycyclic aromatic hydrocarbons	Indeno[1,2,3-cd]fluoranthene	C22H12	193-43-1	276.331	276.093903	31.699	276.094	274.0773
38	Polycyclic aromatic hydrocarbons	Naphthalene	C10H8	91-20-3	128.171	128.062607	6.122	128.0616	127.0533
39	Polycyclic aromatic hydrocarbons	Perylene	C20H12	198-55-0	252.309	252.093903	28.041	252.0971	250.0794
40	Polycyclic aromatic hydrocarbons	Phenanthrene	C14H10	85-01-8	178.229	178.078247	13.484	178.1103	152.0641
41	Polycyclic aromatic hydrocarbons	Pyrene	C16H10	129-00-0	202.251	202.078247	17.61	202.109	200.0697
42	Polybrominated diphenyl ethers	BDE 100	C12H5Br5O	189084-64-8	564.688	559.625671	25.975	563.6215	565.6195
43	Polybrominated diphenyl ethers	BDE 119	C12H5Br5O	189084-66-0	564.688	559.625671	26.237	563.6215	565.6195
44	Polybrominated diphenyl ethers	BDE 126	C12H5Br5O	366791-32-4	564.688	559.625671	28.472	563.6215	565.6195
45	Polybrominated diphenyl ethers	BDE 138	C12H4Br6O	182677-30-1	643.584	637.536194	31.671	483.697	481.6994
46	Polybrominated diphenyl ethers	BDE 153	C12H4Br6O	68631-49-2	643.584	637.536194	30.154	483.6972	481.6994
47	Polybrominated diphenyl ethers	BDE 154	C12H4Br6O	207122-15-4	643.584	637.536194	29.057	483.6975	481.6994
48	Polybrominated diphenyl ethers	BDE 17	C12H7Br3O	147217-75-2	406.895	403.084688	19.005	405.8026	407.8006
49	Polybrominated diphenyl ethers	BDE 183	C12H3Br7O	207122-16-5	722.480	715.446716	32.957	563.6041	561.6048
50	Polybrominated diphenyl ethers	BDE 184	C12H3Br7O	117948-63-7	722.480	715.446716	32.955	563.6041	561.6048
51	Polybrominated diphenyl ethers	BDE 190	C12H3Br7O	189084-68-2	722.480	715.446716	34.381	563.6041	561.6048
52	Polybrominated diphenyl ethers	BDE 191	C12H3Br7O	446255-30-7	722.480	715.446716	33.448	563.6041	561.6048
53	Polybrominated diphenyl ethers	BDE 28	C12H7Br3O	41318-75-6	406.895	403.084688	19.495	405.8026	407.8006

54	Polybrominated diphenyl ethers	BDE 47	C12H6Br4O	5436-43-1	485.791	481.715179	23.146	485.7111	487.7091
55	Polybrominated diphenyl ethers	BDE 66	C12H6Br4O	189084-61-5	485.791	481.715179	23.653	485.7111	487.7091
56	Polybrominated diphenyl ethers	BDE 71	C12H6Br4O	189084-62-6	485.791	481.715179	22.696	485.7111	487.7091
57	Polybrominated diphenyl ethers	BDE 85	C12H5Br5O	182346-21-0	564.688	559.625671	28.263	563.6215	565.6195
58	Polybrominated diphenyl ethers	BDE 99	C12H5Br5O	32534-81-9	564.688	559.625671	26.771	563.6215	565.6195
59	Polychlorinated biphenyls	PCB 101	C12H5Cl5	37680-73-2	326.433	323.883392	17.649	323.8903	325.8855
60	Polychlorinated biphenyls	PCB 103	C12H5Cl5	60145-21-3	326.433	323.883392	16.409	323.8903	325.8855
61	Polychlorinated biphenyls	PCB 105	C12H5Cl5	32598-14-4	326.433	323.883392	20.24	323.8903	255.9464
62	Polychlorinated biphenyls	PCB 110	C12H5Cl5	38380-03-9	326.433	323.883392	18.688	323.8903	325.8855
63	Polychlorinated biphenyls	PCB 118	C12H5Cl5	31508-00-6	326.433	323.883392	19.445	323.8903	325.8855
64	Polychlorinated biphenyls	PCB 128	C12H4Cl6	38380-07-3	360.878	357.844421	21.804	359.8257	361.8455
65	Polychlorinated biphenyls	PCB 138	C12H4Cl6	35065-28-2	360.878	357.844421	20.961	361.8455	359.8257
66	Polychlorinated biphenyls	PCB 153	C12H4Cl6	35065-27-1	360.878	357.844421	20.115	361.8455	359.8257
67	Polychlorinated biphenyls	PCB 170	C12H3Cl7	35065-30-6	395.323	391.805450	23.993	395.8053	323.8903
68	Polychlorinated biphenyls	PCB 18	C12H7Cl3	37680-65-2	257.543	255.961334	13.481	186.0258	220.9937
69	Polychlorinated biphenyls	PCB 180	C12H3Cl7	35065-29-3	395.323	391.805450	23.063	395.8053	323.8903
70	Polychlorinated biphenyls	PCB 187	C12H3Cl7	52663-68-0	395.323	391.805450	21.473	395.8053	323.8903
71	Polychlorinated biphenyls	PCB 194	C12H2Cl8	35694-08-7	429.768	425.766479	25.388	427.7696	429.7686
72	Polychlorinated biphenyls	PCB 195	C12H2Cl8	52663-78-2	429.768	425.766479	24.268	427.7696	429.7686
73	Polychlorinated biphenyls	PCB 198	C12H2Cl8	68194-17-2	429.768	425.766479	24.166	427.7696	429.7686
74	Polychlorinated biphenyls	PCB 199	C12H2Cl8	52663-75-9	429.768	425.766479	26.018	427.7696	429.7686
75	Polychlorinated biphenyls	PCB 200	C12H2Cl8	52663-73-7	429.768	425.766479	23.451	427.7696	431.7624
76	Polychlorinated biphenyls	PCB 205	C12H2Cl8	74472-53-0	429.768	425.766479	26.19	427.7696	429.7686
77	Polychlorinated biphenyls	PCB 206	C12HCl9	40186-72-9	464.213	459.727509	27.205	463.7255	461.7279
78	Polychlorinated biphenyls	PCB 209	C12Cl10	2051-24-3	498.658	493.688538	28.175	497.6867	499.6831
79	Polychlorinated biphenyls	PCB 28	C12H7Cl3	7012-37-5	257.543	255.961334	14.535	259.9586	186.0258
80	Polychlorinated biphenyls	PCB 29	C12H7Cl3	15862-07-4	257.543	255.961334	14.199	259.9586	186.0258
81	Polychlorinated biphenyls	PCB 33	C12H7Cl3	38444-86-9	257.543	255.961334	14.763	259.9586	186.0258
82	Polychlorinated biphenyls	PCB 44	C12H6Cl4	41464-39-5	291.988	289.922363	15.885	293.9201	289.9062
83	Polychlorinated biphenyls	PCB 52	C12H6Cl4	35693-99-3	291.988	289.922363	15.361	293.9201	289.9062
84	Polychlorinated biphenyls	PCB 70	C12H6Cl4	32598-11-1	291.988	289.922363	16.905	293.9201	291.924
85	Polychlorinated biphenyls	PCB 8	C12H8Cl2	34883-43-7	223.098	222.000305	12.562	224.0131	221.9846
86	Polychlorinated biphenyls	PCB 87	C12H5Cl5	38380-02-8	326.433	323.883392	18.405	323.8903	325.8855
87	Polychlorinated dibenzofurans	1,2,3,4,6,7,8-HpCDD	C12HCl7O2	35822-46-9	425.306	421.779633	28.878	423.7766	425.7737
88	Polychlorinated dibenzodioxins	1,2,3,4,6,7,8-HpCDF	C12HCl7O	67562-39-4	409.307	405.784698	27.999	407.7813	409.7788
89	Polychlorinated dibenzofurans	1,2,3,4,7,8,9-HpCDF	C12HCl7O	55673-89-7	409.307	405.784698	29.173	407.7815	409.7788
90	Polychlorinated dibenzofurans	1,2,3,4,7,8-HxCDD	C12H2Cl6O2	39227-28-6	390.861	387.818604	26.159	389.8151	391.8127
91	Polychlorinated dibenzodioxins	1,2,3,4,7,8-HxCDF	C12H2Cl6O	70648-26-9	374.862	371.823669	25.48	373.8205	375.8178
92	Polychlorinated dibenzofurans	1,2,3,6,7,8-HxCDD	C12H2Cl6O2	57653-85-7	390.861	387.818604	26.232	389.8155	391.8127
93	Polychlorinated dibenzofurans	1,2,3,6,7,8-HxCDF	C12H2Cl6O	57117-44-9	374.862	371.823669	25.566	373.8201	375.8178
94	Polychlorinated dibenzofurans	1,2,3,7,8,9-HxCDD	C12H2Cl6O2	19408-74-3	390.861	387.818604	26.471	389.8154	391.8127
95	Polychlorinated dibenzodioxins	1,2,3,7,8,9-HxCDF	C12H2Cl6O	72918-21-9	374.862	371.823669	26.61	373.8206	375.8178
96	Polychlorinated dibenzodioxins	1,2,3,7,8-PCDD	C12H3Cl5O2	40321-76-4	356.416	353.857574	23.557	355.8545	357.8517
97	Polychlorinated dibenzodioxins	1,2,3,7,8-PCDF	C12H3Cl5O	57117-41-6	340.417	337.862640	22.748	339.8593	341.8568
98	Polychlorinated dibenzofurans	2,3,4,6,7,8-HxCDF	C12H2Cl6O	60851-34-5	374.862	371.823669	26.03	373.8204	375.8178
99	Polychlorinated dibenzofurans	2,3,4,7,8-PCDF	C12H3Cl5O	57117-31-4	340.417	337.862640	23.285	339.8592	341.8568
100	Polychlorinated dibenzodioxins	2,3,7,8-TCDD	C12H4Cl4O2	1746-01-6	321.971	319.896545	20.726	321.8937	319.8965
101	Polychlorinated dibenzofurans	2,3,7,8-TCDF	C12H4Cl4O	51207-31-9	305.972	303.901611	20.308	305.8984	303.9016
102	Polychlorinated dibenzodioxins	OCDD	C12Cl8O2	3268-87-9	459.751	455.740662	31.361	459.7339	457.7377
103	Polychlorinated dibenzofurans	OCDF	C12Cl8O	39001-02-0	443.752	439.745728	31.418	443.7398	441.7428
104	Dioxin like-polychlorinated biphenyls	DL-PCB 105	C12H5Cl5	32598-14-4	326.433	323.883392	20.108	325.8804	327.8775
105	Dioxin like-polychlorinated biphenyls	DL-PCB 114	C12H5Cl5	74472-37-0	326.433	323.883392	19.652	325.8804	327.8775
106	Dioxin like-polychlorinated biphenyls	DL-PCB 118	C12H5Cl5	31508-00-6	326.433	323.883392	19.317	325.8804	327.8775
107	Dioxin like-polychlorinated biphenyls	DL-PCB 123	C12H5Cl5	65510-44-3	326.433	323.883392	19.25	325.8804	327.8775
108	Dioxin like-polychlorinated biphenyls	DL-PCB 126	C12H5Cl5	57465-28-8	326.433	323.883392	21.097	325.8804	327.8775
109	Dioxin like-polychlorinated biphenyls	DL-PCB 156	C12H4Cl6	38380-08-4	360.878	357.844421	22.401	359.8415	361.8385

110	Dioxin like-polychlorinated biphenyls	DL-PCB 157	C12H4Cl6	69782-90-7	360.878	357.844421	22.58	359.8415	361.8385
111	Dioxin like-polychlorinated biphenyls	DL-PCB 167	C12H4Cl6	52663-72-6	360.878	357.844421	21.692	359.8415	361.8385
112	Dioxin like-polychlorinated biphenyls	DL-PCB 169	C12H4Cl6	32774-16-6	360.878	357.844421	23.584	359.8415	361.8385
113	Dioxin like-polychlorinated biphenyls	DL-PCB 189	C12H3Cl7	39635-31-9	395.323	391.805450	24.759	393.8025	395.7995
114	Dioxin like-polychlorinated biphenyls	DL-PCB 77	C12H6Cl4	32598-13-3	291.988	289.922363	18.566	291.9194	289.9224
115	Dioxin like-polychlorinated biphenyls	DL-PCB 81	C12H6Cl4	70362-50-4	291.988	289.922363	18.286	291.9194	289.9224
116	Novel brominated flame retardants	ATE	C9H7Br3O	3278-89-5	370.863	367.804688	13.143	209.9692	211.9675
117	Novel brominated flame retardants	BEHTBP	C24H34Br4O4	26040-51-7	706.140	701.919006	36.085	112.1258	464.6621
118	Novel brominated flame retardants	BTBPE	C14H8Br6O2	37853-59-1	687.636	681.562439	34.295	358.7962	356.7974
119	Novel brominated flame retardants	DPTE	C9H7Br5O	35109-60-5	530.671	525.641357	21.753	329.7744	331.7723
120	Novel brominated flame retardants	EHTBB	C15H18Br4O2	183658-27-7	549.918	545.804016	26.716	70.0793	420.6752
121	Novel brominated flame retardants	HBB	C6Br6	87-82-1	551.488	545.510010	22.161	551.5087	553.5062
122	Novel brominated flame retardants	HCDBCO	C13H12Br2Cl6	51936-55-1	540.760	535.743652	26.922	79.0557	107.0869
123	Novel brominated flame retardants	PBEB	C8H5Br5	85-22-3	500.645	495.630768	20.175	499.6314	484.608
124	Novel brominated flame retardants	PBT	C7H3Br5	87-83-2	486.619	481.615112	19.486	485.6162	406.696
125	Synthetic musk compounds	AHTN	C18H26O	1506-02-1	258.398	258.198364	14.275	243.1773	258.2009
126	Synthetic musk compounds	HHCB	C18H26O	1222-05-5	258.398	258.198364	14.149	243.1768	213.1654
127	Synthetic musk compounds	Musk Ketone	C14H18N2O5	81-14-1	294.303	294.121582	15.707	279.1007	294.1242
128	Synthetic musk compounds	Musk Moskene	C14H18N2O4	116-66-5	278.304	278.126648	14.55	263.1054	233.1311
129	Synthetic musk compounds	Musk Xylene	C12H15N3O6	81-15-2	297.264	297.096100	14.258	282.0745	283.0771
130	Benzotriazole ultraviolet stabilizers	UV-234	C30H29N3O	70321-86-7	447.571	447.231049	37.562	432.2163	432.2399
131	Benzotriazole ultraviolet stabilizers	UV-320	C20H25N3O	3846-71-7	323.432	323.199768	22.447	308.1794	323.2023
132	Benzotriazole ultraviolet stabilizers	UV-326	C17H18ClN3O	3896-11-5	315.797	315.113831	23.372	300.0927	315.1197
133	Benzotriazole ultraviolet stabilizers	UV-327	C20H24ClN3O	3864-99-1	357.877	357.160797	24.987	342.1402	357.1634
134	Benzotriazole ultraviolet stabilizers	UV-328	C22H29N3O	25973-55-1	351.485	351.231049	24.854	322.1951	323.1988
135	Benzotriazole ultraviolet stabilizers	UV-329	C20H25N3O	3147-75-9	323.432	323.199768	23.707	252.1154	253.1171
136	Benzotriazole ultraviolet stabilizers	UV-9	C14H12O3	131-57-7	228.243	228.078644	20.428	250.1016	265.1253
137	Benzotriazole ultraviolet stabilizers	UV-P (Drometrizole)	C13H11N3O	2240-22-4	225.246	225.090210	16.751	225.0919	226.0946
138	Polychlorinated naphthalenes	PCN 13	C10H5Cl3	50402-52-3	231.506	229.945679	13.351	229.9448	194.9768
139	Polychlorinated naphthalenes	PCN 2	C10H7Cl	91-58-7	162.616	162.023621	8.611	162.0236	127.0541
140	Polychlorinated naphthalenes	PCN 27	C10H4Cl4	20020-02-4	265.951	263.906708	15.52	265.9048	228.9385
141	Polychlorinated naphthalenes	PCN 28	C10H4Cl4	53555-63-8	265.951	263.906708	15.311	265.9048	228.9385
142	Polychlorinated naphthalenes	PCN 36	C10H4Cl4	67922-22-9	265.951	263.906708	15.248	265.9048	228.9385
143	Polychlorinated naphthalenes	PCN 46	C10H4Cl4	3432-57-3	265.951	263.906708	16.402	265.9048	228.9385
144	Polychlorinated naphthalenes	PCN 48	C10H4Cl4	34588-40-4	265.951	263.906708	15.762	265.9048	228.9385
145	Polychlorinated naphthalenes	PCN 49	C10H3Cl5	67922-25-2	300.396	297.867737	18.822	299.8648	264.8968
146	Polychlorinated naphthalenes	PCN 50	C10H3Cl5	67922-26-3	300.396	297.867737	17.648	299.8648	264.8968
147	Polychlorinated naphthalenes	PCN 52	C10H3Cl5	53555-65-0	300.396	297.867737	17.118	299.8648	264.8968
148	Polychlorinated naphthalenes	PCN 53	C10H3Cl5	150224-24-1	300.396	297.867737	18.397	299.8648	264.8968
149	Polychlorinated naphthalenes	PCN 6	C10H6Cl2	1825-30-5	197.061	195.984650	10.885	195.9847	161.0157
150	Polychlorinated naphthalenes	PCN 63	C10H2Cl6	1335-87-1	334.841	331.828766	21.501	333.8258	298.8575
151	Polychlorinated naphthalenes	PCN 66	C10H2Cl6	103426-96-6	334.841	331.828766	20.237	333.8258	298.8575
152	Polychlorinated naphthalenes	PCN 69	C10H2Cl6	103426-94-4	334.841	331.828766	20.778	333.8258	298.8575
153	Polychlorinated naphthalenes	PCN 72	C10H2Cl6	103426-92-2	334.841	331.828766	20.927	333.8258	298.8575
154	Polychlorinated naphthalenes	PCN 73	C10HCl7	32241-08-0	369.286	365.789795	23.97	367.7868	332.8188
155	Polychlorinated naphthalenes	PCN 75	C10Cl8	2234-13-1	403.731	399.750824	27.09	403.7449	367.7871
156	Phthalates	BBzP	C19H20O4	85-68-7	312.360	312.136169	20.604	149.0215	238.0625
157	Phthalates	DAlP	C14H14O4	131-17-9	246.259	246.089203	12.899	149.0217	189.0546
158	Phthalates	DCHP	C20H26O4	84-61-7	330.418	330.183105	22.948	149.0207	249.1121
159	Phthalates	DEHP	C24H38O4	117-81-7	390.556	390.277008	23.332	167.034	279.1595
160	Phthalates	DEP	C12H14O4	84-66-2	222.237	222.089203	11.185	149.0194	177.0525
161	Phthalates	DiBP	C16H22O4	84-69-5	278.344	278.151794	14.232	150.0193	223.0959
162	Phthalates	DiHpP	C22H32O4	41451-28-9	360.488	360.231171	23.196	149.0186	265.1449
163	Phthalates	DiPrP	C14H18O4	605-45-8	250.290	250.120514	11.924	150.0201	209.0816

KOPRI 극지연구소

164	Phthalates	DMP	C10H10O4	131-11-3	194.184	194.057907	9.501	164.0384	194.0568
165	Phthalates	DnBP	C16H22O4	84-74-2	278.344	278.151794	15.342	149.0188	223.0971
166	Phthalates	DnHxP	C20H30O4	84-75-3	334.450	334.214417	20.441	150.0218	251.1289
167	Phthalates	DnOP	C24H38O4	117-84-0	390.556	390.277008	25.948	149.0205	279.1594
168	Phthalates	DnPeP	C18H26O4	131-18-0	306.397	306.183105	17.802	150.0205	237.1128
169	Phthalates	DnPrP	C14H18O4	131-16-8	250.290	250.120514	13.174	149.0181	191.0708
170	Dechlorane plus	anti-DP	C18H12Cl12	135821-74-8	653.724	647.720154	36.763	271.8125	296.9625
171	Dechlorane plus	syn-DP	C18H12Cl12	135821-03-3	653.724	647.720154	37.92	271.8125	296.9625
172	Siloxanes	D5	C10H30O5Si5	541-02-6	370.770	370.093964	5.434	355.0957	267.0227
173	Siloxanes	D6	C12H36O6Si6	540-97-6	444.924	444.112732	7.769	429.1169	430.0877
174	Siloxanes	L10	C22H66O9Si10	Not Available	755.609	754.239928	16.408	221.0873	147.0671
175	Siloxanes	L11	C24H72O10Si11	Not Available	829.763	828.258726	18.484	221.0873	147.0671
176	Siloxanes	L12	C26H78O11Si12	Not Available	903.917	902.277524	20.632	221.0873	147.0671
177	Siloxanes	L13	C28H84O12Si13	Not Available	978.071	976.296322	22.77	221.0873	147.0671
178	Siloxanes	L14	C30H90O13Si14	Not Available	1052.225	1050.315120	24.842	221.0873	147.0671
179	Siloxanes	L15	C32H96O14Si15	Not Available	1126.379	1124.333918	26.835	221.0873	147.0671
180	Siloxanes	L16	C34H102O15Si16	Not Available	1200.533	1198.352716	28.731	221.0873	147.0671
181	Siloxanes	L17	C36H108O16Si17	Not Available	1274.687	1272.371514	30.525	221.0873	147.0671
185	Siloxanes	L4	C10H30O3Si4	141-62-8	310.685	310.127197	4.297	295.1113	296.1071
186	Siloxanes	L5	C12H36O4Si5	141-63-9	384.839	384.145996	6.651	281.0544	147.0671
187	Siloxanes	L6	C14H42O5Si6	107-52-8	458.993	458.164795	8.889	221.0911	147.068
188	Siloxanes	L7	C16H48O6Si7	541-01-5	533.147	532.183594	10.905	221.0907	147.0674
189	Siloxanes	L8	C18H54O7Si8	556-69-4	607.301	606.202332	12.715	221.0873	147.0671
190	Siloxanes	L9	C20H60O8Si9	2652-13-3	681.455	680.221130	14.475	221.0873	147.0671
191	Chlorobenzenes	1,2,3,4-CBz	C6H2Cl4	634-66-2	215.892	213.891068	8.596	215.9219	178.9282
192	Chlorobenzenes	1,2,3,5-CBz	C6H2Cl4	634-90-2	215.892	213.891068	7.937	215.9219	178.9282
193	Chlorobenzenes	1,2,3-CBz	C6H3Cl3	87-61-6	181.447	179.930038	6.398	179.93	181.9271
194	Chlorobenzenes	1,2,4,5-CBz	C6H2Cl4	95-94-3	215.892	213.891068	7.966	215.9219	178.9282
195	Chlorobenzenes	1,2,4-CBz	C6H3Cl3	120-82-1	181.447	179.930038	5.904	179.93	181.9271
196	Chlorobenzenes	1,3,5-CBz	C6H3Cl3	108-70-3	181.447	179.930038	5.301	179.93	181.9271
197	Chlorobenzenes	PeCBz	C6HCl5	608-93-5	250.337	247.852097	10.393	249.8889	214.8903
198	Organophosphorus esters	CDP	C19H17O4P	26444-49-5	340.310	340.086456	22.483	340.0856	229.0405
199	Organophosphorus esters	EHDPP	C20H27O4P	1241-94-7	362.400	362.164703	21.694	251.0455	77.039
200	Organophosphorus esters	TBEP	C18H39O7P	78-51-3	398.472	398.243347	21.428	199.0721	299.1622
201	Organophosphorus esters	TBP	C12H27O4P	126-73-8	266.314	266.164703	11.761	98.9838	155.0461
202	Organophosphorus esters	TCEP	C6H12Cl3O4P	115-96-8	285.490	283.953888	13.054	248.9841	250.9812
203	Organophosphorus esters	TCPP	C9H18Cl3O4P	13674-84-5	327.570	326.000824	13.475	124.9993	98.9837
204	Organophosphorus esters	TDCPP	C9H15Cl6O4P	13674-87-8	430.905	427.883911	19.492	429.0872	355.0705
205	Organophosphorus esters	TEHP	C24H51O4P	78-42-2	434.633	434.352509	22.274	211.1075	113.1317
206	Organophosphorus esters	TEP	C6H15O4P	78-40-0	182.155	182.070801	6.592	155.1787	127.1472
207	Organophosphorus esters	TiPP	C9H21O4P	513-02-0	224.234	224.117752	6.392	98.9838	155.0461
208	Organophosphorus esters	TiPPP	C27H33O4P	64532-95-2	452.522	452.211639	27.415	452.211	155.0461
209	Organophosphorus esters	TmCP	C21H21O4P	563-04-2	368.363	368.117737	24.803	368.1163	165.0694
210	Organophosphorus esters	TMP	C3H9O4P	512-56-1	140.075	140.023849	5.464	98.9838	155.0461
211	Organophosphorus esters	ToCP	C21H21O4P	78-30-8	368.363	368.117737	24.918	368.1163	165.0694
212	Organophosphorus esters	TpCP	C21H21O4P	1330-78-5	368.363	368.117737	27.232	368.1163	165.0694
213	Organophosphorus esters	TPeP	C15H33O4P	2528-38-3	308.394	308.211639	15.566	98.9838	155.0461
214	Organophosphorus esters	TPhP	C18H15O4P	115-86-6	326.283	326.070801	21.279	326.0696	215.0259
215	Organophosphorus esters	TPrP	C9H21O4P	513-08-6	224.234	224.117752	8.991	98.9838	155.0461

Table S3. The percentage recoveries of each target compound groups analyzed by GC/TOF using 4 different types of SPE cartridge.

	Oasis HLB		C18		Silica gel		Florisil	
	Mean	SD[a]	Mean	SD	Mean	SD	Mean	SD
PCDD/Fs	55.2	10.9	42.4	2.49	50.2	1.27	44.6	4.20
PCBs	76.5	6.76	67.3	3.36	76.9	0.70	71.0	4.14
OCPs	79.9	8.68	67.8	1.76	76.9	2.14	69.5	4.01
PBDEs	61.5	14.0	45.4	2.09	54.6	1.84	44.6	4.87
PAHs	110	5.59	97.4	6.25	90.0	7.84	91.5	4.05
PCNs	60.5	8.35	47.8	4.20	56.5	1.51	52.4	5.39
CLBs	95.3	1.45	90.0	2.65	78.7	5.03	73.5	3.54
DP	53.8	14.4	40.7	1.41	47.5	2.15	37.0	2.96
NBFRs	59.3	10.2	47.1	5.13	56.4	6.05	49.3	11.4
OPFRs	78.6	8.24	72.1	4.35	69.9	6.28	71.6	4.54
Phthalates	99.6	5.41	81.0	2.99	96.0	1.11	87.8	2.84
Siloxanes	81.1	6.96	74.0	3.76	85.6	1.38	72.8	3.70
SMCs	89.0	9.87	73.7	5.10	85.3	2.72	72.2	5.11
BUVSs	85.4	10.1	71.4	4.81	79.1	2.32	69.2	4.37
Total	77.5	19.4	65.1	18.6	71.8	16.3	64.3	17.1

[a]Standard deviation.

극지연구소

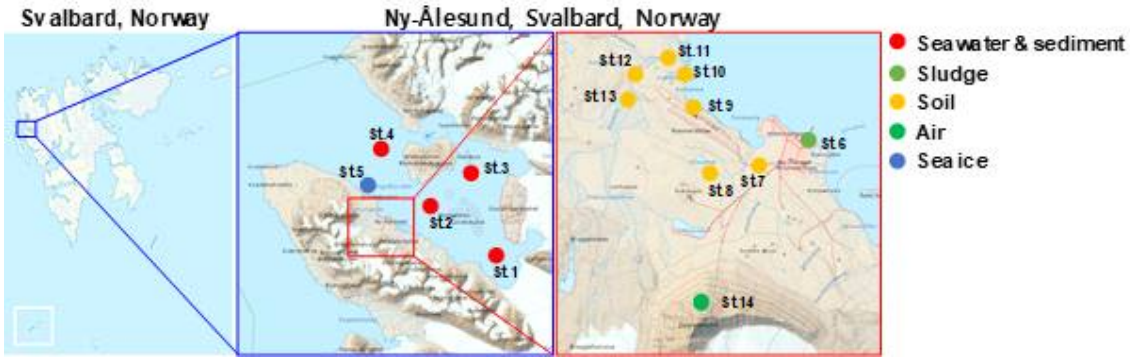

Figure S1. Sampling locations of sludge, seawater, sediment, soil, air, and sea ice samples collected from Ny-Ålesund, Svalbard, Norway.

Figure S2. Total ion chromatogram of sediment sample before (black line) and after passing through an Oasis HLB cartridge (red line) to check cleanup efficiency.

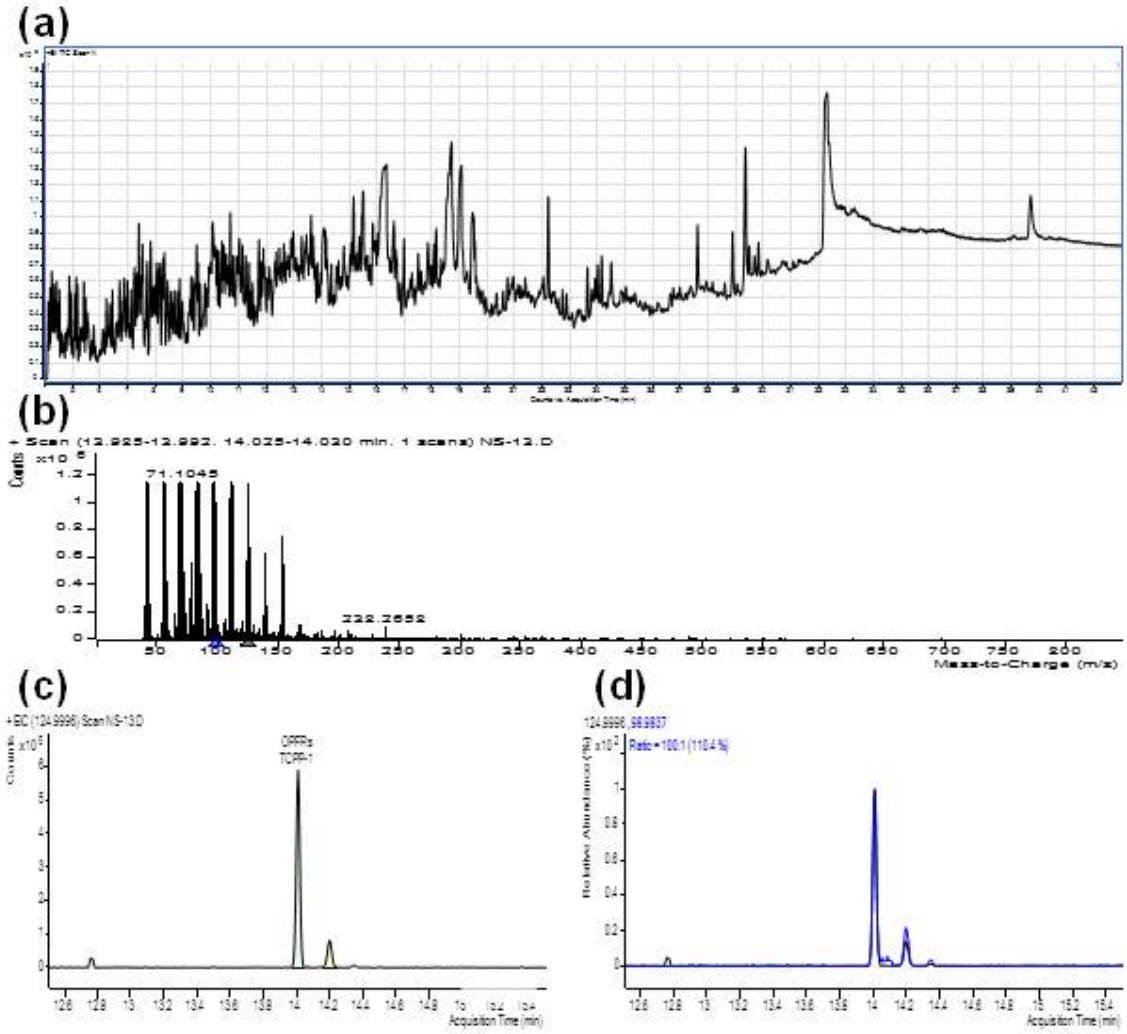

Figure S3. Total ion chromatogram and compounds detected in sediment sample by suspect analysis. (a) total ion chromatogram; (b) the mass spectrum from the total ion chromatogram at 14.004 min; (c) extracted ion chromatogram of qualification ion (m/z: 124.9996) for TCPP at 14.004 min; (d) extracted ion chromatogram of qualifier ion (m/z: 98.9837) for TCPP at 14.004 min.

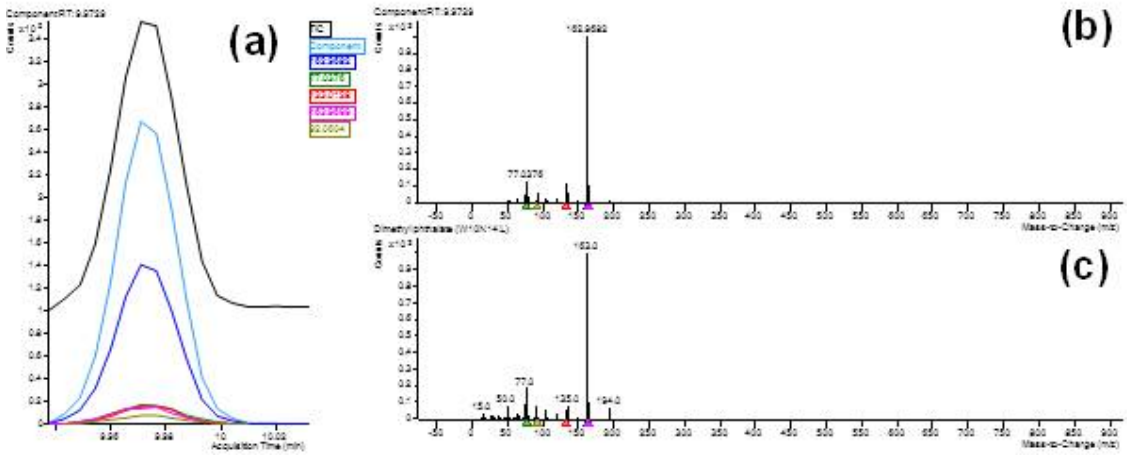

Figure S4. Compounds detected in sediment sample of dimethyl phthalate by non-target analysis. (a) the component detection for dimethyl phthalate at 9.9729; (b) the deconvoluted spectrum from the component at 9.9729; (c) the mass spectrum of dimethyl phthalate from NIST library.

KOPRI
극지연구소

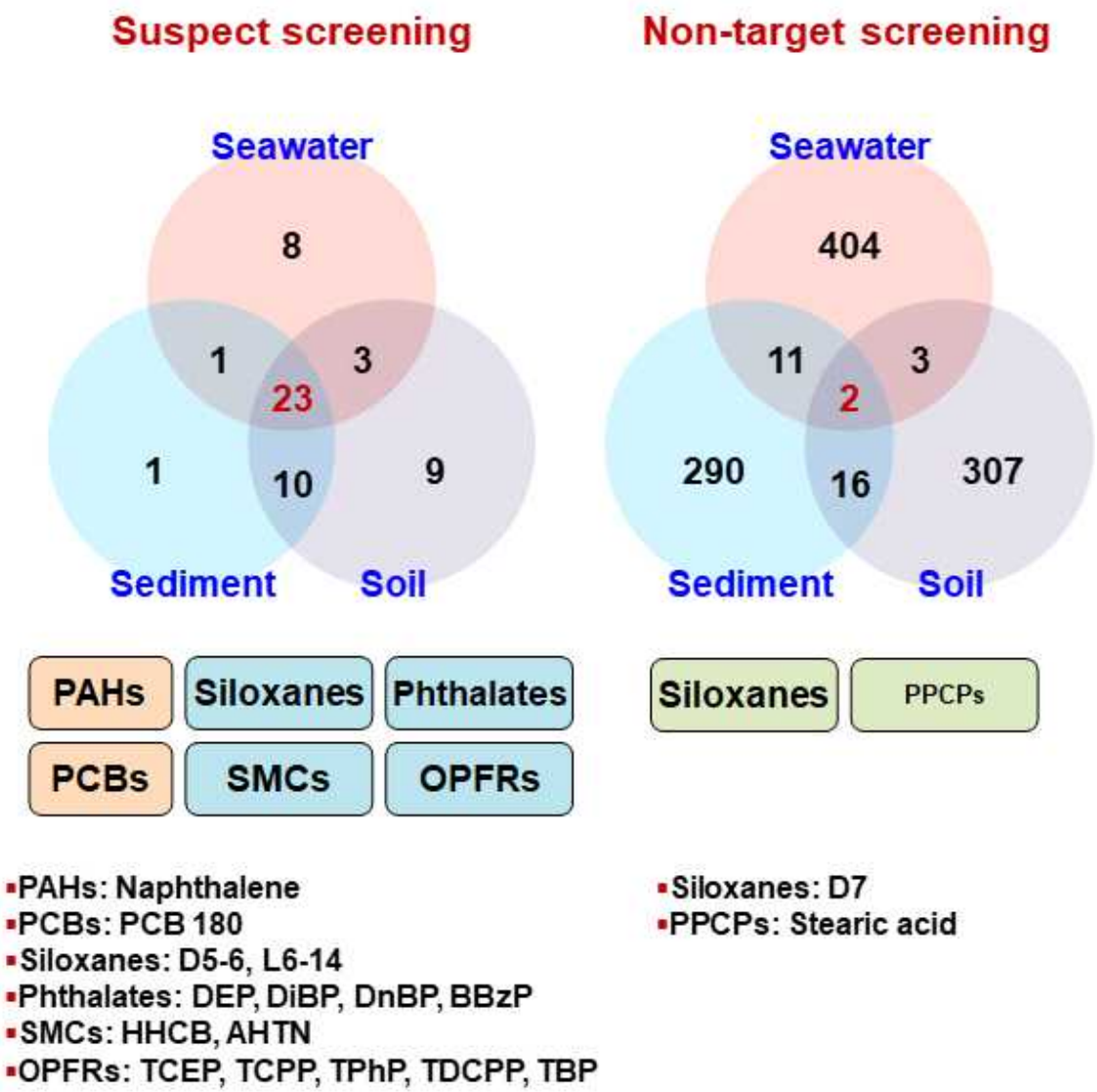

Figure S5. Commonly detected contaminants by suspect and non-target screening analysis in multi matrix.

제 19 절. Ocean Iron Fertilization Experiments: An Overview of the Past, Present, and Future of the Korean Iron Fertilization Experiment in the Southern Ocean (KIFES) Project[12)]

Joo-Eun Yoon[1], Kyu-Cheul Yoo[2], Alison M. Macdonald[3], Ho-Il Yoon[2], Ki-Tae Park[2], EunJin Yang[2], Hyun-Cheol Kim[2], JaeIl Lee[2], MinKyung Lee[2], Jinyoung Jung[2], Jisoo Park[2], Jiyoung Lee[1], Soyeon Kim[1], Seong-Su Kim[1], Kitae Kim[2], and Il-Nam Kim[1]

[1]Department of Marine Science, Incheon National University,
[2]Korea Polar Research Institute
[3]Woods Hole Oceanographic Institution, MS 21, 266 Woods Hold Rd., Woods Hole, USA

1. Introduction

Since the start of the industrial revolution, human activities have caused a rapid increase in atmospheric carbon dioxide (CO_2) from ~280 ppm (pre-industrial revolution) to ~400 ppm (present day) (http://www.esrl.noaa.gov/), which has, in turn, led to global warming and ocean acidification (IPCC, 2013) (Fig. 1). As the Anthropocene climate system has rapidly become more unpredictable, the scientific consensus is that the negative outcomes are a globally urgent issue that should be resolved in a timely manner for the sake of all life on Earth (IPCC, 1990, 1992, 1995, 2001, 2007, 2013). The various ideas/approaches that have been proposed to relieve/resolve the problem of global warming (Matthews, 1996; Lenton and Vaughan, 2009; Vaughan and Lenton, 2011; IPCC, 2014; Leung et al., 2014; Ming et al., 2014) largely fall into two categories: (1) reduction of atmospheric CO_2 by the enhancement of biological CO_2 uptake (including ocean fertilization) and/or the direct capture or storage of atmospheric CO_2 through chemically engineered processes, and (2) control of solar radiation by artificial aerosol injection into the atmosphere to augment cloud formation and cloud brightening to elevate albedo (Fig. 2). One of the most attractive of these proposed approaches is *ocean fertilization*, which targets the drawdown of atmospheric CO_2 by nutrient addition (e.g., iron, nitrogen, or phosphorus compounds) aimed at stimulating phytoplankton growth and, subsequently, carbon export to the deep ocean or sediments via

12) 이 연구는 본 과제 지원으로 수행되었으며 그 결과는 다음의 논문으로 출판되었음: Joo-Eun Yoon, Kyu-Cheul Yoo, Alison M. Macdonald, Ho-Il Yoon, Ki-Tae Park, EunJin Yang, Hyun-Cheol Kim, JaeIl Lee, MinKyung Lee, Jinyoung Jung, Jisoo Park, Jiyoung Lee, Soyeon Kim, Seong-Su Kim, Kitae Kim, and Il-Nam Kim, “Ocean Iron Fertilization Experiments: An Overview of the Past, Present, and Future of the Korean Iron Fertilization Experiment in the Southern Ocean (KIFES) Project”, *Biogeosciences*, 2018, 15, 5847-5889.

the ocean biological pump (ACE CRC, 2015).

The ocean biological pump is frequently depicted as a single combined process, whereby organic matter produced by phytoplankton during photosynthesis in surface waters is quickly transported to intermediate and/or deep waters (Fig. 3a) (Volk and Hoffert, 1985; De La Rocha, 2007). Although the effectiveness of the biological pump is primarily controlled by the supply of macro-nutrients (i.e., nitrate, phosphate, and silicate) from the deep ocean into the mixed layer leading to new production (Sarmiento and Gruber, 2006), iron acts as an essential micro-nutrient to stimulate the uptake of macro-nutrients for phytoplankton growth (Fig. 3b) (Martin and Fitzwater, 1988; Martin, 1990; Morel and Price, 2003). In the subarctic North Pacific (NP), equatorial Pacific (EP), and Southern Ocean (SO), which are well known as high-nutrient and low-chlorophyll (HNLC) regions (Figs. 4a and b), phytoplankton cannot completely utilize the available macro-nutrients (particularly nitrate) for photosynthesis due to a lack of iron. As a consequence, primary production (PP) in these HNLC regions is relatively low, despite the high availability of macronutrients (in particular nitrate and phosphate) (Figs. 4a and b).

Analyses of trapped air bubbles in Arctic/Antarctic ice cores have revealed that atmospheric CO_2 (~180 ppm) during the Last Glacial Maximum (LGM; ~20,000 years ago) was much lower than during pre-industrial times (~280 ppm) (Neftel et al., 1982; Barnola et al., 1987; Petit et al., 1999). Over the last 25 years, several hypotheses have been proposed to explain the lowered atmospheric CO_2 level during the LGM (Broecker, 1982; McElroy, 1983; Falkowski, 1997; Broecker and Henderson, 1998; Sigman and Boyle, 2000). Dust inputs are generally regarded as a major natural iron source for ocean fertilization, and Martin (1990) hypothesized that during the LGM increased dust inputs relieved iron-limitation and, thereby, substantially enhanced the biological pump in HNLC regions, particularly in the SO (Fig. 3b). Since Martin's hypothesis was first published, there has been an enormous interest in ocean iron fertilization (OIF) because only a small amount of iron (C:Fe ratios = 100,000:1, Anderson and Morel, 1982) is needed to stimulate a strong phytoplankton response. Therefore, much of the investigative focus has centered on the artificial addition of iron to HNLC regions as a means of enhancing carbon fixation and subsequent export via the biological pump (ACE CRC, 2008).

To test Martin's hypothesis, two natural OIF (nOIF) and 13 artificial OIF (aOIF) experiments have been performed to date in the subtropical North Atlantic (NA), EP, subarctic NP, and SO (Blain et al., 2007; Boyd et al., 2007; Pollard et al., 2009; Strong et al., 2009) (Fig. 4a and Table 1). These OIF experiments demonstrated, particularly for the SO, that PP could be significantly increased after iron addition (de Baar et al., 2005; Boyd et al., 2007). However, for aOIF to be considered as a useful long-term geoengineering approach (IPCC, 2007), the most critical issue is whether the substantial amounts of

organic carbon produced by aOIF in the surface waters lead to a significant export to intermediate/deep layers and long-term (~1,000 years) storage (Fig. 3c) (Lampitt et al., 2008). A high carbon export was observed in the nOIF experiments in the SO near the Kerguelen Plateau and Crozet Islands (Blain et al., 2007; Pollard et al., 2009). However, all aOIF experiments have shown unexpectedly low carbon exports compared to natural systems (de Baar et al., 2005; Boyd et al., 2007), except for the SO European Iron Fertilization Experiment, EIFEX (Smetacek et al., 2012). The results of these experiments, as well as the potential side effects (e.g., N_2O production and development of hypoxia (Fuhrman and Capone, 1991)), have been scientifically debated amongst those who support and oppose OIF experimentation (Chisholm et al., 2001; Johnson and Karl, 2002; Lawrence, 2002; Buesseler and Boyd, 2003; Smetacek and Naqvi, 2008; Williamson et al., 2012).

In the context of increasing global (social-political-economic) concerns associated with rapid climate change, it is necessary to examine the validity and usefulness of aOIF experimentation as a climate change mitigation strategy. Therefore, the purpose of this paper was to: (1) provide a thorough overview of the aOIF experiments conducted over the last 25 years; (2) discuss aOIF-related important unanswered questions, including carbon export measurement methods, potential side effects, and international law; (3) suggest considerations for the design of future aOIF experiments to maximize the effectiveness of the technique and begin to answer open questions; and (4) introduce design guidelines for a future Korean Iron Fertilization Experiment in the Southern Ocean (KIFES) project.

KOPRI 극지연구소

2. Past: Overview of previous aOIF experiments

A total of 13 aOIF experiments have been conducted in the following areas: 12 experiments were conducted in the three main HNLC (i.e., nitrate >~10 μM) regions: two in the EP, three in the subarctic NP, and seven in the SO (Table 1, Figs. 4a and b). One experiment was conducted in the subtropical NA, known to be a low-nutrient and low-chlorophyll (LNLC) (i.e., nitrate <1 μM) region. These aOIF experiments have been conducted with various/multiple objectives/hypotheses to investigate the biogeochemical responses of ocean environments to artificial iron additions (Table 2). This overview of past aOIF experimentation begins in Section 2.1, with a presentation of the reasons why each experiment was performed and the main hypotheses (Table 2). The unique ocean conditions for the various experiments are described in Section 2.2. Iron addition and the tracing of iron are described in Section 2.3. The biogeochemical responses to the aOIF experiments are presented in Section 2.4, and finally the significant findings from these experiments are summarized in Section 2.5.

2.1 Objectives and hypotheses of previous aOIF experiments

2.1.1 Equatorial Pacific

Initially, Martin's hypothesis was supported by the results of laboratory and shipboard iron-enrichment bottle experiments (Hudson and Morel, 1990; Brand, 1991; Sunda et al., 1991; DiTullio et al., 1993; Hutchins et al., 1993). However, the extrapolation of these results to higher community levels based on the lower trophic levels in a marine ecosystem has been strongly criticized due to possible underestimates in grazing forcing and containment effects. To deal with these issues, in situ iron fertilization experiments at the whole-ecosystem level are required. Under the hypothesis that artificial iron addition would increase phytoplankton productivity by relieving iron limitations on phytoplankton in HNLC regions, the first aOIF, Iron Enrichment Experiment (IronEx-1), was conducted over 10 days in October 1993 in the EP where high intensity light and warm temperatures would assist rapid phytoplankton growth (Martin et al., 1994; Coale et al., 1998).

However, the magnitude of the biogeochemical responses in IronEx-1 were not as large as expected (Martin et al., 1994). Three hypotheses were advanced to explain the weak responses observed: (1) the possibility of other unforeseen micro-nutrient (e.g., zinc, cadmium, and manganese) or macro-nutrient (e.g., silicate) limitations, (2) the short residence time of bioavailable iron in the surface patch due to an unstable water-column structure, and (3) the extremely high grazing pressure (Cullen, 1995). To test the three hypotheses, a second aOIF experiment, IronEx-2, was conducted in May 1995 (Coale et al., 1996). The IronEx-2 research cruise investigated the same area for a longer period (17 days), providing more time to collect information about the biogeochemical, physiological, and ecological responses to the OIF experiment.

2.1.2 Southern Ocean

The SO plays an important role in intermediate and deep-water formation, and has the potential for carbon sequestration associated with artificial iron addition (Martin, 1990; Sarmiento and Orr, 1991; Cooper et al., 1996; Marshall and Speer, 2012). It is known as the largest HNLC region in the World Ocean and models simulating aOIF have predicted that among all HNLC regions, the effect of OIF on carbon sequestration is greatest in the SO (Sarmiento and Orr, 1991). However, a simple extrapolation of the IronEx-2 results to the SO was not deemed appropriate because of the vastly different environmental conditions (Coale et al., 1996) and, therefore, this basin became the next region selected for an aOIF experiment (Frost, 1996). With the hypothesis that iron and light availability may act as key factors that control phytoplankton dynamics, community structure, and grazing in the SO, the Southern Ocean Iron Release Experiment (SOIREE) (Table 1 and Fig. 4a), which was the first *in situ* aOIF experiment performed in the SO, took place in February 1999

(13 days) in the Australasian-Pacific sector (Boyd et al., 2000).

The following year, a second aOIF experiment in the SO, EisenEx ('Eisen' means iron in German), was performed in November within an Antarctic circumpolar current (ACC) eddy in the Atlantic sector (Smetacek, 2001). This region is considered to have a relatively high iron supply, which is supported by dust inputs and sea-ice melt (de Baar et al., 1995; Quéguiner et al., 1997; Smetacek et al., 2002). EisenEx was designed to test the hypothesis that atmospheric dust, an important source of iron in ocean environments, might have led to a dramatic increase in ocean productivity during the LGM due to the relief of iron-limiting conditions for phytoplankton growth.

In addition to iron availability, the supply of silicate is also considered to be an important factor controlling PP in the SO. Silicate-requiring diatoms, which are large-sized phytoplankton, have an important role in the biological pump and are responsible for ~75% of the annual PP in the SO (Tréguer et al., 1995). The silicate concentrations in the SO have a decreasing northward gradient, in particular, on either side of the Antarctic Polar Front (PF), with low silicate concentrations (<5 μM) in the sub-Antarctic waters north of the PF (<61°S) and high silicate concentrations (>60 μM) to the south of the PF (Fig. 4c). Therefore, to address the potential for iron and silicate interactions to regulate the diatom bloom, two aOIF experiments were conducted during January February 2002 in two distinct regions: the Southern Ocean iron experiment-north (SOFeX-N) and -south (SOFeX-S) of the PF (Coale et al., 2004; Hiscock and Millero, 2005) (Table 1). In these two experiments, it was hypothesized that conditions that provided sufficient silicate and iron would lead to high diatom production, while sufficient iron alone would not lead to a diatom bloom (Coale et al., 2004).

Two years later, the Surface Ocean Lower Atmosphere Study (SOLAS) Air - Sea Gas Exchange (SAGE) experiment was conducted during March - April 2004 (15 days) in sub-Antarctic waters, which are HNLC and low silicate concentration waters (HNLCLSi). The aim was to determine the response of phytoplankton dynamics to iron addition in an HNLCSi region (Fig. 4c) (Law et al., 2011). SAGE was designed with the assumption that the response of phytoplankton blooms to artificial iron addition could be detected by enhanced air-sea exchanges of climate-relevant gases (e.g., CO_2 and dimethyl sulfide (DMS)) (Harvey et al., 2010; Law et al., 2011).

These early aOIF experiments demonstrated clear increases in phytoplankton biomass, but the association with export production (i.e., exported carbon from the surface waters into intermediate/deep waters) was obscure (de Baar et al., 2005; Boyd et al., 2007). Therefore, to determine if aOIF could increase export production, EIFEX was conducted during February - March 2004 in a cyclonic eddy core near the PF (Fig. 5). Because it was designed to investigate export production, EIFEX was a much longer experiment (39 days)

compared to earlier studies (~23 days or less) (Smetacek et al., 2012).

To trace the fate of an iron-stimulated phytoplankton bloom and deep carbon export, the Indo-German iron fertilization experiment (LOHAFEX; 'Loha' is iron in Hindi) was conducted during January - March 2009 (40 days), also in a PF cyclonic eddy (Smetacek and Naqvi, 2010; Martin et al., 2013)

2.1.3 Subarctic North Pacific

By the 20th century, the subarctic NP was the only HNLC region in which an aOIF experiment had not been performed (Table 1) (de Baar et al., 2005; Boyd et al., 2007). The subarctic NP shows a strong longitudinal gradient in aeolian dust deposition (i.e., high dust deposition in the west, but low in the east) (Duce and Tindale, 1991; Tsuda et al., 2003; Takeda and Tsuda, 2005), which is different from the other two HNLC regions (i.e., EP and SO). To investigate the relationship between the phytoplankton biomass/community and dust deposition, the Subarctic Pacific iron Experiment for Ecosystem Dynamics Study-1 (SEEDS-1) was conducted in July August 2001 (13 days) in the western subarctic gyre (Tsuda et al., 2003, 2005). In 2004, the experiment was repeated (SEEDS-2) in almost the same location and season. In the intervening year, 2002, the Subarctic Ecosystem Response to Iron Enrichment Study (SERIES) was performed in July August (25 days) in the Gulf of Alaska (representing the eastern subarctic gyre ecosystem) to compare the response of phytoplankton in this area with that in the western subarctic (Boyd et al., 2004, 2005). The SEEDS experiments focused on changes in phytoplankton composition, vertical carbon flux, and climate-relevant gas production stimulated by artificial iron addition (Tsuda et al., 2005, 2007). The main objective of SEEDS-2 and SERIES was to determine the most significant factor (i.e., nutrient supply and/or grazing forcing) controlling the iron induced phytoplankton bloom from its beginning to its end (Boyd et al., 2004).

2.1.4 Subtropical North Atlantic

Unlike HNLC regions, PP in LNLC regions, which are predominantly occupied by N_2 fixers, is generally co-limited by phosphate and iron (Mills et al., 2004). To investigate the impact of iron and phosphate co-limitation on PP, the *in situ* phosphate and iron addition experiment (FeeP) was conducted by adding both phosphate and iron in an LNLC region of the subtropical NA during April May 2004 (21 days) (Rees et al., 2007).

2.2 Environmental conditions prior to iron addition

The initial environment (~1-7 days before iron addition) can affect the outcome of an aOIF experiment, and the experiments described above were conducted under a wide range of physical and biogeochemical conditions. We considered the similarities and differences in

these environments according to the physical and biogeochemical properties of the sites (Steinberg et al., 1998; Coale et al., 1998; Bakker et al., 2001; Boyd and Law, 2001; Gervais et al., 2002; Coale et al., 2004; Boyd et al., 2005; Takeda and Tsuda, 2005; Tsuda et al., 2007; Cisewski et al., 2008; Harvey et al., 2010; Cavagna et al., 2011) (Fig. 6, Tables 3 and 4).

2.2.1 Equatproal Pacific

The first two aOIF experiments, IronEx-1 and IronEx-2, which were both conducted in the EP, were performed in different seasons (i.e., IronEx-1: October, IronEx-2: May). However, the initial surface physical conditions were rather similar, with warm temperatures (mean ± SD = 24.1 ± 1.2°C; SD represents standard deviation), high surface photosynthetic available radiation (PAR) values (51.7 ± 2.1 mol m-2 d-1), and shallow mixed layer depths (MLDs) (27.5 ± 2.5 m) (Figs. 6c and d) (Coale et al., 1996; Coale et al., 1998; Steinberg et al., 1998).

The initial surface biogeochemical conditions were high nutrient (i.e., nitrate = 10.6 ± 0.2 μM, phosphate = 0.9 ± 0.06 μM, and silicate = 4.5 ± 0.6 μM) and low chlorophyll-a concentrations (0.2 ± 0.02 mg m^{-3}). The pico-phytoplankton (0.2 2.0 μm) community, including *Synechococcus* and *Prochlorococcus*, was dominant. Initial surface nutrient concentrations were relatively low compared with other ocean basin aOIF sites (Table 3 and Fig. 6e). Initial photosynthetic quantum efficiency (i.e., Fv/Fm ratio), which is widely used to determine the degree to which iron is the limiting nutrient for phytoplankton growth (the Fv/Fm ratio ranges from 0 to 0.65 where conditions are less iron limited as Fv/Fm approaches 0.65) (Behrenfeld et al., 1996; Boyd et al., 2005), was less than 0.3 (Fig. 6g and Table 4), suggesting severe iron limitation. In aOIF experiments, the initial surface partial pressure of CO_2 (pCO_2) has been recorded using continuous shipboard measurement systems (Wanninkhof and Thoning, 1993; Steinberg et al., 1998; Bakker et al., 2001; Bakker et al., 2005; Hiscock and Millero, 2005; Takeda and Tsuda, 2005; Smetacek et al., 2005; Wong et al., 2006; Tsumune et al., 2009; Currie et al., 2011). In the EP, initial pCO_2 values were 504.5 ± 33.5 μatm, which were much higher than those observed in the SO (355.3 ± 12.5 μatm) or the subarctic NP (370 ± 16.3 μatm) (Steinberg et al., 1998).

2.2.2 Southern Ocean

The initial physical conditions for the aOIF experiments in the SO (SOIREE, EisenEx, SOFeX-N/S, EIFEX, SAGE, and LOHAFEX) were very different from those found in the EP; MLDs were much deeper (52.1 ± 22.7 m) (Fig. 6c) and sea surface temperature (SST) was much lower (4.8 ± 3.5 °C) (Fig. 6d). During SOFeX-N/S, which were conducted along the same line of longitude, on either side of the PF, there were distinct differences in SST:

7.1°C in SOFeX-N and 0.5°C in SOFeX-S (Coale et al., 2004). SAGE was the northernmost of the aOIF experiments in the SO and, therefore, had the highest SST (11.5°C) (Harvey et al., 2010).

The regions used for the aOIF experiments were selected following preliminary surveys to confirm that the sites were subject to HNLC conditions, i.e., nitrate concentration (>~10 μM) and chlorophyll-a concentration (<1 mg m^{-3}). Initial nitrate concentrations ranged from 7.9 μM (SAGE) to 26.3 μM (SOFeX-S) (Fig. 6e and Table 3). Among the various aOIF HNLC experiment sites, the SO had the highest initial nitrate concentrations (21.5 ± 5.0 μM), while the EP had the lowest (10.6 ± 0.2 μM). Initial nitrate and phosphate concentrations at aOIF sites in the SO followed a latitudinal gradient, with higher values to the south of 50°S (nitrate: 24.6 ± 1.6 μM and phosphate: 1.6 ± 0.2 μM) and lower values to the north (nitrate: 17.4 ± 5.1 μM and phosphate: 1.3 ± 0.3 μM) (Table 3, Figs. 4b and 6e). The SO presented the full range of initial silicate concentrations for all aOIF experiments, with values ranging widely from 0.83 μM (SAGE) in the most northernmost site to 62.8 μM (SOFeX-S) in the most southernmost (Table 3, Figs. 4c and 6f). With the specific intent of investigating the co-limitation of iron and silicate to diatom blooms, SOFeX-N, SAGE, and LOHAFEX were all conducted in HNLCLSi regions, with initial silicate concentrations less than 2.5 μM (Figs. 4c and 6f) (Coale et al., 2004; Harvey et al., 2010; Martin et al., 2013). Initial pCO_2 was lowest in the SO (355.3 ± 12.5 μatm) ranging from 330 μatm (SAGE) to 367 μatm (SOFeX-N).

As in the EP, initial SO Fv/Fm values were below 0.3 (Table 4 and Fig. 6g), indicating a severe iron limitation. Prior to iron addition, initial chlorophyll-a concentrations ranged from 0.15 to 0.70 mg m^{-3}. The maximum SO chlorophyll concentrations were found at EIFEX, which was dominated by a micro-phytoplankton (20-200 μm) community of diatoms, while the minimum chlorophyll concentrations were observed at SOFeX-N, which was dominated by a nano-phytoplankton (2.0-20 μm) community, such as prymnesiophytes, pelagophytes, and dinoflagellates.

2.2.3 Subarctic North Pacific

The subarctic NP aOIF experiments (i.e., SEEDS-1/-2 and SERIES) were performed in regions with high nitrate (16.3 ± 3.0 μM) and low chlorophyll-a concentrations (0.7 ± 0.2 mg m-3) (Tables 3 and 4, Figs. 6e and h). Compared with the other aOIF experiments, these subarctic experiments had much higher initial silicate concentrations (27.3 ± 9.6 μM) (Table 3 and Fig. 6f) and shallower MLDs (Fig. 6c). Although SEEDS-1 and SEEDS-2 were conducted in almost the same location and season in the western basin (Tsuda et al., 2007), the MLD in SEEDS-1 (10 m) was shallower than in SEEDS-2 (28 m).

Unlike the latitudinal gradients seen in the aOIF experiments in the SO, there

were longitudinal gradients in physical and biogeochemical properties in the subarctic NP experiments (Tables 3 4, Figs. 4b c, and Figs. 6d h). Initial SSTs in the SO were lower in the western region (7.5°C in SEEDS-1 and 8.1°C in SEEDS-2) than in the eastern region (12.5°C in SERIES) (Fig. 6d). Initial nutrient concentrations were much higher in the west (nitrate: 18.5 ± 0.1 μM and silicate: 34.0 ± 2.2 μM) compared to the east (nitrate: 12 μM and silicate: 16 μM) (Table 3, Figs. 4b c and 6e f). There was also a longitudinal gradient in chlorophyll-a concentrations, with relatively high values in the west (SEEDS-1: 0.9 mg m^{-3} and SEEDS-2: 0.8 mg m^{-3}) and low in the east (SERIES: 0.4 mg m^{-3}) (Fig. 6h). Before the first SEEDS-1 iron infusion, micro-phytoplankton, such as the pennate diatom "*Pseudo-nitzschia turgidula*", were dominant, whereas for SERIES and SEEDS-2 the area was exclusively occupied by pico- and nano-phytoplankton, such as *Synechococcus* and haptophytes (Tsuda et al., 2005; Boyd et al., 2005). Initial Fv/Fm ratios in the subarctic NP aOIF experiments were <0.3, indicating a severe iron limitation (Fig. 6g).

2.3 Iron addition and tracing methods

2.3.1 Iron addition

Iron(II) and sulfate aerosols are ubiquitous in the atmosphere and, therefore, iron-sulfate ($FeSO_4 \cdot H_2O$), a common form of combined iron that enters the ocean environment via dust deposition, has been frequently regarded as a bioavailable iron source during glacial periods (Zhuang et al., 1992; Zhuang and Duce, 1993; Spolaor et al., 2013). Iron-sulfate is a common inexpensive agricultural fertilizer that is relatively soluble in acidified seawater (Coale et al., 1998). Therefore, all aOIF experiments have been conducted by releasing commercial iron-sulfate dissolved in acidified seawater into the propeller wash of a moving ship (Fig. 5), to ensure mixing with surface waters during iron additions.

In general, background dissolved iron concentrations in HNLC regions are <0.2 nM (Table 1). Iron-enrichment bottle incubation experiments performed in deck incubators using ocean water have indicated the maximum phytoplankton growth rates in response to iron additions of 1 - 2 nM (Fitzwater et al., 1996). In aOIF experiments performed in the ocean, targeted iron concentrations within the MLD have ranged between ~1 to 4 nM, depending on the site (Coale et al., 1998; Bowie et al., 2001; Harvey et al., 2010; Martin et al., 2013). If injected iron is well dispersed throughout the mixed layer within 24 h by convective mixing (Martin and Chisolm, 1992), the amount of added iron required to raise the background iron concentration to the target level can be calculated using a volume estimate (i.e., iron-fertilized water patch area × MLD) (Watson et al., 1991). To minimize uncertainty between the first iron addition and phytoplankton response, aOIF experiments have involved multiple-small iron injections to the surface waters in the study area at ~0.4

to 1.5 km intervals over a 1–2-day period (Coale et al., 1998). The patch size fertilized by the first iron addition varied from 25 km^2 (e.g., FeeP; Iron(II) addition of 1840 kg) to 300 km^2 (e.g., LOHAFEX; Iron(II) addition of 2,000 kg), and by the end of these experiments had spread to a maximum ~2500 km^2 (Boyd et al., 2007; Martin et al., 2013) (Table 1, Figs. 6a and b).

During the experiments, dissolved iron concentrations increased to the target ~1.0 4.0 nM (Table 1), but decreased to background concentrations within days. The fast decrease in dissolved iron concentrations indicates that iron was horizontally dispersed and/or rapidly incorporated into particles. These processes occur more rapidly in warmer waters (ACE CRC, 2015). For example, the first aOIF experiment, IronEx-1, showed that the dissolved iron concentration rapidly decreased from 3.6 to 0.25 nM ~2 days after iron addition in the center of the fertilized patch, suggesting a limit to the level required for phytoplankton growth (Gordon et al., 1998). As a result, except for the single iron addition experiments of IronEx-I, SEEDS-1, and FeeP (Martin et al., 1994; Tsuda et al., 2005; Rees et al., 2007), most aOIF experiments have involved multiple iron additions at the patch center, to continuously drive the stimulation of phytoplankton during the experiments. These experiments included: (2 additions) EIFEX, SERIES, SEEDS-2, LOHAFEX (Boyd et al., 2005; Smetacek et al., 2012; Martin et al., 2013); (3 additions) IronEx-2, EisenEx, SOFeX-N (Coale et al., 1996; Gervais et al., 2002; Coale et al., 2004; Nishioka et al., 2005); and (4 additions) SOIREE, SOFeX-S, SAGE (Boyd and Law, 2001; Coale et al., 2004; Harvey et al., 2010) (Table 1).

KOPRI 극지연구소

2.3.2 Tracing iron-fertilized patch

To trace the iron-fertilized patch, aOIF experiments have used a combination of physical and biogeochemical approaches. All the aOIF experiments except EIFEX have used SF_6 as a chemical tracer (Martin et al., 1994; de Baar et al., 2005). Sulfur hexafluoride, which is not naturally found in oceanic waters, is a useful tracer for investigating physical mixing and advection-diffusion processes in the ocean environment due to its nontoxicity, biogeochemically inert characteristics, and low detection limit (Law et al., 1998). The injected SF_6 is continuously monitored using gas chromatography with an electron capture detector system (Law et al., 1998; Tsumune et al., 2005). Usually only one SF_6 injection is necessary because background levels are generally extremely low in the ocean (<1.2 fM; f: femto-, 10^{-15}) (Law et al., 1998; Law et al., 2006; Martin et al., 2013); however, in the SAGE experiment, with its higher mixing and lateral dilution, there were three injections (Harvey et al., 2010). Although these earlier experiments demonstrated that the injection of artificial SF_6 is a useful technique for following iron-fertilized patches, caution is required because artificially high levels of SF_6 injection may negatively impact the interpretation of

low-level SF_6 signals dissolved in seawater via air-sea exchange. These techniques have been widely used to estimate anthropogenic carbon invasion as well as to understand ocean circulation in various ocean environments, with SF_6 being an important time-dependent tracer that has a well-recorded atmospheric history (Fine, 2011). Continuous sampling systems, measuring biogeochemical parameters such as Fv/Fm, pCO_2, and chlorophyll fluorescence, have also been used as an alternative means of following iron-fertilized patches (Gervais et al., 2002; Boyd et al., 2005; Tsuda et al., 2007; Harvey et al., 2010; Smetacek et al., 2012). The Fv/Fm ratio displays a particularly rapid increase (within 24 h) in response to an initial iron addition (Kolber et al., 1994; Behrenfeld et al., 1996; Smetacek et al., 2012), suggesting that it is an easy and convenient tracer for following a fertilized patch.

In addition, surface-drifting buoys equipped with Array for Real-time Geostrophic Oceanography (ARGO) and Global Positioning System (GPS) sensors have been successfully used to track the movement of fertilized patches along with biogeochemical tracers (Coale et al., 1998; Boyd and Law, 2001; Law et al., 2006; Martin et al., 2013). However, floats tend to deviate from the location of fertilized patches under strong wind forcing (Watson et al., 1991; Law et al., 1998; Stanton et al., 1998). NASA airborne oceanographic lidar (AOL) and ocean-color satellites have also been employed to assess the large-scale effects of iron addition on surface chlorophyll in fertilized patches, as compared to surrounding regions (Martin et al., 1994; Westberry et al., 2013).

KOPRI 극지연구소

2.4 Biogeochemical responses

Biogeochemical responses to artificial iron addition, measuring various biogeochemical parameters (e.g., Fv/Fm ratio, chlorophyll-a, PP, nutrients, CO_2 variables, and carbon export fluxes), have been investigated in the HNLC regions (Tables 3 - 5 and Figs. 7 - 8). The results are important, as they have been used as a basis to determine whether the aOIF is effective. Here we address the biogeochemical response in each of the ocean basins to the aOIF experiments to date.

2.4.1 Equatorial Pacific

The IronEx-1 and 2 experiments, which were conducted in similar initial conditions (refer to Section 2.2.1), presented quite different biogeochemical responses (Tables 3 - 4 and Fig. 7). In IronEx-1, there were small increases in the Fv/Fm ratio, chlorophyll-a concentration, and PP, but no significant changes in nutrients and pCO_2 concentrations (Martin et al., 1994). On the other hand, IronEx-2 found dramatic changes in biogeochemical responses, providing support for Martin's hypothesis (Coale et al., 1996). The extremely different results from the two experiments are likely to be associated with additional iron injections

(IronEx-1: no extra addition; IronEx-2: 2 additional injections) and different experimental durations (IronEx-1: 10 days; IronEx-2: 17 days).

The Fv/Fm ratios provided further detail. In IronEx-1 and IronEx-2, Fv/Fm rapidly increased within ~24 h of iron addition and reached a maximum of ~0.60 on the second day (Barber and Hiscok, 2006; Aiken et al., 2008). While the elevated IronEx-1 Fv/Fm ratios promptly disappeared, indicating a rapid iron loss (perhaps indicative of insufficient iron supply), increased IronEx-2 Fv/Fm ratios were maintained for eight days through multiple iron additions, suggesting that additional iron enrichments are likely to be a determining factor in successfully artificially increasing PP through OIF (Kolber et al., 1994; Behrendfeld et al., 1996).

During IronEx-1, chlorophyll-a concentrations increased significantly (3-fold) reaching a maximum value of 0.65 mg m^{-3} in the first four days following iron addition (Martin et al., 1994). In IronEx-2, surface chlorophyll-a increased <27-fold with a maximum of 4 mg m^{-3} after six days (Table 4 and Fig. 7c). To quantify the changes in carbon fixation following iron addition, the depth-integrated PP (from the surface to the critical depth, euphotic depth, or MLD) was estimated in the iron-fertilized patches. The depth-integrated PP values increased significantly compared to the initial values. The IronEx-2 ΔPP (where $\Delta PP = PP_{post\text{-}fertilization\ (postf)} - PP_{pre\text{-}fertilization\ (pref)}$) was the highest (~1800 mg C m^{-2} d^{-1}) of all the aOIF experiments discussed here (Table 4 and Fig. 7e).

The increased ΔPP during IronEx-2 was, in turn, accompanied by drawdowns of pCO_2 ($\Delta pCO_2 = [pCO_2]_{postf} - [pCO_2]_{pref} = -73$ µatm) and dissolved inorganic carbon (DIC) ($\Delta DIC = [DIC]_{postf} - [DIC]_{pref} = -27$ µM) (Steinberg et al., 1998) (Table 3 and Fig. 7f). As the bloom developed, a significant nitrate uptake (e.g., $\Delta NO_3^- = [NO_3^-]_{postf} - [NO_3^-]_{pref} = -4.0$ µM) was observed (Table 3 and Fig. 7b) and silicate concentrations also gradually decreased from 5 to ~1 µM (i.e., limiting diatom growth) over six days (Boyd, 2002). The depletion of macro-nutrients in fertilized patches provides indirect evidence that phytoplankton growth in surface waters is driven by iron fertilization (Boyd and Law, 2001).

Although no phytoplankton community change was observed in IronEx-1, after iron addition in IronEx-2 there was a shift from a pico-phytoplankton dominated community to a micro-phytoplankton dominated community, resulting in diatom-dominated blooms (Behrenfeld et al., 1996; Coale et al., 1996; Cavender-Bares et al., 1999). Diatom biomass increased >70-fold over six days early in the experiment, compared to a less than a 2-fold increase for the pico-phytoplankton (Landry et al., 2000). The biomass of meso-zooplankton (200 2,000 µm), such as copepods, also increased simultaneously, substantially increasing the grazing effect (~50%). However, the grazing force of the increased biomass was insufficient to suppress the diatom bloom over six days early in the

IronEx-2 experiment (Coale et al., 1996). The iron-induced diatom bloom began to decline after day ~7 of the experiment. The decline was probably associated with the combined effects of both the elevated grazing pressure and the onset of nutrient depletion (i.e., limitation in silicate and/or iron) (Boyd, 2002).

To determine whether the biological pump (i.e., export production) is enhanced after iron addition, the export flux of particulate organic carbon (POC) can be estimated using, individually or in combination, chemical tracers such as the natural radiotracer thorium-234 (^{234}Th; half-life = 24.1 days) and the stable carbon isotope of particulate organic matter ($\delta^{13}C_{org}$), sediment traps, beam-transmissometers, and underwater video profilers (UVP) (Table 5) (Bidigare et al., 1999; Nodder et al., 2001; Boyd et al., 2004; Buesseler et al., 2004; Coale et al., 2004; Aono et al., 2005; Tsuda et al., 2007; Smetacek et al., 2012; Martin et al., 2013). The ^{234}Th radionuclide has a strong affinity for particles, and the extent of ^{234}Th removal in the water column is indicative of the export of POC associated with surface PP out of the mixed layer (Buesseler, 1998). IronEx-2 was the first aOIF experiment in which the POC flux was estimated (Bidigare et al., 1999). The ^{234}Th deficiency from the surface to 25 m was measured in the iron-fertilized patch to estimate iron-stimulated export production in the surface layer (Table 5). However, no ^{234}Th measurements were made in the unfertilized patch for comparison, and no measurements in the deep ocean were undertaken to demonstrate deep carbon export (Bidigare et al., 1999).

2.4.2 Southern Ocean

As in the EP IronEx-1/-2 experiments, there were initial rapid increases in the Fv/Fm ratio within 24 h of iron addition aOIF experiments in the SO, indicating that phytoplankton growth was mainly limited by iron availability. Maximum values of the Fv/Fm ratio ranged from 0.5 (SOFeX-N and LOHAFEX) to 0.65 (SOIREE and SOFeX-S). However, the time taken to reach the maximum Fv/Fm ratio was usually longer than ~10 days, i.e., much slower than in IronEx-1/-2 (~2 days) (Table 4 and Fig. 7a) (Boyd and Abraham, 2001; Gervais et al., 2002; Coale et al., 2004; Smetacek et al., 2005; Peloquin et al., 2011; Martin et al., 2013). The slower response time in the SO compared to the EP could be attributed to the colder temperatures (~5°C vs. ~24°C) and/or the deeper MLDs (~50 m vs. ~30 m) (Figs. 6c and d), which were indicative of active physical mixing (Boyd and Abraham, 2001; Boyd, 2002).

The aOIF experiments in the SO recorded >2-fold increases in chlorophyll-a concentrations compared to initial levels (<0.7 mg m^{-3}), and maximum values of between 1.25 mg m^{-3} (LOHAFEX) and 3.8 mg m^{-3} (SOFeX-S) were obtained after artificial iron additions (Table 4 and Fig.7c). Satellite observations were used to investigate the changing spatial and temporal distribution of chlorophyll-a concentrations in response to iron

KOPRI 극지연구소

fertilization in the fertilized patches compared to the surrounding waters (Boyd et al., 2000; Coale et al., 2004; Boyd et al., 2005; Westberry et al., 2013). For example, spatial changes in chlorophyll-a resulting from SOFeX-N/S iron addition were detected using Sea-viewing Wide Field-of-view Sensor (SeaWiFS) and MODerate resolution Imaging Spectrometer (MODIS) Terra Level-2 chlorophyll-a images. The chlorophyll-a image on day ~28 after iron addition in the SOFeX-N showed a phytoplankton bloom distribution resembling a long thread with ~10-fold higher concentrations (~1.0 mg m^{-3}) than the surrounding waters (~0.1 mg m^{-3}), while a chlorophyll-a image on day ~20 of SOFeX-S suggested a somewhat broader bloom pattern (~0.4 mg m^{-3}), with concentrations elevated ~4-fold over the surrounding levels (~0.1 mg m^{-3}) (Fig. 7d) (Westberry et al., 2013).

Following artificial iron enrichment in the SO, ΔPP ranged from ~400 (e.g., LOHAFEX) to ~1400 mg C m^{-2} d^{-1} (e.g., SOFeX-N) (Table 4 and Fig. 7e). In SOIREE, EisenEx, and SOFeX-N/S, the PP increased continuously throughout the duration of the experiments (Boyd et al., 2000; Gervais et al., 2002; Coale et al., 2004). However, in EIFEX, SAGE, and LOHAFEX there was a significant increase in PP for ~10 (SAGE) - 20 (EIFEX) days in response to the iron addition, and decreasing trends after day ~12 (SAGE) - 25 (EIFEX) due to various influences, such as high export production (e.g., EIFEX), lateral dilution with surrounding waters (e.g., SAGE), and high grazing pressure and active bacterial respiration (e.g., LOHAFEX) (Boyd, 2002; Gervais et al., 2002; Buesseler et al., 2004; Coale et al., 2004; Peloquin et al., 2011; Smetacek et al., 2012; Martin et al., 2013).

Using both microscopic and high-performance liquid chromatography (HPLC) pigment analysis, changes in phytoplankton community affected by iron addition have also been investigated. SO iron additions have resulted in blooms of relatively large-sized phytoplankton. During SOIREE and EisenEx, the dominant phytoplankton community shifted from pico- and nano-phytoplankton (e.g., pico-eukaryotes and prymnesiophytes) to micro-phytoplankton (i.e., diatoms) (Boyd and Law, 2001; Gervais et al., 2002). In the iron-limited environment of SOFeX-S and EIFEX, diatoms were already the most abundant group prior to iron addition (Coale et al., 2004; Hoffmann et al., 2006). The contribution of large diatoms became especially clear in EIFEX where ~97% of the phytoplankton bloom was attributed to these species. However, no taxonomic shift toward diatom-dominated phytoplankton communities (<10% of total phytoplankton community) was observed in SAGE and LOHAFEX, which were conducted under silicate-limited conditions (Martin et al., 2013; Harvey et al., 2010; Peloquin et al., 2011). Although SOFeX-N was conducted under low silicate conditions, the diatom biomass increased remarkably making up ~44% of the total phytoplankton community (Coale et al., 2004). This result was partly influenced by the temporary relief of silicate limitation through lateral mixing of the iron-fertilized waters with surrounding waters, with relatively higher silicate concentrations (Coale et al., 2004).

Iron-mediated increases in PP resulted in a significant uptake in macronutrients and pCO_2 throughout the aOIF experiments in the SO (except for SAGE) (Table 3, Figs. 7b and f). The ΔNO_3^- ranged from -3.5 μM (e.g., SOFeX-S) to -1 μM (e.g., EisenEx) and ΔpCO_2 ranged from -38 μatm (e.g., SOIREE) to -7 μatm (e.g., LOHAFEX). Although SOFeX-S had a somewhat greater ΔNO_3^- (-3.5 μM) and ΔpCO_2 (-36 μatm) than EIFEX (ΔNO_3^-: -1.5 μM and ΔpCO_2: -30 μatm) both results suggested that diatoms were abundant in the two experiments. However, the smaller ΔSi observed during SOFeX-S (-4 μM, compared to EIFEX -11 μM) was associated with a decrease in silicification (i.e., the adjustment of frustule thickness toward thinner frustules) of the dominant diatom species (i.e., *Fragilariopsis* sp.) (Twining et al., 2004). In EIFEX, the ratio of heavily silicified diatoms (e.g., *Thalassiothrix antarctica*) to total diatom biomass increased from 0.24 (day 0) to 0.46 (day 37) leading to the larger ΔSi (i.e., more demand for silicate) (Hoffmann et al., 2006). Interestingly, the biogeochemical responses in SAGE were totally different from those seen in other experiments, with increases in ΔNO_3^- (+3.9 μM), ΔpCO_2 (+8 μatm), and ΔDIC (+25 μM) (Table 3, Figs. 7b and f) observed. These contrasting results were thought to be the result of entrainment through vertical and horizontal physical mixing into the iron-fertilized patch of the water, with higher biogeochemical concentrations (Currie et al., 2011; Law et al., 2011).

To investigate export production (Fig. 3c), SOIREE, was the first aOIF experiment in the SO to estimate the downward carbon flux into deep waters. They used a comprehensive suite of methods such as the deployment of a free-drifting sediment trap, ^{234}Th, and $\delta^{13}C_{org}$ estimates derived from high-volume pump sampling, and a beam transmissometer (Nodder and Waite, 2001). However, no measurable change in carbon export was observed in response to iron-stimulated PP (Fig. 8b) (Charette and Buesseler, 2000; Nodder and Waite, 2001; Trull and Armand, 2001; Waite and Nodder, 2001). During EisenEx, an increased downward carbon flux estimated from ^{234}Th deficiency was observed in the iron-fertilized patch as the experiment progressed. However, there were no clear differences between in- and outside-patch carbon fluxes (Buesseler et al., 2005). During SOFeX-S, significantly enhanced POC fluxes outside of the mixed layer after iron enrichment were obtained from ^{234}Th observations (Buesseler et al., 2005). However, the absolute magnitude of these flux increases was similar to that observed in natural blooms. Uniquely, SOFeX-N used only free-profiling robotic Lagrangian carbon explorers equipped with transmissometers to estimate the downward carbon flux without employing chemical tracers, and observed large POC flux events between days 25 and 45 after the first iron addition (Coale et al., 2004; Bishop et al., 2004). However, it was unclear whether surface-fixed carbon was well and truly delivered into intermediate/deep depths. For SAGE and LOHAFEX experiments, which were conducted under silicate limited conditions (Table

3, Figs. 4c and 6f), there was no detection of fertilization-induced export by any method (Table 5) (Peloquin et al., 2011; Martin et al., 2013). This result was likely to be associated with the pico-plankton dominated community, which led to rapid recycling in the mixed layer and less downward carbon flux. In contrast to the other aOIF experiments, EIFEX, which was conducted within the core of an eddy, provided clear evidence of carbon export stimulated by artificial iron addition (Jacquet et al., 2008). During EIFEX, the initial export flux, estimated from ^{234}Th in the upper 100 m of the fertilized patch, was ~340 mg C m^{-2} d^{-1} (Table 5 and Fig. 8a) (Smetacek et al., 2012). This value remained constant for about 25 days after iron addition. Between day ~28 and ~36 a massive increase in carbon export flux (maximum of ~1692 mg C m^{-2} d^{-1}) was observed in the fertilized patch, while the initial value remained constant in the unfertilized patch (Table 5 and Fig. 8a). The profiling transmissometer with high-resolution coverage confirmed this result, showing an increase in exported POC below 200 m after day 24. At least half the iron-induced biomass sank (via the formation of aggregates of diatom species, in particular '*Chaetoceros dichaeta*') to a depth of 1,000 m, with a tenfold higher sinking rate (500 m d^{-1}), compared to the initial conditions (Smetacek et al., 2012). Significant changes in export production were not found in any of the other aOIF experiments and, therefore, the impact of artificial iron addition on this component of the biological pump needs to be resolved in future OIF experiments (Boyd et al., 2004; Smetacek et al., 2012; Martin et al., 2013).

2.4.3 Subarctic North Pacific

The observed increase in the Fv/Fm ratio in response to artificial iron addition in the subarctic NP suggests that the relief in iron limitation may have assisted phytoplankton growth (Table 4 and Fig. 7a). SEEDS-1/-2, which were conducted in the western basin, showed continuous increases in the Fv/Fm ratio, with a maximum value of ~0.4 approximately 10 days after the first iron addition (Tsuda et al., 2003; Tsuda et al., 2007). During SERIES, which was conducted in the eastern basin, the Fv/Fm ratio rapidly increased and reached a maximum value of 0.55 within 24 h of the first iron addition (Boyd et al., 2005). However, the Fv/Fm ratio returned toward the initial value of <0.3 as the dissolved iron concentration decreased to background levels (<0.2 nM) after about day 10 (Tsuda et al., 2003; Boyd et al., 2005; Tsuda et al., 2007).

Increases in chlorophyll-a concentrations were detected in the subarctic NP aOIF experiments in both basins after about the fifth day (Tsuda et al., 2003; Boyd et al., 2004; Suzuki et al., 2009). These increases were especially apparent in SEEDS-1, where they reached a maximum value of 21.8 mg m^{-3} (27 times the initial value of 0.8 mg m^{-3}) (Table 4 and Fig. 7c). This augmentation was the largest among all the aOIF experiments (Tsuda et al., 2003). The dramatic chlorophyll-a increase observed during SEEDS-1 was partly

attributed to the particular range of seawater temperature in the region, which was conducive to diatom growth (i.e., 8 - 13°C) as well as to the shallower MLD (10 m), which provided a relatively longer surface water residence time for the additional iron (Figs. 6c and d) (Noiri et al., 2005; Takeda and Tsuda, 2005; Tsumune et al., 2005). During SERIES, chlorophyll-a concentrations increased substantially from the initial value of 0.35 to 5 mg m^{-3} over 17 days, and the second highest concentration of all aOIF experiments was recorded (Boyd et al., 2004). However, on the 18th day there was a downturn in chlorophyll-a as silicate concentrations decreased to <2 μM (Boyd et al., 2005). Although SEEDS-2 was conducted under similar initial conditions to SEEDS-1 (refer Section 2.2.3), there was a minimal increase in chlorophyll-a (i.e., maximum value of less than 3 mg m^{-3}). This smaller increase was thought to be the result of extensive copepod grazing (SEEDS-2 had almost five times more copepod biomass than SEEDS-1) (Table 4) (Tsuda et al., 2007). A similar spread was seen in depth-integrated PP, which increased by 7-fold or more after various iron enrichments in the subarctic NP aOIF experiments (e.g., from 300 - 420 to ~1,000 - 2,000 mg C m^{-2} d^{-1}) (Table 4 and Fig. 7c).

Changes in the composition of phytoplankton groups were investigated in the subarctic NP aOIF experiments. In SEEDS-1 there was a shift from oceanic diatoms (e.g., *Pseudonitzschia turgidula*), with growth rates of 0.5 - 0.9 d^{-1}, to faster-growing neritic diatoms (e.g., *Chaetoceros debilis*, 1.8 d^{-1}) (Tsuda et al., 2005). The shift in the dominant phytoplankton species during the SEEDS-1 experiment was an important contributor to what became the greatest aOIF-induced increase in phytoplankton biomass yet recorded. During SERIES, the phytoplankton community changed from *Synechococcus* and haptophytes to diatoms, and the highest SERIES chlorophyll-a concentration (day 17) was associated with a peak in diatom abundance (Boyd et al., 2005). However, during SEEDS-2, no significant iron-induced diatom bloom was observed. Instead, pico-phytoplankton (e.g., phytoflagellates) (67% of the total community) dominated throughout the duration of the experiment due to the heavy grazing pressure on diatoms (Tsuda et al., 2007).

In the subarctic NP experiments, significant decreases in macro-nutrient uptake (i.e., ΔNO_3^- and ΔSi), ΔDIC, and ΔpCO_2 in response to artificial iron addition were observed (Table 3 and Figs. 7b and f). SEEDS-1, which saw the largest increases in chlorophyll-a concentrations, also had the largest ΔpCO_2 (-130 μatm) and ΔDIC (-58 μM) (Table 3 and Fig. 7f). These changes led, in turn, to the largest ΔNO_3^- (-15.8 μM) (Fig. 7b) and ΔSi (-26.8 μM) (Table 3) (Tsuda et al., 2003). The second largest increase in the chlorophyll-a concentration was observed in SERIES, where drawdowns of pCO_2 (-85 μatm), DIC (-37 μM), nitrate (-9 μM), and silicate (-14 μM) were recorded. During SEEDS-2, the nitrate concentration decreased remarkably from 18.4 μM to 12.7 μM after five days; however,

there was no significant change in silicate concentrations, which would have been expected as a signal of an iron-induced diatom bloom (Suzuki et al., 2009).

With the formation of a massive iron-induced phytoplankton bloom during SEEDS-1, POC export fluxes in the surface layer (50 m) increased from 296 to 1,000 mg C m^{-2} d^{-1}. However, there was no significant change in the POC export flux estimated from ^{234}Th observations at 200-m depth during the observation period (Table 5) (Aono et al., 2005). These results suggest that most of the exported POC did not reach 200-m depth (Takeda and Tsuda, 2005). During SERIES and SEEDS-2, which allowed comprehensive time-series measurements of the development and decline of the iron-stimulated bloom, POC fluxes estimated by the sediment trap in the fertilized patch displayed temporal variations (Boyd et al., 2004; Aramaki et al., 2009). However, the results suggested that only a small part of the decrease in the mixed layer POC was subsequently captured by the trap, and POC flux losses were mainly governed by bacterial remineralization and mesozooplankton grazing (Boyd et al., 2004; Tsuda et al., 2007).

2.5 Summary of the significant results from aOIF experiments

To test the hypothesis that the addition of iron to the surface layer will efficiently reduce atmospheric CO_2 by increasing PP and enhancing, in turn, the carbon export flux to the deep ocean, aOIF experiments have usually been conducted in HNLC regions, including: the EP, SO, and subarctic NP. The one exception was the FeeP experiment, which was performed in the subtropical NA. The initial environmental conditions associated with the physical and biogeochemical properties were determined at these OIF sites over 1 7 days before iron addition to allow the responses to the aOIF to be evaluated and quantified. Preliminary surveys confirmed that all sites, except FeeP in the subtropical NA, were subject to iron-limited HNLC conditions, with typical levels of iron <0.2 nM, nitrate >~10 μM, and chlorophyll-a <1 mg m^{-3}. The initial Fv/Fm ratios were <0.3, suggesting that phytoplankton growth was severely iron-limited. In SEEDS-1, SOFeX-S, and EIFEX, prior to the addition of iron, the micro-phytoplankton (e.g., diatom) community accounted for half of the population and this was thought to be beneficial to the enhancement of export production. In the other experiments, pico- and nano-phytoplankton (e.g., *Synechococcus* and haptophytes) initially dominated; they are associated with rapid recycling in the mixed layer through the microbial loop rather than export production (Michaels and Silver, 1988; Coale et al., 1998; Landry et al., 2000; Boyd and Law, 2001; Gervais et al., 2002; Tsuda et al., 2005; Coale et al., 2004; Boyd et al., 2005; Hoffmann et al., 2006; Harvey et al., 2010; Tsuda et al., 2007; Martin et al., 2013).

Iron-sulfates dissolved in acidified seawater have been commonly used for artificial iron addition because they are both highly bioavailable and inexpensive. The mixture is

generally released into the ship's wake over a period of 24 h. A sufficient amount of iron was added to reach a target dissolved-iron concentration (at least >1 nM) by volume (defined as the MLD × patch area). To achieve this, a wide range of 225 - 2,000 kg was applied. Except in IronEx-1 and SEEDS-1, the experiments used multiple (2 - 4) iron additions to reinforce the increased iron levels. To trace the iron-fertilized patches, physical tracers (i.e., Argo or other GPS-tracked drifting buoys) and/or chemical tracers such as SF_6 were used. In addition, biogeochemical parameters, such as the Fv/Fm ratio, macro-nutrients, and CO_2 variables, were used to detect responses through a comparison of before and after conditions (i.e., Δ = $[parameter]_{postf}$ - $[parameter]_{pref}$). In particular, it should be noted that the Fv/Fm ratios promptly increased from <0.3 to 0.55 (± 1.5) in the two days following iron addition, indicating a relief in the iron-limitation on phytoplankton growth. The subarctic NP SEEDS-1 experiment, which was conducted under temperature conditions ideal for diatom growth (~8°C) and with shallow MLDs (10 m), produced the greatest changes in biogeochemical parameters.

The aOIF experiments have generally led to changes in the size of the phytoplankton community from pico and nano-phytoplankton to micro-phytoplankton. This effect was particularly noticeable as diatoms became the dominant species during IronEx-2, SOIREE, EisenEx, SEEDS-1, SOFeX-S, EIFEX, and SERIES, with micro-phytoplankton accounting for ~44% of total phytoplankton community in SOFeX-N. The shift to a diatom-dominated community appears be related to the initial availability of silicate (i.e., initial silicate was >3 µM in all the experiments just listed). Diatom-dominated blooms induced >5-fold increases in chlorophyll-a concentrations and accounted for >70% of the chlorophyll-a increase. However, as silicate concentrations decreased to <2 µM due to removal by the elevated diatom abundance, the extent of diatom blooms rapidly declined. SAGE and LOHAFEX, had low initial levels of silicate (< 2 µM), pico and nano-phytoplankton dominated communities, and diatom growth was limited by the lack of available silicate. These results suggest that to develop a massive phytoplankton bloom, a changeover to a diatom-dominated community after iron addition is needed. A necessary, but not sufficient condition, for such a change to occur is the availability of silicate. Silicate alone is not expected to be sufficient because diatom-dominated blooms with distinct increases in the chlorophyll-a concentration were not observed in all experiments with high initial silicate concentrations. IronEx-1 and SEEDS-2 had high initial silicate levels (>4 µM), which were conducive to the development of a diatom-dominated bloom, but the bloom was suppressed due to high grazing pressure. Taken together, the OIF results suggest that both mesozooplankton grazing rates as well as the initial silicate concentrations played a role in limiting the stimulation of diatom-dominated blooms after artificial iron enrichment.

In some experiments (IronEx-1, SEEDS-2, SAGE, and LOHAFEX) there was little change in the carbon export flux, while in others (IronEx-2, SOIREE, EisenEx, SEEDS-1, SOFeX-S, EIFEX, and SERIES) there was a >2-fold increase in PP within the mixed layer, with massive diatom-dominated blooms. However, even in the latter, changes in the carbon export flux differed from experiment to experiment. In SEEDS-1 and SOIREE there was little increase in export flux. However, it has been reported that changes in in the POC concentrations following an increase in PP can take three to four weeks (Buesseler et al., 2005), whereas these two experiments were conducted over only about two weeks, which suggests that the duration of each experiment was too short to detect downward carbon export. In SERIES, there was a distinct increase in the carbon export flux within the mixed layer (30 m), but there was no increase in the export flux below this because the abundance of heterotrophic bacteria was elevated after iron addition rapidly remineralized POC within the mixed layer (Boyd et al., 2004). In SOFeX-S the export flux was enhanced at 100-m depth, below the MLD (45 m). However, the changes in export flux after iron addition were not dramatic compared to natural values. It is possible that the duration of SOFeX-S was also insufficient (~4 weeks) (Table 2). EIFEX was the only aOIF experiment that produced significant carbon export to deeper layers (down to 3,000 m). This high flux was due to aggregate formation with fast sinking rates (Smetacek et al., 2012). EIFEX observed an entire cycle (i.e., development - decline - fate) of the iron-induced phytoplankton bloom during the 39 days of the experiment, which strongly suggests that a sufficient experimental duration is a prerequisite for detecting fully formed diatom aggregates (i.e., carbon export). It should also be noted that the rates of bacterial remineralization and grazing pressure on the diatoms were in the same range inside the fertilized patch as outside, which might have assisted the delivery of iron-induced POC from the MLD to the intermediate/deep depths (Smetacek et al., 2012). These results suggest that to detect significant carbon export to deep waters following an increase in PP, at least three conditions are necessary: (1) a shift to a diatom-dominated community, (2) low bacterial respiration and grazing pressure rates within the mixed layer, and (3) a sufficient experimental duration, enabling both immediate and delayed responses to iron addition to be observed.

3. Present: unanswered aOIF questions - export flux, possible side effects, and international law

OIF has been proposed as a potential technique for rapidly and efficiently reducing atmospheric CO_2 levels at a relatively low cost (Buesseler and Boyd, 2003), but there is still much debate. Over the past 25 years, controlled aOIF experiments have shown that

substantial increases in phytoplankton biomass can be stimulated in HNLC regions through iron addition, resulting in the drawdown of DIC and macronutrients (de Baar et al., 2005; Boyd et al., 2007; Smetacek et al., 2012; Martin et al., 2013). However, the impact on the net transfer of CO_2 from the atmosphere to the intermediate and/or deep ocean layers through the 'biological pump' is not yet fully understood or quantified and appears to vary with environmental conditions, export flux measurement techniques, and other unknown factors (Smetacek et al., 2012). While it is generally agreed that OIF effectiveness needs be determined through both tracking and export flux estimation, there has been no discussion of which export flux measurement techniques are the most effective. In the meantime, concern has been expressed regarding possible environmental side effects in response to iron addition (Fuhrman and Capone, 1991). These side effects include the production of greenhouse gases (e.g., N_2O and CH_4) (Lawrence, 2002; Liss et al., 2005; Law, 2008), the development of hypoxia/anoxia in the water column (Sarmiento and Orr, 1991), and toxic algal blooms (e.g., *Pseudo-nitzschia*) (Silver et al., 2010; Trick et al., 2010). Although they are accidental, these side effects could lead to negative climate and ecosystem changes (Fuhrman and Capone, 1991). Core unanswered questions remain concerning the different carbon export flux results from different measurement techniques (Boyd et al., 2002), the possible side effects that could directly influence the aOIF effectiveness, and the legal framework that is in place to protect any imprudent aOIF operations while simultaneously supporting further studies to increase our understanding of aOIF and its potential risks and benefits (Williamson et al., 2012). With the design of future aOIF experiments in mind, the following section discusses the following core questions: (1) which of the methods are optimal for tracking and quantifying carbon export flux, (2) which of the possible side effects have negative impacts on aOIF effectiveness, and (3) what are the international aOIF experimentation laws and can they be ignored?

3.1 Export flux measurement methods

A traditional, direct method for estimating POC export fluxes in the water column is a sediment trap that collects sinking particles (Suess, 1980). Sediment traps are generally deployed at specific depths for days to years to produce estimates of total dried mass, POC, particulate inorganic carbon (PIC), particulate organic nitrogen (PON), particulate biogenic silica (BSi), $\delta^{13}C_{org}$, and ^{234}Th. A basic assumption for the use of a sediment trap is that it exclusively collects settling particles, resulting from the gravitational sinking of organic matter produced in surface waters. However, although they are designed to ensure the well-defined collection/conservation of sinking particles, they have accuracy issues due to: 1) interference of the hydrodynamic flow across the trap (i.e., strong advective flow), 2) inclusion/invasion (accounting for 14 - 90% of the total POC collected) of metazoan

zooplankton (e.g., copepods, amphipods, and euphausiids) capable of vertical migration (Karl and Knauer, 1989; Buesseler et al., 1991; Buesseler et al., 2007), and 3) loss of trapped particles by bacterial decay and/or dissolution during trap deployment and storage periods (Gardner et al., 1983; Knauer et al.,1984; Kähler and Bauerfeind, 2001). The application of sediment traps for the determination of the carbon export flux is relatively more biased in the upper ocean (surface to ~1,000-m depth) where ocean currents are generally faster and zooplankton are much more active than deeper in the water column. These issues suggest that sediment traps alone may not accurately determine carbon export fluxes.

Even when used at the same depth, traditional sediment traps, such as the surface-tethered drifting trap and bottom-moored trap, can greatly over- or under-estimate particulate ^{234}Th fluxes compared to water-column based estimates (Buesseler et al., 1991). The water column-based total ^{234}Th deficiency method (the sum of dissolved and particulate activities) is less sensitive than sediment traps to the issues mentioned above, and provides better spatial and temporal resolution in flux estimates (Buesseler et al., 1998). For these reasons, traditional sediment trap POC flux estimates have often been calibrated using the total ^{234}Th deficiency measured using a rosette bottle or high-volume pump samples (Coale and Bruland, 1985; Buesseler et al., 2006) as a reference.

Several OIF experiments have used both sediment traps and ^{234}Th deficiency to estimate the iron-induced POC export flux. SOIREE reported distinct differences in POC fluxes estimated from drifting traps (185 mg m^{-2} d^{-1}) at a 110-m depth over days 11 - 13 of the experiment and ^{234}Th (~87 mg m^{-2} d^{-1}) at ~100-m depth (Charette and Buesseler, 2000; Nodder and Waite, 2001). While there was no measurable change in ^{234}Th-based POC fluxes during the 13 days of the SOIREE experiment (Fig. 8b), the traps suggested a 27% increase over the course of the experience (146 mg m^{-2} d^{-1}) (Table 5). It was later discovered that this increase was caused by sampling biases (Nodder and Waite, 2001). Likewise, SEEDS-1 ^{234}Th-based POC fluxes at 50 m on day 13 (when a large iron-induced export event occurred) were estimated to be 1,000 mg m^{-2} d^{-1}, but the drifting trap only recorded 141 mg m^{-2} d^{-1} at 40-m depth over days 12 - 14, ~8 times lower (Aono et al., 2005; Aramaki et al., 2009). This large discrepancy between the two methods was caused by the under-sampling of POC into the sediment traps (Nodder and Waite, 2001; Aono et al., 2005).

To resolve the potential biases in traditional sediment traps, a neutrally buoyant (and freely drifting) sediment trap (NBST) was developed (Valdes and Price, 2000; Valdes and Buesseler, 2006; Lampitt et al., 2008). Through preliminary experiments conducted in June and October 1997 at the Bermuda Atlantic Time-series Study site, Buesseler et al. (2000) showed that an NBST system could reduce the invasion/inclusion of zooplankton into the trap samplers, and that NBST-based ^{234}Th fluxes were comparable with

KOPRI 극지연구소

water-column based estimates. LOHAFEX has been the only OIF experiment so far that has measured particle export using LAGRAngian (PELAGRA) sediment traps based on the NBST system (Martin et al., 2013). However, the PELAGRA sediment traps deployed below the mixed layer (at 200 m and 450 m) did not detect iron fertilization-induced carbon export even though PP did increase within the mixed layer. Water-column based ^{234}Th measurements estimated the POC flux at a 100-m depth to be ~94 mg m^{-2} d^{-1}, whereas the PELAGRA sediment traps estimated the flux at 200 m and 450 m to be only ~12 mg m^{-2} d^{-1}. It should be noted that both sediment traps and water-column based ^{234}Th measurements have a limited ability to fully scan the vertical profile of POC fluxes and, therefore, are of limited used in determining the fate of iron-induced POC in the water column.

To resolve the full column more effectively, LOHAFEX employed a UVP, which provided photographic evidence of sinking particles (particle size ≥100 μm) from the surface down to ~3,000-m depth, with ~0.2 m vertical resolution. Through an analysis of particle size distributions, the UVP also allowed particles to be classified into fecal pellets, aggregates, and live zooplankton. Vertical total particle volume profiles obtained from UVP indicated the maximum particle flux at a 75-m depth (~0.3 μm^3 L^{-1}), with a gradual decrease to 150 m (~0.15 μm^3 L^{-1}). Interestingly, large particles (i.e., zooplankton) were copious between 75-m and 100-m depth, suggesting that there might be high grazing pressure, which might explain the large discrepancy between the 100 m (water-column based ^{234}Th method) and 200 m / 450 m (PELAGRA sediment trap) POC flux estimates (i.e., rather than a sampling bias in sediment trap data) (Martin et al., 2013). To continuously monitor vertical changes in POC flux following iron addition, EIFEX used a transmissometer, providing high vertical resolution (~24 data points per meter) and tracking of the iron-induced flux down to ~3,000 m, even though, unlike UVPs, transmissometers do not allow classification of particles (Smetacek et al., 2012). Improving on this method, SOFeX-N applied autonomous carbon flux explorers equipped with transmissometers, designed to float along with the currents. Three autonomous carbon flux explorers were deployed, two explored the 'iron fertilized in-patch' and one acted as a 'control' outside the patch. Carbon flux explorers can continuously monitor in the field for up to 18 months beyond the initial deployment, which allowed SOFeX-N to observe 'episodic raining' in the iron-fertilized waters (Bishop et al., 2004), indicating a high carbon export flux long after artificial iron addition.

The combination of multiple approaches is essential to the successful detection of the POC produced in response to iron addition and its fate. NBST systems (e.g., the PELAGRA sediment trap) are appropriate for quantifying the aOIF-induced POC flux in the upper waters (<~400-m depth), especially when accompanied by calibration using

water-column based ^{234}Th. Particle profiling systems (e.g., a transmissometer and UVP) mounted on a CTD-Rosette sampler provide continuous quantitative and qualitative information about sinking particles, with high vertical resolution and full coverage of the water column (>3,000-m depth). They are therefore useful for indirectly identifying deep carbon transport. Autonomous carbon flux explorers are an excellent alternative, allowing the continuous observation of POC fluxes during and after an OIF experiment.

3.2 Considering environmental side effects

The purpose of OIF is to reduce the atmospheric CO_2 level by stimulating the sequestration of oceanic carbon through artificial iron additions in the HNLC regions, mitigating the global warming threat. Beyond the benefits of aOIF experimentation, scientists have debated the unintended secondary consequences of OIF, such as production of climate-relevant gases and ocean ecosystem changes. Therefore, it is important to consider the possible negative consequences of OIF to evaluate whether the aOIF experiments are effective (i.e., net profit: positives > negatives).

To investigate changes in climate-relevant gas emissions produced by biological activities and/or photochemical reactions before and after iron additions, the production of CH_4, N_2O, DMS, and halogenated volatile organic compounds (HVOCs) were measured during aOIF experiments (Liss et al., 2005), because their emission may lead to unintended consequences negating the desired effects of aOIF experiments on carbon sequestration. Among the climate-relevant gases, CH_4 has a ~20 times greater warming potential than CO_2. However, CH_4 has been considered to be relatively low risk because most of the CH_4 formed in the ocean is used as an energy source for microorganisms and is converted to CO_2 before reaching the sea surface (Smetacek and Naqvi, 2008; Williamson et al., 2012). During the SOFeX-N experiment, measurements of dissolved CH_4 indicated concentrations were slightly elevated, i.e., by less than 1% (1.74 ppmv in fertilized patches and 1.72 ppmv in outside fertilized patches) (Wingenter et al., 2004). Simulated SO large-scale OIF has suggested that a 20% enhancement of CH_4 emissions would offset only <1% (~4 Tg C yr^{-1}) of the resulting carbon sequestration (Oschlies et al., 2010). Hence, additional CH_4 production from aOIF experiments is not likely to be a serious problem.

On the other hand, N_2O has a relatively long lifetime in the atmosphere (~110 years) and has a global warming potential about 300 times greater than CO_2 (Forster et al., 2007). The ocean is already a significant source of atmospheric N_2O (Nevison et al., 2003). Oceanic N_2O is mainly produced by bacterial remineralization. Therefore, increases in N_2O production after iron additions are expected and, in the long run, contribute to an increase rather than a decrease in the greenhouse effect (Bange, 2006). During the SOIREE experiment, a significant increase (~4 %) in mean N_2O saturation in the pycnocline (65 - 80

m) of the fertilized patch (104.4 ± 2.4%), as compared to outside the fertilized patch (100.3 ± 1.7%), was associated with an increased phytoplankton biomass (Law and Ling, 2001). Measurements of N_2O saturation during SERIES also showed increases of 8% at 30 - 50 m, which were coincident with the accumulation of ammonium and nitrite attributable to increases in bacterial remineralization following increased POC levels (Boyd et al., 2004; Law, 2008). SOIREE-based model estimates suggested that potential N_2O production at timescales longer than six weeks would subsequently offset carbon reduction benefits resulting from the bacterial remineralization of additional carbon fixation by 6 - 12% (Law and Ling, 2001). This estimate is in line with the N_2O offset of 6 - 18% suggested by a modeling study (Jin and Gruber, 2003) and the 5 - 9% suggested by a more recent modeling study investigating the effectiveness of long-term and large-scale SO OIF (Oschlies et al., 2010). Excess N_2O was not found after iron addition in EIFEX, where significant vertical export through the formation of rapidly sinking aggregates was found (Walter et al., 2005; Law, 2008). One explanation for the absence of N_2O accumulation below the EIFEX patch might be the limited bacterial remineralization due to the rapid export of organic matter well below the 500-m depth to the seafloor (Walter et al., 2005). Based on the results of previous studies, no consensus has yet been reached on the exact extent of additional N_2O production after iron additions. However, because there is the potential for excessive N_2O production that would not only impact the effectiveness of aOIF experiments but also positively contribute to global warming, further studies are required to reach a conclusion.

Unlike N_2O emissions, which have the potential to offset the effectiveness of OIF, DMS, a potential precursor of sulfate aerosols that cause cloud formation, may contribute to the homeostasis of the earth's climate by countering the warming due to increased CO_2 emissions (Charlson et al., 1987). DMS is produced by the enzymatic cleavage of planktonic dimethylsulfoniopropionate (DMSP). Microzooplankton grazing on nano-phytoplankton (e.g., haptophytes) is a key factor controlling oceanic DMS production (Dacey and Wakeham, 1986; Gall et al., 2001; Park et al., 2014). The production of DMS in response to iron addition was measured during all aOIF experiments. In the EP and SO, DMS production increased, but in the subarctic NP, it remained constant or decreased (Lawrence, 2002; Boyd et al., 2007). There were significant short-term increases in DMS production in IronEx-2 (from 2.5 to 4.2 nM), SOIREE (from 0.5 to 3.4 nM), EisenEx (from 1.9 to 3.1 nM), and SOFeX-N (from 1.6 to 7.7 nM) (Turner et al., 1996; Turner et al., 2004; Wingenter et al., 2004; Liss et al., 2005). The maximum DMS production observed was a 6.5-fold increase after iron addition in SOIREE (Turner et al., 2004). During an early SOIREE experiment, the dominant phytoplankton species were haptophytes, and DMS production was increased by microzooplankton grazing on DMSP-rich haptophyte species

(i.e., Prymnesiophyceae) (Gall et al., 2001). Similarly, a 5-fold enhancement of DMS production was observed in SOFeX-N. Estimates derived by the extrapolation of SOFeX-N DMS production results suggested that fertilizing 2% of the SO over the course of a week would enhance DMS production by 20%, which would lead to a 2°C decrease in air temperature over the SO (Wingenter et al., 2007). Interestingly, there were no significant changes in DMS production after iron additions in the western subarctic NP SEEDS-1/-2 experiments, despite increases in PP (Turner et al., 1996; Takeda and Tsuda, 2005; Nagao et al., 2009). Furthermore, in the eastern subarctic NP, SERIES DMS production increased from 15.7 nM on day 1 to a maximum of 26.5 nM on day 10, but decreased to 6 nM by the end of the experiment due to an increase in bacterial activity (Levasseur et al., 2006). It is therefore difficult to predict the iron-induced DMS response, because OIF itself is not the only source of DMS. Based on the results of previous aOIF experiments, DMS production was sensitive in the EP and SO, but was less sensitive in the subarctic NP (Law, 2008). These results indicate that further process and modeling studies for each region are required to determine the production and degradation of DMS, both following iron fertilization and in the natural environment.

HVOCs, such as CH_3Cl, CH_3Br, and CH_3I, are well known for their ability to destroy ozone in the lower stratosphere and marine boundary layer (Solomon et al., 1994), and were also measured during past aOIF experiments (Wingenter et al., 2004; Liss et al., 2005). However, no consistent results have been reported for HVOC production (Liss et al., 2005). In SOFeX-N, the impact of iron addition on HVOC was complicated, with CH_3Cl concentrations remaining unchanged, and CH_3Br concentrations increasing by 14% (6.5 pptv in the fertilized patch and 5.7 pptv outside the fertilized patch), while CH_3I concentrations decreased by 23% (4.9 pptv in fertilized patch and 6.4 pptv outside the fertilized patch) (Wingenter et al., 2004). In contrast, CH_3I concentrations increased 2-fold during EisenEx (Liss et al., 2005). Such a complicated response suggests that, as for DMS, further study is needed to fully understand that natural cycling of HVOCs and their responses to iron fertilization.

Secondly, the effectiveness of aOIF may also be offset leading to changes in the ocean ecosystem following OIF, such as a decrease in dissolved oxygen and an increase in domoic acid (DA) levels. The decomposition of iron addition-enhanced biomass may cause decreased oxygen concentrations in subsurface waters (Williamson et al., 2012). Although mid-water oxygen depletion has not been reported from aOIF experiments to date, early modeling studies suggest that anoxic conditions may develop after long-term and large scale OIF (Sarmiento and Orr, 1991). However, more sophisticated and realistic models suggest that OIF produces well-oxygenated conditions, without the development of anoxic conditions, even under climate change scenarios (Oschlies et al., 2010; Keller et al., 2014).

Thus, hypoxia/anoxia development in response to iron additions is unlikely to be a primary concern.

The changes in phytoplankton community composition after iron addition discussed in Section 2.4 may also have unintended consequences; for example, they could lead to potentially toxic species dominating plankton assemblages (Silver et al., 2010; Trick et al., 2010). Some aOIF experiments (e.g., IronEx-2, SOIREE, EisenEx, SOFeX-N/S, and SERIES) generated large blooms dominated by pennate diatoms belonging to the genus '*Pseudo-nitzschia*' (de Baar et al., 2005; Trick et al., 2010). Some '*Pseudo-nitzschia*' species have the capacity to produce the neurotoxin DA that is known to detrimentally affect marine ecosystems. However, no DA was found during EisenEx and SERIES, even though '*Pseudo-nitzschia*' were dominant (Gervais et al., 2002; Marchetti et al., 2006; Assmy et al., 2007). This said, phytoplankton samples used to estimate DA production had been stored for a long time before the analysis, for example, 12 years in IronEx-2 and four years in SOFeX-S (Silver et al., 2010). Trick et al. (2010) argued that phytoplankton samples stored for a long time would have degraded, leading to an under-estimation in DA production. This implies that accurate information about changes in DA production in response to iron addition might not be available. However, the IronEx-2, and SOFeX-S experiments found discernable changes in DA production, even if the original DA might have degraded (Silver et al., 2010). It is likely that several phytoplankton samples (e.g., *Pseudo-nitzschia* abundance: 1.3×10^6 cells L^{-1} in IronEx-2 and 7.5×10^4 cells L^{-1} in SOFeX-S) collected with a net tow were suitable to detect these changes. During IronEx-2 and SOFeX-S, high cell abundances of '*Pseudo-nitzschia*' (10^6 and 10^5 cells l^{-1}, respectively) combined with moderate DA quotas (0.05 and 1 pg DA $cell^{-1}$, respectively) produced toxin levels as high as 45 ng DA l^{-1} in IronEx-2 and 220 ng DA l^{-1} in SOFeX-S, i.e., toxin levels high enough to damage marine communities in coastal waters. Therefore, it is necessary to quantify DA production in response to iron additions, with concentrated phytoplankton samples (i.e., large numbers of cells) using a net tow. This, once again, indicates that such processes need to be better understood in the natural environment before the ramifications of OIF can be fully appreciated

Whether OIF is a viable carbon removal strategy is still under debate (Boyd et al., 2007; Smetacek and Naqvi, 2008). The production of climate-relevant gases such as N_2O, DMS, and HVOCs, which is influenced by the remineralization of sinking particles that follows OIF-induced blooms, and the production of DA are particularly important to understand. They can directly and indirectly modify the effectiveness of carbon sequestration, with the effects being either positive or negative. Therefore, monitoring of the production of climate-relevant gases and DA to evaluate the effectiveness of OIF as a geoengineering approach is essential. This represents only a few of many possible side

effects. The direct and indirect environmental consequences of OIF remain largely unresolved due to the inconsistent and highly uncertain outcomes of the experiments conducted so far, as well as our poor understanding of the processes involved under both nOIF and aOIF conditions (Williamson et al., 2012; Johnson and Karl, 2002; Chisholm et al., 2001). Therefore, considering the increasing evidence for the necessity to keep warming at or below 1.5°C (Rogelj et al., 2015), there continues to be a need to determine the effectiveness of OIF as a means for reducing atmospheric CO_2 through the quantification of OIF side effects.

3.3 Regulation of aOIF: International law of the sea as it applies to aOIF

To prevent pollution of the sea from human activities, the international Convention on the Prevention of Marine Pollution by Dumping of Wastes and Other Matter (London Convention, 1972) was amended in 1972. In 1996, contracting parties to the London Convention adopted the Protocol to the London Convention (London Protocol, 1996). This places legal restrictions on the dumping of wastes and other matter that may cause hazard, harm, and damage in the ocean and/or interfere with the marine environment. However, the London Convention & Protocol (LC/LP) did not establish specific laws to protect the ocean environment against the side-effects of fertilization activities. In 2007, several commercial companies (e.g., GreenSea Venture [http://www.greenseaventure.com] and Climos [http://www.climos.com]) promoted large-scale (~40,000 km2) commercial OIF as a climate mitigation strategy and as a means to gain carbon credits (Chisholm et al., 2001; Buesseler and Boyd, 2003). Assessments of the effectiveness of aOIF have been limited to small, fertilized patches (25 300 km2) (Fig. 6a) due to the time and expense of comparing fertilized and unfertilized areas (ACE CRC, 2008). As discussed earlier, these small-area experiments have left many unanswered scientific questions regarding both the effectiveness and the potential impacts of OIF (Lawrence, 2002; Buesseler and Boyd, 2003). In the same year, noting the potential risks and benefits, the LC/LP scientific group released a statement on large-scale ocean fertilization and recommended that ocean fertilization activities be evaluated carefully to ensure that such operations were not contrary to the aims of the LC/LP.

At the 2008 LC/LP meeting, the contracting parties adopted Resolution LC-LP.1 (2008) on the regulation of ocean fertilization. This resolution prohibited ocean fertilization activities until such time that specific guidance could be developed to justify legitimate scientific research. There was an exception for 'small-scale scientific research studies within coastal waters' to permit the development of proposals that would lead to an assessment framework for scientific ocean fertilization research (Resolution LC-LP.1, 2008). In the meantime, there was a call to develop an assessment framework for ocean

fertilization experiments to assess, accurately, scientific research proposals (Resolution LC-LP.1, 2008). In 2010, LC/LP parties developed Resolution LC-LP.2 (2010), adopting an "Assessment Framework for Scientific Research Involving Ocean Fertilization" to be used to assess, on a case-by-case basis, whether any proposed ocean fertilization activity constitutes legitimate scientific research falling within the aims and scope of Resolution LC-LP.1 (2008) (Fig. 9) (Resolution LC-LP.2, 2010). This framework demands preliminary scientific research prior to any OIF experimentation. There must be a transparent/reasonable scientific rationale/purpose to the experiment and a risk analysis must be undertaken using parameters such as problem formulation, site selection, exposure and effect assessment, and risk characterization and management. Monitoring is also required as an integral component of all approved (i.e., legitimate) scientific OIF research activity to assess ecological impacts and to review actual versus intended geo-engineering benefits (ACE CRC, 2015). In October 2013, the LC/LP parties adopted amendments that categorized aOIF as marine geo-engineering, thereby prohibiting operational OIF activities, but enabling OIF scientific research that meets the permit conditions through the environmental assessment framework (Resolution LP.4 (8), 2013). This means that large-scale (i.e., >~300 km^2 based on previous aOIF experiments; exact areal sizes are not determined in the LC/LP) and/or commercial OIF (e.g., 'the 2012 Haida Gwaii Iron Dump' off the west coast of Canada) are currently banned by international regulations. Under LC/LP, commercial OIF efforts cannot proceed because of the large uncertainties related to large-scale OIF.

KOPRI 극지연구소

4. Future : designing future aOIF experiments

Scientific aOIF research has focused on improving our understanding of the effectiveness, capacity, and risks of OIF as an atmospheric CO_2 removal strategy both in the future and the past (in particular glacial periods). Although the first aOIF experiments took place more than twenty years ago, the legal and economic aspects of such a strategy in terms of the international laws of the sea and carbon offset markets are not yet clear (ACE CRC, 2015). Nonetheless, previous small-scale aOIF experiments have demonstrated a considerable potential for easily and efficiently reducing atmospheric CO_2 levels. Accordingly, physical/biogeochemical/ecological models and nOIF experiments (long-term) have been conducted in an effort to overcome some of the limitations of short-term aOIF experiments (e.g., spatial and temporal scales) and to predict the effectiveness of long-term and large-scale fertilization (Aumont and Bopp, 2006; Blain et al., 2007; Denman, 2008; Pollard et al., 2009). For example, earlier global biogeochemical models have indicated that massive fertilization could draw down atmospheric CO_2 by as much as 107 ppm in 100 years (Joos et al., 1991; Peng and Broecker, 1991; Sarmiento and Orr, 1991; Kurz and Maier-Reimer,

1993). Recent global models, with more realistic ecosystem and biogeochemical cycles predict values closer to a ~33 ppm drawdown in atmospheric CO_2 (Aumont and Bopp, 2006). These results suggest that the amount of carbon sequestration resulting from OIF represents only a modest offset, i.e., a contribution of less than 10% over the range of IPCC future emission scenarios (Aumont and Bopp, 2006; Denman, 2008). The nOIF experiments have also produced much higher carbon sequestration rates than the small-scale aOIF experiments (Morris and Charette, 2013). Furthermore, the results from nOIF experiments do not support the potential negative impacts proposed for OIF experiments, even at larger scales (Belviso et al., 2008). However, these nOIF results do not guarantee that aOIF as a geoengineering approach is able to achieve the high effectiveness associated with carbon sequestration and enable a simple scaling-up as a prediction tool, because the nOIF experiments differ from the aOIF experiments in the mode of iron supply. In particular, nOIF is a continuous and slow process and its iron source is based on the upwelling of iron-rich subsurface waters to the surface layer, whereas aOIF is intended to be episodic, with massive short-term iron additions (Blain et al., 2007). In addition, in nOIF it is difficult to accurately identify iron sources due to the complexity of the system, whereas in aOIF there is quantitative and qualitative information about iron additions and sources (Blain et al., 2008). Contrary to the results of aOIF experiments in the SO (e.g., SOIREE and SOFeX-N), no increase in DMS emissions was found in nOIF experiments in the SO (i.e., Kerguelen Ocean and Plateau compared Study: KEOPS), suggesting that it might be difficult to identify the potential long-term negative effects of aOIF by studying the naturally fertilized systems in the SO. Therefore, it is important to continue undertaking small-scale studies to obtain a better understanding of natural processes in the SO as well as to assess the associated risks, and so lay the groundwork for evaluating the potential effectiveness and impacts of large-scale OIF as a geoengineering solution to anthropogenic climate change. It is therefore of paramount importance that future aOIF experiments continue to focus on the effectiveness and capacity of aOIF as a means of reducing atmospheric CO_2, but they should also carefully consider the location (i.e., 'where'), timing (i.e., 'when'), and duration (i.e., 'how long'), as well as modes of iron addition (i.e., 'how'), tracing methods/parameters measurements/protocols (i.e., 'what') and side effects on marine/ocean ecosystems (i.e., 'what concerns'). This will build on the results of previous aOIF experiments, develop our understanding of the magnitude and sources of uncertainties, and provide confidence in our ability to reproduce results.

Where: The first consideration for a successful aOIF experiment is the location. The dominance of diatoms in phytoplankton communities plays a major role in increasing the biological pump because diatom species can sink rapidly as aggregates or by forming

resting spores (Tréguer et al., 1995). Previous aOIF experiments have shown that silicate concentration is the crucial factor inducing diatom blooms. Therefore, to obtain the greatest possible carbon export flux in response to iron addition, aOIF experiments should be designed in regions with high silicate concentrations, such as in the subarctic NP (e.g., SEEDS-1 experiment) and the south of PF of the SO (e.g., SOFeX-S experiment) >~15 μM (Fig. 4c). In selecting sites for iron fertilization, it is also important to distinguish the iron-fertilized patch from the surrounding unfertilized waters to observe, easily and efficiently, iron-induced changes (Coale et al., 1996). Ocean eddies provide an excellent setting for aOIF experimentation because they tend to naturally isolate interior waters from the surrounding waters. Mesoscale eddies range from 25 - 250 km in diameter and maintain their characteristics for 10 - 100 days after formation (Morrow and Le Traon, 2012). Eddy centers, in which fertilization is performed, tend to be subject to relatively slow current speeds, with low shear and high vertical coherence, providing ideal conditions for tracing the same water column from the surface to the deep layers, as well as minimizing lateral stirring and advection (Smetacek et al, 2012). Therefore, finding an appropriate eddy setting in a study area should be a high priority consideration when conducting an aOIF experiment (Smetacek and Naqvi, 2008).

When: The second consideration for a successful aOIF experiment is timing, which includes when an experiment starts. PP in ocean environment is generally limited by nutrient availability and/or by light availability, and is often referred to as a single- or co-limitation. PP in the SO, a representative HNLC region, is subject to co-limitation by micro/macro-nutrients (i.e., iron and/or silicate) and light availability (Mitchell et al., 1991). In the south PF of SO, phytoplankton blooms usually occur during the early summer (i.e., from late December to early January) due to the increasing nutrient flux from the subsurface waters to the surface waters by the shoaling of MLD, along with the receipt of sufficient solar radiation (Moore and Abbott, 2002). Prior to December, phytoplankton growth is mainly limited due to light availability (Mitchell et al., 1991; Veth et al., 1997; Abbott et al., 2000), while after January (i.e., during late summer and early autumn from February to March) it is mainly limited due to silicate availability. In previous aOIF experiments in the SO that have been conducted between spring and early autumn, PP was mainly limited by iron and/or silicate availability rather than light availability (de Baar et al., 2005; Smetacek and Naqvi, 2008; Peloquin et al., 2011). In addition, the grazing pressure of mesozooplankton (i.e., copepods) on large diatoms was also a major limiting factor in diatom production (Coale et al., 2004; Martin et al., 2013), and was generally higher during late summer and early autumn (February to March) (Le Quéré et al., 2016). Considering the key factors (i.e., micro/macro nutrient availability, light availability, and grazing pressure) controlling PP in the SO, the most appropriate timing for an aOIF

experiment to start in the SO is likely to be the early summertime (i.e., late December to early January).

How long: The third consideration for a successful aOIF experiment is the duration. Although the period that phytoplankton blooms have been maintained by OIF have lasted from ~10 to 40 days (Martin et al., 1994; Coale et al., 1996; Boyd et al., 2000; Tsuda et al., 2005; Coale et al., 2004; Boyd et al., 2004; Smetacek et al., 2012), it has also been suggested that most aOIF experiments did not cover the full response times from onset to termination (Boyd et al., 2005). For example, SOIREE and SEEDS-1 had relatively short observation periods (13 days) and saw increasing trends in PP throughout the experiments (Fig. 10a), suggesting that the observation period should have been extended. Furthermore, after the end of SOIREE, ocean color satellite images showed continued high chlorophyll-a concentrations (~1 mg m^{-3}) in the iron fertilized patch, which was visible as a long ribbon shape that extended some ~150 km for ~45 days; (~6 weeks) after the initial iron addition (Fig. 10b) (Abraham et al., 2000). This indicates that short experimental durations may not be sufficient for detecting the full influence of artificial iron additions on PP and ecosystem (Figs. 8b and 10a) (Boyd et al., 2000; Tsuda et al., 2003; de Baar et al., 2005). SOFeX-S also resulted in relatively low export production despite the high PP due to the experimental duration being insufficient to cover the termination of the phytoplankton bloom. However, SERIES, SEEDS-2, EIFEX, and LOHAFEX did fully monitor all phases of the phytoplankton bloom from onset to termination. EIFEX, the second-longest aOIF experiment, at 39 days, was the only one that observed iron-induced deep export production between days ~28 and ~36 (Table 5 and Fig. 10a) (Smetacek et al., 2012; Assmy et al., 2013). Furthermore, long-term observations covering the later stage of bloom development during nOIF experiments resulted in much higher Fe:C export efficiencies compared to the short-term aOIF (Blain et al., 2007; Pollard et al., 2009). Based on previous aOIF experiments, it would, therefore, be important to detect the full phase of a phytoplankton bloom to determine accurately the amount of iron-induced POC exported out of the mixed layer. The observation period is, therefore, an important factor to consider in budget and effectiveness estimates. It is suggested that the experimental duration should be a minimum of ~40 days based on the SOIREE experiment, which produced the longest iron-induced bloom (i.e., a longevity of ~45 days).

How: The fifth consideration for a successful aOIF experiment lies in the strategy/approach of adding and maintaining dissolved iron within the upper mixed layer to produce a phytoplankton bloom. First, the chemical form for iron addition should be acidified iron-sulfate, which is less expensive and more bioavailable than other iron compounds. The amount of iron-sulfate required is calculated according to the target concentration of the dissolved iron and volume (MLD × patch size). Based on bottle

incubation experiments, target iron concentrations of ~2 - 4 nM are recommended to stimulate maximum phytoplankton growth due to the rapid losses of added iron by horizontal advection/diffusion and oxidation to poorly bioavailable iron(III) (Coale et al., 1996; Coale et al., 1998; Bowie et al., 2001). For patch size, a biogeochemical model study showed that a fertilized patch size of 156 km^2 maintained an iron concentration above 0.3 nM for 56 days, while a longer period of 196 days required a fertilized patch size of 160,000 km^2 (Xiu and Chai, 2010). This is because, compared to larger iron-fertilized patches, a smaller patch size tended to lose iron more rapidly due to dilution effects with unfertilized water. Previous aOIF experiments also produced similar results to this model study. The lateral dilution rate (<0.25 d^{-1}) during SAGE, which had the smallest fertilized patch size (36 km^2) of the SO experiments, was two times higher than the rates (<~0.1 d^{-1}) in the SO experiments with a larger fertilized patch size (e.g., EIFEX fertilized with a patch size of 167 km^2 and SOFeX-N/S fertilized with a patch size of 225 km^2) (Coale et al., 2004; Law et al., 2011; Smetacek et al., 2012). Therefore, it would be more appropriate to fertilize a large area (e.g., LOHAFEX had the largest aOIF experiment at ~300 km^2), which would reduce the dilution effect with unfertilized waters (Xiu and Chai, 2010). Based on a ~2 nM iron concentration for a patch size of 300 km^2 and MLD of 50 m, it would need ~2,000 kg of iron(II) to be applied in a fertilization experiment. Iron should be released into the wake of a ship, with the release track describing an expanding spiral (or square) in the eddy center, with a regular interval of ~1 km throughout the patch, because it is easier to locate a fertilized patch than a point release (Watson et al., 1991). In addition, it should be completed within ~24 h because of the time-dependent phytoplankton response within the iron-fertilized patch. Previous aOIF experiments have shown that multiple iron additions (≥2 infusions) are needed to maintain the dissolved iron concentration required to derive maximum phytoplankton growth within the fertilized patch. For example, in SOIREE it was found that four additions of iron at intervals of about three days led to persistently high levels of both dissolved and particulate iron within the mixed layer, with a rapid reduction at the end of the experiment, combined with an increase in the concentration of iron-binding ligands. In both EIFEX and SOFeX-S, it was also found that multiple iron(II) infusions (in particular, two infusions with intervals of 13 days in EIFEX and four infusions with intervals of four days in SOFeX-S) allowed iron to persist in the mixed layer longer than its expected oxidation kinetics. The relatively low oxidation rates were related to a combination of photochemical production, slow oxidation and, possibly, organic complexation (Croot et al., 2008). Blain et al. (2007) explained that the higher carbon sequestration effectiveness of nOIF experiments compared to aOIF experiments partly resulted from the slow and continuous iron addition that occurs in the natural environment. Large amounts of iron addition at one time can lead to a substantial loss of artificially

added iron. Therefore, for an experimental duration of >~40 days, a minimum of three iron infusions at intervals of ~10 - 15 days would be required to prevent the iron limitation on phytoplankton growth, based on the EisenEx and EIFEX experiments (Nishioka et al., 2005; Smetacek et al., 2012).

What: The fifth consideration for a successful aOIF experiment is the effective tracing of the fertilized patch, including the detection of carbon sequestration (Buesseler and Boyd, 2003). All previous aOIF experiments used physical tracers, in particular GPS and ARGO equipped drifting buoys, to follow the iron fertilized patch. A drifting buoy is a natural and passive system moving along with the currents, but it can be removed from the fertilized patch due to the action of strong winds (Tsumune et al., 2005). Therefore, the release of GPS and ARGO equipped drifting buoys at the center of the patch after the iron infusions would provide a visual map showing the tracked positions of the fertilized patch. An inert chemical tracer, such as SF6, would also be an excellent option for following the fertilized patch after iron addition. Previous aOIF experiments have shown that the SF6 measurements based on underway sampling systems can be used to determine accurately time-dependent vertical and lateral transport of iron-fertilized patches. Many subsequent aOIF experiments have also used tracing methods based on the observation of biogeochemical parameters (such as the Fv/Fm ratio, chlorophyll fluorescence, and underway pCO2) before and after iron addition (Martin et al., 1994; Coale et al., 1996; Boyd et al., 2000; Tsuda et al., 2005; Coale et al., 2004; Boyd et al., 2004; Smetacek et al., 2012). The Fv/Fm ratio can be easily and promptly used as an indicator to track the fertilized patch due to its rapid response to iron addition. Direct measurements of carbon export fluxes to determine the effectiveness of aOIF should be conducted by deploying an NBST at two depths: (1) within the mixed layer to detect increases in iron-induced POC in the surface layer along with the calibration of a water-column based 234Th method, and (2) below the depth of the winter MLD to detect iron-induced export carbon fluxes into intermediate/deeper waters (Bidigare et al., 1999; Nodder et al., 2001; Boyd et al., 2004; Buesseler et al., 2004; Coale et al., 2004; Aono et al., 2005; Tsuda et al., 2007; Smetacek et al., 2012; Martin et al., 2013). Sinking-particle profiling systems mounted on autonomous floats, such as a transmissometer and UVP that measure and photograph sinking particles, could provide a record of the temporal and vertical evolution of iron-induced POC stocks through successive depth layers down to ~3,000-m depth for ~20 months after deployment, once calibrated using POC fluxes measured from sediment traps and/or a water-column based 234Th method (Bishop et al., 2004; Smetacek et al., 2012; Martin et al., 2013). Future OIF experiments would benefit from these technological advances, enabling a more efficient tracing of the carbon export flux and particle size and composition at higher vertical and temporal resolution than has been possible in the past. Hence, the application of an NBST

system and water-column based 234Th method to direct flux estimates, combined with autonomous sinking-particle profiles from a transmissometer and UVP, will enable the quantitative and qualitative evaluation of the effectiveness of aOIF and direct observation of iron-induced carbon export fluxes after artificial iron additions.

What concerns: The sixth consideration for a successful aOIF experiment is the monitoring of possible side effects. The LC/LP parties recently adopted Resolution LC-LP.2 (2010), which includes the "Assessment Framework for Scientific Research Involving Ocean Fertilization". This considers possible side effects on marine/ocean ecosystems after artificial iron additions, such as the production of climate-relevant gases and negative ecosystem changes, which are vital to assess when proposing an aOIF experiment. The emissions of climate-relevant gases, such as N_2O, DMS, and HVOCs, may directly contribute to warming or cooling effects, and toxic DA production may have a negative impact on marine/ocean ecosystems (Law, 2008; Silver et al., 2010; Trick et al., 2010), resulting in significant offsets against the benefits of aOIF experiments. However, there is little quantitative and qualitative information regarding possible side effects following the previous aOIF experiments. Therefore, the future monitoring of these potential side effects is a prerequisite to evaluating accurately the effectiveness of an aOIF experiment in the future.

In summary, to maximize the effectiveness of aOIF experiments in the future, we suggest a design that incorporates several conditions. (1) Experiments are conducted in the center of an eddy structure when grazing pressure is low and silicate levels are high (e.g., in the case of SO, at the southern PF during the early summer). (2) Shipboard observations are made during a minimum of ~40 days, with multiple iron injections (iron infusions of ~2,000 kg at least three times, with an interval of ~10 - 15 days, to fertilize a patch of 300 km^2 to obtain a ~2 nM concentration). (3) The iron-fertilized patch is traced using both physical (e.g., a drifting buoy) and biogeochemical (e.g., SF_6 and the Fv/Fm ratio) tracers. (4) An NBST system and water-column derived ^{234}Th method is employed at two depths (one within the mixed layer and another below it), with autonomous profilers equipped with underwater video profilers and transmissometers to estimate accurately the carbon export flux. (5) The side effects on marine/ocean ecosystems are monitored, including the production of climate-relevant gases (e.g., N_2O, DMS, and HVOCs).

5. Design of the Korean Iron Fertilization Experiment in the Southern Ocean (KIFES)

5.1 A plan for the future : KIFES

The KIFES design entails a The KIFES design entails a 5-year project plan modeled on the EIFEX program that found deep carbon by conducting an aOIF experiment in the center of an eddy structure (Fig. 11). The KIFES project would include a preliminary environmental survey both outside and inside the center of an eddy structure formed in the SO PF, a scientific aOIF experiment, and an assessment of the full KIFES project. In this section, we introduce the major goals, objectives, and main tasks of KIFES.

5.1.1 Year one plan

Goals: (1) Data collection with regard to oceanographic conditions in/near the eastern Bransfield Basin, including both eddy development and distribution. (2) Establishment of the study aims, hypothesis, and site for the KIFES experiment.

Objective: To understand the physical and biogeochemical oceanography of relevance to the eastern Bransfield Basin as an OIF site through an analysis of earlier datasets and a review of published papers.

Main tasks: (1) Review databases of physical and biogeochemical parameters from previous surveys conducted in/near the eastern Bransfield Basin. (2) Review the eastern Bransfield Basin oceanographic conditions using data analysis and references. (3) Establish the study aims, hypothesis, and site in/near the eastern Bransfield Basin for an aOIF experiment, based on the results obtained from tasks (1) and (2). (4) Design an oceanographic cruise map for the first preliminary survey in/near the eastern Bransfield Basin. (5) Analysis of eddy development and distribution using satellite data in/near the eastern Bransfield Basin. (6) Prepare scientific instruments for ocean physical and biogeochemical monitoring. (7) Establish an international collaborative OIF network. (8) KIFES field program proposal submission for the 'Initial Assessment' to determine that KIFES falls within the remit of ocean fertilization and should be evaluated in the LC/LP assessment framework based on the results from tasks (1) and (2).

5.1.2 Year two plan

Goal: First preliminary hydrographic survey to provide a foundational understanding of oceanographic conditions in the SO PF.

Objectives: (1) To obtain information about oceanographic conditions from *in situ* measurements in/near the eastern Bransfield Basin. (2) To provide background information before the KIFES experiment.

Main tasks: (1) Using the ice breaker RV *ARAON*, undertake a field investigation in/near the eastern Bransfield Basin to determine physical and biogeochemical parameters associated with both carbon sequestration and OIF side effects (e.g., production of N_2O, DMS, HVOCs, and DA), based on the first-year results. (2) Prepare an 'Environmental Assessment' for the LC/LP assessment framework based on the first-year results and a preliminary hydrographic survey.

5.1.3 Year three plan

Goals: (1) Preliminary hydrographic survey outside/inside the center of an eddy structure prior to the KIFES experiment. (2) Approval of KIFES from LC/LP. (3) Preparation for making a film on KIFES.

Objective: (1) To compare oceanographic conditions inside and outside the center of an eddy structure formed in/near the eastern Bransfield Basin prior to the KIFES experiment. (2) Obtain permission on the basis that the proposed KIFES is legitimate scientific research from the LC/LP. (3) To prepare the groundwork for making a documentary film on the KIFES expedition.

Main tasks: (1) Using the ice breaker RV *ARAON*, detect an eddy formed in/near the eastern Bransfield Basin using observations from acoustic Doppler current profilers (ADCPs) and satellites. (2) Conduct intensive physical and biogeochemical field investigations both inside and outside the center of an eddy structure. (3) Assess the physical and biogeochemical properties outside vs. inside the center of an eddy structure prior to KIFES. (4) Establish a final design for KIFES. (5) Submit the 'Environmental Assessment' for the LC/LP assessment framework and obtain approval for the KIFES experiment via the 'Decision Making' process from the LC/LP. (6) Contact the director of a Korean science TV channel to make a film about the KIFES expedition.

5.1.4 Year four plan

Goal: Conduction of the KIFES scientific aOIF experiment in the center of an eddy structure during the early summertime (Fig. 11)

Objective: To conduct a scientific aOIF experiment in the center of an eddy structure formed in the SO PF.

Main tasks: (1) Using ice breaker RV *ARAON*, detect an eddy formed in/near the eastern Bransfield Basin using observations from an ADCP and satellites, and investigate the initial environmental conditions for ~4 days before KIFES. (2) Execute the KIFES field campaign during a >~40-day period with the eddy structure maintained. (3) At least three iron additions at intervals of ~15 days, with each iron injection being ~2,000 kg following a spiral ship track, with a regular interval of ~1 km to create a patch size of ~300 km^2

(target dissolved iron concentration of ~2 nM). (4) Trace the fertilized patch with deployments of GPS and ARGO equipped drifting buoys, biogeochemical tracers (SF_6 and Fv/Fm ratio) employing underway-sampling systems, and gliders equipped with biogeochemical sensors. (5) Measure iron-induced carbon export fluxes for the regions both inside and outside the center of an eddy structure using NBST systems at two depths (i.e., just below the in situ MLD and at the winter MLD) along with the calibration of water-column based ^{234}Th measurements and an autonomous profiler equipped with a transmissometer and UVP. (6) Monitor possible side effects, such as the production of climate-relevant gases and toxic DA. (7) Monitor continued responses after KIFES termination using satellite observations and autonomous profilers. (8) Assessment of the effectiveness of carbon sequestration and environmental (ocean and atmosphere) side effects for KIFES and prepare the KIFES assessment for the 'Results of Monitoring' stage of the LC/LP assessment framework. (9) Prepare a documentary film during the KIFES expedition by a Korean government TV channel for a regular series on science for the public.

5.2.5 Year five plan

Goal: Integrated assessment of the KIFES project.

Objective: (1) To evaluate whether small-scale scientific aOIF experimentation can be an effective tool for detecting the effectiveness of artificially iron-induced export production and determining any negative impacts on climate change. (2) To assess the results on basic processes pertaining to the relationship between pelagic ecology and ocean biogeochemistry.

Main tasks: (1) Submit the KIFES assessment report. (2) Submit scientific results to international journals. (3) Collect feedback regarding the KIFES project from international scientific/oceanographic communities. (4) Produce a final aOIF experimental summary (including main tasks (1)-(3). (5) Assess the results for hypothesis testing in the fields of plankton ecology and biogeochemistry using the integrated results of KIFES. (6) Evaluate effectiveness and environmental side effects of large-scale SO aOIF via more realistic simulations under various scenarios with ocean biogeochemical models using the integrated results of KIFES. (7) Submit a final report of the KIFES assessment to the LC/LP.

5.2 Final Remark

The interests of the KIFES project will be all laid out in the detailed investigation of the biogeochemical effects of scientific aOIF in the SO and in aOIF as a possible geoengineering method to mitigate the climate change effects we will face in the future.

We envisage a future where the KIFES, or similar projects, can be resumed following the guidelines formulated by the LC/LP, enabling a more robust assessment of the potential of aOIF as a geoengineering solution to help reduce atmospheric CO_2 concentrations. A continuation of the next aOIF experiment would provide fundamental information and guidelines for future scientific aOIF experiments in HNLC regions, in addition to improving our understanding of SO pelagic ecology - biogeochemistry. The risks and side effects of aOIF should be thoroughly investigated to calm international concerns. Finally, we emphasize that international cooperation is essential for a project as organizationally and scientifically complex as KIFES and that we seek to improve our knowledge and provide a positive outlook for the Earth's future.

6. Summary

To test Martin's hypothesis, a total of 13 scientific aOIF experiments have been conducted in HNLC regions during the last 25 years. These aOIF experiments have resulted in increases in PP and drawdowns of macronutrients and DIC. In most experiments, the phytoplankton group has tended to shift from small-sized to large-sized plankton cells (mostly diatom-dominated). However, their effectiveness in enhancing export production has not been confirmed, except for EIFEX. Likewise, the possible environmental negative side effects in response to iron addition, such as decline in oxygen content and the production of climate-relevant gases and toxic DA, could not be fully evaluated due to the widely differing outcomes, with large uncertainties depending on aOIF experimental conditions and settings. In particular, the monitoring of N2O, DMS, and HVOCs is essential to determine the effectiveness of aOIF as a geoengineering approach, because these potential trace gas emissions can directly and indirectly modify the carbon reduction benefits resulting from aOIF. Furthermore, oxygen decline and toxic DA production may cause serious damage to marine/ocean ecosystems. Therefore, the validation and suitability of aOIF for the mitigation of rapidly increasing atmospheric CO2 levels are a subject of vigorous debate. At present, large-scale and/or commercial aOIF is prohibited by international regulation, while small-scale aOIF experimentation for scientific purposes is permitted. To maximize the effectiveness of aOIF, future aOIF experiments should be conducted by carefully considering the major factors including the methods for iron addition, tracing methods, measurement parameters, location, timing, and experimental duration, under international aOIF regulations. Finally, we envisage a future where the KIFES project, or a similar alternative, becomes a reality so that we may determine whether aOIF is a promising geoengineering solution for climate change mitigation and/or an adequate experimental tool for hypothesis testing in the fields of plankton ecology and ocean biogeochemistry.

7. References

Abbott, M.R., Richman, J.G., Bartlett, J.S.: The spring bloom in the Antarctic Polar Frontal Zone as observed from a mesoscale array of bio-optical sensors. Deep-Sea Res., Part II 47, 3285 - 3314, 2000.

ACE CRC: Position Analysis: Ocean Fertilisation: Science and Policy Issues, ACE CRC, Hobart, 2008.

ACE CRC: Position Analysis: Ocean Fertilisation, ACE CRC, Hobart, 2015.

Anderson, M. A. and Morel, F. M. M.: The influence of aqueous iron chemistry on the uptake of iron by the coastal diatom *Thalassiosira weissflogii*, Limnol. Oceanogr., 27, 789-813, 1982.

Aono, T., Yamada, M., Kudo, I., Imai, K., Nojiri, Y., and Tsuda, A.: Export fluxes of particulate organic carbon estimated from $^{234}Th/^{238}U$ disequilibrium during the Subarctic Pacific Iron Experiment for Ecosystem Dynamics Study (SEEDS 2001), Prog. Oceanogr., 64, 263-282, 2005.

Aramaki, T., Nojiri, Y., and Imai, K.: Behavior of particulate materials during iron fertilization experiments in the Western Subarctic Pacific (SEEDS and SEEDS II), Deep-Sea Res. Pt. II, 56, 2875-2888, 2009.

Assmy, P., Henjes, J., Klaas, C., and Smetacek, V.: Mechanisms determining species dominance in a phytoplankton bloom induced by the iron fertilization experiment EisenEx in the Southern Ocean, Deep-Sea Res. Pt. I, 54, 340-362, 2007.

Assmy, P., Smetacek, V., Montresor, M., Klaas, C., Henjes, J., Strass, V. H., Arrieta, J. M., Bathmann, U., Berg, G. M., Breitbarth, E., Cisewski, B., Friedrichs, L., Fuchs, N., Herndl, G. J., Jansen, S., Krägefsky, S., Latasa, M., Peeken, I., Röttgers, R., Scharek, R., Schüller, S. E., Steigenberger, S., Webb, A., and Wolf-Gladrow, D.: Thick-shelled, grazer-protected diatoms decouple ocean carbon and silicon cycles in the iron-limited Antarctic Circumpolar Current, Proc. Natl. Acad. Sci. USA., 110, 20633-20638, 2013.

Aumont, O. and Bopp, L.: Globalizing results from ocean *in situ* iron fertilization studies, Global Biogeochem. Cycles, 20, GB2017, 2006.

Bahk, J. J., Yoon, H. I., Kim, Y., Kang, C. Y., and Bae, S. H.: Microfabric analysis of laminated diatom ooze (Holocene) from the eastern Bransfield Strait, Antarctic Peninsula, Geosci. J., 7, 135-142, 2003.

Bak, Y.-S., Yoon, H. I., Yoo, K.-C., and Lee, Y.-U.: Diatom succession representing the paleoclimatic change from laminated sediments around Antarctica, J. Korean Earth Sci. Soc., 36, 190-197, 2015.

Bakker, D. C. E., Watson, A. J., and Law, C. S.: Southern Ocean iron enrichment promotes inorganic carbon drawdown, Deep-Sea Res. Pt. II, 48, 2483-2507, 2001.

Bakker, D. C. E., Bozec, Y., Nightingale, P. D., Goldson, L., Messias, M.-J., de Baar, H. J. W., Liddicoat, M., Skjelvan, I., Strass, V., and Watson, A. J.: Iron and mixing affect biological carbon uptake in SOIREE and EisenEx, two Southern Ocean iron fertilisation experiments, Deep-Sea Res. Pt. I, 52, 1001-1019, 2005.

Bange, H. W.: New Directions: The importance of oceanic nitrous oxide emissions, Atmos. Environ., 40, 198-199, 2006.

Barber, R. T. and Hiscock, M. R.: A rising tide lifts all phytoplankton: Growth response of other phytoplankton taxa in diatom-dominated blooms, Global Biogeochem. Cycles, 20, GB4S03, 2006.

Barnola, J. M., Raynaud, D., Korotkevich, Y. S., and Lorius, C.: Vostok ice core provides 160,000-year record of atmospheric CO_2, Nature, 329, 408-414, 1987.

Behrenfeld, M. J., Bale, A. J., Kolber, Z. S., Aiken, J., and Falkowski, P. G.: Confirmation of Iron Limitation of Phytoplankton Photosynthesis in the Equatorial Pacific-Ocean, Nature, 383, 508-511, 1996.

Belviso, S., Bopp, L., Mosseri, J., Tedetti, M., Garcia, N., Griffiths, B., Joux, F., Obernosterer, I., Uitz, J., and Veldhuis, M. J. W.: Effect of natural iron fertilisation on the distribution of DMS and DMSP in the Indian sector of the Southern Ocean, Deep-Sea Res. Pt. II, 55, 893-900, 2008.

Berg, G. M., Mills, M. M., Long, M. C., Bellerby, R., Strass, V., Savoye, N., Röttgers, R., Croot, P. L., Webb, A., and Arrigo, K. R.: Variation in particulate C and N isotope composition following iron fertilization in two successive phytoplankton communities in the Southern Ocean, Global Biogeochem. Cycles, 25, GB3013, 2011.

Bidigare, R. R., Hanson, K. L., Buesseler, K. O., Wakeham, S. G., Freeman, K. H., Pancost, R. D., Millero, F. J., Steinberg, P., Popp, B. N., Latasa, M., Landry, M. R., and Laws, E. A.: Iron-stimulated changes in ^{13}C fractionation and export by equatorial Pacific phytoplankton: Toward a paleogrowth rate proxy, Paleoceanography, 14, 589-595, 1999.

Bishop, J. K. B., Wood, T. J., Davis, R. E., and Sherman, J. T.: Robotic Observations of Enhanced Carbon Biomass and Export at 55°S During SOFeX, Science, 304, 417-420, 2004.

Blain, S., Queguiner, B., Armand, L., Belviso, S., Bombled, B., Bopp, L., Bowie, A., Brunet, C., Brussaard, C., Carlotti, F., Christaki, U., Corbiere, A., Durand, I., Ebersbach, F., Fuda, J.-L., Garcia, N., Gerringa, L., Griffiths, B., Guigue, C., Guillerm, C., Jacquet,

S., Jeandel, C., Laan, P., Lefevre, D., Lo Monaco, C., Malits, A., Mosseri, J., Obernosterer, I., Park, Y.-H., Picheral, M., Pondaven, P., Remenyi, T., Sandroni, V., Sarthou, G., Savoye, N., Scouarnec, L., Souhaut, M., Thuiller, D., Timmermans, K., Trull, T., Uitz, J., van Beek, P., Veldhuis, M., Vincent, D., Viollier, E., Vong, L., and Wagener, T.: Effect of natural iron fertilization on carbon sequestration in the Southern Ocean, Nature, 446, 1070-1074, 2007.

Blain, S., Sarthou, G., and Laan, P.: Distribution of dissolved iron during the natural iron-fertilization experiment KEOPS (Kerguelen Plateau, Southern Ocean), Deep-Sea Res. Pt. II, 55, 594-605, 2008.

Bowie, A. R., Maldonado, M. T., Frew, R. D., Croot, P. L., Achterberg, E. P., Mantoura, R. F. C., Worsfold, P. J., Law, C. S., and Boyd, P. W.: The fate of added iron during a mesoscale fertilisation experiment in the Southern Ocean, Deep-Sea Res. Pt. II, 48, 2703-2743, 2001.

Boyd, P. W., Watson, A. J., Law, C. S., Abraham, E. R., Trull, T., Murdoch, R., Bakker, D. C. E., Bowie, A. R., Buesseler, K. O., Chang, H., Charette, M., Croot, P., Downing, K., Frew, R., Gall, M., Hadfield, M., Hall, J., Harvey, M., Jameson, G., LaRoche, J., Liddicoat, M., Ling, R., Maldonado, M. T., McKay, R. M., Nodder, S., Pickmere, S., Pridmore, R., Rintoul, S., Safi, K., Sutton, P., Strzepek, R., Tanneberger, K., Turner, S., Waite, A., and Zeldis, J.: A mesoscale phytoplankton bloom in the polar Southern Ocean stimulated by iron fertilization, Nature, 407, 695-702, 2000.

Boyd, P. W. and Abraham, E. R.: Iron-mediated changes in phytoplankton photosynthetic competence during SOIREE, Deep-Sea Res. Pt. II, 48, 2529-2550, 2001.

Boyd, P. W. and Law, C. S.: The Southern Ocean Iron RElease Experiment (SOIREE)-introduction and summary, Deep-Sea Res. Pt. II, 48, 2425-2438, 2001.

Boyd, P. W., Law, C. S., Wong, C. S., Nojiri, Y., Tsuda, A., Levasseur, M., Takeda, S., Rivkin, R., Harrison, P. J., Strzepek, R., Gower, J., McKay, R. M., Abraham, E., Arychuk, M., Barwell-Clarke, J., Crawford, W., Crawford, D., Hale, M., Harada, K., Johnson, K., Kiyosawa, H., Kudo, I., Marchetti, A., Miller, W., Needoba, J., Nishioka, J., Ogawa, H., Page, J., Robert, M., Saito, H., Sastri, A., Sherry, N., Soutar, T., Sutherland, N., Taira, Y., Whitney, F., Wong, S.-K. E., and Yoshimura, T.: The decline and fate of an iron-induced subarctic phytoplankton bloom, Nature, 428, 549-553, 2004.

Boyd, P. W., Strzepek, R., Takeda, S., Jackson, G., Wong, C. S., McKay, R. M., Law, C., Kiyosawa, H., Saito, H., Sherry, N., Johnson, K., Gower, J., and Ramaiah, N.: The evolution and termination of an iron-induced mesoscale bloom in the northeast subarctic Pacific, Limnol. Oceanogr., 50, 1872-1886, 2005.

Boyd, P. W., Jickells, T., Law, C. S., Blain, S., Boyle, E. A., Buesseler, K. O., Coale, K. H., Cullen, J. J., de Baar, H. J. W., Follows, M., Harvey, M., Lancelot, C., Levasseur, M., Owens, N. P. J., Pollard, R., Rivkin, R. B., Sarmiento, J., Schoemann, V., Smetacek, V., Takeda, S., Tsuda, A., Turner, S., and Watson, A. J.: Mesoscale Iron Enrichment Experiments 1993-2005: Synthesis and Future Directions, Science, 315, 612-617, 2007.

Broecker, W. S.: Ocean chemistry during glacial time, Geochim. Cosmochim. Acta, 46, 1689-1705, 1982.

Broecker, W. S. and Henderson, G. M.: The sequence of events surrounding Termination II and their implications for the cause of glacial-interglacial CO_2 changes, Paleoceanography, 13, 352-364, 1998.

Buesseler, K. O.: Do upper-ocean sediment traps provide an accurate record of particle flux?, Nature, 353, 420-423, 1991.

Buesseler, K. O.: The decoupling of production and particulate export in the surface ocean, Global Biogeochem. Cycles, 12, 297-310, 1998.

Buesseler, K. O. and Boyd, P. W.: Will Ocean Fertilization Work?, Science, 300, 67-68, 2003.

Buesseler, K. O., Andrews, J. E., Pike, S. M., and Charette, M. A.: The Effects of Iron Fertilization on Carbon Sequestration in the Southern Ocean, Science, 304, 414-417, 2004.

Buesseler, K. O., Andrews, J. E., Pike, S. M., Charette, M. A., Goldson, L. E., Brzezinski, M. A., Lance, V. P.: Particle export during the Southern Ocean Iron Experiment (SOFeX), Limnol. Oceanogr., 1, 311-327, 2005.

Buesseler, K. O., Benitez-Nelson, C. R., Moran, S. B., Burd, A., Charette, M., Cochran, J. K., Coppola, L., Fisher, N. S., Fowler, S. W., Gardner, W. D., Guo, L. D., Gustafsson, Ö., Lamborg, C., Masque, P., Miquel, J. C., Passow, U., Santschi, P. H., Savoye, N., Stewart, G., and Trull, T.: An assessment of particulate organic carbon to thorium-234 ratios in the ocean and their impact on the application of 234Th as a POC flux proxy, Mar. Chem., 100, 213-233, 2006.

Buesseler, K. O. , Antia, A. N. , Chen, M. , Fowler, S. W. , Gardner, W. D. , Gustafsson, Ö. , Harada, K. , Michaels, A. F. , Rutgers v. d. Loeff, M. , Sarin, M. , Steinberg, D. K. and Trull, T.: An assessment of the use of sediment traps for estimating upper ocean particle fluxes, J. Mar. Res., 65(3), 345-416, 2007.

Cavagna, A. J., Fripiat, F., Dehairs, F., Wolf-Gladrow, D., Cisewski, B., Savoye, N., Andrè, L., and Cardinal, D.: Silicon uptake and supply during a Southern Ocean iron

KOPRI 극지연구소

fertilization experiment (EIFEX) tracked by Si isotopes, Limnol. Oceanogr., 56, 147-160, 2011.

Charette, M. A. and Buesseler, K. O.: Does iron fertilization lead to rapid carbon export in the Southern Ocean?, Geochem. Geophys. Geosyst., 1, 2000GC000069, 2000.

Charlson, R. J., Lovelock, J. E., Andreae, M. O., and Warren, S. G.: Oceanic phytoplankton, atmospheric sulphur, cloud albedo and climate, Nature, 326, 655-661, 1987.

Chisholm, S. W., Falkowski, P. G., and Cullen, J. J.: Dis-Crediting Ocean Fertilization, Science, 294, 309-310, 2001.

Cisewski, B., Strass, V. H., Losch, M., and Prandke, H.: Mixed layer analysis of a mesoscale eddy in the Antarctic Polar Front Zone, J. Geophys. Res., 113, C05017, 2008.

Coale, K.H., Bruland, K.W.: ^{234}Th: ^{238}U disequilibria within the California Current. Limn. Oceano., 30 (1), 22 - 33, 1985.

Coale, K. H., Johnson, K. S., Fitzwater, S. E., Gordon, R. M., Tanner, S., Chavez, F. P., Ferioli, L., Sakamoto, C., Rogers, P., Millero, F., Steinberg, P., Nightingale, P., Cooper, D., Cochlan, W. P., Landry, M. R., Constantinou, J., Rollwagen, G., Trasvina, A., and Kudela, R.: A massive phytoplankton bloom induced by an ecosystem-scale iron fertilization experiment in the equatorial Pacific Ocean, Nature, 383, 495-501, 1996.

Coale, K. H., Johnson, K. S., Fitzwater, S. E., Blain, S. P. G., Stanton, T. P., and Coley, T. L.: IronEx-I, an *in situ* iron-enrichment experiment: Experimental design, implementation and results, Deep-Sea Res. Pt. II, 45, 919-945, 1998.

Coale, K. H., Johnson, K. S., Chavez, F. P., Buesseler, K. O., Barber, R. T., Brzezinski, M. A., Cochlan, W. P., Millero, F. J., Falkowski, P. G., Bauer, J. E., Wanninkhof, R. H., Kudela, R. M., Altabet, M. A., Hales, B. E., Takahashi, T., Landry, M. R., Bidigare, R. R., Wang, X., Chase, Z., Strutton, P. G., Friederich, G. E., Gorbunov, M. Y., Lance, V. P., Hilting, A. K., Hiscock, M. R., Demarest, M., Hiscock, W. T., Sullivan, K. F., Tanner, S. J., Gordon, R. M., Hunter, C. N., Elrod, V. A., Fitzwater, S. E., Jones, J. L., Tozzi, S., Koblizek, M., Roberts, A. E., Herndon, J., Brewster, J., Ladizinsky, N., Smith, G., Cooper, D., Timothy, D., Brown, S. L., Selph, K. E., Sheridan, C. C., Twining, B. S., and Johnson, Z. I.: Southern Ocean Iron Enrichment Experiment: Carbon Cycling in High- and Low-Si Waters, Science, 304, 408-414, 2004.

Cooper, D. J., Watson, A. J., and Nightingale, P. D.: Large decrease in ocean-surface CO_2 fugacity in response to *in situ* iron fertilization, Nature, 383, 511-513, 1996.

Croot, P. L., Bluhm, K., Schlosser, C., Streu, P., Breitbarth, E., Frew, R., and Van Ardelan, M.: Regeneration of Fe(II) during EIFeX and SOFeX, Geophys. Res. Lett., 35, L19606, 2008.

Cullen, J. J.: Status of the iron hypothesis after the Open-Ocean Enrichment Experiment, Limnol. Oceanogr., 40, 1336-1343, 1995.

Currie, K. I., Macaskill, B., Reid, M. R., and Law, C. S.: Processes governing the carbon chemistry during the SAGE experiment, Deep-Sea Res. Pt. II, 58, 851-860, 2011.

Dacey, J. W. H.; Wakeham, S. G. Oceanic dimethylsulfide: production during zooplankton grazing on phytoplankton, Science, 233, 1314 - 1316, DOI:10.1126/science.233.4770.1314, 1986.

de Baar, H. J. W., Boyd, P. W., Coale, K. H., Landry, M. R., Tsuda, A., Assmy, P., Bakker, D. C. E., Bozec, Y., Barber, R. T., Brzezinski, M. A., Buesseler, K. O., Boyé, M., Croot, P. L., Gervais, F., Gorbunov, M. Y., Harrison, P. J., Hiscock, W. T., Laan, P., Lancelot, C., Law, C. S., Levasseur, M., Marchetti, A., Millero, F. J., Nishioka, J., Nojiri, Y., van Oijen, T., Riebesell, U., Rijkenberg, M. J. A., Saito, H., Takeda, S., Timmermans, K. R., Veldhuis, M. J. W., Waite, A. M., and Wong, C.-S.: Synthesis of iron fertilization experiments: From the Iron Age in the Age of Enlightenment, J. Geophys. Res., 110, C09S16, 2005.

De La Rocha, C. L.: The Biological Pump, in: Treatise on Geochemistry update, edited by: Holland, H. D. and Turekian, K. K., Elsevier Pergamon, Oxford, 1-29, 2007.

Denman, K. L.: Climate change, ocean processes and ocean iron fertilization, Mar. Ecol.-Prog. Ser., 364, 219 - 225, 2008.

Duce, R. A. and Tindale, N. W.: Atmospheric transport of iron and its deposition in the ocean, Limnol. Oceanogr., 36, 1715-1726, 1991.

Falkowski, P. G.: Evolution of the nitrogen cycle and its influence on the biological sequestration of CO_2 in the ocean, Nature, 387, 272-275, 1997.

Figueiras, F. G., Arbones, B.. Estrada, M.: Implications of bio-optical modeling of phytoplankton photosynthesis in Antarctic waters: Further evidence of no light limitation in the Bransfield Strait, Limnol. Oceanogr., 7, 1599-1608, doi: 10.4319/lo.1999.44.7.1599, 1999.

Fitzwater, S. E., Coale, K. H., Gordon, R. M., Johnson, K. S., and Ondrusek, M. E.: Iron deficiency and phytoplankton growth in the equatorial Pacific, Deep-Sea Res. Pt. II, 43, 995-1015, 1996.

Forster, P., Ramaswamy, V., Artaxo, P., Berntsen, T., Betts, R., Fahey, D. W., Haywood, J., Lean, J., Lowe, D. C., Myhre, G., Nganga, J., Prinn, R., Raga, G., Schultz, M., and

Van Dorland, R.: Changes in atmospheric constituents and in radiative forcing. Cambridge, United Kingdom, Cambridge University Press, 129-234, 2007.

Frew, R. D., Bowie, A. R., Croot, P. L., and Pickmere S.: Macronutrient and trace-metal geochemistry of an *in situ* iron-induced Southern Ocean bloom, Deep-Sea Res. Pt. II, 48, 2467-2481, 2001.

Frost, B. W.: Phytoplankton bloom on iron rations, Nature, 383, 475-476, 1996.

Fuhrman, J. A. and Capone, D. G.: Possible biogeochemical consequences of ocean fertilization, Limnol. Oceanogr., 36, 1951-1959, 1991.

Gardner, W. D., Hinga, K. R., and Marra, J.: Observations on the degradation of biogenic material in the deep ocean with implications on the accuracy of sediment trap fluxes, J. Mar. Res., *41*, 195-214, 1983.

Gervais, F., Riebesell, U., and Gorbunov, M. Y.: Changes in primary productivity and chlorophyll *a* in response to iron fertilization in the Southern Polar Frontal Zone, Limnol. Oceanogr., 47, 1324-1335, 2002.

Gordon, R. M., Johnson, K. S., and Coale, K. H.: The behaviour of iron and other trace elements during the IronEx-I and PlumEx experiments in the Equatorial Pacific, Deep-Sea Res. Pt. II, 45, 995-1041, 1998.

Grelowski, A., Majewicz, A., Pastuszak, M.: Mesoscale hydrodynamic processes in the region of Bransfield Strait and the southern part of Drake Passage during BIOMASS-SIBEX 1983/84, Pol. Polar Res., 7:353 - 369, 1986.

Harvey, M. J., Law, C. S., Smith, M. J., Hall, J. A., Abraham, E. R., Stevens, C. L., Hadfield, M. G., Ho, D. T., Ward, B., Archer, S. D., Cainey, J. M., Currie, K. I., Devries, D., Ellwood, M. J., Hill, P., Jones, G. B., Katz, D., Kuparinen, J., Macaskill, B., Main, W., Marriner, A., McGregor, J., McNeil, C., Minnett, P. J., Nodder, S. D., Peloquin, J., Pickmere, S., Pinkerton, M. H., Safi, K. A., Thompson, R., Walkington, M., Wright, S. W., and Ziolkowski, L. A.: The SOLAS air - sea gas exchange experiment (SAGE) 2004, Deep-Sea Res. Pt. II, 58, 753-763, 2010.

Helbling, E. W., Villafañe, V. E., and Holm-Hansen, O.: Variability of phytoplankton distribution and primary production around Elephant Island, Antarctica, during 1990 - 1993, Polar Biology, 15, 233-246, 1995.

Hiscock, W. T. and Millero, F. J.: Nutrient and carbon parameters during the Southern Ocean iron experiment (SOFeX), Deep-Sea Res. Pt. I, 52, 2086-2108, 2005.

Hoffmann, L. J., Peeken, I., Lochte, K., Assmy, P., and Veldhuis, M.: Different reactions of Southern Ocean phytoplankton size classes to iron fertilization, Limnol. Oceanogr., 51, 1217-1229, 2006.

IPCC: Climate Change: The IPCC Scientific Assessment of Climate Change (Eds. J. T. Houghton, G. J. Jenkins, and J. J. Ephraums), Cambridge Univ. Press, Cambridge, 1990.

IPCC: Climate Change 1992: The Supplementary Report to the IPCC Scientific Assessment (Eds. J. T. Houghton, B. A. Callander, and S. K. Varney), Cambridge Univ. Press, 1992.

IPCC: Climate Change 1995: The Science of Climate Change, Contribution of Working Group 1 to the Second Assessment Report of the Intergovernmental Panel on Climate Change (Eds. J. T. Houghton, L. G. Meira Filho, B. A. Callander, N. Harris, A. Kattenberg, and K. Maskell), Cambridge Univ. Press, Cambridge, 1995.

IPCC: Climate Change 2001: The Scientific Basis, Contribution of Working Group 1 to the Third Assessment Report of the Intergovernmental Panel on Climate Change (Eds. D. J. Griggs, M. Noguer, P. J. van der Linden, X. Dai, K. Maskell, and C. A. Johnson), Cambridge Univ. Press, Cambridge, 2001.

IPCC: Climate Change 2007: The Physical Science Basis, Contribution of Working Group I to the Fourth Assessment Report of the Intergovernmental Panel on Climate Change (Eds. S. Solomon, D. Qin, M. Manning, Z. Chen, M. Marquis, K. B. Averyt, M. Tignor, and H. L. Miller), Cambridge Univ. Press, Cambridge, 2007.

IPCC: Climate Change 2013: The Physical Science Basis, Contribution of Working Group I to the Fifth Assessment Report of the Intergovernmental Panel on Climate Change (Eds. T. F. Stocker, D. Qin, G.-K. Plattner, M. Tignor, S. K. Allen, J. Boschung, A. Nauels, Y. Xia, V. Bex, and P. M. Midgley), Cambridge Univ. Press, Cambridge, 2013.

IPCC: Climate Change 2014: Mitigation of Climate Change, Contribution of Working Group III to the Fifth Assessment Report of the Intergovernmental Panel on Climate Change (Eds. O. Edenhofer, R. Pichs-Madruga, Y. Sokona, E. Farahani, S. Kadner, K. Seyboth, A. Adler, I. Baum, S. Brunner, P. Eickemeier, B. Kriemann, J. Savolainen, S. Schlömer, C. von Stechow, T. Zwickel, and J. C. Minx), Cambridge Univ. Press, Cambridge, 2014.

Jacquet, S. H. M., Savoye, N., Dehairs, F., Strass, V. H., and Cardinal, D.: Mesopelagic carbon remineralization during the European Iron Fertilization Experiment, Global Biogeochem. Cycles, 22, GB1023, 2008.

Jin, X. and Gruber, N.: Offsetting the radiative benefit of ocean iron fertilization by enhancing N_2O emissions, Geophys. Res. Lett., 30, 2249, 2003.

Johnson, K. S. and Karl, D. M.: Is Ocean Fertilization Credible and Creditable?, Science,

KOPRI 극지연구소

296, 467-468, 2002.

Joos, F., Sarmiento, J. L., and Siegenthaler, U.: Estimates of the effect of Southern Ocean iron fertilization on atmospheric CO_2 concentrations, Nature, 349, 772-775, 1991.

Kahru, M., Mitchell, B. G., Gille, S. T., Hewes, C. D., and Holm-Hansen, O.: Eddies enhance biological production in the Weddell-Scotia Confluence of the Southern Ocean, Geophys. Res. Lett., 34, L14603, 2007.

Kang, J.-S., Kang, S.-H., Kim, D., and Kim, D.-Y.: Planktonic centric diatom Minidiscus chilensis dominated sediment trap material in eastern Bransfield Strait, Antarctica, Mar. Ecol. Prog. Ser., 255, 93 99, 2003.

Kang, S. H., Kang, J. S., Lee S., Chung, K. H., Kim, D., Park, M. G., Antarctic phytoplankton assemblages in the marginal ice zone of the northwestern Weddell Sea, J. Plankton Res., 23, 333 - 352, 2001.

Karl, D. M. and Knauer, G. A.: Swimmers, a recapitulation of the problem and a potential solution. Oceanography, *2*, 32-35, 1989.

Keller, D. P., Feng, E. Y., and Oschlies, A.: Potential climate engineering effectiveness and side effects during a high carbon dioxide-emission scenario, Nat. Commun., 5, 3304, 2014.

Khim, B.-K., Kim, D. S., Shin, H. C., and Kim, D. Y.: Stable Carbon and Nitrogen Isotopes of Sinking Particles in the Eastern Bransfield Strait (Antarctica), Ocean Sci. J., 40, 167-176, 2005.

Knauer, G. A., Karl, D. M., Martin, J. H., and Hunter, C. N.: *In situ* effects of selected preservatives on total carbon, nitrogen and metals collected in sediment traps, J. Mar. Res., 42, 445-462, 1984.

Kolber, Z. S., Barber, R. T., Coale, K. H., Fitzwateri, S. E., Greene, R. M., Johnson, K. S., Lindley, S., and Falkowski, P. G.: Iron limitation of phytoplankton photosynthesis in the equatorial Pacific Ocean, Nature, 371, 145-149, 1994.

Koltermann, K. P., Gouretski, V. V., and Jancke, K.: Hydrographic Atlas of the World Ocean Circulation Experiment (WOCE), vol. 3, Atlantic Ocean, edited by M. Sparrow, P. Chapman, and J. Gould, Int. WOCE Proj. Off., Southampton, U. K., 2011.

Kudo, I., Noiri, Y., Cochlan, W. P., Suzuki, K., Aramaki, T., Ono, T., and Nojiri, Y.: Primary productivity, bacterial productivity and nitrogen uptake in response to iron enrichment during the SEEDS II, Deep-Sea Res. Pt. II, 56, 2755-2766, 2009.

Kurz, K. D., Maier-Reimer, E.: Iron fertilization of the austral ocean—the Hamburg model assessment, Global Biogeochem. Cycles, 7, 229 - 244, 1993.

KOPRI 극지연구소

Lampitt, R. S., Achterberg, E. P., Anderson, T. R., Hughes, J. A., Iglesias-Rodriguez, M. D., Kelly-Gerreyn, B. A., Lucas, M., Popova, E. E., Sanders, R., Shepherd, J. G., Smythe-Wright, D., and Yool, A.: Ocean fertilization: a potential means of geoengineering?, Phil. Trans. R. Soc. A, 366, 3919-3945, 2008.

Landry, M. R., Constantinou, J., Latasa, M., Brown, S. L., Bidigare, R. R., and Ondrusek, M. E.: Biological response to iron fertilization in the eastern equatorial Pacific (IronEx II). III. Dynamics of phytoplankton growth and microzooplankton grazing, Mar. Ecol. Prog. Ser., 201, 57-72, 2000.

Latasa, M., Henjes, J., Scharek, R., Assmy, P., Röttgers, R., and Smetacek, V.: Progressive decoupling between phytoplankton growth and microzooplankton grazing during an iron-induced phytoplankton bloom in the Southern Ocean (EIFEX), Mar. Ecol. Prog. Ser., 513, 39-50, 2014.

Law, C. S., Watson, A. J., Liddicoat, M. I., and Stanton, T.: Sulphur hexafluoride as a tracer of biogeochemical and physical processes in an open-ocean iron fertilisation experiment, Deep-Sea Res. Pt. II, 45, 977-994, 1998.

Law, C. S. and Ling, R. D.: Nitrous oxide flux and response to increased iron availability in the Antarctic Circumpolar Current, Deep-Sea Res. Pt. II, 48, 2509-2527, 2001.

Law, C. S., Crawford, W. R., Smith, M. J., Boyd, P. W., Wong, C. S., Nojiri, Y., Robert, M., Abraham, E. R., Johnson, W. K., Forsland, V., and Arychuk, M.: Patch evolution and the biogeochemical impact of entrainment during an iron fertilisation experiment in the sub-Arctic Pacific, Deep-Sea Res. Pt. II, 53, 2012-2033, 2006.

Law, C. S.: Predicting and monitoring the effects of large-scale ocean iron fertilization on marine trace gas emissions, Mar. Ecol. Prog. Ser., 364, 283-288, 2008.

Law, C. S., Smith, M. J., Stevens, C. L., Abraham, E. R., Ellwood, M. J., Hill, P., Nodder, S., Peloquin, J., Pickmere, S., Safi, K., and Walkington, C. M.: Did dilution limit the phytoplankton response to iron addition in HNLCLSi sub-Antarctic waters during the SAGE experiment?, Deep-Sea Res. Pt. II, 58, 786-799, 2011.

Lawrence, M. G.: Side Effects of Oceanic Iron Fertilization, Science, 297, 1993, 2002.

Lenton, T. M. and Vaughan, N. E.: The radiative forcing potential of different climate geoengineering options, Atmos. Chem. Phys., 9, 5539-5561, 2009.

Leung, D. Y. C., Caramanna, G., and Maroto-Valer, M. M.: An overview of current status of carbon dioxide capture and storage technologies, Renew. Sust. Energ. Rev., 39, 426-443, 2014.

Le Quéré, C., Buitenhuis, E. T., Moriarty, R., Alvain, S., Aumont, O., Bopp, L., Chollet, S., Enright, C., Franklin, D. J., Geider, R. J., Harrison, S. P., Hirst, A. G., Larsen, S.,

Legendre, L., Platt, T., Prentice, I. C., Rivkin, R. B., Sailley, S., Sathyendranath, S., Stephens, N., Vogt, M., and Vallina, S. M.: Role of zooplankton dynamics for Southern Ocean phytoplankton biomass and global biogeochemical cycles, Biogeosciences, 13, 4111-4133, 2016.

Levasseur, M., Scarratt, M. G., Michaud, S., Merzouk, A., Wong, C. S., Arychuk, M., Richardson, W., Rivkin, R. B., Hale, M., Wong, E., Marchetti, A., and Kiyosawa, H.: DMSP and DMS dynamics during a mesoscale iron fertilization experiment in the Northeast Pacific－Part I: Temporal and vertical distributions, Deep-Sea Res. Pt. II, 53, 2353-2369, 2006.

Liss, P., Chuck, A., Bakker, D., and Turner, S.: Ocean fertilization with iron: effects on climate and air quality, Tellus B, 57, 269-271, 2005.

London Convention: Convention on the Prevention of Marine Pollution by Dumping of Wastes and Other Matter 1972, 1972.

London Protocol: 1996 Protocol to the Convention on the Prevention of Marine Pollution by Dumping of Wastes and Other Matter, 1972, 1996.

Marshall, J. and Speer, K.: Closure of the meridional overturning circulation through Southern Ocean upwelling, Nat. Geosci., 5, 171-180, 2012.

Martin, J. H. and Fitzwater, S. E.: Iron deficiency limits phytoplankton growth in the north-east Pacific subarctic, Nature, 331, 341-343, 1988.

Martin, J. H.: Glacial-interglacial CO_2 change: The Iron Hypothesis, Paleoceanography, 5, 1-13, 1990.

Martin, J. H. and Chisholm, P.: Design for a mesoscale iron enrichment experiment. Woods Hole Oceanographic Institution, U.S JGOFS Planning Report, 15, 1992.

Martin, J. H., Coale, K. H., Johnson, K. S., Fitzwater, S. E., Gordon, R. M., Tanner, S. J., Hunter, C. N., Elrod, V. A., Nowicki, J. L., Coley, T. L., Barber, R. T., Lindley, S., Watson, A. J., Van Scoy, K., Law, C. S., Liddicoat, M. I., Ling, R., Stanton, T., Stockel, J., Collins, C., Anderson, A., Bidigare, R., Ondrusek, M., Latasa, M., Millero, F. J., Lee, K., Yao, W., Zhang, J. Z., Friederich, G., Sakamoto, C., Chavez, F., Buck, K., Kolber, Z., Greene, R., Falkowski, P., Chisholm, S. W., Hoge, F., Swift, R., Yungel, J., Turner, S., Nightingale, P., Hatton, A., Liss, P., and Tindale, N. W.: Testing the iron hypothesis in ecosystems of the equatorial Pacific Ocean, Nature, 371, 123-129, 1994.

Martin, P., van der Loeff, M. R., Cassar, N., Vandromme, P., d'Ovidio, F., Stemmann, L., Rengarajan, R., Soares, M., González, H. E., Ebersbach, F., Lampitt, R. S., Sanders, R., Barnett, B. A., Smetacek, V., and Naqvi, S. W. A.: Iron fertilization enhanced

KOPRI 극지연구소

net community production but not downward particle flux during the Southern Ocean iron fertilization experiment LOHAFEX, Global Biogeochem. Cycles, 27, 871-881, 2013.

Matthews, B.: Climate engineering: a critical review of proposals, their scientific and political context, and possible impacts, Compiled for scientists for global responsibility, 1996. 〈http://records.viu.ca/earles/geol312o/assignments/mitigation.htm〉.

McElroy, M. B.: Marine biological controls on atmospheric CO_2 and climate, Nature, 302, 328-329, 1983.

Michaels, A. F. and Silver, M. W.: Primary production, sinking fluxes and the microbial food web, Deep-Sea Res. Pt. I, 35, 473 - 490, doi:10.1016/0198-0149(88)90126-4, 1988.

Ming, T., de_Richter, R., Liu, W., and Caillol, S.: Fighting global warming by climate engineering: Is the Earth radiation management and the solar radiation management any option for fighting climate change?, Renew. Sust. Energ. Rev., 31, 792-834, 2014.

Mitchell, B. G., Brody, E. A., Holm-Hansen, O., McClain, C., and Bishop, J.: Light limitation of phytoplankton biomass and macronutrient utilization in the Southern Ocean, Limnol. Oceanogr., 36, 1662-1677, 1991.

Moore, J. K. and Abbott, M. R.: Surface chlorophyll concentrations in relation to the Antarctic Polar Front: seasonal and spatial patterns from satellite observations, Journal of Marine Systems, 37, 69-86, 2002.

Moore, J. K., Doney, S. C., Glover, D. M., and Fung, I. Y.: Iron cycling and nutrient-limitation patterns in surface waters of the world ocean, Deep-Sea Res. Pt. II, 49, 463-507, 2002.

Morel, F. M. M. and Price, N. M.: The Biogeochemical Cycles of Trace Metals in the Oceans, Science, 300, 944-947, 2003.

Morris, P. J. and Charette, M. A.: A synthesis of upper ocean carbon and dissolved iron budgets for Southern Ocean natural iron fertilisation studies, Deep-Sea Res. Pt. II, 90, 147-157, 2013.

Morrow, R. and Le Traon, P.-Y.: Recent advances in observing mesoscale ocean dynamics with satellite altimetry, Adv. Space Res., 50, 1062-1076, 2012.

Nagao, I., Hashimoto, S., Suzuki, K., Toda, S., Narita, Y., Tsuda, A., Saito, H., Kudo, I., Kato, S., Kajii, Y., and Uematsu, M.: Responses of DMS in the seawater and atmosphere to iron enrichment in the subarctic western North Pacific (SEEDS-II),

KOPRI 극지연구소

Deep-Sea Res. Pt. II, 56, 2899-2917, 2009.

Neftel, A., Oeschger, H., Schwander, J., Stauffer, B., and Zumbrunn, R.: Ice core sample measurements give atmospheric CO_2 content during the past 40,000 yr, Nature, 295, 220-223, 1982.

Nelson, D.M., Brzezinski, M.A., Sigmon, D.E., Frank, V.M.: A seasonal progression of Si limitation in the Pacific sector of the Southern Ocean, Deep-Sea Res., Part II 48, 3973 - 3995, 2001.

Nishioka, J., Takeda, S., Baar, H. J. W. D., Croot, P. L., Boye, M., Laan, P., and Timmermans, K. R.: Changes in the concentration of iron in different size fractions during an iron enrichment experiment in the open Southern Ocean, Mar. Chem., 95, 51-63, 2005.

Nodder, S. D., Charette, M. A., Waite, A. M., Trull, T. W., Boyd, P. W., Zeldis, J., and Buesseler, K. O.: Particle transformations and export flux during an *in situ* iron-stimulated algal bloom in the Southern Ocean, Geophys. Res. Lett., 28, 2409-2412, 2001.

Nodder, S. D. and Waite, A. M.: Is Southern Ocean organic carbon and biogenic silica export enhanced by iron-stimulated increases in biological production? Sediment trap results from SOIREE, Deep-Sea Res. Pt. II, 48, 2681-2701, 2001.

Oschlies, A., Koeve, W., Rickels, W., and Rehdanz, K.: Side effects and accounting aspects of hypothetical large-scale Southern Ocean iron fertilization, Biogeosciences, 7, 4017-4035, 2010.

Park, J., Park, T., Yang, E. J., Kim, D., Gorbunov, M. Y., Kim, H.-C., Kang, S. H., Shin, H. C., Lee, S., and Yoo, S.: Early summer iron limitation of phytoplankton photosynthesis in the Scotia Sea as inferred from fast repetition rate fluorometry, J. Geophys. Res. Oceans, 118, 3795 - 3806, doi:10.1002/jgrc.20281, 2013.

Park, K.-T.; Lee, K.; Shin, K.; Yang, E. J.; Hyun, B.; Kim, J.-M.; Noh, J. H.; Kim, M.; Kong, B.; Choi, D. H.; Choi, S.-J.; Jang, P.-G.; Jeong. H. J. Direct linkage between dimethyl sulfide production and microzooplankton grazing, resulting from prey composition change under high partial pressure of carbon dioxide conditions, Environ. Sci. Technol., 48(9), 4750 - 4756, DOI:10.1021/es403351h, 2014.

Peloquin, J., Hall, J., Safi, K., Ellwood, M., Law, C. S., Thompson, K., Kuparinen, J., Harvey, M., and Pickmere, S.: Control of the phytoplankton response during the SAGE experiment: A synthesis, Deep-Sea Res. Pt. II, 58, 824-838, 2011.

Peng, T.-H. and Broecker, W. S.: Factors limiting the reduction of atmospheric CO_2 by iron fertilization, Limnol. Oceanogr., 36, 1919-1927, 1991.

KOPRI 극지연구소

Petit, J. R., Jouzel, J., Raynaud, D., Barkov, N. I., Barnola, J. M., Basile, I., Bender, M., Chappellaz, J., Davis, M., Delaygue, G., Delmotte, M., Kotlyakov, V. M., Legrand, M., Lipenkov, V. Y., Lorius, C., Pepin, L., Ritz, C., Saltzman, E., and Stievenard, M.: Climate and atmospheric history of the past 420,000 years from the Vostok ice core, Antarctica, Nature, 399, 429-436, 1999.

Pollard, R. T., Salter, I., Sanders, R. J., Lucas, M. I., Moore, C. M., Mills, R. A., Statham, P. J., Allen, J. T., Baker, A. R., Bakker, D. C. E., Charette, M. A., Fielding, S., Fones, G. R., French, M., Hickman, A. E., Holland, R. J., Hughes, J. A., Jickells, T. D., Lampitt, R. S., Morris, P. J., Nedelec, F. H., Nielsdottir, M., Planquette, H., Popova, E. E., Poulton, A. J., Read, J. F., Seeyave, S., Smith, T., Stinchcombe, M., Taylor, S., Thomalla, S., Venables, H. J., Williamson, R., and Zubkov, M. V.: Southern Ocean deep-water carbon export enhanced by natural iron fertilization, Nature, 457, 577-580, 2009.

Rees, A. P., Nightingale, P. D., Owens, N. J. P., and Team, P. F.: FeeP－An *in situ* PO_4^{3-} and Fe^{2+} addition experiment to waters of the sub-tropical north-east Atlantic, Geophys. Res. Abstr., 9, 2007.

Resolution LC-LP.1: Regulation of Ocean Fertilization, LC 30/16, Annex 6, 2008.

Resolution LC-LP.2: Assessment Framework for Scientific Research Involving Ocean Fertilization, LC 32/15, Annex 6, 2010.

Resolution LP.4 (8): Amendment to the London Protocol to Regulate the Placement of Matter for Ocean Fertilization and Other Marine Geoengineering Activities, LP.8, LC 35/15, Annex 4, Annex 5, 2013.

Rogelj, J., Michiel, S., Malte, M., Reto, K., Joseph, A., Keywan, R., and William, H.: Zero emission targets as long-term global goals for climate protection, Environ. Res. Lett., 10, 105007, 2015.

Rollwagen Bollens, G.C. and Landry, M.R., Biological response to iron fertilization in the eastern equatorial Pacific (IronEx II). II. Mesozooplankton abundance, biomass, depth distribution and grazing, Mar. Ecol. Pro. Ser., 201, 43 - 56, 2000.

Sarmiento, J. L. and Orr, J. C.: Three-dimensional simulations of the impact of Southern Ocean nutrient depletion on atmospheric CO_2 and ocean chemistry, Limnol. Oceanogr., 36, 1928-1950, 1991.

Sarmiento, J. L. and Gruber, N.: Ocean Biogeochemical Dynamics, Princeton University Press, 2006.

Schlitzer, R.: Ocean Data View, odv.awi.de, 2017.

Sigman, D. M. and Boyle, E. A.: Glacial/interglacial variations in atmospheric carbon

dioxide, Nature, 407, 859-869, 2000.

Silver, M. W., Bargu, S., Coale, S. L., Benitez-Nelson, C. R., Garcia, A. C., Roberts, K. J., Sekula-Wood, E., Bruland, K. W., and Coale, K. H.: Toxic diatoms and domoic acid in natural and iron enriched waters of the oceanic Pacific, Proc. Natl. Acad. Sci. USA., 107, 20762-20767, 2010.

Smetacek, V.: EisenEx: International Team Conducts Iron Experiment In Southern Ocean, U.S. JGOFS News, 11, 11 - 14, 2001.

Smetacek, V., Bathmann, U., and Helmke, E.: The expeditions Antarktis XXI/3-4-5 of the Research Vessel "Polarstern" in 2004. Reports on Polar and Marine Research 500, 2005.

Smetacek, V. and Naqvi, S. W. A.: The next generation of iron fertilization experiments in the Southern Ocean, Philos. Trans. A Math. Phys. Eng. Sci., 366, 3947-3967, 2008.

Smetacek, V. and Naqvi, S. W. A.: The expedition of the research vessel "Polarstern" to the Antarctic in 2009 (ANT-XXV/3 - LOHAFEX), Berichte zur Polar- und Meeresforschung (Reports on Polar and Marine Research). Bremerhaven, Alfred Wegener Institute for Polar and Marine Research, 613, 2010.

Smetacek, V., Klaas, C., Strass, V. H., Assmy, P., Montresor, M., Cisewski, B., Savoye, N., Webb, A., d/'Ovidio, F., Arrieta, J. M., Bathmann, U., Bellerby, R., Berg, G. M., Croot, P., Gonzalez, S., Henjes, J., Herndl, G. J., Hoffmann, L. J., Leach, H., Losch, M., Mills, M. M., Neill, C., Peeken, I., Rottgers, R., Sachs, O., Sauter, E., Schmidt, M. M., Schwarz, J., Terbruggen, A., and Wolf-Gladrow, D.: Deep carbon export from a Southern Ocean iron-fertilized diatom bloom, Nature, 487, 313-319, 2012.

Smetacek, V.: Ocean iron fertilization experiments: The dawn of a new era in applied ocean sciences?, KOPRI, Korea, 2015.

Solomon, S., Garcia, R. R., and Ravishankara, A. R.: On the role of iodine in ozone depletion, J. Geophys. Res., 99, 20491-20499, 1994.

Spolaor, A., Vallelonga, P., Cozzi, G., Gabrieli, J., Varin, C., Kehrwald, N., Zennaro, P., Boutron, C., and Barbante, C.: Iron speciation in aerosol dust influences iron bioavailability over glacial-interglacial timescales, Geophys. Res. Lett., 40, 1618-1623, 2013.

Stanton, T. P., Law, C. S., and Watson, A. J.: Physical evolution of the IronEx-I open ocean tracer patch, Deep-Sea Res. Pt. II, 45, 947-975, 1998.

Steinberg, P. A., Millero, F. J., and Zhu, X.: Carbonate system response to iron enrichment, Mar. Chem., 62, 31-43, 1998.

Strong, A.L., Cullen, J. J., and Chisholm, S. W.: Ocean fertilization: Science, policy, and

commerce. Oceanography, 22, 236 - 261, 2009.

Suess, E.: Particulate organic carbon flux in the oceans - Surface productivity and oxygen utilization, 1980.

Takeda, S. and Tsuda, A.: An *in situ* iron-enrichment experiment in the western subarctic Pacific (SEEDS): Introduction and summary, Prog. Oceanogr., 64, 95-109, 2005.

Talley, L. D.: Hydrographic Atlas of the World Ocean Circulation Experiment (WOCE), Volume 2: Pacific Ocean (eds. Sparrow, M., Chapman, P., and Gould, J.), International WOCE Project Office, Southampton, U.K., ISBN 0-904175-54-5, 2007.

Thiele, S., Fuchs, B. M., Ramaiah, N., and Amann, R.: Microbial Community Response during the Iron Fertilization Experiment LOHAFEX, Appl. Environ. Microbiol., 78, 8803-8812, 2012.

Thompson, A. F., Heywood, K. J., Thorpe, S. E., Renner, A. H. H., and Trasviña, A.: Surface Circulation at the Tip of the Antarctic Peninsula from Drifters, J. Phys. Oceanogr., 39, 3-26, 2009.

Tréguer, P., Nelson, D. M., Van Bennekom, A. J., DeMaster, D. J., Leynaert, A., and Quéguiner, B.: The Silica Balance in the World Ocean: A Reestimate, Science, 268, 375-379, 1995.

Trick, C. G., Bill, B. D., Cochlan, W. P., Wells, M. L., Trainer, V. L., and Pickell, L. D.: Iron enrichment stimulates toxic diatom production in high-nitrate, low-chlorophyll areas, Proc. Natl. Acad. Sci. USA., 107, 5887-5892, 2010.

Trull, T., and Armand, L. K.: Insights into Southern Ocean carbon export from the $\delta^{13}C$ of particles and dissolved inorganic carbon during the SOIREE iron release experiment, Deep-Sea Res. Pt. II, 48, 2655-2680, 2001.

Tsuda, A., Takeda, S., Saito, H., Nishioka, J., Nojiri, Y., Kudo, I., Kiyosawa, H., Shiomoto, A., Imai, K., Ono, T., Shimamoto, A., Tsumune, D., Yoshimura, T., Aono, T., Hinuma, A., Kinugasa, M., Suzuki, K., Sohrin, Y., Noiri, Y., Tani, H., Deguchi, Y., Tsurushima, N., Ogawa, H., Fukami, K., Kuma, K., and Saino, T.: A Mesoscale Iron Enrichment in the Western Subarctic Pacific Induces a Large Centric Diatom Bloom, Science, 300, 958-961, 2003.

Tsuda, A., Kiyosawa, H., Kuwata, A., Mochizuki, M., Shiga, N., Saito, H., Chiba, S., Imai, K., Nishioka, J., and Ono, T.: Responses of diatoms to iron-enrichment (SEEDS) in the western subarctic Pacific, temporal and spatial comparisons, Prog. Oceanogr., 64, 189-205, 2005.

Tsuda, A., Takeda, S., Saito, H., Nishioka, J., Kudo, I., Nojiri, Y., Suzuki, K., Uematsu, M., Wells, M. L., Tsumune, D., Yoshimura, T., Aono, T., Aramaki, T., Cochlan, W. P.,

Hayakawa, M., Imai, K., Isada, T., Iwamoto, Y., Johnson, W. K., Kameyama, S., Kato, S., Kiyosawa, H., Kondo, Y., Levasseur, M., Machida, R. J., Nagao, I., Nakagawa, F., Nakanishi, T., Nakatsuka, S., Narita, A., Noiri, Y., Obata, H., Ogawa, H., Oguma, K., Ono, T., Sakuragi, T., Sasakawa, M., Sato, M., Shimamoto, A., Takata, H., Trick, C. G., Watanabe, Y. W., Wong, C. S., and Yoshie, N.: Evidence for the grazing hypothesis: Grazing reduces phytoplankton responses of the HNLC ecosystem to iron enrichment in the western subarctic pacific (SEEDS II), J. Oceanogr., 63, 983-994, 2007.

Tsuda, A., Saito, H., Machida, R. J., and Shimode, S., Meso- and microzooplankton responses to an in situ iron fertilization experiment (SEEDS II) in the northwest subarctic Pacific, Deep-Sea Res. Part II, 56(26), 2767-2778, DOI: 10.1016/j.dsr2.2009.06.004, 2009.

Tsumune, D., Nishioka, J., Shimamoto, A., Takeda, S., and Tsuda, A.: Physical behavior of the SEEDS iron-fertilized patch by sulphur hexafluoride tracer release, Prog. Oceanogr., 64, 111-127, 2005.

Tsumune, D., Nishioka, J., Shimamoto, A., Watanabe, Y. W., Aramaki, T., Nojiri, Y., Takeda, S., Tsuda, A., and Tsubono, T.: Physical behaviors of the iron-fertilized patch in SEEDS II, Deep-Sea Res. Pt. II, 56, 2948-2957, 2009.

Turner, S. M., Nightingale, P. D., Spokes, L. J., Liddicoat, M. I., and Liss, P. S.: Increased dimethyl sulphide concentrations in sea water from *in situ* iron enrichment, Nature, 383, 513-517, 1996.

Turner, S. M., Harvey, M. J., Law, C. S., Nightingale, P. D., and Liss, P. S.: Iron-induced changes in oceanic sulfur biogeochemistry, Geophys. Res. Lett., 31, L14307, 2004.

Valdes, J. R. and Price, J. F.: A neutrally buoyant, upper ocean sediment trap. J. Atmos. Oceanogr. Technol., 17, 62-68, 2000.

Valdes, J. R. and Buesseler, K. O.: The neutrally buoyant sediment trap (NBST), a new tool for "Twilight Zone" particle exploration, Eos Trans. AGU Ocean Sci. Meeting Suppl., *87(36)*, Abstract OS26A-10, 2006.

Varela, M., Fernandez, E., and Serret, P.: Size-fractionated phytoplankton biomass and primary production in the Gerlache and south Bransfield Straits (Antarctic Peninsula) in Austral summer 1995 - 1996, Deep-Sea Res. Pt. II, 49, 749-768, 2002.

Vaughan, N. E. and Lenton, T. M.: A review of climate geoengineering proposals, Clim. Change, 109, 745-790, 2011.

Veth, C., Peeken, I., and Scharek, R.: Physical anatomy of fronts and surface waters in the ACC near 6°W meridian during austral spring 1992, Deep-Sea Res., Part II 44, 23

KOPRI 극지연구소

- 49, 1997.

Volk, T. and Hoffert, M. I.: Ocean Carbon Pumps: Analysis of Relative Strengths and Efficiencies in Ocean-Driven Atmospheric CO2 Changes, in: The Carbon Cycle and Atmospheric CO2: Natural Variations Archean to Present, edited, Geophys. Monogr. Ser, 99-110, 1985.

Waite, A. M. and Nodder, S. D.: The effect of in situ iron addition on the sinking rates and export flux of Southern Ocean diatoms, Deep-Sea Res. Pt. II, 48, 2635-2654, 2001.

Walter, S., Peeken, I., Lochte, K., Webb, A., and Bange, H. W.: Nitrous oxide measurements during EIFEX, the European Iron Fertilization Experiment in the subpolar South Atlantic Ocean, Geophys. Res. Lett., 32, L23613, 2005.

Wanninkhof, R. and Thoning, K.: Measurement of fugacity of CO_2 in surface water using continuous and discrete sampling methods, Mar. Chem., 44, 189-204, 1993.

Watson, A., Liss, P., and Duce, R.: Design of a small-scale in situ iron fertilization experiment, Limnol. Oceanogr., 36, 1960-1965, 1991.

Watson, A. J., Bakker, D. C. E., Ridgwell, A. J., Boyd, P. W., and Law, C. S.: Effect of iron supply on Southern Ocean CO_2 uptake and implications for glacial atmospheric CO_2, Nature, 407, 730-733, 2000.

Westberry, T. K., Behrenfeld, M. J., Milligan, A. J., and Doney, S. C.: Retrospective satellite ocean color analysis of purposeful and natural ocean iron fertilization, Deep-Sea Res. Pt. I, 73, 1-16, 2013.

Williamson, P., Wallace, D. W. R., Law, C. S., Boyd, P. W., Collos, Y., Croot, P., Denman, K., Riebesell, U., Takeda, S., and Vivian, C.: Ocean fertilization for geoengineering: A review of effectiveness, environmental impacts and emerging governance, Process Saf. Environ. Protect., 90, 475-488, 2012.

Wingenter, O. W., Haase, K. B., Strutton, P., Friederich, G., Meinardi, S., Blake, D. R., and Rowland, F. S.: Changing concentrations of CO, CH_4, C_5H_8, CH_3Br, CH_3I, and dimethyl sulfide during the Southern Ocean Iron Enrichment Experiments, Proc. Nat. Acad. Sci. U.S.A., 101, 8537-8541, 2004.

Wingenter, O. W., Elliot, S. M., and Blake, D. R.: New Directions: Enhancing the natural sulfur cycle to slow global warming, Atmos. Environ., 41, 7373-7375, 2007.

Wong, C. S., Timothy, D. A., Law, C. S., Nojiri, Y., Xie, L., Wong, S.-K. E., and Page, J. S.: Carbon distribution and fluxes during the SERIES iron fertilization experiment with special reference to the fugacity of carbon dioxide (fCO_2), Deep-Sea Res. Pt. II, 53, 2053-2074, 2006.

KOPRI 극지연구소

Xiu, P., Chai, F.: Modeling the Effects of Size on Patch Dynamics of an Inert Tracer, Ocean Sci., 6(1): 413-421, 2010.

Yoo, K.-C., Yoon, H. I., Lee, J. I., Lee, M. K., and Kim, K.: Spectral analysis of time series in marine laminated sediments of the eastern Basin of Bransfield Strait (Antarctic Peninsula), 2016 SCAR Meeting, Kuala Lumpur, p984, 2016.

Zeldis, J., Mesozooplankton community composition, feeding, and export production during SOIREE, Deep-Sea Res. Pt. II, 48, 2615 - 2634, 2001.

Zhuang, G., Yi, Z., Duce, R. A., and Brown, P. R.: Link between iron and sulphur cycles suggested by detection of Fe(II) in remote marine aerosols, Nature, 355, 537-539, 1992.

Zhuang, G. and Duce, R. A.: The adsorption of dissolved iron on marine aerosol particles in surface waters of the open ocean, Deep-Sea Res. Pt. I, 40, 1413-1429, 1993.

KOPRI
극지연구소

Table 1. Summary of ocean iron fertilization (OIF) experiments; time, location, research vessel, added iron(Ⅱ) (values in brackets correspond to the number of days from the first iron addition, e.g., the first iron addition becomes (0), initial iron concentrations, after iron addition concentrations (iron concentrations after iron addition), tracer, initial patch size, experiment duration, and regional characteristics (HNLC: high-nutrient low chlorophyll).

	Experiment	Time	Location	Research vessel	Added iron (Ⅱ) (kg) (day)	Initial iron (nM)	After iron addition (nM)	Tracer	Patch size (km^2)	Duration (days)	Regional characteristics
1	IronEx-1	Oct 1993	Equatorial Pacific 5° S, 90° W	RV *Columbus Iselin*	①450 (0)	0.06	3.60	SF_6	64	10	HNLC
2	IronEx-2	May 1995	Equatorial Pacific 3.5° S, 104° W	RV *Melville*	①225 (0) ②112 (3) ③112 (7)	0.02	2.00 1.00 1.00	SF_6	72	17	HNLC
3	SOIREE	Feb 1999	Southern Ocean-Australasian-Pacific sector 61° S, 141° E	RV *Astrolab*	①768 (0) ②312 (3) ③312 (5) ④353 (7)	0.08	3.80 2.60 2.60 2.50	SF_6	50	13	HNLC
4	EisenEx	Nov 2000	Southern Ocean-Atlantic sector 48° S, 21° E	RV *Polarstern*	①780 (0) ②780 (7) ③780 (16)	0.06	2.00	SF_6	50	23	HNLC
5	SOFeX-N	Jan–Feb 2002	Southern Ocean-Pacific sector 56.23° S, 172° W	RV *Revelle* RV *Melville*	①631 (0) ②631 (5) ③450 (30)		1.20	SF_6	225	40	*HNLCLSi
6	SOFeX-S	Jan–Feb 2002	Southern Ocean-Pacific sector 66.45° S, 171.8° W	RV *Revelle* RV *Melville* RV *Polar star*	①315 (0) ②315 (4) ③315 (7) ④315 (11)		0.70	SF_6	225	28	HNLC
7	EIFEX	Feb–Mar 2004	Southern Ocean-Atlantic sector 50° S, 2° E	RV *Polarstern*	①1406 (0) ②1406 (13)	0.20	1.50 0.34		167	39	HNLC
8	SAGE	Mar–Apr 2004	Southern Ocean-Southeast of New Zealand 46.7° S 172.5° E	RV *Tangaroa*	①265 (0) ②265 (6) ③265 (9) ④265 (12)	0.09	3.03 1.59 0.55 1.01	SF_6	36	15	*HNLCLSi

	Experiment	Time	Location	Research vessel	Added iron (Ⅱ) (kg) (day)	Initial iron (nM)	After iron addition (nM)	Tracer	Patch size (km^2)	Duration (days)	Regional characteristic
9	LOHAFEX	Jan–Mar 2009	Southern Ocean-Atlantic sector 48° S, 15° W	RV *Polarstern*	①2000 (0) ②2000 (21)		2.00	SF_6	300	40	*HNLCLSi
10	SEEDS-1	Jul–Aug 2001	Subarctic North Pacific-Western basin 48.5° N, 165° E	RV *Kaiyo-Maru*	①350 (0)	0.05	2.90	SF_6	80	13	HNLC
11	SERIES	Jul-Aug 2002	Subarctic North Pacific-Eastern basin 50.14° N, 144.75° W	RV *John P. Tully* RV *El Puma* RV *Kaiyo Maru*	①315 (0) ②315 (6)	<0.10	2.00 0.60	SF_6	77	25	HNLC
12	SEEDS-2	Jul–Aug 2004	Subarctic North Pacific-Western basin 48° N, 166° E	RV *Hakuho-Maru* RV *Kilo-Moana*	①332 (0) ②159 (6)	0.17	1.38	SF_6	64	26	HNLC
13	FeeP	Apr–May 2004	Subtropical North Atlantic-North-east Atlantic 27.5° N 22.5° W	RV *Charles Darwin* RV *Poseidon*	①1840 (0)	0.20	3.00	SF_6	25	21	LNLC
Ⅰ	**CROZEX	Nov 2004–Jan 2005	Southern Ocean-South of sub-Antarctic Front 44° S, 50° E	RV *Discovery*		0.04	0.55				HNLC
Ⅱ	**KEOPS	Jan–Feb 2005	Southern Ocean-South of Polar Front 50° S, 73° E	RV *Marion Dufresne*							HNLC

*High Nutrient Low Chlorophyll and Low Silicate (HNLCLSi) region; **nOIF experiments

Sources are Martin et al. (1994) and Coale et al. (1996).

극지연구소

Table 2. Summary of artificial ocean iron fertilization (aOIF) experiments; objectives, significant results, and limitations.

	Experiment	Objective	Significant results	Limitations
1	IronEx-1	* To test the hypothesis that artificial iron addition will increase phytoplankton productivity by relieving the iron limitation of phytoplankton in HNLC regions	* Small increases in the Fv/Fm ratio, chlorophyll-a concentration, and primary production (PP) * Insignificant changes in nutrients and pCO_2 concentrations	* Single iron addition * Insufficient experimental periods to observe the full phases of biogeochemical responses from the onset to termination after iron additions * Micro/macro-nutrient limitations
2	IronEx-2	* To test three hypotheses that were advanced to explain the weak biogeochemical response observed during IronEx-1	* Dramatic changes in biogeochemical responses; close to support for Martin's hypothesis * Taxonomic shift toward diatom-dominated phytoplankton communities	* No export flux measurements conducted in the fertilized patch and deep ocean * Insufficient experimental duration
3	SOIREE	* To test the iron hypothesis in the Southern Ocean (SO)	* Diatom-dominated bloom * No measurable change in carbon export	* Insufficient experimental duration
4	EisenEx	* To test the hypothesis that atmospheric dust inputs might have led to a dramatic increase in ocean productivity during the Last Glacial Maximum (LGM) due to the relief of iron-limited conditions for phytoplankton growth	* Diatom-dominated bloom * No clear differences in carbon flux between in-patch and outside-patch areas	* Light limitation by storms * Insufficient experimental duration
5	SOFeX-N	* To address the potential for iron and silicate interactions to regulate the diatom bloom	* Remarkable increase in diatom biomass * Observation of large export flux event with transmissometers	* Entrainment of dissolved silicate into the fertilized patch by physical mixing * No direct measurement of export fluxes with sediment traps
6	SOFeX-S	* To address the potential for iron and silicate interactions to regulate the diatom bloom	* Significantly enhanced export fluxes out of the mixed layer, but similar to those for natural blooms	* Insufficient experimental duration
7	EIFEX	* To confirm that aOIF experiments can increase export production	* Observation of all the phases of the phytoplankton bloom from onset to termination * Significant carbon export to deeper layers (down to 3,000 m) due to the formation of aggregates with rapid sinking rates * The occurrence of rapidly sinking large aggregates	

To be continued

	Experiment	Objective	Significant results	Limitations
8	SAGE	* To determine the response of phytoplankton dynamics to iron addition in High Nutrient Low Chlorophyll and Low Silicate (HNLCLSi) regions * To test the assumption that the response of phytoplankton blooms to artificial iron addition can be detected by the enhanced air-sea exchanges of climate-relevant gases	* No shift to a diatom-dominated community * No detection of fertilization-induced export	* High dilution rate by small patch size
9	LOHAFEX	* To trace the fate of iron-stimulated phytoplankton blooms and deep carbon export in HNLCSi regions	* Observation of all the phases of the phytoplankton bloom from onset to termination * No shift to a diatom-dominated community * No detection of fertilization-induced export * High grazing pressure and active bacterial respiration	
10	SEEDS-1	* To investigate the relationship between phytoplankton biomass/community and dust deposition in the subarctic North Pacific (NP) * To investigate changes in phytoplankton composition and vertical carbon flux	* A shift from oceanic diatoms to fast-growing neritic ones * The largest changes in biogeochemical parameters of all OIF experiments * No significant increases in export fluxes compared to outside-patch values	* Single iron addition * Insufficient experimental duration
11	SERIES	* To compare the response of phytoplankton in the western subarctic NP ecosystem * To investigate the most significant factor that controls the beginning to the ending of the phytoplankton bloom induced by iron addition	* Observation of all phases of the phytoplankton bloom from onset to termination * No significant increases in export fluxes below the mixed layer depth (MLD) * High bacterial remineralization and mesozooplankton grazing pressure	
12	SEEDS-2	* To investigate the most significant factor that controls the beginning to the ending of a phytoplankton bloom induced by iron addition	* Observation of all phases of the phytoplankton bloom from onset to termination * No shift to a diatom-dominated community * No significant increases in export fluxes * Extensive copepod grazing	
13	FeeP	* To investigate the impact of iron and phosphate co-limitation on PP	*Increases in pico-phytoplankton abundances	

Sources are Martin et al. (1994) and Coale et al. (1996).

Table 3. Initial conditions and changes (Δ values) in chemical parameters during the artificial ocean iron fertilization (aOIF) experiments

	Experiment	Initial NO_3 (μM)	ΔNO_3 (μM)	Initial PO_4 (μM)	ΔPO_4 (μM)	Initial Si (μM)	ΔSi (μM)	Initial pCO_2 (μatm)	ΔpCO_2 (μatm)	Initial DIC (μM)	ΔDIC (μM)
1	IronEx-1	10.8	-0.70	0.92	-0.02	3.90	-0.02	471	-13.0	2044	*-6.00
2	IronEx-2	10.4	-4.00	0.80	-0.25	5.10	-4.00	538	-73.0	2051	*-27.0
3	SOIREE	25.0	-3.00	1.50	-0.24	10.0	-3.00	350	-(38.0–32.0)		-(18.0–15.0)
4	EisenEx	22.0	-1.00	1.60	-0.10	10.0	0	360	-(20–18)		-(15.0–12.0)
5	SOFeX-N	21.9	-1.40	1.40	-0.09	2.50	-1.10	367	-26	2109	-14.0
6	SOFeX-S	26.3	-3.50	1.87	-0.21	62.8	-4.00	365	-36	2176	-21.0
7	EIFEX	25.0	-1.50	1.80	-0.30	19.0	-11.0	360	-30	2135	-13.5
8	SAGE	7.90–10.3	1.50–3.90	0.62–0.85		0.83–0.97		330	8.00	2057	25.0
9	LOHAFEX	20.0	-2.50	1.30	-0.20	0.50–1.40		**357.5	-(15–7)		
10	SEEDS-1	18.5	-15.8			31.8	-26.8	390	-130		-58.0
11	SERIES	10.0–12.0	-(9.00–7.00)	>1.00	-0.50	14.0–16.0	-(14.0–12.0)	350	-85	2030	-37.0
12	SEEDS-2	18.4	-5.72			36.1		370	-6.00		
13	FeeP	<0.01		0.01							<-1.00

*Dissolved inorganic carbon (DIC) in IronEx-1/-2 indicates normalized DIC (normalized DIC = DIC × 35/Salinity). **ΔpCO2 in LOHAFEX was digitized from Fig. 6.1 of Smetacek et al. (2010).

Sources are Martin et al. (1994) and Steinberg et al. (1998).

Table 4. Initial values of biological parameters and the values after fertilization. Note that maximum values were attained after fertilization.

	Experiment	Initial Fv/Fm	After Fv/Fm	Initial Chlorophyll-a (mg m^{-3})	After Chlorophyll-a (mg m^{-3})	Initial PP (mg C m^{-2} d^{-1})	After PP (mg C m^{-2} d^{-1})	Initial Mesozooplankton biomass (mg C m^{-3})	After Mesozooplankton biomass (mg C m^{-3})	Initial Heterotrophic Bacteria abundance (× 10^5 cells ml^{-1})	After Heterotrophic Bacteria abundance (× 10^5 cells ml^{-1})
1	IronEx-1	0.30	0.60	0.24	0.65	*300–450	*805–1330				
2	IronEx-2	0.25	0.57	0.15–0.20	4.00	§~630	§~2430	3.8 (0–55 m)	6.6 (0–55 m)	9.5	
3	SOIREE	0.22	0.65	0.25	2.00	~120	~1300	**22.8 (0–65 m)	**30.1 (0–65 m)	3.7	
4	EisenEx	0.30	0.56	0.50	2.50	130–220	790			4.0	
5	SOFeX-N	0.20	0.5	0.15	2.60	~144	~1500			4.0	
6	SOFeX-S	0.25	0.65	0.30	3.80	~216	~972			4.0	
7	EIFEX	0.28	0.6	0.70	3.16	~750	1500				
8	SAGE	0.27	0.61	0.63	1.33	540	900				
9	LOHAFEX	0.33	0.50	0.50	1.25	<960	1560				
10	SEEDS-1	0.19	0.42	0.80–0.90	21.8	420	1670	**6.8 (0–20 m)	**7.5 (0–20 m)	2.5	
11	SERIES	0.24	0.55	0.35	5.00	300	>2000	**7.3 (0–30 m)		3.5	
12	SEEDS-2	0.29	0.43	0.80	2.48	390	1000	**18.9 (0–20 m)	**38 (0–20 m)		
13	FeeP			0.04	0.07						

*Primary productivity (PP) in IronEx-1 was estimated by multiplying PP (mg C m-3 d-1) with the mixing layer depth (MLD) (initial: 30 m and after: 35 m); §PP in IronEx-2 was digitized from the Figure of de Baar et al. (2005). **Mesozooplankton biomass indicates copepod biomass; Values in brackets correspond to the sampling layer; After mesozooplankton biomass is the mean value averaged for the experimental period after iron addition.

Sources are Kolber et al. (1994) and Martin et al. (1994).

Table 5. Initial values of the export flux and the value after fertilization (mg C m-2 d-1), and the corresponding depth inside and outside the fertilized patch for artificial ocean iron fertilization (aOIF) experiments. Values in brackets correspond to the day of measurement after fertilization.

	Experiment	In-patch Initial (day)	In-patch After (day)	Outside-patch Initial (day)	Outside-patch After (day)	Depth (m)	Method
1	IronEx-1						
2	IronEx-2	84 (0)	600 (7)			25	Water-column ^{234}Th
3	SOIREE		185 (11–13)	146 (0–2)	78 (11–13)	110	Drifting trap
			74 (11–13)	73 (0–2)	38 (11–13)	310	Drifting trap
4	EisenEx						
5	SOFeX-N						
6	SOFeX-S	36 (6)	112 (27)	48 (7)	49 (27)	50	Water-column ^{234}Th
		19 (6)	142 (27)	38 (7)	56 (27)	100	Water-coumn ^{234}Th
7	EIFEX	340 (0)	1692 (32)	396 (0)	516 (32)	100	
8	SAGE						
9	LOHAFEX	~60 (0)	~94 (25)	~78 (4)	~97 (23)	100	Water-column ^{234}Th
10	SEEDS-1	296 (2)	1000 (13)			50	Water-column ^{234}Th
		151 (2)	140 (13)			200	Water-column ^{234}Th
11	SERIES	120 (3)	480 (24)	192 (3)	139 (15)	50	Drifting trap
		48 (3)	192 (24)			100	Drifting trap
12	SEEDS-2	290 (1–4)	580 (19–22)	299 (1–8)	509 (18–31)	40	Drifting trap
		316 (1–4)	336 (19–22)	212 (1–8)	204 (18–31)	100	Drifting trap
13	FeeP						

Sources are Bidigare et al. (1999) and Nodder et al. (2001).

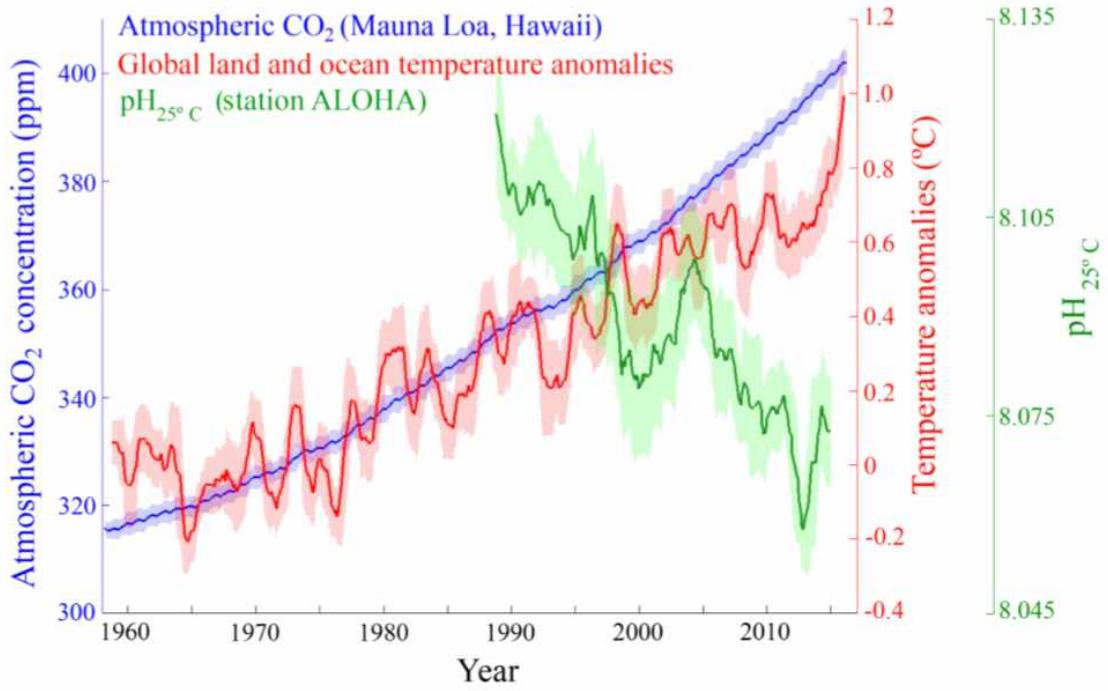

Figure 1. Diagram showing the monthly atmospheric CO_2 concentrations (ppm) (blue) measured at the Mauna Loa Observatory, Hawaii (http://www.esrl.noaa.gov/gmd/ccgg/trends/data.html), global monthly land surface air and sea surface temperature (SST) anomalies (°C) (red) (http://data.giss.nasa.gov/gistemp/), and pH (green) measured at ALOHA station in the central Pacific (http://hahana.soest.hawaii.edu/hot/products/HOT_surface_CO2.txt). The data values represent moving average values for 12 months and shading indicates the standard deviation for 12 months.

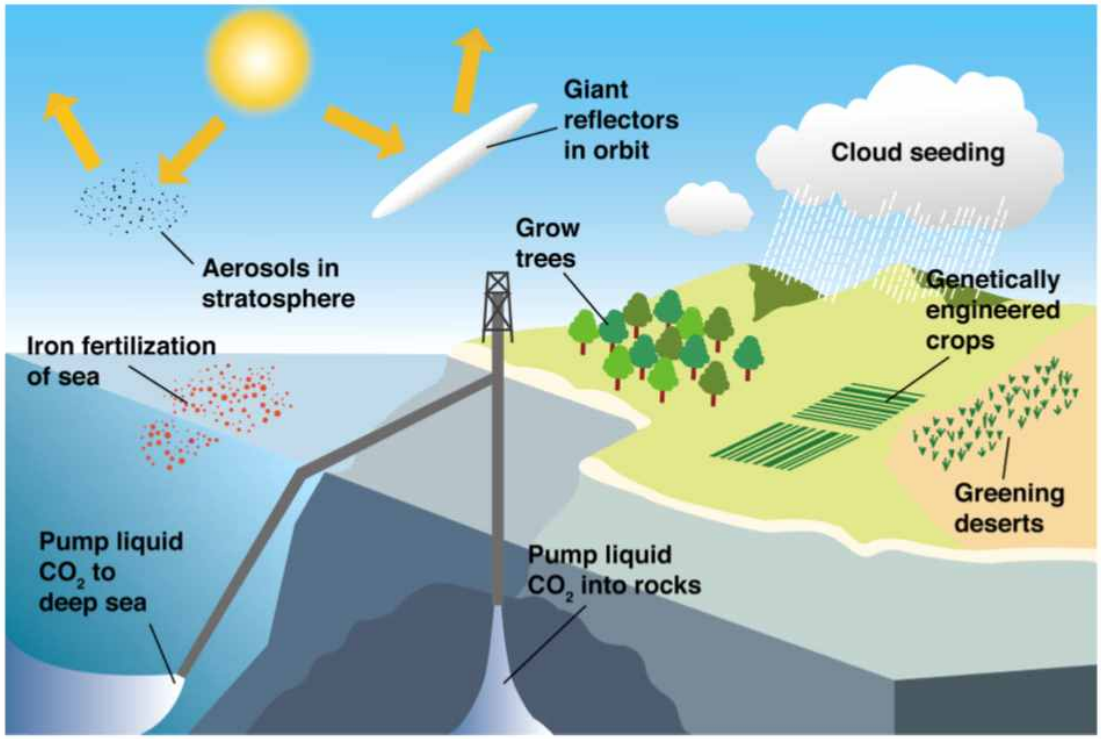

Figure 2. Schematic representation of several proposed climate-engineering methods (modified from Matthews, (1996)).

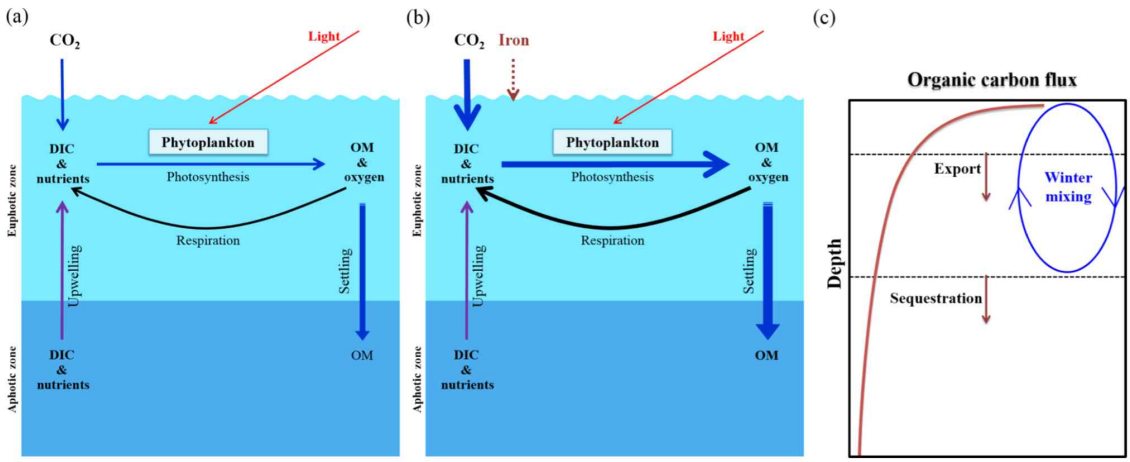

Figure 3. The iron hypothesis, as suggested by Martin (1990). (a) Effectiveness of the biological pump under normal conditions, (b) Effectiveness of the biological pump following iron enrichment (modified from Sarmiento and Gruber, 2006), and (c) Schematic diagram of the decrease in the downward flux of organic carbon as a function of depth in the water column (modified from Lampitt et al. (2008)). OM is organic matter.

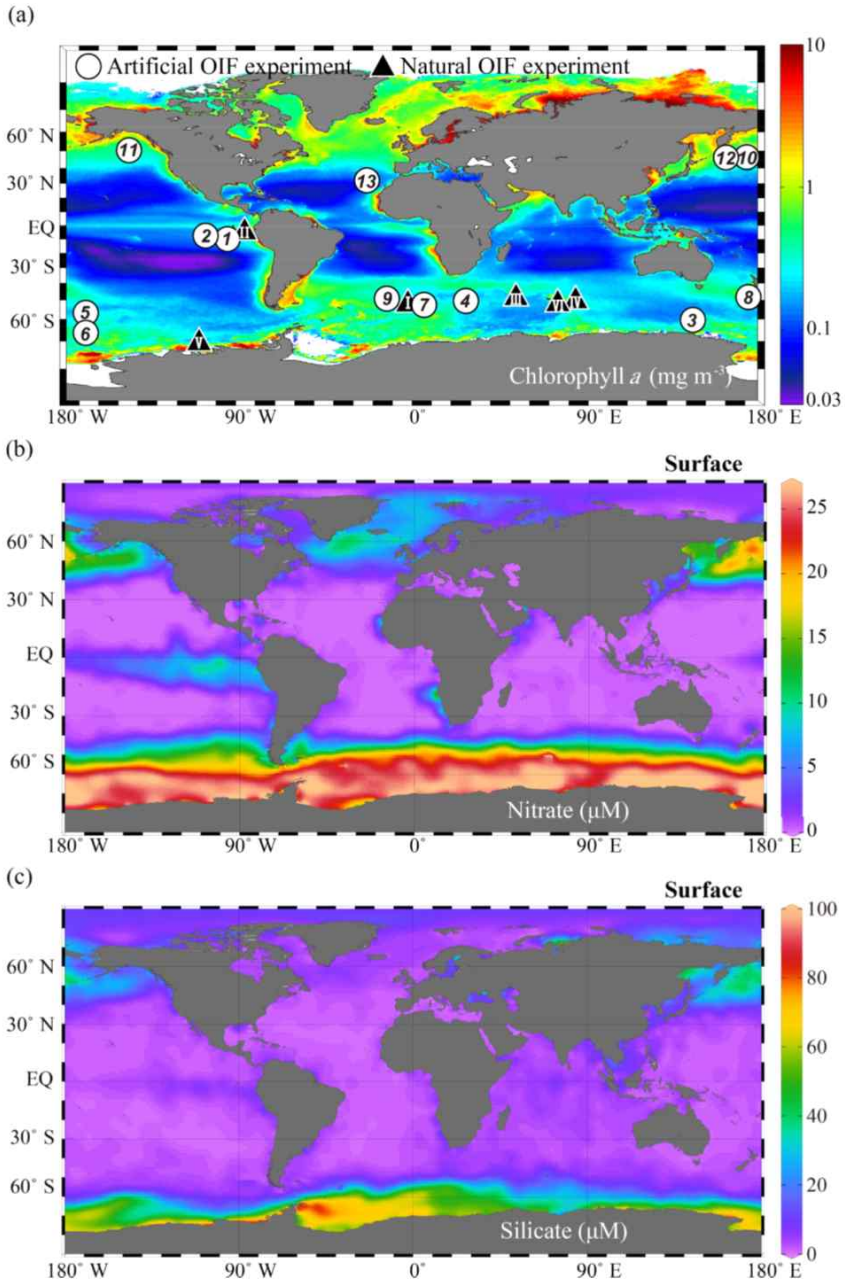

Figure 4. Global annual distribution of surface (a) Chlorophyll concentrations (mg m^{-3}), (b) Nitrate concentrations (μM), and (c) Silicate concentrations (μM). The chlorophyll-a concentration distribution was obtained from the Aqua MODIS chlorophyll-a composite from July 2002 to February 2016 (http://oceancolor.gsfc.nasa.gov/cgi/l3), nitrate and silicate were obtained from the World Ocean Atlas 2013 dataset (https://odv.awi.de/en/data/ocean/world_ocean_atlas_2013) and plotted using Ocean Data View (Schlitzer, 2017). The white circles indicate the locations of 13 artificial ocean iron fertilization (aOIF) experiments and the black triangles indicate the locations of two natural OIF (nOIF) experiments. Note that the numbers indicate the order of the aOIF experiments and the Roman-numerals indicate the order of the nOIF experiments (see Table 1).

Figure 5. Photographs of the iron addition procedure. Panels a–f taken during the European Iron Fertilization Experiment (EIFEX), Surface Ocean Lower Atmosphere Study (SOLAS) Air–Sea Gas Exchange (SAGE), and Indo-German iron fertilization experiment (LOHAFEX): (a) Iron (II) sulfate bags. (b) The funnel used to pour iron and hydrochloric acid. (c) Tank system used for mixing Iron(II) sulfate, hydrochloric acid, and seawater (Smetacek, 2015). (d) Preparation for release: the deck of RV *Tangaroa* with the iron tanks on the left and the SF_6 tracer tanks on the right (Photo: Matt Walkington). (e) Outlet pipe connected to the tank system. (f) Pumping iron into the prop wash during EIFEX (Smetacek, 2015).

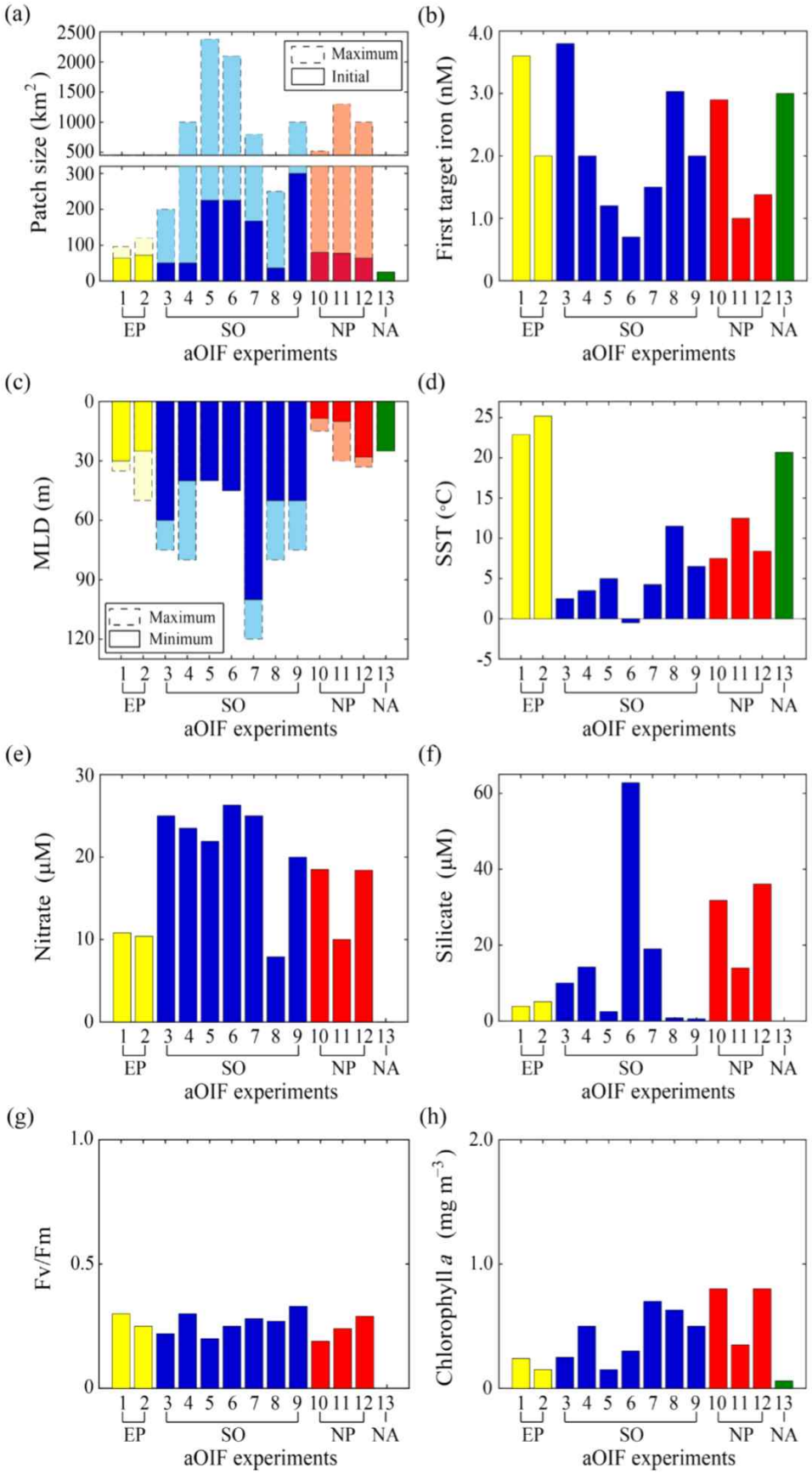

Figure 6. (a) Maximum (bar with dotted line) and initial (bar with solid line) patch size (km^2) during artificial ocean iron fertilization (aOIF) experiments. (b) Total (bar with dotted line) and initial (bar with solid line) iron(Ⅱ) added (kg). (c) Maximum (bar with dotted

line) and minimum (bar with solid line) mixing layer depth (MLD) (m) during aOIF experiments. (d) Average sea surface temperature (SST, °C). (e) Initial nitrate concentrations (μM). (f) Initial silicate concentrations (μM). (g) Initial Fv/Fm ratios. (h) Initial chlorophyll-a concentrations (mg m^{-3}). Note that the numbers indicate the order of aOIF experiments as given in Fig. 4 and Table 1 and are grouped according to ocean basins; East Pacific (EP) (yellow bar), Southern Ocean (SO) (blue bar), subarctic North Pacific (NP) (red bar), and subtropical North Atlantic (NA) (green bar). Sources are Kolber et al. (1994) and Martin et al. (1994).

KOPRI
극지연구소

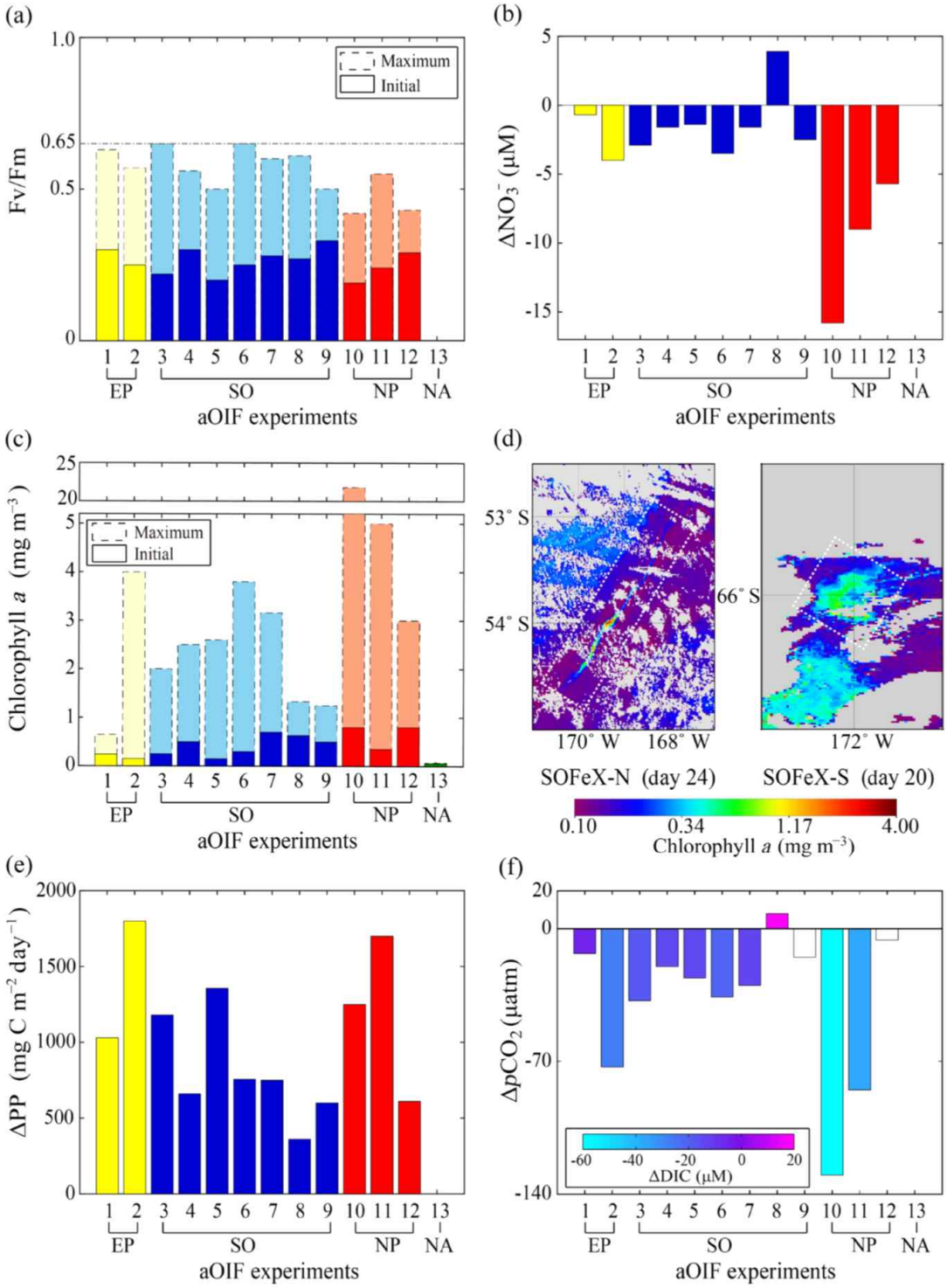

Figure 7. (a) Maximum (bar with dotted line) and initial (bar with solid line) Fv/Fm ratios during artificial ocean iron fertilization (aOIF) experiments, (b) Changes in nitrate concentrations (ΔNO_3^- = $[NO_3^-]_{postf}$ $[NO_3^-]_{pref}$; μM). (c) Maximum (bar with dotted line) and initial (bar with solid line) chlorophyll-a concentrations (mg m^{-3}). (d) Distributions of chlorophyll-a concentrations (mg m^{-3}) on day ~28 after iron addition in the Southern Ocean iron experiment-north (SOFeX-N) and on day ~20 in the SOFeX-south (SOFeX-S) (white dotted box indicates phytoplankton bloom during OIF experiments). (e) Changes in PP (Δ PP = $[PP]_{postf}$ $[PP]_{pref}$; mg C m^{-2} d^{-1}), and (f) Changes in pCO_2 (ΔpCO_2 = $[pCO_2]_{postf}$

$[pCO_2]_{pre-fertilization}$; µatm). The color bar indicates changes in dissolved inorganic carbon (DIC) ($\Delta DIC = [DIC]_{postf} - [DIC]_{pref}$; µM). Note that the primary productivity (PP) (mg C m^{-2} d^{-1}) of aOIF experiment number 1 (IronEx-1) was estimated by multiplying the PP (mg C m^{-3} d^{-1}) with the mixing layer depth (MLD). The numbers on the X axis indicate the order of aOIF experiments as given in Fig. 4 and Table 1 and are grouped according to ocean basins; East Pacific (EP) (yellow bar), Southern Ocean (SO) (blue bar), subarctic North Pacific (NP) (red bar), and subtropical North Atlantic (NA) (green bar). Sources are Kolber et al. (1994) and Martin et al. (1994).

KOPRI
극지연구소

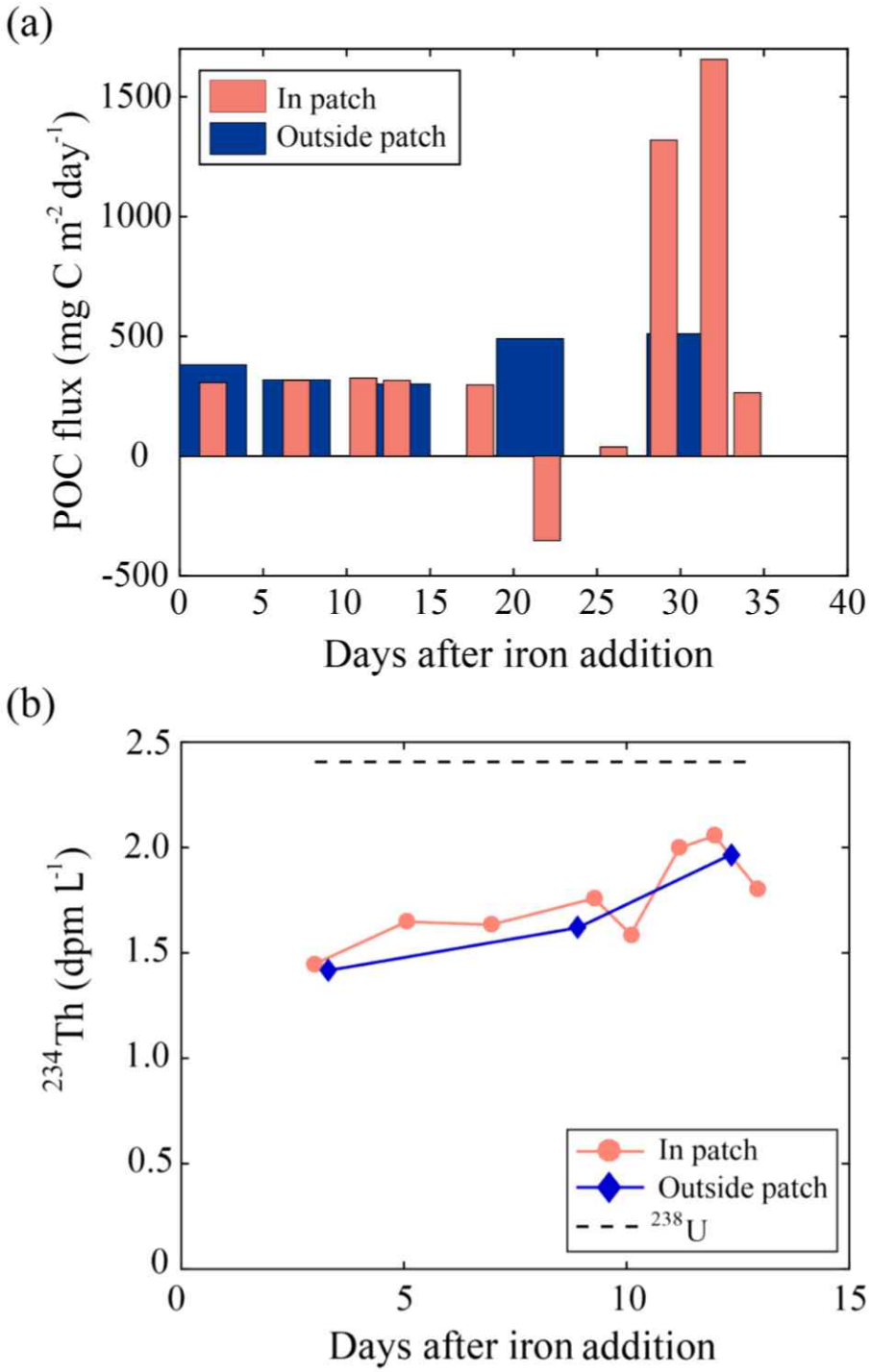

Figure 8. (a) Time-series of particulate organic carbon (POC) fluxes estimated from the water-column based ^{234}Th method (mg m^{-2} d^{-1}) of the upper 100-m layer inside (red bar) and outside the fertilized patch (blue bar) during the European Iron Fertilization Experiment (EIFEX) (modified from Smetacek et al. (2012)) and (b) Time-series of vertically integrated ^{234}Th (dpm l^{-1}) inside (red circles) and outside the fertilized patch (blue diamonds) relative to the parent ^{238}U (dpm l^{-1}; dotted black line) during the Southern Ocean Iron Release Experiment (SOIREE) (modified from Nodder et al. (2001)).

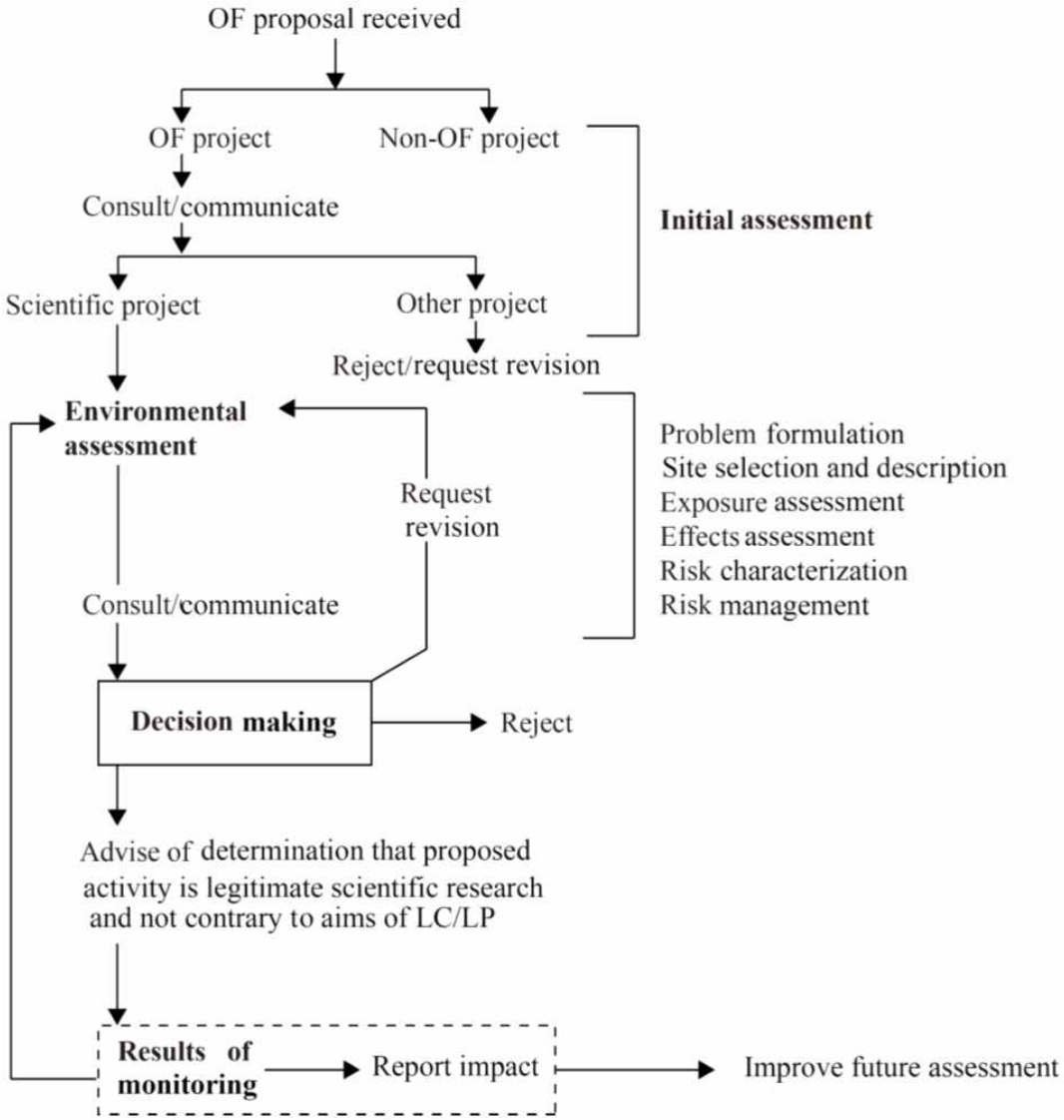

Figure 9. Assessment framework for scientific research involving ocean fertilization (OF) (modified from Resolution LC-LP.2, 2010).

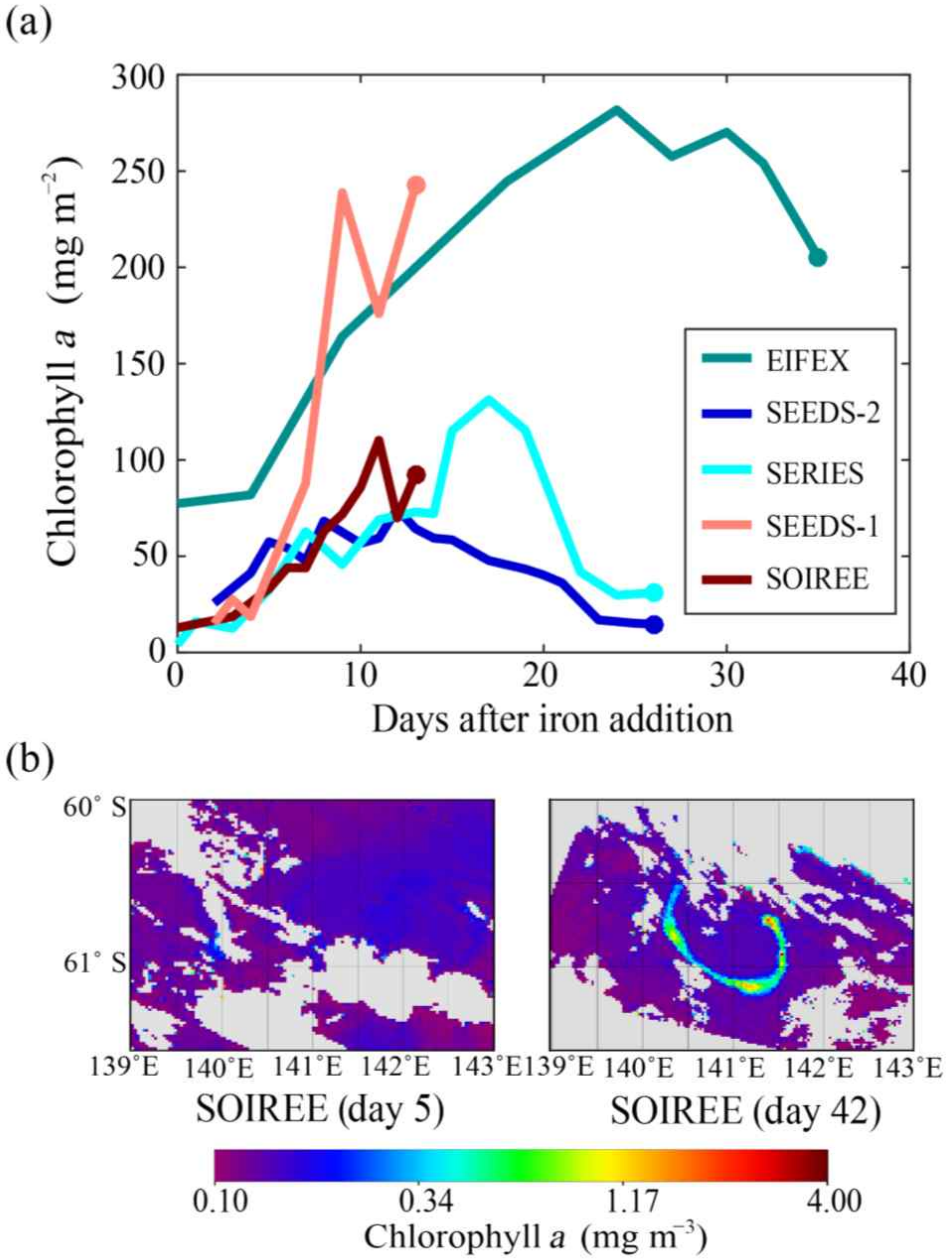

Figure 10. (a) Time-series of mixing layer depth (MLD)-integrated chlorophyll-a concentrations (mg m^{-2}) during the Southern Ocean Iron Release Experiment (SOIREE) (brown line), Subarctic Pacific iron Experiment for Ecosystem Dynamics Study-1 (SEEDS-1) (coral line), Subarctic Ecosystem Response to Iron Enrichment Study (SERIES) (cyan line), SEEDS-2 (blue line), and European Iron Fertilization Experiment (EIFEX) (teal line). (b) The distributions of chlorophyll-a concentrations (mg m^{-3}) on day ~5 and ~46 during SOIREE from SeaWiFS Level-2 daily images. Sources are Boyd and Abraham, (2001); Tsuda et al., (2007); and Assmy et al., (2013).

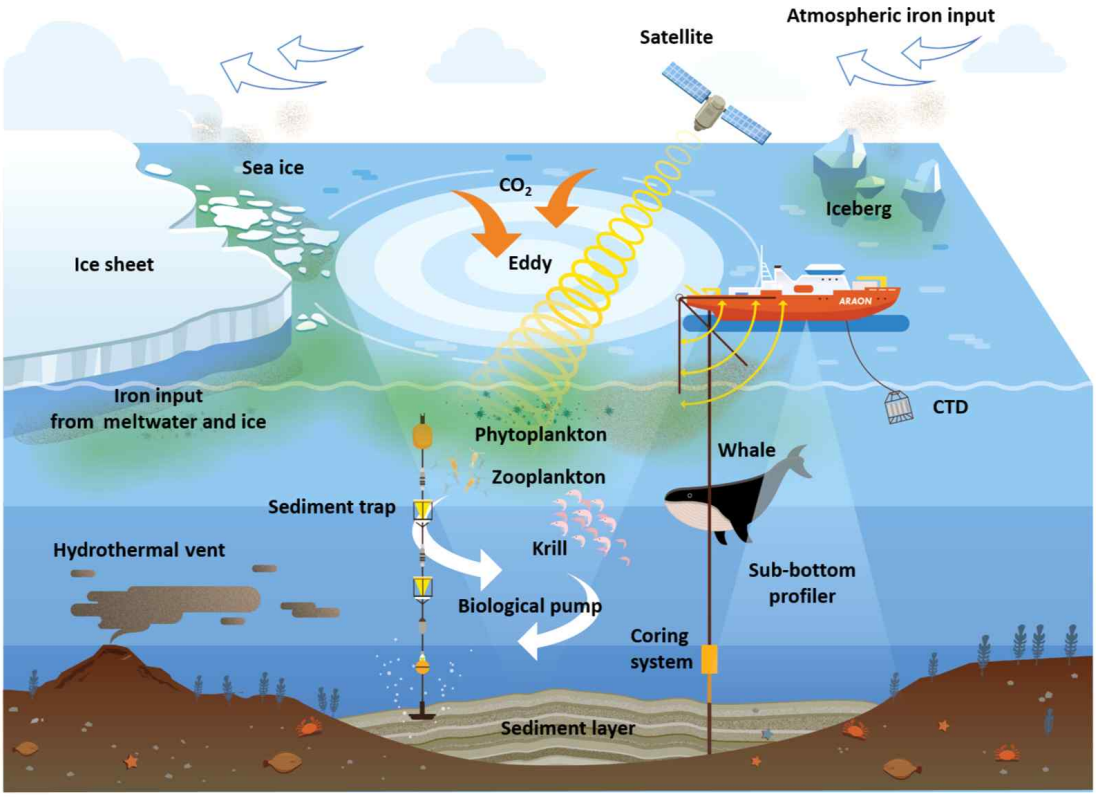

Figure 11. Schematic diagram of the Korean Iron Fertilization Experiment in the Southern Ocean (KIFES) representing the experiment target site (eddy structure) and survey methods (underway sampling systems, multiple sediment traps, sub-bottom profilers, sediment coring systems, and satellite observations).

KOPRI
극지연구소

제 20 절. Enhanced Sensitivity of Fluorescence-based Fe(II) Detection by Freezing[13)]

Yun Hak Lee[1], Peter Verwilst[2], Hyeong Seok Kim[2], Jinjung Ju[3], Jong Seung Kim[2,*], and Kitae Kim[1,*]

[1]Korea Polar Research Institute
[2]Department of Chemistry, Korea University
[3]Department of Environmental Sciences and Biotechnology, Hallym University

Iron, a biologically abundant transition metal in living organisms, is widely distributed in nature, with some common sources including seawater, underground water, soil, and industrial waste.[1,2] In particular, bioavailable iron (mainly Fe(II)) is regarded as a limiting factor for marine primary producers and phytoplankton growth in several oceans, including the Southern ocean.[3] In nature, dissolved iron in water is mainly present in two redox states, namely the ferrous (Fe(II)) and ferric (Fe(III)) forms.[4] Despite the universal distribution of iron around the world, excessive or insufficient quantities of iron can cause significant issues to living organisms and the environment.[5] As such, the quantity of iron in the biosphere should be maintained at an appropriate level, and so the accurate and precise detection of iron is key to understanding the factors that regulate its concentration in nature.

Unlike in the case of industrial waste, the concentration of iron present in the natural water system generally ranges from 61 to 2680 ppm.[6] In addition, although the accurate separation and measurement of divalent and trivalent iron ions is challenging, the selective detection of the more water soluble Fe(II) is necessary due to its importance in redox processes.[7]

Thus, to accurately and sensitively measure Fe(II), the quantitative and qualitative analysis of analytes can be achieved using atomic absorption spectroscopy (AAS), inductively coupled plasma mass spectrometry (ICP-MS), potentiometric stripping analysis (PSA), X-ray fluorescence (XRF), and radioisotopes.[8] Since the above methods are expensive and sophisticated, a simple colorimetric method has been used as an alternative, however this is cumbersome and less selective. To overcome such issues, a rapid and accurate fluorescence method has been proposed for the detection of Fe(II), which allows

13) 이 연구는 본 과제 지원으로 수행되었으며 그 결과는 다음의 논문으로 출판되었음: Yun Hak Lee, Peter Verwilst, Hyeong Seok Kim, Jinjung Ju, Jong Seung Kim, and Kitae Kim, “Enhanced Sensitivity of Fluorescence-based Fe(II) Detection by Freezing”, *Chem. Commun.* 2019, 55, 12136-12139.

the selective detection of certain substances present in the analytes.[9,10]

In addition, in 2013, Nagasawa and co-workers reported the first turn-on fluorescent probe for the selective detection of Fe(II) using N-oxide chemistry in an aqueous solution.[11] The installation of an N-oxide on the fluorophore induces fluorescence attenuation by twisted intramolecular transfer (TICT) and photo-induced electron transfer (PET). The oxidized dialkylarylamine moiety is selectively reduced by only Fe(II)-mediated deoxygenation, thereby resulting in a dramatic increase in fluorescence due to the recovery of π-conjugation in the fluorophore. Indeed, an N-oxide chemistry-based approach for the selective detection of Fe(II) has been widely employed in various biological applications.[12 - 16] However, this method also has limitations since it has low sensitivity and low response rate to the Fe(II) present in aqueous solutions.

To resolve this issue, a new fluorescence-based approach employing the freeze concentration effect was proposed. More specifically, Kim et al. reported that the freezing method increased the interactivity through concentration of the various components in the quasi-liquid layer around the ice crystals, thereby significantly increasing the rate of reaction compared to that in the liquid phase.[17] This system has therefore drawn great interest in recent chemical and environmental studies. For example, a unique reaction between organic and inorganic matter takes place in specific ice region accompanied by low pH conditions.[18 - 21] More recently, this strategy has been applied by Choi et al. for investigating the degradation mechanism of organic pollutants.[22]

Thus, we herein propose a novel idea based on the combination of the freeze concentration effect and N-oxide chemistry to sensitively and selectively detect Fe(II) (Scheme 1). More specifically, we report the design and synthesis of an Fe(II)-specific fluorescent probe (1-Ox) by the combination of a naphthalimide fluorophore and oxidized morpholine as an Fe(II)-selective reaction site (Scheme S1, ESI†). The proposed sensing mechanism of 1-Ox with Fe(II) is based on the modulation of the intramolecular charge transfer (ICT) character of 1, compared to the PET-quenched oxidized morpholine probe 1-Ox, as supported by DFT calculations (Fig. S1 and S2, ESI†). The target compound, 1-Ox, is synthesized according to a previously reported 3-step procedure with minor modifications, as shown in the ESI† (Scheme S1).[23] The identities of the newly synthesized compounds are confirmed by ^{1}H NMR, ^{13}C NMR, and ESI-MS (ESI†).

To evaluate the response to Fe(II) and the effect of freezing, the spectroscopic characterization of probe **1-Ox** and its mother compound **1** was carried out. As shown in Fig. 1A, absorption bands with maxima of 340 and 395 nm were found for **1-Ox** (ε = 1.3 × 10^4 M^{-1} cm^{-1}) and **1** (ε = 0.9 × 10^4 M^{-1} cm^{-1}), respectively. This indicates that a blue shift took place due to a less pronounced ICT character during the excitation, caused by the presence of the *N*-oxide moiety. Moreover, the quantum yield (Φ_F) of **1** and **1-Ox**

with an excitation at 360 nm were measured at 0.31 and 0.02 (quinine sulphate as a standard), respectively (Table S1).

In addition, **1-Ox** exhibited a weak emission band as a result of the PET quenching effect, while **1** gave a relatively strong fluorescence at 540 nm with an excitation at 395 nm (Fig. 1B). When **1-Ox** was treated with 1 equivalent of Fe(II) for 60 min, the fluorescence spectra showed negligible changes due to the low reactivity, in addition to the short reaction time (Fig. 1B). Based on previous results for the combination of an Fe(II)-selective fluorescent probe with *N*-oxide chemistry, a reaction time of at least 60 min is required in addition to >10 equivalents of Fe(II).[12]

To overcome this limitation, we introduced freezing and thawing methods for more efficient fluorescence detection. Preliminary experiments were carried out to determine the optimal conditions. As the reaction time of **1-Ox** with Fe(II) was increased from 0 to 60 min, the change in fluorescence intensity at 25 °C was negligible (Fig. S3, ESI†). Upon extending the freezing time from 30 to 60 min, the fluorescence intensity of the mixture of **1-Ox** with Fe(II) increased significantly (Fig. S4, ESI†). The fluorescence intensity was then measured after thawing at 25 °C for 30 min (Fig. S5, ESI†). Furthermore, the fluorescence intensity of free **1-Ox** was found to be stable under freezing conditions up to 60 min (Fig. S6, ESI†) as well as under solution conditions at 25°C (Fig. S7, ESI†).

Examination of the above results allowed us to determine that freezing and thawing times of 30 min each were suitable. Using this novel analytical method, a mixture of **1-Ox** with 5 μM Fe(II) exhibited a remarkable 130-fold fluorescence enhancement upon freezing (30 min) compared to the previously reported results presented in Fig. 1C. Although the fluorescence intensity of free **1-Ox** also increased with scattering, a significantly greater enhancement in fluorescence (4×) was observed upon the addition of Fe(II). These results indicate that the fluorescence intensity increased due to the freeze concentration effect. In addition, Fig. 1D shows the fluorescence spectra of the thawing **1-Ox** in the absence and presence of Fe(II). Almost no fluorescence was observed for the free **1-Ox**, whereas the fluorescence intensity of **1-Ox** was increased up to 8-fold in the presence of Fe(II). This observation suggests that the deoxygenation reaction between **1-Ox** and 1 equivalent of Fe(II) was enhanced upon freezing.

The fluorescence response of **1-Ox** (5 μM) to Fe(II) over other metal ions was investigated under freezing and thawing conditions, where the fluorescence intensity at 540 nm is plotted in Fig. 2. The obtained results indicate that **1-Ox** can detect Fe(II) selectively over other metal ions. Likewise, none of the other tested biologically relevant reductants caused a notable change in fluorescence intensity (Fig. S8, ESI†).[11-14] Moreover, in the presence of ethylenediaminetetraacetic acid (EDTA) as an Fe(II) capping agent, a low fluorescence was observed, indicating that Fe(II) switched on the fluorescence.

In addition, the fluorescence titration spectra of **1-Ox** with increasing concentrations of Fe(II) are shown in Fig. S9 (ESI†). Upon treatment with Fe(II), the fluorescence intensity of **1-Ox** at 540 nm gradually increased, reaching saturation around at 5 μM under freezing and thawing conditions. The fluorescence response therefore demonstrates a linear relationship between the signal intensity and the Fe(II) concentration, allowing the detection limit to be determined as 0.27 μM under freezing and thawing conditions (Fig. S10, ESI†). However, a detection limit of 1.02 μM was obtained at 25 °C (Fig. S11, ESI†), thereby indicating that the freezing method is favorable for the detection of low concentrations of Fe(II).

As evident from HPLC analysis, the generation of **1** from the deoxygenation of **1-Ox** was induced by Fe(II) using the freezing method (Fig. 3). The retention time of **1** was observed to be 4.30 min upon excitation at 360 nm, whereas the peak of **1-Ox** was detected at 5.50 min. Upon the addition of Fe(II) to **1-Ox** under freezing and thawing conditions, the initial peak at 5.50 min almost disappeared, while a new peak was observed at 4.30 min, i.e., at the same retention time as **1**. These results therefore confirm that Fe(II)-mediated deoxygenation took place to give **1** from **1-Ox**.

To visualize accumulation of the probe in liquid-like layer (LLL), freezing was carried out using a cryostage (Linkam FDCS196) and localization was confirmed by confocal laser microscopy. As can be seen in Fig. S12 (ESI†), it shows the optical and fluorescence images of **1**, where accumulation was observed in ice. In addition, the fluorescence emission from **1-Ox** was found to be lower than that of **1** in the ice phase (Fig. 4A), while the fluorescence intensity of **1-Ox** in the presence of 1 equivalent of Fe(II) was significantly increased (Fig. 4B). In particular, the merged images show an overlap of the fluorescence with differential interference contrast (DIC) from **1-Ox** with that of Fe(II), indicating that the probe settled in LLL. Indeed, magnification images confirm this in detail. Additional studies of these Z-stack images were then carried out for the probes, where the 3-dimensional images of **1-Ox** in the presence of Fe(II) (depth range = 0 - 80 μm) revealed evidence of localization in LLL (Fig. S13, ESI†). It was therefore apparent that these microscopic images gave similar results to the spectroscopic data obtained in ice, thereby implying that the deoxygenation reaction occurred in LLL.

Based on the promising imaging results obtained in ice, we also investigated the applicability of the **1-Ox** probe for the detection of Fe(II) generated by the freezing-enhanced chemical reaction in a cold environment. Indeed, Choi's group previously reported an enhancement in the reduction to Fe(II) from iron oxide in the presence of iodide ions in a frozen solution and its implication for iron bioavailability in cold environments.[24] Thus, the production of Fe(II) was carried out according to the previously reported procedures with minor modifications.[25] Prior to the application of

1-Ox in an environmental system, free **1-Ox** and iron oxide were measured by confocal microscopy. A weak fluorescence in **1-Ox** was observed, whereas iron oxide was clearly concentrated in LLL (Fig. 5). Moreover, the effect of iodide on the fluorescence change of **1-Ox** was negligible (Fig. S14, ESI†). When the iron oxide was pretreated with iodide for 24 h at −20 °C and subsequently thawed at 25 °C then incubated with **1-Ox** for 30 min at −20 °C, the fluorescence of **1-Ox** was significantly enhanced by production of Fe(II) from dissolution of iron oxide with iodide. These results indicate that **1-Ox** is a valuable tool not only for monitoring labile iron ions but also for understanding the accelerated chemical reaction in ice.

In conclusion, we designed and synthesized a novel Fe(II)-selective fluorescent probe, **1-Ox**, which is composed of naphthalimide and an oxidized morpholine moiety. Even in the presence of only 1 equivalent of Fe(II), the probe exhibited a highly sensitive fluorescence enhancement toward Fe(II) upon freezing as opposed to under 25 °C conditions. These results imply that an increased deoxygenation reactivity by Fe(II) in ice was closely related to the freeze concentration effect. Due to its favorable photophysical properties, **1-Ox** therefore appears to be a promising candidate for the sensitive detection of labile Fe(II) in environmental samples, owing to a large Stokes shift, a low detection limit, and a high selectivity. As demonstrated by confocal laser microscopy, the addition of Fe(II) resulted in probe localization in LLL in addition to an enhancement in fluorescence. As such, the combination of **1-Ox** with the appropriate freezing method demonstrates potential for application in the tracking of environmental Fe(II) in nature, and in particular in polar and cold environments. Furthermore, the reported combined strategy is described here for the first time, and we note that this method could be used to provide a better understanding of the environmental implications of Fe(II), while **1-Ox** could be considered a potential analytical tool for identification of the microstructure of ice.

References

(1) R. R. Crichton, S. Wilmet, R. Legssyer and R. J. Ward, *J. Inorg. Biochem.*, 2002, 91, 9-18.

(2) I. A. Mendelssohn, B. A. Kleiss and J. S. Wakeley, Wetlands, 1995, 15, 37-46.

(3) S. Wang and J. K. Moore, *J. Geophys. Res.*, 2011, **116**, C1019.

(4) D. W. Domaille, E. L. Que and C. J. Chang, *Nat. Chem. Biol.*, 2008, **4**, 168.

(5) K. Pantopoulos, S. K. Porwal, A. Tartakoff and L. Devireddy, *Biochemistry*, 2012, **51**, 5705-5724.

(6) E. S. Gurzau, C. Neagu and A. E. Gurzau, *Ecotoxicol. Environ. Saf.*, 2003, **56**, 190-200.

(7) W. Breuer, M. Shvartsman and Z. I. Cabantchik, *Int. J. Biochem. Cell Biol.*, 2008, **40**,

350-354.

(8) S. M. Pyle, J. M. Nocerino, S. N. Deming, J. A. Palasota, J. M. Palasota, E. L. Miller, D. C. Hillman, C. A. Kuharic, W. H. Cole and P. M. Fitzpatrick, *Environ. Sci. Technol.*, 1995, **30**, 204-213.

(9) A. T. Aron, A. G. Reeves and C. J. Chang, *Curr. Opin. Chem. Biol.*, 2018, **43**, 113-118.

(10) W. Xuan, R. Pan, Y. Wei, Y. Cao, H. Li, F.-S. Liang, K.-J. Liu and W. Wang, *Bioconjug. Chem.*, 2015, **27**, 302-308.

(11) T. Hirayama, K. Okuda and H. Nagasawa, *Chem. Sci.*, 2013, **4**, 1250-1256.

(12) T. Hirayama, H. Tsuboi, M. Niwa, A. Miki, S. Kadota, Y. Ikeshita, K. Okuda and H. Nagasawa, *Chem. Sci.*, 2017, **8**, 4858-4866.

(13) T. Hirayama, M. Inden, H. Tsuboi, M. Niwa, Y. Uchida, Y. Naka, I. Hozumi and H. Nagasawa, *Chem. Sci.*, 2019, **10**, 1514-1521.

(14) M. Niwa, T. Hirayama, I. Oomoto, D. O. Wang and H. Nagasawa, *ACS Chem. Biol.*, 2018, **13**, 1853-1861.

(15) G. Liu, W. Chen, Z. Xu, F. Ye, Y. Pan, X. Chen, S.H. Liu, L. Zeng and J. Yin, *Org. Biomol. Chem.*, 2018, **16**, 5517-5523.

(16) G. Liu, X. Han, J. Zhang, Z. Xu, S.H. Liu, L. Zeng and J. Yin, *Dyes Pigm.*, 2018, **148**, 292-297.

(17) K. Kim, W. Choi, M. R. Hoffmann, H.-I. Yoon and B.-K. Park, *Environ. Sci. Technol.*, 2010, **44**, 4142-4148.

(18) K. Kim, H. Y. Chung, J. Ju and J. Kim, *Sci. Total Environ.*, 2017, **590**, 107-113.

(19) J. Ju, J. Kim, Ľ. Vetráková, J. Seo, D. Heger, C. Lee, H.-I. Yoon, K. Kim and J. Kim, *J. Hazard. Mater.*, 2017, **329**, 330-338.

(20) D. Jeong, K. Kim and W. Choi, *Atmospheric Chem. Phys.*, 2012, **12**, 11125-11133.

(21) K. Kim and W. Choi, *Environ. Sci. Technol.*, 2011, **45**, 2202-2208.

(22) Y. Choi, H.-I. Yoon, C. Lee, L. Vetráková, D. Heger, K. Kim and J. Kim, *Environ. Sci. Technol.*, 2018, **52**, 5378-5385.

(23) P.-Y. Gu, C.-J. Lu, Z.-J. Hu, N.-J. Li, T.-T. Zhao, Q.-F. Xu, Q.-H. Xu, J.-D. Zhang and J.-M. Lu, *J. Mater. Chem. C*, 2013, **1**, 2599-2606.

(24) S. P. M. Menacherry, K. Kim, W. Lee, C. H. Choi and W. Choi, *Environ. Sci. Technol.*, 2018, **52**, 13766-13773.

(25) K. Kim, S. P. M. Menacherry, J. Kim, H. Y. Chung, D. Jeong, A. Saiz-Lopez and W. Choi, *Environ. Sci. Technol.*, 2019, **53**, 7355-7362.

KOPRI 극지연구소

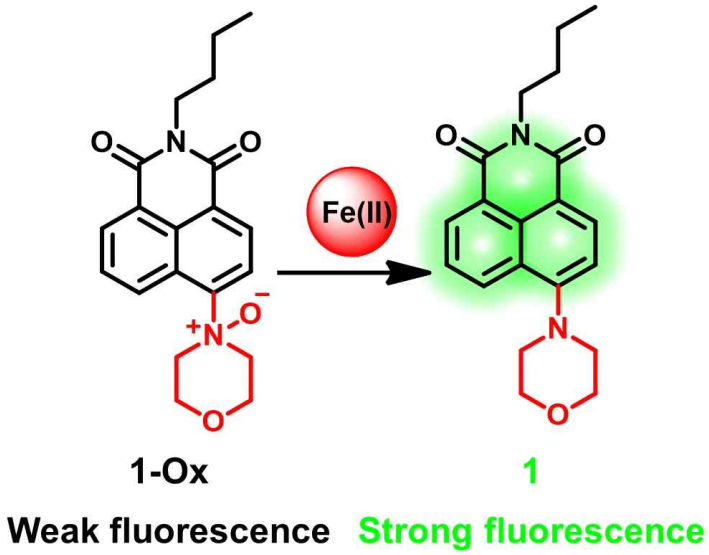

Scheme 1. Proposed reaction between probe 1-Ox and Fe(II).

KOPRI
극지연구소

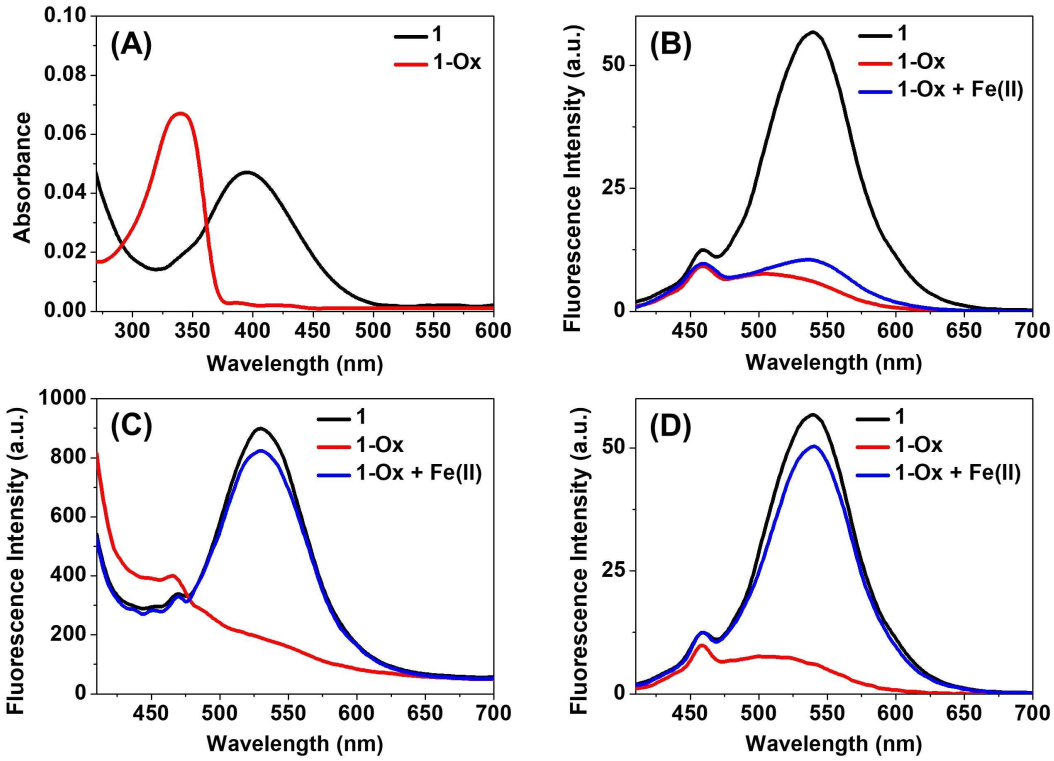

Figure 1. (A) UV-vis absorption spectra of **1** (5 μM) and **1-Ox** (5 μM) in aqueous solution. Fluorescence spectra of **1** and **1-Ox** in the absence and presence of Fe(II) (5 μM) (B) at 25 °C for 60 min, and (C) under freezing (−20 °C) for 30 min, and (D) after thawing (25 °C) for 30 min in aqueous solution containing 0.5% (v/v) acetonitrile. Excitation was at 395 nm.

KOPRI 극지연구소

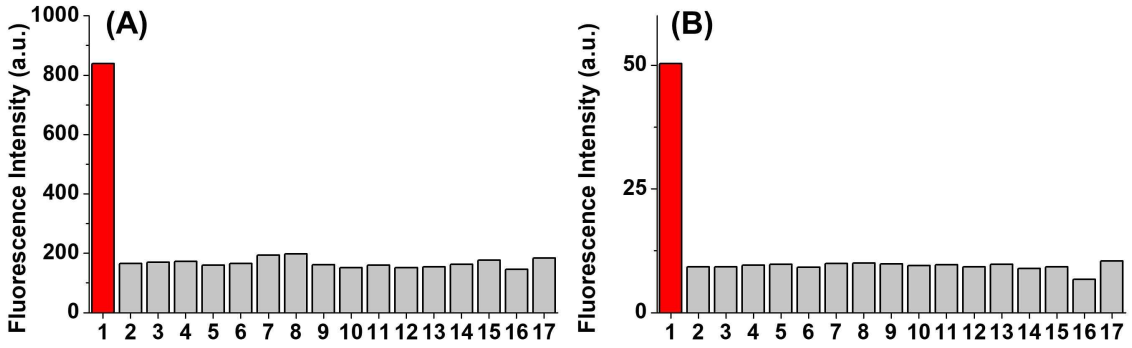

Figure 2. Metal ion selectivity of **1-Ox** (5 μM) toward 5 μM of Fe(II) (1), 50 μM of various chloride salts (2 Fe(III); 3 Ba(II); 4 Co(II); 5 Cr(III); 6 Hg(II); 7 Cu(II); 8 Cu(I); 9 Ni(II); 10 Pb(II); 11 Zn(II); 12 Na(I); 13 K(I); 14 Mg(II); 15 Ca(II)), only 1-Ox (16) and Fe(II) (5 μM) with 50 μM of EDTA (17), under (A) freezing conditions (−20 °C) for 30 min, and (B) after thawing (25 °C) for 30 min in aqueous solution containing 0.5% (v/v) acetonitrile. The results show the fluorescence intensities of **1-Ox** at 540 nm upon excitation at 395 nm.

KOPRI

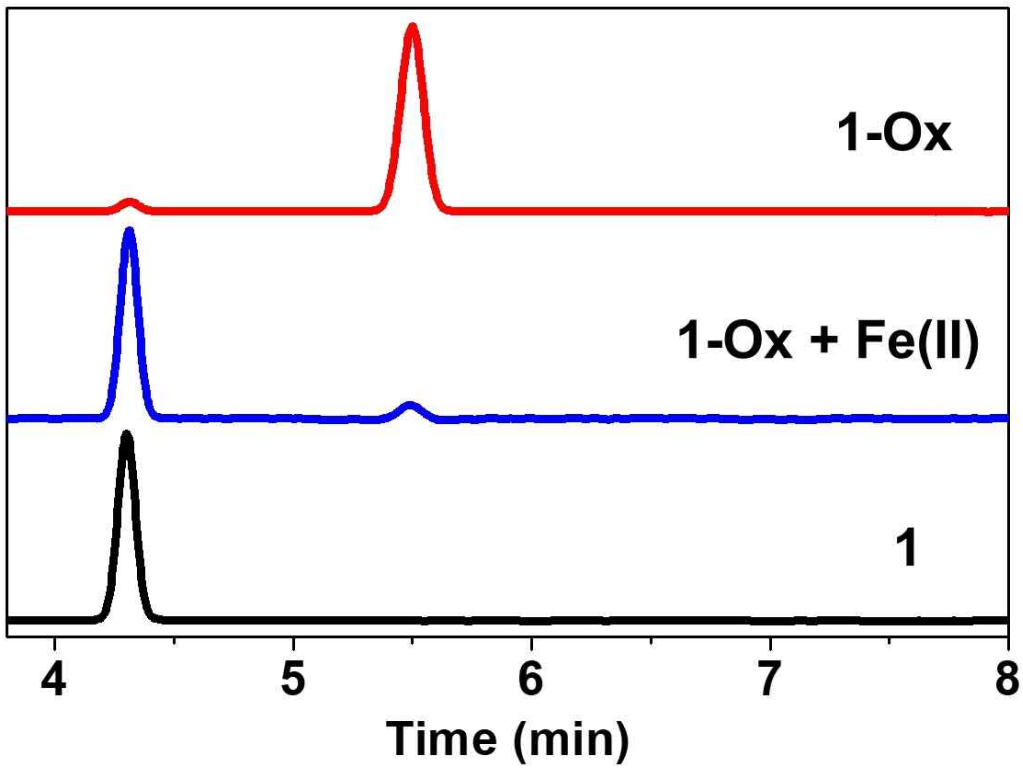

Figure 3. HPLC analysis of **1** and **1-Ox** in the absence and presence of Fe(II) at a single wavelength (360 nm). The eluent was a binary mixture of a 0.1% phosphoric acid solution and acetonitrile (30:70 by volume) at a flow rate of 1.0 mL/min.

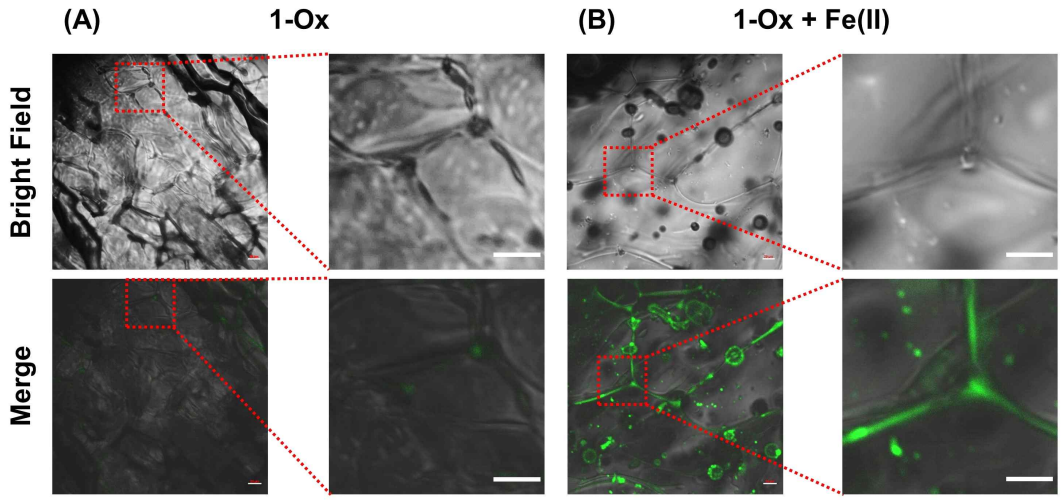

Figure 4. Confocal microscopy images of **1-Ox** (5 μM) in the (A) absence and (B) presence of Fe(II) (5 μM) on the cryostage at −20 °C for 30 min. Merged images were obtained using the DIC and fluorescence images. The excitation and emission wavelengths were 405 and 450 - 600 nm, respectively. Scale bar = 20 μm.

KOPRI

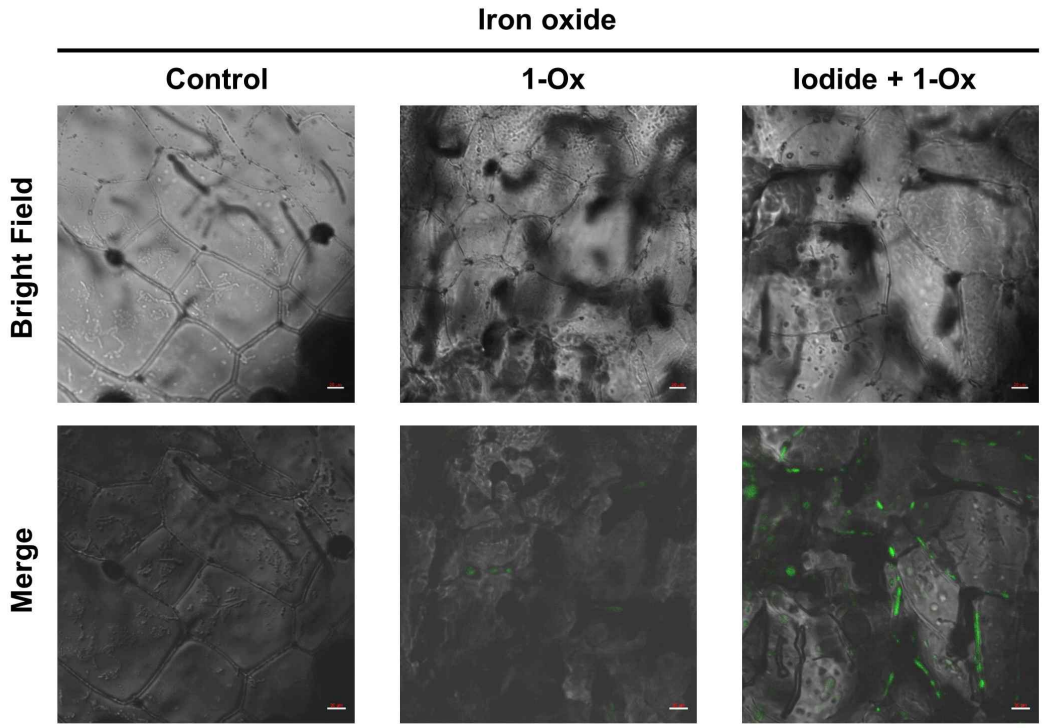

Figure 5. Confocal microscopy images of iron oxide treated with 1-Ox (5 μM) in the absence and presence of iodide on the cryostage at −20 °C for 30 min. Merged images were obtained from the DIC and fluorescence images. The excitation and emission wavelengths were 405 and 450 - 600 nm, respectively. Scale bar = 20 μm.

Supporting Information

General information and materials. All chemicals have been purchased from the commercially available sources (Aldrich, TCI, Samchung, Alfa aesar) and were used as received without further purification. All reactions were carried out under nitrogen atmosphere with flame-dried glassware. Column chromatography purifications were performed using silica gel 60 (Merck Millipore, 0.040 - 0.063 mm) as a stationary phase. 60 silica gel plates (Merck Millipore 60 F254) were used for analytical thin layer chromatography. Water used in all experiments was doubly purified by Milli-Q Systems equipment. All the UV/Vis absorption and fluorescence spectra were recorded with Shimadzu UV-2600 and RF-5301PC spectrophotometer, respectively. Reverse-phase HPLC experiments were conducted using an Agilent 1110 equipped with a UV - vis detector and a ZORBAX 300SB C-18 column (4.6 mm × 150 mm) operated at a flow rates of 1 mL/min using a mobile phase consisting of a binary mixture of a 0.1% phosphoric acid solution and acetonitrile (30:70 by volume). The ^{1}H and ^{13}C NMR spectra were collected on the Bruker 500 MHz spectrometers using $CDCl_3$ with TMS used as an internal reference. Mass spectral analyses were recorded using Bruker Compact QTOF.

DFT calculation methods and results. To gain insight into the photophysical properties of **1** and **1-Ox**, the ground state and excited state structures of **1** and **1-Ox** were calculated using the B3LYP, CAM-B3LYP and ωB97XD functionals at the N07D level of theory. The excitation and emission wavelengths were calculated using the state-specific solvation of their respective architectures. With the exception of B3LYP, all calculated excitation wavelengths, including energy transitions using CAM-B3LYP and ωB97XD on the B3LYP-optimized molecular geometry, provided reasonable approximations of the experimental data. For the emission energies of **1**, it became apparent that B3LYP-optimized calculations provided a poor description of the excited state structure and/or energies, with oscillator strengths approximating or equal to 0. CAM-B3LYP and ω B97XD on the other hand provided a better description of the emission behavior, and among these two functionals ωB97XD resulted in the best match with the experimental data (Fig. S1). For **1**, a significant amount of intramolecular charge transfer occurred during the excitation process, thus resulting in a large Stokes shift. For **1-Ox**, two occupied *N*-oxide oxygen-centered orbitals were identified in between two naphthalimide-centered orbitals, one occupied and one virtual. This observation, together with low HOMO-1→LUMO and HOMO→LUMO dominant vertical transition efficiencies, but a higher HOMO-2→LUMO dominant vertical transition efficiency, is consistent with photo-induced electron transfer (PET) quenching, thus rationalizing the low emission

efficiency of this probe.

The functional and polarizable continuum model screening of the S0→S1 and S0←S1 vertical transition energies, were performed using the Gaussian 16 software package.[S1] The functionals included in the performance test were the B3LYP[S2], CAM-B3LYP[S3], and ωB97XD[S4] functionals on their respective fully unrestrained optimized ground state geometries, and additionally the B3LYP-optimized geometry for the range separated functionals, using the 6-31G-derived N07D basis set.[S5] The excited state calculations for 1 were performed similarly. Polarizable continuum models of acetonitrile were employed, using the default linear response method of the IEFPCM solvation model for structure optimizations and the state-specific approach, as described by Improta et al[S6]. for vertical transition energies. Input file generations were performed using Gabedit 2.5.0.[S7] and structure and orbital visualizations were performed using Gaussview 6.0.[S8]

Spectroscopic data. Stock solutions of compound 1 (1.0 mM) and 1-Ox (1.0 mM) were prepared in acetonitrile. Stock solutions (0.5 mM) of ethylenediaminetetraacetic acid (EDTA) and various metal chlorides including Fe(II), Fe(III), Ba(II), Co(II), Cr(III), Hg(II), Cu(II), Ni(II), Pb(II), Zn(II), Na(I), K(I), Mg(II), and Ca(II) were prepared in deionized water. The stock solution of Cu(I) was prepared from $[Cu(MeCN)_4]PF_6$ in acetonitrile. Samples for absorption and fluorescence measurements were contained in quartz cuvettes. For all measurements of fluorescence spectra, excitation was at 395 nm with all the excitation and emission slit widths at 5.0 nm. All spectroscopic measurements were performed in aqueous solution containing 0.5% acetonitrile.

Determination of fluorescence quantum yields. The quantum yield of the **1** and **1-Ox** in acetonitrile were determined using quinine sulfate in 0.5 M sulfuric acid as a standard. The absorbance values of the solutions at the excitation wavelength were collected with Shimadzu UV-2600. Fluorescence emission spectra of all the sample solutions were measured by RF-5301PC spectrophotometer at an excitation wavelength of 360 nm. The quantum yield was calculated according to the equation as below:

$$\Phi_f^i = \frac{F^i f_s n_i^2}{F^s f_i n_s^2} \Phi_f^s$$

where and represents quantum yield of the sample and that of the standard, respectively; the subscript is used because in most cases one is dealing with fluorescence. F^i and F^s are the integrated intensities (areas) of sample and standard spectra, respectively (in units of photons); is the absorption factor (also known under the obsolete term “absorptance”), the fraction of the light impinging on the sample that is absorbed ($f_x = 1 - 10_x^{-A}$, where A = absorbance); the refractive indices of the sample and reference solution are and ,

respectively.

Freezing method. The disposable fluorescence plastic cells were placed in plastic rack in a cryogenic ethanol bath for the freeze-thaw experiment. Reaction temperature is usually adjusted to -20 ℃ (freeze condition) and 25 ℃ (thaw condition), respectively. The beginning of reaction is determined when the cells were put into ethanol bath. After freezing in the ethanol bath, the sample was measured by fluorescence spectroscopy. Subsequently, measurement of fluorescence was performed by completely thawing the sample at 25 ℃.

Confocal microscopy. Fluorescence images were visualized by a confocal laser scanning microscope (Carl-Zeiss LSM 800 Exciter) with same condition. Fluorescence channel was excited at 405 nm with a Si laser and emission was collected by a 450-600 nm band pass filter. Cold-stage microscopy was performed in cryostage (Linkam FDCS196) for precise temperature control during freezing and thawing. The sample was quickly cooled from 25 ℃ to 0 ℃ and subsequently cooled down to -20 ℃ with a cooling rate of 1 ℃ min^{-1}.

KOPRI
극지연구소

Synthesis

Scheme S1. Synthetic route for 1 and 1-Ox.

Synthesis of 6-bromo-2-butyl-1H-benzo[de]isoquinoline-1,3(2H)-dione (2) 4-Bromo-1,8-naphthalic anhydride was prepared from commercially available, compound **2** was synthesized according to the previously reported method.[S9]

Synthesis of 2-butyl-6-morpholino-1H-benzo[de]isoquinoline-1,3(2H)-dione (1) A solution of compound **2** (200 mg, 0.60 mmol), morpholine (157 mg, 1.8 mmol) in 2-methoxyethanol (5 mL) was refluxing for 6 h. After completion of the reaction by TLC monitoring, the solvent was removed and washed with dichloromethane and brine. After removal of the organic layer, purification by flash column chromatography (methanol :

dichloromethane = 1 : 50, *v*/*v*) afforded the compound **1** (150 mg, 74 %) as a bright yellow solid. ^{1}H NMR ($CDCl_3$, 500 MHz): δ 8.58 (dd, J_1 = 7.3 Hz, J_2 = 1.2 Hz, 1H), 8.52 (d, J = 8.0 Hz, 1H), 8.41 (dd, J_1 = 8.5 Hz, J_2 = 1.2 Hz, 1H), 7.71-7.69 (m, 1H), 7.23 (d, J = 8.0 Hz, 1H), 4.17 (t, J = 7.5 Hz, 2H), 4.02 (t, J = 4.6 Hz, 4H), 3.25 (t, J = 4.6 Hz, 4H), 1.74-1.67 (m, 2H), 1.48-1.40 (m, 2H), 0.97 (t, J = 7.4 Hz, 3H) ppm. ^{13}C NMR ($CDCl_3$, 125 MHz): δ 164.4, 164.0, 155.5, 132.5, 131.1, 130.0, 129.9, 126.1, 125.8, 123.4, 117.3, 115.0, 67.0, 53.5, 40.1, 30.2, 20.4, 13.9 ppm.

Synthesis of 4-(2-butyl-1,3-dioxo-2,3-dihydro-1H-benzo[de]isoquinolin-6-yl) morpholine 4-oxide (1-Ox) Compound 1 (100 mg, 0.30 mmol) was dissolved in anhydrous dichloromethane (5 mL). After stirring at 0 °C for 30 min, m-CPBA (53 mg, 0.31 mmol) was slowly added. The mixture was warmed to 25 °C and stirred for 2 h. The solution was removed in vacuo, and the residue was purified by silica gel column chromatography (methanol : dichloromethane = 1 : 20, *v*/*v*) to give 1-Ox as a pale yellow solid (57 mg, 54 %). ^{1}H NMR ($CDCl_3$, 500 MHz): δ 9.96 (d, J = 8.4 Hz, 1H), 8.67 (dd, J_1 = 7.3 Hz, J_2 = 0.8 Hz, 1H), 8.62 (d, J = 8.2 Hz, 1H), 8.18 (d, J = 7.7 Hz, 1H), 7.87-7.84 (m, 1H), 4.96-4.91 (m, 2H), 4.18 (t, J = 7.6 Hz, 2H), 4.15-4.10 (m, 2H), 4.00 (dd, J_1 = 12.3 Hz, J_2 = 3.0 Hz, 2H), 3.78 (d, J = 10.8 Hz, 2H), 1.76-1.69 (m, 2H), 1.49-1.41 (m, 2H), 0.98 (t, J = 7.4 Hz, 3H) ppm. ^{13}C NMR ($CDCl_3$, 125 MHz): δ 163.8, 163.0, 154.0, 132.8, 131.7, 130.6, 130.2, 127.4, 125.1, 124.3, 123.5, 117.3, 67.2, 62.0, 40.5, 30.1, 20.4, 13.8 ppm.

KOBRA 극지연구소

Characterization spectra and other supporting studies

Table S1. Fluorescent quantum yields of **1** and **1-Ox**.

Sample	Corrected area	Absorbance at 360 nm	Refractive index	Quantum yield at 360 nm
Quinine sulfate	14317.809	0.009	1.339	0.54
1	9997.898	0.011	1.342	0.31
1-Ox	855.922	0.016	1.342	0.02

KOPRI
극지연구소

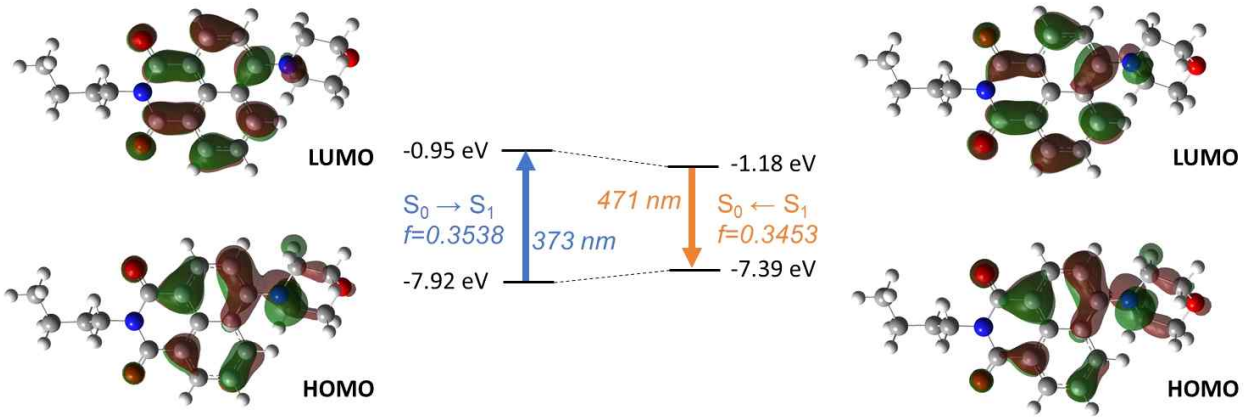

Figure S1. Frontier orbitals and orbital energies of the ground state and excited state structures of 1 calculated at the ωB97XD/N07D level of theory in acetonitrile. Excitation and emission wavelengths were obtained using the state specific solvation. Orbitals are depicted at the 0.03 e/bohr^3 isodensity surface.

KOPRI

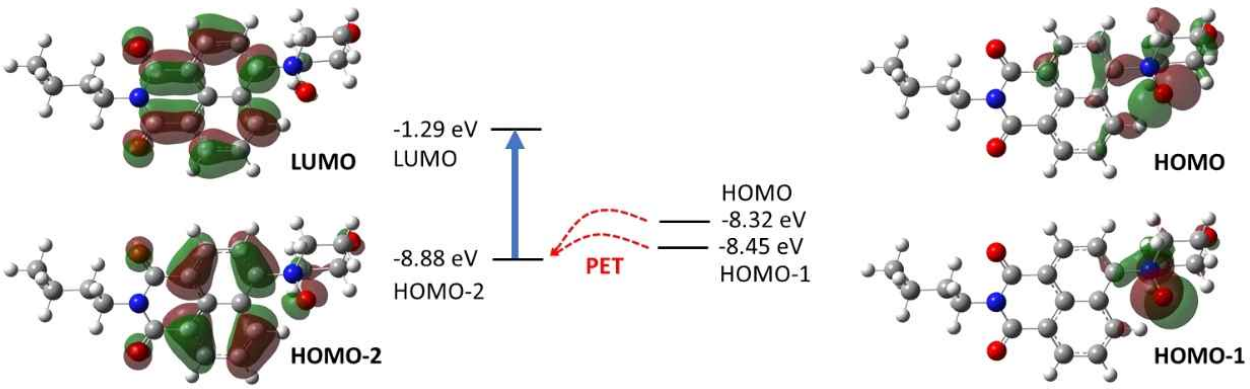

Figure S2. Frontier orbitals and orbital energies of the ground state structure of **1-Ox** calculated at the ωB97XD/N07D level of theory in acetonitrile showing the PET quenching. Orbitals are depicted at the 0.03 e/bohr^3 isodensity surface.

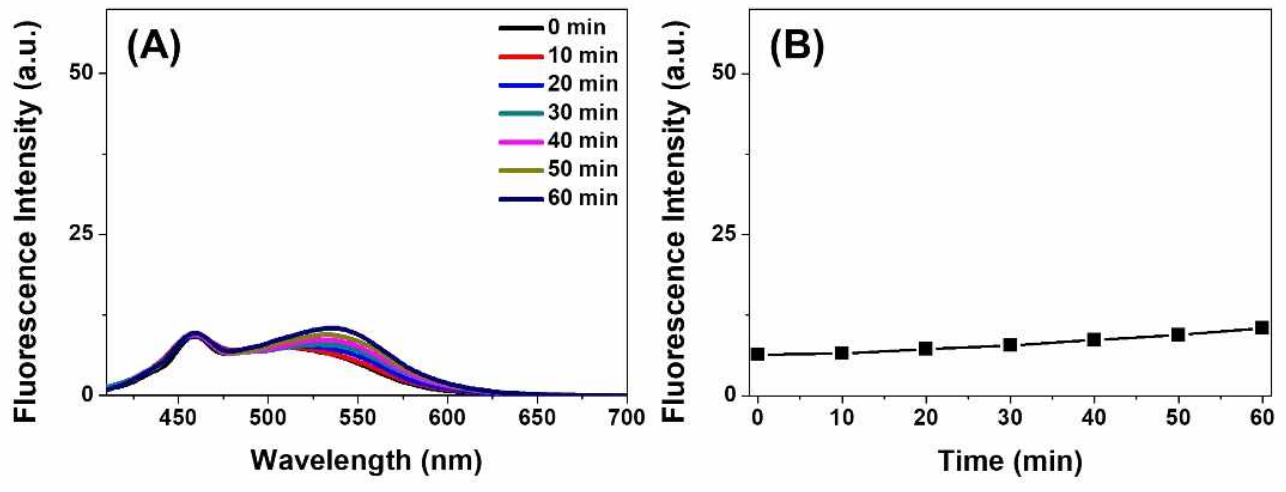

Figure S3. (A) Fluorescence spectra of **1-Ox** (5 μM) with Fe(II) (5 μM) at different time in aqueous solution at 25 °C following excitation at 395 nm. (B) Plot of fluorescence intensity at 540 nm as a function of increasing time.

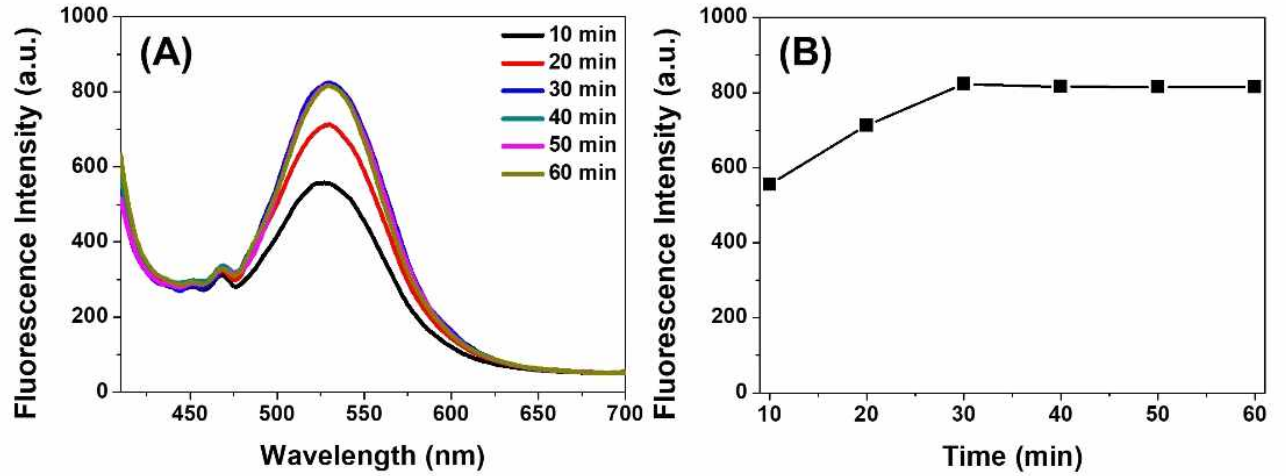

Figure S4. (A) Fluorescence spectra of **1-Ox** (5 μM) with Fe(II) (5 μM) at different time in frozen solution at -20 oC following excitation at 395 nm. (B) Plot of fluorescence intensity at 540 nm as a function of increasing time.

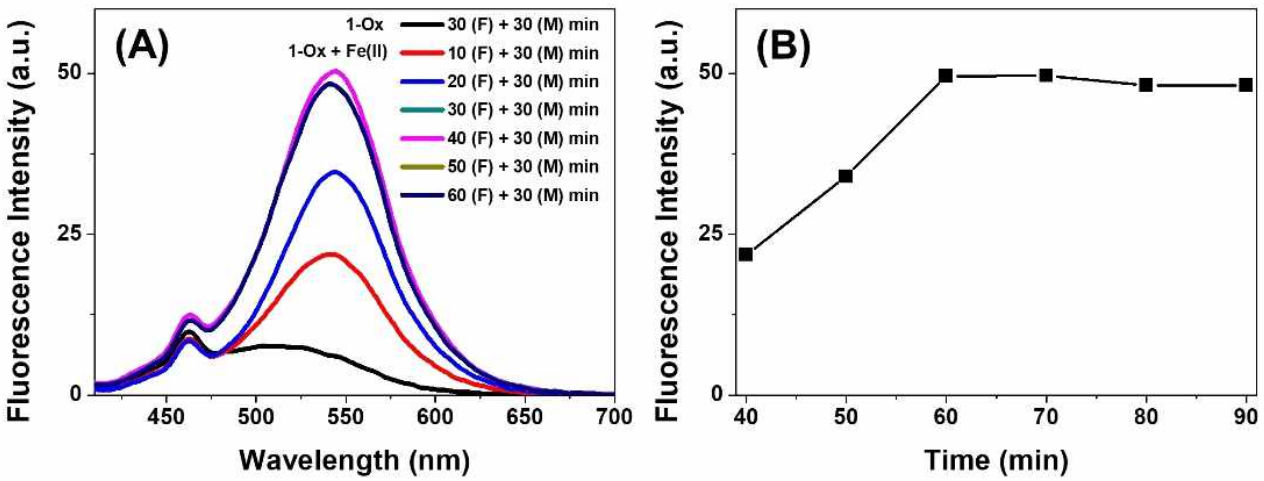

Figure S5. (A) Fluorescence spectra of **1-Ox** (5 μM) in the absence and presence of Fe(II) (5 μM) at different time in frozen solution at -20 oC after thawing (25 oC) for 30 min following excitation at 395 nm. (B) Plot of fluorescence intensity at 540 nm as a function of increasing time.

KOPRI

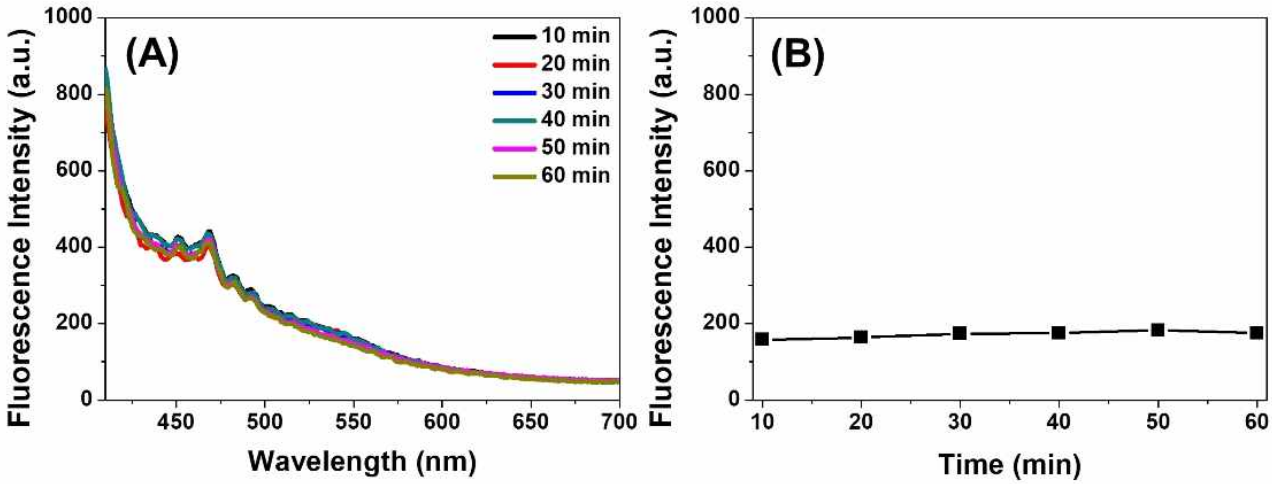

Figure S6. (A) Fluorescence spectra of **1-Ox** (5 μM) at different time in frozen solution at -20 oC following excitation at 395 nm. (B) Plot of fluorescence intensity at 540 nm as a function of increasing time.

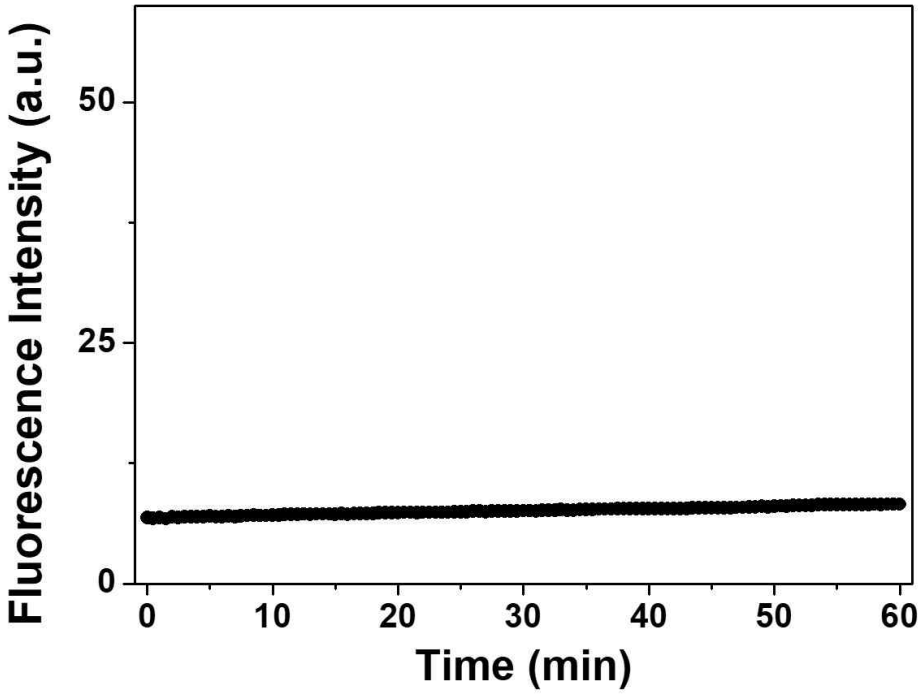

Figure S7. Time-dependent fluorescence intensity of **1-Ox** (5 μM) at 540 nm in aqueous solution at 25 oC, excitation at 395 nm.

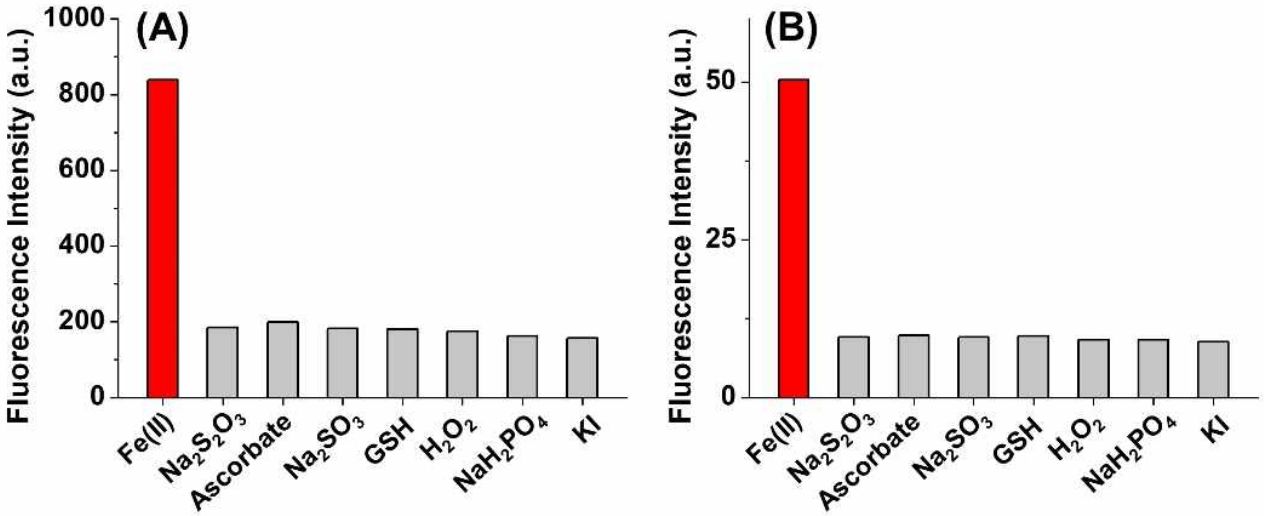

Figure S8. Selectivity studies of **1-Ox** (5 μM) with biologically relevant reductive species under (A) freezing conditions (−20 °C) for 30 min, and (B) after thawing (25 °C) for 30 min in aqueous solutions.

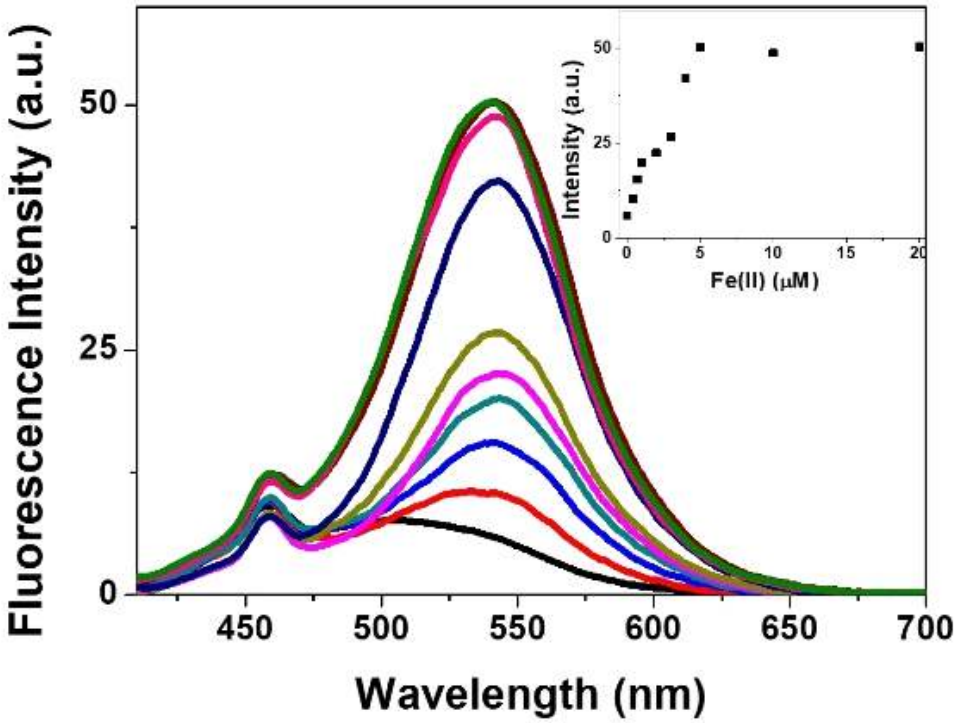

Figure S9. Fluorescence spectra of **1-Ox** (5 μM) in the presence of various concentrations of Fe(II) (0 - 20 μM) for 30 min freezing condition (-20 °C) after thawing (25 °C) for 30 min in aqueous solution following excitation at 395 nm. Inset: Fluorescence intensity at 540 nm as a function of Fe(II) concentration.

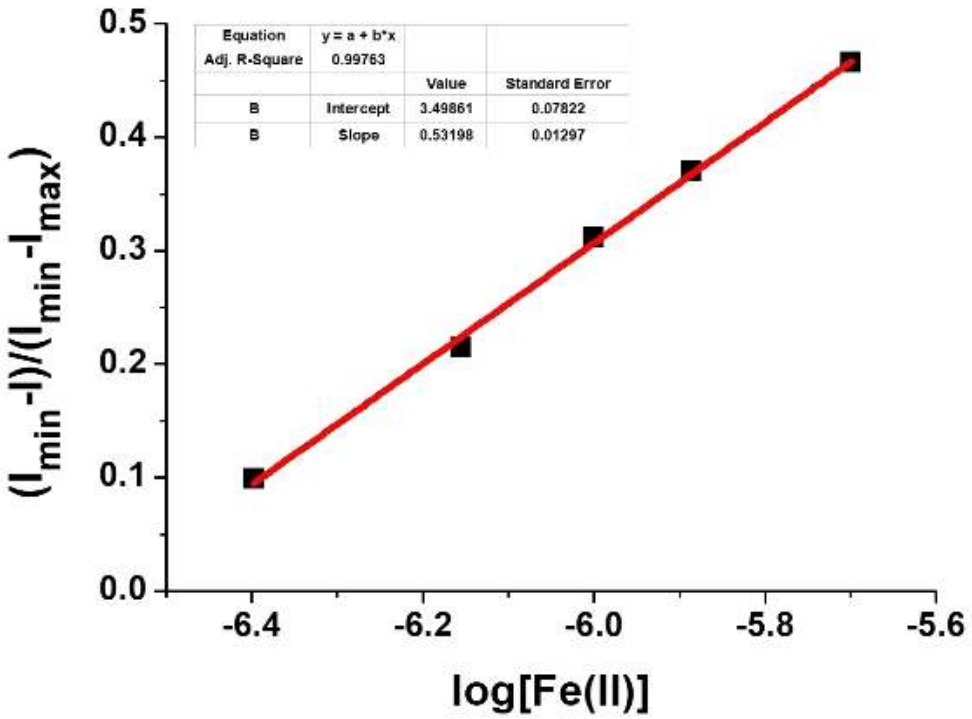

Figure S10. The detection limit of **1-Ox** for Fe(II) in freezing (-20 °C, 30 min) and thawing (25 °C, 30 min) conditions was calculated from the normalized response of the fluorescence signal at 540 nm with excitation affected at 395 nm.

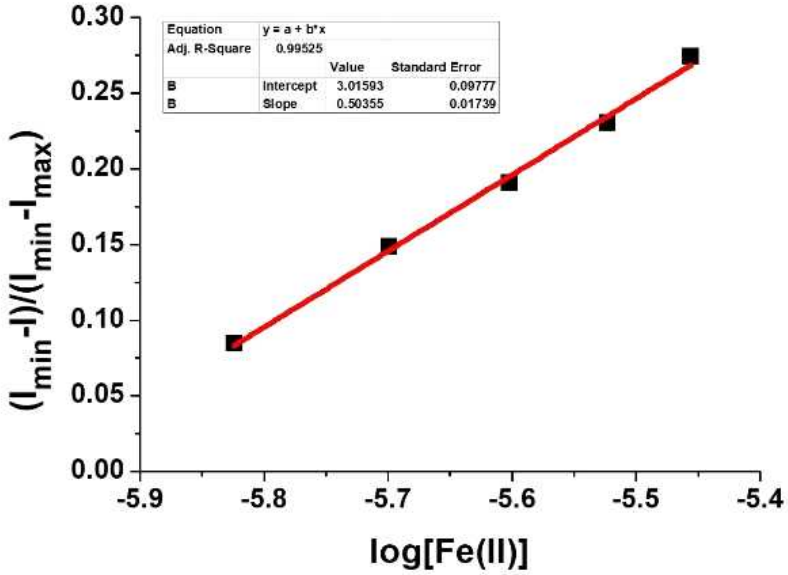

Figure S11. The detection limit of **1-Ox** for Fe(II) at 25 °C was calculated from the normalized response of the fluorescence signal at 540 nm with excitation affected at 395 nm.

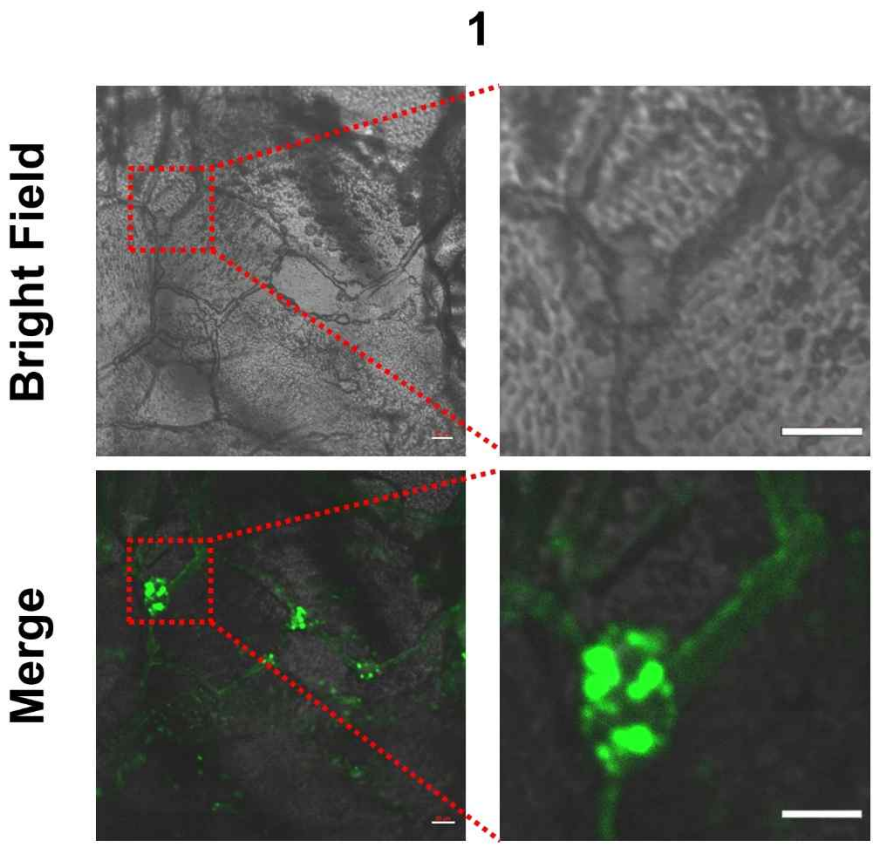

Figure S12. Confocal microscopy images of 1 (5 μM) on the cryostage at -20 °C for 30 min. Merged images were obtained by DIC and fluorescence images. Excitation and emission wavelengths were 405 nm and 450 - 600 nm, respectively. Scale bar is 20 μm.

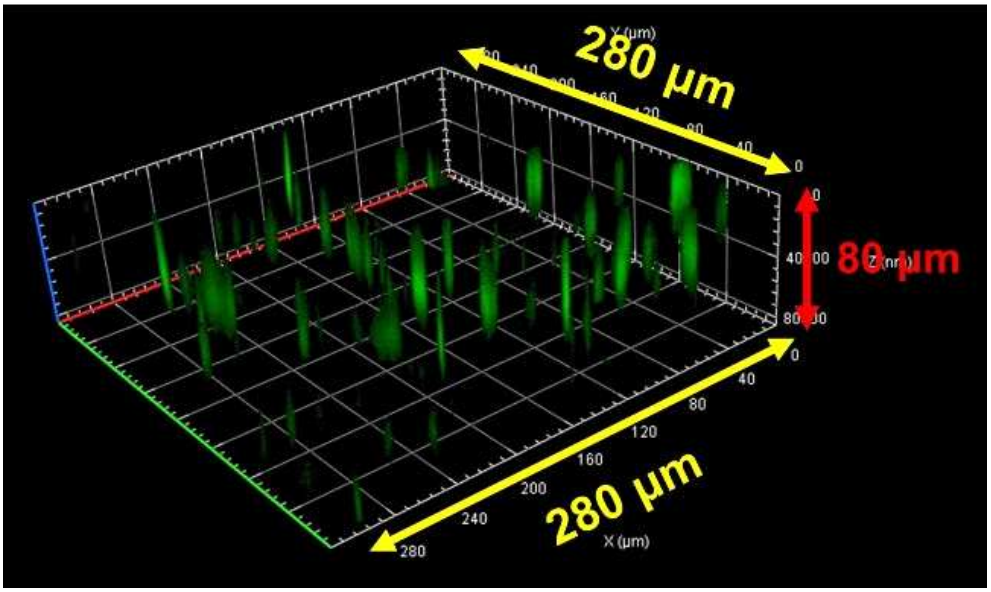

Figure S13. Representative 3D reconstruction images from **1-Ox** (5 μM) with Fe(II) on the cryostage at -20 oC for 30 min were obtained at a depth of 0 - 80 μm.

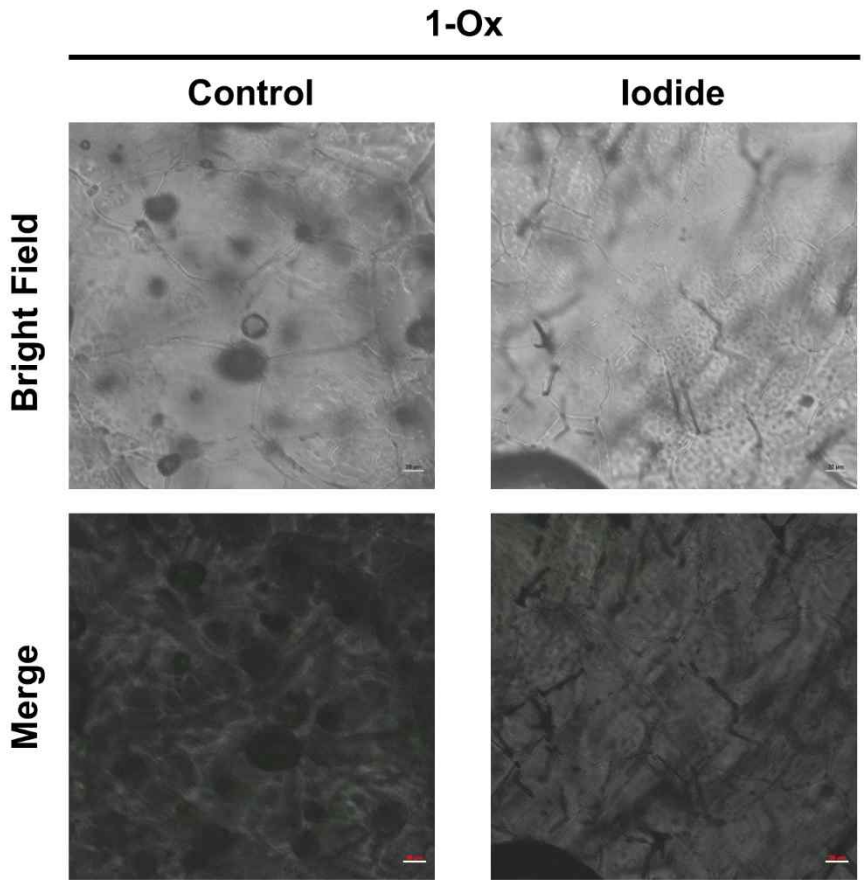

Figure S14. Control experiment for effect of iodide on the fluorescence change of **1-Ox** (5 μM) on the cryostage at -20 oC for 30 min in confocal microscopy images. Merged images were obtained by DIC and fluorescence images. Excitation and emission wavelengths were 405 nm and 450 - 600 nm, respectively. Scale bar is 20 μm.

NMR Spectra and MS Data

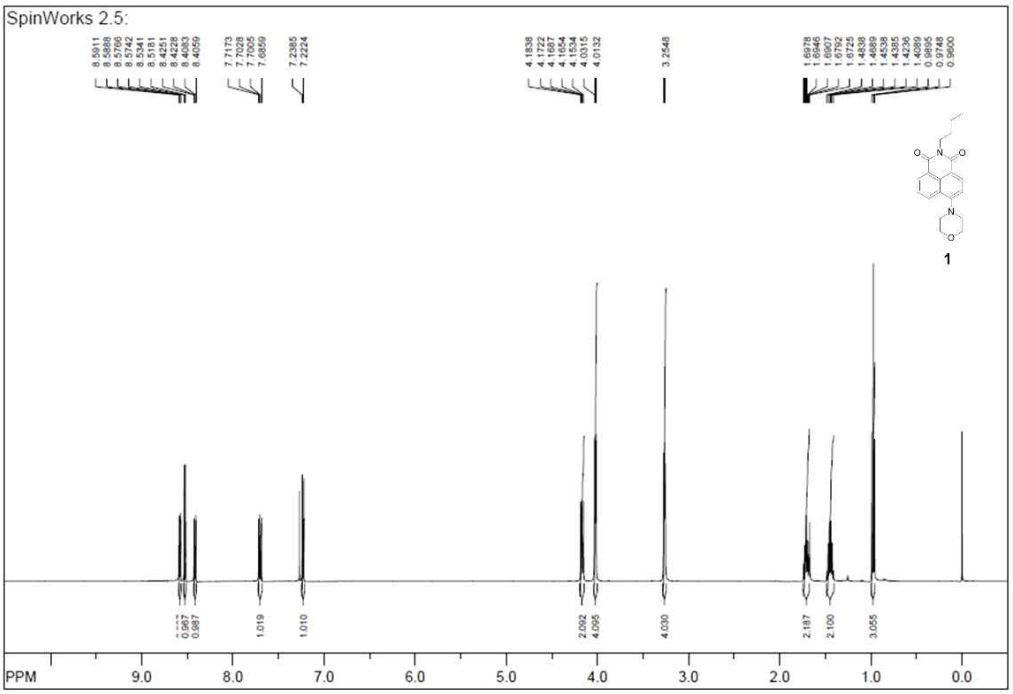

Figure S15. ^{1}H NMR ($CDCl_3$, 500 MHz) spectrum of **1**.

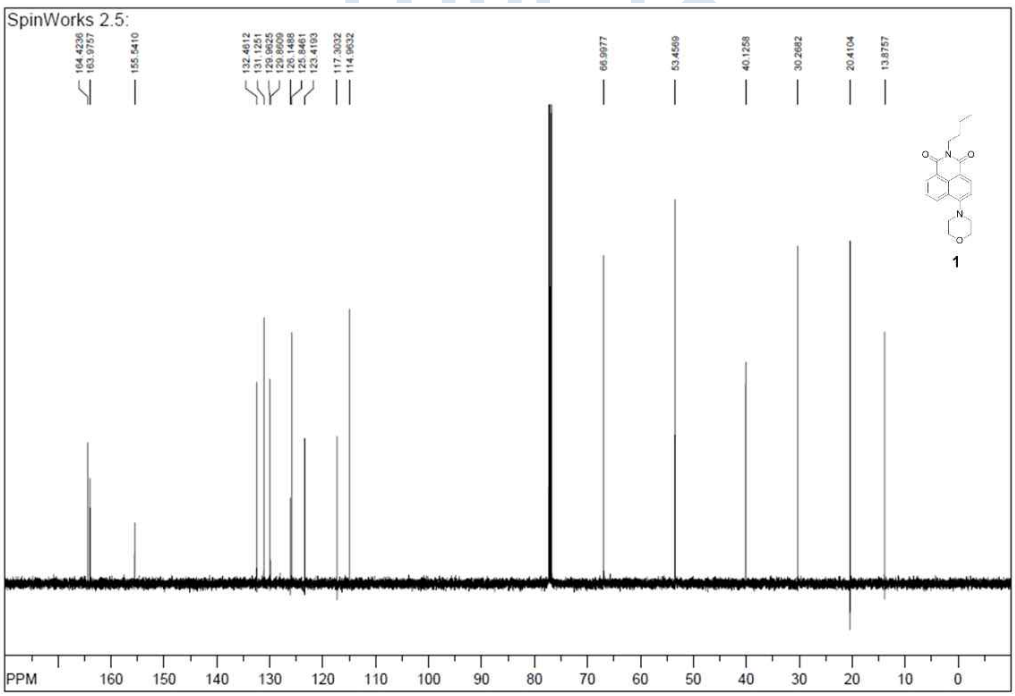

Figure S16. ^{13}C NMR ($CDCl_3$, 500 MHz) spectrum of **1**.

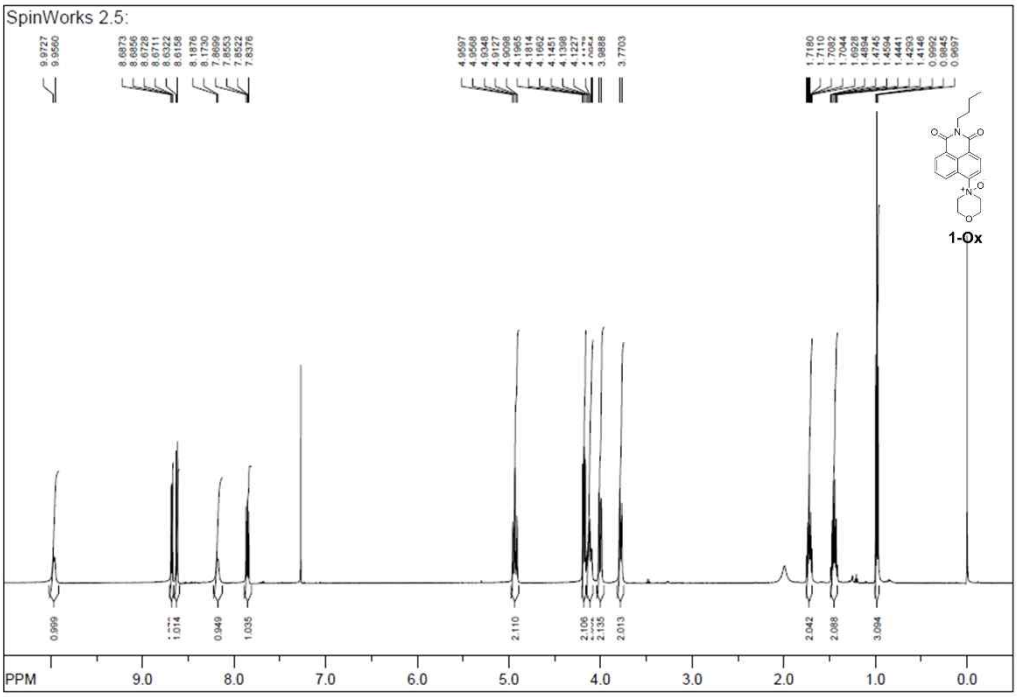

Figure S17. ^{1}H NMR ($CDCl_3$, 500 MHz) spectrum of compound **1-Ox.**

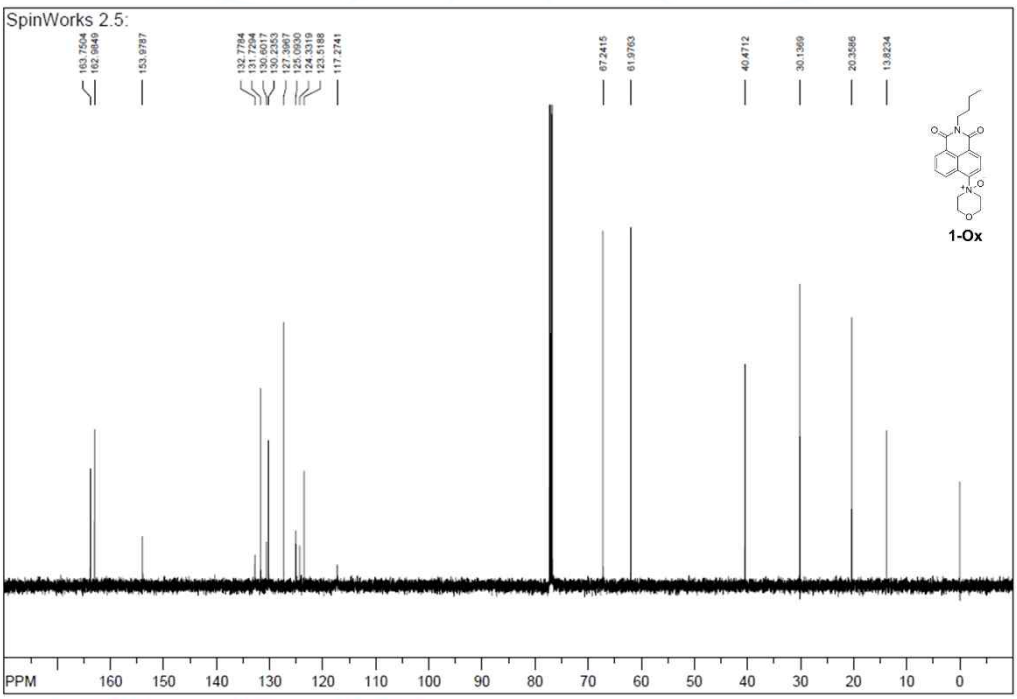

Figure S18. ^{13}C NMR ($CDCl_3$, 500 MHz) spectrum of compound **1-Ox**.

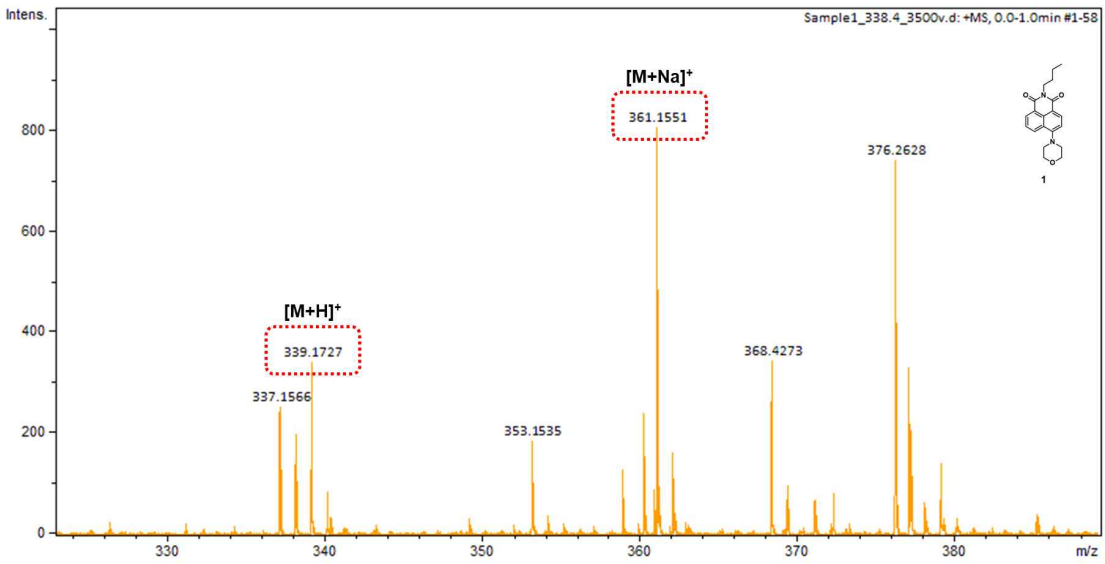

Figure S19. ESI-MS spectrum of compound **1**.

KOPRI

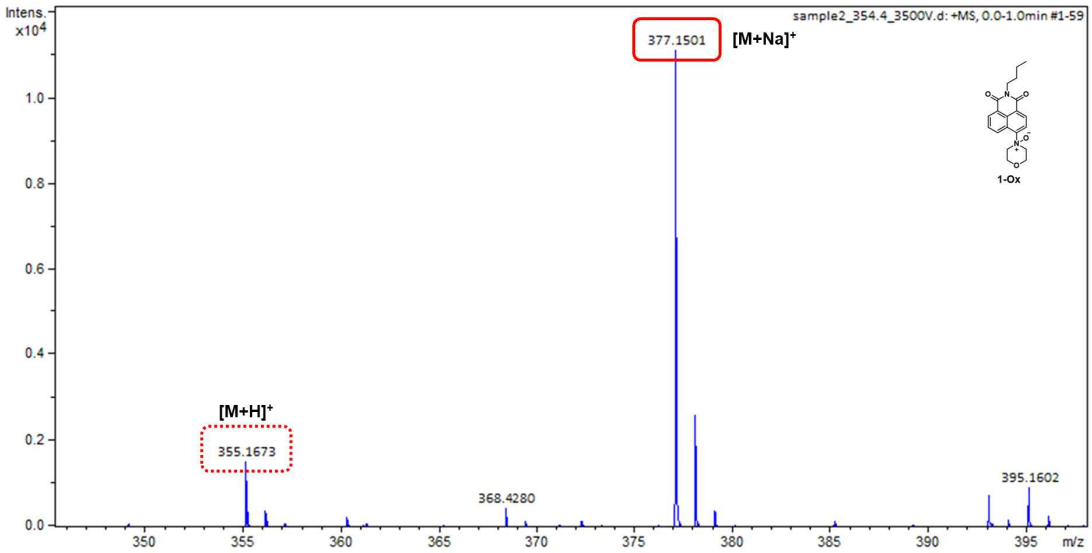

Figure S20. ESI-MS spectrum of compound **1-Ox.**

References in Supporting information

S1. Gaussian 16, M. J. Frisch, G. W. Trucks, H. B. Schlegel, G. E. Scuseria, M. A. Robb, J. R. Cheeseman, G. Scalmani, V. Barone, G. A. Petersson, H. Nakatsuji, X. Li, M. Caricato, A. V. Marenich, J. Bloino, B. G. Janesko, R. Gomperts, B. Mennucci, H. P. Hratchian, J. V. Ortiz, A. F. Izmaylov, J. L. Sonnenberg, D. Williams-Young, F. Ding, F. Lipparini, F. Egidi, J. Goings, B. Peng, A. Petrone, T. Henderson, D. Ranasinghe, V. G. Zakrzewski, J. Gao, N. Rega, G. Zheng, W. Liang, M. Hada, M. Ehara, K. Toyota, R. Fukuda, J. Hasegawa, M. Ishida, T. Nakajima, Y. Honda, O. Kitao, H. Nakai, T. Vreven, K. Throssell, J. A. Montgomery, Jr., J. E. Peralta, F. Ogliaro, M. J. Bearpark, J. J. Heyd, E. N. Brothers, K. N. Kudin, V. N. Staroverov, T. A. Keith, R. Kobayashi, J. Normand, K. Raghavachari, A. P. Rendell, J. C. Burant, S. S. Iyengar, J. Tomasi, M. Cossi, J. M. Millam, M. Klene, C. Adamo, R. Cammi, J. W. Ochterski, R. L. Martin, K. Morokuma, O. Farkas, J. B. Foresman, D. J. Fox, J. Gaussian, Inc., Wallingford CT, 2016..

S2. a) C. T. Lee, W. T. Yang, R. G. Parr, *Phys. Rev. B: Condens. Matter Mater. Phys.*, 1988, **37**, 785 - 789; b) A. D. Becke, *J. Chem. Phys.*, 1993, **98**, 5648 - 5652.

S3. T. Yanai, D. Tew, N. Handy, *Chem. Phys. Lett.*, 2004, 393, 51 - 57.

S4. J.-D. Chai, M. Head-Gordon, *Phys. Chem. Chem. Phys.*, 2008, **10**, 6615 - 6620.

S5. V. Barone, P. Cimino, E. Stendardo, *J. Chem. Theory Comput.*, 2008, **4**, 751 - 764.

S6. a) R. Improta, V. Barone, G. Scalmani, M. Frisch, *J. Chem. Phys.*, 2006, **125**, 054103; b) R. Improta, G. Scalmani, M. Frisch, V. Barone, *J. Chem. Phys.*, 2007, **127**, 074504.

S7. A. R. Allouche, *J. Comput. Chem.*, 2011, 32, 174 - 182.

S8. GaussView, Version 6, R. Dennington, T. A. Keith, J. M. Millam, Semichem Inc., Shawnee Mission, KS, 2016.

S9. P.-Y. Gu, C.-J. Lu, Z.-J. Hu, N.-J. Li, T.-T. Zhao, Q.-F. Xu, Q.-H. Xu, J.-D. Zhang and J.-M. Lu, *J. Mater. Chem. C*, 2013, **1**, 2599-2606.

제 21 절. Activation of Periodate by Freezing for the Degradation of Aqueous Organic Pollutants[14)]

Yejin Choi[1], Ho-Il Yoon[2], Changha Lee[3], Ľubica Vetrakova[4], Dominik Heger[4], Kitae Kim[2,5*], and Jungwon Kim[1*]

[1]Department of Environmental Sciences and Biotechnology, Hallym University
[2]Korea Polar Research Institute
[3]School of Urban and Environmental Engineering, Ulsan National Institute of Science and Technology
[4]Department of Chemistry and Research Centre for Toxic Compounds in the Environment (RECETOX), Faculty of Science, Masaryk University, Czech Republic
[5]Department of Polar Sciences, University of Science and Technology

1. Introduction

Inorganic periodate (IO_4^-) has been used for the oxidation of various organic compounds, such as polysaccharides, alginates, amino compounds, and phenolic compounds.[1-5] However, the application of IO_4^- as a chemical oxidant for water treatment is limited because the IO_4^--mediated oxidation process is usually very slow. To enhance the oxidation ability of IO_4^-, a variety of techniques for IO_4^- activation have been employed including a UV/IO_4^- system [6,7], an ultrasound/IO_4^- system [8], a bimetallic nanoparticle/IO_4^- system [9], and a KOH/IO_4^- system [10]. Short wavelength UV ($\lambda \leq$ 266 nm) or ultrasound irradiation of IO_4^- generates powerful oxidants such as iodyl ($IO_3^{\bullet}$) and hydroxyl ($^{\bullet}OH$) radicals (reactions 1 and 2). The presence of bimetallic nanoparticles (Fe^0/Ni or Fe^0/Cu) converts IO_4^- to $IO_3^{\bullet}$ directly or indirectly through the formation of $H^{\bullet}$ (reactions 3−5). The reaction between IO_4^- and OH^- produces reactive oxygen species (ROS) such as the superoxide radical ($O_2^{\bullet -}$) and singlet oxygen ($^1O_2$) (reactions 6 and 7).

$$IO_4^- + \text{UV light (or ultrasound)} \rightarrow IO_3^{\bullet} + O^{\bullet -} \quad (1)$$

$$O^{\bullet -} + H^+ \rightarrow {}^{\bullet}OH \quad (2)$$

$$2IO_4^- + \text{bimetallic nanoparticle} + 4H^+ \rightarrow 2IO_3^{\bullet} + \text{bimetallic nanoparticle}^{2+} + 2H_2O \quad (3)$$

$$\text{bimetallic nanoparticle} + 2H^+ \rightarrow \text{bimetallic nanoparticle}^{2+} + 2H^{\bullet} \quad (4)$$

$$IO_4^- + H^{\bullet} \rightarrow IO_3^{\bullet} + OH^- \quad (5)$$

14) 이 연구는 본 과제 지원으로 수행되었으며 그 결과는 다음의 논문으로 출판되었음: Yejin Choi, Ho-Il Yoon, Changha Lee, Ľubica Vetrakova, Dominik Heger, Kitae Kim, and Jungwon Kim, “Activation of Periodate by Freezing for the Degradation of Aqueous Organic Pollutants”, *Environ. Sci. Technol.* 2018, 52, 9, 5378-5385.

$$3IO_4^- + 2OH^- \rightarrow 3IO_3^- + 2O_2^{\bullet -} + H_2O \quad (6)$$

$$2O_2^{\bullet -} + 2H_2O \rightarrow {}^1O_2 + H_2O_2 + 2OH^- \quad (7)$$

The activation of IO_4^- generates powerful oxidants such as $IO_3^{\bullet}$, $^{\bullet}OH$, $O_2^{\bullet -}$, and $^1O_2$, which facilitates the application of IO_4^- for water treatment by increasing the degradation rate of aquatic pollutants.

Chemical reactions at temperatures below the freezing point are usually slower than those at temperatures above the freezing point. Therefore, food and unstable chemicals are put in a freezer for long-term storage. However, specific chemical reactions are significantly accelerated during the freezing process due to the existence of thin liquid layer among the solid ice crystals (i.e., ice-ice interface) and on the solid ice crystals (i.e., ice-air interface) at temperatures between the freezing and eutectic points [11-14]. Various terminologies such as liquid brine, ice grain boundary, micropocket have been used to denote this confined liquid layer at temperatures below the freezing point. Solutes and dissolved gases in aqueous solution are expelled from the growing ice crystals and concentrated in the shrinking liquid brine during freezing [15-17]. In addition, protons and hydroxides are accumulated in the liquid brine under acidic and basic conditions, respectively [18]. Therefore, an acidic solution becomes more acidic and a basic solution becomes more basic by freezing. The concentration of solutes, dissolved gases, and protons/hydroxides in the liquid brine during freezing is referred as the “freeze concentration effect”.

This freeze concentration effect during freezing can enhance the chemical reactions in the cold space by increasing the concentrations of reactants and constituting a favorable condition for chemical reactions (i.e., oxygen-rich condition and/or extremely acidic/basic condition). In addition, the reductive/oxidative conversions of pollutants (i.e., chemical reactions between the pollutants or between the pollutants and natural matters) can be accelerated in the cryosphere (e.g., permafrost, polar regions, high-latitudes, and mid-latitudes during the winter season). The oxidation rate of nitrite (NO_2^-) to nitrate (NO_3^-) in the presence of oxygen increased by approximately 10^5 times upon freezing.[19,20] The redox conversions between chromate (Cr^{6+}) and hydrogen peroxide (H_2O_2)[21]/arsenite (As^{3+})[22]/phenolic pollutants[23]/NO_2^-[24] were significantly enhanced during freezing. The reduction of bromate (BrO_3^-) by humic substances, which was negligible in water, was clearly observed when the solution was frozen.[25] The *N*-nitrosation reaction of dimethylamine with NO_2^- was significantly accelerated by freezing.[26] Recently, the freezing process was applied to water treatment, in which the NO_2^--mediated oxidation of sulfamethoxazole was significantly accelerated by freezing.[27]

Although various methods for the activation of IO_4^- have been developed and

applied to the degradation of aquatic pollutants,[6-10] the freezing process has not been tried to activate IO_4^-. The term "activation of IO_4^-" usually refers to "the conversion of IO_4^- to oxidizing species such as $IO_3^{\bullet}$ and reactive oxygen species". However, in a broad sense, the term "activation of IO_4^-" in this study has been used to refer to "providing a reaction medium in which IO_4^- itself favorably acts as an oxidizing species". Herein, we report a new strategy for the activation of IO_4^- and its application for water treatment, i.e., the degradation of aqueous organic pollutants in the presence of IO_4^- by freezing. The degradation of organic pollutants with the simultaneous conversion of IO_4^- during freezing at −20 °C was investigated and compared with that in water at 25 °C. The freezing-induced degradation of organic pollutants in the presence of IO_4^- was measured as a function of various experimental parameters, such as IO_4^- concentration, pH, and freezing temperature. The degradation kinetics of various organic pollutants, such as furfuryl alcohol, cimetidine, tryptophan, phenol, 4-chlorophenol, and bisphenol A, in the IO_4^-/freezing system was compared. Outdoor experiments were performed to verify the practical viability of the IO_4^-/freezing system for water treatment (i.e., the energy-free IO_4^-/freezing system in cold regions). Furthermore, the degradation mechanism of organic pollutants by IO_4^- during freezing is discussed.

2. Experimental Section

Chemicals. All chemicals were used as received without further purification. They include potassium periodate (KIO_4, Sigma-Aldrich, ≥99.8%), potassium iodate (KIO_3, Sigma-Aldrich, ≥99.5%), potassium iodide (KI, Junsei, ≥99.5%), furfuryl alcohol (FFA, $C_5H_6O_2$, Aldrich, ≥98.0%), tryptophan ($C_{11}H_{12}N_2O_2$, Sigma-Aldrich, ≥98.0%), cimetidine ($C_{10}H_{16}N_6S$, Sigma, 100%), phenol (C_6H_5OH, Sigma-Aldrich, ≥99.0%), 4-chlorophenol (ClC_6H_4OH, Aldrich, ≥99.0%), bisphenol A ($C_{15}H_{16}O_2$, Aldrich, ≥99.0%), and cresol red (CR, $C_{21}H_{18}O_5S$, Sigma-Aldrich, ≥95.0%). All solutions were prepared with ultrapure deionized water (resistivity = 18.3 MΩ·cm) that was prepared using a Human-Power I+ water purification system (Human Corporation).

Experimental Procedure. Aliquots of IO_4^- (usually 1 mM, 10 mL) and an organic pollutant (usually FFA, 200 μM, 10 mL) stock solution were added to 80 mL of water in a beaker to yield the desired initial concentration (usually [IO_4^-] = 100 μM and [organic pollutant] = 20 μM). The pH of the solution (100 mL) was adjusted using a $HClO_4$ or NaOH solution to the desired value (usually pH = 3.0). The solution was unbuffered. 10 mL of this solution was put in a polypropylene conical tube (volume = 15 mL, Nest Biotechnology). The conical tube containing the aqueous solution of IO_4^- and organic pollutant was placed in a stainless steel tube rack in a cryogenic ethanol bath, which was

precooled to the desired temperature (usually −20 °C), to freeze the aqueous solution. The moment that the conical tube containing the aqueous solution was put into the cryogenic ethanol bath was defined as “reaction time zero (t = 0)”. After reaction in the cryogenic ethanol bath, the conical tube containing the frozen solution was put into a water bath at 35 °C to thaw the frozen solution. The melted solution was immediately analyzed. The experiments in an ethanol bath preset at 25 °C were also performed as the control experiments. Multiple (two or more) experiments were performed for a given condition to confirm data reproducibility.

Outdoor experiments were performed on a vacant lot beside the Natural Science Building in Hallym University (Chuncheon city, Republic of Korea) (37° 89’ N, 127° 47’ E) at night on December 12, 2017. The wind blew lightly. The temperatures during the outdoor experiments were in the range of −15 ~ −16 °C. 10 mL of aqueous solution containing IO_4^- and FFA ([IO_4^-] = 100 μM, [FFA] = 20 μM, and pH = 3.0) was put in a 100 mL beaker. The beaker was set down on the outside ground.

Chemical Analyses. The concentrations of organic pollutants, such as FFA, cimetidine, tryptophan, phenol, 4-chlorophenol, and bisphenol A, were measured using high-performance liquid chromatography (HPLC, Agilent 1120) equipped with a UV−visible detector and a Zorbax 300SB C-18 column (4.6 mm × 150 mm). The eluent consisted of a binary mixture of 0.1% phosphoric acid solution and acetonitrile, and its flow rate was 1.0 mL/min. The volume ratios (0.1% phosphoric acid solution:acetonitrile) of the eluents and the detection wavelengths were as follows: 85:15 and 218 nm for FFA, 95:5 and 218 nm for cimetidine, 90:10 and 220 nm for tryptophan, 70:30 and 270 nm for phenol, 80:20 and 228 nm for 4-chlorophenol, and 70:30 and 229 nm for bisphenol A, respectively. The concentration of total organic carbon (TOC) was measured using a TOC analyzer (Shimadzu TOC-L_{CPH}) equipped with a nondispersive infrared sensor as a CO_2 detector.

The quantitative analyses of IO_3^- and I^- were performed using an ion chromatograph (IC, Dionex ICS-1100) equipped with a Dionex IonPac AS-14 column (4 mm × 250 mm) and a conductivity detector. A binary mixture of 3.5 mM sodium carbonate and 1 mM sodium bicarbonate was used as the eluent at a flow rate of 1.0 mL/min. The concentration of I_2 was determined by measuring the absorbance at 460 nm (ε = 746 M^{-1} cm^{-1} at 460 nm)[28] using a UV−visible spectrophotometer (Shimadzu UV-2600). Because the absorbance at 353 nm, which is ascribed to the generation of I_3^- (ε = 26400 M^{-1} cm^{-1} at 353 nm and ε = 975 M^{-1} cm^{-1} at 460 nm),[28] was negligible (less than 0.0015 (= 0.06 μM), see Figure S1 in the Supporting Information, SI), only I_2 is responsible for the absorbance at 460 nm.

pH Estimation of the Frozen Solution. The pH of the frozen solution was estimated by measuring the UV−visible absorption spectra of cresol red (CR) as an in situ pH probe after freezing, but without thawing (i.e., in the liquid brine).[29,30] 3 mL of an aqueous solution containing IO_4^- (100 μM) and CR (20 μM) in a cylindrical quartz tube (4 mL) was frozen at −20 °C in a cryogenic ethanol bath and its UV−visible absorption spectrum was immediately recorded using a UV−visible spectrophotometer equipped with a diffuse reflectance accessory (Agilent Cary 5000) after taking the cylindrical quartz tube out from the cryogenic ethanol bath. Nitrogen gas was continuously introduced into the sample compartment to prevent moisture condensation on the cylindrical quartz tube. Pure ice prepared in identical manner was used as a reference.

CR exists in three different forms depending on the pH and exhibits different maximum absorption wavelengths (λ_{max} = 518 nm for diprotonated CR, λ_{max} = 434 nm for monoprotonated CR, and λ_{max} = 573 nm for deprotonated CR).[31] However, the three different CR forms cannot coexist in the equilibrium state because there is a great gap between first and second acid dissociation constants (pK_a) of CR (pK_{a1} = 1.10 and pK_{a2} = 8.15).[32,33] Only diprotonated CR and monoprotonated CR or monoprotonated CR and deprotonated CR can coexist. Therefore, the relative concentrations of the two different CR forms (i.e., [monoprotonated CR]/[diprotonated CR] or [deprotonated CR]/[monoprotonated CR]) can be obtained by fitting the data in the UV−visible absorption spectra of CR to eq 8.[29,30] The non-negative least squares minimization was performed using Matlab. The pH of frozen solution was calculated according to eq 9 using the relative concentrations of the two different CR forms obtained from eq 8 and the pK_a value.

$$\sum_{\lambda = 400\ \mathrm{nm}}^{650\ \mathrm{nm}} (A \cdot a + B \cdot b - X)^2 = \text{minimum value} \qquad (8)$$

where X stands for the absorbance of frozen solution, A and B stand for the absorbances of pure diprotonated CR and monoprotonated CR (or the absorbances of pure monoprotonated CR and deprotonated CR), respectively, and a and b (non-negative parameters) are the relative concentrations of diprotonated CR and monoprotonated CR (or the relative concentrations of monoprotonated CR and deprotonated CR), respectively.

$$pH = pK_{a1} + \log\frac{[\text{monoprotonated CR}]}{[\text{diprotonated CR}]} \quad \left(\text{or} \quad pK_{a2} + \log\frac{[\text{deprotonated CR}]}{[\text{monoprotonated CR}]}\right) \qquad (9)$$

3. Results and Discussion

Degradation of Furfuryl Alcohol (FFA) by IO_4^- during Freezing. The degradation of FFA as a model organic pollutant in the presence of IO_4^- during freezing at −20 °C was investigated (Figure 1a). The degradation of FFA by IO_4^- proceeded rapidly during freezing. The degradation of FFA was initiated after 6 min (i.e., when the aqueous solution was almost solidified) (see Figures S2 and S3 in the SI). After 6 min of induction period, the concentration of FFA gradually decreased with the reaction time, and FFA was completely degraded after 1 h of reaction. The mineralization (i.e., the TOC removal) efficiency was 13.5(±1.2)% after 4 h of reaction. However, FFA was not degraded by IO_4^- in water at 25 °C. In addition, the degradation of FFA during freezing was negligible in the absence of IO_4^-. The results of the control experiments without either freezing or IO_4^- indicate that both freezing and IO_4^- are required for the degradation of FFA.

The degradation of FFA by IO_4^- during freezing was accompanied by the reduction of IO_4^- by FFA. The generation of IO_3^-, I^-, and I_2 was observed in both the presence of IO_4^- and FFA during freezing (Figure 1b). The total iodine mass balance was satisfactory throughout the freezing reaction (i.e., reduced $[IO_4^-]$ = generated $[IO_3^-]$ + generated $[I^-]$ + 2 × generated $[I_2]$) (see Figure S4 in the SI). This result implies that the missing iodine species are negligible. In accordance with the results of control experiments for FFA degradation, IO_4^- was not reduced in the absence of either FFA or freezing (Figure 1b).

Activation Mechanism of IO_4^- by Freezing. IO_4^- exists in various forms, such as H_5IO_6, $H_4IO_6^-$, $H_3IO_6^{2-}$, $H_2IO_6^{3-}$, IO_4^-, and $H_2I_2O_{10}^{4-}$, in water and their molar fraction depends on the pH and the concentration of IO_4^- (see eqs S1−S5 in the SI).[34] The speciation of IO_4^- can be changed during freezing because the concentration of IO_4^- increases and the pH decreases (at acidic conditions) by a freeze concentration effect that accumulates IO_4^- and protons in the liquid brine. It was previously estimated that the solute concentration increases by 10^3-10^6 times[15] and the pH decreases (at acidic conditions) by 2−4 during freezing.[18] Due to the increase in IO_4^- concentration and decrease in pH by freezing, the main iodine^{VII} species in water and during freezing can be different. To estimate the main iodine^{VII} species in water and during freezing, the pH-dependent speciation of IO_4^- was calculated at $[IO_4^-]$ = 100 μM, 100 mM, and 100 M using the MINEQL+ chemical equilibrium modeling system (Figure S5 in the SI). Only IO_4^- is dominant in water under experimental conditions identical to those of Figure 1 (i.e., at pH = 3.0 and $[IO_4^-]$ = 100 μM) (see the results at pH = 3.0 in Figure S5a in the SI). However, both IO_4^- and H_5IO_6 are expected as a main species during freezing assuming that IO_4^- and protons are concentrated in the liquid brine by 10^3-10^6 and 10^2-10^4 times,

respectively (see the results in the pH range of 0−1 in Figures S5b and c in the SI).

Although IO_4^- and H_5IO_6 have a fairly high oxidation power (standard reduction potentials (E^0) of IO_4^- and H_5IO_6 = 1.623 and 1.601 V_{NHE}, respectively),[35] protons are essentially required in the degradation process, as shown in reactions 10 and 11. The negligible degradation of FFA by IO_4^- in water at pH = 3.0 (Figure 1a) implies that 1 mM of protons is not sufficient to drive the degradation of FFA. However, protons are concentrated in the liquid brine by exclusion from ice crystals during freezing, which makes the liquid brine a favorable site for the proton-coupled degradation process (reactions 10 and 11). That is, the degradation of FFA by IO_4^- during freezing is most likely due to the pH decrease by the freeze concentration effect. The generation of IO_3^- as a product of IO_4^- reduction indirectly supports this scenario (see Figure 1b and reactions 10 and 11). Not only IO_3^- but also I^- and I_2 were generated during the freezing-induced degradation of FFA in the presence of IO_4^- (Figure 1b). This result indicates that IO_3^- (E^0 = 1.085 or 1.195 V_{NHE})[35] generated from IO_4^- reduction is also involved in the degradation of FFA during freezing (reactions 12 and 13). When IO_3^- was used instead of IO_4^-, the degradation of FFA was also observed during freezing (see Figure S6 in the SI).

$$IO_4^- + 2H^+ + 2e^- \rightarrow IO_3^- + H_2O,\ E^0 = 1.623\ V_{NHE} \quad (10)$$

$$H_5IO_6 + H^+ + 2e^- \rightarrow IO_3^- + 3H_2O,\ E^0 = 1.601\ V_{NHE} \quad (11)$$

$$IO_3^- + 6H^+ + 6e^- \rightarrow I^- + 3H_2O,\ E^0 = 1.085\ V_{NHE} \quad (12)$$

$$IO_3^- + 6H^+ + 5e^- \rightarrow 0.5I_2 + 3H_2O,\ E^0 = 1.195\ V_{NHE} \quad (13)$$

However, the degradation of FFA by I_2 as well as by I^- was negligible both in water and during freezing (Figure S7 in the SI), which indicates that I^- and I_2 generated from IO_3^- reduction had little involvement in the degradation of FFA. The one-electron reduction of IO_4^- generates $IO_3^{\bullet}$, which is a highly reactive oxidant ($IO_4^- + 2H^+ + e^- \rightarrow IO_3^{\bullet} + H_2O$).[9,36] If the one-electron transfer from FFA to IO_4^- during freezing is kinetically favored, FFA can be degraded not only through the electron transfer mechanism (reactions 10−13) but also through radical mechanism. However, the $IO_3^{\bullet}$-mediated degradation of FFA is only conjecture at this point.

To investigate whether the pH of the aqueous IO_4^- solution really decreases and how much (if any) does the pH decrease by freezing, the UV−visible absorption spectra of cresol red (CR) as an in situ pH probe were measured before and after freezing the aqueous IO_4^- solution containing CR. The maximum absorption wavelength (λ_{max}) of CR varies according to the pH-dependent type of CR (λ_{max} = 518 nm for diprotonated CR, λ_{max} = 434 nm for monoprotonated CR, and λ_{max} = 573 nm for deprotonated CR).[31] The maximum absorbance of CR in aqueous IO_4^- solution at pH = 3.0 was observed at 434 nm

(Figure S8 in the SI) because only monoprotonated CR, which exhibits λ_{max} at 434 nm, exists at pH = 3.0 (see Figure S9 in the SI). The λ_{max} of CR was shifted from 434 nm to 518 nm (i.e., most monoprotonated CR was changed to diprotonated CR) after freezing (Figure S8 in the SI), which indicates that the pH of aqueous IO_4^- solution decreased by freezing. The ratio of [monoprotonated CR] to [diprotonated CR] after freezing was obtained from Figure S8 in the SI and eq 8 and estimated to be approximately 1 to 7.1 (i.e., [monoprotonated CR]/[diprotonated CR] = 0.14). Based on eq 9, the pH of the frozen IO_4^- solution was estimated to be approximately 0.2. The pH decrease from 3.0 to 0.2 by freezing is consistent with the previous result that the pH decreases by 2−4 by freezing.[18]

To provide convincing evidence that supports the activation of IO_4^- by the freezing-induced pH decrease, the degradation of FFA in water was investigated at high concentration of IO_4^- and/or low pH (Figure 2). The degradation of FFA in water was negligible at [IO_4^-] = 100 μM and pH = 3.0. An increase in the IO_4^- concentration by 100 times (100 μM → 10 mM) at pH = 3.0 also did not induce the degradation of FFA. However, the degradation of FFA in water proceeded when the pH decreased by 2 (3.0 → 1.0) at [IO_4^-] = 100 μM. This result clearly indicates that the pH decrease by freezing is primarily responsible for the degradation of FFA by IO_4^-. The degradation of FFA at pH = 1.0 was accelerated when the concentration of IO_4^- increased by 100 times (100 μM → 10 mM). Overall, the decrease in pH and the increase in the IO_4^- concentration in liquid brine by freezing facilitates the proton-coupled degradation processes (reactions 10−13) and enhances the degradation kinetics, respectively. It should be noted that the degradation of FFA during freezing at [IO_4^-] = 100 μM and pH = 3.0 was much faster than that in water at [IO_4^-] = 10 mM and pH = 1.0 (practically possible limit). This should be because freezing increases the concentrations of IO_4^- and protons in the liquid brine much greater than 100 times. In addition, the concentration of FFA in liquid brine should also increase during freezing, which increases the degradation rate of FFA by increasing the chance of contact between IO_4^- and FFA.

Freezing-Induced Degradation of FFA in the Presence of IO_4^- under Various Conditions. The effect of IO_4^- concentration, pH, and freezing temperature on the IO_4^--mediated degradation of FFA during freezing was investigated (Figure 3). The degradation of FFA by IO_4^- in water was negligible under experimental conditions identical to those of Figure 3 except for the reaction temperature. The degradation rate of FFA during freezing increased with increasing IO_4^- concentration (Figure 3a). Even 12.5 μM of IO_4^- completely degraded 20 μM of FFA, which should be ascribed to the fact that IO_3^- generated from IO_4^- reduction is also involved in the degradation of FFA. All previous

methods for the activation of IO_4^- (i.e., a UV/IO_4^- system, an ultrasound/IO_4^- system, a bimetallic nanoparticle/IO_4^- system, and a KOH/IO_4^- system) require high concentrations of IO_4^- because they cannot further activate IO_3^- that is generated from IO_4^- conversion (the concentration of the degraded pollutant is less than the concentration of added IO_4^-).[6-10] On the other hand, the freezing method can activate not only IO_4^- but also IO_3^-, which reduces the dose of IO_4^- for water treatment (the concentration of the degraded pollutant is higher than the concentration of added IO_4^-).

Figure 3b shows the pH-dependent degradation kinetics of FFA in the presence of IO_4^- during freezing. The degradation of FFA was observed below pH = 5.0 but was negligible above pH = 6.0. The pH of the aqueous IO_4^- solution at [IO_4^-] = 100 μM and under acidic conditions decreases by 2.8 after freezing (see Figure S8 in the SI and accompanying discussion). Freezing can reduce the pH from 6.0 to 3.2, which is still an unfavorable condition for the activation of IO_4^- (see Figure 2). Therefore, FFA was not degraded during freezing at the acidic pH = 6.0. Under basic conditions, hydroxides are accumulated, and the pH increases in the liquid brine by freezing, which constitutes a more unfavorable condition for the proton-coupled degradation process. In the pH range of 3−5, the degradation of FFA by IO_4^- during freezing was accelerated as the pH decreased. This behavior is because the lower pH provides a better condition for the proton-coupled degradation process.

We also investigated the effect of freezing temperature on the degradation of FFA by IO_4^- (Figure 3c). The degradation rate of FFA increased with decreasing freezing temperature. The generation of IO_3^-, I^-, and I_2 as products of IO_4^- and IO_3^- reduction was also accelerated with decreasing freezing temperature (Figure S10 in the SI). The concentrations of IO_4^-, FFA, and protons in the liquid brine gradually increase with an increase in the size of ice crystals (i.e., with decreasing volume of liquid brine) during freezing. The larger size of ice crystals (i.e., the smaller volume of liquid brine) at lower freezing temperatures produces higher concentrations of IO_4^-, FFA, and protons in the liquid brine at any reaction time. Overall, a lower freezing temperature increases the degradation rate of FFA by more rapidly concentrating IO_4^-, FFA, and protons in liquid brine.

Applicability of the IO_4^-/Freezing System for Water Treatment. To verify the applicability of the IO_4^-/freezing system for water treatment, the freezing-induced degradation of FFA in the presence of IO_4^- was repeated up to twenty cycles in the same batch by thawing the frozen sample and injecting FFA every 30 min (Figure 4). When IO_4^- (100 μM) was added only at the beginning of first cycle, the nearly complete degradation of FFA (20 μM) was achieved up to ten cycles but was reduced from eleventh cycle

(Figure 4a). Because 10 μM of IO_4^- is consumed for the degradation of 20 μM of FFA (see Figure 1), 100 μM of IO_4^- should be completely consumed after ten cycles. Therefore, the reduced degradation efficiency of FFA from eleventh cycle should be due to the complete depletion of IO_4^-. Although IO_3^-, I^-, and I_2 remain after ten cycles, only IO_3^- can act as an oxidant (see Figures S6 and S7 in the SI). Therefore, the degradation of FFA after tenth cycle (i.e., even in the absence of IO_4^-) should be due to the residual IO_3^-. However, the additional injection of IO_4^- at the beginning of eleventh cycle maintained the degradation efficiency of FFA constant up to twenty cycles (Figure 4b). A stable degradation efficiency throughout the repeated cycles before the complete depletion of IO_4^- makes the IO_4^-/freezing system a practical alternative for water treatment.

We also investigated the degradation of other organic pollutants (i.e., pharmaceutical and phenolic compounds), which are frequently used to evaluate a new water treatment system,[37,38] in the IO_4^-/freezing system (Figure 5). Cimetidine and tryptophan were selected as pharmaceutical pollutants. Phenolic pollutants used in this study include phenol, 4-chlorophenol, and bisphenol A. Although the degradation rate of the other organic pollutants during freezing was lower than that of FFA, the degradation of all organic pollutants tested in this study was clearly observed during freezing. The degradation of cimetidine by IO_4^- was observed even in water because it is very weak against the electrophilic oxidation (Figure 5a).[10] However, even if that was the case, freezing significantly accelerated the degradation of cimetidine (Figure 5b). The degradation of tryptophan, phenol, 4-chlorophenol, and bisphenol A by IO_4^-, which was negligible in water (Figure 5a), continuously proceeded during freezing (Figure 5b). In contrast to the KOH/IO_4^- system that is highly pollutant-specific,[10] the IO_4^-/freezing system can be used for the degradation of various organic pollutants. This non-selective degradation ability of the IO_4^-/freezing system improves its applicability for water treatment.

To identify which organic pollutant (i.e., chemical structure) is more effectively degraded in the IO_4^-/freezing system, the degradation rate of various substituted phenols, such as phenol, 4-chlorophenol, 2-chlorophenol, 4-bromophenol, 2-nitrophenol, 4-nitrophenol, 4-methylphenol, and 2,4-dimethylphenol, was plotted against the Hammett constant (σ^+), which quantitatively represents the electronic distribution of the substituted phenols. The degradation rates of the substituted phenols decreased with increasing Hammett constant (Figure S11 in the SI). This negative Hammett slope signifies that the degradation of more electron-rich organic pollutants proceeds more rapidly in the IO_4^-/freezing system.

The IO_4^-/freezing system for water treatment can be operated without external electrical energy in cold regions such as high-latitudes and mid-latitudes during the winter season. The freezing-induced degradation of organic pollutants in the presence of IO_4^- was tested outdoors without using a cryogenic ethanol bath (external electrical energy) to

confirm the energy-free IO_4^-/freezing system. The beaker containing the aqueous solution of IO_4^- and FFA was only set down on the ground on a cold winter night in the Republic of Korea (−15 ~ −16 °C). In contrast to laboratory experiments, which were performed in a cryogenic ethanol bath, an induction period (i.e., the time required for initiation of the degradation process) was clearly observed during the outdoor experiments. This behavior should be due to the difference between cooling methods (the ethanol cooling system for the laboratory experiments vs. an air cooling system for the outdoor experiments, see Discussion on the effect of cooling method on the induction period in the SI for details). The degradation of FFA was started after 1 h and completed within 2 h. (Figure 6). FFA was not degraded in the absence of IO_4^- under the same conditions. The outdoor experimental results propose that the IO_4^-/freezing system for water treatment is economically feasible in cold regions.

The IO_4^-/freezing system using the artificial freezing method for wastewater treatment may be impractical, because the electrical costs of freezing a large quantity of wastewater will be too high. However, the practical viability of the IO_4^-/freezing system can be established by using a natural freezing method in cold regions, because only IO_4^-, which is a cheap reagent, is required in this case. If wastewater containing IO_4^- is sprayed in the form of small drops using injection nozzles, the degradation process should be immediately initiated without an induction period due to rapid solidification. This method would make the IO_4^-/freezing system for wastewater treatment economically feasible. However, it should be noted that I^- in water treated by the IO_4^-/freezing system may contribute to the formation of toxic iodine-containing products in the chlorine (or manganese dioxide)-mediated oxidation process.[39,40] Therefore, the subsequent cost-effective methods for the removal of iodide, such as adsorption, precipitation, membrane, and ion-exchange,[41-44] should be employed in conjunction with the IO_4^-/freezing system as needed.

4. Conclusion

We investigated the degradation of aqueous organic pollutants by IO_4^- during freezing. Although the degradation of most organic pollutants was negligible in water, it proceeded rapidly during freezing. This unique behavior observed during freezing is due to a freeze concentration effect that provides a favorable site (i.e., liquid brine) for the proton-coupled degradation (i.e., the proton-coupled electron transfer) process by concentrating IO_4^-, organic pollutants, and protons in the liquid brine among the ice crystals. The electron transfer from organic pollutants to IO_4^- during freezing results in the degradation of organic pollutants accompanied by the production of IO_3^-. IO_3^- is further converted to I^- and I_2 as a result of electron transfer from organic pollutants to IO_3^-. Because freezing can

activate not only IO_4^- but also IO_3^- generated from IO_4^- reduction, the freezing method can degrade more organic pollutants than other methods for IO_4^- activation at the same IO_4^- dose. The degradation efficiency of the IO_4^-/freezing system is stable throughout the repeated cycles before IO_4^- is completely depleted. The IO_4^-/freezing system can degrade a variety of organic pollutants (i.e., its application is not restricted to a specific pollutant). In particular, the IO_4^-/freezing system has the potential to be more economical in cold regions because external electrical energy for freezing is not required.

5. References

(1) Kristiansen, K. A.; Potthast, A.; Christensen, B. E. Periodate oxidation of polysaccharides for modification of chemical and physical properties. *Carbohydr. Res.* **2010**, *345*, 1264-1271.

(2) Coseri, S.; Biliuta, G.; Zemljič, L. F.; Srndovic, J. S.; Larsson, P. T.; Strnad, S.; Kreže, T.; Naderi, A.; Lindström, T. One-shot carboxylation of microcrystalline cellulose in the presence of nitroxyl radicals and sodium periodate. *RSC Adv.* **2015**, *5*, 85889-85897.

(3) Kristiansen, K. A.; Tomren, H. B.; Christensen, B. E. Periodate oxidized alginates: depolymerization kinetics. *Carbohydr. Polym.* **2011**, *86*, 1595-1601.

(4) Clamp, J. R.; Hough, L. Some observations on the periodate oxidation of amino compounds. *Biochem. J.* **1966**, *101*, 120-126.

(5) Kamimura, A.; Nokubi, T.; Nasu, K.; Takechi, Y.; Ishihara, Y.; Kato, K.; Noguchi, S.; Watanabe, M.; Shirai, M.; Sumimoto, M.; Uno, H. Facile synthesis of quinone dimer derivatives substituted with sulfanyl groups and their properties. *Chem. Lett.* **2012**, *41*, 950-951.

(6) Chia, L.-H.; Tang, X.; Weavers, L. K. Kinetics and mechanism of photoactivated periodate reaction with 4-chlorophenol in acidic solution. *Environ. Sci. Technol.* **2004**, *38*, 6875-6880.

(7) Lee, C.; Yoon, J. Application of photoactivated periodate to the decolorization of reactive dye: reaction parameters and mechanism. *J. Photochem. Photobiol., A* **2004**, *165*, 35-41.

(8) Lee, Y.-C.; Chen, M.-J.; Huang, C.-P.; Kuo, J.; Lo, S.-L. Efficient sonochemical degradation of perfluorooctanoic acid using periodate. *Ultrason. Sonochem.* **2016**, *31*, 499-505.

(9) Lee, H.; Yoo, H.-Y.; Choi, J.; Nam, I.-H.; Lee, S.; Lee, S.; Kim, J.-H.; Lee, C.; Lee, J. Oxidizing capacity of periodate activated with iron-based bimetallic

nanoparticles. *Environ. Sci. Technol.* **2014**, *48*, 8086-8093.

(10) Bokare, A. D.; Choi, W. Singlet-oxygen generation in alkaline periodate solution. *Environ. Sci. Technol.* **2015**, *49*, 14392-14400.

(11) Bartels-Rausch, T.; Jacobi, H.-W.; Kahan, T. F.; Thomas, J. L.; Thomson, E. S.; Abbatt, J. P. D.; Ammann, M.; Blackford, J. R.; Bluhm, H.; Boxe, C.; Domine, F.; Frey, M. M.; Gladich, I.; Guzmán, M. I.; Heger, D.; Huthwelker, T.; Klán, P.; Kuhs, W. F.; Kuo, M. H.; Maus, S.; Moussa, S. G.; McNeill, V. F.; Newberg, J. T.; Pettersson, J. B. C.; Roeselová, M.; Sodeau, J. R. A review of air-ice chemical and physical interactions (AICI): liquids, quasi-liquids, and solids in snow. *Atmos. Chem. Phys.* **2014**, *14*, 1587-1633.

(12) O'Concubhair, R.; Sodeau, J. R. The effect of freezing on reactions with environmental impact. *Acc. Chem. Res.* **2013**, *46*, 2716-2724.

(13) Park, S.-C.; Moon, E.-S.; Kang, H. Some fundamental properties and reactions of ice surfaces at low temperatures. *Phys. Chem. Chem. Phys.* **2010**, *12*, 12000-12011.

(14) Kong, X.; Thomson, E. S.; Papagiannakopoulos, P.; Johansson, S. M.; Pettersson, J. B. C. Water accommodation on ice and organic surfaces: insights from environmental molecular beam experiments. *J. Phys. Chem. B* **2014**, *118*, 13378-13386.

(15) Heger, D.; Jirkovský, J.; Klán, P. Aggregation of methylene blue in frozen aqueous solutions studied by absorption spectroscopy. *J. Phys. Chem. A* **2005**, *109*, 6702-6709.

(16) Grannas, A. M.; Bausch, A. R.; Mahanna, K. M. Enhanced aqueous photochemical reaction rates after freezing. *J. Phys. Chem. A* **2007**, *111*, 11043-11049.

(17) Takenaka, N.; Bandow, H. Chemical kinetics of reactions in the unfrozen solution of ice. *J. Phys. Chem. A* **2007**, *111*, 8780-8786.

(18) Heger, D.; Klánová, J.; Klán, P. Enhanced protonation of cresol red in acidic aqueous solutions caused by freezing. *J. Phys. Chem. B* **2006**, *110*, 1277-1287.

(19) Takenaka, N.; Ueda, A.; Daimon, T.; Bandow, H.; Dohmaru, T.; Maeda, Y. Acceleration mechanism of chemical reaction by freezing: the reaction of nitrous acid with dissolved oxygen. *J. Phys. Chem.* **1996**, *100*, 13874-13884.

(20) Takenaka, N.; Ueda, A.; Maeda, Y. Acceleration of the rate of nitrite oxidation by freezing in aqueous solution. *Nature* **1992**, *358*, 736-738.

(21) Kim, K.; Kim, J.; Bokare, A. D.; Choi, W.; Yoon, H.-I.; Kim, J. Enhanced removal of hexavalent chromium in the presence of H_2O_2 in frozen aqueous solutions. *Environ. Sci. Technol.* **2015**, *49*, 10937-10944.

KOPRI 극지연구소

(22) Kim, K.; Choi, W. Enhanced redox conversion of chromate and arsenite in ice. *Environ. Sci. Technol.* **2011**, *45*, 2202-2208.

(23) Ju, J.; Kim, J.; Vetráková, Ľ.; Seo, J.; Heger, D.; Lee, C.; Yoon, H.-I.; Kim, K.; Kim, J. Accelerated redox reaction between chromate and phenolic pollutants during freezing. *J. Hazard. Mater.* **2017**, *329*, 330-338.

(24) Kim, K.; Chung, H. Y.; Ju, J.; Kim, J. Freezing-enhanced reduction of chromate by nitrite. *Sci. Total Environ.* **2017**, *590-591*, 107-113.

(25) Min, D. W.; Choi, W. Accelerated reduction of bromate in frozen solution. *Environ. Sci. Technol.* **2017**, *51*, 8368-8375.

(26) Kitada, K.; Suda, Y.; Takenaka, N. Acceleration and reaction mechanism of the *N*-nitrosation reaction of dimethylamine with nitrite in ice. *J. Phys. Chem. A* **2017**, *121*, 5383-5388.

(27) Sun, F.; Xiao, Y.; Wu, D.; Zhu, W.; Zhou, Y. Nitrite-driven abiotic transformation of sulfonamide micropollutants during freezing process. *Chem. Eng. J.* **2017**, *327*, 1128-1134.

(28) Awtrey, A. D.; Connick, R. E. The absorption spectra of I_2, I_3^-, I^-, IO_3^-, $S_4O_6^=$ and $S_2O_3^=$. heat of the reaction $I_3^- = I_2 + I^-$. *J. Am. Chem. Soc.* **1951**, *73*, 1842-1843.

(29) Vetráková, Ľ.; Vykoukal, V.; Heger, D. Comparing the acidities of aqueous, frozen, and freeze-dried phosphate buffers: is there a "pH memory" effect? *Int. J. Pharm.* **2017**, *530*, 316-325.

(30) Krausková, Ľ.; Procházková, J.; Klašková, M.; Filipová, L.; Chaloupková, R.; Malý, S.; Damborský, J.; Heger, D. Suppression of protein inactivation during freezing by minimizing pH changes using ionic cryoprotectants. *Int. J. Pharm.* **2016**, *509*, 41-49.

(31) Rottman, C.; Grader, G.; Hazan, Y. D.; Melchior, S.; Avnir, D. Surfactant-induced modification of dopants reactivity in sol-gel matrixes. *J. Am. Chem. Soc.* **1999**, *121*, 8533-8543.

(32) Perrin, D. D. Buffers of low ionic strength for spectrophotometric p*K* determinations. *Aust. J. Chem.* **1963**, *16*, 572-578.

(33) Dean, J. A. Lange's Handbook of Chemistry, 14th, ed.; McGraw-Hill: New York, 1992.

(34) Weavers, L. K.; Hua, I.; Hoffmann, M. R. Degradation of triethanolamine and chemical oxygen demand reduction in wastewater by photoactivated periodate. *Water Environ. Res.* 1997, *69*, 1112-1119.

(35) Lide, D. R., *CRC Handbook of Chemistry and Physics*, 77th, ed.; CRC Press: Boca

KOPRI 극지연구소

Raton, Florida, 1996.

(36) Yun, E.-T.; Yoo, H.-Y.; Kim, W.; Kim, H.-E.; Kang, G.; Lee, H.; Lee, S.; Park, T.; Lee, C.; Kim, J.-H.; Lee, J. Visible-light-induced activation of periodate that mimics dye-sensitization of TiO_2: simultaneous decolorization of dyes and production of oxidizing radicals. *Appl. Catal., B* **2017**, *203*, 475-484.

(37) Maeng, S. K.; Cho, K.; Jeong, B.; Lee, J.; Lee, Y.; Lee, C.; Choi, K. J.; Hong, S. W. Substrate-immobilized electrospun TiO_2 nanofibers for photocatalytic degradation of pharmaceuticals: the effects of pH and dissolved organic matter characteristics. *Water Res.* **2015**, *86*, 25-34.

(38) Ramasundaram, S.; Seid, M. G.; Lee, W.; Kim, C. U.; Kim, E.-J.; Hong, S. W.; Choi, K. J. Preparation, characterization, and application of TiO_2-patterned polyimide film as a photocatalyst for oxidation of organic contaminants. *J. Hazard. Mater.* **2017**, *340*, 300-308.

(39) Hua, G.; Reckhow, D. A.; Kim, J. Effect of bromide and iodide ions on the formation and speciation of disinfection byproducts during chlorination. *Environ. Sci. Technol.* 2006, *40*, 3050-3056.

(40) Gallard, H.; Allard, S.; Nicolau, R.; von Gunten, U.; Croué, J. P. Formation of iodinated organic compounds by oxidation of iodide-containing waters with manganese dioxide. *Environ. Sci. Technol.* **2009**, *43*, 7003-7009.

(41) Zhang, X.; Gu, P.; Zhou, S.; Li, X.; Zhang, G.; Dong, L. Enhanced removal of iodide ions by nano Cu_2O/Cu modified activated carbon from simulated wastewater with improved countercurrent two-stage adsorption. *Sci. Total Environ.* **2018**, *626*, 612-620.

(42) Liu, Y.; Gu, P.; Yang, Y.; Jia, L.; Zhang, M.; Zhang, G. Removal of radioactive iodide from simulated liquid waste in an integrated precipitation reactor and membrane separator (PR-MS) system. *Sep. Purif. Technol.* **2016**, *171*, 221-228.

(43) Zhang, X.; Gu, P.; Li, X.; Zhang, G. Efficient adsorption of radioactive iodide ion from simulated wastewater by nano Cu_2O/Cu modified activated carbon. *Chem. Eng. J.* **2017**, *322*, 129-139.

(44) Hoskins, J. S.; Karanfil, T. Removal and sequestration of iodide using silver-impregnated activated carbon. *Environ. Sci. Technol.* **2002**, *36*, 784-789.

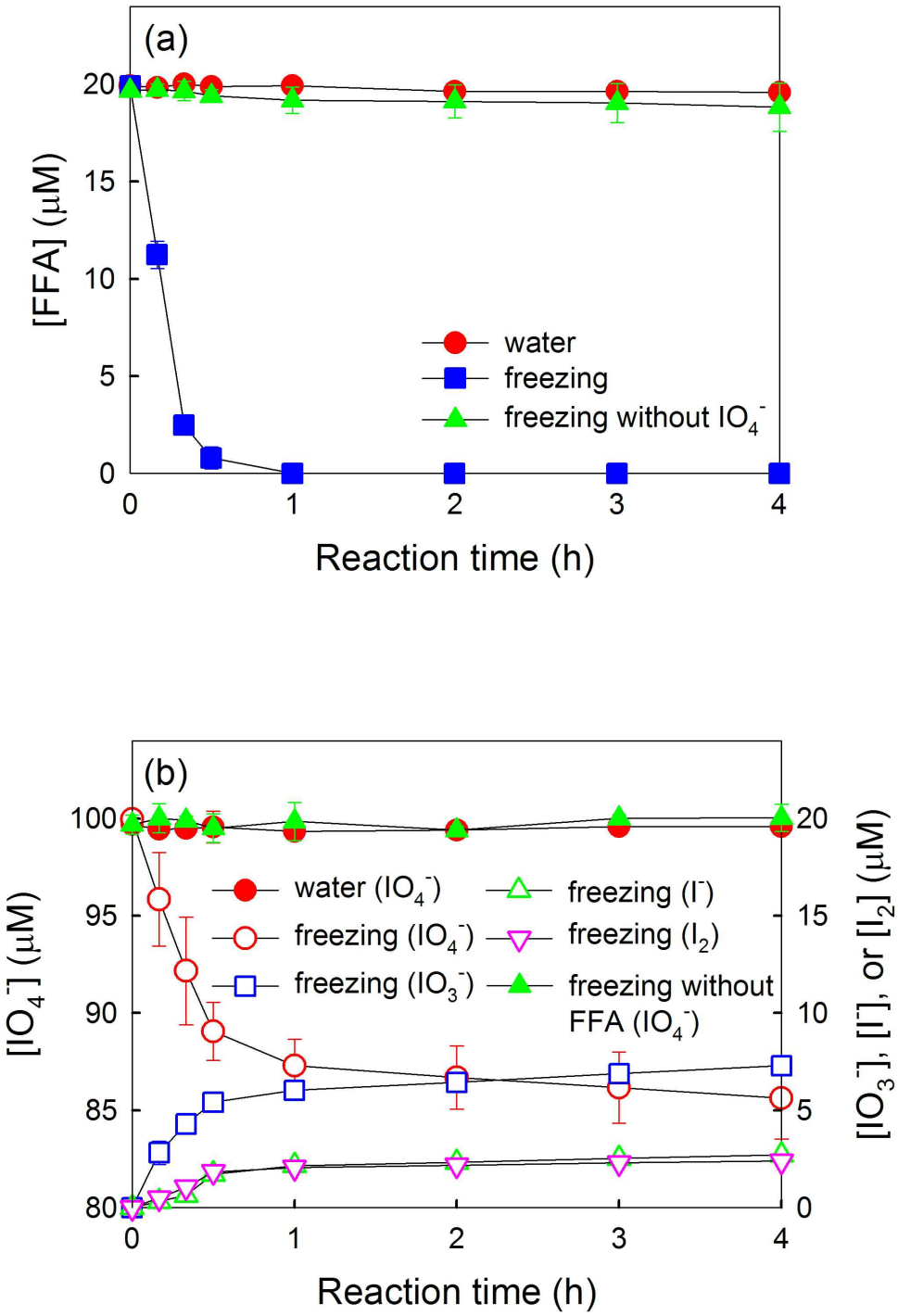

Figure 1. (a) Degradation of FFA in the presence of IO_4^- and (b) the concurrent production of IO_3^-, I^-, and I_2 in water and during freezing. Experimental conditions were as follows: $[IO_4^-]$ = 100 μM, [FFA] = 20 μM, pH = 3.0, water temperature = 25 °C, and freezing temperature = −20 °C.

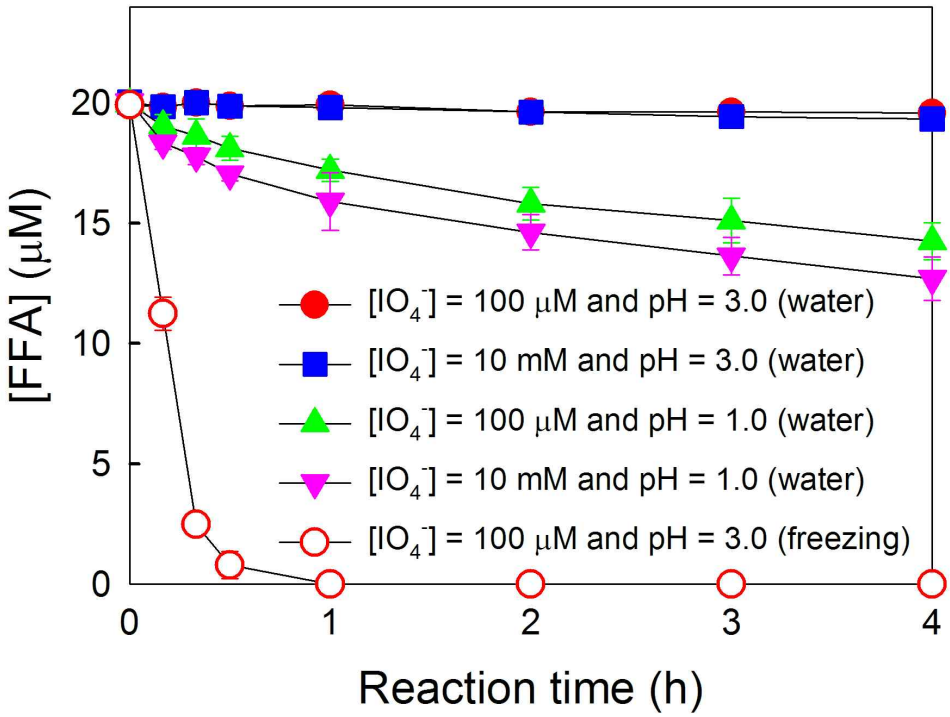

Figure 2. Effect of IO_4^- concentration increase and/or pH decrease on the degradation of FFA by IO_4^- in water. Experimental conditions were as follows: [IO_4^-] = 100 μM or 10 mM, [FFA] = 20 μM, pH = 3.0 or 1.0, water temperature = 25 °C, and freezing temperature = −20 °C.

KOPRI 극지연구소

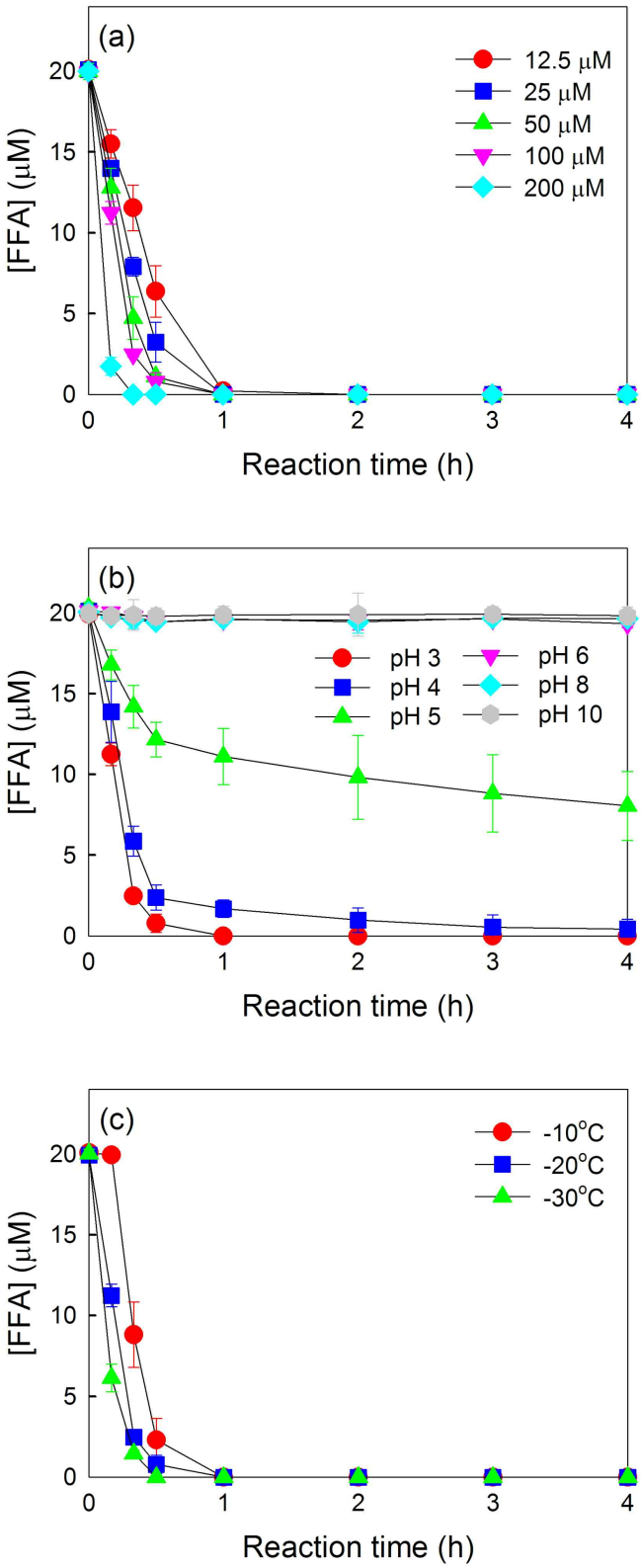

Figure 3. Effect of (a) IO_4^- concentration, (b) pH, and (c) freezing temperature on the IO_4^--mediated degradation of FFA during freezing. Experimental conditions were as follows: $[IO_4^-]$ = 100 μM for parts b and c, [FFA] = 20 μM, pH = 3.0 for parts a and c, and freezing temperature = −20 °C for parts a and b.

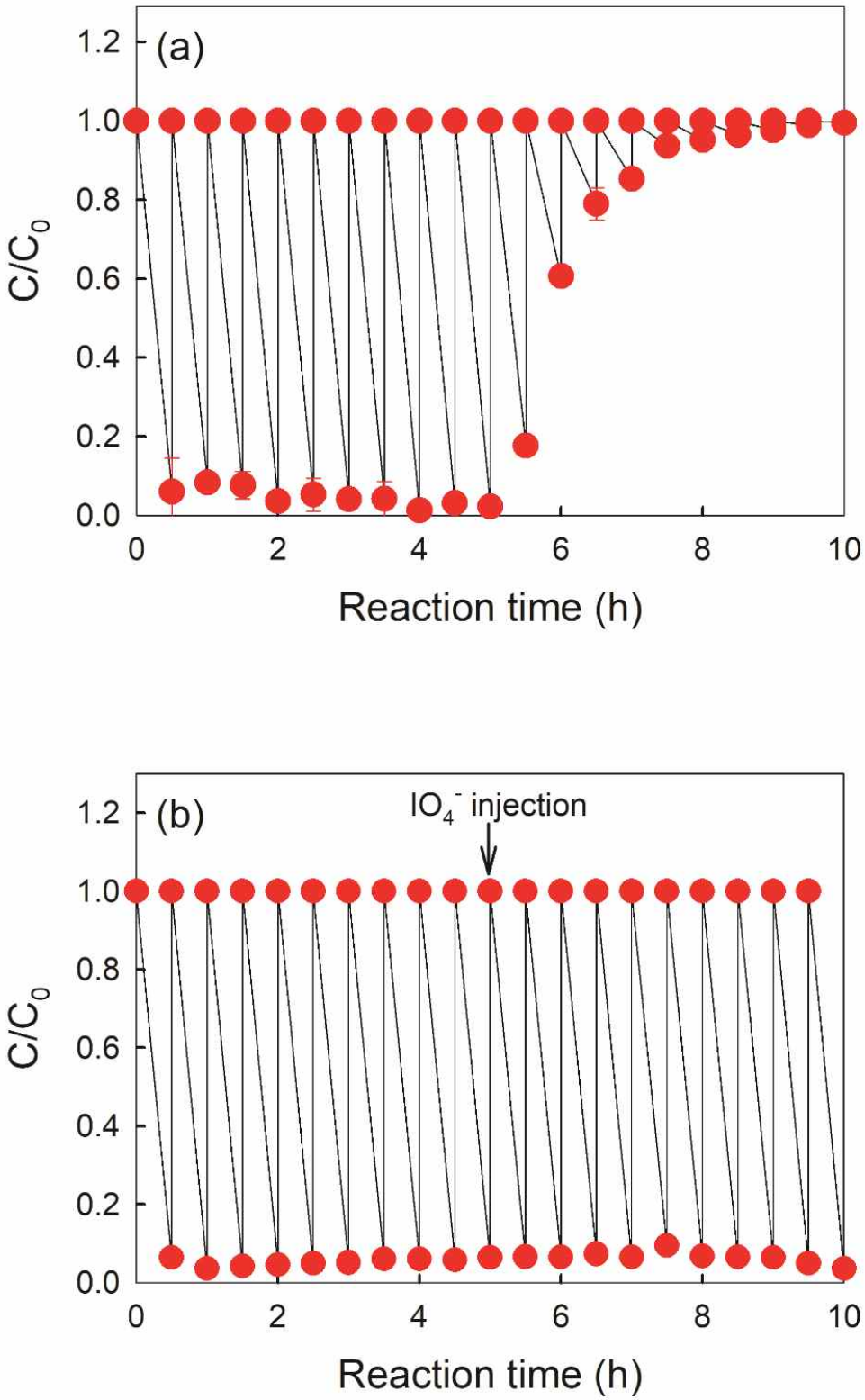

Figure 4. Repeated cycles of FFA degradation by IO_4^- during freezing. FFA was injected at the beginning of each cycle (i.e., every 30 min). For part a, IO_4^- was added only at the beginning of first cycle. For part b, IO_4^- was additionally injected at the beginning of eleventh cycle. Experimental conditions were as follows: initial and injected [IO_4^-] = 100 μM, initial and injected [FFA] = 20 μM, pH = 3.0, and freezing temperature = −20 °C.

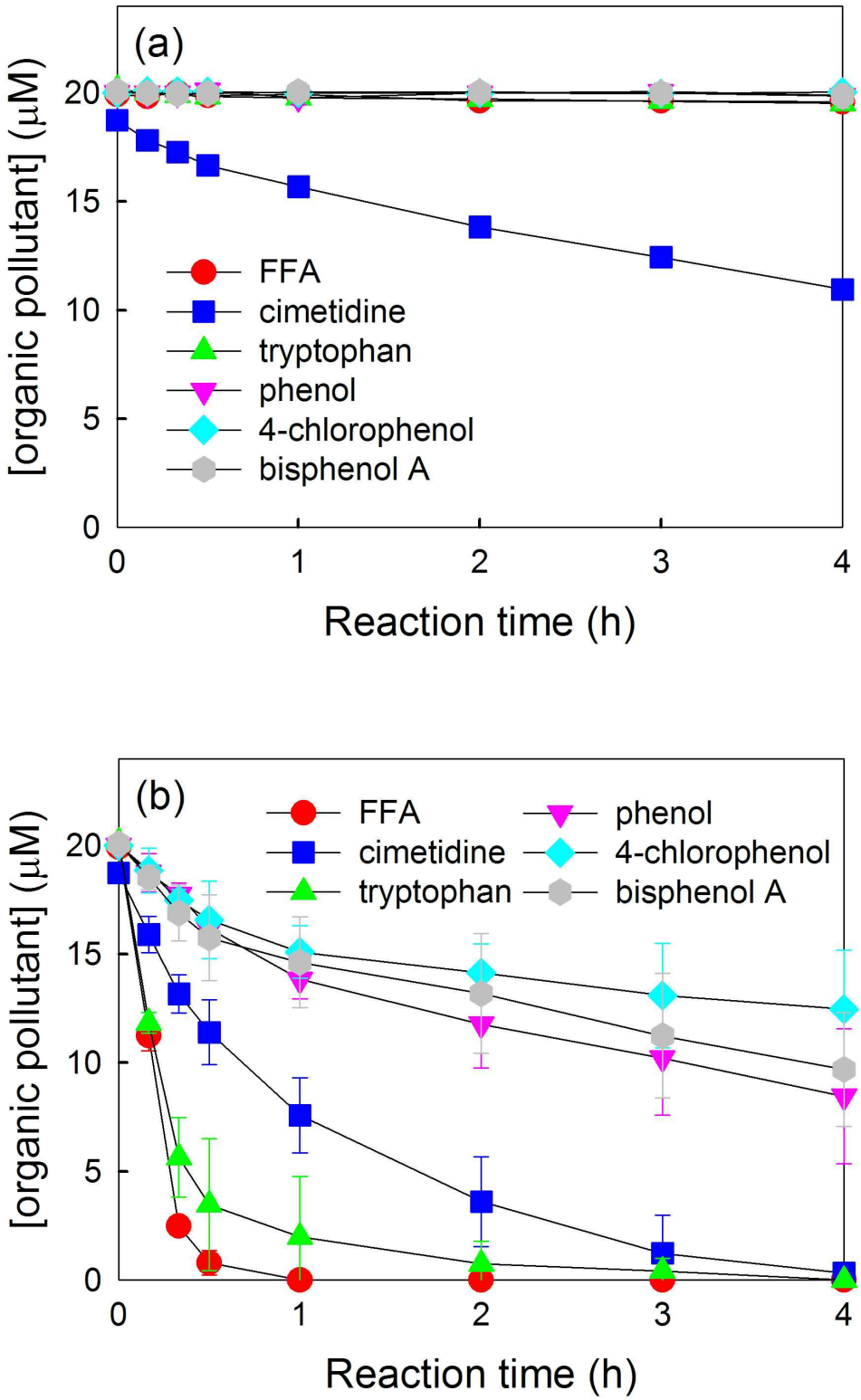

Figure 5. Time profiles of the degradation of various organic pollutants (FFA, cimetidine, tryptophan, phenol, 4-chlorophenol, and bisphenol A) by IO_4^- (a) in water and (b) during freezing. Experimental conditions were as follows: [IO_4^-] = 100 μM, [organic pollutant] = 20 μM, pH = 3.0, water temperature = 25 °C, and freezing temperature = −20 °C.

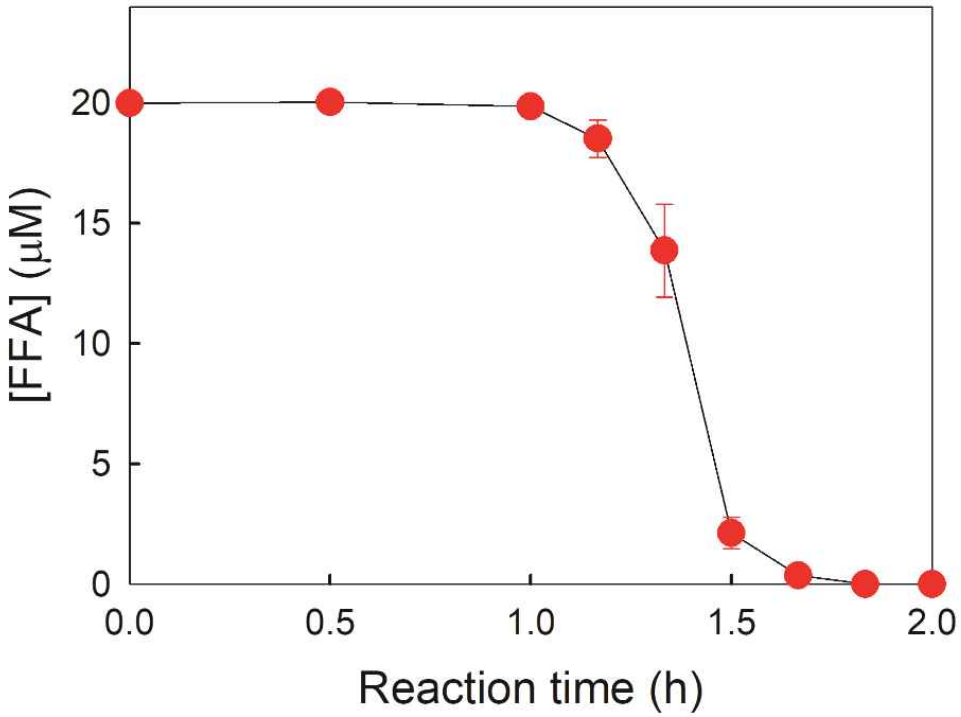

Figure 6. Degradation of FFA in the presence of IO_4^- during freezing (outdoor experiments on a cold winter night in the Republic of Korea). Experimental conditions were as follows: [IO_4^-] = 100 μM, [FFA] = 20 μM, pH = 3.0, and temperature = −15 ~ −16 °C.

KOPRI 극지연구소

Supporting Information

Equations S1-S5

$$H_5IO_6 \leftrightarrow H_4IO_6^- + H^+,\ pK_{a1} = 1.64 \quad (S1)$$

$$H_4IO_6^- \leftrightarrow H_3IO_6^{2-} + H^+,\ pK_{a2} = 8.36 \quad (S2)$$

$$H_3IO_6^{2-} \leftrightarrow H_2IO_6^{3-} + H^+,\ pK_{a3} = 12.20 \quad (S3)$$

$$H_4IO_6^- \leftrightarrow IO_4^- + 2H_2O,\ K_D = 40 \quad (S4)$$

$$2H_3IO_6^{2-} \leftrightarrow H_2I_2O_{10}^{4-} + 2H_2O,\ K_X = 141\ M^{-1} \quad (S5)$$

Equilibria among various iodine^{VII} species, where pK_{a1}, pK_{a2}, and pK_{a3} are the acid dissociation constants, and K_D and K_X are dehydration and dimerization constants, respectively.[S1]

KOPRI
극지연구소

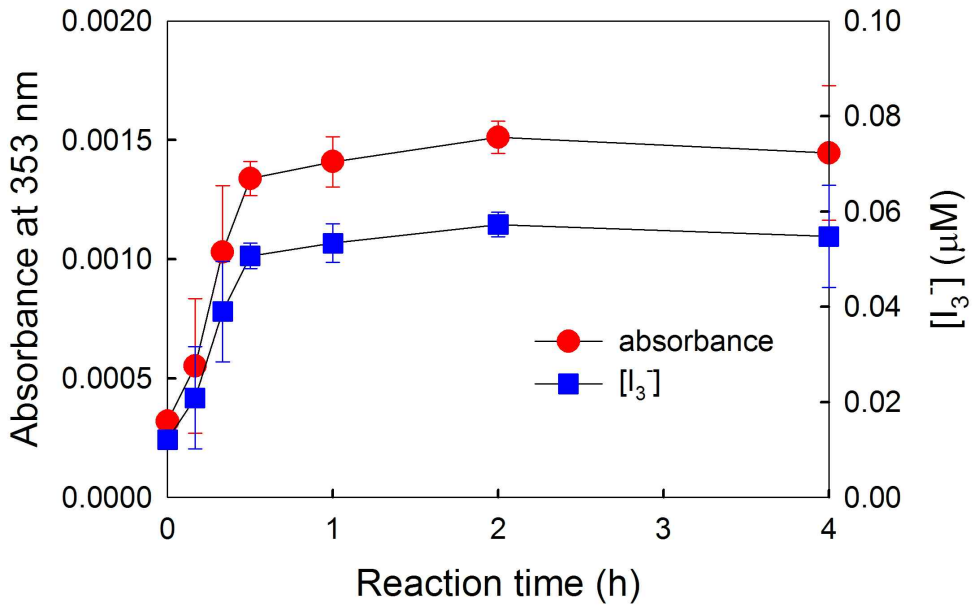

Figure S1. Time profiles of the increase of absorbance at 353 nm and the corresponding production of I_3^- in the presence of IO_4^- and FFA during freezing. Experimental conditions were as follows: $[IO_4^-]$ = 100 μM, [FFA] = 20 μM, pH = 3.0, and freezing temperature = −20 °C. The concentration of I_3^- was calculated by assuming that the absorbance at 353 nm is only due to the generation of I_3^-.

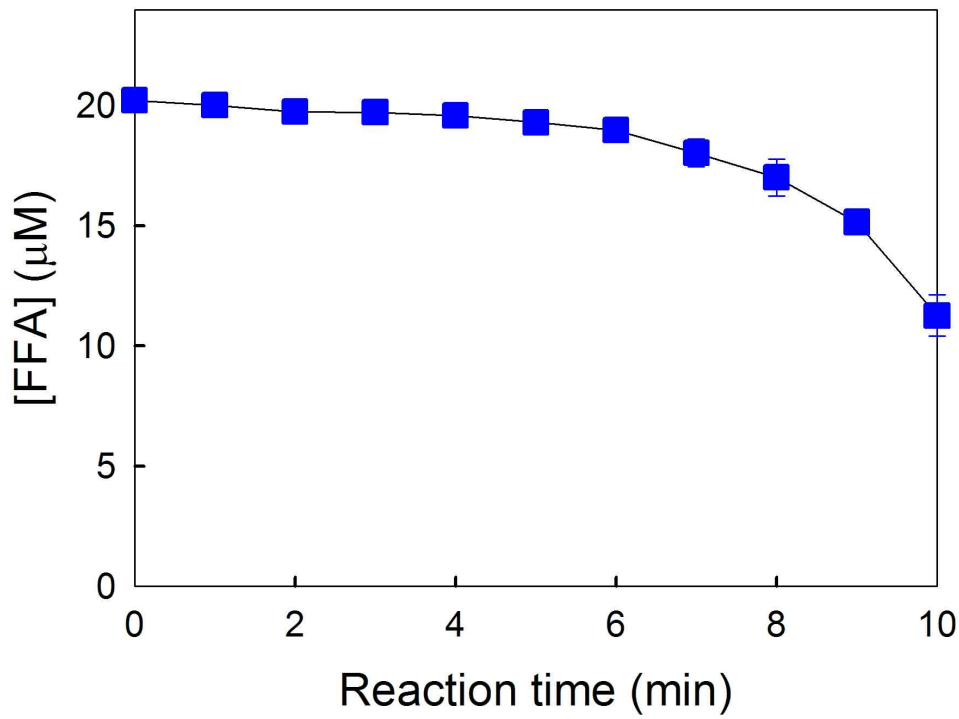

Figure S2. Degradation of FFA in the presence of IO_4^- during freezing. Experimental conditions were as follows: $[IO_4^-]$ = 100 μM, [FFA] = 20 μM, pH = 3.0, and freezing temperature = −20 °C.

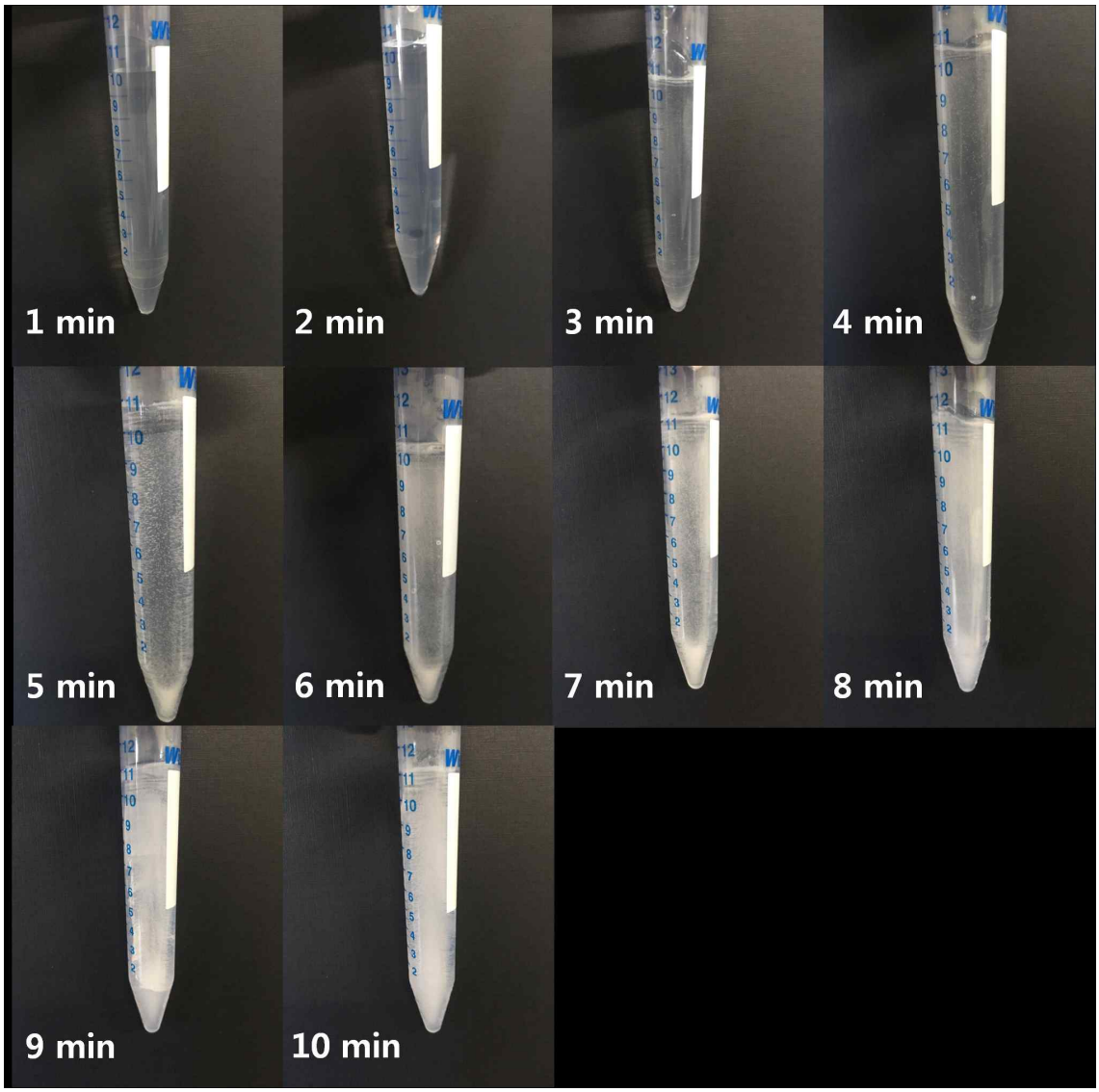

Figure S3. Degree of solidification of the solution containing IO_4^- and FFA as a function of reaction time. Experimental conditions were as follows: [IO_4^-] = 100 μM, [FFA] = 20 μM, pH = 3.0, and freezing temperature = −20 °C.

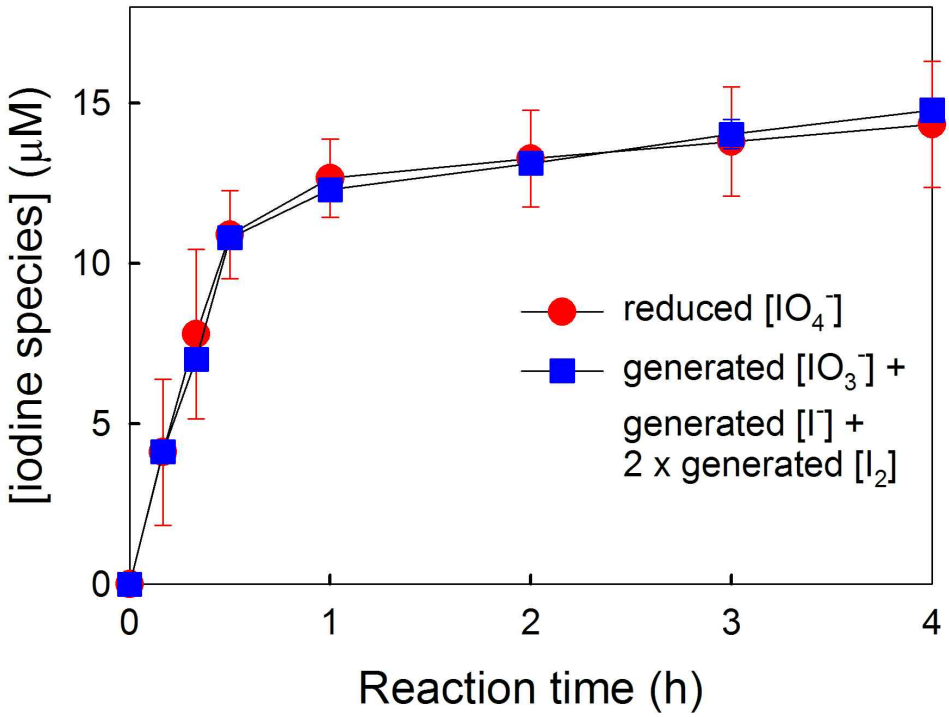

Figure S4. Total iodine mass balance (i.e., reduced [IO_4^-] vs. generated [IO_3^-] + generated [I^-] + 2 × generated [I_2]) in the course of FFA degradation by IO_4^- (IO_4^- reduction by FFA) during freezing. Experimental conditions were as follows: [IO_4^-] = 100 μM, [FFA] = 20 μM, pH = 3.0, and freezing temperature = −20 °C.

KOPRI 극지연구소

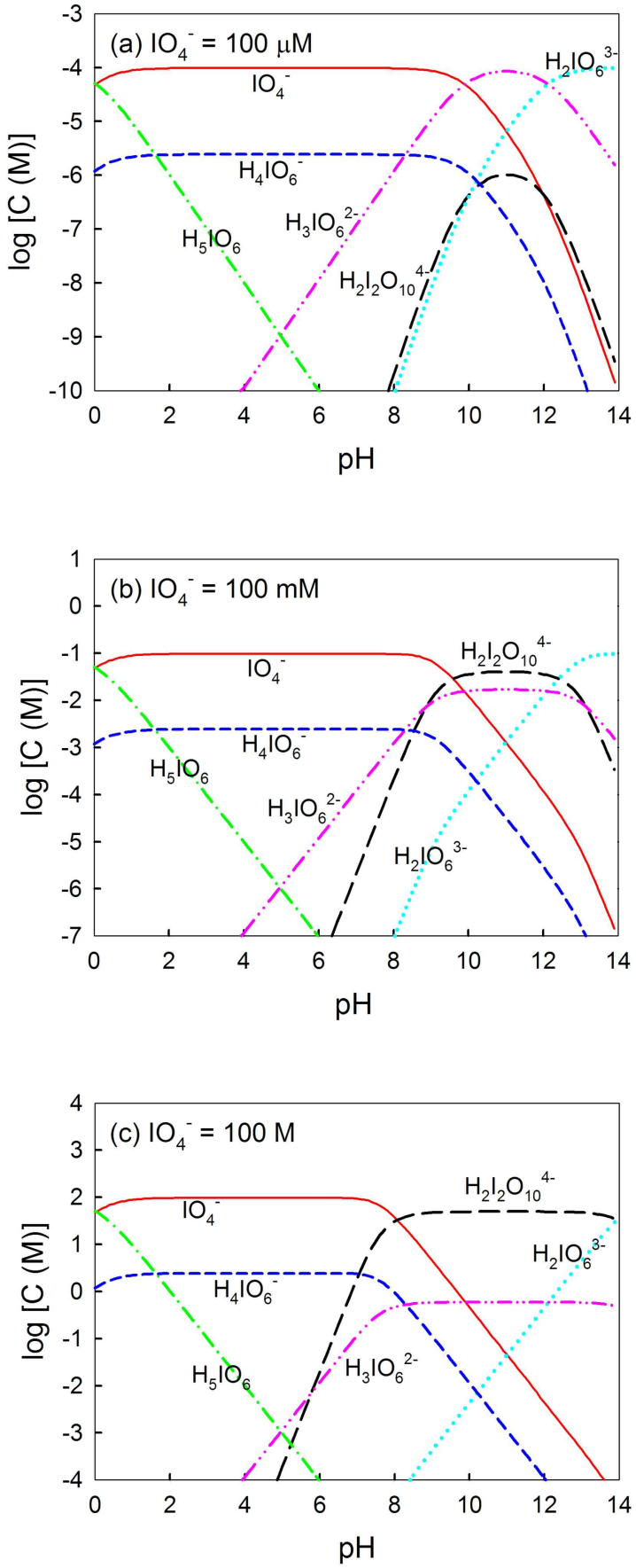

Figure S5. pH-dependent speciation of IO_4^- at [IO_4^-] = (a) 100 μM, (b) 100 mM, and (c) 100 M.

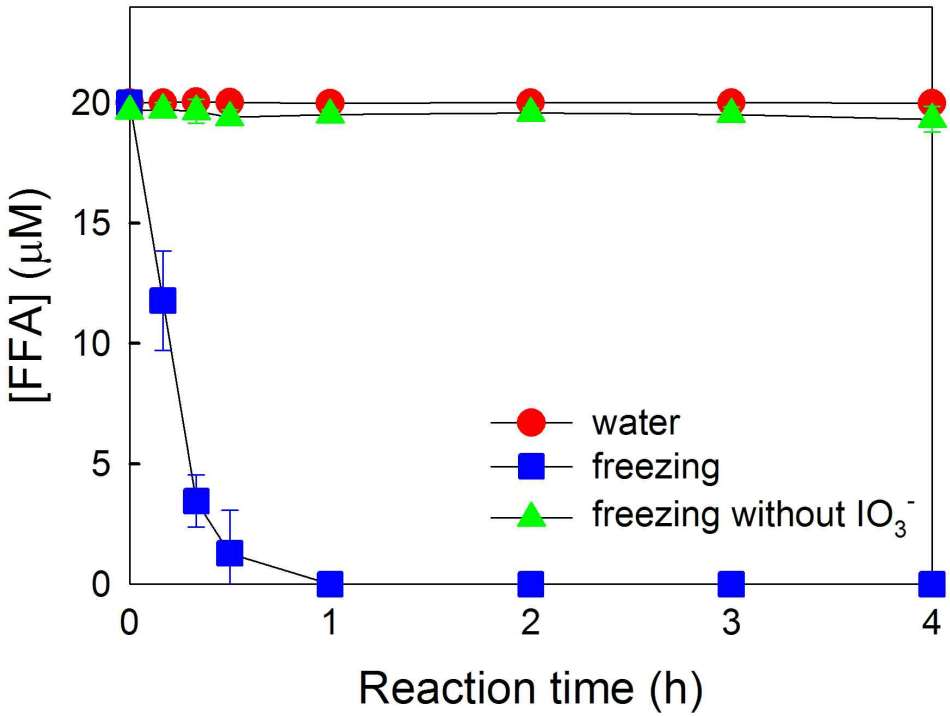

Figure S6. Degradation of FFA in the presence of IO_3^- in water and during freezing. Experimental conditions were as follows: $[IO_3^-]$ = 100 μM, [FFA] = 20 μM, pH = 3.0, water temperature = 25 °C, and freezing temperature = −20 °C.

KOPRI 극지연구소

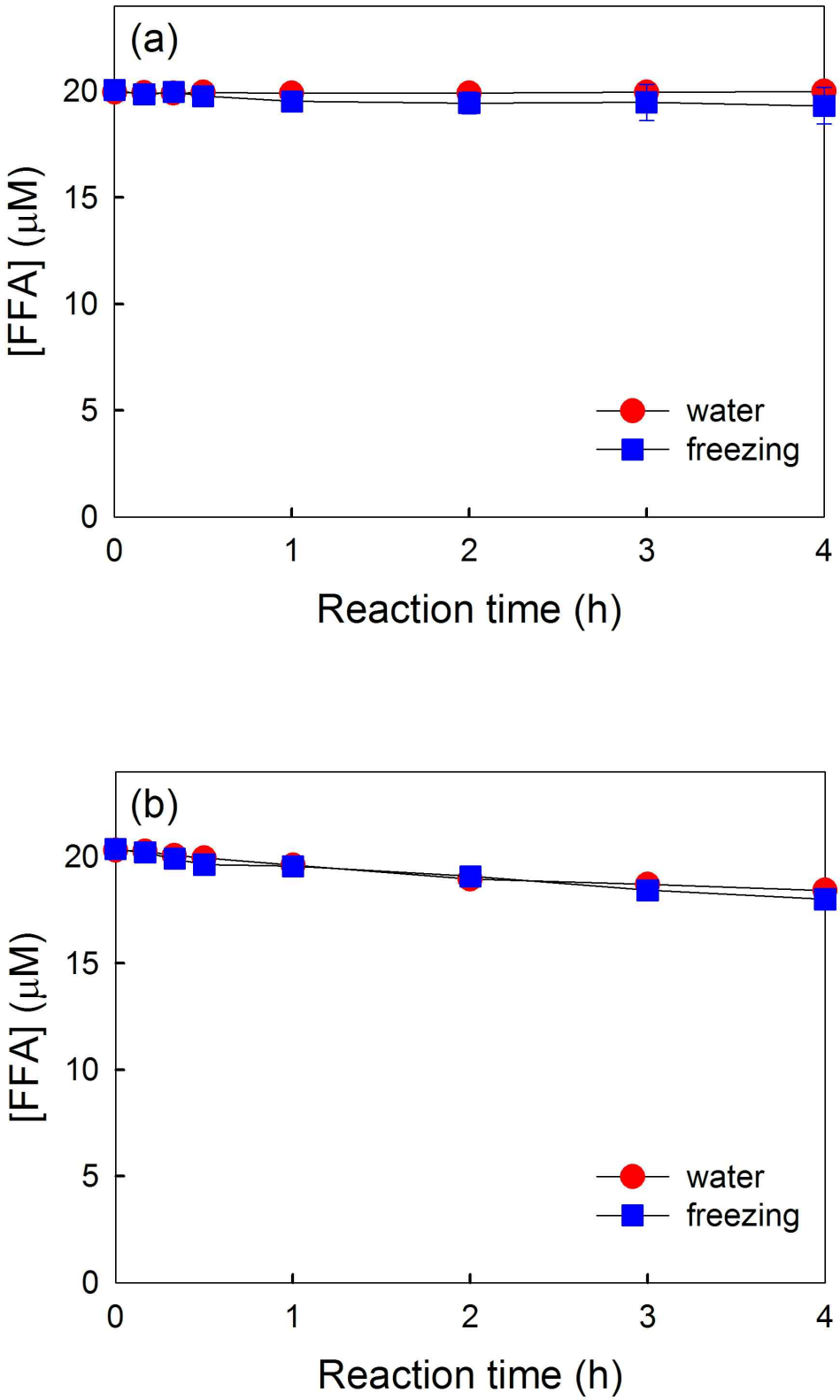

Figure S7. Degradation of FFA in the presence of (a) I^- and (b) I_2 in water and during freezing. Experimental conditions were as follows: $[I^-]$ = 100 μM for part a, $[I_2]$ = 100 μM for part b, [FFA] = 20 μM, pH = 3.0, water temperature = 25 °C, and freezing temperature = −20 °C.

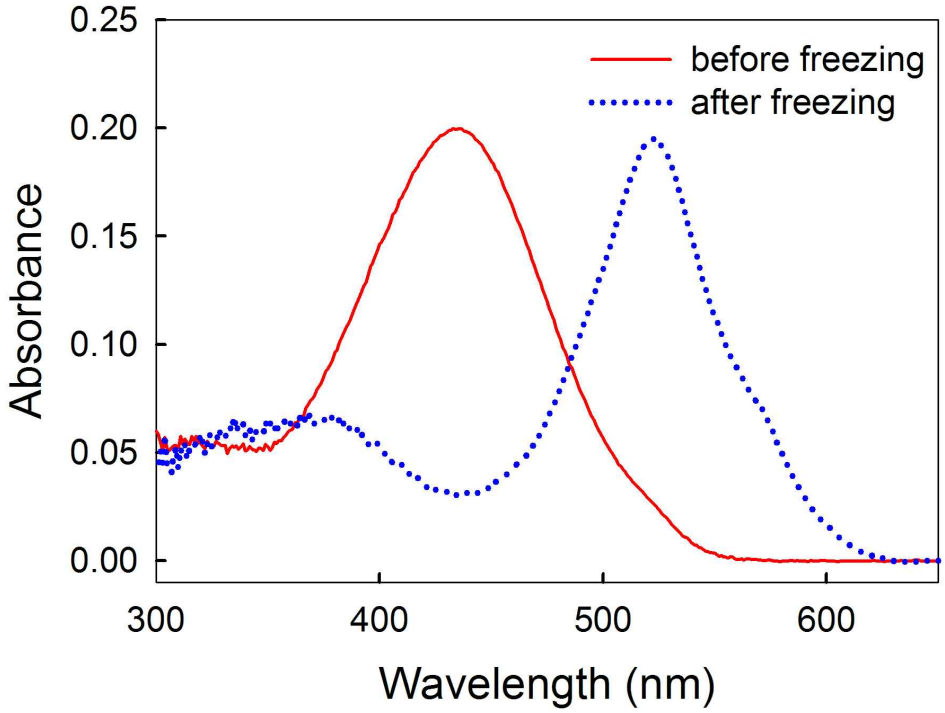

Figure S8. UV−visible absorption spectra of CR as an in situ pH probe before and after freezing the aqueous solution of IO4− and CR. Experimental conditions were as follows: [IO4−] = 100 μM, [CR] = 20 μM, pH = 3.0, water temperature = 25 °C, and freezing temperature = −20 °C.

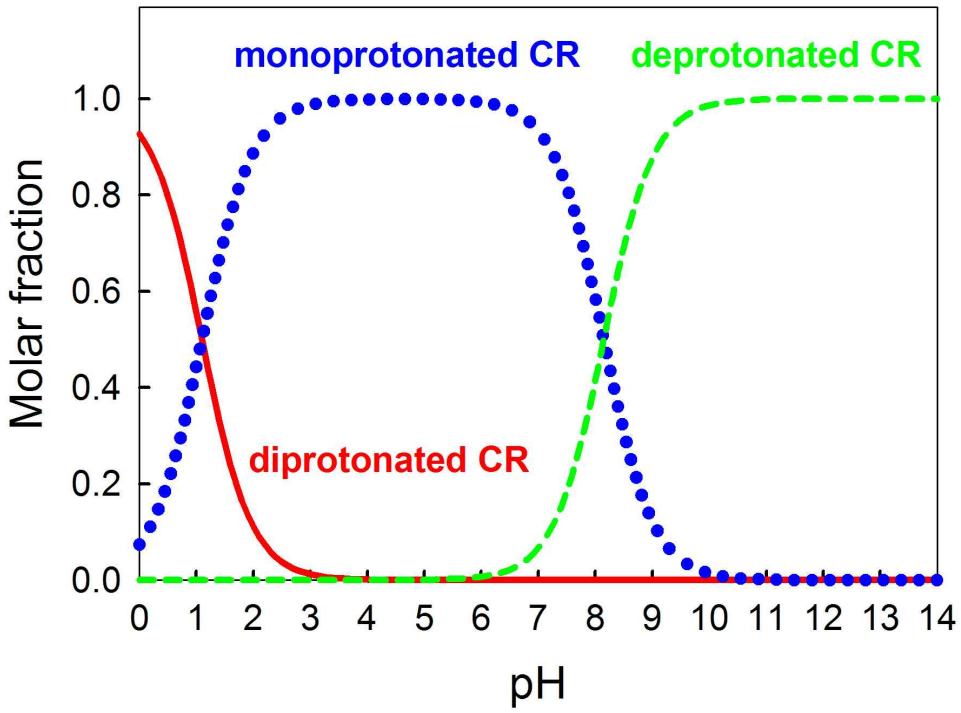

Figure S9. pH-dependent speciation of cresol red (CR). The acid dissociation constants (pK_a) of CR were obtained from references S2 and S3 (pK_{a1} = 1.10 and pK_{a2} = 8.15).

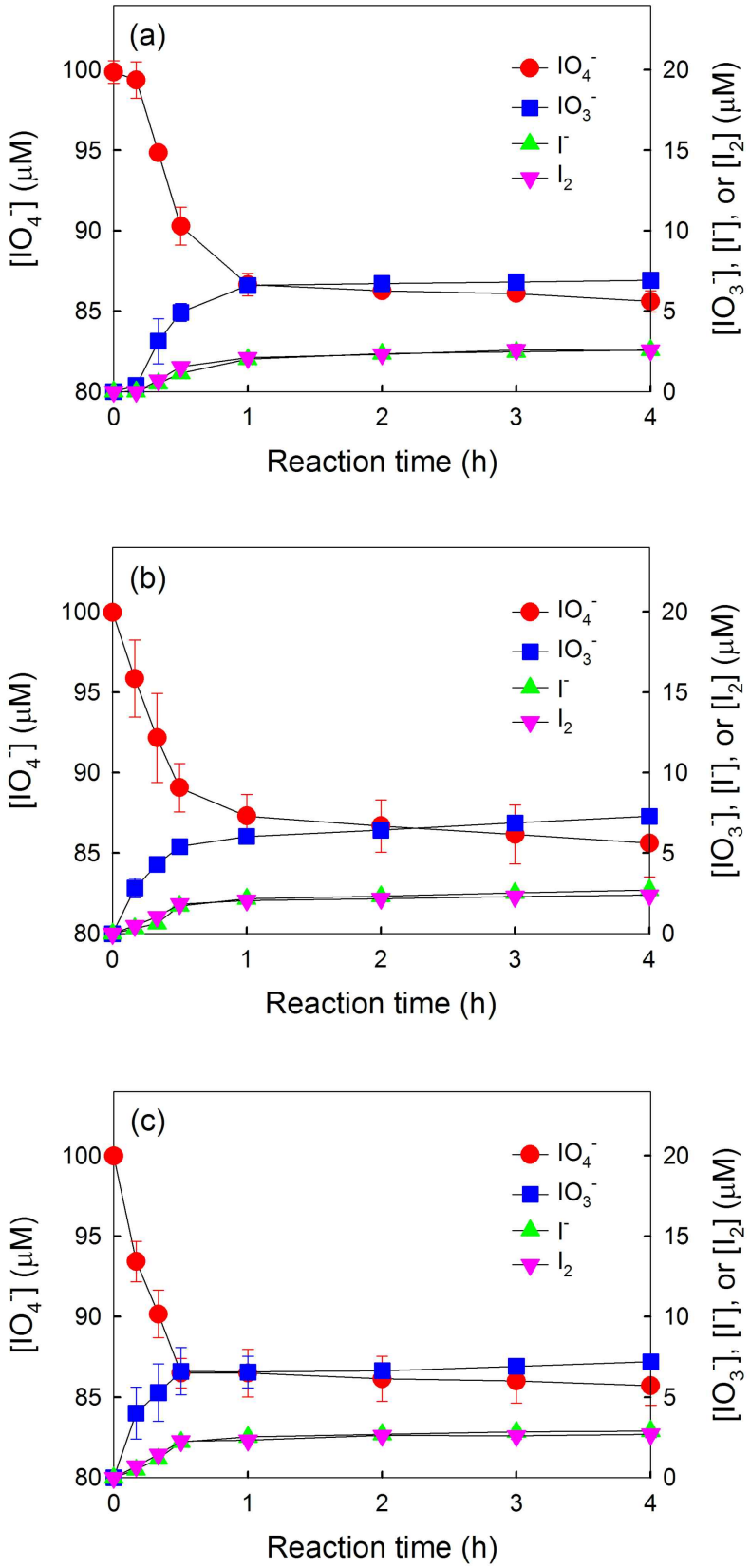

Figure S10. Reduction of IO_4^- by FFA and the concurrent production of IO_3^-, I^-, and I_2 during freezing at (a) −10 °C, (b) −20 °C, and (c) −30 °C. Experimental conditions were as follows: $[IO_4^-]$ = 100 μM, [FFA] = 20 μM, and pH = 3.0.

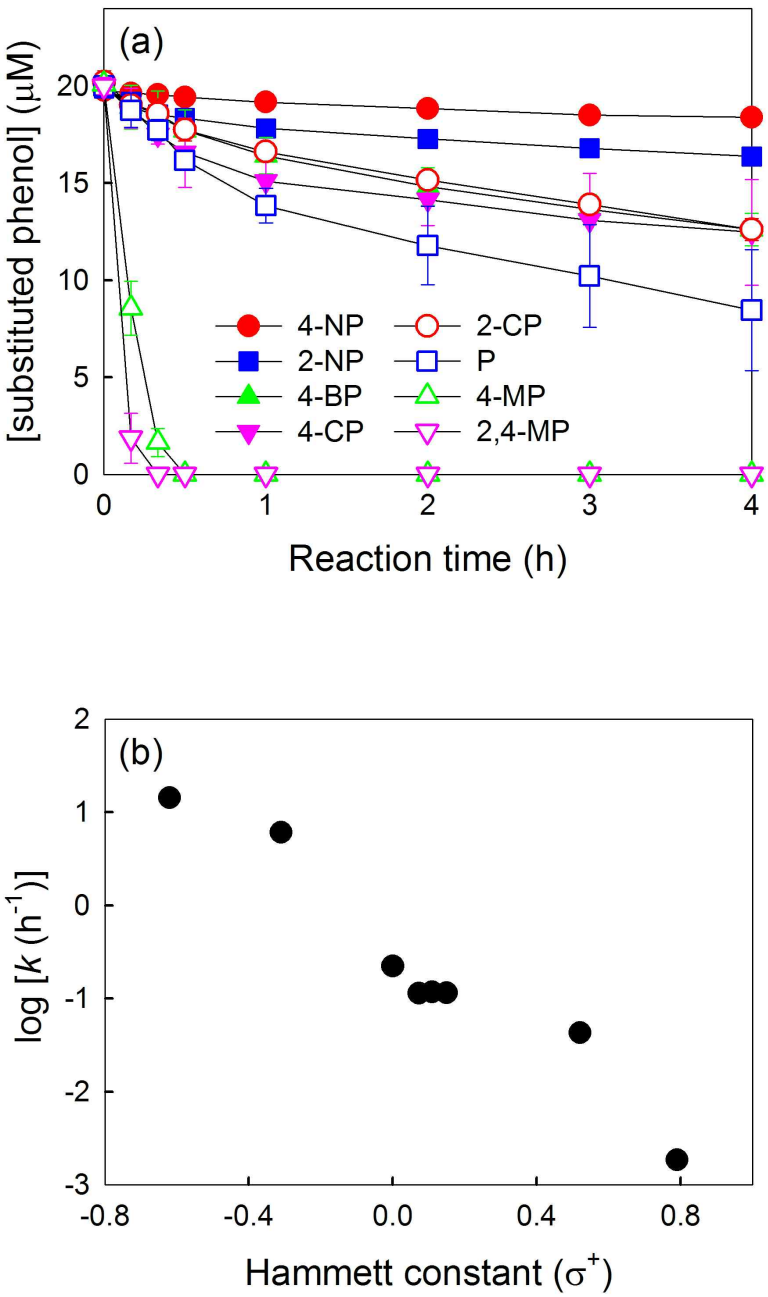

Figure S11. (a) Degradation of various substituted phenols (4-nitrophenol (4-NP), 2-nitrophenol (2-NP), 4-bromophenol (4-BP), 4-chlorophenol (4-CP), 2-chlorophenol (2-CP), phenol (P), 4-methylphenol (4-MP), and 2,4-dimethylphenol (2,4-MP)) in the presence of IO_4^- during freezing. (b) Correlations between degradation rate constants (k) and Hammett constants (σ^+). Experimental conditions were as follows: [IO_4^-] = 100 μM, [substituted phenol] = 20 μM, pH = 3.0, and freezing temperature = −20 °C. The Hammett constants of the substituted phenols were obtained from references S4 and S5.

Discussion on the effect of cooling method on the induction period. The freezing-induced degradation of FFA in the presence of IO_4^- is initiated when the aqueous solution is almost solidified (i.e., when the concentrations of IO_4^-, FFA, and protons reach the minimum level for inducing the degradation process). Therefore, the cooling rate (i.e., the solidification rate) is a key factor in determining the induction period. The aqueous solution is solidified more rapidly when a substance with higher specific heat capacity and density is used as a coolant. The specific heat capacity (C_p) of ethanol is twice that of air (2.0 kJ/kg·°C for ethanol vs. 1.0 kJ/kg·°C for air). The density of ethanol (l) is much higher than that of air (g) (827.0 kg/m^3 for ethanol vs. 1.4 kg/m^3 for air). In addition, the circulation of cold ethanol in a cryogenic ethanol bath contributes to the rapid solidification of the aqueous solution. These can help explain why the induction period in outdoor experiments is much longer than that in laboratory experiments.

References in SI

(S1) Weavers, L. K.; Hua, I.; Hoffmann, M. R. Degradation of triethanolamine and chemical oxygen demand reduction in wastewater by photoactivated periodate. *Water Environ. Res.* **1997**, *69*, 1112-1119.

(S2) Perrin, D. D. Buffers of low ionic strength for spectrophotometric p*K* determinations. *Aust. J. Chem.* **1963**, *16*, 572-578.

(S3) Dean, J. A. *Lange's Handbook of Chemistry*, 14th, ed.; McGraw-Hill: New York, 1992.

(S4) Lee, Y.; Yoon, J.; von Gunten, U. Kinetics of the oxidation of phenols and phenolic endocrine disruptors during water treatment with ferrate (Fe(VI)). *Environ. Sci. Technol.* **2005**, *39*, 8978-8984.

(S5) Guan, C.; Jiang, J.; Pang, S.; Luo, C.; Ma, J.; Zhou, Y.; Yang, Y. Oxidation kinetics of bromophenols by nonradical activation of peroxydisulfate in the presence of carbon nanotube and formation of brominated polymeric products. *Environ. Sci. Technol.* **2017**, *51*, 10718-10728.

KOPRI 극지연구소

제 22 절. 얼음 표면 특성을 이용한 친환경 전도성 신소재 합성 연구

박문정, 김경욱, 강한얼, 합현성

포항공과대학교 화학과

1. 연구개발의 필요성 및 목적

물은 대기압 기준으로 약 0 ℃에서 얼음으로 상변화가 일어난다고 잘 알려져 있음. 한편, 0 ℃보다 낮은 온도에서도 얼음 표면에 액체가 존재한다는 주장이 1842년에 마이클 패러데이에 의해 처음으로 제안되었음. 얼음 표면에 대한 많은 연구가 이루어졌고, 어는점보다 낮은 온도에서도 얼음 표면에 실제로 액체가 존재한다는 사실이 다양한 연구 기법을 통해 확인되었음 [1-4]. 특히 2010년대에 이르러, 원자 힘 현미경(Atomic force microscopy, AFM), 레이저 공초점 기반의 현미경(Laser confocal microscopy combined with differential interference contrast microscopy, LCM-DIM)을 통해 얼음 표면에 있는 액체층을 실제로 관측할 수 있게 되었음 [5-7].

이렇게 물질의 어는점보다 낮은 온도에서도 액체가 존재하는 현상을 표면 녹음(surface melting) 현상이라고 하며, 이때 얼음의 표면에 존재하는 액체층이 액체인 물의 분자 배열과 비슷하지만, 완벽히 동일하지는 않기 때문에 준액체층(liquid-like layer, 또는 quasi-liquid layer)이라고 불리었음 [8-9]. 이처럼 지금까지 얼음 표면의 준액체층에 대한 많은 연구가 있었지만, 이 준액체층을 활용하는 화학 반응에 대한 연구는 아직 심도 있게 다루어지지 않았음.

얼음 표면의 특성 변화에 따른 영향을 확인하기 위해서는 수소결합과 같이 얼음 표면과의 상호작용이 있어야 얼음의 영향을 확인하기 수월하며, 0도 이하의 낮은 온도에서도 진행될 수 있는 화학 반응이어야 함. 이 두 조건을 모두 만족할 수 있는 적절한 화학 반응으로 전도성 고분자의 중합이 있음.

전도성 고분자란, 단일결합과 이중결합이 교대로 이루어져있는 π-공액 구조(π-conjugation system)로 골격을 이루고 있는 고분자로, 이로 인해 넓게 비편재화된 오비탈을 형성하여 전자의 흐름을 가능하게 하여 전기적 특성을 가질 수 있음. 잘 알려진 전도성 고분자로는 poly(3,4-ethylenedioxythiophene) (PEDOT), P3HT (Poly(3-hexylthiophene-2,5-diyl)), 폴리아닐린(polyaniline), 폴리피롤(polypyrrole) 등이 있음. 이 중에서 일부 전도성 고분자는 수소결합이 가능한 싸이트를 가지고 있고, 중합되는 속도 또한 빠르기 때문에, 얼음 표면의 특성이 화학 반응에 미치는 영향을 확인하는 데에 적절함.

나아가, 전도성 고분자는 유연한 특성과 전기 전도 특성을 동시에 가지고 있는 만큼, 차세대 유연 디바이스로서 다양한 미래 활용 분야가 있기 때문에, 얼음 표면의 역할을 규명하

여 좋은 성능을 가진 전도성 고분자를 중합한다면 실용적으로도 매우 큰 의의가 있는 연구가 될 것으로 기대됨.

2. 연구개발 방법

2.1. 목표달성 방법

- 얼음 표면 특성, 특히 물분자의 배열을 얼리는 온도 및 습도를 제어하여 조절.
- 얼음 표면과 전도성 고분자 단량체와의 인력을 규명.
- 챔버를 자체 제작하여 in-situ grazing X-ray 실험 중 얼음 표면의 높은 flatness 확보.
- 극저온 전자현미경으로 온도 및 습도 제어에 따른 얼음 표면의 특성 변화 관찰.
- 제어된 조건에 부합하는 전기 전기전도성 측정 후 얼음 표면의 특성 및 전도성 고분자의 배향과 전기전도성 간의 경향성 파악.

3. 얼음표면에서 합성된 전도성 고분자의 배향 연구

3.1. 얼음표면 위의 전도성 고분자 배향 규명 기술확보

가. 얼음 표면에서 대면적의 전도성 고분자 합성

전도성 고분자란 금속의 높은 전기전도성과 가공이 쉽고 가벼운 플라스틱의 성질을 동시에 나타내는 유기고분자이다. 전도성 고분자는 단일결합과 이중결합이 교대로 이루어져있는 π-공액구조(π-conjugation system)이며, 이로 인해 넓게 비편재화된 오비탈을 형성하여 전자의 흐름을 가능하게 하여 전기적 특성을 가질 수 있다. 잘 알려진 전도성 고분자로는, poly(3,4-ethylenedioxythiophene) (PEDOT), P3HT (Poly(3-hexylthiophene-2,5-diyl)), 폴리아닐린(polyaniline), 폴리피롤(polypyrrole) 등이 있다.

특히 폴리아닐린은 손쉬운 합성, 낮은 가격, 쉬운 doping/dedoping 시스템, 우수한 화학적 안정성 등의 장점으로 인하여 기초적인 학문 연구로 많이 연구되어 왔고, 최근 태양전지, 슈퍼캐패시터 등 많은 첨단 전기화학 장치에 응용되는 연구까지 진행되어 왔다. 하지만 폴리아닐린도 다른 전도성 고분자와 마찬가지로, 고분자의 긴 사슬 구조 사이의 얽힘 현상 때문에 비정질 영역을 다수 포함하고 있어 전자 전이를 저해시키는 결점을 지니고 있고, 이에 따라 전도성 고분자가 발견된 이래로 결정성을 높이기 위한 많은 연구가 진행되어왔다.

본 연구진은 얼음을 기판으로 사용하여 제한된 공간에서 전도성 고분자 중 하나인 폴리아닐린을 합성하였으며(그림 1), 이렇게 합성된 폴리아닐린은 교반을 통해 중합된 일반적인 폴리아닐린보다 매우 높은 결정성과 약 30배이상 높은 전기 전도도를 보였다. 이는 얼음과 단량체인 아닐린 사이의 수소결합으로 인하여 edge-on 배향으로 잘 정렬된 채로 중합되어 electron hopping이 잘 일어나게 되어 나타난 결과라는 것을 확인할 수 있었으며, 전자현미경을 통해 이미지를 확인해본 결과 2차원적인 구조를 가지고 있는 것을 확인할 수 있었다.

나아가, 본 연구진은 폴리아닐린뿐만 아니라, poly(3,4-ethylenedioxythiophene): polystyrene sulfonate (PEDOT:PSS) 전도성 고분자를 얼음 표면에서 합성하고자 하였다. PEDOT:PSS는 그림 2와 같은 화학 구조를 가진 고분자로서, 다른 전도성 고분자와 마찬가지

로 탄소 골격으로 이루어진 유기 고분자이지만, 전도성 고분자 중에서도 전기 전도도가 매우 높은 고분자로 잘 알려져 있으며, 이뿐만 아니라 유연하고 광학적으로 투명한 특성 덕분에 투명 플렉서블 디바이스로 응용되는 연구가 많이 이루어지고 있다.

하지만 PEDOT:PSS는 합성 조건이 폴리아닐린보다 더 까다롭고 합성하기 어렵기 때문에 재현성있는 결과를 위해서는, 조건을 최적화하기 위한 시간이 더 필요할 것으로 판단된다. 이 최적화 조건으로서 얼음의 온도, 얼음의 두께, 얼음의 냉각속도, 전도성 고분자 중합 시간 등 다양한 조건을 제어하여 전도성 고분자를 합성하고자 하였다.

나. 얼음 표면에서 합성한 전도성 고분자의 결정성 및 단위셀 수준의 배향 분석

전도성 고분자는 기본적으로 탄소 기반의 골격으로 이루어진 유기 고분자이기 때문에 일반적인 강한 에너지의 빔에 취약하여 결정을 관측하기가 매우 어렵고, 관측하더라도 주어진 정보를 가지고 결정 구조를 분석하기 매우 어려웠다. 이에, 본 연구진은 얼음 표면에서 합성한 전도성 고분자의 결정 구조를 확인하기 위하여 극저온 투과전자현미경(cryo-TEM)으로 관측하였다. 시료의 결정성을 측정하는 과정에서 시료를 최대한 온전히 보전한 상태로 관측할 수 있기 때문에 오랜 시간 동안 결정을 관측하는 데에 매우 적합하였다. 그림 3은 얼음에서 합성한 전도성 고분자의 제한시야 전자회절(Selected Area Electron Diffraction) 패턴(그림 3a)과 고해상도 투과전자현미경(HRTEM) 사진(그림 3b)으로, 합성한 전도성 고분자 나노시트가 높은 결정성을 가지는 것을 확인할 수 있었다.

이러한 회절 패턴 결과를 통하여 얼음 위에서 합성한 2차원 전도성 고분자 나노시트가 a = 15.20 Å, b = 4.94 Å, c = 13.03 Å, α = γ = 90.00 °, 그리고 β = 92.23 °의 단위 격자 파라미터를 가지는 P121 공간 그룹의 단사(monoclinic) 결정계로 이루어져 있다는 것을 확인할 수 있었다. 또한, GI-WAXS 실험을 통해 합성한 PEDOT:PSS 나노시트가 edge-on 방향으로 우세하게 배향되어있다는 것을 확인할 수 있었다. (그림 4)

3.2. 얼음표면의 액체층 특성과 합성된 고분자 물성 상관관계 정립

가. 얼음 표면에서 합성한 전도성 고분자의 2차원 구조 관찰 및 합성 과정에서 얼음의 역할 분석

본 연구진은 합성된 2차원 고분자의 물성과 얼음표면의 액체층 특성 사이의 상관관계를 확인하기 위하여 감쇠 전반사 퓨리에 변환 적외선 분광 실험을 진행하였다. 그림 5는 전도성 고분자가 각각 건조 상태, 물에 접촉한 상태, 얼음 위에 놓인 상태일때의 polystyrene sulfonate(PSS)에 대한 퓨리에 변환 적외선 분광 실험 결과를 보여준다.

우선, 896 cm^{-1} (ν_{S-O})와 1350 cm^{-1} ($\nu_{S=O}$, symmetric)에서 나타나는 흡수 스펙트럼은 물에 접촉할 때와 얼음 위에 놓일 때 사라지는 것을 알 수 있다. 동시에, 물에 접촉한 상태와 얼음 위에 놓인 상태에서는 각각 1175 cm^{-1}, 1154 cm^{-1} ($\nu_{S=O}$, asymmetric) 에서 흡수 스펙트럼이 나타난다. 이를 통하여, 2차원 PEDOT:PSS가 물에 접촉하거나 얼음 위에 있을 때, PSS의 SO_3H 부분이 축퇴가 깨지고 물과 함께 SO_3H-H_2O를 새롭게 형성한다는 것을 예측할 수 있다.

한편, 앞서 말한 $\nu_{S=O}$ asymmetric 흡수 스펙트럼이 물에 접촉할 때(1175 cm^{-1})보다 얼음 위에 놓일 때(1154 cm^{-1})에 blue shift했으며, aromatic ring in-plane deformation에 해당하는 1001 cm^{-1}와 1123 cm^{-1}에서의 흡수 스펙트럼이 더 넓어지고 조금 red shift한 것을 확인할 수 있다. 이는 PEDOT:PSS가 얼음 표면에 있을 때, 물에서보다 양성자가 적게 해리되며, 인접한 PSS의 SO^3H 부분끼리의 분자간 수소결합이 더 우세하다는 것을 가리킨다. 따라서 PEDOT:PSS에서 PEDOT에 연결된 PSS가, 다른 PEDOT에 연결되어 있는 이웃한 PSS와 서로 연결되면서 얼음 위에서 평면구조로 성장하는 것으로 중합 메커니즘을 예측할 수 있다.

뿐만 아니라, 얼음 위에서 합성한 2차원 PEDOT:PSS 막은 스핀코팅 등 기존의 다른 어떤 2차원 PEDOT:PSS 막 합성 방법보다 가장 빠르게 합성 되는 것으로 확인되었는데, 이는 얼음 표면에 존재하는 준액체층(quasi-liquid layer)에 의한 구속 효과(confinement effect)에 의하여 표면 분자들이 비교적 높은 이동도를 가지기 때문이라고 생각된다. 이러한 구속 효과에 의한 준액체층에서의 빠른 중합은 PEDOT:PSS가 공기-물 계면에서 잘 정렬된 채로 패킹되는 것을 더 용이하게 한다. 결과적으로 얼음 표면의 이러한 액체층 특성에 의하여, 합성된 PEDOT:PSS가 높은 결정성을 가질 수 있는 것으로 예측할 수 있었다.

나. 얼음 표면에서 합성한 PEDOT:PSS의 전기 전도 특성 비교 및 분석

얼음 표면에서 합성한 PEDOT:PSS 막의 전기 전도도를 명확하게 비교하기 위하여, 얼음 표면에서 합성한 PEDOT:PSS 막과 잘 알려져 있는 방법인, 스핀 코팅으로 합성한 PEDOT:PSS 막을 금 전극이 올려져 있는 Si/SiO_2 웨이퍼 위에 준비하였다. 이후 전압을 -1 V부터 1 V까지 가해 전류 전압 곡선을 얻은 결과, 그림 6과 같이 얼음 표면에서 합성한 PEDOT:PSS 막이 스핀 코팅으로 준비한 PEDOT:PSS 막에 비해 훨씬 향상된 전류 흐름을 보였다. 전류 전압 곡선을 얻은 이후, 아래의 식 1을 이용하여 전기 전도도를 계산하였다.

$$\sigma = \frac{L.I}{V.A} \qquad \text{(식 1)}$$

이때 σ는 전기전도도, L은 두 전극간의 거리, A는 시료의 단면적, 그리고 I와 V는 측정된 전류와 전압을 의미한다. 그 결과, 얼음표면에서 합성한 PEDOT:PSS 막의 전기 전도도는 28 $S \cdot cm^{-1}$로, 스핀코팅한 PEDOT:PSS 막의 1.8 S/cm보다 약 15 배 이상 향상된 결과를 보였으며, 기존에 문헌에 보고된 통상적인 값인 1 S/cm에 비하면 30 배 가까이 향상된 결과이다. 이렇게 높은 전기 전도도는, 얼음 표면에서 합성한 PEDOT:PSS 고분자가 얼음과의 수소결합을 통한 높은 결정성을 가지는 것에서 기인한다고 판단할 수 있다.

즉, 얼음은 수소결합을 통해 반응물이 균일하게 배열된 채로 중합될 수 있도록 하는 플랫폼 역할을 할 뿐만 아니라, 표면의 수 나노미터 두께의 액체층을 제공함으로써 빠른 단분자의 확산을 가능하게 하는 독특한 특성을 제공하였고, 이러한 얼음의 특성은 수 분 내의 빠른 반응 시간동안 높은 결정성의 PEDOT:PSS를 합성을 가능하게 하여, 결과적으로 높은 전기 전도 특성을 가진 전도성 고분자를 합성할 수 있다는 것을 확인할 수 있었다.

4. 얼음 표면 특성을 이용한 2차원 구조 전도성 신물질 개발

4.1. 얼음 표면에서 고성능의 2차원 전도성 고분자 신물질 합성

가. 얼음 표면에서 대면적의 2차원 PEDOT:PSS 합성법 개발

poly(3,4-ethylenedioxythiophene):polystyrene sulfonate (PEDOT:PSS)는 전도성 고분자 중에서 유연하고 광학적으로 투명한 특성 때문에 그 전기 전도도를 향상시키는 연구가 활발히 이루어지고 있다. 초기에는 PEDOT:PSS 전도성 고분자는 PSS의 절연 특성과 PEDOT에 연결된 PSS의 낮은 결정성으로 인하여 낮은 전기전도도를 보인다는 단점이 있었지만, 이에 다른 첨가제를 도입함으로써 전기전도도에 큰 향상을 가져왔다.

하지만, 첨가제를 첨가하지 않은 순수한 PEDOT:PSS는 물에서의 쉬운 분산성과 대량의 가공성이라는 장점을 가져, 여전히 전자기기로의 응용에 있어서 순수한 PEDOT:PSS가 많이 선호되고 있다. 따라서 높은 전기전도도를 가지는 순수한 PEDOT:PSS의 개발의 필요성이 대두되었다. 이에 본 연구진은 얼음을 기판으로 도입하여 높은 전기전도도를 가지는 순수한 PEDOT:PSS 막을 합성하는 방법을 개발하였다.

2차원적인 PEDOT:PSS의 합성은 얼음 표면에서 화학적 산화 중합(chemical oxidative polymerization) 방법을 이용하여 진행되었다. 일반적인 용액 중합과 달리, 얼음 표면에서 진행한 중합은 2차원적인 구조로 합성되는 것이 가능하게 하였다. 그림 7a와 같이 EDOT(3,4-Ethylenedioxythiophene)이 포함된 전구체 용액과 PSS가 포함된 전구체 용액을 섞은 뒤 곧바로 -20 ℃의 평평한 얼음 표면에 떨어뜨려서 중합을 시작하였다. 초기에는 밝은 초록색이었던 전구체 혼합물이 약 3분 뒤 밝은 파란색으로 색이 변하였고, 이후 5 분 동안 0 ℃의 조건에서 얼음을 서서히 녹게 하여 공기-물 계면에서 중합을 진행하여 대면적의 2차원적인 PEDOT:PSS 막을 얻을 수 있었다. 합성된 2차원 PEDOT:PSS 막은 그림 7b와 같이 약 10 cm의 크기를 가지도록 대면적으로 합성이 가능하였다.

얼음 표면에서 합성한 전도성 고분자의 구조를 확인하기 위하여 극저온 투과전자현미경으로 관측하였다. 고분자는 강한 에너지의 빔과 열에 취약하기 때문에 극저온 투과전자현미경을 이용하여 관측하였다. 그 결과, 그림 8과 같이 PEDOT:PSS의 2차원적인 구조를 명백하게 확인할 수 있었다. 또한, 원자힘현미경을 통하여 두께를 측정한 결과 약 30 nm의 평균 두께를 가지는 것을 확인하였다. 이렇게 합성된 2차원 PEDOT:PSS는 단순히 얼음 형판을 녹임으로써 FTO, Si/SiO_2 기판, 플라스틱 기판 등 어떤 종류의 기판으로든 쉽게 수집될 수 있었다. 이러한 2차원적인 PEDOT:PSS 막은, 지금까지 보고된 PEDOT에 연결된 PSS 부분이 물에 분산되어 core-shell의 형태로 존재하는 PEDOT:PSS와는 명백하게 다른 결과이다. 따라서 얼음 표면에서의 합성이 2차원적인 PEDOT:PSS 형성에 큰 영향을 미친다는 것을 알 수 있었다.

나. 얼음 표면에서 합성한 2차원 PEDOT:PSS 전도성 고분자의 결정 구조 분석

본 연구진은 얼음표면에서 합성한 전도성 고분자 막의 결정성을 확인하기 위하여 포항 가속기 연구소 5A 빔라인에서 X선 회절 실험을 진행하였다. 이때 일반적인 용액 중합 방법으로 합성한 PEDOT:PSS와 얼음 표면에서 합성한 PEDOT:PSS의 결정성 차이를 명확하게 비교하기 위하여 두 가지 시료를 모두 준비하여 실험을 진행하였다. 그 결과는 그림 9와 같으며 이때

Bulk polymer는 일반적인 용액 중합으로 합성한 PEDOT:PSS를 가리키고, 2D polymer는 얼음 표면에서 합성한 PEDOT:PSS를 가리킨다. 일반적인 용액 중합으로 합성한 PEDOT:PSS는 전체적으로 무정형(amorphous) 영역만 관측된 것에 반해, 얼음에서 합성한 PEDOT:PSS는 몇 개의 강한 결정성 피크들이 관측되었다.

2D polymer의 X선 회절 패턴 중에 5.7 °에서 나타나는 (100) 격자면에 해당하는 결정 피크는 PEDOT의 라멜라 스태킹에 의한 피크이며, 격자면 간 거리(d-spacing)는 15.2 Å에 해당한다. 또한 17.7 °에서 나타나는 (010) 격자면에 해당하는 결정 피크는 PEDOT의 수평 방향으로의 패킹에 의한 것이며 4.9 Å의 격자면 간 거리에 해당한다. 이를 바탕으로 구성한 2D PEDOT:PSS 막의 PEDOT 분자 배열은 그림 9에 있는 삽도와 같다. 이 삽도에 나타낸 PEDOT은 PSS 사슬에 연결되어 있는 PEDOT으로, PEDOT의 배열을 명료하게 나타내기 위해 PSS는 해당 삽도에서 생략하였다.

결과적으로 합성한 2차원 PEDOT:PSS의 결정 구조는 X-ray diffraction (XRD) 실험을 비롯하여, grazing-incidence wide angle X-ray scattering (GI-WAXS) 실험, high-resolution transmission electron microscopy (HRTEM) 실험, 그리고 투과전자현미경을 이용한 전자 회절 패턴 실험을 모두 종합적으로 분석하여 얻을 수 있었으며, 이러한 일련의 실험을 통하여 얼음에서 합성한 전도성 고분자가 훨씬 높은 결정성을 가진다는 것을 확인할 수 있었고, 이렇게 높은 결정성 덕분에 결정 구조를 명확하게 예측할 수 있었다.

다. micro-porous하고 viscoelastic한 특성을 가진 2차원 PEDOT:PSS 나노시트 합성

최근 본 연구진은 전도성 고분자를 미래 wearable 액추에이터에 활용하기 위하여 새로운 형태의 전도성 고분자를 합성하였다. 이러한 미래 유연 소자로의 활용에 있어서는 높은 전기 전도 특성뿐만 아니라, 큰 변형에도 다시 돌아오는 높은 신축성이 필요로 되며, 이를 위해서는 viscoelastic 특성이 필요하다. 또한, porosity는 전극의 capacitance를 높여주기 때문에, porous한 전극을 만드는 것이 실제 응용에 있어서 더 유리하다. 따라서, 현재 본 연구진은 얼음을 활용한 높은 전기적 특성의 2차원 PEDOT:PSS에 porosity 및 viscoelastic 특성을 접목시킨 새로운 2차원 PEDOT:PSS를 합성하는 연구하였다. 이를 위해, 2차원 PEDOT:PSS를 얼음 위에서 합성하는 과정에서 가소제를 도입하였다. 이 과정에서 원하는 porous한 특성을 갖고 우수한 전기화학 특성을 보이는 고분자를 합성하기 위해 가소제의 종류와 함량을 여러 가지 비율로 조절하였다. 그림 10은 가소제 중 하나인 Triton X-100를 도입하기 전의 2차원 PEDOT:PSS 시트의 주사전자현미경(SEM) 사진과, 도입한 뒤의 SEM 사진과 카메라 사진이다. 이를 통해 micro-porous한 특성을 가진 PEDOT:PSS를 합성한 것을 확인할 수 있었고, 가소제 Triton-X의 존재로 인해 viscoelastic 특성을 기대할 수 있었다. 더불어, 카메라 사진에서 확인할 수 있듯이, 대면적의 시트를 합성한 것을 확인할 수 있었다. 이 합성법을 통하여 향후 미래 유연 디바이스의 적용에 더 원활할 것으로 기대하고 있다.

4.2. 얼음표면 특성 제어를 통한 전도성 고분자의 두께 및 전도성 제어기술 확보

가. In-situ X-선 실험을 위한 펠티에 챔버 제작 및 얼음 표면의 온도 제어기술 확보

얼음 표면에는 녹는 점 아래에서도 매우 얇은 준액체층(liquid-like layer)이 존재한다는 것이 다양한 연구를 통해 알려져 있다. 이 준액체층은 얼음의 온도에 따라 두께가 달라지며 얼음의 온도가 올라갈수록 두꺼워지다가 녹는점에 가까워지면 급격하게 상승하는 것으로 보고되었다. 한편, 본 연구진은 얼음 표면에서 합성한 2차원 전도성 고분자가 얼음의 온도에 따라 전기 전도 특성이 달라지는 것을 확인한 바 있으며, 이러한 현상이 얼음 위에 존재하는 준액체층과 밀접한 연관성이 있다고 추측하였다. 따라서, 이를 규명하기 위해 얼음의 온도를 정밀조절하여 전도성 고분자를 합성하였을 때, 각기 다른 온도에서 합성된 전도성 고분자의 특성이 어떻게 달라지는지 확인하는 연구를 진행하고자 하였다. 이를 기반으로, 얼음 표면 위에서 PEDOT:PSS가 합성될 때에 반응 초기부터 높은 결정성을 가지게 되는지, 아니면 일정 시점 이후에 고분자 사슬이 규칙적으로 배열되면서 높은 결정성을 가지는 것인지 정확한 메커니즘을 규명하기 위해, 반응 시간에 따른 전도성 고분자의 특성 변화를 실시간으로 측정하고자 하였다.

우선, 전도성 고분자가 중합될 때 언제 결정성을 가지게 되는지 in-situ로 확인하기 위하여 포항 가속기 연구소 빔라인 3C에서 in-situ grazing-incidence X-ray scattering 실험을 진행하였으며, 꾸준한 실험 진행 중에 있다. 이 실험에 있어서 얼음 표면의 온도가 주변 온도보다 대단히 중요한 요소이며, 이 얼음 표면의 온도를 정밀하게 제어하기 위하여 펠티에 챔버를 제작하였다. 제작한 챔버를 이용한 첫 번째 실험을 수행한 결과, 수증기의 condensation으로 인한 vitrify된 얼음층의 형성되는 등 여러 가지 실험적인 변수들이 많이 확인되었고, 이를 보완하기 위하여 챔버 도면을 수정하여 새롭게 제작하였다. 그림 11a는 펠티에 챔버 모듈을 사용하여 난산란을 일으키지 않는 매우 평평한 표면을 가지는 얼음을 합성한 사진으로, 얼음 표면이 X-선 산란 실험에 필요한 수준으로 매우 평평한 것을 확인할 수 있었다. 그림 11b는 전도성 고분자를 올리기 전의 -20 ℃의 순수한 얼음의 X-선 산란 실험 결과로, 높은 q 범위에서 강한 intensity를 가지는 것을 확인할 수 있어, 높은 결정성의 얼음이 펠티에 챔버 환경에서 제작되었음을 확인할 수 있었다.

나. PEG 고분자 도입을 통한 얼음의 결정성 제어 및 얼음의 특성 변화 분석

앞서 가속기의 X-ray scattering 실험을 통해, 준비한 얼음이 매우 강한 결정성을 가지는 것을 확인할 수 있었다. 본 연구진은 이 얼음의 결정성을 조절하였을 때에 얼음 위에서 합성되는 전도성 고분자의 특성이 어떻게 변화하는지를 관찰하고자, 얼음의 결정성을 조절하고자 하였다. 그 방법으로 DI-water에 polyethylene glycol (PEG)를 혼합하여 얼려서 PEG-mixed water를 준비하였다. 우선, PEG의 분자량과 함량(wt%)을 달리하였을 때 얼음의 결정성이 어떻게 달라지는지를 관찰하여 조건을 최적화하고자 하였다. 그림 12는 분자량이 각각 0.2 k, 2 k, 그리고 20 k인 PEG를 도입하였을 때의 시차주사열량분석법 (Differential Scanning Calorimetry, DSC) 결과이다. DSC의 냉각 과정을 보면, 아무것도 넣지 않은 순수한 DI-water의 경우 crystallization이 약 -15 ℃에서 일어난 것과 달리, PEG를 도입하였을 때에는 -22 ℃에서 -

25 ℃까지 순수한 물에 비하여 훨씬 낮은 온도에서 얼음이 crystallization이 되는 것을 확인할 수 있었다. 특히, 이 실험은 PEG를 각각 1 wt%씩 도입하였는데, 단 1 wt%의 PEG를 섞었음에도 이렇게 결정화를 늦추는 데에 큰 영향을 끼친다는 것을 확인할 수 있었다. 또한, 분자량이 작은 0.2 k부터 큰 20 k까지 특정 분자량에 국한되지 않고 모두 얼음의 결정화를 낮추는 역할을 한다는 것을 확인할 수 있었다.

앞서 보인 DSC 실험을 통하여, 적은 양의 PEG로도 얼음의 결정성 조절에 대한 충분한 효과를 확인할 수 있었다. 본 연구진은 이 데이터를 기반으로 0.2 k부터 20 k 사이의 다양한 분자량의 PEG를 1 %부터 10 %까지의 다양한 함량으로 도입하여 다양한 조건의 얼음을 준비하였다. 그림 13은 이렇게 준비한 얼음 중에 한 시리즈를 찍은 사진으로, 함량을 2.5 %로 고정시키고 PEG를 넣지 않은 순수한 얼음부터, 다양한 분자량의 PEG를 넣은 혼합물 얼음의 결과를 보인 사진이다. 그 결과, PEG의 분자량을 다르게 하여 만든 얼음이 거시적으로는 크게 다르지 않다는 것을 확인할 수 있었다. 하지만, 분자량을 다르게 하였을 때에 DSC 결과에서는 각기 다른 결정화 온도를 보이는 것으로 보아, PEG의 분자량이 얼음의 결정성 조절에 영향을 끼친다는 것을 알 수 있었다. 그 이유로, PEG가 도입된 물을 얼린 얼음의 경우, 순수한 얼음이 crystallization되어 있는 부분과, 얼음-PEG가 섞여서 crystallization되어 있는 부분(PEG-ice eutectic crystallization)으로 두 부분으로 나뉘어서 존재하게 되는데, PEG의 분자량 및 함량을 조절하면 이 두 상의 분포가 달라지기 때문에 결정성이 달라지는 것으로 생각된다. 뿐만 아니라, 얼음을 얼렸을 때에 얼음의 표면 부분과, 반대로 바닥 부분의 PEG 분포가 다를 것으로 예상된다.

다. 얼음 표면 특성 제어를 통한 전도성 고분자의 특성 변화 확인

본 연구진은 반응 시간을 달리하였을 때, 얼음 표면에서 합성되는 2차원 전도성 고분자의 두께 및 전기 전도 특성이 어떻게 달라지는지를 폭넓게 연구 중에 있다. 이때 제어하는 변수로, 얼음의 온도를 -2 ℃, -5 ℃, -10 ℃, -20 ℃와 같이 조절하고 있으며, 반응시간을 5 분, 10 분, 15 분과 같이 조절하고 있다. 그림 14는 이 중 하나의 결과로, -10 ℃ 조건에서 pure ice 표면에서 반응시간을 각각 10 분과 15 분으로 하였을 때의 전도성 고분자의 두께 차이를 보여준다. 그 결과, 반응 10 분일 때와 15 분일 때의 두께가 각각 1 nm와 7 nm로, 10 분과 15 분 사이에 두께가 급격하게 증가한 것을 알 수 있으며, 이는 전도성 고분자의 합성 과정에서 나타나는 oxidative polymerization이 radical polymerization의 일종이므로, 이 시점에 initiation되고 급격하게 중합되는 것이라고 예측할 수 있다.

본 연구진은 위와 같이 얼음의 온도 및 반응시간을 제어할 뿐만 아니라, 얼음의 결정성을 제어하여, 결정성이 다른 얼음에서 합성된 2차원 전도성 고분자를 특성을 비교하는 연구를 수행하였다. 그림 15는 이렇게 PEO 도입을 통하여 결정성을 낮춘 얼음 표면에서 합성한 2차원 PEDOT:PSS의 투과전자현미경 사진으로, 3.4 k 분자량의 PEG를 2.5 %와 5 %만큼 도입하여 만든 얼음 표면에서 합성한 PEDOT:PSS의 결과 사진이다. 이를 보면, 높은 결정성의 얼음 표면에서 합성한 2차원적인 PEDOT:PSS에 비해 더 coarse한 표면을 가지는 것으로 보이며, 두께 또한 더 두꺼운 것으로 보인다.

3. 합성된 소재를 미래 유연 디바이스 전극 소재로의 활용

가. 2차원 PEDOT:PSS 나노시트를 이용하여 광전기화학적 수소 생산 전극 소재로 활용

마치 그래핀이 검은색 기반이지만 투명한 것과 비슷하게, 본 연구진이 합성한 2차원 PEDOT:PSS는 30nm 수준의 얇은 막이기 때문에 약간의 푸른색을 띠면서 투명성을 가졌다. 이에 따라, 2차원 PEDOT:PSS는 태양광을 이용한 실험에 적용하기에 적절하였고, 따라서 이렇게 합성한 고전도성 2차원 PEDOT:PSS에 CdSe 양자점 결합하여 광전기화학적 수소 생산 (photoelectrochemical, PEC) 수소 생산 전극으로의 적용하고자 하였다.

이때, 그림 16a에 이러한 복합물의 TEM 이미지를 보여주고 있는데, 이를 통해 PEDOT:PSS에 약 4.3 nm 크기의 CdSe 양자점이 균일하게 형성된 것을 확인할 수 있었다. 이러한 복합전극에 cobalt-phosphate (CoPi)를 결합하여 표면 전하를 낮추고 태양광을 이용한 수소 생산에 활용하였다. 그림 16b에서 보여주는 바와 같이, 2-전극계 실험에서 백금 상대전극에 대해 수소를 2시간에 걸쳐 약 86 μmol·cm^{-2} 만큼 생산된 것을 확인할 수 있었다. 이러한 결과는 스핀 코팅으로 제작한 PEDOT:PSS에 같은 CdSe 양자점과 CoPi가 도입된 전극 대비 매우 우수한 것으로 드러나 얼음위에서 합성된 2차원 PEDOT:PSS가 디바이스 성능 향상에 긍정적인 영향을 미침을 보여주는 것이다. 뿐만 아니라, PEDOT:PSS의 광학적으로 투명한 특성을 활용하여 ITO / PEDOT:PSS / P3HT:PCBM / Au 형태의 전극을 제조하고 태양전지로 적용 가능성을 확인하였다. 마찬가지로 일반적인 스핀코팅 방법으로 중합한 PEDOT:PSS을 이용한 대조군 전극의 특성도 함께 비교하였다.

그림 16c에서 보여주는 바와 같이, 스핀코팅한 PEDOT:PSS를 이용하였을 경우 단락전류밀도(Jsc) 값이 9.8 mA/cm^2 인 반면, 얼음 위에서 합성한 PEDOT:PSS를 이용하였을 경우 12.67 mA/cm^2 의 값을 보여 약 30% 향상되었고, 개로전압(V_{oc})도 0.61 V에서 0.66 V로 높은 값을 보였고, 그로 인하여 fill factor가 52%에서 63%로 약 11% 향상된 성능을 보였다. 이렇게 향상된 성능을 보이는 요인으로는, 2차원 PEDOT:PSS의 Rq < 1nm 수준의 낮은 표면 roughness에 의하여 2차원적인 전하 전도 특성에 의한 것이 가장 중요한 역할을 하였다고 판단되었다.

나. 2차원 PEDOT:PSS 나노시트를 이용하여 bending motion이 가능한 전극 소재로 활용

앞서 언급한 것과 같이, 인공 근육 등의 미래 유연 전극 소재로 적용되기 위해서는 높은 전기적 특성 외에도 충분한 신축성을 필요로 한다. 따라서 본 연구진은 얼음 위에서 합성한 2차원 PEDOT:PSS 합성 과정에 가소제를 도입하여 viscoelasticity를 부여하고자 하였고, 이와 더불어 micro-porous한 구조의 PEDOT:PSS를 합성하는 데에 성공하였다. 다음으로, 위와 같이 합성한 다공성 2차원 PEDOT:PSS를 이용하여 액추에이터를 제작하였다. 이온성 액체가 포함된 고분자 멤브레인에 다공성 2차원 PEDOT:PSS 전극을 interfacial layer로 이용하여 전기감응성 액추에이터를 제작한 결과, 그림 17과 같이 약 1 V에서 3 V 크기의 비교적 낮은 전압에서도 상당한 수준의 bending motion을 보이는 것을 확인할 수 있었다.

5. 연구개발결과의 활용계획

- 얼음에서 합성한 고분자의 경우, 값비싼 탄소계 물질을 결합하지 않아도 매우 우수한 특성을 보이기 때문에 경제적으로 파급효과가 매우 클 것으로 기대됨.
- 얼음에 합성하고 있는 고분자의 경우 높은 전기 전도 특성을 가지며, 유연하고 투명한 특성을 가지기 때문에, 유기전자디바이스의 탄생을 가능하게 해줄 것으로 여겨져, 실제 태양전지나 다양한 유연 전극에 활용될 가능성이 매우 높아, 경쟁력 있는 지적재산권을 확보할 수 있을 것으로 기대됨.
- 그동안 전도성 고분자의 합성은 전 세계적으로 그 중요성이 강조되고 있는 친환경 프로세스와 거리가 먼 것으로 여겨져 왔으나, 수용액 기반의 친환경 합성법을 제시함으로써 향후 이 합성법을 다양한 화학 반응에 적용할 경우 환경적으로 유익할 것으로 판단됨.
- 나아가, 정립된 합성법을 기반으로 이러한 친환경 소재의 활용범위를 넓혀 태양광하에서 수소를 생산하거나, 연료전지 전극 등으로 활용하기 위해 전도성 고분자/무기나노입자를 합성으로 연구 범위를 넓히고자 하는 것 또한 태양전지/연료전지의 잠재적 시장이 매우 크다는 것을 감안할 때 높은 파급효과가 기대됨.

6. 참고문헌

1. Jellinek, H. H. Liquid-like (transition) layer on ice. *J. Colloid Interface Sci.* **1967**, *25*, 192.
2. Dash, J. G.; Fu, H. Y.; Wettlaufer, J. S. The premelting of ice and its environmental consequences. *Rep. Prog. Phys.* **1995**, *58*, 115-167.
3. Dash, J. G. History of the search for continuous melting. *Rev. Mod. Phys.* **1999**, *71*, 1737-1743.
4. Rosenberg, R. Why is ice slippery? *Phys. Today* **2005**, *58*, 50-55.
5. Sotthewes, K.; Bampoulis, P.; Zandvliet, H. J. W.; Lohse, D.; Poelsema, B. ACS Nano 2017, 11, 12723−12731.
6. Sazaki, G.; Zepeda, S.; Nakatsubo, S.; Yokomine, M.; Furukawa, Y. *Proc. Natl. Acad. Sci. U.S.A.* **2012**, *109*, 1052-1055.
7. Asakawa, H.; Sazaki, G.; Nagashima, K.; Nakatsubo, S.; Furukawa, Y. *Proc. Natl. Acad. Sci. U.S.A.* **2016**, *113*, 1749-1753.
8. Materer, N.; Starke, U.; Barbieri, A.; Van Hove, M. A.; Somorjai, G. A. Molecular surface structure of a low-temperature ice Ih(0001) crystal. *J. Phys. Chem.* **1995**, *99*, 6267-6269.
9. Li, Y.; Somorjai, G. A. Surface premelting of ice. *J. Phys. Chem. C* **2007**, *111*, 9631-9637.

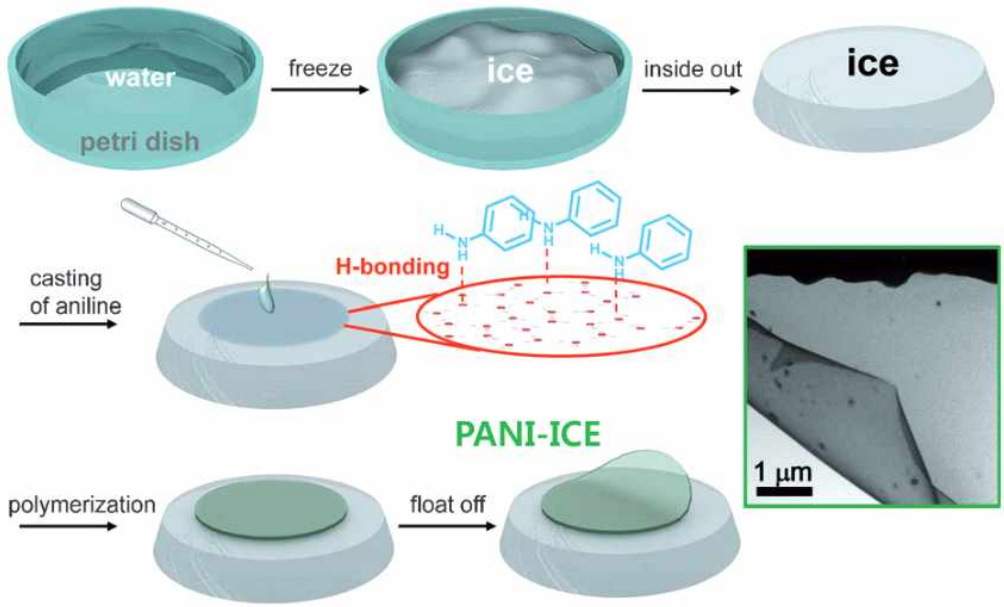

그림 1. 얼음 표면에서의 전도성 고분자 합성 스킴.

KOPRI

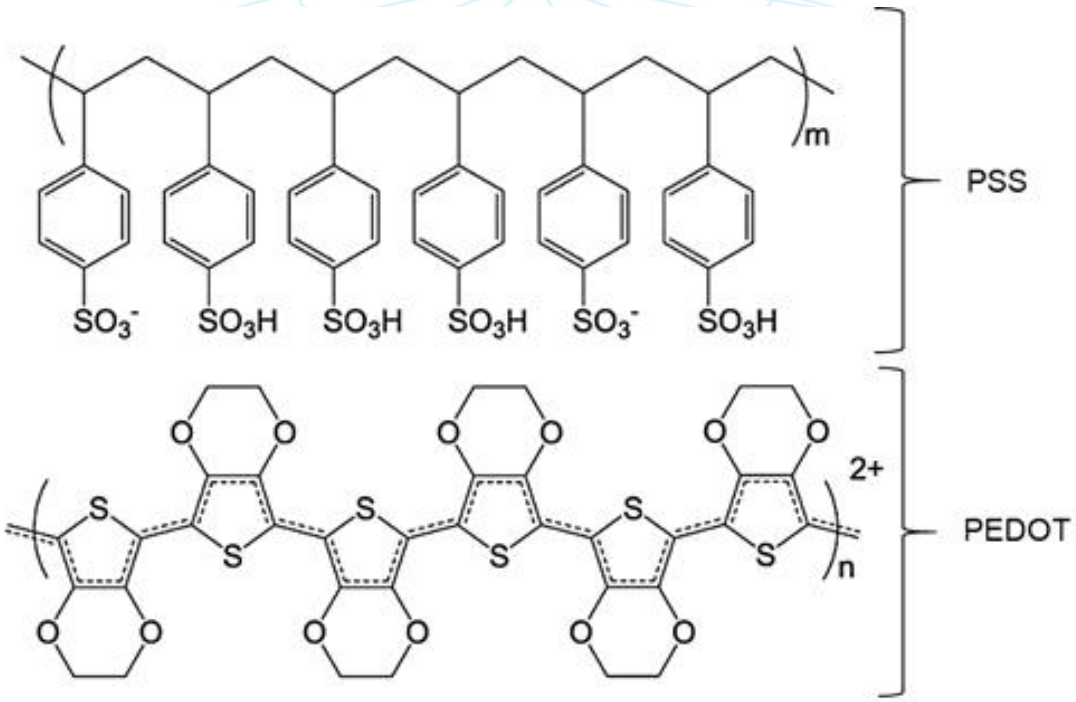

그림 2. 투명한 전도성 고분자인 PEDOT의 화학구조

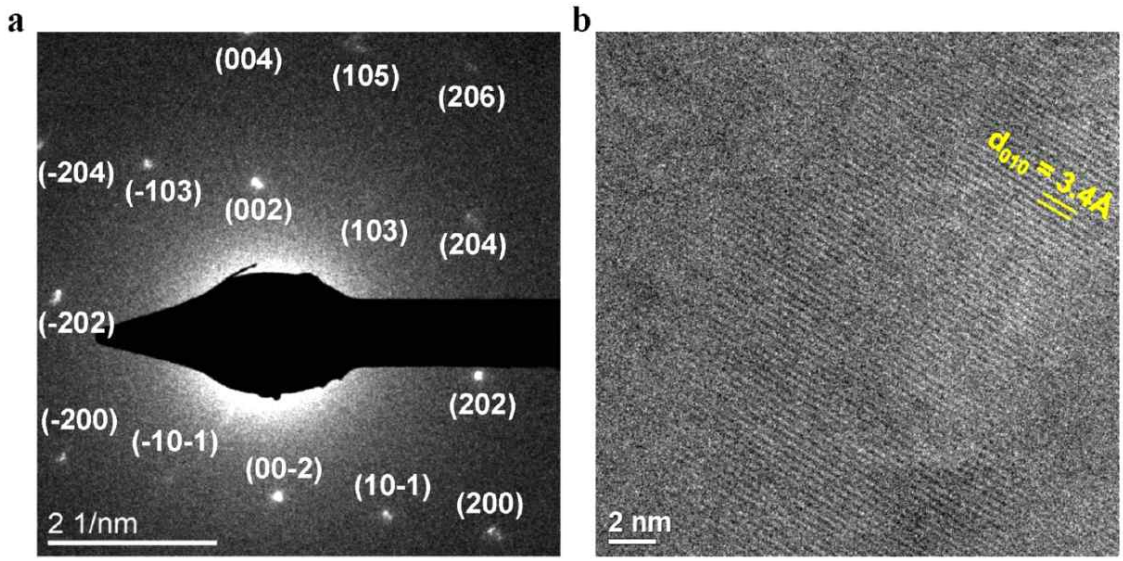

그림 3. 얼음 표면에서 합성한 2차원 전도성 고분자의 (a) 제한시야 전자회절(Selected Area Electron Diffraction) 패턴, (b) 고해상도 투과전자현미경(HRTEM) 사진.

KOPRI

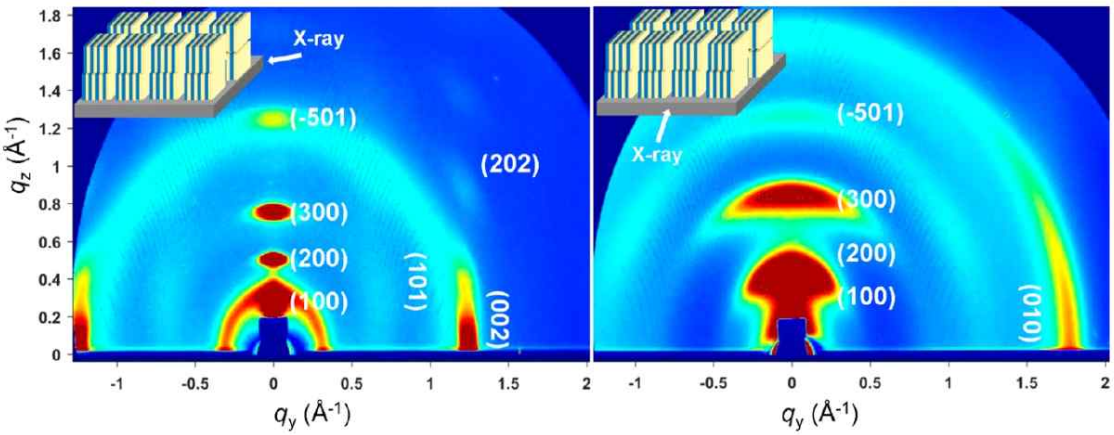

그림 4. 얼음 표면에서 합성한 2차원 PEDOT:PSS의 GI-WAXS 패턴.

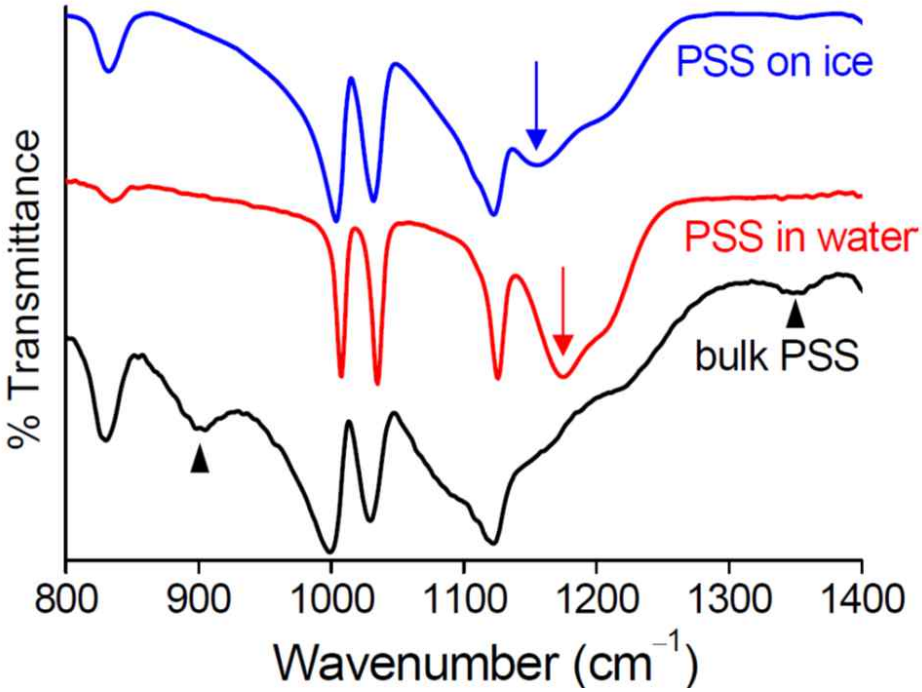

그림 5. 건조 상태(bulk PSS), 물과 접촉한 상태(PSS in water), 그리고 얼음 표면에서의(PSS on ice) PSS의 감쇠 전반사 퓨리에 변환 적외선 분광 스펙트럼.

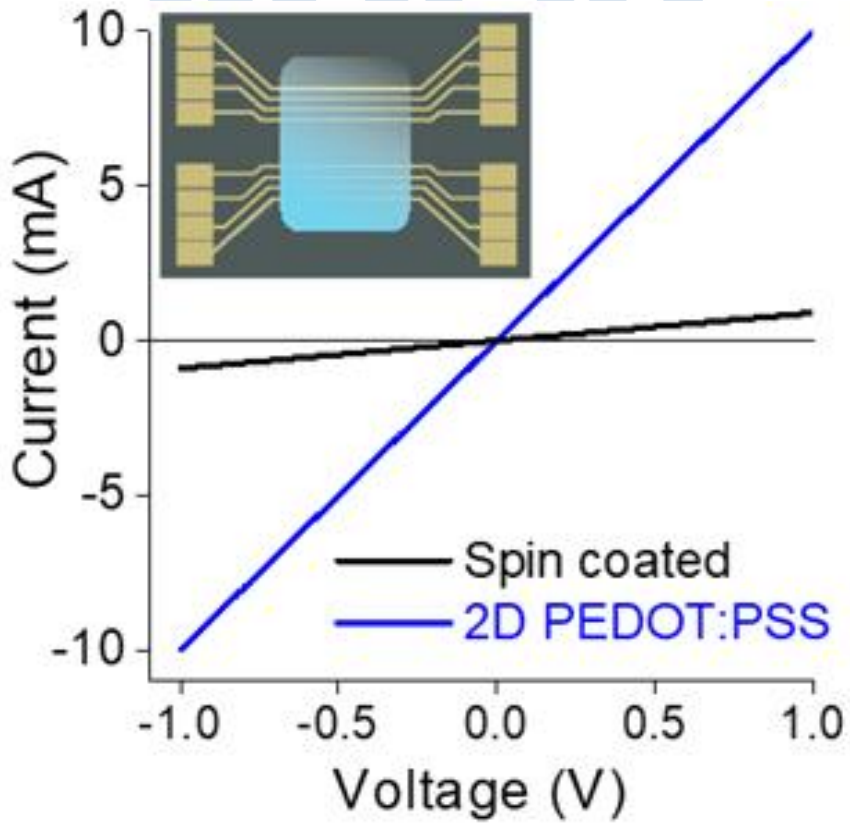

그림 6. 얼음 표면에서 합성한 PEDOT:PSS 막(2D PEDOT:PSS)과 스핀코팅으로 준비한 PEDOT:PSS 막(Spin coated)의 전류 전압 곡선 및 금 전극으로 코팅된 Si/SiO_2 웨이퍼의 삽도.

(a)

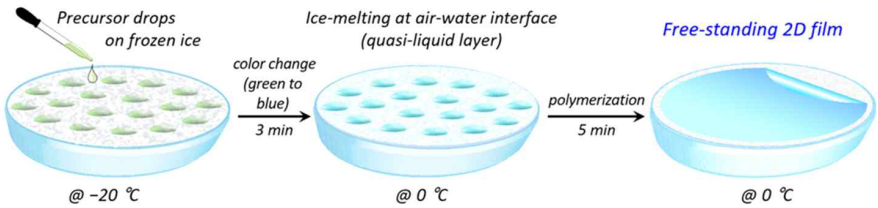

(b)

그림 7. (a) 얼음 표면에서의 PEDOT:PSS 전도성 고분자 막 합성 과정의 도식 (b) 약 10 cm 크기의 대면적으로 합성된 전도성 고분자 막의 사진.

KOPRI

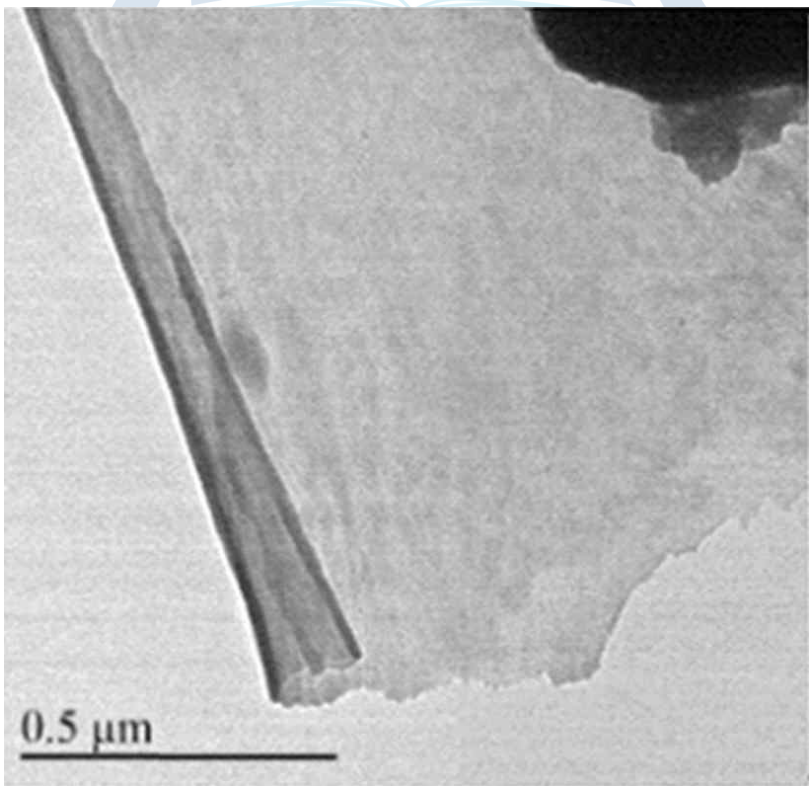

그림 8. 얼음 표면에서 합성한 2차원 PEDOT:PSS 막의 투과전자현미경 사진.

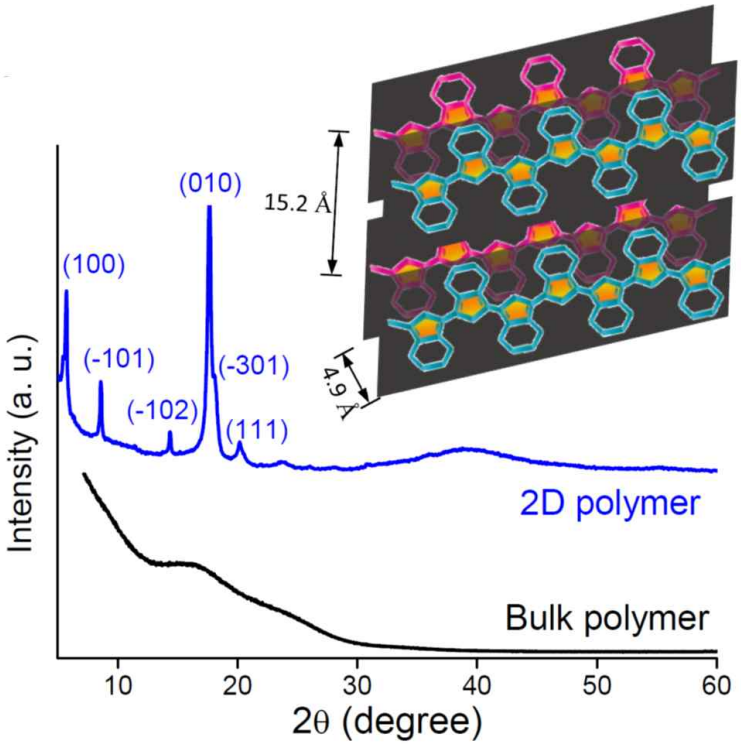

그림 9. 일반적인 용액 중합으로 합성한 PEDOT:PSS (Bulk polymer)와 얼음 표면에서 합성한 PEDOT:PSS 막(2D polymer)의 X선 회절 패턴 및 2D PEDOT:PSS의 PEDOT 분자의 배열을 보이는 삽도.

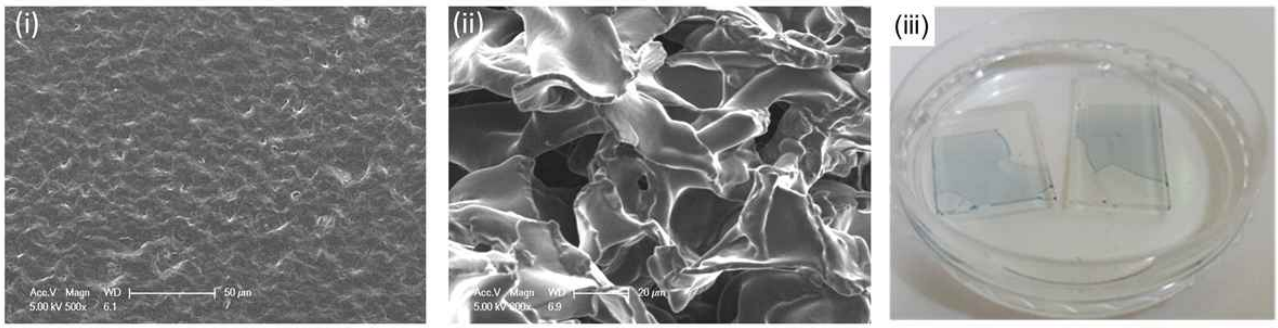

그림 10. (i) 가소제를 넣지 않는 순수한 PEDOT:PSS의 주사전자현미경 사진, (ii) 가소제 Triton X-100를 도입하여 합성한 PEDOT:PSS의 주사전자현미경 사진과 (iii) 가소제를 넣은 PEDOT:PSS의 대면적인 합성을 보여주는 광학 사진.

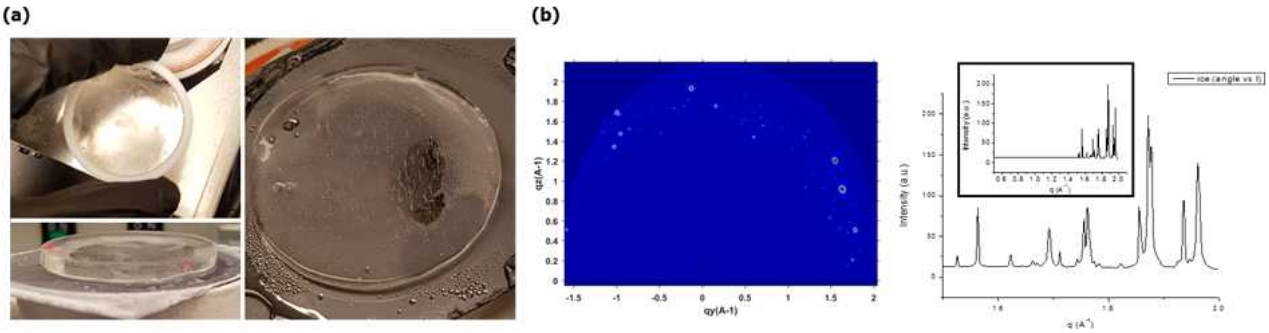

그림 11. (a) 펠티에 모듈을 이용하여 만든 표면이 평평한 얼음, (b) -20 ℃의 순수한 얼음에 대한 grazing-incidence X-ray scattering 실험 결과의 2차원 데이터 및 1차원 데이터.

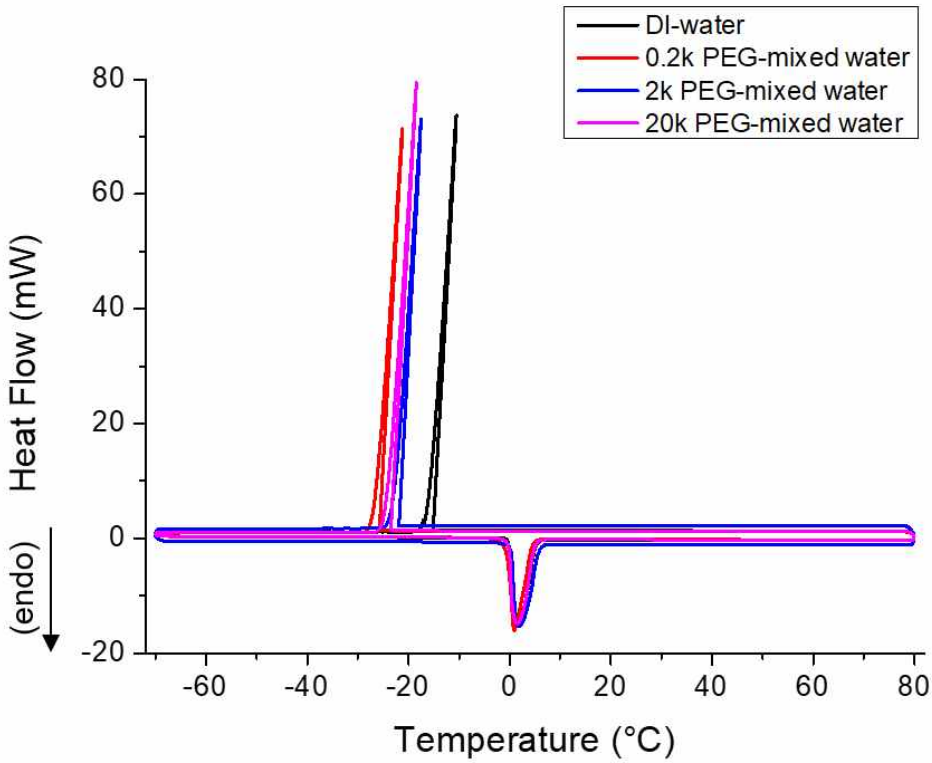

그림 12. 순수한 물과 0.2 k, 2 k, 20 k 분자량의 PEG를 1 %만큼 도입한 물의 시차주사열량 분석법 (Differential Scanning Calorimetry, DSC) 결과

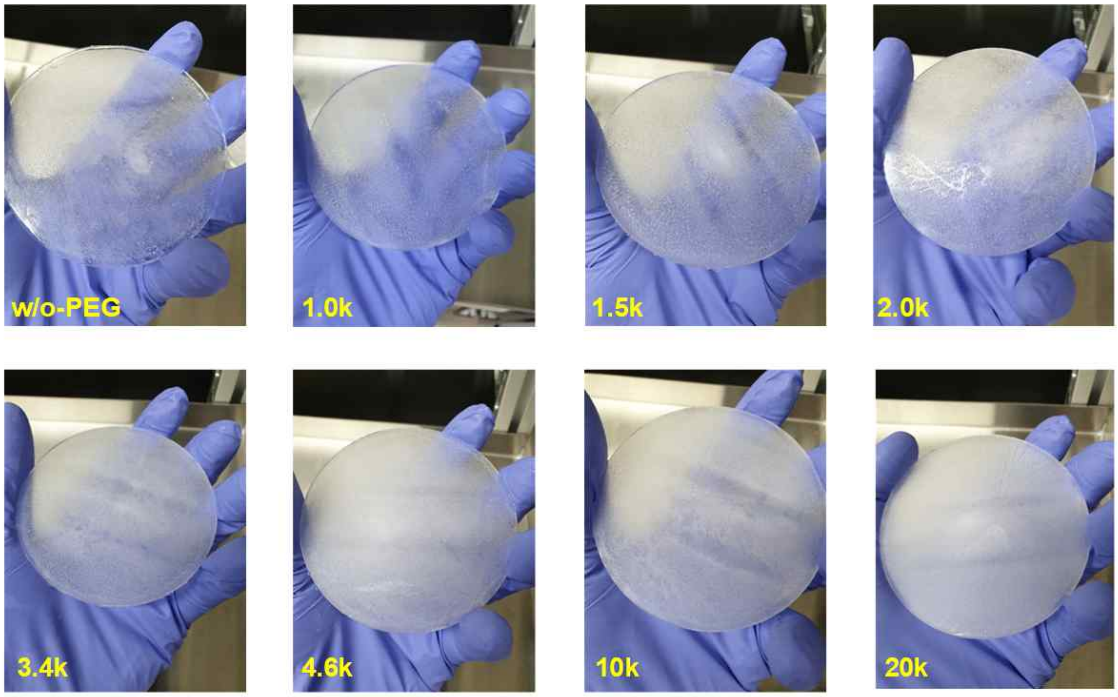

그림 13. 순수한 물을 얼린 얼음과, 다양한 PEG의 함량을 2.5 %로 도입하여 만든 얼음을 찍은 사진.

KOPRI

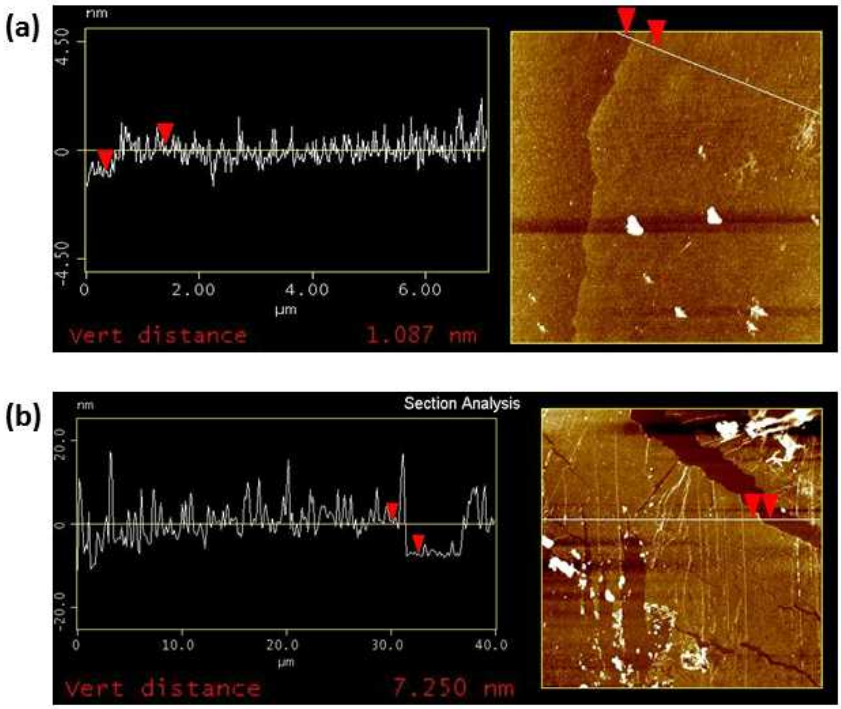

그림 14. (a) -10 ℃에서 반응시간 10 분의 조건에서 합성한 두께 약 1 nm의 전도성 고분자 시트, (b) -10 ℃에서 반응시간 15 분의 조건에서 합성한 두께 약 7 nm의 전도성 고분자 나노 시트.

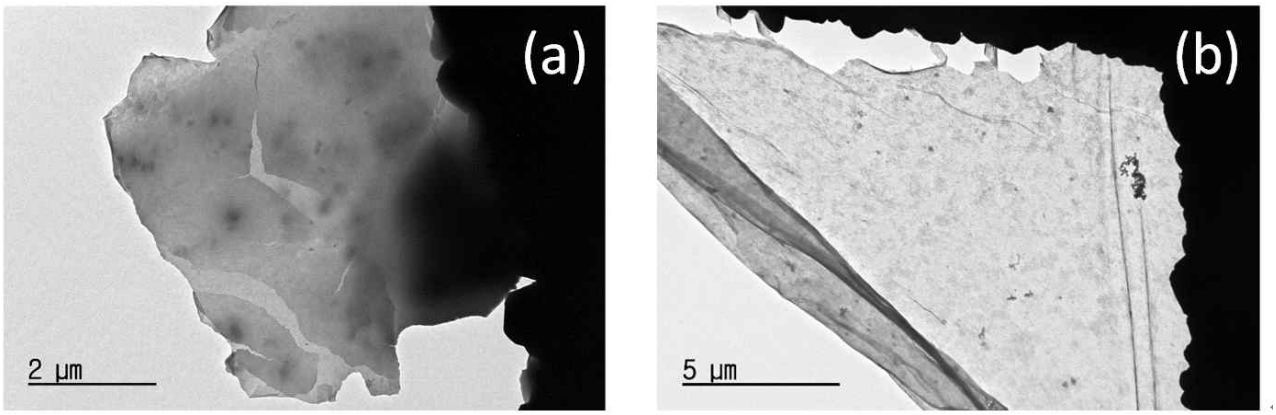

그림 15. 얼음의 결정성을 조절하기 위해 PEG(3.4 k)를 (a) 2.5 wt%, (b) 5 wt% 만큼 도입한 얼음 위에서 합성한 PEDOT:PSS의 투과전자현미경 사진.

KOPRI

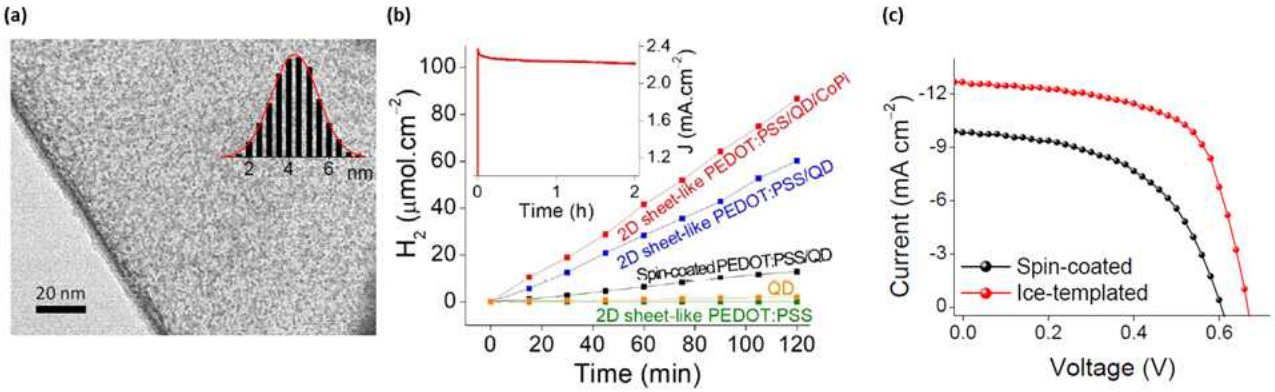

그림 16. (a) 2차원 PEDOT:PSS-CdSe 양자점 복합물의 투과전자현미경 사진 (b) 2D PEDOT:PSS, CdSe 양자점, Spin-coated PEDOT:PSS-CdSe 양자점 복합물, 그리고 2D PEDOT:PSS-CdSe 양자점-CoPi 복합물의 수소 생산 연구 (c) 얼음 위에서 합성한 2차원 PEDOT:PSS (Ice-templated)와 일반적인 스핀코팅 방법으로 합성한 PEDOT:PSS (Spin-coated)을 이용하였을 때의 전압-전류 곡선으로, 실험은 모두 AM 1.5G 조건에서 수행되었음.

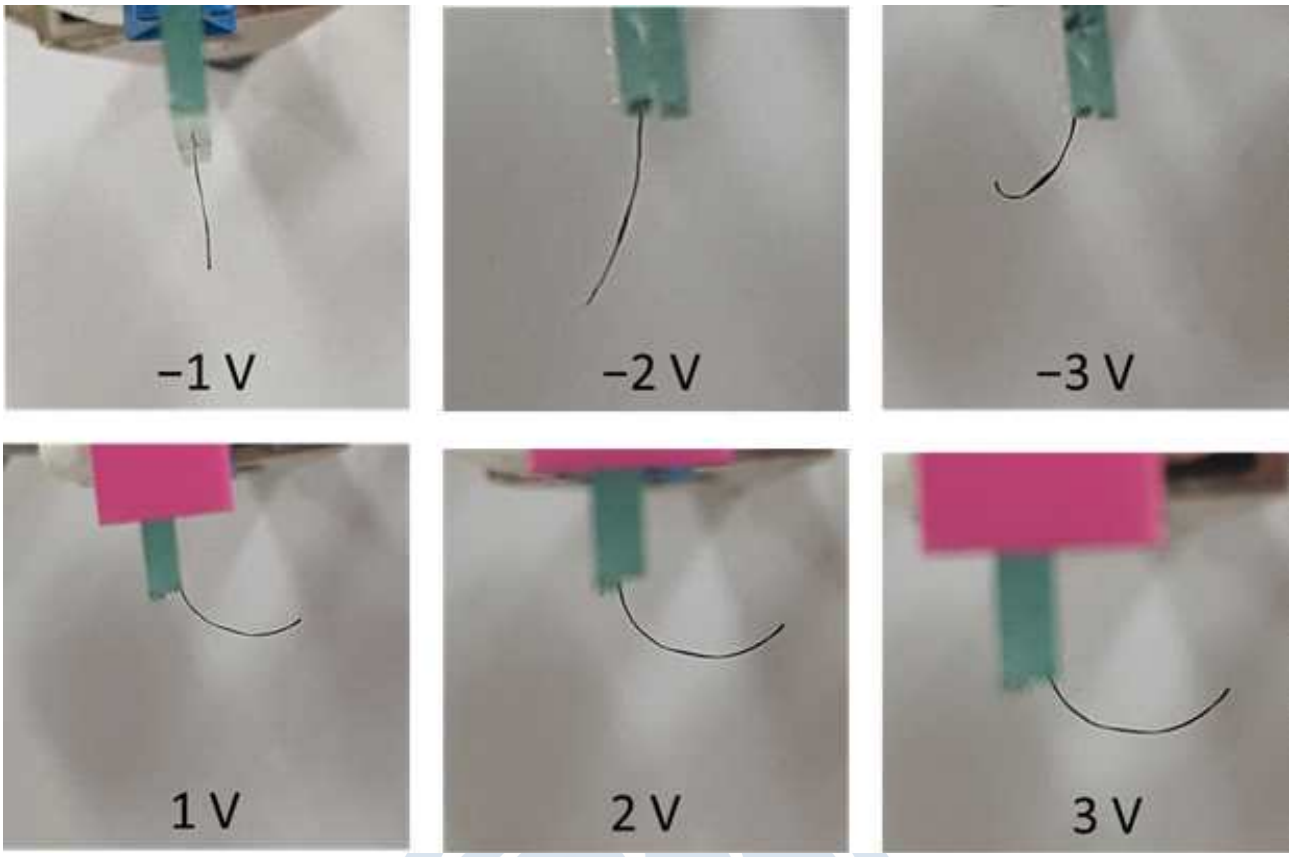

그림 17. 2차원 PEDOT:PSS:Triton X를 이용하여 제작한 액추에이터에 -3V부터 3V 범위의 전압을 인가하였을 때에 각각 어느 수준으로 bending motion을 보이는지를 보여주는 광학 사진.

KOPRI 극지연구소

제 4 장

연구개발목표 달성도 및 대외기여도

제 1 절. 연구개발목표 달성도

1. 연차별 목표 대비 달성도

총연구기간내 연차별 목표 대비 달성율(%)					
구분	연차별 달성내용				연차별 계획대비 연구실적 달성율(B) (%)
	세부연구목표	연구내용	가중치 (A)	달성실적	
1년차 (2018)	1. 얼음화학 연구 인프라 구축 및 기초연구	올바른 얼음 표면모델 완성 및 표면 흡착 구조, 흡착 에너지에 대한 연구를 수행	0.3	1차 얼음표면모델 완성	100
		얼음미구조 입자분석을 위한 장비설치		장비설치 완료	
		얼음표면 흡착반응 계산을 위한 기반 구축 및 얼음-수은 흡착 반응 기초계산 수행		얼음-수은 흡착 반응관련 논문게재완료	
	2. 얼음화학반응에 기초한 극지방 자연현상의 이해	얼음의 저농도 할로겐 원소 및 이온성분 분석 최적화	0.4	최적화 완료	100
		얼음 내 무기요오드 거동 연구		논문게재완료	
		얼음/광물(표준 광물)의 지구화학적 반응 모사 시스템 구축		시스템구축 완료	
		얼음 내 환경유기 물질의 화학 반응 특성 및 메커니즘 이해		논문게재완료	
		얼음 화학반응에 의한 할로겐 물질 발생이 극지 대기 에어로졸 입자 형성에 미치는 영향 규명		MAX-DOAS 구축완료 및 시계열 데이터 획득	
		남극해에서의 휘발성 유기화합물, 할로겐 라디칼 전구물질, 그리고 질소화합물의 분포 분석		현장연구 데이터 획득	
		극지역의 DMS와 할로겐 화합물의 반응 모델링과 해양 및 대기에서의 DMS관측		현장연구 데이터 획득	
	3. 얼음화학기반 응용기술 탐색 및 기초연구	얼음표면 특성을 이용한 전도성 고분자 배향 연구	0.3	신규물질 합성완료	100
		얼음 내에서 오염물질간의 산화·환원 반응에 의한 오염물질 제거 연구		상위 10% 논문게재	
	계		1.0		100

총연구기간내 연차별 목표 대비 달성율(%)					
구분	연차별 달성내용				연차별 계획대비 연구실적 달성율(B) (%)
	세부연구목표	연구내용	가중치 (A)	달성실적	
2년차 (2019)	1. 얼음화학 연구 인프라구축 및 얼음분자모델 개발	얼음 표면 흡착 후 분자들의 추가적인 표면 화학반응의 가능성과 그의 메커니즘을 원자수준에서 연구	0.3	논문게재완료	100
		얼음 표면 연구를 위한 기반 조성. 화학 분자-얼음 간 상호 작용 연구		논문 작성 중	
		저온고압 기초장비 설치 후속작업, 데이터보정 및 기초데이터 획득		초기저온고압장비 구축완료 및 기초데이타 획득	
	2. 얼음화학반응이 극지풍화작용과 할로겐가스 생성에 미치는 영향이해	얼음의 할로겐 화학종 분석법 기초연구	0.4	화학종 분석법 습득완료	100
		얼음 내 요오드물질과 다른 유/무기물과의 화학반응연구		논문게재완료	
		대기 관측을 통한 할로겐 물질 기원 에어로졸 입자 형성 기작 규명		현장데이타 획득	
		세종기지 인근 빙권 변화가 할로겐 물질 및 에어로졸 입자형성에 미치는 영향 연구		현장데이타 획득	
		남극기지 주변 snowpack과 대기 중의 반응성 미량기체 상호 작용 연구		현장데이타 획득	
		얼음-수은 흡착반응의 계산-관찰 결과 상호비교		논문게재완료	
		극지역의 DMS와 할로겐 화합물의 반응 모델링을 통한 현장관측 자료의 분석		현장데이타 획득	
		얼음 내 자연시료의 지구화학적 반응 연구		극지현장시료를 대상으로한 실험완료	
		얼음 내 환경무기 물질의 화학 반응 특성 및 메커니즘 이해		논문게재완료	
	3. 얼음화학기반 응용기술 탐색 및 기반연구	얼음 표면 특성을 이용한 2차원 구조 전도성 신물질 개발	0.3	전도성고분자 신물질 개발완료	100
		얼음 내에서의 화학 반응에 의한 활성산소종 생성 및 이에 의한 오염물질 분해 연구		얼음내 활성산소종을 이용한 오염물 분해실험 완료	
	계		1.0		100

2. 정량적 연구 성과

년도 (과제연차)	성과목표	성과지표	평가기준	가중치 (A)	목표 (B)	달성 (C)	달성도(%) (D=C/B)	달성도(%) (A×D)
2018 (1차년도)	논문게재	상위수준 논문게재	논문 건수	0.6	SCI(E) 논문 mrnIF 80이상 2 편 (※mrnIF 90이상 논문은 1.5편으로 계산)	2편	100	60
		논문게재	논문 건수	0.1	SCI(E) 논문 mrnIF 60이상 1 편	1편	100	10
	얼음화학 연구인프라구축 및 기초연구	얼음화학 기초연구를 위한 실험 인프라 구축	인프라 구축여부	0.025	선진국 대비 30%	30%	100	2.5
		개발된 얼음표면모델 완성도	개발모델제시	0.025	선진국 대비 20%	20%	100	2.5
	얼음화학반응에 기초한 극지방 자연현상의 이해	극지모사 화학분석 및 분석자료	분석결과제시	0.15	실험결과 1세트	2	100	15
		할로겐 물질 관측장비 구축 및 자료확보	관측장비 구축여부 및 자료제시	0.025	아라온 현장연구 시계열자료	1	100	2.5
		국제협력 건수	공동연구여부	0.025	1 건	2	100	2.5
	얼음화학기반 응용기술 탐색 및 기반연구	국내외 지적재산권 확보 건 수	특허출원건수	0.025	1건	1	100	2.5
		얼음의 화학적 특성을 이용한 신소재 합성	합성물제시	0.025	신소재 1 건	1	100	2.5
합 계				1				100

KOPRI 극지연구소

년도 (과제연차)	성과목표	성과지표	평가기준	가중치 (A)	목표 (B)	달성 (C)	달성도(%)	
							(D=C/B)	(A×D)
2019 (2차년도)	논문게재	상위수준 논문게재	논문 건수	0.6	SCI(E) 논문 mrnIF 80이상 3 편 (※mrnIF 90이상 논문은 1.5편으로 계산)	9편	100	60
		논문게재	논문 건수	0.1	SCI(E) 논문 mrnIF 60이상 1 편	2편	100	10
	얼음화학 연구인프라구축 및 얼음분자모델 개발	얼음화학 기초연구를 위한 실험 인프라 구축	구축된 인프라 제시여부	0.025	얼음화학실험 인프라 2건	5건	100	2.5
		개발된 얼음표면모델 완성도	개발모델제시	0.025	선진국 대비 30%	30%	100	2.5
	얼음화학반응이 극지풍화작용과 할로겐가스 생성에 미치는 영향이해	극지풍화작용 화학실험 및 분석자료	분석결과제시	0.05	실험결과 1세트	1set	100	5
		할로겐가스생성 화학실험 및 분석자료	분석결과제시	0.05	실험결과 1세트	1set	100	5
		극지환경화학반응 실험 및 분석자료	분석결과제시	0.05	실험결과 1세트	1set	100	5
		할로겐가스 관측자료확보	관측자료제시	0.025	시계열자료	확보	100	2.5
		국제협력 건수	공동연구여부	0.025	2 건	3건	100	2.5
	얼음화학기반 응용기술 탐색 및 기반연구	동결수처리공정 기초실험수행	분석결과제시	0.02	실험결과 1세트	1set	100	2
		얼음의 화학적 특성을 이용한 신소재 합성	합성물제시	0.02	신소재 1 건	1건	100	2
		지적재산권 확보 건수	특허건수	0.01	1 건	2건	100	1
합 계				1.0				100

AOPR 극지연구소

제 2 절. 대외 기여도

본 과제에서 집중적으로 연구된 얼음의 특성 연구 결과는 극지 자연현상 이해를 포함한 과학 전 분야의 발전에 기여할 수 있다. 정교한 얼음표면모델의 개발은 향후 얼음에서 일어나는 화학 반응 실험 결과를 해석하는데 도움이 될 것이다. 얼음과 연관된 할로겐 물질의 생성 기작 및 거동 연구, 얼음 내 금속 산화물 용출, 얼음에 의한 물질의 독성 변화와 같은 현장 관측 및 실험실 실험 결과는 극지방 및 전지구적 자연 현상 해석에 도움이 될 수 있고, 얼음의 영향을 반영한 기후변화모델과 같은 다양한 시뮬레이션에 사용되어 당면한 문제의 해결 및 미래를 예측하는데 이용될 수 있다.

연구 과정에서 동결 농축 효과를 이용하여 개발한 응용 기술인 미량 철 이온 형광분석, 동결로 인한 활성 산소종 생성 및 이를 이용한 오염물질 분해, 향상된 성능과 기능의 전도성 고분자 합성 기술의 발전과 활용을 위하여 관련 특허를 출원하였다. 이러한 응용 기술들은 향후 추가 연구를 통해 실용화하여 경제적 가치를 창출할 수 있을 것으로 기대된다.

연구 개발 결과로 18건의 논문이 출간되었으며, 그 중 9건은 JCR 기준 상위 20% 이내의 우수 학술지에 출간되었다. 특히 4건의 논문이 표지 논문으로 선정되어, 극지연구소 및 국내 연구진의 우수성을 홍보하여, 향후 얼음 연구를 국제적으로 선도할 수 있음을 드러내었다. 또한 내·외부 참여연구원으로 약 20여명의 학생연구원을 지원하였으며, 박사 3명, 석사 2명, 학사 2명을 배출하여 미래에 연구·개발에 종사할 인력을 양성하는데 공헌하였다.

KOPRI 극지연구소

제 5 장

연구개발결과의 활용계획

“얼음화학 특성연구를 통한 극지방 자연현상 규명 및 응용기술 개발” 과제 수행을 통하여 얼음 연구를 위한 인프라와 연구진, 국내외 연구 네트워크를 구축하였고, 연구 성과를 거두었다. 2020년부터 시작하는 후속 연구과제인 “얼음의 미세구조 특성연구를 통한 저온 정화기술 및 환경에너지 신소재 개발” 과제에서는 본 과제에서 구축된 인프라를 활용하여 얼음의 화학적 특성 뿐 아니라 미세 구조에 기반을 둔 물리적 성질 및 생명활동에서의 역할 규명을 추가함으로 얼음과학에 대한 전반적인 연구를 진행할 것이다. 또한 저온 얼음의 특성을 활용한 응용 기술 개발에 중점을 두어 실용화 가능성이 높은 연구를 할 것이다. 구체적으로 얼음 미세구조 특성연구 분야에서는 저온 분석법을 통한 얼음 표면 및 준액체층 특성연구와 동결농축현상 기작 연구를 하고, 얼음 내에서 일어나는 화학반응 및 생물현상연구를 성과목표로 얼음 내 중금속 정화기작 연구, 얼음 내 유기오염물질 정화기작 연구, 얼음 내 활성 산소종 생성연구, 얼음화학 생성물의 생물독성 평가, 결빙방지단백질 활성에 의한 얼음구조 변화연구, 얼음 미세구조 내에서의 생물 생리연구, 얼음 내 지구환경화학반응 연구를 수행한다. 저온응용기술 기초 연구로 동결을 이용한 친환경 수처리 기술과 얼음특성을 활용한 환경/에너지 신소재를 개발한다.

이외에도 얼음 및 저온, 극지 연구를 위하여 필요한 저온 환경 모사 및 저온 얼음 분석 장치를 연구・개발할 필요성이 있다. 또한 현재까지 구축한 연구 장비 기반은 얼음뿐 아니라 저온 과학기술 연구 전반에 활용할 수 있으므로 극지연구소 내부 또는 외부와 공동으로 이와 관련된 연구도 추진할 예정이다. 본 과제 및 후속 과제를 통해 개발 중인 얼음 특성을 활용한 응용 기술은 향후 환경 정화 및 에너지 관련 기업에 기술을 이전하는 방법으로 실용화가 가능할 것이다.

본 연구 과제를 통하여 얻은 연구 결과는 얼음화학이라는 학문적 미개척 분야를 선도하고 극지방 자연 현상 해석에 있어 얼음화학의 새로운 역할을 규명하였으며, 얼음에서 일어나는 화학반응에 대한 이해로 향후 해빙으로 인한 기후영향 예측, 기후변화모델 개발 및 정확도 향상에 기여할 것이다. 또한 얼음에서 일어나는 특이한 화학 반응에 대한 기초 연구결과는 교육 자료로 활용할 수 수 있으며, 국제 학회 및 위원회 등과 공유해 기후변화/지구온난화 대응책 마련 등 정책 입안에 필요한 지식이 될 것이다.

제 6 장

연구개발과정에서 수집한 해외과학기술정보

이 장에서는 연구개발과정에서 방문한 얼음 관련 연구 기관 및 참가한 얼음 관련 학회에 관한 정보를 기술하였다.

제 1 절. 일본 홋카이도 대학교 저온과학연구소(Institute of Low Temperature Science, Hokkaido University)

저온 과학 연구소(ILTS, Institute of Low Temperature Science)는 빙권(Cryosphere)에서 발생하는 다양한 자연 현상에 대한 학제 간 연구를 위해 홋카이도 대학 부속 연구소로 1941년에 설립됨. 물리학, 기상학, 생물학, 의학, 응용물리학과, 해양학과가 있음.

1. 저온과학연구소 조직 구성

○ 공동연구부(Joint Research Division)
- 남극 빙권-해양 시스템(Antarctic Cryosphere-Ocean System)
- 북극 빙하 및 빙상 변화(Arctic Glacier and Ice Sheet Change)
- 저온 나노 재료 과학(Low-temperature nano-material science)
- 저온 조건에서의 광합성(Photosynthesis under low temperature conditions)
- 육지와 바다를 연결하는 태평양 연안해의 역할(The role of Pacific marginal seas in linking adjacent lands with oceans)
- 국제 남극 연구소 프로그램(International Antarctic Institute Program)

○ 물·물질 순환 연구부(Water and Material Cycles Division)
- 해수, 해빙, 눈/얼음, 구름, 가스에 초점을 맞춘 대기 화학, 빙하학, 수문학, 물리 해양학, 해양 화학 및 지구 화학 등의 연구 수행

○ 얼음·눈 과학 연구부(Frontier Ice and Snow Science Division)
- 얼음 및 눈 과학을 바탕으로 행성 및 지면 현상에 대한 포괄적인 연구 수행

○ 생물 연구부(Environmental Biology Division)
- 극한지 생물 다양성 분석과 생물체 적응 메커니즘 규명 등 극한 환경과 생물간의 상호 작용 연구

○ 팬-오호츠크 리서치 센터(Pan-Okhotsk Research Center)
- 팬-오호츠크 지역(유라시아 대륙, 북태평양, 북극 지역 및 아열대 지역으로 둘러싸인 지역)

과 전지구적 기후변화의 상호작용 평가

○ 기술부(Technical Division), 행정부(Administratie Office)

2. 저온과학연구소 주요 연구 현황

○ 물·물질 순환 연구부, 빙설 신영역 연구부, 생물 환경 연구부

○ 빙설 신영역 연구부(Gen Sazaki 교수; 상전이 역학, Naoki Watanabe 교수: 우주물질 과학, Shigeru Aoki 교수: 해양물리학, 2019 JARA 대장)

○ 현재 저온과학연구소 내에 정규직 기준, 연구원은 40명/기술원 5명/행정인력 15명 정도, 계약직과 학생을 포함하여 100명 이상의 인력이 있으며, 상대적으로 극지연구소 보다 적은 규모이지만, 연구분야의 선택과 집중으로 세계적인 연구성과를 창출하고 있음

○ 저온과학연구소는 이미 PRIC(중), AWI(독) 등 여러 나라와 협력을 하고 있으며, 우리 연구소 또한 협력 분야 발굴 및 공동 연구 수행에 대한 필요성이 요구됨

3. 저온과학연구소 연구실

○ 워크샵(기술실)

- 저온과학연구소에서 사용하는 연구장비 개발 및 커스터마이징을 수행함 (그림 1, 2)
- 기술부는 장비개발실, 첨단 기술 지원실, 공통 장비 관리실로 구성됨

○ -50℃ 챔버실

- 남극과 그린랜드의 빙하 시추의 보관과 저온 실험을 수행 (그림 3)

○ 해양 물리학 실험실

- 저온과학연구소의 남극 기수시스템부의 남극에서의 연구 현황(ROBOTICA; Research of Ocean-ice boundary in Teraction and change around Antarctica 프로그램): 해수면 경계과정, 소야난류의 해류특성 등을 연구
- 저온과학연구소에서 개발한 ROV(Remotely-operated vehicle)을 이용한 남극 빙빙 연구 (그림 4)

○ 우주물질과학 실험실

- 우주와 지구·행성 대기에서 발생하는 원자·분자 - 나노 스케일의 미세한 물리적·화학적 현상 및 과정을 밝히기 위한 다양한 실험 기법 연구
- 최근에는 우주의 저온 영역 또는 지구 대기권에 존재하는 H_2O 고체 (얼음) 미립자에서 일어날 수 있는 물리적·화학적 변화를 중심으로 연구 수행
- 우주에 편재하는 얼음을 연구하고 있으며, 그 중에서도 별·행성 탄생 이전의 극저온 영역(분자 구름 : T ~ 10K)에 존재하는 비정질 얼음 입자 표면에서는 극저온 특유의 원자 터널 반응을 연구 (그림 5)

○ 상전이역학 연구실

- 고해상도 광학현미경(자체개발)을 이용한 얼음 결정 표면의 분자 수준 관찰 (그림 6)
- 얼음 결정의 육각 바닥에서 2차원의 섬모양의 분자층(0.37Å 두께)이 발달하여 퍼지며 결정

KOPRI 극지연구소

이 성장하는 모습 관찰 (그림 7)

- 얼음 결정의 바닥에서 생성되는 2종의 표면 액체상 발견
- 얼음 결정 형태의 비정형(불안정)에 대한 우주 실험 수행

○ 북해도대학 동위원소 영상화 연구실

- Stigmatic Isotope Imaging을 이용한 넓은 영역에서 고해상도 분석 기술 개발
- 2차원의 ^{18}O 이미징(Imaging Depth) 등 구현
- Cryo-SIMS 장비 소개 및 이를 이용한 다양한 분석 영역 연구 (그림 8)

제 2 절. 미국화학회(American Chemical Society)

1. 미국화학회(ACS) 소개

○ 미국화학회는 화학 전 분야 및 인접 분야를 다루는 세계 최대의 과학 학회로, 해마다 전 세계에서 15,000명 이상의 과학자들이 참석하며 12,800개 이상의 연구 결과가 발표됨. 특히 이번 Fall National Meeting에서는 Chemistry and Water이라는 주제로 “Water in the Solid State: Reactions & Interactions with Impurities”이라는 얼음 및 물과 관련된 특별 세션이 개최됨. 얼음과 관련된 다양한 연구 결과가 환경화학, 지화학, 물리화학 등 여러 분과에서 발표되었음.

2. 2019 ACS 학회 내용

○ 주로 발표된 연구는 수증기 또는 물이 얼음으로 상전이하는 과정에 관한 것으로, 얼음 생성에서 가장 어려운 단계인 핵생성을 이론 계산 또는 실험을 이용한 생성 원리 연구부터 이를 이용하여 얼음의 형성을 지연시켜 성에가 발생하기 어렵게 하는 표면 개발 및 결빙방지 단백질에 관한 연구까지 발표되었음.

○ 얼음의 미세 구조, 얼음 내부의 불순물의 분포 및 거동과 같은 얼음화학 반응을 이해하기 위한 기초 연구 및 얼음 내 불순물에 의한 얼음의 물리적 성질 변화 연구도 발표되었음. 상대적으로 분석하기 힘든 얼음 표면 및 내부의 불순물을 Workman-Reynolds 결빙 퍼텐셜, X선 형광, 단층 촬영 등의 분석 장비로 검출 및 정량할 수 있음을 확인함.

○ 얼음의 표면 또는 내부에서 일어나는 화학 반응에 관한 연구가 발표되었음. 저온 얼음 표면에서 질산의 광화학적 해리 과정 및 할로겐화수소의 자발적 해리 과정을 연구한 발표가 있었으며, 동결 농축 효과를 이용한 반응 가속 및 이를 수처리에 응용하는 연구가 제안되었음.

○ 국내외 얼음 화학 연구자들을 접견하고, 최근 연구 진행 상황 및 성과를 교환하였음. 이를 기반으로 향후 연구 시설 공유 및 공동 연구를 추진할 수 있을 것으로 기대됨.

○ 학회장 내 전시장에서는 여러 출판사 및 장비 제작사가 부스를 설치하여 홍보하였으며, 연구에 필요한 화학 분석 장비의 최신 동향을 습득할 수 있었음.

KOPRI 극지연구소

3. 2019 ACS 참가 내용

○ 현재 연구 중이거나 출간된 연구 결과를 구두(이두형, 이윤학, 한태욱) 또는 포스터(김기태, 정현영) 발표하였으며, 발표 및 토론을 통해 현재 연구를 보완할 점 및 향후 연구에 필요한 아이디어를 수집하였음.

○ 발표 제목

- 김기태: Enhanced redox transformation of inorganic iodine species in ice
- 이두형: Acceleration of amorphous solid water crystallization by acidic impurities
- 이윤학: Enhanced fluorescence detection on ferrous ion by freezing
- 한태욱: Application of biochar for removal of hexavalent chromium during freezing process
- 정현영: Redox chemical reaction between chromate and iodide in frozen solution: Mechanism, kinetics, and environmental implications

제 3 절. 미군 공병대 공학연구개발센터 극한지역연구소(Cold Regions Research and Engineering Laboratory, Engineer Research and Development Center, United States Army Corps of Engineers)

미 육군 공병대 산하 공학연구·개발센터 (표 1) 산하 연구소인 극한지역연구소(Cold Regions Research and Engineering Laboratory, CRREL)을 방문하여 극지 과학 및 공학 연구 분야 현황을 파악함.

1. CRREL 소개

○ 미국 뉴햄프셔주 해노버에 위치한 극한지공학연구소(Cold Regions Research and Engineering Laboratory)는 1961년 미 육군 공병대가 추운 환경에서 발생하는 과학·공학적인 문제의 다학제적인 해결을 위해 설립된 기관임. 현재 약 220명의 직원이 Biogeochemical Sciences, Force Protection and Sustainment, Signature Physics, Terrestrial and Cryospheric Sciences 등의 부서로 나뉘어 연구를 수행하고 있음.

○ CRREL의 연구 분야로는 한랭지 자연 환경을 이해하기 위한 생화학적 연구, 극한 지역에서 사용하기 위한 기술 연구, 한랭지에서의 군사력 이동 및 보급을 위한 연구, 지형 및 자연 환경 모니터링을 위한 원격 관측 등이 있음.

○ 뉴햄프셔 해노버와 알래스카 페어뱅크스에 저온과 관련한 다양한 시설을 보유하여 연구에 활용하고 있음. 다양한 크기와 성능을 가진 26개의 냉동 실험실을 비롯하여, 풍동실험실, 성에 연구시설, 재료 특성 연구를 위한 시설, 저온 차량 테스트 시설, 영구동토층 내 실험

실 및 터널 등을 연구용으로 사용 중에 있음.

○ 이 연구소에서 연구·개발된 품목으로는 어는점이 낮아 추운 지방 또는 겨울에도 공사가 가능한 콘크리트, 지표투과레이더를 장착하여 크레바스를 탐사하는 로보틱 로버, 현장에서 얼음이나 토양 내의 성분을 마이크로미터 해상도로 바로 분석할 수 있는 레이저 유도 붕괴 분광기 등이 있음.

○ CRREL의 Emily Asenath-Smith 박사 연구진은 얼음의 표면 접착에 관한 성질을 연구하고 있음. 이를 위해 얼음과 재료 사이의 전단 응력 및 인장 강도를 측정하기 위한 장비를 개발함. 또한 다양한 표면의 내구성을 평가하기 위하여, 외부 환경을 거친 후 얼음 흡착력을 측정하여 실제 환경에서 사용 가능한 표면 코팅제 및 얼음 제거 기술을 개발하고 있음.

2. CRREL 현황

- 설립일자: 1961년 2월 1일
- 기관대표: Joseph L. Corriveau 소장
- 기관현황(2017년도 기준)
  - 직원 220명 (연방정부소속 194, 외주인력 15, 학생 10, 육군소속 1)
    * 연구원 및 기술원 115명(박사 35, 석사 44, 학사 28 / 8명 외부파견)
  - 전체 예산 미상, 인건비 약 16.4백만 달러 (한화 약 192억)
- 기관 목표
  - 미 국방부와 공병대의 활동을 위해 전략적으로 중요한 다학제적 문제를 해결
  - 다양한 기후에 적용 가능한 토목공학, 지리정보공학, 탄력적 시스템 설계 등을 개발
- 연구분야: 국가 안보관련 과학기술, 한랭지 관련 연구, 생지화학, 원격탐사, 지리정보시스템, 육상 및 빙권과학 등
- 연구부서(5개 부서, 1개 센터): Biogeochemical Sciences, Engineering Resources, Signature Physics, Terrestrial and Cryospheric Sciences, Force Projection and Sustainment, Remote Sensing/GIS Center of Excellence

3. 연구소 유관연구사업

- 극한지 도로포장 (Cold Region Pavement Infrastructure Technologies)
  - 연구책임자: Danielle E. Kennedy (Danielle.E.Kennedy@usace.army.mil)
  - 극한지역에서의 신속한 활주로 복구를 위한 급속응결 충전재 개발
  - 영하의 기온에서 사용 가능 한 콘크리트 혼화제 개발
  - 아스팔트 도로 내 전도성 그물망 삽입·전기 공급을 통한 도로 제빙기술 개발
- 얼음의 물체접착력 연구(Ice Adhesion)
  - 연구책임자: Emily Asenath-Smith (emily.asenath-smith@usace.army.mil)
- 분자생물학 연구
  - 연구책임자 Robyn Barbato (robyn.a.barbato@erdc.dren.mil)

• 동토층 해빙으로 인해 나타날 수 있는 새로운 병원균 분석·대응
• 생물자원을 활용한 동토층 오염물질 분해
• 해빙으로 인한 동토층 변화 추적

- 미국 남극프로그램(NSF AIL Division) 지원을 위한 토목공학 연구
• 연구책임자: Rosa T. Affleck (Rosa.T.Affleck@usace.army.mil)
• 2019년 맥머도 얼음부두(ice pier) 파손으로 인한 신규부두 건설 방안연구
• 맥머도 기지 인근 Phoenix Runway 건설(2017년 1월부터 운용)
• 맥머도-아문젠스콧 기지 간 연료 및 화물을 위한 육상 운송루트 확보(1,050 마일) 및 폴리에틸렌 플라스틱 압출 시트이용 연료통 경량화, LC-130을 이용한 항공운송 대비 효율성 36배 증진
• GPR과 원격탐사를 활용한 크레바스 분석
• 다트머스대 연구팀과 협력하여 극한지 운영 가능한 Yeti, Cool Robots 개발
• 맥머도 기지 증축을 위한 지반·배수 분석, 기지내 에너지 효율성 제고를 위한 열센서 시스템 개발

○ 연구시설(하노버 CRREL과, 알라스카주 페어뱅크스 소재)
- CRREL(하노버) 소재 연구시설 및 영구동토층 지하터널 연구시설, 영구동토층 실험기지

4. 중점 연구시설 방문

○ 콜드룸: 연구기자재를 구비한 콜드룸 26실 보유, -30~43°C의 온도 유지 가능 (그림 9)
○ 재료 실험실 : 각종 매질에 대한 실제 환경 모사 실험 (그림 10)
○ 결빙효과 연구시설(Frost Effects Research Facility): 중장비 및 항공기 활주로 실험을 위한 대형 저온시설 (그림 11)
○ 콜드피트(Cold Pit): 쇄빙선박 등의 연구에 사용하는 3m 깊이의 수조시설 (그림 12)
○ 얼음엔지니어링 시설 및 기타 저온소재 연구시설 등

5. 주요 협의 내용

○ 각 기관의 주요 연구 내용 소개(극지기술개발지원부 소개 및 얼음화학 연구 소개)
○ 공학분야 협력 방안 논의 (그림 13)
- 내륙기지 건설, 에너지 효율에 관한 연구 협력
- 남극 Traverse 관련 기술 노하우 공유 협의
- 북극 해빙 관련 연구협력 방안 협의 - 아라온 공동 활용 등
- 심부 빙하 시추, 건설장비의 유지보수 관련 노하우 공유
• 온·오프라인 교신을 통한 구체적인 연구 협력방안 논의
☞ CRREL·다트머스대 연구진 중 연구소 유관분야 연구자를 “제26차 국제 극지과학 심포지엄(2020년 5월 예정)”에 초대하여 구체적인 연구협력 방안을 검토 할 것을 제안
• 양 기관 간 협력연구 구체화 이후 협력약정 등 체결 고려

표 1. 공학연구개발센터 산하 주요 연구소(총 7개)

실험실명	위치
Cold Regions Research and Engineering Laboratory	Hanover, New Hampshire
Geospatial Research Laboratory (co-located with the Army Geospatial Center)	Alexandria, Virginia
Construction Engineering Research Laboratory	Champaign, Illinois
Coastal and Hydraulics Laboratory	Vicksburg, Mississippi
Environmental Laboratory	
Geotechnical and Structures Laboratory	
Information Technology Laboratory	

KOPRI
극지연구소

그림 1. 저온과학연구소 기술실 내부전경 1

그림 2. 저온과학연구소 기술실 내부전경 2

그림 3. -50℃ 챔버 내부, 깊이별 빙하 시료 및 샘플 전시

그림 4. 저온과학연구소에서 개발한 ROV를 이용한 남극 빙붕연구 소개 포스터

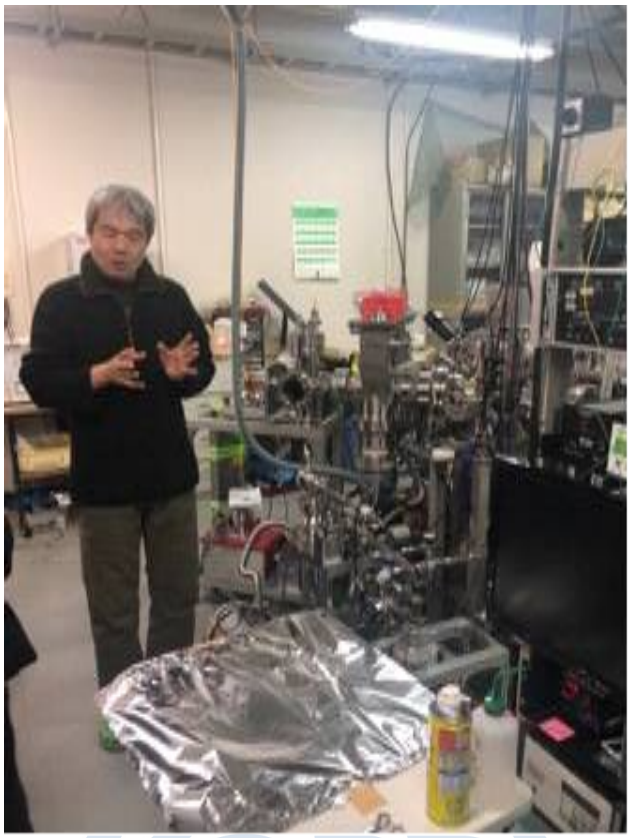

그림 5. 초고진공 실험 장치, 10^{-8} ~ 10^{-6} Pa 정도의 초고진공으로 유지되고 중심으로 냉동기에 의해 10K 정도까지 냉각 가능한 보드가 설치

그림 6. 상전이 역학 연구실 연구 성과 소개(Gen Sazaki 교수)

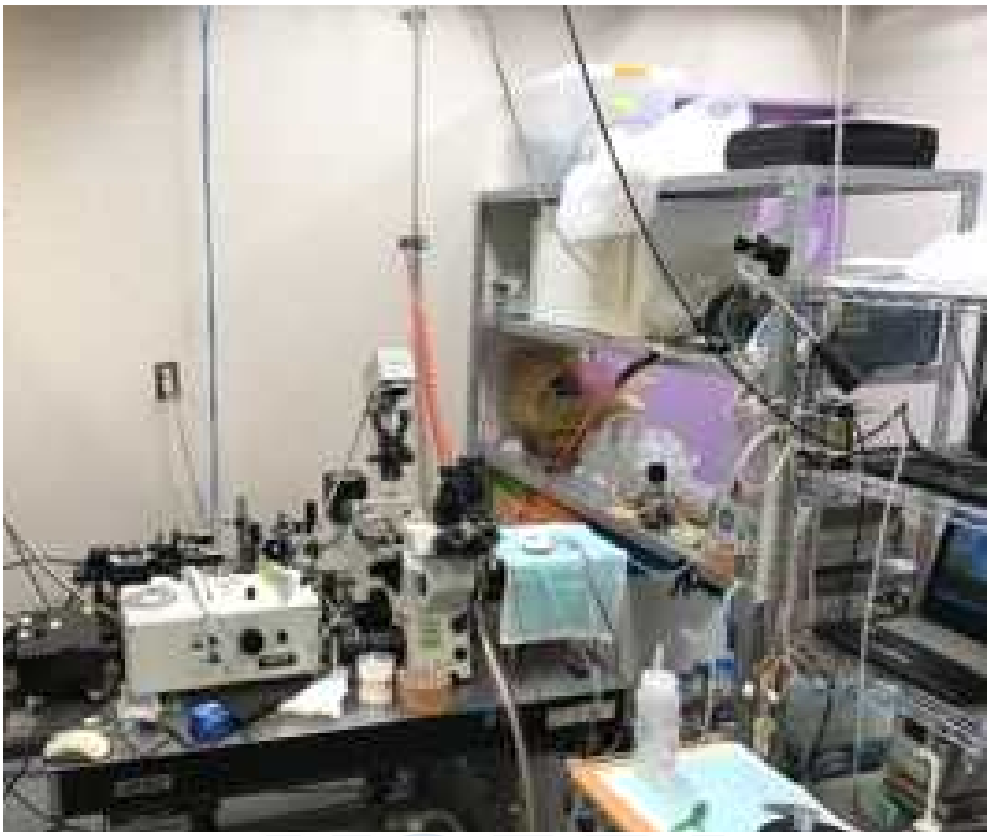

그림 7. Gen Sazaki교수가 개발한 고해상도 광학현미경

그림 8. Cryo-Secondary Ion Mass Spectrometer(SIMS)

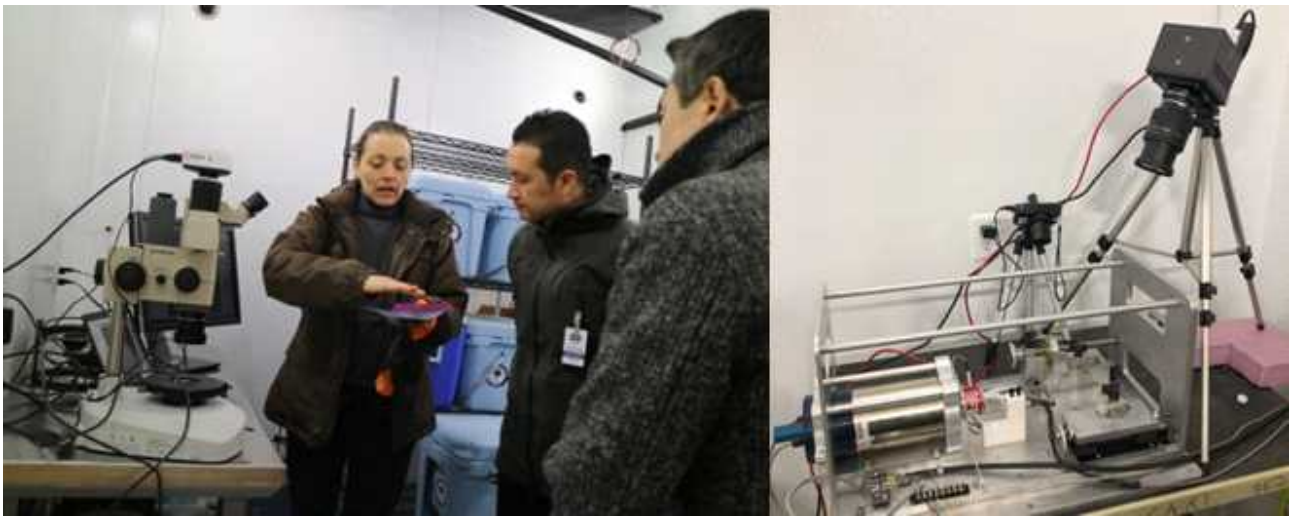

그림 9. 콜드룸 시설. (좌) Ice adhesion 연구, (우) 영상촬영장치

그림 10. 재료 실험실. (좌) 압축강도 실험 장치, (우) 매질의 저항 강도 측정

그림 11. 결빙효과 연구시설. (좌) 대형 저온 시설, (우) 결빙효과 연구시설

그림 12. 얼음엔지니어링 시설 및 기타 저온소재 연구시설. (좌) 얼음 지구물리 연구 시설, (우) 콜드피트(수조)

그림 13. CRREL 본관 방문 및 연구 협의

주 의

1. 이 보고서는 극지연구소에서 수행한 기본연구사업의 연구결과보고서입니다.

2. 이 보고서 내용을 발표할 때에는 반드시 극지연구소에서 수행한 기본연구사업의 연구결과임을 밝혀야 합니다.

3. 국가과학기술 기밀유지에 필요한 내용은 대외적으로 발표 또는 공개하여서는 안 됩니다.

KOPRI
극지연구소